Edited by
Wolfgang Brütting and
Chihaya Adachi

Physics of Organic Semiconductors

Related Titles

Kampen, T. U.

Low Molecular Weight Organic Semiconductors

2005
ISBN: 978-3-527-40653-1

Stallinga, P.

Electrical Characterization of Organic Electronic Materials and Devices

2009
ISBN: 978-0-470-75009-4

Wöll, C. (ed.)

Physical and Chemical Aspects of Organic Electronics

From Fundamentals to Functioning Devices

2009
ISBN: 978-3-527-40810-8

Pagliaro, M., Palmisano, G., Ciriminna, R.

Flexible Solar Cells

2008
ISBN: 978-3-527-32375-3

Schwoerer, M., Wolf, H. C.

Organic Molecular Solids

2007
ISBN: 978-3-527-40540-4

Klauk, H. (ed.)

Organic Electronics

Materials, Manufacturing and Applications

2006
ISBN: 978-3-527-31264-1

Edited by Wolfgang Brütting and Chihaya Adachi

Physics of Organic Semiconductors

2nd completely new revised edition

WILEY-VCH Verlag GmbH & Co. KGaA

The Editors

Prof. Dr. Wolfgang Brütting
University of Augsburg
Institute of Physics
Universitätsstr. 1
86159 Augsburg
Germany

Prof. Dr. Chihaya Adachi
Kyushu University
Center for Future Chemistry
744 Motooka, Nishi
Fukuoka 819-0395
Japan

Cover Picture
Courtesy by H. Nakanotani and C. Adachi (see Chapter 18).

Library of Congress Card No.: applied for

British Library Cataloguing-in-Publication Data
A catalogue record for this book is available from the British Library.

Bibliographic information published by the Deutsche Nationalbibliothek
The Deutsche Nationalbibliothek lists this publication in the Deutsche Nationalbibliografie; detailed bibliographic data are available on the Internet at http://dnb.d-nb.de.

Print ISBN: 978-3-527-41053-8
ePDF ISBN: 978-3-527-65497-0
ePub ISBN: 978-3-527-65496-3
mobi ISBN: 978-3-527-65495-6
oBook ISBN: 978-3-527-65494-9

Cover Design Adam-Design, Weinheim

Typesetting Thomson Digital, Noida, India

Printing and Binding Markono Print Media Pte Ltd, Singapore

Printed on acid-free paper

Foreword

Organic semiconductors now provide an important technology base, supported by a rapidly growing body of science. The field is not new; interest in the semiconducting properties of pi-conjugated molecules was already well established in the 1960s and the foundations of their semiconductor science were built then using molecular materials such as anthracene as model systems. As with inorganic semiconductors, the prospect of engineering toward applications has provided several major boosts to the field. The initial drive in the late 1970s was to use organic photoconductors in place of selenium as the photoactive drum in electrophotography applications. Molecular semiconductor "guests' in polymer "hosts" were successfully engineered and are now the ubiquitous technology for this application. They also provided the working systems for the understanding of electronic transport in disordered semiconductors.

The explosion of interest, dating from the late 1980s, was triggered by the observation of relatively efficient electroluminescence in thin-film diode structures, in both molecular semiconductors and solution-processed polymeric semiconductors. Though electroluminescence had been observed in single-crystal semiconductors in the 1960s, it was the prospect of practical materials processing to deliver useful devices such as pixelated displays that drew industrial and commercial attention, and this has supported a vibrant global research community. Besides light-emitting diodes, now in products such as smart phone displays, other devices have been brought to realistic levels of performance: field-effect transistors today match the performance of thin-film silicon, and solar cells offer realistic energy conversion efficiency, at 10%.

The level of device performance has been achieved on the back of a wide range of scientific and engineering breakthroughs. Perceived obstacles to performance (such as limits to solid-state luminescence efficiency or to field-effect carrier mobility) have been pushed aside and a remarkable landscape of new science and new phenomena is now revealed. This is captured by the excellent series of chapters in this book that cover both the richness of the physics-based science and the global reach of the field, with authors from leading research groups across North America, Europe. and Asia.

Cavendish Laboratory
University of Cambridge, UK

Richard Friend

Preface

With the invention of the transistor around the middle of the last century, inorganic semiconductors like Si or GaAs began to take over the role as dominant materials in electronics from the prevailing metals. At the same time, the replacement of vacuum tube-based electronics by solid-state devices initiated a development that by the end of the twentieth century led to the omnipresence of semiconductor microelectronics in our everyday life. Since the beginning of the twenty-first century, we are facing a new electronics revolution that has become possible due to the development and understanding of a new class of materials, commonly known as *organic semiconductors*. The enormous progress in this field has been driven by the expectation to realize new applications, such as large area, flexible light sources and displays, low-cost printed integrated circuits, or plastic solar cells from these materials.

Strictly speaking, organic semiconductors are not new. The first studies of the dark and photoconductivity of anthracene crystals (a prototype organic semiconductor) date back to the early twentieth century. Later on, triggered by the discovery of electroluminescence in the 1960s, molecular crystals were intensely investigated by many researchers. These investigations could establish the basic processes involved in optical excitation and charge carrier transport. Nevertheless, in spite of the principal demonstration of an organic electroluminescent diode incorporating even an encapsulation similar to the ones used in nowadays commercial display applications, there were several drawbacks preventing practical use of these early devices. Since the 1970s, the successful synthesis and controlled doping of conjugated polymers established the second important class of organic semiconductors. Together with organic photoconductors (molecularly doped polymers), these conducting polymers have initiated the first applications of organic materials as conductive coatings or photoreceptors in electrophotography. The interest in the semiconducting properties of molecular materials revived in the 1980s due to the demonstration of an efficient photovoltaic cell incorporating an organic heterojunction of "p- and n-type" semiconductors as well as the first successful fabrication of thin-film transistors from conjugated polymers and oligomers. The main impetus, however, came from the demonstration of high-performance electroluminescent diodes from vacuum-evaporated molecular films and from conjugated polymers. Owing to the large efforts of both academic and industrial research laboratories

during the past two decades, organic semiconductor devices have progressed rapidly and meanwhile led to first commercial products incorporating displays and light sources made of organic light-emitting diodes (OLEDs), logic circuits utilizing organic field-effect transistors (OFETs) or solar energy harvesting modules on the basis of organic photovoltaic cells (OPVs).

This book focuses on the fundamental physics behind this rapidly developing field of organic electronics. It ties in with the previous edition of "Physics of Organic Semiconductors" published in 2005. Due to the big success of the first edition and the rapidly developing and still growing field, a new edition with completely restructured contents and new contributing authors was put together in order to include novel exciting developments over the past 6 years. In spite of the appearance of first commercial products, there is still a large interest in fundamental issues in the field of organic semiconductors. This book, therefore, tries to bridge the gap between textbook knowledge largely based on crystalline molecular solids on the one side (see, for example, Pope & Swenberg, *Electronic Processes in Organic Crystals and Polymers*, or Schwoerer & Wolf, *Organic Molecular Solids*) and other books focusing more on device applications.

The editors want to thank all contributing authors for writing high-quality up-to-date chapters of their work, including the state of the art in the respective field. Without their efforts this book would not have been possible. Furthermore, we want to thank Russell J. Holmes (University of Minnesota) who acted as consultant editor in the early stages of this book project. We are also indebted to our academic teachers, Prof. Em. Markus Schwoerer (Bayreuth University) and Prof. Em. Tetsuo Tsutsui (Kyushu University), who brought us in touch with this fascinating subject more than 20 years ago.

Wolfgang Brütting and
Chihaya Adachi

Contents

List of Contributors

Chihaya Adachi
Kyushu University
Center for Future Chemistry
744 Motooka
Nishi
Fukuoka 819-0395
Japan

Marc A. Baldo
Massachusetts Institute
of Technology
Department of Electrical
Engineering and Computer Science
Cambridge
MA 02139
USA

Andreas Baumann
Bavarian Center for Applied Energy
Research (ZAE Bayern)
Am Hubland
D - 97074 Würzburg
Germany

David Beljonne
Université de Mons-Hainaut
Service de Chimie des Matériaux
Nouveaux
Place du Parc 20
7000 Mons
Belgium

Peter A. Bobbert
Eindhoven University of Technology
Department of Applied Physics
P.O. Box 513
Eindhoven
5600 MB
The Netherlands

Wolfgang Brütting
University of Augsburg
Institute of Physics
Universitätsstr. 1
86159 Augsburg
Germany

Jui-Fen Chang
Department of Optics and Photonics
National Central University
Chung-Li, 320, R.O.C.
Taiwan

Reinder Coehoorn
Philips Research Laboratories
High Tech Campus 4
Eindhoven
5656 AE
The Netherlands

and

Eindhoven University of Technology
Department of Applied Physics
P.O. Box 513
Eindhoven
5600 MB
The Netherlands

Rafał Czerwieniec
Universität Regensburg
Institut für Physikalische und
Theoretische Chemie
Universitätsstr. 31
93053 Regensburg
Germany

Carsten Deibel
Experimental Physics VI
Julius-Maximilian-University of
Würzburg
Am Hubland
D - 97074 Würzburg
Germany

Vladimir Dyakonov
Experimental Physics VI
Julius-Maximilian-University of
Würzburg
Am Hubland
D - 97074 Würzburg
Germany

and

Bavarian Center for Applied Energy
Research e.V. (ZAE Bayern)
Am Hubland
D - 97074 Würzburg
Germany

Jörg Frischeisen
University of Augsburg
Institute of Physics
Universitätsstr. 1
86159 Augsburg
Germany

Neil Greenham
University of Cambridge
Cavendish Laboratory
J.J. Thomson Avenue
Cambridge CB3 0HE
UK

Hisao Ishii
Chiba University
Center for Frontier Science
1-33 Yayoi-cho
Inage Chiba 263-8522
Japan

Paul-Ludovic Karsenti
Université de Montréal
Département de physique &
Regroupement québécois sur les
matériaux de pointe
C.P. 6128
Succursale Center-ville
Montréal
QC H3C 3J7
Canada

Jang-Joo Kim
Department of Materials Science and
Engineering
Seoul National University
San 56-1
Shillim-dong
Gwanak-gu
Seoul 151-744
Korea

Norbert Koch
Humboldt-Universität zu Berlin
Institut für Physik
Newtonstr. 15
12489 Berlin
Germany

Gianluca Latini
Istituto Italiano di Tecnologia
Centre for Biomolecular
Nanotechnologies @UNILE
Via Barsanti
73010, Arnesano (LE)
Italy

Jae-Hyun Lee
School of Global Convergence Studies
Hanbat National University
San 16-1
Duckmyoung-dong
Daejeon 305-719
Korea

Karl Leo
Technische Universität Dresden
Institut für Angewandte Photophysik
George-Bähr-Str. 1
01069 Dresden
Germany

Björn Lüssem
Technische Universität Dresden
Institut für Angewandte Photophysik
George-Bähr-Str. 1
01069 Dresden
Germany

Yukimasa Miyazaki
Chiba University
Graduate School of Advanced Integration Science
1-33 Yayoi-cho
Inage Chiba 263-8522
Japan

Hajime Nakanotani
Kyushu University
Center for Future Chemistry
744 Motooka
Nishi
Fukuoka 819-0395
Japan

Yasuo Nakayama
Chiba University
Center for Frontier Science
1-33 Yayoi-cho
Inage Chiba 263-8522
Japan

Yutaka Noguchi
Chiba University
Center for Frontier Science
1-33 Yayoi-cho
Inage Chiba 263-8522
Japan

Andreas Opitz
University of Augsburg
Institute of Physics
Universitätsstr. 1
86159 Augsburg
Germany

and

Humboldt-Universität zu Berlin
Institut für Physik
Newtonstr. 15
12489 Berlin
Germany

Francis Paquin
Université de Montréal
Département de physique &
Regroupement québécois sur les matériaux de pointe
C.P. 6128
Succursale Center-ville
Montréal
QC H3C 3J7
Canada

Andreas F. Rausch
Universität Regensburg
Institut für Physikalische und Theoretische Chemie
Universitätsstr. 31
93053 Regensburg
Germany

Sebastian Reineke
Massachusetts Institute of Technology
Department of Electrical Engineering and Computer Science
Cambridge
MA 02139
USA

Moritz Riede
Technische Universität Dresden
Institut für Angewandte Photophysik
George-Bähr-Str. 1
01069 Dresden
Germany

Tomo Sakanoue
Organic Electronics Research Center
Yamagata University, 4-3-16 Jonan
Yonezawa, Yamagata
992-8510
Japan

Maciej Sakowicz
Université de Montréal
Département de physique &
Regroupement québécois sur les matériaux de pointe
C.P. 6128
Succursale Center-ville
Montréal
QC H3C 3J7
Canada

Naoki Sato
Chiba University
Graduate School of Advanced Integration Science
1-33 Yayoi-cho
Inage Chiba 263-8522
Japan

Frank Schreiber
Universität Tübingen
Institut für Angewandte Physik
Auf der Morgenstelle 10
72076 Tübingen
Germany

Carlos Silva
Université de Montréal
Département de physique &
Regroupement québécois sur les matériaux de pointe
C.P. 6128
Succursale Center-ville
Montréal
QC H3C 3J7
Canada

Henning Sirringhaus
Cavendish Laboratory
University of Cambridge
Cambridge CB3 OHE
UK

Natalie Stingelin
Imperial College London
Department of Materials and Centre for Plastic Electronics
South Kensington Campus
London SW7 2AZ
UK

Yuya Tanaka
Chiba University
Graduate School of Advanced Integration Science
1-33 Yayoi-cho
Inage Chiba 263-8522
Japan

Chih-Hung Tsai
National Taiwan University
Graduate Institute of Photonics and Optoelectronics
No. 1, Sec. 4, Roosevelt Rd.
Taipei 10617, Taiwan
Republic of China

Nobuo Ueno
Chiba University
Graduate School of Advanced Integration Science
Inage-ku
Chiba 263-8522
Japan

Linjun Wang
Université de Mons-Hainaut
Service de Chimie des Matériaux Nouveaux
Place du Parc 20
7000 Mons
Belgium

Markus Wohlgenannt
University of Iowa
Department of Physics and Astronomy
Optical Science and Technology Center
205 North Madison Street
126 IATL
Iowa City
IA 52242
USA

Chung-Chih Wu
National Taiwan University
Department of Electrical Engineering
No. 1, Sec. 4, Roosevelt Rd.
Taipei 10617, Taiwan
Republic of China

Hartmut Yersin
Universität Regensburg
Institut für Physikalische und Theoretische Chemie
Universitätsstr. 31
93053 Regensburg
Germany

Part One
Film Growth, Electronic Structure, and Interfaces

Physics of Organic Semiconductors, Second Edition. Edited by Wolfgang Brütting and Chihaya Adachi

1
Organic Molecular Beam Deposition

Frank Schreiber

1.1
Introduction

Organic semiconductors exhibit a range of interesting properties, and their application potential is rather broad, as seen in many other chapters in this book. For the crystalline "small-molecule" systems, grown by organic molecular beam deposition (OMBD), the subject of this chapter, it is generally agreed that the structural definition is important for the functional properties. The following list should serve to illustrate the various aspects:

1) The definition of interfaces (degree of interdiffusion and roughness)
   a) Organic–organic (e.g., in organic diodes)
   b) Organic–metal (e.g., for electrical contacts)
   c) Organic–insulator (e.g., in transistors, insulating layer between gate and semiconductor)
2) The crystal structure
   a) Which structure is present? (Note that polymorphism is very common in organics).
   b) Are different structures coexisting?
   c) Orientation of the structure (epitaxy)?
   d) Is the structure strained (epitaxy)?
3) Crystalline quality/defect structure
   a) Mosaicity (note that in a thin film one has to distinguish between quality in the xy-plane and in z-direction (surface normal)).
   b) Homogeneity within a given film (density of domain boundaries etc.)
   c) Density of defects (and their nature), which also impacts the electronic properties.
4) Issues related to multicomponent systems
   a) Phase segregation versus intermixing; size of "domains."
   b) Possible new structural phases of the mixed system; superstructures?
   c) Tuning of properties by graded concentration profiles?

Physics of Organic Semiconductors, Second Edition. Edited by Wolfgang Brütting and Chihaya Adachi

Since the structure has a strong impact on the functional properties, understanding the structure formation, that is, the growth process, and finding ways to optimize the structural definition is a prerequisite for technological progress. Moreover, understanding the physics of the growth process raises several fundamental challenges.

We will mostly focus on "thicker" films, their growth modes, and the evolution of the morphology for thickness ranges that are typically employed in organic semiconductor applications. We will discuss only to a limited extent the work on the first monolayer, although as the "seed layer" for the following layers this is obviously important. Thus, some of the classical surface science issues, such as binding distances and associated interface dipoles, although very important [1, 2], epitaxial relation, and so on, are not the focus of this chapter. For these issues and also for information on the history of the field, we refer to Refs [3–15]. Also, we will not discuss issues related to chirality, although they are undoubtedly intriguing [11, 16–18].

In terms of growth technology, the equipment is essentially the same as for inorganic molecular beam epitaxy. Evaporation cells on a vacuum chamber are used to provide a flux of molecules at the substrate surface (typically some range around 1 Å/s to 1 Å/min), and ideally the growth can be monitored *in situ*. Virtually, all surface and interface techniques have been used for OMBD-grown films, and we refer to standard textbooks for details of the experimental methodology.

This chapter is organized as follows. We first present some of the general issues in thin film growth and then what is specific and potentially different for organics (Section 1.2). In Section 1.3, we give an overview of the most popular systems. Section 1.4 contains a number of case studies, trying to highlight the issues that we feel are particularly relevant and typical for OMBD. The case studies are based on a few selected compounds and are not intended as an exhaustive list. They are organized according to the (inorganic) substrates, covering, insulators, metals, and semiconductors. In Section 1.7, we briefly indicate the issues for organics-based heterostructures, inorganic–organic, and organic–organic. Some conclusions are given in Section 1.8.

In a review with limited space such as the present one, it cannot be our goal to give a complete and exhaustive overview. Instead, the examples are centered mostly around our own work, which we try to discuss in the context of the general field. This selection is obviously unbalanced, and we apologize for omissions of other important work.

We note that this chapter is an updated version of the 2005 edition of this book and related to Ref. [13]. Important developments since then are, *inter alia*, the precision determination of binding distances of organic semiconductors on metal contacts along with the associated electronic properties (e.g., Refs [1, 2]), the further development of real-time monitoring of growth (e.g., Ref. [19]) and an increased understanding of organic–organic heterostructures, as reviewed at the end of this chapter.

1.2
Organic Molecular Beam Deposition

1.2.1
General Concepts of Thin Film Growth

Crystal and thin film growth are enormously rich subjects with many different facets and theoretical approaches. For a thorough treatment of the underlying concepts, we refer to Refs [20–23]. Here, we shall only briefly touch upon selected aspects that we feel are important in the present context and help to appreciate the issues related to thin film growth (see also Figure 1.1).

One approach to describe the various relevant interactions uses the concept of surface and interface energies, γ, similar to what is done for wetting phenomena. Typically, the surface energies (i.e., the relative contributions of the free substrate surface, γ_s, the film surface, γ_f, and the film–substrate interface, γ_i) are then related to the different growth modes, that is, Frank van der Merwe (layer by layer), Stranski–Krastanov (layer plus islands after a certain critical thickness), and Vollmer–Weber (islands starting at the first monolayer).

We will not discuss issues related to the epitaxial relation in much detail. (For clarity, we should emphasize that under epitaxial relation we understand the crystallographic relation between film and substrate, which does not necessarily imply smooth film growth). However, we should point out that, generally, the surface energies depend on the strain field induced by the lattice mismatch at the film–substrate interface, and thus also on the number of layers of the film. Therefore,

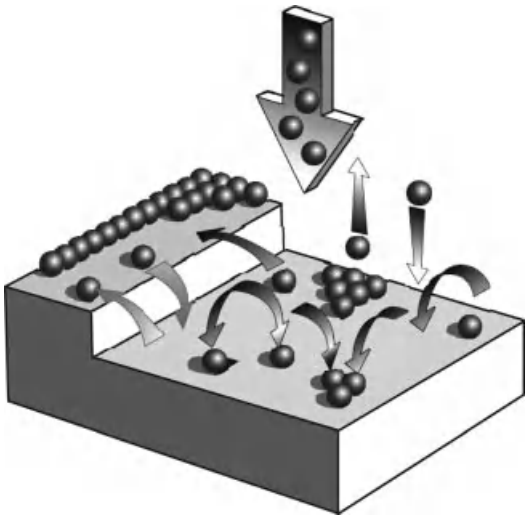

Figure 1.1 Schematic of processes relevant in thin film growth, such as adsorption (as a result of a certain impingement rate), (re-)desorption, intralayer diffusion (on a terrace), interlayer diffusion (across steps), nucleation, and growth of islands.

the epitaxial relation of film and substrate is important not only in a crystallographic sense but also for the growth behavior.

It should be emphasized that growth is actually a nonequilibrium phenomenon, and equilibrium or near-equilibrium energy considerations alone cannot properly account for all growth scenarios. Thus, a dynamic description is needed. This description has to take into account the flux of adsorbates toward the surface (corresponding to a certain supersaturation), the adsorption and redesorption probabilities, and the diffusion processes on the surface (interlayer and intralayer) and their respective barriers. In the past two decades, a theoretical framework has been established, which relates growth mechanisms to a set of scaling exponents describing the dependence of the surface roughness on film thickness and lateral length scale. Much effort has been spent to theoretically predict scaling exponents for certain growth models, as well as to determine them experimentally [20–25].

The scaling theory of growth-induced surface roughness is based on the behavior of the height difference correlation function (HDCF), the mean square height difference $g(R) = \langle [h(x,y) - h(x',y')]^2 \rangle$ of pairs of points laterally separated by $R = \sqrt{(x-x')^2 + (y-y')^2}$. The HDCF displays distinct behaviors for $R \ll \xi$ and $R \gg \xi$, where ξ denotes the correlation length. For $R \ll \xi$ one expects a power law increase as $g(R) \approx a^2 R^{2\alpha}$, where α is the static roughness exponent and the prefactor a is a measure of the typical surface slope. For $R \gg \xi$ the heights at distance R become uncorrelated. Hence, $g(R)$ saturates at the value $g(R \gg \xi) = 2\sigma^2$, where $\sigma = \langle (h - \langle h \rangle)^2 \rangle^{1/2}$ is the standard deviation of the film height (or "rms roughness"). The three parameters σ, ξ, and a evolve with film thickness according to the power laws $\sigma \sim D^{\beta}$, $\xi \sim D^{1/z}$, and $a \sim D^{\lambda}$, defining the growth exponent β, the dynamic exponent z, and the steepening exponent λ. Assuming that the regimes $R \ll \xi$ and $R \gg \xi$ are connected through a scaling form $g(R) = 2\sigma^2 \tilde{g}(R/\xi)$, it follows that the scaling exponents are related by $\beta = \alpha/z + \lambda$. For $\lambda = 0$ (no steepening) one has $\beta = \alpha/z$. Scaling with $\lambda > 0$ is referred to as *anomalous* [22]. The HDCF can be determined experimentally by real space methods (such as atomic force microscopy) or diffuse scattering, each having their advantages [25].

1.2.2
Issues Specific to Organic Thin Film Growth

While the general considerations presented above apply to both inorganic and organic thin-film systems, there are a few issues specific to organics (Figure 1.2), which can lead to quantitatively and qualitatively different growth behavior.

1) Organic molecules are "extended objects" and thus have *internal degrees of freedom*. This is probably the most fundamental difference between growth of atomic and growth of organic systems.
   a) The *orientational degrees of freedom* that are not included in conventional growth models can give rise to qualitatively new phenomena, such as the

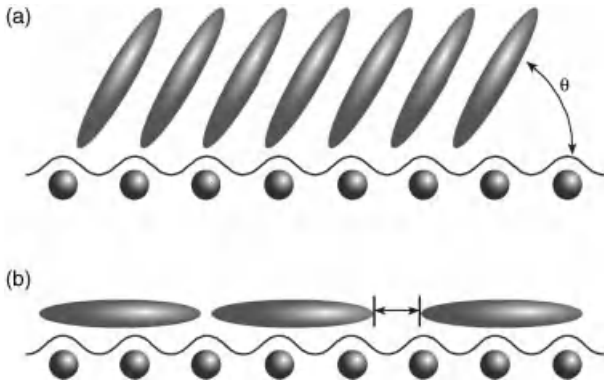

Figure 1.2 Issues specific to organics in the context of thin film growth. (a) Orientational degrees of freedom, potentially leading to orientational domains (additional source of disorder). They can also give rise to orientational transitions during growth. (b) Molecules larger than the unit cells of (inorganic) substrates, thus leading to translational domains. Generally, this can also lead to a smearing-out of the corrugation of the substrate potential experienced by the adsorbate.

change of the molecular orientation during film growth (Figure 1.2). Also, even without considering a *transition* during the growth, the distinction of "lying-down" and "standing-up" films is important and obviously only possible for molecular systems.

b) The *vibrational degrees of freedom* can have an impact on the interaction with the surface as well as the thermalization upon adsorption and the diffusion behavior.

2) The *interaction potential* (molecule–molecule and molecule–substrate) is generally different from the case of atomic adsorbates, and van der Waals interactions are more important.

a) The response to strain is generally different. Potentially, more strain can be accommodated, and in those systems where the build-up of strain leads to a "critical thickness" (before the growth mode changes), this thickness can be greater for "softer" materials.

The different ("softer") interactions with the substrate and the corrugation of the potential have also been discussed in terms of "van der Waals epitaxy" and "quasi-epitaxy."

b) The importance of van der Waals interactions implies that the relevant temperature scales (both for evaporation from a crucible and for diffusion on the substrate) are usually lower. It should be emphasized, however, that the *total* interaction energy of a molecule (integrated over its "contact area" with a surface) can be substantial and comparable to that of strongly interacting (chemisorbing) atomic adsorbates. Nevertheless, in terms of interaction energies *per atom*, the organic molecules considered here are usually weaker.

c) Since we are concerned usually with closed shell molecules and van der Waals-type crystals, there are no dangling bonds at the organic surface, and the surface energies are usually weaker than for inorganic substrates.
d) Importantly, however, if the surface of the *substrate* is "strongly interacting," this results in limited diffusion and thus the evolution of well-ordered films is hampered. In the extreme case of a "very reactive" surface (e.g., with dangling bonds available), the molecules may even dissociate upon adsorption.

3) The *size of the molecules and the associated unit cells* are greater than that of typical (inorganic) substrates.
   a) The effective lateral variation of the potential is smeared out (i.e., averaged over the size of the molecule), making the *effective corrugation* of the substrate as experienced by the molecule generally *weaker* than for atomic adsorbates.
   b) The size difference of the unit cells of adsorbate and substrate implies that there are more translational domains (see Figure 1.2).
   c) Moreover, organics frequently crystallize in low-symmetry structures, which again can lead to multiple domains (not only translational but also orientational domains). Importantly, both are a source of disorder, *in addition* to those known from inorganic systems (e.g., vacancies).

Generally, most of the above points directly or indirectly impact the interactions and thus also the barriers experienced during diffusion. Thus, not only the static structure but also the growth dynamics exhibit differences compared to inorganic systems.

1.2.3 Overview of Popular OMBD Systems

Organic chemistry provides obviously a vast number of dyes and semiconductors, which are potentially interesting for thin film studies, and there is the additional possibility of specifically modifying certain functionalities. A fairly large number of compounds has indeed been employed for thin film work, but not for all of these have detailed growth studies been performed. We will limit ourselves to only selected systems, largely based on examples from our own work (see Figure 1.3).

1.2.3.1 PTCDA

The perylene-derivative PTCDA (3,4,9,10-perylene-tetracarboxylic dianhydride, $C_{24}H_8O_6$, a red dye) has long been regarded as a model system for OMBD [4, 5, 26–33]. Its bulk structure (actually α and β phase) exhibits layered molecular planes, and it was expected that the regular stacking of these planes (along the [102] direction in α phase notation) is favorable for well-behaved film growth, which turned out to be not necessarily correct. The optical properties [34–38] and the vibrational properties [38–41] have been thoroughly studied.

1.2.3.2 DIP

Diindeno(1,2,3,-*cd*,1′,2′,3′-lm)perylene ($C_{32}H_{16}$, DIP, a red dye) has the same perylene core as PTCDA. It has been shown to exhibit interesting out-of-plane

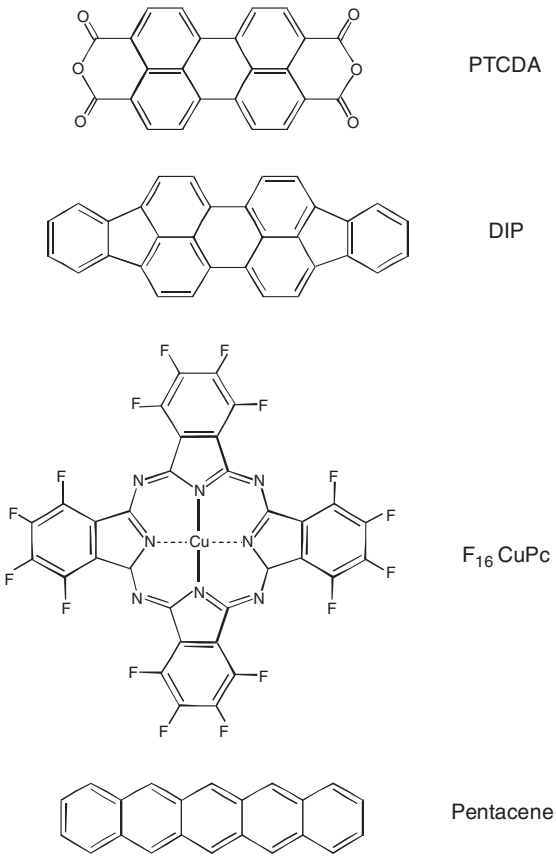

Figure 1.3 Some popular organic semiconductors discussed in this chapter.

ordering behavior [25, 42–44] and, associated with this, good charge carrier transport properties [45, 46]. Recently, its spectroscopic behavior was analyzed in detail [47, 48], and it was also demonstrated to be very promising in OPV devices [49].

1.2.3.3 **Phthalocyanines**

Phthalocyanines (Pc's) are rather popular [50–55], and some of the early work on OMBD has employed Pc's [50]. They exhibit a certain degree of "specific tunability," both due to the possible central metal ion, which can be changed within a broad range, and due to the choice of the side group(s) [51, 52]. F_{16}CuPc is particularly attractive, since it is considered a good candidate as an n-type conducting organic material [56]. As a blue dye [54], it is also interesting for optoelectronic applications [51, 55].

1.2.3.4 Oligoacenes (*Anthracene, Tetracene, and Pentacene*)

The oligoacenes and in particular pentacene have attracted considerable attention, since their charge transport properties were reported to be excellent [9, 45]. An important feature of pentacene seems to be that it can be grown in well-ordered thin films, although the "bulk structure" and a "thin film structure" appear to be competing. A recent development is the synthesis of perfluoropentacene (PFP) [57], which exhibits structural similarities to pentacene (PEN), but electronically of course different [58–61], and allows the preparation of mixed films (see Section 1.7).

There are, of course, many other popular systems. These include, for example, oligothiophenes, oligophenyls, and also "sheets of graphite." Besides the crystalline systems, there are amorphous small-molecule organic semiconductors prepared by OMBD, such as Alq_3 and TPD. In terms of the growth physics, amorphous systems exhibit obviously some differences (no strain due to epitaxy, different diffusion barriers, no crystallographic domains, etc.). They are worth studying in their own right, but we cannot discuss them here. Another interesting case is rubrene, which can form crystals, but for conventional thin-film deposition results in amorphous structures. For examples from various other systems, we refer to Refs [3–15].

1.3 Films on Oxidized Silicon

Silicon wafers are among the most common substrates for thin film growth. They are stable in air with their oxidized surface layer, the thickness of which can be "tuned" by thermal oxidation (from some 15 Å, native oxide, to several 1000 Å). Also, they are very flat and relatively easy to clean.

In the context of organic electronics, of course, they are very popular as substrates for thin-film transistors (TFTs), since the oxide can serve as the insulating layer between the silicon as the bottom contact (gate) and the active organic semiconductor on top.

We should also mention that oxidized silicon surfaces are suitable for surface modification using self-assembled monolayers (SAMs) [62, 63], which has been exploited, for example, for the growth of pentacene [64] and other systems [61].

1.3.1 PTCDA

It was expected that the regular stacking of PTCDA molecules in the [102] direction (in α phase notation) of the bulk structure would give rise to well-behaved film growth. This regular stacking is indeed observed on silicon oxide and many other substrates, unless the growth temperature is too low and no well-defined structure evolves or a too strong interaction with a very "reactive" substrate leads to other orientations of the first PTCDA monolayer. However, it is important to realize that a regular stacking and well-defined orientation of the molecules within the films does not necessarily imply smooth surfaces.

In an early study, it was already found that PTCDA on oxidized silicon exhibits smooth surfaces only for growth at low temperatures ($T < 50\,^{\circ}$C for deposition rates around 1 Å/s), where the crystallinity was not very good [65]. For growth at higher temperatures, the films exhibited good crystallinity, but showed a tendency to island growth ("dewetting").

These results demonstrate a not uncommon feature of growth on substrates with low surface energies. If the films tend to dewet from the substrate near equilibrium, then the above pattern (relatively flat, but low-crystallinity films for low T, and dewetting, that is, rough, morphologies with good crystallinity for high T) is quite frequently found.

1.3.2 DIP

DIP has the same perylene core as PTCDA, but the indeno end groups instead of the anhydride end groups give rise to a completely different structural behavior compared to PTCDA. DIP has been studied in detail both structurally [19, 25, 42–44, 66, 67] and spectroscopically [47, 48, 68–70], and it was found to exhibit excellent out-of-plane order on silicon oxide surfaces.

Films with various film thicknesses (69 Å $\leq D \leq$ 9000 Å) were prepared on oxidized (4000 Å) Si(100) substrates at a substrate temperature of $145 \pm 5^{\circ}$C and at a deposition rate of 12 ± 3 Å/min. The out-of-plane X-ray spectra exhibit well-defined Bragg reflections corresponding to a lattice spacing of $d_{\mathrm{DIP}} \approx 16.55$ Å (suggesting essentially upright-standing molecules) and associated Laue oscillations, the analysis of which shows that the films are coherently ordered across the entire thickness [42]. The rocking width, which is a measure of the distribution of the out-of-plane lattice planes, is 0.01° and lower [42, 44]. The lattice spacing is consistent with a model of molecules standing essentially upright with a tilt angle θ_{tilt} presumably around 15–20°. The large number of higher order Bragg reflections could be used to deconvolute the out-of-plane electron density distribution in a Fourier series (Figure 1.4)

$$\varrho_{el}(z) = \varrho_0 + \sum_n A_n \cos\left(n\frac{2\pi}{d_{\mathrm{DIP}}}z + \phi_n\right) \tag{1.1}$$

where the Fourier amplitude, A_n, is associated with the intensity of the nth Bragg reflection [42]. We can speculate that the shape of DIP with its slightly narrow head and tail may be favorable for an ordering mechanism with some degree of interdigitation of molecules from neighboring (i.e., top and bottom) lattice planes.

On silicon oxide, the in-plane structure is, of course, a 2D powder. The packing appears to follow a herringbone motif. The structure will be discussed also in the context of growth on Au (Ref. [43] and Section 1.5).

The growth including the evolution of the HDCF and the associated growth exponents, α, β, and $1/z$, were studied using AFM and X-ray scattering (specular and diffuse) [25]. Whereas the static roughness exponent α (average of AFM and X-rays 0.684 ± 0.06) is similar to that observed in many other growth experiments [21],

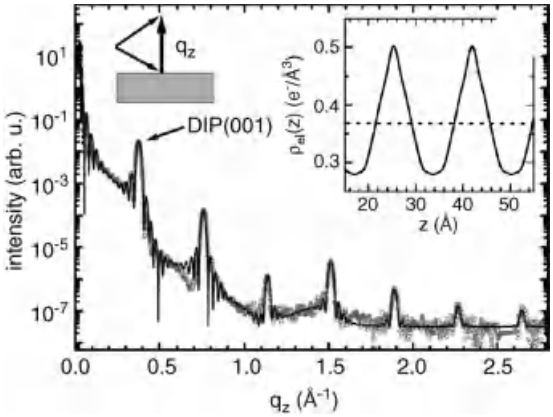

Figure 1.4 Specular X-ray scan of a 206 Å thick DIP film. Many higher order Bragg reflections are observed, which can be used for the reconstruction of the electron density profile using the various Fourier components (close-up shown in the inset). Adapted from Ref. [42].

the values for $1/z$ (0.92 ± 0.20) and β (0.748 ± 0.05) were found to be rather large (Figure 1.5). Specifically, the DIP films belong to the class of systems that display the phenomenon of *rapid roughening*, for which $\beta > 1/2$, that is, the roughness increases faster with thickness D than the random deposition limit $\beta_{RD} = 0.5$ [22]. This effect appears hard to rationalize in the absence of a thermodynamic driving force (e.g., dewetting). A model that is consistent with the scaling exponents involves random spatial inhomogeneities in the local growth rate, which are fixed during the growth process [25, 71]. It is plausible that when certain regions of the

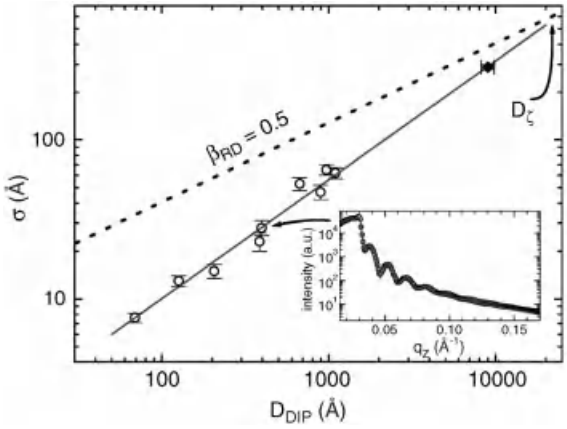

Figure 1.5 Root mean square roughness σ of DIP films as a function of thickness D_{DIP}. The inset shows a typical X-ray reflectivity data set and a fit to the data. The solid line in the main plot is a linear fit to the data and the growth exponent is obtained as $\beta = 0.748 \pm 0.05$. The dotted line denotes the random deposition limit $\beta_{RD} = 0.5$. Adapted from Ref. [25].

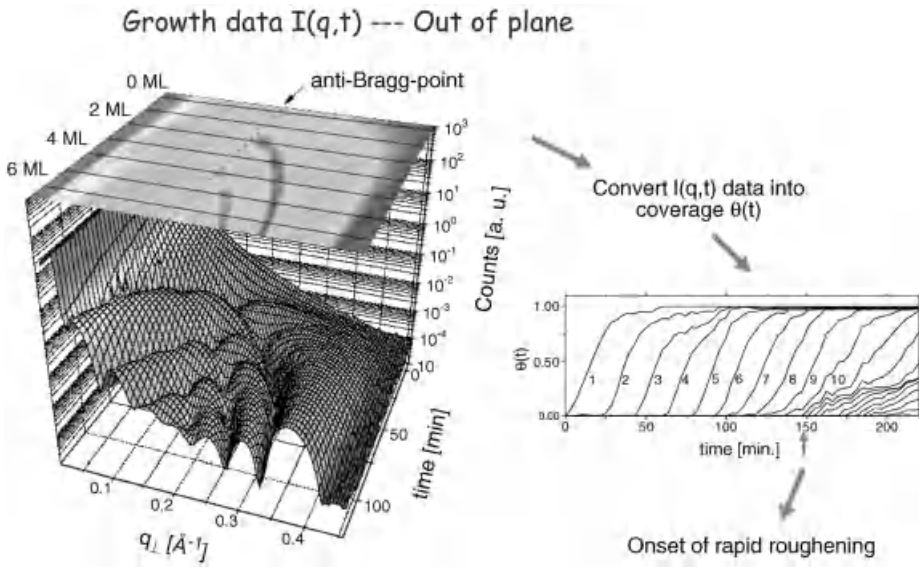

Figure 1.6 (a) The DIP molecule and a schematic of standing (σ) and lying (λ) structures. (b) Evolution of the real-time X-ray reflectivity as a function of time (i.e., film thickness) during growth on silicon oxide (at 130 °C). (c) Layer coverages $\Theta(t)$ as obtained from fits to the above real-time data. A change from layer-by-layer growth to rapid roughening is clearly discernible after about 10 ML (see arrow). Adapted from Ref. [19].

surface persistently grow faster than others, the surface will roughen very rapidly. It was suggested that the spatial inhomogeneities might be related to the different tilt domains of the film and the inevitable grain boundaries in between these [25].

Recently, these issues were followed by X-rays and optical spectroscopy in real-time *in situ* during growth [19, 72, 69] (Figure 1.6), and also steps made visible optically using near-field microscopy with a resolution as good as 17 nm [70].

1.3.3 Phthalocyanines

Phthalocyanines also tend to grow in a standing-up configuration in thicker films on "inert" substrates. Films of F_{16}CuPc between 120 and 450 Å were recently found to exhibit very good crystalline out-of-plane order with rocking widths around 0.01° and well-defined Kiessig interferences and Laue satellites around the out-of-plane Bragg reflection [73].

The in-plane structure is, of course, azimuthally disordered, since the substrate is isotropic. One of the complications for phthalocyanines is a strong anisotropy of the crystal structure and the associated growth properties, which can lead to needle-like features, both for F_{16}CuPc [74] and for H_{16}CuPc [75]. The structure and the optical properties were recently studied in real time [74, 75] revealing changes

during growth. Anomalous scaling behavior and surface roughening for H_2Pc deposition were studied in Ref. [76].

1.3.4 Pentacene

Pentacene on silicon oxide has been studied intensely due to its relevance for OFETs, and it is impossible to provide a complete list of references here [9]. Ruiz *et al*. studied the initial stages of the growth [77]. Their analysis of the island distribution in (sub)monolayer films by dynamic scaling showed that the smallest stable island consisted of four molecules. Meyer zu Heringdorf *et al*. showed that under appropriate growth conditions the single-crystal grain sizes can approach 0.1 mm [78].

For thicker films, pentacene thin films exhibit some complication in the sense that there is a "thin film structure" and a "bulk structure," which can coexist, depending on the growth conditions. Also, the defect structure is of interest [79]. Some light was shed on these issues in real-time growth studies [80, 81].

An interesting idea is that of surface modification involving self-assembled monolayers [63]. Shtein *et al*. studied the effects of film morphology and gate dielectric surface preparation on the electrical characteristics of organic vapor-phase-deposited pentacene thin-film transistors including surface modification using SAMs [64]. Meyer zu Heringdorf *et al*. employed cyclohexene saturation of Si(001) to modify the growth dynamics [78]. Voigt *et al*. studied the growth of tetracene on oil-covered surfaces [82]. While they actually used ITO as solid substrates, the concept might equally well be applicable to silicon oxide surfaces.

1.4 Films on Aluminum Oxide

Interfaces of organics with insulators are of obvious relevance for organic electronics, and aluminum oxide is one of the most commonly used insulators. Unfortunately, sputtered aluminum oxide layers frequently exhibit a rather high roughness and not well-defined starting conditions for growth studies. Sapphire is aluminum oxide (Al_2O_3) in its purest and best ordered form. It is also a popular substrate for epitaxy of metals and inorganic semiconductors, and it can be obtained in very high crystalline quality. We will focus here on sapphire, since it is very suitable for model studies of the growth of organics on insulator surfaces (see Section 1.6 for other substrates).

Surfaces of ionic substrates, which are not charge balanced, tend to be unstable and/or exhibit strong relaxations/reconstructions. In the case of sapphire, the $(11\bar{2}0)$ surface ("A plane") is charge balanced and rather inert, and it has been used for growth studies. An important feature to realize for surfaces of crystals is that they commonly exhibit a miscut, that is, a difference between the physical surface

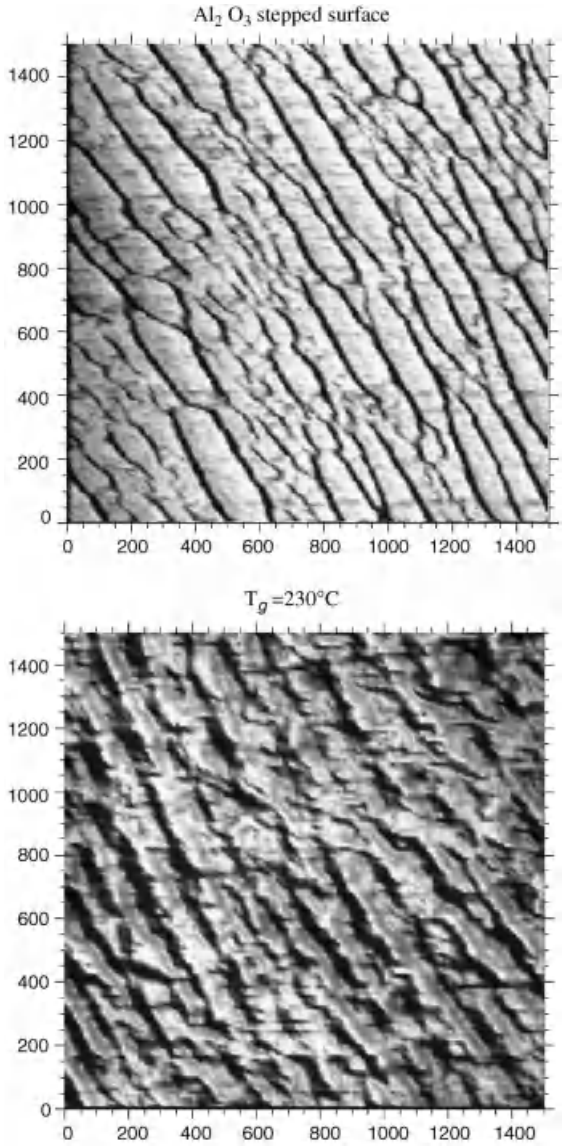

Figure 1.7 Topography of an A-plane sapphire substrate (*top*) and an $F_{16}CuPc$ film (120 Å) (*bottom*) on this substrate determined by noncontact AFM. The step pattern of the substrate serves to azimuthally align the film (see text). Adapted from Ref. [84].

and the (low-index) crystallographic plane. This gives rise to a step pattern, which in the case of essentially perfect crystals like sapphire is the dominating feature of the surface morphology (Figure 1.7). Issues related to the surface preparation have been discussed in Ref. [83].

1.4.1 PTCDA

PTCDA on sapphire has, to our knowledge, not been studied in detail. Test results, however, indicate that the overall behavior is similar to that for PTCDA on oxidized silicon, that is, for growth at high temperatures the films tend to (partially) dewet (Krause et al., unpublished).

The overall growth scenario is most likely not changed significantly by the presence of steps, but the in-plane order of PTCDA may be affected. However, even with alignment at the step edges, PTCDA would most likely still exhibit multiple domains (see also the discussion of PTCDA on metals).

1.4.2 DIP

Based on the results for DIP on silicon oxide it is expected that DIP would also exhibit good out-of-plane ordering on the similarly "inert" sapphire. Preliminary data indicate that this is, in fact, the case (Osso et al., unpublished). In addition, the stepped sapphire substrate can induce in-plane ordering, as first demonstrated for the growth of phthalocyanines [84] (see below), which was also found for DIP (Osso et al., unpublished).

1.4.3 Phthalocyanines

As described above, the regular surface steps associated with miscut sapphire can serve as templates for film growth with azimuthal alignment. While the concept of stepped substrates has been used frequently for monolayer adsorbates, its use for comparatively thick films (5–50 ML) of relatively large molecules was first demonstrated by Osso *et al*. for F_{16}CuPc on A-plane sapphire [84]. The resulting azimuthal ordering has been shown by four methods sensitive to different aspects of order [84]. AFM was used to image the surface morphology of the bare substrate. After film growth, the characteristic step pattern of the bare substrate was shown to be basically replicated, suggesting an azimuthal coupling of the film structure to the substrate morphology (Figure 1.7). In-plane X-ray diffraction (GIXD) showed that the crystal structure of the film was indeed not a 2D powder, but was aligned. The distribution width ("mosaicity" of the in-plane lattice) was several degrees broad, which suggests a rather soft/weak driving force for the ordering. The in-plane order was also visible in the azimuthal intensity distribution of the vibrational modes detected by Raman scattering. Finally, the resulting anisotropy of the dielectric function was studied by spectroscopic ellipsometry, offering the chance to study the "*intrinsic*" behavior of these systems without a strongly reduced disorder-induced broadening of the optical transitions. We should note that the strong optical anisotropies of these systems are an interesting field of study in their own right, and give rise to nontrivial effects in the propagation of light [54].

The out-of-plane ordering was similarly good for F_{16}CuPc or DIP on silicon oxide, that is, a well-defined Bragg reflection with Laue oscillations and mosaicities around 0.01°, although the tendency of phthalocyanines to grow in needles can cause some complications. We note that the tilt angle of the molecules as well as the out-of-plane lattice parameter was found to depend on the growth temperature (and are different from the bulk structure parameters), indicating that the structure may not be in full equilibrium.

1.4.4 Pentacene

Similar concepts and mechanisms as observed for DIP and F_{16}CuPc in terms of azimuthal alignment should be applicable to pentacene on sapphire, but to our knowledge there are no published results yet.

1.5 Films on Metals

Interfaces with metals are of obvious relevance for contacting organic semiconductors. The choice of the metal is frequently determined more by the desired work function and thus electron or hole injection properties than by growth considerations. Nevertheless, there are a wide variety of metals in terms of behavior as substrates for organic thin film growth, and it is important to realize that this can have a profound impact on the growth and the resulting structural and functional properties. Besides issues related to the surface morphology, crystalline quality, potentially crystalline orientation, and size of the unit cell (epitaxy), it is very important how "reactive" or "inert" the metal is, since this determines the mobility of the molecules on the surface and thus the growth.

For strongly reactive substrates, the molecules tend to behave almost in a "hit-and-stick" fashion, that is, without significant mobility and thus no long-range order. Less reactive metals such as noble metals, to which we will limit ourselves here, turned out to be rather popular and suitable.

We will concentrate on metal single crystals. From a practical point of view, for growth studies it is important that their surfaces can be "recycled" by sputtering and annealing, that is, several growth experiments can be performed on the same substrate and on (essentially) the same surface. Less reactive metals are also easier to keep clean before growth. Obviously, with metal substrates the application of electron-based surface science methods is possible, since the signal does not suffer from charging effects. This has been used excessively by the surface science community in particular for molecular monolayers on surfaces of metal single crystals.

We should also mention that metal surfaces are suitable for surface modification using SAMs [62, 63], which has been employed in particular for Au(111). Examples include the growth of PTCDA on alkanethiol SAMs [85–88].

1.5.1 PTCDA

PTCDA on metal surfaces has been thoroughly studied, with the noble metals being particularly popular.

1.5.1.1 Structure and Epitaxy of PTCDA/Ag(111)

On Ag(111), well-defined epitaxial growth of PTCDA(102) has been observed [4, 26, 30, 32]. The 2D structure is characterized by a herringbone arrangement of the flat-lying molecules, which corresponds to a layer of the (102) plane of the bulk structure, with a small degree of distortion (strain). Possible mechanisms leading to the well-behaved 2D structure of PTCDA on Ag(111) were discussed in Ref. [89]. The vertical PTCDA-Ag(111) spacing was found to be 2.85 ± 0.1 Å based on X-ray diffraction [31], but it may differ for low-temperature deposition if the adsorption state differs. Subsequently, still more precise and even element-resolved vertical bonding geometries of PTCDA monolayers were determined using XSW [90, 91].

Overall, in particular monolayers of PTCDA on Ag(111) have been studied in detail using a broad range of techniques; for a collection of references see Refs [92, 93].

For growth extending beyond the monolayer, a more complex azimuthal distribution arises, and, depending on the growth temperature, also domains noncollinear with principal axes of the substrate can form to relieve strain [30]. Interestingly, the epitaxial relations could be rationalized similar to the Nishiyama–Wassermann versus Kurdjumov–Sachs relations for fcc(111)/bcc(110) growth, although the PTCDA structure is not bcc [30].

We note that PTCDA/Ag(111) has also been subject of a number of spectroscopic studies. One of the challenges is understanding the molecule–substrate interaction, which is "between pure van der Waals and clear covalent binding." Details are beyond the scope of this chapter (see Ref. [93] and references therein).

1.5.1.2 Comparison with Other Substrates

The comparison with PTCDA/Au(111) yields a qualitatively similar picture [28, 33, 94], although details of the epitaxy appear to differ, which is not too surprising given that structure is a result of a rather delicate balance of different factors and given that the corrugation of the substrate potential experienced by PTCDA is different.

It is interesting to compare monolayers of PTCDA on different noble metal surfaces. The tendency is as expected from "a stronger chemical interaction" on Cu(111) via the intermediate case on Ag(111) to the weakest interaction on Au(111), which is seen both in the vertical bonding distances and in the valence band spectra [91, 95, 96].

On the more open Ag(110) surface, an entirely different structure already in the monolayer was found, characterized by a "brick-stone" arrangement [26]. Phase transitions of PTCDA/Ag(110) were studied in Ref. [97].

Growth on Cu(110) was studied by Möller's group [98–100]. The monolayer was found to differ from those known from other substrates. For thicker films, Stranski–Krastanov growth was found, similar to the case on Ag(111) (see below).

1.5.1.3 Dewetting and Thermal Properties

While the structure and epitaxy in the monolayer regime are well defined, the later stages of the growth (potentially after a certain threshold thickness) can, of course, exhibit islanding and a very rough resulting morphology. It was found that PTCDA on Ag(111), a well-behaved system in the monolayer regime, indeed exhibits Stranski–Krastanov growth. At growth temperatures $T \lesssim 350\,K$, relatively smooth epitaxial films have been found, whereas at $T \gtrsim 350\,K$, well-separated crystallites with bulk crystalline structure on top of a 2 ML thick wetting layer have been observed [30, 31, 101, 102]. These results are qualitatively the same as those for PTCDA on Au(111) [28].

The thermally induced post-growth dewetting of "low-temperature" grown films was also studied, confirming that the films tend to dewet if given sufficient thermal energy [31]. In these experiments, the thermal expansion of PTCDA was also determined ($1.06 \pm 0.06\,K^{-1}$ out of plane) [31]. For a comparison with other systems (Alq_3 and TPD), see Ref. [103]. While islanding of the films is usually not desirable, it should be pointed out there might also be ways to exploit islanding or dewetting and the formation of small crystallites for "self-organized nanostructures" (similar to Si–Ge quantum dots).

1.5.1.4 Real-Time Growth

In order to shed light on the dynamics and the temperature dependence of the 2D–3D transition (layer by layer to islanding), a real-time X-ray diffraction study of the growth of PTCDA on Ag(111) was performed [102]. The idea is as follows (Figure 1.8). In kinematic theory the specular X-ray scattering intensity is the sum of the scattering contributions from the film and the substrate,

$$I(q_z,t) = |F(q_z,t)|^2 = \left| f_F \sum_{n=1}^{\infty} e^{iq_z d_F (n-1)} \theta_n(t) + f_S \frac{1}{1-e^{-iq_z d_S}} e^{-iq_z d_0} \right|^2 \tag{1.2}$$

where f_F and f_S are the form factors of the film and the substrate, respectively, d_F and d_S are the corresponding lattice spacings, and $d_0 = 2.8\,\text{Å}$ is the distance between the substrate and the first layer of the film [30]. $\theta_n(t)$ is the time-dependent fractional coverage of the nth layer within the organic film. At the anti-Bragg point of the PTCDA film ($q_z^* = \pi/d_F$), the first term in Eq. (1.2) equals $f_F \sum (-1)^{(n-1)} \theta_n(t)$. Therefore, the coverage difference

$$\Delta\theta(t) = \sum_m \theta_{2m+1}(t) - \sum_m \theta_{2m}(t) = \theta_{odd}(t) - \theta_{even}(t) \tag{1.3}$$

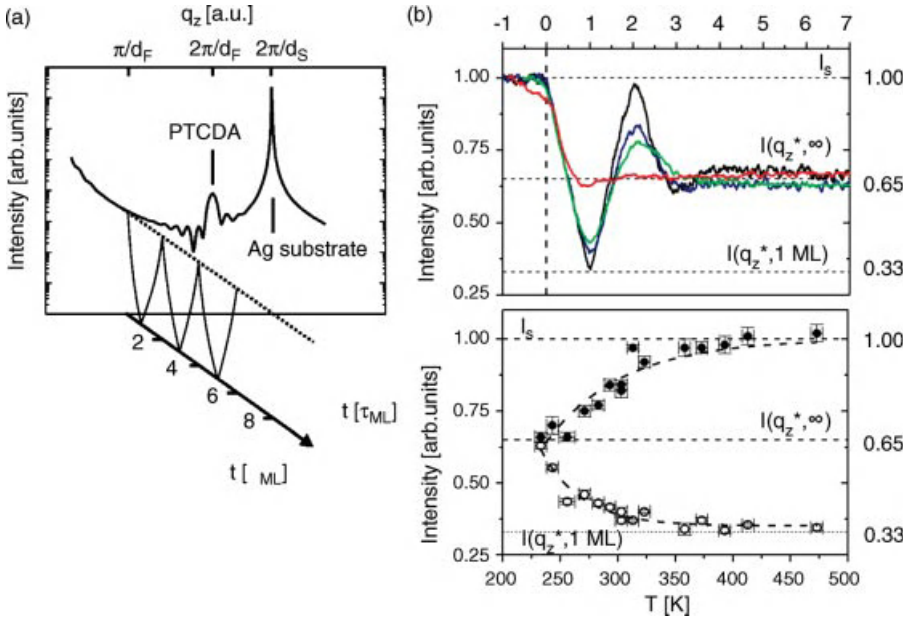

Figure 1.8 Simulation of the specular rod scattering of a thin PTCDA film on Ag(111) as a function of the out-of-plane momentum transfer q_z (*top*). The time axis in this figure (for a fixed q_z) indicates the intensity oscillations at the anti-Bragg point during growth (see text for explanation). The central figure shows the time dependence (in units of monolayer deposition times) of the normalized scattered intensity at the anti-Bragg point for various temperatures (233 K (red), 283 K (green), 303 K (blue), and 358 K (black)). The bottom figure shows the temperature dependence of the deviation from layer-by-layer growth expressed in terms of the intensity of the minimum (open symbols) and of the maximum (filled symbols) of the scattered intensity at 1 ML and 2 ML, respectively (see text for details). Adapted from Ref. [102].

can be deduced from the measured intensity $I(q_z^*, t)$. Specifically, it is possible to distinguish the coverage of the first and the second layer in the initial stage of the growth. In the case of layer-by-layer growth, characteristic intensity oscillations are observed.

Figure 1.8 shows typical time-dependent intensity data during growth in a dedicated chamber [104], measured at various substrate temperatures between 233 and 258 K [102]. $t = 0$ is defined as the starting time of the deposition. The signal is normalized to the substrate scattering intensity, $I_S = I(q_z^*, t < 0)$, and the time is normalized to the deposition time, τ_{ML}, of one monolayer, which corresponds to the intensity minimum. A typical growth measurement exhibits distinct intensity oscillations for $t \lesssim 3\tau_{ML}$, followed by a constant intensity during further deposition, similar to the observations for PTCDA/Au(111) [105]. The intensity oscillations correspond to layer-by-layer growth. The transition to a constant intensity indicates the breakdown of layer-by-layer growth and the onset of islanding characteristic of SK

growth. As can be seen from the transition to a time-independent scattering signal (associated with an equal probability for a given molecule to be accommodated in even and odd layers), the islanding starts rapidly after completion of a 2 ML "wetting" layer.

Comparing the growth data for different temperatures (Figure 1.8), we find that for $T \geq 358$ K the oscillations are not visibly damped for $t < 2\tau_{ML}$. They are followed by a sharp transition to a time-independent intensity (islanding). For lower temperatures, the oscillations are progressively damped, and the 2D–3D transition is smeared out as the temperature is lowered.

The experimental data, that is, in particular the 2D–3D transition, could be modeled by kinetic Monte Carlo simulations using a relatively simple model for the energies/barriers, the most important feature of which is the dependence of the interlayer transport barrier, E_{inter}, on the layer number n, namely, $E_{inter}(n \leq 3) = 0$ and $E_{inter}(n > 3) > 0$ [102].

The growth of PTCDA/Ag(111) could also be monitored in real time in real space using PEEM [106]. Moreover, for elevated temperatures strong postgrowth diffusion was observed [107].

1.5.2 DIP

In the monolayer regime, DIP, like many other organic semiconductors, was studied by STM. The molecules were found to be lying down flat on the substrate [108]. The interaction of DIP with Au was found to be physisorptive. In the regime of thicker films, DIP was studied in detail *on* Au contacts [43] (and as substrate for Au contacts evaporated *on* DIP [43, 66–68]). Importantly, in contrast to growth on silicon oxide, due to the stronger interaction with the Au substrate, the lying-down configuration tends to prevail not only for monolayers but also for multilayers. Since the standing-up configuration (which again followed a herringbone-like motif) appears to have the more favorable surface energy (as seen on silicon oxide), there is obviously a competition between the two configurations (standing-up versus lying-down), and they are found to coexist [43]. From the point of view of growth kinetics, this competition is very interesting, but it is certainly a further complication and an additional source of disorder that is usually undesirable. These issues were recently studied using (electronic) spectromicroscopy [109]. Furthermore, mixed films of DIP and CuPc were studied by STM in the monolayer regime [110].

1.5.3 Phthalocyanines

Phthalocyanines were among the first "large" molecules that were studied by STM with (sub)molecular resolution [50]. In the monolayer regime, the molecules lie down flat on the surface, and the 2D structures have been thoroughly studied.

Recently, the (vertical) bonding distance to the metal substrate was determined using XSW [2, 111, 112]. For thicker films, there is a competition between the lying-down configuration of the first layer and the tendency to stand up. The impact of roughness on the ordering behavior was studied in Ref. [113].

1.5.4 Pentacene

Acenes on metal substrates were studied by several groups. Early work on the orientation of various aromatic hydrocarbons including tetracene on metal surfaces using NEXAFS was done by Koch and coworkers [114].

More recent work focused on pentacene. Pentacene structures on Au(111) as a function of coverage (up to the equivalent of around 2 ML) were studied by Parkinson's group [115]. A very detailed study of pentacene on clean and SAM-modified gold surfaces was presented by Käfer *et al.* [116].

The structure and binding distance as well as associated electronic properties such as work function and interface dipole of PEN and also of PFP on Cu(111) were determined with high precision in Ref. [117].

In the monolayer regime of pentacene on Cu(110), Lukas *et al.* reported a novel mechanism giving rise to long-range order on Cu(110), based on the modulation of the adsorption energy due to charge-density waves related to a surface state [118]. While it is not too surprising that the molecules in the monolayer regime tend to be lying more or less flat on the surface, importantly, for the growth of thicker films on Cu(110) an orientational transition from a lying-down configuration to an essentially standing-up configuration was observed [119].

An interesting study of the "hyperthermal" growth of pentacene (exhibiting hyperthermal energies in a seeded supersonic molecular beam) on Ag(111) was presented by Casalis *et al.* [120]. They found that at low substrate temperatures (200 K), highly ordered films can be grown by hyperthermal deposition when thermal deposition leads only to disordered films. The results were interpreted as a result of "local annealing" due to the impact of the hyperthermal molecules. This technique appears to have the potential to tailor the growth of molecular systems in addition to what is possible by changing the impingement rate and the substrate temperature, and it may be further tested in the future (see Ref. [61] for recent work on PFP).

1.6 Films on Other Substrates

Many substrates other than the above ones have been employed, all of which we cannot review. We shall mention only some of the most important other substrates.

Quite popular for growth studies is graphite, since it is easy to prepare. In our general classification of substrates, graphite would be "weakly interacting." For spectroscopic studies, this offers the opportunity to study the film without strong

"interference" from the substrate; see, for example, Ref. [121] and references therein. Other examples from this group of layered substrates are MoS_2, GeS, and Sb_2S_3 [6].

Also rather weakly interacting would be MgO, which falls essentially in the same category as sapphire and silicon oxide. Mica, which can be easily prepared by cleavage, may also be seen in the category of rather inert substrates. It can also be used well for real-time differential reflectance spectroscopy (DRS) [122].

Alkalihalogenides, such as NaCl and KCl, are quite popular as simple substrates for growth studies, since they are easy to prepare. For some studies, they have the additional benefit that they can be easily dissolved and the film can be studied by TEM.

Metals, as indicated above, span a broad range from the noble metals to very reactive substrates.

A very important class of substrates are certainly (inorganic) semiconductors such as Si and GaAs, since they may be used in the integration of organic–inorganic hybrid devices. Moreover, they are very well defined in terms of their surface and overall structural quality, which is favorable for growth studies. If the surface is clean, however, they can exhibit "dangling bonds" and be rather reactive. In these cases, the organic adsorbates then tend to "hit and stick," that is, they usually do not diffuse over significant distances, hence they do not form long-range ordered structures. A strategy to avoid these problems, but still benefit from the above advantages, is the use of surface-passivated semiconductors, such as H–Si or Se–GaAs.

Polymeric substrates and possible routes for oriented growth of pentacene have been studied in Ref. [123].

1.7
More Complex Heterostructures and Technical Interfaces

Organic semiconductor devices frequently do not only consist of a film on a substrate, but involve additional layers such as metal contacts or insulating layers or also different organic components in a multilayer structure.

1.7.1
Inorganic–Organic Heterostructures

Metal contacts are one obvious requirement for many applications of organic semiconductors. It turns out that the controlled deposition of metals *on* organics ("top electrode") is nontrivial. In order to reduce problems related to interdiffusion (and ultimately short-circuiting) and traps related to surface states, different strategies can be pursued.

1) Deposition at low temperatures to "freeze in" the interdiffusion.
2) Deposition at (moderately) high rates with the idea that the metals are quickly forming larger aggregates that are then less mobile and diffuse less far into the organic film.

3) The use of "suitably reactive" metals and/or organics, so that a strong interaction at the top layer(s) of the organic material prevents interdiffusion.
4) "Soft deposition" by "thermalizing" or at least reducing the energy of the impinging metal atoms by "baffling" these using a noble gas or other means [124].
5) Miscellaneous other nonthermal deposition strategies including, for example, electrochemical deposition may be attempted.

Our group performed studies of the deposition of gold, which is widely used as a hole injection material, onto well-defined DIP thin-film surfaces to study the interdiffusion (Figure 1.9). The study followed the "classical" approach without specific precaution against interdiffusion except for variation in the temperature and the rate [43, 44, 66–68]. The important result was that under rather typical deposition conditions near room temperature, the metal interdiffusion was already significant, and the layers would exhibit electrical shorts (Figure 1.9). If the substrate, however, is cooled, fairly well-defined interfaces could be obtained. We note that Faupel"s group studied similar issues in detail for metal deposition on polymers [125, 126].

Sellner *et al*. [127, 128] have studied aluminum oxide/DIP interfaces, which exhibit a very different interdiffusion behavior. Even the use of aluminum oxide capping layers, giving rise to significantly enhanced thermal stability of the underlying organic layer, are possible and may be used for encapsulation of devices.

We should note that for device structures one also has to take into account the effect of the morphology of technical interfaces and surfaces on the growth behavior of organics [113].

1.7.2 Organic–Organic Heterostructures

Another important interface, which has not been excessively studied with regard to growth and structure, is the organic–organic interface as found, for example, in OLEDs and in OPV devices. Some early work on superlattices and bilayers can be found, for example, in Refs [129–132]. PTCDA on self-assembled monolayers as well-defined organic model surfaces has been studied in Refs [85–88]. PTCDA on hexa-peri-hexabenzocoronene (HBC) was investigated in Ref. [133]. A number of different polynuclear aromatic hydrocarbons including DIP and perylene were studied by Kobayashi's group [134]. Other studies were concerned with the post-growth stability of the organic–organic interface and the interdiffusion behavior [103, 135].

Recently, the study of organic–organic structures has attracted increased interest, and different architectures have been studied in more detail. For an up-to-date review on this specific topic, see Ref. [136].

For A-on-B-type structures, which in device terminology correspond to "planar heterojunctions" (PHJ), in addition to the interface stability, there are other issues.

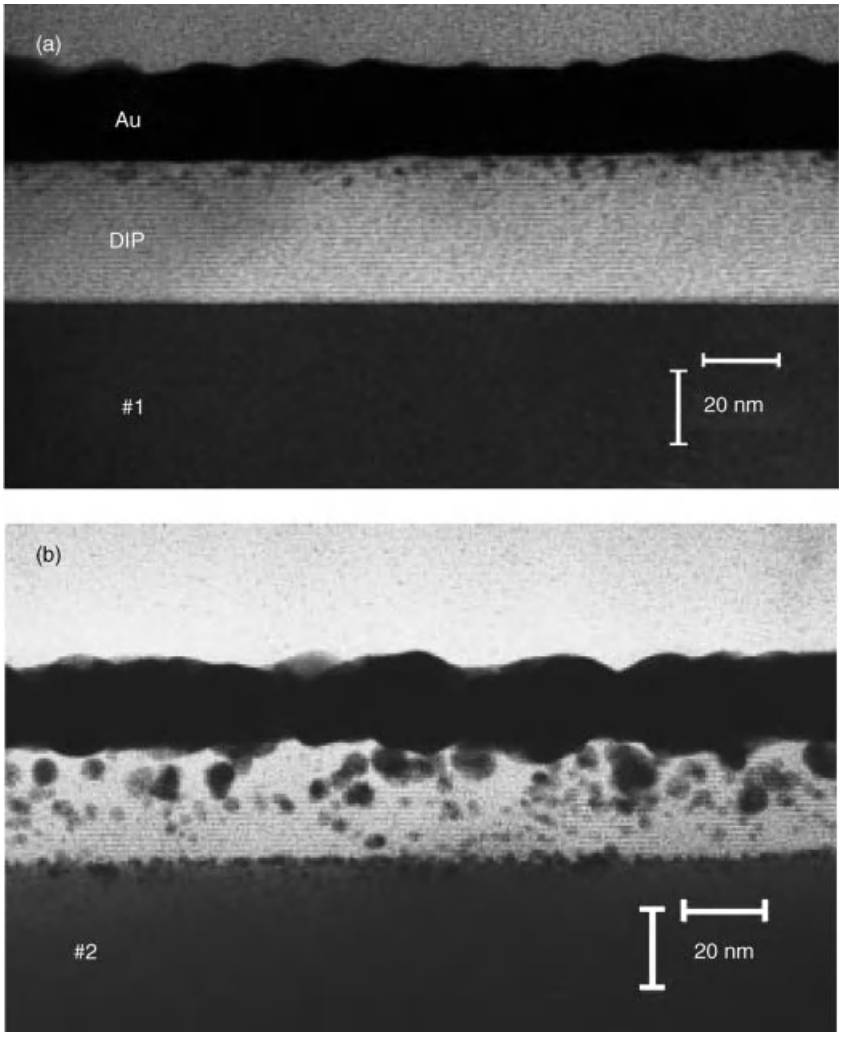

Figure 1.9 Cross-sectional TEM images of two Au/DIP/silicon oxide heterostructures. While the Au contact prepared at −120 °C and at a rate of 23 Å/min (a) exhibits rather well-defined interfaces, the Au contact prepared at 70 °C and at a rate of 0.35 Å/min (b) shows strong interdiffusion. Note that individual lattice planes of the DIP film can be resolved. Adapted from Ref. [66].

One of these issues is related to the evolution of roughness. An interesting effect is smoothing (see Figure 1.10), which was observed for PFP on DIP and PEN on PFP [137]. For both systems, surface smoothing during thermal evaporation of the second material on top of the first is observed. The smoothing can be rationalized by a, compared to homoepitaxy, lowered step edge barrier for one species diffusing on the other, but more details have yet to be explored.

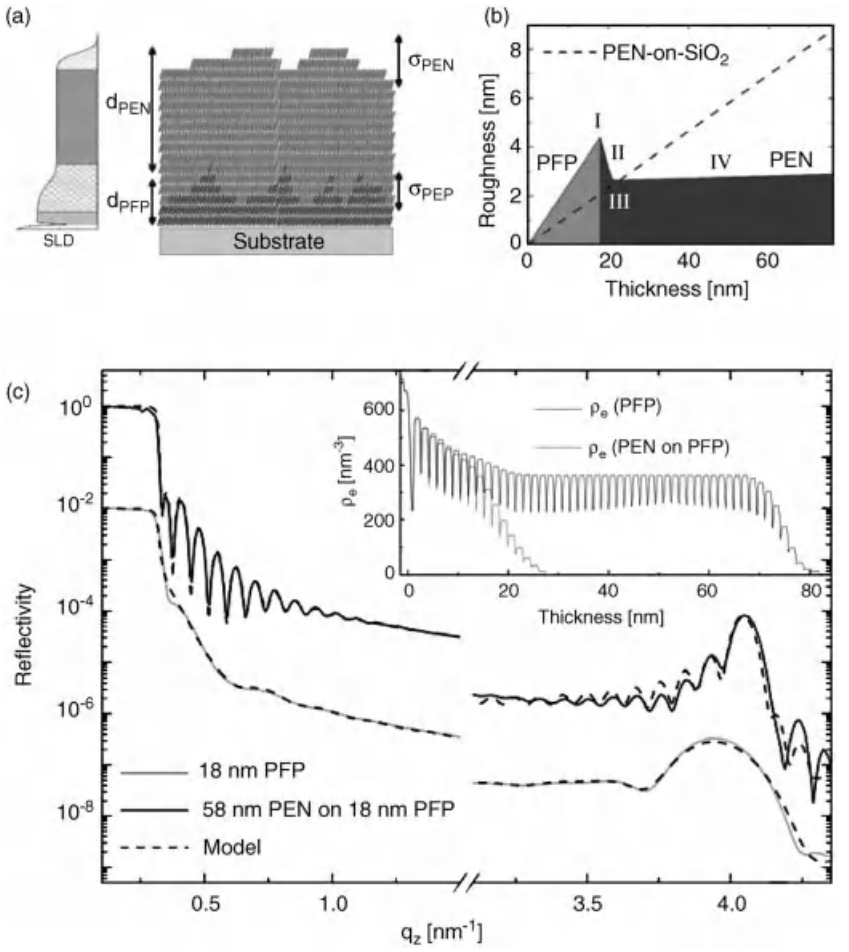

Figure 1.10 (a) Heterostructure with thicknesses of the organic layers d_{PFP} and d_{PEN} and roughness of the intermediate interface σ_{PFP} and the top roughness σ_{PEN}. (b) Roughness evolution during film growth. (c) Reflectivity data and fits from a 18 nm thick PFP film, and from a PEN-on-PFP heterostructure with $d_{PFP} = 18$ nm and $d_{PEN} = 58$ nm. The inset shows ϱ_e for both fits. Adapted from Ref. [137].

In contrast to the above scenario, for the system DIP on F_{16}CuPc, Stranski–Krastanov growth was reported [138], underlining that, of course, the growth scenario depends on the specific system.

Another important question concerns the molecular orientation (in particular, "lying down" versus "standing up" for rod-like molecules) at the interface or induced by the interface. The orientation may be changed (compared to single-component film growth on, say, silicon oxide) by an underlying organic layer, for example, by the balance of the interface energies. It may also be influenced by a

specific step pattern or its height, which for organics is obviously greater than for typical inorganic substrates. In this context, one may observe templating effects, that is, the growth behavior of the top layer may depend on the structural and morphological properties of the bottom layer. This was demonstrated, for example, for PFP on DIP. Two main effects were observed: PFP molecules in the top layer adopt partly the orientation of the DIP molecules in the bottom layer and the crystalline quality of the PFP layer correlates with the crystalline quality of the DIP layer underneath in terms of the coherent in-plane island size [142].

Apart from the various combinations of PEN, PFP, F_{16}CuPc, and DIP mentioned above, other A-on-B heterostructures were studied [136]. Here, we shall not attempt to provide a complete list but rather refer to other chapters in this book and to the paragraph further below on work relating different architectures to device performance.

For A-mixed-with-B-type structures, in particular coevaporated (50 : 50) films, which correspond to "bulk heterojunctions" (BHJs) in OPV devices, there are several fundamental structural issues to be addressed. First of all, there is the question of intermixing versus phase segregation. As an "ordered form of intermixing," one may even find the formation of a true superstructure ("A-B-A-B-A- . . . ," to be seen most directly from a superlattice reflection), in contrast to a "statistical occupancy" of the different lattice sites by A and B [139, 140]. These are classical issues in the physics of metals (ordered versus disordered alloys).

Entropy, which will always favor intermixing, has to be compared to the balance of the interactions (A with A and B with B versus A with B), which then determines whether intermixing is indeed found. In addition to direct ("conventional") interactions, there are steric issues. For instance, CuPc and C60 are structurally/sterically apparently incompatible (platelet versus sphere), so that an ordered structure and intermixing on the molecular level is not expected, and indeed is not found [49].

A promising system for good intermixing appears to be PEN:PFP, since this may exhibit favorable interactions for intermixing and very little steric difficulties, since the two compounds are derived from the same molecular structure. Consequently, the system PEN:PFP was studied in detail both structurally [139, 141] and spectroscopically [142–144]. Indeed, it could be shown that PEN:PFP does tend to intermix and form its own structure with 1 : 1 stoichiometry. However, the situation for continuous variation in the composition is actually rather complex. Scenarios with different coexisting structures are possible, for example, if the structure with 1 : 1 stoichiometry is favorable, for compositions different from 1 : 1, the "ordered 1 : 1 regions" may coexist with regions with excess molecules of one or the other compound, if there is no "continuous intermixing." For a detailed discussion of the subtleties of X-ray diffraction on this system, see Ref. [138]; for aspects related to the microstructure studied by X-ray microscopy and micro-NEXAXS including dichroism, see Ref. [145].

In addition to the above cases (PHJ and BHJ), other (intermediate) possible architectures have been studied, for example, mixed layers sandwiched between

pure layers (planar-mixed heterojunction, PM-HJ) [49]. The impact of the organic–organic architecture on device performance has also been studied. These issues are discussed in, for example, in OPV cells using the rather promising new donor–acceptor pair of DIP and C_{60} as PHJ versus BHJ versus PM-HJ geometry, together with X-ray, AFM, optical, and electronic characterization [49]. For other work on organic–organic heterostructures combining structural and spectroscopic characterization with transport or other device performance parameters, we refer to Refs [146–149] and references therein and of course other chapters in this book.

1.8 Summary and Conclusions

This chapter does not claim to be complete in any way. We have rather presented a few case studies, which we hope serve to highlight a few of the issues specific to the growth of organic thin films. We shall summarize some of these.

1) Epitaxial relations can be complicated, and the films can exhibit a large number of symmetry-equivalent domains. Moreover, the coexistence of different phases can give rise to complications.
2) Islanding (after some critical thickness) is not uncommon, and is, of course, not prevented by well-defined structural relation between film and substrate.
3) Even for systems that tend to "wet" the substrate, overproportional roughening may occur, and the growth exponents may be very different from those expected based on conventional theories.
4) The controlled preparation of organic-based heterostructures can be particularly difficult, given the tendency for interdiffusion of, for example, metal contacts.
5) The growth of organic–organic heterostructures, whether A-on-B or A-mixed-with-B or other architectures, can be a complex endeavor, but offers many ways to further manipulate and engineer device performance.

Despite the "additional complications" of organics, well-ordered thin films can be grown by OMBD. We hope the improvement of the understanding of the growth mechanisms will further promote the applications of organics.

Moreover, organics with their specific features promise to give rise to fundamentally new growth phenomena such as orientational transitions and new universality classes (scaling exponents), which is an exciting subject in its own right.

Acknowledgments

We wish to thank the many students, collaborators, and colleagues who contributed in various ways to the work reviewed here. Valuable comments on the manuscript

were made by A. Gerlach, S. Kowarik, W. Brütting, and J. Pflaum. We wish to acknowledge financial support from the Deutsche Forschungsgemeinschaft.

References

1 Romaner, L., Heimel, G., Bredas, J.L., Gerlach, A., Schreiber, F., Johnson, R.L., Zegenhagen, J., Duhm, S., Koch, N., and Zojer, E. (2007) *Phys. Rev. Lett.*, **99**, 256801.

2 Yamane, H., Gerlach, A., Duhm, S., Tanaka, Y., Hosokai, T., Mi, Y., Zegenhagen, J., Koch, N., Seki, K., and Schreiber, F. (2010) *Phys. Rev. Lett.*, **105**, 046103.

3 Koma, A. (1995) *Prog. Cryst. Growth Charact.*, **30**, 129.

4 Umbach, E., Sokolowski, S., and Fink, R. (1996) *Appl. Phys. A*, **63**, 565.

5 Forrest, S.R. (1997) *Chem. Rev.*, **97**, 1793.

6 Karl, N. and Günther, C. (1999) *Cryst. Res. Technol.*, **34**, 243.

7 Hooks, D.E., Fritz, T., and Ward, M.D. (2001) *Adv. Mater.*, **13**, 227.

8 Fraxedas, J. (2002) *Adv. Mater.*, **14**, 1603.

9 Dimitrakopoulos, C.D. and Malenfant, P. R.L. (2002) *Adv. Mater.*, **14**, 99.

10 Rosei, F., Schunack, M., Naitoh, Y., Jiang, P., Gourdon, A., Laegsgaard, E., Stensgaard, I., Joachim, C., and Besenbacher, F. (2003) *Prog. Surf. Sci.*, **71**, 95.

11 Barlow, S.M. and Raval, R. (2003) *Surf. Sci. Rep.*, **50**, 201.

12 Witte, G. and Wöll, C. (2004) *J. Mater. Res.*, **19**, 1889.

13 Schreiber, F. (2004) *Phys. Stat. Sol. (a)*, **201**, 1037.

14 Gerlach, A., Sellner, S., Kowarik, S., and Schreiber, F. (2008) *Phys. Stat. Sol. (a)*, **205**, 461.

15 Kowarik, S., Gerlach, A., and Schreiber, F. (2008) *J. Phys. Condens. Matter*, **20**, 184005.

16 Lorenzo, M.O., Baddeley, C.J., Muryn, C., and Raval, R. (2000) *Nature*, **404**, 376.

17 Shen, Q., Frankel, D., and Richardson, N.V. (2002) *Surf. Sci.*, **497**, 37.

18 Toomes, R.L., Kang, J.H., Woodruff, D. P., Polcik, M., Kittel, M., and Hoeft, J.T. (2003) *Surf. Sci. Lett.*, **522**, L9.

19 Kowarik, S., Gerlach, A., Sellner, S., Schreiber, F., Cavalcanti, L., and Konovalov, O. (2006) *Phys. Rev. Lett.*, **96**, 125504.

20 Barabási, A.-L. and Stanley, H.E. (1995) *Fractal Concepts in Surface Growth*, Cambridge University Press, Cambridge.

21 Krim, J. and Palasantzas, G. (1995) *Int. J. Mod. Phys. B*, **9**, 599.

22 Krug, J. (1997) *Adv. Phys.*, **46**, 139.

23 Pimpinelli., A. and Villain, J. (1999) *Physics of Crystal Growth*, Cambridge University Press, Cambridge.

24 Biscarini, F., Samori, P., Greco, O., and Zamboni, R. (1997) *Phys. Rev. Lett.*, **78**, 2389.

25 Dürr, A.C., Schreiber, F., Ritley, K.A., Kruppa, V., Krug, J., Dosch, H., and Struth, B. (2003) *Phys. Rev. Lett.*, **90**, 016104.

26 Glöckler, K., Seidel, C., Soukopp, A., Sokolowski, M., Umbach, E., Böhringer, M., Berndt, R., and Schneider, W.-D. (1998) *Surf. Sci.*, **405**, 1.

27 Möbus, M., Karl, N., and Kobayashi, T. (1992) *J. Cryst. Growth*, **116**, 495.

28 Fenter, P., Schreiber, F., Zhou, L., Eisenberger, P., and Forrest, S.R. (1997) *Phys. Rev. B*, **56**, 3046.

29 Seidel, C., Awater, C., Liu, X.D., Ellerbrake, R., and Fuchs, H. (1997) *Surf. Sci.*, **371**, 123.

30 Krause, B., Dürr, A.C., Ritley, K., Schreiber, F., Dosch, H., and Smilgies, D. (2002) *Phys. Rev. B*, **66**, 235404.

31 Krause, B., Dürr, A.C., Schreiber, F., Dosch, H., and Seeck, O.H. (2003) *J. Chem. Phys.*, **119**, 3429.

32 Krause, B., Dürr, A.C., Ritley, K.A., Schreiber, F., Dosch, H., and Smilgies, D. (2001) *Appl. Surf. Sci.*, **175**, 332.

33 Schmitz-Hübsch, T., Fritz, T., Sellam, F., Staub, R., and Leo, K. (1997) *Phys. Rev. B*, **55**, 7972.

34 Hoffmann, M., Schmidt, K., Fritz, T., Hasche, T., Agranovich, V.M., and Leo, K. (2000) *Chem. Phys.*, **258**, 73.

35 Leonhardt, M., Mager, O., and Port, H. (1999) *Chem. Phys. Lett.*, **313**, 24.

36 Vragović, I., Scholz, R., and Schreiber, M. (2002) *Europhys. Lett.*, **57**, 288.

37 Alonso, M.I., Garriga, M., Karl, N., Ossó, J.O., and Schreiber, F. (2002) *Org. Electron.*, **3**, 23.

38 Scholz, R. (2003) Habilitation Thesis, Chemnitz.

39 Scholz, R., Kobitski, A.Y., Kampen, T.U., Schreiber, M., Zahn, D.R.T., Jungnickel, G., Elstner, M., Sternberg, M., and Frauenheim, T. (2000) *Phys. Rev. B*, **61**, 13659.

40 Tautz, F.S., Sloboshanin, S., Schaefer, J. A., Scholz, R., Shklover, V., Sokolowski, M., and Umbach, E. (2000) *Phys. Rev. B*, **61**, 16933.

41 Wagner, V., Muck, T., Geurts, J., Schneider, M., and Umbach, E. (2003) *Appl. Surf. Sci.*, **212**, 520.

42 Dürr, A.C., Schreiber, F., Münch, M., Karl, N., Krause, B., Kruppa, V., and Dosch, H. (2002) *Appl. Phys. Lett.*, **81**, 2276.

43 Dürr, A.C., Koch, N., Kelsch, M., Rühm, A., Ghijsen, J., Johnson, R.L., Pireaux, J. J., Schwartz, J., Schreiber, F., Dosch, H., and Kahn, A. (2003) *Phys. Rev. B*, **68**, 115428.

44 Dürr, A.C., Schreiber, F., Kelsch, M., and Dosch, H. (2003) *Ultramicroscopy*, **98**, 51.

45 Karl, N. (2001) *Organic Electronic Materials*, vol. **2** (eds R. Farchioni and G. Grosso), Springer, Berlin.

46 Kurrle, D. and Pflaum, J. (2008) *Appl. Phys. Lett.*, **92**, 133306.

47 Heinemeyer, U., Scholz, R., Gisslén, L., Alonso, M.I., Ossó, J.O., Garriga, M., Hinderhofer, A., Kytka, M., Kowarik, S., Gerlach, A., and Schreiber, F. (2008) *Phys. Rev. B*, **78**, 085210.

48 Scholz, R., Gisslen, L., Schuster, B.-E., Casu, M.B., Chassé, T., Heinemeyer, U., and Schreiber, F. (2011) *J. Chem. Phys.*, **134**, 014504.

49 Wagner, J., Gruber, M., Hinderhofer, A., Wilke, A., Bröker, B., Frisch, J., Amsalem, P., Vollmer, A., Opitz, A., Koch, N., Schreiber, F., and Brütting, W. (2010). *Adv. Funct. Mater.*, **20**, 4295.

50 Lippel, P.H., Wilson, R.J., Miller, M.D., Wöll, C., and Chiang, S. (1989) *Phys. Rev. Lett.*, **62**, 171.

51 Leznoff, C.C. and Lever, A.B.P. (1989) *Phthalocyanines: Properties and Applications*, VCH Publishers Inc., New York.

52 Schlettwein, D. (2001) *Supramolecular Photosensitive and Electroactive Materials* (ed. H.S. Nalwa), Academic Press, San Diego.

53 Yim, S. and Jones, T.S. (2002) *Surf. Sci.*, **521**, 151.

54 Alonso, M.I., Garriga, M., Ossó, J.O., Schreiber, F., Barrena, E., and Dosch, H. (2003) *J. Chem. Phys.*, **119**, 6335.

55 Rogers, J.A., Bao, Z., Dodabalapur, A., and Makhija, A. (2000) *IEEE Electron. Dev. Lett.*, **21**, 100.

56 Bao, Z., Lovinger, A.J., and Brown, J. (1998) *J. Am. Chem. Soc.*, **120**, 207.

57 Inoue, Y., Sakamoto, Y., Suzuki, T., Kobayashi, M., Gao, Y., and Tokito, S. (2005) *Jpn. J. Appl. Phys. 1*, **44**, 3663.

58 Hinderhofer, A., Heinemeyer, U., Gerlach, A., Kowarik, S., Jacobs, R.M. J., Sakamoto, Y., Suzuki, T., and Schreiber, F. (2007) *J. Chem. Phys.*, **127**, 194705.

59 Koch, N., Vollmer, A., Duhm, S., Sakamoto, Y., and Suzuki, T. (2007) *Adv. Mater.*, **19**, 112.

60 Kowarik, S., Gerlach, A., Hinderhofer, A., Milita, S., Borgatti, F., Zontone, F., Suzuki, T., Biscarini, F., and Schreiber, F. (2008) *Phys. Stat. Sol. (RRL)*, **2**, 120.

61 Desai, T.V., Woll, A.R., Schreiber, F., and Engstrom, J.R. (2010) *J. Phys. Chem. C*, **114**, 20120.

62 Schreiber, F. (2004) *J. Phys. Condens. Matter*, **16**, R881.

63 Schreiber, F. (2000) *Prog. Surf. Sci.*, **65**, 151.

64 Shtein, M., Mapel, J., Benziger, J.B., and Forrest, S.R. (2002) *Appl. Phys. Lett.*, **81**, 268.

65 Möbus, M. and Karl, N. (1992) *Thin Solid Films*, **215**, 213.

66 Dürr, A.C., Schreiber, F., Kelsch, M., Carstanjen, H.D., and Dosch, H. (2002) *Adv. Mater.*, **14**, 961.

67 Dürr, A.C., Schreiber, F., Kelsch, M., Carstanjen, H.D., Dosch, H., and Seeck, O.H. (2003) *J. Appl. Phys.*, **93**, 5201.

68 Koch, N., Dürr, A.C., Ghijsen, J., Johnson, R.L., Pireaux, J.J., Schwartz, J., Schreiber, F., Dosch, H., and Kahn, A. (2003) *Thin Solid Films*, **441**, 145.

69 Heinemeyer, U., Broch, K., Hinderhofer, A., Kytka, M., Scholz, R., Gerlach, A., and Schreiber, F. (2010) *Phys. Rev. Lett.*, **104**, 257401.

70 Zhang, D., Heinemeyer, U., Stanciu, C., Sackrow, M., Braun, K., Hennemann, L. E., Wang, X., Scholz, R., Schreiber, F., and Meixner, A.J. (2010) *Phys. Rev. Lett.*, **104**, 056601.

71 Krug, J. (1995) *Phys. Rev. Lett.*, **75**, 1795.

72 Kowarik, S., Gerlach, A., Skoda, M., Sellner, S., and Schreiber, F. (2009) *Eur. Phys. J. Special Topics*, **167**, 11.

73 Ossó, J.O., Schreiber, F., Alonso, M.I., Garriga, M., Barrena, E., and Dosch, H. (2004) *Org. Electron.*, **5**, 135.

74 de Oteyza, D., Barrena, E., Osso, J., Sellner, S., Dosch, H. (2006) *J. Am. Chem. Soc.*, **128**15052.

75 Hosokai, T., Gerlach, A., Hinderhofer, A., Frank, C., Ligorio, G., Heinemeyer, U., Vorobiev, A., and Schreiber, F. (2010) *Appl. Phys. Lett.*, **97**, 063301.

76 Yim, S. and Jones, T.S. (2006) *Phys. Rev. B*, **73**, 161305.

77 Ruiz, R., Nickel, B., Koch, N., Feldman, L.C., Haglund, R., Jr., Kahn, A., Family, F., and Scoles, G. (2003) *Phys. Rev. Lett.*, **91**, 136102.

78 Meyer zu Heringdorf, F.-J., Reuter, M.C., and Tromp, R.M. (2001) *Nature*, **412**, 517.

79 Nickel, B., Barabash, R., Ruiz, R., Koch, N., Kahn, A., Feldman, L.C., Haglund, R. F., and Scoles, G. (2004) *Phys. Rev. B*, **70**, 125401.

80 Mayer, A., Kazimirov, A., and Malliaras, G. (2006) *Phys. Rev. Lett.*, **97**, 105503.

81 Kowarik, S., Gerlach, A., Leitenberger, W., Hu, J., Witte, G., Wöll, C., Pietsch, U., and Schreiber, F. (2007) *Thin Solid Films*, **515**, 5606.

82 Voigt, M., Dorsfeld, S., Volz, A., and Sokolowski, M. (2003) *Phys. Rev. Lett.*, **91**, 026103.

83 Becker, T., Birkner, A., Witte, G., and Wöll, C. (2002) *Phys. Rev. B*, **65**, 115401.

84 Ossó, J.O., Schreiber, F., Kruppa, V., Dosch, H., Garriga, M., Alonso, M.I., and Cerdeira, F. (2002) *Adv. Funct. Mater.*, **12**, 455.

85 Schreiber, F., Gerstenberg, M.C., Dosch, H., and Scoles, G. (2003) *Langmuir*, **19**, 10004.

86 Schreiber, F., Gerstenberg, M.C., Edinger, B., Toperverg, B., Forrest, S.R., Scoles, G., and Dosch, H. (2000) *Phys. B*, **283**, 75.

87 Gerstenberg, M.C., Schreiber, F., Leung, T.Y.B., Bracco, G., Forrest, S.R., and Scoles, G. (2000) *Phys. Rev. B*, **61**, 7678.

88 Staub, R., Toerker, M., Fritz, T., Schmitz-Hübsch, T., Sellam, F., and Leo, K. (2000) *Surf. Sci.*, **445**, 368.

89 Eremtchenko, M., Schaefer, J., and Tautz, F.S. (2003) *Nature*, **425**, 602.

90 Hauschild, A., Karki, K., Cowie, B.C.C., Rohlfing, M., Tautz, F.S., and Sokolowski, M. (2005) *Phys. Rev. Lett.*, **94**, 036106.

91 Gerlach, A., Sellner, S., Schreiber, F., Koch, N., and Zegenhagen, J. (2007) *Phys. Rev. B*, **75**, 045401.

92 Tautz, F.S. (2007) *Prog. Surf. Sci.*, **82**, 479.

93 Ziroff, J., Forster, F., Schöll, A., Puschnig, P., and Reinert, F. (2010) *Phys. Rev. Lett.*, **104**, 233004.

94 Chizhov, I., Kahn, A., and Scoles, G. (2000) *J. Cryst. Growth*, **208**, 449.

95 Henze, S.K.M., Bauer, O., Lee, T.-L., Sokolowski, M., and Tautz, F.S. (2007) *Surf. Sci.*, **601**, 1566.

96 Duhm, S., Gerlach, A., Salzmann, I., Bröcker, B., Johnson, R., Schreiber, F., and Koch, N. (2008) *Org. Electron.*, **9**, 111.

97 Seidel, C., Poppensieker, J., and Fuchs, H. (1998) *Surf. Sci.*, **408**, 223.

98 Stöhr, M., Gabriel, M., and Möller, R. (2002) *Europhys. Lett.*, **59**, 423.

99 Stöhr, M., Gabriel, M., and Möller, R. (2002) *Surf. Sci.*, **507–510**, 330.

100 Gabriel, M., Stöhr, M., and Möller, R. (2002) *Appl. Phys. A*, **74**, 303.

101 Chkoda, L., Schneider, M., Shklover, V., Kilian, L., Sokolowski, M., Heske, C., and Umbach, E. (2003) *Chem. Phys. Lett.*, **371**, 548.

102 Krause, B., Schreiber, F., Dosch, H., Pimpinelli, A., and Seeck, O.H. (2004) *Europhys. Lett.*, **65**, 372.

103 Fenter, P., Schreiber, F., Bulovic, V., and Forrest, S.R. (1997) *Chem. Phys. Lett.*, **277**, 521.

104 Ritley, K.A., Krause, B., Schreiber, F., and Dosch, H. (2001) *Rev. Sci. Instrum.*, **72**, 1453.

105 Fenter, P., Eisenberger, P., Burrows, P., Forrest, S.R., and Liang, K.S. (1996) *Phys. B*, **221**, 145.

106 Marchetto, H., Groh, U., Schmidt, T., Fink, R., Freund, H.-J., and Umbach, E. (2006) *Chem. Phys.*, **325**, 178184.

107 Krause, B., Dürr, A.C., Schreiber, F., Dosch, H., and Seeck, O.H. (2004) *Surf. Sci.*, **572**, 385.

108 Strohmaier, R.PhD thesis, Stuttgart (1997)

109 Casu, M.B., Schuster, B.-E., Biswas, I., Raisch, C., Marchetto, H., Schmidt, T., and Chassé, T. (2010) *Adv. Mater.*, **22**, 3740.

110 Huang, H., Huang, Y., Pflaum, J., Wee, A.T.S., and Chen, W. (2009) *Appl. Phys. Lett.*, **95**, 263309.

111 Gerlach, A., Schreiber, F., Sellner, S., Dosch, H., Vartanyants, I.A., Cowie, B.C. C., Lee, T.-L., and Zegenhagen, J. (2005) *Phys. Rev. B*, **71**, 205425.

112 Stadler, C., Hansen, S., Pollinger, F., Kumpf, C., Umbach, E., Lee, T.-L., and Zegenhagen, J. (2006) *Phys. Rev. B*, **74**, 035404.

113 Peisert, H., Schwieger, T., Auerhammer, J.M., Knupfer, M., Golden, M.S., Fink, J., Bressler, P.R., and Mast, M. (2001) *J. Appl. Phys.*, **90**, 466.

114 Yannoulis, P., Dudde, R., Frank, K.H., and Koch, E.E. (1987) *Surf. Sci.*, **189/190**, 519.

115 France, C.B., Schroeder, P.G., Forsythe, J. C., and Parkinson, B.A. (2003) *Langmuir*, **19**, 1274.

116 Käfer, D., Ruppel, L., and Witte, G. (2007) *Phys. Rev. B*, **75**, 085309.

117 Koch, N., Gerlach, A., Duhm, S., Glowatzki, H., Heimel, G., Vollmer, A., Sakamoto, Y., Suzuki, T., Zegenhagen, J., Rabe, J.P., and Schreiber, F. (2008) *J. Am. Chem. Soc.*, **130**, 7300.

118 Lukas, S., Witte, G., and Wöll, C. (2002) *Phys. Rev. Lett.*, **88**, 028301.

119 Lukas, S., Söhnchen, S., Witte, G., and Wöll, C. (2004) *Chem. Phys. Chem*, **5**, 266.

120 Casalis, L., Danisman, M.F., Nickel, B., Bracco, G., Toccoli, T., Iannotta, S., and Scoles, G. (2003) *Phys. Rev. Lett.*, **90**, 206101.

121 Kera, S., Yamane, H., Fukagawa, H., Hanatani, T., Okudaira, K.K., Seki, K., and Ueno, N. (2007) *J. Electron. Spectrosc. Relat. Phenom.*, **156**, 135.

122 Proehl, H., Dienel, T., Nitsche, R., and Fritz, T. (2004) *Phys. Rev. Lett.*, **93**, 097403.

123 Brinkmann, M., Graff, S., Straupé, C., Wittmann, J.-C., Chaumont, C., Nuesch, F., Aziz, A., Schaer, M., and Zuppiroli, L. (2003) *J. Phys. Chem. B*, **107**, 10531.

124 Okazaki, N. and Sambles, J.R. (2000) Extended Abstr. Int. Symp. Org. Mol. Electron. (Nagoya, Japan), May 18–19 pp. 66–67.

125 Faupel, F., Willecke, R., and Thran, A. (1998) *Mater. Sci. Eng.*, **R22**, 1.

126 Scharnberg, M., Hu, J., Kanzow, J., Ratzke, K., Adelung, R., Faupel, F., Pannemann, C., Hilleringmann, U., Meyer, S., and Pflaum, J. (2005) *Appl. Phys. Lett.*, **86**, 024104.

127 Sellner, S., Gerlach, A., Schreiber, F., Kelsch, M., Kasper, N., Dosch, H., Meyer, S., Pflaum, J., Fischer, M., and Gompf, B. (2004) *Adv. Mater.*, **16**, 1750.

128 Sellner, S., Gerlach, A., Schreiber, F., Kelsch, M., Kasper, N., Dosch, H., Meyer, S., Pflaum, J., Fischer, M., Gompf, B., and Ulbricht, G. (2006) *J. Mater. Res.*, **16**, 1750.

129 So, F.F., Forrest, S.R., Shi, Y.Q., and Steier, W.H. (1990) *Appl. Phys. Lett.*, **56**, 674.

130 Anderson, M.L., Williams, V.S., Schuerlein, T.J., Collins, G.E., England, C.D., Chau, L.-K., Lee, P.A., Nebesny, K. W., and Armstrong, N.R. (1994) *Surf. Sci.*, **307–309**, 551.

131 Akimichi, H., Inoshita, T., Hotta, S., Noge, H., and Sakaki, H. (1993) *Appl. Phys. Lett.*, **63**, 3158.

132 Nonaka, T., Mori, Y., Nagai, N., Nakagawa, Y., Saeda, M., Takahagi, T., and Ishitani, A. (1994) *Thin Solid Films*, **239**, 214.

133 Sellam, F., Schmitz-Hübsch, T., Toerker, M., Mannsfeld, S., Proehl, H., Fritz, T., Leo, K., Simpson, C., and Müllen, K. (2001) *Surf. Sci.*, **478**, 113.

134 Hoshino, A., Isoda, S., and Kobayashi, T. (1991) *J. Cryst. Growth*, **115**, 826.

135 Heutz, S., Salvan, G., Jones, T.S., and Zahn, D.R.T. (2003) *Adv. Mater.*, **15**, 1109.

136 Hinderhofer, A., and Schreiber, F. (2012) Organic-organic heterostructures: Concepts and applications. *Chem. Phys. Chem.* **13**, 628.

137 Hinderhofer, A., Gerlach, A., Kowarik, S., Zontone, F., Krug, J., and Schreiber, F. (2010) *Europhys. Lett.*, **91**, 56002.

138 Barrena, E., de Oteyza, D.G., Sellner, S., Dosch, H., Ossol, J.O., and Struth, B. (2006) *Phys. Rev. Lett.*, **97**, 076102.

139 Hinderhofer, A., Frank, C., Hosokai, T., Resta, A., Gerlach, A., and Schreiber, F. (2011). Structure and morphology of co-evaporated pentacene-perfluoropentacene thin films. *J. Chem. Phys.* **134**, 104702.

140 Vogel, J.-O., Salzmann, I., Duhm, S., Oehzelt, M., Rabe, J.P., and Koch, N. (2010) *J. Mater. Chem.*, **20**, 4055.

141 Salzmann, I., Duhm, S., Heimel, G., Rabe, J.P., Koch, N., Oehzelt, M., Sakamoto, Y., and Suzuki, T. (2008) *Langmuir*, **24**, 7294.

142 Salzmann, I., Duhm, S., Heimel, G., Oehzelt, M., Kniprath, R., Johnson, R.L., Rabe, J.P., and Koch, N. (2008) *J. Am. Chem. Soc.*, **130**, 12870.

143 Broch, K., Heinemeyer, U., Hinderhofer, A., Anger, F., Scholz, R., Gerlach, A., and Schreiber, F. (2011) Optical evidence for intermolecular coupling in mixed films of pentacene and perfluoropentacene. *Phys. Rev. B*, **83**, 245307.

144 Anger, F., Ossó, J. O., Heinemeyer, U., Broch, K., Scholz, R., Gerlach, A., and Schreiber, F. (2012) Photoluminescence spectroscopy of pure pentacene, perfluoropentacene and mixed thin films. *J. Chem. Phys.* **136**, 054701.

145 Kowarik, S., Broch, K., Hinderhofer, A., Schwartzberg, A., Ossó, J.O., Kilcoyne, D., Schreiber, F., and Leone, S.R. (2010) *J. Phys. Chem. C*, **114**, 13061.

146 Opitz, A., Ecker, B., Wagner, J., Hinderhofer, A., Schreiber, F., Manara, J., Pflaum, J., and Brütting, W. (2009) *Org. Electron.*, **10**, 1259.

147 Opitz, A., Wagner, J., Ecker, B., Hörmann, U., Kraus, M., Bronner, M., Brütting, W., Hinderhofer, A., and Schreiber, F. (2009) *Mater. Res. Soc. Proc.*, **1154**, 9.

148 Opitz, A., Wagner, J., Brütting, W., Hinderhofer, A., and Schreiber, F. (2009) *Phys. Stat. Sol. (a)*, **206**, 2683.

149 Opitz, A., Wagner, J., Brütting, W., Salzmann, I., Koch, N., Manara, J., Pflaum, J., Hinderhofer, A., and Schreiber, F. (2010) *IEEE J. Sel. Top. Quant.*, **99**, 1.

2
Electronic Structure of Interfaces with Conjugated Organic Materials

Norbert Koch

2.1
Introduction

The function and efficiency of most organic (opto)electronic devices, such as light-emitting diodes (OLEDs), thin-film transistors (OTFTs), and photovoltaic cells (OPVCs), are significantly depending on the electronic structure of the interfaces within the devices. For instance, in OLEDs and OTFTs, charges must be injected from electrodes into the organic semiconductor, which requires that energy barriers for charge injection must be minimized to achieve low operation voltages. Several layers of different organic semiconductors are used in OLEDs to separate charge injection/transport from the region of exciton formation and recombination, which necessitates proper adjustment of the energy levels at such organic heterojunctions to facilitate electron (hole) transport across the interface while holes (electrons) should be blocked simultaneously. The contact between an electron acceptor and an electron donor organic semiconductors represents the most important element of OPVCs because only at that very interface, the exciton dissociation can occur with high probability; once the electron and hole are separated, they can be transported to the respective electrodes. Consequently, the energy levels at these interfaces must be matched to allow optimal charge separation and thus energy conversion efficiency. The key electronic levels and energy parameters of such interfaces are summarized in Figure 2.1. Most commonly, the relative energy positions of electrode Fermi level (E_F) and the highest occupied molecular orbital (HOMO) as well as the lowest unoccupied molecular orbital (LUMO) are used to characterize interface energetics, because these levels predominantly govern charge transport and optical excitations. HOMO and LUMO are the frontier orbitals of the conjugated molecules that comprise organic semiconductors. In the case of long-chain polymers, these localized orbitals delocalize along the chains, which leads to the formation of one-dimensional bands (in full analogy to those known from inorganic semiconductors). Consequently, one can also use the terms valence band maximum and conduction band minimum when

Physics of Organic Semiconductors, Second Edition. Edited by Wolfgang Brütting and Chihaya Adachi

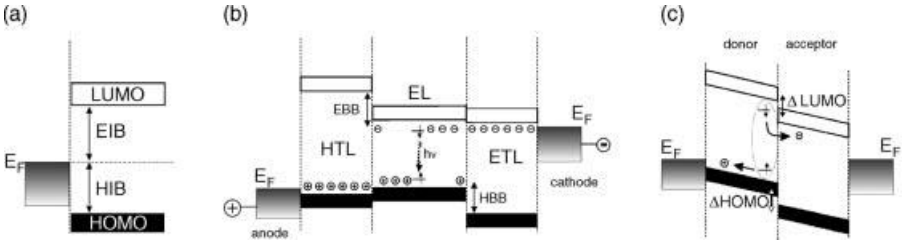

Figure 2.1 Definition of energy level parameters at interfaces with organic semiconductors. Gray shaded boxes: (metal) electrode density of states; open boxes: lowest unoccupied molecular orbital (LUMO); black boxes: highest unoccupied molecular orbital (HOMO), Fermi level (E_F). (a) Organic semiconductor/electrode interface with electron injection barrier (EIB) and hole injection barrier (HIB). (b) Multiheterolayer stack of an OLED comprising hole transport layer (HTL), electron transport layer (ETL), and electroluminescent layer (EL) with hole-blocking barrier (HBB) and electron-blocking barrier (EBB). (c) Donor/acceptor organic semiconductors in an OPVC with LUMO offset (ΔLUMO) and HOMO offset (ΔHOMO).

polymeric organic semiconductors are under consideration. As plotted in Figure 2.1a, the energy offset between E_F and the HOMO defines the hole injection barrier (HIB), and that between E_F and the LUMO corresponds to the electron injection barrier (EIB). Note that this frequently used terminology is a simplification that results from the way that HIB and EIB are measured by ultraviolet photoelectron spectroscopy (UPS) and inverse photoelectron spectroscopy (IPES), which are the most widely used methods to infer interface electronic properties. These methods do not yield the actual HOMO and LUMO energy positions of the organic semiconductor in the ground state, rather they provide the ionization and electron affinity (EA) levels, that is, the energies required to remove or add one electron to a conjugated molecule. The charged species of organic semiconductor molecules are the structurally and energetically relaxed (on the order of a few 100 meV compared to the neutral molecule energy levels) polarons, which represent the actual charge carriers. Therefore, UPS and IPES return the energy of the positive and negative polarons with respect to E_F, that is, the HIB and EIB indeed. Because the polaron levels are directly derived from the respective HOMO and LUMO levels, literature has thus adopted the use of the terms for the ground state rather than the charged state. Keeping this in mind should not lead to further ambiguities when studying pertinent literature.

Other frequently used interface energy level parameters include the electron-blocking barrier (EBB) and hole-blocking barrier (HBB) at organic semiconductor heterojunctions (Figure 2.1b exemplifying the situation in an OLED) and the energy offset between the two HOMO and the two LUMO levels (ΔHOMO and ΔLUMO) at donor/acceptor interfaces in OPVCs (Figure 2.1c).

As just discussed, the energy level alignment at interfaces in organic electronic devices is crucial to their function and efficiency. Consequently, device engineers long for rules that allow predicting the energy levels in devices based

on parameters of the individual materials, such as work function, ionization energy (IE), and electron affinity. For instance, a common vacuum level upon interface formation is often assumed. However, the physics and chemistry of interfaces involving conjugated materials can be rather complex, which causes simple models to predict energy levels of two materials in contact often unreliably and can result in errors on the order of several 100 meV. Thorough fundamental investigations of organic/inorganic and organic/organic interfaces over the past two decades have enabled, nonetheless, to derive a few general guidelines that – within limits – enable knowledge-based engineering of interface energy levels. In the following sections, some considerations regarding the intrinsic electronic properties of conjugated materials are discussed, followed by the most important physicochemical phenomena occurring upon interface formation, first of organic semiconductors with electrodes and then at organic semiconductor heterojunctions. Where applicable, methods to predictably tune the energy level alignment will also be introduced.

2.2
Energy Levels of Organic Semiconductors

While an isolated individual molecule has only one ionization potential, multiple values are generally found for molecules in ordered assemblies. The existence of a surface dipole (SD) built into molecular layers was reported [1]; its origin lies in details of the molecular electronic structure and its magnitude depends on the orientation of molecules relative to the surface of an ordered assembly. As prototypical planar conjugated molecule with an extended π-electron system, the simplest aromatic molecule benzene (C_6H_6) is now used to introduce the general concept of molecular electrostatics. The π-electrons reside in molecular orbitals (MOs) that have a node in the plane of the molecule and extend into space on either side, as indicated in Figure 2.2a. In contrast, the atomic nuclei and the charge distribution of all other electrons, that is, those residing in core- and σ-orbitals, are centered in the molecular plane. This leads to the situation where negatively charged π-clouds on either side of the symmetry plane are compensated by a positive charge within the plane of the overall charge-neutral molecule. This particular arrangement of charges corresponds to a quadrupole, which can also be seen as two dipoles μ pointing toward each other (Figure 2.2a). A 3D surface plot of the electron potential energy in a plane cutting through the molecule (Figure 2.2b) reveals regions of higher potential energy directly outside the negatively charged π-electron clouds, whereas regions of lower potential energy are next to the hydrogen atoms within the plane of the molecule. Importantly, the potential around the isolated benzene molecule converges rapidly (within a few angstroms) in all directions toward one common value, which corresponds to the vacuum level far away from any matter.

A molecular solid can thus be represented as an assembly of many such quadrupolar charge distributions, which has profound consequences when the molecules within the solid are not randomly oriented but preferentially ordered or even

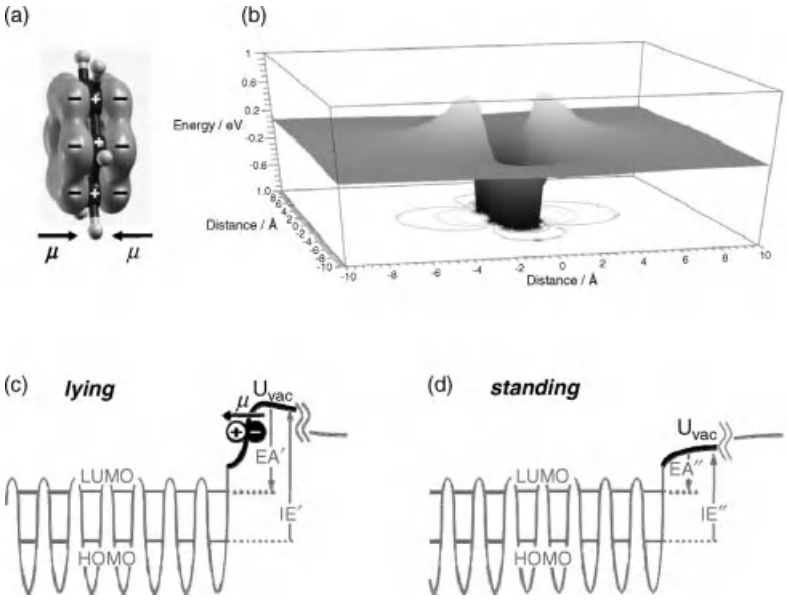

Figure 2.2 (a) Schematic of the quadrupolar charge distribution within a benzene (C_6H_6) molecule. (b) Plot of the calculated electron potential energy in a plane cutting through the molecule. (c) Sketch of the energy levels in an ordered molecular assembly where the planes of the molecules coincide with the exposed surface. The dipole layer (μ) with the negative π-electron clouds above the positive molecular planes terminates the surface. Also indicated are the highest occupied (HOMO) and the lowest unoccupied molecular orbitals (LUMO) as well as the ionization energy (IE′), the electron affinity (EA′), and the electron potential energy in the vacuum immediately outside the surface (U_{vac}). (d) Same as (c) with the planes of the constituent molecules perpendicular to the exposed surface. The energy differences from HOMO and LUMO to U_{vac}, IE″, and EA″ are smaller than that in (c). Reprinted with permission from Ref. [2].

crystalline. The collective surface electrostatic potential created by all molecules will depend critically on the molecular orientation at the surface. For instance, if the benzene molecules are oriented on the surface such that the molecular plane is parallel to the surface (i.e., lying), the electron potential energy just outside the surface (U_{vac}) is raised by the surface-terminating dipolar layer μ, as shown in Figure 2.2c. Far away from the surface, the electrostatic potential will yet assume the common vacuum level, resulting in a potential well-being present at the surface of the organic solid. Recalling the definition of ionization energy (electron affinity) as the energy required to remove from (attach to) the sample an electron into (from) infinite distance, it transpires that the IE and EA values for this lying molecular surface orientation are increased by the amount of the potential well that electrons have to overcome, resulting in IE′ and EA′. On the other hand, U_{vac} is lower than the common vacuum level at infinity when the benzene molecules are upright standing at the surface of the solid, as depicted in Figure 2.2d. Consequently, the values IE″ and EA″ for such a molecular arrangement are lower than

those found for the lying molecule case. The quadrupolar charge distribution of benzene can readily be extended to practically relevant molecules in organic electronics, such as pentacene (PEN) or α-sexithienylene. For ordered molecular layers of these, the differences in IE and EA for lying and standing surface orientation were found to be 0.4 eV [1].

Numerous molecules have, in addition to the electrostatic quadrupoles resulting from the π-electron distribution, strong intramolecular dipoles that also contribute to the surface electrostatic potential U_{vac}. In addition, molecular orientations different from just lying and standing result on yet other IE and EA values. For example, perfluoropentacene (PFP) (Figure 2.3, inset), which is the completely fluorinated analogue to pentacene, grows lying in the first monolayer on clean metal surfaces [3]. The bottom UPS spectrum in Figure 2.3 is that of a lying PFP monolayer on Au (111) [4]. The first clear peak is attributed to the molecular HOMO with an onset that yields $IE' = 5.80$ eV. For multilayer PFP, the molecules are still oriented with their long molecular axes parallel to the substrate, but with the molecular plane inclined relative to the surface (Figure 2.3, center), that is, the molecules assume their typical "herringbone" arrangement as in the bulk crystal structure [5]. As the entire molecular periphery is terminated with electronegative fluorine atoms, a surface dipole layer (negative on the outside) is thus formed, which raises U_{vac} above the sample. Consequently, the ionization energy increases to $IE_{tilted} = 6.00$ eV. Layers of PFP can be grown with the long molecular axes standing (almost) upright on silicon oxide surfaces, yielding a UPS spectrum as shown in the topmost trace

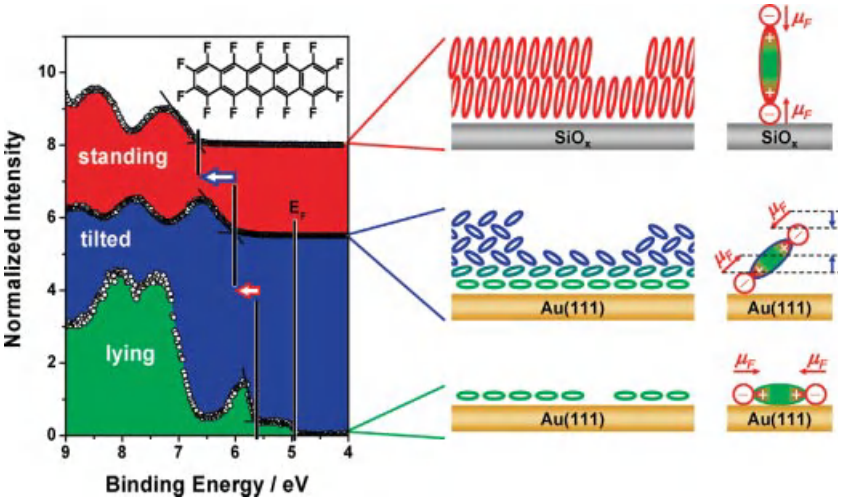

Figure 2.3 Experimental UPS spectra of perfluoropentacene (*inset*: chemical structure). The spectrum of a lying monolayer on Au(111) is shown at the bottom, that of inclined molecules in the multilayer in the center, and that of a film of standing molecules on silicon oxide at the top. On metals, the Fermi level is marked with E_F. The center panels indicate the molecular orientation in each case and the right panels highlight the respective orientation of the dipole moment μ_F, arising from the polar intramolecular F–C bonds relative to the surface and its projection on the surface normal. Reprinted with permission from Ref. [6].

of Figure 2.3. As the projection of the polar F–C bonds onto the surface normal is higher in this case than for the "tilted" molecules, the ionization energy further increases to $IE'' = 6.65$ eV. As expected, the situation is now reversed compared to pentacene. There, layers of standing molecules have a lower IE than layers of lying molecules due to the surface dipole caused by the π-electron clouds. In contrast, layers of standing PFP have a higher IE than layers of lying molecules, owing to the presence of intramolecular polar bonds that, collectively, form a surface dipole layer.

In all further discussions of the energy levels at interfaces with ordered molecular layers, we thus have always to consider molecular orientation as a decisive factor that will influence the actually obtained level alignment. Only for organic semiconductors that exhibit strictly amorphous solids, the above considerations need not be taken into account.

2.3
Interfaces between Organic Semiconductors and Electrodes

Barriers for charge injection at organic/electrode interfaces have commonly been estimated by assuming "vacuum level (E_{vac}) alignment" across the interface (i.e., the Schottky–Mott limit, as shown in Figure 2.4a) using values for electrode work function (ϕ) and organic material ionization energy and electron affinity determined separately for individual samples. The neglect of physicochemical processes occurring at such interfaces often results in wrong barrier height (HIB and EIB) values (sometimes more than 1 eV) estimated from vacuum level alignment, except for justified cases (Section 2.3.2). Instead, significant work function changes $\Delta\phi$ after the deposition of organic molecules were found, predominantly for atomically clean metal surfaces under ultrahigh vacuum (UHV) conditions. Consequently, the change of ϕ results in concomitantly different HIB′ and EIB′ values compared to vacuum level alignment (Figure 2.4b). $\Delta\phi$ can have positive or negative sign,

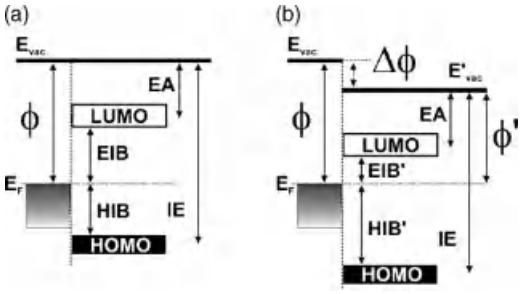

Figure 2.4 Organic semiconductor/electrode interface energy levels for Schottky–Mott limit ("vacuum level E_{vac} alignment" (a)) and the general case involving interface formation-induced work function changes $\Delta\phi$ (b).

depending on the specific materials in contact. The origin of this phenomenon, often also termed "vacuum level shift" or "interface dipole" in literature, is – in general terms – a rearrangement of the electron density distribution at the metal surface *and* on the molecules due to the mutual interaction at the interface, and thus inducing changes in the electrostatic potential above the surface. The individual processes that lead to $\Delta\phi$ can be manifold, and will be discussed in the following. Given that atomically clean metal electrodes in UHV have no practical relevance for fabrication of organic electronic devices, which typically occurs in high vacuum (HV) or inert gas, this section is rather brief, and emphasis will be given to application-relevant electrode materials, which may include a certain level of contamination from ambient.

2.3.1
Atomically Clean Metal Electrodes

The interaction between conjugated molecules and clean metal surfaces is a rather complex issue. Despite the huge number of material systems that have been investigated, no generally applicable rules to predict the energy level alignment have yet emerged. The possible types of interaction could be classified into physisorption (van der Waals) or chemisorption with certain degrees of charge transfer and covalent bond formation. A physisorbed molecule retains its chemical integrity and orbital structure upon adsorption. If chemisorption occurs, the ordering of orbitals of the adsorbed molecule differs from that of the free (gas phase) molecule, due to hybridization with electron wave functions of the metal and a change in orbital population. Chemisorption can often be readily identified due to the appearance of a new density of states (DOS), for instance, in UPS and IPES experiments, different from those of the bulk molecular solid and the clean metal.

For the case of weak (physisorptive) organic–metal interaction (e.g., occurring at many interfaces between conjugated organic materials and clean Au), a qualitative picture of the interface energetics is shown in Figure 2.5. On the left-hand side, the clean metal surface and the molecule with its LUMO and HOMO levels are at large distance without interaction. The metal ϕ has two contributions: the bulk chemical potential of electrons relative to the mean electrostatic potential inside the metal

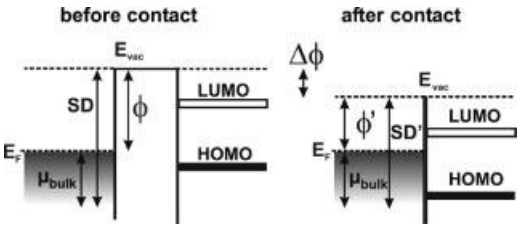

Figure 2.5 Molecule physisorption-induced metal surface dipole (SD) changes, leading to the effective work function change $\Delta\phi$.

μ_{bulk} and the surface dipole SD, which is due to electrons spilling out into the vacuum at the free surface [7]; thus, $\phi = \text{SD} - \mu_{\text{bulk}}$. The HIB/EIB could easily be estimated from ϕ and IE/EA assuming vacuum level alignment. However, it is observed that after contact (i.e., molecule adsorption), ϕ is *reduced* by $\Delta\phi$ to ϕ', which leads to a higher HIB′ and lower EIB′ than expected. Effectively, the SD of the clean metal surface is reduced to SD′ due to the "pushback effect" (also known as "cushion effect" or Pauli repulsion [8,9]); the adsorption of the organic molecule "pushes back" the electron density of the metal surface that was spilling out into vacuum. The magnitude of the metal surface electron pushback depends on the details of how the molecules adsorb on the surface, for example, on the molecule conformation, bonding distance, and surface density. Typical values of $\Delta\phi$ for clean Au electrodes upon organic semiconductor deposition are in the range of 0.5–1.2 eV. Since ϕ of clean Au in UHV is typically 5.4 eV, this means that the effective ϕ of a gold electrode after molecule adsorption is only 4.2–4.9 eV, that is, much less favorable for hole injection than expected. On other metal surfaces, such as Ag and Cu, $\Delta\phi$ is typically on the order of 0.5 eV. Purely physisorptive interactions between conjugated materials and these metals, as well as those with even lower intrinsic work function are found only in rare cases because of the higher chemical reactivity of such metals.

The exact change in total electron density distribution upon pushback at the organic–metal interface can be rather complex [9], and even more so when strong chemical interactions occur. In the following, a prototypical example for strong conjugated molecule–metal interaction is discussed. We consider the conjugated molecule tetrafluoro-tetracyanoquinodimethane (F4TCNQ) with an IE of 5.24 eV [10] on a Cu(111) surface with a ϕ of 5.0 eV [11]. Assuming a common vacuum level at this interface would place the LUMO of F4TCNQ *below* the Fermi level (E_F) of Cu, that is, the lowest unoccupied level of the molecule being below filled states of the metal. In the Schottky–Mott limit, this is thus a nonequilibrium situation, and charge transfer across the interface is needed to establish equilibrium. In the simplest possible model for interface charge transfer, one- or two-electron transfer from the metal into the LUMO of F4TCNQ may be assumed, resulting in the molecular negative polaron (anion) or bipolaron (dianion), with the now (partially) filled LUMO shifted below E_F. Photoemission spectroscopy in conjunction with theoretical modeling indeed showed that a new DOS just below E_F appeared upon F4TCNQ deposition on Cu(111), which can be derived from the filled molecular LUMO (Figure 2.6a) [11]. Since this DOS did not cross E_F, which is expected for a negative polaron state, it can be concluded that the LUMO is filled with two electrons, that is, bipolarons might be formed. The negatively charged molecule and the positive charge remaining in the metal result in a reaction-induced surface dipole, whose magnitude can be estimated by taking into account a typical binding distance of conjugated molecules on metal surfaces of 2.5 Å. Using the Helmholtz equation,

$$\Delta\phi = \frac{eN\mu}{\varepsilon_0\varepsilon} \tag{2.1}$$

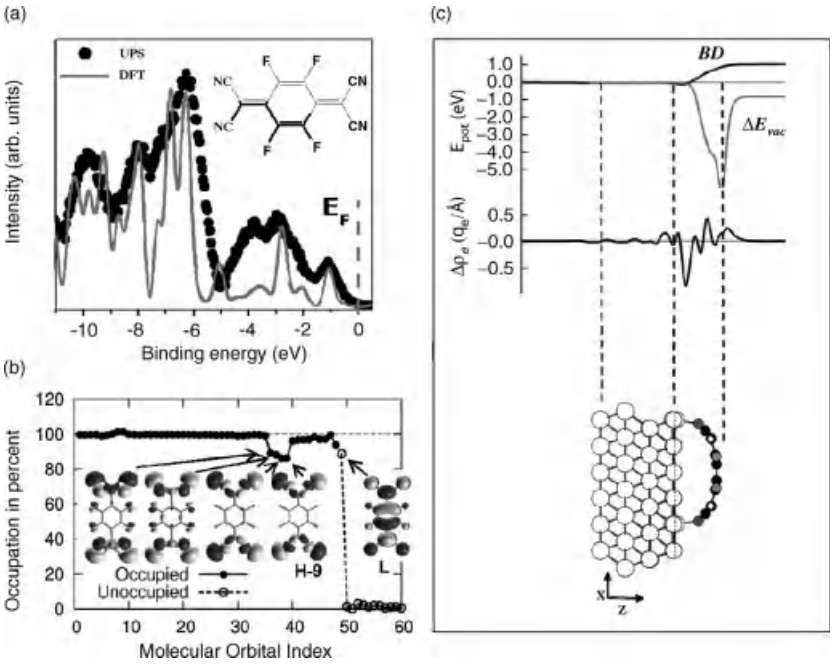

Figure 2.6 Chemisorbed conjugated molecule on a metal electrode. (a) UPS spectrum (circles) and DFT-calculated DOS (solid line) of the F4TCNQ layer on Cu(111). The experimental spectrum was obtained by subtracting the UPS signal of the bare Cu(111) surface from that of monolayer covered surface. The calculated DOS does not take into account photoemission cross sections. (b) Occupation (in percent) of the lowest 60 F4TCNQ molecular orbitals after adsorption on Cu(111). The full (open) circles and solid (dashed) lines correspond to the orbitals that are occupied (unoccupied) in the isolated molecule. (c) Charge rearrangement $\Delta\varrho_e$ and related potential energy E_{pot} of an electron (black lines) along the direction of the surface normal z. q_e is the charge of an electron. $\Delta\varrho_e$ is calculated by subtracting the noninteracting electron density from the electron density of the interacting molecule/metal system and averaging in the x–y plane. ΔE_{vac} represents the geometry-induced contribution to the work function modification and BD is the bond dipole due to charge density rearrangement. (Adapted from Ref. [11]).

which relates a dipole induced the surface work function change $\Delta\phi$ to the area–density of dipoles (N) and the dipole moment (μ) (with elementary charge e, relative permittivity ε, and vacuum permittivity ε_0), $\Delta\phi$ for a full monolayer of F4TCNQ on Cu(111) can be estimated to be about 5 eV. However, the experiment yielded a $\Delta\phi$ of only 0.6 eV, evidencing that the simple model employing one- or two-electron transfer is not adequate. Two important phenomena occurring at this interface are missing: details of the adsorption-induced interfacial charge density rearrangement and the molecular conformation changes. The chemical interaction between F4TCNQ and Cu(111) is thus far more complex. Detailed theoretical modeling showed that a strong hybridization of (also deep lying) molecular orbitals and metal

states occurred, involving bidirectional charge transfer across the interface. This is represented through the orbital occupation analysis in Figure 2.6b, where the calculated DOS of the interacting molecule/metal system was partitioned into contributions from the molecular orbitals of the isolated molecule, and the degree of occupation of the individual orbitals was obtained via integration of the projections up to the calculated E_F [11]. This reveals that the original empty LUMO π-electron orbital of F4TCNQ becomes filled to 90% (1.8 electrons) through charge transfer from Cu, but at the same time deeper lying σ-orbitals become depleted of electrons. Summing over all molecular orbitals, the net charge on F4TCNQ is only 0.6 electrons. Furthermore, the molecule does not remain planar upon adsorption on the metal surface, but it becomes significantly distorted, as schematically shown in Figure 2.6c. The negatively charged cyano groups of the molecule are bent toward the metal, which induces a dipole that actually counteracts that of the net charge transfer. This conformation effectively decreases the work function (ΔE_{vac} in Figure 2.3c). In conjunction with the dipole due to charge transfer (the bond dipole BD), the calculated $\Delta\phi$ is 0.7 eV, in good agreement with the experimental value of 0.6 eV.

It is important to emphasize that many studies on organic/metal interfaces, similar to the ones mentioned, were conducted starting from atomically clean metal surfaces in UHV (residual pressure $<10^{-9}$ mbar), which is markedly different from the situations that prevail during the actual organic device fabrication. In high vacuum (typically 10^{-6} mbar) or inert gas atmospheres, and also in air, any surface is covered with about a monolayer of various molecular species (e.g., hydrocarbons, oxygen, and water) within seconds. As shown above, even physisorbed molecules induce significant changes of ϕ. In addition, some adsorbed species may have permanent dipoles with some preferred orientation relative to the surface, leading to additional ϕ changes ($\Delta\phi$) according to the Helmholtz equation (2.1). For instance, while an atomically clean Au surface has a ϕ of $\sim$5.4 eV in UHV, it drops to $\sim$4.5–4.9 eV after exposure to HV or air, as a rule of thumb (the exact value will depend on the composition of the actual atmosphere) [12,13]. For more reactive metals, the formation of a surface oxide proceeds rapidly, forming a comparably inert interlayer, which electronically decouples molecules and metal. Molecules or polymers deposited on such "dirty" metal surfaces exhibit an energy level alignment that is markedly different from that obtained on clean surfaces in UHV. As a consequence, energy level alignment mechanisms differ from those of atomically clean metals, and the chemically more inert character of contaminated metals even permits employing rather simple rules for energy level alignment at organic/electrode contacts, as is presented in Section 2.3.

Another kind of "contamination," however, introduced on purpose, can significantly lower the HIB at organic/Au interfaces: the exposure of Au surfaces to UV/ozone. Such treatment leads to the formation of a thin surface Au oxide layer that is accompanied by the adsorption of oxidized hydrocarbon species. This combination leads to an increase of ϕ to up to 5.5 eV, that is, even larger than ϕ of clean Au in UHV, which is stable in air for up to an hour. When depositing conjugated

molecular materials or polymers onto UV/ozone-treated Au, the HIB can be reduced significantly (e.g., by 1.4 eV for the blue electroluminescent organic semiconductor *p*-sexiphenyl) [12] compared to both atomically clean and air-exposed Au. Furthermore, the energy level alignment achieved after deposition of the organic semiconductor layer is remarkably stable even in air over many days. Contrary to that, an organic/metal interface that was fabricated under UHV conditions changes its energy levels upon exposure to air, mainly because oxygen and/or water can diffuse through a thin organic film toward the metal, and thus modifies its effective work function.

2.3.2
Application-Relevant Electrodes

To keep manufacturing and material costs for organic (opto)electronic devices at an acceptable level, common fabrication environments are high vacuum, inert gas atmospheres, and ambient air (e.g., for printed electronics). Practically relevant electrode materials include polycrystalline (evaporated, sputtered, or printed) metals, transparent conductive oxides [the most frequently used being indium tin oxide (ITO)], and conductive polymers [the presently dominating one being poly(3,4-ethylenedioxythiophene):poly(styrenesulfonate); (PEDT:PSS)]. All these electrode materials and the employed film fabrication methods render the surfaces chemically rather inert, either due to intrinsic properties or due to ubiquitous surface contamination with oxides/hydrocarbons. Consequently, the electronic coupling between these electrodes and conjugated materials is weak, and a comparably simple general behavior for energy level alignment was found. Figure 2.7 shows how HIB/EIB values depend on electrode ϕ. Apparently, there is a range of ϕ values where interface energetics essentially follow the Schottky–Mott limit, that is, the HIB decreases by the same amount as the electrode ϕ increases (and the EIB increases by that same amount) and the vacuum level alignment prevails (not valid

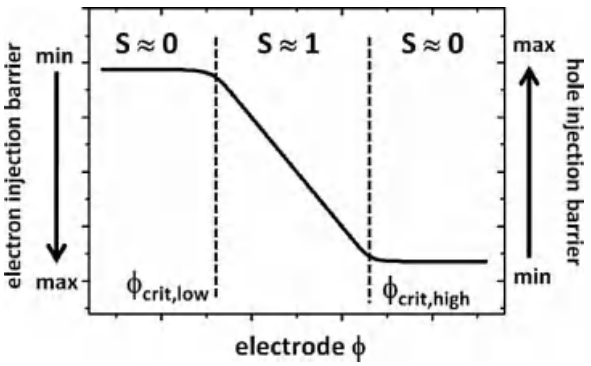

Figure 2.7 Dependence of electron and hole injection barrier heights of organic semiconductors on the work function of chemically inert electrodes.

for clean metal surfaces) (Figure 2.4). The behavior of HIB/EIB as function of ϕ can be characterized by the S parameter:

$$S = \frac{\mathrm{d}E_{\mathrm{F}}^{\mathrm{gap}}}{\mathrm{d}\phi} \tag{2.2}$$

which yields the shift of the electrode Fermi level in the energy gap of the organic semiconductor ($E_{\mathrm{F}}^{\mathrm{gap}}$) as ϕ changes [14]. For a certain ϕ range, the Schottky–Mott limit applies $S \approx 1$. However, at the upper and lower critical ϕ values ($\phi_{\mathrm{crit,high}}$ and $\phi_{\mathrm{crit,low}}$), there is a transition to $S \approx 0$. This means that the HIB (EIB) does not change notably upon further increasing (decreasing) the electrode ϕ, and $E_{\mathrm{F}}^{\mathrm{gap}}$ remains essentially at the same position within the gap of the semiconductor; as a result, vacuum level alignment does no longer occur and $\Delta\phi$ at such interfaces assumes a value that equals the difference of ϕ_{crit} and ϕ of the electrode before contact. This is referred to as Fermi level pinned regime. The reason for E_{F} pinning to occur beyond ϕ_{crit} is that due to the high (low) electrode work function, E_{F} moves into the occupied (unoccupied) DOS of the organic semiconductor. This, as discussed above, results in a nonequilibrium situation, which is brought into equilibrium by interfacial charge transfer. In principle, one might expect that E_{F} can actually approach the HOMO/LUMO or valence band/conduction band edges closely, resulting in zero HIB or EIB values. However, in UPS/IPES experiments, finite values for HIB/EIB on the order of a few 100 meV are predominantly found [12,15–17]. At the time of writing this chapter, the origin of E_{F} pinning at comparably large energy distances from the frontier energy levels is not unequivocally resolved, and the presently discussed models will be summarized in the following. The first one is frequently referred to as the integer charge transfer (ICT) model [18], based on the justified assumption that in the absence of interfacial chemical reactions, only integer charges can be transferred (e.g., via tunneling) between the electrode and the organic semiconductor. Consequently, equilibrium is established by the formation of positive or negative polarons (depending on whether pinning occurs at $\phi_{\mathrm{crit,high}}$ and $\phi_{\mathrm{crit,low}}$) in the organic material right at the contact. Theoretical modeling of conjugated organic materials predicted that the energy levels of these charged entities come to lie in the gap of the neutral organic material, as sketched in Figure 2.8. For the positive polaron P_{pos}, one electron is removed from the HOMO of the neutral molecule N; while for the negative polaron P_{neg}, one electron is added to the LUMO of N. In the ICT model, these polaron levels are the

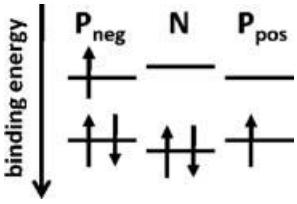

Figure 2.8 Schematic ground-state energy levels of a neutral (N) molecule and a negative (P_{neg}) and a positive (P_{pos}) polaron.

energy levels at which E_F gets pinned. But since only a small fraction of a molecular layer in contact with the electrode needs to be in these charged states to induce $\Delta\phi$ sufficient to establish equilibrium, these levels are not observed in experiments, and only the levels of the majority N are observed, which have then indeed a binding energy typically few 100 meV (polaron relaxation energy) [17,18] below E_F. Most likely, the ICT model can be extended as certain ambiguities exist, such as that the positive polaron states have not been clearly observed to date, and the energy distance from E_F at which pinning occurs is not found constant for a given material but may vary by several 100 meV in different experiments.

An appropriate extension may be based on the model suggested by Hwang *et al.* [19,20]. Here, the density of states of an organic semiconductor is not assumed to be as sharp as typically plotted in schematics, but it takes into account a broadening of the DOS into the energy gap. The existence of such tail states into the gap of an actual organic material is realistic because structural disorder and/or chemical impurities indeed result in such intragap states. For instance, pentacene, as a prototypical example for rodlike molecules, can form highly ordered layered structures (with almost upright standing molecules) on even quite rough surfaces. Actually, an individual layer can conform very tightly to substrate morphological features, covering the surface like a "soft carpet." This was observed for substrates such as insulating [21] and conducting polymers [22]. This ability to include vertical offsets between neighboring molecules is exemplified in the AFM micrograph and side view sketch in Figure 2.9 for pentacene single-layer islands on native silicon oxide with bunched steps of Si(111) atomic height (about 3 Å). The single molecular height islands extend over many substrate steps, and no apparent influence of the substrate morphology can be observed. Such vertical sliding of neighboring pentacene molecules along the long molecular axis can induce traps for electrons and holes on the order of 100 meV, as was quantified theoretically (Figure 2.9c) [23].

The exact energy and density distribution of such tail states (gap states) is *a priori* unknown, and will vary from sample to sample; for modeling, often Gaussian or exponential forms have been assumed [25,26]. To explain E_F pinning for a high work function electrode, the tail states would come to lie above E_F before contact and will thus be filled with holes up to the point where $\Delta\phi$ is sufficient to ascertain equilibrium, which then pins E_F, as shown in Figure 2.10. This scenario can successfully explain why the majority DOS is usually found far from E_F and why the pinning energy often varies depending on the specific sample (i.e., different degrees of disorder or chemical impurities).

2.3.2.1 Low Work Function Electrodes

The most straightforward choice for electrodes with low ϕ (to facilitate good electron injection) are metals such as Al, Mg (also Mg:Ag mixtures), Ca, and Ba. As these metals are highly reactive, tabulated values of ϕ (usually determined in UHV) can be rather misleading when estimating EIBs. First, these metals often react with organic semiconductors, and second, residual oxygen in the vacuum vessel during metal deposition in HV (or subsequent exposure to air) leads to (partial) metal oxide formation [27], whose work function can be rather different from that of the

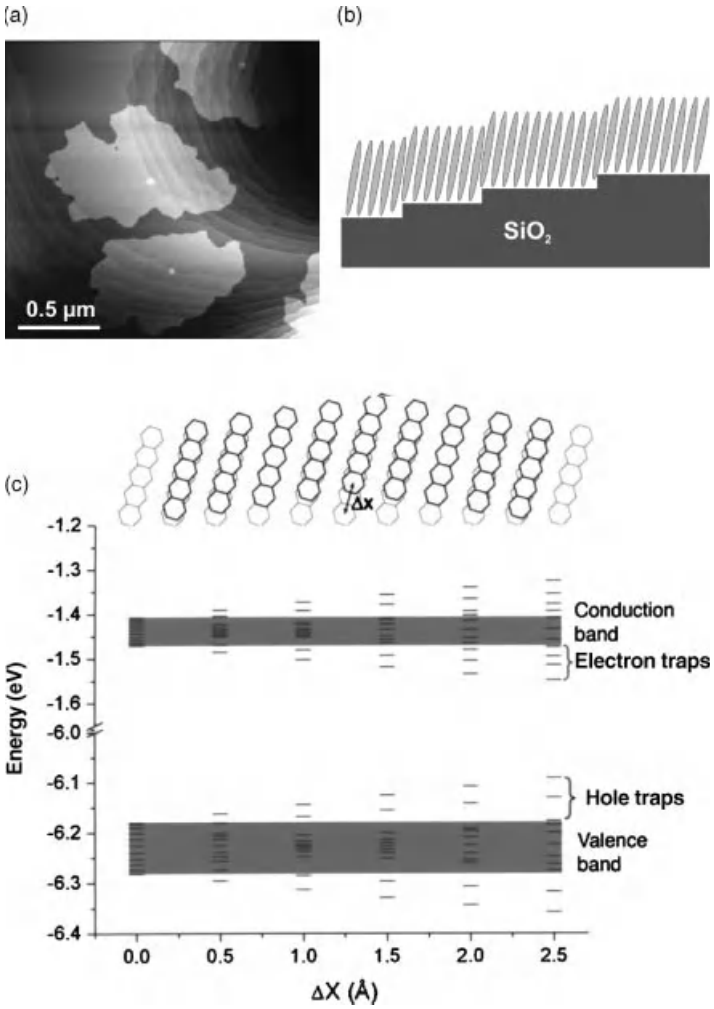

Figure 2.9 AFM image (a) of submonolayer pentacene on native silicon oxide with atomic steps. The pentacene islands extend over many steps (step height: 3 Å), as indicated in the schematic side view (b). (c) Illustration of sliding defect (by DX in the vertical direction)-induced local energy variations for pentacene from theoretical modeling. Gray molecules are perfectly stacked, while darker molecules represent displaced molecules. Reprinted with permission from Ref. [24].

pristine metal. For instance, one of the most prominent luminescent and electron-transporting materials, Alq_3, reacts with Al and Mg to form organometallic complexes [28–33], which exhibit intragap states that pin E_F. Also, many other conjugated materials [34–36] react with Al and Mg, leading to a new distribution of occupied and unoccupied levels at such organic/metal interfaces. The description of details of the interaction depends very much on the actual material pairing, and cannot be readily generalized. Furthermore, there are examples of organic

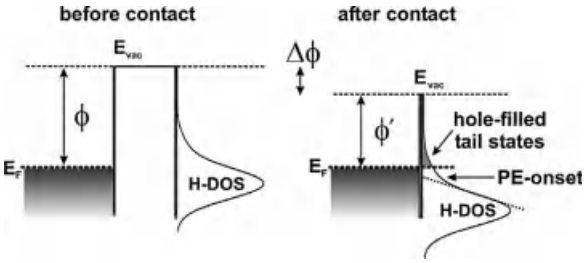

Figure 2.10 Schematic organic/electrode interface energy levels before and after contact. The frontier-occupied organic semiconductor energy levels (H-DOS) are broadened (e.g., due to structural disorder) (see text). Pinning at E_F occurs due to filling of tail states with holes. PE onset indicates the onset of majority of DOS observed in photoemission experiments.

materials that do not react with Al (*p*-sexiphenyl [37], methyl-substituted ladder-type poly(*p*-phenylene)) [38] or Mg [39]. However, a more general trend for the interaction with conjugated systems can be stated for alkali and alkaline earth metals, which are also frequently used to improve electron injection. Commonly, the interaction is mainly governed by charge transfer from the metal atoms to the LUMO of the conjugated system, resulting in the formation of polarons and/or bipolarons stabilized by the presence of the metal counterions) (cf. Figure 2.8), which are occupied states within the otherwise empty energy gap [40–46]. Bipolarons are formed by adding another charge to the polaron states, that is, leading to a doubly occupied (empty) LUMO (HOMO)-derived state. The Fermi level becomes pinned at these states, and as they are close in energy to the LUMO of the pristine conjugated system (typically within <0.4 eV), rather low EIBs can be achieved.

However, since metal cathodes are typically evaporated onto the organic layer, unwanted diffusion of metal atoms into the organic layer has to be prevented (e.g., the presence of metal atoms and ubiquitous chemical reactions with molecules can quench luminescence). Several studies clearly show that metal atom can diffuse several 10 nm into an organic layer [47–49]. In this context, the use of alkali halides (e.g., LiF and CsF) has turned out to be very helpful in confining the organic/metal-reacted region. A detailed analysis has suggested that alkali halides undergo dissociation when Al is deposited on top, thus releasing the alkali atom to react with the organic semiconductor in immediate proximity [50–53]. A particularly interesting low work function metal is Sm ($\phi \approx 2.8$ eV). In conjunction with several organic semiconductors, Sm provides for low electron injection barriers; and due to the comparably large atom diameter, diffusion into the organic bulk seems to be limited [54,55].

2.3.2.2 **Conducting Polymer Electrodes**

The insertion of an intrinsically conducting polymer layer between a highly conductive inorganic electrode (e.g., transparent conductive oxide, such as indium tin oxide) and the active organic semiconductor layer has proven to be very favorable for hole injection. In addition to doped polyaniline [56,57], the prototypical conductive polymer used in the majority of applications today is

poly(3,4-ethylenedioxythiophene):poly(styrenesulfonate) (chemical structure is shown in Figure 2.11) [58], which is available in various formulations. In this polymer mixture, positive charges on PEDT are stabilized by negative charges on PSS, which renders the conjugated PEDT highly conductive. The PEDT part of the mixture is hydrophobic and PSS is hydrophilic, which results in the formation of few nanometer-sized core–shell agglomerates in aqueous dispersions, where PSS forms the outer shell. After spin-coating and drying, the conductive PEDT-rich domains are separated by insulating PSS-rich domains. The spatial distribution of alternating volumes of high and low local conductivity can be changed by varying the ratio of PEDT:PSS [59,60] and the processing conditions, including the use of additives. By controlling this nanomorphology, it is possible to change the conductivity of thin films, ranging from about 10^{-5} S/cm (PEDT:PSS ratio of 1 : 20) to over 100 S/cm (1 : 2.5). While low-conductivity polymers are mainly used for applications in flat panel displays (to reduce cross talk between pixels), the high-conductivity variants even allow to completely replace the inorganic supporting electrode. The properties of conductive polymers lead to two primary beneficial effects when used in organic electronic devices. First, the use of a few 10 nm thick conductive polymer layer significantly flattens the comparably rough inorganic electrode surface (typically RMS roughness of PEDT:PSS about 1 nm), thus providing a smooth surface for the deposition of subsequent layers. This reduces the probability of microshort formation in devices during operation. Second, high ϕ values can be obtained with conductive polymers, resulting in low hole injection barriers. Reported values of PEDT:PSS films ϕ vary from about 4.8 eV up to over 6.0 eV. Care has to be taken when comparing results obtained from samples/devices comprising PEDT:PSS when different processing conditions were used. It was shown that ϕ of PEDT:PSS is influenced by water in spin-coated thin films [61]. As shown in Figure 2.11, annealing (in UHV) of PEDT:PSS films spin-cast on ITO changes ϕ

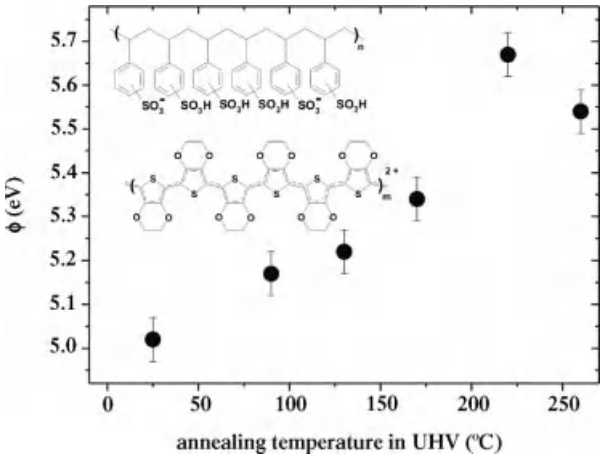

Figure 2.11 Work function (ϕ) variation of PEDT:PSS (chemical structure shown as inset) as function of annealing temperature in ultrahigh vacuum (UHV).

from about 5.0 eV (room temperature drying) to over 5.6 eV (annealed at 220 °C), indicating that the intrinsic work function of this polymer can be much higher than that of atomically clean Au. Subsequent exposure of high ϕ samples to water vapor reduced ϕ to its original value of 5.0 eV. For comparison, PEDT:PSS samples annealed in air at 200 °C typically exhibit a ϕ of 5.2 eV. Samples that were UHV annealed to have $\phi = 5.6$ eV and then exposed to the simulated atmosphere of a typical inert gas box (residual water content of about 1 ppm H_2O) for 30 min also had a ϕ of 5.2 eV, indicating that already this level of residual water content of the atmosphere is sufficient to saturate PEDT:PSS uptake of water. The changes in ϕ (and thus water content) are then accompanied by changes of the polymer surface composition. While air- and vacuum-annealed sample surfaces are PSS rich, water vapor-exposed samples had an increased PEDT concentration near the surface. This water-induced swelling can partially account for the observed ϕ changes, as it was suggested that PSS surface-rich PEDT:PSS films have higher ϕ because of the preferential orientation of near-surface dipoles (due to the presence of $PEDT^+$ and PSS^-) [22]; swelling modifies this preferential dipole orientation. In addition, the incorporation of water in the polymer film may reduce the effect of the local dipoles, as the dipole-induced work function changes scale with $1/\varepsilon$ (Eq. (2.1)), and the dielectric constant ε of water is rather large ($\varepsilon_{H_2O} = 78$). Even higher ϕ conductive polymers are available, which often comprise fluorinated hydrocarbon polymer species additives, yielding ϕ values of ~6 eV [15,17]. According to the energy level alignment rules outlined above and shown in Figure 2.7, the use of high ϕ electrodes is preferred in devices, even when the critical ϕ for E_F pinning has already been reached. For instance, the critical high ϕ for the conjugated molecular donor diindenoperylene (DIP) is 4.9 eV [62], which pins the HOMO onset of 0.45 eV below E_F. When instead a high ϕ polymer electrode (5.7 eV) is used, the energy levels only at the intimate interface between the DIP and the polymer are modified. Charge transfer-induced density of states of only 0.3 eV below E_F was found for the DIP in direct contact with this electrode, but the HIB into bulk DIP was not affected. However, the positive charges induced in the DIP close to the electrode were sufficient to reduce the contact resistance substantially, as evidenced by the improved electrical characteristics of photovoltaic cells employing the high ϕ electrode [62].

2.3.2.3 Adjusting the Energy Level Alignment at Electrodes

For practical reasons, certain materials like metals or conductive oxides will be chosen as electrodes. However, often adjusting ϕ of a given electrode material to render good electrical contact to the organic semiconductors is desired. In general, one would strive to reach ϕ values above (below) $\phi_{crit,high}$ ($\phi_{crit,low}$) of the organic material to reach the E_F pinning regime. As a result, a number of methods have been devised to change ϕ of metal, conductive oxide, and conductive polymer electrodes in a rational manner. The conceptual base for most methods is the Helmholtz equation (Eq. (2.1)), by anchoring dipoles on an electrode surface. The work function of the electrode can be adjusted via the magnitude and direction of the dipole moment μ perpendicular to the surface plane and the dipole area–density N. For a given dipolar species, ϕ of a surface will vary as shown in Figure 2.12 as function of

N. The maximum (minimum) of ϕ will be achieved at the highest possible packing density of dipoles on the surface, referred to as complete monolayer. Deposition of an organic HTL (ETL) on these modified electrodes will lead to HIB (EIB) values according to the plots in Figure 2.12, reaching the respective minima at the critical ϕ values. In principle, a second or more layers of oriented dipoles might be employed to further change ϕ, but in practice this is difficult to achieve. Two reliable ways of controlled electrode surface dipole formation will be discussed in the following sections: (i) the use of strong electron acceptor and donor molecules, and (ii) the self-assembled monolayers (SAMs).

Strong Electron Acceptor and Donor Molecules A method that allows continuous adjustment of metal and conductive oxide ϕ and thus HIB/EIB values at organic/metal interfaces is the precoverage of the electrode surface with strong electron acceptor or donor molecules [63]. The chemisorption reaction of such molecules is accompanied by an electron density redistribution (compared to the isolated species) such that local dipoles μ with their negative ends oriented away from the surface (acceptors) or toward the surface (donors) occur, thus increasing or decreasing ϕ. A specific example for the chemisorption of the acceptor F4TCNQ on Cu(111) was discussed in Section 2.3.1. The area-averaged work function of the electrode can thus be adjusted by controlling the area density *N* of such dipoles according to Figure 2.12. If depolarization effects are small or two-dimensional island growth of the acceptor/donor occurs, there exists a linear relationship between the effective ϕ and the molecular coverage from about 10% coverage onward to one monolayer. Subsequently deposited conjugated organic molecules feel this modified average

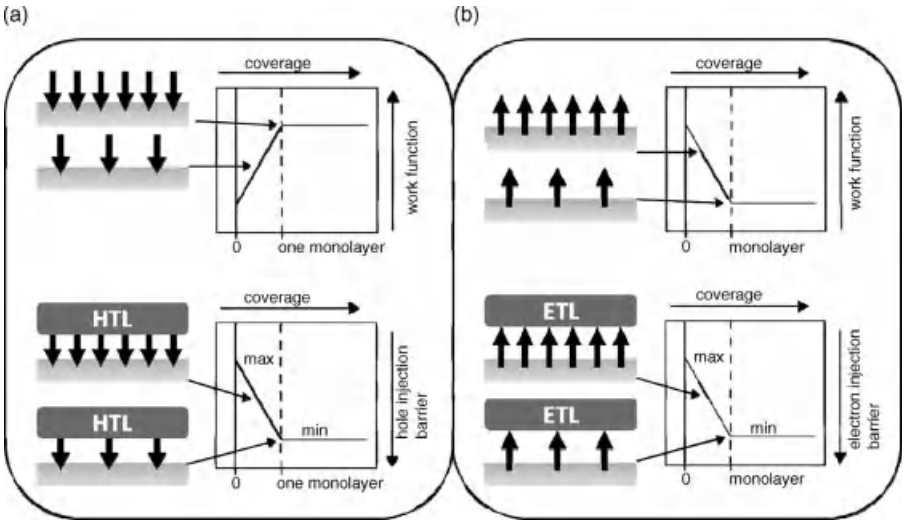

Figure 2.12 Conceptual use of dipoles (arrows) to adjust the work function and charge injection barriers at contacts between electrodes and hole transport layers (HTL) and electron transport layers (ETL).

surface potential, and the energy levels are shifted relative to E_F accordingly. For electron acceptors, the occupied levels of virtually any organic material deposited on top of this modified metal surface shift rigidly toward E_F, thus reducing the HIB (Figure 2.12a), and the opposite occurs for donors (Figure 2.12b). Any value for HIB/EIB between the two extreme values HIB_{max}/EIB_{max} (pristine metal surface) and HIB_{min}/EIB_{min} (monolayer acceptor/donor coverage) can be adjusted predictably by choosing the appropriate acceptor coverage [63]. Acceptor/donor molecules adsorbed onto the chemisorbed monolayer just physisorb and thus do not induce any dipoles and further work function changes.

A particularly potent acceptor to reduce HIBs toward organic semiconductors is F4TCNQ, for which the largest reduction of the HIB achieved was 1.2 eV for the organic molecular blue light emitter *p*-sexiphenyl on F4TCNQ precovered Au [64]. Strong electron donor molecules are often not stable in air due to their low IE. A donor that is strong enough to induce dipoles on metal surfaces while still being air-stable is neutral methyl viologen (1,1′-dimethyl-1*H*,1′*H*-[4,4′]bipyridinylidene; MV0) [65]. A monolayer of MV0 adsorbed on Au, Ag, and Cu surfaces yields a work function of only 3.3 eV, which is a significant reduction of ϕ compared to the pristine metal surfaces (Au: 5.5 eV, Ag: 4.5 eV, and Cu: 4.9 eV). Accordingly, EIB values for prototypical ETLs were reduced by up to 0.8 eV.

Self-Assembled Monolayers with Dipoles The use of electrode surface-attached self-assembled monolayers comprising dipolar moieties has been shown to allow adjusting charge injection barriers toward organic semiconductors, having the Helmholtz equation also as conceptual basis [66–68]. SAMs based on alkyl chains with thiol end groups for covalent bonding to metals are frequently used. However, the wide energy gap of alkyl chains counteracts the beneficial effect of ϕ tuning by introducing a wide gap of several angstroms through which charge carriers have to tunnel to reach the organic semiconductor. Furthermore, the toxicity of thiolate compounds may be problematic. A good alternative consists of using phosphonic acid derivatives of conjugated molecules, which can self-assemble on metal oxide surfaces to form a dense monolayer. Subsequent annealing leads to the formation of covalent bonds from every molecule to the oxide, forming a highly stable interface. This has been demonstrated for α-quarterthiophene-2-phosphonic acid (4TPA), which forms a stable covalently bonded monolayer of α-quarterthiophene-2-phosphonate (4TP) on indium tin oxide [69]. This SAM can then be rendered highly conductive by immersion in a solution of F4TCNQ, which forms a charge transfer complex with the thiophene part of 4TP (as schematically shown in Figure 2.13). In addition to providing energy levels close to E_F due to the charge transfer complex right at the interface, ϕ of ITO is also increased, leading to highly favorable hole injection properties of such an anode. Highly efficient OLEDs with small molecular materials and polymers were demonstrated using 4TP/F4TCNQ-modified ITO. In addition, further ϕ optimization can be achieved by substitution of the SAM molecule with electron-withdrawing or electron-donating groups to include additional dipole effects.

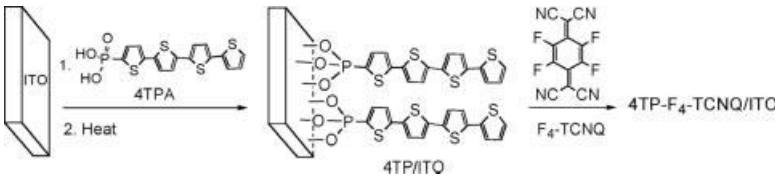

Figure 2.13 Schematic preparation of 4TP/F4-TCNQ on ITO.

2.4
Energy Levels at Organic Semiconductor Heterojunctions

The relative energy position of the frontier molecular or polymer levels at organic semiconductor heterojunctions is critical for the efficiency of OLEDs and OPVCs, as can be seen from Figure 2.1. The charge-blocking behavior at interfaces between ETL, HTL, and EL determines the extent to which exciton formation can be confined to the EL. Conversely, exciton dissociation in OPVCs occurs at the donor/acceptor interface, and ΔHOMO and ΔLUMO must be sufficient for stable charge separation. Furthermore, the open-circuit voltage is limited by the energy offset between the electron transport level in the acceptor and the hole transport level in the donor [70], which are the quantities derived from direct and inverse photoemission (cf. Section 2.1). Numerous investigations on the energy levels at organic semiconductor heterojunctions show that vacuum level alignment does indeed often occur [14,28,71], and one might estimate the interfacial energy level alignment by combining literature values of IE and EA of individual materials. However, there are four situations where the invalidity of this simple rule has been demonstrated:

- There exist multiple IE and EA values for an ordered organic material because these are orientation dependent (Figure 2.3).
- IE of one organic material is smaller than EA of the other.
- The contact between the electrode and one organic material enforces energy level pinning on the second organic material.
- Molecular dipoles at interfaces.

The following examples illustrate how these situations require involving further considerations beyond isolated IE and EA values.

2.4.1
Molecular Orientation Dependence

As described in Section 2.2, intramolecular dipoles lead to orientation-dependent multiple IE and EA values for one organic semiconductor as long as ordered or crystalline assemblies are formed. Consequently, predicting the level alignment at an organic/organic heterojunction is impossible as long as the orientation of molecules at the heterojunction is unknown. Let us assume the interface between

pentacene and perfluoropentacene. In literature, we find IE values, for example, obtained for individual PEN and PFP films on Au(111), of 5.15 and 5.60 eV, respectively [4]. The optical energy gaps of both materials differ by only 0.1 eV [72], and we can assume similar exciton binding energies for both (0.35 eV) [28], yielding EA values of 2.95 eV for PEN and 3.50 eV for PFP. Assuming a common vacuum level upon PEN/PFP interface formation, we arrive at an interfacial energy level diagram as depicted in Figure 2.14a. From this we could predict that this PEN/PFP heterojunction might have ideal energy levels for an OPVC, facilitating stable electron and hole separation as well as a high open-circuit voltage of up to 1.65 eV. Note that this assumption is invalidated by the fact that singlet exciton fission in pentacene is highly efficient [73]. However, OPVCs fabricated from this material pair show no photovoltaic function. The reason for this is that the level alignment drawn in Figure 2.14a does not occur in an actual OPVC. The IE/EA values used from Ref. [4] are valid only for flat-lying PEN and PFP. In contrast, both materials exhibit an almost upright standing molecular orientation on practical electrodes that are used for OPVC fabrication (e.g., ITO and PEDT:PSS). UPS measurements of the PEN/PFP heterojunction with upright standing molecular orientation yield the energy level diagram shown in Figure 2.14b, making it apparent that photovoltaic action would indeed no longer be expected. Rather the small energy separation between the PEN hole transport level and the PFP electron transport level turns this particular heterojunction into a charge generation layer, as may be used as contact for interfacing two active subcells in a tandem OPVC [72].

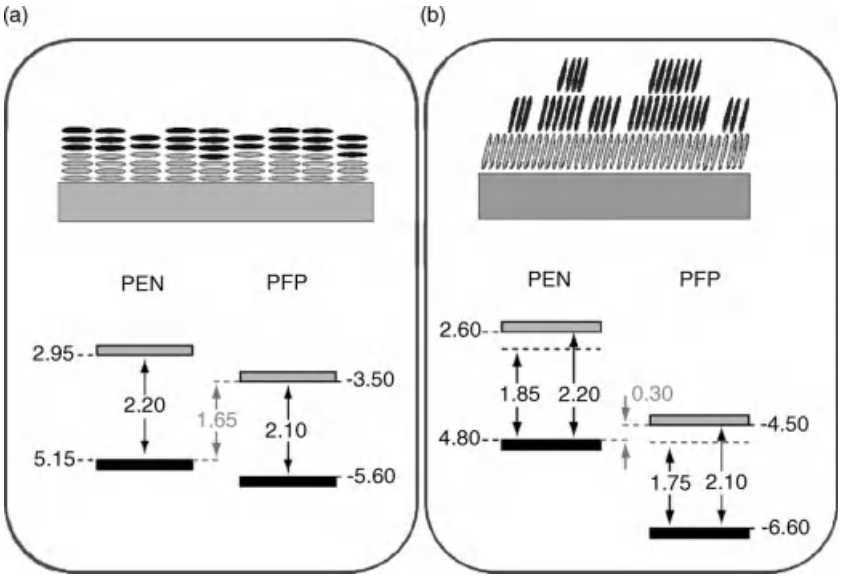

Figure 2.14 (a) Energy level alignment at a PEN/PFP heterojunction expected for flat-lying molecules. (b) Experimentally determined energy level alignment for PEN and PFP molecules essentially standing at the contact.

The example described above is not unique, as numerous examples on the orientation dependence of organic semiconductor heterojunction energy level alignment can be found, for example, for rod- and disklike molecules [74–76].

2.4.2 Interfacial Charge Transfer

When the IE of one organic semiconductor is lower than the EA of another, it appears quite naturally that interfacial charge transfer will occur upon contact formation as vacuum level alignment would result in a nonequilibrium situation. The charge transfer establishes an interface dipole that realigns the energy levels on both sides such that electronic equilibrium is established. For instance, the organic donor tetrathiafulvalene (TTF) and the acceptor tetracyanoquinodimethane (TCNQ) form heterojunctions where charge transfer across the interface leads to substantial interface dipoles, on the order of 0.6 eV [77]. More generally, charge transfer and the associated interface dipoles may also result when the intragap density of states tail from the HOMO side of one material (as schematically shown in Figure 2.10) overlaps energetically with the analogous tail from the LUMO side of the second material. The density of such states is often too small to be detected by photoemission spectroscopy, and the interface dipoles observed at numerous organic heterojunctions could be caused by charge transfer between tail states.

2.4.3 Electrode-Induced Pinning of Energy Levels

The third situation where simple vacuum level alignment at organic/organic heterojunctions fails to correctly predict the energy levels is characterized by an influence brought about by the sheer presence of an electrode making contact with (one of) the organic semiconductors. As example, we discuss the heterojunction formed by the donor diindenoperylene (DIP) and the acceptor C_{60}, which can also be used to form efficient OPVCs [62]. As long as the effective work function of the underlying organic semiconductor (in contact with an electrode) falls within the interval of $\phi_{\mathrm{crit,low}}$ and $\phi_{\mathrm{crit,high}}$ (Figure 2.7), one essentially observes vacuum level alignment at the DIP/C_{60} interface, regardless of deposition sequence (Figure 2.15a and b) [62]. The energy offset between the HOMO levels of DIP and C_{60}, however, depends somewhat on the deposition sequence due to the different effective substrate work function values. For the presented material pair, this is achieved, for example, by employing medium ϕ PEDT:PSS as electrode ($\phi = 5.1$ eV). However, when the initial ϕ of the electrode is chosen such that the effective work function of the first organic layer is beyond the critical ϕ values of the second organic material, vacuum level shifts are induced. In our example, this situation can be achieved by selecting a PEDT:PSS variant with high ϕ as substrate for C_{60} (Figure 2.15c). The effective ϕ of C_{60} on the high ϕ PEDT:PSS is 5.5 eV, which is higher than $\phi_{\mathrm{crit,high}}$ of DIP (IE of upright standing DIP is 5.4 eV). Vacuum level alignment at the interface

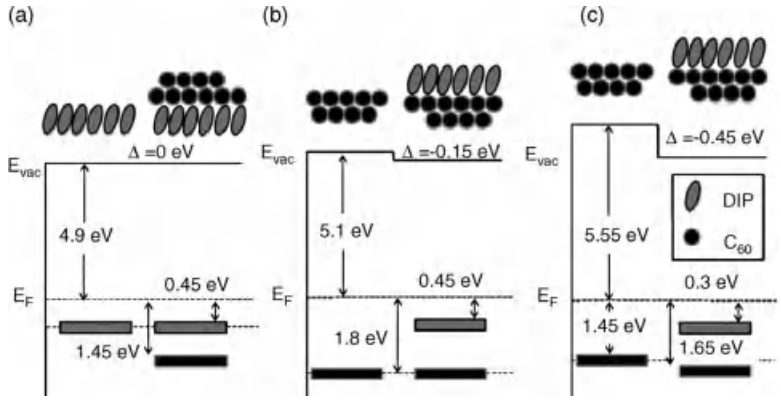

Figure 2.15 Energy level alignment at interfaces comprising DIP and C_{60}. Essentially vacuum level alignment at (a) DIP/C_{60} and (b) C_{60}/DIP interfaces on medium work function PEDT:PSS substrates. (c) Huge vacuum level shift across the C_{60}/DIP interface for high work function substrates.

to the subsequently deposited DIP would result in the HOMO of DIP being placed above E_F, that is, a nonequilibrium situation. To achieve equilibrium at this interface, charge density rearrangement at the C_{60}/DIP interface occurs, which results in the formation of an interface dipole of −0.45 eV that shifts the DIP HOMO below E_F (Figure 2.15c) [78]. Unfortunately, at present we cannot unequivocally resolve in which way the charge density rearrangement at the organic/organic interface occurs. Two possible scenarios are still discussed at present: direct charge transfer and mutual polarization. While direct interfacial charge transfer would result in the presence of positive and negative polaron states on the respective sides of the heterojunction, polarization is characterized mainly by charge density rearrangements within the first molecular layer that form the contact and the charge transfer becomes negligible [79]. Polarization at organic/organic interfaces can generally occur due to permanent dipoles and/or quadrupoles of molecules in conjunction with the asymmetry of the interface [80]. Further experimental and theoretical work is required to fully resolve the mechanisms here.

2.4.4
Molecular Dipoles for Energy Level Tuning

Based on the concept of using dipole layers to shift the electrostatic potential across an interface, the energy level alignment at organic/organic heterojunctions can be adjusted. This is very similar to the energy level tuning approaches discussed for organic–electrode interfaces in Section 2.3.2.3. Proof that this concept is applicable comes from the work of Tada *et al.* [81]. The organic donor/acceptor interface frequently investigated in the context of OPVCs formed by [6,6]-phenyl-C_{61}-butyric acid methyl ester (PCBM) and poly(3-hexylthiophene) (P3HT), chemical structures

shown in Figure 2.16, was modified by employing interfacial dipolar layers. By using surface-segregated monolayers of fluorinated compounds, they succeeded in altering the energy level offset between the frontier levels of P3HT and PCBM in both possible directions. As schematically shown in Figure 2.16, the insertion of [6,6]-phenyl-C_{61}-butyric acid 1*H*,1*H*-perfluoro-1-nonyl ester (FC_8) led to an upward shift of the P3HT levels with respect to those of PCBM, that is, reduction of the photovoltaic gap ΔE_{HL}. Conversely, the insertion of poly(4′-dodecyl-3-[1*H*,1*H*,2*H*,2*H*-perfluorooctyl]-2,2′-bithiophene (P3DDFT), with an oppositely oriented dipole increased ΔE_{HL}. Noteworthy, these changes of the energy level alignment between the active materials P3HT and PCBM directly impacted the open-circuit voltage of OPVCs that employed these structures.

More generally, it needs to be stated that molecules that possess permanent dipoles can result in energy level shifts at organic/organic heterojunctions, as well as also within the individual layers as function of thickness [82].

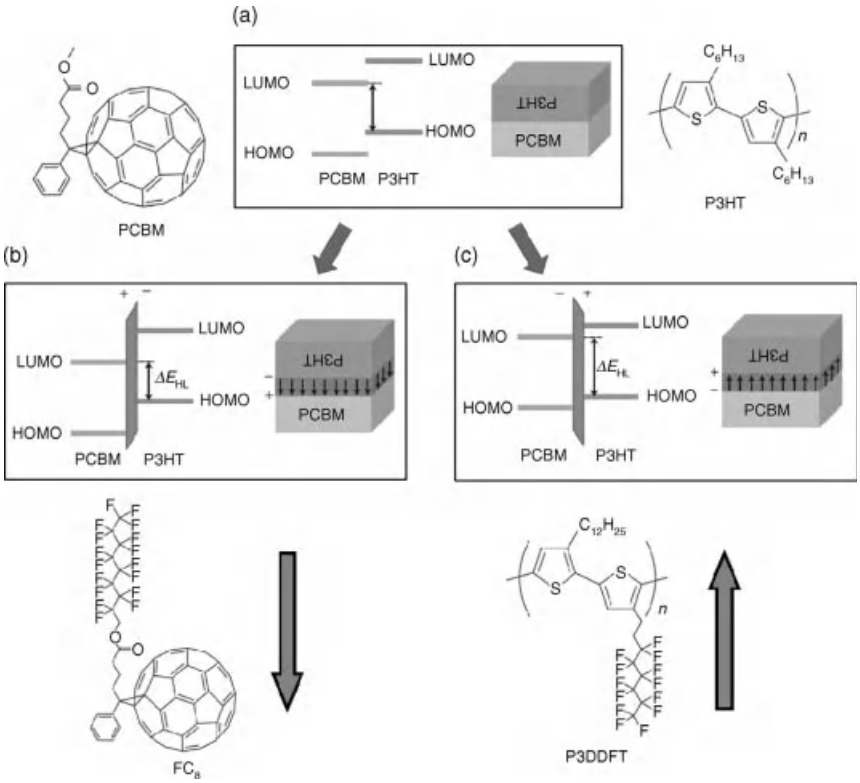

Figure 2.16 Schematic representation and energy diagrams of P3HT/PCBM bilayer structures. (a) Without interfacial dipoles. (b) With interfacial dipoles of FC_8. (c) With oppositely oriented interfacial dipoles of P3DDFT. Adapted with permission from Ref. [81], copyright 2011 McMillan Publishers Ltd.

2.5 Conclusions

Interfaces between dissimilar organic and also organic and inorganic materials are of great importance for (opto)electronic device function and efficiency, and the level of understanding interface properties will contribute decisively to the success of organic-based technology. Despite the huge number of investigations, there is still a lack of a truly comprehensive picture of the mechanisms that determine the properties of such interfaces, and how interfaces can predictably be designed and fabricated to satisfy certain requirements. However, as outlined in this chapter, a number of reliable methods to control the energy levels at interfaces with organic materials do already exist. It must be stressed that researchers and engineers should be cautious to utilize these methods without proper knowledge about their inherent limitations. Oversimplified models about interface energetics will rarely result in adequate predictions, and subsequent correlations to actual device performance can be misleading. At present, it remains good advice to experimentally determine the electronic structure of interfaces with organic semiconductors when they are critical for the performance of devices.

Acknowledgments

Financial support by the DFG and the EC is gratefully acknowledged.

References

1 Duhm, S., Heimel, G., Salzmann, I., Glowatzki, H., Johnson, R.L., Vollmer, A., Rabe, J.P., and Koch, N. (2008) Orientation-dependent ionization energies and interface dipoles in ordered molecular assemblies. *Nat. Mater.*, **7** (4), 326–332.

2 Heimel, G. and Koch, N. (2010) Electronic structure engineering through intramolecular polar bonds, in *Functional Supramolecular Architectures* (eds. P. Samori and F. Cacialli), Wiley-VCH Verlag GmbH, Weinheim.

3 Koch, N., Gerlach, A., Duhm, S., Glowatzki, H., Heimel, G., Vollmer, A., Sakamoto, Y., Suzuki, T., Zegenhagen, J., Rabe, J.P., and Schreiber, F. (2008) Adsorption-induced intramolecular dipole: correlating molecular conformation and interface electronic structure. *J. Am. Chem. Soc.*, **130** (23), 7300–7304.

4 Koch, N., Vollmer, A., Duhm, S., Sakamoto, Y., and Suzuki, T. (2007) The effect of fluorination on pentacene/ gold interface energetics and charge reorganization energy. *Adv. Mater.*, **19** (1), 112.

5 Sakamoto, Y., Suzuki, T., Kobayashi, M., Gao, Y., Inoue, Y., and Tokito, S. (2006) Perfluoropentacene and perfluorotetracene: syntheses, crystal structures, and FET characteristics. *Mol. Cryst. Liq. Cryst.*, **444**, 225–232.

6 Heimel, G., Salzmann, I., Duhm, S., and Koch, N. (2011) Design of organic semiconductors from molecular electrostatics. *Chem. Mater.* **23**, 359–377.

7 Lang, N.D. and Kohn, W. (1971) Theory of metal surfaces: work function. *Phys. Rev. B*, **3**, 1215.

8 Ishii, H., Sugiyama, K., Ito, E., and Seki, K. (1999) Energy level alignment and interfacial electronic structures at organic metal and organic/organic interfaces. *Adv. Mater.*, **11** (8), 605.

9 Bagus, P.S., Hermann, K., and Woll, C. (2005) The interaction of C_6H_6 and C_6H_{12} with noble metal surfaces: electronic level alignment and the origin of the interface dipole. *J. Chem. Phys.*, **123** (18), 184109.

10 Gao, W.Y. and Kahn, A. (2002) Electronic structure and current injection in zinc phthalocyanine doped with tetrafluorotetracyanoquinodimethane: interface versus bulk effects. *Org. Electron.*, **3** (2), 53–63.

11 Romaner, L., Heimel, G., Bredas, J.L., Gerlach, A., Schreiber, F., Johnson, R.L., Zegenhagen, J., Duhm, S., Koch, N., and Zojer, E. (2007) Impact of bidirectional charge transfer and molecular distortions on the electronic structure of a metal–organic interface. *Phys. Rev. Lett.*, **99** (25), 256801.

12 Rentenberger, S., Vollmer, A., Zojer, E., Schennach, R., and Koch, N. (2006) UV/ozone treated Au for air-stable, low hole injection barrier electrodes in organic electronics. *J. Appl. Phys.*, **100** (5), 053701.

13 Wan, A., Hwang, J., Amy, F., and Kahn, A. (2005) Impact of electrode contamination on the α-NPD/Au hole injection barrier. *Org. Electron.*, **6**, 47–54.

14 Hill, I.G., Milliron, D., Schwartz, J., and Kahn, A. (2000) Organic semiconductor interfaces: electronic structure and transport properties. *Appl. Surf. Sci.*, **166**, 354–362.

15 Koch, N. and Vollmer, A. (2006) Electrode-molecular semiconductor contacts: work-function-dependent hole injection barriers versus Fermi-level pinning. *Appl. Phys. Lett.*, **89** (16), 162107.

16 Crispin, A., Crispin, X., Fahlman, M., Berggren, M., and Salaneck, W.R. (2006) Transition between energy level alignment regimes at a low band gap polymer–electrode interfaces. *Appl. Phys. Lett.*, **89** (21), 213503.

17 Tengstedt, C., Osikowicz, W., Salaneck, W. R., Parker, I.D., Hsu, C.-H., and Fahlman, M. (2006) Fermi-level pinning at conjugated polymer interfaces. *Appl. Phys. Lett.*, **88** (5), 053502.

18 Fahlman, M., Crispin, A., Crispin, X., Henze, S.K.M., Jong, M.P.D., Osikowicz, W., Tengstedt, C., and Salaneck, W.R. (2007) Electronic structure of hybrid interfaces for polymer-based electronics. *J. Phys. Condens. Matter*, **19** (18), 183202.

19 Hwang, J., Kim, E.-G., Liu, J., Bredas, J.-L., Duggal, A., and Kahn, A. (2007) Photoelectron spectroscopic study of the electronic band structure of polyfluorene and fluorene-arylamine copolymers at interfaces. *J. Phys. Chem. C*, **111**, 1378–1384.

20 Hwang, J., Wan, A., and Kahn, A. (2009) Energetics of metal–organic interfaces: new experiments and assessment of the field. *Mater. Sci. Eng.*, **R64**, 1–31.

21 Stadlober, B., Haas, U., Maresch, H., and Haase, A. (2006) Growth model of pentacene on inorganic and organic dielectrics based on scaling and rate-equation theory. *Phys. Rev. B*, **74** (16), 165302.

22 Koch, N., Elschner, A., Rabe, J.P., and Johnson, R.L. (2005) Work function independent hole-injection barriers between pentacene and conducting polymers. *Adv. Mater.*, **17** (3), 330.

23 Kang, J.H., da Silva, D., Bredas, J.L., and Zhu, X.Y. (2005) Shallow trap states in pentacene thin films from molecular sliding. *Appl. Phys. Lett.*, **86** (15), 152115.

24 Kang, J.H., da Silva, D., Bredas, J.L., and Zhu, X.Y. (2005) Shallow trap states in pentacene thin films from molecular sliding. *Appl. Phys. Lett.*, **86** (15), 152115.

25 Bässler, H. (1993) Charge transport in disordered organic photoconductors: a Monte Carlo simulation study. *Phys. Status Solidi B*, **175** (1), 15–56.

26 Vissenberg, M.C.J.M. and Matters, M. (1998) Theory of the field-effect mobility in amorphous organic transistors. *Phys. Rev. B*, **57**, 12964.

27 Koch, N., Pogantsch, A., List, E.J.W., Leising, G., Blyth, R.I.R., Ramsey, M.G., and Netzer, F.P. (1999) Low-onset organic blue light emitting devices obtained by better interface control. *Appl. Phys. Lett.*, **74** (20), 2909–2911.

28 Kahn, A., Koch, N., and Gao, W.Y. (2003) Electronic structure and electrical properties of interfaces between metals and π-conjugated molecular films. *J. Polym. Sci. Polym. Phys.*, **41** (21), 2529–2548.

29 Ishii, H., Yoshimura, D., Sugiyama, K., Narioka, S., Hamatani, Y., Kawamoto, I., Miyazaki, T., Ouchi, Y., and Seki, K. (1997) *Synth. Met.*, **85**, 1389.

30 Lee, S.T., Hou, X.Y., Mason, M.G., and Tang, C.W. (1998) Energy level alignment at Alq/metal interfaces. *Appl. Phys. Lett.*, **72** (13), 1593–1595.

31 Rajagopal, A. and Kahn, A. (1998) Photoemission spectroscopy investigation of magnesium–Alq3 interfaces. *J. Appl. Phys.*, **84**, 355–358.

32 Shen, C.F., Hill, I.G., Kahn, A., and Schwartz, J. (2000) Organometallic chemistry at the magnesium-tris(8-hydroxyquinolino)aluminum interface. *J. Am. Chem. Soc.*, **122**, 5391.

33 Jönsson, S.K.M., Salaneck, W.R., and Fahlman, M. (2005) Photoemission of Alq3 and C_{60} films on Al and LiF/Al substrates. *J. Appl. Phys.*, **98**, 014901.

34 Baier, F., von Ludowig, F., Soukopp, A., Vaterlein, C., Laubender, J., Bauerle, P., Sokolowski, M., and Umbach, E. (1999) A combined photoelectron spectroscopy and capacity-voltage investigation of the aluminum oligothiophene interface. *Opt. Mater.*, **12** (2–3), 285–290.

35 Schlaf, R., Merritt, C.D., Picciolo, L.C., and Kafafi, Z.H. (2001) Determination of the orbital lineup at reactive organic semiconductor interfaces using photoemission spectroscopy. *J. Appl. Phys.*, **90**, 1903.

36 Tang, J.X., Lee, C.S., and Lee, S.T. (2006) Chemical bonding and electronic structures at magnesium/copper phthalocyanine interfaces. *Appl. Surf. Sci.*, **252**, 3948–3952.

37 Koch, N., Yu, L.M., Parente, V., Lazzaroni, R., Johnson, R.L., Leising, G., Pireaux, J.J., and Bredas, J.L. (1998) Evidence for physisorption of aluminum on the surface of electroluminescent sexiphenyl. *Adv. Mater.*, **10** (13), 1038.

38 Koch, N., Pairleitner, R., Le, Q.T., Forsythe, E.W., Gao, Y., and Leising, G. (2000) Photoemission spectroscopic investigation on the interface formation of a ladder-type poly(*para*-phenylene) with aluminum. *Appl. Phys. Lett.*, **76** (25), 3738–3740.

39 Oji, H., Ito, E., Furuta, M., Kajikawa, K., Ishii, H., Ouchi, Y., and Seki, K. (1999) *J. Electron. Spectrosc.*, **103**.

40 Salaneck, W.R., Friend, R.H., and Bredas, J.L. (1999) Electronic structure of conjugated polymers: consequences of electron–lattice coupling. *Phys. Rep.*, **319** (6), 231–251.

41 Logdlund, M., Dannetun, P., Stafstrom, S., Salaneck, W.R., Ramsey, M.G., Spangler, C.W., Fredriksson, C., and Bredas, J.L. (1993) Soliton pair charge storage in doped polyene molecules: evidence from photoelectron-spectroscopy studies. *Phys. Rev. Lett.*, **70** (7), 970–973.

42 Logdlund, M., Dannetun, P., Fredriksson, C., Salaneck, W.R., and Bredas, J.L. (1996) Theoretical and experimental studies of the interaction between sodium and oligothiophenes. *Phys. Rev. B*, **53** (24), 16327–16333.

43 Ramsey, M.G., Schatzmayr, M., Leising, G., and Netzer, F.P. (1994) The electronic structure of alkali doped ultra thin sexiphenyl films. *Mol. Cryst. Liq. Cryst.*, **256** (1), 679–684.

44 Ramsey, M.G., Steinmüller, D., and Netzer, F.P. (1990) Explicit evidence for bipolaron formation: Cs-doped biphenyl. *Phys. Rev. B*, **42**, 5902.

45 Greczynski, G., Fahlman, M., Salaneck, W.R., Johansson, N., dos Santos, D.A., Dkhissi, A., and Bredas, J.L. (2002) Electronic structure of poly(9,9-dioctylfluorene) in the pristine and reduced state. *J. Chem. Phys.*, **116** (4), 1700–1706.

46 Koch, N., Rajagopal, A., Ghijsen, J., Johnson, R.L., Leising, G., and Pireaux, J.J. (2000) Bipolaron: the stable charged species in n-doped *p*-sexiphenyl. *J. Phys. Chem. B*, **104** (7), 1434–1438.

47 Durr, A.C., Koch, N., Kelsch, M., Ruhm, A., Ghijsen, J., Johnson, R.L., Pireaux, J.J., Schwartz, J., Schreiber, F., Dosch, H., and Kahn, A. (2003) Interplay between morphology, structure, and electronic properties at diindenoperylene-gold interfaces. *Phys. Rev. B*, **68** (11), 115428.

48 Koch, N., Chan, C., Kahn, A., and Schwartz, J. (2003) Lack of thermodynamic equilibrium in conjugated organic molecular thin films. *Phys. Rev. B*, **67** (19), 195330.

49 Schamberg, M., Hu, J., Kanzow, J., Rätzke, K., Adelung, R., Faupel, F., Pannemann, C., Hilleringmann, U., Meyer, S., and Pflaum, J. (2005) Radiotracer measurements as a sensitive tool for the detection of metal penetration in molecular-based organic electronics. *Appl. Phys. Lett.*, **86** (2), 024104–024104-3.

50 Yoshimura, D., Yokoyama, T., Ito, E., Ishii, H., Ouchi, Y., Hasegawa, S., and Seki, K. (1999) Electronic structure of Alq3/LiF/Al interfaces studied by UV photoemission *Synth. Met.*, **102** (1–3), 1145–1146.

51 Le, Q.T., Yan, L., Gao, Y.G., Mason, M.G., Giesen, D.J., and Tang, C.W. (2000) Photoemission study of aluminum/tris-(8-hydroxyquinoline) aluminum and aluminum/LiF/tris-(8-hydroxyquinoline) aluminum interfaces. *J. Appl. Phys.*, **87** (1), 375–379.

52 Mason, M.G., Tang, C.W., Hung, L.S., Raychaudhuri, P., Madathil, J., Giesen, D. J., Yan, L., Le, Q.T., Gao, Y., Lee, S.T., Liao, L.S., Cheng, L.F., Salaneck, W.R., dos Santos, D.A., and Bredas, J.L. (2001) Interfacial chemistry of Alq(3) and LiF with reactive metals. *J. Appl. Phys.*, **89** (5), 2756–2765.

53 Greczynski, G., Salaneck, W.R., and Fahlman, M. (2001) An experimental study of poly(9,9-dioctyl-fluorene) and its interfaces with Al, LIF and CsF. *Appl. Surf. Sci.*, **175**, 319–325.

54 Koch, N., Ghijsen, J., Johnson, R.L., Schwartz, J., Pireaux, J.J., and Kahn, A. (2002) Physisorption-like interaction at the interfaces formed by pentacene and samarium. *J. Phys. Chem. B*, **106** (16), 4192–4196.

55 Koch, N., Zojer, E., Rajagopal, A., Ghjisen, J., Johnson, R.L., Leising, G., and Pireaux, J.J. (2001) Electronic properties of the interfaces between the wide bandgap organic semiconductor *para*-sexiphenyl and samarium. *Adv. Funct. Mater.*, **11** (1), 51–58.

56 Scott, J.C., Carter, S.A., Karg, S., and Angelopoulos, M. (1997) Polymeric anodes for organic light-emitting diodes original research. *Synth. Met.*, **85**, 1197–1200.

57 Yang, Y., Pei, Q., and Heeger, A.J. (1996) Efficient blue polymer light-emitting diodes from a series of soluble poly(paraphenylene)s. *J. Appl. Phys.*, **79**, 934.

58 Kirchmeyer, S. and Reuter, K. (2005) Scientific importance, properties and growing applications of poly(3,4-ethylenedioxythiophene). *J. Mater. Chem.*, **15** (21), 2077–2088.

59 Jukes, P.C., Martin, S.J., Higgins, A.M., Geoghegan, M., Jones, R.A.L., Langridge, S., Wehrum, A., and Kirchmeyer, S. (2004) Controlling the surface composition of poly(3,4-ethylene dioxythiophene)poly (styrene sulfonate) blends by heat treatment. *Adv. Mater.*, **16** (9–10), 807.

60 Greczynski, G., Kugler, T., and Salaneck, W.R. (1999) Characterization of the PEDOT-PSS system by means of X-ray and ultraviolet photoelectron spectroscopy. *Thin Solid Films*, **354** (1–2), 129–135.

61 Koch, N., Vollmer, A., and Elschner, A. (2007) Influence of water on the work function of conducting poly(3,4-ethylenedioxythiophene)/poly (styrenesulfonate). *Appl. Phys. Lett.*, **90** (4), 043512.

62 Wagner, J., Gruber, M., Hinderhofer, A., Wilke, A., Broker, B., Frisch, J., Amsalem, P., Vollmer, A., Opitz, A., Koch, N., Schreiber, F., and Brutting, W. (2010) High fill factor and open circuit voltage in organic photovoltaic cells with diindenoperylene as donor material. *Adv. Funct. Mater.*, **20** (24), 4295–4303.

63 Koch, N. (2007) Organic electronic devices and their functional interfaces. *ChemPhysChem*, **8** (10), 1438–1455.

64 Koch, N., Duhm, S., Rabe, J.P., Vollmer, A., and Johnson, R.L. (2005) Optimized hole injection with strong electron acceptors at organic-metal interfaces. *Phys. Rev. Lett.*, **95** (23), 237601.

65 Broker, B., Blum, R.P., Frisch, J., Vollmer, A., Hofmann, O.T., Rieger, R., Mullen, K., Rabe, J.P., Zojer, E., and Koch, N. (2008) Gold work function reduction by 2.2eV with an air-stable molecular donor layer. *Appl. Phys. Lett.*, **93** (24), 243303.

66 Appleyard, S.F.J., Day, S.R., Pickford, R. D., and Willis, M.R. (2000) Organic electroluminescent devices: enhanced carrier injection using SAM derivatized ITO electrodes. *J. Mater. Chem.*, **10** (1), 169–173.

67 Zuppiroli, L., Si-Ahmed, L., Kamaras, K., Nüesch, F., Bussac, M.N., Ades, D., Siove, A., Moons, E., and Grätzl, M. (1999) Self-assembled monolayers as interfaces for organic opto-electronic devices *Eur. Phys. J. B*, **11** (3), 505–512.

68 Miozzo, L., Yassar, A., and Horowitz, G. (2010) Surface engineering for high performance organic electronic devices: the chemical approach. *J. Mater. Chem.*, **20** (13), 2513–2538.

69 Hanson, E.L., Guo, J., Koch, N., Schwartz, J., and Bernasek, S.L. (2005) Advanced surface modification of indium tin oxide for improved charge injection in organic devices. *J. Am. Chem. Soc.*, **127** (28), 10058–10062.

70 Rand, B.P., Burk, D.P., and Forrest, S.R. (2007) Offset energies at organic semiconductor heterojunctions and their influence on the open-circuit voltage of thin-film solar cells. *Phys. Rev. B*, **75** (11), 115327.

71 Vázquez, H., Gao, W., Flores, F., and Kahn, A. (2005) Energy level alignment at organic heterojunctions: role of the charge neutrality level. *Phys. Rev. B*, **71** (4), 041306.

72 Duhm, S., Salzmann, I., Heimel, G., Oehzelt, M., Haase, A., Johnson, R.L., Rabe, J.P., and Koch, N. (2009) Controlling energy level offsets in organic/organic heterostructures using intramolecular polar bonds. *Appl. Phys. Lett.*, **94** (3), 033304.

73 Wilson, M.W.B., Rao, A., Clark, J., Kumar, R.S.S., Brida, D., Cerullo, G., and Friend, R.H. (2011) Ultrafast dynamics of exciton fission in polycrystalline pentacene. *J. Am. Chem. Soc.*, **133** (31), 11830–11833.

74 Chen, W. (2008) Molecular orientation dependent interfacial dipole at the F16CuPc/CuPc organic heterojunction interface. *Appl. Phys. Lett.*, **92** (6), 063308.

75 Chen, W., Qi, D.C., Huang, Y.L., Huang, H., Wang, Y.Z., Chen, S., Gao, X.Y., and Wee, A.T.S. (2009) Molecular orientation dependent energy level alignment at organic–organic heterojunction interfaces. *J. Phys. Chem. C*, **113** (29), 12832–12839.

76 Chen, W., Qi, D.-C., Huang, H., Gao, X., and Wee, A.T.S. (2011) Organic–organic heterojunction interfaces: effect of molecular orientation. *Adv. Funct. Mater.*, **21** (3), 410–424.

77 Braun, S., Liu, X., Salaneck, W.R., and Fahlman, M. (2010) Fermi level equilibrium at donor–acceptor interfaces in multi-layered thin film stack of TTF and TCNQ. *Org. Electron.*, **11**, 212–217.

78 Wilke, A., Amsalem, P., Frisch, J., Broker, B., Vollmer, A., and Koch, N. (2011) Electric fields induced by energy level pinning at organic heterojunctions. *Appl. Phys. Lett.*, **98** (12), 123304.

79 Rissner, F., Rangger, G.M., Hofmann, O. T., Track, A.M., Heimel, G., and Zojer, E. (2009) Understanding the electronic structure of metal/SAM/organic–semiconductor heterojunctions. *ACS Nano*, **3** (11), 3513–3520.

80 Linares, M., Beljonne, D., Cornil, J.R.M., Lancaster, K., Brédas, J.-L., Verlaak, S., Mityashin, A., Heremans, P., Fuchs, A., Lennartz, C., Idé, J., Méreau, R.l., Aurel, P., Ducasse, L., and Castet, F.D.R. (2010) On the interface dipole at the pentacene–fullerene heterojunction: a theoretical study. *J. Phys. Chem. C*, **114** (7), 3215–3224.

81 Tada, A., Geng, Y.F., Wei, Q.S., Hashimoto, K., and Tajima, K. (2011) Tailoring organic heterojunction interfaces in bilayer polymer photovoltaic devices. *Nat. Mater.*, **10** (6), 450–455.

82 Sugi, K., Ishii, H., Kimura, Y., Niwano, M., Ito, E., Washizu, Y., Hayashi, N., Ouchi, Y., and Seki, K. (2004) Characterization of light-erasable giant surface potential built up in evaporated Alq3 thin films. *Thin Solid Films*, **464–465** (0), 412–415.

3
Electronic Structure of Molecular Solids: Bridge to the Electrical Conduction

Nobuo Ueno

3.1
Introduction

Organic semiconductors, discovered in the mid-twentieth century [1–3], have larger bandgap and smaller bandwidth than their inorganic counterparts. The number of thermally excited carriers in the organic films is not enough to give sufficient current. We thus need injection of carriers into the organic film from electrodes to realize sufficient current in organic devices. This chapter describes fundamental aspects of electronic structure of organic semiconductors and the method to bridge the electronic structure and electrical property using ultraviolet photoemission spectroscopy (UPS).

As it is well known, the electrical conductivity (σ) is given by

$$\sigma = nq\mu \tag{3.1}$$

where n is the carrier concentration, q is the charge of the carrier concerned, and μ is the charge-carrier mobility. This relation simply indicates that we must increase n and μ, if we need larger conductivity and electrical current. To obtain sufficient current in organic films, we need to inject charge carriers effectively from electrodes to increase n. As the carrier injection is dominated by the charge injection barrier height that is the energy difference between the Fermi level (E_F) and the highest occupied molecular orbital (HOMO) state (for hole) or the lowest unoccupied molecular orbital (LUMO) state (for electron) of the organic film, a large number of studies using UPS have been carried out to study the energy level alignment at organic/metal interfaces [4–9]. These experiments have provided quantitative information on the position of E_F in the HOMO–LUMO bandgap of an organic layer at organic/metal or organic/organic heterojunctions and motivated studies on the origin of the Fermi level pinning to give models such as the charge neutrality level and/or the induced density of interface states [10–18] and the integer charge transfer states (ICT model) due to polaron [19–21] in the bandgap at the interfaces. Unfortunately, however, direct experimental evidence of such bandgap

Physics of Organic Semiconductors, Second Edition. Edited by Wolfgang Brütting and Chihaya Adachi

states has been missing for weakly interacting interfaces that show pinning of the Fermi level near HOMO or LUMO. In relation to this Fermi level pinning effect, we observe n-or p-type charge transport property without intentional impurity doping. These effects seem to be determined by the host molecule itself. There have also been some direct measurements on gap states that have not been detected by conventional UPS, which have pointed out the role of the gap states in the energy level alignment and band bending phenomena [22–26].

To increase μ, on the other hand, we need to know principal origin of μ of organic material concerned, namely, coherent band conduction or hopping conduction. The band mobility, which is derived by coherent carrier motion and generally larger than the hopping mobility, is dominated by the energy band dispersion [27, 28], whereas the hopping mobility is dominated by the charge reorganization energy that is related to electron or hole/vibration coupling [28–32]. Unfortunately, however, quantum mechanical/chemical information on the charge mobility has been completely left to be elusive in experimental field till 2002 due to difficulty in realizing high-energy resolution UPS measurements on organic thin films [33, 34]. Such fundamental understanding based on experimental evidences is critical if we are going to improve charge-carrier mobility from quantum chemical molecular design and material engineering.

In this way, electronic structure of the organic semiconductor is of critical importance to unravel electrical conduction in organic devices [28]. Many of the electrical properties of organic devices have not been discussed based on quantum mechanical or quantum chemical ways, but on classical electromagnetism. In this chapter, we describe a feature of electronic states of an organic molecular solid in relation to the charge transport property.

3.2
General View of Electronic States of Organic Solids

3.2.1
From Single Molecule to Molecular Solid

We will first learn the evolution of electronic structure from single molecule to molecular solid and then discuss the energy bands typically appearing in the solid. Figure 3.1a schematically shows the electronic structure of a polyatomic molecule, where the molecule is made of three atoms. The ordinate is the electron energy. The potential well is formed by the Coulombic potential of each atomic nucleus. The effective potential well of the molecule for an electron is formed by the atomic nuclei as well as other electrons. However, we here neglect contribution of other electrons for simplicity. The wells of the nuclei are merged in the upper part to form a broad well, where various molecular orbitals (MOs) exist and produce discrete energy levels that are different from atomic energy levels. Each MO level (energy level) is occupied by two electrons with spin up and down, respectively. The horizontal part of the potential well is the vacuum level (VL), at which an electron that exists outside the

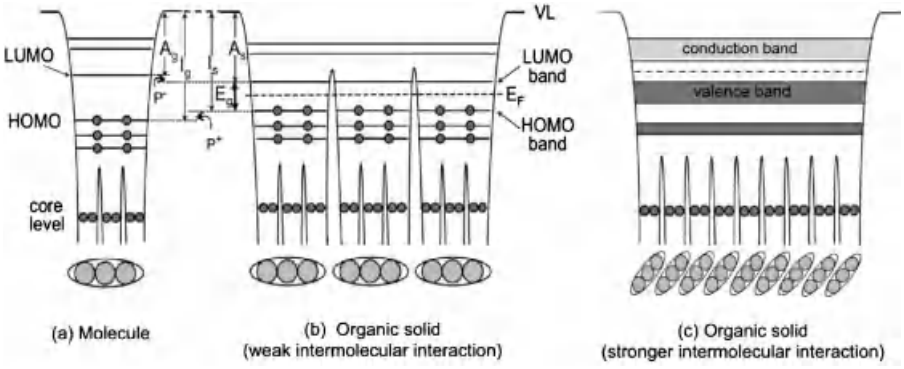

Figure 3.1 Evolution of electronic structure, from single molecule (a) to solid (b and c). When intermolecular electronic interaction is weak, the width of energy bands is very narrow (b). With increase in the intermolecular interaction, the bandwidth becomes larger (c). VL: the vacuum level, E_F: Fermi level, A_g: electron affinity of gas phase, A_s: electron affinity of solid, I_g: ionization energy of gas phase, I_s: ionization energy of solid, P^-: polarization energy for negative ion in solid, P^+: polarization energy for positive ion in solid, E_g: bandgap.

molecule stops moving and its kinetic energy is zero. The electron excited above the VL can escape from the molecule to vacuum. Electrons at deeper levels are localized in the atomic potential well (core levels), and thus have the feature of those in atomic orbitals because of very high potential barrier between the atoms. The upper energy levels, MO levels, involve interatomic interaction to form delocalized molecular orbitals. The energy separations from the HOMO or the LUMO to the VL are defined as the gas-phase ionization energy (I_g) or the electron affinity (A_g) of the molecule, respectively. When molecules come together to form an organic solid, the electronic structure becomes like that shown in Figure 3.2b. Since the molecules interact only by the weak van der Waals interaction in many organic solids, wave functions of the occupied valence states (or valence bands) and the lower unoccupied states (conduction bands) are mainly localized in each molecule, yielding narrow intermolecular energy band of the bandwidth approximately <0.2 eV [28]. Thus, the electronic structure of an organic solid approximately preserves that of a molecule, and the validity of usual band theory is often limited in discussing charge transport in an organic solid [28], which means that such an organic solid often shows two faces, in some cases face of single molecule and in other cases face of solid state. This situation in the electronic structure of the solid allows us to simply write the band structure such as the HOMO and the LUMO levels by using "line" due to very narrow bandwidth as in Figure 3.1b. When intermolecular interaction becomes larger, both the occupied (valence) and unoccupied (conduction) bands become wider because of larger overlapping of relevant wave functions (MOs) of adjacent molecules. This also means that the HOMO does not necessarily show the widest band in occupied valence bands, since the bandwidth is related to spatial spread of the MO as well as the intermolecular distance. Such an example can be seen in the intermolecular band dispersion results on perylene-3,4,9,10-tetracarboxilic dianhydride (PTCDA) [35].

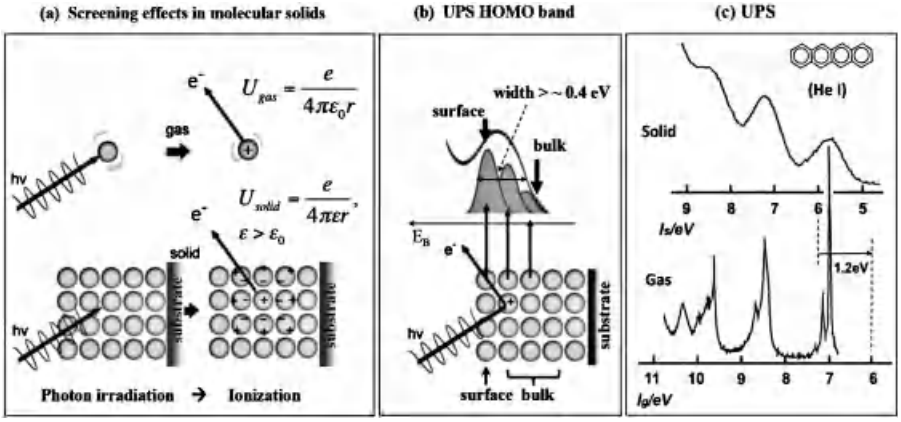

Figure 3.2 Screening effects in an organic semiconductor film and in a gas-phase molecule (a) and origin of the bandwidth of a UPS feature for a thin film of weakly interacting molecules (b). The potential (U) of the photogenerated hole (positive ion) acting on the photoelectron is described in (a). Panel (b) illustrates a historical model that UPS bandwidth is determined by superposition of photoelectrons from surface molecules (with low kinetic energy/higher binding energy) and bulk molecules (with higher kinetic energy/lower binding energy), where screening effects depend on the number of molecules surrounding the ion. Panel (c) show comparison of gas and thin-film UPS on naphthacene, where the ionization energy of gas-phase spectrum is shifted by ~1.2 eV, polarization energy (P^+), to align the HOMO positions.

From a molecule to a solid, the energy levels change from Figure 3.1a to b, where I_g and A_g become the ionization energy (I_s) and the electron affinity (A_s) of the solid, respectively. They are defined as the energy separation of the HOMO and the LUMO from the VL, as in the case of a molecule (Figure 3.1b). When a hole (electron) is introduced into the HOMO (LUMO) of the solid, the electronic polarization of the molecules surrounding the ionized molecule stabilizes the ion by screening effects, leading to a lowering of I and an increase in A from those in the gas phase, as shown in Figure 3.1a and b. As the polarization effect may be different for the hole (cation) and the electron (anion) because a molecular solid is not complete continuum medium, there are two polarization energies P^+ and P^- for the hole and the electron, respectively [36, 37]; thus, we write

$$I_s = I_g - P^+, \quad A_s = A_g + P^- \tag{3.2}$$

This relation is easily understandable by considering the case of photoionization of a molecule and a molecular solid. The potential energy of an electron in the attractive force field of the ion is $U = e^2/4\pi\varepsilon_0 r$ in vacuum, where ε_0 is the vacuum permittivity, and $U = e^2/4\pi\varepsilon r$ in the solid with the permittivity ε that reflects screening of the ion by surrounding molecules, where the molecules are polarized as shown in Figure 3.2. UPS of organic thin films gives I_s that is smaller by P^+ than I_g, and inverse photoemission spectroscopy (IPES) provides A_s larger by P^- than A_g.

Although we usually do not write a hole in the occupied MO level but two electrons in the energy level scheme, the scheme always means that the occupied MO

level corresponds to that of one hole state and the unoccupied MO level to one electron state by assuming Koopmans' theorem [38, 39]. For ionization, Koopmans' theorem gives

$$E_N - E_{N-1} = \varepsilon_i \tag{3.3}$$

where E_N and E_{N-1} are total electron energies of N and $N-1$ electron systems in closed-shell Hartree–Fock approximation, respectively, and ε_i is the orbital energy of ith level from which an electron is ejected. Therefore, the computed MO energy corresponds to its ionization energy. The valence band is thus called as hole band and the conduction band as electron band. This is why we can use the energy level diagram in Figure 3.1 for UPS and IPES, and also for hole and electron conduction in organic solid.

3.2.2
Polaron and Charge Transport

In the UPS experiment, as the ionization time can be defined by the time from the photoexcitation to the photoelectron detection, the polarization that is faster than the ionization time contributes to the P^+. This is generally contribution of very rapid electron rearrangement after photoionization. If we consider slower ionization process such as charge hopping (with low mobility), polarization associated with deformation of geometrical structure of the molecular ion (change in the atomic positions within the ion that is related to local phonon/molecular vibration) and of surrounding molecules (crystal phonon) contributes to P^+. In this way, there are three polarization contributions: (i) electronic polarization (fast, and called electronic polaron from quasi-particle picture), (ii) intramolecular geometrical polarization (slower than (i) and here we call as very small polaron,) and (iii) intermolecular geometrical polarization (small polaron if the geometrical deformation is in the scale of the unit cell of the crystal, and large polaron for a larger scale deformation, expected to be slower than (ii)). Thus, P^+ in UPS may mainly involve electronic polarization effects (i), and contribution of (ii) and (iii) has been considered to be too slow to be detected effectively by conventional UPS. Accordingly, UPS measures mainly a positive electronic polaron, while the hopping mobility in devices also involves effects of the very small, small, and large polarons (positive/negative polaron for hole/electron) depending on timescale of the hopping as well as the electronic polaron. Therefore, information on these polarons, especially on polaron binding energy (E_{Pol}: stabilization energy by polarization) and the timescale, is important in discussion of photoionization and charge transport.

3.2.3
Requirement from Thermodynamic Equilibrium

There is key concept for considering electronic state of solid and the energy level alignment at the interface of interacting two solids. The electron system of solid is

specified by the Fermi–Dirac distribution with the Fermi level (E_F). E_F is the chemical potential of the electron (fermion) system. If an organic solid is free from impurity and effective masses (m^*) of the HOMO hole and the LUMO electrons are the same, E_F locates at the center of the HOMO–LUMO gap. Since the electrons fill the energy levels strictly following the Fermi–Dirac distribution, an interface system consisting of two solids must have single E_F throughout the interacting solids when the electrons in this system are in thermodynamic equilibrium after exchange through the interface. This concept should be strictly valid for the electron system in thermodynamic equilibrium.

The work function ϕ of the solid is defined as the energy separation between the E_F and the VL.

3.3 Electronic Structure in Relation to Charge Transport

3.3.1 Ultraviolet Photoemission Spectroscopy

Photoemission spectroscopy, particularly ultraviolet photoemission spectroscopy, is a well-established and the most widely used technique in characterizing valence electronic structure at interfaces, including metal–molecule interfaces and solids (thin films of high resistivity). A schematic UPS process is shown in Figure 3.3, where the energy and momentum conservation rules are used in analyzing observed spectra. As the photogenerated hole exists during the photoionization of a molecular solid, the spectrum reflects the one hole state. Thus, for example, the binding energy (E_B) from E_F can be obtained by the energy conservation rule as

$$E_B = h\nu - E_k - \phi \tag{3.4}$$

where E_k and ϕ are the kinetic energy of photoelectron and the work function of molecular film, respectively. The vacuum level (E_{vac}), at which $E_k = 0$, is identified by the cutoff position of the secondary electron. E_F is measured by UPS of the conductive/metal substrate. In some cases, the binding energy (E_B^v) is measured from E_{vac} as

$$E_B^v = E_B + \phi = h\nu - E_k \tag{3.5}$$

Elimination of the photogenerated hole by electron transfer from the substrate contributes to the broadening of the observed spectral width, if the attractive Coulombic potential acting on the photoelectron disappears by the elimination of the hole before detection of the photoelectron.

In order to obtain the energy band dispersion from UPS experiments, a three-step model is generally adopted for the photoemission process, consisting of an optical dipole excitation in the bulk, followed by transport to the surface and emission to the vacuum [40, 41]. General assumptions are (i) both the energy and the momentum of the electrons are conserved during the optical transition, (ii) the

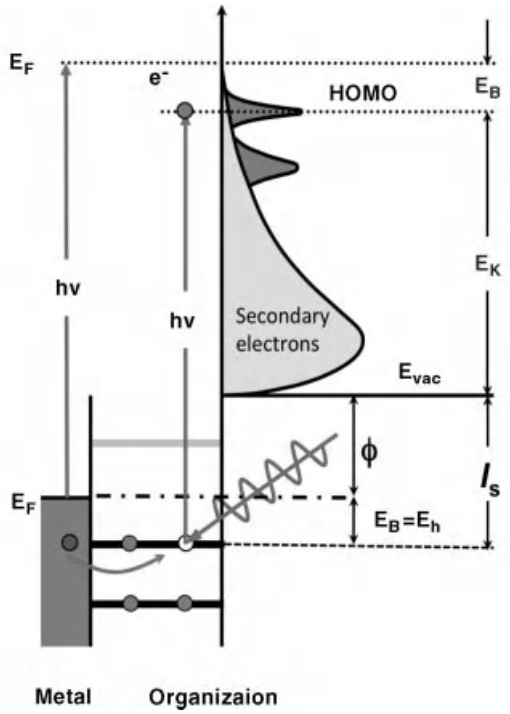

Figure 3.3 Electronic structure probed by ultraviolet photoemission spectroscopy (UPS) and important parameters in discussing organic devices. Here, binding energy (E_B) refers to the Fermi level (E_F). E_k, ϕ, and E_h are the kinetic energy of the photoelectron, work function, and hole injection barrier, respectively.

momentum component parallel to the surface is conserved, while the electron escapes through the surface, and (iii) the final continuum state in the solid is a parabolic free electron-like band in a constant inner potential V_0 :,

$$E = \frac{\hbar^2 \mathbf{k}^2}{2m^*} + V_0 \tag{3.6}$$

where m^* is the effective mass of the photoexcited electron in the final state (conduction band) and $\boldsymbol{k}$ is the electron wave vector (Figure 3.4). V_0 represents the effective potential step to be crossed by the photoexcited electron to leave the surface. The kinetic energy E_{kin} and the wave vector $\boldsymbol{K}$ of observed photoelectron is described by the following relation, with the surface normal ($K^{\perp}$) and parallel ($K^{//}$) components of $\boldsymbol{K}$, respectively,

$$E_{\text{kin}} = \frac{\hbar^2 K^2}{2m_0} = \frac{\hbar^2 \left(K^{\perp^2} + K^{//^2} \right)}{2m_0} \tag{3.7}$$

$$K^{\perp} = K\cos\theta, \quad K^{//} = K\sin\theta \tag{3.8}$$

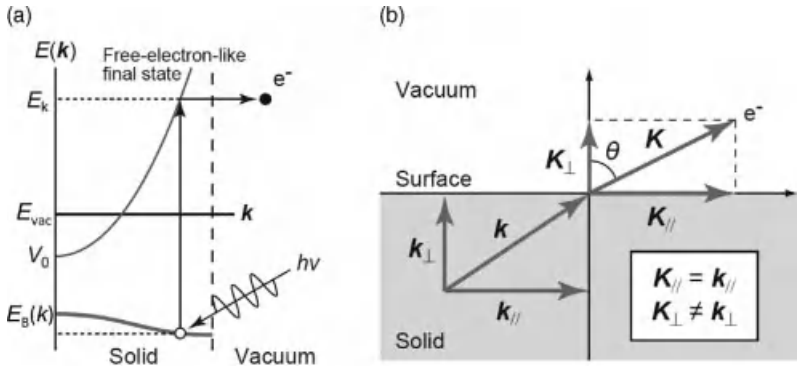

Figure 3.4 Energy and momentum conservation rules for measurements of valence band dispersion $E_B(k)$ (a) and the momentum conservation upon photoelectron escape to vacuum (b).

where m_0 is the free electron mass and θ is the photoelectron emission angle from surface normal (Figure 3.4b). The surface normal and parallel components of the wave vector $\boldsymbol{k}$ of the photoexcited electron in the solid, respectively, can be expressed as

$$k_{\perp} = \sqrt{\frac{2m^*}{\hbar^2}}\sqrt{E_{\mathrm{kin}}\cos^2\theta + V_0} \tag{3.9}$$

$$k_{//} = \sqrt{\frac{2m_0}{\hbar^2}}\sqrt{E_{\mathrm{kin}}}\sin\theta = 0.51A^{-1}\sqrt{E_{\mathrm{kin}}(eV)}\sin\theta \tag{3.10}$$

The binding energy (E_B^v) from E_{vac} of the electron in the initial state is written as Eq. (3.5). The free electron mass m_0 is often assumed for m^* in the computation of $k_{\perp}$. The band dispersion along either $k_{//}$ or $k_{\perp}$ in the organic film may be investigated by changing the electron emission angle θ or E_{kin} of the photoelectrons via tuning of the energy of the incident photons $h\nu$. As understood from Eqs. (3.9) and (3.10), however, the inner potential V_0 must be determined in obtaining $k_{\perp}$, while $k_{//}$ can be determined without V_0. Thus, the simplest way to obtain band dispersion is to measure angle-resolved UPS (ARUPS) of a single-crystal specimen as a function of θ in order to tune $k_{//}$ (method I). A principal difficulty in measuring $k_{//}$ for organic semiconductors and insulators is that electrical conductivity is very low and thus charging of the specimen upon photoemission has hindered to use single-crystal organic samples in ARUPS. Thus, one needs to use oriented thin films on conductive substrates to realize the measurement. Organic thin films, being free from charging, are divided into two groups: (i) uniaxially oriented thin films where direction of the periodic structure or molecular stacking direction is along the surface normal, and (ii) oriented thin films where direction of the periodic structure (one-dimensional molecules) or molecular stacking direction is along the surface. For the former, in order to tune $k_{\perp}$ and probe the electronic band existing along the periodic direction perpendicular to the substrate, experimental setup is chosen such that the electrons are collected normal to the surface ($\theta = 0°$), that is, $k_{//}$ is

zero, while varying $h\nu$ of the incident photons (method II). The latter is similar to the measurements of the single crystal with method I.

The use of actual single crystal in UPS measurements requires elimination of the charging effects by using high-quality single crystal with less charge-trapping centers as well as using photoinduced-electron injection from the substrate to the crystal to reduce the number of the trapped holes. An example of the dispersion measurements of single crystals will be discussed in 3.3.2.

3.3.2
Energy Band Dispersion and Band Transport Mobility

If the intermolecular band dispersion [$E_B = E_B(k)$] is measured with angle-resolved UPS (ARUPS), the effective mass of hole (m_h^*) is obtained experimentally as [28]

$$m_h^* = \hbar^2 \left[\frac{d^2 E_B(k)}{dk^2} \right]^{-1} \tag{3.11}$$

In the case that the band dispersion is described by a tight binding model, $E_B(k) = E_0 - 2t\cos(ak)$, m_h^* becomes

$$m_h^* = \hbar^2 \left[\frac{d^2 E_B(k)}{dk^2} \right]^{-1} = \frac{\hbar^2}{2ta^2} \tag{3.12}$$

where E_0 is the energy of the band center, t is the transfer integral that specifies the intermolecular interaction, and a is the lattice constant for relevant direction. Here, for the tight binding dispersion, the cosine curve is approximated by a parabola near the top of the band. In a broadband model (bandwidth (W) $> k_B T$), the drift mobility of a hole (μ_h) can be estimated from the uncertainty principle [27]:

$$\tau \geq \frac{\hbar}{W}, \quad \tau \geq \frac{\hbar}{k_B T} \tag{3.13}$$

$$\mu_h = \frac{e\tau}{m_h^*} \geq \frac{e\hbar}{m_h^* W} \cong 20 \frac{m_0}{m_h^*} \cdot \frac{300}{T} \tag{3.14}$$

where τ is the relaxation time of the hole due to scattering and T is the temperature.

The first experimental determination of intermolecular band dispersion was reported by Hasegawa *et al.* [42] for an oriented thin film of bis(1,2,5-thiadiazolo *p*-quinobis(1,3-dithiole) (BTQBT). They used an oriented multilayer (30 Å) grown on a cleaved MoS_2 single-crystal surface with the molecular planes nearly parallel to the surface, as confirmed by the quantitative analysis of the photoelectron angular distribution [43]. The $h\nu$ dependence of the normal-emission ARUPS in the HOMO and HOMO-1 region is shown in Figure 3.5a, where the periodic binding energy shifts are seen for both the HOMO and the HOMO-1 bands. The band dispersions obtained from these results are shown in Figure 3.5b, where V_0 was used as an adjustable parameter to obtain the expected periodicity in the extended Brillouin zone scheme from the tight binding model. Although the accuracy of the determined k values depends also on the number of the repeating units, the experimental dispersion relation shows a cosine curve, suggesting both bands can be

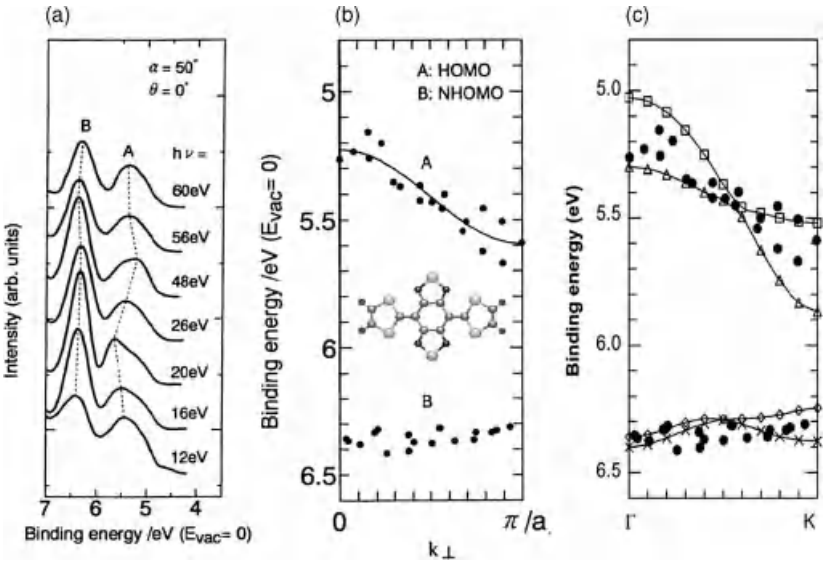

Figure 3.5 $h\nu$ dependence of ARUPS at normal emission for BTQBT thin film on MoS_2 (a) [43]. The HOMO and HOMO-1 bands are labeled A and B, respectively. HOMO and HOMO-1 band dispersion of BTQBT measured with ARUPS with a best-fit tight binding dispersion (b) [43]. Comparison with recent theoretical HOMO (□, △) and HOMO-1 (◇, ×)-derived band structure along Γ–K compared with ARUPS-derived results (●) (c) [45]. The binding energy of the theoretical bands was obtained by setting the HOMO-1-derived bands to have the same binding energy as the experimental value at Γ point. Figures a and b were reprinted with permission from Ref. [43]. Copyright (1993) by the American Physical Society, and Figure c were reprinted with permission from Ref. [45]. Copyright (2005) American Chemical Society.

approximated by the tight binding model. The experimental bandwidth W is about 0.4 eV for the HOMO band and 0.1 eV for the HOMO-1 band. Since W is given by $4t$ in the tight binding model in one dimension, the cosine curve fitting with t, $a_\perp$ (lattice spacing), and V_0 as adjustable parameters yielded $t_{\mathrm{HOMO}} = 0.092$ eV and $t_{\mathrm{HOMO\text{-}1}} = 0.02$ eV, with $a_\perp = 3.4$ Å and $V_0 = -12.5$ eV, respectively. This lattice spacing corresponds well to that (3.45 Å) of the molecular sheets in the reported crystal structure [44]. The hole mobility is then estimated as $\mu_h \geq 6.5\,\mathrm{cm}^2/(\mathrm{V\,s})$ at 290 K. Huang and Kertesz computed the band structure of BTQBT using first-principle density functional theory (DFT) and compared with the experimental dispersion [45]. The results are shown in Figure 3.5c, indicating that the data scattering in the experimental results came from two bands of the HOMO.

In Figures 3.6 and 3.7, the results of PTCDA on MoS_2 [35] and pentacene on Cu(110) [46] are shown, respectively. For pentacene (Pn), the values of m_h^* in the Γ–X_{Pn} and Γ–Y_{Pn} directions at 300 K are $3.02m_0$ and $1.86m_0$, respectively. This result also demonstrates the presence of the anisotropy of the hole mobility in pentacene crystals at higher temperatures. Furthermore, by comparing with the other experimental $E(k)$ relations in pentacene films [47–49], it was confirmed that the band structure of pentacene films is very sensitive to the minor difference in the film structure, especially molecular tilt angle, because of bumpy spatial-distribution

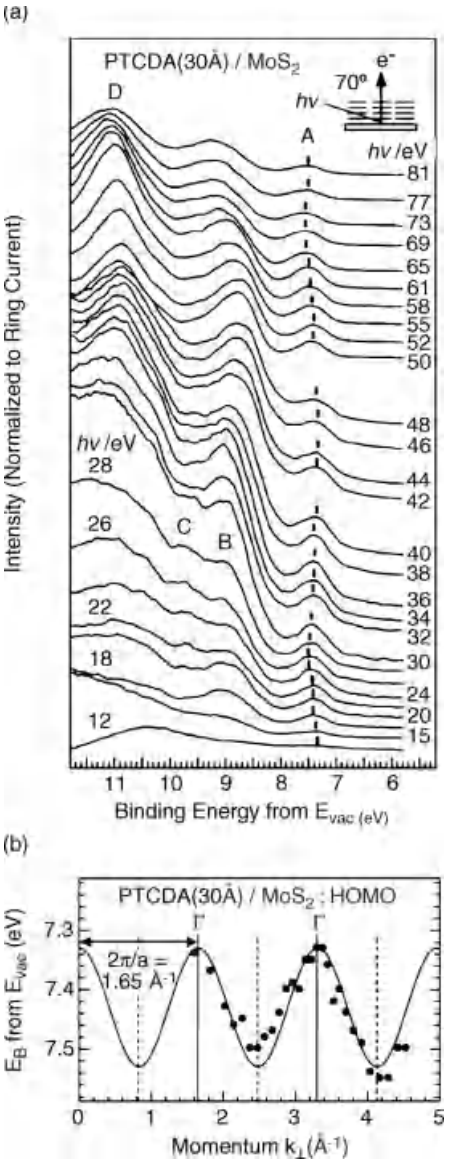

Figure 3.6 $h\nu$ dependence of ARUPS spectra along the surface normal for the 30 Å thick PTCDA multilayer (~8 ML) prepared on the MoS_2 surface (a) and the HOMO band dispersion (b) [35]. The binding energy (E_B) scale refers to the vacuum level (E_{vac}). The energy of the band center, the transfer integral, the lattice spacing normal to the surface, and the inner potential are $E_0 = 7.43$ eV, $t = 0.05$ eV, $a_\perp = 3.8$ Å, and $V_0 = -5.1$ eV, respectively. Figures were reprinted with permission from Ref. [35]. Copyright (2003) by the American Physical Society.

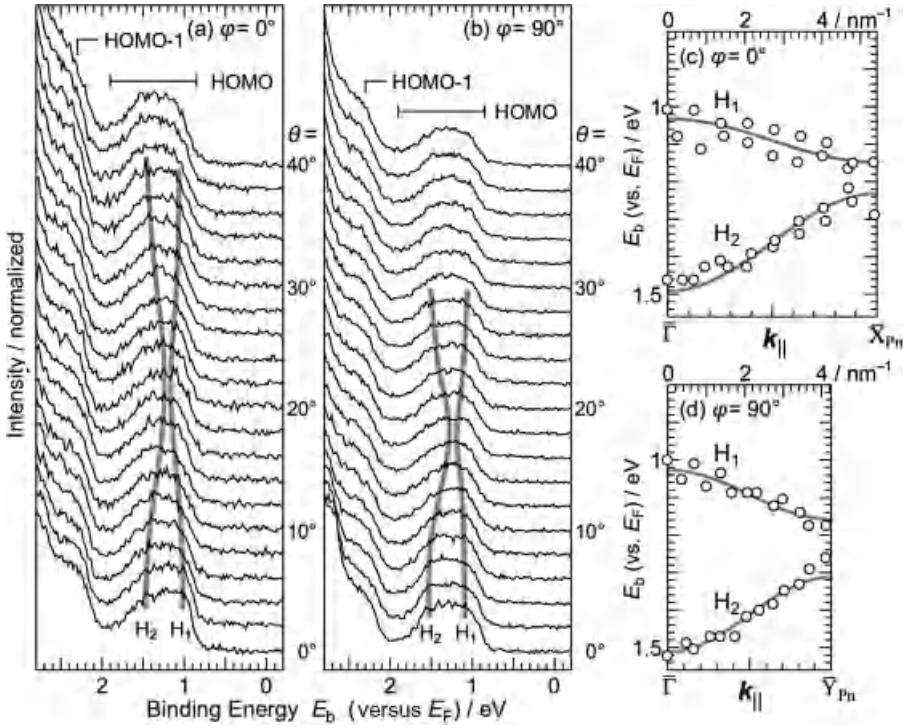

Figure 3.7 Photoelectron takeoff angle (θ) dependence of the ARUPS spectra for the highly ordered upright standing pentacene multilayer film on Cu(110) measured at (a) $\phi = 0°$ and (b) $\phi = 90°$ and the experimental HOMO band dispersion [46]. The incidence photon energy is 20 eV and the sample temperature is 300 K. E_b is the binding energy relative to the Fermi level (E_F) of the substrate. (c and d) $E(k_{||})$ relation for the highly ordered upright standing pentacene multilayer film on Cu(110) at sample azimuthal angle (c) $\phi = 0°$ and (d) $\phi = 90°$. ϕ is measured from [110] direction. Figures were reprinted with permission from Ref. [46]. Copyright (2008) Wiley.

of MO of the molecule. This was also shown with band structure calculation [50]. Further studies on the correlation between the band structure and the film structure would lead to a breakthrough for the understanding of the charge transport mechanism in organic solids.

So far some other dispersion measurements are available for oriented thin films [28]. These measurements used oriented thin films to avoid charging effects upon photoionization.

Recently, band dispersion measurement of a single crystal was realized by Machida *et al*. for rubrene that showed the largest mobility so far [51]. The results are shown in Figure 3.8. The HOMO band dispersion width was found to be 0.4 eV along the Γ–Y direction (well-stacked *b*-direction), whereas it is very small along the Γ–X direction (*a*-direction). The dispersion along the Γ–Y direction gives $m_h^* = 0.65(\pm 0.1)m_0$ using Eq. (3.12). In the case of rubrene single crystal, if the reliable μ_h is known, we can also obtain τ or mean free path (l_h)

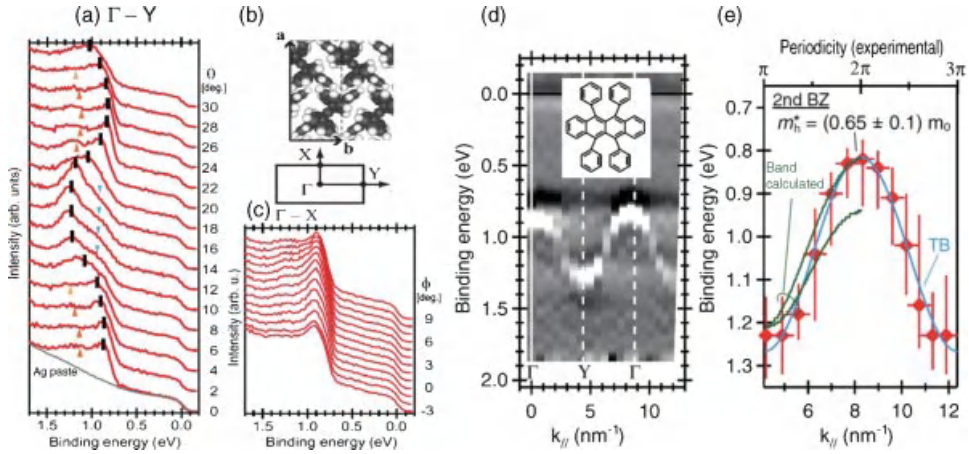

Figure 3.8 ARUPS spectra of a rubrene single crystal and band dispersion [51]. (a) The spectra along the Γ–Y direction (*b*-direction of the crystal). The upward and downward triangles indicate the high and low E_B shoulders, respectively. The bottom curve represents a spectrum of the silver paste. (b) Schematics of molecular orientation of the crystalline *a*–*b* plane ($a = 1.44$ nm, $b = 0.72$ nm) [52] and the corresponding reciprocal lattice. (c) ARUPS spectra along the Γ–X direction. The main peak position at each θ is marked with a thick bar. (d) Second derivative of the ARUPS spectra mapped on the E–$k_{//}$ plane. Center and boundary of the Brillouin zone are also indicated by dashed lines. (e) E–$k_{//}$ diagram of the main peaks along the Γ–Y direction in the second BZ. Theoretical band dispersions [53] and a fitting curve obtained by the tight binding approximation (TB) are also shown. Figures were reprinted with permission from Ref. [51]. Copyright (2010) by the American Physical Society.

of the HOMO hole by combining experimental m_h^* and μ_h to be $\tau = 15$ fs and $l_h = 2.1$ nm or longer. This distance is three times larger than the lattice constant, suggesting that the transport behavior in the HOMO band of the rubrene single crystal may be described by coherent band transport. Similar results were obtained by Ding *et al.* [54].

3.3.3
Density-of-States Effects in Polycrystalline Film

The HOMO band dispersion in pentacene suggests that there is a density-of-states (DOS) structure and, therefore, the DOS may be observed even for polycrystalline films. Such evidences were observed by Fukagawa *et al.* [55] prior to the band dispersion measurements and accelerated the ARUPS experiments. The DOS structure in the HOMO band of polycrystalline pentacene is shown in Figure 3.9. Actually the maximum difference in binding energy between the higher E_B band and the lower E_B one in Figure 3.9, 460–500 meV, is in good agreement with the largest energy separation between two components of the HOMO (Figure 3.7) [46, 49]. The two DOS components of polycrystalline pentacene were better resolved even for polycrystalline monolayer when it is prepared

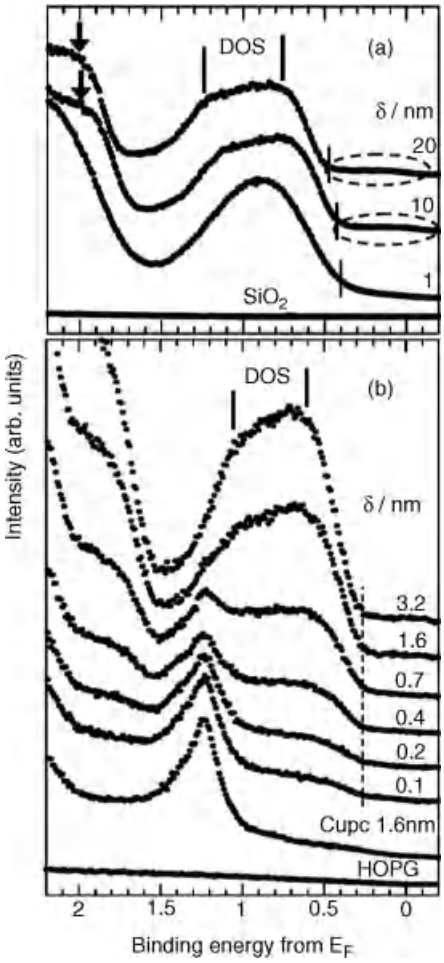

Figure 3.9 He I UPS spectra of pentacene/SiO_2/Si(100) (a) and pentacene/CuPc/HOPG (b) as a function of the deposition amount of pentacene (δ) in the HOMO region [55]. In part (b), the underlying CuPc film consists of flat-lying CuPc. All the spectra were measured at 295 K. Bars indicate density-of-states (DOS) structure of the pentacene HOMO band. Figures were reprinted with permission from Ref. [55]. Copyright (2006) by the American Physical Society.

on CuPc(ML)/GeS(001) and CuPc(ML)/HOPG [56], where the surfaces of GeS(001) and HOPG are passivated by flat-lying CuPc(ML). Note that one can obtain a clear evidence of the intermolecular band dispersion even for the poly-crystalline film of monolayer range when the molecular packing structure in each grain is sufficiently good. If such DOS splitting is not observed, one should understand that the molecular packing in the film is not sufficient, thus yielding a very low μ_h in pentacene field-effect transistor (organic field-effect transistor OFET).

3.4
Electron–Phonon Coupling, Hopping Mobility, and Polaron Binding Energy

3.4.1
Basic Background

Traveling charges couple strongly with phonons, and the hopping charge mobility is dominated by the so-called electron–phonon coupling. Here, phonons involve both delocalized lattice phonons and localized phonons at each molecule in a molecular solid. The latter corresponds well to molecular vibrations of a free molecule; thus, in many cases, we use electron–vibration coupling as the keyword when we consider the coupling with localized phonons. For hole transport, it is necessary to consider hole–vibration coupling, which in principle can be measured by UPS as vibration-related shake-up satellites of a spectral peak (HOMO for hole conduction in organic devices).

Direct experimental evidence of HOMO hole–vibration coupling in organic semiconductor film was published in 2002 [33]. A HOMO band in UPS involves information on the coupling between the conduction hole and vibrations of the molecular ion. UPS measurements can thus offer key information that is necessary to unravel the fundamental mechanism in the carrier transport properties of organic devices.

Charge hopping dominates the mobility of molecular systems with very narrow bandwidths and systems with larger bandwidths if the mean free path of the conduction charge is on the order of the intermolecular distance. Charge transfer processes and carrier dynamics of organic molecules have been widely studied in various fields and detailed theoretical descriptions can be found in several reviews [29–32, 57]. According to general microscopic models, total mobility can be expressed as the sum of two contributions, that is, (i) coherent charge tunneling that dominates transport at low temperatures, and (ii) incoherent charge hopping that becomes dominant at high temperatures. The relative contributions of either mechanism depend on the film structures, where key parameters are the charge (electron or hole)–phonon (molecular vibration) coupling, the electronic bandwidth, and phonon bandwidths. For ideal crystalline films, the model has been satisfactorily described in the theoretical work for two limiting cases, that is, weak and strong electronic coupling limits; however, a model that exhibits intermediate coupling with dependence on temperature has not yet been well explained.

The Holstein polaron model [58, 59] has been applied within the limits of weak intermolecular interactions. There is also a detailed theoretical description in a review [31, 32]. Since the electronic state concerned is well localized, charge transport occurs via hopping from one molecule to the next. Transport in a wide band is also described by hopping when the mean free path of the mobile charge is very short [28]. Moreover, changes in the hopping rate due to variation of relative intermolecular geometry need to be considered for static disorder systems, which are often found in actual organic solids. When an electron or a hole is injected into a

molecular solid, electronic–nuclear coupling leads to localization and transport occurs via localized charge hopping, which is closely related to Marcus electron transfer theory [29]. The semiclassical Marcus hopping model for self-exchange charge transfer has been widely studied. Here, we present one semiclassical approach to obtain hopping mobility. These molecular parameters have appeared in the following equations, which have also often been used in other theoretical models and can experimentally be obtained by using high-resolution UPS measurements.

The hopping mobility (μ) in the high-temperature regime can be approximated from the electron transfer rates by considering the Einstein relation for diffusive motion [28, 31]:

$$\mu = \frac{ea^2}{k_B T} k_{CT} \quad \text{and} \quad k_{CT} = \frac{2\pi}{\hbar} t^2 \sqrt{\frac{1}{4\pi\lambda k_B T}} \exp\left[-\frac{\lambda}{4k_B T}\right] \tag{3.15}$$

where a is the intermolecular distance, k_{CT} is the charge transfer/hopping probability per unit time, λ denotes the reorganization energy induced by the charge transfer, and t corresponds to the intermolecular transfer integral that describes the strength of the electronic interaction between adjacent molecules, as in Eq. (3.12). Thus, there are two major parameters that determine the charge hopping mobility: (i) the electronic coupling (transfer integral t) between adjacent molecules, which needs to be large, and (ii) the reorganization energy λ, which needs to be small for obtaining efficient hopping mobility. For the hole, transport t can be experimentally obtained from the HOMO band dispersion of a molecular stacking system or from the splitting of the HOMO level of a dimer molecule. λ corresponds to the sum of the geometry relaxation energies ($\lambda_{rel}^{(1)}$ and $\lambda_{rel}^{(2)}$) in Figure 3.10. The contribution of each vibration mode to relaxation energy $\lambda_{rel}^{(2)}$ can be determined by the intensities of vibration satellites in high-resolution UPS. The satellite intensities

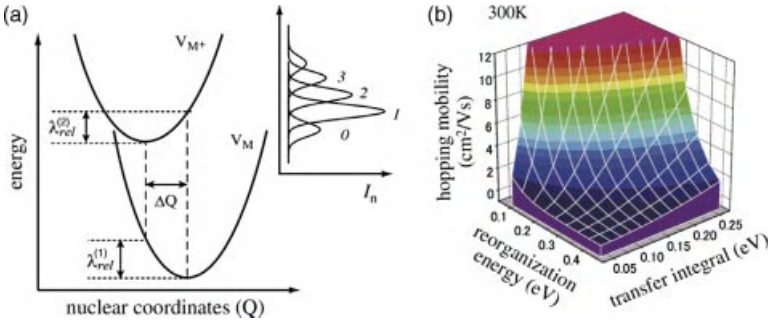

Figure 3.10 (a) Typical adiabatic energy surfaces of neutral (V_M) and ionized (V_{M+}) states and two relaxation energies $\lambda_{rel}^{(1)}$ and $\lambda_{rel}^{(2)}$ at ionization ($M \rightarrow M^+$) and neutralization ($M^+ \rightarrow M$) processes. The UPS intensity of vibration satellites I_n on photoionization is shown on the right. $\lambda_{rel}^{(2)}$ is obtained by measuring I_n. (b) Typical simulation results of charge hopping mobility as function of transfer integral (t) and reorganization energy ($\lambda = 2\lambda_{rel}^{(2)}$ using Eq. (3.15) at 300 K and $a = 0.32$ nm. Figures were reprinted with permission from Ref. [34]. Copyright (2009) Elsevier.

are described by the values of the Huang–Rhys factors S, which in the harmonic approximation are related to $\lambda_{\mathrm{rel}}^{(2)}$ by

$$\lambda_{\mathrm{rel}}^{(2)} = \sum_i S_i h\nu_i \tag{3.16}$$

There are two λ_{rel} components $\lambda_{\mathrm{rel}}^{(1)}$ and $\lambda_{\mathrm{rel}}^{(1)}$, corresponding to going to the ionized state and returning to the neutral state (Figure 3.10). If $\lambda_{\mathrm{rel}}^{(1)}$ is not too different from $\lambda_{\mathrm{rel}}^{(2)}$, λ can be written as

$$\lambda = \lambda_{\mathrm{rel}}^{(1)} + \lambda_{\mathrm{rel}}^{(2)} \approx 2\lambda_{\mathrm{rel}}^{(2)} \tag{3.17}$$

One thus obtains λ using the following relation:

$$\lambda \approx 2\lambda_{\mathrm{rel}}^{(2)} = 2\sum_i S_i h\nu_i \tag{3.18}$$

When the neutral state is in the vibrational ground state, the intensities of the vibrational progression resemble a Poisson distribution:

$$I_n = \frac{S^n}{n!} e^{-S} \tag{3.19}$$

where I_n is the intensity of the nth vibrational satellite. These relations mean that λ can be experimentally estimated by measuring $h\nu_i$ and I_n with high-resolution UPS. As Eq. (3.15) is too simplified when we calculate μ using experimental λ obtained at low temperatures, one should refer, for example, to Refs. [31, 32]. To our knowledge, however, no good theoretical description is available so far to obtain μ or k_{CT} from the analyses of the vibration satellites in the thin-film UPS measured at low temperatures.

Here, one should be careful in considering the hopping mobility obtained by above-described approach, since (i) the validity of the Einstein relationship has been debated for nonequilibrium conditions, for example, in an actual organic field-effect transistor, and (ii) the above-described hopping mobility corresponds to that in an ideal crystalline region, where there is no energy distribution/-spread of the HOMO. For nonideal crystals, which have various band gap states/trap states due to crystal imperfectness and domain boundaries, we need to consider distributions of the electronic energy levels, the intermolecular distance that depends on relative molecular orientation of relevant adjacent molecules and t, and thus the progress of theoretical study on these contributions as well as on the effects of polaron, as discussed in Section 3.2.2 [32, 57]. It is true, however, that μ in actual devices of poor molecular packing should be smaller than that estimated with above-described method.

As the polaron binding energy (E_{pol}) is defined as a stabilization energy when the hole (electron) is localized on a single lattice site, E_{pol} is directly related to the relaxation energy and thus the reorganization energy [32]. For intramolecular relaxation (for a very small positive polaron) in the limit of weak intermolecular electronic

interaction ($t \sim 0$), E_{pol} may be obtained by using $\lambda_{rel}^{(2)}$ determined from the UPS vibration satellites:

$$E_{pol} = \lambda_{rel}^{(2)} \cong \frac{\lambda}{2} \tag{3.20}$$

This relation means that the high-resolution UPS gives E_{pol} even for molecular systems with $\lambda_{rel}^{(1)} \neq \lambda_{rel}^{(2)}$.

3.4.2
Experimental Reorganization Energy and Polaron Binding Energy

The bandwidth of UPS features contains information on electron/hole–phonon/vibration interaction, electron (hole) lifetime, and electron-defect scattering provided that the final state band structure (dispersion) effects are not taken into account. It is necessary to obtain high-resolution UPS spectra to observe vibration satellites for HOMO band. There are few examples of molecular adsorbates on metal surfaces where vibrational features can be resolved in a valence photoemission spectrum and where structural heterogeneity can be eliminated from molecule–metal interfaces to allow the bandwidth to be quantitatively determined.

The first result for a CuPc submonolayer (ML) on HOPG [33] is shown in Figure 3.11, where the molecular plane is parallel to the surface. This result was

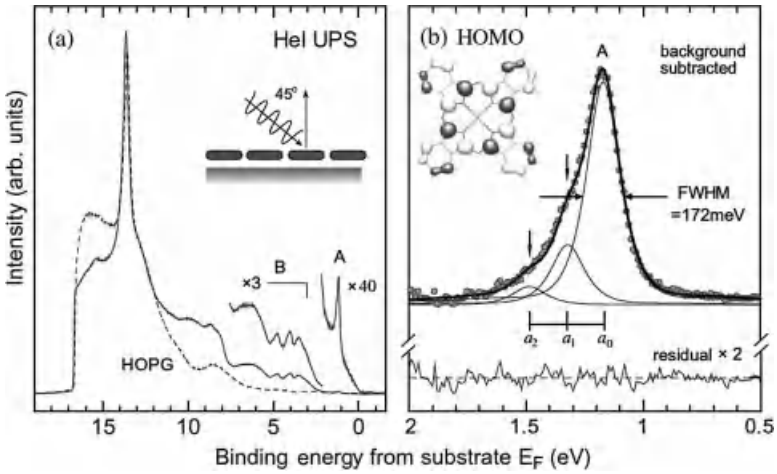

Figure 3.11 (a) He I UPS of CuPc (0.2 nm) on a highly oriented pyrolytic graphite (HOPG) substrate (solid curve) and clean HOPG (dashed curve) at the sample temperature of 295 K at $\theta = 0^\circ$ [33]. (b) Expanded spectrum of top band (A) (HOMO) region after subtraction of background. Circles represent observed spectrum after subtraction of background. Three components (a_0–a_2) of pseudo-Voigt profiles used in curve fitting are indicated by thin solid curves. Solid curve that overlaps observed spectrum is convolution of three fitting curves. Residual of curve fitting is also shown at bottom of (b). Orbital pattern of HOMO of CuPc is also illustrated. Caution should be taken with vibration energy (170 meV) obtained from this result. More precise measurements give smaller vibration energy (153 meV) as shown in Figure 3.12 Figures were reprinted with permission from Ref. [33]. Copyright (2002) Elsevier.

obtained at room temperature (295 K), since the molecular orientation becomes tilted to yield a larger spectral bandwidth at a lower temperature due to the appearance of a nonuniform packing structure [60]. Nevertheless, the experiment was successfully realized in obtaining a much sharper HOMO band for the CuPc/HOPG system, which will be discussed later, by properly controlling the method of cooling. The HOMO (labeled A) in Figure 3.11a appears as a sharp peak at 1 eV below E_F. Panel (b) shows an enlarged view of the HOMO peak after the contribution from the HOPG substrate has been subtracted. The peak is asymmetric and can be decomposed into three vibrational features ($\nu = 0, 1, 2$) with an energy separation of 170 meV (this value has been improved in recent work) (Figure 3.12). This gives a full width at half maximum (FWHM) of 172 meV for the main component ($\nu = 0$). Considering an instrument resolution (ΔE) of 80 meV, the intrinsic linewidth was obtained as 150 meV, which corresponds to a lifetime of 2.2 fs under the

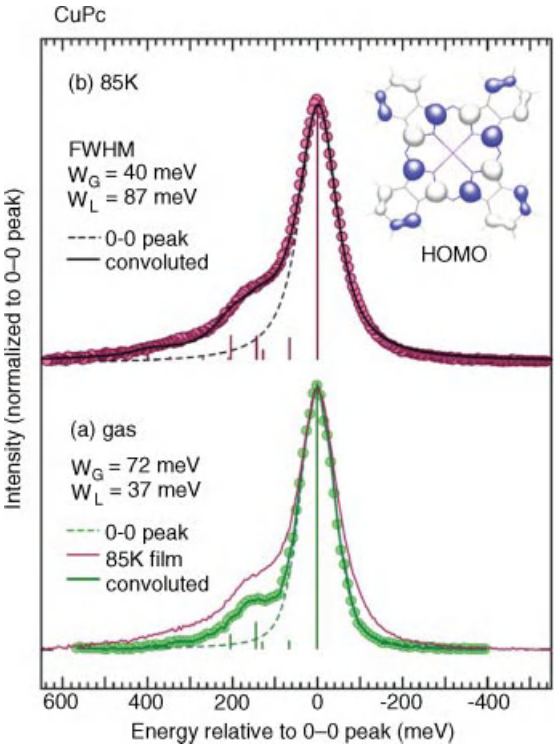

Figure 3.12 Gaseous (green circles) and angle-integrated-ML UPS spectra (red circles) for CuPc, compared with convoluted curves of eight vibrational modes (solid curves) [34]. Energy is relative to 0–0 transition peak (dashed curve). (a) Convolution curve obtained by Voigt functions ($W_G = 72$ meV, $W_L = 37$ meV) with S_{gas} and $h\nu_{gas}$, compared with gas-phase and 85 K film spectra (thin curve). Vertical bars indicate 0–0, 0–1, and 0–2 transition intensities. (b) Convolution curve obtained by Voigt functions ($W_G = 40$ meV and $W_L = 87$ meV) with S_{film} and $h\nu_{gas}$. Each S_{film} in this analysis was determined by least-squares fitting. Gas spectrum is after Evangelista *et al.* [66]. Figure was reprinted with permission from Ref. [34]. Copyright (2009) Elsevier.

assumption of using an uncertainty relation. The lifetime effect on the line shape will be discussed elsewhere without using the uncertainty relation. This value can be an upper limit for the lifetime of the hole generated by the photoemission process. The transient hole was considered to be filled by electron transfer from the HOPG substrate; thus, the lifetime of the HOMO hole may correspond to the electron transfer rate to the HOMO.

Figure 3.13 shows the angle-integrated UPS spectra ($\theta = 0°$–$60°$) of a pentacene (ML)/HOPG system compared with the convoluted curves of 18 A_g modes [61]. The energy scale is relative to the 0–0 transition peak. Here, the thin-film spectra have also been integrated for the azimuthal angle around the surface normal by the azimuthal disorder of the single-crystal domains in the HOPG surface. The convolutions were carried out using Voigt functions, in which the

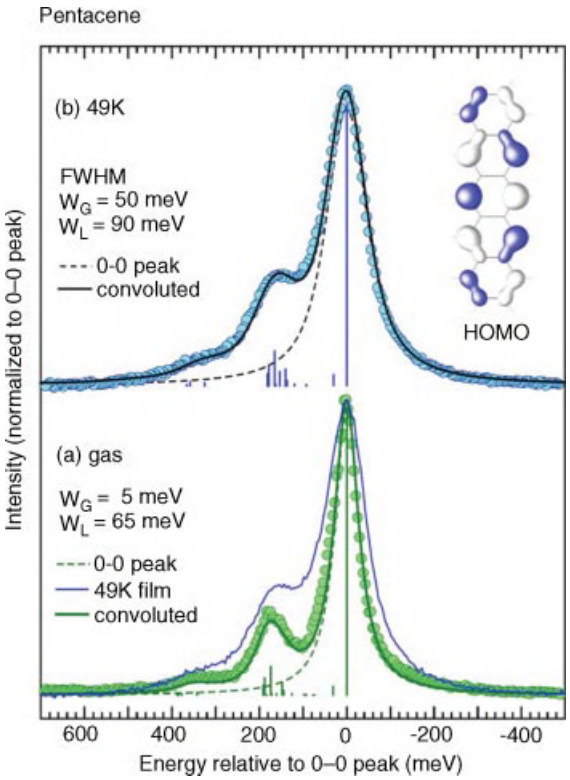

Figure 3.13 Gaseous (green circles) and angle-integrated ML UPS spectra (blue circles) for pentacene compared with convoluted curves of 18 A_g vibrational modes (solid curves) [34, 61]. Energy is relative to 0–0 transition peak (dashed curve). (a) Convolution curve obtained by Voigt functions ($W_G = 5$ meV and $W_L = 65$ meV) with S_{gas} and $h\nu_{gas}$, compared with gas-phase and 49 K film spectra (thin curve). Vertical bars indicate 0–0, 0–1, and 0–2 transition intensities. (b) Convolution curve obtained by Voigt functions ($W_G = 50$ meV and $W_L = 90$ meV), assuming values of 1.2 S_{gas} and 0.95 $h\nu_{gas}$. Gas spectrum is after Malagoli *et al.* [62]. Figure was reprinted with permission from Ref. [34]. Copyright (2009) Elsevier.

intensity of the vibration satellite is given by 0–0, 0–1, and 0–2 transitions as represented by the Poisson distribution. The convoluted curve with $W_G = 5$ meV and $W_L = 65$ meV for Voigt functions and with the vibration intensities given by the gas-phase S factor (S_{gas}) and the gas-phase vibration energies (h_{ngas}), which were used to analyze the gas-phase spectrum [62], is in excellent agreement with the gas-phase spectrum to yield a λ_{gas} of 97 meV. However, there was marked disagreement between this convoluted curve and the 49 K spectrum both in the satellite intensities and the linewidth. Better agreement between the 49 K and the convoluted spectrum is obtained for $W_G = 50$ meV, $W_L = 90$ meV, and $S_{film} = 1.2S_{gas}$ for all A_g vibrational modes, in which all $h\nu_{gas}$'s are contracted by 0.95, which is obtained from direct measurements of the vibration energy for the satellite peak (158 meV for 49 K film and 167 meV for gas-phase UPS). Therefore, λ for the pentacene/HOPG (λ_{film}) was obtained from Eq. (3.18) as $\lambda_{film} = 109$ meV at 49 K. The value was slightly revised to $\lambda_{film} = 110$ meV (Kera, S. and Ueno, N. *et al.*, unpublished). λ_{film} is larger than λ_{gas} [62, 63], indicating that the hole mobility at the interface and in the bulk of oligoacene crystal is smaller than that expected from the gas-phase results.

Paramonov *et al.* [64] calculated on the hole–vibration coupling on the pentacene/graphite system and demonstrated that the effects of molecule/substrate interaction on hole–vibration coupling are larger than those of intermolecular interaction. Using Eq. (3.15), the hopping mobility in a crystalline pentacene can be estimated as 1–2 cm^2/Vs from $\lambda_{film} = 0.10$–0.11 eV obtained from monolayer film, $t = 0.04$–0.06 eV from band dispersion measurements [46, 49], $a = 0.32$ nm, and $T = 300$ K. Note that λ_{film} and t depend on the direction of hopping in the crystal. In passing, Nan *et al.* reported that the semiclassical Marcus theory is valid only for very small λ and at very high temperatures by considering electronic coupling [65].

Figure 3.12 plots new angle-integrated UPS spectra ($\theta = 0$–$60°$) for the CuPc (ML)/HOPG system with the gas-phase results [66] and FC analysis on the Pc system by Kera *et al.* [34, 56]. Here, sharper HOMO bands are observed for ML film than those were evident in the previous results (Figure 3.11) by measuring the UPS using the electron energy analyzer with a higher energy resolution ($\Delta E < 20$ meV) and by controlling the sample preparation more carefully. The FWHM of the 0–0 peak for the integrated spectrum is about 120 meV. The convolutions were done using Voigt functions as was described for pentacene. The convoluted curve with $W_G = 72$ meV and $W_L = 37$ meV for the Voigt functions was used for the gas-phase spectrum. The vibrational fine structure of the gas-phase CuPc was reproduced well using eight vibrational modes (A_g and B_{1u}) whose intensities satisfied the linear coupling model. We used up to eight vibration modes with the largest S factors to reduce computation costs, that is, other modes with smaller S factors were considered in a spectral width. We found that the k for the CuPc was $\lambda_{gas} = 63$ meV from the gas-phase results. This value is similar to the results recently estimated from theoretical calculations for TiOPc [67].

In Figure 3.14, we show values of the relaxation energy $\lambda_{rel}^{(2)}$, namely, $\lambda_{film} \cong 2\lambda_{rel}^{(2)}$ and polaron binding energy E_{pol} (intramolecular polaron), which have been

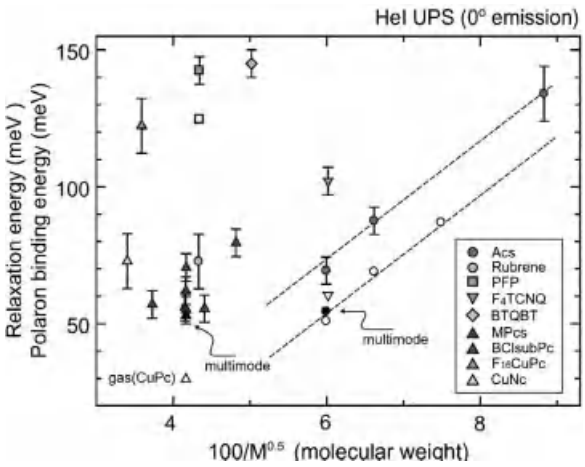

Figure 3.14 Experimental relaxation energy ($\lambda_{rel}^{(2)}$) and polaron binding energy (E_{pol}) versus $100/M^{0.5}$ (M: molecular weight) for various organic monolayer films. Reorganization energy $\lambda \cong 2\lambda_{rel}^{(2)}$ [34]. Results are for oligoacene (Ac: pentacene, tetracene#, naphthalene#), perfluoropentacene (PFP#), rubrene#, tetrafluoro-tetracyanoquinodimethane (F_4TCNQ#), bis(1,2,5-thiadiazolo)-*p*-quinobis (1,3-dithiole) (BTQBT#), metal–phthalocyanine (MPc; M = H_2, OV, OTi, ClAl, Cu, and Pb), Cu–naphthalocyanine(CuNc#), Cu–hexadecafluorophthalocyanine (F_{16}CuPc#), and chloro(subphthalocyaninato)boron (BClsubPc#). Open symbols are from gaseous results: Acs (pentacene, tetracene, and anthracene) [4], PFP#, CuPc (spectra) [66], and F_4TCNQ#, and closed symbols are for multimode analysis of pentacene and CuPc films (Figures 3.12 and 3.13). Dashed lines are visual guides. HOMO band measured at normal emission (acceptance angle of 12°) is fitted with Gaussian functions. Single normal mode (typically 150–170 meV) was considered to determine relaxation energy. Errors are estimated from residual spectra. Hash marks (#) represent that original spectra have not yet been published [34]. Figure was reprinted with permission from Ref. [34]. Copyright (2009) Elsevier.

measured so far [34], where $\lambda_{rel}^{(2)}$ and E_{pol} obtained by single-mode analysis are plotted as a function of the square root of the molecular weight (M). The relaxation energies for the films were estimated using the spectra at $\theta = 0°$ with acceptance angle of 12° and some of the solid-state effects have also been included [34]. Nevertheless, one can clearly see a correlation between the relaxation energy and the size of the π electron system for oligoacenes (Acs), as has been described in theoretical papers [31, 63]. It is interesting to see that the polaron binding energy is 0.05–0.15 eV, while the electronic polarization energy (electronic polaron binding energy) is around 1.2–1.8 eV [37].

3.5 Summary

Although many works were carried out on electrical properties of organic devices, most of them discussed *I–V* curves under classical electromagnetism with charge injection barrier estimated by UPS on organic films on polycrystalline

substrates/electrodes. In order to develop key technologies to increase device functions, it is clear that we need to understand relation between the electronic states and the electrical property.

We described what we have learnt so far, but it is more important to realize what we do not know currently. Emphasis in this chapter was therefore placed on high-precision UPS studies that can provide deeper insights into the charge mobility of organic molecular systems that have been elusive in past experimental studies on electrical conduction. The accurate information on the electronic states described here would provide a way to reach the goal of organic electronics. As impacts of imperfect molecular packing on the electronic structure are also important to unravel the energy level alignment and band bending, we will describe this issue elsewhere.

As understood from this chapter, we must know the relaxation time or mean free path of the conduction charge, namely, the mean free path of very low-energy electron and hole in an organic solid, in obtaining the drift mobility more quantitatively. Experimental challenges on this issue have been left.

Acknowledgments

The author is very grateful to the late Prof. K. Seki of Nagoya University for close collaboration for more than 30 years. He also thank Prof. S. Kera of Chiba University, Dr. H. Yamane of Institute for Molecular Science, and Dr. H. Fukagawa of NHK for their collaboration.

References

1 Akamatsu, H. and Inokuchi, H. (1950) *J. Chem. Phys.*, **18**, 810.
2 Akamatsu, H., Inokuchi, H., and Matsunaga, Y. (1954) *Nature*, **173**, 168.
3 Inokuchi, H. (2006) *Org. Electron.*, **7**, 62.
4 Ishii, H., Sugiyama, K., Ito, E., and Seki, K. (1999) *Adv. Mater.*, **11**, 605.
5 Salaneck, W.R., Seki, K., Kahn, A., and Pireaux, J.-J. (eds.) (2002) *Conjugated Polymers and Molecular Interfaces: Science and Technology for Photonic and Optoelectronic Applications*, Marcel Dekker, New York.
6 Koch, N. (2007) *ChemPhysChem.*, **8**, 1438.
7 Hwang, J., Wan, A., and Kahn, A. (2009) *Mater. Sci. Eng. R*, **64**, 1.
8 Gao, Y. (2010) *Mater. Sci. Eng. R*, **68**, 39.
9 Heimel, G., Salzmann, I., Duhm, S., and Koch, N. (2011) *Chem. Mater.*, **23**, 359.
10 Heine, V. (1965) *Phys. Rev.*, **138**, A1689.
11 Tejedor, C., Flores, F., and Louis, E. (1977) *J. Phys. C*, **10**, 2163.
12 Flores, F. and Tejedor, C. (1987) *J. Phys. C*, **20**, 145.
13 Mönch, W. (1994) *Surf. Sci.*, **299**, 928.
14 Vázquez, H., Oszwaldowski, R., Pou, P., Ortega, J., Pérez, R., Flores, F., and Kahn, A. (2004) *Europhys. Lett.*, **65**, 802.
15 Vázquez, H., Gao, W., Flores, F., and Kahn, A. (2005) *Phys. Rev. B*, **71**, 041306 (R).
16 Kahn, A., Zhao, W., Gao, W., Vázquez, H., and Flores, F. (2006) *Chem. Phys.*, **325**, 129.
17 Vázquez, H., Dappe, Y.J., Ortega, J., and Flores, F. (2007) *J. Chem. Phys.*, **126**, 144703.
18 Vázquez, H., Flores, F., and Kahn, A. (2007) *Org. Electron.*, **8**, 241.

19 Braun, S. and Salaneck, W.R. (2007) *Chem. Phys. Lett.*, **438**, 259.
20 Braun, S., Salaneck, W.R., and Fahlman, M. (2009) *Adv. Mater.*, **21**, 1.
21 Braun, S., Liu, X., Salaneck, W.R., and Fahlman, M. (2010) *Org. Electron.*, **11**, 212.
22 Ono, M., Sueyoshi, T., Zhang, Y., Kera, S., and Ueno, N. (2006) *Mol. Cryst. Liq. Cryst.*, **455**, 251.
23 Fukagawa, H., Kera, S., Kataoka, T., Hosoumi, S., Watanabe, Y., Kudo, K., and Ueno, N. (2007) *Adv. Mater.*, **19**, 665.
24 Sueyoshi, T., Fukagawa, H., Ono, M., Kera, S., and Ueno, N. (2009) *Appl. Phys. Lett.*, **95**, 183303.
25 Sueyoshi, T., Kakuta, H., Ono, M., Sakamoto, K., Kera, S., and Ueno, N. (2010) *Appl. Phys. Lett.*, **96**, 093303.
26 Mao, H.Y., Bussolotti, F., Qi, D.-C., Wang, R., Kera, S., Ueno, N., Wee, A.T. S., and Chen, W. (2011) *Org. Electron.*, **12**, 534.
27 Meier, H. (1974) Chapter 10, in *Organic Semiconductors*, vol. **2** (ed. H.F. Ebel), Verlag Chemie, Weinheim.
28 Ueno F N. and Kera, S. (2008) *Prog. Surf. Sci.*, **83**, 490.
29 Marcus, R.A. (1993) *Rev. Mod. Phys.*, **65**, 599.
30 Silinsh, E.A. and Čápek, V. (1994) *Organic Molecular Crystals: Interaction, Localization and Transport Phenomena*, Springer, Berlin.
31 Brédas, J.-L., Beljonne, D., Coropceanu, V., and Cornil, J. (2004) *Chem. Rev.*, **104**, 4971.
32 Coropceanu, V., Cornil, J., da Silva Filho, D.A., Oliver, Y., Silbey, R., and Brédas, J.-L. (2007) *Chem. Rev.*, **107**, 926 (see also Erratum, *Chem. Rev.* 2007, 107, 2165).
33 Kera, S., Yamane, H., Sakuragi, I., Okudaira, K.K., and Ueno, N. (2002) *Chem. Phys. Lett.*, **364**, 93.
34 Kera, S., Yamane, H., and Ueno, N. (2009) *Prog. Surf. Sci.*, **84**, 135.
35 Yamane, H., Kera, S., Yoshimura, D., Okudaira, K.K., Seki, K., and Ueno, N. (2003) *Phys. Rev. B*, **68**, 33102.
36 Gutmann, F. and Lyons, L.E. (1967) *Organic Semiconductors*, John Wiley & Sons, Inc., New York.
37 Seki, K. (1989) *Mol. Cryst. Liq. Cryst.*, **171**, 255.
38 Koopmans, T. (1933) *Physica*, **1**, 104.
39 Phillips, J.C. (1961) *Phys. Rev.*, **123**, 420.
40 Berglund, C.N. and Spicer, W.E. (1964) *Phys. Rev. A*, **136**, 1030.
41 Feibelman, P.J. and Eastman, D.E. (1974) *Phys. Rev. B*, **10**, 4932.
42 Hasegawa, S., Mori, T., Imaeda, K., Tanaka, S., Yamashita, Y., Inokuchi, H., Fujimoto, H., Seki, K., and Ueno, N. (1994) *J. Chem. Phys.*, **100**, 6969.
43 Hasegawa, S., Tanaka, S., Yamashita, Y., Inokuchi, H., Fujimoto, H., Kamiya, K., Seki, K., and Ueno, N. (1993) *Phys. Rev.*, **B48**, 2596.
44 Yamashita, Y., Tanaka, S., Imaeda, K., and Inokuchi, H. (1991) *Chem. Lett.*, **7**, 1213.
45 Huang, J. and Kertesz, M. (2005) *J. Phys. Chem. B*, **109**, 12891.
46 Yamane, H., Kawabe, E., Yoshimura, D., Sumii, R., Kanai, K., Ouchi, Y., Ueno, N., and Seki, K. (2008) *Phys. Status Solidi B*, **245**, 793.
47 Koch, N., Vollmer, A., Salzmann, I., Nickel, B., Weiss, H., and Rabe, J.P. (2006) *Phys. Rev. Lett.*, **96**, 156803.
48 Annese, E., Viol, C.E., Zhou, B., Fujii, J., Vobornik, I., Baldacchini, C., Betti, M.G., and Rossi, G. (2007) *Surf. Sci.*, **601**, 4242.
49 Kakuta, H., Hirahara, T., Matsuda, I., Nagao, T., Hasegawa, S., Ueno, N., and Sakamoto, K. (2007) *Phys. Rev. Lett.*, **98**, 247601.
50 Yoshida, H. and Sato, N. (2008) *Phys. Rev. B*, **77**, 235205.
51 Machida, S., Nakayama, Y., Duhm, S., Xin, Q., Funakoshi, A., Ogawa, N., Kera, S., Ueno, N., and Ishii, H. (2010) *Phys. Rev. Lett.*, **104**, 156401.
52 Chapman, B.D., Checco, A., Pindak, R., Siegrist, T., and Kloc, C. (2006) *J. Cryst. Growth*, **290**, 479.
53 Filho, D.A.d.S., Kim, E.-G., and Brédas, J.-L. (2005) *Adv. Mater.*, **17**, 1072.
54 Ding, H., Reese, C., Mäkinen, A.J., Bao, Z., and Gao, Y. (2010) *Appl. Phys. Lett.*, **196**, 222106.
55 Fukagawa, H., Yamane, H., Kataoka, T., Kera, S., Nakamura, M., Kudo, K., and Ueno, N. (2006) *Phys. Rev.*, **B73**, 245310.
56 Ueno, N., Kera, S., Sakamoto, K., and Okudaira, K.K. (2008) *Appl. Phys.*, **A92**, 495.
57 Zhu, X.-Y. (2004) *Surf. Sci. Rep.*, **56**, 1.

58 Holstein, T. (1959) *Ann. Phys.*, **8**, 325.

59 Holstein, T. (1959) *Ann. Phys.*, **8**, 343.

60 Kataoka, T., Fukagawa, H., Hosoumi, S., Nebashi, K., Sakamoto, K., and Ueno, N. (2008) *Chem. Phys. Lett.*, **451**, 43.

61 Yamane, H., Nagamatsu, S., Fukagawa, H., Kera, S., Friedlein, R., Okudaira, K.K., and Ueno, N. (2005) *Phys. Rev. B*, **72**, 153412.

62 Malagoli, M., Coropceanu, V., da Silva Filho, D.A., and Brédas, J.-L. (2004) *J. Chem. Phys.*, **120**, 7490.

63 Coropceanu, V., Malagoli, M., da Silva Filho, D.A., Gruhn, N.E., Bill, T.G., and Brédas, J.-L. (2002) *Phys. Rev. Lett.*, **89**, 275503.

64 Paramonov, P.B., Coropceanu, V., and Brédas, J.-L. (2008) *Phys. Rev. B*, **78**, 041403 (R).

65 Nan, G., Wang, L., Yang, X., Shuai, Z., and Zhao, Y. (2009) *J. Chem. Phys.*, **130**, 024704.

66 Evangelista, F., Carravetta, V., Stefani, G., Jansik, B., Alagia, M., Nazionale, L., Stranges, S., and Ruocco, A. (2007) *J. Chem. Phys.*, **126**, 124709.

67 Norton, J.E. and Brédas, J.-L. (2008) *J. Chem. Phys.*, **128**, 034701.

4
Interfacial Doping for Efficient Charge Injection in Organic Semiconductors

Jae-Hyun Lee and Jang-Joo Kim

4.1
Introduction

The discovery of charge conduction in polymers and organic thin films has led to the application of new materials in electronic devices such as light-emitting diodes (OLED), lasers, field-effect transistors (OFETs), photovoltaics (OPVs), sensors, memory chips, and integrated circuits. The most fundamental characteristic of electronic devices is the electrical one represented by the current density–voltage (J–V) relationship.

The J–V characteristics of an organic semiconductor (OS) device are controlled by the charge injection at the electrode/organic and organic/organic interfaces and by the transport in bulk organic semiconductors. The energy level alignment at the interfaces dominantly controls the charge injection at the junctions. Lowering the energy barrier at the interfaces is important to facilitate efficient charge injection through the interfaces. In general, organic materials have low electrical conductivities due to the low intrinsic charge-carrier density and low mobility coming from the hopping transport of charges. The increasing charge density in organics is beneficial by increasing the conductivity of the organics.

Lowering of the injection barriers can be achieved through the proper selection of a metal electrode and an organic material so that the work function of the metal and the highest occupied molecular orbital (HOMO) energy level or the lowest unoccupied molecular energy level (LUMO) of the organic material are aligned for a low energy difference with efficient hole or electron injection through the junction, respectively. The organic materials must also possess high hole or electron mobility for efficient charge transport after charge injection. This method has been utilized to synthesize proper materials for the hole or electron injection layer (HIL and EIL) for organic electronic devices. However, the synthesis of adequate HILs and EILs requires large efforts because other properties such as thermal and electrochemical stabilities and carrier mobility along with the HOMO and LUMO

Physics of Organic Semiconductors, Second Edition. Edited by Wolfgang Brütting and Chihaya Adachi

energy levels must be tuned at the same time. Moreover, the vacuum level shift at the interface makes the energy level alignment sometimes unpredictable.

Various methods other than the synthesis of materials have been proposed up to now, including the modification of the electrode work function, insertion of an interfacial layer, and interfacial doping in HILs or EILs. In this chapter, methods to lower the injection barrier will be described with emphasis on the interfacial doping method because this method is applicable to a wide variety of electrode materials, organic materials, and organic electronic devices.

4.2
Insertion of an Interfacial Layer in the Organic/Electrode Junction

4.2.1
Electron Injection

Low work function metals such as Mg or Ca have been used as cathodes with efficient electron injection for organic semiconductors [1]. Unfortunately, the low work function metals are unstable to air exposure. Due to this, alloys containing elements such as Mg:Ag or Li:Al have been developed with increased stability [2, 3]. Depositing alkali metals such as Li and Cs between an organic layer and the Al cathode turned out to be an effective method to increase electron injection through the reaction of Li with either the underlying organic layer or the upper Al electrode [4–6]. Along with the modification of the electrode material itself, the technique of inserting an interfacial layer between an organic or a polymer layer and the stable Al electrode was developed. Kim *et al.* used a very thin poly(methyl methacrylate) (PMMA) Langmuir–Blodgett (LB) film as the interfacial layer between the poly[2-methoxy-5-(2-ethylhexyloxy)-1,4-phenylene-vinylene] (MEHPPV) and an Al electrode [7]. They found that the emission efficiency of the electroluminescence (EL) devices increased without increasing the driving voltage (Figure 4.1) and was attributed to enhanced electron injection from the Al electrode, even though the interfacial layer was an insulation material [7]. Different insulating materials such as Al_2O_3 or MgO have been used as the interfacial layer with similar observed effects [8, 9].

Soon after the first report of an interfacial layer, Hung *et al.* inserted a thin LiF layer between the tris-(8-hydroxyquinoline) aluminum (Alq_3) and the Al cathode to significantly reduce the driving voltage [10]. The current density in the device with the LiF/Al electrode was one order of magnitude higher than that of the Mg:Ag electrode and two orders of magnitude higher than that of the Al electrode (Figure 4.2) [10]. The LiF/Al electrode is widely used as a cathode these days, especially as a stable and efficient cathode in OLEDs. Various mechanisms have been proposed to explain the enhanced electron injection in the Alq_3/LiF/Al junction, including tunneling injection [10], interface dipole formation [11, 12], band bending [13], dissociation of LiF [14, 15], or a chemical reaction among Al, LiF, and Alq_3 [11, 16]. One of the mechanisms is the large vacuum level shift, which reduces the electron injection barrier due to the large dipole moment of LiF (6.33D) [11]. Figure 4.3 shows the energy diagram of Al/Alq_3, Al/LiF (0.5 nm)/Alq_3 (5 nm), and Al/LiF (2 nm)/Alq_3 (5 nm) interfaces [12].

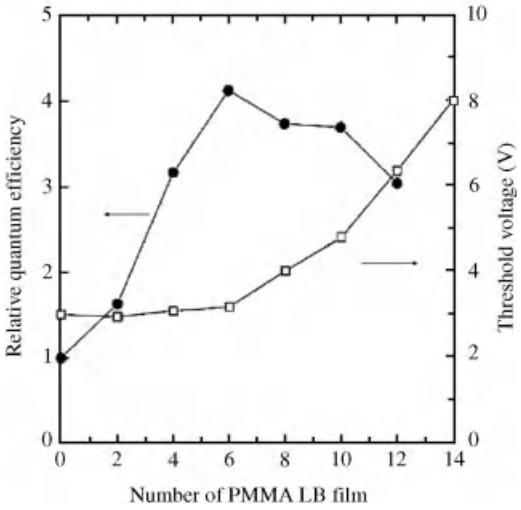

Figure 4.1 Relative quantum efficiency and threshold voltage of the EL devices (ITO/MEHPPV/LB layers/Al) for different numbers of PMMA LB layers where the thickness of the PMMA LB monolayer is 1 nm [7].

Based on ultraviolet photoemission spectroscopy (UPS), X-ray photoemission spectroscopy (XPS), and metastable atom electron spectroscopy (MAES) analyses, a very thin LiF layer on an Al layer was investigated and found to have a similar electronic structure with a thick LiF film, even though LiF was expected to form nano-sized clusters under the thickness of 1.5 nm. LiF layers with thicknesses of 0.5 and 2 nm induced a large vacuum level shift of 0.9 and 0.7 eV at the interface of Al/LiF and 1.6 and 0.1 eV at the interface of LiF/Alq_3, respectively. These large vacuum

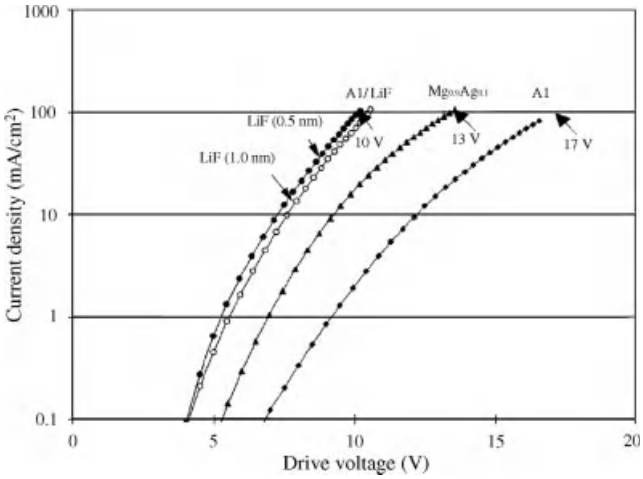

Figure 4.2 The *J–V* characteristics of three OLEDs with Al, $Mg_{0.9}Ag_{0.1}$, and Al/LiF electrodes, respectively [10].

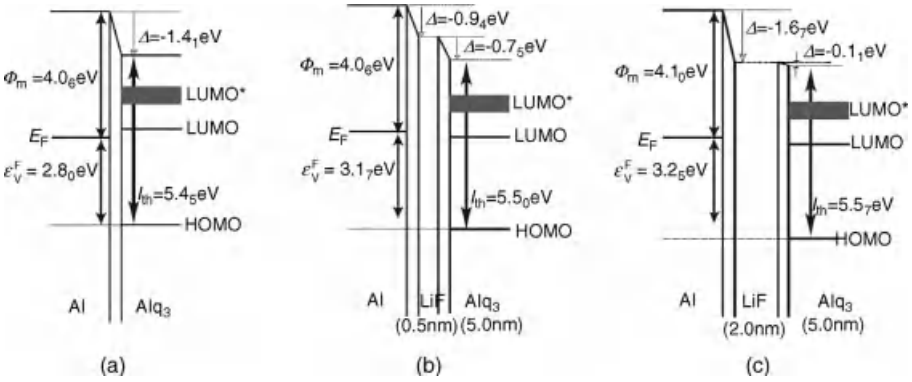

Figure 4.3 Energy diagram of the Alq_3/LiF/Al systems with a LiF layer of (a) 0 nm, (b) 0.5 nm, and (c) 2.0 nm thickness [12].

level shifts decreased the electron injection barrier between the work function of the cathode and the LUMO level of the Alq_3 layer.

The other proposed mechanism is the dissociation of LiF or the chemical reaction of LiF with Alq_3 and Al, which in turn, behaves as an electrical dopant in Alq_3. Figure 4.4 shows the high-resolution electron energy loss spectroscopy (HREELS) spectra of each step in the layered structures of Si/LiF/Al and Si/Alq_3/LiF/Al, respectively [15].

The loss peak of LiF after the deposition of Al did not change in intensity, but shifted from 73 to 68 meV due to the weakening of the Li—F bond by the interaction between the Al and LiF, indicating that the deposition of Al on LiF alone did not induce a chemical reaction (Figure 4.4a). The deposition of LiF on the Alq_3 layer

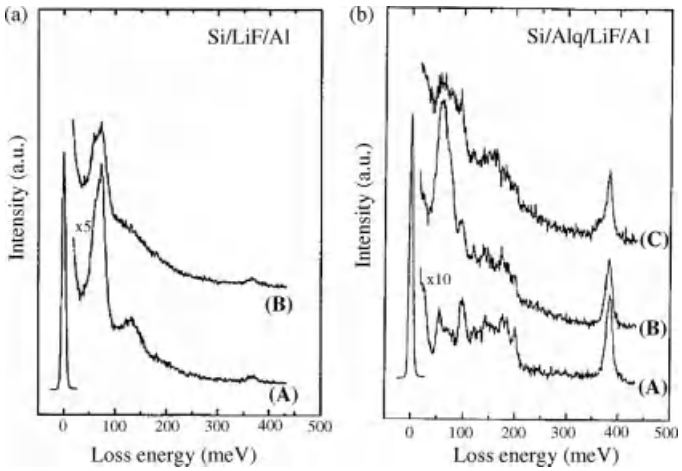

Figure 4.4 (a) HREELS spectra of (A) Si/LiF (0.52 nm) and (B) Si/LiF (0.52 nm)/Al (0.23 nm). (b) (A) Si/Alq_3 (2 nm), (B) Si/Alq_3 (2 nm)/LiF (0.26 nm), and (C) Si/Alq_3 (2 nm)/LiF (0.26 nm)/Al (0.23 nm) [15].

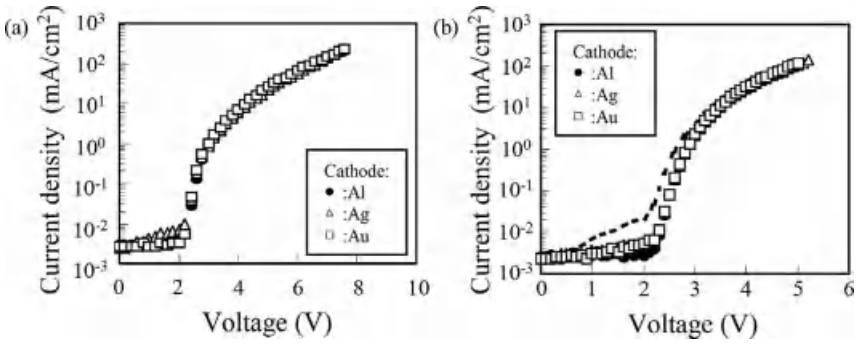

Figure 4.5 The *J–V* characteristics of devices with cathodes of Al, Ag, or Au (a) with thin Cs_2CO_3 as EIL (b) with coevaporated EILs [20].

again did not induce a chemical reaction indicated by no significant change in the loss peak of Alq_3 at 384 meV (Figure 4.4b). However, when the Al layer was deposited on the LiF layer, the loss peak of LiF at around 62 meV was significantly reduced. These results indicate that the dissociation of Li from LiF took place in the presence of Alq_3 and Al [15]. Dissociated Li atoms were expected to act as a n-type dopant in the Alq_3 layer, which enhances the electron injection. If this interpretation is the case explaining the enhancement of the electron injection, the insertion of the LiF layer may correspond to the first report of interfacial doping in organic semiconductors.

Besides alkali metal halides such as LiF, NaF, MgF_2, CsF, and NaCl layers [10, 16–19], alkali metal carbonates have also been investigated for their excellent electron injection properties [20]. The *J–V* characteristics of OLEDs with an EIL of Cs_2CO_3 and with a Cs_2CO_3 doped layer are shown in Figure 4.5a and b, respectively [20]. Thin Cs_2CO_3 and Cs_2CO_3 doped layers with various cathodes have facilitated good electron injection into devices.

Other alkali metal carbonates such as Rb_2CO_3 and Na_2CO_3 have also been investigated as an EIL and a n-type dopant [21, 22]. These materials were used not only as thin EILs but also as n-type dopants. The enhancement of electron injection by doping will be discussed in next section.

4.2.2
Hole Injection

Similar strategies developed for electron injection have been utilized for hole injection. A simple way to enhance hole injection is to modify the electrode. Metal electrodes with a high work function (Pt or Au), metal oxides (ZnO, TiO_2, Pr_2O_3, etc.), and surface modifications such as UV ozone treatment or plasma treatment of ITO were investigated to increase the work function of electrode [23–27]. However, these electrodes still formed the Schottky contact with organic semiconductors due to surface contamination or vacuum level shift at the interface with the organic layers [28]. Insertion of a charge injection layer such as fluorocarbon (CF_4), polytetrafluoroethylene (Teflon), self-assembled

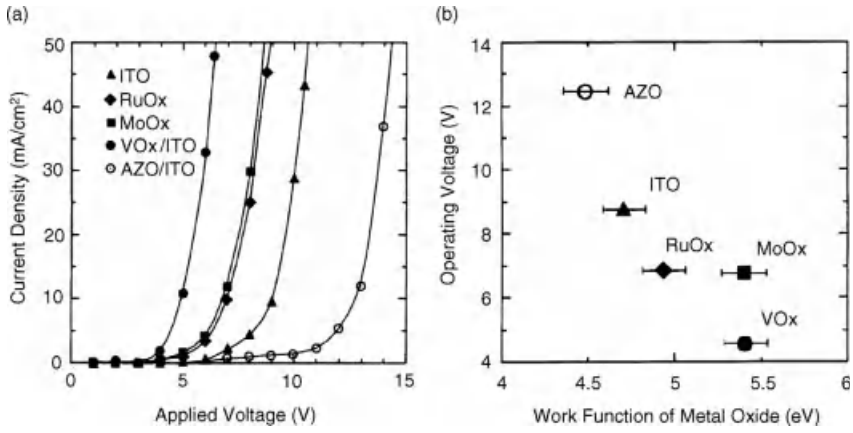

Figure 4.6 (a) The *J–V* characteristics and (b) operating voltage of OLEDs with VO_x, MoO_x, RuO_x, and AZO layers as the HIL on the ITO layer [33].

monolayers (SAMs), and poly(3,4-ethylenedioxythiophene):polystyrene sulfonic acid (PEDOT:PSS) enhanced hole injection from electrodes [29–32]. These additional layers reducing the charge injection barriers commonly have a large vacuum level shift due to the interface dipole between the electrode and charge injection layer. Recently, effective charge injection by insertion of a thin metal oxide layer has been widely investigated [33–36].

Transition metal oxide (TMO) layers such as ruthenium oxides (RuO_x), molybdenum oxides (MoO_x), vanadium oxide (VO_x), and so on have been used as hole injection layers in OLEDs [33]. These metal oxides possessing high work functions enhanced hole injection into the devices when deposited on an ITO anode, reducing the operating voltage of the devices from 9 to 4.5 V (Figure 4.6). Other TMOs such as tungsten oxide (WO_3) and rhenium oxide (ReO_3) and the organic material 1,4,5,8,9,11-hexaazatriphenylene hexacarbonitrile (HATCN) with a very low LUMO level near 5.6 have been widely used [37–40]. HATCN is also an important material, which is used in practical OLEDs as a HIL and in charge generation layers [39]. Its application in organic devices such as OLEDs or OPVs will be summarized in the next section.

It is interesting to note that hole injection through TMOs is affected by the work function of the electrodes. Figure 4.7 shows the *J–V* characteristics of hole-only devices with V_2O_5 or MoO_3 (3 nm) as a hole injection layer and 1,4-bis[*N*-(1-naphthyl)-*N*′-phenylamino]-4,4′ diamine (NPB) as the hole transporting layer on Al and Ag. The hole injection barriers of the devices with the MoO_3 layer were 0.55 and 0.39 eV on the Al or Ag electrodes, respectively, with the hole injection barriers extracted from the thermionic emission plots ($\ln(J)$–$V^{0.5}$) [41]. Without the MoO_3 layer, the hole injection barriers were 1.2 and 1.7 eV on the Al or Ag electrodes, respectively [42, 43].

A few mechanisms have been proposed to explain the reduction of the hole injection barrier with the insertion of very thin TMOs. In the early research, MoO_3 was

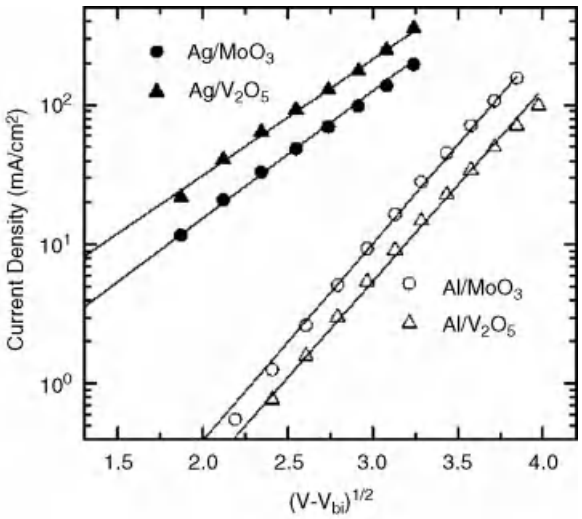

Figure 4.7 Measured (symbols) and calculated (lines) *J–V* characteristics of single hole-transporting layer devices, plotted as ln *J* versus $(V - V_{bi})^{1/2}$ [41].

reported as a semiconductor with ionization energy and electron affinity near 5.3 and 2.3 eV, respectively [44, 45]. Therefore, when MoO_3 was used as a hole injection layer, this ionization energy with the intermediate energy level between the work function of the electrode and the HOMO level of the organic layer explained the enhanced hole injection [46]. Recently, however, UPS and XPS analyses revealed that MoO_3 and WO_3 are n-type semiconductors with a deep electron affinity near 6.7 eV if deposited in an ultrahigh vacuum [47, 48]. This deep electron affinity induces large positive vacuum level shifts (0.5–2.5 eV) [48–51] at the anodes/MoO_3 junction originating from the electron transfer of electrodes such as ITO (W_F of 4.7 eV), Al (4.3 eV), or Ag (4.6 eV) to TMOs (Figure 4.8) [48]. Deposition of an additional organic layer on the MoO_3 layer resulted in a negative vacuum level shift indicating a charge transfer from the organic layer to the MoO_3, even though the vacuum level shift was reported with a large deviation of 0.1–2.1 eV due to the different sample preparation or measurement conditions [48, 50, 51]. These large vacuum level shifts decrease the energy difference between the Fermi level of the electrodes and the HOMO level of the organic layers, resulting in a reduced hole injection barrier from the ITO to the organic layers.

A similar but subtle different mechanism was proposed by Murata and coworkers [52]. They suggested with hole-only devices consisting of ITO/MoO_3 (*X* nm)/NPD (100 nm)/MoO_3 (10 nm)/Al that electron transfer from the HOMO level of the organic layer to the work function of the MoO_3 layers forms electron–hole pairs. Then, the pairs are separated under an electric field; the resultant electrons move though the n-type MoO_3 layer, and the holes move through the p-type organic layer (Figure 4.9) [52, 53].

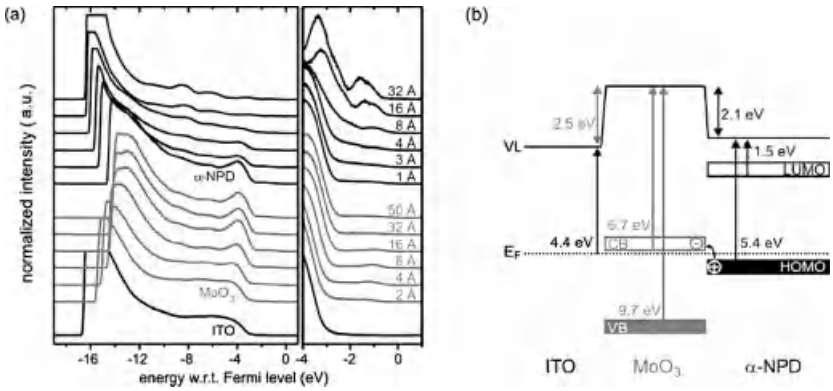

Figure 4.8 (a) UPS spectrum corresponding to MoO_3 and NPD deposition on ITO with MoO_3 and NPD thickness. (b) Schematic energy level alignment of the ITO/MoO_3/α-NPD junction [48].

On the other hand, a few groups have reported that evaporated thin MoO_3 layers on ITO or Au electrodes form a gap state in the MoO_3 layer [50, 54]. Based on theoretical modeling and experimental results, Mo^{5+}, which is generated by the oxygen vacancy in the MoO_x or by the electron transfer, is considered as the origin of the gap state [50, 55, 56]. This gap state is nearly aligned with the HOMO level of an organic layer on the MoO_x, resulting in a reduced hole injection barrier [50]. Recently, various theoretical modelling for energy level alignment have been designed to explain the Fermi level pinning between TMOs and organic semiconductors [57, 58].

It would be worth noting that the work function of MoO_3 depends on the sample preparation conditions. The work function of the MoO_3 layer was 5.6 eV when exposed to oxygen, which is 1.2 eV smaller than uncontaminated MoO_3 [49, 54]. There is also a different report against the UPS results that MoO_3 has electron-blocking properties in an organic solar cell and has an electron affinity near 2.3 eV [59]. Therefore, the energy level alignment with the MoO_3 layer for effective hole injection needs further investigation.

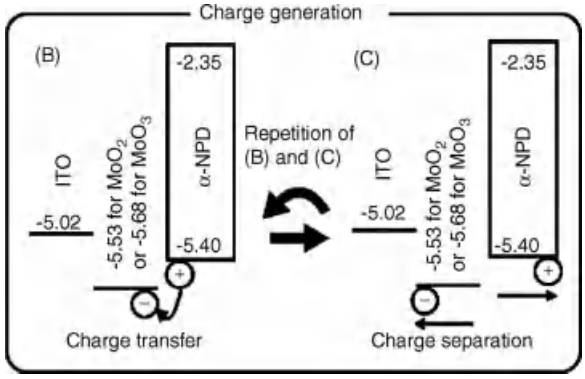

Figure 4.9 Illustrations of energy level diagrams to explain charge generation consisting of charge transfer (B) and charge separation (C) [52].

4.3
Doped Organic/Electrode Junctions

Doping in semiconductors is one of the most important techniques in inorganic semiconductors. Electrical doping is the process of intentionally introducing impurities into an intrinsic semiconductor for modulating its electrical properties. Carrier type and density can be controlled by doping. Increased free carrier density by doping also modifies the contact properties at the junctions with an electrode or other semiconductors. For instance, heavy doping of semiconductors is one of the most widely used methods to form ohmic contacts at metal/semiconductor junctions by reducing the depletion width of the semiconductor as follows [60]:

$$W = \sqrt{\frac{2\varepsilon_s}{qN}(V_{bi} - 2kT/q)}$$

where ε_s is the dielectric constant of the semiconductor, q is the charge of the carrier, N is the carrier density, V_{bi} is the built-in potential, k is the Boltzmann constant, and T is the absolute temperature. Therefore, sharp band bending (thin depletion width) at a high doping concentration (high carrier density) yields ohmic contact with the electrode by tunneling of the charges through the thin depletion region (Figure 4.10).

4.3.1
"Doping" in Organic Semiconductors

Electrical doping in organic semiconductors is similar to that of inorganic semiconductors. However, the concept of the "free carrier" may not be suitable in organic semiconductors since the transport mechanism in organic semiconductors,

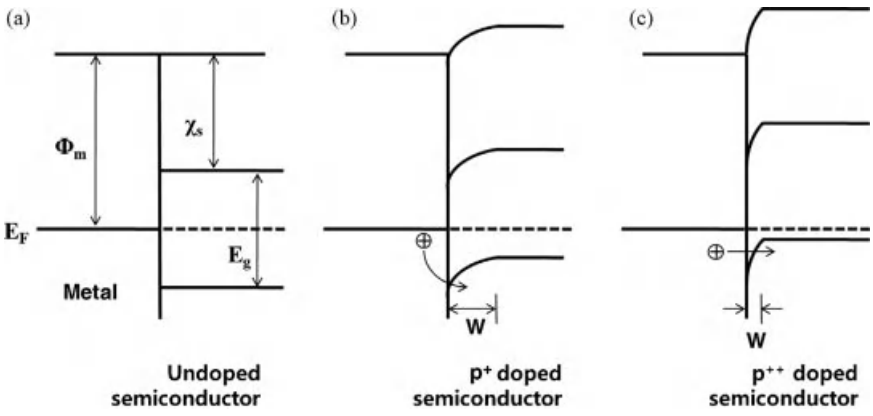

Figure 4.10 Energy band diagrams of metal/semiconductor junctions with (a) undoped semiconductor, (b) lightly p-doped semiconductor and (c) heavily p-doped semiconductor.

especially in amorphous structures, is governed by hopping transport rather than band transport. "Doping" in organic semiconductors, nevertheless, enhances the conductivity of the organics by generating charge carriers through the process of introducing impurities into an organic semiconductor [61]. The doping mechanism in organic semiconductors is a little different from that of inorganic semiconductors. Instead of the generation of free carriers from the dopants by the ionization of electrons or holes in inorganic semiconductors, the "charge transfer" from the HOMO level of a host (dopant) material to the LUMO level of a dopant (host) material for p-(n-) doping, respectively, and the "separation" of bounded charges are the main mechanisms in organic semiconductors [62].

Electrical doping in organic semiconductors can be easily confirmed by the modified optical characteristics of the doped films. Charge transfer from the host to the dopant for p-type doping generates cation host molecules, which exhibit additional peaks that do not originate from the intrinsic host and dopant molecules [37, 38]. Figure 4.11a shows an example of an ultraviolet-visible-near infrared (UV-Vis-NIR) absorption spectrum of 4,4′,4″-tris(*N*-(2-naphthyl)-*N*-phenyl-amino)-triphenylamine (2TNATA) doped with copper iodide (CuI), MoO_3, and ReO_3 [63]. Additional peaks at 450 and 1200 nm appear originating from the reaction of the charge transfer between the host and dopant molecules. The charge transfer reaction can be further confirmed by Fourier transform-Infrared (FT-IR) spectroscopy [63, 64]. Charge transfer from the 2TNATA molecule to the metal complex dopant will modify the charge distribution of the 2TNATA molecule and rearrange the binding energy between the atoms in the molecule of the charge transfer complex. In Figure 4.11b, doped 2TNATA films showed additional absorption peaks at 1167 and 1567 cm^{-1}, at the expense of the C=C stretching bands of the *para*-substituted benzene group of the 2TNATA molecule at 1108 and 1497 cm^{-1}. It was confirmed by molecular simulation through density function theory calculations that the HOMO electron of the 2TNATA molecule was almost entirely located on the nitrogen atom and the *para*-substituted benzene [63].

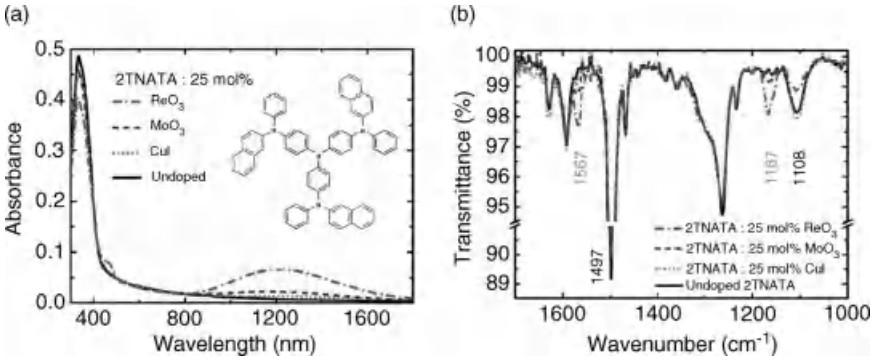

Figure 4.11 (a) UV-Vis-NIR absorption spectrum and (b) FT-IR spectrum of the doped 2TNATA films with 25 mol% ReO_3, MoO_3, and CuI and undoped 2TNATA film [63].

4.3.2
Dopants in Organic Semiconductors

Organic dopants possessing low LUMO levels such as tetracyano-quinodimethane (TCNQ) and tetrafluoro-tetracyano-quinodimethane (F_4-TCNQ) are used as p-dopants and the doping characteristics of F_4-TCNQ in organic semiconductors, such as zinc phthalocyanine (ZnPc), copper phthalocyanine (CuPc), or 4,4′,4″-tris (3-methylphenylphenylamino triphenylamine (mTDATA) were actively investigated by Leo and coworkers [62]. However, F_4-TCNQ has a LUMO level of 5.2 eV and is applicable only to host molecules with a HOMO level higher than 5.2 eV. Then, halide materials with strong electron affinities such as iodine (I_2), ferric chloride ($FeCl_3$), antimony pentachloride ($SbCl_5$), or CuI were introduced as p-dopants in OLEDs [65–68]. Even with their efficient electron-accepting properties, the use of metal halide dopants in organic vacuum chambers may cause contamination problems.

TMOs such as MoO_3, WO_3, V_2O_5, and ReO_3, which have been used as a thin interfacial layer between an electrode and an organic semiconductor, have been adopted as p-dopants [21, 33, 69–71]. Their high work functions facilitate electron transfer from various hosts [48, 72]. Low-temperature evaporation is also an important characteristic of electrical dopants in organic semiconductors. Dopant materials with a relatively low evaporation temperature compatible with common organic materials are preferred for practical applications. MoO_3 has been extensively used as a p-dopant since it has a lower melting temperature than WO_3 or V_2O_5. The evaporation temperature of ReO_3 is about 250–300 °C, which is even lower than MoO_3 (400–500 °C) and a little higher than NPB (165 °C at 0.1 nm/s).

Recently, tris[1,2-bis(trifluoromethyl)ethane-1,2-dithiolene] [$Mo(tfd)_3$] and 1,3,4,5,7,8-hexafluorotetracyanonaphthoquinodimethane (F6-TNAP) were introduced as a new organic p-dopants, which have a low LUMO level of 5.59 and 5.57 eV, respectively [73, 74].

Alkali metals (Li, Cs, Rb, Mg, K, and Na) [5, 75–80], metal nitrides [81], metal quinolines [82], and alkali metal carbonates (Cs_2CO_3, Rb_2CO_3) [83–85] have been used as n-type dopants. Their work functions are around 2–2.5 eV and are located above the LUMO level (∼3.0 eV) of most ETLs. Among them, metal carbonates are easy to use as n-dopants since they are more stable in moist conditions and evaporate more easily than alkali metals with a very low evaporation temperature near room temperature. Recently, organic materials such as cesium azide (CsN_3) were introduced as n-type dopants [81, 86]. CsN_3 was stable under ambient conditions and thermally deposited at a low evaporation temperature similar to organic materials.

4.3.3
Charge Generation Efficiencies of Dopants

Higher carrier density in organic semiconductors is desired to form an ohmic contact between an electrode and an organic layer. A dopant generating high carrier

density under a given doping concentration is preferred to yield high carrier density from the doping [85, 86]. Therefore, an investigation of the factors affecting the charge generation efficiency is necessary to develop an efficient dopant, where the charge generation efficiency is defined as follows [87]

$$\text{Charge generation efficiency} = \frac{\text{number density of carriers generated by doping}}{\text{number density dopant molecules}}$$

Since electrical doping is taking place by charge transfer from host molecules to dopants for p-doping, the energy difference between the HOMO level of the host and the LUMO level of the dopants is expected to certainly affect the charge generation efficiency. Systematic investigation of the effect of the energy level difference on doping efficiency was done by Lee *et al*. [63, 87]. They found indeed that the host with a higher lying HOMO level generated a larger carrier density than a host with a lower lying HOMO level for a dopant [63]. The carrier density generated by the doping was quantitatively estimated by the capacitance–voltage (*C*–*V*) measurement with a metal–insulator–semiconductor (MIS) structure [88, 89]. The total capacitance of a MIS device is governed by the insulator layer and the width of the depletion layer in the semiconductor layer, which depends on the charge-carrier density and external electric field.

Figure 4.12 shows the carrier density extracted from the *C*–*V* measurements for ReO_3-doped 2TNATA, NPB, 1,1-bis-(4-methylphenyl)-aminophenyl-cyclohexane (TAPC), and *N*,*N*′-dicarbazolyl-4-4′-biphenyl (CBP) films as a function of the doping concentration [87]. The carrier density increased almost linearly with the doping concentration up to 25 mol%. One can clearly notice that the carrier density becomes smaller as the HOMO level of the hosts becomes lower. ReO_3-doped 2TNATA ($E_{HOMO} = 5.0$ eV) showed the highest carrier density for the entire doping concentration range, followed by NPB ($E_{HOMO} = 5.4$ eV), 1,1-bis-(4-methylphenyl)-

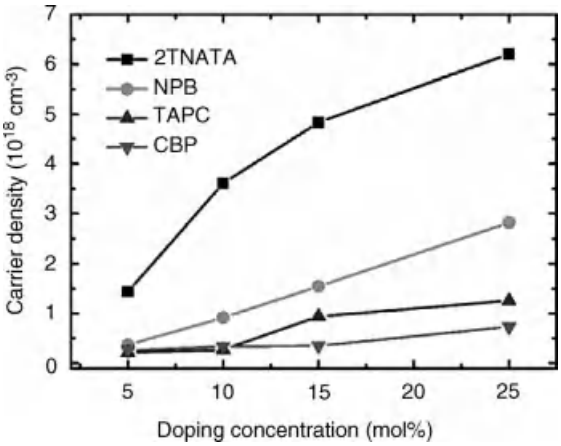

Figure 4.12 Carrier density versus doping concentrations for ReO_3-doped 2TNATA, NPB, TAPC, and CBP films [87].

aminophenyl-cyclohexane (TAPC) ($E_{HOMO} = 5.8$ eV), and CBP ($E_{HOMO} = 6.0$ eV) in decreasing order [68, 90, 91], resulting in a charge generation efficiency in the same decreasing order: 2TNATA (3.8%) > NPB (0.75%) > TAPC (0.38%) > CBP (0.29%) [87]. The same tendency was found for the doping of different dopants in a host. Three different dopants of CuI, MoO_3, and ReO_3 doped in 2TNATA showed that a larger difference between the HOMO of the host and the LUMO of the dopants resulted in a higher doping efficiency (Figure 4.11) [63].

It is interesting to note that the charge generation efficiencies of metal oxide dopants remain very low, in the range of 0.3–4% in the above experiments. The organic dopant F_4-TCNQ also exhibits a low charge generation efficiency [92].

Recently, Kim and coworkers reported that the low charge generation efficiency of metal oxide dopants in organic semiconductor hosts originated from the formation of dopant nanoclusters [93, 94]. Figure 4.13 shows bright-field transmission electron microscopy (TEM) images of (a) undoped NPB and (b) ReO_3-, (c) $Mo(tfd)_3$-, and (d) F_4-TCNQ-doped NPB films with a doping concentration of 2 mol%. The undoped NPB film shows a featureless image due to its amorphous structure. The NPB films doped with the metal oxide (ReO_3), however, show dark spots due to the nanoclusters of the dopant having a larger electron scattering cross section (Figure 4.13b). On the other hand, the $Mo(tfd)_3$-doped NPB film showed a featureless image with no dark spots. The nanoclusters of organic dopant molecules possessing a metal atom could be distinguished from an organic host by TEM analysis [95]. Therefore, the featureless image of the $Mo(tfd)_3$-doped NPB film clearly indicates that the organic dopant of $Mo(tfd)_3$ is uniformly dispersed in the NPB host. Even though the featureless image of the F_4-TCNQ-doped film does not necessarily prove that it is homogeneously dispersed in the host, the F_4-TCNQ molecules are expected to have homogeneous dispersion in the NPB host. Based on

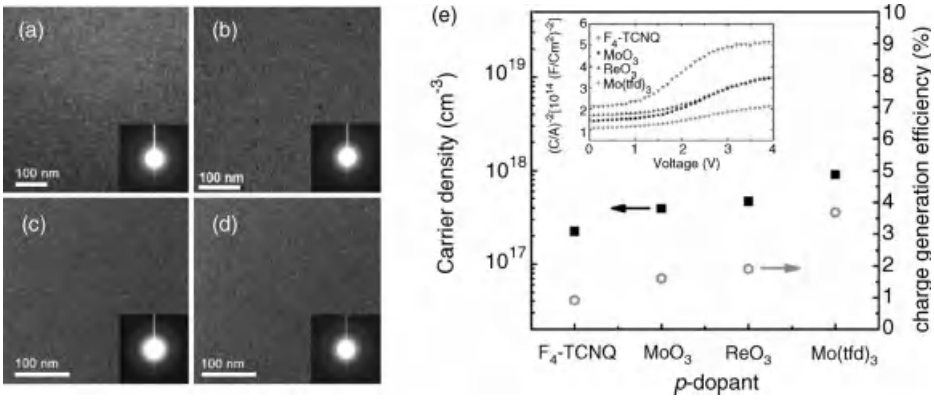

Figure 4.13 Bright-field TEM images of (a) undoped NPB and (b) ReO_3-, (c) $Mo(tfd)_3$-, and (d) F_4-TCNQ-doped NPB (2 mol%). The insets show the corresponding diffraction patterns. (e) The carrier density and the doping efficiency of 2 mol% doped with F_4-TCNQ, MoO_3, ReO_3, and $Mo(tfd)_3$-doped NPB films. *Inset*: The *C*–*V* curves of the MIS structured devices [93].

these results, $Mo(tfd)_3$ is expected to show high charge generation efficiency because of its homogeneous dispersion characteristics and low LUMO level of 5.59 eV [73].

The carrier densities for different dopants generated by the doping and the corresponding charge generation efficiencies are shown in Figure 4.13e. The charge generation efficiency is as follows: $Mo(tfd)_3$ (3.7%) > ReO_3 (1.9%) > MoO_3 (1.6%) > F_4-TCNQ (0.9%). Notably, $Mo(tfd)_3$ generates a higher hole density than ReO_3 and MoO_3, even though $Mo(tfd)_3$ has a higher LUMO level than the metal oxides. This is attributed to the homogeneous dispersion of the organic complex in the organic semiconductor as demonstrated by TEM analysis. Homogeneous dispersion leads to a larger number of contacts between the dopant and host molecules resulting in a larger number of carriers compared to inhomogeneously doped metal oxide dopants with the same doping concentrations. When we compare the organic dopants $Mo(tfd)_3$ and F_4-TCNQ since the pair is expected to have similar dispersion characteristics, the dopants with a lower LUMO level ($Mo(tfd)_3$ ~5.59 eV) resulted in a higher charge generation efficiency compared to the dopants with a higher LUMO (F_4-TCNQ ~5.2 eV), respectively. This confirms that a higher energy difference between the LUMO level of the dopant and the HOMO level of the host results in a higher charge generation efficiency when the dispersion characteristics of the dopants are similar. This observation leads to the conclusion that the charge generation efficiency (η_{CG}) of a dopant can be expressed by the product of the dispersion efficiency (η_{dis}) of the dopant and the charge transfer efficiency (η_{CT}) of a dopant molecule from or to a host molecule as follows:

$$\eta_{CG} = \eta_{dis} \cdot \eta_{CT}$$

4.3.4
Hole Injection through the p-Doped Organic Layer/Anode Junction

The charge injection barrier between an electrode and an organic semiconductor is determined by the energy level difference between the W_F of the electrode and the HOMO (LUMO) level of the organic layer before contact, the vacuum level shift at the electrode/organic junction, and the depletion width in the doped semiconductor layers, which depends on the carrier density or doping concentration. The electrical doping characterized by the increased carrier density and Fermi energy level shift toward the HOMO or LUMO levels modifies the junction characteristics. One example is shown in Figure 4.14. The doping of F_4-TCNQ in ZnPc reduces (i) the vacuum level shift at the junction, (ii) the depletion width in the organic semiconductor at the junction, and (iii) the energy level difference between the Fermi level and the HOMO level of the organic layer . All three of these factors contribute to the improved hole injection at the electrode/organic semiconductor junction.

The *J–V* characteristics of the hole-only devices with these doped organic semiconductors are shown in Figure 4.15 [96]. The *J–V* characteristics of the hole-only devices with Au/undoped organic layer/Au layers were in good agreement with the

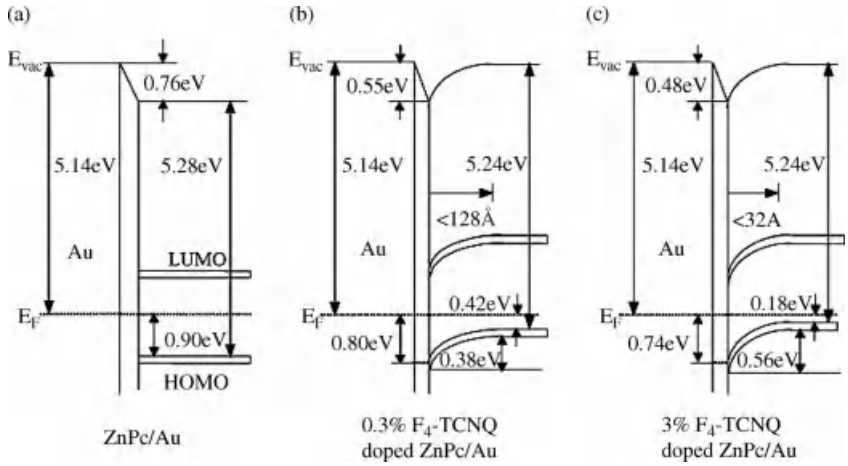

Figure 4.14 Energy of the molecular levels near the interface between Au and (a) undoped ZnPc; (b) ZnPc:0.3%F_4-TCNQ; and (c) ZnPc:3% F_4-TCNQ. The measured width of the depletion region is shown in (b) and (c). Interface dipole and the work function of Au and ZnPc ionization energy are indicated in each case [96].

thermionic emission model. These results indicate that the current density through the undoped ZnPc layer was controlled by the injection-limited current due to a high hole injection barrier of 0.9 eV (Figure 4.14). However, the *J–V* characteristics of devices with doped ZnPC (ZnPc:0.3%F_4-TCNQ) were in good agreement with the space charge-limited current (SCLC) model, indicating that the current density of the devices was controlled not by the injection-limited current but by the transport-limited current. Due to the hole injection barrier that was measured by UPS analysis and was similar to the undoped case, the transport-limited current of doped devices indicates that charge injection takes place mostly by tunneling injection. Conclusively, a reduced depletion width from doping in the organic layer yielded near ohmic contact with the anode, even though a large negative vacuum level shift at the junction increased the hole injection barrier.

Similar behavior was observed when TMOs were used as the dopant. One important difference between the MoO_3 or WO_3-doped NPB or CBP film and the F_4-TCNQ-doped ZnPc layer is the direction of the vacuum level shift [51, 56, 97–99]. The MoO_3-doped organic layer makes a positive vacuum level shift with the ITO electrode due to the charge transfer from the ITO to the doped organic layer (Figure 4.16). An abrupt work function increase (Figure 4.16 inset) can be separated from the vacuum level shift by band bending. This additional reduction of the hole injection barrier due to the vacuum level shift at the MoO_3-doped organic layer/electrode junction and a reduction in the depletion width similar to that of the F_4-TCNQ-doped case facilitate easier hole injection into the organic layer.

In addition to the vacuum level shift and the reduction in the depletion width, there are reports that the electronic and chemical interactions between MoO_3 and NPB resulted in the formation of gap states in MoO_3-doped NPB layers similar to

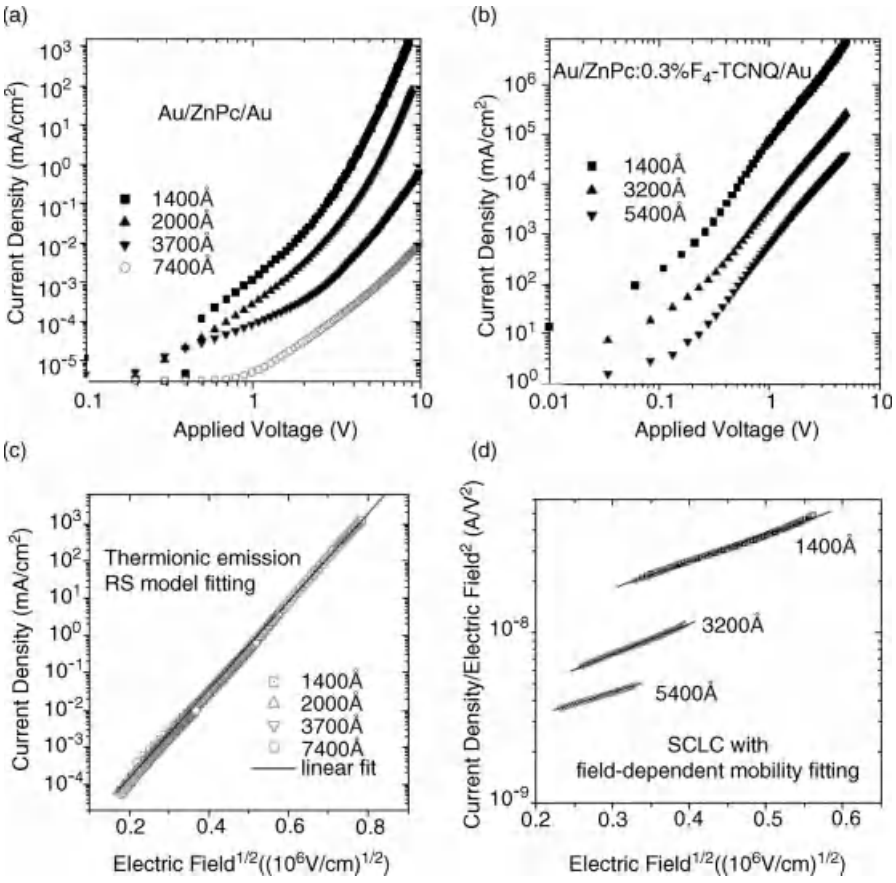

Figure 4.15 Thickness dependence of the *I–V* characteristics measured *in situ* for the Au/ZnPc/Au structures. (a) Undoped ZnPc. (b) ZnPc:0.3%F_4-TCNQ. (c) Current density versus (electric field)$^{1/2}$ compared to the thermionic emission (Richardson-Schottky equation) model for the devices of Au/undoped ZnPc/Au structures. (d) Current density/(electric field)^2 versus (electric field)$^{1/2}$ in terms of SCLC with the field-dependent mobility fitting for devices of the Au/ZnPc:0.3%F_4-TCNQ/Au structures [96].

that of the MoO_3/NPB interface due to the charge transfer from the NPB molecules to the MoO_3 (Figure 4.17) [51, 56, 99]. These gap states are suggested as another reason of a reduction in the hole injection barrier.

The *J–V* characteristics of the hole-only devices with a ReO_3-doped NPB layer are shown in Figure 4.18 (Lee, J.-H. and Kim, J.-J. (unpublished).). As the doping concentration increases, the current density through the hole-only device is also enhanced. Such enhanced current density must be interpreted by both the effect of the reduced hole injection barrier and the enhanced conductivity of the doped organic layer. Generally, measured conductivity from the slope of the *J–V* curve of hole-only devices contains a portion of contact resistance. Therefore, enhanced

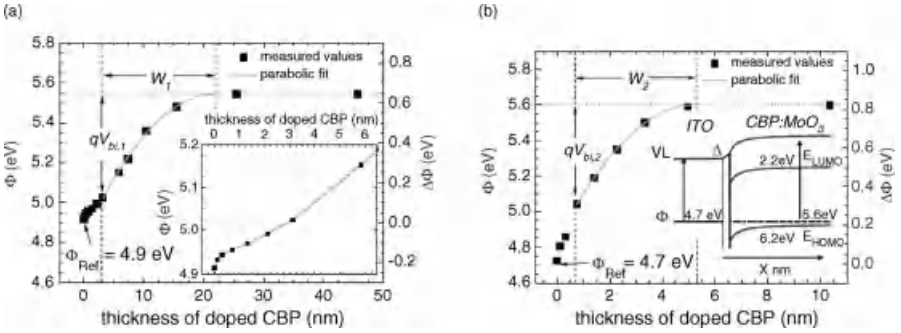

Figure 4.16 (a) Work function of MoO_3 (2.2 mol%)-doped CBP deposited stepwise onto ITO. *Inset*: Magnified view of the progression of the work function within the first 6 nm of CBP:MoO_3. (b) Work function of MoO_3 (17.3 mol%)-doped CBP deposited stepwise on ITO. *Inset*: Energy level alignment at the n¯p junction (V_L: vacuum level, *W*: depletion width) [97].

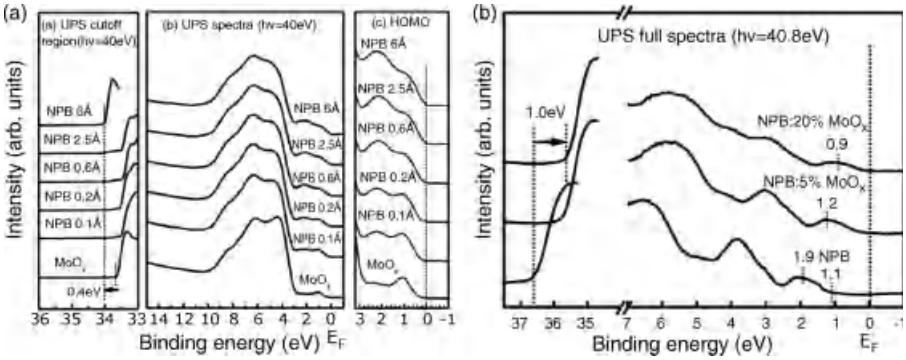

Figure 4.17 (a) UPS spectrum of MoO_3 with incremental deposition of NPB. (b) UPS spectrum of pristine NPB and NPB:MoO_3 (5% and 20%) [56].

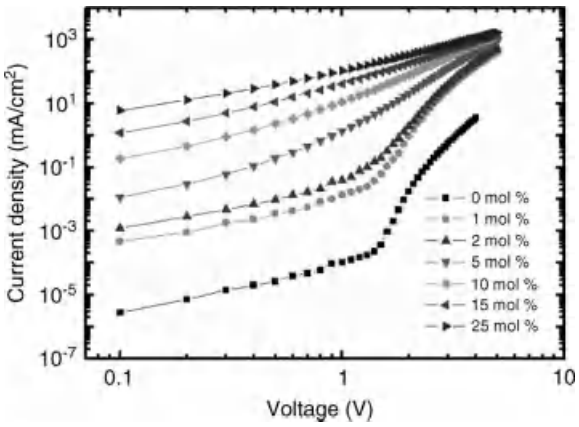

Figure 4.18 The *J–V* characteristics of hole-only devices with a ReO_3-doped NPB layer versus doping concentrations of 0–25 (mol%) (Lee, J.-H. and Kim, J.-J. (unpublished).).

conductivity depending on the doping concentration must be measured by a four-point or four-lead method, which can neglect the contact resistance from the conductivity measurement [87].

4.3.5
Electron Injection through the n-Doped Organic Layer/Cathode Junction

Enhanced electron injection through n-type doping is similar to the mechanism for hole injection through p-doping, in which alkali metals, alkali metal carbonates, and chlorides have been utilized as n-dopants.

The UPS analysis of 4,7-diphenyl-1,10-phenanthroline (BPhen):8% Rb_2CO_3/Al structure clearly shows that the onset and the valance band spectra largely shift toward the higher binding energy side by 1.0 eV compared to that of the pristine BPhen layer (Figure 4.19). The doping of Rb_2CO_3 in BPhen induces the movement of the Fermi level toward the LUMO level and consequently reduces the electron injection barrier. In addition, extra states are formed in the forbidden gap as indicated by the arrow for the BPhen:8% Rb_2CO_3/Al system, facilitating effective charge-carrier injection and transport. The BPhen/LiF/Al reference also exhibits a large shift of onset and valence band spectra toward a higher binding energy. Both the reduction in the barrier height for electron injection and the creation of gap states in the BPhen:Rb_2CO_3/Al system contribute to the enhancement of electron injection and electron transport characteristics of the n-doped organic layer. Energy barrier lowering by electrical doping is attributed to efficient charge-carrier injection (Figure 4.20) [84].

The devices with a doped layer exhibit higher current density than the undoped devices, confirming the effectiveness of Rb_2CO_3 doping in ETL. Specifically, the device with a BPhen/BPhen:15% Rb_2CO_3 layer exhibits a relatively low threshold voltage as well as high current density at the same voltage compared to that with a BPhen/BPhen:8% Rb_2CO_3 layer. The *J–V* curves of the devices with

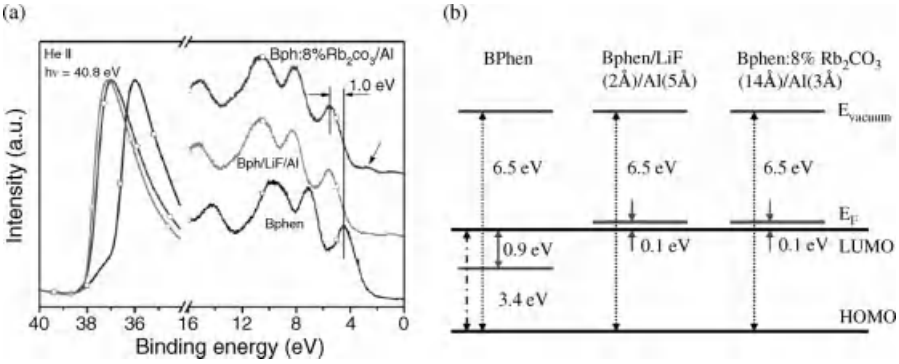

Figure 4.19 UPS spectrum of the pristine BPhen, BPhen/Rb_2CO_3:Bphen/Al, and BPhen/LiF/Al cases. (b) The associated energy band diagram [84].

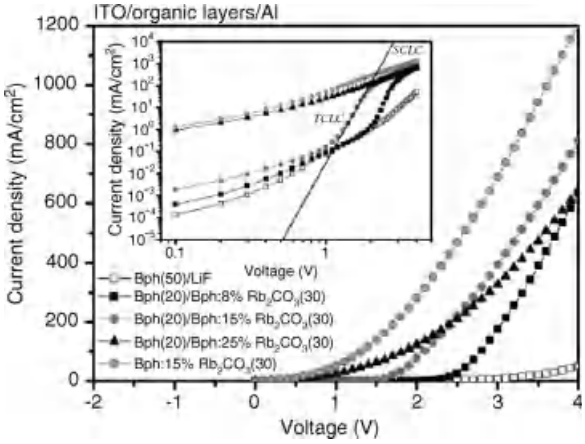

Figure 4.20 The *J–V* characteristics of an electron-only device with ITO/BPhen (20)/BPhen: 8–25% Rb_2CO_3 (30)/Al and ITO/BPhen (50)/LiF/Al [84].

BPhen/BPhen:8–15% Rb_2CO_3 layers with an undoped–doped organic junction exhibit characteristics similar to that of the device with the undoped BPhen-only layer. The *J–V* characteristics depending on the organic–organic junction will be discussed in the next section.

4.4
Doped Organic/Undoped Organic Junction

Charge-carrier injection between a doped organic layer and undoped organic layer is also important as much as the interface between the electrode and organic layer. Generally, a doped organic layer is inserted between the electrode and the active layer in OLEDs and OPVs to modify the injection characteristics of the electrode. In such device structures, the doped/undoped organic junction sometimes plays a significant role in the injection characteristics of the active layer [100, 101]. Charge transfer between the doped organic and undoped organic layers can modify the electronic structure of the doped/undoped organic junctions (DO/UO junctions). For instance, the DO/UO junction between F_4-TCNQ-doped α-NPD or ZnPc and undoped 2,9-dimethyl-4,7-diphenyl-1,10-phenanthroline (BCP) exhibited a vacuum level shift by the interface dipole (0.6–0.9 eV) compared to the undoped–undoped junction (Figure 4.21) [101].

Based on the induced density of the interface states and the charge neutrality level (IDIS/CNL) model, the downward shifted CNL and enhanced dielectric constant from doping were suggested as the reason of the interface dipole at the junction with the undoped layer [101].

n-DO/UO homojunctions for electron injection have been investigated with three different ETLs of bis-4,6-(3,5-di-3-pyridylphenyl)-2-methylpyrimidine

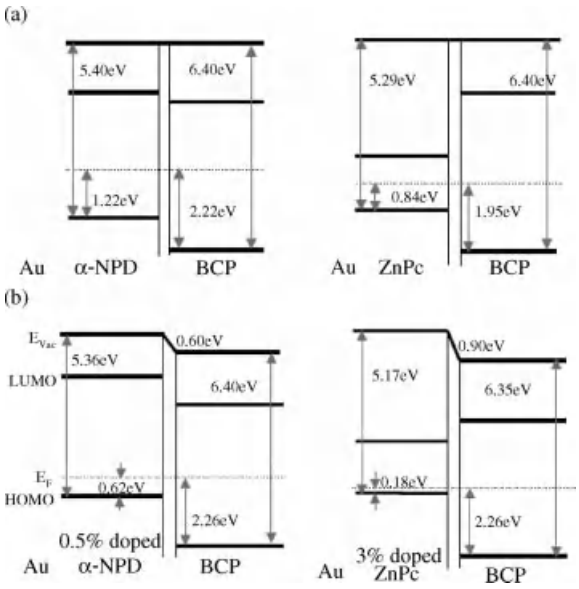

Figure 4.21 Electronic structures of the DO/UO heterojunctions, α-NPD/BCP, and ZnPc/BCP with (a) undoped NPD or ZnPc and (b) F_4-TCNQ-doped NPD or ZnPc on an Au electrode [101].

(B3PYMPM), BPhen, and 2,2′,2″-(1,3,5-benzenetriyl)tris-[1-phenyl-1*H*-benzimidazole] (TPBi) doped with 15% Rb_2CO_3 [102]. Figure 4.22 shows little change in the onset spectra (a) and the valence band spectra (b) when pristine B3PYMPM is deposited on n-doped B3PYMPM, indicating that there is no interface dipole and HOMO offset between n-doped B3PYMPM and pristine B3PYMPM. In contrast, Bphen and TPBi exhibit the shift of 0.2 and 0.25 eV toward the lower binding energy, respectively, both in the vacuum level and the HOMO level between the n-doped and the undoped layers. The energy level diagrams of the ITO/n-ETL/ETL structure extracted from the UPS spectra are displayed in the insets of Figure 4.22. B3PYMPM had the smallest electron injection barrier from ITO due to a large vacuum level shift and no energy barrier at the DO/UO junction, while the energy barrier in BPhen and TPBi were 0.2 and 0.25 eV at the DO/UO junction, respectively. These results are in good agreement with the *J–V* characteristics of the electron-only devices with the ITO/n-ETL (20 nm)/undoped ETL (30 nm)/Al structure (Figure 4.23) [102].

When negative bias was applied to the ITO electrode for electron injection from ITO to the ETLs, the current density of the electron-only devices with B3PYMPM dramatically increased as the voltage increased over 0.1 V than in that of other devices. This fact suggests that the barrier height for electron injection between an n-ETL and an ETL even in homojunctions plays an important role in efficient carrier injection.

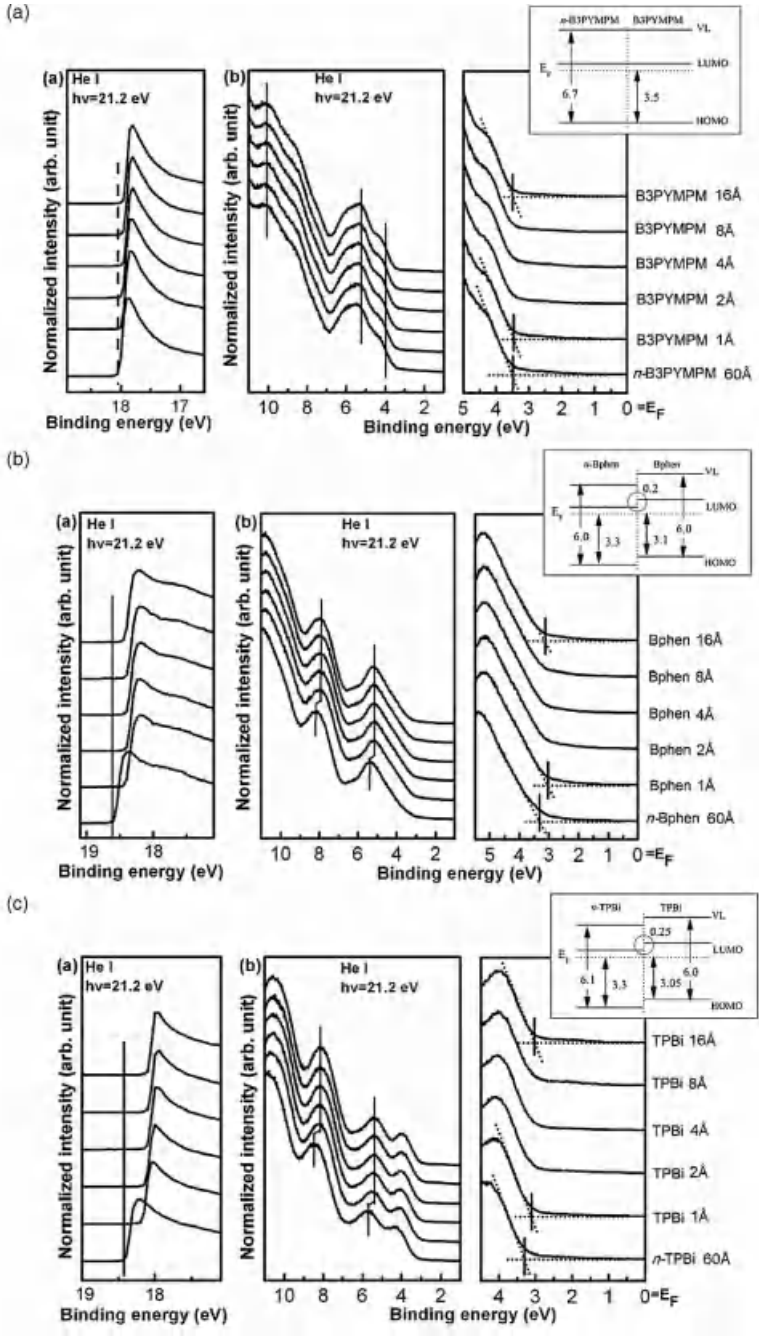

Figure 4.22 UPS spectra near (a) the onset and (b) the valence band region of DO/UO homojunction on ITO electrode of Rb_2CO_3 doped (1) B3PYMPM, (2) BPhen and (3) TPBi (inset: energy level diagram) [102].

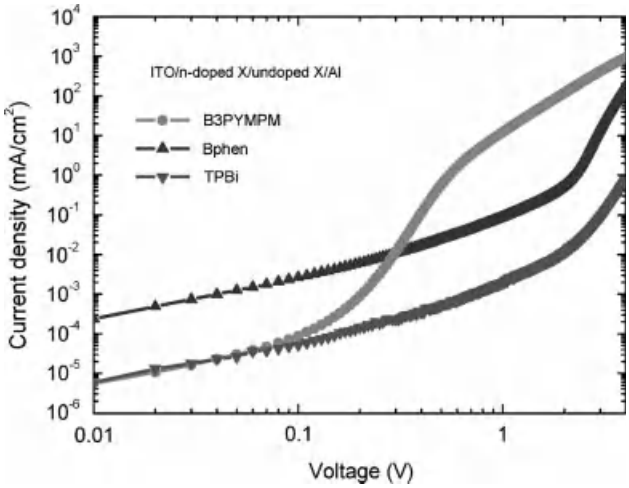

Figure 4.23 The J-V characteristics of electron only devices with the inverted structure of (a) ITO/Rb_2CO_3 doped ETL (50 nm, 15 wt%)/Al (open symbol) or (b) ITO/Rb_2CO_3 doped ETL (20 nm, 15 wt%)/undoped ETL (30 nm)/Al (solid symbol) [102].

4.5 Applications

4.5.1 OLEDs

Interfacial doping has been widely used to reduce the driving voltage by reducing the injection barrier, leading to the p-doped/intrinsic/n-doped (p–i–n) OLEDs structure [84, 103, 104]. Moreover, p–n junctions are widely used as the interconnection unit (ICU) in tandem OLEDs exhibiting a low operation voltage, high efficiency, and long lifetime [21, 105–108].

One example of the p–i–n OLED structures comprised of ITO/4 wt% ReO_3-doped NPB (80 nm), undoped NPB (20 nm), a double-emission layer (30 nm) of 8 wt% tris(2-phenylpyridyl)iridium(III) [$Ir(ppy)_3$]-doped CBP and BPhen, undoped BPhen (x nm), 15 wt% Rb_2CO_3-doped BPhen (γ nm) is shown in Figure 4.24 [84].

All the devices with different thicknesses of undoped and doped layers show very low driving voltage near 3.1 V at 100 cd/m^2 and 3.6 V at 1000 cd/m^2 due to the reduced charge injection barrier from the anode and the cathode by doping. The whole p–i–n OLEDs show high device efficiencies (max 61–68 cd/A and 68–76 lm/W) (Figure 4.24b) [84].

4.5.2 OPVs

Organic solar cells are under active research due to their advantages of flexibility, low processing cost, and a thin active layer with a high absorption coefficient [109].

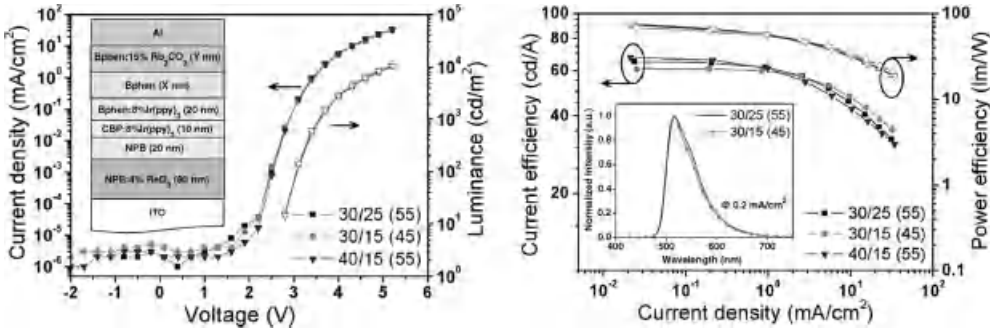

Figure 4.24 (a) The *J–V–L* characteristics of p–i–n OLEDs. *Inset*: The schematic illustration of p–i–n OLEDs with different thicknesses of BPhen and BPhen:15% Rb_2CO_3 layers. (b) The current efficiency and power efficiency–current density plots of part (a). *Inset*: Electroluminescence spectrum of the devices [84].

However, the Schottky contact in the organic/electrodes interface and additional organic layers as an optical spacer to optimize the position of the active layer can reduce the open-circuit voltage (V_{oc}) and short-circuit current (J_{sc}) of the OPVs [110]. To overcome the poor electrical properties of organic semiconductors, the p–i–n structure or tandem p–i–n structure of OPVs have also been investigated [111, 112]. These doped organic layers must have a high conductivity, low charge injection barriers with an electrode, and transparency to pass the light into the active layer [113, 114].

Figure 4.25 shows the characteristics of the OPVs comprised of an ITO/CuPc/C60/n-doped electron-transporting layer. This ETL acts as the

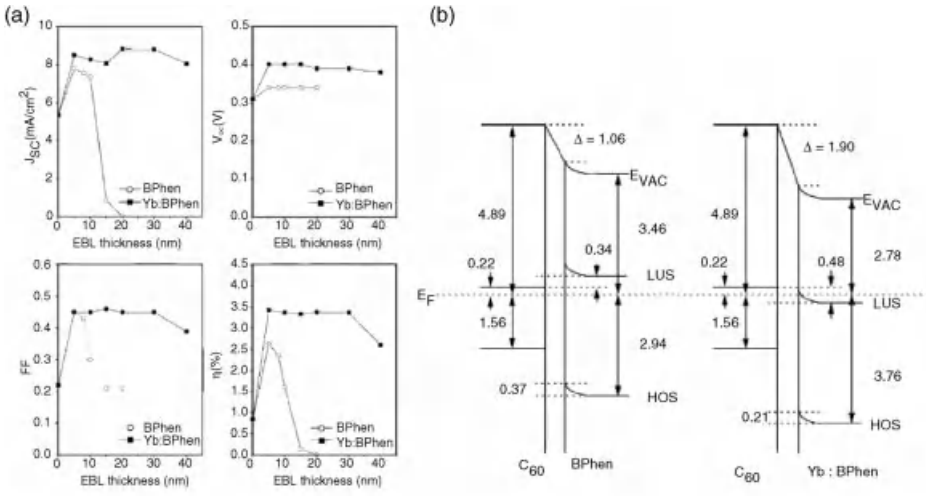

Figure 4.25 (a) Photovoltaic response of OPVs, where EBL is either BPhen or Yb:BPhen. (b) Energy level diagram for the C60/BPhen and the C60/Yb:BPhen contacts [115].

exciton-blocking layer (EBL) and optical spacer. When the EBL was inserted between C60 and the electrode to prevent exciton quenching at the electrode surface, OPVs with doped or undoped BPhen layers showed an enhanced J_{sc} and V_{oc}. When the undoped and doped EBLs were compared, the J_{sc} of the device with an undoped layer was however suddenly suppressed due to the low conductivity of the undoped layer as the thickness of EBL increases. In addition, V_{oc} and J_{sc} were enhanced with a doped BPhen layer as the EBL due to the near ohmic contact by a larger vacuum level shift at the interface of C60 and the doped EBL.

4.5.3 OFETs

OFETs have the potential for application in low-cost and flexible electronics such as radio-frequency identification tags and driving circuits for flexible displays [116–118]. However, the poor contact with the electrode and the low mobility of the organic semiconductor are the limitations of OFETs [119]. There was a lot of research about the surface modification of substrates by SAMs and the film formation of organic semiconductors such as polythiophenes (P3HT) or pentacene [120, 121]. Doping in OFETs has also been an effective way of controlling and improving the charge injection from the source electrode similar to the conventional inorganic semiconductors [60, 122]. Figure 4.26a and b show the typical device structure of a top-contact pentacene OFET with a $Mo(tfd)_3$-doped pentacene layer (1:1) between the Au electrodes (source and drain) and pentacene layer [123]. When the doped layer was inserted, contact resistance was effectively reduced and the current density through the source and drain was enhanced.

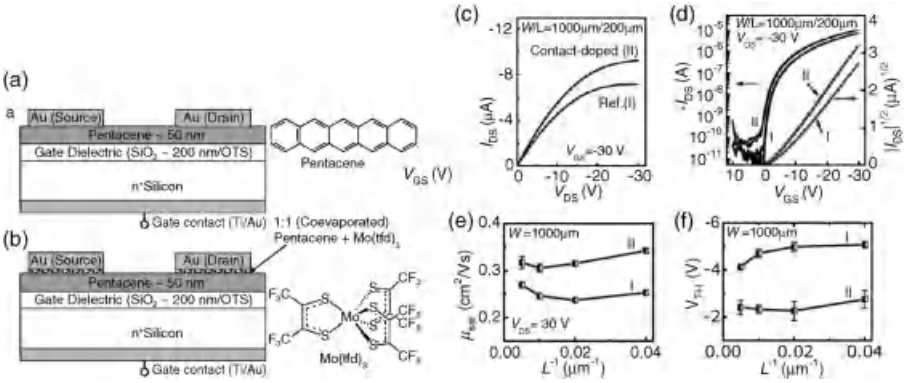

Figure 4.26 Device structures of a reference top-contact pentacene OFET (a) and that of a device in which the contact region under the source and drain electrodes has been doped with $Mo(tfd)_3$ (b); chemical structures of pentacene and $Mo(tfd)_3$ are shown on the right. Comparison of the output and transfer characteristics of reference (I) and contact-doped (II) pentacene OFETs with $W/L = 1000/200\,\mu m$ (c and d). (e) Dependence of I_{sat} on L^{-1} and (f) dependence of V_{TH} on L^{-1} for both types of OFETs [123].

The source–drain current and the mobility of the devices with a doped injection layer increased and the threshold voltage decreased (Figure 4.26c–f). The contact resistance in devices with a doped layer dropped to 0.5 kΩ cm compared to 3.4 kΩ cm of the reference devices [123].

4.6 Conclusions

In this chapter, we have described interfacial doping in organic semiconductors for efficient charge injection through the interfaces of organic devices. Electrical doping reduces the charge injection barrier by reducing the vacuum level shift and depletion width at the junction with the electrode and increases the conductivity of the organic semiconductors by enhancing the carrier density. Applications of the doping technique in organic devices have exhibited improved *J–V* characteristics of the devices with enhanced performance of the device. Further quantitative and systematized analyses on doping characteristics and on the development of efficient dopants must be continued in the field of organic semiconductors.

References

1 Parker, I.D. (1993) *J. Appl. Phys.*, **75**, 1656.
2 VanSlyke, S.A. and Tang, C.W. (1987) *Appl. Phys. Lett.*, **51**, 913.
3 Wakimoto, T., Fukuda, Y., Nagayama, K., Nakada, H., and Tsuchida, M. (1997) *IEEE Trans. Elec. Dev.*, **44**, 1245.
4 Haskal, E., Curioni, A., Seidler, P., and Andreoni, W. (1997) *Appl. Phys. Lett.*, **71**, 1151.
5 Kido, J. and Matsumoto, T. (1998) *Appl. Phys. Lett.*, **73**, 2866.
6 Oyamada, T., Sasabe, H., Adachi, C., Murase, S., Tominaga, T., and Maeda, C. (2005) *Appl. Phys. Lett.*, **86**, 033503.
7 Kim, Y.E., Park, H., and Kim, J.-J. (1996) *Appl. Phys. Lett.*, **69**, 599.
8 Tang, H., Li, F., and Shinar, J. (1997) *Appl. Phys. Lett.*, **71**, 2560.
9 Choi, H.W., Kim, S.Y., Kim, W.K., and Lee, J.L. (2005) *Appl. Phys. Lett.*, **87**, 082102.
10 Hung, L.S., Tang, C.W., and Mason, M.G. (1997) *Appl. Phys. Lett.*, **70**, 152.
11 Shaheen, S., Jabbour, G., Morrell, M., Kawabe, Y., Kippelen, B., Peyghambarian, N., Nabor, M.F., Schlaf, R., Mash, E., and Armstrong, N. (1998) *J. Appl. Phys.*, **84**, 2324.
12 Yokoyama, T., Yoshimura, D., Ito, E., Ishii, H., Ouchi, Y., and Seki, K. (2003) *Jpn. J. Appl. Phys.*, **42**, 3666.
13 Schlaf, R., Parkinson, B., Lee, P., Nebesny, K., Jabbour, G., Kippelen, B., Peyghambarian, N., and Armstrong, N. (1998) *J. Appl. Phys.*, **84**, 6729.
14 Le, Q.T., Yan, L., Gao, Y., Mason, M., Giesen, D., and Tang, C. (2000) *J. Appl. Phys.*, **87**, 375.
15 Hung, L.S., Zhang, R.Q., He, P., and Mason, G. (2002) *J. Phys. D Appl. Phys.*, **35**, 103.
16 Lee, J., Park, Y., Kim, D., Chu, H., Lee, H., and Do, L.M. (2003) *Appl. Phys. Lett.*, **82**, 173.
17 Park, Y., Lee, J., Lee, S., and Kim, D. (2001) *Appl. Phys. Lett.*, **79**, 105.
18 Kang, S., Park, D., Kim, S., Whang, C., Jeong, K., and Im, S. (2002) *Appl. Phys. Lett.*, **81**, 2581.
19 Chan, M.Y. (2004) *J. Appl. Phys.*, **95**, 5397.
20 Hasegawa, T., Miura, S., Moriyama, T., Kimura, T., Takaya, I., Osato, Y., and

Mizutani, H. (2004) *SID Int. Symp. Dig. Tech.*, **35**, 154.
21 Leem, D.-S., Lee, J.-H., Kim, J.-J., and Kang, J.-W. (2008) *Appl. Phys. Lett.*, **93**, 103304.
22 Kao, P.C., Wang, J.Y., Lin, J.H., and Chen, S.H. (2010) *J. Electrochem. Soc.*, **157**, J135.
23 Diao, L., Frisbie, C.D., Schroepfer, D.D., and Ruden, P.P. (2007) *J. Appl. Phys.*, **101**, 014510.
24 Shen, Y., Jacobs, D.B., Malliaras, G.G., Koley, G., Spencer, M.G., and Ioannidis, A. (2001) *Adv. Mater.*, **13**, 1234.
25 Sugiyama, K., Ishii, H., Ouchi, Y., and Seki, K. (2000) *J. Appl. Phys.*, **87**, 295.
26 Ishii, M., Mori, T., Fujikawa, H., Tokito, S., and Taga, Y. (2000) *J. Lumin.*, **87**, 1165.
27 Qiu, C., Xie, Z., Chen, H., Wong, M., and Kwok, H.S. (2003) *J. Appl. Phys.*, **93**, 3253.
28 Ishii, H., Sugiyama, K., Ito, E., and Seki, K. (1999) *Adv. Mater.*, **11**, 605.
29 Li, Y. (2004) *Chem. Phys. Lett.*, **386**, 128.
30 Wu, Z., Wang, L., Wang, H., Gao, Y., and Qiu, Y. (2006) *Phys. Rev. B*, **74**, 165307.
31 Appleyard, S.F.J., Day, S.R., Pickford, R. D., and Willis, M.R. (2000) *J. Mater. Chem.*, **10**, 169.
32 Jonas, F. and Schrader, L. (1991) *Synth. Met.*, **41**, 831.
33 Tokito, S., Noda, K., and Taga, Y. (1996) *J. Phys. D Appl. Phys.*, **29**, 2750.
34 Chen, C.-W., Hsieh, P.-Y., Chiang, H.-H., Lin, C.-L., Wu, H.-M., and Wu, C.-C. (2003) *Appl. Phys. Lett.*, **83**, 5127.
35 Kim, S.Y., Lee, J.-L., Kim, K.-B., and Tak, Y.-H. (2005) *Appl. Phys. Lett.*, **86**, 133504.
36 Kanno, H., Sun, Y., and Forrest, S.R. (2005) *Appl. Phys. Lett.*, **86**, 263502.
37 Chang, C.-C., Hsieh, M.-T., Chen, J.-F., Hwang, S.-W., and Chen, C.H. (2006) *Appl. Phys. Lett.*, **89**, 253504.
38 Leem, D.-S., Park, H.-D., Kang, J.-W., Lee, J.-H., Kim, J.W., and Kim, J.-J. (2007) *Appl. Phys. Lett.*, **91**, 011113.
39 Liao, L.-S., Slusarek, W.K., Hatwar, T.K., Ricks, M.L., and Comfort, D.L. (2008) *Adv. Mater.*, **20**, 324.
40 Liao, L.S. and Klubek, K.P. (2008) *Appl. Phys. Lett.*, **92**, 223311.
41 Zhu, X., Sun, J., Yu, X., Wong, M., and Kwok, H.-S. (2007) *Jpn. J. Appl. Phys.*, **46**, 1033.
42 Wu, J., Hou, J., Cheng, Y., Xie, Z., and Wang, L. (2007) *Semicond. Sci. Technol.*, **22**, 824.
43 Lee, J.Y. (2006) *Appl. Phys. Lett.*, **88**, 073512.
44 Shrotriya, V., Li, G., Yao, Y., Chu, C.W., and Yang, Y. (2006) *Appl. Phys. Lett.*, **88**, 073508.
45 Cox, P.A. (1992) *Transition Metal Oxides: An Introduction to Their Electronic Structure and Properties*, Clarendon, Oxford.
46 Chu, C.-W., Li, S.-H., Chen, C.-W., Shrotriya, V., and Yang, Y. (2005) *Appl. Phys. Lett.*, **87**, 193508.
47 Lee, H., Cho, S.W., Han, K., Jeon, P.E., Whang, C.-N., Jeong, K., Cho, K., and Yi, Y. (2008) *Appl. Phys. Lett.*, **93**, 043308.
48 Kröger, M., Hamwi, S., Meyer, J., Riedl, T., Kowalsky, W., and Kahn, A. (2009) *Appl. Phys. Lett.*, **95**, 123301.
49 Meyer, J., Shu, A., Kröger, M., and Kahn, A. (2010) *Appl. Phys. Lett.*, **96**, 133308.
50 Kanai, K., Koizumi, K., Ouchi, S., Tsukamoto, Y., Sakanoue, K., Ouchi, Y., and Seki, K. (2010) *Org. Electron.*, **11**, 188.
51 Wang, F., Qiao, X., Xiong, T., and Ma, D. (2008) *Org. Electron.*, **9**, 985.
52 Matsushima, T. and Murata, H. (2009) *Appl. Phys. Lett.*, **95**, 203306.
53 Kabra, D., Lu, L.P., Song, M.H., Snaith, H.J., and Friend, R.H. (2010) *Adv. Mater.*, **22**, 3194.
54 Irfan, H., Ding, Y., Gao, C., Small, C., Kim, D.Y., Subbiah, J., and So, F. (2010). *Appl. Phys. Lett.*, **96**, 243307.
55 Scanlon, D.O., Watson, G.W., Payne, D.J., Atkinson, G.R., Egdell, R.G., and Law, D.S.L. (2010) J. *Phys. Chem. C*, **114**, 4636.
56 Wu, C.I., Lin, C.T., Lee, G.R., Cho, T.Y., Wu, C.C., and Pi, T.W. (2009) *J. Appl. Phys.*, **105**, 033717.
57 Braun, S., Salaneck, W.R., and Fahlman, M. (2009) *Adv. Mater.*, **21**, 1450.
58 Greiner, M.T., Helander, M.G., Tang, W.M., Wang, Z.B., Qiu, J., and Lu, Z.H. (2012) *Nature Mater.*, **11**, 76.
59 Tong, X., Lassiter, B.E., and Forrest, S.R. (2010) *Org. Electron.*, **11**, 705.

60 Sze, S.M. (1981) *Physics of Semiconductor Device*, 2nd edn, Wiley-Interscience, New York.

61 Klauk, H. (2006) *Organic Electronics: Materials, Manufacturing and Applications*, Wiley-VCH Verlag GmbH.

62 Walzer, K., Maennig, B., Pfeiffer, M., and Leo, K. (2007) *Chem. Rev.*, **107**, 1233.

63 Lee, J.-H., Leem, D.-S., Kim, H.-J., and Kim, J.-J. (2009) *Appl. Phys. Lett.*, **94**, 123306.

64 Salmeron-Valverde, A., Robles-Martinez, J., Garcia-Serrano, J., Gomez, R., Ridaura, R.M., Quintana, M., and Zehe, A. (1999) *Mol. Eng.*, **8**, 419.

65 Ganzorig, C. and Fujihira, M. (2000) *Appl. Phys. Lett.*, **77**, 4211.

66 Endo, J., Matsumoto, T., and Kido, J. (2002) *Jpn. J. Appl. Phys.*, **41**, L358.

67 Huang, F., MacDiarmid, A.G., and Hsieh, B.R. (1997) *Appl. Phys. Lett.*, **71**, 2415.

68 Lee, J.-H., Leem, D.-S., and Kim, J.-J. (2008) *Org. Electron.*, **9**, 805.

69 Ikeda, H., Sakata, J., Hayakawa, M., Aoyama, T., Kawakami, T., Kamata, K., Iwaki, Y., Seo, S., Noda, Y., Nomura, R., and Yamazaki, S. (2006) *SID Int. Symp. Dig. Tech. Papers*, **37**, 923.

70 Yun, J.Y., Noh, S.U., Shin, Y.C., Baek, H.I., and Lee, C.H. (2006) Low operating voltage and long lifetime organic light-emitting diodes with vanadium oxide (V_2O_5) doped hole transport layer, International Meeting on Information Display, p. 1038.

71 Chang, C.-C., Hsieh, M.-T., Chen, J.-F., Hwang, S.-W., Ma, J.-W., and Chen, C.H. (2006) *SID Int. Symp. Dig. Tech.*, **6**, 1106.

72 Meyer, J., Hamwi, S., Schmale, S., Winkler, T., Johannes, H.-H., Riedl, T., and Kowalsky, W. (2009) *J. Mater. Chem.*, **19**, 702.

73 Qi, Y., Sajoto, T., Barlow, S., Kim, E.G., Marder, S.R., and Kahn, A. (2009) *J. Am. Chem. Soc.*, **131**, 12530.

74 Koech, P.K., Padmaperuma, A.B., Wang, L., Swensen, J.S., Polikarpov, E., Darsell, J.T., Rainbolt, J.E., and Gaspar, D.J. (2010) *Chem. Mater.*, **22**, 3926.

75 Blochwitz, J., Pfeiffer, M., Fritz, T., and Leo, K. (1998) *Appl. Phys. Lett.*, **73**, 729.

76 Chen, M.H., Chen, Y.H., Lin, C.T., Lee, G.R., Wu, C.I., Leem, D.S., Kim, J.-J., and Pi, T.W. (2009) *J. Appl. Phys.*, **105**, 113714.

77 Chen, M.H. and Wu, C.I. (2008) *J. Appl. Phys.*, **104**, 113713.

78 Johansson, N., Osada, T., Stafstrom, S., Salaneck, W.R., Parente, V., Dos Santos, D.A., Crispin, X., and Brédas, J.L. (1999) *J. Chem. Phys.*, **111**, 2157.

79 Lee, J.H., Wu, M.H., Chao, C.C., Chen, H.L., and Leung, M.K. (2005) *Chem. Phys. Lett.*, **416**, 234.

80 Oyamada, T., Maeda, C., Sasabe, H., and Adachi, C. (2003) *Jpn. J. Appl. Phys.*, **42**, 1535.

81 Yook, K.S., Jeon, S.O., Min, S.Y., Lee, J.Y., Yang, H.J., Noh, T., Kang, S.K., and Lee, T.W. (2010) *Adv. Funct. Mater.*, **20**, 1797.

82 Khan, M.A., Xu, W., Haq, K., Bai, Y., Wei, F., Jiang, X.Y., Zhang and, Z.L., and Zhu, W.Q. (2007) *J. Phys. D Appl. Phys.*, **40**, 6535.

83 Wu, C.I., Lin, C.T., Chen, Y.H., Chen, M. H., Lu, Y.J., and Wu, C.C. (2006) *Appl. Phys. Lett.*, **88**, 152104.

84 Leem, D.-S., Kim, S.-Y., Kim, J.-J., Chen, M.-H., and Wu, C.-I. (2009) *Electrochem. Solid-State Lett.*, **12**, J8.

85 Yang, C.-J., Cho, T.-Y., Lin, C.-L., and Wu, C.-C. (2007) *Appl. Phys. Lett.*, **90**, 173507.

86 Lee, J.Y., Yook, K.S., Jeon, S.O., Joo, C.W., Lee, T.-W., Noh, T., Yang, H.-J., and Kang, S.-K. (2008) CsN_3 as an air stable and low temperature evaporable novel n doping material for high efficiency and low driving voltage in organic light emitting diodes, International Meeting on Information Display, p. 1319.

87 Lee, J.-H., Leem, D.-S., and Kim, J.-J. (2010) *Org. Electron.*, **11**, 486.

88 Grecu, S., Bronner, M., Opitz, A., and Brütting, W. (2004) *Synth. Met.*, **146**, 359.

89 Lee, J.-H., Leem, D.-S., Kim, H.-J., and Kim, J.-J. (2009) *SID Int. Symp. Dig. Tech.*, **40**, 1719.

90 Aonuma, M., Oyamada, T., Sasabe, H., Miki, T., and Adachi, C. (2007) *Appl. Phys. Lett.*, **90**, 183503.

91 Hill, I. and Kahn, A. (2009) *J. Appl. Phys.*, **86**, 4515.

92 Olthof, S., Tress, W., Meerheim, R., Lüssem, B., and Leo, K. (2009) *J. Appl. Phys.*, **106**, 103711.

93 Lee, J.-H., Kim, H.-M., Kim, K.-B., Kabe, R., Anzenbacher, P., Jr., and Kim, J.-J. (2011) *Appl. Phys. Lett.*, **98**, 173303.

94 Lee, J.H., Kim, H.M., Kim, K.B., and Kim, J.-J. (2011) *Org. Electron.*, **12**, 950

95 Noh, Y.-Y., Lee, C.-L., Kim, J.-J., and Yase, K. (2003) *J. Chem. Phys.*, **118**, 2853.

96 Gao, W. and Kahn, A. (2002) *Org. Electron.*, **3**, 53.

97 Hamwi, S., Meyer, J., Winkler, T., Riedl, T., and Kowalsky, W. (2009) *Appl. Phys. Lett.*, **94**, 253307.

98 Wang, F., Qiao, X., Xiong, T., and Ma, D. (2009) *J. Appl. Phys.*, **105**, 084518.

99 Kwon, J.W., Lim, J.T., and Yeom, G.Y. (2010) *Thin Solid Films*, **518**, 6339.

100 Braun, S., Liu, X., Salaneck, W.R., and Fahlman, M. (2010) *Org. Electron.*, **11**, 212.

101 Kahn, A., Zhao, W., Gao, W., Vazquez, H., and Flores, F. (2006) *Chem. Phys.*, **325**, 129.

102 Lee, J.-H., Wang, P.-S., Park, H.-D., Wu, C.-I, and Kim, J.-J. (2011) *Org. Electron.*, **12**, 1763.

103 Huang, J., Pfeiffer, M., Werner, A., Blochwitz, J., Leo, K., and Liu, S. (2002) *Appl. Phys. Lett.*, **80**, 139.

104 Leem, D.-S., Kim, S.-Y., Lee, J.-H., and Kim, J.-J. (2009) *J. Appl. Phys.*, **106**, 063114.

105 Shen, Z., Burrows, P.E., Bulovic, V., Forrest, S.R., and Thompson, M.E. (1997) *Science*, **276**, 2009.

106 Matsumoto, T., Nakada, T., Endo, J., Mori, K., Kawamura, N., Yokoi, A., and Kido, J. (2003) Multiphoton emission oled: structure and property, Proceedings of the International Display Workshops, pp. 1285.

107 Law, C. W., Lau, K. M., Fung, M. K., Chan, M. Y., Wong, F. L., Lee, C. S., and Lee, S. T. (2006) *Appl. Phys. Lett.* **89**, 133511.

108 Lee, S., Lee, J.-H., Lee, J.-H., and Kim, J.-J. (2012) *Adv. Funct. Mater.*, **22**, 855.

109 Tang, C.W. (1986) *Appl. Phys. Lett.*, **48**, 183.

110 Yu, G., Zhang, C., and Heeger, A.J. (1994). *Appl. Phys. Lett.*, **64**, 1540.

111 Xue, J., Uchida, S., Rand, B.P., and Forrest, S.R. (2004) *Appl. Phys. Lett.*, **85**, 5757.

112 Drechsel, J., Mannig, B., Kozlowski, F., Pfeiffer, M., Leo, K., and Hoppe, H. (2005) *Appl. Phys. Lett.*, **86**, 244102.

113 Drechsel, J. (2004) *Org. Electron.*, **5**, 175.

114 Lee, J., Kim, S.-Y., Kim, C., and Kim, J.-J. (2010) *Appl. Phys. Lett.*, **97**, 083306.

115 Chan, M.Y., Lai, S.L., Lau, K.M., Lee, C. S., and Lee, S.T. (2006) *Appl. Phys. Lett.*, **89**, 163515.

116 Baude, P., Ender, D., Haase, M., Kelley, T., Muyres, D., and Theiss, S. (2003) *Appl. Phys. Lett.*, **82**, 3964.

117 Zhou, L., Wanga, A., Wu, S.C., Sun, J., Park, S., and Jackson, T.N. (2006) *Appl. Phys. Lett.*, **88**, 083502.

118 Zaumseil, J. and Sirringhaus, H. (2007) *Chem. Rev.*, **107**, 1296.

119 Puntambekar, K.P., Pesavento, P.V., and Frisbie, C.D. (2003) *Appl. Phys. Lett.*, **83**, 5539.

120 Salleo, A., Chabinyc, M., Yang, M., and Street, R. (2002) *Appl. Phys. Lett.*, **81**, 4383.

121 de Boer, B., Hadipour, A., Mandoc, M.M., van Woudenbergh, T., and Blom, P.W.M. (2005) *Adv. Mater.*, **17**, 621.

122 Kwon, J.H., Shin, S.I., Kim, K.H., Cho, M.J., Kim, K.N., Choi, D.H., and Ju, B.K. (2009) *Appl. Phys. Lett.*, **94**, 013506.

123 Tiwari, S.R., Potscavage, W.J., Jr., Sajoto, T., Barlow, S., Marder, S.R., and Kippelen, B. (2010) *Org. Electron.*, **11**, 860.

5
Displacement Current Measurement for Exploring Charge Carrier Dynamics in Organic Semiconductor Devices

Yutaka Noguchi, Yuya Tanaka, Yukimasa Miyazaki, Naoki Sato, Yasuo Nakayama and Hisao Ishii

5.1 Introduction

Organic semiconductor (OSC) devices, particularly organic field effect transistors (OFETs), photovoltaic cells (OPVCs), and light-emitting diodes (OLEDs) have been extensively studied in recent decades because of their promising applications in electronics [1–7]. The basic structures of OSC devices were established in the mid-1980s. The first OFETs, composed of small molecules (1984) and polymers (1987), were realized by fabricating a thin OSC layer on a SiO_2/doped Si substrate in contact with top or bottom source–drain electrodes [8–10]. In 1986, Tang demonstrated the first efficient OPVC by introducing a bilayer system composed of donor and acceptor layers analogous to the p–n junction used in inorganic devices [11]. The bilayer structure was also applied to OLEDs by Tang and VanSlyke in 1987, significantly enhancing the device performance [12]. These and following works have indicated the importance of developing good interfaces in OSC devices, which has been a key issue in the research in this field. Furthermore, extensive research has been conducted to overcome the interface problems, and resulted in elaborate multilayer structures and various surface treatments in modern OSC devices [4, 6, 7]. The structural optimization of OSC devices has significantly enhanced their performance; however, the underlying mechanisms of device operation have not been sufficiently well understood mainly owing to enormous variations in the materials used in the devices and their complex interactions with other materials.

Since most OSC materials have a relatively wide energy gap between occupied and unoccupied states, and are not intentionally doped in most cases, they contain very few thermally excited carriers. Consequently, charge injection from the electrode to the OSC layer often initiates the functioning of the OSC devices. Hence, the potential barrier at the electrode/OSC layer interface is a highly essential parameter to understand the device operation mechanisms. Previous studies on OSC interfaces through photoelectron spectroscopy (PES) have revealed the

Physics of Organic Semiconductors, Second Edition. Edited by Wolfgang Brütting and Chihaya Adachi

presence of interface dipoles, that is, a vacuum-level shift at the metal/organic interfaces due to the interactions between the metal surface and the molecules [13]. The vacuum-level shift typically exceeds the thermal energy by a few hundred meV; this difference can greatly influence the charge injection properties of OSC devices. However, even if the presence of an interface dipole is taken into account, the electronic structures observed through PES cannot always explain the properties of actual OSC devices. The reasons are often believed to be (i) the differences in experimental situations and (ii) the presence of a small density of states in the energy gap.

PESs are usually performed in ultrahigh vacuum (UHV) conditions, while the actual devices are often fabricated and operated in high vacuum (HV), inert gas, or even air. Surfaces in HV conditions are easily contaminated by residual gases such as water vapor and hydrocarbons. These contaminants can form an interlayer between the OSC layer and the electrode and lead to a different energy structure at the interface [1]. Furthermore, the purity of the OSC materials is not sufficiently controlled with regard to the electronic properties of the devices. Device operation may also be significantly affected by unintentional doping from the environment. The electronic states due to such contaminants may exist between the highest occupied molecular orbital (HOMO) and the lowest unoccupied molecular orbital (LUMO), and the charge injection and transport properties can be modified by the presence of such intergap states; however, the detailed characteristics are yet to be clarified. At present, research is aimed at exploring the real principle behind the driving mechanisms of the OSC devices, for example, direct observation of the electronic structure and carrier dynamics in actual devices, fabrication of ideal devices with highly ordered films (crystals) of ultrapure materials, and so on. We believe that such efforts bridge the gap between the ideal and the actual device (interface) properties and aid in gaining a comprehensive understanding of the device physics.

We have studied the fundamental operation mechanisms of OSC devices and have specifically focused on their interface properties. To achieve a clear understanding, the carrier dynamics in OSC devices should be analyzed based on the electronic structure at their interfaces. We have been mainly developing two experimental techniques, photoelectron yield spectroscopy (PYS) and displacement current measurement (DCM), to investigate the device physics of actual OSC devices. PYS is a classical technique that measures the total amount of photoelectrons emitted from a material surface as a function of the wavelength of the incident ultraviolet (UV) light [14]. Thus far, several variations of PYS methods have been reported, in which photoelectrons were detected (i) simply as photoelectrons using an electron multiplier [15, 16], (ii) as the motion of ionized small particles floating in a Millikan chamber [17], (iii) as oxygen anions using an open-counter analyzer [18], and (iv) as electric current using an amperemeter [19–22]. Although PYS is based on a simple principle, it allows us to evaluate the ionization energy and energy barrier at the metal/organic and organic/organic interfaces under various conditions such as UHV, HV, air, and so on [19, 23, 24]. Moreover, we found that our PYS method overcomes the sample

charging problem, which often limits the application of PES, and can hence be used on thick organic films, organic crystals, and even insulators [25]. Based on these advantages, we are exploring the electronic structures at device-related interfaces in similar situations to the actual devices. On the other hand, many experimental techniques have been developed to investigate the charge carrier dynamics in OSC devices. Because of the complex structures and various functions of modern OSC devices, one should take appropriate combinations of measurement techniques among them. Here, we briefly review some typical methods used in this research field to specify our experimental technique, DCM.

Current–voltage (*I*–*V*) measurement, which involves detection of the actual current at a steady state as a function of applied voltage, is the most fundamental method for investigating the charge carrier transport in electronic devices [26–28]. The *I*–*V* curves of OSC devices are often analyzed within two limiting regimes, that is, the injection and space-charge-limited regimes. In the former regime, for instance, when the energy barrier at the electrode/OSC interface is high, the Fowler–Nordheim and/or Richardson–Schottky models are applied to analyze the current behaviors [26, 27]. On the other hand, when the charge injection across the electrode/OSC interface is suitable, space charge-limited current (SCLC) and/or trap-charge-limited current (TCLC) become predominant [28]. For simplified model devices rather than the actual ones, the models well explain the *I*–*V* curves of the device and are useful in determining some physical parameters, such as carrier mobility, energy barrier, and charge trap density.

Capacitance–voltage (*C*–*V*) measurement is another standard method, in which, typically, an alternating current (AC) bias modulation superimposed on a direct current (DC) offset is applied to the device. In *C*–*V* measurement, the behavior of mobile charges is detected in response to the given AC modulation. Unlike the case of *I*–*V* measurement, carrier transport in the device can be investigated even below the threshold voltage of the actual DC current. The *C*–*V* measurement has been often applied to study the charge injection and accumulation properties and to determine the dopant concentration in OSC devices [10, 26, 29]. In general, *C*–*V* and capacitance–frequency (*C*–*f*) measurement can be expanded to impedance spectroscopy (IS), in which response signals including the amplitude and phase shift are measured with reference to the applied AC modulation [30]. Impedance spectroscopy has been applied for various processes related to OSC devices, such as the determination of the carrier mobility, trap density, barrier heights, built-in voltage, and so on [31–36].

The above methods are mainly applied to the device in the (quasi-)static state. Even though they can extract information related to charge dynamics, such as carrier mobility, the analyses usually require certain assumptions. To determine the carrier mobility in a straightforward manner, a transient carrier response should be measured. Time of flight (TOF) is a typical example, in which the transit time of a photogenerated carrier across the device is measured as the displacement current [37]. Because of the simple principle and experimental setup, TOF has been widely accepted as a standard technique to evaluate the carrier mobility in organic materials. However, a device with a relatively thick film (typically on a micrometer scale) is

necessary for obtaining a photogenerated carrier sheet of negligible thickness. Recently, Manaka *et al*. developed a technique called time-resolved microscopic optical second-harmonic generation (TRM-SHG) for visualizing the carrier motion in OFETs [38]. This method detects carrier motion as an SHG signal instead of current; the SHG signal is induced by the local electric field owing to the presence of a charge in the channel region.

In addition to the above techniques, various other techniques have been developed to verify the charge carrier behaviors in OSC devices, such as Kelvin force microscopy (KFM) to determine the potential profile [39], electroabsorption spectroscopy (EA) to evaluate the averaged electric field [40], and charge extraction by linearly increasing voltage (CELIV) to explore bulk transport properties [41]. Our experimental technique, DCM, probes the behavior of carriers and trapped charges as well as dielectric properties in actual devices [42–47]. DCM is a type of *C*–*V* measurement, but it uses a triangular wave as the applied voltage and measures both quasi-static and transient current responses. Although the quasi-static DCM is similar to the conventional *C*–*V* measurement, DCM can detect both injected and extracted charge carriers and can consequently detect the amount of trapped charge in the device, as well as polarization switching; this is because the true current (not the root mean square) is measured as function of time and applied voltage. DCM was specifically introduced to analyze organic diodes [48, 49]. Egusa *et al*. conducted pioneering research on DCM to investigate the interface properties of OLEDs [47]. Ogawa and Ishii then expanded this technique to analyze charge carrier dynamics in OFETs [44–46]. DCM has mainly been used to analyze quasi-static carrier behavior; however, the DCM signal contains a current due to transient carrier behavior and it increases when the sweep rate of the applied triangular wave is high. From the sweep rate dependence of the DCM curve, we can obtain the information of the contact and bulk resistance of the device [50]. Moreover, the dynamic carrier behavior can be directly examined by using a combined waveform consisting of a constant voltage following a ramp voltage [51].

In this chapter, we introduce the basic concept and recent advances of the DCM technique with some typical experimental results. These results include charge injection, extraction, and accumulation properties in organic metal insulator semiconductor (MIS) structures (Section 5.2.1); estimation of the depth profile of the dopant concentration in an archetypical OLED (Section 5.2.1); detection of contact and bulk resistance from the sweep rate dependence of the applied voltage (Section 5.2.2); and transient current analysis results using a DC bias following a ramp voltage supported by IS data (Section 5.2.2). Moreover, charge accumulation behavior at OLED-related interfaces, where the orientation polarization of organic films plays a significant role, were studied using a combination of DCM, IS, Kelvin probe (KP), and ultraviolet photoelectron spectroscopy (UPS) (Sections 5.3.1 and 5.3.2). We also show light-induced space charges in a tris-(8-hydroxyquinolate) aluminum (Alq_3) film, originating from the light

absorption of Alq_3 during the film formation (Section 5.3.3). Finally, we state the conclusions of our recent works.

5.2
Displacement Current Measurement

The principle of DCM is simple: A triangular wave bias is applied to the device and the current response is measured. The total current density flowing through the system (i_{total}) consists of the actual and displacement current densities, i_{act} and i_{dis}, respectively; thus,

$$i_{total} = i_{act} + i_{dis} \tag{5.1}$$

In a device consisting of organic semiconductor layers between two parallel electrodes, where a voltage source and current meter are connected to the electrodes (Figure 5.1a), i_{dis} corresponds to the time derivative of the induced charge on the electrode. For instance, if one positive charge (q) is at a distance x from the electrode next to voltage source in a single-layer device with capacitance C, applied voltage V, and thickness d, then the induced charge on the current meter side Q_{elec} is given by

$$-Q_{elec} = CV + \frac{x}{d}q \tag{5.2}$$

The first term of Eq. (5.2) denotes the charges supplied from the voltage source, while the second term shows the contribution of the induced charges due to the (injected) charges in the organic layer. The equation can be generalized by

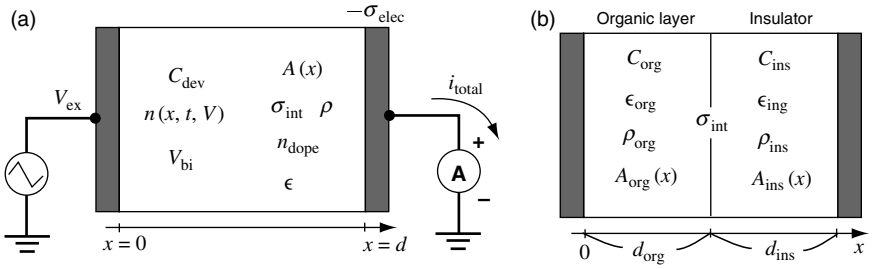

Figure 5.1 Schematic illustrations of the system under study. (a) The device is connected to the voltage source (left side) and current meter (right side). C_{dev}: capacitance of the device; $n(x, t, V)$: carrier density; V_{bi}: built-in voltage; $A(x)$: charge induction efficiency depending on the device structure; σ_{int}: interface charge density; ϱ: trapped charge density; n_{dope}: dopant density; ε: dielectric constant. (b) A typical bilayer system consisting of an organic layer and insulator sandwiched by two electrodes. The parameter of each layer is specified by the subscripts. Here, $C_{dev}^{-1} = C_{org}^{-1} + C_{ins}^{-1}$, $A_{org}(x) = (x/\varepsilon_{org})C_{dev}$, and $A_{ins}(x) = (C_{org}^{-1} + (x - d_{org}/\varepsilon_{ins}))C_{dev}$ can be obtained.

assuming a charge distribution along the x-axis as,

$$-\sigma_{\mathrm{elec}} = C_{\mathrm{dev}} V + \int_0^d A(x)\{qn(x,t,V) + \varrho\}\mathrm{d}x \tag{5.3}$$

where σ_{elec} is the charge density induced on the current meter side electrode, C_{dev} is the capacitance of the device per unit area, $A(x)$ is the charge induction efficiency, which depends on the device structure (corresponding to x/d in Eq. (5.2)), $n(x,t,V)$ is the carrier (mobile charge) density, ϱ is the trapped (immobile) charge density, and $V(= V_{\mathrm{ex}} - V_{\mathrm{bi}})$ is the effective applied voltage. V_{ex} and V_{bi} are the external applied voltage and built-in voltage, respectively. The displacement current is then given by

$$i_{\mathrm{dis}} = \frac{\partial \sigma_{\mathrm{elec}}}{\partial t} \tag{5.4}$$

The symbol i_{dis} includes both quasi-static and transient carrier behavior in the device. On the other hand, i_{act} is $qn(d,t,V)\mu E|_{x=d} - Dq\partial n(x,t,V)/\partial x|_{x=d}$, where μ is the carrier mobility, E is the electric field, and D is the diffusion constant. When the carriers move sufficiently fast compared to the change in the applied voltage, the device immediately achieves the quasi-static state at a given voltage; thus, $n(x,t,V)$ can be revised as $n(x,V)$. Eq. (5.4) corresponds to $i_{\mathrm{dis}} = C_{\mathrm{app}}(\mathrm{d}V/\mathrm{d}t)$, where the apparent capacitance, $C_{\mathrm{app}} = \mathrm{d}\sigma_{\mathrm{elec}}/\mathrm{d}V$, is used. C_{app} directly provides us the information related to the charge injection/extraction and accumulation properties of the device. At a higher sweep rate (corresponding to a large $\mathrm{d}V/\mathrm{d}t$), the contribution of the transient current increases and the system is no longer considered to be "quasi-static." In this situation, analyzing i_{dis} is not easy; however, the dynamic response can be derived from i_{dis} by holding the sweep voltage at a certain voltage $(\mathrm{d}V/\mathrm{d}t = 0)$, as discussed in Section 5.2.2. We can obtain transport characteristics of the device from the transient current behavior. In the following sections, we explain the basic concepts of DCM with some experimental data.

5.2.1 DCM for Quasi-Static States

5.2.1.1 Basic Concepts of DCM

To explain typical DCM characteristics, we assume a bilayer device consisting of an organic semiconductor layer and an insulator between two metal electrodes (Figures 5.1b and 5.2). When the device with a negligible i_{act} is in a quasi-static state, the measured current i_{total} corresponds to $C_{\mathrm{app}}(\mathrm{d}V/\mathrm{d}t)$. When the applied voltage to the device is lower than the built-in voltage of the device (V_{bi}), no carrier injection occurs and both the organic and the insulator layers act as insulators (defined as depletion state, (i) in Figure 5.2d). C_{app} is then considered as the serially combined capacitance of the organic and insulator layers, that is, $C_{\mathrm{app}}^{-1} = C_{\mathrm{dev}}^{-1} = C_{\mathrm{org}}^{-1} + C_{\mathrm{ins}}^{-1}$ (Figure 5.2c). Here, C_{org} and C_{ins} are the capacitances of the organic and insulator layers, respectively. When the carrier injection to the organic layer occurs at

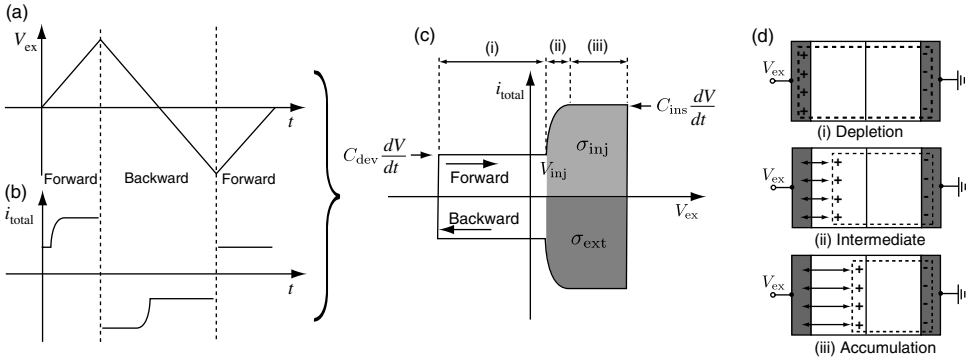

Figure 5.2 Schematic illustration of (a) the applied triangular wave voltage, (b) current response, and (c) DCM curve of bilayer device. The DCM curve represents the capacitance of the depletion and accumulation state, injection/extraction voltage, and amount and polarity of injected/extracted charge. In this case, the positive charge carrier behavior is detected because the displacement current increases in the positive bias side. (d) (i)–(iii) Schematic illustration of charge location in each state in (c).

voltages larger than V_{bi}, the organic layer is no longer regarded as a simple capacitor and the injected carriers mainly accumulate at the organic/insulator interface within the quasi-static regime ((iii) in Figure 5.2d). Consequently, C_{app} increases to C_{ins} at this voltage region (defined as accumulation state, Figure 5.2c). The total amount of charges (per unit area) injected from the electrode into the organic layer (σ_{inj}) is given by

$$\sigma_{inj} = \int_{t_{inj}}^{t} i_{dis} dt' = \int_{V_{inj}}^{V} C_{app} dV' \tag{5.5}$$

where $t_{inj}(V_{inj})$ is the time (voltage) when the carrier injection begins. Similarly, charge extraction processes from the organic layer to the electrode are observed in the backward sweep. Here, we define $dV/dt > 0$ as a forward sweep, and $dV/dt < 0$ as a backward sweep. The amount of the extracted charge σ_{ext} and the charge extraction voltage V_{ext} is also obtained from i_{dis}. Figure 5.2 shows a schematic illustration of an ideal DCM curve obtained by applying one cycle of triangular wave voltage.

5.2.1.2 Trapped Charges and Injection Voltage

If a part of the injected charge is trapped in the device during a sweep cycle of the applied voltage, then the extracted charge is less than the injected charge and the DCM curve appears asymmetric. The total amount of trapped charge can be determined as $\sigma_{trap} = \sigma_{inj} - \sigma_{ext}$ (Figure 5.3a). Although σ_{trap} is easily obtained, further analyses are required to estimate the trapped charge distribution in the film. Because the trapped charges form an electric field to prevent charge injection, V_{inj} for the subsequent voltage sweep shifts to the higher side. The analysis of V_{inj} provides us information of the trapped charge distribution. Assuming trapped charges

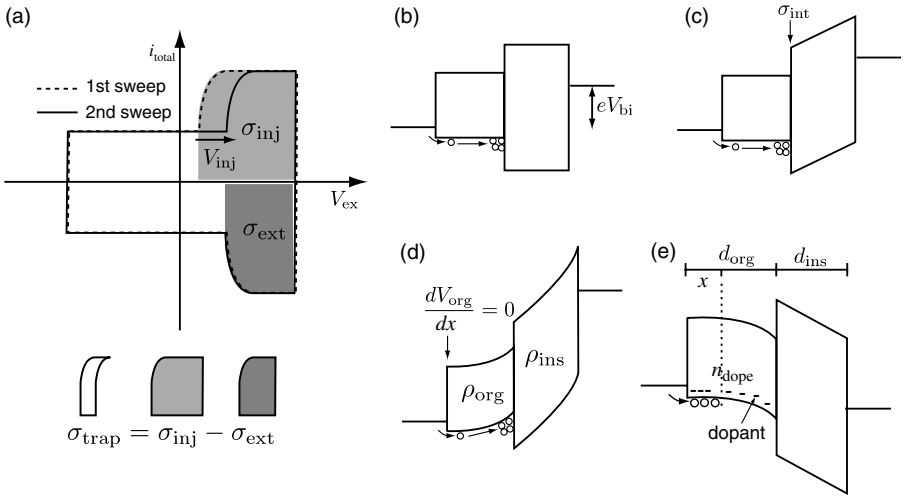

Figure 5.3 (a) Schematic illustration of typical DCM curve when a part of the injected charge is trapped in the device. The DCM curve becomes asymmetric and V_{inj} shifts to a higher side with the subsequent voltage sweep. σ_{trap} can be estimated from $\sigma_{inj} - \sigma_{ext}$. (b)–(d) Schematic energy diagram at V_{inj}: (b) $\varrho_{org} = \varrho_{ins} = 0$, $\sigma_{int} = 0$, (c) $\varrho_{org} = \varrho_{ins} = 0$, and (d) $\sigma_{int} = 0$. (e) Schematic energy diagram of the device in an intermediate state.

in the organic layer and insulator with a density of ϱ_{org} and ϱ_{ins}, respectively (Figure 5.1b), the potential distribution in the device is given by Poisson's equation,

$$\frac{d^2}{dx^2} V_{org} = -\frac{\varrho_{org}}{\varepsilon_{org}}, \quad (0 \le x \le d_{org}) \tag{5.6}$$

$$\frac{d^2}{dx^2} V_{ins} = -\frac{\varrho_{ins}}{\varepsilon_{ins}}, \quad (d_{org} \le x \le d_{org} + d_{ins}) \tag{5.7}$$

with boundary conditions of

$$V_{org} = V_{ex} - V_{bi} \quad (x = 0),$$
$$V_{org} = V_{ins} \quad (x = d_{org}),$$
$$V_{ins} = 0 \quad (x = d_{org} + d_{ins}),$$

and

$$\varepsilon_{org} \frac{d}{dx} V_{org} - \varepsilon_{ins} \frac{d}{dx} V_{ins} = \sigma_{int} \quad (x = d_{org})$$

Here, V_{org} (V_{ins}), d_{org} (d_{ins}), and ε_{org} (ε_{ins}) are the potential, thickness, and dielectric constant of the organic layer (insulator), respectively, and σ_{int} is the interface charge density. These equations provide the potential distribution of the bilayer system; V_{inj} can be obtained by assuming that the charge injection starts when $(d/dx)V_{org} = 0$ $(x = 0)$, for instance, in the case of the flat band condition.

If there is no trapped charge, that is, $\varrho_{org} = \varrho_{ins} = 0$ and $\sigma_{int} = 0$, $V_{inj} = V_{bi}$ is obtained from the above equations (Figure 5.3b), but the presence of the interface

charge results in

$$V_{\mathrm{inj}} = V_{\mathrm{bi}} + \frac{\sigma_{\mathrm{int}} d_{\mathrm{ins}}}{\varepsilon_{\mathrm{ins}}} \tag{5.8}$$

V_{inj} is proportional to d_{ins} and σ_{int}, when the interface charge exists at the interface (Figure 5.3c). Brütting *et al.* discovered such an interface charge in Alq_3-based OLEDs [28]; we have found that the interface charges exist at several organic heterointerfaces of the materials related to OLEDs. The interface charge is critical to V_{inj} from the anode to the hole transport layer (HTL); and this interface charge determines the minimum amount of accumulated holes at the HTL/Alq_3 interface during device operation. Moreover, the interface charge is directly related to the degradation in OLEDs [43, 52]. We will return to this discussion in Section 5.3.

Similarly, in the case that constants ϱ_{org} and ϱ_{ins} exist in the device (but no interface charge), V_{inj} is given as

$$V_{\mathrm{inj}} = V_{\mathrm{bi}} + \varrho_{\mathrm{org}} d_{\mathrm{org}} \left(\frac{d_{\mathrm{org}}}{2\varepsilon_{\mathrm{org}}} + \frac{d_{\mathrm{ins}}}{\varepsilon_{\mathrm{ins}}} \right) + \varrho_{\mathrm{ins}} \frac{d_{\mathrm{ins}}^2}{2\varepsilon_{\mathrm{ins}}} \tag{5.9}$$

Thus, the shift in V_{inj} is proportional to ϱ_{org} and ϱ_{ins} but is also a quadratic of the film thicknesses (Figure 5.3d). If the interface charge exists in addition to the constant space charges, $\sigma_{\mathrm{int}}(d_{\mathrm{ins}}/\varepsilon_{\mathrm{ins}})$ should be added to Eq. (5.9). The thickness dependence of V_{inj} is helpful to analyze the trapped charge distribution in the device.

5.2.1.3 Intermediate State between Depletion and Accumulation

In the above discussions, we ignored the intermediate state between the depletion and the accumulation, although this intermediate state often appears in the DCM curves. As discussed in the next section, the intermediate state is frequently observed in the DCM curves measured at a high sweep rate, though it can be attributed to the transient current (due to the contact and film resistance). However, even within a quasi-static regime (at sufficiently slow sweep rates), the intermediate state still appears in the DCM curves. The curve in the intermediate state can be attributed to the depletion width in the device, which can be formed by the presence of intentional or unintentional dopants. For example, the $1/C^2$–V plot has often been used to analyze dopant characteristics, and one can estimate the dopant density from its slope [10, 26, 48]. Here, we consider how C_{app} changes from the depletion (C_{dev}) to accumulation (C_{ins}) state as a function of the applied voltages within the quasi-static regime.

If a sufficient reverse bias is applied to the device, carriers in the device are completely extracted and all thermally active dopants are ionized. Then, by increasing the applied bias, the injected charges penetrate into the organic layer, compensating for the ionized dopants, namely, $n(x, V) = n_{\mathrm{dope}}$. Here, n_{dope} is the dopant density. The carrier penetration reduces the thickness of the depletion region, and an intermediate capacitance is observed between C_{dev} and C_{ins}. Here, the following equation can be assumed (Figure 5.3e).

$$\sigma_{\mathrm{inj}} = \int_{V_{\mathrm{inj}}}^{V} C_{\mathrm{app}} \mathrm{d}V' = \int_{0}^{x} -qn_{\mathrm{dope}} \mathrm{d}x'. \tag{5.10}$$

This equation corresponds to

$$-qn_{\mathrm{dope}} = C_{\mathrm{app}} \frac{\mathrm{d}V}{\mathrm{d}x} \tag{5.11}$$

with a boundary condition of $V = V_{\mathrm{inj}}$ at $x = 0$. On the other hand,

$$C_{\mathrm{app}}^{-1} = C_{\mathrm{ins}}^{-1} + \left(\frac{\varepsilon_{\mathrm{org}}}{d_{\mathrm{org}} - x} \right)^{-1} \tag{5.12}$$

where x is the penetration depth of the carrier from the electrode. The equation can be rewritten as

$$x = \varepsilon_{\mathrm{org}} \left(C_{\mathrm{dev}}^{-1} - C_{\mathrm{app}}^{-1} \right) \tag{5.13}$$

Here, C_{dev} and $C_{\mathrm{app}}[= i_{\mathrm{total}}/(\mathrm{d}V/\mathrm{d}t)]$ are measurable parameters; thus, if $\varepsilon_{\mathrm{org}}$ is known, one can obtain x at a given voltage V. $\mathrm{d}V/\mathrm{d}x$ is numerically obtained from the list of (x, V). Finally, n_{dope} is given by Eq. (5.11). On the other hand, assuming a constant n_{dope}, C_{app} can be derived as

$$C_{\mathrm{app}} = \left\{ C_{\mathrm{dev}}^{-2} + \frac{2(V - V_{\mathrm{inj}})}{\varepsilon_{\mathrm{org}} q n_{\mathrm{dope}}} \right\}^{-1/2} \tag{5.14}$$

Therefore, the $1/C_{\mathrm{app}}^2$ versus V plot is a straight line with a slope of $2/\varepsilon_{\mathrm{org}} q n_{\mathrm{dope}}$, as often used to analyze the dopant density. However, it is available only for the case in which the dopant density in the film is assumed to be constant. The proposed method enables us to obtain the dopant density profile from the measured DCM curves within the quasi-static regime.

Typical DCM Curve at Quasi-Static State Figure 5.4b shows typical DCM curves of an archetypical bilayer OLED, which has an indium-tin oxide (ITO)/4,4′-bis(*N*-(1-naphthyl)-*N*-phenylamino)-biphenyl (α-NPD) (70)/Alq_3 (50)/Ca/Al structure (Figure 5.4a), at a sweep rate of 10 V/s – 1 kV/s, where the number in the parentheses denotes the film thickness (nm). The vertical axis is the current density normalized by the sweep rate to specify the curve shape. The device was fabricated and encapsulated without exposure to air. The DCM curves at 10 V/s are almost identical to those at 100 V/s; thus, one can assume that the device was in a quasi-static state at sweep rates of 10–100 V/s. The depletion, intermediate, and accumulation states are clearly seen in these curves. Moreover, the charge injection begins at −1.2 V, which is lower than V_{bi} of the device (typically 1.9 V). At voltages larger than V_{bi}, the actual current increases. The result indicates the presence of negative interface charge, as discussed in detail in Section 5.3. According to the above equations, x and n_{dope} are obtained from the DCM curve (Figure 5.4c), where $\varepsilon_{\mathrm{NPD}}/\varepsilon_0 = 3.0$ was used (ε_0 is the dielectric permittivity of vacuum). The estimated dopant density increases near the interfaces, namely, ITO/α-NPD and α-NPD/Alq_3, but the tail of the dopant density at the α-NPD/Alq_3 interface is longer than that at the

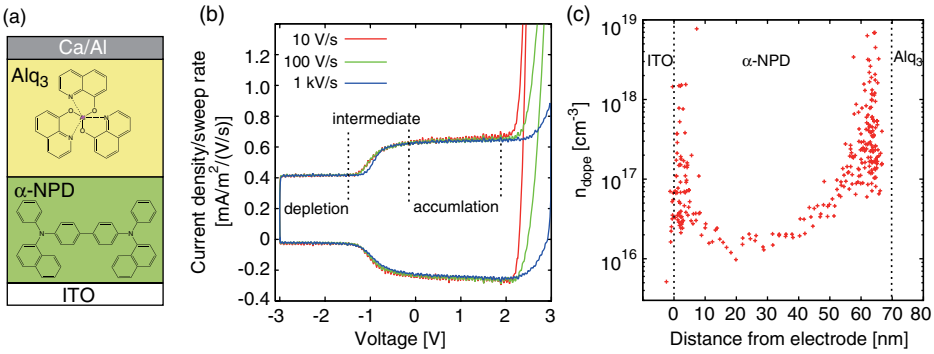

Figure 5.4 (a) The structure of the device. The chemical structure of α-NPD and Alq_3 is also shown. (b) Typical DCM curves of the device (10 V/s–1 kV/s). (c) Depth profile of n_{dope} in the α-NPD layer derived from the DCM curve.

ITO/α-NPD interface. From 15 to 40 nm, the dopant density appears constant ($\sim 2 \times 10^{16}$ (cm^{-3})). The typical molecular density of the evaporated films of OSC is $\sim 10^{21}$ (cm^{-3}); thus, the estimated dopant density is on the order of 10 ppm. This value agrees with the previously reported value for nondoped OSC films [53, 54]. The results imply that the α-NPD layer was unintentionally doped, although the exact origin of the "dopant" is not clear at the moment. For example, although O_2 is often considered to be the dopant, recent ultrahigh sensitivity UPS measurements revealed that even N_2 induces the gap states [55]. We believe that small amounts of electronic states in the energy gap (e.g., HOMO–LUMO gap) formed due to such unintentional doping play important roles in the charge injection and transport characteristics. We are also conducting high-resolution PYS experiments to understand the device physics in OSC devices based on direct observations of electronic structures in the gap states.

5.2.2
DCM for Transient States

When a triangular wave voltage with a higher sweep rate is applied, the system is no longer regarded as "quasi-static." One must also consider the contribution of the transient current. Assuming a bilayer device consisting of an organic layer and insulator between two electrodes without charge traps, the charge injected from the electrode transports through the organic layer and accumulates at the organic/insulator interface. Since the transport process takes a finite time, depending on the mobility μ and electric field distribution E in the material, it caused a delay in the charging process of the device. When the applied bias voltage changes faster than the charging process, a transient current due to the delay is enhanced in the current–voltage curve. In addition, the contact resistance at the electrode/organic film also appears in the DCM curves, even though the charge transport through the film is sufficiently fast, because the contact resistance restricts the amount of charge injected in the device.

The transient current results in a complicated DCM curve, which includes information on transport properties and contact resistance of the device. Analysis of the transient current in the DCM curve is thus an important factor to be considered when exploring the charge carrier behaviors in the device. In this section, we discuss what we can obtain from the sweep rate dependence of the DCM curve and how we can derive the dynamic current from the DCM curves. The conventional *C–V* and *C–f* analysis is helpful to understand the transient behavior; thus, we conducted both DCM and IS measurements on the identical samples [51].

5.2.2.1 **Sweep rate Dependence in DCM Curves**

Two types of devices, A and B, were fabricated as model OFET structures (Figure 5.5) for investigation of the charge injection/extraction and accumulation properties at metal/organic and organic/gate dielectric interfaces. Device A contains a pentacene (Pn) film and Au top electrode, both with the same area to avoid spreading of charge at the Pn/SiO_2 interface. Device B contains an organic film with an area larger than that of the electrode; thus, charge spreading is allowed in this device. Figure 5.6a and b shows typical DCM curves of Au/Pn/SiO_2/p-doped Si structures as OFET models, measured as a function of the sweep rate of the applied triangular wave voltage. The vertical axis is the current normalized by the sweep rate and electrode area.

The DCM curves of device B contains a transient carrier response, that is, a current peak at −10 V at 80 V/s, and a gradual increase in current in the negative bias region at 800 V/s – 80 kV/s; the DCM curves of device A show a typical quasi-static behavior at low sweep rates (80 V/s – 8 kV/s). The current peak appears as the accumulated charges at the Pn/SiO_2 interface under the electrode area (corresponding to the region (ii) in Figure 5.6b and d) spread over the interface (region (iii)); the line shape strongly depends on the sweep rate of the applied voltage. The peak structure in the DCM curves of device B is pushed to the negative side, and at the same time, the curves in the backward sweep are strongly distorted as the sweep

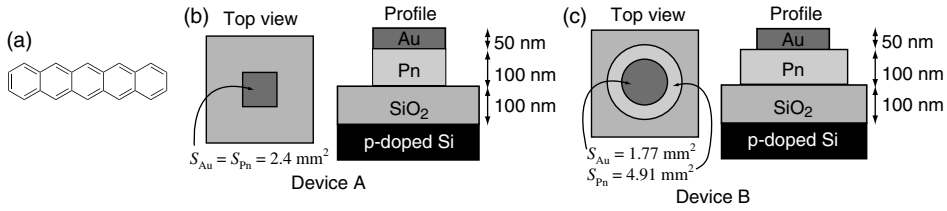

Figure 5.5 (a) The chemical structure of pentacene. (b)–(c) Schematic illustration of the top view and profile of devices A and B. S_{Au} and S_{Pn} are the areas of the Au and Pn layers, respectively. The resistivity of the p-doped Si is 0.02 Ω cm.

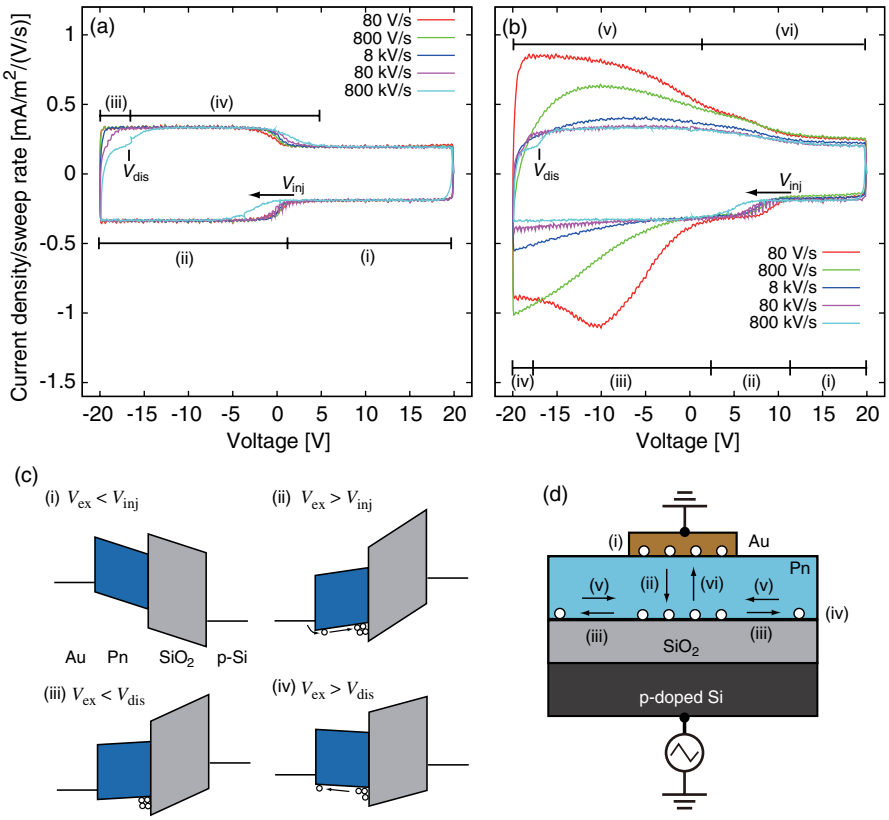

Figure 5.6 (a, b) DCM curves as a function of sweep rate of applied voltage in devices A and B, respectively. (c) Schematic illustrations of energy diagram expected in the voltage regions of (i)–(iv) in (a) at a sweep rate of 800 kV/s. (d) Schematic illustration of charge carrier behaviors at the voltage regions of (i)–(vi) in (b). The sweep rate corresponds to 80 V/s.

rate is increased. Finally, at the sweep rate of 800 kV/s, the signals from the peak structure disappear and the DCM curve of device B becomes almost coincident with that of device A.

The results suggest that the current peak originates from the transient carrier moving along the Pn/SiO_2 interface. The current due to the charge injection from the electrode is similar in both devices, that is, the injection voltage V_{inj} slightly shifts to the negative side as the sweep rates increase to more than 80 kV/s. This result indicates that the charge injection and accumulation processes under the electrode area are much faster than the charge filling process due to the spreading of charge over the interface region. Liang *et al.* recently analyzed the peak structure in DCM curves and utilized these carriers to evaluate the carrier transport characteristics at the interface [56, 57].

Even though the sweep rate dependence of the DCM curves provides us qualitative information of the interface and film resistances, a quantitative analysis is still

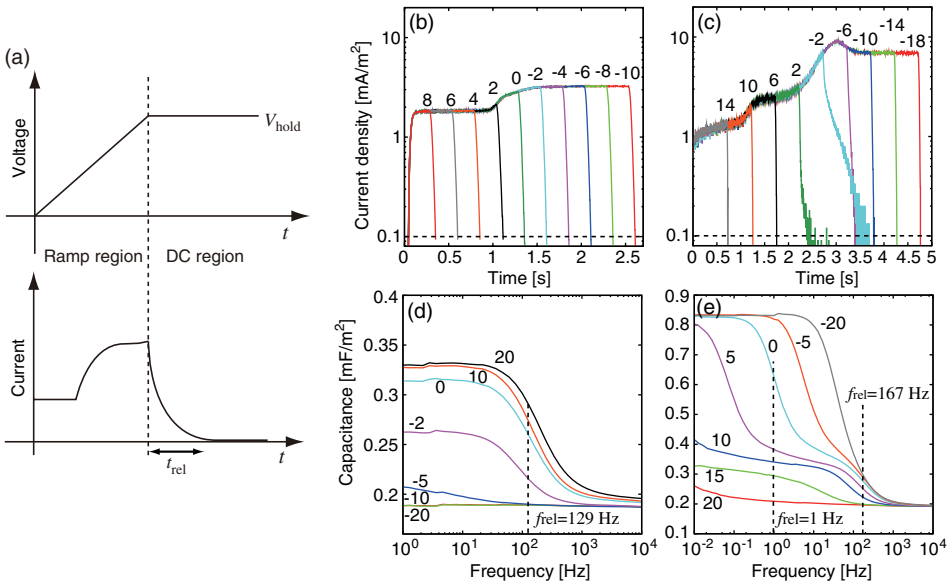

Figure 5.7 (a) Schematic illustration of the applied voltage (*top*) and measured current (*bottom*) in the combined waveform DCM. (b, c) Combined waveform DCM curves of device A (b) and B (c). The numbers near the line show V_{hold}, in units of V, for each curve. The sweep rate of the applied ramp voltages was 8 kV/s. (d, e) *C–f* curves of device A (d) and B (e). The applied DC bias in units of V and the relaxation frequencies (f_{rel} at 0 V) are shown in the figure.

difficult without making assumptions about the transport mechanisms in the organic films; this is because the DCM curves contain the contributions from both the quasi-static and the transient current. In order to separate the transient current from the observed total current in DCM, we proposed the use of a waveform that is a combination of a constant voltage following a ramp voltage instead of a triangular wave voltage (upper part of Figure 5.7a). When a ramp voltage is applied to the device, both the quasi-static and dynamic currents are observed, but after the ramp is switched to constant voltage, only the transient current remains (the bottom graph in Figure 5.7a). By changing V_{hold}, we can directly examine the transient current in various (depletion, intermediate, and accumulation) states of the device.

Figure 5.7b and c shows the combined waveform DCM curves for devices A and B, respectively. V_{hold} of each curve is indicated in the figures. In device A, the transient current decays immediately after the applied voltage form is switched to DC, almost independent of the holding voltage. If we define t_{rel} as is the time required for the current to decay less than 0.1 mA/m^2 from the beginning of the constant voltage region, then t_{rel} is less than 0.1 s for device A. On the other hand, the transient current in device B drastically changes when the holding voltages vary from 2 to −2 V corresponding to the charge spreading region. The transient current at these biases persists as long as about 1 s. The dynamic current with the large t_{rel} is observed only during the hole-spreading process at the Pn/SiO_2 interface.

Interestingly, after the charge sheet is formed completely at the interface ($V_{hold} < -10$ V), t_{rel} becomes much smaller again. The transient current with long decay time is obviously the origin of the peak structure in the DCM curve.

Figure 5.7d and e shows the *C–f* curves of devices A and B, respectively, at various applied voltages. The *C–f* curve reflects how fast the charges in the device respond at a given bias voltage. For instance, in Figure 5.7c, the capacitance at 0 V corresponds to C_{dev} ($\sim$0.2 mF/m^2) at higher frequencies ($> 10^3$ Hz), indicating that the charges in the organic layer do not follow the AC modulation at these frequencies. However, the capacitance increases with decreasing frequency, and finally drops to around C_{ins}, because the charges in the organic layer sufficiently move with the applied AC modulation. The inflection point in *C–f* curves is defined as f_{rel}; and for device A, it can be estimated to be 129 Hz. Two f_{rel} are observed in the *C–f* curves of device B, corresponding to the vertical (across the Pn film) and lateral (along the Pn/SiO_2 interface) charge transport. From the *C–f* curve at 0 V, the relaxation frequencies are determined as 167 and 1 Hz for the vertical and lateral carrier motion, respectively. The observed f_{rel} agrees with the inverse of t_{rel} estimated from the combined waveform DCM curves. This result demonstrates that the combined waveform DCM can properly extract the dielectric relaxation time of the carrier motion in the devices.

The charge injected into device B is immediately accumulated at the interface below the electrode area, but an additional voltage is required to start the charge spreading along the interface ((ii) in Figure 5.6b). This result suggests that the potential below the electrode is lower than that in other regions, possibly due to the presence of hole traps at the interface. Although trapped holes below the electrode can be extracted by a stronger electric field, those in other regions are likely to remain, and a potential barrier to initiate hole spreading can be formed between these regions. The suggested hole traps may also prevent the charge spreading along the interface. However, after the charge is completely spread over the interface, the carriers can move smoothly because the hole traps are filled and the interface region becomes equipotential. This mechanism might lead to the current with a long decay time, however, only during charge spreading.

Another interesting feature observed in Figure 5.6a and b is the hump in the forward sweep of DCM curve, for example, (iv) in Figure 5.6a. The discharge of the holes accumulated at the interface does not start until the applied bias becomes lower than a certain voltage (V_{dis} in Figure 5.6a and b). The presence of the hump can be attributed to the contact resistance at the electrode/Pn interface rather than the transport delay in the Pn film, although this hump also appears as decay current just after the polarity of applied voltage is switched. It should be noted that the capacitance corresponding to C_{dev} appears in the DCM curve before the discharging process begins in the backward sweep. The result indicates that the charges in the device do not move at these voltages, otherwise the intermediate capacitance should be observed. In other words, there are no carriers in the bulk region of the Pn layer.

The carrier behavior in the device can be described as follows. In the backward sweep, the hole injection into the Pn layer begins at V_{inj}. The injected charges

immediately cross the Pn layer and accumulate at the Pn/SiO_2 interface ((ii) in Figure 5.6c). However, the presence of the contact resistance prevents sufficient hole injection ($\sigma_{inj} < C_{ins}V$), leading to a reduction in the observed capacitance in the backward sweep at 800 kV/s. As a result, an electric field for hole conduction is formed in the Pn layer. In the forward sweep, the discharging process of the accumulated holes does not start until the forward electric field disappears ((iii) and (iv) in Figure 5.6c). As a result, the whole device works as a capacitor and C_{dev} is observed at biases higher than V_{dis}. By further decreasing the applied bias, the electric field for the discharge of the holes is established in the Pn layer, and the accumulated holes are then extracted from the interface. The current due to this process thus forms a hump in the forward sweep.

To see the hump in the DCM curve can be a test of the contact resistance in the device. Figure 5.8 shows the sweep rate dependence of the DCM curves of the α-NPD/Alq_3-based OLEDs with/without a copper phthalocyanine (CuPc) interlayer between the ITO and the α-NPD layers. The hole injection behavior in the device

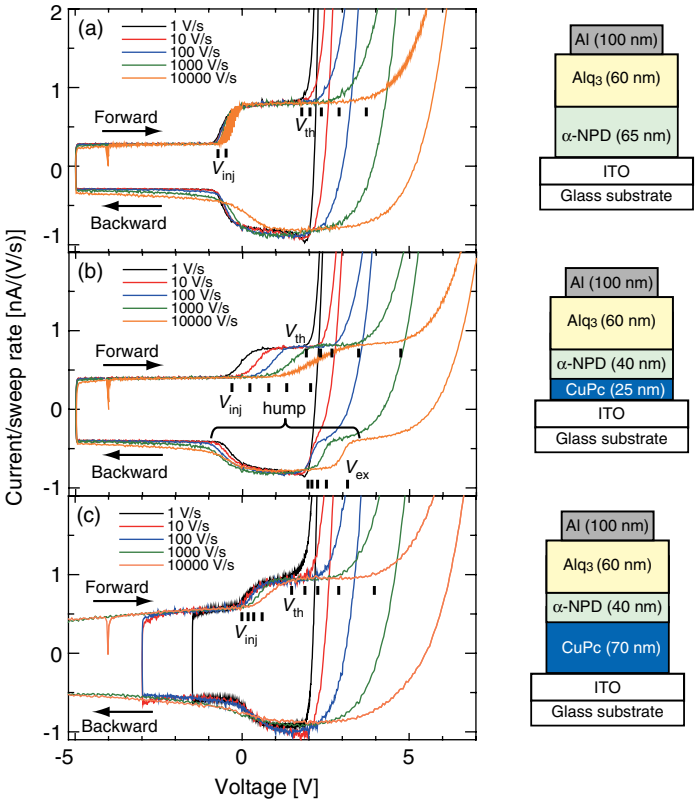

Figure 5.8 Typical DCM curves of ITO/(CuPc)/α-NPD/Alq_3/Al device (1 V/s–10 kV/s). The thickness of the CuPc layer is (a) 0 nm, (b) 25 nm, and (c) 70 nm. Schematic illustrations of the device structure are also shown on the right side of the corresponding DCM curves.

with the CuPc interlayer depends significantly on the sweep rate, and a hump appears in the backward sweep of the DCM curves. On the other hand, there is no significant change in the DCM curves of the device without the CuPc interlayer. Although the role of the CuPc layer is controversial, with regard to whether it enhances or deteriorates the hole injection from the anode [58–66], our results indicate that the presence of the CuPc interlayer leads to a higher contact resistance. Interestingly, the DCM curves of the device with a thick (70 nm) CuPc interlayer show no significant dependence on the sweep rate, indicating a smaller contact resistance than that in the thin-CuPc device. This peculiar thickness dependence can be attributed to the band bending in the CuPc layer. The details have been reported elsewhere [50].

5.3
Charge Accumulation at Organic Heterointerfaces

Since most OSC devices have multilayer structures, understanding the charge accumulation properties at the heterointerfaces is essential for improving the device performance [28, 58, 67–71]. For example, in OLEDs, the accumulated charges tune the electric field distribution to achieve a better charge balance and those in the emission layer increase the probability of exciton formation, leading to better efficiency [67, 68]. On the other hand, charged molecules near the emissive region can also act as exciton quenchers in an Alq_3-based OLED [71, 72]; the presence of the Alq_3 and α-NPD cation species is considered to be responsible for device degradation [58, 73]. In this section, we review our recent studies on charge accumulation problems in OLEDs, especially focusing on the orientation polarization in OSC films.

5.3.1
Elements of Charge Accumulation at Organic Heterointerfaces

Charge accumulation behavior has been extensively studied using various methods and theoretical models [29, 40, 46, 67, 68, 70, 72, 74–76]. In this section, we briefly explain the parameters responsible for the charge accumulation properties at organic heterointerfaces. The charge accumulation occurs where the current is prevented. In this situation, the divergence of the current takes a finite value, as shown in the continuity equation as follows:

$$\frac{\partial i_{\mathrm{act}}}{\partial x} = -q\frac{\partial n}{\partial t} \tag{5.15}$$

On the other hand, using the carrier mobility, the actual current flowing in the device is given by

$$i_{\mathrm{act}} = qn\mu E. \tag{5.16}$$

Here, we omit the diffusion current for simplicity. From these two equations,

$$-\frac{q}{i_{\mathrm{act}}}\frac{\partial n}{\partial t}=\frac{1}{n}\frac{\partial n}{\partial x}+\frac{1}{\mu}\frac{\partial \mu}{\partial x}+\frac{1}{E}\frac{\partial E}{\partial x} \tag{5.17}$$

is derived. This equation indicates three elements of charge accumulation. The energy barrier at the interface ΔE appears in the first term on the right-hand side of the equation, assuming that the carrier density is given by the Boltzmann's equation. The second term indicates that the mobility mismatch of the materials induces charge accumulation. This is a type of carrier congestion when they move from a "fast" to "slow" material [62]. The final term can be rewritten by using the Poisson's equation,

$$\frac{\partial D}{\partial x}=qn+\varrho_t \tag{5.18}$$

where $D=\varepsilon E+P_0$ is the electric flux density and P_0 is the orientation polarization due to a permanent dipole moment ordering. n and ϱ_{t} are the carrier (mobile) and trapped (immobile) charge densities, respectively. Thus,

$$\frac{\partial E}{\partial x}=\frac{1}{\varepsilon}(qn+\varrho_{\mathrm{t}}+\varrho_{\mathrm{b}}) \tag{5.19}$$

is derived, where $\partial P_0/\partial x=-\varrho_{\mathrm{b}}$ is the boundary charge density.

Orientation polarization is indeed very important to understand the charge accumulation at organic heterointerfaces. Many OSC molecules possess a permanent dipole moment, and some of them spontaneously form a polarized film with a constant P_0 [77–79]. Orientation polarization induces the interface charge in multilayer devices. Here, we consider a bilayer device that consists of polar films with no space charges (Figure 5.9a). At the interface ($x=d_1$), the electron flux density of these polar films (D_1, D_2) should be continuous; thus, the boundary condition is

$$D_1-D_2=-\varepsilon_1\frac{d}{\mathrm{d}x}V_1+\sigma_1+\varepsilon_2\frac{d}{\mathrm{d}x}V_2-\sigma_2=0\quad(x=d_1) \tag{5.20}$$

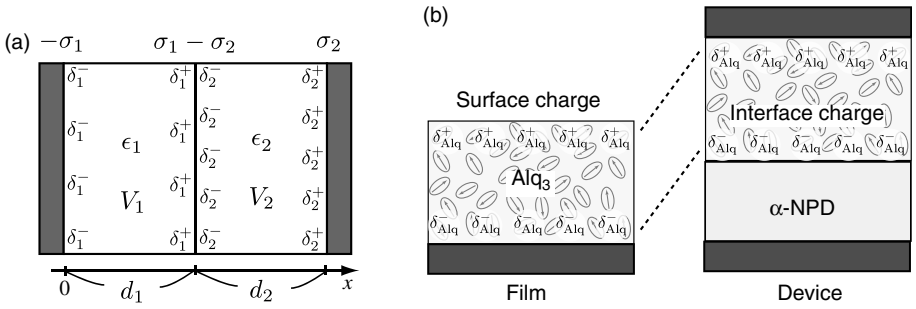

Figure 5.9 (a) Schematic illustration of an organic/organic interface with an orientation polarization. (b) Surface charge on the Alq_3 film and interface charge in Alq_3-based OLED.

where $\sigma_{1,2}$ is the sheet density of the interface charge due to the orientation polarization ($= P_{1,2}$). The above equation indicates that the orientation polarization of the film generates the interface charge at the heterointerface ($\sigma_{int} = \sigma_1 - \sigma_2$), leading to charge accumulation, as discussed in the next section. Importantly, the film itself maintains charge neutrality even though the interface charges seem like actual charges and the same amount of interface charges with opposite polarity exist at the backside of the film. The interface charge at the surface of a polar film is intrinsically formed without any charges from the outside and remains as long as the orientation polarization persists.

According to the above discussions, three elements of charge accumulation can be obtained as follows:

1) Energy barrier at the interface.
2) Mobility mismatch between the materials.
3) Mobile, trapped, polarized charge distribution in the device.

Among them, charge accumulation due to the charge distribution can occur at biases lower than V_{bi}, as discussed in Section 5.2.1 (Eqs. (5.8) and (5.9)). The mobility mismatch and energy barrier are not responsible for charge accumulation, because no carriers cross the interface at $V_{ex} \leq V_{bi}$. Thus, the contribution of the charge distribution to the charge accumulation is more clearly examined than the contribution of other parameters. However, in general, it is difficult to realize the physical origins of the charge accumulation at higher biases ($>V_{bi}$), because conventional electric measurements detect a combination of factors responsible for the accumulation, and signals from the bulk and multilayers often appear in optical spectroscopy analyses. Thus, the accurate estimation of these parameters in the device itself or under similar conditions is very important to understand the details of charge accumulation properties.

PESs and PYS are powerful tools for evaluating the ionization energy of materials and the barrier height at their interfaces. However, the energy levels such as HOMO levels determined independently for each material are not sufficient to estimate the energy barrier at actual interfaces; this is because a vacuum-level shift is often observed due to the presence of interface dipoles (electric double layers) [13]. Moreover, some organic films possess an orientation polarization, indicating that the film is asymmetric along the direction of thickness, as discussed below. This asymmetry indicates that the barrier height may depend on whether the contacts are formed on the front or back of the film and thus a direct measurement of the electronic structures should be done on the interfaces according to the stacking order in the actual device.

5.3.2
Interface Charges and Orientation Polarization

Brütting *et al.* discovered that hole injection from the anode to the α-NPD layer in Alq_3-based OLEDs occurs at biases lower than V_{bi} and that V_{inj} shifts to the negative side proportionally with the increase in the Alq_3 film thickness [28, 29]. They

reported the presence of a fixed negative charge at the α-NPD/Alq_3 interface with a constant density of about $-1.1\,mC/m^2$ (see Eq. (5.8)). Their interface charge model is very suitable for explaining the hole injection property of Alq_3-based OLEDs; however, the microscopic origin of this charge still remains to be clarified.

We recently proposed that the orientation polarization of the film is the origin of the interface charge, based on the observations of the giant surface potential (GSP) [80]. The GSP was first found in the Alq_3 film formed on a gold substrate under dark conditions [77]. The GSP grows linearly as a function of film thickness (reaching 28 V at a film thickness of 560 nm) due to the dipole moment ordering in the Alq_3 film or, in other words, the orientation polarization of Alq_3 film ($P_{Alq} = n_{Alq} p_{Alq} \langle \cos\theta \rangle$, where n_{Alq} is the molecular density, p_{Alq} is the dipole moment, and $\langle \cos\theta \rangle$ is the order parameter with reference to the surface normal). The result indicates that P_{Alq} induces a constant surface charge on the Alq_3 film (σ_{Alq}) independent of its thickness; a surface charge of $1.32\,mC/m^2$ is obtained from the boundary condition at the vacuum/Alq_3 film, that is, $\sigma_{Alq} = \varepsilon_{Alq} dV/dx$. This value is similar to the charge density found at the α-NPD/Alq_3 interface in the device ($-1.1\,mC/m^2$), though the polarity is opposite. However, the same amount of negative charge should exist at the bottom of the Alq_3 film, and this negative charge should act as the fixed charge at the α-NPD/Alq_3 interface, if P_{Alq} persists in the actual OLEDs (Figure 5.9b).

Most studies have focused on the energy barrier and mobility mismatch for understanding the charge accumulation properties, even though the interface charge is important not only for device operation but also for device degradation [43, 52, 81]. One reason for such a specific focus may be that the interface charge has been considered as a unique problem of Alq_3-based OLEDs. However, GSP has actually been found in the films of several compounds such as metal complexes, TPBi, and BCP [78, 82, 83], and the presence of the interface charge has also been suggested at the α-NPD/OXD-7 interface [28]. Moreover, Kondakov *et al.* also showed voltammetry data of several devices where the hole injection voltage appears at negative voltages [84, 85]. These studies indicate that the interface charge exists even in common OLEDs; however, a direct comparison between GSP and the interface charge has not been demonstrated. Realizing the physical origin of the interface charge is an important task leading to a comprehensive understanding of the charge accumulation properties. Here, we conducted DCM and KP measurements on the interfaces containing polar and nonpolar molecules (Figure 5.10) and found that the interface charge in the devices actually relates to the GSP of their constituents. Based on the experimental results, we conclude that the orientation polarization is the origin of the interface charge.

Figure 5.11 shows the typical surface potential of the α-NPD and Alq_3 film as a function of the film thickness. These films were successively deposited on an ITO substrate under high vacuum and dark conditions. It should be noted here that light absorption of the deposited film causes a decay of the surface potential, and thus, the experiments were performed excluding such light irradiation. As shown in Figure 5.11, a clear GSP behavior with a slope of 48 mV/nm is observed for the Alq_3 film. The corresponding surface charge density is $1.3\,mC/m^2$ with the

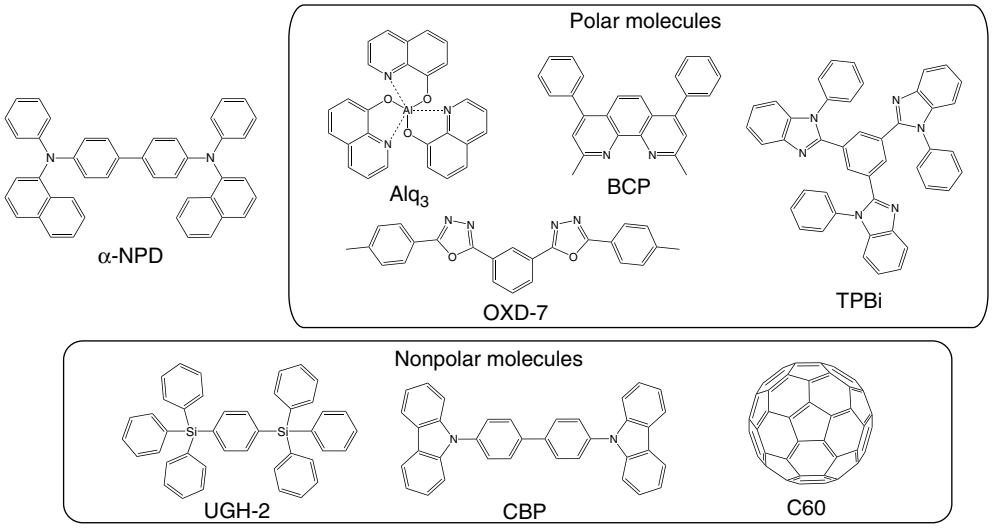

Figure 5.10 Chemical structures of the molecules used in this study, where α-NPD: 4,4′-bis(N-(1-naphthyl)-N-phenylamino)-biphenyl; Alq_3: tris-(8-hydroxyquinolate) aluminum; BCP: 2,9-dimethyl-4,7-diphenyl-1,10-phenanthroline; TPBi: 1,3,5-tris(1-phenyl-1*H*-benzimidazol-2-yl)benzene; OXD-7: 1,3-bis(2-(4-*tert*-butylphenyl)-1,3,4-oxadiazo-5-yl) benzene; CBP: 4,4′-bis(N-carbazolyl)-1,1′-biphenyl; and UGH2: 1,4-bis(triphenylsilyl) benzene.

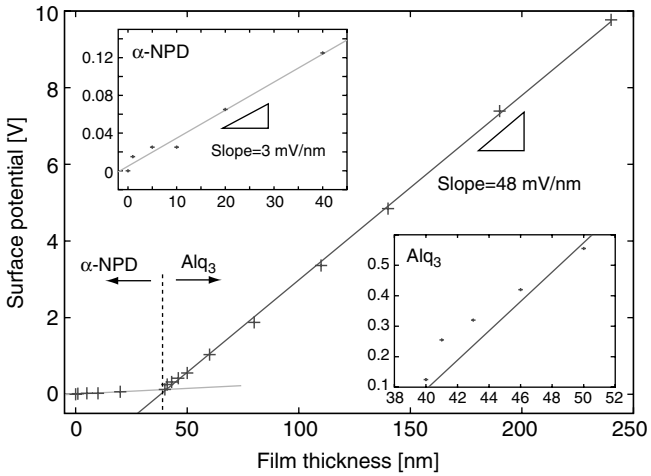

Figure 5.11 A typical surface potential of Alq_3 and α-NPD film as a function of the film thickness. The Alq_3 film was deposited on an α-NPD film on the ITO substrate. The α-NPD/Alq_3 interface locates at the film thickness of 40 nm. The surface potential of the Alq_3 film grows linearly with a slope of 48 mV/nm, though a nonlinear region appears within several nanometers from the interface (bottom inset). The α-NPD film also shows a weak GSP behavior (3 mV/nm, top inset).

Table 5.1 Interface properties of OLED-related materials.

	TPBi	BCP	Alq_3	OXD-7	CBP	UGH2	C_{60}	α-NPD
Dipole moment (D)	1.9	2.9	4.1	6.6	0	0	0	0.3
ΔIP (eV)	1.3[a)]	0.8[b)]	0.5[a)]	1.3[c)]	0.8[b)]	2.0[d)]	1.0[e)]	/
ΔE_{UPS} (eV)	1.3	1.0[b)]	0.3[f)]	1.6	0.7	2.0	0.4[g)]	/
GSP (mV/nm)								
-on α-NPD	76[i)]	37[h)]	48	68	—	-2[i)]	—	/
-on ITO	—	42	34	64	—	—	0	3
-on Au	—	—	50	82	—	—	—	—
$(V_{th} - V_{inj}/d_{ETL})$ (mV/nm)	39	23	49	110	0	0	—	/
σ_{int} (mC/m^2)	-1.4	-0.7	-1.2	-2.6	0	0	—	/

The dipole moment was calculated by Gaussian 03 with a basis set of B3LYP/6-31G(d). ΔIP denotes the difference in the independently determined ionization energy of each compound with that of α-NPD (5.2 eV). ΔE_{UPS} is the HOMO energy offset directly measured through UPS, where the sample was the ETL on the α-NPD film interface unless explicitly stated. The interface charge density is estimated by integrating DCM curves.

a) [87].
b) [59].
c) [88].
d) [89].
e) [90].
f) α-NPD on Alq_3 [86].
g) α-NPD on C_{60} [91].
h) On C_{60}.
i) On 4,4′,4″-tris(*N*-(1-naphthyl)- *N*-phenylamino)triphenylamine (1-TNATA) [82].
j) The surface potential is not proportional to but gradually decreases with increasing film thickness.
—: not available;/: not applicable.

assumption that the relative dielectric constant of the Alq_3 film is 3. A potential jump of about 0.2 eV is observed at the interface region (see the bottom inset); this jump is possibly due to the vacuum-level shift [86]. Interestingly, even the α-NPD film shows a weak GSP behavior ($\sim$3 mV/nm, top inset); thus, the total σ_{int} of the α-NPD/Alq_3 interface can be estimated as -1.2 mC/m^2 (Eq. (5.20)). We performed similar experiments on films of several compounds and confirmed that GSP appeared in the films of the polar compounds. Our experimental results and some data from the literature are summarized in Table 5.1.

To examine σ_{int} at the interfaces in bilayer devices, the DCM curves of the ITO/α-NPD/electron transport layer (ETL)/cathode devices were measured. We note here that the devices were fabricated while ensuring the exclusion of the light absorption of the films during the deposition process, because it can lead to the change in the charge accumulation properties of the resultant devices [92]. Figure 5.12 shows typical DCM curves of the device, where the Alq_3 film was used as the ETL. The carrier behavior of this device can be explained as follows. The triangular bias sweep starts at -3 V. Around the start voltage, the current density is maintained at a lower level ($\sim$0.02 μA/cm^2). C_{app} corresponds to C_{dev} in this bias region, indicating that the

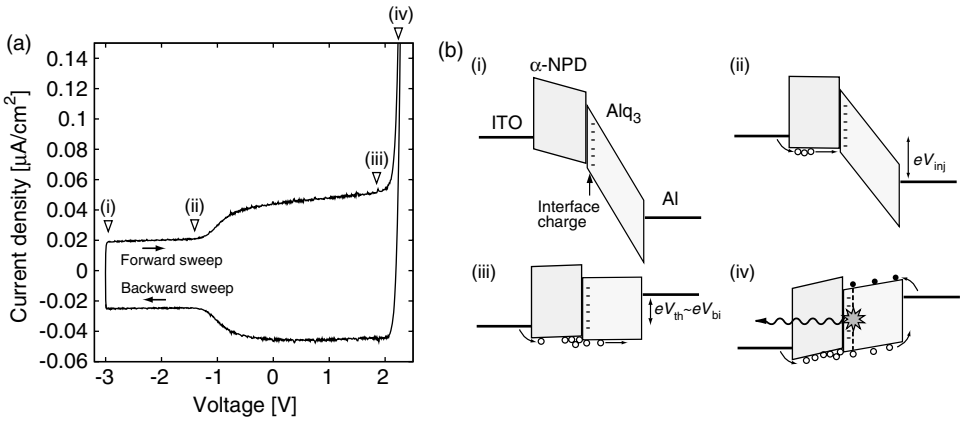

Figure 5.12 (a) A typical DCM curve of the ITO/α-NPD/Alq_3/Ca/Al device at a sweep rate of 1 V/s. (b) Schematic illustrations of energy diagram at the applied biases, corresponding to (i)–(iv) in (a).

device is in the depletion state ((i) in Figure 5.12b). Subsequently, the current rises at a voltage of -1.48 V (V_{inj}) due to charge injection from electrodes (the injected charges are holes from the ITO, as discussed later) ((ii) in Figure 5.12b). The current again shows constant intensity until the biasing voltage reaches 1.80 V(V_{th}). C_{app} in this bias region indicates that the hole accumulation occurs at the α-NPD/Alq_3 interface. V_{th} corresponds to the threshold voltage of the actual current and agrees well with the V_{bi} of the device (typically, $\sim$1.9 V), estimated from the open-circuit voltage during intense white light irradiation. The accumulated charge density $\sigma_{NPD/Alq}$ is estimated to be 1.3 mC/m^2 by integrating the current density from V_{inj} to V_{th}.

Figure 5.13a and b shows the DCM curves of the ITO/α-NPD/Alq_3/Al devices containing various combinations of the film thicknesses. The current density at the accumulation state depends only on the Alq_3 film thickness, indicating that the injected charges are holes from the ITO. Moreover, the V_{th} is independent of the film thicknesses in all devices, but the V_{inj} shifts to the negative side with increasing Alq_3 film thickness. Thus, the polarity of the interface charge should be negative (Eq. (5.8)). The interface charge density estimated from the DCM curves is almost constant over all the devices with varying combinations of film thicknesses.

Similar characteristics were observed in the DCM curves of all the bilayer devices containing the polar films (corresponding to the films exhibiting a GSP behavior), that is, OXD-7, BCP, and TPBi. These similar characteristics indicate the presence of a negative interface charge independent of the film thickness. On the other hand, V_{inj} coincides with V_{th} in devices with nonpolar films, corresponding to no interface charge in the devices. Figure 5.14a shows a typical DCM curve of the ITO/α-NPD/UGH2/Al device. V_{inj} appears at about 1.2 V, but V_{th} is unclear. We, hence, extract i_{dis} and i_{act} from the DCM curve. In the quasi-static limit, one can

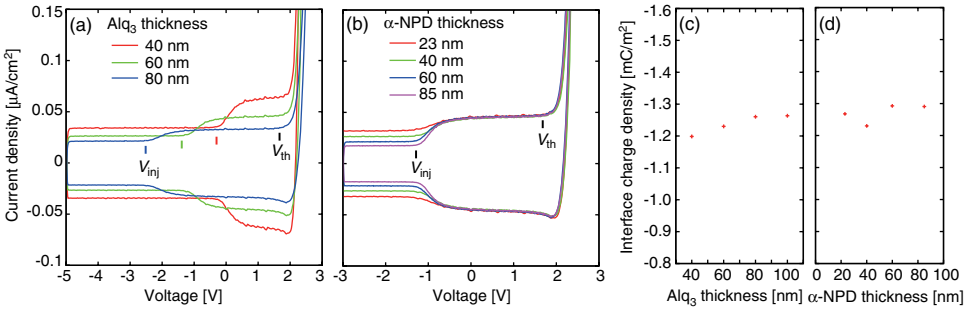

Figure 5.13 (a, b) DCM curves of the ITO/α-NPD/Alq_3/Al device with various combinations of the film thickness. The α-NPD and Alq_3 film thickness is fixed at 40 nm (a) and 60 nm (b), respectively. The current density at the accumulation state depends only on the Alq_3 film thickness, indicating that the injected charges are holes. The threshold voltage of the actual current V_{th} is independent of the combinations of the film thickness, while the V_{inj} shifts to the negative side as the Alq_3 film thickness is increased. Thus, the polarity of the interface charge is negative. (c, d) The interface charge density estimated from the DCM curves. It is almost independent of the combinations of the film thickness.

assume $i_{dis} = C_{app}(dV/dt)$; thus, i_{act} and i_{dis} are derived from $(i_+ + i_-)/2$ and $(i_+ - i_-)/2$, respectively. Here, i_+ is the DCM current observed in the forward sweep while i_- is that observed in the backward sweep. Since i_{dis} divided by the sweep rate corresponds to C_{app}, the C_{app}–V curve is finally obtained. Figure 5.14b shows the extracted C_{app}–V and i_{act}–V curves, where V_{inj} and V_{th} are observed at 1.2 V.

We summarized the DCM, KP, and UPS data in Table 5.1. The relationship between the GSP and the dipole moment and that between the GSP and the interface charge are shown in Figure 5.15a and b, respectively. The slope of the GSP

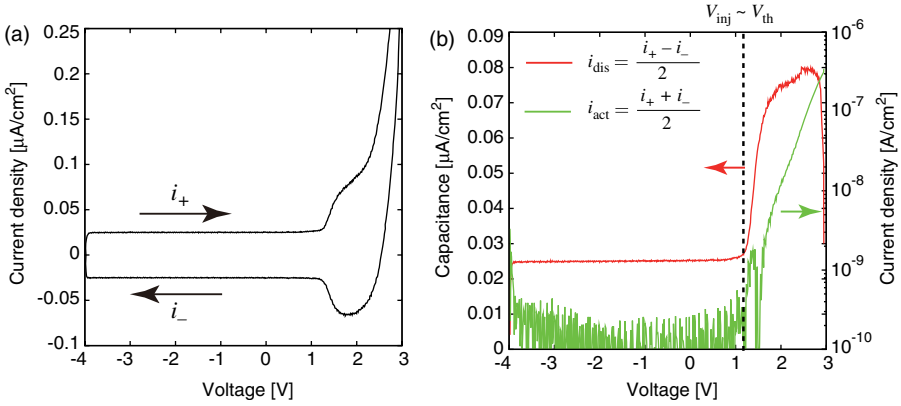

Figure 5.14 (a) A typical DCM curve of the ITO/α-NPD/UGH2/Al device at a sweep rate of 1 V/s. (b) Capacitance–voltage and actual current–voltage curves derived from the DCM curve.

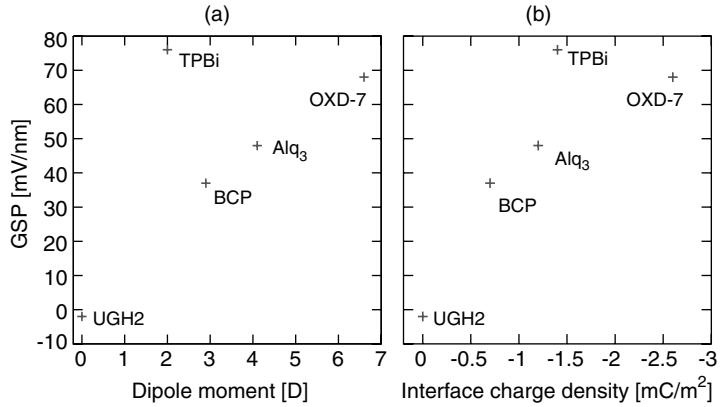

Figure 5.15 (a) The slope of GSP versus dipole moment of the molecule. (b) The slope of GSP versus interface charge density. The GSP data are measured on the films formed on 1-TNATA for TPBi [82], α-NPD for Alq_3 and OXD-7, and C_{60} for BCP.

seems to relate to the interface charge density, that is, a larger GSP leads to a higher negative interface charge density, except in the case of TPBi. This exception possibly originates from the difference in the experimental conditions. Surface potential, especially GSP, is sensitive to temperature, ambient light, and substrate, rather than the interface charge observed in the device; this is because GSP changes irreversibly due to the presence of compensation charges traveling from the electrode (as thermally injected carriers), the bulk of the film (as photoinduced carriers), and environment [77, 79]. Even though there still remains a quantitative disagreement, the data strongly suggest that the orientation polarization remains and leads to the interface charge in the actual devices.

A permanent dipole moment is a very important parameter in understanding and controlling the operation properties of the OSC devices. As discussed above, it is the origin of the interface charge and predominates the charge injection and accumulation properties in the device, along with the energy barrier and mobility mismatch at the heterointerface. Moreover, the presence of dipole moments near the interface can suppress the charge spreading along the interface [80]. Recently, we found that the *C–V* and *C–f* curves of the devices containing polar films (polar devices) show different behaviors from that of nonpolar devices. The capacitances in the polar devices are well defined; in other words, the *C–V* and *C–f* curves are maintained at a constant value and show a clear step feature due to the charge accumulation at the heterointerface; on the other hand, the capacitances of nonpolar devices increased with increasing applied DC voltages at low frequencies. The results suggest that charge spreading at the organic heterointerface is unlikely to occur in polar devices. A possible origin of the charge behavior at the interfaces is a local electric field formed by the dipole moment in the vicinity of the interface, leading to a potential roughness. Similar behavior has been reported as the gate dielectric dependence of the charge mobility in OFETs, in which the dipolar disorder in the gate dielectric layer results in a lower mobility [93, 94]. Furthermore,

in our case, the dipolar disorder may reduce the mobility at the interface. However, unlike the case of OFETs, the charge spreading should be suppressed in OLEDs to achieve an efficient charge recombination and avoid cross-talk between neighboring pixels. The use of polar molecules is reasonable for these purposes.

5.3.3
Light-Induced Space Charges in Alq_3 Film

Interestingly, we recently found that light irradiation during the Alq_3 film deposition leads to additional negative space charges with a constant density in the bulk of the resultant film [92]. Figure 5.16 shows the DCM curves of the devices fabricated under (a) dark conditions and (b)–(f) light irradiation. V_{inj} and V_{th} shift to the lower side with an increase in the incident light intensity, I_{in}, when the wavelength, λ_p, is 400 nm (Figure 5.1b and c). On the other hand, no shift was observed for $\lambda_p = 525, 630$ nm (Figure 5.16e and f), which are longer than the wavelength of the absorption edge of the Alq_3 film (~450 nm). We have confirmed that light irradiation after the device fabrication has no significant effect on the DCM curves.

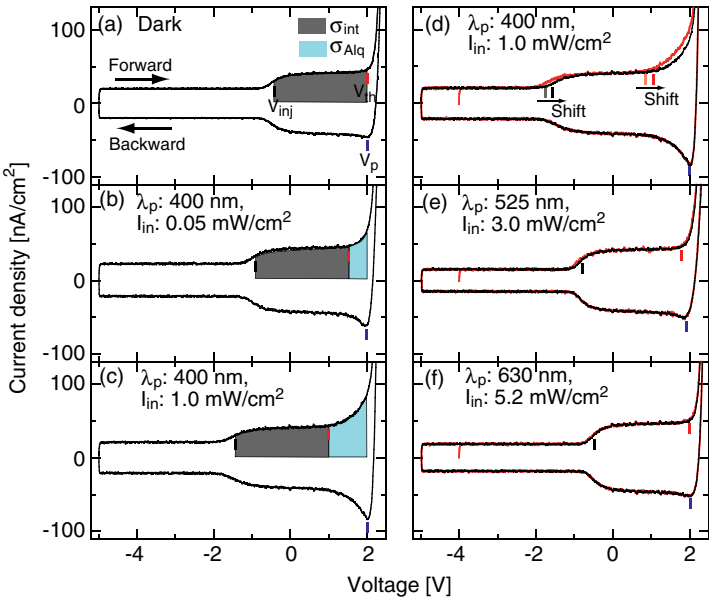

Figure 5.16 Typical DCM curves of devices fabricated under (a) dark conditions and (b–f) light irradiation. λ_p and I_{in} for each device are shown in the figure. V_{inj}, V_{th}, and V_p are indicated by short bars. The halftone area shown in (a–c) corresponds to the amount of accumulated charge at the α-NPD/Alq_3 interface, σ_0, and in the bulk of the Alq_3 layer, σ_{Alq}. The DCM curves in (d–f) were obtained by applying the first (red) and second (black) bias sweeps. All curves were measured at a sweep rate of 1 V/s. The sweep direction is indicated by arrows in (a).

The shift appears to result from the light absorption of the Alq_3 film during the film deposition. The 400 nm light irradiation also induced a current peak at V_p, as shown in Figure 5.16b and c. The increase in the displacement current at the biases between V_{th} and V_p indicates that C_{app} in this bias region was larger than that of the Alq_3 layer. This result indicates that the dielectric thickness of the Alq_3 layer, d_{dielec}, was reduced, that is, the injected holes were accumulated in the bulk of the film. We note here that V_p is independent of light irradiation and corresponds to the typical V_{bi} of the ITO/α-NPD/Alq_3/Al devices. The results indicate that the light-treated devices were negatively charged.

The λ_p dependence is also observed in the DCM curves as a function of the sweep cycles (Figure 5.16d–f). V_{inj} and V_{th} in the second sweep shifted to a higher side relative to those in the first sweep for the device fabricated under 400 nm light irradiation. This sweep cycle dependence indicates that some of the injected holes were trapped in the device during the first sweep and that the hole injection voltage in the next sweep shifted to a higher side relative to the previous one due to the additional electric field formed by the trapped holes (Section 5.2.1).

Figure 5.17a shows the $1/C_{app}^2 - V$ plots of the light-treated devices. A linear relationship is clearly observed, suggesting that the negative space charge is distributed uniformly in the Alq_3 layer (Section 5.2.1.3): The potential profile in the Alq_3 layer is similar to that in a strong depletion layer with fully ionized acceptors of p-type inorganic semiconductors (Figure 5.17b). The slope of the $1/C_{app}^2 - V$ plot corresponds to $2/\varepsilon_{Alq} q n_{dope}$ (Eq. (5.14)), where ε_{Alq} is the dielectric constant of the Alq_3 film. The n_{dope} of our light-treated devices is estimated to be $\sim 10^{17}$ cm^{-3}, assuming $\varepsilon_{Alq}/\varepsilon_0 = 3$.

We consider two possible origins for the negative space charges in the Alq_3 film. One is the polarization charge owing to the spatial inhomogeneity of P_{Alq} and the other is the electrons trapped in the Alq_3 film. At the present stage, the dominant origin has not been determined conclusively; however, according to the previous

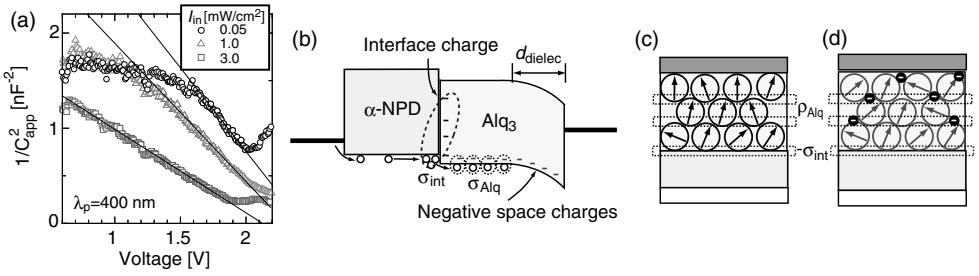

Figure 5.17 (a) The $1/C_{eff}^2 - V$ plot of the devices fabricated under 400 nm light irradiation at $I_{in} = 0.05$, 1.0, and 3.0 μW/cm^2. The linear lines are a guide to the eye. (b) Schematic energy diagrams of the light-treated device. The holes surrounded by the broken lines indicate that they are compensated by the interface charge or the negative space charge. (c) Schematic illustration of the negative space charge due to the spatial inhomogeneity of P_{Alq}. (d) Schematic illustration of the negative space charge due to trapped electrons.

studies on the GSP of the Alq_3 film, we can propose the following two possible models for the negative space charge formation (Figure 5.17c and d).

The GSP of the Alq_3 film, originating from P_{Alq}, grows linearly as a function of the film thickness; however, it decays upon light irradiation during or after film deposition if the photon energy exceeds the absorption edge of Alq_3 [77]. Two models have been proposed for the decay mechanism: (i) formation of compensation charges and (ii) dipole moment disordering in the Alq_3 film [77, 79, 95–97]. If the dipole moment disordering occurs, the interface charge should also disappear. However, based on the observation of the interface charge, even in the irradiated devices during or after the fabrication, the former model should be responsible for the photoinduced decay of GSP. Therefore, if the film is deposited under light irradiation, one can expect that the compensation charge is constantly induced on the film surface. The presence of the compensation charge reduces the electrostatic energy stored in the film, which relaxes the Coulomb repulsion between the adjacent dipoles aligned in the same direction. We can thus expect that the dipole moment ordering of Alq_3 is enhanced in the light-treated film. The compensation charge can be removed by applying an external voltage during device operation; however, the spatial inhomogeneity of P_{Alq}, that is, $\partial P_{Alq}/\partial x = -\varrho_{Alq}$, remains in the film (Figure 5.17c). This spatial inhomogeneity could be the reason why light irradiation leads to the distribution of the negative space charges in the Alq_3 film.

The other possible model is the formation of deep electron traps in the Alq_3 layer. Sugi *et al*. reported that even if the GSP of the Alq_3 film is removed by light irradiation, it builds again with the constant P_{Alq} for further deposition of the Alq_3 film on that surface [95]. This result may suggest that the electrons compensating the surface charge were captured in deep traps and did not move to the newly deposited area; otherwise, the compensating electrons would move to the new surface to negate the GSP. If the film was formed under continuous light irradiation, the deep traps were uniformly distributed, and the captured electrons remained in the resultant film (Figure 5.17d). The electrons in the deep traps can work as shallow traps for holes (Figure 5.17a), where the trapped holes are easily released by thermal energy at room temperature. Because Alq_3 is a photosensitive molecule, these traps might originate from a photooxidized Alq_3 or other photoinduced derivatives [98, 99]. Studies on the electronic structure and molecular orientation of a light-treated Alq_3 film should be conducted to gain a better understanding of the mechanism of negative space charge formation.

Alq_3 films have been mainly investigated to understand the mechanisms of spontaneous buildup and photoinduced decay of GSP by several research groups. However, the mechanisms have not been sufficiently clarified, mainly due to the experimental difficulties of this system, such as the small order parameter even at the initial state (typically, $\langle \cos\theta \rangle \sim 0.05$, indicating almost random but slightly ordered on average) and the irreversible decay of GSP caused by the light irradiation and thermal fluctuations. Although the mechanisms of spontaneous ordering in the evaporated film of polar molecules are still an open problem, the correlations between the Coulomb interactions and the molecular packing should be responsible for the structure of the resultant film. Here, we consider, as the

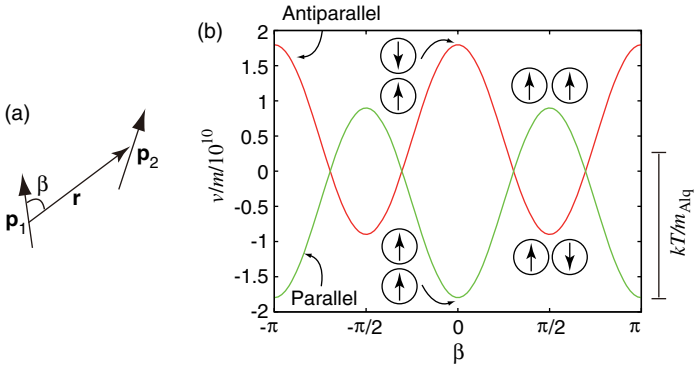

Figure 5.18 (a) The simplest model for determination of the potential energy of two dipole moments. (b) The calculated potential energy normalized by m.

simplest case, the interaction between two permanent dipoles, $\mathbf{p}_1$ and $\mathbf{p}_2$ (Figure 5.18a). The potential energy of these two dipoles is given by [100]

$$\mathcal{V} = \frac{1}{4\pi\varepsilon_0}\frac{\mathbf{p}_1 \cdot \mathbf{p}_2 - 3(\mathbf{p}_1 \cdot \hat{\mathbf{r}})(\mathbf{p}_2 \cdot \hat{\mathbf{r}})}{r^3} \tag{5.21}$$

where $\hat{\mathbf{r}}$ is the unit vector pointing to molecule 2 with reference to molecule 1 and r is the distance between two molecules. Assuming a parallel configuration and identical molecule ($p_1 = p_2 = p$), the equation can be simplified to

$$\mathcal{V}_{\uparrow\uparrow} = -\frac{1}{4\pi\varepsilon_0}\frac{p^2}{r^3}(3\cos^2\beta - 1) \tag{5.22}$$

where $\cos\beta = \mathbf{p} \cdot \hat{\mathbf{r}}/|\mathbf{p}|$. Similarly, the potential of the antiparallel configuration can be obtained as $\mathcal{V}_{\uparrow\downarrow} = -\mathcal{V}_{\uparrow\uparrow}$. Figure 5.18b shows the potential energy distribution of $\mathcal{V}_{\uparrow\downarrow}$ and $\mathcal{V}_{\uparrow\uparrow}$ normalized by the molecule-dependent factor $m = p^2/r^3$. The parallel configuration with $\beta = 0$ is the most stable. For Alq_3, using $p = 4.1$ D$(= 1.4 \times 10^{-29}$ Cm) and $r \sim 1.0$ nm, $m_{Alq} = 1.96 \times 10^{-31}$ C^2/m is obtained; the thermal energy (kT) at 300 K normalized by this value (2.11×10^{10} J/(C^2/m)) is shown on the right-hand side of Figure 5.18b. It should be noted that the thermal energy is comparable to the potential energy of two dipoles in the case of Alq_3, implying that dipole moment ordering in the film phase is possible. Although a real system may be much more complex, it can be expected to have a similar property (e.g., GSP and interface charge) if m of the molecule is $\sim 10^{-31}$.

5.4 Conclusions

In this chapter, we reviewed the basics and recent progress of DCM with some experimental data. DCM is based on a simple principle but is a powerful tool to examine the charge carrier behavior in OSC devices. In particular, charge

injection/extraction voltages, accumulation density, and trapped charge density can be evaluated from the DCM curves of the device in the quasi-static state. Although the dopant density in the device is generally obtained from the slope of the $1/C^2 - V$ plot, an analysis of the intermediate state in terms of the penetration depth of the injected charge may be helpful to estimate the depth profile of the dopant density. When the sweep rate of the applied voltage increases, the contributions of the transient current are more pronounced in the DCM curves. The transient current often leads to complicated DCM curves, but provides important information of the contact and bulk resistance in the device. We proposed a modified DCM to extract the dynamic carrier behavior from the DCM curve using a combined waveform of a DC following a ramp voltage. As a result, the transient current with a long relaxation time ($\sim$1 s) was found in the peak structure of the DCM curve of the Au/Pn/SiO_2/p-doped Si structure, originating from the charge spreading over the Pn/SiO_2 interface. Furthermore, we recently succeeded in analyzing the *C*–*V* and DCM curves of operating OFETs; in these curves, the pinch-off point is clearly observed, depending on the applied source–drain voltage [101].

Since most OSC devices have a multilayer structure and their functions originate from the interfaces, understanding the charge accumulation properties at heterointerfaces in the OSC devices is a very important issue. We discussed the charge accumulation mechanisms that can be attributed to (i) energy barrier height, (ii) mobility mismatch, and (iii) mobile, trapped, polarized charge distribution in the device. Among these parameters, we especially focused on the charge accumulation due to the interface charge; DCM, KP, and UPS measurements were performed on OLED-related interfaces. We proposed the orientation polarization of the OSC film as the origin of the interface charge and actually found that GSP (corresponding to the orientation polarization) of the constituent film correlates with the interface charge density in the devices. It should be emphasized that many OSC molecules possess a permanent dipole moment, and thus, the interface charge can also exist in common OSC devices. Moreover, the presence of dipole moments near the interface can also suppress the charge spreading along the interface. We also showed that light irradiation during the Alq_3 film formation induces negative space charges in the resultant film. Permanent dipole moment should be considered a very important parameter to understand and control the operation properties of the OSC devices. Although the mechanisms of spontaneous ordering in the evaporated film of polar molecules are still an open problem, investigations of the properties of the interface charge may be helpful in understanding the mechanism of the molecular ordering.

There still exists a gap between the physics and the actual properties of the OSC devices. The present situation requires research to explore the real principle behind the driving mechanisms of the OSC devices, for instance, through direct observations of the electronic structures and carrier behavior in actual devices, fabrication of the ideal devices with highly ordered films (crystals) of ultrapure materials, and so on. We hope that our efforts will contribute to bridge the gap between the ideal and the actual device properties and lead to a comprehensive understanding of the device physics.

Acknowledgment

We would like to thank Wolfgang Brütting (Universität Augsburg), Syun Egusa (Toshiba Corp.), Satoshi Ogawa (Epson Corp.), Yoshinori Fukuda (ex. Pioneer Corp.), and members of Ishii's group (Chiba University) for fruitful discussions. Y. Noguchi thanks members of Brütting's group (Universität Augsburg) for their kind cooperation in our experiments. This research is granted by the Japan Society for the Promotion of Science (JSPS) through the "Funding Program for World-Leading Innovative R&D on Science and Technology (FIRST Program)," initiated by the Council for Science and Technology Policy (CSTP), the Global-COE Project of Chiba University (Advanced School for Organic Electronics), and KAKENHI (Grant Nos. 21245042, 22750167).

References

1 Koch, N. (2007) Organic electronic devices and their functional interfaces. *ChemPhysChem*, **8** (10), 1438–1455.
2 Malliaras, G. and Friend, R. (2005) An organic electronics primer. *Phys. Today*, **58** (5), 53–58.
3 Sirringhaus, H. (2009) Materials and applications for solution-processed organic field-effect transistors. *Proc. IEEE*, **97** (9), 1570–1579.
4 Braga, D. and Horowitz, G. (2009) High-performance organic field-effect transistors. *Adv. Mater.*, **21** (14–15), 1473–1486.
5 Günes, S., Neugebauer, H., and Sariciftci, N.S. (2007) Conjugated polymer-based organic solar cells. *Chem. Rev.*, **107** (4), 1324–1338.
6 Walzer, K., Maennig, B., Pfeiffer, M., and Leo, K. (2007) Highly efficient organic devices based on electrically doped transport layers. *Chem. Rev.*, **107** (4), 1233–1271.
7 Zaumseil, J. and Sirringhaus, H. (2007) Electron and ambipolar transport in organic field-effect transistors. *Chem. Rev.*, **107** (4), 1296–1323.
8 Kudo, K., Yamashita, M., and Moriizumi, T. (1984) Field effect measurement of organic dye films. *Jpn J. Appl. Phys.*, **23** (1), 130.
9 Koezuka, H., Tsumura, A., and Ando, T. (1987) Field-effect transistor with polythiophene thin film. *Synth. Met.*, **18** (1–3), 699–704.
10 Burroughes, J.H., Jones, C.A., and Friend, R.H. (1988) New semiconductor device physics in polymer diodes and transistors. *Nature*, **335** (6186), 137–141.
11 Tang, C.W. (1986) Two-layer organic photovoltaic cell. *Appl. Phys. Lett.*, **48** (2), 183–185.
12 Tang, C.W. and VanSlyke, S.A. (1987) Organic electroluminescent diodes. *Appl. Phys. Lett.*, **51** (12), 913–915.
13 Ishii, H., Sugiyama, K., Ito, E., and Seki, K. (1999) Energy level alignment and interfacial electronic structures at organic/metal and organic/organic interfaces. *Adv. Mater.*, **11** (8), 605–625.
14 Kazda, C. (1925) The photo-electric threshold for mercury. *Phys. Rev.*, **26** (5), 643–654.
15 Schäfer, J., Ristein, J., Ley, L., and Ibach, H. (1993) High sensitivity photoelectron yield spectroscopy with computer-calculated electron optics. *Rev. Sci. Instrum.*, **64**, 653–658.
16 Sebenne, C., Bolmont, D., Guichar, G., and Balkanski, M. (1975) Surface states from photoemission threshold measurements on a clean, cleaved, Si (111) surface. *Phys. Rev. B*, **12** (8), 3280–3285.
17 Altwegg, L., Pope, M., Arnold, S., Fowlkes, W., and El Hamamsy, M. (1982) Modified Millikan capacitor for

photoemission studies. *Rev. Sci. Instrum.*, **53** (3), 332–337.
18 Kirihata, H. and Uda, M. (1981) Externally quenched air counter for low-energy electron emission measurements. *Rev. Sci. Instrum.*, **52** (1), 68–70.
19 Inumaru, K., Okubo, Y., Fujii, T., and Yamanaka, S. (2000) Effects of organic vapour adsorption on the photoelectron emission from Au thin films in atmospheric air. *Phys. Chem. Chem. Phys.*, **2** (16), 3681–3685.
20 Watanabe, I. (1994) Optical oxidation potential: a new measure for reducing power. *Anal. Sci.*, **10**, 229.
21 Yoshikawa, G., Kiguchi, M., Ueno, K., Koma, A., and Saiki, K. (2003) Visible light photoemission and negative electron affinity of single-crystalline CsCl thin films. *Surf. Sci.*, **544** (2–3), 220–226.
22 Ishii, H., Tsunami, D., Suenaga, T., Sato, N., Kimura, Y., and Niwano, M. (2007) Photoelectron yield spectroscopy for electronic structures of organic electronic materials and their interfaces. *J. Surf. Sci. Soc. Jpn.*, **28** (5), 264–270.
23 Honda, M., Kanai, K., Komatsu, K., Ouchi, Y., Ishii, H., and Seki, K. (2007) Atmospheric effect of air, N_2, O_2, and water vapor on the ionization energy of titanyl phthalocyanine thin film studied by photoemission yield spectroscopy. *J. Appl. Phys.*, **102** (10), 103 704-1–10.
24 Nakayama, Y., Machida, S., Minari, T., Tsukagishi, K., Noguchi, Y., and Ishii, H. (2008) Direct observation of the electronic states of single crystalline rubrene under ambient condition by photoelectron yield spectroscopy. *Appl. Phys. Lett.*, **93** (17), 173305.
25 Nakayama, Y., Machida, S., Tsunami, D., Kimura, Y., Niwano, M., Noguchi, Y., and Ishii, H. (2008) Photoemission measurement of extremely insulating materials: capacitive photocurrent detection in photoelectron yield spectroscopy. *Appl. Phys. Lett.*, **92** (15), 153306.
26 Ebisawa, F., Kurokawa, T., and Nara, S. (1983) Electrical properties of polyacetylene/polysiloxane interface. *J. Appl. Phys.*, **54** (6), 3255–3259.
27 Karg, S., Meier, M., and Riess, W. (1997) Light-emitting diodes based on poly-*p*-phenylene-vinylene: I. Charge-carrier injection and transport. *J. Appl. Phys.*, **82** (4), 1951–1960.
28 Brütting, W., Berleb, S., and Mückl, A.G. (2001) Device physics of organic light-emitting diodes based on molecular materials. *Org. Electron. Phys. Mater. Appl.*, **2** (1), 1–36.
29 Berleb, S., Brütting, W., and Paasch, G. (2001) Interfacial charges in organic hetero-layer light emitting diodes probed by capacitance–voltage measurements. *Synth. Met.*, **122** (1), 37–39.
30 Barsoukov, E. and Macdonald, J.R. (eds) (2005) *Impedance Spectroscopy: Theory, Experiment, and Applications*, Wiley-Interscience.
31 Meier, M., Karg, S., and Riess, W. (1997) Light-emitting diodes based on poly-*p*-phenylene-vinylene: II. Impedance spectroscopy. *J. Appl. Phys.*, **82** (4), 1961–1966.
32 Scherbel, J., Nguyen, P.H., Paasch, G., Brütting, W., and Schwoerer, M. (1998) Temperature dependent broadband impedance spectroscopy on poly-(*p*-phenylene-vinylene) light-emitting diodes. *J. Appl. Phys.*, **83** (10), 5045–5055.
33 Berleb, S. and Brütting, W. (2002) Dispersive electron transport in tris(8-hydroxyquinoline) aluminum (Alq3) probed by impedance spectroscopy. *Phys. Rev. Lett.*, **89** (28), 286601.
34 Tsang, S.W., So, S.K., and Xu, J.B. (2006) Application of admittance spectroscopy to evaluate carrier mobility in organic charge transport materials. *J. Appl. Phys.*, **99** (1), 013706.
35 Van Mensfoort, S.L.M. and Coehoorn, R. (2008) Determination of injection barriers in organic semiconductor devices from capacitance measurements. *Phys. Rev. Lett.*, **100** (8), 086802.
36 Okachi, T., Nagase, T., Kobayashi, T., and Naito, H. (2009) Determination of localized-state distributions in organic light-emitting diodes by impedance spectroscopy. *Appl. Phys. Lett.*, **94** (4), 043301.

37 Kepler, R.G. (1960) Charge carrier production and mobility in anthracene crystals. *Phys. Rev.*, **119** (4), 1226–1229.

38 Manaka, T., Lim, E., Tamura, R., and Iwamoto, M. (2007) Direct imaging of carrier motion in organic transistors by optical second-harmonic generation. *Nat. Photon.*, **1** (10), 581–584.

39 Palermo, V., Palma, M., and Samori, P. (2006) Electronic characterization of organic thin films by Kelvin probe force microscopy. *Adv. Mater.*, **18** (2), 145–164.

40 Rohlfing, F., Yamada, T., and Tsutsui, T. (1999) Electroabsorption spectroscopy on tris-(8-hydroxyquinoline) aluminum-based light emitting diodes. *J. Appl. Phys.*, **86** (9), 4978–4984.

41 Pivrikas, A., Sariciftci, N.S., Juška, G., and Osterbacka, R. (2007) A review of charge transport and recombination in polymer/fullerene organic solar cells. *Prog. Photovolt. Res. Appl.*, **15** (8), 677–696.

42 Noguchi, Y., Sato, N., Tanaka, Y., Nakayama, Y., and Ishii, H. (2008) Threshold voltage shift and formation of charge traps induced by light irradiation during the fabrication of organic light-emitting diodes. *Appl. Phys. Lett.*, **92** (20), 203306.

43 Kondakov, D.Y., Sandifer, J.R., Tang, C. W., and Young, R.H. (2003) Nonradiative recombination centers and electrical aging of organic light-emitting diodes: direct connection between accumulation of trapped charge and luminance loss. *J. Appl. Phys.*, **93** (2), 1108–1119.

44 Ogawa, S., Kimura, Y., Ishii, H., and Niwano, M. (2003) Carrier injection characteristics in organic field effect transistors studied by displacement current measurement. *Jpn. J. Appl. Phys. 2*, **42** (10B), L1275–L1278.

45 Ogawa, S., Naijo, T., Kimura, Y., Ishii, H., and Niwano, M. (2005) Photoinduced doping effect of pentacene field effect transistor in oxygen atmosphere studied by displacement current measurement. *Appl. Phys. Lett.*, **86** (25), 1–3.

46 Ogawa, S., Naijo, T., Kimura, Y., Ishii, H., and Niwano, M. (2005) Displacement current measurement as a tool to characterize organic field effect transistors. *Synth. Met.*, **153** (1–3), 253–256.

47 Egusa, S., Miura, A., Gemma, N., and Makoto, A. (1994) Carrier injection characteristics of organic electroluminescent devices. *Jpn J. Appl. Phys.*, **33**, 2741–2745.

48 Twarowski, A.J. and Albrecht, A.C. (1979) Depletion layer studies in organic films: low frequency capacitance measurements in polycrystalline tetracene. *J. Chem. Phys.*, **70** (5), 2255–2261.

49 Iriyama, K., Shiraki, M., Thuda, K., Okada, A., Sugi, M., Iizima, S., Kudo, K., Shiokawa, S., Moriizumi, T., and Yasuda, T. (1980) Photoelectric effects in organic diodes. *Jpn J. Appl. Phys.*, **19** (Supplement 19–2), 173–177.

50 Noguchi, Y., Sato, N., Miyazaki, Y., Nakayama, Y., and Ishii, H. (2010) Higher resistance to hole injection and electric field distribution in organic light-emitting diodes with copper phthalocyanine interlayer. *Jpn J. Appl. Phys.*, **49** (1 Part 2), 01AA01.

51 Tanaka, Y., Noguchi, Y., Kraus, M., Brütting, W., and Ishii, H. (2011) Displacement current measurement of a pentacene metal–insulator–semiconductor device to investigate both quasi-static and dynamic carrier behavior using a combined waveform. *Org. Electron. Phys. Mater. Appl.*, **12**(9), 1560–1565.

52 Jarikov, V.V. and Kondakov, D.Y. (2009) Studies of the degradation mechanism of organic light-emitting diodes based on tris(8-quinolinolate)aluminum Alq and 2-*tert*-butyl-9,10-di(2-naphthyl) anthracene *t*BADN. *J. Appl. Phys.*, **105** (3), 034905.

53 Chan, C.K. and Kahn, A. (2009) N-doping of pentacene by decamethylcobaltocene. *Appl. Phys. A Mater.*, **95** (1), 7–13.

54 Laubender, J., Chkoda, L., Sokolowski, M., and Umbach, E. (2000) Influence of oxygen and air on the characteristics of organic light-emitting devices studied by *in vacuo* measurements. *Synth. Met.*, **111**, 373–376.

55 Sueyoshi, T., Kakuta, H., Ono, M., Sakamoto, K., Kera, S., and Ueno, N. (2010) Band gap states of copper

phthalocyanine thin films induced by nitrogen exposure. *Appl. Phys. Lett.*, **96** (9), 093303.

56 Chang, H., Ruden, P.P., and Liang, Y., and Frisbie, C.D. (2010) Transient effects controlling the charge carrier population of organic field effect transistor channels. *J. Appl. Phys.*, **107** (10), 104502.

57 Liang, Y., Frisbie, C.D., Chang, H., and Ruden, P.P. (2009) Conducting channel formation and annihilation in organic field-effect structures. *J. Appl. Phys.*, **105** (2), 024514.

58 Aziz, H., Popovic, D., Hu, N.X., Hor, A. M., and Xu, G. (1999) Degradation mechanism of small molecule-based organic light-emitting devices. *Science*, **283** (5409), 1900–1902.

59 Hill, I.G. and Kahn, A. (1999) Combined photoemission/*in vacuo* transport study of the indium tin oxide/copper phthalocyanine/*N*,*N*′-diphenyl-*N*,*N*′-bis (l-naphthyl)-1,1′biphenyl-4, 4″diamine molecular organic semiconductor system. *J. Appl. Phys.*, **86** (4), 2116–2122.

60 Forsythe, E.W., Abkowitz, M.A., and Gao, Y. (2000) Tuning the carrier injection efficiency for organic light-emitting diodes. *J. Phys. Chem. B*, **104** (16), 3948–3952.

61 Forsythe, E.W., Abkowitz, M.A., Gao, Y., and Tang, C.W. (2000) Influence of copper phthalocynanine on the charge injection and growth modes for organic light emitting diodes. *J. Vac. Sci. Technol. A*, **18** (4), 1869–1874.

62 Brütting, W., Riel, H., Beierlein, T., and Riess, W. (2001) Influence of trapped and interfacial charges in organic multilayer light-emitting devices. *J. Appl. Phys.*, **89** (3), 1704–1712.

63 Tadayyon, S.M., Grandin, H.M., Griffiths, K., Norton, P.R., Aziz, H., and Popovic, Z.D. (2004) CuPc buffer layer role in OLED performance: a study of the interfacial band energies. *Org. Electron. Phys. Mater. Appl.*, **5** (4), 157–166.

64 Divayana, Y., Chen, B.J., Sun, X.W., Wong, T.K.S., Sarma, K.R., and Hu, X. (2006) Hole injection or blocking? The role of CuPc in Alq3-based organic light-emitting devices. *J. Cryst. Growth*, **288** (1), 105–109.

65 Luo, Y., Aziz, H., Popovic, Z.D., and Xu, G. (2007) Degradation mechanisms in organic light-emitting devices: metal migration model versus unstable tris(8-hydroxyquinoline) aluminum cationic model. *J. Appl. Phys.*, **101** (3), 034510.

66 Goushi, K., Yoshida, M., Yamamoto, H., Brown, J., Sasabe, H., and Adachi, C. (2007) *Organic Electron Devices and Applications*, Research Signpost, Chapter 2.

67 Malliaras, G.G. and Scott, J.C. (1998) The roles of injection and mobility in organic light emitting diodes. *J. Appl. Phys.*, **83** (10), 5399–5403.

68 Ruhstaller, B., Carter, S.A., Barth, S., Riel, H., Riess, W., and Scott, J.C. (2001) Transient and steady-state behavior of space charges in multilayer organic light-emitting diodes. *J. Appl. Phys.*, **89** (8), 4575–4586.

69 Wang, H., Klubek, K.P., and Tang, C.W. (2008) Current efficiency in organic light-emitting diodes with a hole-injection layer. *Appl. Phys. Lett.*, **93** (9), 093306.

70 Matsumura, M., Ito, A., and Miyamae, Y. (1999) Accumulation of positive charges in organic light-emitting diodes with a double-layer structure. *Appl. Phys. Lett.*, **75** (8), 1042–1044.

71 Young, R.H., Tang, C.W., and Marchetti, A.P. (2002) Current-induced fluorescence quenching in organic light-emitting diodes. *Appl. Phys. Lett.*, **80** (5), 874–876.

72 Haskins, T., Chowdhury, A., Young, R. H., Lenhard, J.R., Marchetti, A.P., and Rothberg, L.J. (2004) Charge-induced luminescence quenching in organic light-emitting diodes. *Chem. Mater.*, **16** (23), 4675–4680.

73 Kondakov, D.Y. and Young, R.H. (2010) Variable sensitivity of organic light-emitting diodes to operation-induced chemical degradation: nature of the antagonistic relationship between lifetime and efficiency. *J. Appl. Phys.*, **108** (7), 074513.

74 Tamura, R., Lim, E., Manaka, T., and Iwamoto, M. (2006) Analysis of pentacene field effect transistor as a Maxwell–Wagner effect element. *J. Appl. Phys.*, **100** (11), 114515.

75 Taguchi, D., Inoue, S., Zhang, L., Li, J., Weis, M., Manaka, T., and Iwamoto, M. (2010) Analysis of organic light-emitting diode as a Maxwell–Wagner effect element by time-resolved optical second harmonic generation measurement. *J. Phys. Chem. Lett.*, **1** (5), 803–807.

76 Watanabe, S., Ito, K., Tanaka, H., Ito, H., and Marumoto, K., and Kuroda, S. (2007) Electron spin resonance observation of gate-induced charge carriers in organic field-effect devices fabricated on silicon substrates. *Jpn. J. Appl. Phys. 2*, **46** (33–35), L792–L795.

77 Ito, E., Washizu, Y., Hayashi, N., Ishii, H., Matsuie, N., Tsuboi, K., Ouchi, Y., Harima, Y., Yamashita, K., and Seki, K. (2002) Spontaneous buildup of giant surface potential by vacuum deposition of Alq_3 and its removal by visible light irradiation. *J. Appl. Phys.*, **92** (12), 7306–7310.

78 Hayashi, N., Imai, K., Suzuki, T., Kanai, K., Ouchi, Y., and Seki, K. (2004) Substrate dependence of giant surface potential of Alq3 and the examination of surface potential of related materials, in *Proc. Int. Symp. Super-Functionality Organic Devices, IPAP Conf. Series*, vol. 6, pp. 69–72.

79 Yoshizaki, K., Manaka, T., and Iwamoto, M. (2005) Large surface potential of Alq_3 film and its decay. *J. Appl. Phys.*, **97** (2), 023703.

80 Noguchi, Y., Miyazaki, Y., Tanaka Y., Sato, N., Nakayama, Y., Schmidt, T. D., Brütting, W., and Ishii, H. (2012) Charge accumulation at organic semiconductor interfaces due to a permanent dipole moment and its orientational order in bilayer devices. *J. Appl. Phys.* **111**(11), 114508.

81 Noguchi, Y., Tamura, T., Kim., H. J., and Ishii, H. (2012) Device properties of Alq_3-based organic light emitting diodes studied by displacement current measurement. *J. Photon. Energy*, **2**, 021214.

82 Kröger, M., Hamwi, S., Meyer, J., Dobbertin, T., Riedl, T., Kowalsky, W., and Johannes, H. (2007) Temperature-independent field-induced charge separation at doped organic/organic interfaces: experimental modeling of electrical properties. *Phys. Rev. B*, **75** (23), 235321.

83 Kajimoto, N. (2008) *Dielectric relaxation processes in organic semiconductor films*, Ph. D. thesis, Tokyo Institute of Technology.

84 Kondakov, D.Y. (2006) Voltammetric study of Bphen electron-transport layer in contact with LiFAl cathode in organic light-emitting diodes. *J. Appl. Phys.*, **99** (2), 024901.

85 Marchetti, A.P., Sassin, K.E., Young, R. H., Rothberg, L.J., and Kondakov, D.Y. (2011) Integer charge transfer states in organic light-emitting diodes: optical detection of hole carriers at the anode–organic interface. *J. Appl. Phys.*, **109** (1), 013709.

86 Lee, S.T., Wang, Y.M., Hou, X.Y., and Tang, C.W. (1999) Interfacial electronic structures in an organic light-emitting diode. *Appl. Phys. Lett.*, **74** (5), 670–672.

87 Ng, A.M.C., Djurisic, A.B., Tam, K.H., Cheng, K.W., Chan, W.K., Tam, H.L., Cheah, K.W., Lu, A.W., Chan, J., and Rakic, A.D. (2008) 3,4,9,10-perylenetetracarboxylicdiimide as an interlayer for ultraviolet organic light emitting diodes. *Opt. Commun.*, **281** (9), 2498–2503.

88 Ichikawa, M., Kobayashi, K., Koyama, T., and Taniguchi, Y. (2007) Intense and efficient ultraviolet electroluminescence from organic light-emitting devices with fluorinated copper phthalocyanine as hole injection layer. *Thin Solid Films*, **515** (7–8), 3932–3935.

89 Holmes, R.J., D'Andrade, B.W., Forrest, S.R., Ren, X., Li, J., and Thompson, M.E. (2003) Efficient, deep-blue organic electrophosphorescence by guest charge trapping. *Appl. Phys. Lett.*, **83** (18), 3818–3820.

90 Lai, S.L., Lo, M.F., Chan, M.Y., Lee, C.S., and Lee, S.T. (2009) Impact of dye interlayer on the performance of organic photovoltaic devices. *Appl. Phys. Lett.*, **95** (15), 153303.

91 Cho, S.W., Yoo, K., Jeong, K., Whang, C., and Yi, Y., and Noh, M. (2007) Interfacial electronic structure of *N, N′*-bis(1-naphthyl)- *N, N′*-diphenyl-1, 1′-biphenyl-4, 4′-diamine/copper phthalocyanine:

C_{60} composite/Au studied by ultraviolet photoemission spectroscopy. *Appl. Phys. Lett.*, **91** (5), 052102.

92 Noguchi, Y., Sato, N., Miyazaki, Y., and Ishii, H. (2010) Light- and ion-gauge-induced space charges in tris-(8-hydroxyquinolate) aluminum-based organic light-emitting diodes. *Appl. Phys. Lett.*, **96** (14), 143305.

93 Veres, J., Ogier, S.D., Leeming, S.W., Cupertino, D.C., and Khaffaf, S.M. (2003) Low-*k* insulators as the choice of dielectrics in organic field-effect transistors. *Adv. Funct. Mater.*, **13** (3), 199–204.

94 Veres, J., Ogier, S., Lloyd, G., and De Leeuw, D. (2004) Gate insulators in organic field-effect transistors. *Chem. Mater.*, **16** (23), 4543–4555.

95 Sugi, K., Ishii, H., Kimura, Y., Niwano, M., Ito, E., Washizu, Y., Hayashi, N., Ouchi, Y., and Seki, K. (2004) Characterization of light-erasable giant surface potential built up in evaporated Alq_3 thin films. *Thin Solid Films*, **464–465**, 412–415.

96 Kajimoto, N., Manaka, T., and Iwamoto, M. (2007) Cooperative molecular field effect on the surface potential of tris (8-quinolinato)aluminum films. *Jpn. J. Appl. Phys.*, **46** (4B), 2740–2744.

97 Ozasa, K., Nemoto, S., Isoshima, T., Ito, E., Maeda, M., and Hara, M. (2008) Photoinduced reduction and pattern preservation of giant surface potential on tris(8-hydroxyquinolinato) aluminum(iii) thin films. *Appl. Phys. Lett.*, **93** (26), 103501.

98 Priestley, R., Sokolik, I., Walser, A.D., Tang, C.W., and Dorsinville, R. (1997) Photooxidation effects on picosecond photoluminescence and photoconductivity in tris-(8-hydroxyquinoline) aluminum (Alq_3). *Synth. Met.*, **84** (1–3), 915–916.

99 Thangaraju, K., Amaladass, P., Bharathi, K.S., Mohanakrishnan, A.K., Narayanan, V., and Kumar, J. (2009) Studies on influence of light on fluorescence of tris-(8-hydroxyquinoline)aluminum thin films. *Appl. Surf. Sci.*, **255** (11), 5760–5763.

100 Schwoerer, M. and Wolf, H. (2007) *Organic Molecular Solids*, Wiley-VCH Verlag GmbH., Weinheim

101 Tanaka, Y., Noguchi, Y., and Ishii, H. (2011) Capacitance–voltage measurement of an ambipolar pentacene field effect transistor in operation by using displacement current measurement. *MRS Proc.*, 1287, mrsf10-1287-f03-06.

Part Two
Charge Transport

Physics of Organic Semiconductors, Second Edition. Edited by Wolfgang Brütting and Chihaya Adachi

6
Effects of Gaussian Disorder on Charge-Carrier Transport and Recombination in Organic Semiconductors

Reinder Coehoorn and Peter A. Bobbert

6.1
Introduction

Common fabrication technologies of organic semiconductor materials, such as high vacuum evaporation deposition of small molecule-based materials or solution processing of polymers, often lead to a disordered, amorphous or nearly amorphous structure. In such systems, with only a weak intermolecular interaction, injected electrons or holes reside on distinct molecular sites or (in the case of polymers) on distinct conjugated segments. The charge transport is due to hopping, that is, due to thermally assisted quantum mechanical tunneling in between the localized sites. Experimental evidence favoring this picture is the observation of an increase of the charge-carrier mobility with increasing temperature, as measured in unipolar devices in which the transport is due to a small concentration of charges injected from the electrodes. At high carrier concentrations, as obtained, for example, by strong molecular doping, a crossover to metallic transport can take place, characterized by a decrease of the conductivity with increasing temperature [1].

In this chapter, we discuss recent advances in our understanding of the charge-carrier transport in disordered organic semiconductors in the hopping regime. We focus on OLEDs and include a discussion of the effect of disorder on charge-carrier recombination and an application to single-layer OLEDs showing that predictive modeling of the current density and light emission efficiency is presently feasible. In the remainder of this section, we give a brief overview of the developments and state of the art.

In its most ambitious form, building a charge transport model for a disordered organic semiconductor would require the realization of the sequence of the following three steps:

1) Prediction of the molecular scale (disordered) structure using molecular dynamics (MD) or Monte Carlo (MC) methods, appropriately taking the deposition conditions into account.

Physics of Organic Semiconductors, Second Edition. Edited by Wolfgang Brütting and Chihaya Adachi

2) Calculation of the electronic structure and interaction parameters that determine the hopping rates between pairs of molecules, using density functional theory (DFT).
3) Calculation of the charge-carrier mobility as a function of the temperature, electric field, charge-carrier density, and other relevant parameters, by solving the hopping problem on a large grid of sites representing the molecules.

Recently, for the first time, this approach was indeed followed to develop a mobility model, namely, for hole transport in the archetypical OLED material tris(8-hydroxyquinoline)-aluminum(III) (Alq_3) [2, 3]. Figure 6.1 shows the result of a supercomputer simulation of a $10 \times 10 \times 10\,nm^3$ box containing 1137 molecules, showing their disordered packing and revealing the nonuniformity of the hole transport. A Gaussian shape of the density of states (DOS) was found, with a width $\sigma \approx 0.18\,eV$. As a result of the disorder, the current density is not uniform but filamentary, so that only a small fraction of the molecules participates in the transport process. This pioneering work has opened the prospect that predicting the mobility from first principles will become a feasible option. However, no complete analysis of the accuracy of the methods used and of comparisons with experiment has yet been made. Making such an analysis is hampered by the CPU intensiveness

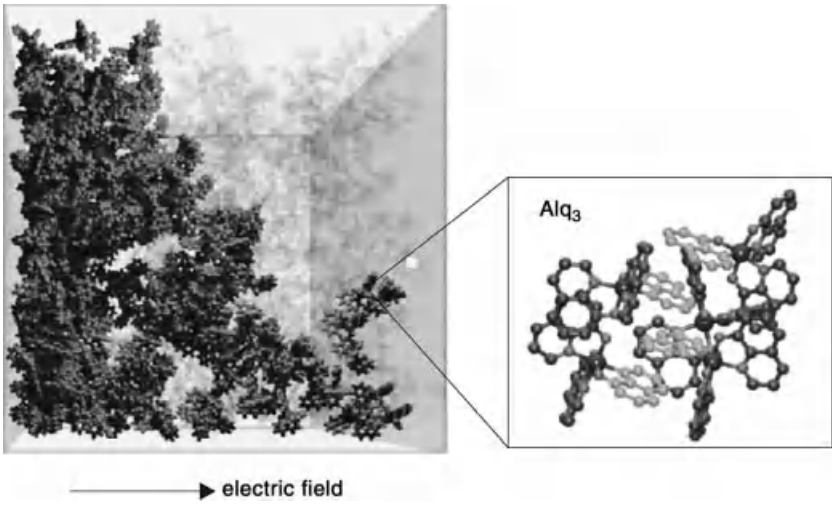

Figure 6.1 Result of a supercomputer simulation of the morphology and hole transport in the organic semiconductor Alq_3 in a $10 \times 10 \times 10\,nm^3$ box containing 1137 molecules, revealing the nonuniformity of the hole transport [2]. In the simulation, the disordered structure has been obtained from Monte Carlo simulations. Subsequently, the trajectories were calculated of 2000 holes that were released on randomly chosen molecules in the leftmost layer and that traveled to the right under influence of a uniform electric field. The highlighted molecules are those that were at least once visited by a hole. The right part of the figure shows schematically the arrangement of a few Alq_3 molecules (H-atoms not shown), with typical π–π stacking structures drawn in a lighter gray tone. Left and right parts of the figure are reproduced from Refs [2] and [3], respectively.

of the computational tasks involved and by the well-known sensitivity of the thin-film structure and the resulting mobility of organic electronic materials such as Alq_3 to the deposition conditions.

Debates about the appropriateness of more simple models have been a recurring theme in the literature. Such simplifications concern the description of the energy level structure (shape of the DOS and spatial correlations between the energy levels of nearby molecules), the molecular positions (positional disorder), and the hopping mechanism. Most fundamentally, the question has been raised whether the energetic disorder is actually the dominant factor determining the mobility. Energetic disorder leads to a wide distribution of the intermolecular hopping rates and the resulting percolative nature of the transport process is an obstacle for obtaining a large mobility. However, it has been argued that often the limiting factor for the mobility is not the disorder, but the Marcus reorganization energy, that is, the energy involved in the change of the atomic structure of a molecule upon positive or negative charging [4–7] during the hopping process. Both models have been discussed in a review by Coropceanu *et al*. [8]. Experimentally, a distinction between both points of view can be made from a study of the temperature (T) dependence of the low-field mobility of single carriers, which is expected to be proportional to $\exp[-(E_{A,1}/k_BT)^2]$ in the specific case of strong Gaussian disorder and to $\exp(-E_{A,2}/k_BT)$ in the case of a predominant intramolecular reorganization energy. Here, $E_{A,1}$ and $E_{A,2}$ are temperature-independent effective activation energies that depend on the energetic disorder and the reorganization energy, respectively, and k_B is the Boltzmann constant. The $1/T^2$ dependence was obtained within the Gaussian disorder model (GDM) developed by Bässler [9], who investigated the effects not only of the energetic disorder but also of the positional disorder. Time-of-flight (TOF) mobility measurements [10, 11] and analyses of the current–voltage ($J(V)$) characteristics of unipolar sandwich-type single-layer devices often yield a $1/T^2$ temperature dependence, as expected when disorder prevails, although a $1/T$ dependence has also been obtained from such studies [10–13].

Recently, it has been shown that this controversy may be solved by taking into account that in the case of energetic disorder, the mobility is a function not only of the temperature and electric field but also of the charge-carrier density. This was already known to be a relevant effect in organic field-effect transistors based on amorphous organic semiconductors with an exponential shape of the DOS [14]. The application of a gate voltage can then give rise to a large carrier concentration (charge per molecule) in the accumulation channel near the gate dielectric, up to 0.01 or even higher. However, analyses of the $J(V)$ characteristics of unipolar sandwich-type single-layer devices revealed that the mobility can also be strongly carrier density dependent at much lower concentrations [15]. Three-dimensional (3D) numerical modeling using a master equation (ME) approach [16] and a theoretical semianalytical study [17] showed that a carrier density dependence of the mobility is expected not only for the case of an exponential DOS but also for a Gaussian DOS. Pasveer *et al*. showed for the case of a spatially uncorrelated Gaussian DOS that the results of 3D ME

calculations can be used in a one-dimensional (1D) transport model in conjunction with effective expressions for the temperature, field, and carrier density dependence of the mobility, in spite of the fact that the current density is filamentary instead of uniform, providing an excellent explanation of available experimental results [18]. This extension of the GDM, including the carrier density dependence of the mobility, has been called the extended Gaussian disorder model (EGDM). It is now evident that in many transport experiments, the density dependence of the mobility plays an important role, and that in simplified analyses of the $J(V)$ characteristics of unipolar sandwich-type single-layer devices that neglect this effect, the *effective* mobility will often show to a good approximation a $1/T$ temperature dependence, whereas the value of the mobility in the low-concentration limit as determined properly from the experiments shows a $1/T^2$ dependence [19, 20]. It thus follows that the observation of a $1/T$ dependence of the effective mobility is not necessarily inconsistent with the point of view that the effect of disorder on the mobility is significant.

In Figure 6.2, our view on the development of OLED modeling is visualized. Conventionally, OLED models [14, 21–26] employed a mobility function with an empirical Poole–Frenkel (PF) ($\exp[\gamma_{PF}(T)\sqrt{F}]$) electric field ($F$) dependence (with γ_{PF} an empirical temperature-dependent Poole–Frenkel factor) and a $1/T$ temperature dependence as would be expected in the absence of (substantial) disorder. No charge-carrier density dependence was assumed. Within these one-dimensional "first-generation" models, the current density is assumed to be spatially uniform. The "second-generation" OLED models are based on 3D supercomputer modeling using master equation or Monte Carlo methods of the transport between mathematical point sites, in practice situated on a regular lattice, taking the energetic

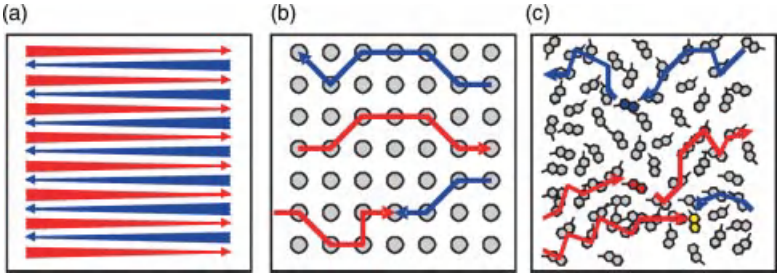

Figure 6.2 Three generations of OLED models. Red (blue) arrows denote hole (electron) currents in a small region of an organic semiconductor under the influence of a horizontally directed electric field. (a) In the first-generation models, the current density is a continuous and laterally uniform function of the position. (b) In the second-generation OLED models, as discussed in this chapter, the discreteness and energetic randomness of the molecular states is taken into account, but the molecules are treated as mathematical points on a regular lattice. "Translation" of three-dimensional modeling results to fast 1D PC models makes efficient applications possible. (c) The future third-generation OLED models will take the spatially and orientationally random molecular structure into account, as well as the change of the intramolecular structure when a hole, electron, or exciton is present on the molecule (red, blue, and yellow molecules) ("reorganization").

disorder into account but neglecting the molecular scale details such as orientational disorder and the Marcus reorganization energy. The resulting current density is filamentary and the recombination preferentially takes place at a small fraction of the molecular sites. The EGDM is a "translation" of the 3D modeling results to a 1D analytical description of the mobility function and recombination. An analogous 3D–1D translation step has been made for the case of spatially correlated disorder, resulting in the extended correlated disorder model (ECDM) [27]. Recently, OLED simulation software tools based on both models have become commercially available [28, 29]. Future "third-generation" OLED models will include all molecular-scale details on the charge-carrier transport, as in the pioneering work on Alq_3 discussed above, and molecular-scale modeling of excitonic processes.

It has been a purpose of our work in the past years to investigate whether a complete second-generation OLED model can be consistently made, based on 3D–1D translations. This will be the main subject of this chapter. The EGDM and ECDM are both examples of such a translation. Within both models, the mobility depends only on a few physically meaningful parameters, although if needed additional parameters describing a trap density of states can be included. We also show how the modeling of injection at the electrode interfaces and transport across organic–organic interfaces are included, and to what extent the EGDM and ECDM may be applied to application-relevant materials and devices.

6.2
Mobility Models for Hopping in a Disordered Gaussian DOS

6.2.1
The Extended Gaussian Disorder Model

The extended Gaussian disorder model [18] has been developed on the basis of 3D master equation modeling of the current density due to hopping between the sites on a cubic lattice with a spacing a. The energy level E_i on each site i is taken randomly from a Gaussian distribution with a shape $g(E) = (N_t/\sqrt{2\pi\sigma^2})\ \exp[-E^2/(2\sigma^2)]$, with $N_t \equiv a^{-3}$ being the total volume density of hopping sites and σ the width. For a fixed carrier concentration c and for a uniform electric field F, the *time-averaged* occupation probabilities p_i on each site are calculated in a self-consistent way, taking into account that the hopping probability to a neighbor site j is reduced by a factor $(1 - p_j)$ due to the onsite Coulomb repulsion, which prevents double occupation of a site. The hopping rate w_{ij} from a site i at position $\vec{r}_i$ to a site j at a position $\vec{r}_j$ is assumed to be given by the Miller–Abrahams (MA) expression:

$$w_{ij} = \nu_0 \exp\left(-2\alpha|\vec{r}_i - \vec{r}_j|\right) \exp\left(\frac{H[E_j - E_i - (\vec{r}_j - \vec{r}_i)\cdot\vec{F}]}{k_B T}\right) \tag{6.1}$$

where ν_0 is a hopping attempt frequency, α is the inverse of an effective wave function decay length, and H is the Heaviside step function ($H(x) = 0$ for $x \leq 0$ and $H(x) = 1$ for $x > 0$). The hopping rate thus varies exponentially with hopping distance and with the site energy difference. The MA approach is known to be a good approximation if all hops are accompanied by single-phonon processes. The range of validity of the MA approach and the sensitivity of the calculated transport properties to the hopping model used are subjects of continued debate in the literature [2, 30]. In the 3D supercomputer modeling using master equation or Monte Carlo methods, cells containing 10^6 sites or more are considered, with periodic boundary conditions, in order to appropriately model the filamentary current. The current density is obtained from a summation of the currents through a plane perpendicular to the field direction.

In all published 3D modeling work on the (E)GDM, a fixed value of the product αa, equal to 10, has been used. This choice was motivated by Bässler, who noted that a typical value for the nearest-neighbor hopping distance is 1 nm, whereas the effective value of the wave function decay length that follows from experimental studies of the site density dependence of the mobility in dilute host–guest systems is typically 0.1 [9]. When using a cubic lattice, the current density is then under common conditions almost exclusively due to the nearest-neighbor hops, so that varying the αa product has no significant effect on the temperature, field, or carrier density dependence of the mobility (van der Holst, J.J.M. (unpublished).

Figure 6.3a and c (symbols) shows the mobility for various values of the dimensionless disorder parameter $\hat{\sigma} \equiv \sigma/(k_B T)$ as a function of the carrier concentration and the dimensionless electric field $\tilde{F} \equiv eaF/\sigma$ (with e being the elementary charge), respectively, as obtained in Ref. [18] from ME calculations. The mobility is found to be independent of the carrier concentration for sufficiently small carrier densities, when each carrier may be viewed as independent. The average carrier energy is then independent of the carrier concentration, and equal to the so-called thermal equilibrium energy:

$$E_0 = -\frac{\sigma^2}{k_B T} \tag{6.2}$$

In this so-called Boltzmann regime, the zero-field mobility is to an excellent approximation described by the expression

$$\mu_{0,\mathrm{EGDM}}(T) = c_1 \frac{a^2 \nu_0 e}{\sigma} \exp\left(-c_2 \hat{\sigma}^2\right) \tag{6.3}$$

where $c_1 = 1.8 \times 10^{-9}$ and $c_2 = 0.42$. These are empirical parameters, determined from a fit to the numerical data. We note, however, that c_1 is very close to the value of the factor $\exp(-2\alpha a) = 2.1 \times 10^{-9}$, which would be expected for the case of nearest-neighbor hopping in the high-temperature limit. Furthermore, we note that c_2 is very close to the value of $\sim$0.44 obtained by Bässler from Monte Carlo calculations [9].

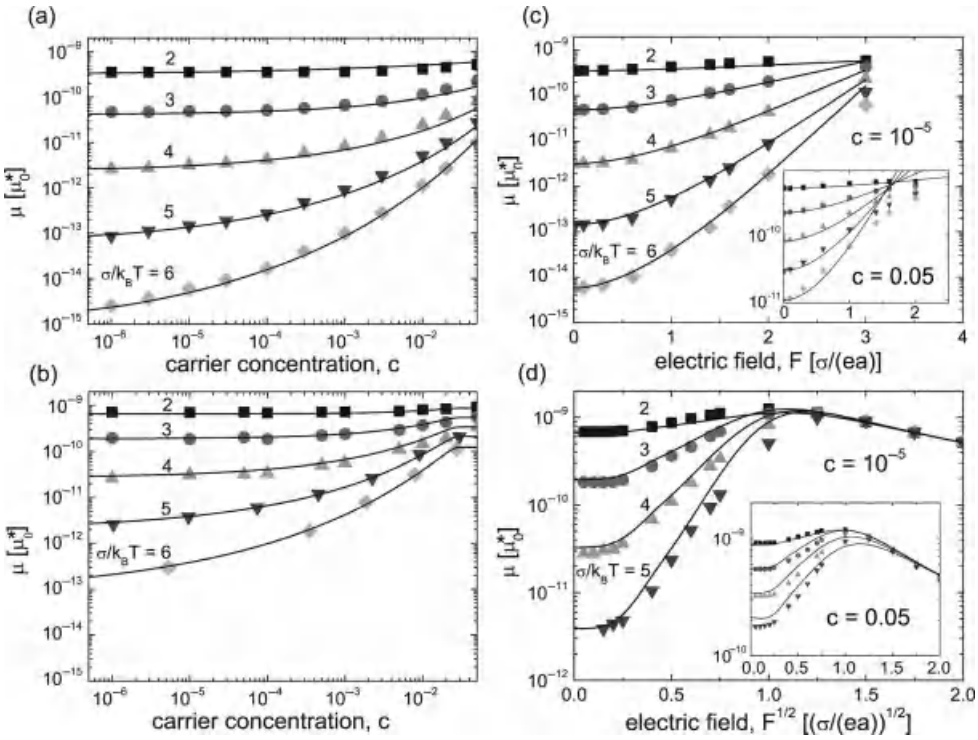

Figure 6.3 Carrier density dependence at zero field and electric field dependence of the mobility for various values of the disorder parameters within the EGDM (a and c) and the ECDM (b and d), as obtained from 3D master equation calculations [18, 27]. Note the square-root field scale used in figure (d). The mobility is expressed in units $\mu_0^* \equiv a^2\nu_0 e/\sigma$. Figures taken from Ref. [27].

A crossover to a regime in which the mobility is carrier density dependent is found to take place when the Fermi energy E_F exceeds E_0, which may be shown to correspond to a crossover concentration given by

$$c_{\text{crossover}} = \frac{1}{2}\exp\left(-\frac{1}{2}\hat{\sigma}^2\right) \tag{6.4}$$

For $\hat{\sigma} = 4$, corresponding at room temperature to $\sigma \approx 0.1\,\text{eV}$, $c_{\text{crossover}} \approx 10^{-4}$. With decreasing temperature or increasing σ, $c_{\text{crossover}}$ decreases rapidly. Percolation theory shows that for sufficiently small carrier concentrations, the mobility may be viewed as being determined by the energy difference between the Fermi energy in the tail of the DOS, which increases with increasing carrier concentration, and by a fixed so-called "transport level," more close to the top of the DOS [31–33]. It may be shown that the carrier concentration dependence of the mobility is then to a good approximation given by [19]

$$\mu(c) = \mu_{0,\text{EGDM}}\frac{1}{c}\exp\left(\frac{E_F(c)}{k_B T} + \frac{1}{2}\hat{\sigma}^2\right) \tag{6.5}$$

It follows from Eqs. (6.2), (6.4) and (6.5) that at the crossover concentration, the enhancement is precisely equal to a factor of 2. The effect becomes important for $E_F > E_0$ when, due to filling of the deepest states, the average charge-carrier energy starts to increase with increasing energy. Trapping in the already highly occupied deepest states is then less probable, so the mobility starts to increase. Note that this is purely a density of occupied states effect and is independent of the specific transport model assumed. Figure 6.3a shows that the carrier concentration dependence of the mobility can give rise to an enhancement of the mobility over many orders of magnitude, as expected from Eq. (6.5).

Figure 6.3b shows that an electric field also enhances the mobility, as might have been anticipated from Eq. (6.1), until for $F \approx 4\sigma/(ea)$ the field is so large that most forward hopping attempts are actually "downhill." The current density is then field and temperature independent and the mobility is proportional to $1/F$. Up to high values of the carrier concentration, essentially equal results are obtained using Monte Carlo modeling [34], within which the *actual* trajectories between carriers are calculated, taking into account that hops to already occupied sites are forbidden. At concentrations above $c = 0.01$, depending on the site density, the repulsive Coulomb interaction that was neglected in the ME calculations starts to give rise to a decrease of the mobility [34].

It was shown in Ref. [18] that these 3D modeling results can be described well using an analytical 1D expression for the mobility of the form

$$\mu(T, c, F) = \mu_{0,\mathrm{EGDM}}(T) \exp\left[\frac{1}{2}(\hat{\sigma}^2 - \sigma)(2c)^{\delta}\right] \exp\left[0.44(\hat{\sigma}^{3/2} - 2.2)\left(\sqrt{1 + 0.8\hat{F}^2} - 1\right)\right] \tag{6.6}$$

where $\delta \equiv 2[\ln(\hat{\sigma}^2 - \hat{\sigma}) - \ln(\ln 4)]/\hat{\sigma}^2$. The carrier density and the field dependence occur as separate factors. A motivation for the specific parameterization function used to describe the carrier density dependence and an analysis of its precision have been given in Appendix D of Ref. [19]. The parameterization is shown by the full curves in Figure 6.3a and b. No attempts have been made so far to develop an accurate parameterization for the large carrier concentration and high-field regimes. In actual calculations using the EGDM, often a cutoff is introduced at $c = 0.1$ and at high fields $\hat{F} = 2$ [35]. The actual value of the cutoff concentration and the precise assumptions made concerning the very high mobility close to that concentration are seldom of significant impact to calculated device properties. Such very high concentrations would in practice occur only in very thin regions near the interfaces of well-injecting metallic electrodes, whereas the device properties are determined by the much lower mobilities in the bulk of the layers. The dimensionless cutoff field would typically correspond to $F \approx 0.2$ V/nm, which will only rarely be attained under realistic measurement conditions.

Within the EGDM, the mobility is in practice described by three material-specific parameters, namely, σ, N_t, and $\mu_{0,\mathrm{EGDM}}$. The consistency can be judged from the measured temperature dependence of $\mu_{0,\mathrm{EGDM}}$, which is expected to vary as $1/T^2$ with a slope parameter c_2 in the range of 0.38–0.50 (see Eq. (6.3)) [19].

6.2.2
The Extended Correlated Disorder Model

In TOF experiments, the field dependence of the mobility is often found to be described well by the empirical Poole–Frenkel expression $\mu \propto \exp[\gamma_{PF}\sqrt{F}]$. Within the (E)GDM, such a field dependence is indeed found, but only in a narrow field range. Gartstein and Conwell argued that obtaining a PF field dependence in a wider field range requires that the energy levels are assumed to be spatially correlated [36]. The physical origin of such correlations could be the dipole moments present on some organic molecules [36–38], the quadrupolar moments inherently present for all π-conjugated systems, long-range thermal fluctuations in the molecular geometries (for the case of a polymer) [10], or short-range order due to a specific molecular packing [39]. An extended range of validity of the PF law was indeed found from 1D [37] and 3D [38] calculations of the mobility in the Boltzmann regime (correlated disorder model (CDM)). Using a 3D ME approach analogous to that described above, Bouhassoune *et al.* [27] developed an extension of the CDM including the effect of the carrier density dependence of the mobility (ECDM). The site energies were obtained by assuming correlated disorder resulting from randomly oriented electrical dipole moments, as in Ref. [38]. This leads to a Gaussian DOS with a pair correlation function of the site energies that decreases by a factor of ∼2 within approximately 1.5 average intersite distances and that decreases at large distances (r) as $1/r$ [36]. Figure 6.4 shows the distribution of energies on a part of the system containing $31 \times 31 \times 31$ sites.

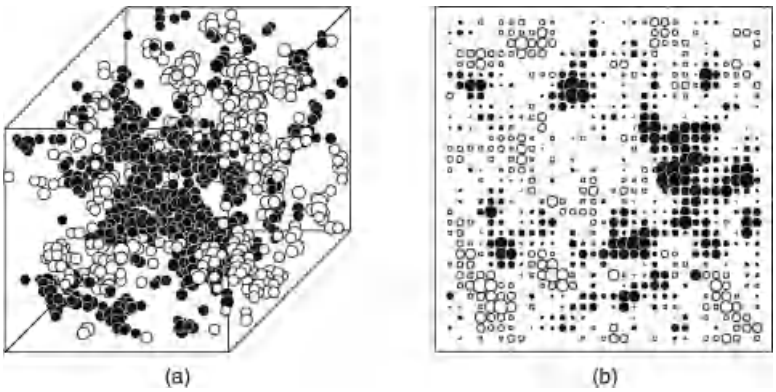

Figure 6.4 (a) Distribution of the potential in the case of correlated disorder, as obtained from randomly oriented dipoles for a part of the system consisting of $31 \times 31 \times 31$ sites on a cubic grid. Black and white spheres represent sites with positive and negative values of the local energy E_i, and the sphere radii are proportional to $|E_i|$. For the sake of clarity, sites with $|E_i| < 2\sigma$ are not shown. (b) Two-dimensional cross section of the system shown in (a). Reproduced from Ref. [38b] with permission from the authors.

Figure 6.3b and d (symbols) shows the mobility for various values of the dimensionless disorder parameter as a function of the carrier concentration and the dimensionless electric field. As in the case of the EGDM, the mobility is independent of the carrier concentration for sufficiently small carrier densities, when each carrier may be viewed as independent, whereas it becomes carrier concentration dependent above a value of $c_{\text{crossover}}$ close to that given by Eq. (6.4). However, the carrier concentration dependence is smaller than that for the EGDM, whereas the field dependence is stronger. The square-root field axis used in Figure 6.3d reveals that over a substantial field range, an approximate Poole–Frenkel behavior holds. The crossover to the downhill hopping regime already takes place when $F \approx \sigma/(ea)$, corresponding for the case of $\hat{\sigma} = 4$ and $a = 1\,\text{nm}$ to a field equal to $0.1\,\text{V/nm}$. This relatively low field, which could be realistically obtained in actual devices, made it necessary to develop a parameterization scheme including the high-field range [27]. In the low-field regime, the mobility is written as

$$\mu(T, c, F) = \mu_{0,\text{ECDM}}(T) g(T, c) f(T, F, c) \tag{6.7}$$

with g and f dimensionless mobility enhancement functions described by analytical expressions given in Ref. [27] and with

$$\mu_{0,\text{ECDM}}(T) = c_3 \frac{a^2 \nu_0 e}{\sigma} \exp\left(-c_4 \hat{\sigma}^2\right) \tag{6.8}$$

where $c_3 = \exp(-20) = 2.1 \times 10^{-9}$ and $c_4 = 0.29$. Within the ECDM, the temperature dependence of the mobility is thus smaller than that within the EGDM [18], reflecting that for a given value of σ, the energy level landscape is effectively smoother than that in the EGDM due to the spatial correlation: close to each occupied state, many other low-lying states are present to which hops can take place that contribute significantly to the total mobility. The full curves in Figure 6.3b and d show the results of the parameterization, using for the carrier density dependence a high-concentration cutoff at $c = 0.025$.

6.2.3
Mobility in Host–Guest Systems

The EGDM and the ECDM can under certain conditions also be used to accurately describe the mobility of host–guest systems, within which the DOS deviates from a simple Gaussian shape due to the presence of additional low-lying guest-derived states. Such a situation often arises when describing the electron mobility, as a result of a nonintentional small concentration of low-lying trap states, or when describing the mobility in emissive layers containing a relatively large concentration of fluorescent or phosphorescent dye molecules.

Experimental studies show that, in general, four transport regimes may be distinguished, depending on the relative guest molecule concentration x [40], as illustrated in Figure 6.5. We emphasize that the boundaries between the regimes depend on the details of the material system studied and that a strict separation in

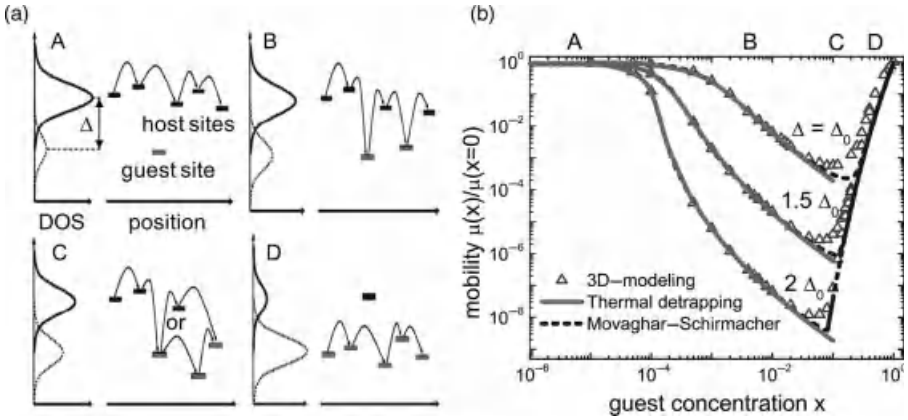

Figure 6.5 (a) The four transport regimes (A–D) in a disordered host–guest systems with a bimodal Gaussian DOS, as described in the text. (b) Dependence of the mobility on the guest concentration x, normalized by the mobility in the pure host ($x = 0$), obtained for three values of the average trap depth Δ using numerically exact 3D modeling (3D master equation or 3D percolation model), the thermal detrapping model, and the Movaghar–Schirmacher model. Parameter values used are $T = 298$ K, $\sigma_{\text{host}} = \sigma_{\text{guest}} = 4k_BT$, $\Delta_0 = 0.30$ eV, and $c_{\text{total}} = 10^{-4}$ (total carrier concentration). Adapted from Ref. [41].

four regimes is not always possible. As a concrete example, we consider the case of a bimodal Gaussian DOS without spatial correlations, for which the guest concentration dependence of the mobility was obtained from ME modeling or from a basically equivalent percolation model [41]. Within this example, equal widths of the host and guest DOS, $\hat{\sigma}_h = \hat{\sigma}_g = 4$ (i.e., $\sigma \approx 0.1$ eV at room temperature), and equal values of their wave function decay length α^{-1} were assumed. Three values of the depth Δ of the trap states are considered, corresponding to 0.3, 0.45, and 0.6 eV at room temperature and the carrier concentration is 10^{-4}.

Figure 6.5a shows the four transport regimes. At very small guest concentrations (regime A), the mobility is only due to host–host hopping so that it is not affected by the guest molecules (a). For very high guest concentrations (here for $x > 0.3$, regime D), the mobility is exclusively due to hopping between the guest sites. The increase of the mobility with increasing guest site density as a result of the decreasing intersite distance is described well using the EGDM (not shown).

A more interesting situation arises in regime B, when the guest molecules start to act as trap sites. For very small electric fields, the mobility is then to an excellent approximation given by a multiple trap-and-release "thermal detrapping" model, used in conjunction with the EGDM. Within this approach, the mobility is equal to the fraction of carriers which according to Fermi–Dirac (FD) statistics populate the host states, times the EGDM host mobility at the corresponding (lowered) "free" carrier density [42]. The mobility is carrier density dependent for two reasons: (i) the occupation of the host states increases with increasing carrier density, and (ii) the mobility of the carriers in the host states increases with increasing carrier density (if the carrier concentration is above the critical value given by Eq. (6.4)). In the

earlier theoretical work [43–45], the latter effect was not taken into account. In Figure 6.5b, the prediction as obtained from this model (full curves, thermal detrapping) is compared with the results as obtained from the benchmark ME model (symbols), showing excellent agreement in the relevant guest concentration range ($10^{-4} < x < 5 \times 10^{-2}$).

At finite values of the electric field, this simple picture is not anymore applicable, as the field creates a "hot" nonequilibrium occupation of the density of states. More electrons than would be obtained from the FD distribution then occupy host states, so that the mobility is larger than expected. The effect is called field-induced detrapping (FID). It is illustrated in Figure 6.6 for a system with a set of parameters as given in the figure caption. The figure shows that under realistic conditions, for fields up to approximately 0.15 V/nm, the thermal detrapping model can underestimate the mobility by a factor up to approximately 3. Recent work by Cottaar *et al.* [46] has shown that it is not possible to solve this problem by replacing the actual temperature by an effective larger temperature in conjunction with the standard FD expression. Instead, it was shown to be solvable with high accuracy by making use of a field-dependent generalized FD distribution that depends only on the shape of the host DOS

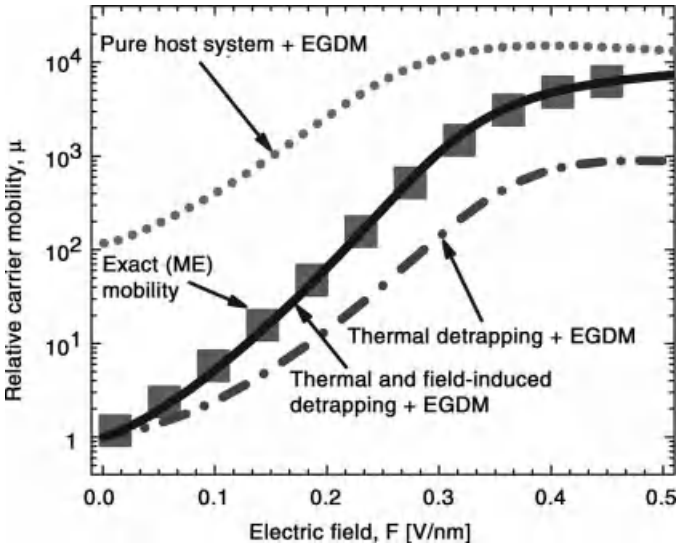

Figure 6.6 Effect of the electric field on the mobility in a host–guest system (relative to the mobility at zero field) with a bimodal Gaussian DOS with $\sigma_{host} = \sigma_{guest} = 0.13$ eV, average trap depth $\Delta = 0.65$ eV, site density $N_t = 6 \times 10^{26}$ m^{-3}, and guest concentration $x = 0.01$. The carrier concentration is $c = 0.01$ and $T = 298$ K. The squares give the exact ME results, which are found to be described well using the "thermal detrapping + FID + EGDM" approach developed in Ref. [46]. The dotted and dash–dotted curves show the mobility in the absence of traps and as calculated using the thermal detrapping model and the EGDM, but neglecting field-induced detrapping, respectively. Adapted from Ref. [46].

and *not* on that of the guest DOS. An easy-to-use parameterization scheme for this distribution was derived from 3D ME calculations. Its accuracy is excellent, as may be judged from Figure 6.6 by comparing the exact 3D ME results with the "thermal detrapping + FID + EGDM" prediction. When the mobility in the host can be described within the EGDM, a full extension to include a guest DOS with any arbitrary shape is thus available within regime B. For systems described by the ECDM, the FID effect has not yet been investigated.

The most complex situation arises when at intermediate guest concentrations, the hopping takes place via host and guest sites ($5 \times 10^{-2} < x < 0.3$, regime C). Figure 6.5b shows that the mobility as obtained from the benchmark ME model is then underestimated by the application of the EGDM in conjunction with the thermal detrapping model as well as by an application of the EGDM that assumes that all transport is due to guest–guest hopping. The figure shows that even the highly refined semianalytical Movaghar–Schirmacher percolation model (see also Refs. [42, 47] for details) underestimates the mobility in this regime. The ME results indicate that close to the mobility minimum random statistical variations of the local guest concentration, to smaller and to larger concentrations, lead to regions with an enhanced mobility. This intermediate transport regime occurs in many emissive layer materials used in OLEDs, within which typical phosphorescent dye concentrations are 1–10%. It would therefore be important to extend the EGDM (and the ECDM) to include this situation.

6.3
Modeling of the Recombination Rate

6.3.1
Recombination in Systems with a Gaussian DOS

The position ($\vec{x}$) dependent exciton formation rate in OLEDs is generally described using the Langevin formula,

$$R(\vec{x}) = \frac{e}{\varepsilon}(\mu_e(\vec{x}) + \mu_h(\vec{x}))n_e(\vec{x})n_h(\vec{x}) \tag{6.9}$$

where ε is the dielectric permittivity, μ_e and μ_h are the electron and hole mobility, and n_e and n_h are the electron and hole carrier density [48]. R is often called "recombination rate," as it is equal to the total rate of all radiative and nonradiative electron–hole recombination processes if no exciton dissociation takes place. The derivation is based on a consideration of the interaction between a single electron and a single hole and assumes that even when the electron and hole are within each other's capture radius, approximately 15 nm at room temperature for typical organic semiconductors with a relative dielectric permittivity $\varepsilon_r \sim 3$, diffusive transport characterized by multiple hops precedes the final exciton formation process [49]. The mobility can be position dependent as a result of its carrier density and field dependence. In the case of large carrier density or field gradients, Eq. (6.9) is

obviously expected to be a zeroth-order approximation at best. Furthermore, one might wonder whether (i) in the case of a wide Gaussian DOS, the capture process is described well using the same carrier density and field-dependent mobilities as used for describing the (filamentary) charge transport, (ii) the recombination rate is affected by the Coulomb interactions between carriers at high densities, and (iii) (deep) trap states would affect the applicability of Eq. (6.9).

The effect of Gaussian disorder on the recombination rate has for the first time been investigated by Albrecht and Bässler [50] using MC calculations of the capture process in systems containing a single electron–hole pair. Their studies showed that Eq. (6.9) is applicable in the zero-density limit and up to intermediate fields ($\sim$0.05 V/nm) for systems studied at room temperature with a wide range of disorder parameters σ, up to 0.25 eV. More recently, Groves and Greenham [51] and van der Holst *et al.* [52] carried out MC calculations for systems with Gaussian disorder as a function of the electron and hole density. Both groups found that the recombination rate can be significantly smaller than that expected from the Langevin formula, up to 70%. However, van der Holst *et al.* found that the Langevin formula is well obeyed if the *bipolar mobilities* as obtained for the actual double-carrier (DC) devices are used, instead of the unipolar mobilities that are obtained in single-carrier devices (Figure 6.7a). In a bipolar system with a sufficiently high carrier concentration, the electrostatic fields created by the second carrier give rise to additional disorder, so that the bipolar mobilities are smaller than the unipolar mobilities. The difference was found to be larger for the case of perfectly anticorrelated HOMO and LUMO site energies than for the case of perfectly correlated energies (Figure 6.7b). Varying local electrostatic potentials (anticorrelation) could occur as a result of randomly oriented molecular dipole moments. Varying energy gaps (correlation) could occur as a result of varying degree of conjugation (e.g., in the case of polymers with varying conjugation lengths). The correlation between the HOMO and LUMO energy levels in actual materials is not well known.

The applicability of the Langevin formula when bipolar mobilities are used and the effect of correlation are shown in Figure 6.7c for a wide range of disorder parameters, for electron and hole concentrations equal to 10^{-4}, and for the zero-field limit. The difference between unipolar and bipolar mobilities increases with increasing disorder parameter. At finite realistic fields ($<$0.1 V/nm), only small deviations from the Langevin formula were found. Interestingly, the location of the sites at which the recombination takes place preferentially was found to be independent of the location of the current filaments (see the next section) in the corresponding single-carrier devices (studied when switching off the current due to the other carrier). Instead, these locations coincide with the energetically low-lying sites for electrons or holes.

So far, this study of the validity of the Langevin formula and the effect of using bipolar mobilities has not yet been extended to cases with unequal electron and hole densities or unequal disorder parameters, nor to systems with correlated disorder (ECDM). Furthermore, there is not yet an easy-to-use parameterization scheme for the bipolar mobility. Another issue that needs further attention is the

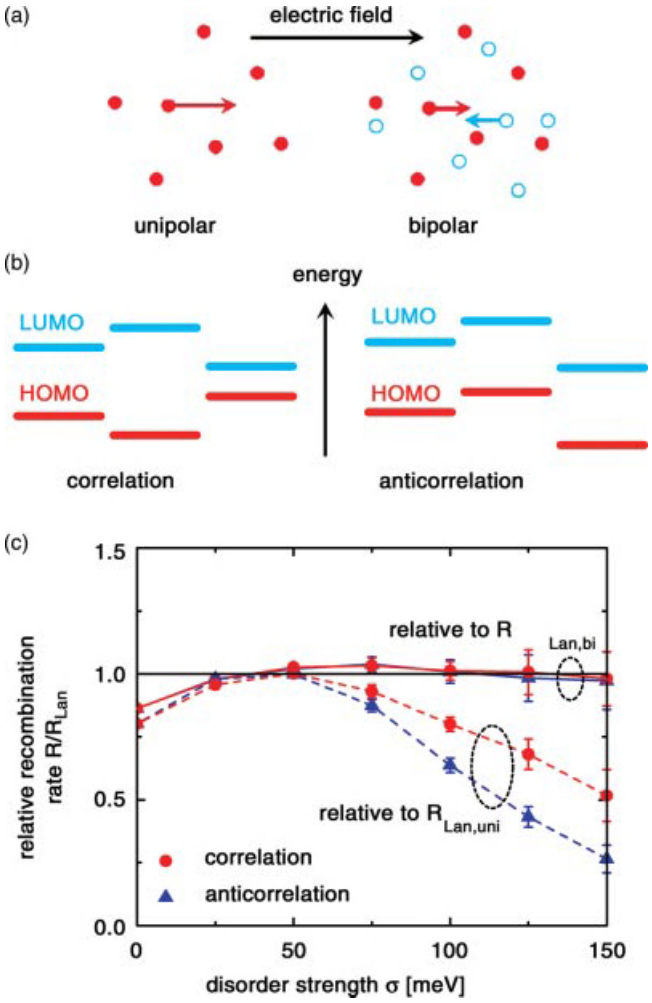

Figure 6.7 (a) Charge transport in a unipolar and bipolar device, giving rise to unipolar and bipolar mobilities. (b) Correlated and anticorrelated electron and hole onsite energies. (c) Zero-field recombination rate R relative to the Langevin recombination rate R_{Lan} as a function of disorder energy σ, obtained at temperature $T = 300$ K from MC calculations, for electron and hole carrier concentrations both equal to $c = 10^{-4}$. Red circles (blue triangles): correlated (anticorrelated) electron and hole energies. Solid (dashed) lines: Langevin recombination rate calculated with bipolar (unipolar) mobilities. Taken from Ref. [53].

electric field dependence of the recombination rate. Albrecht and Bässler [50] found from 3D MC calculations in the Boltzmann regime that at finite (large) fields, the actual rate is slightly larger than as obtained from Eq. (6.9) (including the field dependence of the mobility). Van Mensfoort and Coehoorn [35] rationalized this result by describing the recombination process on a cubic grid as a result of

contributions from two longitudinal hops (parallel and antiparallel to the field), with rates determined by F, and from four transverse hops, with rates independent of F. We have adopted this approach in all our 1D device simulations presented in this chapter. However, van der Holst *et al.* [52] obtained from 3D MC calculations outside the Boltzmann regime a more complex picture, with an (small) initial decrease of the recombination rate with increasing field.

6.3.2
Recombination in Host–Guest Systems with a Gaussian Host DOS

In actual OLEDs, the densities of HOMO and LUMO states are seldomly both single Gaussians. For example, the electron transport in polymer and small-molecule organic semiconductors is often significantly influenced by the presence of electron traps (Section 6.4). A natural extension of the Langevin formula within which the effect of electron traps is included is given by [53]

$$R = \frac{e}{\varepsilon}\left(n_{\mathrm{e,free}} n_{\mathrm{h}} \mu_{\mathrm{e}}(n_{\mathrm{e,free}}) + n_{\mathrm{h}} n_{\mathrm{e}} \mu_{\mathrm{h}}(n_{\mathrm{h}})\right) \tag{6.10}$$

For notational simplicity, the position dependence is not explicitly given here. Equation (6.10) expresses that the total recombination rate is a sum of contributions due to the capture of "free" electrons, that is, electrons residing in the Gaussian host DOS, by holes and capture of holes (which are all "free") by electrons ("free" or "trapped"). The electron and hole mobilities used are given by the EGDM expressions, evaluated for the "free" electron density and the total hole density. An application of this expression is discussed in Section 6.5.2.

We note that Eq. (6.10) may be rewritten as

$$\begin{aligned} R &= \frac{e}{\varepsilon} n_{\mathrm{e,free}} n_{\mathrm{h}} \left(\mu_{\mathrm{e}}(n_{\mathrm{e,free}}) + \mu_{\mathrm{h}}(n_{\mathrm{h}})\right) + \frac{e}{\varepsilon} n_{\mathrm{h}} n_{\mathrm{e,trapped}} \mu_{\mathrm{h}}(n_{\mathrm{h}}) \\ &= R_{\mathrm{L,free}} + R_{\mathrm{trap\text{-}assisted}} \end{aligned} \tag{6.11}$$

that is, as the sum of a Langevin-type term resulting from the bimolecular recombination between "free" carriers and a term resulting from the trap-assisted recombination of free holes with trapped electrons. A similar approach was recently presented by Kuik *et al.* [54], within which the trap-assisted recombination term was calculated using the Schottky–Read–Hall (SRH) formalism [55]. Both approaches are equivalent if within the SRH formalism the coefficient describing the rate of electron capture in a trap state is taken essentially infinite, so that the hole capture process becomes the rate-determining step (as we have silently assumed above). The hole capture coefficient used within the SRH formalism, which is treated as a free parameter in Ref. [54], is then equal to $C_{\mathrm{h}} = (e/\varepsilon)\mu_{\mathrm{h}}$.

The trap-assisted recombination is expected to be most important and in some cases even dominant over the free carrier contribution at low voltages, when the fraction of electrons occupying trap states is largest. This was indeed seen in the two studies referred to above [53, 54] for the case of two different polymer OLED systems.

6.4
OLED Device Modeling

6.4.1
Single-Layer OLEDs: Analytical Drift-Only Theory

In order to be able to analyze the effects of energetic disorder on the current density and on recombination in OLEDs, we first give a brief review on the device physics of metal/organic semiconductor/metal sandwich systems based on intrinsic semiconductors with a constant mobility [56, 57] and taking only the drift contribution $J_{\text{drift}} = e\mu nF$ to the current density into account. The contribution due to charge-carrier diffusion is neglected. For unipolar devices with equal and ideally injecting metallic contacts, that is, with an infinite carrier density at the injecting electrodes, the current density is then given by the Mott–Gurney square law formula:

$$J = \frac{9}{8}\varepsilon\mu\frac{V^2}{L^3} \tag{6.12}$$

where L is the thickness of the organic semiconductor layer. The space charge and the field are not uniform. For the case of hole transport with the anode and cathode at $x = 0$ and $x = L$, they vary as

$$n(x/L) = \sqrt{\frac{L}{2x}}n_{1/2} \tag{6.13a}$$

and

$$F(x/L) = \sqrt{\frac{2x}{L}}F_{1/2} \tag{6.13b}$$

where $n_{1/2} = (\sqrt{9/8})(\varepsilon/e)(V/L^2)$ and $F_{1/2} = (\sqrt{9/8})(V/L)$. Under these assumptions, the device is thus completely empty at $V = 0$, and is filled upon the application of a voltage difference. Also, for the steady-state mobility in systems with traps [58] and for the transient current density as obtained, for example, in capacitance–voltage [59] and dark injection [60] experiments, useful analytical drift-only expressions are available.

If the electrodes are not ideal, so that there are energy differences Δ_0 and Δ_1 between the states in the organic semiconductor responsible for the charge-carrier transport and the Fermi level in the electrodes at the injecting and exit contacts, respectively, the device stays empty and no current flows until at the built-in voltage $V_{\text{bi}} = (\Delta_1 - \Delta_0)/e$, the so-called flat band condition ($F = 0$) is reached. This term is actually not very appropriate for disordered organic semiconductor devices within which the transport is due to hopping between localized states instead of transport of delocalized charge carriers in a valence or conduction band. Nevertheless, it is often used, and will be adopted as well in this chapter. For the case of an ideal injecting contact at $x = 0$, the current is for $V > V_{\text{bi}}$ given in Eq. (6.12) after replacing V by $(V - V_{\text{bi}})$. In the presence of an injection

barrier at the $x = 0$ contact, the effective carrier density at that contact decreases to a value that depends on the detailed charge-carrier injection model assumed. Often, local thermal equilibrium at the electrode contacts is assumed, resulting from the large rates of hopping expected between the "reservoirlike" electrodes in which the carrier density is very large and the molecules directly adjacent to the electrodes. Using Fermi–Dirac statistics, the charge-carrier density at the interface is then given by

$$n_0 = \frac{N_t}{1 + \exp((\Delta_0/(k_B T))} \tag{6.14}$$

where N_t is the total hopping site density. It may be shown that the current density is not significantly affected by the injection barrier as long as $n_0 \gg n_{1/2}$. This is called the space-charge limited current (SCLC) regime, and the contact is called Ohmic. On the other hand, if $n_0 \ll n_{1/2}$, the carrier density and the field are uniform across the device and equal to n_0 and V/L, respectively. In this so-called injection-limited current (ILC) regime, the current density is given by

$$J_{ILC} = e\mu n_0 \frac{V}{L} \tag{6.15}$$

where again V should be replaced by $V - V_{bi}$ in the case of a built-in voltage. In the ILC regime, $J(V/L)$ curves measured for different layer thicknesses thus coincide. Under the assumptions made (no diffusion and no disorder), the boundary between the SCLC and ILC regimes is reached when $n_0 = n_{1/2}$, that is, at a barrier height of $\Delta_0 \approx k_B T \ln [eN_t L^2/(\varepsilon V)]$. For typical devices, with $N_t = 10^{27}\,m^{-3}$, $L = 100\,nm$ and $\varepsilon_r = 3$, studied at $T = 300\,K$ and $V = 5\,V$, this happens for $\Delta_0 \approx 0.25\,eV$.

Properly modeling charge-carrier injection is actually more involved than as discussed above, as the injection barrier is effectively lowered due to the interaction of the injected charge with its image charge in the electrode. The situation is most simple if the injection barrier is very high, so that it is sufficient to consider only a single carrier and its image charge. In the presence of a positive applied field F_0, the local image charge-induced field gives rise to the position dependence of the potential shown in Figure 6.8b (full curve), so that the effective injection barrier is lowered. As argued by Emtage and O'Dwyer, the effective carrier density boundary condition may then be taken equal to the value given by Eq. (6.13a) with a reduced injection barrier

$$\Delta_{0,eff} = \Delta_0 - e\sqrt{\frac{eF_0}{4\pi\varepsilon\varepsilon_r}} \tag{6.16}$$

Deep in the ILC regime, F_0 is equal to V/L. However, in general, F_0 is affected by the space charge in the device, from which it must be calculated self-consistently using the Poisson equation. In the SCLC regime, F_0 is negative (Figure 6.8a) due to the space charge near the injecting electrode, so that Eq. (6.16) cannot be applied. In Sections 6.4.2 and 6.4.3, we further discuss the carrier density boundary condition in the SCLC regime.

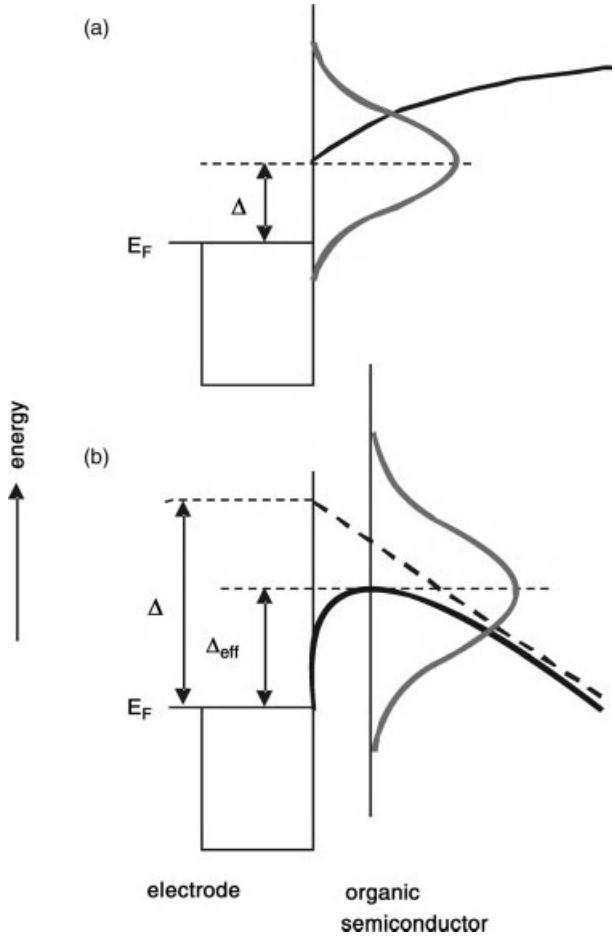

Figure 6.8 Energy level structure near a metal–organic interface for (a) the case of a small injection barrier (SCLC regime) and (b) deep in the ILC regime. The full black curves give the position-dependent electrostatic potential, which in the case of a Gaussian DOS (gray curves) is defined as the position of the top of the DOS. The thick dashed line in figure (b) gives the top of the Gaussian DOS in the absence of the image charge interaction.

For the case of double-carrier OLEDs with (i) ideally injecting electron and hole contacts, (ii) equal and constant electron and hole mobilities, and (iii) bimolecular recombination as given by the Langevin formula (Eq. (6.9)), Parmenter and Ruppel have shown that the drift-only current density shows the same voltage and layer thickness dependence as given by the Mott–Gurney formula, but that the current density is a factor of $256/(9\pi^2) \approx 2.88$ larger than the corresponding single-carrier current density [61]. This factor is larger than 2 as the positive and negative space charges cancel partially, so that the applied field is to a smaller extent opposed by the presence of space charge in the device. When

holes are injected at $x = 0$ and electrons are injected at $x = L$, the space charge and the field are given by

$$n_h(x/L) = (\sqrt{L/x - 1})n_{1/2} \tag{6.17a}$$

$$n_e(x/L) = (\sqrt{L/x - 1})^{-1} n_{1/2} \tag{6.17b}$$

$$F(x/L) = (\sqrt{L/x - 1} + 1/\sqrt{L/x - 1})^{-1} F_{1/2} \tag{6.17c}$$

where $n_{1/2} = (\sqrt{16/\pi^2})(\varepsilon/e)(V/L^2)$ and $F_{1/2} = (\sqrt{16/\pi^2})(V/L)$, respectively. The hole and electron densities at the cathode and anode are zero, which already shows that the recombination efficiency is equal to 1: all injected carriers give rise to recombination. The recombination rate is uniform across the device, as the product of the electron and hole densities is position independent and equal to $R = (J/e)/L$. Parmenter and Ruppel have also given solutions for the case of an arbitrary ratio between the electron and hole mobilities and for the case Langevin recombination as enhanced or decreased by an arbitrary prefactor γ_L [61]. A methodology for obtaining exact semianalytical solutions of the drift-only single-layer double-carrier problem for arbitrary values of the injection barriers has been developed by Martin [62]. For $\gamma_L > 1$ or $\gamma_L < 1$, the recombination becomes peaked in the device center or near the two electrodes, respectively. A large μ_h/μ_e ratio yields recombination peaked near the cathode. And large injection barriers can give rise to a decreased recombination efficiency, namely, when the carrier density in the device is so low that not all carriers meet an oppositely charged carrier before reaching the other electrode.

6.4.2
The Role of Charge-Carrier Diffusion

In the presence of a gradient in the charge-carrier density, diffusion gives rise to an additional contribution $J_{diff} = -qD(dn/dx)$ to the current density, where q is the charge and D is the diffusion coefficient. In the absence of disorder, the diffusion coefficient is related to the mobility via the Einstein equation $D = (k_B T/e)\mu$.

In single-layer OLEDs, the effect of charge-carrier diffusion is most prominent at low voltages. Within the drift-only approximation, the current density in devices with ideal contacts varies quadratically with V as the voltage fulfills two functions: it gives rise to an injected space charge and it provides the driving force for the current. However, charge-carrier diffusion gives even at $V = 0$ already rise to a space charge in the device. At small voltages, the diffusion contribution to the current density is therefore linear in V and larger than the drift-only current density. For the case of a constant mobility, exact semianalytical expressions are available for the current density, including diffusion, and for arbitrary charge-carrier density boundary conditions [63]. In the case of ideal contacts ($n_0 = n_1 = \infty$), the carrier density at $V = 0$ is given by

$$n(x/L) = \frac{1}{\cos^2[\pi((x/L) - (1/2))]} n_{1/2} \tag{6.18}$$

where $n_{1/2} \equiv 2\pi^2\tilde{n} = 2\pi^2\varepsilon k_B T/(eL)^2$ [63]. The current density at low voltages may be obtained by viewing the device as a resistor with a position-dependent resistivity $\varrho(x) = 1/[e\mu n(x)]$, which yields

$$J_0 = 4\pi^2 \frac{k_B T}{e} \varepsilon\mu \frac{V}{L^3} \tag{6.19}$$

From a comparison with the Mott–Gurney formula, it follows that a crossover between diffusion and drift-dominated transport is expected around a voltage $V_{\text{crossover}} = (32\pi^2/9) \times k_B T/e$. At room temperature, $V_{\text{crossover}} \approx 0.9\,\text{V}$. The effect of including diffusion is shown in Figure 6.9, where in both panels curves A and B give the current density without and with diffusion for a symmetric

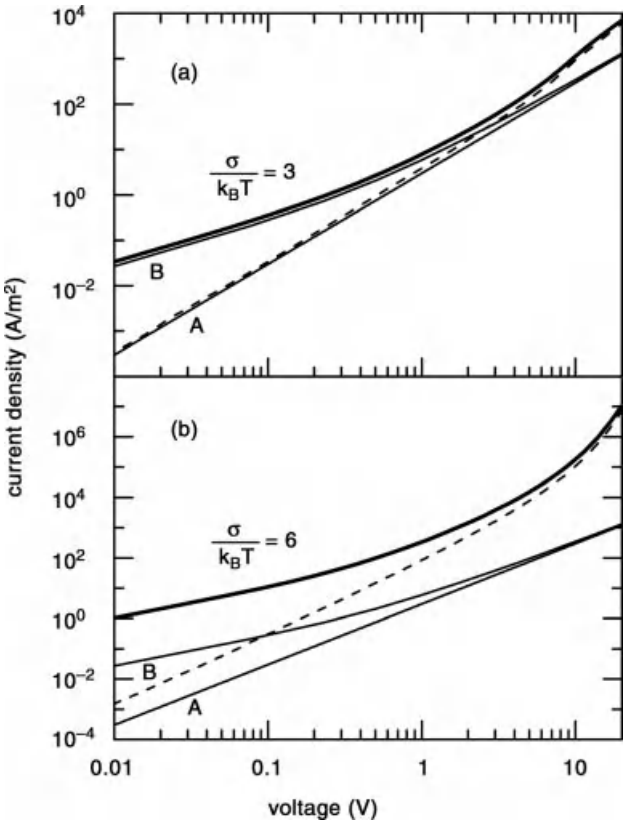

Figure 6.9 Effects of diffusion and disorder on the $J(V)$ curves for 100 nm symmetric sandwich-type single-carrier devices with equal electrodes with $\Delta = 0$ (no injection barriers), based on a material with a Gaussian DOS with $N_t = 4.26 \times 10^{26}\,\text{m}^{-3}$, for (a) $\sigma/(k_B T) = 3$ and (b) $\sigma/(k_B T) = 6$ (thick curves). The calculations were carried out for $T = 298$ K using the EGDM with $\mu_{0,\text{EGDM}} = 1.0 \times 10^{-10}\,\text{m}^{-2}/(\text{V s})$. The full thin curves A and B give the result for the case of a constant mobility $\mu = \mu_{0,\text{EGDM}}$, without and with diffusion, respectively, and the dashed curves give the results including disorder but without diffusion. Taken from Ref. [35].

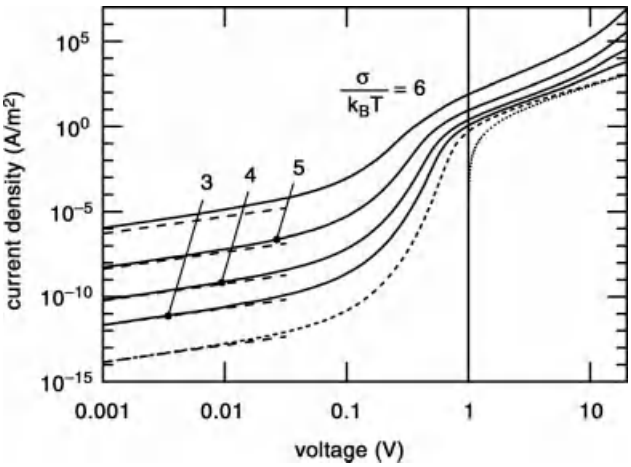

Figure 6.10 Effects of Gaussian disorder on the $J(V)$ curves for 100 nm sandwich-type single-carrier devices with a perfectly injecting contact ($\Delta_0 = 0$) and a large barrier at the exit contact ($\Delta_0 = 1$ eV, $V_{bi} = 1$ V). As in Figure 6.9, the calculations were carried out for $T = 298$ K using the EGDM with $\mu_{0,EGDM} = 1.0 \times 10^{-10}\,m^{-2}/(V\,s)$ and $N_t = 4.26 \times 10^{26}\,m^{-3}$. The dotted and short-dashed curves give the current density for the case of a constant mobility $\mu = \mu_{0,EGDM}$, without and with diffusion, respectively. The long-dashed lines give the current density in the $V = 0$ limit, neglecting the effect of disorder on the mobility and diffusion coefficient. Taken from Ref. [35].

device with ideal contacts and with a material with a constant mobility. At 1 V, the diffusion contribution is still significant, but at 10 V it is almost negligible. This explains why the effect of diffusion is often most important in thin devices, which are investigated at relatively small voltages. Crăciun *et al.*, for example, studied the hole transport in single-layer PPV-based devices and found for devices with a thickness well below 100 nm an effective mobility (as deduced from an analysis of the $J(V)$ curves using the drift-only Mott–Gurney formula) exceeding the value obtained for devices thicker than 100 nm by more than one order of magnitude [64].

In Figure 6.10, calculated $J(V)$ curves are given for devices for which $V_{bi} = 1$ V, due to a 1 V barrier at the exit contact. The dotted and dashed $J(V)$ curves give the drift-only and total current density (including diffusion) for devices with a constant mobility. The figure shows that as a result of diffusion, the effective onset voltage V_{onset} is significantly smaller than the built-in voltage. This implies that V_{bi} cannot be obtained accurately from an analysis of the $J(V)$ curve using the Mott–Gurney formula. In our view, the built-in voltage is given by the value of the onset voltage, extrapolated to zero temperature. A temperature-dependent difference between the onset voltage and V_{bi} has indeed been observed [65]. The square root of the current density is down to voltages close to V_{bi} a linear function of the voltage [66], so that V_{onset} can be defined by extrapolation. Its value is to an excellent approximation given by (R. Coehoorn (unpublished)).

$$V_{\text{onset}} = V_{\text{bi}} - \frac{k_B T}{e} \ln \frac{n_0}{\tilde{n}} \tag{6.20}$$

For the case of a good injecting contact $n_0 \approx 10^{27}\,\text{m}^{-3}$ (i.e., on the order of the site density) and for $\tilde{n} \approx 10^{21}\,\text{m}^{-3}$ (using $L = 100\,\text{nm}$ and $T = 300\,\text{K}$), V_{onset} can at room temperature be 0.3 eV smaller than V_{bi}.

Methods that show in alternative ways the shift of the effective onset voltage due to diffusion include (i) measurements of the low-frequency capacitance, which show a distinct peak close to V_{onset} [67], (ii) electroabsorption experiments [68], and (iii) measurement of the compensation voltage as obtained from the net photocurrent density [69]. All these experiments yield characteristic voltages that are close to (although not precisely identical to) V_{onset}. If the temperature dependence of V_{onset} is not available, V_{bi} and the injection barriers Δ_0 and Δ_1 can be deduced using device modeling. It is shown in the next section that the presence of disorder gives rise to an enhanced onset voltage shift.

The effect of diffusion on the boundary conditions in the case of a large injection barrier, deep in the ILC regime, has been discussed by Scott and Malliaras [70]. In the bulk of the device, diffusion then plays no role, as the carrier density is in that regime uniform and equal to n_0, but at the interface the field is position dependent due to the image potential effect. The authors find an expression for n_0 that is very close to the image potential-modified expression given by Eqs. (6.15) and (6.16), modified by a weakly field-dependent prefactor on the order of 1. Experimental support for the prediction that in the ILC regime the effective boundary condition n_0 does not depend on the mobility, so that the $J_{\text{ILC}} \propto V$ (Eq. (6.15)), has been given by Shen *et al.* [71].

6.4.3
The Role of Gaussian Disorder: One-Dimensional Device Simulations

Methods for performing one-dimensional OLED device simulations including the effects of Gaussian disorder as described by the EGDM or the ECDM, have been developed by various groups [35, 72, 73]. The first additional element of such calculations is the use of the generalized Einstein equation $D = n/[e(\text{d}n/\text{d}E_F)]\mu$, where E_F is the Fermi energy, to obtain the diffusion coefficient from the mobility [74]. As a result, the diffusion coefficient in a Gaussian DOS is enhanced with respect to the value $(k_B T/e)\mu$, which would be expected in the absence of disorder by a factor that increases with increasing carrier concentration (see Figure 1 in Ref. [35]). The enhancement is precisely equal to a factor of 2 for the concentration at which $E_F = E_0/2$ (see Appendix A in Ref. [35]), where E_0 is the thermal equilibrium energy given by Eq. (6.2). This characteristic concentration is relatively large, ranging from $\sim 10^{-1}$ to $\sim 2 \mid 10^{-3}$ for $\hat{\sigma} = 3$ and 6, respectively. As in OLEDs the carrier density is generally smaller, except in certain cases at the electrodes and near-internal interfaces, the effect on the $J(V)$ curves is in practice quite moderate. However, it affects the low-voltage parts of the curves and the effective onset voltage.

Second, the effect of disorder on the carrier density boundary conditions should be taken into account. As suggested in Refs. [35, 75], this may be done by assuming (again) thermal equilibrium at the electrode interfaces. The carrier density boundary condition for the case of a Gaussian DOS with width σ and site density N_t is then given by the Gauss–Fermi integral:

$$n_0 = \int_{-\infty}^{\infty} \frac{N_t}{\sqrt{2\pi\sigma^2}} \frac{\exp\left(-(E^2/2\sigma^2)\right)}{1+\exp\left((E+\Delta_{0,\mathrm{eff}})/(k_\mathrm{B}T)\right)} \mathrm{d}E \tag{6.21}$$

where $\Delta_{0,\mathrm{eff}}$ is obtained from the self-consistently determined electric field using Eq. (6.16) when $F_0 > 0$. When $F_0 < 0$, a situation that arises as a result of charge-carrier diffusion in the case of sufficiently small barriers, no image charge correction will be included. In another way, an image potential effect is then still taken into account, viz. as the laterally uniform space charge density gives rise to a surface charge density on the electrodes. The effect of disorder on n_0 is twofold. First, at a given temperature and injection barrier, it gives rise to a larger value of n_0, due to the filling of low-energy tail states. A higher value of the injection barrier is then needed to enter the ILC regime. Second, it may be readily verified that the decrease of n_0 with decreasing temperature is much smaller than that in the absence of disorder, which is again consistent with the picture that the effective activation barrier for injection is smaller than that in the absence of disorder. These effects were already predicted by Arkhipov *et al.* [76], although the temperature dependence of the predicted current density is not in good agreement with the results of more recent 3D device modeling [75]. The strong effect of disorder on the temperature dependence of the transport in the ILC regime was demonstrated experimentally by van Woudenbergh *et al.* in a study of PPV-based devices [77]. We refer to the publications mentioned above for the technical details of the 1D simulations, and focus in this section on the results of calculations for model systems.

Figure 6.9 shows the effect of including disorder on the current density of a symmetric single-carrier device ($V_{\mathrm{bi}} = 0$) with essentially ideal contacts, as obtained from 3D ME modeling [75]. At $V = 0$, the carrier concentration in the center of the device is approximately 10^{-5}. In the case of weak disorder ($\hat{\sigma} = 3$) (Figure 6.9a), this concentration is well within the Boltzmann regime, so that the effect of disorder is visible only at high voltages where the carrier density is outside the Boltzmann regime and where the mobility becomes field dependent. However, in the case of strong disorder ($\hat{\sigma} = 6$) (Figure 6.9b), the carrier density dependence of the mobility already gives at small voltages, in the diffusion regime, rise to a significant increase of the current density compared to the reference constant-mobility case (curve B). It was shown in Ref. [35] that in the latter case, apparent mobilities that vary over more than two orders of magnitude with the layer thickness are obtained if the $J(V)$ curves are (incorrectly) analyzed using the drift-only Mott–Gurney formula. Meaningful analyses of transport in OLED materials should thus take the carrier density and field dependence of the mobility induced by the disorder into account.

Figure 6.10 (full curves) shows the effect of disorder on the current density in asymmetric single-carrier devices, with an ideal injecting contact at $x = 0$ and a 1 eV barrier at the exit contact, so that $V_{bi} = 1$ V. In this case, the linear current density in the diffusion regime is determined by the carrier density at the exit contact [35], which from Eq. (6.21) can be shown to increase with increasing disorder. The figure furthermore shows that with increasing disorder, the effective current density onset voltage shift, caused by the diffusion of charge near the injecting electrode (Section 6.4.2), increases. This is consistent with experimental analyses. For example, electroabsorption [68] experiments on a polyfluorene-based copolymer with $\hat{\sigma} \cong 5.1$ have revealed shifts of approximately 0.6 V.

Gaussian disorder has also a strong effect on the current density and recombination profile in double-carrier devices [72]. As an example, Figure 6.11 shows

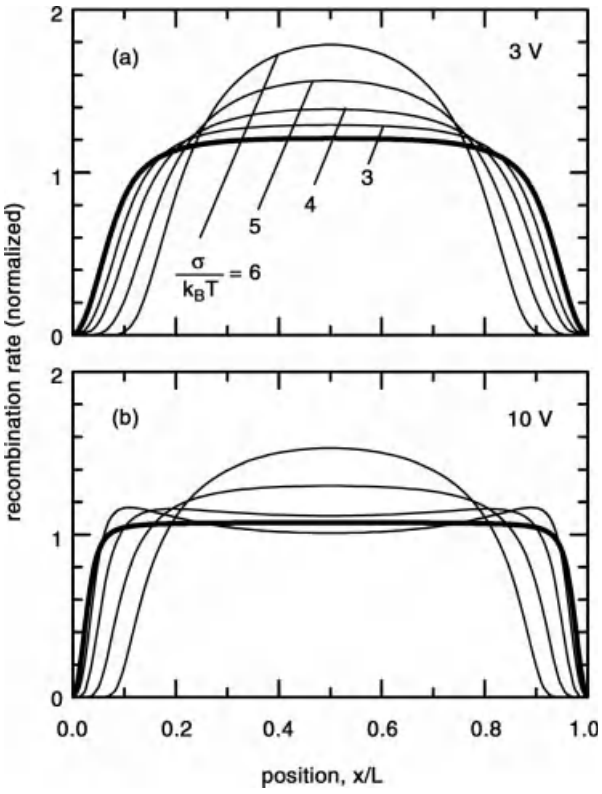

Figure 6.11 Position dependence of the normalized recombination density in symmetric 100 nm OLEDs with a Gaussian electron and hole DOS with various values of $\hat{\sigma}$ (thin full curves) and for the case of a constant mobility with $\mu = \mu_{0,EGDM}$ (thick full curve). No electron and hole barriers at the injecting contacts. Parameter values used are $N_t = 1 \times 10^{27}$ m^{-3}, $V_{bi} = 2$ eV, $\varepsilon_r = 3$, and $T = 298$ K. Taken from Ref. [72].

the calculated recombination profiles (thin curves) as a function of the disorder parameter for 100 nm symmetric OLEDs with ideal contacts and equal electron and hole mobilities, at 3 V and 10 V. The thick curves show for comparison the profiles in the absence of disorder. As a result of charge-carrier diffusion and the assumption of thermal equilibrium at the interfaces, the recombination rate goes to zero in thin regions near the electrodes. It may be seen that the effect of diffusion is more important at low voltage. In the center of the device, the recombination rate is uniform, as expected from the drift-only Parmenter–Ruppel theory (Section 6.4.1). The effect of disorder is seen to depend on the detailed conditions. In the case of weak disorder and a large voltage, the field dependence of the mobility gives rise to a double-peaked profile, as known already for materials with a Poole–Frenkel-type mobility [78]. The carrier density in the device center (where the field is largest (Eq. (6.17c)) is then relatively small, due to the mobility enhancement, so that the recombination becomes largest in regions more close to the electrodes. Upon the introduction of strong disorder, the recombination profile becomes more confined to the device center. This striking effect is a result of the carrier density dependence of the mobility. At either side of the device center, the carrier densities are strongly unbalanced, as may be already seen from Eqs. (6.17a) and (6.17b)). In the case of disorder, this effect is enhanced as the mobility then drops strongly for those carriers that have just passed the device center, entering a low-density region. On the other hand, the mobility of the other carrier then increases. Therefore, most carriers that just passed the device center will recombine quickly. In the same study, disorder was found to have a strong effect on the emission profiles in devices with unequal hole mobilities. Surprisingly, stronger disorder was found to give rise to *wider* profiles, less strongly confined to a narrow region close to one of the electrodes.

In Ref. [72], the disorder was also found to have a strong effect on the current density. Although the Parmenter–Ruppel theory would predict that the current density in double-carrier devices is enhanced by a factor of 2.88 compared to that in otherwise identical single-carrier devices, the enhancement factor as calculated for the case $\hat{\sigma} = 6$ is almost a factor of 8. The effect was shown to be to a large extent due to the enhanced carrier density and field in the device center as a result of the disorder and the corresponding mobility enhancement.

6.4.4
The Role of Gaussian Disorder: Three-Dimensional Device Simulations

The emergence of a filamentary current density as a result of energetic disorder has been revealed from various three-dimensional studies, for example, for systems with a uniform field and a uniform (average) carrier density [16, 79], in studies of the injection from a metallic electrode [80], of the unipolar [81] and bipolar [82] transport across organic–organic heterojunctions, and in devices with two metallic electrodes with varying injection conditions [75, 83]. The filamentarity is strongest at small fields, decreases with increasing field, and vanishes at very high fields when almost all forward hops are "downhill" so that

disorder has no effect anymore on the hop rates [16, 79]. The filamentarity resulting from injection into a system with correlated disorder is much stronger than that for the case of spatially random disorder [80]. In case of charge transport across an organic–organic interface, with a step in the average onsite energies, a thin highly charged layer will be present just in front of this step. Because of the steep gradients in the carrier density, the usual continuum approaches for charge transport break down and one has to resort to Monte Carlo approaches in which the Coulomb interaction between the carriers is explicitly accounted for [81]. The Coulomb repulsion in this thin layer pushes away the charges from each other, leading to charge ordering. The reduced charge density around a specific charge leads to an electric field felt by that charge that is much smaller than that in the case of a continuum treatment, in which charges are assumed to be smeared out in this layer [81]. In condensed matter theories, this would be called a "self-energy" effect. We expect that by accounting for this effect, it might be possible to construct continuum theories that do properly describe the current across organic–organic interfaces.

Jurić *et al.* [82] investigated the effect of 3D disorder on the recombination rate near an organic–organic heterojunction at which there are equal hole and electron barriers. With increasing disorder energy, a decreased effective recombination cross section at the barrier (leading to exciton or exciplex charge pairs) was found, as may be expected from the presence of rare low-energy states that lead to an increased transmission probability through the barrier. A similar effect was found when comparing the transmission through a molecularly sharp interface and through an interface with one or two mixed interface layers.

Important questions to be solved are to what extent the current density, recombination profiles, and other observables predicted from such 3D calculations can be obtained as well from 1D device simulations, and to what extent the filamentarity of the current density gives rise to statistical variations. For the case of single-layer devices, this issue has been studied by van der Holst *et al.* [75]. Figure 6.12 shows the three-dimensional current density across 22 nm thick symmetric single-carrier devices with a 1 eV injection barrier, studied at room temperature at 2 V using a 3D ME approach. The calculation was done for a box with $13 \times 50 \times 50$ sites on a cubic grid, with periodic boundary conditions in the lateral direction. The intersite distance is 1.6 nm. The figures show that the current density is already weakly filamentary for $\sigma = 75$ meV, and becomes strongly filamentary for $\sigma = 150$ meV. In the latter case, almost all the current flows through a relatively small number of sites.

As a consequence of the filamentarity of the current density, the total current through a certain small area varies statistically. Figure 6.13 shows the current density distributions for the same $80 \times 80\,\text{nm}^2$ devices as studied in Figure 6.12, as obtained using the ME model (light gray) and as obtained using the Burin–Ratner (BR) ILC model (dark) within which the current density is viewed as a sum of strictly one-dimensional filaments [84]. For $\sigma = 75$ meV, the current density distribution is relatively narrow. It is centered around the average current density (arrow in the figure), with a full width at half maximum equal to

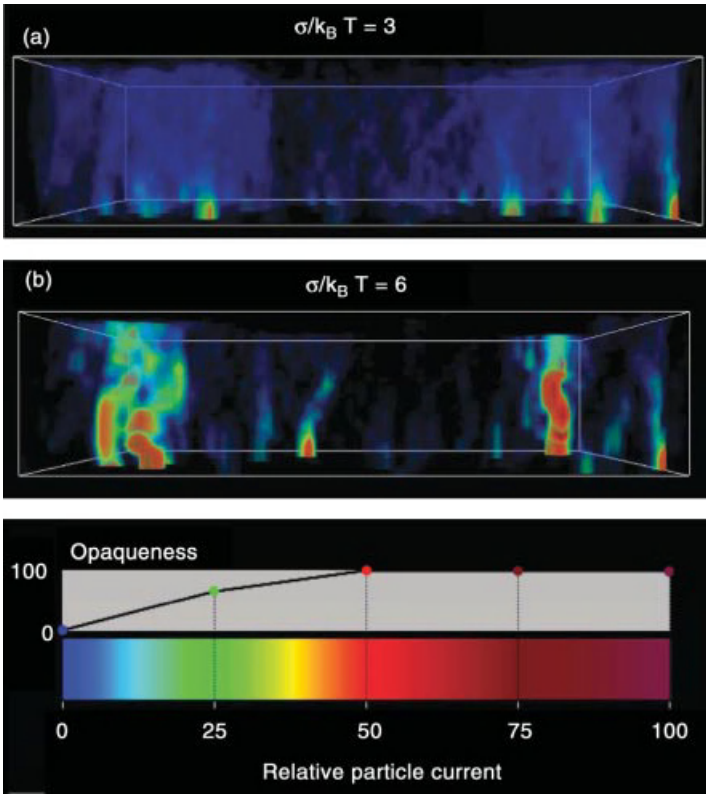

Figure 6.12 Filamentary current densities at room temperature as obtained from 3D ME calculations in single-carrier devices based on organic semiconductors with a Gaussian DOS with (a) $\sigma/(k_BT) = 3$ and (b) $\sigma/(k_BT) = 6$, that is, for $\sigma = 0.075$ eV and 0.15 eV, respectively. The calculations were carried out for symmetric 22 nm devices, with 1 eV injection barriers and intersite distance $a = 1.6$ nm, at $V = 2$ V. The figures show the local current density with respect to the average current density, using a color scheme and opaqueness as given in part (c) of the figure. The boundaries of the part of the device considered, with dimensions $80 \times 80 \times 22$ nm^3, are shown as a white box. Taken from Ref. [75].

approximately 40% of the average current density. In contrast, for $\sigma = 150$ meV, the distribution is quite asymmetric, with a long high-current tail. In the ensemble of 3200 samples studied, even a case with a current density slightly larger than 40 times, the average value was found. In both cases, the distributions as obtained using the BR model were found to be displaced to lower current densities, showing that the actual filaments are not strictly one dimensional and that side jumps play a role.

Figure 6.14 gives an analysis of the current density calculated as a function of the injection barrier using various methods. The 1D continuum model (full curve) yields for $\sigma = 75$ meV an excellent approximation to the results of the 3D ME method (full spheres) if the image charge effect is included when $F_0 > 0$

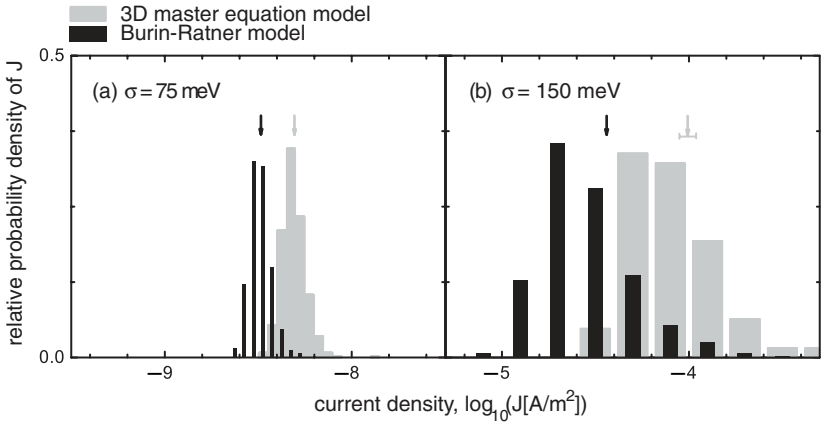

Figure 6.13 Probability distribution of the average current density J in $80 \times 80\,\mathrm{nm}^2$ single-carrier devices, as discussed in Figure 6.12, with (a) $\sigma/(k_BT) = 3$ and (b) $\sigma/(k_BT) = 6$. The gray (black) distributions were obtained from 3D ME calculations and from the Burin–Ratner model within only 1D filaments, respectively, by calculating J for large ensembles of devices with site energies taken randomly from a Gaussian DOS. Their width is seen to increase with increasing disorder. Arrows indicate the ensemble-averaged current densities. Taken from Ref. [75].

(Section 6.4.3). For $\sigma = 150\,\mathrm{meV}$, the overall trend is excellent, but in the SCLC and ILC regimes, the continuum model underestimates the current density by a factor of $\sim$4 and $\sim$8, respectively. The discrepancy observed for the ILC regime has been attributed to a breakdown of the mobility concept: the assumption, underlying the 1D calculations, of a local mobility that varies continuously breaks down for thin devices [83]. For thicker (102 nm) devices, the agreement was found to be excellent. Concerning the SCLC regime, it should be noted that within both methods, the image charge effects were treated in an approximate way. In the 3D ME model, a layer-averaged potential was calculated from the laterally averaged charge density, and a site-specific image potential correction was added to the energy at each site. In the 1D continuum model, no image potential correction to the injection barrier was made in the SCLC regime. Within a more recent MC study for the same devices, no such approximations were made [83]. The open spheres show the results obtained for four values of the injection barrier. At 2 V, the current density is for $\Delta = 0$, and for $\sigma = 75\,\mathrm{meV}$ it was found to be only $\sim$25% *smaller* than the 1D continuum model result; whereas for $\sigma = 150\,\mathrm{meV}$, the discrepancy at 2 V was found to be even smaller. Apparently, the 1D continuum model provides a rather good approximation, although improvements would still be required when using it, for example, for the purpose of accurate parameter extraction. In particular, refined modeling to remove the unphysical discontinuity in the slope of the $J(\Delta)$ curves at the cross-over from the SCLC regime to the ILC regime (Figure 6.14, arrows) would be needed.

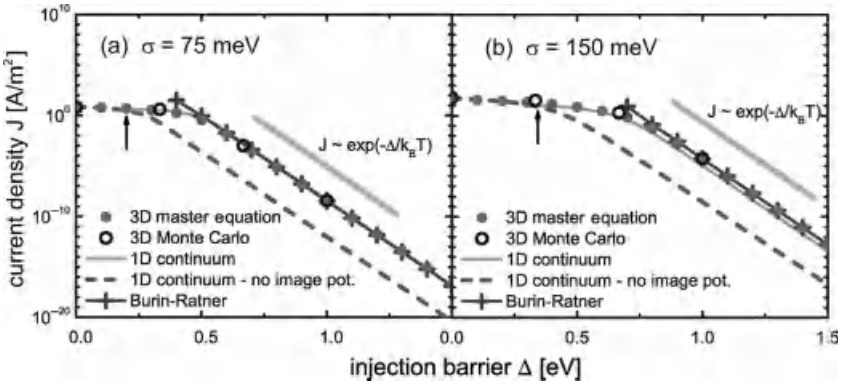

Figure 6.14 Dependence of the current density J on the injection barrier Δ as obtained from 3D ME calculations (full spheres) [75] and from 3D MC calculations within which no approximation concerning short-range Coulomb interactions are made [85] (open sphere). The parameters used are the same as in Figure 6.12. For comparison, the current density is shown as obtained from 1D continuum drift-diffusion modeling using the EGDM with (full curve) and without (dashed curve) the image potential effect (taken from Ref. [75]) and from the Burin–Ratner model (1D filaments) [84]. The crossover points between the SCLC and ILC regimes are indicated by arrows. As shown by the gray line, the $J(V)$ curves are deep in the ILC regime proportional to $\exp[-\Delta/(k_BT)]$.

6.5 Experimental Studies

6.5.1 Overview

The theoretical discussion on the device physics of OLEDs, presented in the previous section, has made clear that the effects of disorder can be strong, so that they cannot be neglected when developing a predictive model. The second-generation modeling methods, based on the EGDM or the ECDM, take the effects of Gaussian disorder into account. An important consequence is that, in practice, no simple relationship between the directly measured observables and the parameters describing the mobility function exists. The Mott–Gurney square law, for example, cannot be used as a simple means for deducing the mobility. It does not include the effect of diffusion and it disregards the fact that the mobility is actually a complex function that in sandwich-type devices is position dependent and that varies as a function of the voltage due a field and carrier density dependence. Methods used to determine the OLED materials parameters are therefore nowadays based on least-squares fitting algorithms [28, 29]. Such approaches are already used successfully in many other fields in which inverse problems are solved, for example, seismology and 3D X-ray medical imaging, but they have only recently emerged in the field of OLED materials parameter extraction. In its generalized form, the outcome of a

parameter extraction procedure is a set of optimal parameters plus a covariance matrix stating the uncertainties of each parameter and their correlation coefficients [86]. A similar inverse approach is also needed for obtaining other information about the functioning of OLEDs. The internal recombination profile, for example, may be deduced using least-squares algorithms from the complete wavelength, angular and polarization-dependent emission intensity [85, 87]. Simulation-assisted methods are also needed for deducing the built-in voltage from the results of $C(V)$ measurements or electroabsorption measurements (Section 6.4.2).

Traditionally, the mobility in OLED materials has often been studied using TOF measurements [10]. In such experiments, the carrier concentration used is relatively small, typically 10^{-5}. One has to carefully judge in each case whether the transport in the Boltzmann regime is probed, yielding correctly $\mu_{0,\mathrm{EGDM}}$ or $\mu_{0,\mathrm{ECDM}}$, or whether an error is made due to the carrier density dependence of the mobility outside that regime. Clear evidence for such an error was found for the case of a TOF study of host–guest systems, providing a solution to a previously puzzling guest concentration dependence of the mobility [42]. It is now evident that the TOF mobility cannot be used in predictive OLED models, as it provides at best a lower limit to the real, concentration-dependent mobility. A further complication, which arises in any transient experiment, is the role of charge-carrier relaxation [32]. As a result of a sudden increase of the carrier density in a disordered organic semiconductor, the mobility is initially high, and decreases subsequently due to energetic relaxation to lower energy states. The effect is directly observable as a time dependence of the mobility in TOF experiments, and will also affect the analysis of other transient experiments. It has been demonstrated recently for the case of capacitance–voltage experiments how the effect can be included as an extension of the EGDM in device modeling, without the introduction of additional parameters [88].

For all these reasons, we do presently regard the use of steady-state $J(V)$ measurements on sandwich-type devices, carried out for a wide range of voltages, temperatures, and layer thicknesses, as the preferred method for determining the validity of the EGDM or the ECDM (including if needed a trap distribution) and for deducing the EGDM or ECDM parameters. In Table 6.1, an overview is given of such studies, performed so far only for a small number of polymers and small-molecule systems. Examples of systems studied are the copolymer PF–TAA (Section 6.5.2) and the small-molecule materials α-NPD [89] and BAlq [90]). The picture that emerges, based on this limited work, is as follows:

1) EGDM and ECDM are more appropriate to polymers and small-molecule materials, respectively. However, it is not clear how general this is. In all the cases studied, a distinction between both models has been made from the hopping site density N_t as obtained from an analysis of a large set of measured $J(V)$ curves for various layer thicknesses and temperatures. For the small-molecule materials α-NPD and BAlq, for example, an ECDM analysis was found to yield

Table 6.1 Examples of analyses of the charge-carrier mobility and OLED luminance using second-generation OLED modeling.

Material	Carrier	Methods	References
PF–TAA	Holes	Analysis of $J(V)$ curves, EGDM, and ECDM	[20, 91]
PF–TAA	Holes	Analysis of built-in voltage using electroabsorption and capacitance–voltage measurements, EGDM	[68]
PF–TAA	Holes	Charge-carrier relaxation	(Germs, W.Chr., van der Holst, J.J.M., van Mensfoort, S.L.M., Bobbert, P.A., and Coehoorn, R. (unpublished).)
PF–TAA	Electrons	Analysis of $J(V)$ curves, EGDM + traps	[92]
PF–TAA	Double carrier	Predictive OLED modeling: analysis of $J(V)$ curves, luminous efficiency, and emission profile	[53]
PF–TAA	Double carrier	Measurement of singlet exciton fraction and emission profile modeling	[93]
PFB, F8BT	Holes	Analysis of $J(V)$ curves, EGDM. Polyfluorene-based polymers	[94]
α-NPD	Holes	Analysis of $J(V)$ curves, EGDM, and ECDM	[89, 95]
BAlq	Electrons	Analysis of $J(V)$ curves, EGDM, and ECDM	[90]

values of N_t within a factor of ∼2 from the known molecular density. For some materials, a consistent model could not yet be obtained [94].

2) For describing hole transport, a Gaussian density of states is found most appropriate, whereas for electron transport, a density of states formed by the superposition of a Gaussian and an exponential DOS is often used. The nature of the (additional) exponential DOS for electrons (intrinsic or extrinsic trap states?) is yet not known.
3) The size of injection barriers is often *a priori* not very clear due to uncertainties related to the interpretation of spectroscopic measurements and due to the possible formation of interface dipole layers, for example, due to the presence of a net polarization of organic thin film [96]. It is therefore advantageous to make use of symmetric sandwich-type devices within which the electrodes are made of equal and highly conductive molecularly n- or p-doped layers with small injection barriers [95].
4) So far no *direct* methods have emerged from which the shape of the (tail of the) DOS can be deduced from experiment with sufficient (∼10 meV) accuracy.

In Section 6.5.2, a full model based on experimentally determined mobility functions is discussed for the case of a single-layer blue-emitting OLED based on the copolymer PF–TAA. The second-generation modeling of full multilayer white OLEDs, also based on separately measured electron and hole mobility functions for each of the layers, is in progress.

6.5.2
PF–TAA-Based Polymer OLEDs

Intensive studies have been carried out of the effects of disorder on the charge-carrier transport in blue-emitting polyfluorene–(7.5 mol% triarylamine) (PF–TAA) copolymers, from the Lumation™ Blue Series commercially available from Sumation Co., Ltd. The structure of these copolymers is given as an inset in Figure 6.15 and a schematic energy level scheme is given in the top part of Figure 6.16 for the hole-only (HO) and electron-only (EO) devices studied. The hole transport is due to hopping in between the TAA units, whereas the electron transport is due to hopping via the PF–LUMO states. Experimental evidence that for the 7.5% concentration used, the hole transport is in the guest–guest hopping regime has been obtained from a study of the current density of otherwise identical devices as a function of the TAA concentration, shown in Figure 6.15 [91]. The presence of the TAA units gives rise to an improved efficiency by (a) facilitating the injection of holes (there is a ∼0.6 eV injection barrier from the PEDOT:PSS anode to the polyfluorene HOMO states) and (b) by reducing the hole mobility so that it is better

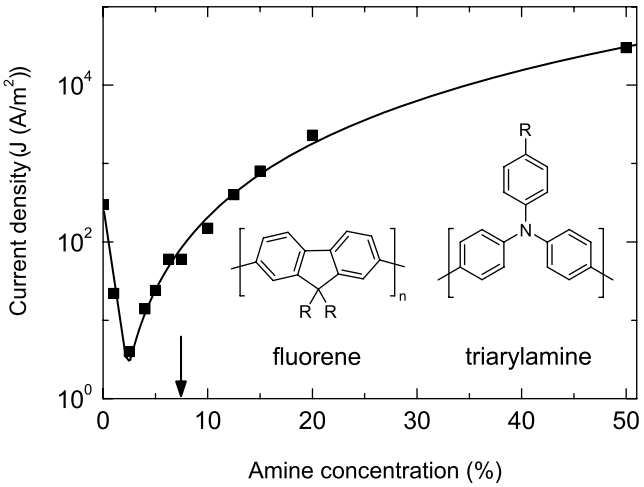

Figure 6.15 Current density in hole-only PEDOT:PSS/80 nm PF–TAA/Au devices, measured at 6 V, as a function of the triarylamine (TAA) concentration. The inset shows the structure of the fluorene and TAA monomer units of which the random copolymer is comprised. The arrow shows the 7.5% concentration used in the study discussed in this section. Taken from Ref. [91].

balanced with the electron mobility. Studies on similar types of OLEDs were reported in Refs. [97, 98].

Based on separate EGDM hole-only [20] and electron-only [92] device studies, a combined experimental and modeling study of the current density and luminous efficacy of double-carrier devices was recently presented by van Mensfoort *et al.* [53]. The devices studied were as follows:

HO: Glass/ITO/PEDOT:PSS/PF–TAA/Pd
EO: Glass/AlO_x/PF–TAA/LiF/Ca/Al
DC: Glass/ITO/PEDOT:PSS/PF–TAA/LiF/Ca/Al

Figure 6.16a and b show that for the HO devices, the conventional model (including diffusion but neglecting the carrier concentration dependence of the mobility and assuming a PF field dependence) would lead to a rather good fit at room temperature, but that a clear inconsistency is found when studying the layer thickness dependence at low temperatures. In contrast, the $J(V)$ curves were found to be described excellently using the EGDM, as shown in Figure 6.16c and d. Similarly,

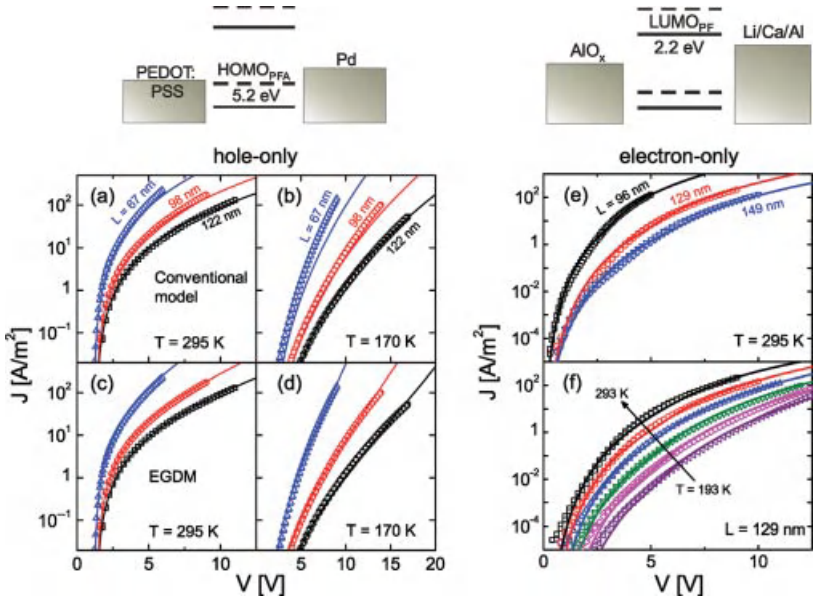

Figure 6.16 (a–d) Measured (symbols) and calculated (curves) hole-only $J(V)$ curves for PF–TAA-based devices, analyzed using the conventional model (a and b) and the EGDM (c and d) [20]. (e and f) Measured (symbols) and calculated (curves) electron-only $J(V)$ curves for PF–TAA-based devices, analyzed using the EGDM including an exponential trap DOS [92]. The top parts of the figure show the device structures used and a schematic energy level scheme in which the full (dashed) lines indicate PF- and TAA-based states. The energies of the PF-derived HOMO states and TAA-derived LUMO states are approximately 5.8 and 1.6 eV, respectively, with respect to the vacuum level [99]. Figure 6.17 gives the parameter values used.

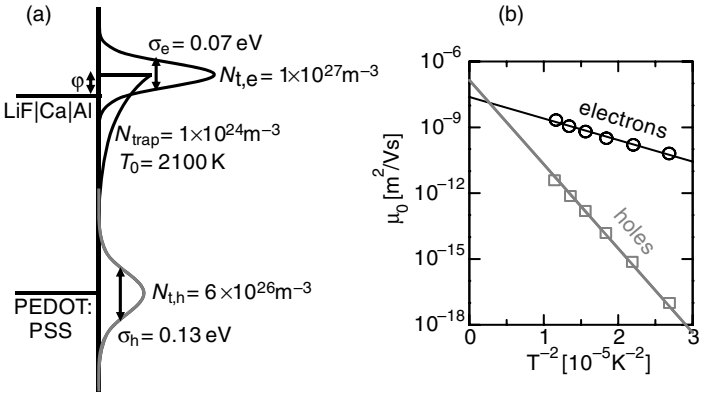

Figure 6.17 (a) Parameter values describing the hole (gray) and electron (black) DOS of PF–TAA. (b) Temperature dependence of the mobility in the low-density and zero-field limit, $\mu_{0,\mathrm{EGDM}}$, as obtained from analyses of $J(V)$ curves (see Figure 6.16) [20, 92]. Taken from Ref. [53].

the EGDM was found to provide a good description of the $J(V)$ curves of the EO devices, as shown in Figure 6.16e and f for three-layer thicknesses and for a range of temperatures, provided that in addition to the Gaussian DOS, an additional exponential density of low energy (trap) states was assumed. In Figure 6.17a, an overview is given of the parameters describing the shapes of the HOMO and LUMO densities of states. The analysis revealed hole and electron injection barriers from the PEDOT:PSS and LiF/Ca/Al electrodes equal to $\sim$0 eV and 0.3 ± 0.1 eV, respectively.

The width of the hole DOS, $\sigma_{\mathrm{h}} = 0.13 \pm 0.01$ eV, is close to the value obtained for two different PPV derivatives [18]. The HOMO site density obtained, $N_{\mathrm{t,h}} = (6 \pm 1) \times 10^{26}\,\mathrm{m}^{-3}$, may be compared with the estimated TAA volume density, $\sim 1.8 \times 10^{26}\,\mathrm{m}^{-3}$ [99]. De Vries *et al.* [91] showed that an analysis within the framework of the ECDM could provide an equally good fit to the data, for all layer thicknesses and temperatures, with $\sigma_{\mathrm{h}} = 0.085 \pm 0.005$ eV and $N_{\mathrm{t,h}} = (5 \pm 2) \times 10^{27}\,\mathrm{m}^{-3}$. This showed that a successful analysis of the $J(V)$ curves using the EGDM or the ECDM by itself does not yet convincingly prove that the disorder is completely random or correlated. However, the large value obtained using the ECDM for N_{t}, more than one order of magnitude larger than the estimated experimental value, was argued to provide a clear indication that for PF–TAA, the site energies are uncorrelated. In the same study, it was shown that, in general, the EGDM and the ECDM lead to distinctly different predictions concerning the mobility in devices in which large carrier densities can occur, for example, in OLEDs with internal interfaces at which blocking takes place.

For the case of electron transport, van Mensfoort *et al.* [92] observed that the width of the Gaussian DOS, 0.07 ± 0.02 eV, is significantly smaller than that of the hole DOS. It coincides with the 0.07–0.10 eV range reported for *hole* transport in poly-octyl-fluorene (PFO) [100, 101]. This is consistent with the point of

view that the electron transport is due to hopping in a Gaussian DOS formed by the PF-derived LUMO states, with a width of the DOS similar to that of the PF-derived HOMO states in a polymer that does not contain TAA units. The site density obtained, $N_{t,e} = (1.0 \pm 0.5) \times 10^{27}\,m^{-3}$, is consistent with the estimated average intersite distance $a \approx 1.1\,nm$ as obtained from the volume density of fluorene monomer units in PF–TAA. The authors demonstrated that the electron transport could not be described properly without the assumption of the presence of an additional trap DOS. As shown in Figure 6.17a, the authors assumed an exponential electron trap DOS of the form $g(E) = N_{trap}/(k_B T_0)\ \exp[E/(k_B T_0)]$. Following the earlier literature, the $1/e$ decay length is expressed as $k_B T_0$, with T_0 being the "characteristic trap temperature." In the figure, the trap DOS is strongly enlarged in order to make it clearly visible. Only the low-energy tail of the trap states is relevant to the transport process. At higher energies, the large Gaussian DOS dominates. The detailed shape of the trap DOS in that energy region is not probed by transport measurements. In the figure, we have depicted the trap DOS as if it continues until the top of the Gaussian DOS. N_{trap} is then equal to the total volume density of trap states. With no consequence to the predicted transport properties, it would be possible to assume a different shape of the part of the exponential DOS in the energy region in which it is buried under the high Gaussian DOS, for example, by choosing a cutoff at a lower energy or by assuming a peak in the trap DOS [102]. That was not done in order to avoid the introduction of additional parameters that could not be validated experimentally. The parameter values describing the trap DOS, $N_{trap} = (1.0 \pm 0.5) \times 10^{24}\,m^{-3}$ and $T_0 = 2100 \pm 300\,K$, are similar to the values obtained in previous reports on a variety of organic semiconductors.

Figure 6.17b shows the temperature dependence of μ_0, the mobility in the limit of zero carrier density and field. As expected from the EGDM, it varies with temperature as $\exp[-C \cdot \hat{\sigma}^2]$, with a slope parameter C equal to 0.39 ± 0.01 for hole transport [20] and 0.34 ± 0.10 for electron transport [92]. Both values are consistent with the range of values of 0.38–0.46, following from semianalytical percolation theory (Section 6.4) [19], depending on the wave function decay length.

A comparison of the current–voltage curves of the HO and EO devices shows that the latter curves are much steeper and that for an equal device thickness, the curves cross at a certain voltage. The large slope of the EO curves is the result of the presence of traps, as may be understood semiquantitatively from the (oversimplified) Mark–Helfrich model [58]. For 100 nm single-carrier PF–TAA devices, equal electron and hole current densities are observed at approximately 2.8 V above V_{bi}. The DC devices, with $V_{bi} \approx 3\,V$, would then be expected to be optimally efficient around 6 V. This highly simplified picture was indeed found to provide a useful view on the functioning of these OLEDs, as shown below.

Figure 6.18 shows the experimental and modeling results obtained for the DC devices with a 100 nm PF–TAA layer. Figure 6.18a shows that for a wide range of temperatures, the measured current–voltage curves (symbols) are in excellent agreement with the prediction (full curves) from a 1D ME double-carrier OLED

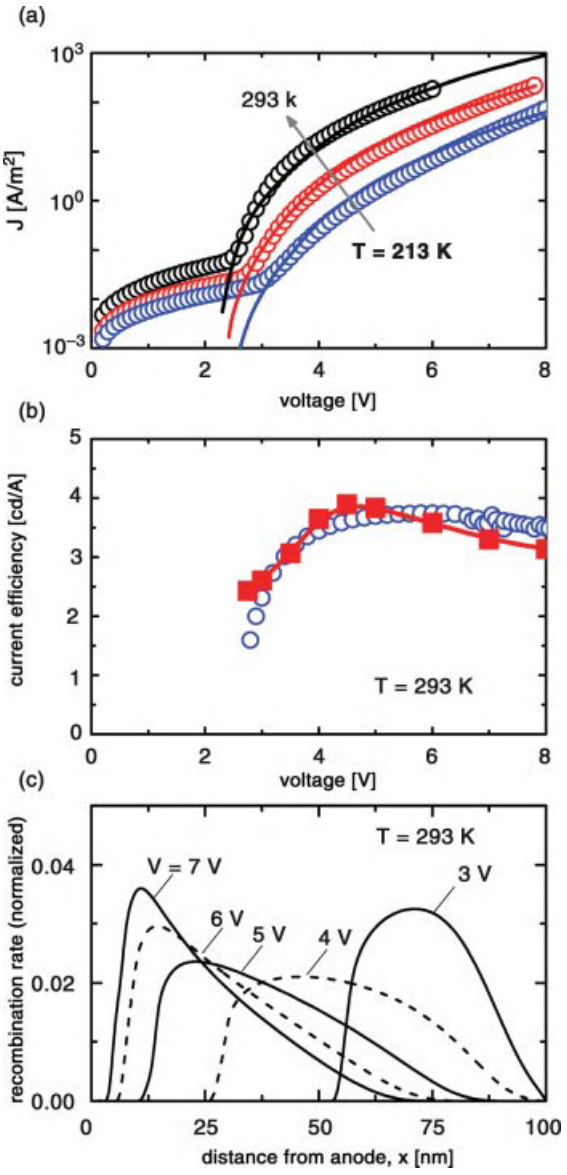

Figure 6.18 (a) Measured (open spheres) and calculated (solid curves) $J(V)$ curves for 100 nm PF–TAA-based double-carrier devices at $T = 293$, 253, and 213 K. (b) Measured (open spheres) and calculated (closed squares, connected by a solid curve) current efficiency as a function of the applied voltage at 293 K. (c) Calculated normalized recombination rate distributions at 293 K at various voltages. Taken from Ref. [53].

model using the electron and hole mobility functions obtained from the separate studies discussed above. Langevin recombination was assumed, including recombination of holes with trapped electrons as described in Section 6.3.2. Figure 6.18b shows the current efficiency at room temperature, as measured (open spheres) and predicted (closed squares) for the case of perpendicular emission. The emission was obtained from the calculated voltage dependence of the recombination profile, using an optical microcavity light outcoupling model (LIGHTEX) [103] in a manner described in detail in Ref. [53]. Only the fraction of singlet excitons formed was regarded as a free parameter. The best fit, shown in the figure, yielded $\eta_S = 22\%$, very close to the quantum statistical value of 25% and within the interval obtained from an independent study for the same material yielding 10–25% [93]. The figure shows that the model excellently predicts the measured maximum in the current efficiency, and it explains this maximum as the result of a voltage dependence of the light outcoupling efficiency. As shown in Figure 6.18c, the emission profile is predicted to shift from a region more close to the cathode at low voltages to a region more close to the anode at high voltages. At intermediate voltages, the recombination is least quenched due to the presence of nearby electrodes. The light outcoupling efficiency and hence the current efficiency are then largest. This shows that predictive one-dimensional device modeling of OLEDs is feasible.

6.6 Conclusions and Outlook

On the basis of 3D master equation and Monte Carlo modeling, we have developed a set of compact expressions describing the temperature, electric field, and charge-carrier density dependence of the mobility in organic semiconductors for the cases of random and spatially correlated Gaussian disorder. The resulting EGDM and ECDM mobility models are the basis of "second-generation" OLED device models, which also include the consequences of the disorder on the recombination rate (bipolar mobility) (Section 6.3), the injection from the electrodes, and the transport across internal organic–organic interfaces. The commercial second-generation simulation tools have recently become available [28, 29]. In order to theoretically validate these OLED device models, the 1D modeling results were compared with the results of 3D modeling of complete devices including the effects of energetic disorder, injection barriers, and short-range Coulomb interactions on the current density and showing its filamentarity. Furthermore, experimental validation studies using steady-state $J(V)$ curves of single-carrier devices were carried out for various OLED-relevant materials. Predictive EGDM-based OLED modeling was demonstrated for single-layer OLEDs based on a blue-emitting copolymer. We find that extending the 3D simulations to complete multilayer OLEDs, including the effects of internal interfaces and of fluorescent or phosphorescent emitters, is computationally feasible

(van der Holst, J.J.M., van Oost, F.W.A., Cottaar, J., Mesta, M., Coehoorn, R., and Bobbert, P.A. (unpublished)). That work is beyond the scope of the present chapter, and will be reported elsewhere.

Even if a complete theoretical framework is available for describing the mobility in OLED materials, the development of an accurate description of the mobility function of a specific novel material has turned out to be more involved than was thought some years ago. Due to the carrier density dependence of the mobility and the role of diffusion, often-used simple analytical expressions describing the steady-state or transient current density are usually not applicable. Simulation-assisted parameter extraction methods are required, making use of data sets that are sufficiently "rich" by including experimental results for at least a wide range of voltages, temperatures, and layer thicknesses, and if necessary by also including the results of nonsteady-state measurements.

There are several unresolved or only partially resolved issues concerning the description of the mobility in disordered organic semiconductors, such as the occurrence and type of spatially correlated disorder, the microscopic origin of electron trap states, the description of the mobility in host–guest systems at intermediate guest concentrations (as occurring in many phosphorescent OLEDs), the effect on the transport across the interfaces of a net polarization of layers due to nonrandom molecular dipole orientation [24], the effect of disorder on excitonic processes such as diffusion and exciton–exciton or exciton–charge interactions and the relationship between the experimental parameters (σ and μ_0) and the molecular structure and deposition conditions. The development of novel or refined experimental and theoretical methods will therefore be of high value. Within the "third-generation" OLED modeling methodology that we envision (Figure 6.2), the material-specific mobility parameters will be predicted by microscopic modeling of the morphology of OLED materials by molecular dynamics or Monte Carlo methods and the determination of the hopping rates from density functional theory calculations of the charge transfer integrals and reorganization energies. After extending such studies to the interfaces, this will allow fully predictive modeling of the charge transport through OLED devices. A further extension, to include the motion and interactions of singlet and triplet excitons, will open the perspective of obtaining a fully predictive electro-optical OLED model.

The complexity of high-efficiency OLEDs presently grows rapidly due to the use of many layers of different organic semiconductors with specialized functions. As a result, improving the performance of OLEDs using trial-and-error methods is becoming less feasible. We envisage that the use of "second-generation" OLED modeling as described in this chapter can contribute to solving this problem by providing rational design strategies and by providing a predictive description of their functioning, based on measured materials parameters for each layer. The future development of "third-generation" OLED modeling would further contribute by providing deepened insights into the relationships between the molecular and thin-film structure of the organic semiconductors used and the resulting charge transport and excitonic properties.

Acknowledgments

We gratefully acknowledge the contributions to the work presented in this chapter by J. Billen, M. Bouhassoune, M. Carvelli, J. Cottaar, W.Chr. Germs, H. Greiner, J.J. M. van der Holst, H.-P. Loebl, R.A.J. Janssen, S.L.M. van Mensfoort, F.W.A van Oost, W.F. Pasveer, B. Ramachandhran, V. Shabro, R.J. de Vries, S.I.E. Vulto, and Y.Y. Yimer. The research described has received funding from the European Community's Seventh Framework Program under Grant No. 213708 (AEVIOM, contribution R.C.).

References

1 (a) Yoon, C.O., Reghu, M., Moses, D., and Heeger, A.J., (1994) *Phys. Rev. B*, **49**, 10851; (b) Ahlskog, M., Reghu, M., Heeger, A.J., Noguchi, T., and Ohnishi, T. (1997) *Phys. Rev. B*, **55**, 6777.

2 Kwiatkowski, J.J., Nelson, J., Li, H., Bredas, J.L., Wenzel, W., and Lennartz, C. (2008) *Phys. Chem. Chem. Phys.*, **10**, 1852.

3 Nagata, Y. and Lennartz, C. (2008) *J. Chem. Phys.*, **129**, 034709.

4 Marcus, R.A. (1956) *J. Chem. Phys.*, **24**, 966.

5 Barbara, P.F., Meyer, T.J., and Ratner, M. A. (1996) *J. Phys. Chem.*, **100**, 13148.

6 Sakanue, K., Motoda, M., Sugimoto, M., and Sakaki, S. (1999) *J. Phys. Chem. A*, **103**, 5551.

7 Malagoli, M. and Brédas, J.L. (2000) *Chem. Phys. Lett.*, **327**, 13.

8 Coropceanu, V., Cornil, J., da Silva Filho, D.A., Olivier, Y., Silbey, R., and Brédas, J.-L. (2007) *Chem. Rev.*, **107**, 926.

9 Bässler, H. (1993) *Phys. Status Solidi B*, **175**, 15.

10 Borsenberger, P.M. and Weiss, D.S. (1998) *Organic Photoreceptors for Xerography*, Marcel Dekker, Inc., New York.

11 Blom, P.W.M. and Vissenberg, M.C.J.M. (2000) *Mater. Sci. Eng.*, **27**, 53.

12 Pai, D.M. (1970) *J. Chem. Phys.*, **52**, 2285.

13 (a) Schein, L.B., Glatz, D., and Scott, J.C., (1990) *Phys. Rev. Lett.*, **65**, 472; (b) Pautmeier, L.Th., Scott, J.C., and Schein, L.B. (1992) *Chem. Phys. Lett.*, **197**, 568.

14 Vissenberg, M.C.J.M. and Matters, M. (1998) *Phys. Rev. B*, **57**, 12964.

15 (a) Tanase, C., Meijer, E.J., Blom, P.W.M., and de Leeuw, D.M., (2003) *Phys. Rev. Lett.*, **91**, 216601; (b) Tanase, C., Blom, P. W.M., and de Leeuw, D.M. (2004) *Phys. Rev. B*, **70**, 193202.

16 Yu, Z.G., Smith, D.L., Saxena, A., Martin, R.L., and Bishop, A.R. (2001) *Phys. Rev. B*, **63**, 085202.

17 Tessler, N. and Roichmann, Y. (2005) *Org. Electron.*, **6**, 200.

18 Pasveer, W.F., Cottaar, J., Tanase, C., Coehoorn, R., Bobbert, P.A., Blom, P.W. M., de Leeuw, D.M., and Michels, M.A.J. (2005) *Phys. Rev. Lett.*, **94**, 206601.

19 Coehoorn, R., Pasveer, W.F., Bobbert, P. A., and Michels, M.A.J. (2005) *Phys. Rev. B*, **72**, 155206.

20 van Mensfoort, S.L.M., Vulto, S.I.E., Janssen, R.A.J., and Coehoorn, R. (2008) *Phys. Rev. B*, **78**, 085208.

21 Davids, P.S., Saxena, A.S., and Smith, D. L. (1996) *J. Appl. Phys.*, **78**, 4244.

22 (a) Scott, J.C., Brock, P.J., Salem, J.R., Ramos, S., Malliaras, G.G., Carter, S.A., and Bozano, L., (2000) *Synth. Met.*, **111–112**, 289; (b) Ruhstaller, B., Carter, S.A., Barth, S., Riel, H., Riess, W., and Scott, J.C. (2001) *J. Appl. Phys.*, **89**, 4575.

23 Staudigel, J., Stößel, M., Steuber, F., and Simmerer, J. (1999) *J. Appl. Phys.*, **86**, 3895.

24 Brütting, W., Berleb, S., and Mückl, A.G. (2001) *Org. Electron.*, **2**, 1.

25 (a) Houili, H., Tutiš, E., Lütjens, H., Bussac, M.N., and Zuppiroli, L., (2003) *Comput. Phys. Commun.*, **156**, 108–122; (b) Berner, D., Houili, H., Leo, W., and

Zuppiroli, L. (2005) *Phys. Status Solidi A*, **202**, 9.
26 Walker, A.B., Kambili, A., and Martin, S. J. (2002) *J. Phys. B Condens. Matter*, **14**, 9825.
27 Bouhassoune, M., van Mensfoort, S.L. M., Bobbert, P.A., and Coehoorn, R. (2009) *Org. Electron.*, **10**, 437.
28 Simulation software SETFOS3.2 (2011), product of Fluxim (www.fluxim.com).
29 Simulation software SimOLED (2011), product of Sim4tec (www.sim4tec.com).
30 (a) Emin, D., (1975) *Adv. Phys.*, **24**, 305; (b) Emin, D., (1986) *Handbook of Conducting Polymers*, vol. **2** (ed. T.A. Skolheim), Dekker, New York, p. 915; (c) Fishchuk, I.I., Kadashchuk, A., Sudha Devi, L., Heremans, P., Bässler, H., and Köhler, Anna (2010) *Phys. Rev. B*, **78**, 045211.
31 Monroe, D. (1985) *Phys. Rev. Lett.*, **54**, 146.
32 Böttger, H. and Bryksin, V.V. (1985) *Hopping Conduction in Solids*, Akademie-Verlag, Berlin.
33 (a) Baranovskii, S.D., Faber, T., Hensel, F., and Thomas, P., (1997) *J. Phys. Condens. Matter*, **9**, 2699; (b) Baranovskii, S.D., Cordes, H., Hensel, F., and Leising, G. (2000) *Phys. Rev. B*, **62**, 7934.
34 Zhou, J., Zhou, Y.C., Zhao, J.M., Wu, C. Q., Ding, X.M., and Hou, X.Y. (2007) *Phys. Rev. B*, **75**, 153201.
35 van Mensfoort, S.L.M. and Coehoorn, R. (2008) *Phys. Rev. B*, **78**, 085207.
36 Gartstein, Y.N. and Conwell, E.M. (1995) *Chem. Phys. Lett.*, **245**, 351.
37 Dunlap, D.H., Parris, P.E., and Kenkre, V.M. (1996) *Phys. Rev. Lett.*, **77**, 542.
38 (a) Novikov, S.V., Dunlap, D.H., Kenkre, V.M., Parris, P.E., and Vannikov, A.V., (1998) *Phys. Rev. Lett.*, **81**, 4472; (b) Novikov, S.V. and Vannikov, A.V. (1995) *J. Phys. Chem.*, **99**, 14573.
39 Yu, Z.G., Smith, D.L., Saxena, A., Martin, R.L., and Bischop, A.R. (2000) *Phys. Rev. Lett.*, **84**, 721.
40 Pai, D.M., Yanus, J.F., and Stolka, M. (1984) *J. Phys. Chem.*, **88**, 4717.
41 Yimer, Y.Y., Bobbert, P.A., and Coehoorn, R. (2008) *J. Phys. Condens. Matter*, **20**, 335204.
42 Coehoorn, R. (2007) *Phys. Rev. B*, **75**, 155203.
43 (a) Wolf, Y., Bässler, H., Borsenberger, P. M., and Gruenbaum, W.T., (1998) *Chem. Phys.*, **222**, 259; (b) Borsenberger, P.M., Gruenbaum, W.T., Wolf, U., and Bässler, H. (1998) *Chem. Phys.*, **234**, 277.
44 (a) Fishchuk, I.I., Kadashchuk, A.K., Bässler, H., and Weiss, D.S., (2002) *Phys. Rev. B*, **66**, 205208; (b) Fishchuk, I.I., Kadashchuk, A.K., Vakhnin, A., Korosko, Yu., Bässler, H., Souharce, B., and Scherf, U. (2006) *Phys. Rev. B*, **73**, 115210.
45 Arkhipov, V.I., Heremans, P., Emelianova, E.V., Adriaenssens, G.J., and Bässler, H. (2002) *J. Phys. Condens. Matter*, **14**, 9899.
46 Cottaar, J., Coehoorn, R., and Bobbert, P. A. (2010) *Phys. Rev. B*, **82**, 205203.
47 Movaghar, B. and Schirmacher, W. (1981) *J. Phys. C*, **14**, 859.
48 Langevin, M.P. (1903) *Ann. Chim. Phys.*, **28**, 433.
49 Pope, M. and Swenberg, C.E. (1999) *Electronic Processes in Organic Crystals and Polymers*, Oxford University Press, New York.
50 (a) Albrecht, U. and Bässler, H. (1995) *Phys. Status Solidi B*, **191**, 455; (b) Albrecht, U. and Bässler, H. (1995) *Chem. Phys.*, **199**, 207.
51 Groves, C. and Greenham, N.C. (2008) *Phys. Rev. B*, **78**, 155205.
52 J.J.M. van der Holst, F.W.A. van Oost, R. Coehoorn and P.A. Bobbert (2009), *Phys. Rev. B* **80**, 235202.
53 van Mensfoort, S.L.M., Billen, J., Carvelli, M., Vulto, S.I.E., Janssen, R.A.J., and Coehoorn, R. (2011) *J. Appl. Phys.*, **109**, 064502.
54 Kuik, M., Nicolai, H.T., Lenes, M., Wetzelaer, G.-J.A.H., Lu, M., and Blom, P.W.M. (2011) *J. Appl. Phys.*, **98**, 093301.
55 (a) Shockley, W. and Read, W.T., (1952) *Phys. Rev.*, **87**, 835; (b) Hall, R.N. (1952) *Phys. Rev.*, **87**, 387.
56 Lampert, M.A. and Mark, P. (1970) *Current Injection in Solids*, Academic, New York.
57 Kao, K.C. and Hwang, W. (1981) *Electrical Transport in Solids*, Pergamon Press, Oxford.

58 Mark, P. and Helfrich, W. (1962) *J. Appl. Phys.*, **33**, 205.

59 (a) Shao, J., and Wright, G.T., (1961) *Solid State Electron.*, **3**, 291; (b) Kassing, R. (1975) *Phys. Status Solidi A*, **28**, 107.

60 Many, A. and Rakavi, G. (1962) *Phys. Rev.*, **126**, 1980.

61 Parmenter, R.H. and Ruppel, W. (1959) *J. Appl. Phys.*, **30**, 1548.

62 Martin, B.G. (1994) *J. Appl. Phys.*, **75**, 4539.

63 (a) de Levie, R. and Moreira, H., (1972) *J. Membr. Biol.*, **9**, 241; (b) de Levie, R., Seidah, N.G., and Moreira, H. (1972) *J. Membr. Biol.*, **10**, 171.

64 Crăciun, N.I., Brondijk, J., and Blom, P.W.M. (2008) *Phys. Rev. B*, **77**, 035206.

65 Kemerink, M., Kramer, J.M., Gommans, H.H.P., and Janssen, R.A.J. (2006) *Appl. Phys. Lett.*, **88**, 192108.

66 van Mensfoort, S.L.M. (2009) PhD thesis: Effects of disorder on the charge transport and recombination in organic light-emitting diodes. Eindhoven University of Technology.

67 van Mensfoort, S.L.M. and Coehoorn, R. (2008) *Phys. Rev. Lett.*, **100**, 086802.

68 de Vries, R.J., van Mensfoort, S.L.M., Janssen, R.A.J., and Coehoorn, R. (2010) *Phys. Rev. B*, **81**, 125203.

69 Malliaras, G.G., Salem, J.R., Brock, P.J., and Scott, J.C. (1998) *J. Appl. Phys.*, **84**, 1583.

70 Scott, J. and Malliaras, G. (1999) *Chem. Phys. Lett.*, **299**, 115.

71 Shen, Y., Klein, M.W., Jacobs, D.B., Scott, J.C., and Malliaras, G.G. (2001) *Phys. Rev. Lett.*, **86**, 3867.

72 Coehoorn, R. and van Mensfoort, S.L.M. (2009) *Phys. Rev. B*, **80**, 085302.

73 Knapp, E., Häusermann, R., Schwarzenbach, U., and Ruhstaller, B. (2010) *J. Appl. Phys.*, **108**, 054504.

74 Roichman, Y. and Tessler, N. (2002) *Appl. Phys. Lett.*, **80**, 1948.

75 van der Holst, J.J.M., Uijttewaal, M.A., Ramachandhran, B., Coehoorn, R., Bobbert, P.A., de Wijs, G.A., and de Groot, R.A. (2009) *Phys. Rev. B*, **79**, 085203.

76 (a) Arkhipov, V., Emelianova, E., Tak, Y., and Bässler, H., (1998) *J. Appl. Phys.*, **84**, 848; (b) Arkhipov, V., Wolf, U., and Bässler, H. (1999) *Phys. Rev. B*, **59**, 7514.

77 van Woudenbergh, T., Blom, P.W.M., Vissenberg, M., and Huiberts, J. (2001) *Appl. Phys. Lett.*, **79**, 1697.

78 (a) Crone, B.K., Davids, P.S., Campbell, I. H., and Smith, D.K. (1998) *J. Appl. Phys.*, **84**, 833; (b) Konezny, S.J., Smith, D.L., Galvin, M.E., and Rothberg, L.J. (2006) *J. Appl. Phys.*, **99**, 064509.

79 Meisel, K.D., Pasveer, W.F., Cottaar, J., Tanase, C., Coehoorn, R., Bobbert, P.A., Blom, P.W.M., de Leeuw, D.M., and Michels, M.A.J. (2006) *Phys. Status Solidi C*, **3**, 267.

80 Tutiš, E., Batistić, I., and Berner, D. (2004) *Phys. Rev. B*, **70**, 161202(R).

81 Houili, H., Tutiš, E., Batistić, I., and Zuppiroli, L. (2006) *J. Appl. Phys.*, **100**, 033702.

82 Jurić, I., Batistić, I., and Tutiš, E. (2008) *Phys. Rev. B*, **77**, 165304.

83 van der Holst, J.J.M., van Oost, F.W.A., Coehoorn, R., and Bobbert, P.A. (2011) *Phys. Rev. B*, **83**, 085206.

84 Burin, A. and Ratner, M. (2000) *J. Chem. Phys.*, **113**, 3941.

85 van Mensfoort, S.L.M., Carvelli, M., Megens, M., Greiner, H., Wehenkel, D., Bartyzel, M., Janssen, R.A.J., and Coehoorn, R. (2010) *Nat. Photonics*, **4**, 329.

86 Aster, R.C., Borchers, B., and Thurber, C. H. (2005) *Parameter Estimation and Inverse Problems*, Elsevier Academic Press, Oxford.

87 Perucco, B., Reinke, N.A., Rezzonico, D., Moos, M., and Ruhstaller, B. (2010) *Opt. Express*, **18**, A246.

88 Germs, W. Chr., van der Holst, J.J.M., van Mensfoort, S.L.M., Bobbert, P.A., and Coehoorn, R. (2011) *Phys. Rev. B* **84**, 165210.

89 van Mensfoort, S.L.M., Shabro, V., Janssen, R.A.J., and Coehoorn, R. (2010) *J. Appl. Phys.*, **107**, 113710.

90 van Mensfoort, S.L.M., de Vries, R.J., Shabro, V., Loebl, H.P., Janssen, R.A.J., and Coehoorn, R. (2010) *Org. Electron.*, **11**, 1408.

91 de Vries, R.J., van Mensfoort, S.L.M., Shabro, V., Vulto, S.I.E., Janssen, R.A.J., and Coehoorn, R. (2009) *Appl. Phys. Lett.*, **94**, 163307.

92 van Mensfoort, S.L.M., Billen, J., Vulto, S.I.E., Janssen, R.A.J., and Coehoorn, R. (2009) *Phys. Rev. B*, **80**, 033202.

93 Carvelli, M., Janssen, R.A.J., and Coehoorn, R. (2011) *Phys. Rev. B*, **83**, 075203.

94 Blakesley, J.C., Clubb, H.S., and Greenham, N.C. (2010) *Phys. Rev. B*, **81**, 045210.

95 Schober, M., Olthof, S., Furno, M., Lüssem, B., and Leo, K. (2010) *Appl. Phys. Lett.*, **97**, 013303.

96 Ishii, H., Sugiyama, K., Ito, E., and Seki, K. (1999) *Adv. Mater.*, **11**, 605.

97 Doi, S., Sekine, C., Tsubata, Y., Ueda, M., Noguchi, T., and Ohnishi, T. (2003) *J. Photopolym. Sci. Technol.*, **16**, 303.

98 Harkema, S., Kicken, R.A.H.J., Langeveld-Voss, B.M.W., van Mensfoort, S.L.M., de Kok, M.M., and Coehoorn, R. (2010) *Org. Electron.*, **11**, 755, and references therein.

99 Coehoorn, R., Vulto, S.I.E., van Mensfoort, S.L.M., Billen, J., Bartyzel, M., Greiner, H., and Assent, R. (2006) *Proc. SPIE*, **6192**, 61920O.

100 Redecker, M., Bradley, D.D.C., Inbasekaran, M., and Woo, E.P. (1998) *Appl. Phys. Lett.*, **73**, 1565.

101 Poplavskyy, D., Su, W., and So, F. (2005) *J. Appl. Phys.*, **98**, 014501.

102 Mandoc, M.M., de Boer, B., Paasch, G., and Blom, P.W.M. (2007) *Phys. Rev. B*, **75**, 1932022.

103 Greiner, H. and Martin, O.J.F. (2004) *Proc. SPIE*, **5214**, 249.

7
Charge Transport Physics of High-Mobility Molecular Semiconductors

Henning Sirringhaus, Tomo Sakanoue, and Jui-Fen Chang

7.1
Introduction

There has been tremendous progress in discovering new classes of organic semiconductors that provide field-effect mobilities μ above $1\,cm^2/(V\,s)$ and allow addressing increasingly demanding thin-film electronic applications [1]. For many years, the performance of organic field-effect transistors (OFETs) seemed to be inherently lower than that of their inorganic counterparts, in particular, compared to amorphous silicon (a-Si) and polycrystalline FETs that have characteristic mobilities on the order of 0.5–1 and $100\,cm^2/(V\,s)$, respectively. Due to extensive materials development and evaluation of different classes of organic semiconductors, there is now a broad range of organic semiconductors, both vacuum and solution processable, as well as small molecule and conjugated polymer based, which are able to reach mobility values exceeding that of a-Si. The processing characteristics of these materials make them suitable for applications that cannot be easily addressed by many inorganic materials. Organic semiconductors are inherently low-temperature materials. Because of the absence of covalent bonding between molecules, they can be processed at temperatures below typically 100–150 °C from either vapor phase or solution into high-quality thin films that exhibit a low density of electronic defects. This makes them suitable for applications with a limited temperature window during manufacturing, such as those that require a flexible plastic substrate or applications that require integration with other low-temperature materials such as biological molecules. It also makes these materials compatible with direct-write printing-based manufacturing techniques.

As a result of these improved performance and unusual processing characteristics, organic FETs are now in advanced stages of development for commercial applications in flexible active matrix displays, such as active matrix, and electrophoretic displays on plastic substrates. OFET-driven, active matrix OLED displays on plastic substrates have been demonstrated [2]. Circuit applications in RFID tags and ambient intelligent devices are also being pursued. Very recently, a first 8-bit

Physics of Organic Semiconductors, Second Edition. Edited by Wolfgang Brütting and Chihaya Adachi

microprocessor was realized by an OFET integrated circuit [3]. For an excellent, recent review on applications of organic FETs, refer to Ref. [4].

In spite of extensive research efforts, there is still considerable controversy about the correct physical description of the charge carriers and the mechanism of charge transport in organic semiconductors, particularly in high-mobility systems. In low-mobility, disordered organic semiconductors, it is well established that charge transport is limited by static, energetic, and positional disorder and proceeds by hopping of localized charge carriers in an energetically disordered landscape of sites. This transport regime is very well investigated from studies on amorphous organic semiconductors, as used in xerographic applications [5]. In contrast, charge transport in high-mobility molecular semiconductors with mobilities of $1\,cm^2/(V\,s)$ or higher is intermediate between the classical bandlike Bloch electron conduction of crystalline inorganic semiconductors and the molecular hopping conduction in disordered, low-mobility organic semiconductors. At least at room temperature (RT), a description in terms of band transport remains controversial because the mean free path of charges is estimated to be on the order of the molecular distance [6]. However, a clear understanding of the nature of the charge carriers, their charge transport mechanism, and the factors that limit charge-carrier mobilities in this high mobility regime is essential for providing clear guidelines to materials chemists for design and synthesis of materials that allow achieving even higher levels of performance.

This review is focused on understanding of the charge transport physics of high-mobility organic semiconductors at a molecular level. It is less concerned with other important aspects of the device physics of organic FETs, such as the role of the gate dielectric [7], the importance of efficient charge injection from the source–drain contacts, as well as the nature of defect states and their role in device stability that have been reviewed elsewhere [8, 9]. In Section 7.2, we review recent high-mobility small-molecule and conjugated polymer materials with a focus on crystalline materials that have been able to exceed mobilities of $0.5–1\,cm^2/(V\,s)$. In Section 7.3, we discuss some of the main competing factors that govern charge transport in these materials and present theoretical approaches that have been developed to describe systems in which moderately strong intermolecular electronic interactions and strong electron–phonon interactions are present. In Section 7.4, we review recent experimental results that have aimed to address the important question whether at room temperature charge carriers in these high-mobility organic semiconductors are in fact simply extended Bloch electrons that undergo occasional scattering processes or are localized on individual molecules and move by hopping.

7.2 Review of Recent High-Mobility Small-Molecule and Polymer Organic Semiconductors

The field-effect mobility of an organic FET critically depends on the local intramolecular structure and the intermolecular packing between the molecules. These

determine the reorganization energy and the transfer integral that are the main parameters that govern charge transport [10]. For the design of a high-mobility material as a rule of thumb, the reorganization energy should be small and the transfer integral large. However, equally important is how uniform the molecular environment is along the interface. Static structural and energetic disorder encountered by the charges moving along the interface results in percolation motion with certain sites becoming rate limiting for the transport along the interface. The effect that such sites have on mobility can easily mask the more intrinsic dependence of mobility on molecular structure and packing [11]. The disorder might also be dynamic due to fluctuations in the intermolecular packing that occur on the same timescale as carrier motion and require charge carriers to remain localized on particular lattice sites until a favorable molecular configuration for charge transfer occurs dynamically [12–14]. The transport physics of organic semiconductors will be discussed in more detail. In this section, we first discuss recently discovered small-molecule semiconductors that provide field-effect mobilities $>1\,cm^2/(V\,s)$ (Figure 7.1) and then review recent high-mobility conjugated polymers (Figure 7.2). The discussion will be focused on materials that exhibit high hole mobilities in FET

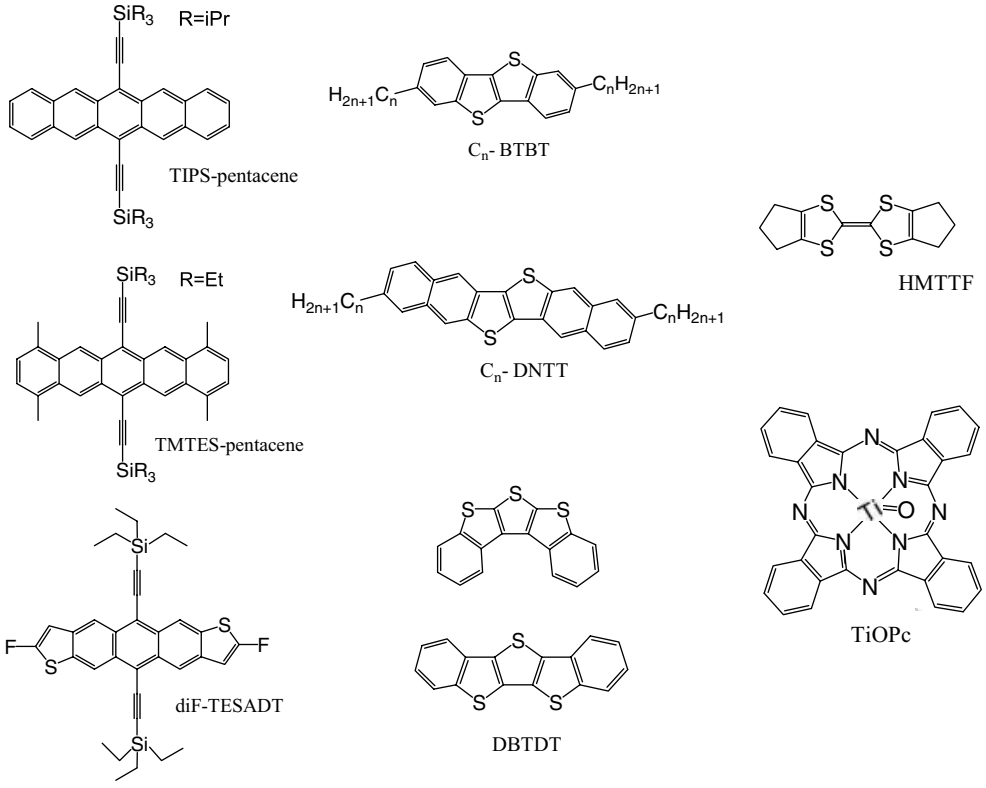

Figure 7.1 Examples of the molecular structure of high-mobility molecular semiconductors.

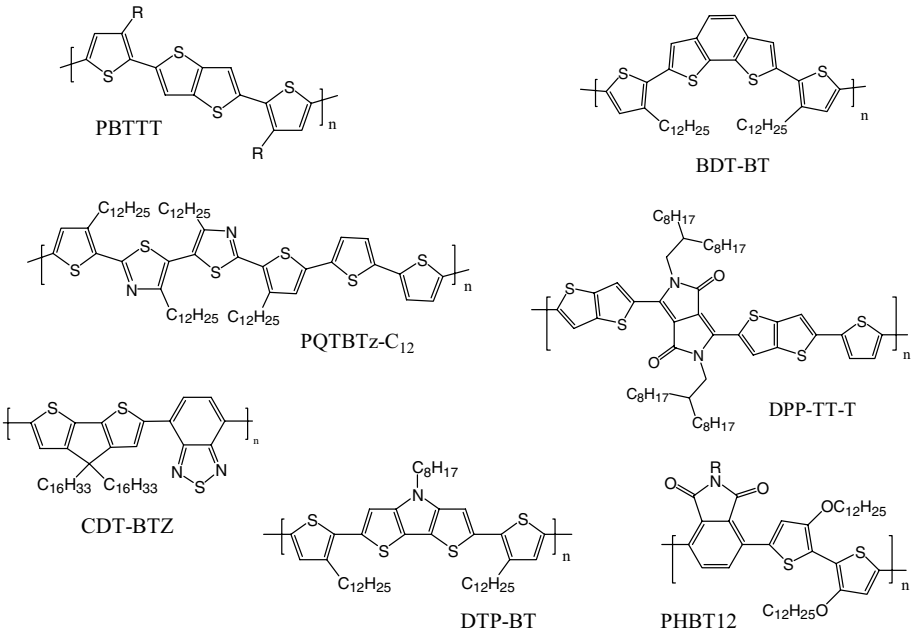

Figure 7.2 Examples of the molecular structure of high-mobility conjugated polymer semiconductors.

configurations. Due to space constraints we are unable to discuss the wide range of materials for n-type FETs. We only state here that similarly high carrier mobilities exceeding 1 $cm^2/(V s)$ are also achievable for electron transport and we refer to the recent excellent review by Anthony *et al.* on this subject [15].

A focus area for new materials development continues to be the class of acenes and fused heteroacene materials. The extensive work on systems such as pentacene and rubrene has established such fused, extended π-systems to be good candidates for achieving high mobility. Recent synthetic efforts have been devoted to developing acene-based materials with better chemical stability and solution processability. An important class of solution-processable acenes were developed by Anthony *et al.* [16] based on the excellent solubility characteristics of the trialkylsilylethynyl group, such as triisopropyl-silylethynyl (TIPS), substituted in the central 6- and 13-position of a pentacene core. TIPS-pentacene (TIPS-P) shows a high degree of crystallinity, even in spin-coated films, and exhibits a 2D brickwall and cofacial π–π-stacking motif in the plane of the films with the side chains oriented near normal to the substrate surface. Mobilities exceeding 1 $cm^2/(V s)$ can be obtained in films of neat TIPS-P provided that care is taken to carefully adjust the growth and substrate conditions to control the nucleation of the crystalline grains [17]. A variety of heteroacene derivatives, such as triethylsilylethynyl anthradithiophene (TESADT) [18] or difluorinated (di-F) TESADT [19], exhibit similarly high levels of performance. Some derivatives substituted with electron-withdrawing groups, such as 7,8,9,

10-tetrafluoro-5,12-bis(TIPSethynyl)tetraceno[2,3-*b*]thiophene [20], have been shown to exhibit high-mobility ambipolar transport with electron and hole mobilities exceeding 0.1 $cm^2/(V s)$. Anthony's group has investigated the structure–property relationships of a large number of solution-processable, trialkylsilylethynyl-substituted acenes and has studied the correlation between the crystal packing motif and carrier mobility. It was concluded that generally 1D π–π stacking tends to result in lower mobility than 2D brickwall packing [21]. An interesting derivative, which possibly does not follow this simple rule as discussed below, is 1,4,8,11-tetramethyl-6,13-triethylsilylethynyl pentacene (TMTES-P) that exhibits one-dimensional π–π stacking, but allows reaching field-effect mobilities up to 3 $cm^2/(V s)$ [22]. Several groups have reported more straightforward control of film growth and more uniform electrical characteristics when blending the TIPS-pentacene molecules with a polymer binder [23]. In blend films of TIPS-P and diF-TESADT, respectively, Hamilton *et al.* reported mobilities of 1 and 2.4 $cm^2/(V s)$, respectively [24]. The high performance is associated with a segregation of the small molecule to the surface and interface of the films.

Another class of molecules that has recently attracted significant attention are end-substituted phenylene–thiophene, selenophene, or thiazine fused ring systems. In vacuum-sublimed films of unsubstituted diphenyl-benzothienobenzothiophenes and dinaphtho-chalcogenopheno-chalcogenophenes based on thiophene (DNTT) or selenophene (DNSS) mobilities of 1–3 $cm^2/(V s)$ were reported [25, 26]. Single crystals of DNTT laminated onto a Cytop gate dielectric showed mobilities up to 8.3 $cm^2/(V s)$ [27]. In vapor-grown single crystals of pyrrolobisbenzothiazine with cofacial 2D π–π stacking mobilities of up to 3.6 $cm^2/(V s)$ were reported on octadecyltrichlorosilane (OTS)-modified SiO_2. Derivatives substituted with C_8H_{17} on the central nitrogen position exhibited more 1D π–π stacking and reduced mobilities up to 0.4 $cm^2/(V s)$ [28]. Interestingly, in 3,10-dimethyl-substituted DNTT, an unusual 3D Herringbone stacking was observed due to slippage of one of the molecules in the unit cell along the c-direction. Surprisingly, this 3D Herringbone stacking still supports only slightly degraded mobility of 0.8 $cm^2/(V s)$ compared to that of DNTT.

Spin-coated films of dialkyl end-substituted derivatives of benzothienobenzothiophene (BTBT) exhibit a highly ordered, crystalline microstructure with alternating layers of aliphatic side chains and conjugated layers parallel to the substrate and Herringbone stacking within the conjugated layers. High mobilities of 1–3 $cm^2/(V s)$ were initially reported for C_n-BTBT ($n = 11$–13). C_n-BTBT with longer sides chains tended to exhibit slightly higher mobility than C_n-BTBT with shorter side chains, because the stronger hydrophobic interaction induced by the longer side chains enhances the conjugated molecular overlap. By drop-casting onto an inclined substrate, the film morphology for C_8-BTBT could be optimized and bottom-gate FETs with mobilities of 5 $cm^2/(V s)$ were reported [29]. Attempts to replace sulfur by selenium surprisingly resulted in poorer device performance as the thin films of C_n-BSBS adopt a microstructure with larger inclination of the molecular axis from the substrate normal and poorer electronic overlap than in the corresponding C_n-BTBT films. Attempts to incorporate the BTBT conjugated core into a

conjugated polymer were initially unsuccessful, but a closely related copolymer based on naphthodithiophene–bithiophene (PNDBT) with semicrystalline, lamellar microstructure exhibits high hole mobilities up to 0.54 $cm^2/(V s)$ [30]. In contrast to C_n-BTBT, dialkylated C_n-DNTT exhibits only moderate solubility too low for forming films by spin-coating, but shows excellent device performance with mobilities up to 7.6 $cm^2/(V s)$ in vacuum-sublimed thin films of C_{10}-DNTT [31]. By using a drop-casting method from hot solution with growth directed by an inclined surface solution-deposited films of C_{10}-DNTT were incorporated into both bottom- and top-gate FETs with mobilities up to 11 $cm^2/(V s)$ [32].

Hu and coworkers compared linear-shaped dibenzothienodithiophene (DBTDT) [33] and sickle-shaped bisbenzothienothiophene (BBTT) [34] and found that while DBTDT adopts a Herringbone π–π stacking with mobility of 0.5 $cm^2/(V s)$ in vacuum-deposited thin films, BBTT has significantly higher solubility, adopts a cofacial π–π stacking, and solution-grown crystals exhibit field-effect mobilities of 0.2–0.6 $cm^2/(V s)$ in bottom-gate FETs on OTS-modified SiO_2. Gao *et al*. investigated end-substituted dialkyl-dithienobenzodithiophene with cofacial, 2D π–π stacking and demonstrated mobilities of 1–1.7 $cm^2/(V s)$ in drop-cast films on untreated SiO_2 [35].

Recent discoveries of molecules with high carrier mobilities >1 $cm^2/(V s)$ have by no means been confined to acenes or fused thiophene–phenylene systems. Due to space constraints, we cannot provide a complete account, but as examples we quote titanylphtaolocyanine (TiOPc) that has a nonplanar square pyramid shape and exhibits mobilities of up to 3.6 $cm^2/(V s)$ in vacuum-grown films on OTS-modified SiO_2 [36]. Derivatives of tetrathiafulvalene (TTF) have also attracted significant attention. In solution-grown crystals of dithiophene-TTF, field-effect mobilities of 3.6 $cm^2/(V s)$ were reported for bottom-gate FETs on hexamethyldisilazane (HMDS) or OTS-modified SiO_2 [37]. In solution-grown crystals of hexamethylene-TTF (HMTTF) contacted with TTF-TCNQ source–drain electrodes and a parylene gate dielectric mobilities of 10 $cm^2/(V s)$ were reported. The molecules adopt a 2D cofacial, brick-wall π–π stacking motif [38].

We now shift our discussion to high-mobility conjugated polymers. Although it is possible to achieve reasonably high mobilities of 10^{-3}–10^{-2} $cm^2/(V s)$ using amorphous materials as long as the polymer is designed to minimize energetic disorder [11, 39, 40], it is easier to ensure this in semicrystalline materials. It appears that many of the recently discovered high-mobility polymers adopt a lamellar microstructure similar to that found in P3HT [41] or poly(3,3′-dialkylquaterthiophene) (PQT) [42]. Through the formation of alternating layers of conjugated backbones separated by layers of flexible side chains with the layers oriented in the plane of the film, efficient charge transport in the plane of the film along the active interface of the FET is facilitated, because the motion of charges is not impeded by the presence of the inevitable flexible, insulating side chains. One focus of recent attention has been on thienothiophene-based copolymers after the discovery of high mobilities of up to 1.1 $cm^2/(V s)$ in poly(2,5-bis(3-alkylthiophen-2-yl)thieno(3,2-*b*)thiophene) (PBTTT) [43, 44]. The lower density of side chains in thiophene–thienothiophene copolymers such as

PBTTT not only slightly increases the ionization potential and improves the stability but also allows better side chain interdigitation and more highly crystalline structures. This work has recently been reviewed by McCulloch *et al*. [45].

A number of groups have successfully investigated different classes of donor–acceptor copolymers [46]. A copolymer of benzothiadiazole and cyclopentadithiophene (CDT-BTZ) was recently shown to exhibit mobilities up to 1.4 $cm^2/(V s)$. It was originally claimed that thin films of this polymer had an amorphous microstructure [47], but it was later discovered in dip-coated films of higher molecular weight that the polymer is in fact semicrystalline [48]. It adopts an anisotropic lamellar structure, again resembling that of P3HT, with the polymer backbone and the direction of π–π stacking in the plane of the film. The exceptionally high mobility values achieved in this polymer have been attributed to its donor–acceptor character that increases the interchain attraction and result in a small π–π stacking distance of 3.7–3.9 Å. Bao and coworkers have reported several low bandgap, donor–acceptor polymers [49, 50], including poly(didodecylquaterthiophene-*alt*-didodecylbithiazole) (PQTBTz-C_{12}) [51] that adopts a highly crystalline lamellar microstructure and allows achieving mobilities of 0.3 $cm^2/(V s)$ and excellent bias stress stability comparable to that of a-Si thin-film transistors. Guo *et al*. [52] copolymerized phtalimide acceptor units with thiophene (Ph-BT12) and achieved small π–π stacking distance of 3.6 Å and field-effect mobilities of 0.2 $cm^2/(V s)$. Liu *et al*. [53] showed that a high degree of crystallinity is not always a prerequisite for high mobility. They reported copolymers based on *N*-alkyl-dithienopyrrole and thiophene (DTP-BT) and showed that mobilities of up to 0.2 $cm^2/(V s)$ could be achieved in as-spun films of the polymer with a seemingly amorphous microstructure. Rieger *et al*. investigated copolymers of thiophene and benzodithiophene (BDT-BT) with a curved backbone that affords a good compromise between solubility and aggregation and exhibits mobilities up to 0.5 $cm^2/(V s)$ in top-gate devices with polystyrene gate dielectric [54].

A new class of low-bandgap conjugated polymers that has recently attracted significant attention are low-bandgap copolymers of diketopyrrolopyrrole (DPP). Bürgi *et al*. were first to report a low-bandgap copolymer based on DPP and thiophene, which exhibited not only high hole mobilities of 0.1 $cm^2/(V s)$ but also electron mobilities of the same magnitude and could be operated as an ambipolar, infrared light-emitting transistor [55]. Nelson *et al*. demonstrated that in semicrystalline, spin-coated films of a copolymer of electron-donating dithienopyrrole (DTP) and electron-accepting DPP mobilities of 0.3–0.4 $cm^2/(V s)$ on OTS-modified SiO_2 can be achieved [56]. Li *et al*. investigated copolymers of DPP and thienothiophene and demonstrated high hole mobilities of up to 0.94 $cm^2/(V s)$ in spin-coated films annealed at 200 °C with a semicrystalline, lamella microstructure on OTS-modified SiO_2 [57]. Electron mobilities were much lower. In bottom-gate OFETs with SiO_2, modified SiO_2 copolymers of DPP with electron-accepting thiophene–benzothiadiazole–thiophene (TBT) exhibit ambipolar transport with high electron mobilities of 0.4 $cm^2/(V s)$ and hole mobilities of 0.35 $cm^2/(V s)$ were observed [58]. In top-gate FETs with PMMA, gate dielectric and copolymers of DPP and silaindacenodithiophene electron mobilities of 0.1 $cm^2/(V s)$ and hole mobilities of 0.4 $cm^2/(V s)$ were

found [59]. Even higher mobilities have recently been reported for top-gate FETs with PMMA gate dielectric and copolymers of DPP and thienothiophene (DPP-TT-T). Record hole mobilities for a conjugated polymer FET of $1.95\,\mathrm{cm}^2/(\mathrm{V\,s})$ and electron mobilities of $0.03\,\mathrm{cm}^2/(\mathrm{V\,s})$ were achieved [60], which demonstrate the potential for reaching with conjugated polymers similarly high charge-carrier mobilities as in the small-molecule systems described above.

7.3 General Discussion of Transport Physics/Transport Models of Organic Semiconductors

The charge transport physics of a specific organic semiconductor system can be considered to be governed by several key physical parameters: the intrinsic bandwidth J due to the intermolecular interactions in a perfectly periodic molecular solid, the static diagonal and nondiagonal disorder parameters σ and Σ, respectively, that characterize the distribution in site energies and transfer integrals due to static disorder in the real molecular solid, the reorganization energy λ_{reorg} that is a measure of the strength of the local electron–phonon/electron–ion interaction and the strength of the nonlocal electron–phonon coupling that reflects phonon-induced, dynamic fluctuations in the transfer integrals. The origin of these parameters can be seen from the Hamiltonian of the electron–phonon system in a molecular solid:

$$\begin{aligned} H &= H^0_{\mathrm{el}} + H^0_{\mathrm{ph}} + V^{\mathrm{local}}_{\mathrm{el-ph}} + V^{\mathrm{nonlocal}}_{\mathrm{el-ph}} \\ H^0_{\mathrm{el}} &= \textstyle\sum_j \varepsilon_j a_j^+ a_j + \sum_{ij} J_{ij} a_i^+ a_j \\ H^0_{\mathrm{ph}} &= \textstyle\sum_{\vec{q}\ s} \hbar\omega_{\vec{q}\ s}\left(b^+_{\vec{q},s} b_{\vec{q}s} + \frac{1}{2}\right) \\ V^{\mathrm{local}}_{\mathrm{el\text{-}ph}} + V^{\mathrm{nonlocal}}_{\mathrm{el\text{-}ph}} &= \textstyle\sum_{\vec{q}s}\sum_j \hbar\omega_{\vec{q}s} g_{jj,\vec{q}s}\left(b^+_{\vec{q},s} + b_{-\vec{q}s}\right) a_j^+ a_j \\ &\quad + \textstyle\sum_{\vec{q}s}\sum_{i\neq j} \hbar\omega_{\vec{q}s} g_{ij,\vec{q}s}\left(b^+_{\vec{q},s} + b_{-\vec{q}s}\right) a_i^+ a_j \end{aligned} \tag{7.1}$$

Here, $a_j^+(a_j)$ are creation (annihilation) operators for an electron onsite j. $b^+_{\vec{q},s}(b_{\vec{q}s})$ are creation (annihilation) operators for a phonon with wave vector $\vec{q}$ and polarization index s and frequency $\omega_{\vec{q}s}$. ε_j is the energy of a charge sitting on a molecule on site j. The transfer integral J_{ij} characterizes the strength of the intermolecular, electronic interaction between neighboring molecules on sites i and j of the crystal causing charges to move between sites. $g_{jj,\vec{q}s}$ and $g_{ij,\vec{q}s}$ are the respective local and nonlocal electron–phonon coupling constants that measure the strength of the interaction between electrons and intramolecular and intermolecular vibrations. As can be seen from Eq. (7.1) the local electron–phonon coupling gives rise to a modification of the site energies, while the nonlocal electron–phonon coupling modulates the transfer integrals due to fluctuations in molecular distances and/or orientation.

i) **Transfer integral J_{ij}:** If there was no static disorder in the values of ε_i and J_{ij} and the electron–phonon coupling could be ignored, one would expect the electron states of a molecular crystal comprising a perfectly periodic array of molecules to be simply Bloch waves with a defined wave vector $\vec{k}$, just like in crystalline inorganic semiconductors. The only difference would be that in a tight binding description, these Bloch states would be constructed not from the atomic orbitals of isolated atoms, but from the molecular orbitals of isolated molecules. J_{ij} determines the bandwidth B of the energy–momentum dispersion of these Bloch states. A simple tight binding model of a one-dimensional molecular stack would predict, for example, a bandwidth $B = 4J$. The transfer integral can be calculated from $J_{ij} = \langle \psi_i \| H_{\mathrm{el}} \left| \psi_j \right\rangle$, where ψ_i and ψ_j are the relevant HOMO and LUMO orbitals in the case of hole and electron transport, respectively, of the isolated molecules and H_{el} is the effective one-electron Hamiltonian of the crystal. It can often simply be estimated as half the energy splitting between the HOMO and HOMO-1 (LUMO + 1 and LUMO) of a dimer of the molecule computed in the intermolecular packing configuration encountered in the full crystal [61].

J_{ij} has been calculated for a broad range of organic molecules using quantum chemical or density functional theory (DFT) techniques (for a detailed discussion see, Ref. [61]). From these calculations several important insights have been gained, in particular regarding the expected magnitude of J_{ij} and its dependence on intermolecular packing. Since the intermolecular distances in van der Waals bonded molecular solids are significantly larger than in covalently bonded inorganic semiconductors, such as silicon, the typical bandwidth in molecular crystals is comparatively small, but not negligible. Typical values predicted by band structure calculations are on the order of several 100 meV (Figure 7.3). Experimental investigations of the band structure of thin, single crystals of pentacene by angle-resolved ultraviolet photoemission spectroscopy (ARUPS) have shown that the bandwidth at 140 K in the $\Gamma\bar{M}$ direction of the surface Brillouin zone is indeed on the order of 330 meV (Figure 7.4) [62].

The bandwidth, however, is very sensitive to intermolecular separation and decreases approximately exponentially with intermolecular distance. Within a range of π–π stacking distances of 3.4–4 Å typically encountered in organic semiconductors, the transfer integral can vary by a factor of 3–4. For the different molecular pairs in the crystal structure of pentacene, values for the hole transfer integrals in the range of 35–85 meV have been estimated from DFT calculations [63]. These values are comparable in magnitude to typical intra-/intermolecular vibrational modes. Values for electrons and holes can exhibit significant differences reflecting the different wave function of the HOMO and LUMO states. These calculations have also demonstrated that the transfer integral is very sensitive to the exact intermolecular stacking arrangement. Small relative shifts of intermolecular positions can cause large variations in the magnitude and sign of the transfer integral reflecting changes in the overlap between the peaks and nodes of the molecular wave functions (Figure 7.7a)

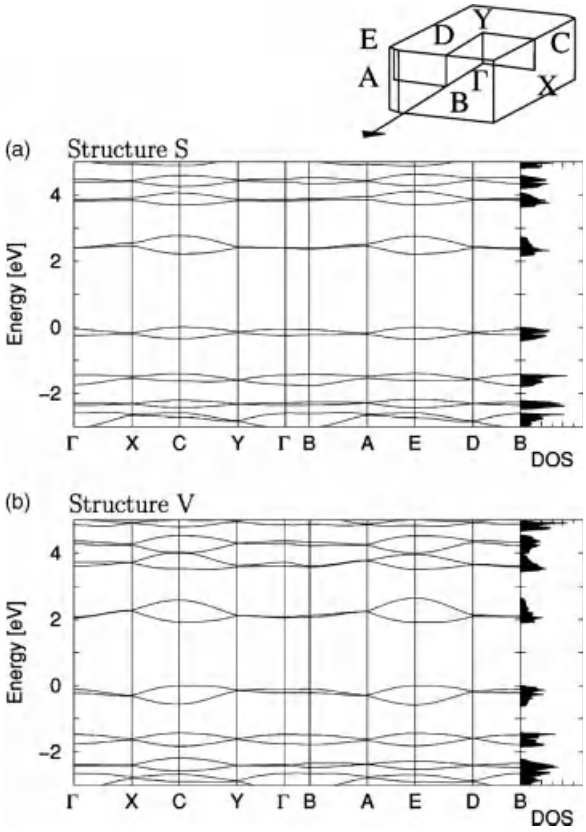

Figure 7.3 *Ab initio* band structure calculation of two different polymorphs of pentacene: *S* – phase grown from solution **(a)**, *V* – phase grown from vapor **(b)**. The density of states is shown in the right panel. Energies are referenced with respect to the valence band maximum. With permission from Ref. [120].

[61]. This is the reason why transport properties in molecular crystals can depend sensitively on polymorph structure; however, it also suggests that non-diagonal electron–phonon coupling might be particularly relevant to the transport physics of these materials as will be discussed below.

If static disorder and electron–phonon coupling were sufficiently weak such that the standard Bloch electron description of covalently bonded semiconductors could indeed be applied to molecular crystals, one would expect the charge-carrier mobility to exhibit a characteristic bandlike temperature dependence $\mu = (e\tau(T))/m$, with effective mass m^*. The temperature-dependent scattering time $\tau(T)$ should exhibit a decrease with increasing temperature reflecting thermally induced excitation of the various scattering mechanisms, such as phonons. However, even in the purest and highest-mobility molecular crystals, the electron–phonon coupling might be too strong in order to be

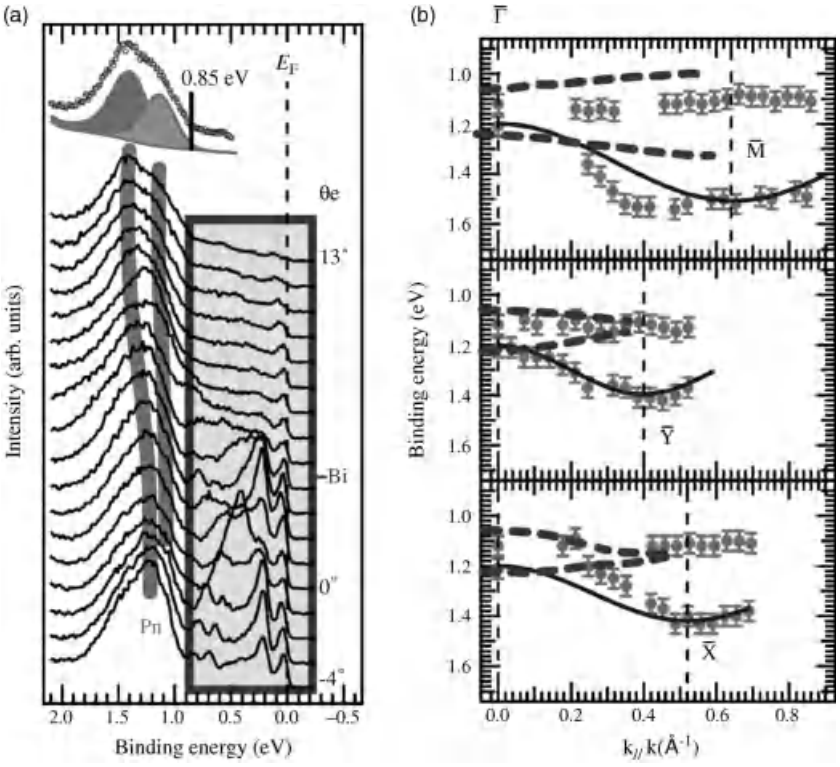

Figure 7.4 (a) Surface band structure of pentacene measured by ARUPS. (a) ARUPS spectra of 1 monolayer of pentacene on Bi(001) measured at 140 K along the $\Gamma - Y$ direction. The uppermost spectrum shows the decomposition of the pentacene-induced structure at a photoelectron emission angle θ_e of 13°. (b) Band dispersions of the two HOMO-derived bands of the 1 monolayer pentacene film adsorbed on Bi(001). Theoretical dispersions of the HOMO-derived bands are indicated by dashed lines. Solid curves are the dispersion obtained by analyzing the higher binding energy HOMO-derived band using a simple tight binding model. With permission from Ref. [62].

taken into account merely as an occasional scattering mechanism. Much of the theoretical effort in the field has been devoted to methods of treating and understanding the potential effects of the electron–phonon interaction terms in the above Hamiltonian.

ii) **Reorganization energy λ:** To get an understanding of the effects of diagonal electron–phonon coupling, it is helpful to discuss the limit in which disorder, intermolecular interactions and nonlocal electron–phonon coupling can be considered weak. Holstein showed in a series of papers in 1959 [64, 65] that if the transfer integral was strictly zero, the local electron–phonon coupling would result in full localization of the charge onto a single site. The energy of the localized charge is stabilized by the so-called polaron binding energy $E_b = (1/N)\sum_{\vec{q}s}\hbar\omega_{\vec{q}s}|g_{jj,\vec{q}s}|^2 = \lambda/2$ associated with a local molecular distortion

induced by the charge. E_b and the so-called reorganization energy λ, which is twice the polaron binding energy, play an important role in theories of electron transfer in a transport regime in which the reorganization energy can be considered to be large compared to the transfer integral. The reorganization energy can also be expressed in terms of the energies of the neutral (E) and charged (E^+) molecule computed for both the ground-state nuclear configuration of the neutral (M) and charged molecule (M^+) or in terms of the difference in the configuration coordinates between the neutral and charged ground-state configuration ΔQ_s (neglecting the dispersion of the phonon modes): $\lambda = E^+(M) - E^+(M^+) + E(M^+) - E(M) = (1/2)\sum_s \hbar\omega_s \Delta Q_s^2$.

Reliable values of reorganization energy have been computed for a range of molecules by taking into account the contributions from all individual vibrational and rotational modes (Figure 7.5) (for a review, see Ref. [61]). The intramolecular modes correspond to local molecular distortions associated with charge injection. However, intermolecular lattice modes involving the relative

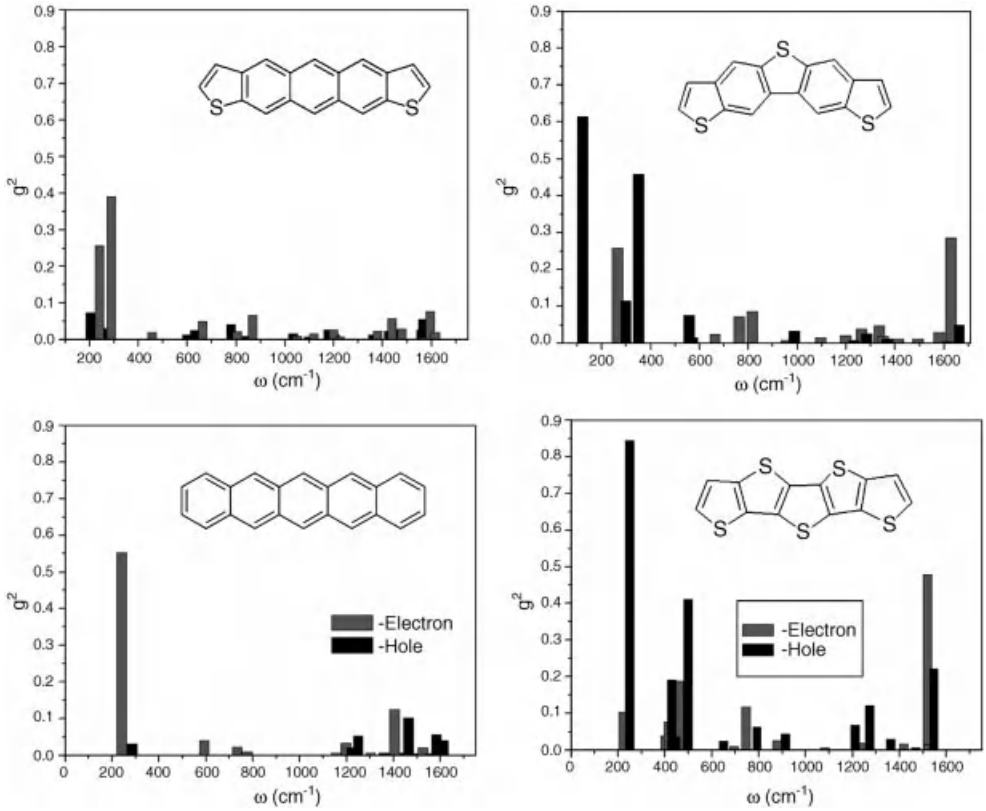

Figure 7.5 DFT-calculated diagonal electron– and hole–vibration couplings for different organic semiconductors. With permission from Ref. [61].

displacement of molecules also make contributions to the charge-carrier polarization energy, which should not be ignored for a reliable estimate of λ. The reorganization energy sensitively depends on molecular structure and substitution and also on the polarity of the charge carrier. λ tends to decrease with increasing conjugation length and increase in the presence of polar substitution groups. Hole charge carriers in pentacene have been found to exhibit a particularly low value of $\lambda = 90$ meV, while sexithiophene has a significantly higher value of 320 meV. It should be noted that the value of λ for pentacene is in excellent agreement with gas-phase ultraviolet photoelectron spectroscopy (UPS) measurements [66].

Holstein considered a model for charge transport in which the nondiagonal electron–phonon coupling is neglected and the diagonal electron–phonon coupling constant g to optical vibrational modes is large [65]. Although Holstein's perturbation theory approach for taking into account the effect of finite J is limited to systems with small electronic bandwidth and is probably not applicable to systems like pentacene where λ is of comparable magnitude to the estimated transfer integral, we discuss it here because its identification of two different transport regimes – an extended polaron bandlike transport regime at low temperature and a localized, small-polaron hopping regime at high temperatures – is widely believed to be more generally valid. As stated above in the limit $J = 0$, the charge is localized on an individual lattice site p and is accompanied with a vibrational state characterized by occupation numbers N_k for each vibrational mode. For finite J, Holstein applied perturbation theory to calculate the probability for transitions to a neighboring site ($p \rightarrow p \pm 1$). At low temperatures, this transition probability is dominated by diagonal transitions in which none of the N_k are altered and Bloch-type extended polaron states are formed. The polaron bandwidth is renormalized and is expected to be significantly smaller than the electron bandwidth B due to the dependence on a vibrational overlap integral. The polaron bandwidth is also predicted to drop rapidly with increasing temperature. Such narrowing of the bandwidth has recently been observed experimentally in ARUPS measurements on thin films of pentacene on graphite [67]. In this regime, the effect of nondiagonal transitions can be taken into account as a scattering mechanism and the mobility drops rapidly with increasing temperature. For a 1D system with lattice constant a and single optical vibration mode with frequency ω_0, the mobility in this polaron band transport regime can be expressed as

$$\mu_{\text{band}} = \frac{ea^2\omega_0}{k_B T}\left(\frac{g^2 \operatorname{csc} h((\hbar\omega_0)/(2k_B T))}{\pi}\right)^{1/2} \exp\left(-2g^2 \operatorname{csc} h\left(\frac{\hbar\omega_0}{2k_B T}\right)\right) \tag{7.2}$$

Holstein estimated that at a transition temperature T_t of around the Debye temperature, that is, typically $(k_B T_t)/(\hbar\omega_0) < 0.5 - 1$, the lifetime of these states becomes so short that the associated energy uncertainty becomes

comparable to the bandwidth. At higher temperature nondiagonal transitions, in which some of the N_k are altered as a result of the electron transfer, dominate and transport can be described as a hopping process of small polarons that are localized on individual lattice sites and hop between pairs of sites with a mobility:

$$\mu_{\text{hopping}} = \frac{ea^2J^2}{\hbar^2\omega_0 k_B T}\left(\frac{\pi}{g^2 \operatorname{csc} h((\hbar\omega_0)/(2k_B T))}\right)^{1/2} \exp\left(-2g^2 \tanh\left(\frac{\hbar\omega_0}{4k_B T}\right)\right) \tag{7.3}$$

At high temperatures ($\hbar\omega_0 \ll k_B T$), this reduces to an Arrhenius temperature behavior with an activation energy $E_a = \lambda/4$, which is identical to the one predicted by Marcus electron transfer theory. At very high temperatures ($E_{\text{pol}} = \hbar\omega_0 g^2 \ll 2k_B T$), the mobility is expected to drop again with a $T^{-(3/2)}$ temperature dependence. Holstein also established that for transfer integrals that exceed a critical value perturbation theory can no longer be applied and an adiabatic treatment of the electron transfer process is required. The DFT and QC calculations discussed above suggest that in systems such as pentacene λ is of comparable magnitude to J, which suggests that simple, nonadiabatic hopping models for electron transfer are probably not applicable.

Several authors developed approaches to solving the Holstein Hamiltonian for a broader range of parameters, while still ignoring nondiagonal couplings. Silbey and Munn [68] showed using a density matrix approach that the existence of two transport regimes, a polaron band transport regime at low temperatures ($(k_B T)/\hbar\omega < 0.5 - 1$) with mobility decreasing rapidly with increasing temperature and a high-temperature, small-polaron hopping regime is still expected over a wider range of parameter values for J and g than those accessible by Holstein's approach. As g increases, the overall mobility in the band regime is reduced, but the hopping contribution is enhanced (Figure 7.6). In the high-temperature hopping regime, a thermally activated regime as predicted by Holstein is observed only for very large values of $g > 3$, which are probably not realized in many molecular systems, as they would imply too large values for λ. For intermediate and small values of g, the effect of the contribution from the hopping transport is to slow the decrease of mobility with increasing temperature experienced by the band transport contribution and lead to a relatively weak temperature dependence of the mobility near room temperature mobility. Kenkre *et al.* [69] used a generalized master equation approach to extend the Holstein model to higher dimensions and to fit the theoretical mobility expression to the experimental data of naphthalene molecular crystals. They estimated a ratio of $(g^2\hbar\omega_0)/B \approx 5 - 7$ for diagonal coupling to a librational mode with $\hbar\omega_0 = 16$ meV. More recently, Munn and Silbey used a generally applicable variational method to study the crossover from the bandlike to the hopping transport [70]. A different approach to explain the bandlike temperature dependence of the mobility near room temperature in molecular crystals was recently proposed by Nan *et al.* who

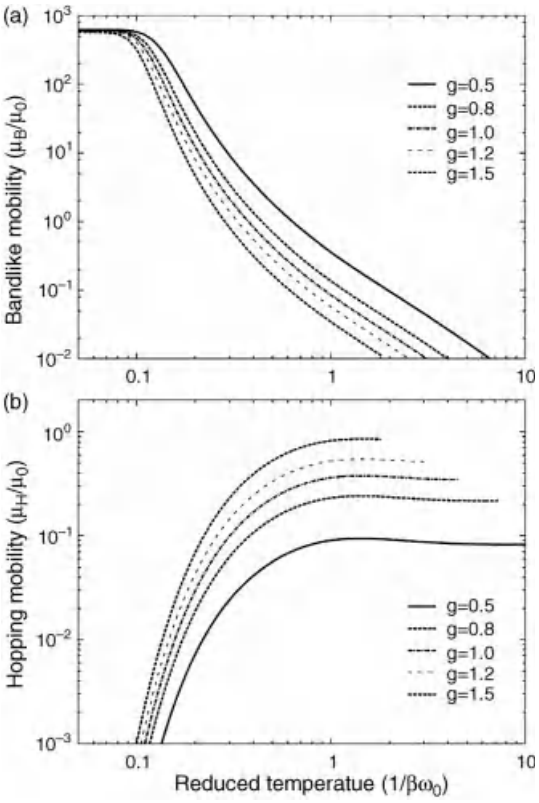

Figure 7.6 Bandlike and hopping contributions to conduction in 1D Holstein system. A comparison of bandlike (a) and hopping (b) mobilities for a 1D Holstein system with $J_0/\omega_0 = 2$ for different diagonal electron coupling constants. With permission from Ref. [70].

considered a quantum mechanical expression of the charge transfer rate in the localized hopping regime conventionally described by Marcus theory and showed that a mobility decreasing with increasing temperature can also be obtained in a hopping transport regime [71].

iii) **Nonlocal electron–phonon coupling constant:** The nonlocal electron–phonon coupling modulates the transfer integrals. It arises mainly from lattice modes that modulate the molecular distances, relative positions, and/or orientation. A number of authors have developed approaches to include these terms in the treatment of the Hamiltonian. Although an exact diagonalization of the Hamiltonian as in the limit considered by Holstein is not possible, Munn and Silbey showed using a unitary transformation method that in the presence of nonlocal coupling, it is still possible to distinguish clearly between a bandlike polaron low-temperature regime and a small-polaron hopping regime at higher temperatures [72, 73]. In the bandlike regime, the inclusion of nonlocal coupling increases the scattering rate and decreases the mobility. However, in

the high-temperature hopping regime, nonlocal couplings give rise to phonon-assisted currents and increase the mobility. Overall, inclusion of nonlocal coupling was predicted to further weaken the temperature dependence of the mobility in the hopping regime and lead to a near temperature-independent diffusion coefficient and a mobility temperature dependence $\mu \propto T^{-1}$. More recently, Hannewald and Bobbert [74, 75] used a similar unitary transformation method with *ab initio* estimates of the various coupling constants to calculate the mobility in the Kubo formalism of linear response theory. They showed in particular that nondiagonal coupling gives rise to contributions to the mobility that exhibit a pronounced anisotropy in their temperature dependence.

A different approach to investigating the effects on nondiagonal electron–phonon coupling was recently proposed by Troisi *et al.* [76, 77]. The approach is motivated by the realization from quantum chemical computations that the transfer integrals in molecular crystals are extremely sensitive to the relative molecular positions and orientations. Small translations of two acene molecules along their long axis by only 0.5–1 Å can result in large changes of the transfer integrals by more than an order of magnitude (Figure 7.7a) [61]. The origin of this high sensitivity of J to intermolecular packing is the complex shape of the HOMO and LUMO wave functions. Furthermore, it appears that in many common molecular crystals, the equilibrium molecular stacking configuration does not correspond to a maximum or minimum of the transfer integral, such that small displacements of any molecule from the equilibrium structure are associated with significant changes in the relevant transfer integrals. This is illustrated in Figure 7.7b for the case of different solution-processable pentacene derivatives derived from TIPS pentacene, in which π–π stacking does not occur in the conventional Herringbone motif but in a cofacial manner [78]. The two dimensional contour map shows the expected variation of the transfer integral as a function of relative translations of two pentacene molecules in x- and y-directions. The contour line labeled with an asterisk corresponds to a zero value of J. The plot also shows the actual relative positions that are found in the equilibrium structure of five different pentacene derivatives (a–e). It is clear from this plot that (a) the transfer integral varies strongly as a function of relative position and (b) that the equilibrium structures are located in regions in the vicinity of which significant variations of transfer integral as a function of position are expected.

At or near room temperature, significant thermal fluctuations in relative molecular positions and orientations are expected due to the soft, van der Waals bonding in these materials. This is illustrated in Figure 7.7c where the individual dots show fluctuations in molecular configuration that were detected in a molecular dynamics simulation at room temperature. There is a significant thermal broadening of the values of the transfer integral that are encountered in the array of molecules during the MD simulation and the standard deviation of these fluctuations is comparable to the magnitude of the average transfer integral. By combining DFT

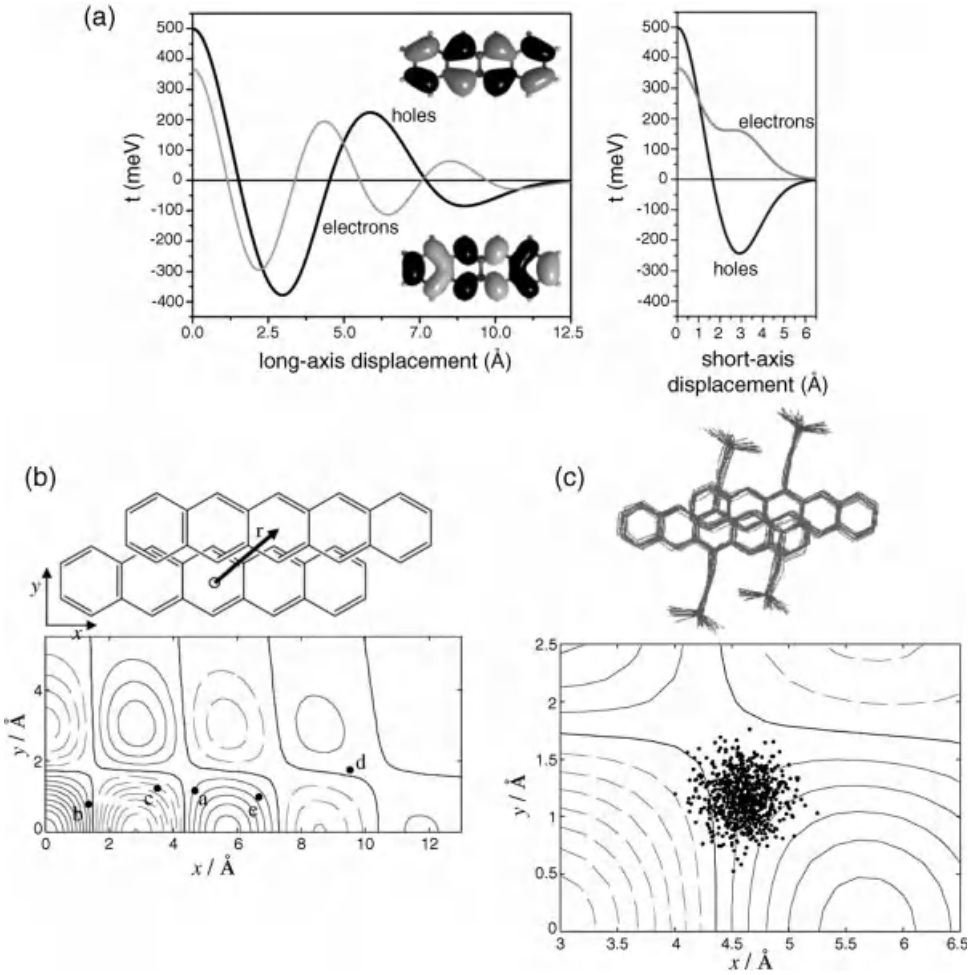

Figure 7.7 **(a)** Evolution of the quantum chemical transfer integrals for electrons and holes in a tetracene cofacial dimer as a function of the degree of translation of one molecule along its long axis (left) and short axis (right); the intermolecular distance is set at 3.74 Å (which is the intermolecular separation found in the rubrene crystal along the *a*-direction). The HOMO (top) and LUMO (bottom) wave functions are also presented in the figure on the left. With permission from Ref. [61]. **(b)** Map of the hopping integral between coaxial pentacene molecules sliding one with respect to the other in two parallel planes distant 3 Å. Contour lines are plotted at the interval of 700 cm^{-1} (dashed and solid lines are negative and positive contour lines, respectively, the contour lines with null coupling are indicated by solid black lines). The labeled points a–e indicate the actual position of typical pentacene pairs as found in different materials. (c) The black dots in a smaller region of the same map represent the relative position of the pentacene pairs a sampled during a short molecular dynamics simulation at 300 K. With permission from Ref. [78].

calculations with molecular dynamics simulations, Coropceanu came to similar conclusions about the strength of thermal fluctuations of the transfer integral of acene crystals and estimated quantitative values for the nondiagonal electron–phonon coupling constants for different inter- and intramolecular modes [79]. The fluctuations of the transfer integral occur on a picosecond timescale. From the Fourier transform of the corresponding autocorrelation function, it can be concluded that there is a distribution of vibrational modes that contribute to the modulation of transfer integrals centered around $40\,\mathrm{cm}^{-1}$, while modes above $160\,\mathrm{cm}^{-1}$ make only negligible contributions [80].

It is clear from these simulations that at and near room temperature, electrons moving through such a solid are expected to experience significant dynamic disorder in the transfer integrals with strong fluctuations occurring on a picosecond timescale. If one considers a frozen lattice configuration at a specific point in time, an electron will see a disordered lattice of molecules. This disorder in the transfer integrals fundamentally affects the nature of the electron states and is expected to result in localization of at least some of the electron states if the disorder is strong enough [81]. Troisi found that at room temperature the disorder is in fact strong enough to localize all the states in the density of states (DOS) within a computed localization length on the order of several 10 Å [76]. States near the edge of the DOS are more strongly localized. The localization length increases as a function of decreasing temperature because of the decreasing thermal fluctuations. Troisi's approach allows to build up a microscopic model of the DOS and localization length for such dynamically disordered systems as a function of temperature. The specific molecular and crystal structure can be taken into account and the results can be compared with experimental results, as discussed in more detail below. Fratini and Ciuchi [82] used a Green's function method to consider localization induced by dynamic disorder in a 1D model system and predicted a density of states with a tail of states that are strongly localized by dynamic disorder, while states in the center of the DOS were found to be significantly more delocalized.

Troisi also developed a model for the mobility in such a dynamically disordered system [76]. The model treats the motion of the nuclei classically and assumes one effective vibrational mode of a specific frequency to represent the more complex distribution of modes of the real crystal. It is based on integrating the time-dependent Schrödinger equation for electrons to predict the time evolution of the electron wave function starting with an initial electron wave function that is localized over a characteristic localization length by the dynamic disorder as discussed above. By calculating the charge-carrier diffusion length as a function of time, Boltzmann averaging over different initial wave functions and fitting the averaged diffusion length to obtain a diffusion coefficient, a mobility value is predicted from the Einstein relation. Troisi demonstrated that the simple transport model can reproduce the order of magnitude of the mobility observed at room temperature in rubrene and pentacene [77]. It predicts a bandlike temperature dependence of the mobility, $\mu \propto T^{-\alpha}$, because as the temperature is decreased, the dynamic disorder is reduced and the localization length of the electronic states is increased.

Troisi's original model has been criticized for treating the phonons classically, for approximating the complex dynamics with a single effective mode to include in the Hamiltonian, and for being a 1D model. Dynamic disorder might possibly be a strong effect in one dimension only, but in two dimension one could argue it should affect the electronic states significantly less. However, recent work on an extension of the model to two dimension has shown that the basic prediction of the model, that the electronic states become localized by dynamic disorder in the transfer integrals, remains valid also in two dimension [83]. The model was also recently extended to systems that exhibit dynamical fluctuations over a wide frequency range of typically 0–200 cm^{-1} [84, 85]. The classical treatment of the phonons is clearly a limitation of the model and warrants further study. However, at room temperature, the condition $\hbar\omega \ll k_B T$, which renders such classical treatment valid, should be valid for the low-energy lattice modes that appear to be responsible for the dynamic disorder.

To better understand the charge transport in this regime, it is helpful to consider the different timescales that are relevant. The intermolecular interactions with transfer integrals $J \approx 100$ meV should, in principle, give rise to formation of mesoscopically extended Bloch electrons on a timescale $\tau_b = \hbar/J \approx 10$ fs. However, as stated above, we need to consider the coupling of the electrons to intramolecular vibrational modes ($\hbar\omega_v \approx 100$ meV) as well as intermolecular librations and other acoustic and optical phonon modes ($\hbar\omega_p < 10$ meV) [86]. Intramolecular reorganization occurs on a typical timescale comparable to the timescale of charge delocalization and might therefore be considered to lead primarily to renormalization of the transfer integral [87]. Intermolecular reorganization, on the other hand, occurs on a slower timescale of $\tau_p > 100$ fs and it is therefore expected that on a sub-100 fs timescale, charge carriers see a dynamically disordered potential landscape into which they can extend over only a small length scale. A short time later, the lattice configuration changes and the charges then extend into the new configuration. In this process, the charges can be considered to "surf" on the potential created by the lattice phonon modes. A similar argument for dynamic localization was put forward by Zuppiroli *et al.*, who argued that fluctuations in the polarization energy due to intermolecular phonons can also result in similar dynamic disorder-driven carrier localization [87].

7.3.1
Static Disorder Parameters σ and Σ

In a real molecular solid, structural or chemical defects, such as branching defects, regioregularity defects, conjugation defects, chemical impurities, point or line defects, dipolar disorder due to random orientation of polar groups of the organic semiconductor, or the gate dielectric, lead to time-independent, spatial variations of the energy and hopping distances from site to site. Again, according to Anderson [81], in the presence of such static disorder, some of the electronic states, particularly those close to the band edge, are no longer delocalized but become localized. If the disorder is sufficiently strong, all states become localized. This regime is

encountered in many disordered, amorphous low-mobility organic solids and conjugated polymers. Charge transport can be described by hopping between pairs of localized molecular states. The distribution of site energies can often be approximated by a Gaussian distribution with standard deviation σ. Similarly, the off-diagonal disorder can be described by a Gaussian distribution with standard deviation Σ, reflecting the distribution in hopping distances.

The transport of charges injected into a molecular solid dominated by the effects of disorder is well understood from the work on molecularly doped polymers and other organic photoconductors used in xerography [5]. Assuming a disorder-broadened Gaussian density of transport states with a characteristic width σ, Bässler [88] has shown on the basis of Monte Carlo simulations that an injected carrier hopping through such an otherwise empty density of states relaxes to a dynamic equilibrium energy $\langle \varepsilon_\infty \rangle = -(\sigma^2/kT)$ below the center of the DOS leading to a characteristic $log\,\mu \propto 1/T^2$ temperature dependence of the mobility. The model has been improved by Novikov *et al.* [89], who showed that the dominant source of diagonal disorder is due to charge–dipole interactions and that spatial correlations of such interactions need to be taken into account in order to explain the commonly observed Poole–Frenkel dependence of the mobility on the electrical field and derived an expression for the electric field and temperature dependence of the mobility in a correlated DOS with both diagonal and nondiagonal, positional disorder:

$$\mu = \mu_0 \cdot \exp\left[-\left(\frac{3\sigma}{5 \cdot k_B \cdot T}\right)^2 + 0.78 \cdot \left(\left(\frac{\sigma}{k_B \cdot T}\right)^{3/2} - 2\right)\sqrt{\frac{e \cdot a \cdot E}{\sigma}}\right] \tag{7.4}$$

The model describes the transport of individual injected carriers at zero/small carrier concentrations, that is, should in principle not be directly applicable to the relatively high carrier concentrations $p = 10^{18}$–$10^{19}\,cm^{-3}$ present in the accumulation layer of FETs. Vissenberg and Matters [90] have developed a percolation model for variable range hopping transport in the accumulation layer of a FET assuming an exponential DOS with width T_0. An expression for the field-effect mobility as a function of carrier concentration p was derived:

$$\mu_{FE} = \frac{\sigma_0}{e}\left[\frac{(T_0/T)^4 \sin(\pi(T/T_0))}{(2 \cdot \alpha)^3 \cdot B_c}\right]^{T_0/T} p^{(T_0/T)-1} \tag{7.5}$$

where σ_0 is the prefactor for the conductivity, α is the effective overlap parameter between localized states, and $B_c \cong 2.8$ is the critical number for onset of percolation. Transport in this model can be effectively described as activation from a gate voltage-dependent Fermi energy to a specific transport energy in the DOS.

An alternative theoretical framework for understanding the effects of disorder is the multiple trapping model, which is well established for describing transport in amorphous silicon, and has been claimed to be more appropriate for describing the charge transport in microcrystalline polymers such as P3HT [91] and poly(bis(alkylthienyl-bithiophene) [92]. This model assumes that the static disorder is sufficiently

weak, that in a certain energy range the DOS becomes high enough, and that electronic states above the so-called mobility edge are extended, while electronic states below the mobility edge remain localized. The current is assumed to be transported by carriers that are thermally activated into the delocalized states above the mobility edge, while carriers in localized states are effectively trapped. Assuming a specific DOS and a mobility for carriers above the mobility edge, the FET current can be obtained by first determining the position of the quasi-Fermi level at the interface for a particular gate voltage and then calculating the number of free carriers that are thermally excited above the mobility edge using Fermi–Dirac statistics. A common feature of all transport models that assume that transport is determined by energetic disorder is that they predict a temperature-dependent mobility that increases with increasing temperature and it is generally challenging to distinguish between the different models on the basis of an analysis of this temperature dependence alone.

7.4
Transport Physics of High-Mobility Molecular Semiconductors

In this section, we review the recent experimental characterization of the charge transport physics of high-mobility molecular semiconductor FETs. Our discussion is limited to transport in single crystals or polycrystalline thin films with large grain size that allow studying the more intrinsic charge transport properties and electronic structure within the single-crystalline grains in the absence of grain boundaries. The general transport physics of molecular single-crystal FETs has been reviewed in an excellent review article by Gershenson *et al*. [93], which includes discussions on the experimentally determined mobility anisotropy, the role of the gate dielectric, effects observed at high carrier concentration, and understanding of the nature of defect and trap states. When studying charge transport in organic semiconductors using FET configurations, one should always keep in mind that the electronic properties of the surface might differ significantly from those in the bulk, not only because the presence of the dielectric can induce significant electronic disorder and polarization effects [8] but also because the molecular structure in the first layer on the surface/interface might differ significantly from that in the bulk as recently demonstrated for rubrene single crystals by X-ray diffraction [94]. In this section, we focus on recent attempts to answer one of the fundamental, remaining open questions, which is whether the transport in highly crystalline molecular semiconductors at or near room temperature is governed by band transport or hopping transport, that is, whether the wave function of the charge carriers at or near room temperature is extended over many molecules or confined to a single molecule. As discussed in Section 7.3, this remains the subject of considerable debate.

Important experimental insight into this question comes from the temperature dependence of the FET mobility in high-mobility rubrene single crystals with room temperature mobility values of 10–40 $cm^2/(V\,s)$ which exhibit bandlike temperature

dependence between room temperature and 200 K, that is, the mobility decreases with increasing temperature (Figure 7.8a) [95]. The temperature dependence can be fitted to a $\mu \propto T^{-\gamma}$ ($\gamma \approx 2$) power law dependence. At lower temperatures, the mobility enters a trap-dominated thermally activated regime. Similar temperature dependence has also been observed for transport in the bulk, for example, by transient photoconductivity experiments [96, 97]. It is in reasonably good qualitative

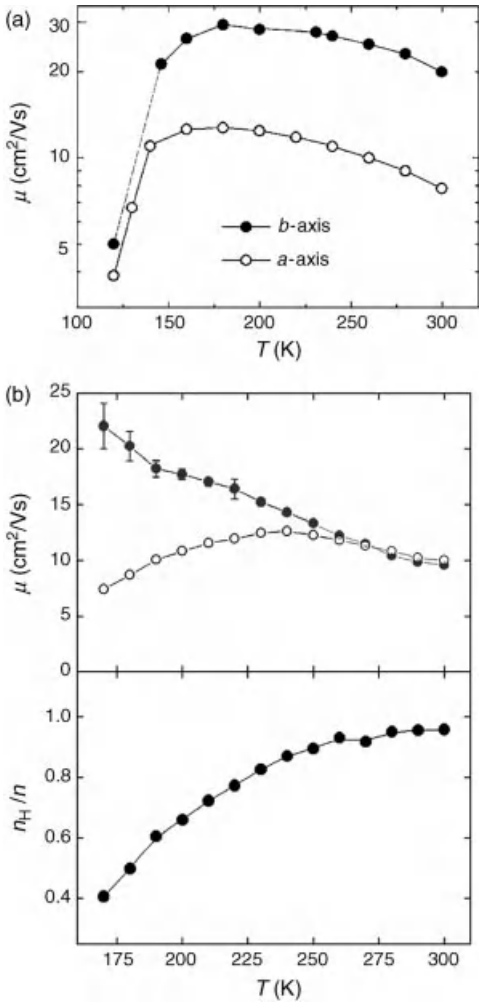

Figure 7.8 (a) Temperature dependence of the field-effect mobility measured along the *a*- and *b*-axes of a rubrene single-crystal FET with an air gap dielectric.With permission from Ref. [95]. (b) *Upper panel*: The temperature dependence of the Hall mobility μ_H (solid circles) and the field-effect mobility μ extracted from the conductivity using the density n calculated from the gate-channel capacitance (open circles). *Lower panel*: The temperature dependence of the ratio of the Hall carrier density n_H to the density n. With permission from Ref. [95].

agreement with the theoretical predictions by Hannewald discussed above. However, as our discussion of theoretical approaches to describe system with strong electron–phonon coupling has shown, considering the temperature dependence of the mobility alone is not necessarily a very sound basis for distinguishing extended-state bandlike transport from localized hopping transport.

Complementary evidence that is supporting a bandlike conduction mechanism includes the observation of a Drude-like optical conductivity induced by the formation of an accumulation layer in rubrene single crystals at room temperature. The effective mass of the carriers was estimated to be close to that of the free electron mass [98, 99], suggesting that polaronic effects are absent or too weak to lead to significant mass enhancement. It was also claimed that in the optical spectra range close to the bandgap, there are no characteristic charge-induced absorptions that are characteristic for isolated radical cations, also suggesting absence of pronounced polaronic relaxation effects [98]. We note, however, that in the raw experimental charge modulation spectrum of these devices, there are strong interference artifacts, which make it difficult to investigate any charge-induced absorptions in the optical spectral range.

Measurements of the Seebeck coefficient S also provide a means of assessing the relevance of electron–phonon coupling in molecular semiconductors. S is a measure of the entropy transported by a thermally excited charge carrier and can be determined from the thermoelectric voltage generated between two electric contacts between which a temperature gradient ΔT is established, $S = V_{\text{thermoel}}/\Delta T$. In inorganic semiconductors with negligible electron–phonon coupling, S is determined mainly by a configurational, electronic entropy contribution that depends on the electronic density of states and the energy-dependent conductivity $\sigma(E)$ [100]:

$$S = \frac{k_B}{e}\int \frac{E_F - E}{k_B T}\frac{\sigma(E)}{\sigma} = \frac{k_B}{e}\frac{E_F - E_{tr}}{k_B T} + A \tag{7.6}$$

where E_{tr} (E_F) is the transport (Fermi) energy level, that is, the edge of the valence band, and A is a quantity that depends on the detailed shape of $\sigma(E)$. For many inorganic semiconductors, A is on the order of 1. In contrast, in a system with strong polaronic effects, in which the charges lead to significant softening of the vibrational modes, there should be additional vibrational contributions to the Seebeck coefficients that would make S significantly larger than what is expected from the pure electronic configurational entropy term in Eq. (7.6) [101].

The main challenge of interpreting Seebeck measurements on molecular semiconductors is an accurate knowledge of the energy difference $E_F - E_{tr}$. Von Muhlenen reported thermopower measurements on relatively low-mobility polycrystalline pentacene FETs on SiO_2 and found relatively high values of the Seebeck coefficient on the order of 240–500 μV/K [101]. No significant dependence on the gate voltage was detected. $E_F - E_{tr}$ was estimated from a comparison of the activation energy of the thin-film conductivity and the activation energy of the field-effect mobility. From this analysis, the contribution to the Seebeck coefficient from the configurational entropy term was found to be small and it was claimed that the main reason for the large

Seebeck coefficient stems from the vibrational entropy contribution due to phonon mode softening associated with charge formation. Pernstich *et al.* reported contradictory results [102]. In their thermopower measurements on rubrene single crystals and pentacene thin films, DOS modeling of the temperature-dependent FET characteristics was used to estimate $E_F - E_{tr}$ and it was concluded that the magnitude of S is well within what could be expected for nonpolaronic transport ($A = 2$–4) and suggestions that there is no significant charge–vibration coupling. In this study, a significant decrease of $S \propto -\log|V_g|$ with increasing carrier concentration/gate voltage was also detected.

Electron spin resonance (ESR) provides a microscopic probe for distinguishing between transport regimes that involve hopping of localized charges and those that involve delocalized electrons [103]. In a standard ESR measurement, a DC magnetic field applied to the sample causes a Zeeman splitting of the energy levels of spin-1/2 charge carriers, the magnitude of which is measured by the absorption of a microwave field. The position of the ESR resonance allows extracting the g-factor of the electron and its anisotropy as a function of direction of the applied field. The ESR linewidth provides information about the hyperfine coupling between the electron spin density distribution and the protons of the molecule. For localized electrons, hyperfine interactions should in principle give rise to a broad Gaussian line shape, while for delocalized electrons the motional narrowing effect tends to result in narrow Lorentzian line shape. Kuroda used field-induced ESR measurements on pentacene FETs to determine the anisotropy of the g-factor [104]. For thin-film pentacene FETs with a relatively low mobility of $0.01\,cm^2/(V\,s)$, they claimed a Gaussian temperature-independent line shape indicating that the charge carriers were static and displayed no motional narrowing. From an analysis of the linewidth broadening due to hyperfine coupling ($\Delta B_{1/2} \propto N^{-(1/2)}$), the number of molecules N over which the charge-carrier wave function is extended was estimated to be on the order of 10. Matsui *et al.* [105] used similar pentacene FETs, but with higher mobility up to $0.6\,cm^2/(V\,s)$. They claimed that the ESR spectra in fact exhibit a Lorentzian line shape, which were found to narrow considerably at high temperatures and high gate voltages, providing experimental evidence for motional narrowing due to polaron diffusion. According to the theory of motional narrowing in a system in which transport is determined by a multiple trapping and release the full width at half maximum of the ESR spectrum, $\Delta B_{1/2}$, is related to the typical residence time of charges in a trap state, τ_c, through $\Delta B_{1/2} = \gamma(\Delta B_{inhomo})^2\tau_c$, where γ is the gyromagnetic ratio and ΔB_{inhomo} is the inhomogeneity of the local magnetic field due to the hyperfine interaction. Values for pentacene films of $\tau_c = 0.7 - 2$ ns were extracted. A similar analysis was also applied to ESR measurement on single-crystal rubrene FETs [106] for which shorter values of $\tau_c = 60 - 700$ ps were extracted reflecting the higher mobility of 1–$8\,cm^2/(V\,s)$ compared to thin-film pentacene. A correlation between ESR linewidth and mobility was reported for rubrene device with different chemical modification of the gate dielectric–rubrene interface. Recently, Matsui *et al.* presented a careful analysis on pentacene FETs to explain why the ESR spectrum retains a near-Lorentzian line shape even at low temperatures [107]. From saturation experiments and an absence of linewidth broadening

with increasing microwave power at low temperatures, it was concluded that below a temperature of 50 K, the charges become strongly trapped and no motional narrowing effect is present, that is, the trap residence time becomes larger than $(\gamma \Delta B_{\text{inhomo}})^{-1}$. They were able to explain the near-Lorentzian line shape at low temperatures by assuming the existence of three different trap states in which the trapped charge is distributed over $N = 1.5$, 5, and 6–20 molecules, each trap state contributing a Gaussian shaped peak with a linewidth $\sigma_0 N^{-(1/2)}$ (Figure 7.9). A theoretical Holstein polaron analysis of the expected binding energy for these trap states predicted binding energies of 140 meV ($N = 1.5$), 22 meV ($N = 5$), and 5–15 meV ($N = 6$–20). At room temperature, this estimate of N does not apply because of the linewidth being determined by motional narrowing.

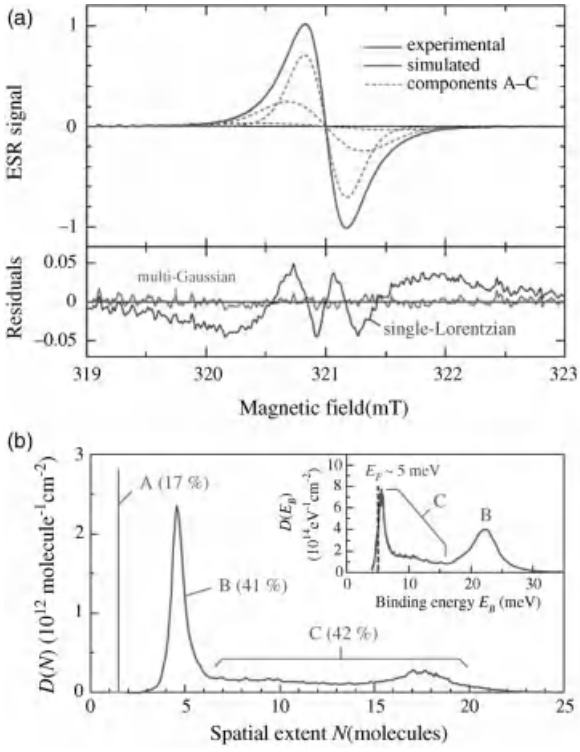

Figure 7.9 (a) *Top:* High-precision field-induced ESR spectrum of pentacene TFT measured at 20 K and at a gate voltage of 200 V. Also shown is a simulated curve reproduced by multiple Gaussian fitting, with three components indicated by dashed lines. *Bottom:* Residuals for the stochastic optimization analysis for different fits (solid line). (b) Distribution of trap states in pentacene TFTs are plotted against the spatial extent N of the wave function as obtained by stochastic optimization analysis of the ESR spectrum in (a). The inset shows the distribution of trap states as a function of theoretically computed polaron binding energy E_B. With permission from Ref. [107].

Hall effect measurements have also been used because they might provide a more direct way of probing the intrinsic charge transport properties of organic semiconductors than measurements of the longitudinal conductivity. In a Hall experiment on a FET, a magnetic field is applied perpendicular to the plane of the accumulation layer and a transverse voltage on opposite sides of the channel is measured as a longitudinal current is flowing along the channel. The main quantities that are measured is the Hall resistance R_H and the longitudinal conductivity σ of the accumulation layer. These define a Hall carrier concentration n_H as well as a Hall mobility μ_H according to

$$R_H \equiv \frac{1}{B}\frac{U_H}{I} \equiv \pm\frac{1}{en_H}$$

$$\mu_H \equiv R_H\sigma = \frac{1}{B}\frac{U_H}{V}\frac{L^*}{W} \approx \frac{n}{n_H}\mu$$

U_H is the transverse Hall voltage measured by two voltage probes on opposites sides of the channel separated by the channel width W, V is the longitudinal voltage drop associated with the current I measured between two voltage probes along the channel separated by a distance L^*, and the $\pm$ sign applies to electrons and hole charge carriers, respectively.

For an ideal, wide bandgap semiconductor or metal with an isotropic band structure and no trap states, the Hall carrier concentration should be equal to the total carrier concentration n and the Hall mobility should be equal to the longitudinal drift mobility μ. This situation we will refer to as the ideal Hall effect. In a FET configuration, it is possible to check whether a Hall signature is ideal since the total carrier concentration is known accurately from $n = C_i(V_g - V_T)$. In fact, one of the main applications of Hall measurements for systems where the carrier n is not known is the independent determination of n. If the system has some trap states, such that at any point in time a fraction of charges reside in localized trap states, these charges do not have a velocity and, consequently, do not experience a Lorentz force. In this situation, n_H can be interpreted as the fraction of the total carrier concentration, which is in mobile band states and are able to contribute to the Hall voltage. μ_H continues to provide a measure of the band mobility, while the drift mobility extracted by dividing the longitudinal conductivity by the total carrier concentration would be reduced reflecting the influence of the traps.

In a hopping system, the situation is more complicated. A simple interpretation of n_H is not possible and the key quantity that needs to be computed in order to interpret the Hall effect in such systems is the transverse conductivity $\sigma_{xy}(B)$ in the presence of the magnetic field. A number of authors have developed theoretical approaches to calculate the Hall mobility for different hopping transport models [108]. The magnetic field manifests itself through the interference of the transition amplitudes associated with the carrier moving between two sites via different paths. Emin considered the Holstein polaron

model in the high-temperature hopping limit and showed that the key quantity that determines the transverse conductivity and the Hall mobility are three-site hopping probabilities [109]. Generally, in hopping systems, μ_H and R_H differ significantly from μ and $(en)^{-1}$, respectively. In this sense, Hall effect measurements should constitute a powerful, qualitative test for whether a system exhibits hopping transport or whether the charge carriers are associated with well-defined velocities.

Hall measurements in organic semiconductors are challenging due to the high longitudinal sheet resistance associated with the relatively low field-effect mobilities, high contact resistance and threshold voltage, and current instabilities on the timescale of the Hall measurements. They were first reported for high-mobility FETs based on rubrene single crystals [110, 111]. Podzorov *et al.* showed that at room temperature, rubrene FETs with air gap dielectric exhibit an ideal Hall effect with $n_H = C_i(V_g - V_T)$ and $\mu_H = \mu_{FET}$ suggesting that all carriers induced by the gate voltage have well-defined velocity and contribute to the Hall voltage (Figure 7.8b). At temperatures <250 K, n_H and μ_{FET} were found to exhibit thermally activated behavior as a result of charge-carrier trapping, while μ_H exhibited a bandlike temperature dependence from RT to 170 K below which the Hall signature could not be measured due to increased noise [111]. Takeya showed for rubrene FETs in contact with a relatively high-k gate dielectric of polyvinylphenol (PVP) that the Hall mobility drops sensitively with increasing gate voltage suggesting that high-mobility charge transport is possible, while at the interface the mobility is reduced by surface scattering [112]. The first Hall measurements on thin-film OFETs were reported for pentacene bottom-gate OFETs with a mobility of 0.4 $cm^2/(V s)$ [113]. The inverse Hall resistance was a factor 2–3 larger than the gate-induced charge-carrier concentration in the temperature range of 250–380 K [114]. Below 250 K, this difference increased further. This cannot be interpreted in terms of a trapping effect as discussed above, which would lead to $n_H < C_i(V_g - V_T)$, but rather indicates that charge transport in such relatively, low-mobility polycrystalline OFETs exhibits characteristics of hopping transport. Different behavior was recently observed for vacuum-evaporated polycrystalline FETs based on DNTT with slightly higher field-effect mobility of 0.4–1.2 $cm^2/(V s)$. Here, the Hall effect was observed to be ideal at room temperature as well as at low temperatures down to 160 K, suggesting that the presence of grain boundaries alone does not prevent the observation of an ideal Hall effect in organic semiconductors [115]. The extracted Hall mobility in the thin films was found to be thermally activated, while reference measurements on single crystals of DNTT revealed a near temperature-independent Hall mobility. This was interpreted in terms of a contribution from grain boundary resistance to the Hall mobility of the thin films.

One of the important questions that was left unanswered by these Hall effect studies is an understanding of the extent to which the observation of an ideal or nonideal Hall effect system reflects any microscopic charge transporting states in a particular materials system. It remained unclear, for example, why a molecular semiconductor such as unsubstituted pentacene shows a

nonideal Hall effect, while DNTT is able to exhibit an ideal Hall effect, when the field-effect mobilities of the two systems are quite comparable. In a recent series of papers [116, 117], we have proposed an experimental methodology to address these questions by combining temperature-dependent FET measurements with Hall effect measurements, optical spectroscopy of charges that provides a direct spectroscopic assessment of the presence of polaronic relaxation effects and theoretical simulations of dynamic disorder for the specific molecular structures investigated experimentally. In the following, we illustrate this methodology by comparing two solution-processable pentacene derivatives, 6,13-bistriisopropyl-silylethynyl pentacene (TIPS-P) [16] and 1,4,8,11-tetramethyl-6,13-triethylsilylethynyl pentacene (TMTES-P) [22]. Both systems exhibit high charge-carrier mobilities in spin-coated thin films in contact with a low-k, Cytop gate dielectric with room temperature values of 1.5–2 $cm^2/(V\,s)$ for TIPS-P and even higher values of 2.6–3.5 $cm^2/(V\,s)$ for TMTES-P. The measurements are performed on thin polycrystalline films, but the grain size is large, $>10\,\mu m$, typically, such that it should be possible to study more intrinsic charge transport properties in these devices. The main advantage of using thin films compared to single crystals is that it is easier to extend the temperature range of electrical and optical measurements to temperatures close to 4 K. With single-crystal FETs, this has proven challenging due to problems with mismatch of thermal expansion coefficients between the crystals and the substrate/other layers.

The temperature dependence of TIPS-P top-gate FETs with mobilities of 1.5–2 cm^2/Vs was found to be similar to that observed for rubrene single crystal FETs [116]. Between room temperature and 200K the mobility increases with decreasing temperature, providing clear evidence that even in solution-processed molecular thin films a band-like temperature dependence of the mobility can be observed. At lower temperature, again similarly to single crystals, the mobility becomes thermally activated with a relatively small activation energy of 5–15 meV. The nature of the static, shallow traps states that are most likely responsible for the temperature-activated behavior is unknown, but they could be associated with dislocations, point defects, or other structural defects incorporated into the film during solution growth.

This observation of bandlike transport characteristics in thin films similar to that observed in rubrene single crystals warranted a more in-depth investigation using Hall effect measurements. The sign of the Hall coefficient R_H was found to be positive in both materials, consistent with the FETs operating in p-type accumulation mode. $1/R_H$ increases monotonically with $|V_g - V_{th}|$ (Figure 7.10b). In TIPS-P, $1/R_H$ is about twice larger than the gate-induced charge density $Q \equiv C_i(V_g - V_{th})$, which is similar to the behavior reported for vacuum-sublimed pentacene [113]. The Hall mobility μ_H is about half the field-effect mobility μ_{FET} at all temperatures from room temperature to 150 K. In contrast, TMTES-P exhibits a remarkably ideal Hall effect with $1/R_H$ coinciding with Q for $|V_g| > 20$ V, not only at room temperature, but for all temperatures from RT to 150 K.

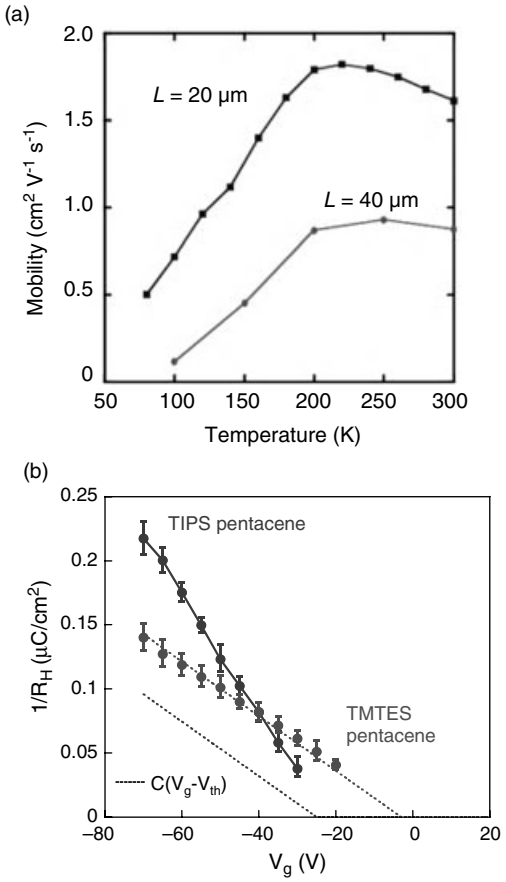

Figure 7.10 (a) Temperature dependence of effective mobility of TIPS-P FETs for devices with channel length of L = 20 and 40 μm. With permission from Ref. [116]. (b) Inverse Hall coefficient $1/R_H$ and gate-induced charge density $Q \equiv C_i(V_g - V_{th})$ as a function of gate voltage for TIPS-P and TMTES-P FETs measured at room temperature. With permission from Ref. [117].

The observation of an ideal Hall effect in TMTES-P suggests unambiguously that, at least in TMTES-P, the charge carriers are not localized on individual molecules and move by hopping, but that their wave function must be sufficiently delocalized, such that it is possible to define a wave vector and group velocity that can couple to the magnetic field through a semiclassical Lorentz force expression. The observation of an ideal Hall signature raises the question whether charge carriers in these molecular crystals are in fact best described as conventional Bloch electrons that are only weakly coupled to phonons and delocalized on mesoscopic length scales or in which way the transport properties reflect any molecular reorganization and localization processes.

The degree to which molecular reorganization associated with charge formation is present can directly be investigated by optical charge modulation spectroscopy (CMS) of the charges in the FET accumulation layer as a function of temperature. If molecular reorganization is present, charges in organic semiconductors are expected to have characteristic charge-induced optical absorptions, which differ from those of the neutral molecule and reflect the degree of intramolecular reorganization and polarization associated with charge formation [8]. For both TIPS-P and TMTES-P FETs, we observed pronounced charge-induced absorption bands ($\Delta T/T < 0$) around 1.2 and 2.6 eV together with an associated bleaching signal ($\Delta T/T > 0$) of the neutral molecule absorption around 1.8–2.2 eV (Figure 7.11) [116]. To identify the nature of these transitions, we performed quantum chemical calculations at the semiempirical AM1 level with full configuration interaction (FCI). Calculations were performed on an isolated TIPS-P monomer molecule as well as on a dimer. If one takes into account the typical errors in estimating transition energies by quantum chemical computations in the gas phase, the theoretical spectrum is in good agreement with the experimental CMS spectrum of TIPS-P [116]. The calculations on the dimer predict the charge to be fully delocalized over the two molecules. The calculations predict subtle differences between the monomer and the dimer spectrum, which might suggest that the temperature dependence of the CMS spectra can be interpreted as temperature-dependent changes in the degree of charge delocalization. We interpret the broad spectral features in the room temperature CMS spectrum of TIPS-P as a manifestation of an ensemble average over charges that are delocalized over different numbers $N = 2,3, \ldots$ of molecules. The sharper CMS spectrum at low temperature is believed to reflect the capturing of the charges in shallow static trap states, which is consistent with the observed temperature dependence of the mobility at low lateral electric field. In general, the surprisingly good agreement of the experimental charge-induced absorption spectrum with the calculations on small molecular clusters implies that charges in TIPS-P and TMTES-P cannot be in extended Bloch electron states delocalized over hundreds or thousands of molecules, but can only be delocalized over a small number of molecules. For mesoscopically extended states, the reorganization would be significantly reduced [118] and we would expect any residual charge-induced absorption features to appear at energies close to those of the neutral system and not result in such strongly spectrally shifted induced absorptions.

To investigate the generality of these results, we also performed CMS measurements on rubrene single-crystal FETs with mobilities $>5\,\mathrm{cm}^2/(\mathrm{V\,s})$ (Figure 7.12). As discussed above, it had been concluded from the previous CMS measurements [98] that in rubrene no such induced absorptions were present in the optical spectral range. We optimized the device configuration for CMS measurements on rubrene single crystals to remove any interference artifacts in the spectrum. To our surprise, we found that the rubrene CMS spectra are qualitatively very similar to TIPS-P and TMTES-P, with a low-energy charge-induced absorption at 1.6 eV and a higher lying transition at 2.8 eV. There is no spectroscopic evidence that charge carriers in TMTES-P, TIPS-P, and rubrene single crystals are fundamentally different. Since

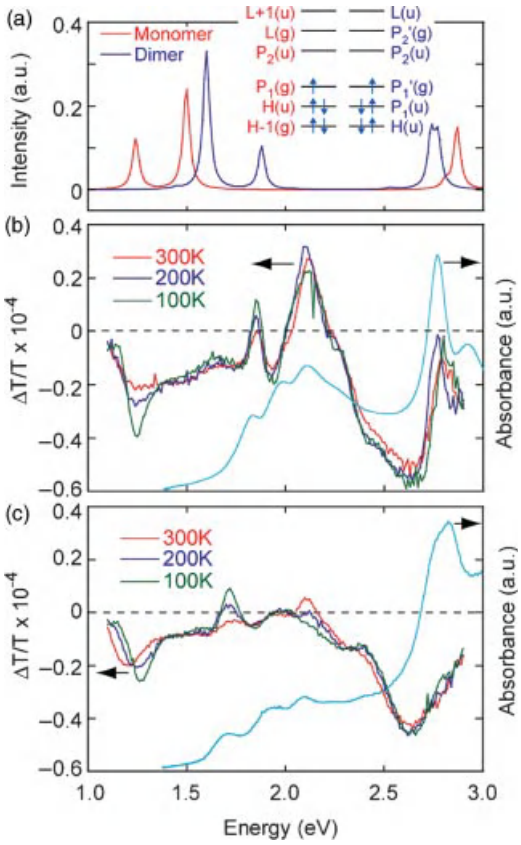

Figure 7.11 (a) Quantum chemical simulation of the absorption spectrum of TIPS-P radical cation monomer (red) and dimer (blue), including schematic energy level diagram. Temperature-dependent differential transmission CMS spectra of TIPS-P (b) and TMTES-P (c) FETs. The thin-film absorption spectra of the two molecules are shown as light blue curves. With permission from Ref. [117].

TMTES-P and rubrene [111] exhibit an ideal Hall effect to which *all* charge carriers must contribute, we concluded that charges, which are delocalized over only a small molecular cluster and result in radical cationlike, charge-induced absorptions, are indeed capable of producing an ideal Hall signature and a bandlike temperature dependence of the field-effect mobility.

These observations of limited charge delocalization over only a few molecules emerging from CMS and the ideal Hall effect and bandlike temperature dependence of the mobility normally associated with extended-state transport can be rationalized consistently in the dynamic disorder transport model proposed by Troisi and Orlandi [76, 83] discussed above. Fluctuations in the hopping integrals for TIPS-P and TMTES-P were computed using a combination of molecular

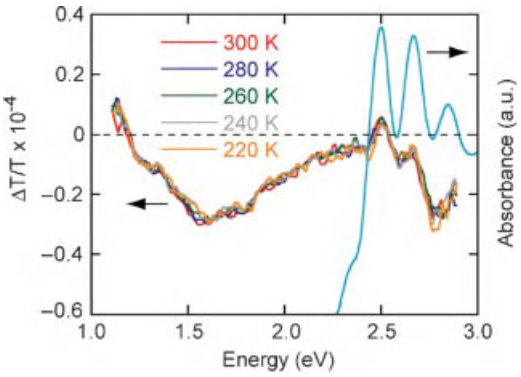

Figure 7.12 Temperature dependent differential transmission CMS spectrum of a rubrene single-crystal FET with top-gate architecture and parylene gate dielectric. The absorption spectrum of rubrene is shown as a light blue curve.l With permission from Ref. [117].

dynamics and quantum chemical calculations [77] and the dynamically disordered DOS and localization length at room temperature were calculated for the crystal structure of the two molecules that had been determined by X-ray diffraction. For both molecules, there is substantial DOS broadening due to thermal motions, accompanied by considerable localization of the wave function in the tail of the DOS. Within few k_BT from the DOS edge, the states are localized within few molecules. The DOS shape for the two molecules is different. In both molecules, the π–π stacking is cofacial and the π–π stacking distance are similar, but TMTES-P has a quasi-one-dimensional dispersion reflecting its one-dimensional crystal packing and smaller broadening due to a smaller fluctuation of the coupling, whereas TIPS-P has a two-dimensional brick wall packing motif (Figure 7.13a). When integrating the DOS to a charge concentration of $10^{19}\,\mathrm{cm}^{-3}$ typical for the FET accumulation layer, the Fermi level comes to lie in a region with larger delocalization length for TMTES-P than for TIPS-P. This provides a possible explanation for the more ideal Hall signature observed in TMTES-P. The computed isotropic mobilities of 5.1 and $12.4\,\mathrm{cm}^2/(\mathrm{V\,s})$ for TIPS-P and TMTES-P, respectively, are also in a similar ratio as found experimentally for the Hall mobilities and also close to the experimental values in absolute terms. From this analysis, it appears that the wave function localization length predicted by the dynamic disorder model for systems such as TMTES-P is small enough to provide an explanation for observing the signature of localized states in CMS, but large enough to allow observation of an ideal Hall effect. In fact, Hall transport in organic semiconductors might be qualitatively similar to that in bad metals with weak electron correlation effects, where R_H remains ideal when the scattering length approaches the interatomic distance [119].

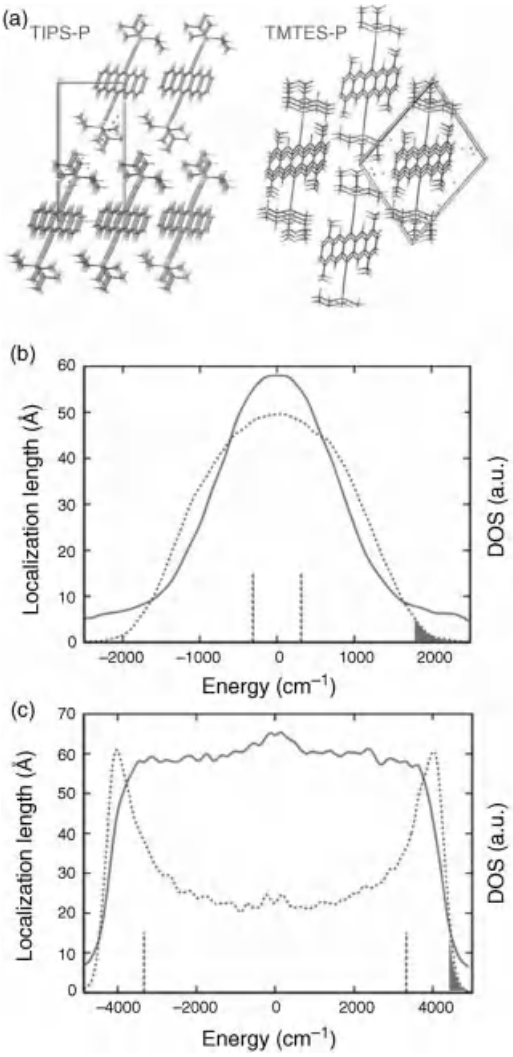

Figure 7.13 (a) View of the single-crystal structure of TIPS-P and TMTES-P along (near) the *a*-axis. The one- and two-dimensional stackings of molecules along the *a*-axis can be clearly seen. Localization length (solid) and DOS (dotted) for TIPS-P (b) and TMTES-P (c). The vertical dashed lines represent the bandwidth in the absence of dynamic disorder. The shaded area indicates the portion of the DOS that is expected to be occupied for a carrier concentration of $10^{19}\,cm^{-3}$. With permission from Ref. [117].

7.5 Conclusions

In this chapter, we have discussed the materials and charge transport physics of high-mobility organic semiconductors. In spite of extensive research efforts, it has been difficult to answer the simple but fundamental question whether at or near room temperature the wave function of the charge carriers in these materials are extended over many molecules and transport is best described in terms of Bloch electrons with occasional scattering or whether the charge carriers are localized on individual molecules and move by hopping. Over recent years, there has been increasing experimental evidence that at least in high-mobility molecular crystals with mobility values exceeding 1–10 $cm^2/(V\,s)$, a description in terms of Bloch electron transport might be more appropriate to explain the bandlike temperature dependence of the mobility or the observation of an ideal Hall effect. However, as we have argued in this chapter, there are also experimental observations that clearly indicate the importance of molecular relaxation effects, such as the presence of a pronounced optical charge-induced absorption that resembles that of radical cations localized on small molecular clusters. To explain these observations consistently, we have proposed that at room temperature the intermolecular interaction is sufficiently strong and the diagonal electron–phonon coupling is sufficiently weak, such that the charge carriers would in principle be able to form extended Bloch electron states, however, they are hindered in their ability to delocalize fully by nondiagonal electron–phonon coupling due to thermal lattice fluctuations. At room temperature, charges remain localized on a picosecond timescale over small clusters of molecules and they undergo a diffusive motion with the fluctuations in the intermolecular lattice. In such a model, it is possible to explain not only both the bandlike temperature dependence of the mobility and the occurrence of an ideal Hall effect but also the observation of pronounced charge-induced absorption. These descriptions of charge transport point to dynamic disorder as one of the main factors limiting charge-carrier mobilities at room temperatures. Higher mobilities can be expected in molecular architectures that effectively reduce fluctuations in relative molecular positions and orientations and associated fluctuations in the transfer integrals. Molecular modeling of dynamic disorder should provide a simulation tool at the molecular level to guide the design and development of new mobility organic semiconductors.

References

1 McCulloch, I. (2010) *Adv. Mater.*, **22** (34), 3760–3761.

2 Sirringhaus, H. and Ando, M. (2008) *MRS Bull.*, **33** (7), 676–682.

3 Myny, K., van Veenendaal, E., Gelinck, G.H., Genoe, J., Dehaene, W., and Heremans, P., An 8b organic microprocessor on plastic foil (2011) Proceedings of the ISSCC 2011, San Francisco.

4 Gelinck, G., Heremans, P., Nomoto, K., and Anthopoulos, T.D. (2010) *Adv. Mater.*, **22** (34), 3778–3798.

5 Borsenberger, P.M. and Weiss, D.S. (1993) BT *Organic Photoreceptors for Imaging Systems,* Marcel Dekker, New York.
6 Karl, N. (2003) *Synth. Met.*, **133**, 649–657.
7 Ortiz, R.P., Facchetti, A., and Marks, T.J. (2010) *Chem. Rev.*, **110** (1), 205–239.
8 Sirringhaus, H. (2005) *Adv. Mater.*, **17** (20), 2411–2425.
9 Sirringhaus, H. (2009) *Adv. Mater.*, **21** (38–39), 3859–3873.
10 Bredas, J.L., Calbert, J.P., da Silva, D.A., and Cornil, J. (2002) *Proc. Natl. Acad. Sci. USA*, **99** (9), 5804–5809.
11 Sirringhaus, H. (2005) *Adv. Mater.*, **17** (20), 2411–2425.
12 Troisi, A. and Orlandi, G. (2006) *Phys. Rev. Lett.*, **96** (8), 086601.
13 Cheung, D.L., McMahon, D.P., and Troisi, A. (2009) *J. Phys. Chem. B*, **113** (28), 9393–9401.
14 Troisi, A., Cheung, D.L., and Andrienko, D. (2009) *Phys. Rev. Lett.*, **102** (11), 116602.
15 Anthony, J.E., Facchetti, A., Heeney, M., Marder, S.R., and Zhan, X.W. (2010) *Adv. Mater.*, **22** (34), 3876–3892.
16 Anthony, J.E., Brooks, J.S., Eaton, D.L., and Parkin, S.R. (2001) *J. Am. Chem. Soc.*, **123** (38), 9482–9483.
17 Payne, M.M., Parkin, S.R., Anthony, J.E., Kuo, C.C., and Jackson, T.N. (2005) *J. Am. Chem. Soc.*, **127** (14), 4986–4987.
18 Lee, S.S., Kim, C.S., Gomez, E.D., Purushothaman, B., Toney, M.F., Wang, C., Hexemer, A., Anthony, J.E., and Loo, Y.L. (2009) *Adv. Mater.*, **21** (35), 3605.
19 Gundlach, D.J., Royer, J.E., Park, S.K., Subramanian, S., Jurchescu, O.D., Hamadani, B.H., Moad, A.J., Kline, R.J., Teague, L.C., Kirillov, O., Richter, C.A., Kushmerick, J.G., Richter, L.J., Parkin, S. R., Jackson, T.N., and Anthony, J.E. (2008) *Nat. Mater.*, **7** (3), 216–221.
20 Tang, M.L., Reichardt, A.D., Miyaki, N., Stoltenberg, R.M., and Bao, Z. (2008) *J. Am. Chem. Soc.*, **130** (19), 6064.
21 Anthony, J.E. and Purushothaman, B. (2007) BT Organic Field-Effect Transistors VI, vol. **6658** (eds. Z. Bao and D.J. Gundlach), SPIE, Bellingham, pp. L6580–L6580.
22 Llorente, G.R., Dufourg-Madec, M.B., Crouch, D.J., Pritchard, R.G., Ogier, S., and Yeates, S.G. (2009) *Chem. Commun.*, (21), 3059–3061.
23 Kang, J., Shin, N., Jang, D.Y., Prabhu, V.M., and Yoon, D.Y. (2008) *J. Am. Chem. Soc.*, **130** (37), 12273.
24 Hamilton, R., Smith, J., Ogier, S., Heeney, M., Anthony, J.E., McCulloch, I., Veres, J., Bradley, D.D.C., and Anthopoulos, T.D. (2009) *Adv. Mater.*, **21** (10–11), 1166–1171.
25 Takimiya, K., Ebata, H., Sakamoto, K., Izawa, T., Otsubo, T., and Kunugi, Y. (2006) *J. Am. Chem. Soc.*, **128** (39), 12604–12605.
26 Yamamoto, T. and Takimiya, K. (2007) *J. Am. Chem. Soc.*, **129** (8), 2224.
27 Haas, S., Takahashi, Y., Takimiya, K., and Hasegawa, T. (2009) *Appl. Phys. Lett.*, **95** (2), 022111.
28 Wei, Z.M., Hong, W., Geng, H., Wang, C.L., Liu, Y.L., Li, R.J., Xu, W., Shuai, Z. G., Hu, W.P., Wang, Q.R., and Zhu, D.B. (2010) *Adv. Mater.*, **22** (22), 2458.
29 Uemura, T., Hirose, Y., Uno, M., Takimiya, K., and Takeya, J. (2009) *Appl. Phys. Express*, **2** (11), 111501.
30 Osaka, I., Abe, T., Shinamura, S., Miyazaki, E., and Takimiya, K. (2010) *J. Am. Chem. Soc.*, **132** (14), 5000.
31 Kang, M.J., Doi, I., Mori, H., Miyazaki, E., Takimiya, K., Ikeda, M., and Kuwabara, H. (2011) *Adv. Mater.*, **23** (10), 1222.
32 Nakayama, K., Hirose, Y., Soeda, J., Yoshizumi, M., Uemura, T., Uno, M., Li, W.Y., Kang, M.J., Yamagishi, M., Okada, Y., Miyazaki, E., Nakazawa, Y., Nakao, A., Takimiya, K., and Takeya, J. (2011). *Adv. Mater.*, **23** (14), 1626.
33 Gao, J.H., Li, R.J., Li, L.Q., Meng, Q., Jiang, H., Li, H.X., and Hu, W.P. (2007) *Adv. Mater.*, **19**, 3008.
34 Li, R.J., Dong, H.L., Zhan, X.W., He, Y.D., Li, H.X., and Hu, W.P. (2010) *J. Mater. Chem.*, **20** (29), 6014–6018.
35 Gao, P., Beckmann, D., Tsao, H.N., Feng, X.L., Enkelmann, V., Baumgarten, M., Pisula, W., and Mullen, K. (2009) *Adv. Mater.*, **21** (2), 213.
36 Li, L.Q., Tang, Q.X., Li, H.X., Yang, X.D., Hu, W.P., Song, Y.B., Shuai, Z.G., Xu, W., Liu, Y.Q., and Zhu, D.B. (2007) *Adv. Mater.*, **19**, 2613.

37 Leufgen, M., Rost, O., Gould, C., Schmidt, G., Geurts, J., Molenkamp, L.W., Oxtoby, N.S., Mas-Torrent, M., Crivillers, N., Veciana, J., and Rovira, C. (2008) *Org. Electron.*, **9** (6), 1101–1106.

38 Zhang, L., Tan, L., Wang, Z.H., Hu, W.P., and Zhu, D.B. (2009) *Chem. Mater.*, **21** (9), 1993–1999.

39 Veres, J., Ogier, S.D., Leeming, S.W., Cupertino, D.C., and Khaffaf, S.M. (2003) *Adv. Funct. Mater.*, **13** (3), 199–204.

40 Veres, J., Ogier, S., Lloyd, G., and de Leeuw, D. (2004) *Chem. Mater.*, **16** (23), 4543–4555.

41 Sirringhaus, H., Brown, P.J., Friend, R. H., Nielsen, M.M., Bechgaard, K., Langeveld-Voss, B.M.W., Spiering, A.J.H., Janssen, R.A.J., Meijer, E.W., Herwig, P., and de Leeuw, D.M. (1999) *Nature*, **401** (6754), 685–688.

42 Ong, B.S., Wu, Y.L., Liu, P., and Gardner, S. (2004) *J. Am. Chem. Soc.*, **126** (11), 3378–3379.

43 McCulloch, I., Heeney, M., Bailey, C., Genevicius, K., Macdonald, I., Shkunov, M., Sparrowe, D., Tierney, S., Wagner, R., Zhang, W.M., Chabinyc, M.L., Kline, R. J., McGehee, M.D., and Toney, M.F. (2006). *Nat. Mater.*, **5** (4), 328–333.

44 Hamadani, B.H., Gundlach, D.J., McCulloch, I., and Heeney, M. (2007) *Appl. Phys. Lett.*, **91** (24), 243512.

45 McCulloch, I., Heeney, M., Chabinyc, M. L., DeLongchamp, D., Kline, R.J., Coelle, M., Duffy, W., Fischer, D., Gundlach, D., Hamadani, B., Hamilton, R., Richter, L., Salleo, A., Shkunov, M., Sporrowe, D., Tierney, S., and Zhong, W. (2009). *Adv. Mater.*, **21** (10–11), 1091–1109.

46 Osaka, I., Sauve, G., Zhang, R., Kowalewski, T., and McCullough, R.D. (2007) *Adv. Mater.*, **19** (23), 4160.

47 Zhang, M., Tsao, H.N., Pisula, W., Yang, C.D., Mishra, A.K., and Mullen, K. (2007) *J. Am. Chem. Soc.*, **129** (12), 3472.

48 Tsao, H.N., Cho, D., Andreasen, J.W., Rouhanipour, A., Breiby, D.W., Pisula, W., and Mullen, K. (2009) *Adv. Mater.*, **21** (2), 209.

49 Becerril, H.A., Miyaki, N., Tang, M.L., Mondal, R., Sun, Y.S., Mayer, A.C., Parmer, J.E., McGehee, M.D., and Bao, Z. A. (2009) *J. Mater. Chem.*, **19** (5), 591–593.

50 Mondal, R., Miyaki, N., Becerril, H.A., Norton, J.E., Parmer, J., Mayer, A.C., Tang, M.L., Bredas, J.L., McGehee, M.D., and Bao, Z.A. (2009) *Chem. Mater.*, **21** (15), 3618–3628.

51 Kim, D.H., Lee, B.L., Moon, H., Kang, H. M., Jeong, E.J., Park, J.I., Han, K.M., Lee, S., Yoo, B.W., Koo, B.W., Kim, J.Y., Lee, W.H., Cho, K., Becerril, H.A., and Bao, Z. (2009). *J. Am. Chem. Soc.*, **131** (17), 6124–6132.

52 Guo, X.G., Kim, F.S., Jenekhe, S.A., and Watson, M.D. (2009) *J. Am. Chem. Soc.*, **131** (21), 7206.

53 Liu, J.Y., Zhang, R., Sauve, G., Kowalewski, T., and McCullough, R.D. (2008) *J. Am. Chem. Soc.*, **130** (39), 13167–13176.

54 Rieger, R., Beckmann, D., Pisula, W., Steffen, W., Kastler, M., and Mullen, K. (2010) *Adv. Mater.*, **22** (1), 83.

55 Burgi, L., Turbiez, M., Pfeiffer, R., Bienewald, F., Kirner, H.J., and Winnewisser, C. (2008) *Adv. Mater.*, **20** (11), 2217.

56 Nelson, T.L., Young, T.M., Liu, J.Y., Mishra, S.P., Belot, J.A., Balliet, C.L., Javier, A.E., Kowalewski, T., and McCullough, R.D. (2010) *Adv. Mater.*, **22** (41), 4617–4621.

57 Li, Y.N., Singh, S.P., and Sonar, P. (2010) *Adv. Mater.*, **22** (43), 4862.

58 Sonar, P., Singh, S.P., Li, Y., Soh, M.S., and Dodabalapur, A. (2010) *Adv. Mater.*, **22** (47), 5409.

59 Ashraf, R.S., Chen, Z.Y., Leem, D.S., Bronstein, H., Zhang, W.M., Schroeder, B., Geerts, Y., Smith, J., Watkins, S., Anthopoulos, T.D., Sirringhaus, H., de Mello, J.C., Heeney, M., and McCulloch, I. (2011). *Chem. Mater.*, **23** (3), 768–770.

60 Bronstein, H., Chen, Z.Y., Ashraf, R.S., Zhang, W.M., Du, J.P., Durrant, J.R., Tuladhar, P.S., Song, K., Watkins, S.E., Geerts, Y., Wienk, M.M., Janssen, R.A.J., Anthopoulos, T., Sirringhaus, H., Heeney, M., and McCulloch, I. (2011) *J. Am. Chem. Soc.*, **133** (10), 3272–3275.

61 Coropceanu, V., Cornil, J., da Silva, D.A., Olivier, Y., Silbey, R., and Bredas, J.L. (2007) *Chem. Rev.*, **107** (5), 2165–2165.

62 Kakuta, H., Hirahara, T., Matsuda, I., Nagao, T., Hasegawa, S., Ueno, N., and

Sakamoto, K. (2007) *Phys. Rev. Lett.*, **98** (24), 247601.
63 Cheng, Y.C., Silbey, R.J., da Silva, D.A., Calbert, J.P., Cornil, J., and Bredas, J.L. (2003) *J. Chem. Phys.*, **118** (8), 3764–3774.
64 Holstein, T. (2000) *Ann. Phys.*, **281** (1–2), 706–724.
65 Holstein, T. (2000) *Ann. Phys.*, **281** (1–2), 725–773.
66 Coropceanu, V., Malagoli, M., da Silva, D.A., Gruhn, N.E., Bill, T.G., and Bredas, J.L. (2002) *Phys. Rev. Lett.*, **89** (27), 275503.
67 Koch, N., Vollmer, A., Salzmann, I., Nickel, B., Weiss, H., and Rabe, J.P. (2006) *Phys. Rev. Lett.*, **96** (15), 156803.
68 Silbey, R. and Munn, R.W. (1980) *J. Chem. Phys.*, **72** (4), 2763–2773.
69 Kenkre, V.M., Andersen, J.D., Dunlap, D. H., and Duke, C.B. (1989) *Phys. Rev. Lett.*, **62** (10), 1165–1168.
70 Cheng, Y.C. and Silbey, R.J. (2008) *J. Chem. Phys.*, **128** (11), 114713.
71 Nan, G.J., Yang, X.D., Wang, L.J., Shuai, Z.G., and Zhao, Y. (2009) *Phys. Rev. B*, **79** (11), 115203.
72 Munn, R.W. and Silbey, R. (1985) *J. Chem. Phys.*, **83** (4), 1854–1864.
73 Munn, R.W. and Silbey, R. (1985) *J. Chem. Phys.*, **83** (4), 1843–1853.
74 Hannewald, K. and Bobbert, P.A. (2004) *Phys. Rev. B*, **69** (7), 075212.
75 Hannewald, K. and Bobbert, P.A. (2004) *Appl. Phys. Lett.*, **85** (9), 1535–1537.
76 Troisi, A. and Orlandi, G. (2006) *Phys. Rev. Lett.*, **96** (8), 086601–086604.
77 Troisi, A. (2007) *Adv. Mater.*, **19** (15), 2000–2004.
78 Troisi, A., Orlandi, G., and Anthony, J.E. (2005) *Chem. Mater.*, **17** (20), 5024–5031.
79 Coropceanu, V., Sanchez-Carrera, R.S., Paramonov, P., Day, G.M., and Bredas, J.L. (2009) *J. Phys. Chem. C*, **113** (11), 4679–4686.
80 Troisi, A. (2011) *Chem. Soc. Rev.*, **40** (5), 2347–2358.
81 Anderson, P.W. (1958) *Phys. Rev.*, **109** (5), 1492–1505.
82 Fratini, S. and Ciuchi, S. (2009) *Phys. Rev. Lett.*, **103** (26), 266601–266604.
83 Troisi, A. (2011) *J. Chem. Phys.*, **134** (3), 034702.
84 Troisi, A., Cheung, D.L., and Andrienko, D. (2009) *Phys. Rev. Lett.*, **102** (11), 116602.
85 Feng, X.L., Marcon, V., Pisula, W., Hansen, M.R., Kirkpatrick, J., Grozema, F., Andrienko, D., Kremer, K., and Mullen, K. (2009) *Nat. Mater.*, **8** (5), 421–426.
86 Silinsh, E.A. and Capek, V. (1994) BT *Organic Molecular Crystals: Interaction, Localisation and Transport Phenomena*, AIP Press, New York.
87 Picon, J.D., Bussac, M.N., and Zuppiroli, L. (2007) *Phys. Rev. B*, **75** (23), 235106–235115.
88 Bässler, H. (1993) *Phys. Status Solidi B*, **175**, 15.
89 Novikov, S.V., Dunlap, D.H., Kenkre, V.M., Parris, P.E., and Vannikov, A.V. (1998) *Phys. Rev. Lett.*, **81** (20), 4472–4475.
90 Vissenberg, M.C.J.M. and Matters, M. (1998) *Phys. Rev. B*, **57**, 12964–12967.
91 Sirringhaus, H., Tessler, N., and Friend, R.H. (1998) *Science*, **280**, 1741–1744.
92 Salleo, A., Chen, T.W., Volkel, A.R., Wu, Y., Liu, P., Ong, B.S., and Street, R.A. (2004) *Phys. Rev. B*, **70** (11), 115311.
93 Gershenson, M.E., Podzorov, V., and Morpurgo, A.F. (2006) *Rev. Mod. Phys.*, **78** (3), 973–989.
94 Okada, Y., Uno, M., Nakazawa, Y., Sasai, K., Matsukawa, K., Yoshimura, M., Kitaoka, Y., Mori, Y., and Takeya, J. (2011) *Phys. Rev. B*, **83** (11), 113305.
95 Podzorov, V., Menard, E., Borissov, A., Kiryukhin, V., Rogers, J.A., and Gershenson, M.E. (2004) *Phys. Rev. Lett.*, **93** (8).
96 Ostroverkhova, O., Cooke, D.G., Hegmann, F.A., Anthony, J.E., Podzorov, V., Gershenson, M.E., Jurchescu, O.D., and Palstra, T.T.M. (2006) *Appl. Phys. Lett.*, **88** (16).
97 Moses, D., Soci, C., Chi, X., and Ramirez, A.P. (2006) *Phys. Rev. Lett.*, **97** (6), 067401.
98 Li, Z.Q., Podzorov, V., Sai, N., Martin, M. C., Gershenson, M.E., Di Ventra, M., and Basov, D.N. (2007) *Phys. Rev. Lett.*, **99** (1), 016403–016406.
99 Fischer, M., Dressel, M., Gompf, B., Tripathi, A.K., and Pflaum, J. (2006) *Appl. Phys. Lett.*, **89** (18), 182103–182105.

100 Fritzsche, H. (1971) *Solid State Commun.*, **9**, 1813–1815.

101 von Muhlenen, A., Errien, N., Schaer, M., Bussac, M.N., and Zuppiroli, L. (2007) *Phys. Rev. B*, **75** (11).

102 Pernstich, K.P., Rossner, B., and Batlogg, B. (2008) *Nat. Mater.*, **7** (4), 321–325.

103 Feher, G. (1959) *Phys. Rev.*, **114** (5), 1219.

104 Marumoto, K., Kuroda, S., Takenobu, T., and Iwasa, Y. (2006) *Phys. Rev. Lett.*, **97** (25), 256603.

105 Matsui, H., Hasegawa, T., and Tokura, Y. (2008) *Phys. Rev. Lett.*, **100** (12).

106 Marumoto, K., Arai, N., Goto, H., Kijima, M., Murakami, K., Tominari, Y., Takeya, J., Shimoi, Y., Tanaka, H., Kuroda, S., Kaji, T., Nishikawa, T., Takenobu, T., and Iwasa, Y. (2011). *Phys. Rev. B*, **83** (7).

107 Matsui, H., Mishchenko, A.S., and Hasegawa, T. (2010) *Phys. Rev. Lett.*, **104** (5), 056602.

108 Friedman, L. and Holstein, T. (1963) *Ann. Phys.*, **21** (3), 494–549.

109 Emin, D. (1971) *Ann. Phys.*, **64** (2), 336.

110 Takeya, J., Tsukagoshi, K., Aoyagi, Y., Takenobu, T., and Iwasa, Y. (2005) *Jpn. J. Appl. Phys. 2*, **44** (46–49), L1393–L1396.

111 Podzorov, V., Menard, E., Rogers, J.A., and Gershenson, M.E. (2005) *Phys. Rev. Lett.*, **95** (22), 226601–226604.

112 Takeya, J., Kato, J., Hara, K., Yamagishi, M., Hirahara, R., Yamada, K., Nakazawa, Y., Ikehata, S., Tsukagoshi, K., Aoyagi, Y., Takenobu, T., and Iwasa, Y. (2007) *Phys. Rev. Lett.*, **98** (19).

113 Sekitani, T., Takamatsu, Y., Nakano, S., Sakurai, T., and Someya, T. (2006) *Appl. Phys. Lett.*, **88** (25), 253508–253510.

114 Takamatsu, Y., Sekitani, T., and Someya, T. (2007) *Appl. Phys. Lett.*, **90** (13), 133516.

115 Yamagishi, M., Soeda, J., Uemura, T., Okada, Y., Takatsuki, Y., Nishikawa, T., Nakazawa, Y., Doi, I., Takimiya, K., and Takeya, J. (2010) *Phys. Rev. B*, **81** (16).

116 Sakanoue, T. and Sirringhaus, H. (2010) *Nat. Mater.*, **9** (9), 736–740.

117 Chang, J.-F., Sakanoue, T., Oliviera, Y., Uemura, T., Dufourg-Madec, M.B., Yeates, S.G., Cornil, J., Takeya, J., Troisi, A., and Sirringhaus, H. (2011) *Phys. Rev. Lett.*, **107**, 066601.

118 Bromley, S.T., Illas, F., and Mas-Torrent, M. (2008) *Phys. Chem. Chem. Phys.*, **10** (1), 121–127.

119 Dai, P.H., Zhang, Y.Z., and Sarachik, M.P. (1993) *Phys. Rev. Lett.*, **70** (13), 1968–1971.

120 Tiago, M.L., Northrup, J.E., and Louie, S.G. (2003) *Phys. Rev. B*, **67**, 115212–115218.

8
Ambipolar Charge-Carrier Transport in Molecular Field-Effect Transistors

Andreas Opitz and Wolfgang Brütting

8.1
Introduction

Molecular or polymeric materials used as organic semiconductors in thin-film devices are traditionally reported as electron- or hole-transporting materials [1, 2]. Most of the polymeric materials, like poly-phenylenevinylenes or poly-thiophenes, and some classes of molecular materials, like acenes or phthalocyanines, are typically p-conducting materials, whereas fullerenes or fluorinated acenes or phthalocyanines are mainly n-conducting materials. In contrast, bipolar transport was reported for single crystals as obtained by time-of-flight (TOF) measurements [3]. In this technique, electron–hole pairs are generated by light absorption close to one electrode and the drift of one charge carrier type toward the counter electrode is measured in an electric field. The sign of this applied voltage determines the charge carrier type that is transported through the whole crystal and is analyzed by the transit time.

In thin-film devices, charge carriers are generated either by the field effect or by injection. Here the misalignment of the metal work function to the respective transport levels induces more or less large injection barriers. Furthermore, the transport in field-effect transistors (FETs) can be limited by trap states at the semiconductor/insulator interface. Especially, the often-used gate oxides, like silica or alumina, have electron traps at their surfaces in the form of hydroxyl groups [4]. Thus, multilayer structures comprising different organic materials with spatially separated electron and hole transport layers were used to fabricate efficient organic light-emitting diodes (OLED) [5]. On the other hand, photovoltaic devices are usually realized by mixing p- and n-conducting materials in one single layer yielding the so-called bulk heterojunction structure [6, 7]. This is necessary to bring the materials in close contact because organic materials have a short exciton diffusion length. This mixing leads to ambipolar transport in the blended film. In this context, ambipolar means the transport of both electrons and holes at the same time in a given material. In contrast, with bipolar transport as described before, we denote the ability of a material to transport both species, where the charge carrier type can

Physics of Organic Semiconductors, Second Edition. Edited by Wolfgang Brütting and Chihaya Adachi

be chosen by the applied voltage used for TOF or by the electrode material used for electron- or hole-transporting layers in multilayer devices like OLEDs.

In a field-effect transistor, the current flowing in the accumulation channel between two electrodes, called source (S) and drain (D), can be modulated via a third electrode, called gate (G), which is separated from the channel between source and drain by an insulating layer. Organic FETs (OFETs) are typically produced as thin-film transistors where the active layer is a normally undoped organic semiconductor that is deposited as thin film. Schematic cross-sectional sketches of such thin-film transistors are shown in Figure 8.1 for the bottom-gate/bottom-contact geometry. The operation regimes of a field-effect transistor are defined by the relation of the applied drain voltage V_D (between drain and source) and the effective gate voltage $V_{G,eff} = V_G - V_T$ (applied between gate and source, with respect to the threshold voltage V_T). The unipolar transistor saturates if the drain voltage is higher than the effective gate voltage, as it is evident from the constant drain current at high drain voltages in the output characteristics. Examples for p-conductive copper phthalocyanine (CuPc) and n-conductive fullerene (C_{60}) (for chemical structure, see Figure 8.2) are shown in Figure 8.3a and b. The pinch-off point

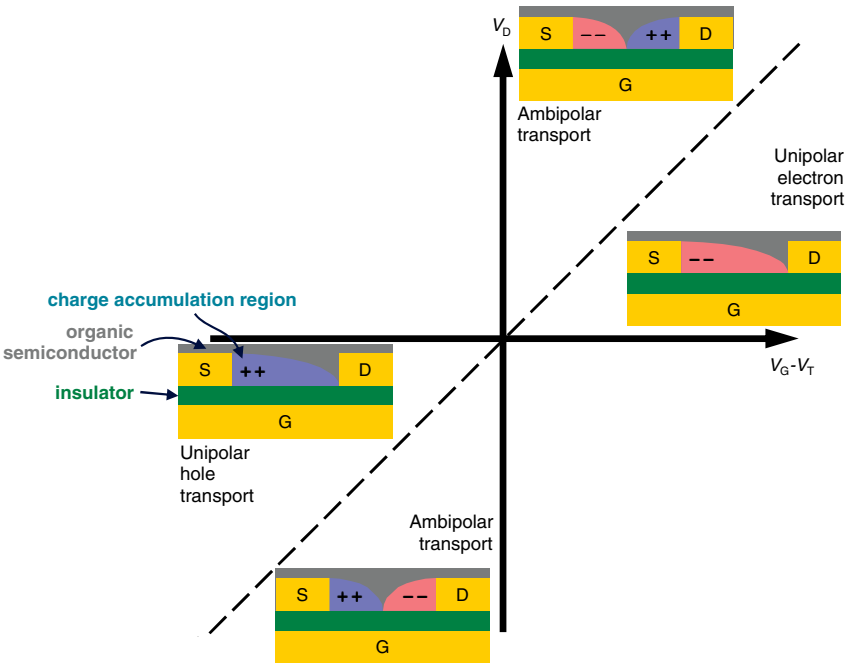

Figure 8.1 Sketch for the unipolar and ambipolar operation regimes of an organic field-effect transistor represented by the distribution of accumulated charge carriers. The pinch-off point is located at the drain electrode for the unipolar transport regime. In the case of ambipolar transport, the pinch-off point lies inside the channel and electrons and holes can be injected from the opposite electrodes. V_D denotes the drain voltage, V_G and V_T are gate and threshold voltages, respectively. Figure adapted from Ref. [19].

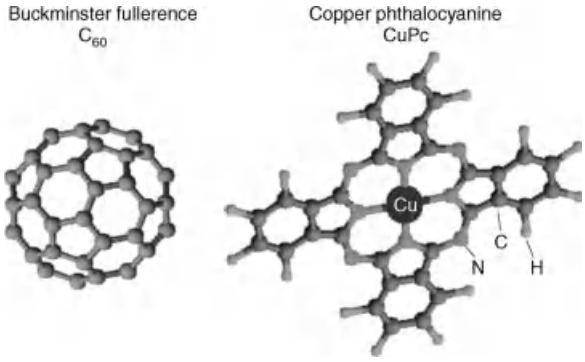

Figure 8.2 Chemical structures of the used semiconductors Buckminster fullerene (C_{60}) as n-conductive and copper–phthalocyanine (CuPc) as p-conductive semiconductors.

(channel potential equates to the gate potential) shifts into the channel as illustrated in Figure 8.1. The potential of this point lies between that of the source and the drain voltages. Below the threshold voltage, which is determined by the energy levels of the electrodes as well as by the volume and interface trap density [8], the accumulation channel is switched off and no current flows as visible in the transfer characteristics in Figure 8.3c and d.

In an ambipolar transistor, the situation is different because in the saturation range of the output characteristics as well as in the off-range of the transfer characteristics, the drain current increases for the ambipolar transport behavior as shown in Figure 8.4 for $|V_D| > |V_{G,eff}|$. While the majority charge carriers will be injected from the source, the minority charge carriers can also be injected from the drain

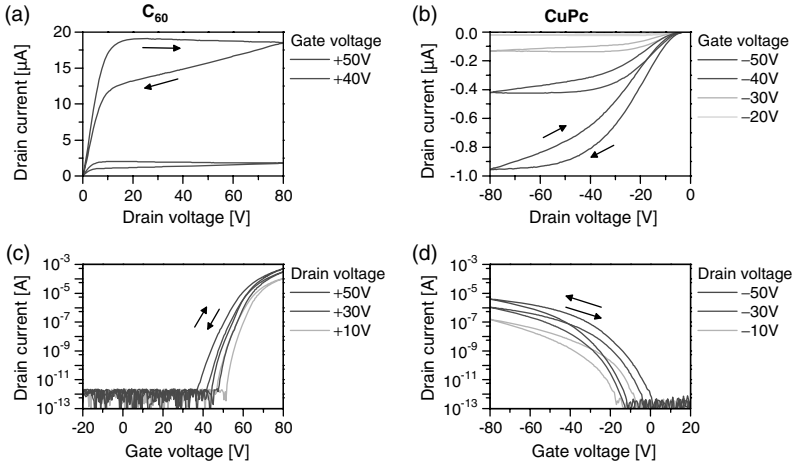

Figure 8.3 Output (a and b) and transfer (c and d) characteristics of unipolar field-effect transistors with neat C_{60} (a and c) and neat CuPc (b and d) films (for chemical structure, see Figure 8.2). The direction of the hysteresis is indicated by arrows. Figure adapted from Ref. [19].

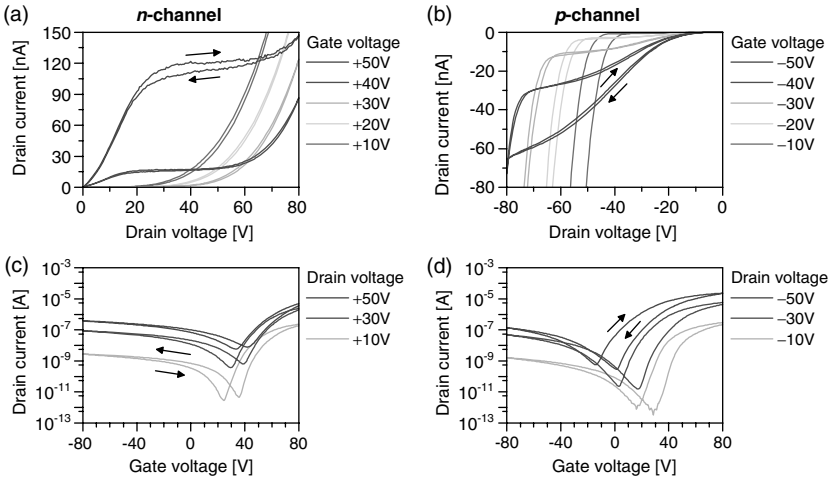

Figure 8.4 Output (a and b) and transfer (c and d) characteristics of ambipolar field-effect transistors for a mixing ratio between C_{60} and CuPc of 1 : 1 measured in the n-channel regime (a and c) as well as the p-channel regime (b and d). The direction of the hysteresis is indicated by arrows. Figure adapted from Ref. [19].

electrode as observed for the first time in hydrogenated amorphous silicon [9]. The pinch-off point (Figure 8.1) now indicates the transition from electron to hole accumulation.

An analytical model to describe the ambipolar behavior was proposed by Schmechel *et al.* [10] as extension of the standard Shockley model [11] for inorganic FETs, which allows the determination of electron and hole mobilities and the respective threshold voltages. If both charge carrier types can be injected and transported in the transistor channel, the model assumes a complete recombination of electrons and holes as shown by the sharp transition between positive and negative carriers in Figure 8.1. This recombination zone can be detected as light emission zone in light-emitting organic field-effect transistors (LE-OFET) (see Section 8.6) [12, 13]. In this model, the drain currents of electrons $I_{D,e}$ and of holes $I_{D,h}$, respectively, are given by

$$I_{D,e} = \frac{W}{2L} C_{ins} \times \left\{ \mu_e \left(\left[V_G - V_{T,e} \right]^2 - \left[\left(V_G - V_{T,e} \right) - V_D \right]^2 \right) + \mu_h \left(\left[V_D - \left(V_G - V_{T,h} \right) \right]^2 \right) \right\}$$

and

$$I_{D,h} = -\frac{W}{2L} C_{ins} \times \left\{ \mu_h \left(\left[V_{T,h} - V_G \right]^2 - \left[V_D - \left(V_G - V_{T,h} \right) \right]^2 \right) + \mu_e \left(\left[\left(V_G - V_{T,e} \right) - V_D \right]^2 \right) \right\}$$

$$\text{with } [x] = \frac{1}{2} x + \frac{1}{2} |x| \tag{8.1}$$

It can be shown that the mobilities as determined from saturation and from the ambipolar regime are in excellent agreement [14]. This model assumes band transport like in inorganic single-crystalline semiconductors and neglects hopping transport as found in organic systems. The latter problem has been treated by Smits *et al*. [15] who developed a consistent description for ambipolar OFETs based on variable range hopping, including such important features like density-dependent charge-carrier mobility. Two-dimensional simulations in organic system were performed by Paasch *et al*. [16]. Their simulations show that ambipolar transport is possible for parameters allowing the injection of both charge carrier types. However, the analytical model by Schmechel *et al*. [10] turned out to be sufficient in order to work out the important features of devices used for this report.

The realization of injection and transport of both carrier types in terms of lowering the injection barriers and the trap concentrations at interfaces is an important feature of OFETs. Therefore, two approaches are reported here to analyze the ambipolar transport in OFETs. As a first approach, ambipolar field-effect transistors were realized by mixtures of p-conducting and n-conducting materials. As a second approach, bipolar transport was achieved in a neat semiconductor layer by a modification of the gate dielectric in combination with a controlled variation of the electrode materials used for carrier injection. The transport levels of the organic semiconductor need to be aligned with the Fermi level of the respective electrode to decrease the injection barrier. This is possible with one common electrode in blends of hole- and electron-conducting materials due to their different energy levels as shown in Figure 8.5a. Otherwise, the injection barriers can be tuned for neat organic semiconductors by varying the electrode material (Figure 8.5b). Thus, the work function of the electrode can be aligned with one of the transport levels [17, 18]. Normally, a high work function material is used for hole injection and a low work function material for electron injection. Ambipolar transport can be achieved by balancing the injection barriers for holes and electrons.

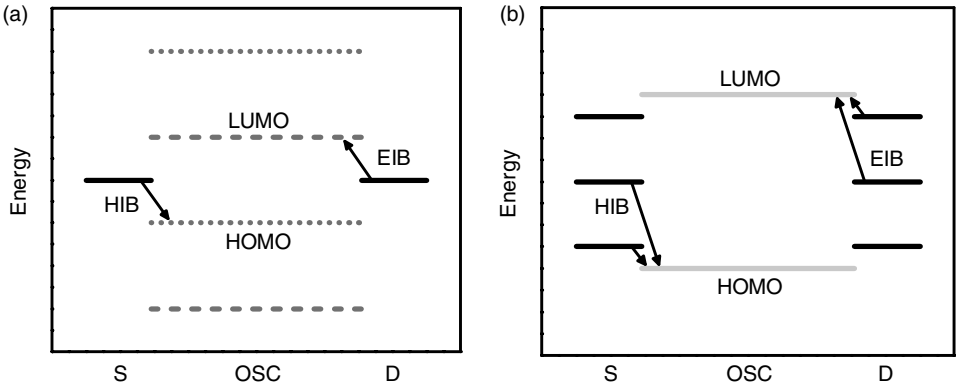

Figure 8.5 Schematic energy diagrams to show the charge-carrier injection into a blend (a) or a neat organic semiconductor (OSC) (b) to realize ambipolar transport. EIB means electron injection barrier and HIB hole injection barrier. Electrodes of an FET are source (S) and drain (D).

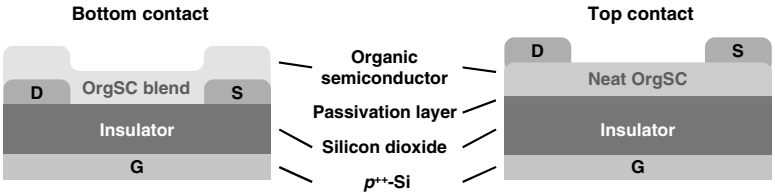

Figure 8.6 Schematic cross section of bottom- and top-contact transistors.

Experimentally, the OFETs for analyzing the blended films were realized in bottom-gate/bottom-contact geometry [14, 19], whereas the OFETS for analyzing the neat semiconductor films were fabricated in bottom-gate/top-contact geometry [20–23], as shown in Figure 8.6. As already mentioned, electron traps on oxide surfaces need to be prevented. Therefore, a trap-free polymethylmethacrylate (PMMA) or tetratetracontane (TTC) layer was introduced as passivating interlayer on top of the silicon dioxide prior to the deposition of the organic semiconductor [24, 25].

8.2 Ambipolar Charge-Carrier Transport in Blends of Molecular Hole- and Electron-Conducting Materials

Figures 8.3 and 8.4 show typical transfer characteristics of OFETs with neat CuPc and neat C_{60} in comparison to a 1 : 1 mixture of both materials. For the former two, only unipolar transport is observed in the used bottom-contact geometry. The drain current reaches higher values for the C_{60} FET resulting in a higher mobility. The obtained mobilities are $\mu_h = 1.7 \times 10^{-3}\,cm^2/(V\,s)$ and $\mu_e = 6.8 \times 10^{-2}\,cm^2/(V\,s)$ for hole transport in CuPc and electron transport in C_{60}, respectively.

The ambipolar current increase in the off-state of a unipolar OFET appears for mixed films of C_{60} and CuPc both in the n- and p-channel regimes and is shown in Figure 8.4c and d for a mixing ratio of 1 : 1. In addition, a 1 : 3 and a 3 : 1 mixing ratio were investigated and analyzed. The shift of the minimum in the ambipolar transfer curve is related to a shift of the ambipolar region in the transistor channel with the drain voltage and can be described by the model of Schmechel *et al.* [10].

Using the transfer length method (TLM) [28, 29], mobilities (Figure 8.7a) and contact resistances (Figure 8.7b) were determined for OFETs with different mixing ratios in both transport regimes. By this method, mobility and contact resistance can be estimated independently and, therefore, the transport can be separated from the injection behavior. The dependence of both quantities on the mixing ratio is summarized in Figure 8.7. The mobilities of electrons and holes are found to decrease exponentially with decreasing concentration of the respective transport material. Ambipolar transport occurs for all three investigated mixtures; however, for a mixture with only about 35% C_{60} content, one would obtain equal electron and hole mobilities. As reported previously [27, 30, 31], C_{60} and CuPc are electronically noninteracting so that there is no charge transfer in the ground state. This

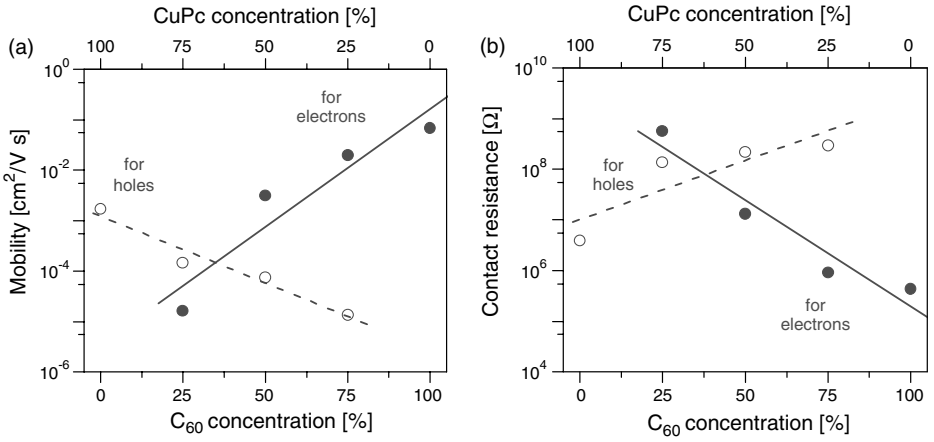

Figure 8.7 Dependence of the mobility (a) and of the contact resistance (b) on the concentration in blended CuPc:C_{60} films. The mobilities and the contact resistances are determined applying the transfer length method. The concentration ratios are taken from the deposition rates. Adapted from Ref. [20].

implies that transport in blends is possible by only separate percolation pathways of electrons and holes in the respective transport material. The decrease of both mobilities upon dilution can then be related to an increased hopping distance between molecules or grains of one material.

In contrast to the mobilities, the contact resistances for electron and hole injections increase with decreasing concentration of the respective transport material. This is at first glance rather unexpected, since the injection barriers as derived from photoelectron spectroscopy are found to decrease upon diluting one material with the other species (Figure 8.8) [19, 27, 32]. This suggests a correlation between contact resistance and mobility for each charge carrier type giving a reciprocal relation $R_C \sim \mu^{-1}$, indicating that the low mobility limits the injection of charge carriers. This behavior can be explained by diffusion-limited injection [11] following the equation

$$j_{inj} \sim \mu \cdot \exp\left[-\frac{\Phi_B}{kT}\right] \tag{8.2}$$

Here, Φ_B denotes the injection barrier, which also exhibits some variation as shown in Figure 8.8 [19, 27, 32], but due to the large changes of the mobility, the composition of the blend is not the dominant factor. A similar behavior was observed in both hole-only diodes [33], where the mobility was varied by mixing semiconducting and insulating molecules, and in unipolar OFETs [34], where the mobility was changed by the charge-carrier concentration.

Figure 8.9 shows the surface morphologies for different mixing ratios as investigated by noncontact scanning force microscopy (SFM) for small areas. Neat CuPc films have a needlelike structure showing low roughness. For neat C_{60} films, a

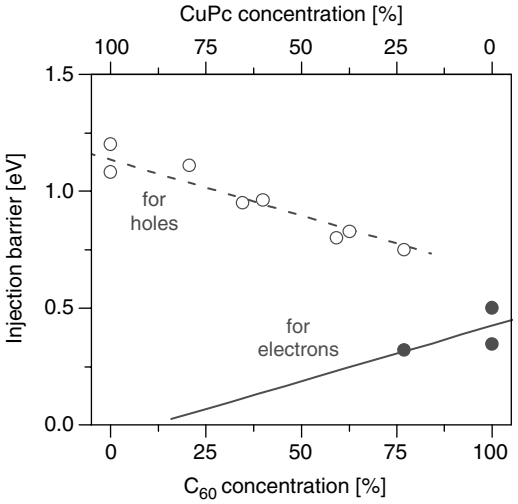

Figure 8.8 Dependence of the injection barrier on the concentration in blended CuPc:C_{60} films. The hole injection barriers are calculated from the onset of CuPc HOMO level measured by ultraviolet photoelectron spectroscopy, and the electron injection barriers are estimated from the onset of the C_{60} HOMO levels assuming a transport gap of 2.3 eV [26]. The concentration ratios are determined from X-ray photoelectron spectroscopy [27]. Adapted from Ref. [19].

rough and granular structure is observed. Compared to the CuPc film, the roughness of the films is increasing with increasing C_{60} content. The different surface morphologies for neat and blended films lead to the conclusion that phase separation occurs in the blended films. Altogether, film morphology and structure of blends of flat CuPc and spheric C_{60} molecules are still not very well understood and need further investigation. This will become particularly important in photovoltaic cells, where this material combination is potentially a promising candidate for so-called bulk heterojunction cells [35, 36]. The phase separation for CuPc and C_{60} blends was shown for the deposition onto solar cell-related substrates by X-ray scattering [37].

8.3
Ambipolar Charge-Carrier Transport in Molecular Semiconductors by Applying a Passivated Insulator Surface

Bipolar transport in molecular systems was described before for highly pure and well-defined single crystals [38]. To transfer this behavior to thin-film devices, the reduction of bulk and interface trap states [4, 39, 40] as well as the adjustment of the injection barriers [41] is necessary. Especially, organic insulating passivation layers were introduced to prevent the effect of electron traps on oxide surfaces [4, 24, 25]. For this purpose, polymeric materials like polymethylmethacrylate (PMMA) [25] or molecular materials like tetratetracontane (TTC) [24] were reported.

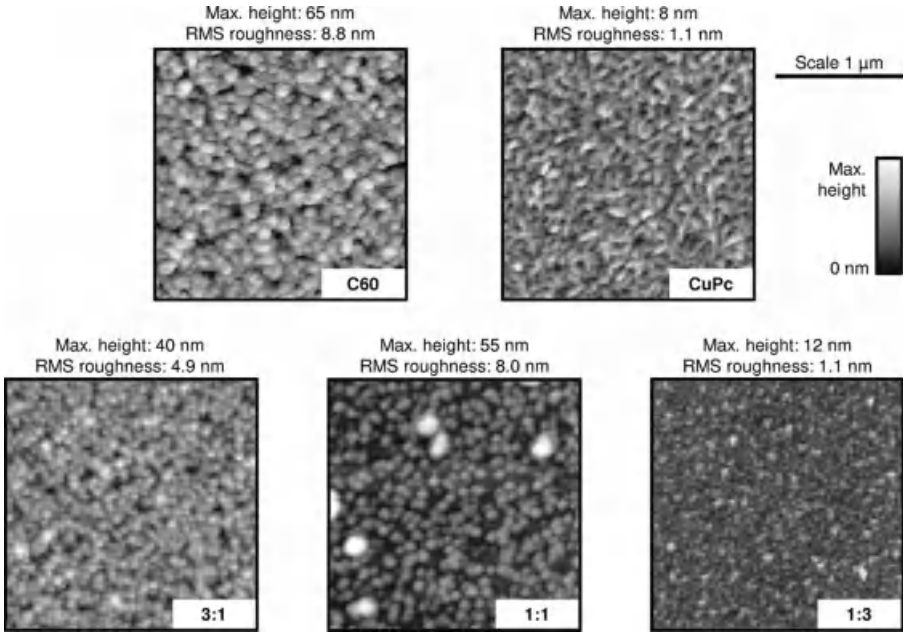

Figure 8.9 Scanning force microscopy images taken in noncontact mode for neat C_{60} and CuPc films as well as for three mixed films grown at 375 K. The total image size is $2 \times 2\,\mu m^2$. The maximum height is given as the difference between the lowest value (dark) and the highest value (white) in each of the images. Adapted from Ref. [19].

Figure 8.10 shows the comparison of charge-carrier transport with transfer characteristics in neat CuPc FETs without and with passivation layer. The studied passivation layers were PMMA (about 20 nm, spin-coated from toluene) and TTC (about 8 nm, evaporated in high vacuum) [21]. While PMMA forms a smooth and unstructured layer, TTC grows as well-crystallized film with a step height of about 6 nm that is close to the length of the molecules. A scanning force microscopy image of a 10 nm TTC layer on SiO_2 is shown in Figure 8.11a. Without passivation layer, no electron transport was observed in CuPc FETs. Applying the insulating organic layers, the electron transport also becomes measurable. The determined mobilities (summarized in Table 8.1) are higher for TTC as passivation layer than for PMMA, where the hole mobility is comparable to the hole mobility on bare SiO_2. This is related to the higher structural ordering of CuPc on TTC as shown in Figure 8.11b. On TTC layers, CuPc forms elongated crystallites with a length of up to 250 nm, whereas the CuPc crystallites on PMMA are round with an average diameter of 50 nm. Grain boundaries in the transport channel always hinder the transport, so the lower number of grain boundaries in the CuPc film on top of the molecular insulator and its very high crystallinity [21] are the reasons for the better transport and the higher mobilities.

TTC as passivation layer is also useful for other molecular semiconductors like diindenoperylene (DIP) [23], pentacene (Pen) [24], 6,13-bis(triisopropylsilylethynyl)

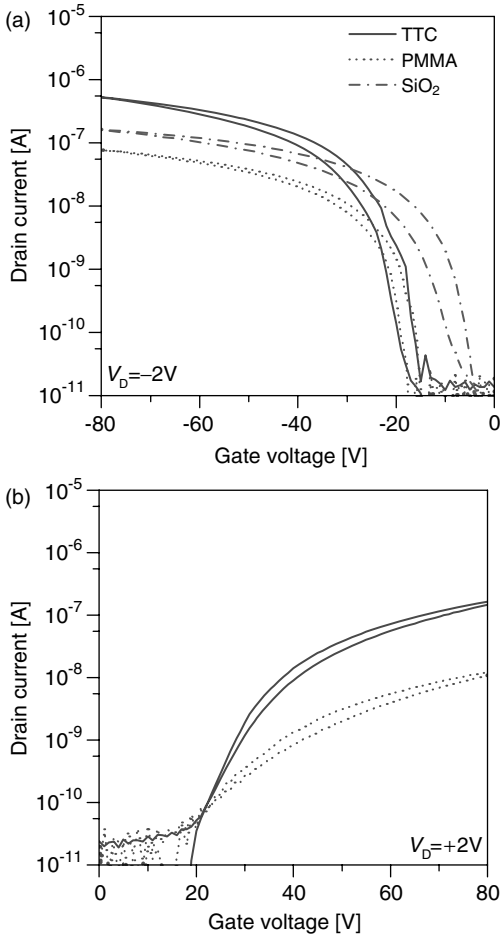

Figure 8.10 Transfer characteristics of CuPc OFETs (channel length 50 μm) without (dot-dashed line) and with different passivation layers, namely, PMMA (dashed line) and TTC (solid line). Without passivation layer, no electron transport is observed.

pentacene (TIPS-Pen), and α-sexithiophene (6T). The chemical structures of the molecules are shown in Figure 8.12. The transfer characteristics are summarized in Figure 8.13. The electrode materials to realize bipolar injection depend on the energy levels of the semiconductor and are given together with the observed electron and hole mobilities in Table 8.1. From these results, TTC seems to be a well-suited passivation layer for evaporated molecular semiconductors. For typical electron-transporting materials, like fluorinated CuPc or the fullerene C_{60}, the injection of holes in the low-lying HOMO is a problem. Nevertheless, the transport of electrons can also be improved with a TTC interlayer (not shown here). Unfortunately, however, TTC shows a good solubility in most organic solvents. So spin-coating of an organic semiconductor layer, like poly(3-hexylthiophene) or TIPS pentacene, on top of the TTC film dissolves TTC and removes the passivation layer.

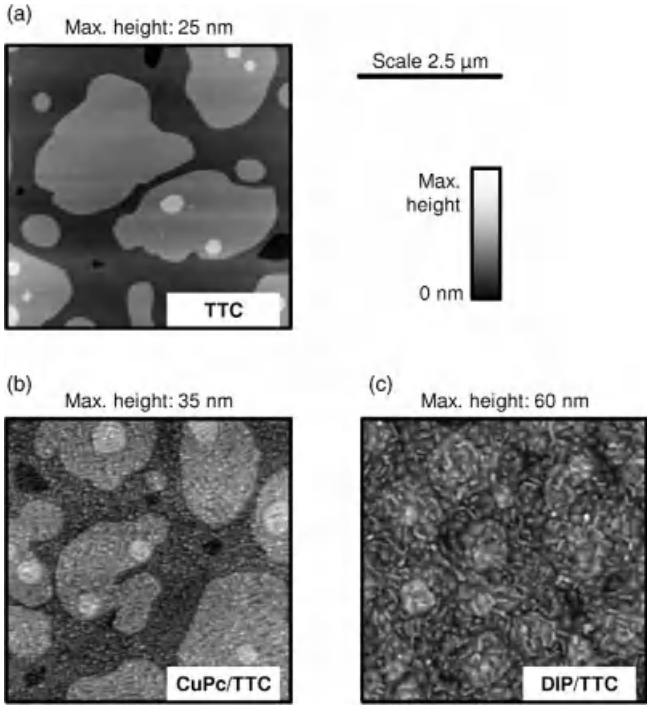

Figure 8.11 Scanning force microscopy images taken in noncontact mode for a 10 nm TTC film (a) as well as for a 25 nm CuPc (b) and a 25 nm DIP (c) film on top of a TTC film. The total image size is $5 \times 5\,\mu m^2$. The maximum height is given as the difference between the lowest value (dark) and the highest value (white) in each of the images.

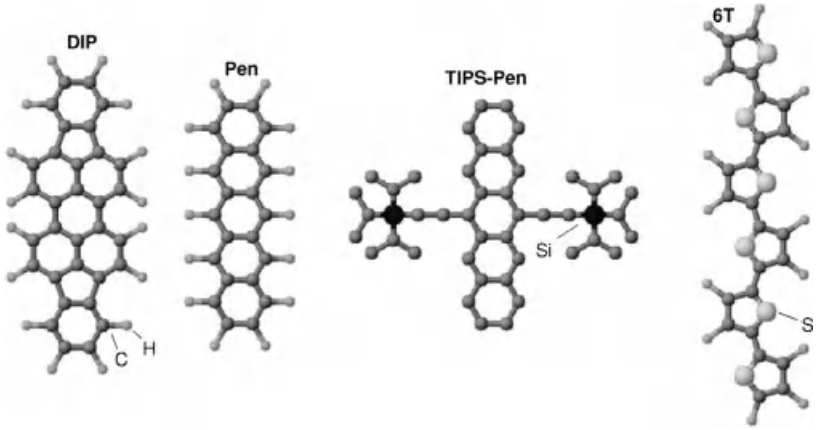

Figure 8.12 Chemical structures of additionally used semiconductors diindenoperylene (DIP), pentacene (Pen), TIPS pentacene (TIPS-Pen), and α-sexithiophene (6T). The hydrogen atoms are not shown in the case of TIPS-Pen for simplification.

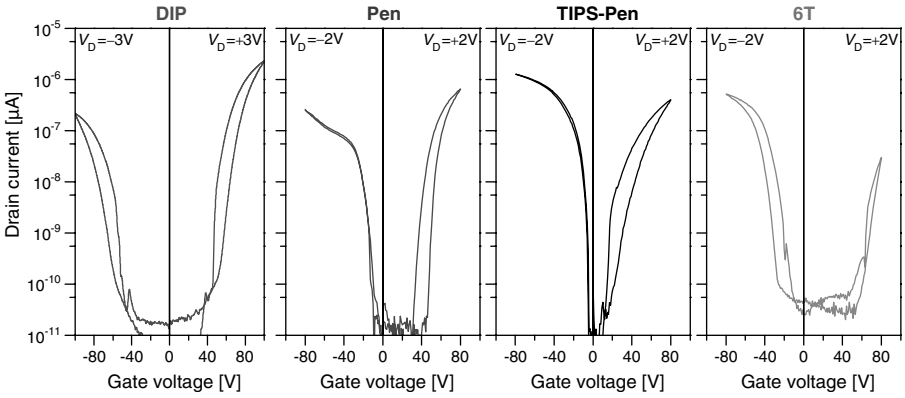

Figure 8.13 OFET transfer characteristics (channel length 70 μm) for the organic semiconductors diindenoperylene (DIP), pentacene (Pen), TIPS pentacene (TIPS-Pen), and α-sexithiophene (6T) with 10 nm TTC as passivation layer.

The TTC layer used for evaporated molecular semiconductors not only prevents the influence of interface traps on electron transport but also improves the transport in terms of increased crystallinity of the semiconducting film as shown for CuPc. However, the TTC layer becomes very rough if the film thickness is larger than 10 nm [22]. To smoothen the TTC layer, the samples were annealed at 60 °C under inert atmosphere. Subsequently, the transport properties on annealed TTC films are further improved. Figure 8.14a shows the dependence of the electron and hole mobilities for CuPc OFETs on the thickness of the annealed TTC layer. No electron transport appears if the TTC layer covers the substrate only partially below about 6 nm, which is necessary for a closed monolayer. Up to 3 monolayers of TTC (about 18 nm), the electron and hole mobilities increase continuously. This can be explained with a further improvement of the crystallinity [22] and a reduction of the induced polarization in the oxide insulator [42] or interface traps at the oxide surface, which act

Table 8.1 Summary of bipolar mobilities for different evaporated organic semiconductors.

Organic semiconductor	Passivation layer	Electrode materials	Hole mobility [$cm^2/(V\,s)$]	Electron mobility [$cm^2/(V\,s)$]
Copper phthalocyanine [21]	PMMA	Ag, Au	2×10^{-3}	3×10^{-4}
Copper phthalocyanine [22]	TTC	Ag, Au	2×10^{-2}	2×10^{-2}
Diindenoperylene [23]	TTC	Ag, Au	2×10^{-2}	1×10^{-1}
Pentacene	TTC	Ag, Al	1×10^{-1}	3×10^{-2}
TIPS pentacene	TTC	Ag, Al	4×10^{-2}	1×10^{-1}
α-Sexithiophene	TTC	Ag	1×10^{-2}	✓

The electron mobility in 6T was not able to determine due to the high threshold voltages, as visible in Figure 8.12.

differently for electrons and holes since traps can be charged. For thicker films, the mobilities stay constant at equal level.

The dependence of the transport properties for DIP OFETs on the TTC layer thickness is slightly different compared to the CuPc behavior as shown in

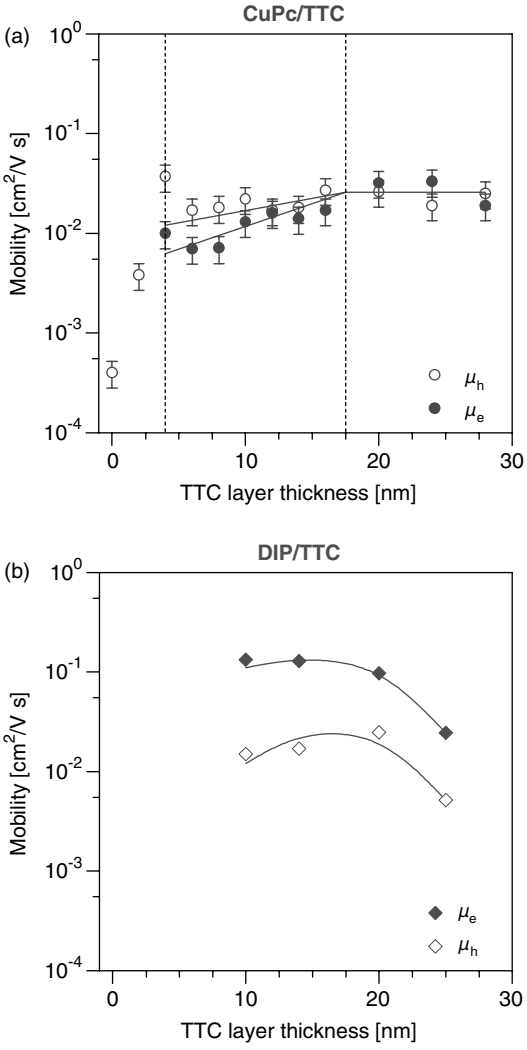

Figure 8.14 Dependence of the ambipolar mobilities determined by transfer length method for CuPc and DIP transistors on the thickness of the TTC 1passivation layer. The lines are to guide the eyes. The mobilities in DIP transistors were also determined for a lower TTC thickness from the linear regime and are lower than that for the 10 nm transistors. Part (a) adapted from Ref. [22].

Figure 8.14b. The electron mobility is always higher than the hole mobility and for a film thickness larger than 20 nm, the mobilities start to decrease. This should be related to the different growth behaviors of CuPc and DIP on top of the TTC passivation layer. While the CuPc grows only on top of the TTC islands, the DIP grains are exceeding the individual TTC islands as shown in Figure 8.11c. In addition, preferred orientations of the CuPc grains can be seen, which are aligned perpendicular to each other. Thus, the growth of CuPc on TTC can be considered as some kind of "pseudoepitaxial" growth [21].

In summary, the morphology of molecular semiconducting layers depends strongly on the surface properties of the underlying substrate. So differences for CuPc films on PMMA or TTC layers as well as for CuPc and DIP films on TTC layers were observed. However, TTC works as passivation layer for a wide range of evaporated molecular semiconductors.

8.4 Electrode Variation for Ambipolar and Bipolar Transport

In the previous section, the ability to transport electrons and holes in molecular semiconductors was described by applying an aliphatic passivation layer. In addition, the transported charge carrier type can be influenced by the choice of the used electrode material. In this context, the injection barrier for electrons and holes depends on the electrode work function [18]. So a high work function electrode is typically used for hole injection and a low work function electrode for electron injection.

Gold and silver electrodes are usually applied for hole injection as shown for CuPc in Section 8.2. In the top-contact geometry, as used for ambipolar transport in OFETs with a passivation layer, however, the gold electrodes allow both electron and hole injections. Thus, varying the top-contact material while the interface between the insulating passivation layer and the molecular semiconductor stays the same and using the transfer length method, we have separately analyzed the injection and the transport behavior [28, 29]. Figure 8.15 shows transfer characteristics for CuPc (part a) and DIP (part b) transistors with different electrode materials and a TTC passivation layer. It can be seen that low work function electrodes like Ca or Al only allow electron injection. For pure hole injection, the organic metal tetrathiafulvalene-tetracyanoquinodimethane (TTF-TCNQ) (for chemical structure of the molecules, see Figure 8.16a and b) is used. The determined mobilities and contact resistances are compiled in Table 8.2. The results for CuPc transistors with PMMA as passivation layer and Pen transistors with TTC as passivation layer are also shown. Apart from organic metal contacts [21], a doping of the interface between the semiconductor and gold or silver electrodes by fluorinated tetracyanoquinodimethane (F_4TCNQ) (for chemical structure, see Figure 8.16c) was implemented for hole injection [20]. This interface doping is based on a charge transfer between the semiconductor and the dopant [43], resulting in a p-type doping of the semiconductor near the interface, and was applied here only for CuPc.

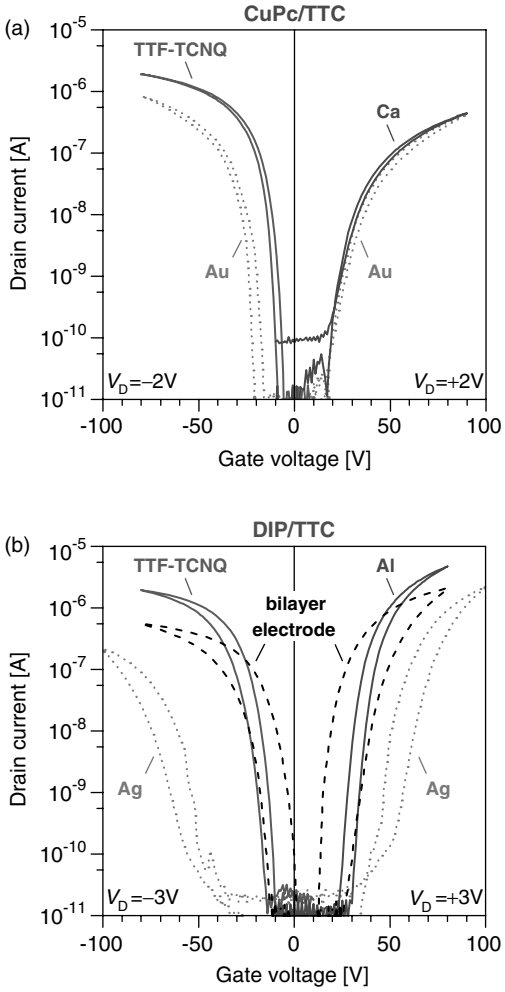

Figure 8.15 Transfer characteristics for OFETs with different electrode materials (CuPc: channel length 50 μm, DIP: channel length 70 μm). The thicknesses of the TTC layer are 8 nm for CuPc and 10 nm for DIP OFETs. The curves for the unipolar (ambipolar) devices are shown with solid (dotted), gray lines. The "bilayer electrode" device with Al and TTF-TCNQ as electrode materials has a channel length of 63 μm (dashed, black lines). Part (b) adapted from Ref. [23].

To compare the injection behavior for the different electrode materials, the work function of the metal contacts were measured under inert gas atmosphere by Kelvin probe [20]. In this experiment, the metals were deposited under the same high-vacuum conditions as for device production. It is important to mention that the work function of the free surface, as measured here, is different from measurements in ultrahigh vacuum [46] and also differs for

Table 8.2 Summary of bipolar mobilities for CuPc, DIP, and Pen OFETs with different electrode materials.

Electrode		Hole transport		Electron transport	
Material	**Work function [eV]**	**Mobility [$cm^2/(V\,s)$]**	**Contact resistance [MΩ]**	**Mobility [$cm^2/(V\,s)$]**	**Contact resistance [MΩ]**
CuPc transistors with PMMA as passivation layer [20]					
Ca	3.3	—	—	3×10^{-4}	n.d.
Ag	4.9	1×10^{-3}	n.d.	5×10^{-4}	n.d.
F_4TCNQ/Ag	5.3	2×10^{-3}	n.d.	—	—
CuPc transistors with TTC as passivation layer [45]					
Ca	3.3	—	—	1×10^{-2}	1.1
Au	5.0	3×10^{-2}	3.2	2×10^{-2}	4.8
TTF-TCNQ	4.7	4×10^{-2}	0.9	—	—
DIP transistors with TTC as passivation layer [23]					
Al	3.6	—	—	1×10^{-1}	0.1
Ag	4.9	2×10^{-2}	9.5	1×10^{-1}	0.9
TTF-TCNQ	4.7	5×10^{-2}	1.0	—	—
Al/TTF-TCNQ	3.6/4.7	7×10^{-3}	1.0	3×10^{-2}	0.1
Pen transistors with TTC as passivation layer					
Al	3.6	6×10^{-2}	5.2	3×10^{-2}	0.6
Ag	4.9	1×10^{-1}	2.1	9×10^{-3}	19.2
TTF-TCNQ	4.7	8×10^{-2}	1.7	—	—

The contact resistances for the first experiments with CuPc transistors and PMMA as passivation layer were not determined (n.d.) by transfer length method. The work function of Ca, Al, Ag, Au, and Ag/F_4TCNQ were determined at free surfaces by Kevin probe technique [20]. The work function of TTF-TCNQ is taken from Ref. [44].

the devices with top-contact geometry, where the surface dipole of the metals is reduced by the pushback effect [47]. The effective work function can be further changed by damages of the molecules occurring during deposition [48, 49], by formation of metal clusters inside the semiconductor film [50–52], by contaminations due to adsorbants during the production process [27], and by chemical reactions during deposition under high-vacuum conditions [53]. Nevertheless, the values can be used to classify the materials for electron injection – Ca and Al – as low work function materials and the materials for bipolar injection – Ag and Au – as medium work function materials. The deposition of the interface dopant F_4TCNQ increases the work function further and together with the effect of p-doping at the interface, only hole injection is then observed. Due to the low charge-carrier density in the organic metal TTF-TCNQ, the pushback effect is absent and the Fermi level can align with the HOMO levels of the organic semiconductors. The different injection behavior can be seen also from the contact resistances. The higher the work function of the contact material, the lower the contact resistance for hole

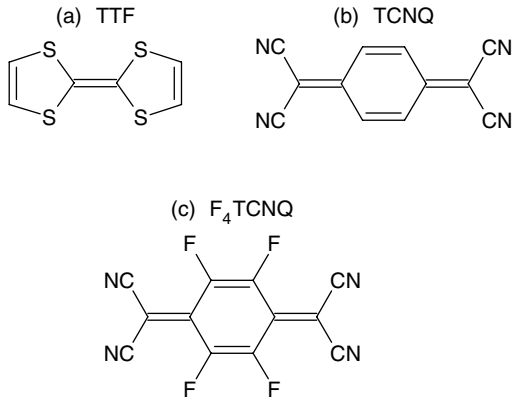

Figure 8.16 Chemical structure of materials used for contact variation. The organic metal tetrathiafulvalene-tetracyanoquinodimethane (TTF-TCNQ) contains the two molecules TTF (a) and TCNQ (b). Fluorinated tetracyanoquinodimethane (F_4TCNQ) (c) was used for interface doping deposited prior the deposition of the metal contact.

injection and vice versa and the higher the contact resistance for electron injection. At the same time, the contact resistance is lower and herewith the transistor current is also higher for unipolar devices than for ambipolar devices. This observation gives the possibility to tune the transport behavior from electron-only transistors via ambipolar to hole-only transistors by changing the electrode work function.

The interface between the organic passivation layer and the molecular semiconductor in transistors will be unchanged due to the variation of top contacts [20, 21, 23]. This can be seen from the fact that the mobilities for electron and hole transport are quite similar for a given combination of passivation layer and semiconductor. The variation in the mobilities for such a combination is within the scattering of mobilities between different samples produced in the same way. Therefore, the mobilities are independent of the electrode material. Thus, the mobility can be considered as an intrinsic property of a given film morphology and interface geometry. In the configuration shown here, the hole mobility is higher for CuPc and for Pen, whereas the electron mobility is higher for DIP. This intrinsic asymmetry between electron and hole transport should be related to differences in the π–π overlap of LUMO and HOMO between the molecules in the crystallites or at the grain boundaries as well as to differences in trap densities. A higher trap density for electrons was determined for CuPc OFETs [22], whereas similar trap densities for electrons and holes were found for DIP OFETs [23]. For thicker TTC films, the mobility asymmetry in CuPc OFETs vanishes (Figure 8.14a). However, the detailed explanation remains unclear. Further analysis might be possible by density functional theory calculations and drift diffusion modeling to separate the influence of contact coupling, trap distributions, grain boundaries, and intermolecular overlap [54, 55].

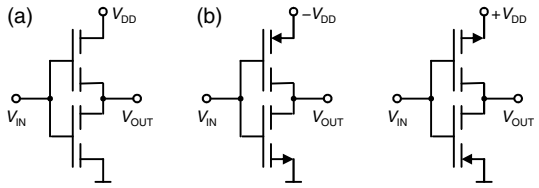

Figure 8.17 (a) Electrical circuit for an ambipolar inverter. (b) The two operation regimes (positive and negative supply voltages) for ambipolar and complementary inverters.

8.5 Applications of Bipolar Transport for Ambipolar and Complementary Inverters

As already mentioned, there was the suggestion of using ambipolar FETs to realize complementary organic integrated circuits [56–58]. Ambipolar inverters or complementary inverters are based on two ambipolar transistors (Figure 8.17a). These inverters are working with positive and negative supply voltages, where the sign of the driving voltage determines which of the two transistors works as n- and p-transistor (Figure 8.17b). Complementary inverters, in contrast, are based on unipolar n- and p-type transistors with a predefined power supply as shown in Figure 8.17b. However, to realize such a circuit patterning of the organic semiconductor [59], locally different surface functionalization or application of different electrode materials for the two transistors are required to achieve spatially separated p- and n-conducting regions, which is not necessary in the case of ambipolar inverters. In order to evaluate the performance of these different concepts, we have fabricated both ambipolar and complementary inverters and compared their output characteristics by both experimental studies and simulations.

Figure 8.18a and b shows the characteristics of ambipolar inverters using CuPc: C_{60} blends grown on SiO_2 with mixing ratios of 3 : 1 and 1 : 3. The upper part presents the transfer characteristics of the inverters (output voltage versus input voltage) and the lower part presents the corresponding current supplied by a driving voltage of $V_{DD} = \pm 90$ V, which directly gives the dissipated current in the circuit.

A characteristic feature of ambipolar inverters is their operation in the first as well as in the third quadrant of the output versus input diagrams, depending only on the sign of the supply voltage. Ideally, an inverter should have a sharp transition from the low to the high state at half of the driving voltage and the dissipated current should be negligible except for a narrow range around the transition voltage. Both inverters, based on two ambipolar transistors, show this transition at about half of the supply voltage ($V_{DD}/2 = \pm 45$ V) and reach high gain (about 13 for the 1 : 3 mixture and about 18 for the 3 : 1 mixture), which is defined as the steepness of the characteristics at the transitions between the high and the low states. However, they do not reach zero in the low state at the driving voltage in the high state. Also, the voltages at the high and the low states are not constant. Significant differences between the two ambipolar inverters are observed in the dissipated current. Although for the inverter with a 1 : 3 mixing ratio the power dissipation is symmetric around ± 45 V, the device with a 3 : 1 mixture shows an asymmetry of about

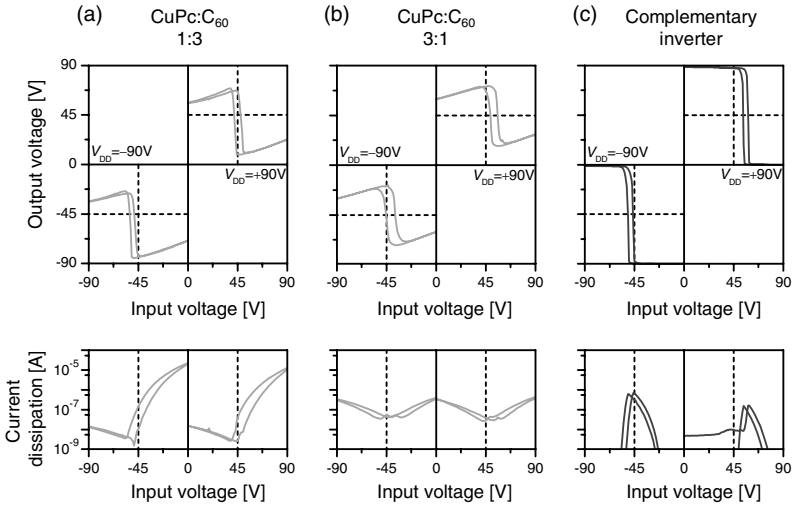

Figure 8.18 Characteristics of ambipolar inverters with mixing ratios CuPc: C_{60} of 3 : 1 (a) and 1 : 3 (b) in the semiconducting layer and a complementary inverter (c) consisting of a neat C_{60} and a neat CuPc transistor. The driving voltage is $V_{DD} = \pm 90$ V. Transfer characteristics (top) and current dissipation (bottom) are shown. Adapted from Ref. [19].

three orders of magnitude. Moreover, the dissipated current is as high as 10^{-5} A, which is 1.5 orders of magnitude larger than in the previous case. Thus, it is remarkable that a huge asymmetry in electron and hole mobilities of more than three orders of magnitude, as observed for the 3 : 1 mixture, has drastic consequences for the power dissipation of the inverter, although it does not lead to a significant asymmetry in the transition voltage.

For comparison, we have also fabricated a complementary inverter by connecting a p-channel transistor (neat CuPc) and an n-channel transistor (neat C_{60}) together, its characteristics being shown in Figure 8.18c. In order to make it operate in the first quadrant, it is necessary to connect the p-channel transistor to $+V_{DD}$ and the n-channel transistor to ground and, likewise, the n-channel transistor to $-V_{DD}$ and the p-channel transistor to ground in order make it operate in the third quadrant, as seen in Figure 8.17. These inverters also show slightly asymmetric transitions with respect to $\pm V_{DD}/2$ due to the unbalanced electron and hole mobilities in neat CuPc and C_{60}, but they reach the ground potential in the low state and the supply voltage in the high state. The gain is about 38 for a positive supply voltage and 34 for a negative supply voltage. So these values are about twice as large as those of the ambipolar inverters. A characteristic difference in the ambipolar inverter type is the current dissipation being high only in the vicinity of the transition. This is because at any time one of the two transistors is being switched off in each of the logic states, whereas an ambipolar transistor always shows a nonnegligible current.

Ambipolar and complementary inverters can also be produced on the basis of a single organic semiconductor, for example, by neat CuPc layers with a TTC passivation layer [45]. Thus, gold electrodes were used for the ambipolar inverter as shown

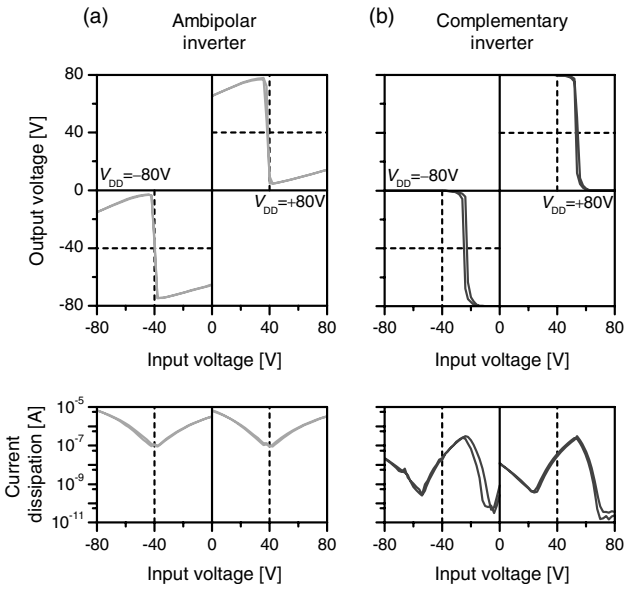

Figure 8.19 Characteristics of (a) an ambipolar inverter (both OFETs with gold electrodes) and (b) a complementary inverter (one OFET with Al and one OFET with TTF-TCNQ electrodes) consisting of neat CuPc films as semiconducting layer. The driving voltage is $V_{DD} = \pm 80$ V. Transfer characteristics (top) and current dissipation (bottom) are shown. All transistors contain a passivation layer of TTC.

in Figure 8.19a. Different electrode materials – Al for the n-type transistor and TTF-TCNQ for the p-type transistor – were used to fabricate the complementary inverter. The shifted transition between the two logic states for the complementary inverter away from half of the supply voltage is related to asymmetric threshold voltages (Figure 8.15). This asymmetry does not occur for Au contacts in the case of ambipolar inverters. The increase of loss current for the negative input voltages is caused by a slightly ambipolar behavior of the Al transistor (not shown).

For a better understanding of inverter characteristics, we performed numerical simulations based on the analytical model of Schmechel *et al.* [10] for both ambipolar and complementary inverters. The output voltage as well as the current dissipation was calculated to demonstrate the differences between ambipolar and complementary inverters and the influence of device parameters like mobility and threshold voltage.

Figure 8.20 shows simulated transfer characteristics of ambipolar and complementary inverters. In part (a), balanced mobilities ($\mu_e = \mu_h$) and symmetric threshold voltages ($V_{T,e} = -V_{T,h} = 30$ V) were used for the simulation. The part (b) shows the characteristics for symmetric threshold voltages ($V_{T,e} = -V_{T,h} = 30$ V) but different mobilities ($\mu_e = 100\mu_h$). In part (c), the balanced mobilities ($\mu_e = \mu_h$) and different threshold voltages ($V_{T,e} = +30$ V, $V_{T,h} = -10$ V) were used. In all cases, as observed before in the measurements, the output voltage of the complementary inverter reaches the driving and the ground voltage in the high and the

low states, respectively, whereas the output voltage of the ambipolar inverter does not [58]. Nevertheless, the gain for both types of inverters is comparable. As expected, the current dissipation in the complementary inverter has a maximum at the transition between the logic levels, whereas the ambipolar inverter has its minimum at this point.

A closer look at the simulations in Figure 8.20a, which are based on symmetric mobilities and threshold voltages, shows that the transition between the logic states is at half of the driving voltage for both the ambipolar and the complementary inverters. An asymmetry in carrier mobilities (Figure 8.20b) and/or in threshold voltages (Figure 8.20c) leads to a shift of the transition voltage in both cases. Nevertheless, the transition voltages of the measured inverters (Figure 8.18a and c) are still more or less symmetric, although the mobilities are largely different. The reason is that in both cases, the shift of the transition voltage due to the higher mobility in the n-channel is compensated by a lower threshold voltage in the p-channel. One can further see that different mobilities have no influence on the gain, whereas different, especially lower, threshold voltages decrease the gain. Experimentally, we have a decrease in the threshold voltage in the p-channel by diluting CuPc with C_{60} and accordingly the gain in the measured ambipolar inverters is lower than in the complementary inverter. Finally, it is evident that the current dissipation of an ambipolar inverter is increasing drastically in the case of asymmetric mobilities. Altogether, complementary inverters are clearly superior to their ambipolar counterparts, but in both cases equal mobilities and symmetric threshold voltages are required to achieve optimal inverter characteristics.

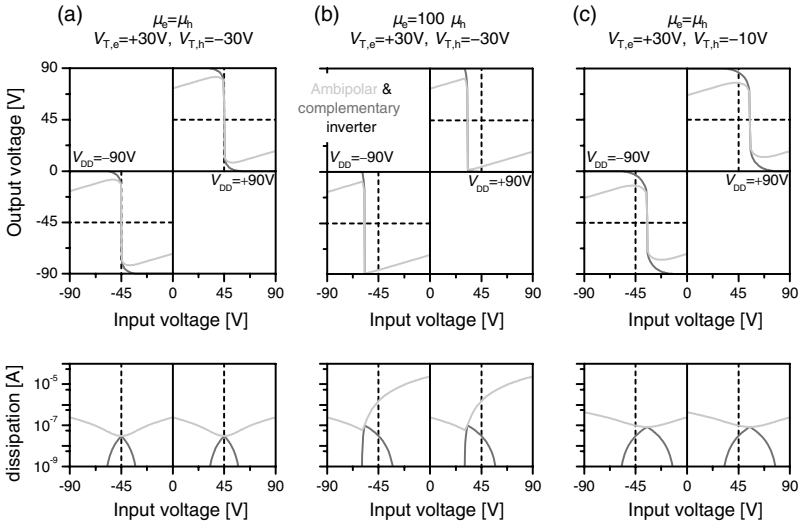

Figure 8.20 Simulations of ambipolar and complementary inverter transfer characteristics and current dissipation with (a) symmetric mobilities and threshold voltages for p- and n-channels in comparison to (b) asymmetric mobilities and (c) asymmetric threshold voltages. Adapted from Ref. [19].

8.6
Realization of Light-Emitting Transistors with Combined Al and TTF-TCNQ Electrodes

When electrons and holes are ever in the same area, recombination can take place. So the emission of light from ambipolar transistors was described before [12, 13]. For this reason, full recombination of injected electrons and holes is assumed for simplified derivation of equations for ambipolar transistors, as the ones given in Eq. (8.2) [10].

While CuPc shows fluorescence in the near infrared range and only at low temperatures [60], DIP already has strong fluorescence in the visible range at room temperature [61]. Therefore, DIP OFETs with a passivation layer of TTC and two different electrode materials – Al and TTF-TCNQ – were analyzed. The schematic structure of this OFET is illustrated in Figure 8.21a. The effect of two different electrodes giving a good unipolar injection is transferred to an ambipolar field-effect transistor with "bilayer electrodes" [62], as sketched in Figure 8.15, by deposition of the electrodes by a parallactic shadow mask displacement technique [10]. Somewhat lower mobilities are observed for the FETs with combined Al/TTF-TCNQ electrodes, as given in Table 8.2. Also, the determination of the channel length is slightly inaccurate in the device with two electrode materials so that the same values for the contact resistances are used as for the unipolar devices. However, the differences in the mobilities due to the fixed contact resistances are negligible. In addition, using different materials for source and drain contacts causes a built-in potential for the drain current that is not considered in the analysis.

As shown in Figure 8.1, at large drain voltages, this means in the ambipolar region, both electrons and holes are injected. At the same time, the pinch-off point,

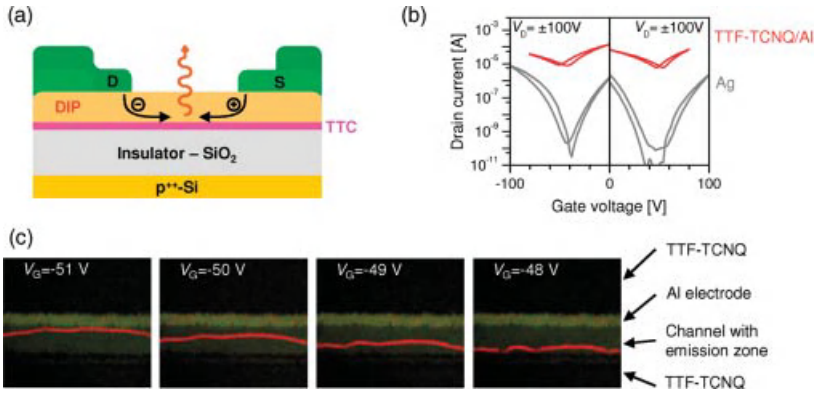

Figure 8.21 (a) Schematic cross section of LE-OFET. (b) Ambipolar transfer characteristics in the saturation regime for single-layer (Ag) and "bilayer" electrodes. (c) Photographs of the LE-OFET with emission zone.

where the recombination takes place and the charge-carrier density is zero, can be shifted through the channel by changing either the drain or the gate voltage (see below).

In comparison to Ag electrodes (Figure 8.21b), the "bilayer" electrodes also allow higher currents in this transistor regime [62]. Thus, using the "bilayer" electrodes, light emission was detected as can bee seen in Figure 8.21c. By varying the gate voltage at a constant drain voltage, the spatial position of the recombination and emission zone can be shifted [63]. This is predicted by the model of Schmechel *et al.* [10] where the position of the recombination zone is given by

$$\frac{L_h}{L_e} = \frac{\mu_h}{\mu_e} \cdot \frac{(V_G - V_{T,h})^2}{(V_G - V_D - V_{T,e})^2} \tag{8.3}$$

Here, L_h is the distance of the recombination zone to the hole-injecting electrode and L_e is the distance of the recombination zone to the electron-injecting electrode.

Due to the upright standing DIP molecules [64] and the concomitant orientation of the transition dipole moment parallel to the long axis of the molecules [65], the emission is mainly in the plane of the substrate. However, this is suitable as pumping device for organic lasers (for details, see Chapter 18) [66]. A further increase of emission efficiency can be realized by separated electron and hole transport as well as an additional emission layer [67].

8.7 Conclusion

In the recent years, bipolar transport was transferred from an effect occurring only in single crystals using photogenerated charge carriers to a feature that can be used in devices containing polycrystalline thin films like molecular FETs. Basically, two different approaches were realized:

1) The application of blended semiconductor films composed of classical electron- and hole-transporting materials.
2) The application of neat semiconductor films in combination with an almost trap-free insulator/semiconductor interface.

This shows once more the importance of understanding interface traps at the semiconductor/insulator interface as well as injection behavior at the semiconductor/contact interface.

An asymmetry between electron and hole transport is observed for the same material, either by direct asymmetry of the mobilities or by the differences in trap densities. However, the transport behavior seems to be an intrinsic property of a given insulator/semiconductor interface defining the growth behavior via the interaction of the molecules with the substrate (see Chapter 1) and the electric and electronic interaction of traps and polarization.

Ambipolar transport has also been reported for single-crystal FETs [68–70]. Even though unipolar single-crystal FETs show mobilities higher than $10\,cm^2/(V\,s)$ [71], the ambipolar transport in thin-film devices reported here is widely comparable to results reported in the literature for ambipolar transport in single crystals.

Acknowledgments

The authors thank the German Research Foundation (DFG) for funding over recent years (SPP1121 and SFB484). We are grateful to colleagues from the groups of Frank Schreiber (University of Tübingen, Germany), Jens Pflaum (University of Würzburg, Germany), and Tatsuo Hasegawa (National Institute for Advanced Industrial Science and Technology in Tsukuba, Japan) for continuous support and fruitful discussions.

Furthermore, the contributions of Markus Bronner, Michael Kraus, Julia Wagner, Simon Haug, Matthias Horlet, Marc Kiwull, and Stefan Richler at Augsburg University to part of the results shown in this chapter are gratefully acknowledged.

References

1 Horowitz, G. (1998) Organic field-effect transistors. *Adv. Mater.*, **10**, 365–377.
2 Dimitrakopoulos, C. and Malenfant, P. (2002) Organic thin film transistors for large area electronics. *Adv. Mater.*, **14**, 99–117.
3 Warta, W. and Karl, N. (1985) Hot holes in naphthalene: high, electric-field-dependent mobilities. *Phys. Rev. B*, **32**, 1172–1182.
4 Chua, L.L., Zaumseil, J., Chang, J.F., Ou, E.C.W., Ho, P.K.H., Sirringhaus, H., and Friend, R.H. (2005) General observation of n-type field-effect behaviour in organic semiconductors. *Nature*, **434**, 194–199.
5 Tang, C.W. and van Slyke, S.A. (1987) Organic electroluminescent diodes. *Appl. Phys. Lett.*, **51**, 913–915.
6 Yu, G., Gao, J., Hummelen, J.C., Wudl, F., and Heeger, A.J. (1995) Polymer photovoltaic cells: enhanced efficiencies via a network of internal donor–acceptor heterojunctions. *Science*, **270**, 1789–1791.
7 Rostalski, J. and Meissner, D. (2000) Monochromatic versus solar efficiencies of organic solar cells. *Sol. Energy Mater. Sol. Cell.*, **61**, 87–95.
8 Scheinert, S. and Paasch, G. (2004) Fabrication and analysis of polymer field-effect transistors. *Phys. Status Solidi A*, **201**, 1263–1301.
9 Neudeck, G.W. and Malhotra, A.K. (1975) Field-effect conductance modulation in vacuum-evaporated amorphous silicon films. *J. Appl. Phys.*, **46**, 239–247.
10 Schmechel, R., Ahles, M., and von Seggern, H. (2005) A pentacene ambipolar transistor: experiment and theory. *J. Appl. Phys.*, **98**, 084511.
11 Sze, S. (1982) *Physics of Semiconductor Devices*, John Wiley & Sons, Inc., New York.
12 Hepp, A., Heil, H., Weise, W., Ahles, M., Schmechel, R., and von Seggern, H. (2003) Light-emitting field-effect transistor based on a tetracene thin film. *Phys. Rev. Lett.*, **91**, 157406.
13 Loi, M.A., Rost-Bietsch, C., Murgia, M., Karg, S., Rieß, W., and Muccini, M. (2006) Tuning optoelectronic properties of ambipolar organic light-emitting

transistors using a bulk-heterojunction approach. *Adv. Funct. Mater.*, **16**, 41–47.
14 Opitz, A., Bronner, M., and Brütting, W. (2007) Ambipolar charge carrier transport in mixed organic layers of phthalocyanine and fullerene. *J. Appl. Phys.*, **101**, 063709.
15 Smits, E.C.P., Anthopoulos, T.D., Setayesh, S., van Veenendaal, E., Coehoorn, R., Blom, P.W.M., de Boer, B., and de Leeuw, D.M. (2006) Ambipolar charge transport in organic field-effect transistors. *Phys. Rev. B*, **73**, 205316.
16 Paasch, G., Lindner, T., Rost-Bietsch, C., Karg, S., Rieß, W., and Scheinert, S. (2005) Operation and properties of ambipolar organic field-effect transistors. *J. Appl. Phys.*, **98**, 084505.
17 Crispin, A., Crispin, X., Fahlman, M., Berggren, M., and Salaneck, W.R. (2006) Transition between energy level alignment regimes at a low band gap polymer-electrode interfaces. *Appl. Phys. Lett.*, **89**, 213503.
18 Koch, N. and Vollmer, A. (2006) Electrode–molecular semiconductor contacts: work-function-dependent hole injection barriers versus Fermi-level pinning. *Appl. Phys. Lett.*, **89**, 162107.
19 Bronner, M., Opitz, A., and Brütting, W. (2008) Ambipolar charge carrier transport in organic semiconductor blends of phthalocyanine and fullerene. *Phys. Status Solidi A*, **205**, 549–563.
20 Opitz, A., Kraus, M., Bronner, M., Wagner, J., and Brütting, W. (2008) Bipolar transport in organic field-effect transistors: organic semiconductor blends versus contact modification. *New J. Phys.*, **10**, 065006.
21 Kraus, M., Richler, S., Opitz, A., Brütting, W., Haas, S., Hasegawa, T., Hinderhofer, A., and Schreiber, F. (2010) High-mobility copper–phthalocyanine field-effect transistors with tetratetracontane passivation layer and organic metal contacts. *J. Appl. Phys.*, **107**, 094503.
22 Kraus, M., Haug, S., Brütting, W., and Opitz, A. (2011) Achievement of balanced electron and hole mobility in copper–phthalocyanine field-effect transistors by using a crystalline aliphatic passivation layer. *Org. Electron.*, **12**, 731–735.
23 Horlet, M., Kraus, M., Brütting, W., and Opitz, A. (2011) Diindenoperylene as ambipolar semiconductor: influence of electrode materials and mobility asymmetry in organic field-effect transistors. *Appl. Phys. Lett.*, **98**, 233304.
24 Ogawa, S., Kimura, Y., Niwano, M., and Ishii, H. (2007) Trap elimination and injection switching at organic field effect transistor by inserting an alkane ($C_{44}H_{90}$) layer. *Appl. Phys. Lett.*, **90**, 033504.
25 Benson, N., Melzer, C., Schmechel, R., and Seggern, v.H. (2008) Electronic states at the dielectric/semiconductor interface in organic field effect transistors. *Phys. Status Solidi A*, **205**, 475–487.
26 Lof, R.W., Vanveenendaal, M.A., Koopmans, B., Jonkman, H.T., and Sawatzky, G.A. (1992) Band-gap, excitons, and Coulomb interaction in solid C_{60}. *Phys. Rev. Lett.*, **68**, 3924–3927.
27 Opitz, A., Bronner, M., Brütting, W., Himmerlich, M., Schaefer, J.A., and Krischok, S. (2007) Electronic properties of organic semiconductor blends: ambipolar mixtures of phthalocyanine and fullerene. *Appl. Phys. Lett.*, **90**, 212112.
28 Luan, S. and Neudeck, G.W. (1992) An experimental study of the source/drain parasitic resistance effects in amorphous silicon thin film transistors. *J. Appl. Phys.*, **72**, 766–772.
29 Klauk, H., Schmid, G., Radlik, W., Weber, W., Zhou, L., Sheraw, C.D., Nichols, J.A., and Jackson, T.N. (2003) Contact resistance in organic thin film transistors. *Solid State Electron.*, **47**, 297–301.
30 Molodtsova, O.V. and Knupfer, M. (2006) Electronic properties of the organic semiconductor interfaces CuPc/C_{60} and C_{60}/CuPc. *J. Appl. Phys.*, **99**, 053704.
31 Lozzi, L., Granato, V., Picozzi, S., Simeoni, M., La Rosa, S., Delly, B., and Santucci, S. (2006) CuPc:C_{60} blend film: a photoemission investigation. *J. Vac. Sci. Technol. A*, **24**, 1668–1675.
32 Akaike, K., Opitz, A., Wagner, J., Brütting, W., Kanai, K., Ouchi, Y., and Seki, K. (2010) Unoccupied states in copper phthalocyanine/fullerene blended films determined by inverse photoemission

spectroscopy. *Org. Electron.*, **11**, 1853–1857.
33 Shen, Y.L., Klein, M.W., Jacobs, D.B., Scott, J.C., and Malliaras, G.G. (2001) Mobility-dependent charge injection into an organic semiconductor. *Phys. Rev. Lett.*, **86**, 3867–3870.
34 Hamadani, B.H. and Natelson, D. (2004) Temperature-dependent contact resistances in high-quality polymer field-effect transistors. *Appl. Phys. Lett.*, **84**, 443–445.
35 Xue, J., Rand, B., Uchida, S., and Forrest, S. (2005) A hybrid planar-mixed molecular heterojunction photovoltaic cell. *Adv. Mater.*, **17**, 66–71.
36 Stübinger, T. and Brütting, W. (2002) Photocurrent spectra of bilayers and blends of the organic donor–acceptor system CuPc/C_{60}. *SPIE Proc.*, **4465**, 102–112.
37 Opitz, A., Wagner, J., Bronner, M., Brütting, W., Hinderhofer, A., and Schreiber, F. (2009) Molecular semiconductor blends: microstructure, charge carrier transport and application in photovoltaic cells. *Phys. Status Solidi A*, **206**, 2683–2694.
38 Karl, N. (2000) Organic semiconductors, Group III, in *Landolt-Boernstein (New Series)*, updated edn, vol. **41E** (eds. O. Madelung, M. Schulz, and H. Weiss), Springer, Berlin.
39 Probst K.H. and Karl, N. (1975) Energy levels of electron and hole traps in the band gap of doped anthracene crystals. *Phys. Status Solidi A*, **27**, 499–508.
40 Pflaum, J., Niemax, J., and Tripathi, A. (2006) Chemical and structural effects on the electronic transport in organic single crystals. *Chem. Phys.*, **325**, 152–159.
41 Yasuda, T., Goto, T., Fujita, K., and Tsutsui, T. (2004) Ambipolar pentacene field-effect transistors with calcium source–drain electrodes. *Appl. Phys. Lett.*, **85**, 2098–2100.
42 Hulea, I.N., Fratini, S., Xie, H., Mulder, C. L., Iossad, N.N., Rastelli, G., Ciuchi, S., and Morpurgo, A.F. (2006) Tunable Frohlich polarons in organic single-crystal transistors. *Nat. Mater.*, **5**, 982–986.
43 Pfeiffer, M., Beyer, A., Plonnigs, B., Nollau, A., Fritz, T., Leo, K., Schlettwein, D., Hiller, S., and Wöhrle, D. (2000) Controlled p-doping of pigment layers by cosublimation: basic mechanisms and implications for their use in organic photovoltaic cells. *Sol. Energy Mater. Sol. Cell.*, **63**, 83–99.
44 Takahashi, Y., Hasegawa, T., Abe, Y., Tokura, Y., and Saito, G. (2006) Organic metal electrodes for controlled p- and n-type carrier injections in organic field-effect transistors. *Appl. Phys. Lett.*, **88**, 073504.
45 Kraus, M. (2011) *Charge carrier transport in organic field-effect devices based on copper-phthalocyanine*. PhD thesis. Universität Augsburg.
46 Michaelson, H.B. (1977) The work function of the elements and its periodicity. *J. Appl. Phys.*, **48**, 4729–4733.
47 Koch, N. (2007) Organic electronic devices and their functional interfaces. *ChemPhysChem*, **8**, 1438–1455.
48 Parthasarathy, G., Burrows, P.E., Khalfin, V., Kozlov, V.G., and Forrest, S.R. (1998) A metal-free cathode for organic semiconductor devices. *Appl. Phys. Lett.*, **72**, 2138–2140.
49 Xue, J.G., Rand, B.P., Uchida, S., and Forrest, S.R. (2005) Mixed donor–acceptor molecular heterojunctions for photovoltaic applications. II. Device performance. *J. Appl. Phys.*, **98**, 124903.
50 Scharnberg, M., Hu, J., Kanzow, J., Rätzke, K., Adelung, R., Faupel, F., Pannemann, C., Hilleringmann, U., Meyer, S., and Pflaum, J. (2005) Radiotracer measurements as a sensitive tool for the detection of metal penetration in molecular-based organic electronics. *Appl. Phys. Lett.*, **86**, 024104.
51 Dürr, A.C., Schreiber, F., Kelsch, M., Carstanjen, H., and Dosch, H. (2002) Morphology and thermal stability of metal contacts on crystalline organic thin films. *Adv. Mater.*, **14**, 961–963.
52 Dürr, A.C., Schreiber, F., Kelsch, M., Carstanjen, H.D., Dosch, H., and Seeck, O.H. (2003) Morphology and interdiffusion behavior of evaporated metal films on crystalline diindenoperylene thin films. *J. Appl. Phys.*, **93**, 5201–5209.

53 Ohring, M. (1992) *The Material Science of Thin Films*, Academic Press, San Diego.

54 Lugli, P., Erlen, C., Pecchia, A., Brunetti, F., Latessa, L., Bolognesi, A., Csaba, G., Scarpa, G., and di Carlo, A. (2007) The simulation of molecular and organic devices: a critical review and look at future developments. *Appl. Phys. A*, **87**, 593–598.

55 Schuster, C., Kraus, M., Opitz, A., Brütting, W., and Eckern, U. (2009) Transport properties of copper phthalocyanine based organic electronic devices. *Eur. Phys. J. Spec. Top.*, **180**, 117–134.

56 Meijer, E.J., De Leeuw, D.M., Setayesh, S., Van Veenendaal, E., Huisman, B.H., Blom, P.W.M., Hummelen, J.C., Scherf, U., and Klapwijk, T.M. (2003) Solution-processed ambipolar organic field-effect transistors and inverters. *Nat. Mater.*, **2**, 678–682.

57 Anthopoulos, T.D., Setayesh, S., Smith, E., Cölle, M., Cantatore, E., de Boer, B., Blom, P.W.M., and de Leeuw, D.M. (2006) Air-stable complementary-like circuits based on organic ambipolar transistors. *Adv. Mater.*, **18**, 1900–1904.

58 Inoue, Y., Sakamoto, Y., Suzuki, T., Kobayashi, M., Gao, Y., and Tokito, S. (2005) Organic thin-film transistors with high electron mobility based on perfluoropentacene. *Jpn. J. Appl. Phys.*, **44**, 3663–3668.

59 Crone, B., Dodabalapur, A., Lin, Y.Y., Filas, R.W., Bao, Z., LaDuca, A., Sarpeshkar, R., Katz, H.E., and Li, W. (2000) Large-scale complementary integrated circuits based on organic transistors. *Nature*, **403**, 521–523.

60 Yoshino, K., Hikida, M., Tatsuno, K., Kaneto, K., and Inuishi, Y. (1973) Emission-spectra of phthalocyanine crystals. *J. Phys. Soc. Jpn.*, **34**, 441–445.

61 Heilig, M., Domhan, M., and Port, H. (2004) Optical properties and morphology of thin diindenoperylene films. *J. Lumin.*, **110**, 290–295.

62 Gwinner, M.C., Vaynzof, Y., Banger, K.K., Ho, P.K.H., Friend, R.H., and Sirringhaus, H. (2010) Solution-processed zinc oxide as high-performance air-stable electron injector in organic ambipolar light-emitting field-effect transistors. *Adv. Funct. Mater.*, **20**, 3457–3465.

63 Zaumseil, J., Friend, R.H., and Sirringhaus, H. (2006) Spatial control of the recombination zone in an ambipolar light-emitting organic transistor. *Nat. Mater.*, **5**, 69–74.

64 Dürr, A.C., Schreiber, F., Münch, M., Karl, N., Krause, B., Kruppa, V., and Dosch, H. (2002) High structural order in thin films of the organic semiconductor diindenoperylene. *Appl. Phys. Lett.*, **81**, 2276–2278.

65 Heinemeyer, U., Scholz, R., Gisslén, L., Alonso, M.I., Ossó, J.O., Garriga, M., Hinderhofer, A., Kytka, M., Kowarik, S., Gerlach, A., and Schreiber, F. (2008) Exciton–phonon coupling in diindenoperylene thin films. *Phys. Rev. B*, **78**, 085210.

66 Takenobu, T., Bisri, S.Z., Takahashi, T., Yahiro, M., Adachi, C., and Iwasa, Y. (2008) High current density in light-emitting transistors of organic single crystals. *Phys. Rev. Lett.*, **100**, 066601.

67 Capelli, R., Toffanin, S., Generali, G., Usta, H., Facchetti, A., and Muccini, M. (2010) Organic light-emitting transistors with an efficiency that outperforms the equivalent light-emitting diodes. *Nat. Mater.*, **9**, 496–503.

68 de Boer, R.W.I., Stassen, A.F., Craciun, M. F., Mulder, C.L., Molinari, A., Rogge, S., and Morpurgo, A.F. (2005) Ambipolar Cu- and Fe-phthalocyanine single-crystal field-effect transistors. *Appl. Phys. Lett.*, **86**, 262109.

69 Tripathi, A.K. and Pflaum, J. (2006) Correlation between ambipolar transport and structural phase transition in diindenoperylene single crystals. *Appl. Phys. Lett.*, **89**, 082103.

70 Takenobu, T., Watanabe, K., Yomogida, Y., Shimotani, H., and Iwasa, Y. (2008) Effect of postannealing on the performance of pentacene single-crystal ambipolar transistors. *Appl. Phys. Lett.*, **93**, 073301.

71 Gershenson, M.E., Podzorov, V., and Morpurgo, A.F. (2006) *Colloquium*: Electronic transport in single-crystal organic transistors. *Rev. Mod. Phys.*, **78**, 973–989.

9
Organic Magnetoresistance and Spin Diffusion in Organic Semiconductor Thin-Film Devices

Markus Wohlgenannt

9.1
Introduction

The field of organic electronics, that is, electronic devices that are based on π-conjugated organic semiconductors, has progressed at a rapid pace and electronics based on organic thin-film materials could soon become a mainstay of semiconductor technology. Recently, commercial products based on organic light-emitting diodes (OLEDs), organic photovoltaic cells (OPV), and organic field-effect transistors (OFETs) have entered on the market. The future may see an even wider range of application for this technology. One specific area that organic semiconductors may be applied to is spintronics.

The study of electron-spin transport through metallic and semiconducting devices is an extremely active field called spintronics, because of the rich physics involved and the important applications in the area of magnetic sensors. Spintronics deals with controlling and utilizing the electron-spin degree of freedom through a variety of spin-dependent phenomena. The spin valve is the principal spintronic device and consists, in its most basic form, of two ferromagnetic electrodes separated by a nonmagnetic spacer layer (Figure 9.1). The two ferromagnetic electrodes are chosen to exhibit two distinct switching fields, and the device can be switched between a parallel and antiparallel magnetization configuration using an applied magnetic field B. The significant difference in resistance between the two configurations is referred to as giant magnetoresistance (GMR). Fert and Grünberg were awarded the Nobel Prize in 2007 for their pioneering work on giant magnetoresistance. In GMR devices, typically metallic spacer layers are used, and the spin-polarized current is injected into and transported through the spacer layer. If a thin layer of insulator is chosen as the spacer layer instead of a metal, the corresponding effect is called tunneling magnetoresistance (TMR) [1, 2], because the spin-

Physics of Organic Semiconductors, Second Edition. Edited by Wolfgang Brütting and Chihaya Adachi

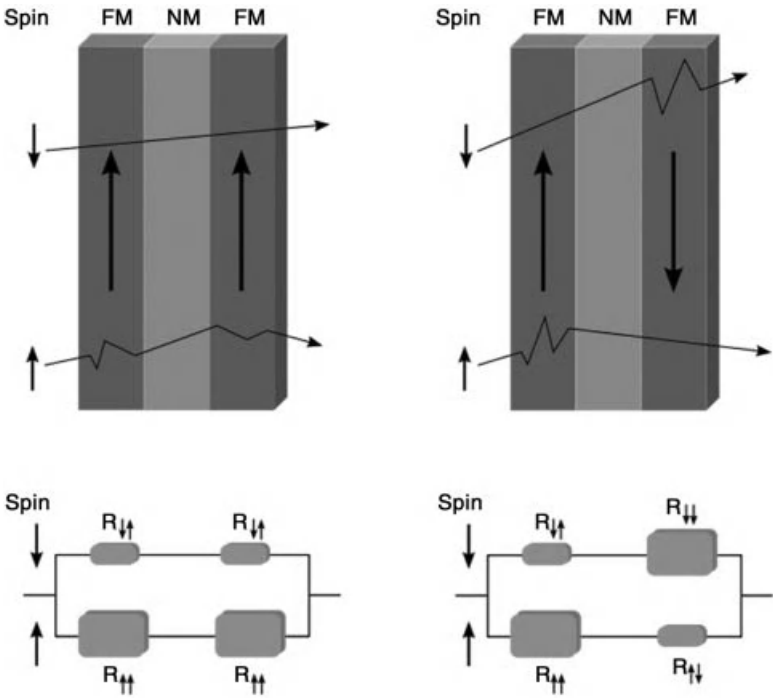

Figure 9.1 *Top panel*: Schematic drawing for spin valve in parallel magnetization configuration (left) and antiparallel magnetization configuration (right). *Bottom panel*: corresponding electrical resistor models. Reprinted from http://en.wikipedia.org/wiki/Giant_magnetoresistance.

polarized carriers tunnel through the insulating layer. More recently, semiconductor-based spintronic devices have been investigated [3]. Organic semiconductors are an interesting materials class for spintronics because of the enormous versatility of organic chemistry and because the light atoms from which they are composed cause very little spin–orbit coupling [4].

9.1.1 Organization of This Chapter

In this chapter, we investigate a variety of spin-dependent transport phenomena in organic semiconductor sandwich devices. The overarching theme is therefore organic spintronics, and we study several questions that have arisen in this field. Figure 9.2 shows a flowchart for the outline and various topics of this chapter, and some introductory remarks will be given now.

We study, *inter alia*, a recently discovered magnetoresistive effect, dubbed organic magnetoresistance (OMAR), which, although based on spin-dependent transport, does not require the injection of a spin-polarized current from magnetic electrodes. The mechanism underlying OMAR is currently not known with

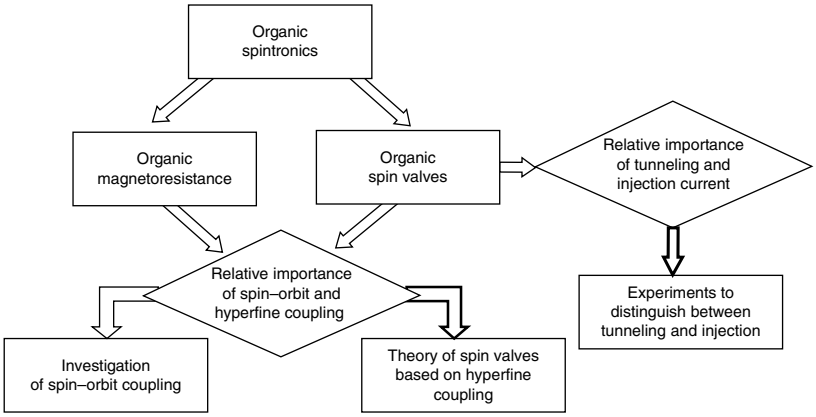

Figure 9.2 Flowchart for this chapter.

certainty, but it has been shown that OMAR is caused by hyperfine interaction in the organic semiconductor material. Indeed, as we will show throughout this chapter, hyperfine coupling is the dominant spin-scattering mechanism in organic spintronics. Spin–orbit coupling, which is often the dominant spin-scattering mechanism in inorganic spintronics, is usually much weaker than the hyperfine coupling in organic materials, but can be important in organic materials containing heavy atoms. To substantiate this claim, we also examine spin–orbit coupling in singly charged π-conjugated polymer chains theoretically and show that spin–orbit coupling is quenched to first order because the diagonal matrix elements vanish and the energy levels in polymers are orbitally nondegenerate. Even the off-diagonal matrix elements are zero or negligibly small unless a twisted, nonplanar polymer chain is considered.

Next, we consider organic semiconductor spintronic devices where a spin-polarized current is injected from ferromagnet electrodes, that is, organic spin valves. Building on the results of the OMAR studies, we present a theory for spin diffusion in disordered organic semiconductors based on incoherent hopping of a charge carrier and coherent precession of its spin in an effective magnetic field, composed of the random hyperfine field of hydrogen nuclei and an applied magnetic field. We perform Monte Carlo simulations and discuss a comparison between this theory and experiments on organic spin valves.

There has always been a substantial discussion on the proper analysis of the spin valve phenomena, both spin injection and spin-polarized tunneling have been considered. In the final section of this chapter, we introduce a criterion for distinguishing between tunneling and injection conductivity. This criterion is based on measurements of the current–voltage (I–V) characteristics of the devices as a function of the spacer layer thickness d. A case study is presented in a typical device structure, specifically Co/AlO_x/rubrene/Fe junctions with a rubrene spacer layer. For $d \leq 10$ nm, the I–V traces are typical of tunnel junctions. At $d > 15$ nm, the tunneling current becomes negligibly small. At larger biases, however, a second

type of conductivity sets in, which we identify with injection into the organic layer followed by hopping transport.

9.2 Organic Magnetoresistance

Organic magnetoresistance is a recently discovered, large (10% or more in some materials), low-field, room temperature magnetoresistive effect in organic semiconductor devices with *nonmagnetic* electrodes [5–8]. Similar magnetic field effects have also been observed in photoconductivity (Figure 9.3), conductivity, and electroluminescence experiments and have led to the conclusion that the hydrogen hyperfine fields are involved, influencing reactions between spin-carrying radicals (polarons and triplet excitons) [9–12]. However, the exact mechanism behind OMAR is still debated. Figure 9.4 shows typical OMAR traces for the prototypical small-molecule tris-(8-hydroxyquinoline) aluminum (Alq_3) (see inset in Figure 9.4 for molecular structure). It is seen that the magnetoconductive effect is typically about 10%, and the OMAR traces have a typical full width at half maximum of $\approx$20 mT. For fields in excess of 100 mT, the effect essentially saturates.

Next, we will briefly summarize some basic experimental results regarding OMAR that are common to most devices independent of the particular organic material that is used in the devices [13]: (i) OMAR is an effect associated with the bulk resistance of the organic semiconductor layer, rather than with the semiconductor/electrode interface resistance. (ii) The effect is independent of the magnetic field direction. (iii) OMAR can be of positive or negative sign, depending on material and/or operating conditions of the devices. (iv) OMAR obeys the empirical laws

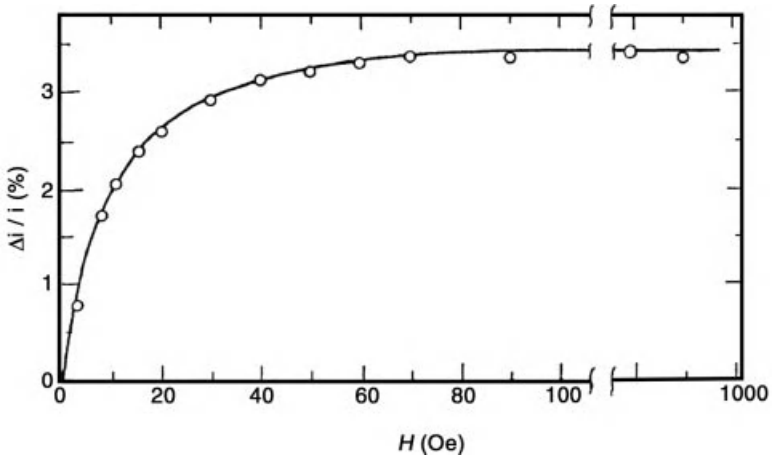

Figure 9.3 Typical dependence of the photocurrent *i* on the magnetic field strength *H* in an organic semiconductor device. Reprinted with permission from Ref. [9].

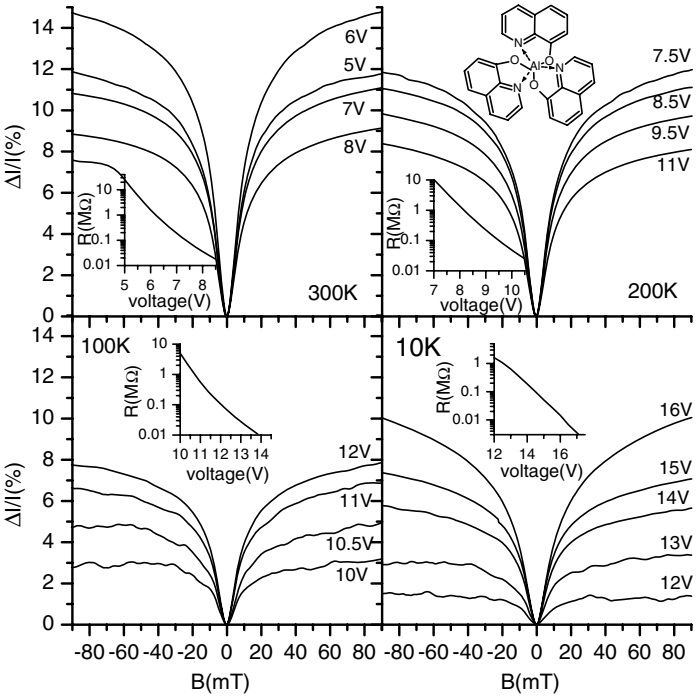

Figure 9.4 Magnetoconductance $\Delta I/I$ curves measured in an ITO/PEDOT/Alq_3 ($\approx$ 100 nm)/Ca device at different voltages and different temperatures. The insets show the device resistance as a function of the applied voltage. Reprinted with permission from Ref. [16].

$\Delta I(B)/I \propto B^2/(B^2 + B_0^2)$ or $\Delta I(B)/I \propto B^2/(|B| + B_0)^2$ dependent on material , where $B_0 \approx 5$ mT in most materials (see Figure 9.5 for a summary of OMAR traces in several different materials). The parameter B_0 is a measure of the strength of the effective magnetic field and sets the characteristic magnetic field scale of OMAR. As we will show, the magnetic field scale of OMAR is set by hyperfine coupling, and B_0 is equal to the hyperfine coupling strength (up to a factor of order unity). The value of B_0 can be directly read off the experimental data, since it is the half-saturation field and quarter-saturation field for the empirical laws $\Delta I(B)/I \propto B^2/(B^2 + B_0^2)$ and $\Delta I(B)/I \propto B^2/(|B| + B_0)^2$, respectively.

9.2.1
Dependence of Organic Magnetoresistance on Hyperfine Coupling Strength

Hyperfine coupling occurs in atoms possessing a nonzero nuclear magnetic dipole moment, that is, generally in atoms with unpaired nucleons. The most common isotope of C therefore does not exhibit any hyperfine coupling. In organic compounds, hyperfine coupling is predominantly due to the hydrogen atoms. Hyperfine coupling can be effectively eliminated by using an organic semiconductor

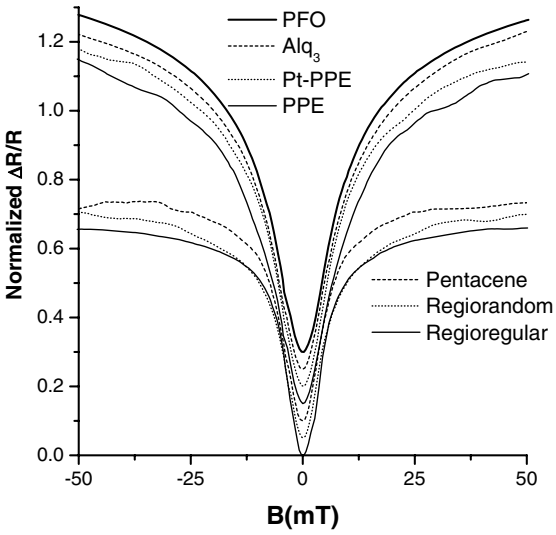

Figure 9.5 Summary of OMAR traces in a variety of organic semiconductor devices. The upper group of traces obey the empirical law $\Delta R(B)/R \propto B^2/(|B| + B_0)^2$, whereas the lower group obey $\Delta R(B)/R \propto B^2/(B^2 + B_0^2)$. Reprinted with permission from Ref. [13].

carbon-60 (C_{60}) that does not contain hydrogen atoms, and this allows one to show that OMAR is indeed caused by hyperfine coupling [14]. Strictly speaking, hyperfine interaction with the carbon isotope ^{13}C is still present, but its strength is only 6 μT [15], three orders of magnitude below the fields relevant for OMAR. Figure 9.6 reports on the *nonobservation* (with a sensitivity of less than 0.05%) of any OMAR effect in ITO/C_{60}/Ca/Al and Au/C_{60}/Ca/Al devices.

Next, we deliberately reintroduce hyperfine coupling by replacing C_{60} with a substituted fullerene derivative with a hydrocarbon side group. Specifically, PCBM, a compound similar to C_{60}, with similar electron transport properties, but which contains a hydrogen-containing side group substituent (Figure 9.7, inset), was used. Figure 9.7 shows a clear OMAR signal. The solid lines show the fit to the empirical law $B^2/(|B| + B_0)^2$. Apparently, introducing even a small amount of hydrogen atoms into the chemical structure leads to a clearly detectable OMAR signal.

9.2.2
Organic Magnetoresistance in a Material with Strong Spin–Orbit Coupling

In the study of C_{60} devices presented in Section 9.2.1, we investigated what happens to OMAR if spin-coupling is reduced by eliminating the hyperfine coupling. We will now investigate what happens if we increase the strength of the spin-coupling by introducing strong spin–orbit coupling into the organic semiconductor. For this purpose, the well-known heavy atom effect is exploited. Figure 9.8 shows

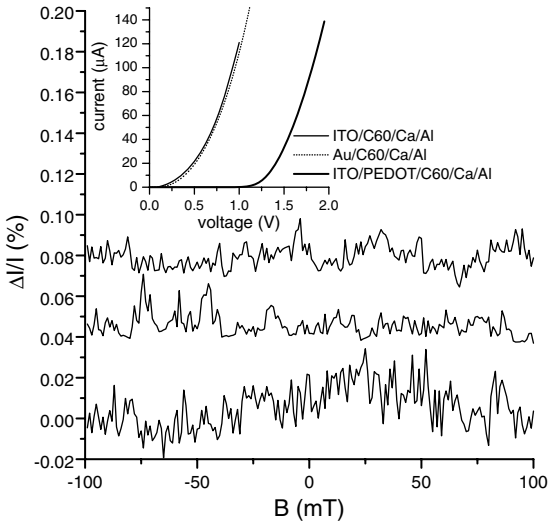

Figure 9.6 Magnetoconductance traces $\Delta I/I$ in the Au/C60/Ca/Al device at 100, 200, and 300 K from top to bottom. The data sets were offset along the vertical axis for clarity. The inset shows the current–voltage characteristics of C_{60} (150 nm) sandwich devices using different electrode materials at 300 K. Reprinted with permission from Ref. [14].

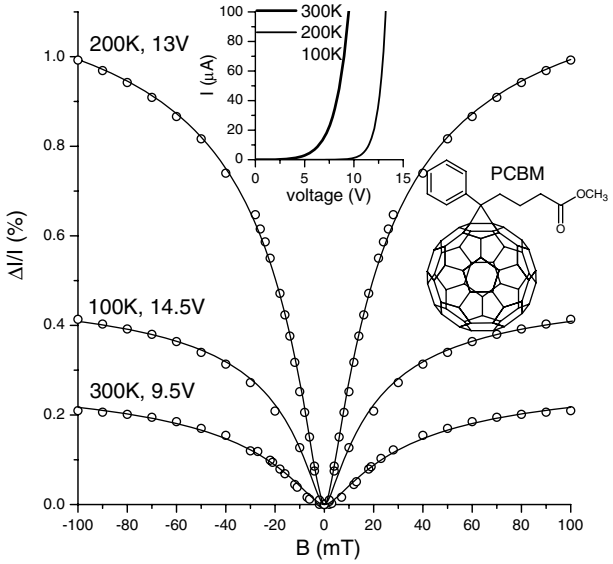

Figure 9.7 Magnetoconductance ratio $\Delta I/I$ in an ITO/PCBM (≈160 nm)/Ca devices measured at three different temperatures (scatter plot). The solid line is a fit to the law $\Delta I/I \propto B^2/(|B| + B_0)^2$. The molecular structure of PCBM and current–voltage characteristics of the device are shown as insets. Reprinted with permission from Ref. [14].

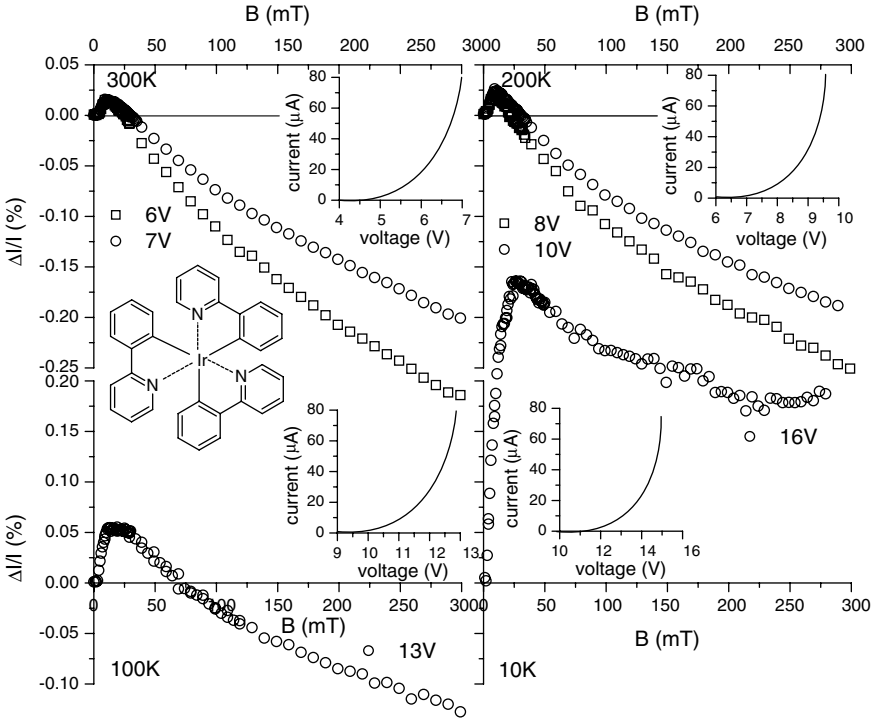

Figure 9.8 Magnetoconductance $\Delta I/I$ curves measured in an ITO/PEDOT/Ir(ppy)$_3$ ($\approx$100 nm)/Ca device at different voltages and different temperatures. The insets show the device current resistance as a function of the applied voltage. Reprinted with permission from Ref. [16].

the measured OMAR effect in an ITO/PEDOT/Ir(ppy)$_3$/Ca device [16], at different voltages and different temperatures. This material was chosen because of its chemical structure similar to that of the Alq$_3$ standard, except for the Ir atom that introduces strong spin–orbit coupling. Figures 9.4 and 9.8 show that the behavior of OMAR in Alq$_3$ and Ir(ppy)$_3$ devices differs dramatically: the magnitude of OMAR in Ir(ppy)$_3$ is about two orders of magnitude smaller than that in Alq$_3$. Moreover, it is evident that the OMAR traces in Ir(ppy)$_3$ are comprised of low-field and high-field effects of opposite signs. In terms of a possible analysis of the Ir(ppy)$_3$ data, this behavior implies that there are at least two relevant coupling strengths in materials with strong spin–orbit coupling, in contrast to Alq$_3$, where only a single coupling strength is evident. It appears natural to assign the second coupling strength in Ir(ppy)$_3$ to the spin–orbit coupling. In particular, two models have been suggested to account for the high-field cone. One model, proposed by Sheng *et al.* [17], treats spin precession about the orbital magnetic moment in much the same way as spin precession about the nuclear magnetic moment (i.e., hyperfine coupling), and another model, proposed by Wang *et al.* [18], considers the so-called delta-g

mechanism. In the delta-g mechanism, the high-field cone is related to a relative dephasing of the electron and hole spins that make up an electron–hole pair.

9.2.3
Organic Magnetoresistance in Doped Devices

So far we have limited ourselves to the study of OMAR in devices based on undoped, intrinsically semiconducting organic layers. In this section, we use the conducting polymer poly(3,4-ethylenedioxythiophene)-poly(styrenesulfonate) (PEDOT) (Figure 9.9, inset) as a prototypical doped conducting polymer and investigate whether the OMAR effect may also be observed in highly doped conducting polymer films. Figure 9.9 shows OMAR traces for several forward bias voltages in a ITO/PEDOT(100 nm)/Ca device for four different temperatures between 300 and 10 K. Essentially identical results were also obtained under reverse bias [16]. This is distinct from undoped devices for which the *I–V* curves are asymmetric for asymmetric electrode materials, and OMAR is observed only in forward bias. This shows that the conductivity in the PEDOT devices is due to the charges provided by the

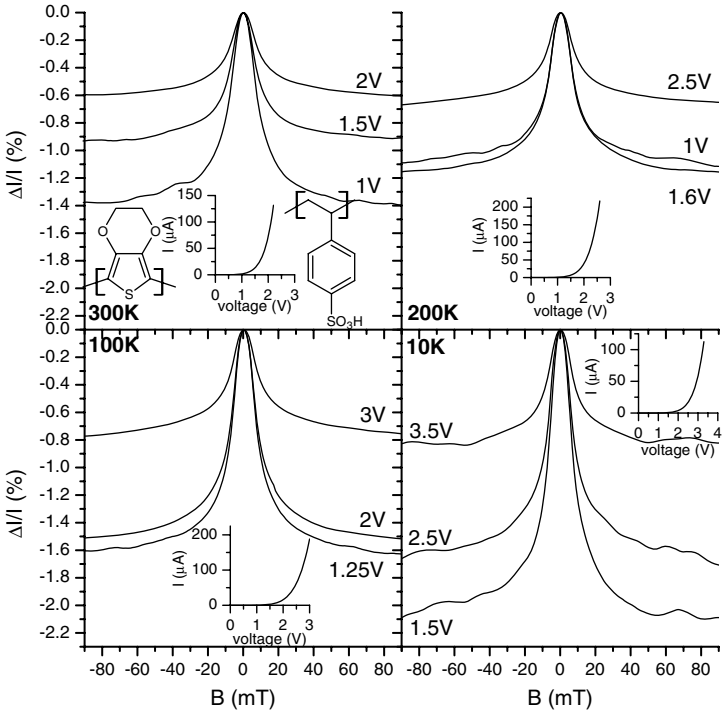

Figure 9.9 Magnetoconductance ratio in an ITO/PEDOT (≈100 nm)/Ca device measured at several different constant forward bias voltages at different temperatures. The current–voltage characteristics of the device are shown as insets. Reprinted with permission from Ref. [16].

dopant, rather than the injected charges that dominate undoped sandwich devices. OMAR effects of about 1% were observed at room temperature for forward and reverse bias voltages, and the OMAR effect increases by about a factor of 2 at 10 K [16].

However, it has to be noted that the OMAR effect observed in PEDOT devices is different from that observed in semiconducting device. As we will show now, the OMAR effect in PEDOT occurs at the PEDOT/Ca interface and is not a bulk effect. Figure 9.10 shows the *I–V* curves of ITO/PEDOT/Ca/Al devices with different PEDOT layer thickness. For bulk-limited devices, we would expect that the *I–V* curves shift to higher voltages in proportion to the film thickness. Experimentally however, a much smaller shift is observed. This conclusion that the device resistance is primarily due to the PEDOT/Ca interface can be confirmed by varying the electrode materials. If the electrode interface resistance is indeed dominant, a strong dependence on the electrode material, for example, its work function, is expected. Figure 9.10 shows the *I–V* curves of ITO/PEDOT/metal devices using Al and Au as the cathodes. It is seen that these devices show the linear *I–V* curves expected for metallic devices with ohmic contacts rather than the nonlinear *I–V* curves observed in the PEDOT/Ca devices. The great difference in behavior between the low-work function Ca and that of higher work function Al and Au may be caused by either of the two possibilities: (i) The particularly large difference in work function between Ca and PEDOT's "valence" bands that house the majority p-carriers leads to a large Schottky-like interface resistance. (ii) The Ca electrode locally dedopes the PEDOT film close to the interface . To the best of our knowledge, no OMAR effect has been reported in conducting devices with ohmic

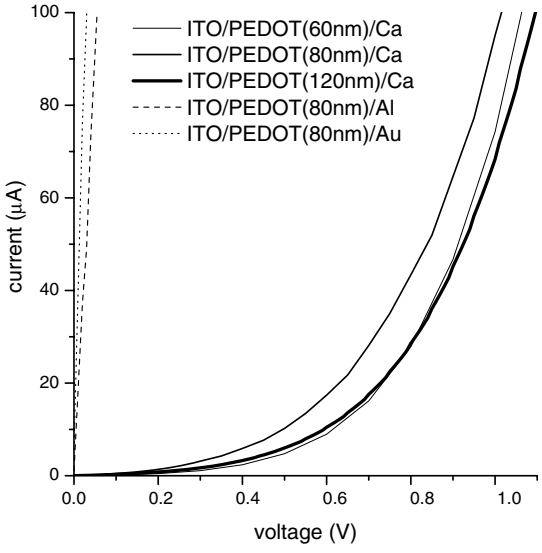

Figure 9.10 Current–voltage characteristics of a set of sandwich devices with different PEDOT:PSS thicknesses and cathode electrodes at 300 K. Reprinted with permission from Ref. [16].

contacts, suggesting that the OMAR effect observed in PEDOT/Ca devices occurs at the interface.

9.2.4
Conclusions for Organic Spintronics

In summary of Section 9.2, the analysis of the OMAR effect shows that spins in organic semiconductors couple primarily with nuclear hyperfine fields. Spin–orbit coupling is significantly weaker than hyperfine coupling, unless materials containing heavy atoms are employed. In the next section, we will study spin–orbit coupling theoretically to further explore this conclusion.

9.3
Theory of Spin–Orbit Coupling in Singly Charged Polymer Chains

Organic materials are a promising route to spintronics because the spin–orbit coupling strength is expected to be weak in organic semiconductors, promising long spin relaxation times. This expectation is based on the observation that these materials are mainly composed of the light elements carbon and hydrogen and on the well-known scaling of the spin–orbit coupling strength with the fourth power of the effective charge. However, the atomic carbon spin–orbit coupling strength equals ≈ 6 meV for p-states [19], which is actually quite strong since it must be compared with the very small interchain hopping matrix elements in organic thin-film devices (typical mobilities are $10^{-5}\,\mathrm{cm}^2/(\mathrm{V\,s})$ or less). Therefore, spin–orbit coupling has been proposed by some as the dominant spin scattering mechanism in organic spin valve devices [20]. Moreover, spin–orbit coupling in excitons appears to be quite strong because relatively large intersystem crossing rates between singlet and triplet states can be observed [21].

On the other hand, studies of OMAR (which we reviewed in the preceding sections) suggest that spin–orbit coupling in organics is weaker than the hyperfine coupling. The hyperfine coupling in organics has a strength of about 1 μeV, and if spin–orbit coupling were indeed weaker than hyperfine coupling, a significant further reduction of the spin–orbit coupling strength compared to the atomic value must result from the binding structure of π-conjugated molecules. These questions prompt us to explore the theory of spin–orbit coupling in singly charged conjugated polymer chains in this section. We note that although there exist a few works on spin–orbit coupling pertaining to intersystem crossing between singlet and triplet excitons (Ref. [22] and references therein), comparatively little seems to be known about spin–orbit coupling in singly charged polymer chains.

Because of the chainlike structure of polymers, the expression for the spin–orbit coupling Hamiltonian H_{SO} for a nonspherical potential must be employed:

$$H_{\mathrm{SO}} = \frac{1}{2m^2c^2}(\nabla V \times \mathbf{p})\mathbf{S} \tag{9.1}$$

where m is the electron mass, c is the speed of light, V is the potential energy, and **p** and **S** are the linear momentum and spin operators, respectively. Before inclusion of spin–orbit coupling, the wave function for the molecular orbitals factors into a spatial part and a spin part. Rybicki and Wohlgenannt [23] pointed out that the "diagonal" elements of the spin–orbit Hamiltonian that connect the spin-up and spin-down states for the same orbital wave function must vanish. This is because the spatial part of H_{SO} is both Hermitian and purely imaginary, whereas the orbital wave function is purely real. By the Hermitian property, the diagonal matrix elements are real. However, they must also be imaginary because the operator is imaginary. Therefore, they must be zero to satisfy the two conditions. This has important consequences for spin–orbit coupling in π-conjugated polymers, because orbitals in π-conjugated polymers are generally nondegenerate (not considering spin). This is because the symmetry group of polymer chains is typically low, allowing only one-dimensional (1D) irreducible representations. Therefore, the spin–orbit coupling matrix elements connect only states of different energies, and spin–orbit coupling is quenched in first order, since the first-order transitions must conserve energy. The situation is distinctly different in atomic carbon: Although the spin–orbit coupling matrix elements between, for example,p_x-orbitals is zero by the same argument as presented above, the spin–orbit coupling is not quenched since it can occur between, for example, p_x- and p_y-orbitals and still conserve energy, as they are degenerate. One can easily estimate the energy splitting in a polymer chain between the lowest and second lowest orbital: If the wave function is delocalized over the polymer chain (or rather one of its conjugation segments), the first excited state will be separated from the lowest state by at least the quantum confinement energy. Or, if the carrier forms a self-localized polaron, the first excited state is higher in energy by the polaron binding energy. In both cases, the energy difference should be on the order of 100 meV [24] and, therefore, much larger than the spin–orbit coupling energy.

To calculate the off-diagonal spin–orbit coupling matrix elements, we treat the polymer chain in the independent particle approximation using an effective π-electron tight binding model, including electron–phonon coupling, to allow bond dimerization (the so-called Su–Schrieffer–Heeger (SSH) model) [25]. The matrix elements for H_{SO} are calculated between wave functions obtained using this tight binding model based on p_z atomic orbitals. The calculated matrix elements between the orbital ground and first excited states are shown in Figure 9.11 for a 32 site *trans*-polyacetylene chain. The *x*-axis denotes the dihedral angle θ between neighboring carbon atoms connected by a double bond. Importantly, Figure 9.11 shows that nonvanishing spin–orbit coupling between π-electron orbitals require twisted chains. In the completely planar chain, the spin–orbit coupling for π-electrons vanishes. Figure 9.11 containing results for two different twist patterns shows a dependence approximately proportional to $\sin\theta$. For realistic twist angles of up to ≈ 10 degrees, Figure 9.11 shows that we have $H_{SO} = 10\,\mu eV$. This is still an order of magnitude larger than the hyperfine

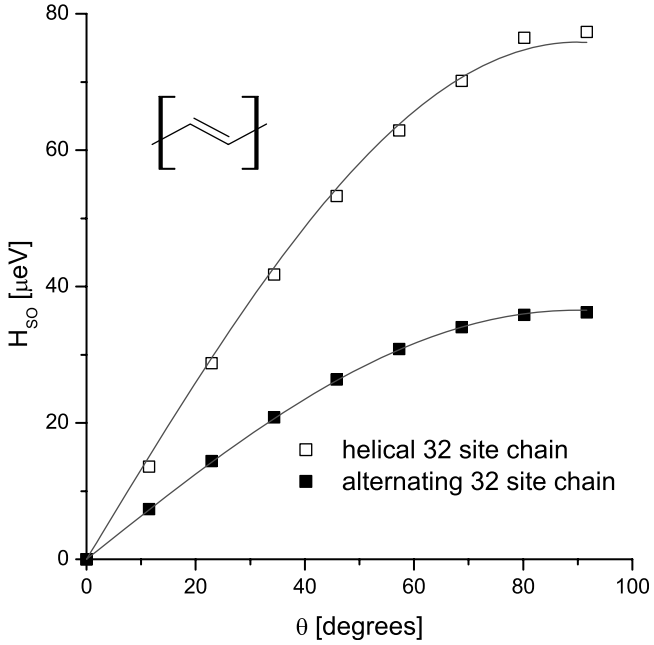

Figure 9.11 Calculated matrix elements for spin–orbit coupling H_{SO} as a function of the twist angle θ. The matrix element was taken between the orbital ground and first excited states in a singly charged *trans*-polyacetylene (inset) chain of 32 repeat units. Results are shown both for the case of a helical chain as well as a chain with alternating twist (scatter plots). The solid lines are fits to the law $H_{SO} \propto \sin\theta$. Reprinted with permission from Ref. [23].

coupling strength. However, since the diagonal matrix elements are zero, a spin-flip transition cannot occur in first order.

However, even higher order matrix elements do not lead [23] to spin randomization (spin precession). This follows from time-reversal symmetry, which dictates that in singly charged polymer chains that have an odd number of electrons, the energy levels must be (at least) doubly degenerate, the so-called Kramers degeneracy. Spin–orbit coupling will indeed mix the pure spin states into pseudo-spin states, and a pure spin state is a superposition of pseudo-spin states. Such a superposition, however, will still lie in the degenerate subspace spanned by the pseudo-spin states and will therefore be conserved. To avoid possible misunderstandings, we point out that the treatment by Rybicki and Wohlgenannt [23] is valid for stationary electron wave functions. In band transport systems that support itinerant Bloch-type electron wave functions, spin precession due to spin–orbit coupling is possible in crystals that lack inversion symmetry. This is the so-called Dyakonov–Perel [26] mechanism. We do not believe that this mechanism applies to organic hopping systems.

9.4
Theory of Spin Diffusion in Disordered Organic Semiconductors

Many spintronic devices rely on the injection and detection of spin-polarized current. For a large signal, it is essential that the spin polarization is maintained during the transport from the injector to the detector. Spin relaxation in the inorganic materials traditionally used in these structures, containing relatively heavy atoms, is mainly caused by spin–orbit coupling [27]. Organic semiconductors are a very interesting alternative because of the enormous versatility of organic chemistry and the small spin–orbit coupling [23, 28]. Recent years have seen the first demonstrations of GMR devices (Figure 9.12) [29–36] as well as magnetic tunnel junctions [37, 38] using organic semiconductors as the spacer layer (Figure 9.13). The experiments reported so far have shown that when the thickness of the organic semiconductor spacer layer increases, the GMR effect in these devices disappears on a typical length scale on the order of 10–100 nm. Two very important questions therefore arise: What is the cause of the remaining spin relaxation? What factors

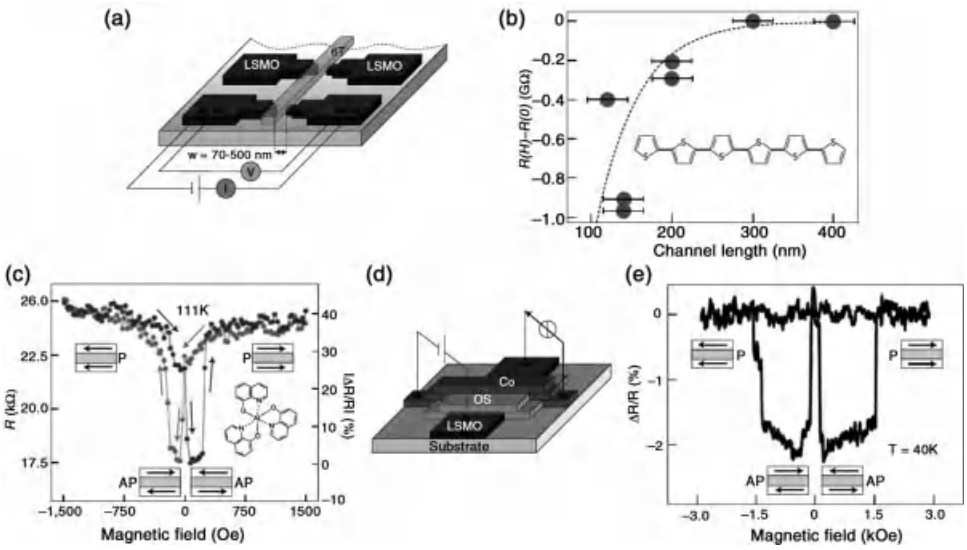

Figure 9.12 Organic spintronic devices. (a) Lateral spin device. In this device, two ferromagnetic LSMO electrodes patterned by electron beam lithography were separated by 70–500 nm and bridged by a 6T channel. (b) Magnetoresistance ($H = 0.3$ T, where H is the magnetic field) of the lateral spin device depicted in (a) as a function of the channel length. (c) Magnetoresistance loop of a LSMO (100 nm)/Alq_3 (130 nm)/Co (3.5 nm) spin valve device measured at 11 K. As indicated in the figure, an antiparallel (AP) configuration of the magnetization of the electrodes corresponds to a low-resistance state. (d) Schematic of a typical vertical inorganic–organic spin valve. In this case, LSMO is the bottom electrode and Co is the top one. (e) Magnetoresistance loop of a LSMO (20 nm)/6T (100 nm)/Al_2O_3 (2 nm)/Co (20 nm) vertical spin valve device measured at 40 K. Reprinted with permission from Ref. [4].

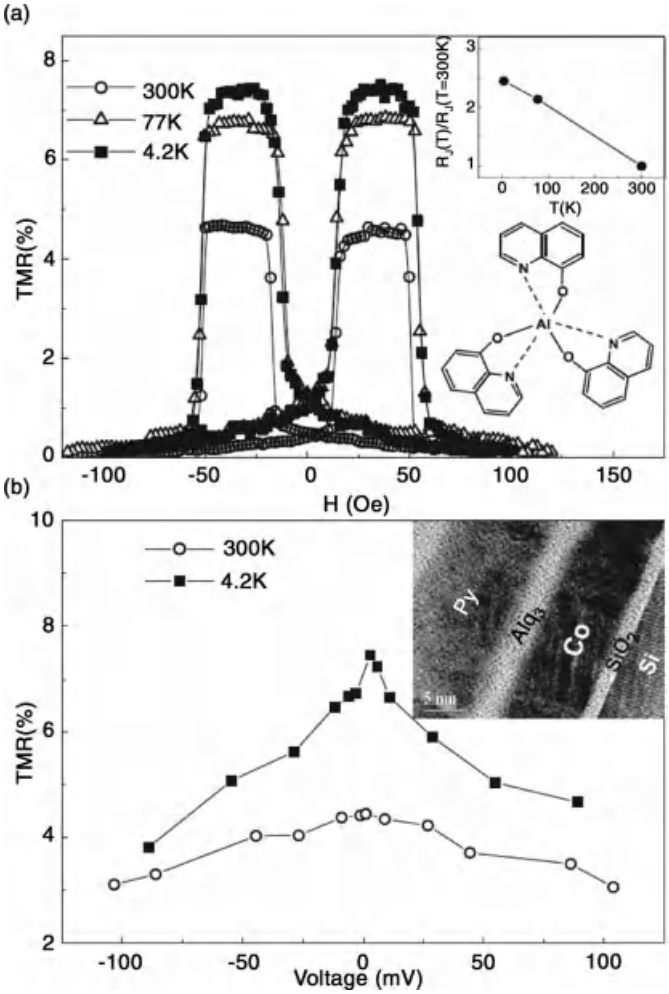

Figure 9.13 Tunneling magnetoresistance (TMR) for a 8 nm Co/1.6 nm Al_2O_3/6 nm Alq_3/10 nm Py junction. (a) TMR measured with 10 mV bias. The inset shows the temperature dependence of the junction resistance and the chemical structure of the Alq_3 molecule. (b) Bias dependence of the TMR. The inset is a cross-sectional HRTEM image, showing the continuous Alq_3 barrier. Reprinted with permission from Ref. [37].

determine the spin diffusion length? The study of the OMAR effect provides strong evidence that hyperfine coupling is the dominant spin relaxation mechanism in organic spin valves. In this section, we therefore review a theory of spin diffusion based on hyperfine coupling due to Bobbert *et al.* [39].

Since typically many (∼10 or more) hydrogen nuclear spins couple to the spin of a charge carrier in organic semiconductors, we can replace the hyperfine coupling by a classical, quasi-static, and random field, distributed according to a three-

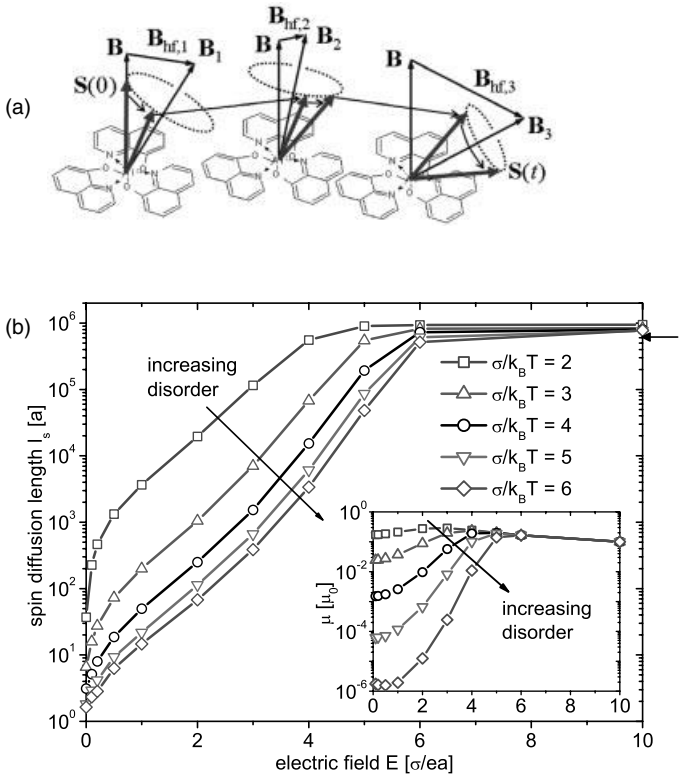

Figure 9.14 (a) Mechanism for spin diffusion, in this case for the molecular semiconductor Alq_3. (b) Spin diffusion length l_s (as multiples of the lattice constant) versus electric field E at zero magnetic field, for $r \equiv \omega_{hop}/\omega_{hf} = 1000$ and different $\hat{\sigma} \equiv \sigma/k_B T$. The arrow at the right axis indicates the result for a one-dimensional chain at large E. *Inset*: Corresponding mobility μ versus E, in units of $\mu_0 \equiv ea^2\omega_{hop}/\sigma$. Reprinted with permission from Ref. [39].

dimensional (3D) Gaussian [40], with standard deviation B_{hf}. In addition, we model charge transport in disordered organic semiconductor films by hopping of carriers between localized sites with random site energies, distributed according to a Gaussian density of states (GDOS) with standard deviation σ [41]. Therefore, this model describes spin diffusion in these materials by a combination of *incoherent* hopping of a carrier in a GDOS together with *coherent* precession of its spin around a local effective magnetic field (Figure 9.14).

We consider the situation that a carrier with unit charge e (electron or hole) and spin fully polarized in the z-direction is injected by an electrode into the organic material at $x = 0$ and moves to the opposite electrode under the influence of the applied electric field E. Clearly, the ratio $r \equiv \omega_{hop}/\omega_{hf}$ of hopping frequency and hyperfine precession frequency is an important parameter. If r is large, the influence of the hyperfine field is small and large spin diffusion lengths can be expected, while the opposite holds if r is small. For derivatives of the familiar

π-conjugated polymer poly-(*para*-phenylene vinylene) (PPV), we obtain an estimate of 10^9–$10^{11}\,s^{-1}$ for ω_{hop} [42]. Hence, for this class of organic semiconductors, r is on the order of 10–1000, but the large variation even within this class shows that very different values can be expected for different organic semiconductors.

It is instructive to first consider a one-dimensional chain of sites for the case $E \gg \sigma/ea$, when all hops are downfield with the same rate ω_{hop}, leading to equal average waiting times $1/\omega_{hop}$ at each site. By solving the time-dependent Schrödinger equation for the spinor in the effective magnetic field and performing an average over the random hyperfine fields (in cylindrical coordinates ϱ, ζ), one can easily derive the following expression for the relative preservation λ of spin polarization p during the waiting time of the carrier at a site:

$$\begin{aligned} \lambda &= \frac{1}{\sqrt{2\pi}} \int_0^\infty \varrho d\varrho \int_{-\infty}^{\infty} d\zeta e^{-((\varrho^2+\zeta^2)/2)} \frac{r^2 + (\zeta + b)^2}{r^2 + \varrho^2 + (\zeta + b)^2} \\ &\approx \exp\left\{ -\left[1/\ln(3) + r^2/2 + b^2/2 \right]^{-1} \right\} \end{aligned} \tag{9.2}$$

where $b \equiv B/B_{hf}$ denotes the relative strength of the applied magnetic field compared to the random hyperfine fields. From the exponentially decaying polarization $p(x) = \exp(-x/l_s)$, the spin diffusion length is extracted:

$$l_s = -a/\ln\lambda \approx a[1/\ln(3) + r^2/2 + b^2/2] \tag{9.3}$$

where a is the average nearest-neighbor distance. The increase of l_s with increasing b and r can readily be understood qualitatively: with increasing b, the Zeeman coupling becomes increasingly dominant over the hyperfine coupling and the carrier spin becomes effectively pinned. The quadratic increase with r results from "motional narrowing" well known in magnetic resonance spectroscopy.

For the three-dimensional situation, Bobbert *et al.* [39] performed Monte Carlo simulations for hopping of a single carrier in a homogeneous electric field of arbitrary magnitude on a cubic lattice of sites. Sufficiently far from the injecting layer, $p(x)$ decreases exponentially, from which the spin diffusion length l_s is extracted. In Figure 9.14b, we show l_s as a function of E for different reduced disorder strengths $\hat{\sigma} \equiv \sigma/k_B T$, for $r = 1000$ and $B = 0$. The arrow at the right axis shows the value obtained for the 1D model discussed above, which is quite close to the present results at large E. For $r \leq 1$ (slow hopping), Bobbert *et al.* found $l_s \sim a$, indicating that for this case no significant spin diffusion length is found.

We now undertake a comparison between this theory and experimental results in organic spin valves, as far as they are available at the moment. We have no information about the hopping frequencies of the organic semiconductors used in the spin valves of Refs [29–31]: sexithienyl, tris-(8-hydroxyquinoline) aluminum (Alq_3), and poly-3-hexylthiophene, respectively. Since the mobilities in these materials are higher than those of the PPV derivatives investigated in Ref. [42], we expect that the hopping frequencies are such that $r > 1000$. A calculated value of $\sigma = 0.26$ eV for the energetic disorder of electrons in Alq_3 [43] leads to $\hat{\sigma} \approx 10$ at room temperature, which is clearly in the strong disorder limit. We can conclude that with a typical value of $a \approx 1$ nm, the spin diffusion lengths of about 10–100 nm found in

Refs [29–31] and recently confirmed with muon spin resonance studies [33] are compatible with the theoretical results.

This theory [39] predicts a rather weak dependence of l_s on the relative disorder strength of σ/k_BT and hence on temperature, in agreement with experiments [30, 34, 35]. In the experiments with $La_{2/3}Sr_{1/3}MnO_3$ (LSMO) as one of the electrodes, the GMR effect decreases significantly above $T \approx 100$ K, but this can be fully attributed to a reduction of the spin polarization of the injected current [34, 35]. Finally, it is important to note that in the experiments, the GMR effect rapidly disappears with growing bias voltage [30, 34, 35] on a voltage scale ($\sim$1 V) that corresponds in the theory to electric fields for which $eEa/\sigma \ll 1$. At such fields, l_s has saturated to its value at $E = 0$. Therefore, our view is that the measured bias voltage dependence is not caused by a dependence of l_s on the electric field. This view is supported by experiments that find an asymmetric behavior in the bias dependence of organic spin valves depending on which of the two unequal electrode materials is positively biased [30, 34]. Several possible explanations for the steep decrease of spin valve efficiency with increasing bias have been suggested [34], but it is clear that this issue requires much further study. If efficient spin injection can be realized with high biases such that $eEa/\sigma > 1$, then the theory predicts greatly enhanced spin diffusion lengths on the order of several hundreds of nanometers, up to even millimeters (Figure 9.14a).

9.5 Distinguishing between Tunneling and Injection Regimes of Ferromagnet/Organic Semiconductor/Ferromagnet Junctions

Utilizing semiconductors as spacer layers is particularly attractive because of the possibility of implementing spintronic logic devices. However, spin injection into semiconductors continues to be challenging, in part because of the conductivity mismatch problem [44]. The search for new materials systems is therefore ongoing.

Recently, there has been increasing interest in using organic semiconductors for spintronics, motivated, in part, by their long spin relaxation times [4, 45]. The first demonstration of an organic spintronic device employed a planar structure of LSMO electrodes separated by an $\approx$ 100 nm long channel of α-sexithiophene [29]. The first vertical organic spin valve device, which utilized LSMO and Co as the ferromagnetic layers, was demonstrated by Xiong *et al.* [30] and exhibited a clear spin valve effect. The relatively thick (>100 nm) spacer layers employed in Ref. [30] suggest that spin injection into the organic layer (rather than tunneling through it) must have occurred. However, these devices display a surprisingly low resistance at low-bias (<100 mV), weakly temperature-dependent I–V curves and approximately parabolic differential conductance traces. All these properties are characteristic of tunneling and are uncharacteristic of organic semiconductor devices that function by carrier injection and hopping transport (cf. organic light-emitting diodes) [46], as we will

show below. Recently, TMR using the organic semiconductor rubrene was demonstrated with tunneling distances as long as 15 nm [38].

Apparently, both spin injection and spin tunneling are possible, and a criterion for a clear distinction between tunneling and injection is required for the proper analysis of spin valve effects in organics. Since tunneling is expected to dominate in thin junctions, but decays exponentially with increasing thickness [47], there will be a critical thickness beyond which tunneling is improbable and injection will become the dominant mode of conductivity. Lin *et al*. [48] and Yoo *et al*. [49] recently looked for and identified this transition between the two modes of conductivity.

The distinction between tunneling and spin injection is crucially important for possible semiconductor spintronics applications: only if the spin gets injected into the semiconductor (i.e., its wave function is entirely contained within the semiconductor) is the effective manipulation of its spin state, necessary for logic gates [50, 51]. We note that in inorganic semiconductor spintronics, identification of spin injection is possible using the spin–orbit coupling-based methods and Hanle effect measurements. In organic semiconductors, however, the minuteness of spin–orbit coupling [23] makes such measurements extremely difficult [52]. Furthermore, the very slow carrier drift velocity requires very small Hanle magnetic fields. The presence of hyperfine fields [39] will mask the Hanle effect. We note that two methods for detecting spin injection in organics have recently been demonstrated [33, 53] using two-photon photoemission and low-energy muon spin rotation, respectively. However, these are very complex experiments that are not widely available.

Figure 9.15a and b shows measured [48] *I*–*V* traces in typical organic spin valve devices (using Co and Fe as the ferromagnetic spin injector and spin detector and thermally evaporated rubrene as the organic semiconductor spacer) with two different rubrene thicknesses of 10 and 20 nm, respectively, at various temperatures ranging from room temperature to ≈13 K. Figure 9.16a and b shows room temperature *I*–*V* data of devices with several different rubrene thicknesses *d*, this time plotted as differential conductance versus the average electric field. Comparison of the data shown in Figures 9.15a and 9.16a and that shown in Figures 9.15b and 9.16b clearly shows that there exist two entirely different modes of conductivity in these devices. The mode shown in Figures 9.15a and 9.16a displays weak temperature dependence and near-parabolic differential conductance traces typical of tunneling conduction and occurs in devices with thickness $d \leq 15$ nm. The tunneling nature of this mode is confirmed by plotting the junction current measured at a bias voltage of 0.5 V versus *d*. As expected for tunneling, the dependence is exponential, from a fit to the dependence $\ln(I) \propto -d/d_0$ the tunneling decay length $d_0 \approx 1$ nm is obtained.

The mode shown in Figures 9.15b and 9.16b, on the contrary, is strongly temperature dependent, and the *I*–*V* curves are typical of those commonly measured in OLEDs: They possess an onset voltage below which hardly any current flows, and above which the current increases in a highly nonlinear fashion. The similarity to OLEDs is clearly demonstrated by comparison with Figure 9.15c that depicts data measured in a rubrene OLED. Both parts (b) and (c) of Figure 9.15 show a very similar functional dependence between current and voltage, as well as a

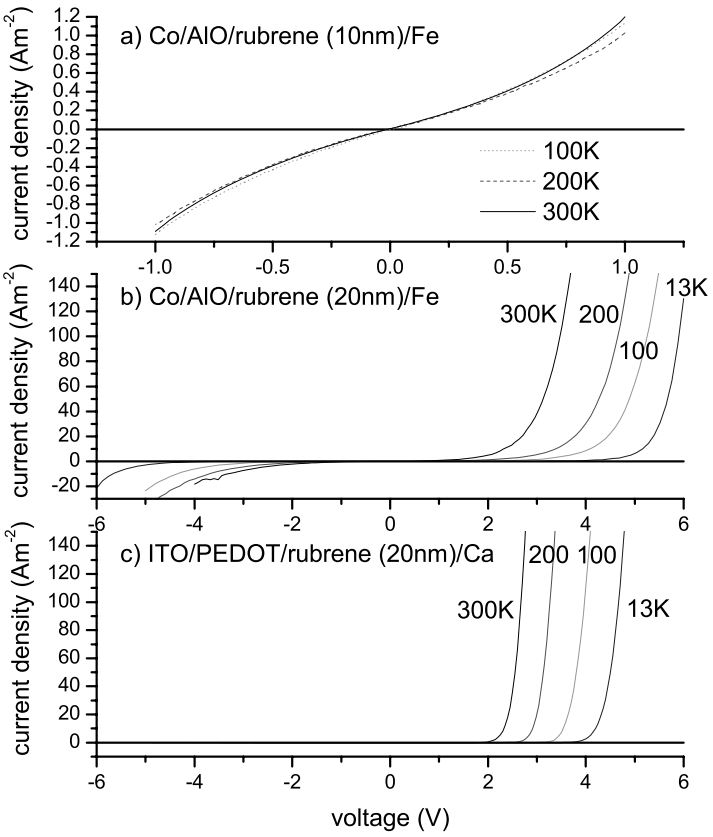

Figure 9.15 (a) and (b) Current–voltage (*I–V*) characteristics of Co/AlO/rubrene/Fe junctions at different temperatures. (a) Device with rubrene thickness of 10 nm. Note that the *I–V* curves for 100, 200 and 300 K are almost overlapping. (b) Device with rubrene thickness of 20 nm. (c) *I–V* characteristics of a PEDOT/rubrene (20 nm)/Ca OLED at different temperatures. Reprinted with permission from Ref. [48].

characteristic temperature dependence where, with decreasing temperature, larger and larger biases are required to obtain a certain conductivity. Since current conduction in OLEDs is well known to occur by carrier injection followed by carrier hopping [54], the second mode observed in these ferromagnet/organic semiconductor/ferromagnet junctions should be assigned to carrier injection/hopping.

OLED *I–V* curves are commonly explained by either a space charge-limited current model [54] or modeled by Monte Carlo simulations considering (nearest-neighbor) hopping in a disordered density of states [41]. In both models, the high nonlinearity is caused by a distribution of deep traps. Figure 9.16a shows that the tunneling current is barely detectable for the 15 nm devices (note that the data are plotted on two different *y*-scales, left and right *y*-axes), and it also shows the beginning of the injection mode at a bias of ≈75 mV/nm. The 15 nm data are replotted

in Figure 9.16b on a larger *y*-scale to demonstrate the dominance and high nonlinearity of the injection mode at larger biases. Figure 9.16b also shows the differential conductance of a much thicker device ($d = 50$ nm) demonstrating injecting behavior.

In a recent work, Yoo *et al.* [49] performed a study of LSMO/rubrene/Fe junctions. They identified two modes of conductivity: tunneling and a mode that they called phonon-assisted field emission. In the latter mode, carriers are injected into the organic layer even at low bias, resulting in *I*–*V* curves that look similar to the tunneling case. This mode of injection is different from the injection mode we just discussed, for which the conductivity at low bias is negligible. Injection due to field emission at low bias can occur only as a temperature-activated process because the carriers must overcome a significant energy offset between electrode work function and unoccupied energy levels in the organic. As a result, this injection mode is highly temperature dependent, but even at room temperature the electrode injection resistance is quite large and the device conductivity is injection limited.

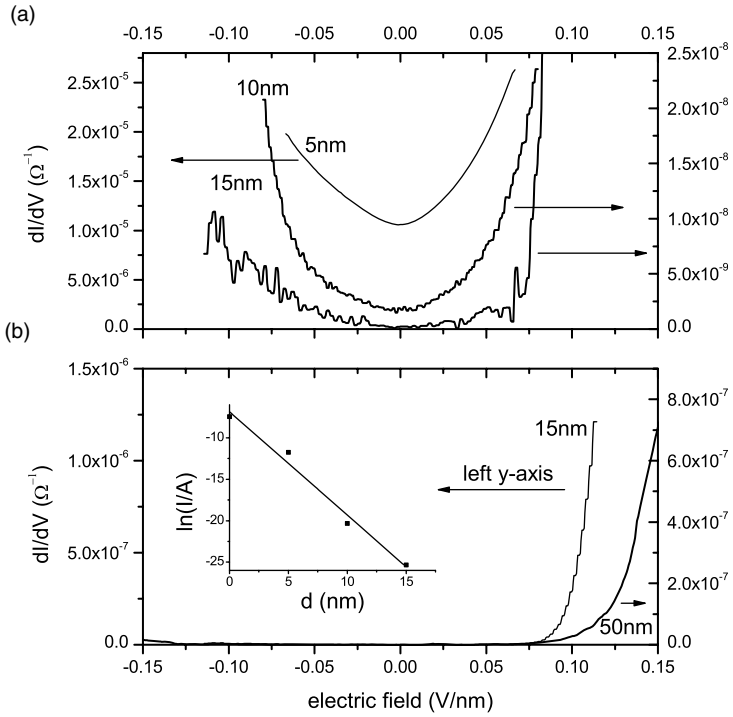

Figure 9.16 Differential conductance versus average electric field of Co/AlO/rubrene/Fe junctions at room temperatures for different rubrene thicknesses *d*. (a) $d = 5$, 10, and 15 nm. (b) $d = 15$ and 20 nm. Note that the data in both panels are plotted on two different *y*-scales, left and right *y*-axes. The corresponding *y*-axis is assigned using an arrow. *Inset*: Natural logarithm of the tunneling current *I* measured in *A* at a bias voltage of 0.5 V versus *d*. The 0 nm data refer to a Co/AlO/Fe junction. The line is a fit to an exponential. Reprinted with permission from Ref. [48].

Figure 9.17 shows magnetoconductivity traces, $\Delta I/I \equiv (I(B) - I(B_{max}))/(I(B_{max}))$, measured in the Co/AlO/rubrene/Fe devices discussed earlier, one with $d = 5$ nm (thin lines) and the other with $d = 10$ nm (thick lines) at two different temperatures, 300 and 100 K (panels (a) and (b), respectively). B_{max} is the maximum reported field in the respective graphs and corresponds to a parallel orientation of the two electrodes. At 100 K, both devices show a maximum MR ratio of 5–6%, which shows that spin-polarized tunneling can occur over lengths of $\geq$10 nm. Similar results were also obtained by the MIT group for rubrene [38]. For the 10 nm device, a similar MR ratio is also achieved at room temperature, whereas the MR ratio for the 5 nm device is significantly smaller than that at 100 K. This possibly indicates a competing pinhole transport mechanism active at room temperature in the very thin junction. The figures also demonstrate that the coercive field of the electrodes increases significantly with decreasing temperature. Such behavior was also previously observed in organic spin valves [30] and may indicate pinning of domains on the organic semiconductor surface. For the

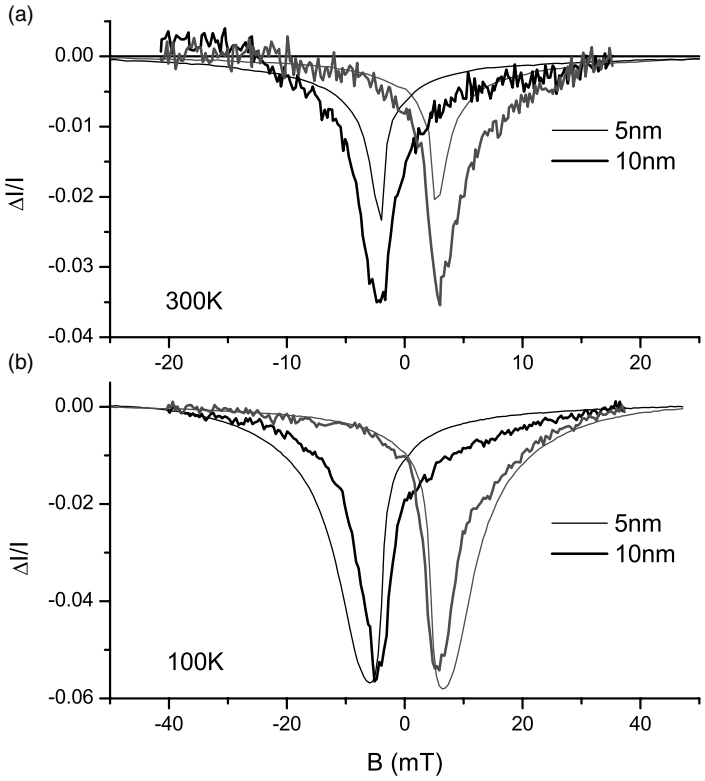

Figure 9.17 Magnetoconductivity traces measured at a bias of 0.2 V in a Co/AlO/rubrene(5 nm)/Fe device (thin lines) and a Co/AlO/rubrene(10 nm)/Fe device (thick lines), at room temperature (a) and 100 K (b). Reprinted with permission from Ref. [48].

15 nm device, the tunneling current has become very small even at larger biases (Figure 9.16a), and no MR (with about 0.1% accuracy) could be detected in these experiments [48]. No MR could be detected for thicker devices either.

The experiments just discussed [48] yield a value of ≈1 nm for the tunnel decay length in rubrene (Figure 9.16, inset). A measurable tunneling conductivity through the organic semiconductor layer is limited to devices of ≈15 nm thickness or thinner. Reports of GMR effects in organic spin valves with a thickness in excess of 100 nm [30, 35, 55] clearly seem beyond the tunneling range. Tunneling scenarios in such thick devices would only be plausible if there existed locally thin regions in the organic layer (i.e., the film quality is poor or effects occurring at sharp edges of devices) or if the effective barrier height for tunneling through the organic layer were exceptionally low. The latter scenario is however highly unlikely: d_0 is proportional to the square root of the barrier height, and a 10-fold larger d_0 would require a tunnel barrier 100-fold smaller than that in our devices.

If one rejects tunneling through the thick organic layer as a possibility for the spin valves reported in Refs [30, 35, 55], then an alternative explanation is required for their *I–V* curves that are clearly characteristic of tunneling, and not of injection, devices. This is possible with modeling the devices as a series of (at least) two resistors. One corresponds to the resistance to carrier injection from the electrodes into the organics. Another represents the resistance to the transport of the carrier/spin through the organics. In OLEDs, efficient hole and electron injection electrodes are employed (such as PEDOT and Ca, as in the case of the OLED data we discussed here) resulting in small injection resistance and bulk-limited devices. However, in devices using LSMO, Co, or Fe, the injection resistance will be much larger than in OLEDs, since these materials are much less efficient injectors due to their unfavorable work functions. Assuming that the devices in Refs [30, 35, 55] are (tunneling) injection limited rather than bulk limited, their *I–V* curves would mimic tunneling even though carriers get injected into the organic layers.

Such a scenario could also explain the recent observation of injection GMR in LSMO/rubrene/Fe junctions in the regime of phonon-assisted field emission [49]. In these devices, conduction is still injection limited. Because the spin-dependent injection resistance is much greater than the spin-independent bulk resistance, the possible conductivity mismatch problem is overcome [56, 57]. We note that although the conductivity mismatch problem is well established for inorganic semiconductor spintronics, the situation is much less understood in organic spintronics. Nevertheless, significant progress in the modeling of organic spintronics devices has been made (Refs [4, 58, 59] and references therein).

9.6 Conclusion

Organic magnetoresistance is a recently discovered magnetoresistive effect in nonmagnetic organic semiconductor devices. In devices made from the prototypical small-molecule Alq_3, OMAR reaches values of 10% or more at room temperature.

Analysis of OMAR reveals that hyperfine coupling is the dominant spin coupling mechanism. Spin–orbit coupling, on the other hand, is important only in organic semiconductor materials containing heavy atoms. Reasons for the weak spin–orbit coupling in hydrocarbon organic semiconductors also lie in symmetries: Diagonal spin–orbit coupling matrix elements vanish because the operator is imaginary–Hermitian, and off-diagonal elements connect only nondegenerate energy levels. Spin–orbit coupling therefore vanishes in first-order perturbation theory. Kramers degeneracy prevents spin–orbit-induced spin precession, even when taking into account these off-diagonal matrix elements. Furthermore, even the off-diagonal matrix elements are zero in planar molecules due to the symmetry of π-orbitals.

Next, we applied the conclusions drawn from OMAR studies to organic spintronics. We presented a theory for spin diffusion in disordered organic semiconductors with hyperfine coupling, based on a combination of incoherent carrier hopping and coherent spin precession in a random effective magnetic field. The calculated spin diffusion lengths are in agreement with experiments on spin valves.

Both spin injection and tunnel junctions have recently been demonstrated with organic spacer layers. It is important to determine the experimental fingerprints of the two spin valve modes. We presented a case study in Co/AlO/rubrene/Fe junctions. Tunneling occurs in relatively thin junctions less than 15 nm thick and is characterized by a conductivity that decays exponentially with increasing organic layer thickness. The tunneling mode is also characterized by a weak temperature dependence and a nearly parabolic differential conductance. Injection followed by carrier hopping occurs in relatively thick devices and can be identified by strongly temperature-dependent, highly nonlinear current–voltage traces that are similar to those commonly measured in OLEDs.

Acknowledgments

The work reported in this chapter that was completed at the University of Iowa was supported by the National Science Foundation of the United States under Grant Nos ECS 04-23911 and ECS 07-25280, and by ARO MURI under Grant No. W911NF- 08-1-0317. M.W. is indebted to the students who worked on these projects and to Dr. Fujian Wang. A large fraction of this work was completed in collaboration with Profs Bobbert and Koopmans from the Technical University of Eindhoven, NL. The author also acknowledges fruitful discussions with Profs M. E. Flatté and Z. V. Vardeny.

References

1 Julliere, M. (1975) Tunneling between ferromagnetic films. *Phys. Lett. A*, **54** (3), 225.

2 Moodera, J.S., Kinder, L.R., Wong, T.M., and Meservey, R. (1995) Large magnetoresistance at room temperature

in ferromagnetic thin film tunnel junctions. *Phys. Rev. Lett.*, **74** (16), 3273.
3 Wolf, S.A., Awschalom, D.D., Buhrman, R.A., Daughton, J.M., von Molnar, S., Roukes, M.L., Chtchelkanova, A.Y., and Treger, D.M. (2001) Spintronics: a spin-based electronics vision for the future. *Science*, **294** (5546), 1488.
4 Dediu, V.A., Hueso, L.E., Bergenti, I., and Taliani, C. (2009) Spin routes in organic semiconductors. *Nat. Mater.*, **8** (9), 707.
5 Francis, T.L., Mermer, O., Veeraraghavan, G., and Wohlgenannt, M. (2004) Large magnetoresistance at room temperature in semiconducting polymer sandwich devices. *New J. Phys.*, **6**, 185.
6 Prigodin, V.N., Bergeson, J.D., Lincoln, D. M., and Epstein, A.J. (2006) Anomalous room temperature magnetoresistance in organic semiconductors. *Synth. Met.*, **156** (9–10), 757.
7 Hu, B. and Wu, Y. (2007) Tuning magnetoresistance between positive and negative values in organic semiconductors. *Nat. Mater.*, **6** (12), 985.
8 Bloom, F.L., Wagemans, W., Kemerink, M., and Koopmans, B. (2007) Separating positive and negative magnetoresistance in organic semiconductor devices. *Phys. Rev. Lett.*, **99** (25), 257201.
9 Frankevich, E.L., Lymarev, A.A., Sokolik, I., Karasz, F.E., Blumstengel, S., Baughman, R.H., and Horhold, H.H. (1992) Polaron-pair generation in poly (phenylene vinylenes). *Phys. Rev. B*, **46** (15), 9320.
10 Kalinowski, J., Cocchi, M., Virgili, D., Di Marco, P., and Fattori, V. (2003) Magnetic field effects on emission and current in Alq_3-based electroluminescent diodes. *Chem. Phys. Lett.*, **380** (5–6), 710.
11 Desai, P., Shakya, P., Kreouzis, T., Gillin, W.P., Morley, N.A., and Gibbs, M.R.J. (2007) Magnetoresistance and efficiency measurements of Alq_3-based OLEDs. *Phys. Rev. B*, **75** (9), 094423.
12 Bobbert, P.A., Nguyen, T.D., van Oost, F. W.A., Koopmans, B., and Wohlgenannt, M. (2007) Bipolaron mechanism for organic magnetoresistance. *Phys. Rev. Lett.*, **99** (21), 216801.
13 Mermer, O., Veeraraghavan, G., Francis, T.L., Sheng, Y., Nguyen, D.T., Wohlgenannt, M., Kohler, A., Al-Suti, M. K., and Khan, M.S. (2005) Large magnetoresistance in nonmagnetic π-conjugated semiconductor thin film devices. *Phys. Rev. B*, **72** (20), 205202.
14 Nguyen, T.D., Sheng, Y., Wohlgenannt, M., and Anthopoulos, T.D. (2007) On the role of hydrogen in organic magnetoresistance: a study of C_{60} devices. *Synth. Met.*, **157** (22–23), 930.
15 Zhang, D., Norris, J.R., Krusic, P.J., Wasserman, E., Chen, C.C., and Lieber, C. M. (1993) Time-resolved EPR and Fourier-transform EPR study of triplet C_{60} determinations of T1 and the C_{13} hyperfine coupling constant. *J. Phys. Chem.*, **97** (22), 5886.
16 Nguyen, T.D., Sheng, Y.G., Rybicki, J., Veeraraghavan, G., and Wohlgenannt, M. (2007) Magnetoresistance in π-conjugated organic sandwich devices with varying hyperfine and spin–orbit coupling strengths, and varying dopant concentrations. *J. Mater. Chem.*, **17** (19), 1995.
17 Sheng, Y., Nguyen, T.D., Veeraraghavan, G., Mermer, O., and Wohlgenannt, M. (2007) Effect of spin–orbit coupling on magnetoresistance in organic semiconductors. *Phys. Rev. B*, **75** (3), 035202.
18 Wang, F.J., Bassler, H., and Vardeny, Z.V. (2008) Magnetic field effects in π-conjugated polymer–fullerene blends: evidence for multiple components. *Phys. Rev. Lett.*, **101** (23), 236805.
19 Min, H., Hill, J.E., Sinitsyn, N.A., Sahu, B. R., Kleinman, L., and MacDonald, A.H. (2006) Intrinsic and Rashba spin–orbit interactions in graphene sheets. *Phys. Rev. B*, **74** (16), **165**, 310.
20 Pramanik, S., Stefanita, C.G., Patibandla, S., Bandyopadhyay, S., Garre, K., Harth, N., and Cahay, M. (2007) Observation of extremely long spin relaxation times in an organic nanowire spin valve. *Nat. Nanotechnol.*, **2** (4), 216.
21 Burrows, H.D., de Melo, J.S., Serpa, C., Arnaut, L.G., Miguel, M.D., Monkman, A. P., Hamblett, I., and Navaratnam, S. (2002) Triplet state dynamics on isolated conjugated polymer chains. *Chem. Phys.*, **285** (1), 3.

22 Beljonne, D., Shuai, Z., Pourtois, G., and Bredas, J.L. (2001) Spin–orbit coupling and intersystem crossing in conjugated polymers: a configuration interaction description. *J. Phys. Chem. A*, **105** (15), 3899.

23 Rybicki, J. and Wohlgenannt, M. (2009) Spin–orbit coupling in singly charged π-conjugated polymers. *Phys. Rev. B*, **79** (15), 153202.

24 Wohlgenannt, M., Jiang, X.M., and Vardeny, Z.V. (2004) Confined and delocalized polarons in π-conjugated oligomers and polymers: a study of the effective conjugation length. *Phys. Rev. B*, **69** (24), 241204.

25 Heeger, A.J., Kivelson, S., Schrieffer, J.R., and Su, W.P. (1988) Solitons in conducting polymers. *Rev. Mod. Phys.*, **60** (3), 781.

26 Dyakonov, M.I. and Perel, V.I. (1971) Spin relaxation of conduction electrons in noncentrosymmetric semiconductors. *Sov. Phys. Solid State*, **13**, 3023.

27 Zutic, I., Fabian, J., and Das Sarma, S. (2004) Spintronics: fundamentals and applications. *Rev. Mod. Phys.*, **76** (2), 323.

28 Rocha, A.R., Garcia-Suarez, V.M., Bailey, S.W., Lambert, C.J., Ferrer, J., and Sanvito, S. (2005) Towards molecular spintronics. *Nat. Mater.*, **4** (4), 335.

29 Dediu, V., Murgia, M., Matacotta, F.C., Taliani, C., and Barbanera, S. (2002) Room temperature spin polarized injection in organic semiconductor. *Solid State Commun.*, **122** (3–4), 181.

30 Xiong, Z.H., Wu, D., Vardeny, Z.V., and Shi, J. (2004) Giant magnetoresistance in organic spin valves. *Nature*, **427** (6977), 821.

31 Majumdar, S., Laiho, R., Laukkanen, P., Vayrynen, I.J., Majumdar, H.S., and Osterbacka, R. (2006) Application of regioregular polythiophene in spintronic devices: effect of interface. *Appl. Phys. Lett.*, **89** (12), 122114.

32 Petta, J.R., Slater, S.K., and Ralph, D.C. (2004) Spin-dependent transport in molecular tunnel junctions. *Phys. Rev. Lett.*, **93** (13), 136601.

33 Drew, A.J., Hoppler, J., Schulz, L., Pratt, F. L., Desai, P., Shakya, P., Kreouzis, T., Gillin, W.P., Suter, A., Morley, N.A., Malik, V.K., Dubroka, A., Kim, K.W., Bouyanfif, H., Bourqui, F., Bernhard, C., Scheuermann, R., Nieuwenhuys, G.J., Prokscha, T., and Morenzoni, E. (2009) Direct measurement of the electronic spin diffusion length in a fully functional organic spin valve by low-energy muon spin rotation. *Nat. Mater.*, **8** (2), 109.

34 Wang, F.J., Yang, C.G., Vardeny, Z.V., and Li, X.G. (2007) Spin response in organic spin valves based on la2/3sr1/3mno3 electrodes. *Phys. Rev. B*, **75** (24), **245**, 324.

35 Dediu, V., Hueso, L.E., Bergenti, I., Riminucci, A., Borgatti, F., Graziosi, P., Newby, C., Casoli, F., De Jong, M.P., Taliani, C., and Zhan, Y. (2008) Room-temperature spintronic effects in Alq_3-based hybrid devices. *Phys. Rev. B*, **78** (11), 115203.

36 Yoo, J.W., Chen, C.Y., Jang, H.W., Bark, C. W., Prigodin, V.N., Eom, C.B., and Epstein, A.J. (2010) Spin injection/detection using an organic-based magnetic semiconductor. *Nat. Mater.*, **9** (8), 638.

37 Santos, T.S., Lee, J.S., Migdal, P., Lekshmi, I.C., Satpati, B., and Moodera, J. S. (2007) Room-temperature tunnel magnetoresistance and spin-polarized tunneling through an organic semiconductor barrier. *Phys. Rev. Lett.*, **98** (1), 016601.

38 Shim, J.H., Raman, K.V., Park, Y.J., Santos, T.S., Miao, G.X., Satpati, B., and Moodera, J.S. (2008) Large spin diffusion length in an amorphous organic semiconductor. *Phys. Rev. Lett.*, **100** (22), 226603.

39 Bobbert, P.A., Wagemans, W., van Oost, F. W.A., Koopmans, B., and Wohlgenannt, M. (2009) Theory for spin diffusion in disordered organic semiconductors. *Phys. Rev. Lett.*, **102** (15), 156604.

40 Schulten, K. and Wolynes, P.G. (1978) Semi-classical description of electron-spin motion in radicals including effect of electron hopping. *J. Chem. Phys.*, **68** (7), 3292.

41 Bassler, H. (1993) Charge transport in disordered organic photoconductors: a Monte Carlo simulation study. *Phys. Status Solidi B*, **175** (1), 15.

42 Pasveer, W.F., Cottaar, J., Tanase, C., Coehoorn, R., Bobbert, P.A., Blom, P.W. M., de Leeuw, D.M., and Michels, M.A.J. (2005) Unified description of charge-carrier mobilities in disordered semiconducting polymers. *Phys. Rev. Lett.*, **94** (20), 206601.

43 Nagata, Y. and Lennartz, C. (2008) Atomistic simulation on charge mobility of amorphous tris(8-hydroxyquinoline) aluminum (Alq_3): origin of Poole-Frenkel-type behavior. *J. Chem. Phys.*, **129** (3), 034709.

44 Schmidt, G., Ferrand, D., Molenkamp, L. W., Filip, A.T., and van Wees, B.J. (2000) Fundamental obstacle for electrical spin injection from a ferromagnetic metal into a diffusive semiconductor. *Phys. Rev. B*, **62** (8), R4790.

45 Naber, W.J.M., Faez, S., and van der Wiel, W.G. (2007) Organic spintronics. *J. Phys. D Appl. Phys.*, **40** (12), R205.

46 Burrows, P.E. and Forrest, S.R. (1994) Electroluminescence from trap-limited current transport in vacuum-deposited organic light-emitting devices. *Appl. Phys. Lett.*, **64** (17), 2285.

47 Butler, W.H., Zhang, X.G., Schulthess, T. C., and MacLaren, J.M. (2001) Spin-dependent tunneling conductance of *Fe*/|MgO/||Fe sandwiches. *Phys. Rev. B*, **63** (5), 054416.

48 Lin, R., Wang, F., Rybicki, J., Wohlgenannt, M., and Hutchinson, K.A. (2010) Distinguishing between tunneling and injection regimes of ferromagnet/organic semiconductor/ferromagnet junctions. *Phys. Rev. B*, **81** (19), 195214.

49 Yoo, J.W., Jang, H.W., Prigodin, V.N., Kao, C., Eom, C.B., and Epstein, A.J. (2009) Giant magnetoresistance in ferromagnet/organic semiconductor/ferromagnet heterojunctions. *Phys. Rev. B*, **80** (20), 205207.

50 Datta, S. and Das, B. (1990) Electronic analog of the electrooptic modulator. *Appl. Phys. Lett.*, **56** (7), 665.

51 Fiederling, R., Keim, M., Reuscher, G., Ossau, W., Schmidt, G., Waag, A., and Molenkamp, L.W. (1999) Injection and detection of a spin-polarized current in a light-emitting diode. *Nature*, **402** (6763), 787.

52 Vardeny, Z.V. (2009) Spintronics organics strike back. *Nat. Mater.*, **8** (2), 91.

53 Cinchetti, M., Heimer, K., Wustenberg, J. P., Andreyev, O., Bauer, M., Lach, S., Ziegler, C., Gao, Y.L., and Aeschlimann, M. (2009) Determination of spin injection and transport in a ferromagnet/organic semiconductor heterojunction by two-photon photoemission. *Nat. Mater.*, **8** (2), 115.

54 Blom, P.W.M. and Vissenberg, M. (2000) Charge transport in poly(*p*-phenylene vinylene) light-emitting diodes. *Mater. Sci. Eng. R Rep.*, **27** (3–4), 53.

55 Liu, Y., Watson, S.M., Lee, T., Gorham, J. M., Katz, H.E., Borchers, J.A., Fairbrother, H.D., and Reich, D.H. (2009) Correlation between microstructure and magnetotransport in organic semiconductor spin-valve structures. *Phys. Rev. B*, **79** (7), 075312.

56 Rashba, E.I. (2000) Theory of electrical spin injection: tunnel contacts as a solution of the conductivity mismatch problem. *Phys. Rev. B*, **62** (24), R16267.

57 Fert, A. and Jaffres, H. (2001) Conditions for efficient spin injection from a ferromagnetic metal into a semiconductor. *Phys. Rev. B*, **64** (18), 184420.

58 Ruden, P.P. and Smith, D.L. (2004) Theory of spin injection into conjugated organic semiconductors. *J. Appl. Phys.*, **95** (9), 4898.

59 Ren, J.F., Fu, J.Y., Liu, D.S., Mei, L.M., and Xie, S.J. (2005) Diffusion theory of spin injection into organic polymers. *J. Phys. Condens. Matter*, **17** (15), 2341.

Part Three
Photophysics

Physics of Organic Semiconductors, Second Edition. Edited by Wolfgang Brütting and Chihaya Adachi

10
Excitons at Polymer Interfaces

Neil Greenham

10.1
Introduction

Many of the interesting processes occurring in polymer electronic devices take place at interfaces between different materials. These include charge injection and extraction at electrodes, charge generation and recombination in photovoltaics, and exciton (energy) transfer in both LEDs and photovoltaics. Even the most basic process of charge transport involves *inter*molecular hopping between sites, and often this happens close to the interface with another material (e.g., the dielectric in a polymer transistor). These intermolecular processes are frequently challenging to model theoretically and to measure experimentally. Although crucial in determining device performance, the regions close to the interface often comprise only a small fraction of the total volume, and the optoelectronic transitions associated directly with the interface are always much weaker than those occurring within a single polymer chain.

The importance of interfaces is not unique to organic semiconductors. However, molecular semiconductors, and polymer semiconductors in particular, bring some unique advantages in studying interfacial processes. At the free surface of an inorganic semiconductor, there is inevitably a plane of dangling bonds, sometimes accompanied by a surface reconstruction of the crystal structure. This fundamentally alters the electronic structure, producing new electronic states within the bandgap that dominate the observed properties. Although clean heterojunctions can be fabricated between different inorganic semiconductors, for example by molecular beam epitaxy, there are severe constraints on the chemical and crystal structures, lattice constants, and deposition methods if defect-free interfaces are to be achieved. The surface of a polymer semiconductor is fundamentally different in character, since no bonds are broken to form the surface. Furthermore, there is no requirement for an adjacent material to share the same chemical or structural properties. Hence, rather than looking at the interface and its electronic structure as a completely new entity, it is possible to understand how interfacial processes occur starting from a simple combination of what remain "bulk-like" materials on either

Physics of Organic Semiconductors, Second Edition. Edited by Wolfgang Brütting and Chihaya Adachi

side of the interface. The details of these processes, which form the basis of this chapter, are subtle and interesting, but can be set within a framework based on the well-established properties of the individual semiconductors. The lack of broken bonds at interfaces allows polymer heterojunctions to be fabricated very easily by deposition of films from a solution containing two polymers.

This chapter will examine the electronic processes occurring at interfaces between conjugated polymers, particularly concentrating on the processes of energy transfer, charge transfer, charge separation, and recombination that are important in light-emitting diodes and photovoltaics. Understanding the operation of polymer photovoltaic devices is an important goal, since it should allow further improvement in device efficiencies. In these devices, light is absorbed to generate excitons, and these excitons diffuse to an interface with a second material where charge transfer takes place. The state formed after charge transfer must then be dissociated into free charges that are transported to and collected at the electrodes. For efficient device operation, all these processes must take place without losses of excited states to recombination, and without unnecessary losses in energy of the excited states between generation and collection. Here, we will focus on the interfacial processes that are important in the early stages of device operation; the later processes of charge separation and transport are discussed in more detail elsewhere in this volume (Chapter 17). The majority of work on polymer photovoltaics uses fullerene derivatives as the electron acceptor, since these devices at present give the highest efficiencies [1]. In this chapter, most of the examples are taken specifically from polymer:polymer interfaces, although much of the physics applies in a similar manner to both systems. Polymer:fullerene devices are discussed in more detail in Chapter 17. The chemical structures and names of the polymers discussed in this chapter are summarized in Table 10.1.

10.2
Fabrication and Structural Characterization of Polymer Heterojunctions

Films of conjugated polymers are typically deposited from solution using spin-coating or printing techniques, but since most commonly used materials are soluble in the same (nonpolar) solvents it is difficult to fabricate simple "bilayer" heterojunctions by successive deposition since the bottom layer will dissolve while the top layer is being deposited. This is very different from the situation in small-molecule semiconductors, where highly complex multilayer structures can easily be fabricated by vacuum sublimation [2]. Nevertheless, various techniques can be used to form polymer bilayers. Some polymers can be found with orthogonal solubilities, for example, the materials used by Greenham *et al*. in 1993 to fabricate the first conjugated polymer bilayer LED [3]. Here, the bottom, hole-transporting, layer was unsubstituted poly(*p*-phenylenevinylene) [PPV] processed via a precursor route. After conversion to the final material, it was completely insoluble, allowing the top layer of CN-PPV to be spin-coated directly from chloroform (Figure 10.1). Alternatively, cross-linking can be used to render a previously soluble layer insoluble [4],

Table 10.1 Abbreviations, chemical names, and structures of the polymers discussed in this chapter.

Abbreviation	Chemical name	Structure
PPV	Poly(*p*-phenylenevinylene)	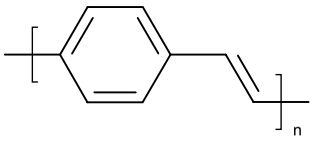
CN-PPV	Poly(2,5-di(hexyloxy)cyanoterephthalylidene)	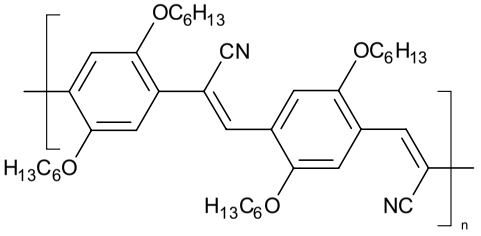
PFB	poly(9,9-dioctylfluorene-*co*-bis-*N*,*N*-(4-butylphenyl)-bis-*N*,*N*-phenyl-1,4-phenylenediamine)	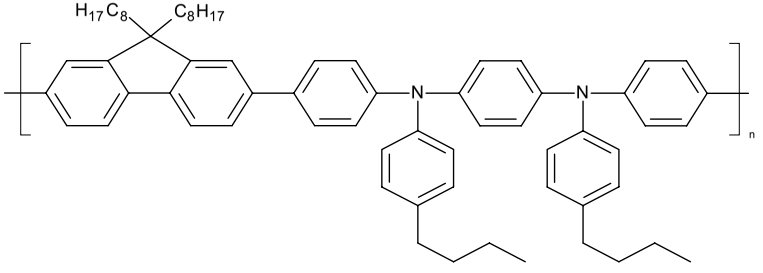

(*continued*)

Table 10.1 (*Continued*)

Abbreviation	Chemical name	Structure
TFB	poly(9,9-dioctylfluorene-*co*-*N*-(4-butylphenyl)diphenylamine)	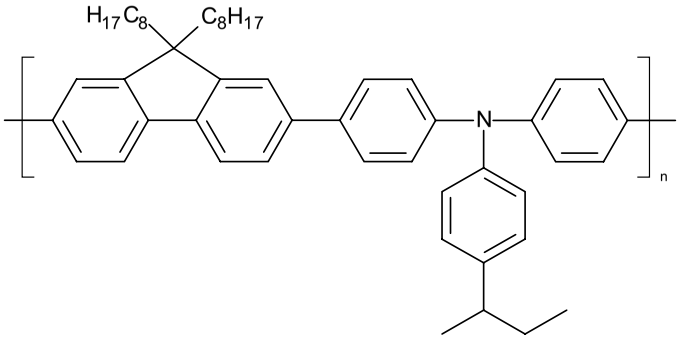
F8BT	poly(9,9-dioctylfluorene-*co*-benzothiadiazole)	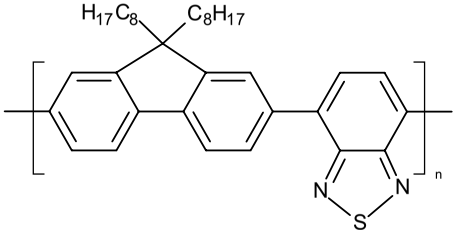

Poly(*p*-phenylene) ladder polymer (generic structure)		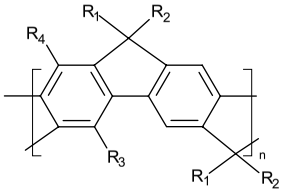
MEH-PPV	Poly(2-methoxy-(2′-ethyl)-5-hexyloxy-*p*-pheneylenevinylene)	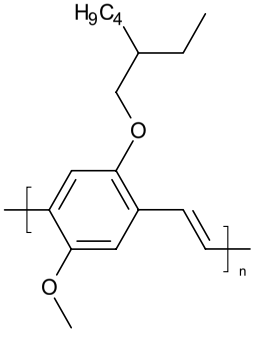
P3HT	Poly(3-alkylthiophene)	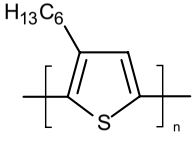
F8TBT	Poly((9,9-dioctylfluorene)-2,7-diyl-*alt*-[4,7-bis(3-hexylthien-5-yl)-2,1,3-benzothiadiazole]-2′,2″-diyl)	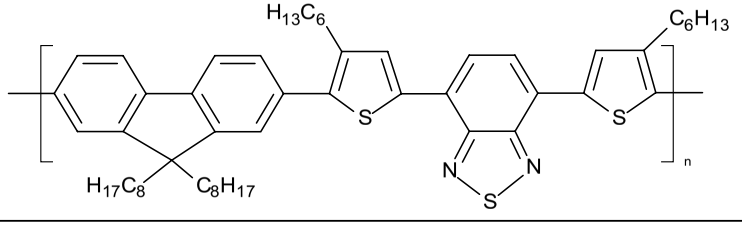

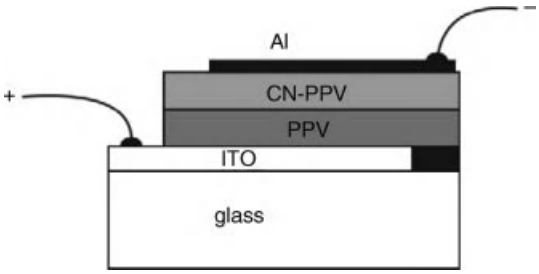

Figure 10.1 Structure of a polymer LED based on a bilayer of PPV and CN-PPV.

although this requires specially modified polymers. Ho and coworkers have used cross-linkers that operate on the alkyl chains of unmodified polymers [5], allowing efficient polyfluorene-based bilayer LEDs to be fabricated. For some polymers on appropriate substrates, annealing forms a thin insoluble layer next to the substrate, onto which a second material can be deposited after rinsing away the initial soluble material. This approach has been used by Kim *et al*. to fabricate bilayer LEDs based on the TFB/F8BT combination [6]. Another way to form bilayers of soluble materials is by lamination, for example by spin coating one material onto a substrate with a water-soluble sacrificial layer and floating off the polymer onto the surface of a water trough [7]. The second material is spin-coated onto a separate substrate and then used to pick up the first polymer layer from the water surface. Embossing and imprint lithography methods can also be used, which allow patterning of the interface. For example, imprinting in the presence of solvent vapor allows modest pressures to be used for imprinting at room temperatures. Interdigitated polymer:polymer structures with feature sizes as small as 50 nm can be fabricated by this method, using a first imprinted polymer layer as a stamp to protrude into a second layer (Figure 10.2) [8]. Although these methods based on lamination are unlikely to be practical for large-scale manufacture, the fact that the resulting structures show clean device characteristics is testament to the robustness of polymer surfaces under ambient or aqueous conditions.

Characterizing the physical structure of the interface in a polymer:polymer bilayer is far from straightforward, since the buried interface is not accessible to the usual techniques of surface science such as photoelectron spectroscopy and scanning probe microscopy. Although roughnesses of <1 nm are easy to achieve at the surface of an individual polymer layer, it is important to understand the degree of intermixing that occurs when a bilayer is formed, particularly when the sample is subsequently annealed. One technique that can be applied to gain more detailed information is resonant soft X-ray reflectivity. This synchrotron-based technique observes the interference pattern formed by the reflection of X-rays from different planar interfaces in a multilayer film. Normally, the X-ray refractive index contrast between different polymers is very small, so it is necessary to tune the X-ray energy close to a resonance (in the soft X-ray region) in order to achieve a significant reflection from the buried interface. Changes in the sharpness of this interface can then

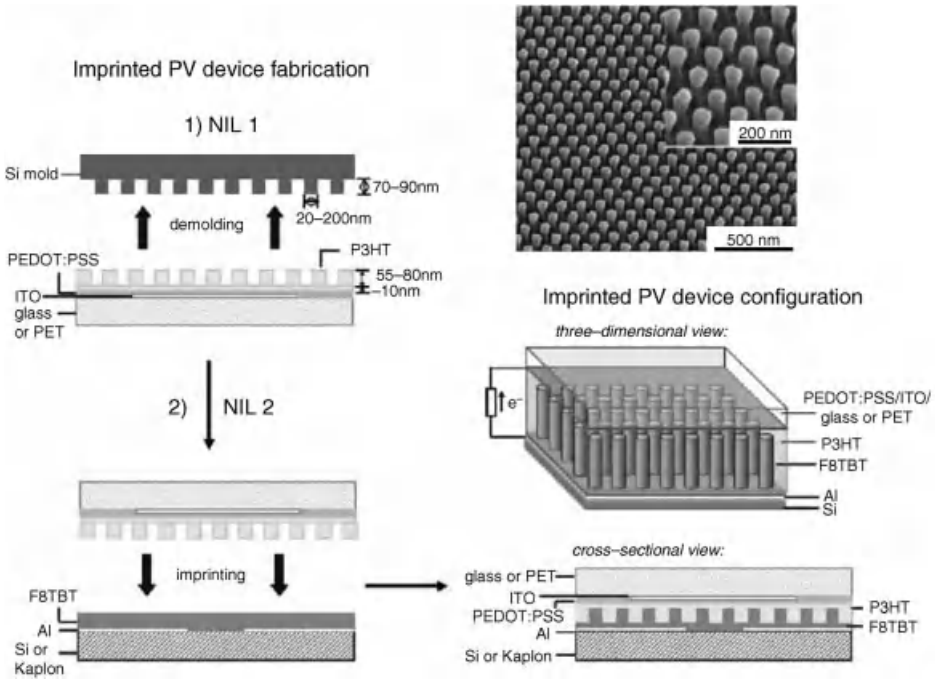

Figure 10.2 Formation of a nanostructured polymer photovoltaic device based on P3HT and F8TBT by the process of solvent-assisted nanoimprint lithography. A scanning electron micrograph of an imprinted film of P3HT is also shown. Reproduced from Ref. [8]. © 2010 American Chemical Society.

be observed as a change in the visibility of the interference fringes. This technique was recently applied by Yan *et al*. to bilayers of PFB and F8BT fabricated by the "float-off" method described above [9]. On annealing, the interface was found to roughen, with the characteristic interfacial width increasing from 1.6 nm for unannealed films to 15 nm after annealing at 180 °C for 10 min (Figure 10.3). In a photovoltaic device based on these bilayers, the intermixing allowed excitons to be harvested from a larger fraction of the film, but was found to constrain the process of charge-carrier separation at the interface (see Section 10.8).

A particularly important way in which large quantities of polymer:polymer interface can be formed is in polymer blends, where two polymers are mixed in solution and codeposited from a common solvent [10]. In donor–acceptor (D–A) blends for photovoltaics [11, 12], this structure is known as a "bulk heterojunction." Due to their low entropy of mixing, polymers tend to phase separate into relatively pure phases. For spin-coated or printed blends, the structure becomes frozen during the phase separation process when the solvent has evaporated to the extent that the mobility of the polymers becomes negligible. Rapid processing, therefore, leads to fine blends with close to a molecular scale of intermixing, whereas slower processing (e.g., using high-boiling-point solvents) can lead to the formation of much

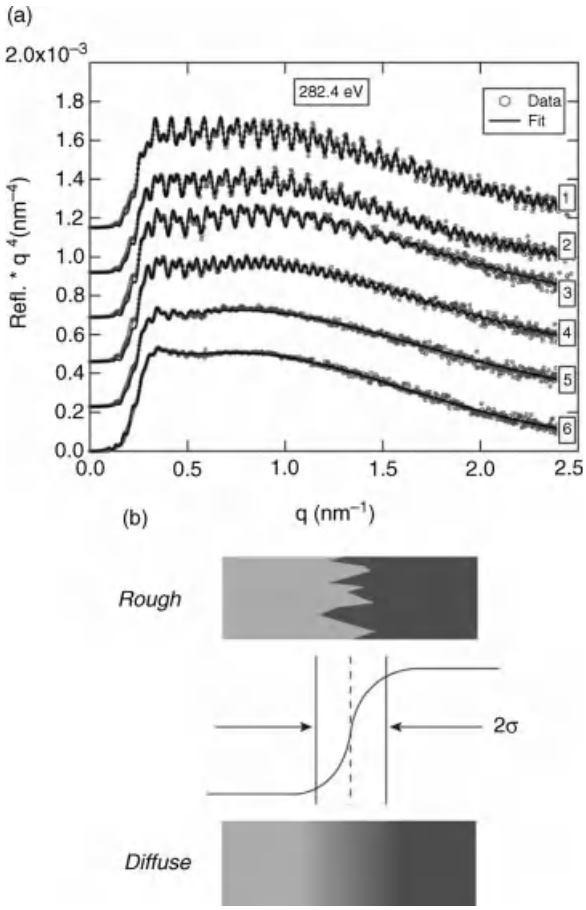

Figure 10.3 (a) X-ray reflectivity at 282.4 eV as a function of scattering vector for F8BT/PFB bilayers annealed at temperatures of (1) as-prepared, (2) 100 °C, (3) 120 °C, (4) 140 °C, (5) 160 °C, and (6) 200 °C. (b) Schematic showing rough or diffuse interfaces leading to loss of fringe contrast. Reproduced from Ref. [9], © 2010 Wiley-VCH.

larger domains with feature sizes up to hundreds of microns, often with a complex hierarchical structure [13]. The blend structure can be evolved by thermal annealing [14] or solvent vapor annealing [15], and the initial structure can be influenced not only by the choice of solvent but also by the processing conditions and the use of solvent additives [16, 17]. The large-scale structure of polymer blends can be characterized using optical techniques such as luminescence microscopy and Raman microscopy [18], with scanning near-field optical microscopy allowing the resolution to be reduced below the diffraction limit [19]. X-ray microscopy (based on contrast in the near-edge X-ray absorption fine structure (NEXAFS)) allows chemical resolution (averaged through the film thickness) to be determined on length scales below 50 nm [20, 21]. Transmission electron microscopy is often used

to characterize bulk heterojunction films [22], although it is typically difficult to achieve contrast between different conjugated polymers, requiring staining [11] or energy filtering [23] to be used to obtain high-quality images. Scanning probe techniques such as AFM are routinely applied to image the surface topography and composition; this gives useful information about the form of phase separation [13]; however, the surface composition can sometimes differ from that of the bulk [24, 25]. Scattering and diffraction techniques including light scattering [26], X-ray diffraction [27], and (for blends containing a deuterated component) neutron scattering [24, 28] are all useful for investigating blend structures, but relating them directly to real-space structure is not straightforward. In general, to obtain full three-dimensional information is difficult, but recent advances in transmission electron tomography have provided important progress [29].

The processing and structural characterization of conjugated polymer blends is a complex area, and is reviewed in detail in Ref. [10]. Our focus here is more on the microscopic properties of electronic states formed at polymer interfaces, and at the relevant molecular and intermolecular length scales most of the imaging techniques mentioned above fail. For sufficiently crystalline materials, X-ray diffraction can provide some information about the details of intermolecular packing (at least for the crystalline regions of a sample) [30], but for mixed systems it is only when the two components form a particularly well-ordered structure that diffraction techniques provide useful information about the intermolecular structure [31]. Therefore, it is necessary to use spectroscopic methods to *infer* information about the intermolecular interactions at the microscopic scale.

10.3
Electronic Structure at Polymer/Polymer Interfaces

Two distinct types of interfacial processes are of interest in device operation. In an LED, it is often desirable to tune the emission spectrum, for example to obtain white emission for lighting applications. One way to achieve this is to add small amounts of red- and green-emitting "dopant" materials into a blue-emitting "host." Excitons formed in the high-energy host, if they come into the vicinity of a dopant, can transfer their energy to that lower-energy dopant, where they can emit. By tuning the concentration and type of dopant, it is possible to fine-tune the emission color. In a photovoltaic device, the desired process is for an exciton arriving at an interface to dissociate into a charge transfer state, with the electron predominantly localized on one material (the acceptor), and the hole localized on the other (the donor). This state can then be further dissociated into free charges, which are ultimately collected at the electrodes.

To distinguish between these two processes, energy transfer and charge transfer, it is helpful to consider the alignment of highest occupied molecular orbital (HOMO) and lowest unoccupied molecular orbital (LUMO) levels shown in Figure 10.4. In the absence of coulombic interactions between the electron and the hole, it is clear that a type-I (nested) structure will lead to energy transfer (from

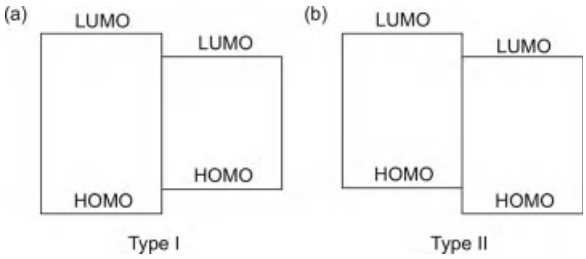

Figure 10.4 Energies (vertical scale) of highest unoccupied molecular orbital and lowest unoccupied molecular orbitals at (a) type-I and (b) type-II semiconductor heterointerfaces.

high-gap to low-gap material), whereas a type-II (staggered or offset) structure will lead to charge transfer. In reality, electron–hole interactions are strong in organic materials, with coulombic binding energies of several tenths of an eV both in the intramolecular neutral exciton and in the charge transfer state. Hence, it is better to consider the outcome in terms of the total energies of the various neutral and charge-transfer states. Provided that fast competing processes do not occur at earlier stages, the lowest energy state is the one that will eventually be produced. Charge transfer will, therefore, occur when the charge-transfer state is lower in energy than neutral excitonic states on either material. In terms of the single-particle energy diagrams in Figure 10.4, this can be expressed as requiring HOMO and LUMO offsets that are both larger than the difference in coulombic binding energy between the exciton and the charge-transfer states [32]. Where the two materials (A and D) have different energy gaps (here we consider $E_A > E_D$), the charge transfer state can be formed by a number of different routes as shown in Figure 10.5: (i) excitation of D followed by electron transfer to A, (ii) excitation of A followed by hole transfer to D, (iii) excitation of A followed by energy transfer to D followed by electron transfer to A .

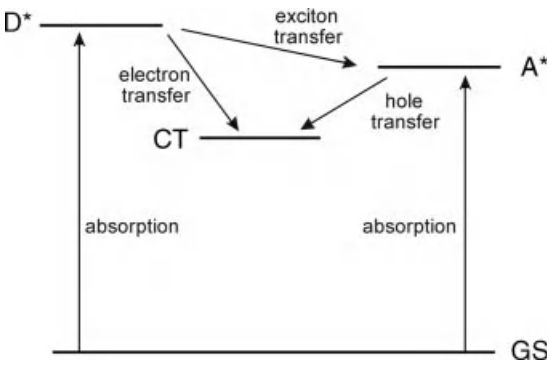

Figure 10.5 Pathways for CT state formation after photoexcitation of a donor–acceptor (D–A) system where the bandgap of D is larger than the bandgap of A.

The energy levels shown in diagrams such as Figure 10.4 should be treated with a good deal of caution. Typically, the HOMO levels are measured either by cyclic voltammetry or by ultraviolet photoelectron spectroscopy (UPS). Since UPS measures unrelaxed states and cyclic voltammetry measures the energy of relaxed states, the values should not necessarily match, and there is debate about the magnitude of these polaronic effects [33, 34]. Furthermore, the environment of the final charged state is very different in an electrochemical cell surrounded by electrolyte from that inside a device, which could significantly affect the energy. Determining the LUMO levels adds further complications – sometimes these can be measured directly as a reduction peak in cyclic voltammetry, and very occasionally inverse photoelectron spectroscopy is applied to find the LUMO level [35]. But more usually, they are estimated from the HOMO level and the optical bandgap, adding further uncertainties due to relaxation and coulombic effects. Even if the energy levels of the individual materials are perfectly known, ground-state interactions when the two materials are placed in contact can, in principle, change the offsets at the interface [36, 37]. This "vacuum-level shift" is generally thought to be small, but is difficult to measure directly in polymer/polymer systems. At interfaces between small-molecule layers, where these effects can be more easily measured by *in situ* deposition during a UPS experiment, offsets in the range of 0–0.5eV have been reported [36].

10.4 Excitons at Homointerfaces

Before considering processes at interfaces between different materials, we first review the intermolecular excitonic processes occurring within a single material. These processes are important since, for example, they determine how excitons are transported to a heterojunction. The properties of excitons in ordered organic systems such as molecular crystals are treated in great detail in a number of books, for example, those by Pope and Swenberg [38], and Schwoerer and Wolf [39], so we will only briefly review them here.

For the simple situation of two identical interacting molecules (a dimer), with an interaction Hamiltonian V_{12}, the excited states will be linear superpositions of the excited state wavefunctions of the individual molecules ϕ_1 and ϕ_2

$$\Phi^*_{\pm} = \frac{1}{\sqrt{2}}\left(\phi_1\phi_2^* \pm \phi_1^*\phi_2\right)$$

with energies $E^*_{\pm} = E^* + D' \pm J_{12}$, where E^* is the energy of the excited state of an individual molecule, $D' = \langle \phi_1^*\phi_2 | V_{12} | \phi_1^*\phi_2 \rangle = \langle \phi_1\phi_2^* | V_{12} | \phi_1\phi_2^* \rangle$, and $J_{12} = \langle \phi_1^*\phi_2 | V_{12} | \phi_1\phi_2^* \rangle$. The splitting of the states, by an energy $2J_{12}$, is known as Davydov splitting. For parallel molecules, the optical transition from the ground state and one of the new excited states is forbidden, and the other allowed. Where the molecules are side-by-side, it is the lower energy transition that is forbidden, so the observed optical absorption is blueshifted. After absorption to the higher

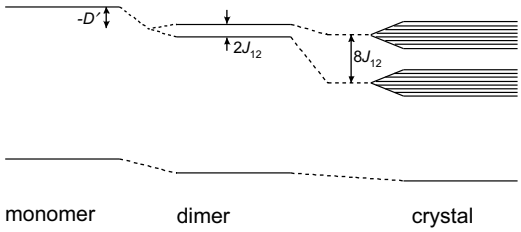

Figure 10.6 Splitting of exciton states on formation of dimers and crystals in a molecular semiconductor. D' and J_{12} are defined in the text.

energy state, interaction with the environment will typically lead the system to relax to the lower energy, forbidden, state, so the luminescence will be redshifted and slow. In the presence of competing nonradiative processes, it is therefore likely to have a low efficiency of emission.

In the solid state, each molecule can interact with more than one neighbor, so the Davydov splitting must be summed over more than one interacting molecule, typically over the nearest neighbors. Furthermore, for an extended, crystalline system in the absence of disorder and vibrational coupling, the exciton can, in principle, form a coherent superposition over all the molecules in the system, leading to the formation of a band of energy states, each labeled by the exciton momentum $\hbar\mathbf{k}$. In that case, Davydov splitting occurs due to interactions with translationally inequivalent neighboring molecules, followed by additional splitting due to band formation (Figure 10.6). Only the states close to $k = 0$ are probed in optical absorption.

In practice, for polymer systems, it is rare to achieve the level of intermolecular order required for the formation of exciton bands. It is therefore the direct interactions with near neighbors that are most important when considering intermolecular effects. Even when a conjugated polymer has close π–π stacking between neighboring chains, quantum chemical calculations have shown that intramolecular delocalization of the exciton wave function along the polymer significantly reduces the intermolecular transfer integral J_{12} compared to small molecular systems [40].

A region of a conjugated polymer film where intermolecular interactions play an important role in the photophysics is generally known as an *aggregate*. Given that most conjugated polymers have a rather low degree of structural order, aggregates typically comprise only a small fraction of the total film, and hence are difficult to detect in absorption measurements. The high-energy transition is buried under the nonaggregate absorption and the low-energy transition usually has low oscillator strength. (In the case of side-by-side parallel chromophores, an H-aggregate, it is formally forbidden but may be partially allowed if the alignment is not perfect.) An easier way to detect the presence of aggregates is to look for a redshifted emission (compared to solution measurements). Since excitations can migrate to low-energy sites, even a small concentration of aggregates can dominate the emission. Low-energy emission due to aggregates is seen in films of CN-PPV [41], MEH-PPV

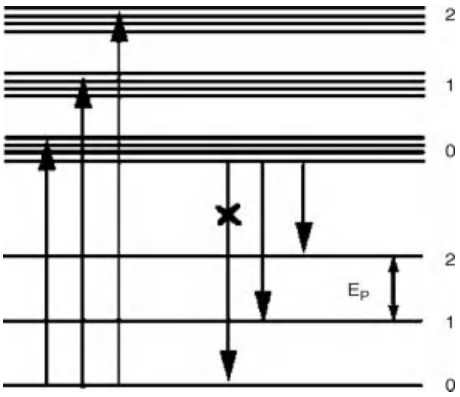

Figure 10.7 Absorption and emission processes in P3HT aggregates. 0, 1, 2 represent the respective vibrational levels of the ground and excited states. Reproduced with permission from Ref. [45]. © 2007 American Physical Society.

[42, 43], and ladder poly(phenylene)s [44]. In addition to being redshifted, aggregate emission is usually broad, and has a longer radiative lifetime than intrachain exciton emission.

A particularly clear example of the role of intermolecular interactions in conjugated polymer films is given by regioregular poly(3-hexylthiophene) [45]. With appropriate processing, this polymer π-stacks in a two-dimensional lamellar structure with a π–π spacing of 3.8 Å [30, 46]. The intermolecular transfer integral is small compared to the energy of the dominant vibrational mode that couples to the absorption and emission, so the splitting due to intermolecular effects can be considered to apply separately to each vibrational level, giving an energy-level structure as shown in Figure 10.7. In this H-aggregate structure, the allowed optical transitions are to the top of the bands associated with each of the vibrational states. Furthermore, intermolecular coupling reduces the strength of the 0–0 absorption peak (A_{0-0}) compared to the 0–1 absorption (A_{0-1}). The ratio of these peaks can be used to estimate the width of the exciton band, W, where $W = 4J$. For a Huang–Rhys parameter of 1, the peak ratio is given by

$$\frac{A_{0-0}}{A_{0-1}} \approx \frac{n_{0-1}}{n_{0-0}} \left(\frac{1 - 0.24W/E_p}{1 + 0.073W/E_p} \right)^2,$$

where n represents the refractive index at the respective wavelength, and E_p is the energy of the dominant vibrational energy. Looking at the measured absorption data (Figure 10.8), the 0–0 absorption peak is found to be stronger in samples with a higher degree of microstructural order. For example, the value of W for a film processed from isodurene (which evaporates slowly) is found to be ∼20 meV, whereas for films processed from chloroform (which evaporates quickly and gives a more disordered structure), it is found to be ∼120 meV. This behavior is rather

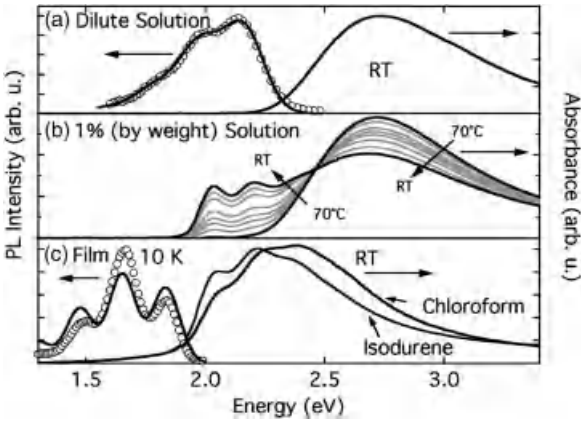

Figure 10.8 Absorption and emission in P3HT. (a) In dilute solution. (b) In 1% solution at various temperatures. (c) In films spun from different solvents (absorption at room temperature, emission at 10 K for films spun from chloroform). Reproduced with permission from Ref. [45]. © 2007 American Physical Society.

counterintuitive since one might expect that improved order would lead to enhanced interchain interactions. In fact, the interchain spacing is relatively insensitive to the processing route; what changes is the degree of intrachain order. In the more ordered sample, the excitons can delocalize over a longer region of polymer chain, and this one-dimensional delocalization reduces the amount of interchain overlap, as demonstrated by quantum chemical calculations [40].

Turning now to the transport of excitons, if we stay within the band picture of exciton processes presented above, it is possible to envisage a coherent band-like motion of excitons within a perfect crystalline structure. In practice, though, for most polymers the intermolecular interactions are sufficiently weak that the exciton can be considered as localized on a single polymer chain. Even when intermolecular interactions are significant, the combination of disorder and vibrational coupling typically leads to a localized exciton that is spread over a small number of molecules. For localized excitons, their transport can be considered as an incoherent hopping process between localized states. For singlet excitons (which are radiatively coupled to the ground state), this can occur via the process of Förster energy transfer [47], a nonradiative transfer mechanism based on near-field dipole–dipole coupling. The rate of this Förster transfer from an energy donor D to an energy acceptor A separated by a distance R is given by

$$k_f = \frac{1}{\tau_D}\frac{1}{R^6}\frac{3f}{4\pi}\int \frac{c^4}{\omega^4 n^4} F_D(\omega)\sigma_A(\omega)d\omega,$$

where τ_D is the radiative lifetime of the donor, f is a factor related to the relative orientation of the two molecules, c is the speed of light, n is the refractive index of the medium, $F_D(\omega)$ is the normalized emission spectrum of the donor, and $\sigma_A(\omega)$ is the acceptor absorption cross section [38]. It can be seen that Förster transfer has

an R^{-6} dependence on distance, and relies on overlap between the emission and the absorption spectra of the donor and acceptor molecules. It therefore generally favors transfer to sites that are lower in energy than the donor site. The treatment above assumes that the exciton can be treated as a point dipole; this is usually a poor assumption in conjugated polymers, where the exciton is delocalized along the chain over a distance that is significantly larger than the intermolecular spacing. A better approximation can be obtained using the distributed monopole method, where the electronic coupling is summed over atomic transition charges [48].

Förster transfer rates can be maximized by choosing a lower energy acceptor with particularly good spectral overlap, but Förster transfer is also important in films of a single material, where the combination of homogeneous and inhomogeneous broadening of emission and absorption spectra allows spectral overlap to occur. The hopping of excitons from site to site within a single material can be thought of as a diffusive process, whereby excitons will typically diffuse over a distance L_D within their lifetime τ. The exciton diffusion length is given by $L_D = \sqrt{D_{ex}\tau}$, where D_{ex} is the diffusion constant for excitons, related to the Förster transfer rates. This length can best be measured in bilayer samples in which polymer films of different thickness are in contact with a nonabsorbing layer where exciton quenching occurs by charge transfer (a short-range process requiring diffusion of excitons to the heterojunction). When the film thickness is comparable to the exciton diffusion length, then most excitons generated in the film will be quenched, and by studying the luminescence efficiency of these structures for films of different thickness it is thus possible to deduce exciton diffusion length (Figure 10.9) [49], although great

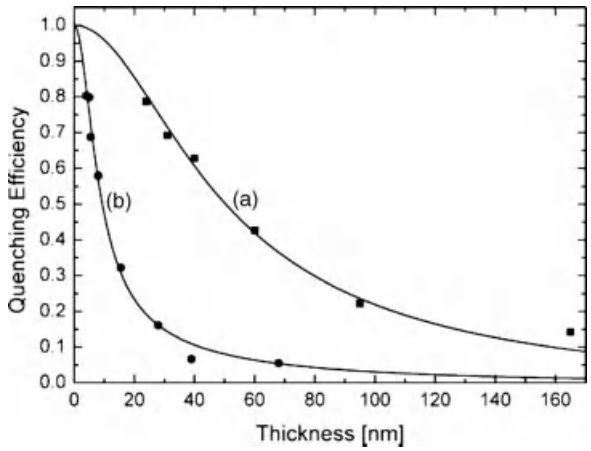

Figure 10.9 Relative photoluminescence quenching for a PPV derivative as a function of film thickness, for structures where the polymer is in contact with (a) an evaporated C_{60} film; (b) a cross-linked C_{60} derivative film. The data in (b) are consistent with the true exciton diffusion length of 5 nm, whereas the data in (a) show quenching that appears to take place over longer distances, due to diffusion of C_{60} into the polymer. Reproduced with permission from Ref. [49]. © 2005, American Chemical Society.

care must be taken to ensure that intermixing of the two materials does not occur. Time-resolved measurements of photoluminescence decay in these structures also allow diffusion lengths to be determined, and this has enabled diffusion lengths of 5–6 nm to be measured in a range of PPV derivatives with differing degrees of energetic disorder [50].

Diffusion of excitons is crucial in the performance of organic photovoltaics, since the fraction of excitons that can diffuse to a heterojunction interface places a fundamental limit on device efficiency. In bilayer photovoltaics, comparing the measured quantum efficiency with the expected absorption can be used to estimate the exciton diffusion length [51]. The diffusion length is typically much smaller than the device thickness required to absorb most of the incident light, hence the need for bulk heterojunction structures. In these structures, the exciton diffusion length sets the maximum dimension of pure phases that can be tolerated in the bulk heterojunction nanostructure. One way to assist exciton diffusion to the heterojunction is to choose a donor–acceptor pair where one material has a significantly lower gap than the other. In this case, due to the improved spectral overlap, excitons in the higher gap material can undergo Förster transfer to the lower gap material without having to diffuse all the way to the interface [52]. Having transferred to a low-gap molecule close to the interface, an exciton can readily undergo charge transfer to produce the same charge transfer state that would have been formed after diffusion of the exciton to the interface in the high-gap material, as shown in Figure 10.5.

10.5 Type-I Heterojunctions

The simplest way to observe the effects of a type-I heterojunction is to dope a small amount of low-gap material into a high-gap host. Even at doping levels of a small percentage, excitons created on the host can diffuse close enough to a dopant site to be able to undergo Förster transfer. For example, doping less than 1% of a red-emitting polymer into a blue-emitting ladder polyphenylene host was sufficient for red emission to dominate the photoluminescence spectrum [53]. An obvious application for this effect is in LEDs, where low-energy dopants can be added to a high-gap device in order to tune the emission spectrum (Figure 10.10) [54]. This is an attractive approach toward obtaining white emission for lighting applications [55]. However, in real polymer blend LEDs, the process of recombination on the host followed by energy transfer is only one of the pathways by which emission can occur. The dopants will typically also act as traps for charge carriers, so recombination may occur directly on the dopant when a trapped carrier on the dopant captures an opposite carrier from the host. At higher dopant concentrations, injection onto and transport between dopant molecules can also contribute. These processes are illustrated in Figure 10.11 [10]. For a review of the structure and performance of polymer blend LEDs, see Refs. [10, 56]. LEDs based on type-II heterojunctions are discussed in more detail below.

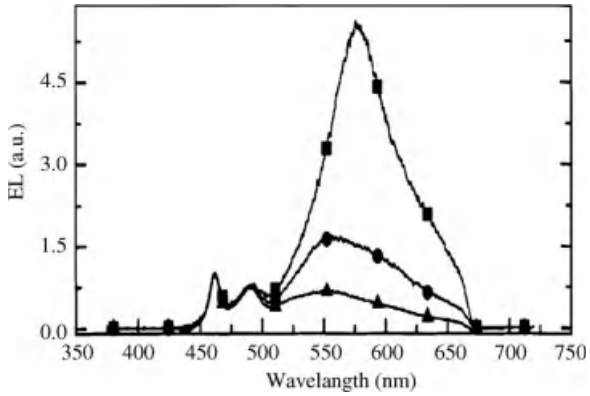

Figure 10.10 Electroluminescence spectra from blends of the blue-emitting polyphenylene ladder polymer *m*-LPPP with the lower gap poly(decylthiophene) at concentrations of 0.5% (triangles), 1% (circles), and 2%(squares) by weight. The effect of energy transfer to and/or recombination on the low-energy dopant can be clearly seen. Reproduced with permission from Ref. [54]. © 1999 Elsevier.

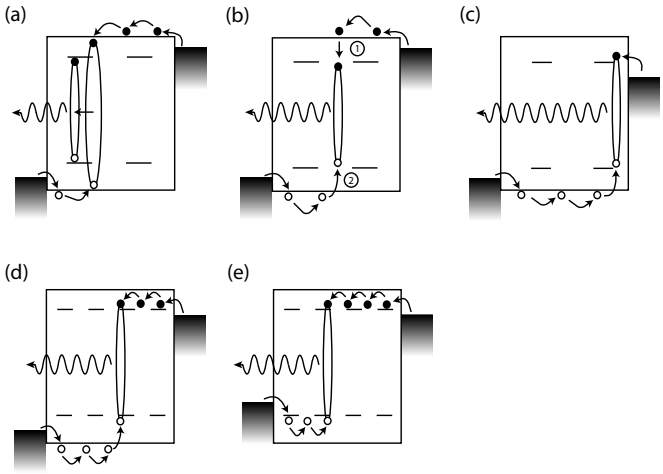

Figure 10.11 Charge injection, transport, and recombination in polymer-blend electroluminescent devices based on type-I heterojunctions. (a) Transport and recombination on the host, followed by energy transfer to the guest. (b) Electron trapping on the guest, followed by capture of a hole from the host to form an exciton on the guest. (c) Electron injection directly onto the host, followed by capture of a hole from the host. (d) Electron injection onto and transport through the guest, followed by capture of a hole from the host. (e) Injection, transport, and recombination of both carriers on the guest. Adapted from Ref. [10]. © 2008, Wiley-VCH.

10.6
Type-II Heterojunctions

As discussed in Section 10.3, the lowest energy state at a type-II heterojunction involves charge transfer, with the electron predominantly localized on the acceptor and the hole on the donor. This state can be formed by dissociation of an exciton created on either donor or acceptor (Figure 10.12), or by capture of an electron and a hole on either side of the interface.

Once an exciton reaches a type-II heterojunction interface, for example on the donor side, electron transfer to the acceptor can take place. The rate of this process can be found using Marcus theory (Figure 10.13), which predicts an electron transfer rate

$$k_{\mathrm{et}} = \frac{2\pi}{\hbar\sqrt{4\pi\,\lambda\,k_{\mathrm{B}}T}}\,V^2 \exp\left(\frac{-\left(\Delta G^0 + \lambda\right)^2}{4\lambda\,k_{\mathrm{B}}T}\right),$$

where V is the tunneling matrix element, ΔG^0 is the energy difference between final (charge transfer) and initial (exciton) states at the bottoms of their vibrational potentials, and λ is the structural relaxation energy required for the initial state to vibrate into the configuration associated with the equilibrium geometry of the final state. Generally, the process of electron transfer at suitable polymer/polymer or polymer/fullerene heterojunctions is found to be fast, occurring on picosecond or even subpicosecond timescales. The amount of driving force required for efficient photovoltaic operation is a matter of some debate, and this is an important question since if too much energy is used to drive the initial electron transfer reaction then the voltage that can be obtained from the cell will be reduced. However, if the

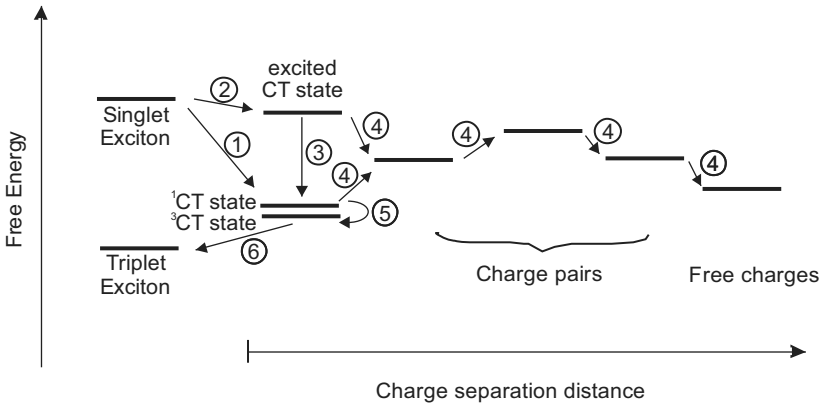

Figure 10.12 Charge separation processes at a donor–acceptor heterojunction. (1) Electron transfer to form CT state. (2) Electron transfer to higher lying CT state. (3) Relaxation to lowest CT state. (4) Charge separation. (5) Intersystem crossing from singlet to triplet CT state. (6) Formation of intrachain triplet exciton.

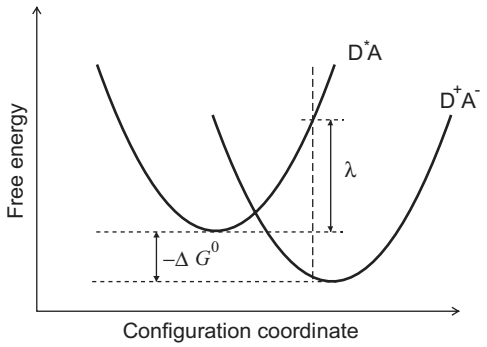

Figure 10.13 Potential energy surfaces relevant to Marcus theory of electron transfer. Free energy is shown as a function of configuration coordinate for the initial state (excited donor, D^*A) and the final state (D^+A^-).

driving force is too small, then the electron transfer rate may be reduced such that electron transfer cannot compete effectively with other exciton decay processes. LUMO offsets of 0.3–0.4 eV are often quoted [57], but this does not translate directly into ΔG^0 values since coulombic effects also contribute to ΔG^0, as discussed in Section 10.3. Veldman *et al.* have reported that ΔG^0 values of -0.1 eV are sufficient to observe charge transfer [58], although, as we discuss below, when the driving force is small the process of thermally activated electron back transfer to reform the exciton can also take place [59].

The charge-transfer state formed by electron transfer differs in two important ways from a free electron and free hole in acceptor and donor phases, respectively. When the two charges are immediately adjacent to the interface, there can be significant overlap between electron and hole wavefunctions (which can lead to recombination), and there is also a significant coulombic attraction between electron and hole (which tends to prevent the electron and hole from separating). As the electron and hole are separated further on either side of a polymer heterojunction (Figure 10.12), the wave function overlap decreases rapidly, but the coulomb attraction remains significant over much longer distances. There is, of course, a spectrum of states with different spatial separations, ranging from the tightly bound state formed where electron and hole are adjacent on either side of the interface (which we term a charge-transfer, or CT, state), to a more distant, but still coulombically bound, state (termed a charge pair), to a completely separated electron and hole [60].

In general, it is difficult to measure the properties of CT states directly, since they are weakly absorbing and show absorption features that are hard to distinguish from those of separated charges. However, in some cases emission can be directly seen from CT states, and this redshifted emission provides a convenient way to monitor their population. A system where these effects are prominent and have been extensively studied is provided by blends of fluorene-based polymers comprising F8BT mixed with PFB or TFB [61]. At low temperatures, the emission of these

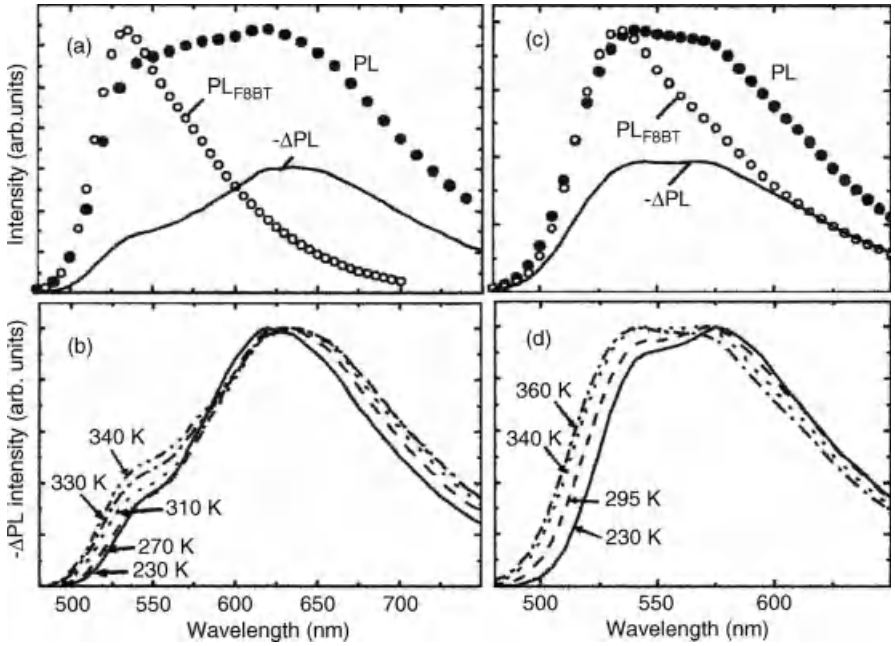

Figure 10.14 Emission spectra of PFB:F8BT and TFB:F8BT blends. (a) Photoluminescence intensity (PL, solid circles) and reduction of photoluminescence intensity due to an applied reverse bias of 10 V (ΔPL, continuous line) for a PFB:F8BT blend device at 340 K. (b) ΔPL spectra (at 10 V) from the same device as in (a) at different temperatures. (c) PL (solid circles) and ΔPL at a reverse bias of 15 V (continuous line) for a TFB:F8BT blend device at 340 K. (d) ΔPL spectra from the same device as in (c) at different temperatures. For comparison, the PL spectrum from an F8BT-only device (open circles) is plotted in both parts (a) and (c). Reproduced with permission from Ref. [59]. © 2004, American Physical Society.

blends is dominated by a red-emitting species ascribed to a CT state. The CT state has a lifetime of tens of nanoseconds and thus is much longer-lived than the exciton emission seen in pure films of the individual polymers. PFB is a stronger hole acceptor than TFB, and this correlates with the lower energy of the CT emission seen in PFB blends (Figure 10.14). The emitting state is often termed an "exciplex," although this terminology is not universally accepted since an exciplex usually refers to a CT-like state that is stabilized by an attractive physical interaction between the molecules that is present only in the excited state. Like an excimer between two identical molecules, a classical exciplex is thus visible only in emission, and does not appear as a low-energy feature in the absorption spectrum. The exciplex terminology is supported by the fact that there is no obvious evidence for such a feature in the F8BT:PFB and F8BT:TFB absorption spectra, but it is difficult to rule out a very weak absorption.

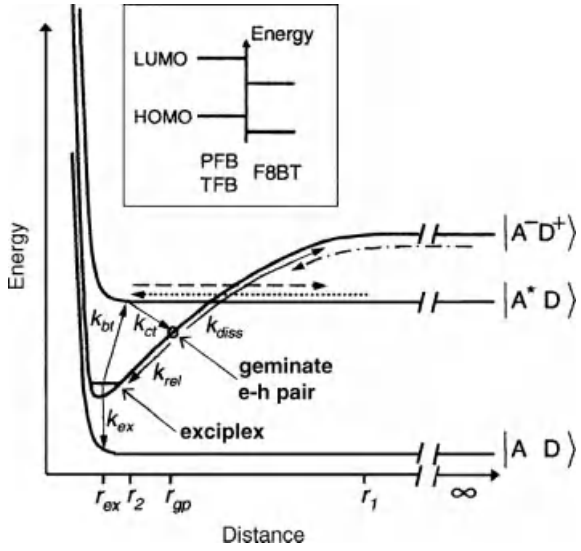

Figure 10.15 Potential energy diagram describing the energetic and kinetics at type-II polymer heterojunctions. Reproduced with permission from Ref. [59]. © 2004, American Physical Society.

The character of the exciton states in F8BT:PFB blends and the rates of CT state formation have been found to be highly sensitive to the exact arrangement of the two polymer chains at the polymer heterojunction [62]. Due to the significant degree of intramolecular charge transfer character of the excitons in these polymers, the PFB exciton is stabilized by up to 160 meV when the amine groups on the PFB chain are in close proximity to the benzothiadiazole groups on the F8BT, compared to the case when its fluorene units are in close proximity to the benzothiadiazole groups. These different configurations are argued to have different rates for CT state formation.

At room temperature, the F8BT:TFB system in particular has an unusual dominant decay channel, namely, the CT state becomes thermally reexcited to form an exciton on F8BT (Figure 10.15) [59]. These excitons then have a chance to emit before undergoing electron transfer again, particularly if they diffuse away from the interface. The emission thus has the spectrum of F8BT excitons, but its dynamics are much slower, since they are dominated by the reservoir of long-lived CT states awaiting "recycling" to form excitons. The ratio of exciton to CT emission in F8BT:TFB is found to have an activation energy of 100 meV, consistent with thermally assisted recycling. A similar process occurs in F8BT:PFB, but with an activation energy of 200 meV, such that exciton recycling is less prominent. This is consistent with the relatively high quantum efficiency for emission in F8BT:TFB blends at room temperature (35%, compared to 80% in pure F8BT), in contrast to the low PL efficiency seen in F8BT:PFB blends (4%) where most excitations decay nonradiatively via the CT state.

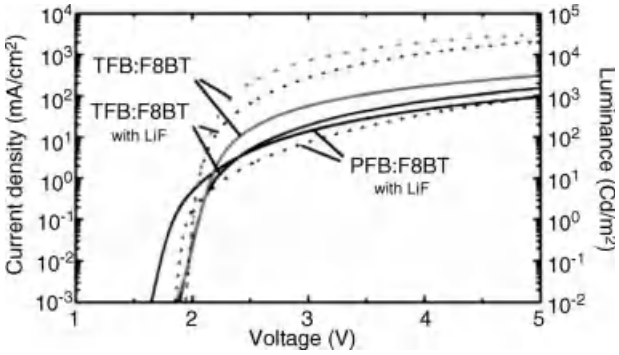

Figure 10.16 Current–voltage–luminance characteristics of LEDs based on TFB:F8BT and PFB:F8BT blends. Reproduced from Ref. [61]. © 2003, Wiley-VCH.

This process of exciton formation via intermolecular CT states has proved to be very important in obtaining highly efficient polymer LEDs [61]. LEDs formed from F8BT:TFB blends allow easy injection of electrons and holes onto the F8BT and TFB components, respectively, and thus operate at low turn-on voltages (Figure 10.16). Electrons and holes arriving at the heterojunction encounter a barrier to further transport, thus preventing efficiency losses due to carrier extraction. In a traditional model for multilayer or blended LEDs, one carrier needs to be injected over the heterojunction barrier, where it will encounter an opposite carrier, recombining to form an exciton. In F8BT:TFB blends, however, an additional recombination route is available, whereby electrons and holes remain in the F8BT and TFB phases, respectively, close to the heterojunction interface, but move under the influence of their mutual coulomb attraction until the CT state is formed [63]. This state can then be thermally recycled to form an exciton, which can finally emit green light with high efficiency. This process can take place without the need for high electric fields or high charge densities at the heterojunction, and assists in achieving low drive voltages in the LED. F8BT:TFB LEDs were found to give display brightnesses of 100 cd/m^2 at voltages of only 2.1 V, with high efficiencies above 19 lm/W.

Recently it has started to become apparent that direct emission from CT states is visible in a wider range of donor–acceptor blends than previously thought, including the polymer:PCBM blends that are extensively used in photovoltaics [58, 64–68]. Although weak, this CT emission is useful since it provides an accurate measure of the energy of the CT state, and it is this energy that sets the maximum voltage that can be obtained in a photovoltaic device based on the blend [69].

In many of these blends, it is also possible to detect absorption into CT states. Scattering and reflection effects make it difficult to resolve weak absorptions below the usual bandgap in transmission experiments, but the technique of photothermal deflection spectroscopy avoids these problems and allows accurate measurements to be made [70]. Another way to detect absorption into CT states is to look for a small contribution to the photocurrent action spectrum below the bandgap of either donor or acceptor [70, 71].

10.7
CT State Recombination

In any photovoltaic device, high efficiency requires that for each incident photon an electron and hole are collected at the respective electrode. Assuming that photon absorption is efficient, quantum efficiencies less than unity imply recombination of electrons with holes within the device. In an organic photovoltaic device, this involves recombination of an electron in the acceptor phase with a hole in the donor phase. Since some degree of wave function overlap is required for recombination, the state formed immediately before recombination is likely to closely resemble the CT states discussed above. The rate and mechanism of CT state recombination is, therefore, of great interest. We have already discussed the possibilities for CT state decay by radiative emission, and by recycling to form an exciton that then emits. In practice, two other mechanisms are likely to dominate: nonradiative decay to the ground state, and in some systems intersystem crossing to the triplet state followed by nonradiative decay of the triplet. Here, we discuss these two possibilities.

Nonradiative recombination is essentially an electron transfer process, so its rate should be described by Marcus theory, following a very similar framework to the electron transfer process from exciton to CT state. Fortunately for the operation of photovoltaics, recombination to the ground state turns out to be much slower than the forward electron transfer reaction. The origin of this difference in rates is normally ascribed to the very different driving forces ($-\Delta G^0$) for the two processes, typically a few 10ths of an eV for forward electron transfer and 1–2 eV for recombination. This places the recombination process firmly in the inverted Marcus regime where $-\Delta G^0$ is much larger than the structural reorganization energy, hence providing a significant thermal activation barrier to recombination. To zeroth order, the tunneling matrix element for the two processes should be rather similar. Another factor assisting the forward process is the presence of higher lying electronic states into which the electron can tunnel, followed by internal conversion to reach the lowest electronic state on the donor. This provides additional channels that may have more optimal balance of reorganization energies and $-\Delta G^0$. In contrast, for the recombination process the ground state is the only option for the final state.

Although Marcus theory provides a starting point for modeling recombination, the measured recombination dynamics in donor–acceptor blends are often highly nonexponential, with a long tail of recombination stretching into the microsecond and millisecond regime [72]. Clearly, these long-lived charges cannot be tightly bound pairs with significant wave function overlap across the interface. At least one of the charges in these pairs must have moved further from the interface to a site where it is either out of the attractive range of its geminate twin or is energetically stabilized such that the coulomb attraction cannot immediately cause it to rejoin its twin. The latter situation can arise due to the presence of energetic disorder or due to the presence of distinct trap states. Recombination then requires either tunneling over a large distance (a slow process) or thermal activation out of the trap site.

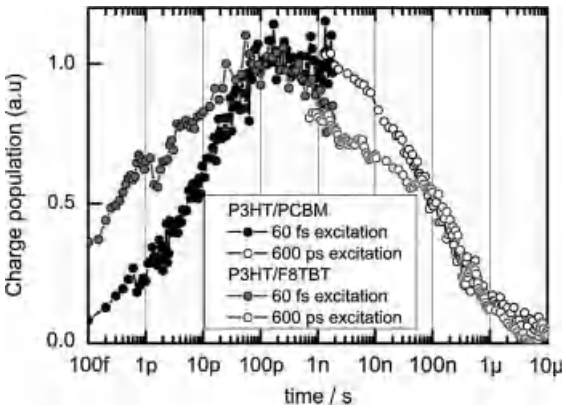

Figure 10.17 Charge population kinetics for P3HT:F8TBT blends compared with P3HT:PCBM. Charge generation following exciton diffusion to the interface can be resolved, followed by recombination. Reproduced with permission from Ref. [73]. © 2010, American Physical Society.

As discussed above, in systems where the CT state is clearly emissive time-resolved luminescence provides a convenient way to track the population of CT states. Further information can be gained from transient absorption measurements that monitor absorptions in the near infrared to track the population of charges. These measurements do not discriminate between tightly bound CT states, weakly bound charge pairs, or free charges. In P3HT:F8TBT blends, which show good photovoltaic performance, there is no obvious sign of emission from CT states, and hence transient absorption is the only way to follow the recombination of charges. Hodgkiss *et al*. have studied the recombination dynamics in this system over a wide range of timescales, and find that 30% of the charges recombine within 2 ns, with the remainder decaying with characteristic timescales of 200 ns (Figure 10.17) [73]. This contrasts with the behavior seen in P3HT:PCBM blends, where the rapid recombination component is absent. Clearly, the presence of a rapid recombination channel is undesirable for photovoltaic operation, but the microscopic origin of the difference in recombination behavior between the two systems is not yet established.

The final recombination process we must consider involves intersystem crossing to form triplet states (Figure 10.12) [74, 75]. Photon absorption in a polymer produces singlet ($S = 0$) excitons, and only a small fraction of these usually undergo intersystem crossing to form the lower energy triplet ($S = 1$) state. The reason for this low yield is that, in the absence of heavy atoms, spin–orbit coupling is weak, and the singlet lifetime is short so intersystem crossing cannot compete with radiative and nonradiative decay. However, when electron transfer occurs to produce a CT state, more possibilities arise. In a CT state, the wave function overlap between electron and hole is much smaller than for an intrachain exciton, so the exchange energy (the difference in energy between singlet and triplet CT states) will be small. This will facilitate mixing between singlet and triplet states. In addition, CT states

have a longer lifetime, so there is more time for spin mixing to occur. The mechanism for spin mixing is under some debate, but hyperfine interaction with proton spins is believed to play an important role [76]. CT states produced by charge transfer will initially be in a singlet spin state, and may then undergo intersystem crossing to form a triplet CT state. As far as the process of charge separation is concerned, it makes no difference whether the CT state is a singlet or a triplet, but the spin state can significantly influence the recombination process. Triplet CT states should give slower recombination to the ground state, but a major new recombination route can arise when the intrachain triplet exciton on either polymer lies lower in energy than the CT state. In this case, charge transfer can take place from the CT state to form an intrachain triplet exciton. Since the triplet exciton is the lowest energy excited state in the system, it is unlikely to be dissociated again, and will eventually decay (most likely nonradiatively) to the ground state.

A clear example of recombination via triplet states is found in F8BT:PFB blends [74]. Triplet states here can be detected since they have a characteristic absorption in the near infrared. In pure materials, the yield of triplet states after photoexcitation is only 1–2%, but in blends (where excitons are dissociated to form CT states), the yield of triplet states is much higher. Transient absorption measurements can resolve the transition from rapidly formed charge transfer states to triplet excitons (Figure 10.18) [77, 78]; it has been found that the characteristic timescale for triplet state formation is 40 ns and that the yield of triplet states can be as high as 75% (Figure 10.19) [78]. In F8BT:PFB, it was found that application of

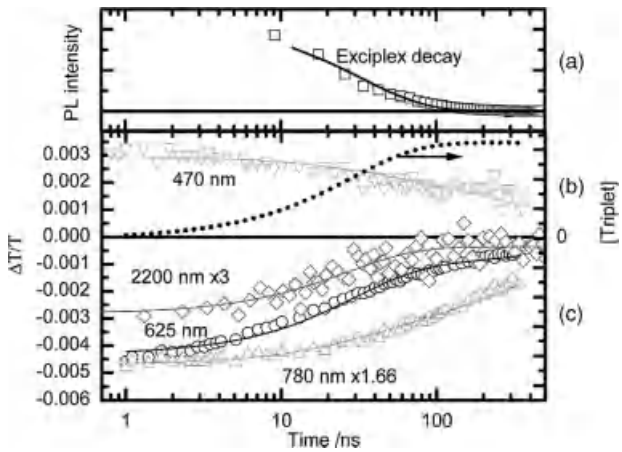

Figure 10.18 Time-resolved spectra for PFB:F8BT blends, together with numerical fits (lines). (a) Photoluminescence decay of the exciplex as measured by time-correlated single-photon counting at 650 nm. (b) Transient absorption kinetics measured at various wavelengths shown. 470 nm (ground-state bleach) tracks the total excited state population, 2200 nm tracks the charge population, 670 nm tracks mostly the charge population, and 780 nm tracks mostly the triplet population. The dashed line is the triplet density reconstructed from the fit. Reproduced from Ref. [78]. © 2008, American Chemical Society.

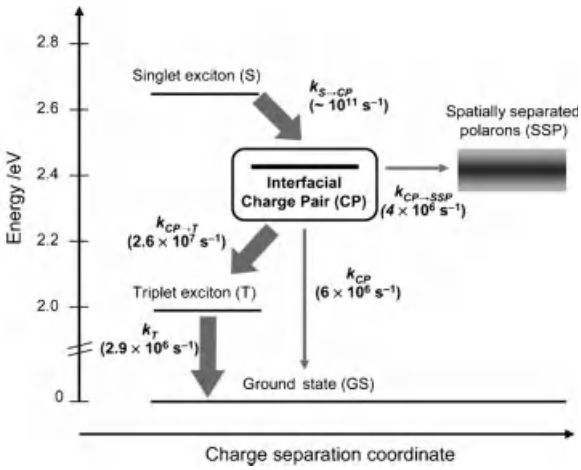

Figure 10.19 Rates for charge transfer, charge separation, recombination and triplet formation in PFB:F8BT blends, deduced from the data shown in Figure 10.18. Reproduced from Ref. [78]. © 2008, American Chemical Society.

an electric field suppresses the formation of triplet states, presumably by dissociating charge pairs before intersystem crossing can occur [74]. In blends of PPV derivatives, however, it was found that an electric field enhanced the yield of triplet state; this was ascribed to nongeminate recombination of separated charge carriers [75].

The issue of triplet state formation is not unique to polymer:polymer blends, and is a general problem in organic photovoltaics [79, 80]. The most obvious way to avoid it is to use a strong electron acceptor such that the CT state is lower in energy than the triplet exciton. However, since the exchange energy (the difference in energy between singlet and triplet excitons) in organic materials is typically 0.7 eV, this strategy involves a major sacrifice in open-circuit voltage, which is not acceptable in high-efficiency photovoltaics. There is limited scope to control exchange energies directly or to manipulate spin mixing times for CT states, so it is, therefore, necessary to ensure that separation of CT states occurs sufficiently rapidly to compete with spin mixing.

10.8
Charge Separation and Photovoltaic Devices based on Polymer:Polymer Blends

The natural application of type-II polymer heterojunctions is in photovoltaic devices, where the CT states formed can be further dissociated into free charges and collected at electrodes. Here, we will briefly discuss the separation of CT states and review the performance of photovoltaics based on polymer:polymer blends. More detailed discussion of the role of CT states, focused on polymer:fullerene blends, can be found in two recent reviews [60, 81].

We have discussed above the processes of CT state formation and recombination. For photovoltaic operation, a number of additional questions become important: (i) how easily can CT states be dissociated into free carriers? (ii) What is the role of electric field in this process? (iii) Are CT states the only product of charge transfer or is there some intermediate state that can either dissociate into free charges or relax to a tightly bound CT state? The answers to these questions are still under debate, and it is likely that the answers depend on the material system considered and on its detailed nanostructure.

Models for charge pair separation were initially developed by Onsager, and were combined with recombination dynamics in a kinetic model (known as the Braun–Onsager model [82]) that considered the competition between recombination and dissociation rates for a charge pair with some initial separation, *a*. Although this model has been widely applied to parameterize the process of charge generation in bulk heterojunction solar cells [83], it is conceptually unsatisfactory since it assumes that the processes of charge separation and recombination are in direct competition, whereas the recombination, in fact, occurs only when the carriers are adjacent and the separation process occurs over a much wider range of distances. More rigorous models have been developed by Tachiya and coworkers [84–86], based on a more satisfactory conceptual framework. It is also possible to perform Monte Carlo simulations of charge separation; these models allow the effects of hopping transport within a disordered density of states to be considered directly [87], and can also include the effects of the presence of heterojunction interfaces, either planar [88–90] or in a blend structure [91, 92]. The qualitative picture emerging from these models is clear: the probability of successful charge separation at a given electric field is increased by a large initial separation, high charge carrier mobility, and slow recombination at the interface. However, the quantitative results show that it is remarkably difficult to separate charge carriers successfully within these models. It is reasonable to assume an initial separation of $\sim$1 nm for a charge pair formed by electron transfer at a heterojunction, and to use mobilities measured in independent experiments. Under these assumptions, in order to reproduce the dissociation efficiencies measured in photovoltaic devices, it is necessary to invoke interfacial recombination times that are considerably longer than those measured in spectroscopic experiments. Some important physics must, therefore, be missing from the models.

Various proposals have been made to resolve this issue. Arkhipov proposed the existence of interfacial dipoles at the heterojunction that assist in the process of charge separation [93], although it is not clear why these dipoles should be universally present. It is also possible that local mobilities close to the regions where charges are generated are significantly higher than the bulk mobilities. Deibel *et al.* considered the effect within a Monte Carlo model of delocalization of the charges along segments of a polymer chain, and this was found to reduce the recombination probability [94]. Groves *et al.* investigated the effect of correlated disorder, that is, the energy of a given hopping site tends is not entirely random but is more likely to be close to the energy of its neighbors [95]. This increases the bulk mobility, but the effect on charge separation yield is more than what would be

expected based on this increase in mobility. Since charge separation is a local process, it is particularly sensitive to the presence of low-energy sites that may cause one of the carriers to become trapped. Correlated disorder makes it easier to escape from these sites since it increases the chances of finding a neighboring site to which the carrier can hop with a relatively small activation barrier.

Another effect that could enhance charge pair separation is the formation of intermediate states immediately following charge transfer (see Figure 10.12). The state formed after charge transfer will not initially be vibrationally relaxed, and it is possible that the excess vibrational energy might assist in the subsequent dissociation. In addition, higher lying electronic states might play a role in the charge transfer, and a charge carrier in one of these states might find it easier to escape from the interface, perhaps because the higher lying states are more delocalized. These effects are likely to be more prominent when the driving force for charge transfer is large. Although these higher lying electronic states to the lowest excited state should be rapid, it has been argued that charge hopping away from the interface might also be rapid [96]. Durrant and coworkers have reported a strong correlation between driving force and yield of long-lived charges in a series of polythiophene: fullerene [97] and polythiophene:perylene [98] blends. However, the driving force for charge separation is certainly not the sole determinant of charge generation yield, since donor–acceptor polymers with small driving forces for charge transfer to fullerenes have been found to give high yields of separated charges [99]. In polymer:polymer systems such as PFB:F8BT and TFB:F8BT, the role of an intermediate state in charge photogeneration was demonstrated by Morteani *et al.*, who studied the effect of electric field on exciplex and exciton emission [59]. They found that that relatively modest electric fields caused significant quenching of the luminescence, but without changing its lifetime. These data show that the state dissociated by the electric field is not the exciplex, but instead some intermediate precursor state. Analysis of the field dependence of the quenching within the Onsager framework suggested initial pair separations of 2.2 nm (TFB:F8BT) and 3.1 nm (PFB: F8BT) for the state that is affected by the field, larger than would be expected for a tightly bound exciplex. Furthermore, it was found that the photocurrent correlated directly with the PL quenching, showing that the dissociated charges are collected at the electrodes [100].

If intermediate states (or the excess thermal energy from the charge transfer process) play a significant role in assisting charge separation, then exciting the CT state directly in a photovoltaic device should give a lower probability of charge collection than when intramolecular exciton states are excited and diffuse to the heterojunction. Quantitative measurements of these effects are challenging, since the measured photocurrent must be compared with the number of absorbed photons, but absorption into the CT transition is very much weaker than into the exciton transition. Drori *et al.* reported that CT excitation does not contribute significantly to the photocurrent in P3HT:PCBM blends [101], but more recent measurements by Lee *et al.* found no difference in internal quantum efficiency in P3HT:fullerene and PPV-derivative:fullerene blend devices with excitation wavelength across the CT and exciton absorption bands [102].

Given the relative ease of charge separation found experimentally, there is some question about the role of CT state separation and its field dependence in determining the current–voltage characteristics of photovoltaic devices. The relative roles of geminate, trap-assisted, and bimolecular recombination are likely to highly depend on materials. In polymer:polymer devices, it is rather clear that geminate recombination plays an important role [14, 103], but in polymer:fullerene systems the situation is less obvious. Transient absorption measurements on device structures where electric fields can be applied are a powerful tool to study the field dependence of charge separation and recombination. These measurements can now be done at sufficiently low excitation densities to be relevant to conditions of device operation, and it has been found that in P3HT:PCBM devices the amount of geminate recombination on sub-100 ns timescales is greatly reduced by the application of a strong reverse bias to the device (Figure 10.20) [104]. The detailed behavior depends on the morphology of the blends, but these measurements clearly identify the importance of coulombically bound charge pairs in limiting the photocurrent in this system.

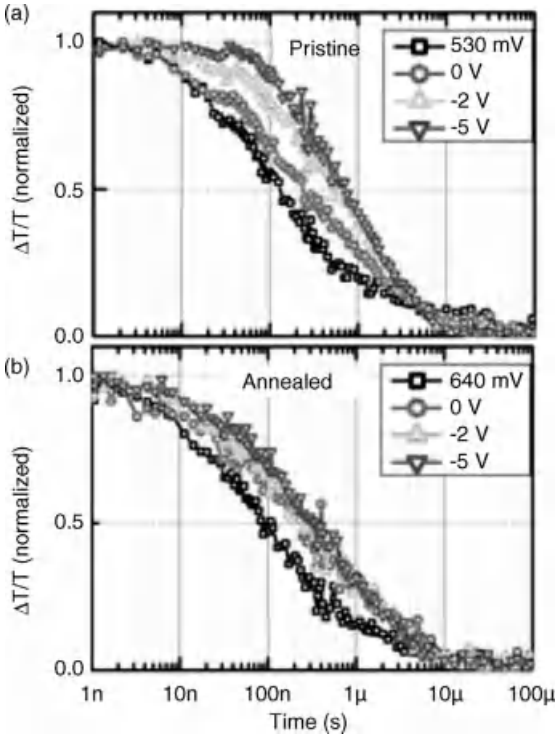

Figure 10.20 Bias-dependent charge recombination kinetics for pristine (a) and annealed (b) P3HT:PCBM devices. Reproduced with permission from Ref. [104]. © 2010, Wiley-VCH.

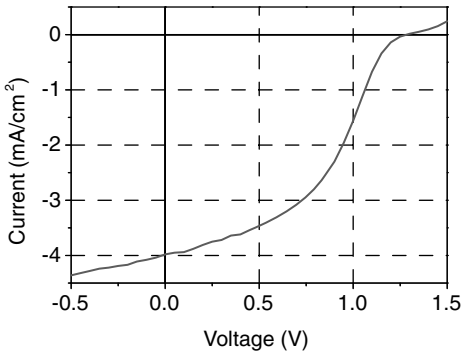

Figure 10.21 Current–voltage characteristic for an F8TBT:P3HT photovoltaic device under AM1.5G 1 sun illumination. Adapted with permission from Ref. [14]. © 2005, American Institute of Physics.

Photovoltaic devices based on blends of donor and acceptor polymers were reported as some of the earliest bulk heterojunction structures [11, 12], but have received less attention than polymer:fullerene blends over recent years. The F8BT:PFB system has been widely studied as a model system [13, 105, 106], but its absorption does not extend far enough to the red for it to give high photovoltaic power conversion efficiencies. More recently, a number of red-absorbing polymer:polymer blends have been studied, and these have given efficiencies in the range 1.5–2% [14, 107, 108]. The performance of a device based on a P3HT:F8TBT blend is shown in Figure 10.21. It seems that geminate recombination in polymer:polymer blends is a more severe problem than in the best polymer fullerene blends, and in the P3HT:F8TBT system, for example, the presence of a rapid (ns) recombination pathway [73] (see Section 10.7) is obviously not helpful in obtaining high charge separation yields. Strong electron trapping effects have also been seen in this system [109, 110], and these may hinder charge separation, promote recombination, or lead to space charge effects. Polymer:polymer blends have allowed useful studies to be carried out of the effect of crystallinity and nanostructure on device efficiency [103]. In particular, it was found that the ease of geminate pair separation increased as the device was annealed to increase the characteristic length scale of phase separation. In F8BT:PFB blends, for example, it was found that typical domain sizes of 20 nm were found to be required for efficient charge separation [106]. This is consistent with Monte Carlo simulations of charge separation in nanostructured blends, which found that geminate recombination was enhanced in structures with characteristic length scales of phase separation below about 15 nm (Figure 10.22) [90]. Although carriers separating at a planar heterojunction are unlikely to recombine geminately once they have been separated to a distance of 5 nm, in a fine blend structure they can be prevented from separating

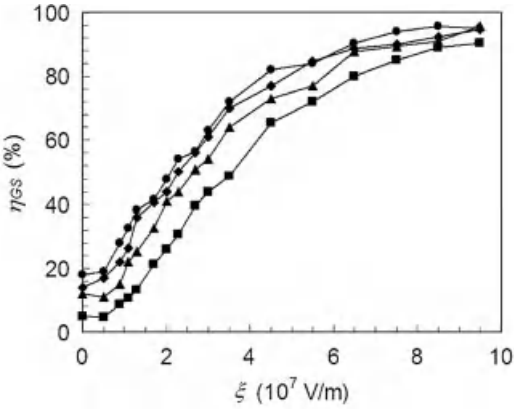

Figure 10.22 Monte Carlo simulations of the charge separation yields, η_{CS} as a function of electric field, ξ, for characteristic donor–acceptor blend feature sizes of l = 4 nm (squares), 8 nm (triangles), 12 nm (diamonds), and 16 nm (circles). Reproduced with permission from Ref. [90]. © 2008, American Institute of Physics.

fully by the structure of the blend, thus increasing the probability that they will return to smaller separations such that geminate recombination becomes likely.

10.9 Future Directions

It is already clear that the fine-tuning of polymer interfaces is very important in optimizing the efficiency of organic photovoltaics. The demands of simultaneously maximizing quantum efficiency and minimizing energy losses will be very exacting if further efficiency improvements are to be achieved. We rely largely on empirical optimization of materials and processing to control the interface, and it would certainly be desirable to be able to modify the interface more directly. Although one could imagine ways to modify planar interfaces during their fabrication, it is hard to do this for interfaces formed within a bulk heterojunction structure. One possible way forward might involve donor–acceptor block copolymers, which can assemble into well-ordered nanostructures where the phase separation between donor and acceptor blocks is constrained by the covalent linkage between the blocks. Modifying the chemical structure in the region of the linkage might allow the interfacial electronic structure to be designed so as to enhance exciton diffusion toward the heterojunction and to favor charge separation or suppress recombination at the interface. Such materials could also be added to a blend of homopolymers as an interfacial modifier, where they can assemble at the interface between the two phases. The synthetic chemistry is very challenging, but preliminary results using this approach have recently been reported [111].

References

1 Liang, Y., Xu, Z., Xia, J., Tsai, S.-T., Wu, Y., Li, G., Ray, C., and Yu, L. (2010) *Adv. Mater.*, **22**, E135.
2 Reineke, S., Lindner, F., Schwartz, G., Seidler, N., Walzer, K., Lussem, B., and Leo, K. (2009) *Nature*, **459**, 234.
3 Greenham, N.C., Moratti, S.C., Bradley, D.D.C., Friend, R.H., and Holmes, A.B. (1993) *Nature*, **365**, 628.
4 Zuniga, C.A., Barlow, S., and Marder, S. R., (2011) *Chem. Mater.*, **23**, 658.
5 Png, R.Q., Chia, P.J., Tang, J.C., Liu, B., Sivaramakrishnan, S., Zhou, M., Khong, S.H., Chan, H.S.O., Burroughes, J.H., Chua, L.L., Friend, R.H., and Ho, P.K.H. (2010) *Nat. Mater.*, **9**, 152.
6 Kim, J.S., Friend, R.H., Grizzi, I., and Burroughes, J.H. (2005) *Appl. Phys. Lett.*, **87**, 023506.
7 Ramsdale, C.M., Barker, J.A., Arias, A.C., MacKenzie, J.D., Friend, R.H., and Greenham, N.C. (2002) *J. Appl. Phys.*, **92**, 4266.
8 He, X., Gao, F., Tu, G., Hasko, D., Huettner, S., Steiner, U., Greenham, N. C., Friend, R.H., and Huck, W.T.S. (2010) *Nano Lett.*, **10**, 1302.
9 Yan, H., Swaraj, S., Wang, C., Hwang, I., Greenham, N.C., Groves, C., Ade, H., and McNeill, C.R. (2010) *Adv. Funct. Mater.*, **20**, 4329.
10 McNeill, C.R. and Greenham, N.C. (2009) *Adv. Mater.*, **21**, 3840.
11 Halls, J.J.M., Walsh, C.A., Greenham, N. C., Marseglia, E.A., Friend, R.H., Moratti, S.C., and Holmes, A.B. (1995) *Nature*, **376**, 498.
12 Yu, G. and Heeger, A.J. (1995) *J. Appl. Phys.*, **78**, 4510.
13 Arias, A.C., MacKenzie, J.D., Stevenson, R., Halls, J.J.M., Inbasekaran, M., Woo, E.P., Richards, D., and Friend, R.H. (2001) *Macromol.*, **34**, 6005.
14 McNeill, C.R., Abrusci, A., Zaumseil, J., Wilson, R., McKeirnan, M.J., Burroughes, J.H., Halls, J.J.M., Greenham, N.C., and Friend, R.H. (2007) *Appl. Phys. Lett.*, **90**, 193506.
15 Zhao, Y., Xie, Z., Qu, Y., Geng, Y., and Wang, L. (2007) *Appl. Phys. Lett.*, **90**, 043504.
16 Lee, J.K., Ma, W.L., Brabec, C.J., Yuen, J., Moon, J.S., Kim, J.Y., Lee, K., Bazan, G. C., and Heeger, A.J. (2008) *J. Am. Chem. Soc.*, **130**, 3619.
17 Campbell, A.R., Hodgkiss, J.M., Westenhoff, S., Howard, I.A., Marsh, R. A., McNeill, C.R., Friend, R.H., and Greenham, N.C. (2008) *Nano Lett.*, **8**, 3942.
18 Kim, J.S., Ho, P.K.H., Murphy, C.E., and Friend, R.H. (2004) *Macromol.*, **37**, 2861.
19 Chappell, J., Lidzey, D.G., Jukes, P.C., Higgins, A.M., Thompson, R.L., O'Connor, S., Grizzi, I., Fletcher, R., O'Brien, J., Geoghegan, M., and Jones, R. A.L. (2003) *Nat. Mater.*, **2**, 616.
20 McNeill, C.R., Watts, B., Thomsen, L., Ade, H., Greenham, N.C., and Dastoor, P.C. (2007) *Macromol.*, **40**, 3263.
21 McNeill, C.R., Watts, B., Thomsen, L., Belcher, W.J., Greenham, N.C., Dastoor, P.C., and Ade, H. (2009) *Macromol.*, **42**, 3347.
22 Martens, T., D'Haen, J., Munters, T., Beelen, Z., Goris, L., Manca, J., D'Olieslaeger, M., Vanderzande, D., De Schepper, L., and Andriessen, R. (2003) *Synth. Met.*, **138**, 243.
23 Loos, J., Yang, X.N., Koetse, M.M., Sweelssen, J., Schoo, H.F.M., Veenstra, S.C., Grogger, W., Kothleitner, G., and Hofer, F. (2005) *J. Appl. Polym. Sci.*, **97**, 1001.
24 Parnell, A., Dunbar, A., Pearson, A., Staniec, P., Dennison, A., Hamamatsu, H., Skoda, M., Lidzey, D., and Jones, R. (2010) *Adv. Mater.*, **22**, 2444.
25 Vaynzof, Y., Kabra, D., Zhao, L., Chua, L. L., Steiner, U., and Friend, R.H. (2011) *ACS Nano*, **5**, 329.
26 Jukes, P.C., Heriot, S.Y., Sharp, J.S., and Jones, R.A.L. (2005) *Macromol.*, **38**, 2030.
27 Staniec, P., Parnell, A., Dunbar, A., Yi, H., Pearson, A., Wang, T., Hopkinson, P., Kinane, C., Dalgliesh, R., Donald, A., Ryan, A., Iraqi, A., Jones, R., and Lidzey, D. (2011) *Adv. Energy Mater.*, **1**, 499.
28 Higgins, A.M., Martin, S.J., Thompson, R.L., Chappell, J., Voigt, M., Lidzey, D.G., Jones, R.A.L., and Geoghegan, M. (2005) *Adv. Funct. Mater.*, **17**, 1319.

29 Bavel, S., Sourty, E., With, G., and Loos, J. (2009) *Nano Lett.*, **9**, 507.

30 Sirringhaus, H., Brown, P.J., Friend, R. H., Nielsen, M.M., Bechgaard, K., Langeveldvoss, B.M.W., Spiering, A.J.H., Janssen, R.A.J., Meijer, E.W., Herwig, P., and de Leeuw, D.M. (1999) *Nature*, **401**, 685.

31 Mayer, A.C., Toney, M.F., Scully, S.R., Rivnay, J., Brabec, C.J., Scharber, M., Koppe, M., Heeney, M., McCulloch, I., and McGehee, M.D. (2009) *Adv. Funct. Mater.*, **19**, 1173.

32 Halls, J.J.M., Cornil, J., dos Santos, D.A., Silbey, R., Hwang, D.H., Holmes, A.B., Bredas, J.L., and Friend, R.H. (1999) *Phys. Rev. B*, **60**, 5721.

33 Hwang, J., Wan, A., and Kahn, A. (2009) *Mater. Sci. Eng. Rep.*, **64**, 1.

34 Blakesley, J.C. and Greenham, N.C. (2009) *J. Appl. Phys.*, **106**, 034507.

35 Hwang, J., Kim, E.G., Liu, J., Bredas, J.L., Duggal, A., and Kahn, A. (2007) *J. Phys. Chem. C*, **111**, 1378.

36 Ishii, H., Sugiyama, K., Ito, E., and Seki, K. (1999) *Adv. Mater.*, **11**, 972.

37 Beljonne, D., Cornil, J., Muccioli, L., Zannoni, C., Brédas, J.L., and Castet, F. (2011) *Chem. Mater.*, **23**, 591.

38 Pope, M. and Swenberg, C.E. (1999) *Electronic Processes in Organic Crystals and Polymers*, Oxford University Press, Oxford.

39 Schwoerer, M. and Wolf, H.C. (2007) *Organic Molecular Solids*, Wiley-VCH Verlag GmbH, Weinheim.

40 Beljonne, D., Cornil, J., Silbey, R., Millie, P., and Bredas, J.L. (2000) *J. Chem. Phys.*, **112**, 4749.

41 Samuel, I.D.W., Rumbles, G., and Collison, C.J. (1995) *Phys. Rev. B*, **52**, 11573.

42 Jakubiak, R., Collison, C.J., Wan, W.C., Rothberg, L.J., and Hsieh, B.R. (1999) *J. Phys. Chem. A*, **103**, 2394.

43 Nguyen, T.Q., Martini, I.B., Liu, J., and Schwartz, B.J. (2000) *J. Phys. Chem. B*, **104**, 237.

44 Lemmer, U., Heun, S., Mahrt, R.F., Scherf, U., Hopmeier, M., Siegner, U., Gobel, E.O., Mullen, K., and Bässler, H. (1995) *Chem. Phys. Lett.*, **240**, 373.

45 Clark, J., Silva, C., Friend, R.H., and Spano, F.C. (2007) *Phys. Rev. Lett.*, **98**, 206406.

46 McCullough, R.D., Tristram-Nagle, S., Williams, S.P., Lowe, R.D., and Jayaraman, M. (1993) *J. Am. Chem. Soc.*, **115**, 4910.

47 Förster, T. (1948) *Ann. Phys. VI*, **2**, 55.

48 Beljonne, D., Pourtois, G., Silva, C., Hennebicq, E., Herz, L.M., Friend, R.H., Scholes, G.D., Setayesh, S., Müllen, K., and Brédas, J.L. (2002) *Proc. Natl. Acad. Sci. USA*, **99**, 10982.

49 Markov, D.E., Amsterdam, E., Blom, P. W.M., Sieval, A.B., and Hummelen, J.C. (2005) *J. Phys. Chem. A*, **109**, 5266.

50 Markov, D.E., Tanase, C., Blom, P.W.M., and Wildeman, J. (2005) *Phys. Rev. B*, **72**, 6.

51 Halls, J.J.M., Pichler, K., Friend, R.H., Moratti, S.C., and Holmes, A.B. (1996) *Appl. Phys. Lett.*, **68**, 3120.

52 Liu, Y.X., Summers, M.A., Edder, C., Frechet, J.M.J., and McGehee, M.D. (2005) *Adv. Mater.*, **17**, 2960.

53 Tasch, S., List, E.J.W., Hochfilzer, C., Leising, G., Schlichting, P., Rohr, U., Geerts, Y., Scherf, U., and Müllen, K. (1997) *Phys. Rev. B*, **56**, 4479.

54 List, E.J.W., Holzer, L., Tasch, S., Leising, G., Scherf, U., Müllen, K., Catellani, M., and Luzzati, S. (1999) *Solid State Commun.*, **109**, 455.

55 Granstrom, M. and Inganäs, O. (1996) *Appl. Phys. Lett.*, **68**, 147.

56 Moons, E. (2002) *J. Phys. C.*, **14**, 12235.

57 Scharber, M.C., Wuhlbacher, D., Koppe, M., Denk, P., Waldauf, C., Heeger, A.J., and Brabec, C.L. (2006) *Adv. Mater.*, **18**, 789.

58 Veldman, D., Meskers, S.C.J., and Janssen, R.A.J. (2009) *Adv. Funct. Mater.*, **19**, 1939.

59 Morteani, A.C., Sreearunothai, P., Herz, L.M., Friend, R.H., and Silva, C. (2004) *Phys. Rev. Lett.*, **92**, 247402.

60 Clarke, T.M. and Durrant, J.R. (2010) *Chem. Rev.*, **110**, 6736.

61 Morteani, A.C., Dhoot, A.S., Kim, J.S., Silva, C., Greenham, N.C., Friend, R.H., Murphy, C., Moons, E., Ciná, S., and Burroughes, J.H. (2003) *Adv. Mater.*, **15**, 1708.

62 Sreearunothai, P., Morteani, A.C., Avilov, I., Cornil, J., Beljonne, D., Friend, R.H., Phillips, R.T., Silva, C., and Herz, L.M. (2006) *Phys. Rev. Lett.*, **96**, 117403.

63 Bobbert, P.A. and Greenham, N.C. (2003) *Phys. Rev. B*, **68**, 245301.

64 Benson-Smith, J.J., Goris, L., Vandewal, K., Haenen, K., Manca, J.V., Vanderzande, D., Bradley, D.D.C., and Nelson, J. (2007) *Adv. Funct. Mater.*, **17**, 451.

65 Loi, M.A., Toffanin, S., Muccini, M., Forster, M., Scherf, U., and Scharber, M. (2007) *Adv. Funct. Mater.*, **17**, 2111.

66 Hallermann, M., Haneder, S., and Da Como, E. (2008) *Appl. Phys. Lett.*, **93**, 3.

67 Kim, H., Kim, J.Y., Park, S.H., Lee, K., Jin, Y., Kim, J., and Suh, H. (2005) *Appl. Phys. Lett.*, **86**, 3.

68 Zhou, Y., Tvingstedt, K., Zhang, F.L., Du, C.X., Ni, W.X., Andersson, M.R., and Inganas, O. (2009) *Adv. Funct. Mater.*, **19**, 3293.

69 Vandewal, K., Tvingstedt, K., Gadisa, A., Inganas, O., and Manca, J.V. (2009) *Nat. Mater.*, **8**, 904.

70 Goris, L., Poruba, A., Hod'akova, L., Vanecek, M., Haenen, K., Nesladek, M., Wagner, P., Vanderzande, D., De Schepper, L., and Manca, J.V. (2006) *Appl. Phys. Lett.*, **88**, 3.

71 Vandewal, K., Gadisa, A., Oosterbaan, W. D., Bertho, S., Banishoeib, F., Van Severen, I., Lutsen, L., Cleij, T.J., Vanderzande, D., and Manca, J.V. (2008) *Adv. Funct. Mater.*, **18**, 2064.

72 Nogueira, A.F., Montanari, I., Nelson, J., Durrant, J.R., Winder, C., and Sariciftci, N.S. (2003) *J. Phys. Chem. B*, **107**, 1567.

73 Hodgkiss, J.M., Campbell, A.R., Marsh, R.A., Rao, A., Albert-Seifried, S., and Friend, R.H. (2010) *Phys. Rev. Lett.*, **104**, 177701.

74 Ford, T.A., Avilov, I., Beljonne, D., and Greenham, N.C. (2005) *Phys. Rev. B*, **71**, 125212.

75 Offermans, T., van Hal, P.A., Meskers, S. C.J., Koetse, M.M., and Janssen, R.A.J. (2005) *Phys. Rev. B*, **72**, 045213.

76 Nguyen, T.D., Hukic-Markosian, G., Wang, F.J., Wojcik, L., Li, X.G., Ehrenfreund, E., and Vardeny, Z.V. (2010) *Nat. Mater.*, **9**, 345.

77 Ford, T.A., Ohkita, H., Cook, S., Durrant, J.R., and Greenham, N.C. (2008) *Chem. Phys. Lett.*, **454**, 237.

78 Westenhoff, S., Howard, I.A., Hodgkiss, J.M., Kirov, K.R., Bronstein, H.A., Williams, C.K., Greenham, N.C., and Friend, R.H. (2008) *J. Am. Chem. Soc.*, **130**, 13653.

79 Ohkita, H., Cook, S., Astuti, Y., Duffy, W., Heeney, M., Tierney, S., McCulloch, I., Bradley, D.D.C., and Durrant, J.R. (2006) *Chem. Commun.*, 3939.

80 Schueppel, R., Uhrich, C., Pfeiffer, M., Leo, K., Brier, E., Reinold, E., and Baeuerle, P. (2007) *ChemPhysChem*, **8**, 1497.

81 Deibel, C., Strobel, T., and Dyakonov, V. (2010) *Adv. Mater.*, **22**, 4097.

82 Braun, C.L. (1984) *J. Chem. Phys.*, **80**, 4157.

83 Mihailetchi, V.D., Koster, L.J.A., Hummelen, J.C., and Blom, P.W.M. (2004) *Phys. Rev. Lett.*, **93**, 216601.

84 Sano, H. and Tachiya, M. (1979) *J. Chem. Phys.*, **71**, 1276.

85 Wojcik, M. and Tachiya, M. (2009) *J. Chem. Phys.*, **130**, 104107.

86 Wojcik, M. and Tachiya, M. (2005) *Rad. Phys. Chem.*, **74**, 132.

87 Barth, S., Hertel, D., Tak, Y.H., Bässler, H., and Hörhold, H.H. (1997) *Chem. Phys. Lett.*, **274**, 165.

88 Peumans, P. and Forrest, S.R. (2004) *Chem. Phys. Lett.*, **398**, 27.

89 Offermans, T., Meskers, S.C.J., and Janssen, R.A.J. (2005) *Chem. Phys.*, **308**, 125.

90 Groves, C., Marsh, R.A., and Greenham, N.C. (2008) *J. Chem. Phys.*, **129**, 114903.

91 Watkins, P.K., Walker, A.B., and Verschoor, G.L.B. (2005) *Nano Lett.*, **5**, 1814.

92 Marsh, R.A., Groves, C., and Greenham, N.C. (2007) *J. Appl. Phys.*, **101**, 083509.

93 Arkhipov, V.I., Heremans, P., and Bässler, H. (2003) *Appl. Phys. Lett.*, **82**, 4605.

94 Deibel, C., Strobel, T., and Dyakonov, V. (2009) *Phys. Rev. Lett.*, **103**, 036402.

95 Groves, C., Blakesley, J.C., and Greenham, N.C. (2010) *Nano Lett.*, **10**, 1063.

96 Brédas, J.L., Norton, J.E., Cornil, J., and Coropceanu, V. (2009) *Acc. Chem. Res.* **42**, 1691.

97 Ohkita, H., Cook, S., Astuti, Y., Duffy, W., Tierney, S., Zhang, W., Heeney, M., McCulloch, L., Nelson, J., Bradley, D.D. C., and Durrant, J.R. (2008) *J. Am. Chem. Soc.*, **130**, 3030.

98 Shoaee, S., Clarke, T.M., Huang, C., Barlow, S., Marder, S.R., Heeney, M., McCulloch, I., and Durrant, J.R. (2010) *J. Amer. Chem. Soc.*, **132**, 12919.

99 Clarke, T., Ballantyne, A., Jamieson, F., Brabec, C., Nelson, J., and Durrant, J. (2009) *Chem. Commun.*, 89.

100 Gonzalez-Rabade, A., Morteani, A.C., and Friend, R.H. (2009) *Adv. Mater.*, **21**, 3924.

101 Drori, T., Sheng, C.X., Ndobe, A., Singh, S., Holt, J., and Vardeny, Z.V. (2008) *Phys. Rev. Lett.*, **101**, 037401.

102 Lee, J., Vandewal, K., Yost, S.R., Bahlke, M.E., Goris, L., Baldo, M.A., Manca, J.V., and Voorhis, T.V. (2010) *J. Am. Chem. Soc.*, **132**, 11878.

103 McNeill, C.R., Halls, J.J.M., Wilson, R., Whiting, G.L., Berkebile, S., Ramsey, M. G., Friend, R.H., and Greenham, N.C. (2008) *Adv. Funct. Mater.*, **18**, 2309.

104 Marsh, R.A., Hodgkiss, J.M., and Friend, R.H. (2010) *Adv. Mater.*, **22**, 3672.

105 Halls, J.J.M., Arias, A.C., Mackenzie, J. D., Wu, W.S., Inbasekaran, M., Woo, E. P., and Friend, R.H. (2000) *Adv. Mater.*, **12**, 498.

106 McNeill, C.R., Westenhoff, S., Groves, C., Friend, R.H., and Greenham, N.C. (2007) *J. Phys. Chem. C*, **111**, 19153.

107 Kietzke, T., Horhold, H.H., and Neher, D. (2005) *Chem. Mater.*, **17**, 6532.

108 Koetse, M.M., Sweelssen, J., Hoekerd, K. T., Schoo, H.F.M., Veenstra, S.C., Kroon, J.M., Yang, X.N., and Loos, J. (2006) *Appl. Phys. Lett.*, **88**, 083504.

109 Brenner, T.J.K., Hwang, I., Greenham, N.C., and McNeill, C.R. (2010) *J. Appl. Phys.*, **107**, 114501.

110 Hwang, I., McNeill, C.R., and Greenham, N.C. (2009) *J. Appl. Phys.*, **106**, 094506.

111 Mulherin, R.C., Jung, S., Huettner, S., Johnson, K., Kohn, P., Sommer, M., Allard, S., Scherf, U., and Greenham, N.C. (2011) *Nano Lett.*, **11**, 4846.

11
Electronic Processes at Organic Semiconductor Heterojunctions: The Mechanism of Exciton Dissociation in Semicrystalline Solid-State Microstructures

Francis Paquin, Gianluca Latini, Maciej Sakowicz, Paul-Ludovic Karsenti, Linjun Wang, David Beljonne, Natalie Stingelin, and Carlos Silva

11.1
Introduction

Unraveling primary electronic processes in polymeric semiconductors opens a fundamental window to their materials physics. The steps to generate charge by optical absorption are currently the subject of wide interest (see Ref. [1] for a comprehensive review). Here, we focus on charge generation and recombination dynamics in *neat* regioregular poly(3-hexylthiophene) (P3HT). This semicrystalline polymer adopts π-stacked lamellar microstructures in the solid state [2], leading to two-dimensional electronic dispersion [3]. Crystallinity induced by molecular organization results in the formation of interfaces between amorphous and crystalline domains, thus profoundly influencing the electronic properties of the material, exemplified by the high yield (η) of apparently direct charge photogeneration. Although in general $\eta \ll 1\%$ in less organized polymeric semiconductors [4], various groups have reported η up to 30% over ultrafast timescales in P3HT films at 300 K [5–9]. However, photoemission spectroscopy measurements place the energy for free polaron generation ~0.7 eV above the optical gap in neat P3HT [10]. Weak interchain electronic coupling in the lamellar architecture leads to a free exciton bandwidth – the pure electronic bandwidth due to dispersion neglecting coupling to vibrations – that is well below this energy [11–14]. Are charges indeed generated *intrinsically* (directly by photoexcitation due to the crystalline electronic structure) or *extrinsically* (due to a driving force for exciton dissociation)?

Charge photogeneration in neat P3HT has been studied previously by means of transient absorption spectroscopy [7, 9], which measures directly the dynamics of nascent polarons. We implement time-resolved photoluminescence (PL) spectroscopy at 10 K to probe charge photogeneration and recombination dynamics. Our strategy is to exploit the intricate details of electronic structure, structural relaxation, and correlated disorder afforded by the spectral bandshape

Physics of Organic Semiconductors, Second Edition. Edited by Wolfgang Brütting and Chihaya Adachi

of the PL spectrum [14], over timescales where it is known that charge photogeneration is important. We probe the recombination environment via the bandshape and decay dynamics of delayed PL from charge pair recombination, which also probes the environment in which photogeneration occurs, since photoexcitations are frozen at 10 K. We find that charge generation occurs over subnanosecond timescales by dissociation of excitons created at interfaces between lamellar (aggregate) and poorly stacked (nonaggregate) domains, driven by energetic disorder. Thus, prompt charge photogeneration is an *extrinsic* process, and film microstructure determines the surface area and the energy landscape of interfaces between domains. In order to explore the generality of these photophysics, we explore various films of different molecular weights, which form distinct solid-state microstructure. We find that the distribution of electron–hole radii depends upon microstructure.

11.2
Experimental Methods

PL measurements were carried out with a 40 fs, 532 nm (2.33 eV) pulse train derived from an optical parametric amplifier (Light Conversion TOPAS), pumped by a Ti:sapphire laser system (KMLabs Dragon). Time-resolved PL spectra were measured with an optically triggered streak camera (Axis-Photonique, 6 ps instrument response). Alternatively, an intensified CCD camera (Princeton-Instruments PIMAX 1024HB) was used. Except for the work described in Section 11.3.2, we studied P3HT films of $M_w = 47.8$ kg/mol, $M_n = 26.2$ kg/mol, and polydispersity = 1.83 (Merck), spun from trichlorobenzene solution (6 wt%), resulting in film thickness of 150 nm. In Section 11.3.2, we explored films of different molecular weights, which we specify in that section.

11.3
Results and Analysis

11.3.1
Photophysics of Charge Photogeneration and Recombination Probed by Time-Resolved PL Spectroscopy

11.3.1.1 Absorption and Steady-State PL

In P3HT films, the PL spectrum is understood within the framework of a weakly coupled H-aggregate model [13], resulting from the weak resonance Coulomb coupling (J) of transition moments aligned cofacially in neighboring polymer chains [11, 12]. In contrast, the absorption spectrum contains contributions from both the aggregate and nonaggregate regions [13]. Figure 11.1 displays the absorption and PL spectra of a P3HT film studied in this section. We have analyzed the absorption spectrum using a modified Franck–Condon model that takes into account the

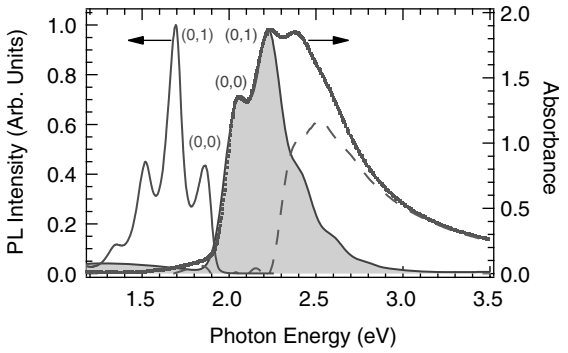

Figure 11.1 Absorption (room temperature) and PL (10 K) spectra of P3HT. The continuous line filled to the baseline displays the absorption spectrum of the H-aggregate obtained via a Franck–Condon model [15]. The broken line is the difference between the modeled aggregate spectrum and the measured absorption spectrum.

H-aggregate nature of P3HT lamellar stacks in the weak coupling limit [15]. The continuous line filled to the baseline is the fit to this model using the same parameters as in Ref. [15], except for $W = 4J = 100 \pm 3$ meV. Following the analysis in Ref. [15], we have separated the contribution of nonaggregate regions of the film, shown as a broken curve. This could be either due to very disordered lamellar stacks in which the electronic coupling is poor, such that absorption resembles that of noninteracting polymer chains, or due to amorphous regions of the film. We estimate a volume fraction of $52 \pm 5\%$ for photophysical aggregates from the modeled contribution of the H-aggregate spectrum.

11.3.1.2 **Time-Resolved PL Measurements**

In order to explore exciton dynamics on picosecond timescales, we have carried out time-resolved PL spectroscopy by means of a spectrometer incorporating a streak camera. Figure 11.2a displays time-resolved PL measurements at 10 K. The PL spectrum decays substantially over subnanosecond timescales, and it redshifts by > 40 meV with weak evolution of the spectral bandshape. We examine this spectral evolution in Figure 11.2b. Figure 11.2c displays the early-time PL anisotropy, defined as $r = (I_{\parallel} - I_{\perp})/(I_{\parallel} + 2I_{\perp})$, where $I_{\parallel(\perp)}$ is the instantaneous PL intensity parallel (perpendicular) to the linear polarization of the pump pulse. At 10 K (open circles), r decays to 0.22 ± 0.03 within the instrument response of several picoseconds due to exciton self-trapping in the photophysical aggregate [16, 17], and does not evolve further on a subnanosecond window. In contrast, r decays to zero after 500 ps at room temperature. PL anisotropy decay is a signature of exciton diffusion. Note that we excite both H-aggregates and nonaggregates with similar probability at 2.33 eV (Figure 11.1), so exciton diffusion would result in a dynamic memory loss of the ensemble average transition dipole moment orientation. We observe this at 300 K because exciton diffusion is thermally activated, but not at 10 K (see Ref. [18] for relevant modeling). Therefore, at 10 K, excitons are immobile over the timescale of the dynamic redshift in Figure 11.2a. Another possibility could

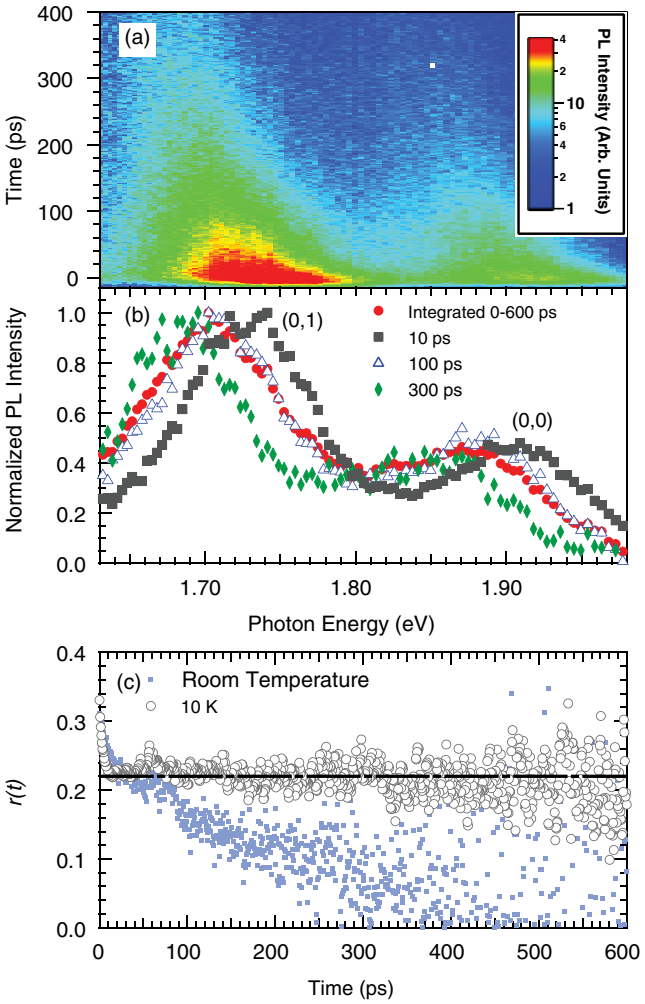

Figure 11.2 (a) Time-resolved PL spectrum (10 K, 19 μJ/cm^2 per pulse). (b) Normalized slices of (a) at various times. (c) Time-resolved PL anisotropy r at 10 K (open circles) and at room temperature (dots). The horizontal line indicates the average anisotropy between 20 and 600 ps.

be relaxation of excess vibrational energy following ultrafast excitation of the sample. Parkinson *et al.* [19] have reported that torsional relaxation of the backbone leads to more cofacial lamellar structures (more extended correlation of site energies in the aggregate) [14], leading to a dynamic loss of (0,0) intensity over ~13 ps at 300 K. We do not observe significant relaxation of the (0,0) relative intensity over the timescale of Figure 11.2a. Furthermore, upon increasing the temperature even slightly, the steady-state PL spectrum broadens significantly at 10 K [13], so we rule out thermal relaxation. We suggest that the dynamic spectral redshift of the PL

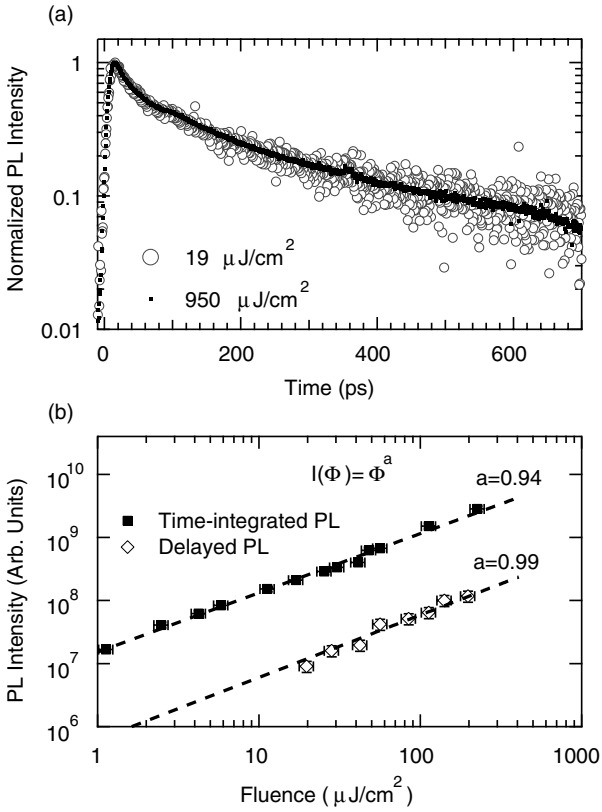

Figure 11.3 (a) Spectrally integrated PL intensity as a function of time following excitation at 2.33 eV, at two different fluences shown in the legend. (b) Fluence (Φ) dependence of the time-integrated, spectrally integrated PL intensity, and that of the spectrally integrated, delayed PL intensity over a temporal gate of 100 ns–500 μs. All measurements were carried out at 10 K.

spectrum results from an evolving electric field distribution [20] from photogenerated charges in the aggregate, which is consistent with charge photogeneration yields reported in the literature. If so, charges are generated over all timescales spanning 1 ns, by a mechanism not involving exciton diffusion.

We have investigated the fluence dependence of the excitation laser pulse train on the time-resolved and time-integrated PL intensity. Figure 11.3a displays the time-resolved PL intensity shown in Figure 11.2a, integrated spectrally over the range shown in that figure. Also shown in the figure is a similar measurement carried out with a laser fluence that is a factor of 50 higher. The PL decay dynamics do not depend on fluence over this range. Figure 11.3b displays the fluence dependence of the time-integrated PL intensity and the delayed PL intensity over a long temporal gate spanning up to 500 μs. Both PL signals show linear fluence dependence. Therefore, we can exclude the second-order phenomena such as singlet

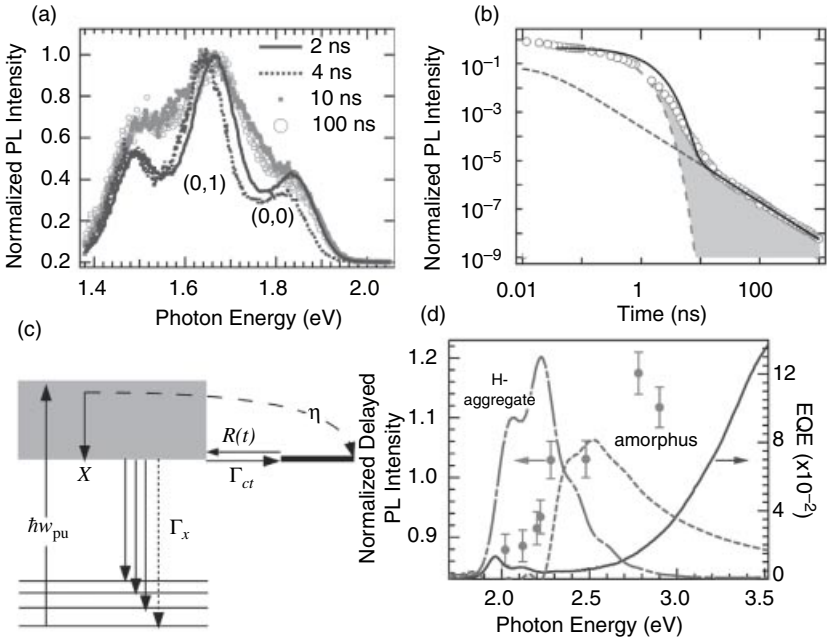

Figure 11.4 (a) Time-resolved PL spectra at 10 K. (b) Spectrally integrated PL intensity versus gate delay. Data from Figure 11.2 are included over subnanosecond timescales. The dashed lines represent a two-exponential fit with $\langle\tau\rangle = 235 \pm 23$ ps and an asympototic power law $[1/(1+(t/\tau')^{\alpha})]$ with $\alpha = 1.54 \pm 0.08$ and $\tau' \ll \langle\tau\rangle$. A fit to the model (Eq. (11.1)), represented schematically in (c), is shown as a continuous line (for $\eta = 0.03$, $\Gamma_{ct} = 0.35\ \text{ns}^{-1}$, $\Gamma_x = 1.23\ \text{ns}^{-1}$, $\nu = 4.37 \times 10^{13}\ \text{s}^{-1}$, $\mu = 0.54$). (d) Delayed PL excitation spectrum at 10 K, measured by phase-sensitive methods, superimposed on the H-aggregate and nonaggregate absorption spectra [15]. Also shown is the external quantum efficiency spectrum measured at 300 K in a ITO/PEDOT:PSS/P3HT/LiF/Al diode fabricated and encapsulated in a N_2-filled glove box.

exciton bimolecular annihilation dynamics as a mechanism for the PL spectral evolution observed in Figure 11.2.

We next consider delayed PL dynamics due to charge recombination from charges generated on picosecond timescales. Figure 11.4a displays time-gated PL spectra at 10 K. After a few nanoseconds, the aggregate spectrum is superimposed with a broader component with similar dynamics on those of the H-aggregate since this composite bandshape persists over microseconds. Figure 11.5 displays two time-resolved PL spectra shown in Figure 11.4a. In order to demonstrate that the spectra at 10 ns and longer times is a superposition of the aggregate spectrum (still evident after 4 ns) and a broad, less featured component, we have subtracted the 10 ns spectrum, normalized arbitrarily, from the 4 ns spectrum. The arbitrary normalization was chosen such that the vibronic structure of the aggregate is subtracted (note that the residual structure around 1.8 eV is probably due to unequal

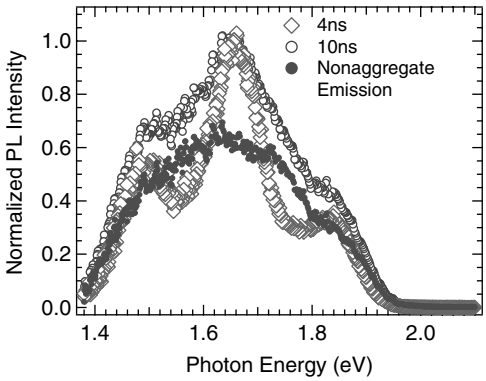

Figure 11.5 PL spectra at two temporal gates, taken from Figure 11.4a. The solid circles are the difference of the spectrum at 10 ns and 0.38 times its peak intensity at 4 ns.

(0,0) intensity of the two spectra). We base our conjecture that the delayed PL spectrum is a superposition of the spectrum of the H-aggregate and a featureless "nonaggregate" component on this procedure. While we know that the aggregate spectrum arises from lamellar stacks, we conjecture that the featureless spectrum arises from nonaggregate regions. It is reminiscent of red-emitting species found in amorphous polymer films, often referred to as excimers [21]. This emission has not been reported in steady-state or time-resolved PL spectra of P3HT in any solid-state microstructure. It is a product of delayed charge recombination, and it decays with the same power law dynamics as the regenerated H-aggregate. From the delayed PL bandshape in Figure 11.4a, we conclude that recombination occurs at the interface between H-aggregate and nonaggregate regions and can populate either species.

The total PL intensity decays exponentially over picosecond timescales, but asymptotically as a power law ($I(t) \propto t^{-1.54}$) for times much longer than the exciton lifetime (Figure 11.4b). This behavior can arise from unimolecular charge recombination [22] or by triplet bimolecular annihilation [23, 24]. We find that the delayed PL intensity varies linearly with the pump fluence (Figure 11.3), which permits us to assign the power law decay to exciton regeneration by charge recombination with a distribution of rates, as the other two possibilities would lead to a nonlinear fluence dependence. The power law decay is independent of temperature (Figure 11.3b), suggesting recombination by tunneling. We note that we cannot reproduce the measured time-resolved PL intensity as a simple superposition of a multiexponential and an asymptotic power law decay, as the time window spanning 1–10 ns features a PL decay over nearly three orders of magnitude that deviates significantly from either decay function (Figure 11.4b). This indicates that the two PL decay phenomena are not independent, but that one decay regime evolves into the other, with competing kinetics on nanosecond timescales. By integrating the PL intensity over timescales where the decay is nonexponential, we find that $\geq 12\%$ of

the time-integrated intensity is accounted for by slow recombination. This reflects a significant density of charge pairs.

Based on the results of Figures 11.2 and 11.4 and building upon previous reports [5–9], we construct the following photophysical picture, depicted schematically in Figure 11.4c. Upon photoexcitation, charge pairs are generated with efficiency η, and the rest of the population relaxes to self-trapped excitons x in < 1 ps[17]. These decay to the ground state with rate constant Γ_x, or charge separate with rate constant Γ_{ct}. Charge pairs may recombine to regenerate x with a temporal distribution $R(t)$. Thus,

$$\frac{dx}{dt} = -(\Gamma_x + \Gamma_{ct})x + \eta R(t) + \int_0^t \Gamma_{ct} x(t') R(t - t') dt' \tag{11.1}$$

Assume a distribution of charge pair distances $f(r) = \varepsilon e^{-\varepsilon r}$. The tunneling rate is $k(r) = \nu e^{-\beta r}$ and its time distribution is $R(t) = \int_0^\infty f(r) k(r) e^{-k(r)t} dr$. With $x(0) = 1 - \eta$, the Laplace transform of Eq. (11.1) is

$$\hat{x}(s) = \frac{1 - \eta + \eta \hat{R}(s)}{s + \Gamma_x + \Gamma_{ct}\left[1 - \hat{R}(s)\right]} \tag{11.2}$$

where $\hat{R}(s) = \mu \int_0^\infty e^{-(1+\mu)\chi} / (s/\nu + e^{-\chi}) d\chi$, $\chi = \beta r$, and $\mu = \varepsilon/\beta$. The model predicts biphasic dynamics with PL intensity $I(t) \propto \Gamma_x x(t)$, evolving as $I(t) \propto \exp(-\Gamma_x t)$ at short times and as $I(t) \propto t^{-(1+\mu)}$ at long times. We evaluate Eq. (11.2) as described elsewhere to recover $I(t)$[25].

The most robust parameter in this model is the ratio of the characteristic electron–hole separation (ε) and the distance dependence of charge tunneling (β): $\mu = \varepsilon/\beta = 0.54 \pm 0.08$, as it defines uniquely the slope of the power law decay at long times. Hence, $\varepsilon \approx 0.54\beta$; a significant fraction of charge pairs do not recombine in the microsecond timescale, as the tail of $f(r)$ extends beyond the characteristic length scale of $k(r)$. The charge pair population is expected to survive on much longer timescales, which is consistent with reports of a high residual charge density in P3HT at steady state [26, 27].

We next consider η. We cannot extract it uniquely from the model, as it is coupled to Γ_{ct}. Both parameters affect the amplitude of the power law decay without altering the decay rate. We probe the range of η that is consistent with the literature, and explore the consequences on Γ_{ct}. With $\Gamma_x = 1.23\ ns^{-1}$ (fixed by the slow part of the biexponential decay in Figure 11.3a) and $\nu = 4.37 \times 10^{13}\ s^{-1}$ (corresponding to the frequency of the aromatic C–C stretch measured by Raman spectroscopy) [28], we find that if we set $\eta = 3\%$, we require $\Gamma_{ct} = 0.35 \pm 0.05\ ns^{-1}$; but if $\eta = 30\%$, we can reproduce the data with $\Gamma_{ct} = 0$. With $\eta = 40\%$, we can no longer obtain a satisfactory fit of the amplitude of the power law component, which is overestimated. We have interpreted the dynamic redshift of the PL spectrum (Figure 11.2) as a consequence of an evolving electric field on the subnanosecond timescale, which is comparable to the exciton lifetime. In order to rationalize our time-resolved spectroscopic data, we therefore consider that $\Gamma_{ct} \Gamma_x$, which from the modeling, would imply that $\eta < 10\%$ in the solid-state microstructure of our films.

11.3.1.3 Quantum Chemical Calculations

If the two slow decaying emissive species in Figure 11.4a are due to regeneration of aggregate and nonaggregate excitations by charge tunneling, we propose that charges are initially generated at the interface between the two domains. To explore this further, we have carried out quantum chemical calculations. Semiempirical INDO/SCI excited state calculations (including 200 molecular orbitals in the active space) have been performed on the basis of snapshots extracted from molecular dynamics simulations of the stack, using a force field parameterized against high-level *ab initio* calculations (further details will be reported elsewhere). These calculations were carried out on a stack of 10 oligothiophene chains (Figure 11.6a) to represent the crystalline moieties in the higher molecular weight (i.e., longer chain) P3HT used in our experimental study. We note higher conformational disorder at the top/bottom of the stack, leading to a higher excitation energy in those regions

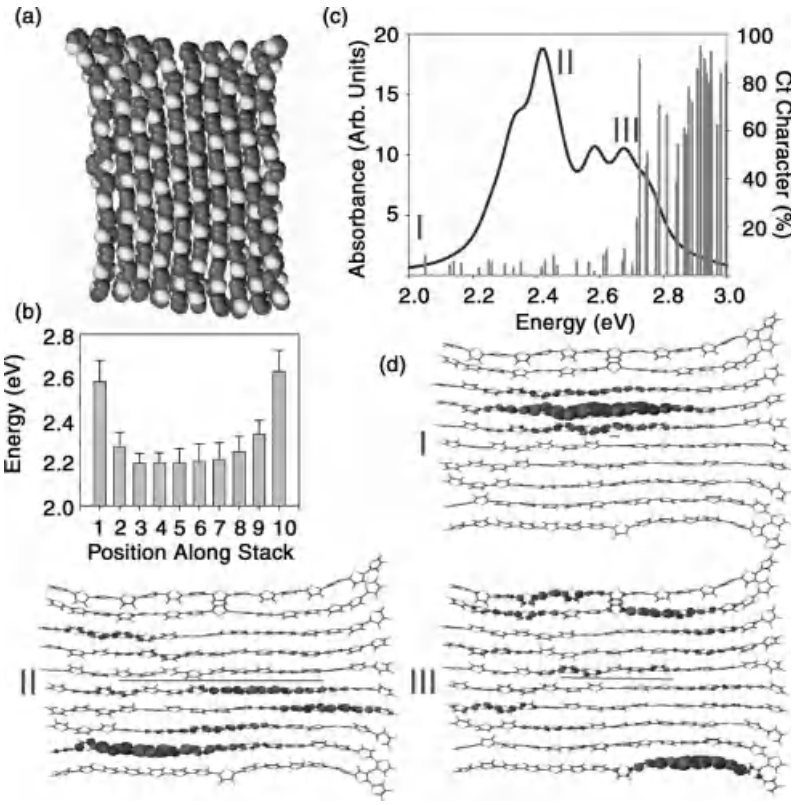

Figure 11.6 Results of quantum chemical calculations described in the text. (a) Snapshot of an aggregate architecture (15 mers in a 10 chain stack, see text for details). (b) Average site excitation energy (uncertainty is the variance), averaged over many excited state calculations on isolated conformers extracted from the stack. (c) Absorption spectrum for one configuration of the full stack superimposed on the corresponding CT character. (d) Transition densities (ground state–excited state overlap) for excitations of increasing energy.

compared to the center (Figure 11.6b). Figure 11.6c displays the calculated absorption spectrum in a given configuration. For all stack configurations studied, we always observe a shoulder at ~2.7 eV on the blue side of the main absorption band at ~2.4 eV. (Note that these energies are overestimated, but the ~0.3 eV difference is meaningful.) The excited states that are generated in this spectral region are quasi-degenerate with the lowest-lying charge transfer (CT) states, shown by the superimposed plot of CT character as a function of excitation energy. We can identify three regimes of the spatial distribution of transition densities, shown in Figure 11.6d. The excitation with the lowest transition energy (I) is always confined to the center of the stack over two to three sites as a result of disorder and is weakly emissive (H-aggregate); the intermediate excitation (II) carries most of the oscillator strength and is delocalized in the center of the stack; the higher lying excitation (III) is dominated by conformationally disordered chains at the ends of the stack, but it communicates with chains in the center so that charge separation of these higher energy states is possible. In our measurements, we excite ~0.3 eV above the (0,0) absorption, placing us at the limit of CT excitation predicted by Figure 11.6c. We have measured the delayed PL excitation spectrum, shown in Figure 11.4d. This reveals that excitation on the edge of the component of the absorption spectrum due to less ordered or amorphous species enhances the delayed PL yield, consistent with the significant CT character of excitons at these photon energies. Photocurrent measurements reveal that a further 0.4 eV energy is required to produce charge carriers (Figure 11.4d), underlining that our delayed PL measurements probe recombination of tightly bound geminate polaron pairs (not carriers) produced by excitation with energies 3 eV. Deibel *et al.* [10] reported that 0.42 eV excess energy above the optical gap is required to produce polaron pairs, and then a further 0.3 eV to generate photocarriers, consistent with our findings.

11.3.2 Solid-State Microstructure Dependence

11.3.2.1 Polymer Microstructure

With increasing molecular weight (i.e., chain length), most classical (semi-)flexible crystallizable polymers feature in their solid state a transition from an extended chain conformation (schematically depicted in Figure 11.7, bottom panel) to a structure consisting of alternating crystalline lamellae and amorphous (largely unordered) regions [29, 30]. The number of entanglements (or intertwinings) between individual chains in the system determines at what molecular weight this transition occurs. The reason for this is that they act as macromolecular friction loci, which result in an increased molecular connectivity and, as a consequence, a reduced mobility of the individual polymer chains. During solidification, flexible polymers of a molecular weight above a certain value, typically a few times the molecular weight between entanglements M_e (Figure 11.8), therefore normally only partially disentangle and, hence, only partially extend, even when they are constituted of perfectly regular chain molecules. Such macromolecules will usually form *semicrystalline* solids. In the melt, M_e is essentially independent of the chain

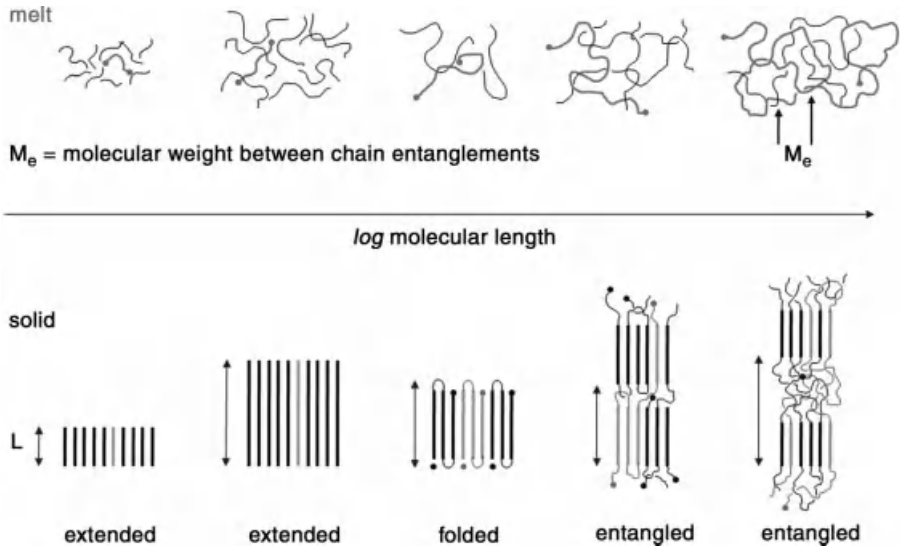

Figure 11.7 Development with molecular length (i.e., weight) of the macromolecular structure of a (semi)flexible polymer in the melt (top panel) and in the solid state (bottom panel). The molecular weight between entanglements M_e and long period L, that is, the total thickness of the crystalline and amorphous region, are defined as indicated.

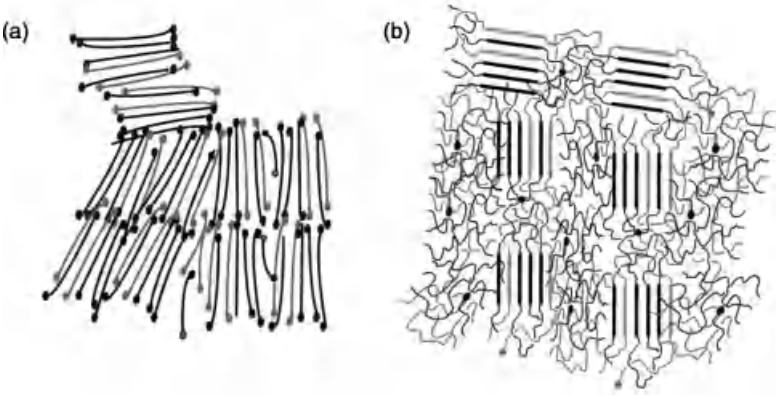

Figure 11.8 Schematic illustration of the solid-state microstructure of (a) low molecular weight, nonentangled macromolecules, and (b) high molecular weight material that is strongly entangled leading to a typical semicrystalline microstructure of molecularly ordered crystalline lamellae embedded in an amorphous matrix. The short-chain nature of low molecular weight materials provides for little interconnectivity between the extended-chain crystals, while for high molecular weight material, the individual domains are bridged with so-called tie molecules.

length and, hence, the number of entanglements per chain $N : N \propto M$ (with M being the molecular weight of the macromolecule). In solution, however, M_e depends on the volume fraction of the polymer ϕ_P, approximately as M_e (solution) $\sim M_e$ (melt)$/\phi_P$, and, thus, $N \propto M \cdot \phi$. Note also that the molecularly ordered lamellae in the resulting semicrystalline architectures resemble "building blocks" similar to those found in single crystals, for instance, grown from dilute solutions [31, 32], with the principal differences being in size, perfection, and macromolecular connectivity. The crystal thickness can generally only be assessed indirectly, for example, from the long period L, which is the total thickness of the crystalline and amorphous region.

Conjugated macromolecules, such as P3HT follow the same structural development [33, 34]. As a consequence, varying the molecular weight of, for example, P3HT, changes the solid-state microstructure from a single phase of randomly oriented chain-extended crystals (Figure 11.8a) to a two-phase amorphous/crystalline morphology as the molecular weight increases (Figure 11.8b). The latter creates interfaces between the amorphous and crystalline entities. Employing processing tools, such as solid-state processing [35], the amount of interfaces can be manipulated by varying the degree of crystallinity and the extent of chain extension.

11.3.2.2 Dependence of Time-Resolved PL on Molecular Weight

In order to explore the dependence of the time-resolved PL behavior reported in Figure 11.4b on the solid-state microstructure, we have studied two other films with a lower ($M_w = 12.4$ kg/mol) and higher ($M_w = 347$ kg/mol) molecular weights than that used for the studies in Section 11.3.1.2 ($M_w = 47.8$ kg/mol). We show the spectrally integrated, time-resolved PL dynamics in Figure 11.9. Although the low molecular weight sample shows a power law decay at long times that is similar to that reported in Figure 11.4b ($\mu = 0.5$), the high molecular weight sample displays significantly slower decay of the power law component ($\mu \approx 0.2$). In the higher molecular weight sample, the two-phase amorphous/crystalline

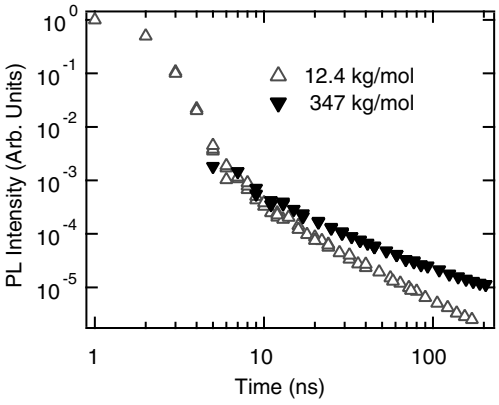

Figure 11.9 Time-resolved PL spectra at 10 K. for thin films of P3HT of two different molecular weights (M_w), indicated in the inset of the figure.

morphology (Figure 11.8b) results in a higher density of gradual interfaces between amorphous and crystalline domains. Consequently, the disordered energy landscape around these interfaces is likely to be more rugged, such that the distribution of electron–hole separation features a longer characteristic length ε^{-1}. The distance dependence for tunneling β is not expected to show a significant dependence on solid-state microstructure, so $\mu = \varepsilon/\beta$ is smaller quantity in the high molecular weight sample than in the low molecular weight one. The clear dependence of μ on film microstructure supports further our conclusion that exciton dissociation on picosecond timescales occurs at interfaces between aggregate and nonaggregate regions.

11.4 Conclusions

We have presented compelling evidence that excitons with sufficient energy dissociate *extrinsically* near interfaces between molecularly organized and less organized domains, underlining the importance of the disordered energy landscape in semicrystalline microstructures. This points to the importance of hot exciton dissociation in *neat* P3HT, which competes with dissociation at heterojunctions in photovoltaic diodes [1].

Acknowledgments

C.S. acknowledges NSERC and CRC in Organic Semiconductor Materials. G.L. and N.S. acknowledge the EC 7th Framework Program ONE-P project (Grant Agreement 212311). G.L. thanks the Royal Society. D.B., Research Director of FNRS, is also partly supported by ONE-P (NMP3-LA-2008-212311), the Inter-university Attraction Pole IAP 6/27 of the Belgian Federal Government, and FNRS/FRFC. P.L.K. thanks FQRNT, and M.S. thanks MELS/FQRNT.

References

1 Clarke, T.M. and Durrant, J.R. (2010) Charge photogeneration in organic solar cells. *Chem. Rev.*, **110** (11), 6736–6767.

2 Sirringhaus, H., Brown, P.J., Friend, R.H., Nielsen, M.M., Bechgaard, K., Langeveld-Voss, B.M.W., Spiering, A.J.H., Janssen, R.A.J., Meijer, E.W., Herwig, P., and de Leeuw, D.M. (1999) Two-dimensional charge transport in self-organized, high-mobility conjugated polymers. *Nature*, **401** (6754), 685–688.

3 Spano, F.C. (2006) Excitons in conjugated oligomer aggregates, films, and crystals. *Annu. Rev. Phys. Chem.*, **57**, 217–243.

4 Silva, C., Russell, D., Dhoot, A., Herz, L., Daniel, C., Greenham, N., Arias, A., Setayesh, S., Mullen, K., and Friend, R. (2002) Exciton and polaron dynamics in a step-ladder polymeric semiconductor: the influence of interchain order. *J. Phys. Condens. Mater.*, **14** (42), 9803–9824.

5 Hendry, E., Schins, J.M., Candeias, L.P., Siebbeles, L.D.A., and Bonn, M. (2004) Efficiency of exciton and charge carrier photogeneration in a semiconducting polymer. *Phys. Rev. Lett.*, **92** (19), 196601.

6 Ai, X., Beard, M.C., Knutsen, K.P., Shaheen, S.E., Rumbles, G., and Ellingson, R.J. (2006) Photoinduced charge carrier generation in a poly(3-hexylthiophene) and methanofullerene bulk heterojunction investigated by time-resolved terahertz spectroscopy. *J. Phys. Chem. B*, **110** (50), 25462–25471.

7 Sheng, C., Tong, M., Singh, S., and Vardeny, Z.V. (2007) Experimental determination of the charge/neutral branching ratio eta in the photoexcitation of pi-conjugated polymers by broadband ultrafast spectroscopy. *Phys. Rev. B*, **75** (8), 085206.

8 Cunningham, P.D. and Hayden, L.M. (2008) Carrier dynamics resulting from above and below gap excitation of P3HT and P3HT/PCBM investigated by optical-pump terahertz-probe spectroscopy. *J. Phys. Chem. C*, **112** (21), 7928–7935.

9 Piris, J., Dykstra, T.E., Bakulin, A.A., van Loosdrecht, P.H.M., Knulst, W., Trinh, M. T., Schins, J.M., and Siebbeles, L.D.A. (2009) Photogeneration and ultrafast dynamics of excitons and charges in P3HT/PCBM blends. *J. Phys. Chem. C*, **113** (32), 14500–14506.

10 Deibel, C., Mack, D., Gorenflot, J., Schoell, A., Krause, S., Reinert, F., Rauh, D., and Dyakonov, V. (2010) Energetics of excited states in the conjugated polymer poly(3-hexylthiophene). *Phys. Rev. B*, **81** (8), 085202.

11 Spano, F.C. (2005) Modeling disorder in polymer aggregates: the optical spectroscopy of regioregular poly(3-hexylthiophene) thin films. *J. Chem. Phys.*, **122** (23), 234701.

12 Spano, F.C. (2007) Erratum: Modeling disorder in polymer aggregates: the optical spectroscopy of regioregular poly (3-hexylthiophene) thin films. *J. Chem. Phys.*, **126**, 159901.

13 Clark, J., Silva, C., Friend, R.H., and Spano, F.C. (2007) Role of intermolecular coupling in the photophysics of disordered organic semiconductors: aggregate emission in regioregular polythiophene. *Phys. Rev. Lett.*, **98** (20), 206406.

14 Spano, F.C., Clark, J., Silva, C., and Friend, R.H. (2009) Determining exciton coherence from the photoluminescence spectral line shape in poly(3-hexylthiophene) thin films. *J. Chem. Phys.*, **130** (7), 074904.

15 Clark, J., Chang, J.F., Spano, F.C., Friend, R.H., and Silva, C. (2009) Determining exciton bandwidth and film microstructure in polythiophene films using linear absorption spectroscopy. *Appl. Phys. Lett.*, **94** (16), 163306.

16 Chang, M.H., Frampton, M.J., Anderson, H.L., and Herz, L.M. (2007) Intermolecular interaction effects on the ultrafast depolarization of the optical emission from conjugated polymers. *Phys. Rev. Lett.*, **98** (2), 027402.

17 Collini, E. and Scholes, G.D. (2009) Coherent intrachain energy migration in a conjugated polymer at room temperature. *Science*, **323** (5912), 369–373.

18 Beljonne, D., Hennebicq, E., Daniel, C., Herz, L., Silva, C., Scholes, G., Hoeben, F., Jonkheijm, P., Schenning, A., Meskers, S., Phillips, R., Friend, R., and Meijer, E. (2005) Excitation migration along oligophenylenevinylene-based chiral stacks: delocalization effects on transport dynamics. *J. Phys. Chem. B*, **109** (21), 10594–10604.

19 Parkinson, P., Mueller, C., Stingelin, N., Johnston, M.B., and Herz, L.M. (2010) Role of ultrafast torsional relaxation in the emission from polythiophene aggregates. *J. Phys. Chem. Lett.*, **1** (19), 2788–2792.

20 Kersting, R., Lemmer, U., Mahrt, R.F., Leo, K., Kurz, H., Bässler, H., and Gobel, E.O. (1993) Femtosecond energy relaxation in π-conjugated polymers. *Phys. Rev. Lett.*, **70** (24), 3820–3823.

21 Schwartz, B.J. (2003) Conjugated polymers as molecular materials: how chain conformation and film morphology influence energy transfer and interchain interactions. *Annu. Rev. Phys. Chem.*, **54**, 141–172.

22 Schweitzer, B., Arkhipov, V.I., Scherf, U., and Bässler, H. (1999) Geminate pair

recombination in a conjugated polymer. *Chem. Phys. Lett.*, **313** (1–2), 57–62.

23 Gerhard, A. and Bassler, H. (2002) Delayed fluorescence of a poly (*p*-phenylenevinylene) derivative: triplet–triplet annihilation versus geminate pair recombination. *J. Chem. Phys.*, **117** (15), 7350–7356.

24 Rothe, C. and Monkman, A. (2005) Regarding the origin of the delayed fluorescence of conjugated polymers. *J. Chem. Phys.*, **123** (24), 244904.

25 Brosseau, C.N., Perrin, M., Silva, C., and Leonelli, R. (2010) Carrier recombination dynamics in $In_xGa_{1(x}N$/GaN multiple quantum wells. *Phys. Rev. B*, **82** (8), 085305.

26 Dicker, G., de Haas, M.P., and Siebbeles, L.D.A. (2005) Signature of exciton annihilation in the photoconductance of regioregular poly(3-hexylthiophene). *Phys. Rev. B*, **71** (15), 155204.

27 Ferguson, A.J., Kopidakis, N., Shaheen, S. E., and Rumbles, G. (2008) Quenching of excitons by holes in poly(3-hexylthiophene) films. *J. Phys. Chem. C*, **112** (26), 9865–9871.

28 Gao, Y., Martin, T.P., Thomas, A.K., and Grey, A.K. (2010) Resonance Raman spectroscopic and photocurrent imaging of polythiophene/fullerene solar cells. *J. Phys. Chem. Lett.*, **1** (1), 178–182.

29 Wunderlich, B. (1973) *Macromolecular Physics. Volume 1: Crystal Structure, Morphology, Defects*, vol. 1, Academic Press, New York.

30 Flory, P.J. and Yoon, D.Y. (1978) Molecular morphology in semicrystalline polymers. *Nature*, **272**, 226–229.

31 Keller, A. (1957) A note on single crystals in polymers: evidence for a folded chain configuration. *Philos. Mag.*, **2**, 1171–1175.

32 Keller, A. (1958) *Growth and Perfection of Crystals*, John Wiley & Sons, Inc., New York, p. 498.

33 Brinkmann, M. and Ramnou, P. (2007) Effect of molecular weight on the structure and morphology of oriented thin films of regioregular poly(3-hexylthiophene) grown by directional epitaxial solidification. *Adv. Mater.*, **17**, 101–108.

34 Vikar, A.A., Mannsfield, S., Bao, Z., and Stingelin, N. (2010) Organic semiconductor growth and morphology considerations for organic thin-film transistors. *Adv. Mater.*, **22**, 3857–3875.

35 Baklar, M.A., Koch, F., Kumar, A., Domingo, E.B., Campoy-Quiles, M., Feldman, K., Yu, L., Wobkenberg, P., Ball, J., Wilson, R.M., McCulloch, I., Kreouzis, T., Heeney, M., Anthopoulos, T., Smith, P., and Stingelin, N. (2010) Solid-state processing of organic semiconductors. *Adv. Mater.*, **22** (35), 3942–3947.

12
Recent Progress in the Understanding of Exciton Dynamics within Phosphorescent OLEDs

Sebastian Reineke and Marc A. Baldo

12.1
Introduction

Phosphorescence is now widely adopted in commercial organic light-emitting devices (OLEDs). It has reached its position as the premier high-efficiency technology after a long development effort. Despite this, many of the underlying mechanisms remain unclear, attracting continuing research interest and the attention of regular scientific reviews [1–3]. Here, we focus on recent developments in three areas of particular relevance to the operation of phosphorescent OLEDs. Following the lifecycle of the excited states, we first review advances in the understanding of exciton formation, with a particular focus on emerging competitors to phosphorescence. Then, we review progress in the understanding and control of exciton transport and harvesting, before concluding with a summary of present knowledge about exciton quenching.

12.2
Exciton Formation

12.2.1
Background

In an OLED, the conversion of electrical energy into light is mediated by excitons. It is the properties of the excitons that primarily determine the overall luminescent efficiency of the device.

An exciton may be thought of as a two-electron system: one electron is excited into a previously unfilled orbital of a given molecule or polymer, while the second remains in a partially filled ground state. The partially filled ground state is often known as a hole, and imagined to possess a positive charge.

The exciton formation process in OLEDs begins with electrons and holes injected at the electrodes. As the charges drift together under the influence of an electric field, there are two principal interactions between them: coulombic and

Physics of Organic Semiconductors, Second Edition. Edited by Wolfgang Brütting and Chihaya Adachi

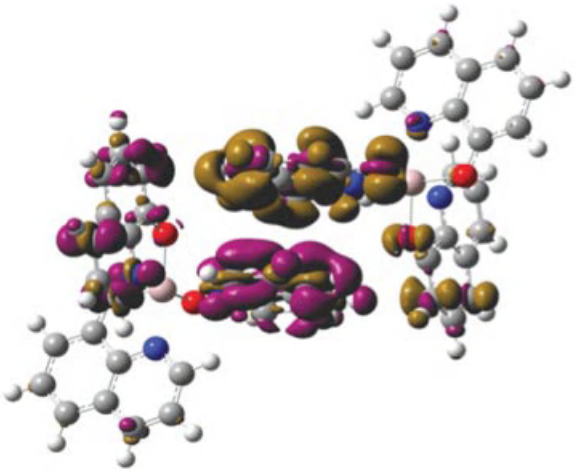

Figure 12.1 The calculated charge density difference between the singlet and the triplet CT states, and the ground state, in a δ-AlQ_3 dimer [1]. The molecule on the right (left) hand is constrained to be negatively (positively) charged, and gold (purple) surfaces enclose volumes where the CT state has more (fewer) electrons. Analogous plots for the triplet CT state are visually indistinguishable from the above plot. Reproduced from Ref. [4].

exchange. At separations of a few nanometers, the coulombic attraction binds the charges together and they are no longer able to escape one another by thermal diffusion. Typically, this occurs before the electron and hole form an exciton on a single molecule or polymer chain. For example, Figure 12.1 shows an electron and a hole on two adjacent molecules of the archetype OLED material tris(8-hydroxyquinoline) aluminum (AlQ_3) [4]. This combination of an electron and hole is also bound and forms what is known as a charge transfer (CT) state.

Exchange effects are weaker than coulombic interactions but they have a profound effect on the operation of an OLED. The total spin of the two electron system may be either $S=0$ or $S=1$. The $S=0$ state is antisymmetric under particle exchange, but the $S=1$ contains three possible states, all symmetric under particle exchange. The degeneracies of each state are reflected in their titles, the $S=0$ state is known as a singlet and the $S=1$ is a triplet. Crucially, the opposite sign of the exchange interaction in singlet and triplet states creates an energetic difference. The exchange splitting between singlets and triplets is usually substantial in excitons (>0.1 eV) [5]. But exchange interactions are more controversial in the CT states. Measurements suggest appreciable splittings [4,6], but theory suggests that the exchange interaction may also be very weak [7]. Also, the ordering of the CT states is debated [6–8]; in some cases, the singlet CT state is predicted to have the lowest energy [8].

In addition to its effect on exchange interactions, the spin of the exciton controls its luminescence. The ground state of most molecules is a singlet state, and because the emission of a photon conserves spin, typically only singlet excited

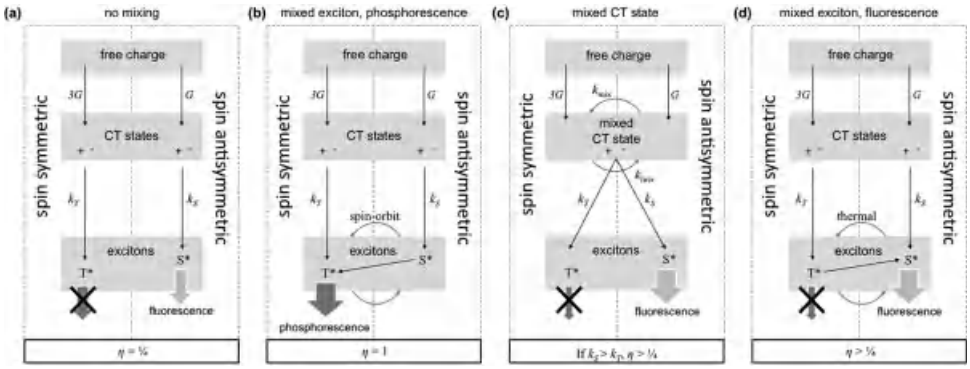

Figure 12.2 A model of exciton formation [9]. The formation rates of triplet and singlet excitons are k_S and k_T, respectively. The mixing rate at room temperature is k_{mix}. G is a constant determined by the formation rate of charge transfer states. η is the maximum quantum efficiency of light emission.

states can emit light. Radiation of singlet excitons is fast, often efficient, and is known as fluorescence. The probability of luminescence from the remaining triplet states is generally so low that almost all their energy is lost to nonradiative processes.

A model of exciton formation [1,9] is summarized in Figure 12.2. Excitons are formed from CT states, which in turn are formed from injected electrons and holes. Most importantly, the model predicts that in the absence of a process that mixes the singlet and triplet channels, only one quarter of the injected charges will form luminescent (singlet) excitons, irrespective of the relative formation rates of singlets and triplets.

12.2.2
Spin Mixing for Higher Efficiency

There are two opportunities for spin mixing in OLEDs: the exciton and the CT state. Below, we briefly summarize two methods of exciton mixing, phosphorescence and thermally activated delayed fluorescence (TADF), and we also review progress toward higher efficiencies by exploiting CT state mixing.

12.2.2.1 Exciton Mixing and Phosphorescence

It is well known now that heavy atoms such as platinum or iridium can enhance spin–orbit coupling within a molecule or polymer [10–12]. This in turn can mix the excited singlet and triplet states such that the triplet gains some singlet character and the decay of the triplet state is partially allowed (cf. Figure 12.2b). The emission of light is still significantly slower than fluorescence, but if singlet–triplet mixing in the exciton state yields a radiative decay rate that is faster than the nonradiative rate, then the luminescence can be efficient. This emission of light from a "disallowed" transition is known as phosphorescence.

The exciton mixing required for efficient phosphorescence enhances intersystem crossing (ISC) from the singlet exciton to the lower energy triplet exciton. Thus, phosphorescence can harness 100% of the injected carriers [13]. Also, by making the lowest energy state in the system emissive, phosphorescence is naturally robust to the presence of mixing anywhere in the formation path. This is not true for enhanced fluorescence following CT state mixing, where exciton mixing can generate nonemissive triplet excitons.

Next, we describe alternatives before returning to summarize the technological prospects of phosphorescence.

12.2.2.2 CT State Mixing and Enhanced Fluorescence

If the emissive material does not possess sufficient exciton mixing to enable strong phosphorescence, it is still theoretically possible to obtain light from 100% of the injected charges. The mixing process can instead be performed in the CT state. Including CT mixing yields a maximum quantum efficiency (photons/electrons) of [7],

$$\eta = \frac{1 + k_{\mathrm{mix}}/k_{\mathrm{T}}}{4 + k_{\mathrm{mix}}/k_{\mathrm{T}}(1 + 3k_{\mathrm{T}}/k_{\mathrm{S}})} \tag{12.1}$$

There are two important parameters: the rate of singlet–triplet CT state mixing, k_{mix}, and the ratio of exciton formation rates, $k_{\mathrm{S}}/k_{\mathrm{T}}$. If $k_{\mathrm{mix}} \gg k_{\mathrm{T}}$ then η becomes a function of the exciton formation rates, that is, $\eta = k_{\mathrm{S}}/(k_{\mathrm{S}} + 3k_{\mathrm{T}})$. These rates have been calculated by numerous groups. While the predictions are highly material dependent [14], k_{S} is generally expected to be faster than k_{T} because the energetic separation between the CT state and the singlet exciton is smaller than the gap between the CT state and the triplet exciton. Consequently, singlet exciton formation is less Marcus inverted than triplet exciton formation [5].

The general expectation that $k_{\mathrm{S}}/k_{\mathrm{T}} > 1$ suggests that $\eta > {}^{1}/_{4}$ in many fluorescent OLEDs. These predictions, however, assumed that the mixing rate is fast ($k_{\mathrm{mix}} \gg k_{\mathrm{T}}$). The rate of singlet–triplet CT mixing is governed by the strength of the coupling between singlet and triplet CT states, which is typically less than 10^{-4}–10^{-5} eV in purely organic systems due to weak spin–orbit and spin–lattice interactions [7].

Thermally stimulated luminescence measurements [15] by Kadashchuk *et al.* have demonstrated that CT state mixing does occur over long timescales (seconds) [6]. Perhaps, the first measurement of the CT mixing rate at shorter timescales was performed by Reufer *et al.* [16]. In that work, excitons in the prototypical conjugated polymer ladder-type poly(*para*-phenylene) (PhLPPP) were generated by an optical pulse, then separated into charges using an electric field pulse, before finally being allowed to reform and emit [16]. The singlet exciton population is monitored by the fluorescence [16]. But very weak Pd doping in the polymer enhances phosphorescence and also allows the triplet exciton population to be measured [16].

The data in Figure 12.3 shows a decrease in both fluorescence and phosphorescence during the electrical pulse [16]. Then, both the singlet and the triplet channels are observed to rebound as the charges separated by the field recombine [16].

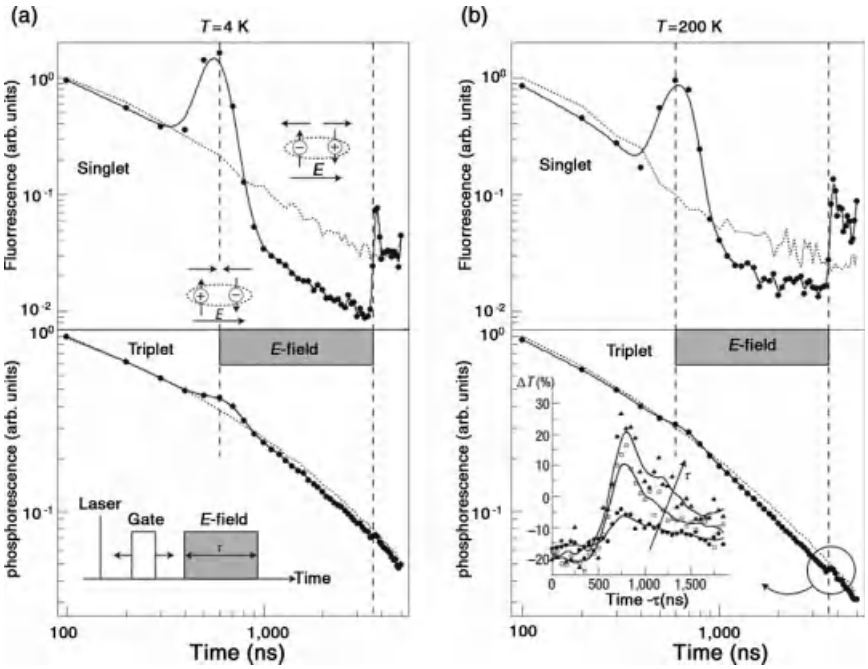

Figure 12.3 Field modulated recombination of optically generated singlet and triplet charge carrier pairs. (a) At 4 K. (b) At 200 K (electric field: ~1 MV/cm; duration marked by vertical dashed lines). Dotted lines indicate the PL dynamics in the absence of a field. All spectra were recorded in 200 ns gate windows. The inset in (b) shows the effect of pulse length *T*on the triplet overshoot post-turn-off for 3 μs (circles), 7 μs (squares), and 11 μs (triangles) long pulses. Reproduced from Ref. [16].

Crucially, the inset shows that the phosphorescent "rebound" scales approximately linearly with the length of the electrical pulse [16]. This, together with the overall similarity of both singlet and triplet channel dynamics, confirms that there is no appreciable mixing of the CT states prior to recombination [16].

While Reufer *et al.* found mixing rates slower than $10^5\,s^{-1}$ in PhLPPP [16], a later study by Ford *et al.* established a *minimum* rate of $2 \times 10^6\,s^{-1}$ in blends of poly(9,9-dioctylfluorene-*co*-benzothiadiazole) (F8BT) with poly(9,9-dioctylfluorene-*co*-bis-*N*,*N*′-(4- butylphenyl)-bis-*N*,*N*′-phenyl-1,4-phenylene-diamine) (PFB) [17]. Although the latter measurement may be consistent with much faster mixing rates, if the results of Reufer *et al.* hold generally, then fluorescent materials do not possess sufficient mixing in their CT states to achieve $\eta > {}^1/_4$. As discussed previously [1,14], direct measurements of η are contradictory. Some measurements suggest that $\eta > {}^1/_4$ and others that $\eta = {}^1/_4$ [1,14]. Studies have also suggested that $\eta > {}^1/_4$ in fluorescent polymers but not in small molecules [18]. Unfortunately, no measurement technique appears unimpeachable, with comparisons between electroluminescence and photoluminescence prone to underestimation of the photoluminescent efficiency because 70–80% of the emitted light is waveguided and

subject to self-absorption [19] and OLED-based measurements subject to the uncertainty of charge quenching and exciton formation in traps [14]. The quantum efficiency of fluorescent OLEDs is the ultimate measure, and to date, it has remained substantially below that of phosphorescent OLEDs.

The apparent absence of sufficient CT mixing in some fluorescent materials suggests that to enhance fluorescence, an OLED could be engineered to specifically mix CT states *but not excitons* [4]. It is important not to mix the exciton state because that results in triplet exciton formation, which lowers the fluorescent efficiency. Figure 12.4a shows an OLED with a selective CT mixing layer (X-OLED). As in other heterostructure OLEDs, excitons are formed on the lower energy side of the interface between the hole transport layer (HTL) and the electron transport layer (ETL). The emissive material is the red fluorophore 4-(dicyanomethylene)-2-methyl-6-julolidyl-9-enyl-4*H*-pyran (DCM2). It is inserted between the HTL/ETL interface, doped into a wide band-gap host material, in a narrow layer just 50 Å thick, to minimize the possibility of efficiency artifacts caused by shifts in the exciton formation zone [20].

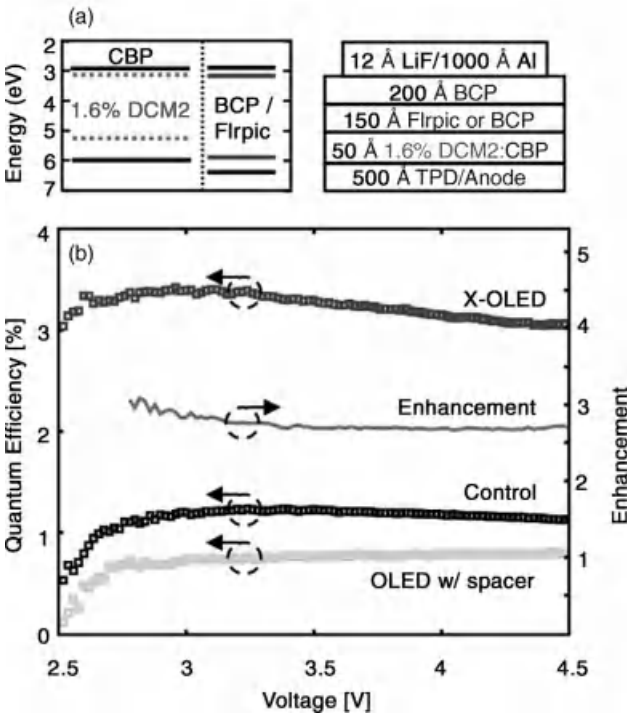

Figure 12.4 Compares the performance of the enhanced fluorescent OLED to the control device. The external quantum efficiency of the OLED with mixing reaches a maximum of 3.4% or 2.8 times larger than the control. An OLED identical to the X-OLED, but with the FIrpic layer spaced from DCM2 by 100 Å of BCP does not show enhanced efficiency. This is consistent with the enhancement in fluorescence resulting from spin mixing at the exciton formation interface. Reprinted from Ref. [4].

To obtain CT state mixing and enhanced fluorescence (cf. Figure 12.2c), the ETL consists of a thin film of iridium(III) bis [(4,6-difluorophenyl) pyridinato-N,$C^{2'}$] picolinate (FIrpic), followed by an additional conventional ETL (BCP) [21]. The presence of iridium in FIrpic enhances spin–orbit coupling and mixes the spin state of the electron it carries. The spin of the CT state consisting of an electron on FIrpic and a hole on DCM2 is, therefore, also mixed. Furthermore, calculations similar to those described above give a singlet–triplet CT gap of 60 meV for a $FIrpic^{-}/DCM2^{+}$ heterodimer [4]. Thus, the interfacial CT states should be appreciably split. FIrpic will not quench DCM2, as FIrpic phosphoresces in the blue green. It is employed here, however, purely as an ETL. Indeed, its electroluminescent quantum efficiency is only 0.2% in a neat film. In addition, FIrpic's spin mixing effect on neighboring molecules is reduced by the bulky side groups that surround its central heavy metal atom, reducing intersystem crossing effects in DCM2. In a control device, the FIrpic ETL is replaced by an ETL with low spin–orbit coupling: 2,9-dimethyl-4,7-diphenyl-1,10-phenanthroline (BCP) [14]. Figure 12.4b shows the external quantum efficiency of control- and X-OLED together with the corresponding improvement obtained by employing CT mixing.

Based on this study, CT mixing could be used to enhance the efficiency of OLEDs without appreciably lengthening the excited state lifetime. Much work remains, however, to extend the approach to other fluorescent emitters and demonstrate an improvement at high brightness.

12.2.2.3 **Thermally Activated Delayed Fluorescence**

Another route to enhancing the overall luminescence efficiency from fluorescent materials makes use of excitons that are mixed back to the fluorescent channel from a nonradiative reservoir in the molecular triplet manifold by means of thermal activation (cf. Figure 12.2d) [22]. For this mixing process to be efficient, the energetic splitting of singlet and triplet states (ΔE_{ST}) must be comparable to $k_B T$. The first observation of TADF in OLEDs was reported by Endo *et al.* [23], discussing various tin(IV) fluoride–porphyrin complexes, which possess energetic splittings of approximately 0.4 eV, which still is too large for efficient reverse ISC from the triplet back to the singlet.

From the quantum mechanical viewpoint, the energy difference ΔE_{ST} is proportional to the exchange integral K between spatial overlap of the highest occupied and lowest unoccupied molecular orbital. Thus, the splitting can be reduced by minimizing K (it is worth noting that fullerenes also show TADF [22] because of moderate ΔE_{ST}, which is caused by the molecules' symmetry rather than by a small K). The same group (Endo *et al.*) succeeded in developing a hybrid molecule 2-biphenyl-4,6-bis(12-phenylindolo[2,3-*a*]carbazole-11-yl)-1,3,5-triazine (PIC-TRZ) as shown in Figure 12.5a containing donor (indolocarbazole) and acceptor (triazine) units [24], respectively, resulting in vanishing spatial overlap (cf. Figure 12.5a) and strongly reduced splitting of $\Delta E_{ST} = 0.11$ eV (cf. Figure 12.5b). This leads to a very high reverse ISC efficiency of 29%. Figure 12.5c gives clear evidence for TADF showing that both the prompt and the delayed emission coincide. Further promising results about TADF-based electroluminescence have been discussed by Deaton *et al.* for a bis(phosphine)diarylamido dinuclear copper(I) complex with

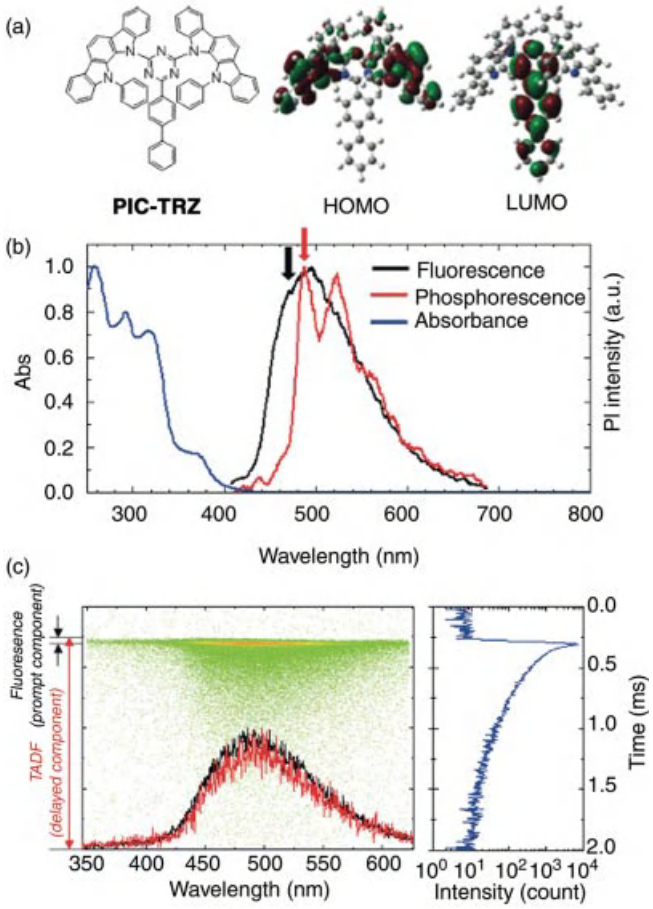

Figure 12.5 (a) Molecular structure and calculated HOMO and LUMO orbital distributions as obtained from a Gaussian 03 (B3LYP/cc-pVDZ) calculation of PIC-TRZ. (b) Photophysical properties of PIC-TRZ: Fluorescence and phosphorescence are obtained at 5 K for a 6 wt% mixed film of 1,3-bis (9-carbazolyl)benzene:PIC-TRZ. (c) Streak-camera image of the samples. Reproduced from Ref. [24].

$\Delta E_{ST} = 0.10$ eV [25]. At low excitation levels, OLEDs based on this copper complex reach an external quantum efficiency of 16%, clearly outperforming the 5% limit for conventional fluorescent materials.

The triplet reservoir that feeds the luminescent singlet state is the major source of loss in this concept because triplet excitons pile up if the thermally activated intersystem crossing is slow. Thus, triplet–triplet annihilation [26] becomes a severe issue that strongly reduces the device efficiency at high excitation levels. All reports on TADF to date exhibit a pronounced roll-off in efficiency with increasing current density. For instance, Figure 12.6 shows the quantum efficiency versus current density of a device based on the copper complex of Deaton *et al.* dropping to

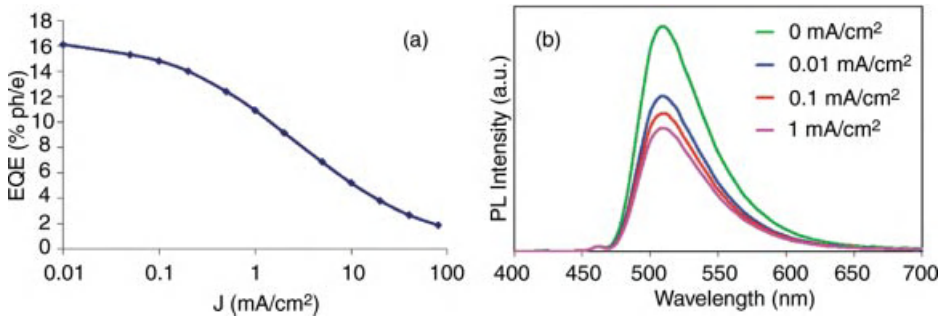

Figure 12.6 (a) EQE and (b) EL spectra both as a function of current density of a TADF device based on the copper complex of Deaton *et al.* The initial EQE drops to half its value at only a few mA/cm^2. Reproduced from Ref. [25].

half its initial value at only a few mA/cm^2 [25]. In contrast, a similar drop in efficiency is observed at roughly two orders of magnitude higher current density for phosphorescent devices [27,28].

12.2.2.4 Summary: Comparison between Phosphorescence, Extrafluorescence, and TADF

Although extrafluorescence from CT state mixing and TADF have shown promise, it seems unlikely that either approach will soon replace phosphorescence in mainstream applications. The challenge in extrafluorescence is to design systems where the CT state mixing competes with rapid exciton formation rates while also not mixing the exciton. TADF will require smaller singlet–triplet splittings to increase the intersystem crossing rate and reduce the density of triplet excitons. Thus, phosphorescence appears likely to remain the preferred technology in high-efficiency OLEDs. Its only important weaknesses are the relatively long lifetime of the excited state (see 12.4), which enhances quenching processes and a reliance at present on expensive metals such as iridium or platinum to perform the spin mixing.

12.3 Distributing Excitons in the Organic Layer(s)

Once an exciton is formed in the organic semiconductor within an OLED, it is a challenge to efficiently direct it to the desired emissive state. Here, we will address key requirements for efficient phosphorescence and point out strategies to exploit the nature of triplet excitons to manage the exciton distribution, especially for white light-emitting devices.

12.3.1.1 Excitonic Confinement: Host–Guest Systems

Many phosphorescent emitters exhibit a noticeable reduction in luminescence quantum yield for bulk layers [12,29]. On the other hand, strongly improved quantum yields are obtained whenever the phosphor is diluted into another

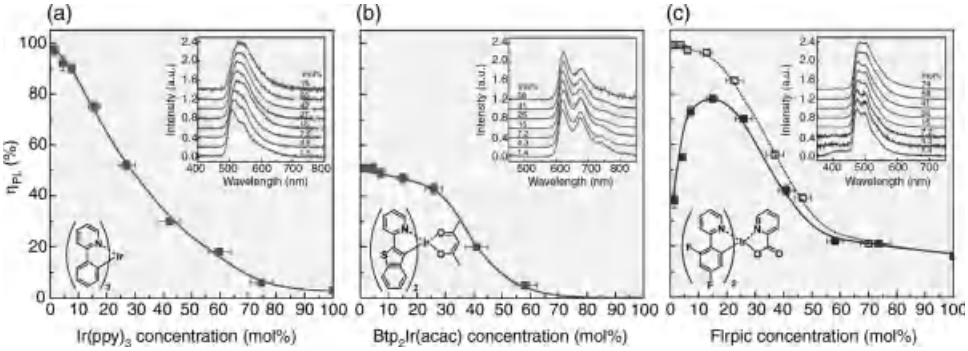

Figure 12.7 Concentration dependence of three different phosphorescent emitters ($Ir(ppy)_3$, $BtpIr_2(acac)$, and FIrpic) as dispersed into a proper host material. For the blue emitter FIrpic, data are shown for an endothermic and an exothermic system. Reproduced from Ref. [29].

material – the host material (cf. Figure 12.7). The phosphorescent dopant is accordingly referred to as guest material. This effect is called concentration or aggregation quenching [30,31]. High quantum yields are typically achieved with a concentration of the phosphor in the host–guest system in the range of $1 - 10$ wt%.

The host material must be selected carefully with respect to its and the phosphor's energy levels. It is a prerequisite for efficient emission that the excitation created on host sites be transferred to the phosphor, unless emission from the host is desired. Here, singlet excitons are mainly transferred via dipole–dipole energy transfer (Förster mechanism [32]) while triplet excitons migrate from site to site, ultimately reaching a phosphorescent molecule, based on Dexter-type [33] transfer steps (hopping). Once the excitation is transferred to guest sites, it is necessary to confine the excitation on the phosphor so that radiative recombination can occur efficiently [28,34]. In case the phosphorescent emitter is in its lowest T_1 state, migration to other molecules proceeds via highly efficient Dexter-type triplet–triplet energy exchange steps. Therefore, the relative position of the matrix triplet level with respect to the phosphor T_1 state is important. The highest phosphorescence quantum yield of the mixed system can be expected for an exothermic system, where the triplet level of the matrix is higher in energy compared to the phosphor. By reducing the energy of the host triplet level to a resonant or endothermic system, respectively, the phosphorescent quantum yield of the mixed film will decrease accordingly as more excitations remain on host sites [35].

12.3.1.2 **Exciton Generation Zone**

The way excitons are spatially distributed within the device is vastly determined by the electrical (transport) properties of the various materials used. And, equally true for fluorescent and phosphorescent OLEDs, excitons are typically formed in a thin slab of an organic layer in the proximity of an interface to an adjacent material layer. This is because truly ambipolar materials, which transport electrons and holes equally well, are rare. Furthermore, both carrier species often need to pass different

energy barriers on their way to the emission layer. Typically, the width of the generation zone is below 5 nm [36], and even its approximation as a delta distribution often holds [37]. Especially for multicolor devices, as adding thickness or layers to the device will not automatically broaden the exciton generation zone, it remains a key challenge to address more spatially displaced emissive states.

One way of increasing the width of exciton generation zone is to bring two host materials together in a way that one is predominately hole conductive, the other electronconductive, thus forming a double emission layer (DEML). Here, excitons are formed on either side of the interface between these two layers. This concept has successfully been used for demonstrating high-efficiency monochrome [38] and white [35] phosphorescent devices. The exciton generation zone can also be broadened by mixing materials with altering transport properties to form a blend with ambipolar character [39]. Ultimately, inherently ambipolar materials are desired that spatially distribute charges efficiently, enabling exciton formation throughout the layer. At present, much synthetic effort is spent on developing these materials.

12.3.1.3 **Exciton Migration**

Owing to the relatively long excited state lifetime of phosphors – typically in the range of microseconds – the exciton is likely to be transferred to other energetically accessible states. Because the donor (D) is an excited phosphor in its triplet state, it can transfer its energy efficiently to the singlet or triplet state of an acceptor (A) molecule via Förster type [32]:

$$^3D^* + {}^1A \rightarrow {}^1D + {}^1A^* \tag{12.2}$$

or Dexter-type [33]

$$^3D^* + {}^1A \rightarrow {}^1D + {}^3A^* \tag{12.3}$$

energy transfer, respectively. Here, the asterisks indicate excited states. The latter triplet–triplet transfer requires two simultaneous spin-flips, which are only possible incorporating exchange interactions. Energy transfer between one species of phosphorescent molecules should solely follow Dexter transfer-mediated hopping steps, because the fluorescent state of the identical acceptor it too high in energy. In contrast, however, Kawamura *et al.* investigated the intraspecies energy transfer (triplet–triplet transfer) of the phosphorescent systems shown in Figure 12.7 based on Förster's theory with good agreement [30]. For these emitters, they derived corresponding Förster radii of 1.4, 0.8, and 1.1 nm for fac-tris(2-phenylpyridine) iridium [$Ir(ppy)_3$], bis[2-(2′-benzothienyl)pyridinato-$N,C^{3\prime}$]acetylacetonato)iridium(III) [$BtpIr_2$(acac)], and FIrpic, respectively [30]. It is argued that multiple dipole–dipole transfers that lead to a dampening of energy are the cause of the observed concentration quenching (reduction of PL efficiency with increasing phosphor content – cf. Figure 12.7). This interpretation is in contrast to the publication of Kobayashi *et al.*, where the authors introduce a nonemissive state 121 meV above the lowest $Ir(ppy)_3$–^{3}MLCT (metal-to-ligand CT) state with much higher decay rates compared

to the triplet sublevels to explain the concentration quenching [31]. Even so results published to date cannot establish a secure interpretation of the mechanism behind the concentration dependence of phosphors, the above stated results of Kawamura *et al.* clearly indicate that the energy exchange between phosphorescent molecules occurs efficiently up to distances of 2 nm. This coincides with the limit of the interaction range of the Dexter-type hopping steps.

The consequence of this discussion for energy migration is simple. While phosphors that differ in their emission wavelength will undergo cascade energy transfer from high to low energy sites with efficiencies approaching unity when in close proximity to each other, spatial distances down to 2 nm can decouple these excited states. Figure 12.8 shows a set of samples comprising three phosphors, that is, FIrpic, $Ir(ppy)_3$, and $Ir(MDQ)_2(acac)$ [iridium(III)bis(2-methyldibenzo[f,h]quinoxaline) (acetylacetonate)]. Each emitter is doped with 10 wt% into a wide-gap material 4,4′,4″-tris(*N*-carbazolyl)-triphenylamine (TCTA) having a T_1 level of 2.83 eV above the respective emitter levels, forming a 1 nm thin layer. The different slabs of emitter doped films are intermitted by TCTA interlayers (see Figure 12.8 for the sample layout). Thus, in addition to a spatial separation, the TCTA interlayer is used as an energetic barrier for triplet exciton movement based on Dexter-type hopping steps. Figure 12.8 shows that even a 2 nm spacing of different emitters can maintain strong emission from all emitters. In contrast, without the interlayers the emission

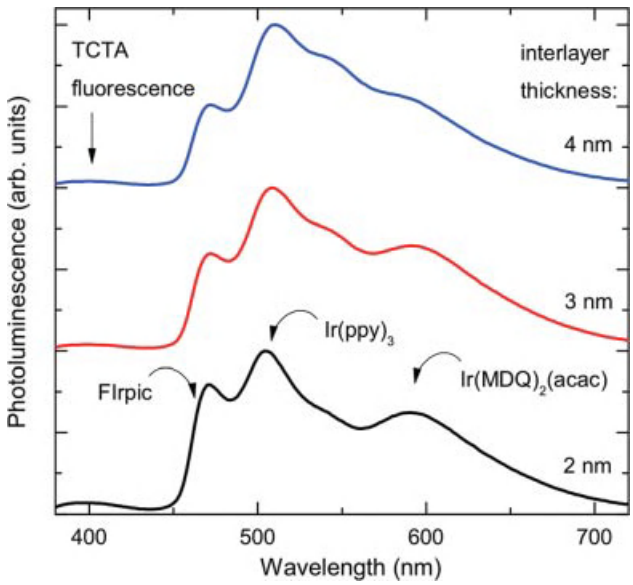

Figure 12.8 Photoluminescence spectra of an emission layer consisting of multiple thin phosphor-doped layers (1 nm and 10 wt% each) that are intermitted by intrinsic layers of the host material TCTA of various thickness (2, 3, or 4 nm). The samples have the following general sequence (with R = $Ir(MDQ)_2(acac)$, G = $Ir(ppy)_3$, B = FIrpic, and I = TCTA): TCTA:R/I (x nm)/TCTA:G/I (x nm)/TCTA:B/I (x nm)/TCTA:B/I (x nm)/TCTA:G/I (x nm)/TCTA:R.

from the high-energy phosphors (FIrpic and $Ir(ppy)_3$) is fully quenched, resulting in solely red emission.

These finding go hand in hand with known concepts for white light-emitting devices incorporating phosphors. D'Andrade *et al.* made use of the same properties dispersing three different emitters into one wide-gap material at different concentration varying from 0.5 to 20 wt% that effectively assures interspecies spacing [40]. Another way is to unite the concept of the DEML with intrinsic interlayers to suppress complete energy transfer to low-energy emitters [35].

12.3.1.4 **Triplet Harvesting**

The combination of a fluorescent blue emitter with phosphorescent green and red phosphors to form a hybrid emission layer is attracting much interest because it provides an alternative to the use of blue phosphors. The latter are the current bottleneck in white devices because they noticeably increase the operating voltage and remain chemically unstable. Sun *et al.* first proposed white OLEDs with hybrid fluorescent/phosphorescent emission layers to efficiently utilize both singlets and triplets [41]. However, the authors used a fluorescent emitter with a triplet level below the corresponding energies of the phosphors [42]. Thus, the blue fluorophor still remains a potential triplet exciton trap within the system. In order to avoid exciton losses in the triplet manifold of the blue fluorophor, special emitters have been introduced possessing a small singlet–triplet splitting [42–44].

The hybrid fluorescence–phosphorescence concept dates to the first paper on phosphorescent OLEDs, where it was employed to demonstrate different singlet and triplet exciton diffusion length and triplet exciton harvesting by phosphors [10]. For *N,N′*-di-1-naphthalenyl-*N,N′*-diphenyl-[1,1′:4′,1″:4″,1‴-quaterphenyl]-4,4″-diamine (4P-NPD), the first material known to be used for white OLEDs in this approach, the triplet diffusion length in the bulk material has been determined to 11 nm [37]. Figure 12.9a illustrates the working principle of triplet harvesting: the exciton generation zone is fixed to one interface within the blue bulk fluorophor. This is followed by host–guest system formed by the blue fluorescent and a red phosphorescent emitter. By increasing the thickness of the intrinsic blue layer it

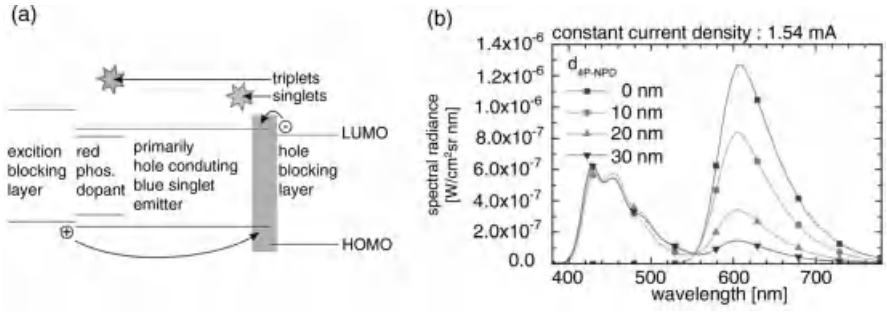

Figure 12.9 (a) Diagram illustrating the working principle of triplet harvesting. (b) Electroluminescence of a set of OLEDs varying in the blue fluorescent spacer layer (4P-NPD) thickness. Adapted from Ref. [45].

also acts as a spacer that decouples the red phosphor from the site of exciton generation. While singlet excitons, as a result of their short lifetime, recombine at the position of the generation interface, the triplet excitons diffuse further into the spacer layer ultimately being harnessed by the phosphor. This effect can be seen in Figure 12.9b [45]: For a large thickness of the blue spacer (30 nm), almost only blue fluorescence is observed. By reducing the spacing, the contribution of the red phosphor increases noticeably while the intensity of the fluorescence remains constant. This is a clear indication that the phosphorescent material diffusively harvests triplets of the blue fluorophor. Finally with no spacer, solely red phosphorescence is observed, indicating that singlet excitons are also transferred to the phosphor.

12.4 High Brightness Effects in Phosphorescent Devices

Phosphorescent OLEDs pay for their fourfold increase in internal quantum efficiency with at least one order of magnitude longer excited state lifetime compared to conventional fluorescent dyes. Thus, these excitons are highly exposed to nonlinear quenching processes that limit the inherently high device efficiency at high excitation levels. Generally, three processes account for triplet exciton quenching: (i) triplet-polaron quenching, (ii) electric field-induced exciton dissociation, and (iii) triplet–triplet annihilation (TTA) [46,47]. Among those, TTA is the only process that scales with the square of the exciton density n, for which it dominates the decrease in efficiency at high exciton densities [36]. It is worth noting that field-induced dissociation, as suggested by Kalinowski *et al.* to be the dominant effect [47], is not observed for state-of-the-art OLEDs [36]. Furthermore, the overall effect of triplet-polaron quenching on the efficiency roll-off easily can vary over orders of magnitude as it strongly depends on the device charge carrier balance.

Generally, the dynamics of the guest triplet exciton density $n(t)$ upon short, pulsed excitation is governed by the following rate equation:

$$\frac{\mathrm{d}n(t)}{\mathrm{d}t} = -\frac{n(t)}{\tau} - f\, k_{\mathrm{T}}(t) n(t)^2 \tag{12.4}$$

where f accounts for the number of triplet states that are deactivated. Consequently, it can have values of 1/2 or 1. Typically, $f = 1/2$ is assumed, that is, the acceptor state will ultimately keep its excited configuration. The first term represents the monomolecular deactivation of the triplet exciton density n that is inversely proportional to the excited state lifetime τ. Furthermore, $k_{\mathrm{T}}(t)$ describes the TTA rate.

TTA in solid mixed films can have different underlying mechanisms [48]. One of them is a single-step long-range interaction (dipole–dipole coupling), based on Förster-type energy transfer (cf. Figure 12.10a). It marks the limit for every phosphorescent mixed system as it solely depends on the spectral properties of the emitting guest. Interestingly, Staroske *et al.* recently introduced this mechanism as the intrinsic limit for any phosphorescent system [49]. Triplet–triplet annihilation mediated by Förster-type energy transfer is possible if the donor is a

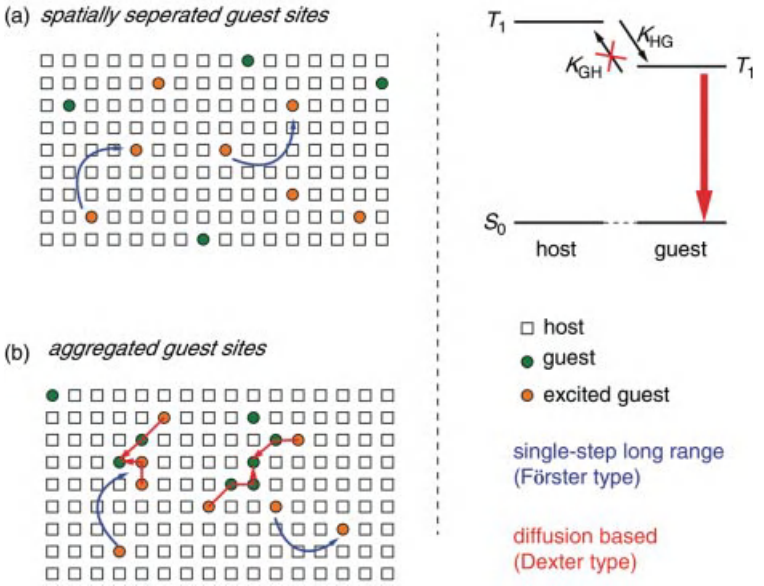

Figure 12.10 Scheme illustrating TTA based on (a) single-step long-range energy transfer for an exothermic host–guest system. In the scenario (b), an additional TTA channel is shown mediated by hopping-assisted migration of triplet excitons in clusters of guest molecules. Adapted from Ref. [48].

phosphorescent material, because then transition moment for $T_1 \rightarrow S_0$ is nonzero. Moreover, the transition of the acceptor molecule, that is, $T_1 \rightarrow T_n$, lies within the triplet manifold and is therefore an allowed transition. According to Förster's theory of energy transfer [32], the rate of TTA is proportional to the spectral overlap of phosphorescent emission of the donor and the excited triplet state absorption of the acceptor. Within the Förster framework, the rate constant $k_{T,F}(t)$ can be approximated to [50]

$$k_{T,F}(t) = \frac{2}{3}\pi R_F^3 \sqrt{\frac{\pi}{\tau t}} \tag{12.5}$$

with the Förster radius R_F for the transfer to an excited guest molecule. Note that there is no regime for which the transfer rate is time independent. Furthermore, this model suggests that TTA does not depend on the dopant concentration and that TTA breaks down if the intermolecular spacing between the phosphorescent molecules exceeds R_F.

If the host–guest system is exothermic, that is, the triplet level of the host is higher than the one of the guest, the single-step long-range mechanism should be the only channel for TTA for typical guest concentrations ranging from 1 to 10 mol%. In their analysis, Staroske *et al.* pointed out that the phosphorescent systems comprising the archetype emitter $Ir(ppy)_3$ suffer from stronger TTA than predicted by their model. They suggested that efficient triplet migration, taking place in locally

dense clusters of guest molecules by means of exciton hopping (Dexter-type energy transfer), leads to the unexpected impact of TTA (cf. Figure 12.10b) [49].

The corresponding TTA rate constant for hopping-assisted exciton motion reads [51]

$$k_{T,D}(t) = 8\pi D\bar{a}\left(1 + \frac{\bar{a}}{\sqrt{2\pi Dt}}\right) \tag{12.6}$$

with the interaction distance $\bar{a}$ and the diffusion constant D. For times much greater than the nearest-neighbor hopping time $\bar{a}/6D$, this rate constant can be approximated to a time-independent form: $k_{T,D} = 8\pi D\bar{a}$ [50]. Note that TTA within this model is – in contrast to the single-step long-range model – concentration dependent, which is accounted for in the diffusion constant D [48].

In the following, experimental evidence will be provided that supports the picture of guest aggregates in the mixed film that ultimately leads to strongly enhanced triplet–triplet annihilation. Time-resolved spectroscopy is commonly used to investigate TTA. Here, the sample of interest is excited with a short laser pulse and the luminescence response of the sample is resolved as a function of time. When visualized in semilogarithmic plot, TTA leads to a curvature in the transient signal directly after the excitation pulse, which will transform into a monoexponential decay at longer times/lower excitation levels (cf. Figure 12.11c). Now solely by analyzing the decay curve it is not possible to distinguish which mechanism (single-step long- range and/or hopping assisted) contributes to TTA. Thus, indirect methods need to be applied to differentiate between those two.

For this purpose, three mixed films of TCTA:Ir(ppy)$_3$ were prepared with a thickness of 20 nm and varying guest concentrations from 0.1 to roughly 10 mol% [52]. The highly diluted sample is used to assure spatial separation of the guest molecules (taking into account their expected tendency to aggregate). In Figure 12.11a, the solid box indicates the triplet exciton densities that can be created in the system without seeing a TTA signature in the transient signal, that is, the decay curve is fully monoexponential. Now, the monoexponential data with highest triplet density can be used to determine an upper limit for the Förster radius R_F. Based on Eqs. (12.4) and (12.5), calculated fits can be used to approach the monoexponential decay shown in Figure 12.11b from large R_F (with stronger TTA impact) to small values. Within experimental error, 6 nm was found to be an upper limit, while $\leq$3 nm showed best agreement with this set of data [52]. In comparison, based on photophysical properties of Ir(ppy)$_3$, Staroske *et al.* estimated the Förster radius for this TTA process to be 2.9 nm [49].

Figure 12.11c plots decay curves of the two samples with higher guest concentration, of which the 9.3 mol% sample is closest to application in real devices [36,46]. The solid lines correspond to fit calculations on the single-step long-range model yielding radii of 9 and 10.5 nm for 1.1 and 9.3 mol% of guest concentration, respectively. Two important facts prove that an additional TTA channel in this system must be present: (i) In contrast to model predictions, these fits show concentration dependence (because R_F is increased from 9 to 10.5 nm). Note that this is a noticeable difference as the TTA rate constant $k_{T,F}$ is proportional to the third power of

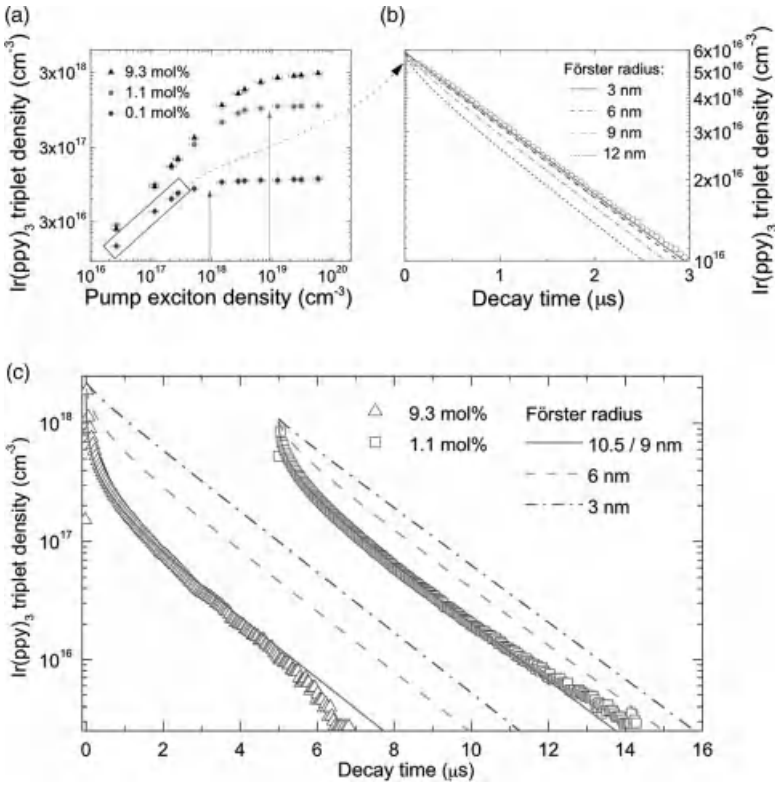

Figure 12.11 (a) Guest triplet exciton density versus pump exciton density (initial singlet states formed on the matrix material) for three different $Ir(ppy)_3$ concentrations in the matrix TCTA. (b) Transient signal of the phosphorescence of the highly diluted sample at highest triplet density in the linear regime, as indicated in (a). In addition, shown are calculated fits according to Eqs. (12.4) and (12.5). (c) Decay curves of two samples with 9.3 and 1.1 mol% guest concentration, respectively (split in time for clarity). Fits according to the single-step long-range model (cf. Eqs. (12.4) and (12.5)) are plotted for various Förster radii. Adapted from Ref. [48].

the Förster radius R_F. (ii) The derived values by far exceed both the upper limit and the estimated value of 2.9 nm. To illustrate this discrepancy, Figure 12.12 plots the external quantum efficiency of a standard OLED structure comprising this TCTA:Ir $(ppy)_3$ emitter system. Going to higher brightness, the efficiency strongly decreases. However, using the data of the decay curves from Figure 12.11c and a simple expression, $n(j) = \nu\,\tau j/(ew)$, to relate the exciton density n to current density j luminance [53], it is possible to determine the impact of Förster-based TTA. Here, ν is the probability of exciton formation, e the elementary charge, and w the width of exciton generation zone. Assuming 3 nm as the Förster radius, which yields almost perfect monoexponential curves in Figure 12.11c, the external quantum efficiency of this TCTA:$Ir(ppy)_3$-based OLED should remain constant up to an approximate device brightness of 30 000 cd/m^2, as indicated by the solid line.

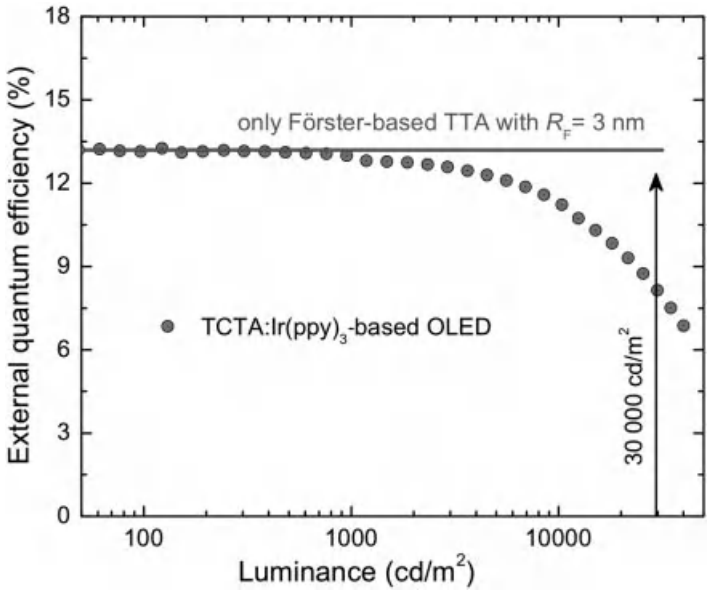

Figure 12.12 External quantum efficiency of a state-of-the-art green phosphorescent OLED comprising $Ir(ppy)_3$ as emitter molecule (for device details, see, for example, Ref. [36]). Thick solid line indicates that the EQE would remain constant up to a brightness of 30 000 cd/m^2, if only the single-step long-range model would contribute to TTA with a Förster radius of 3 nm, as suggested by Staroske *et al.* [49] and Reineke *et al.* [52].

The best proof to support the picture of guest aggregates is their visualization. Therefore, a 50 nm thick TCTA:$Ir(ppy)_3$ mixed film with a high concentration of roughly 10 wt% was analyzed by high-resolution transmission electron microscopy (TEM) (for details see Ref. [52]). The TEM image is shown in Figure 12.13. Here, the dark contrast refers to atoms with higher mass, that is, the iridium atoms in the mixed film. Clearly, clustered features with sizes up to 10 nm are visible, resulting in a strong nonuniformity of the material mixture.

It is worth mentioning that there is more experimental evidence supporting the picture of guest aggregation and efficient triplet migration in these clusters that is beyond the scope of this review. Relevant data includes the suppression of triplet motion by inserting high T_1 material acting as a barrier [27] and the spectral red-shift of phosphor emission with increasing guest concentration [29,54]. The latter effect can be used to reduce the aggregation and thus TTA by using phosphorescent emitter molecules with smaller dipole moments [53].

To conclude, the discussion of TTA annihilation and guest aggregation may give an answer to a very general question regarding phosphorescence: Considering the exciton densities needed for bright OLEDs and the sufficiently short excited lifetime of phosphors that are compatible with the RC-time of the devices [55], why are high guest concentrations typically ranging from 5 to 20 mol% necessary for optimal OLED efficiency? Note here that the photoluminescence efficiency of phosphorescent

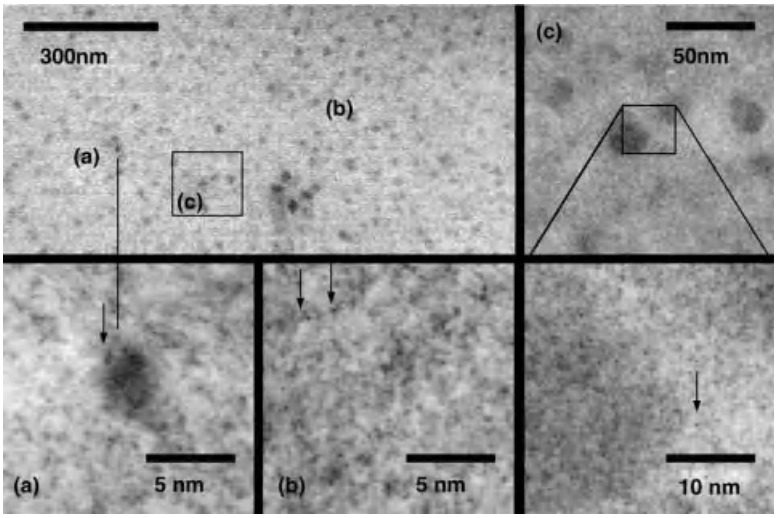

Figure 12.13 High-angle annular dark field (HAADF) transmission electron microscopy image of a 50 nm mixed film of a TCTA:$Ir(ppy)_3$ with a concentration of 10 wt% [52]. Higher resolution images are taken for the regions (a), (b), and (c). Image (c) is additionally shown with a further zoom-in on the bottom right. Dark contrast refers to atoms with high mass, that is, iridium atoms. Arrows point to single iridium atoms in the focal plane of the image. Adapted from Ref. [48].

emitters at these concentrations are already up to 10% lower than their maximum values at low densities (cf. Figure 12.7) [29]. The clusters of phosphorescent molecules leave regions that are well below the average guest concentration. Thus, whenever an exciton is formed on the host material in these regions, it may be unable to find a phosphorescent site for recombination, ultimately reducing the efficiency of the system. Hence, a system with spatially well-distributed emitters may be used at lower emitter concentration and consequently yield higher internal efficiencies.

Acknowledgments

This work was supported as part of the Center for Excitonics, an Energy Frontier Research Center funded by the US Department of Energy, Office of Science, Office of Basic Energy Sciences under Award Number DE-SC0001088 (MIT).

References

1 Baldo, M.A. and Segal, M. (2004) *Physics of Organic Semiconductors* (ed. W. Brütting), Wiley-VCH Verlag GmbH, Weinheim.

2 Hartmut, Y. (ed.) (2007) *Highly Efficient OLEDs with Phosphorescent Materials*, Wiley-VCH Verlag GmbH, Weinheim.

3 Pfeiffer, M. and Forrest, S.R. (2003) *Nanoelectronics and Information Technology* (ed. R. Waser), Wiley-VCH Verlag GmbH, Weinheim.

4 Segal, M., Singh, M., Rivoire, K., Difley, S., Van Voorhis, T., and Baldo, M.A. (2007) *Nat. Mater.*, **6**, 374.

5 Pope, M. and Swenberg, C. (1982) *Electronic Processes in Organic Crystals*, 1st edn, Oxford University Press, Oxford.

6 Kadashchuk, A., Vakhnin, A., Blonski, I., Beljonne, D., Shuai, Z., Bredas, J.L., Arkhipov, V.I., Heremans, P., Emelianova, E.V., and Bassler, H. (2004) *Phys. Rev. Lett.*, **93**, 066803.

7 Barford, W., Bursill, R.J., and Makhov, D.V. (2010) *Phys. Rev. B*, **81**, 035206.

8 Difley, S., Beljonne, D., and Van Voorhis, T. (2008) *J. Am. Chem. Soc.*, **130**, 3420.

9 Wohlgenannt, M., Tandon, K., Mazumdar, S., Ramasesha, S., and Vardeny, Z.V. (2001) *Nature*, **409**, 494.

10 Baldo, M.A., O'Brien, D.F., You, Y., Shoustikov, A., Sibley, S., Thompson, M.E., and Forrest, S.R. (1998) *Nature*, **395**, 151.

11 Baldo, M.A., Thompson, M.E., and Forrest, S.R. (1999) *Pure Appl. Chem.*, **71**, 2095.

12 Baldo, M.A., Lamansky, S., Burrows, P.E., Thompson, M.E., and Forrest, S.R. (1999) *Appl. Phys. Lett.*, **75**, 4.

13 Adachi, C., Baldo, M.A., Thompson, M.E., and Forrest, S.R. (2001) *J. Appl. Phys.*, **90**, 5048.

14 Segal, M., Baldo, M.A., Holmes, R.J., Forrest, S.R., and Soos, Z.G. (2003) *Phys. Rev. B*, **68**, 075211.

15 Kadashchuk, A., Skryshevskii, Y., Vakhnin, A., Ostapenko, N., Arkhipov, V. I., Emelianova, E.V., and Bassler, H. (2001) *Phys. Rev. B*, **63**, 115205.

16 Reufer, M., Walter, M.J., Lagoudakis, P.G., Hummel, A.B., Kolb, J.S., Roskos, H.G., Scherf, U., and Lupton, J.M. (2005) *Nat. Mater.*, **4**, 340.

17 Ford, T.A., Ohkita, H., Cook, S., Durrant, J.R., and Greenham, N.C. (2008) *Chem. Phys. Lett.*, **454**, 237.

18 Wilson, J.S., Dhoot, A.S., Seeley, A.J.A.B., Khan, M.S., Köhler, A., and Friend, R.H. (2001) *Nature*, **413**, 828.

19 Currie, M.J., Mapel, J.K., Heidel, T.D., Goffri, S., and Baldo, M.A. (2008) *Science*, **321**, 226.

20 Kim, J.-S., Ho, P.K.H., Greenham, N.C., and Friend, R.H. (2000) *J. Appl. Phys.*, **88**, 1073.

21 Holmes, R.J., Forrest, S.R., Tung, Y.-J., Kwong, R.C., Brown, J.J., Garon, S., and Thompson, M.E. (2003) *Appl. Phys. Lett.*, **82**, 2422.

22 Baleizao, C., Nagl, S., Borisov, S.M., Schäferling, M., Wolfbeis, O.S., and Berberan-Santos, M.N. (2007) *Chem. Eur. J*, **13**, 3643.

23 Endo, A., Ogasawara, M., Takahashi, A., Yokoyama, D., Kato, Y., and Adachi, C. (2009) *Adv. Mater.*, **21**, 4802.

24 Endo, A., Sato, K., Yoshimura, K., Kai, T., Kawada, A., Miyazaki, H., and Adachi, C. (2011) *Appl. Phys. Lett.*, **98**, 083302.

25 Deaton, J.C., Switalski, S.C., Kondakov, D. Y., Young, R.H., Pawlik, T.D., Giesen, D.J., Harkins, S.B., Miller, A.J.M., Mickenberg, S.F., and Peters, J.C. (2010) *J. Am. Chem. Soc.*, **132**, 9499.

26 Kepler, R.G., Avakian, P., Lewis, J.C., and Abramson, E. (1963) *Phys. Rev. Lett.*, **10**, 400.

27 Reineke, S., Schwartz, G., Walzer, K., and Leo, K. (2007) *Appl. Phys. Lett.*, **91**, 123508.

28 Su, S.J., Gonmori, E., Sasabe, H., and Kido, J. (2008) *Adv. Mater*, **20**, 4189.

29 Kawamura, Y., Goushi, K., Brooks, J., Brown, J.J., Sasabe, H., and Adachi, J. (2005) *Appl. Phys. Lett.*, **86**, 071104.

30 Kawamura, Y., Brooks, J., Brown, J.J., Sasabe, H., and Adachi, C. (2006) *Phys. Rev. Lett.*, **96**, 017404.

31 Kobayashi, T., Ide, N., Matsusue, N., and Naito, H. (2005) *Jap. J. Appl. Phys.*, **44**, 1966.

32 Förster, T. (1948) *Ann. Physik*, **2**, 55.

33 Dexter, D.L. (1953) *J. Chem. Phys.*, **21**, 836.

34 Goushi, K., Kwong, R., Brown, J.J., Sasabe, H., and Adachi, C. (2004) *J. Appl. Phys.*, **95**, 7798.

35 Reineke, S., Lindner, F., Schwartz, G., Seidler, N., Walzer, K., Lüssem, B., and Leo, K. (2009) *Nature*, **459**, 234.

36 Reineke, S., Walzer, K., and Leo, K. (2007) *Phys. Rev. B*, **75**, 125328.

37 Wünsche, J., Reineke, S., Lüssem, B., and Leo, K. (2011) *Phys. Rev. B*, **81**, 245201.

38 Zhou, X., Qin, D.S., Pfeiffer, M., Blochwitz-Nimoth, J., Werner, A., Drechsel, J., Maennig, B., Leo, K., Bold, M., Erk, P., and Hartmann, H. (2002) *Appl. Phys. Lett.*, **81**, 4070.

39 Hsiao, C.H., Chen, Y.H., Lee, T.C., Hsiao, C.C., and Lee, J.H. (2006) *Appl. Phys. Lett.*, **89**, 163511.

40 D'Andrade, B.W., Holmes, R.J., and Forrest, S.R. (2004) *Adv. Mater.*, **16**, 624.

41 Sun, Y.R., Giebink, N.C., Kanno, H., Ma, B.W., Thomspon, M.E., and Forrest, S.R. (2006) *Nature*, **440**, 908.

42 Schwartz, G., Reineke, S., Rosenow, T.C., Walzer, K., and Leo, K. (2009) *Adv. Funct. Mater.*, **19**, 1219.

43 Schwartz, G., Pfeiffer, M., Reineke, S., Walzer, K., and Leo, K. (2007) *Adv. Mater.*, **19**, 3672.

44 Kondakova, M.E., Deaton, J.C., Pawlik, T. D., Giesen, D.J., Kondakov, D.Y., Young, R.H., Royster, T.L., Comfort, D.L., and Shore, J.D. (2010) *J. Appl. Phys.*, **107**, 014515.

45 Rosenow, T.C., Furno, M., Reineke, S., Olthof, S., Lüssem, B., and Leo, K. (2010) *J. Appl. Phys.*, **108**, 113113.

46 Baldo, M.A., Adachi, C., and Forrest, S.R. (2000) *Phys. Rev. B*, **62**, 10967.

47 Kalinowski, J., Stampor, W., Mezyk, J., Cocchi, M., Virgili, D., Fattori, V., and Di Marco, P. (2002) *Phys. Rev. B*, **66**, 235321.

48 Reineke, S. (2011) Controlling excitons: concepts for phosphorescent organic LEDs at high brightness, PhD thesis (Akademische Verlagsgemeinschaft München).

49 Staroske, W., Pfeiffer, M., Leo, K., and Hoffmann, M. (2007) *Phys. Rev. Lett.*, **98**, 197402.

50 Engel, E., Leo, K., and Hoffmann, M. (2006) *Chem. Phys.*, **325**, 170.

51 Chandrasekhar, S. (1943) *Rev. Mod. Phys.*, **15**, 0001.

52 Reineke, S., Schwartz, G., Walzer, K., Falke, M., and Leo, K. (2009) *Appl. Phys. Lett.*, **94**, 163305.

53 Reineke, S., Rosenow, T.C., Lüssem, B., and Leo, K. (2010) *Adv. Mater.*, **22**, 3189.

54 Baldo, M.A., Soos, Z.G., and Forrest, S.R. (2001) *Chem. Phys. Lett.*, **347**, 297.

55 Thompson, M.E. (2007) *MRS Bull.*, **32**, 694.

13
Organometallic Emitters for OLEDs: Triplet Harvesting, Singlet Harvesting, Case Structures, and Trends

Hartmut Yersin, Andreas F. Rausch, and Rafał Czerwieniec*

13.1
Introduction

During the last years, organotransition metal compounds have attracted much attention due to outstanding emission properties. For example, colors over the whole visible range are realizable and high quantum yields at relatively short emission decay times are obtainable. Accordingly, these compounds have successfully been used as emitters in organic light-emitting diodes (OLEDs) [1–11] and in many other applications that are connected with light emission [12–23]. In most cases, the emitting state is a triplet (T_1 state), while the ground state S_0 is a singlet. Rarely, for example, for selected Cu(I) complexes, the emitting state at ambient temperature is the lowest excited singlet state S_1 [24–28]. The knowledge about the states' properties is still much less common or even less developed than for purely organic compounds [29–31]. Thus, it seems to be justified to focus on the properties of these metal complexes. From detailed spectroscopic investigations, new insights can be extracted that lead to valuable stimulations also for the development of new emitter materials.

In particular, a transition between the triplet state and the singlet ground state is formally forbidden, but can become distinctly allowed by spin–orbit coupling (SOC) induced by the heavy metal central ion, such as Pt(II) or Ir(III). SOC normally also leads to fast intersystem crossing (ISC) from higher lying singlet states to the emitting triplet. Therefore, in an electroluminescence process, both singlet and triplet excitons can contribute to the emission from the triplet state. This so-called triplet harvesting effect can lead to a four times higher internal electroluminescence quantum yield than achievable with fluorescent emitters [32–35]. The triplet harvesting mechanism will be explained below in this chapter.

On the other hand, the effects of SOC seem to be limited, at least in the group of materials that are usually applied as OLED emitters so far. This is displayed, for example, in the emission decay time. Investigations show that a lower limit exists for the (radiative) emission decay time [36]. This has significant implications for the roll-off of efficiency of an OLED with increasing current density due to saturation

Physics of Organic Semiconductors, Second Edition. Edited by Wolfgang Brütting and Chihaya Adachi

and triplet–triplet annihilation effects [37–44]. Therefore, it is advantageous to involve energy states with short (radiative) decay times in the emission process, such as singlet states. Indeed, this is possible, if the energy separation between the lowest triplet state and the next higher lying singlet state is small enough to allow for a delayed fluorescence [24, 36]. Interestingly, Cu(I) complexes represent attractive candidates. Applying these, it is possible to harvest both singlet and triplet excitons; however, in this case, the emitting state at ambient temperature is the lowest singlet state. In an electroluminescence application, this effect is called singlet harvesting [24, 36, 45–48]. This mechanism will also be explained below and examples based on Cu(I) complexes will be given.

In this chapter, we introduce in Section 13.2 the important triplet harvesting and singlet harvesting effects, both, at least in principle, allowing 100% gathering of all excitons formed by the electron–hole recombination and their conversion into light, in contrast to the situation as normally found for purely organic emitters. These allow to use only up to 25% of the total number of excitons when applied as emitters in OLEDs. In Section 13.3, we discuss important properties of triplet emitters and summarize some guidelines for an assessment of OLED emitters. For the red and green spectral regions, efficient emitters have been reported, achieving emission quantum yields of up to 80% or even up to almost 100% [36]. However, organotransition metal complexes that exhibit a blue emission of high quantum yield and sufficient stability are still rare. Therefore, in Section 13.4, we focus on properties of blue light emitting materials based on triplet state emission. Interestingly, blue light emission can also be generated with Cu(I) complexes. Recently, it was reported that Cu(I) compounds show at ambient temperature very efficient singlet emission of ϕ_{PL} up to 90% as delayed fluorescence. Therefore, these compounds represent potentially attractive materials for singlet harvesting [24, 36, 45]. Examples will be presented in Section 13.5. A short conclusion ends this introductory contribution.

13.2 Electroluminescence

In an emission layer of an OLED, electrons and holes combine and form excitons. Since both particles carry a spin of $\hbar/2$, singlet and triplet [30, 31] excitons are generated. In a statistical limit, they are formed in a ratio of 1: 3 [32]. In subsequent relaxation processes, these populate the emitting states of the doped complexes. The corresponding mechanisms are discussed in Refs [34, 35]. Here, we want to refer to this model and explain the triplet harvesting effect.

13.2.1 Triplet Harvesting

Figure 13.1 describes the triplet harvesting effect schematically. After the electron–hole recombination, the three triplet excitons relax to the lowest triplet

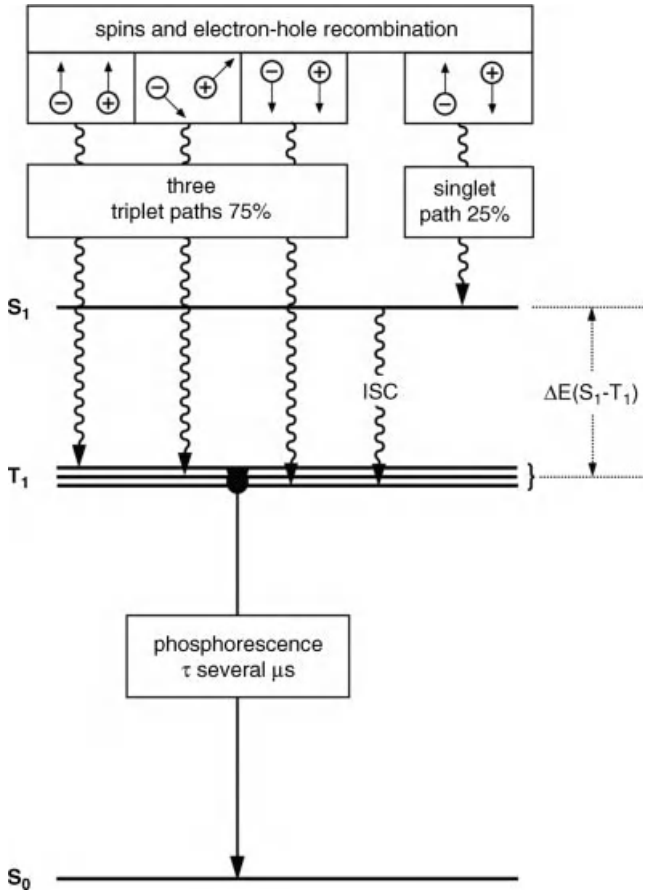

Figure 13.1 Schematic diagram to illustrate the effect of triplet harvesting. In an emitter layer of an OLED, electrons and holes recombine and form triplet and singlet excitons in a ratio of 3 : 1. They relax to the triplet state T_1 and the singlet state S_1 of the dopants (emitter molecules), respectively. Induced by SOC, the singlet excitation relaxes efficiently from the S_1 state to the T_1 state (intersystem crossing). Finally, all excitons are harvested in the lowest triplet state. SOC is also responsible for the occurrence of phosphorescence from the T_1 state [33–35].

state T_1, while the singlet exciton populates the S_1 state. These relaxations occur with a time constant of $\approx 10^{-12}$ s or even faster [30]. For organotransition metal compounds, SOC is usually very effective and then results in a very short ISC time. In Ref. [49], a time constant of 50 fs has been determined for a Pt(II) compound (from the Lorentzian line shape of the singlet absorption line). Recently, it has been shown by time-resolved investigations that the ISC time constant for $Ir(ppy)_3$ (**23**)[1)] is shorter than 100 fs [50]. Consequently, an emission from the

1) Chemical structures for the compounds are shown in Figure 13.7.

singlet state S_1 is practically absent, at least for a large energy separation between the singlet and the triplet state, for example, for $\Delta E(S_1–T_1) > 3000\,cm^{-1}$. In this case, only down-ISC but no up-ISC processes occur at ambient temperature. An alternative behavior will be discussed below. Moreover, if SOC between the T_1 state and higher lying singlet states is large enough, the T_1 state can show an efficient and relatively short-lived phosphorescence of almost 100% quantum yield (see Section 13.3) [51, 52]. In summary, all excitons of singlet and triplet character that are formed can, at least in principle, be harvested in the lowest triplet state T_1. Hence, *triplet harvesting* occurs.

For completeness, it is mentioned that in purely organic molecules, the S_1 and the T_1 states are similarly populated as discussed above, but often the ISC time is, for example, two orders of magnitude longer than the fluorescence decay time from the S_1 state (order of 1 ns) [30]. As a consequence, emission from the S_1 state can occur. However, the three paths that populate the triplet state will not induce an emission (phosphorescence), since the nonradiative decay strongly dominates the radiative decay [30]. Consequently, the triplet excitons cannot be used for light generation, their energy is simply transferred into heat. Thus, at most 25% of all excitons formed, namely, the singlet excitons, will lead to light generation in purely organic molecules.

13.2.2 Singlet Harvesting

Figure 13.2 displays a similar situation with respect to electron–hole recombination and the formation of singlet and triplet excitons, as discussed in Section 13.2.1. However, in the present situation, the energy separation between the lowest singlet and triplet states is assumed to be relatively small, for example, of $\Delta E(S_1–T_1) \leq 1000\,cm^{-1}$. Furthermore, if these states experience sufficient SOC, which is usually the case for organotransition metal compounds, both down-ISC and up-ISC processes are fast. At low temperatures, the fast relaxation populates the triplet state T_1, which emits with its intrinsic decay time, for example, of several 100 µs as found for a number of Cu(I) complexes (Section 13.5). This decay time is much too long for OLED operation (due to saturation and $T_1–T_1$ annihilation effects). However, with temperature increase, the S_1 state is populated according to a Boltzmann distribution and, thus, at sufficiently high temperatures, the emission stems dominantly from the S_1 state. This is a consequence of the fact that the probability for the radiative $S_1 \rightarrow S_0$ decay is much higher than for the $T_1 \rightarrow S_0$ decay. For example, for Cu(I) complexes, we determined (experimentally) a ratio of the radiative rates of three to four orders of magnitude (Section 13.5). Although the radiative decay represents a $S_1 \rightarrow S_0$ emission, one does not measure the intrinsic (prompt) S_1 fluorescence decay time, since the long-lived T_1 reservoir leads to a delayed process, that is, a thermally activated delayed fluorescence and a decay time of τ_{DF} is observed [30, 53–55]. It can be as long as several microseconds, as found for the examples discussed below.

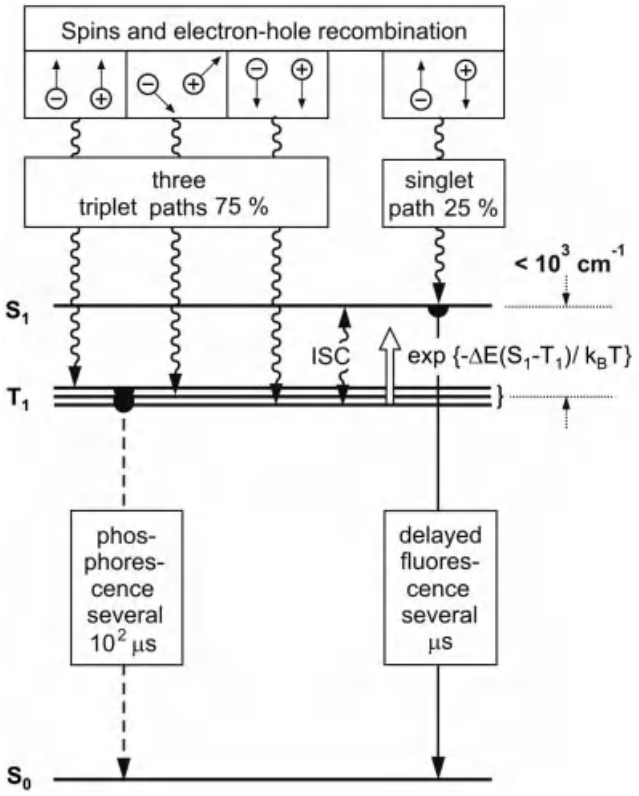

Figure 13.2 Schematic illustration of the effect of singlet harvesting [24, 36, 45–48]. The S_1 and T_1 states are populated similarly as described in the caption of Figure 13.1. Fast up- and down-ISC processes lead to a thermal equilibration of the two states governed by a Boltzmann distribution. Due to the much higher radiative decay rate of $S_1 \rightarrow S_0$ than of $T_1 \rightarrow S_0$, the emission stems essentially from the singlet S_1 state. The emission represents a delayed fluorescence [30, 53–55]. The decay times given refer to Cu(I) complexes, as discussed in Section 13.5.

In summary, in an electroluminescence excitation process, using suitable emitter compounds, all triplet and singlet excitons can be harvested. In the situation discussed, the emission does not stem from the lowest triplet state, but results from the energetically higher lying singlet state S_1. Hence *singlet harvesting* occurs.

13.3
Triplet Emitters: Basic Understanding and Trends

Electronic transitions are often described in terms of excitations from the highest occupied molecular orbital (HOMO) to the lowest unoccupied molecular orbital (LUMO). These HOMO–LUMO considerations are often indicative, since in

suitable cases they can provide information about some properties of the lowest excited states. However, the HOMO–LUMO model does not contain energy states. Thus, singlets or triplets are not described by this model. Therefore, relations between the two descriptions, that is, MO model versus state model, will shortly be discussed. Furthermore, the emission behavior is crucially determined by effects of spin–orbit coupling between the lowest triplet state T_1 and higher lying singlet and triplet states. These effects are difficult to handle quantitatively, but simple guidelines and coupling routes resulting from theoretical considerations can be given. Moreover, assessments based on experiments are presented that use the systematics of zero-field splittings (ZFS) of the triplet into substates. In particular, SOC determines these splittings as well as the radiative decay times of the T_1 substates to the singlet ground state. Relating these properties, it is indicated that the (radiative) emission decay time will have a lower limit of $\approx 1\,\mu s$ for the type of compounds being discussed in this section.

13.3.1 Energy States

In this section, we want to present some considerations on a schematic basis to help to develop a better understanding about excitations between molecular orbitals (MOs) and energy states (compare also Ref. [56]). Figure 13.3 shows a small number of frontier orbitals, which are often expected to be mainly responsible for a qualitative description of the lower energy states. The diagram displays orbitals for a (distorted) octahedral organotransition metal complex, such as $Ir(ppy)_3$, with

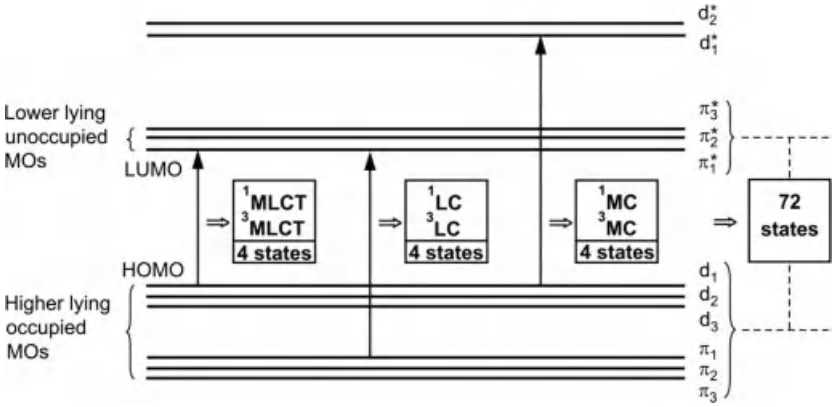

Figure 13.3 Schematic diagram for selected molecular orbitals (MOs) to specify different types of MO excitations for a (distorted) octahedral complex. The metal-to-ligand charge transfer transitions of d–π^* character lead to ^{1,3}MLCT (^{1,3}dπ^*) states, while the ligand-centered π–π^* and metal-centered d–d* excitations result in ^{1,3}LC ($^{1,3}\pi\pi^*$) and ^{1,3}MC (^{1,3}dd*) states, respectively. Inclusion of the orbitals, marked with brackets, gives 72 different energy states. Here, the three substates of a triplet term are counted as three states.

three chelating ligands that have π and π* orbitals in the relevant energy range. In a metal complex, these ligand orbitals will combine to MOs of the complex. For example, one π-orbital of one single ligand can combine differently with the π-orbitals of the other two ligands. This leads to three MOs of the complex. If the symmetry is lower than C_3, all three MOs will energetically split. Moreover, three occupied and two unoccupied d-orbitals, representing the split t_{2g} and e_g orbitals, respectively, are also shown in Figure 13.3. The designation, particularly in the range of the higher lying occupied MOs, gives only the leading contribution of these MOs. For example, a d-orbital can also contain π-admixtures, or a π-orbital can be admixed with some d-character.

Restricting attention to closed-shell ground states, each occupied orbital of the compounds being of interest here contains two electrons with opposite spins. Thus, the configuration $\pi_3^2\pi_2^2\pi_1^2d_3^2d_2^2d_1^2$ gives the electronic singlet ground state S_0. For example, a HOMO–LUMO excitation, representing an MLCT (metal-to-ligand charge transfer) transition, leads to the excited state configuration $\pi_3^2\pi_2^2\pi_1^2d_3^2d_2^2d_1^1\pi_1^{*1}$. Let us designate this excitation as $d_1\pi_1^*$ or $MLCT_1$ excitation. Taking the spins and spin-flips into account, one obtains one singlet state ($^1d_1\pi_1^*$ or $^1MLCT_1$) and one triplet term ($^3d_1\pi_1^*$ or $^3MLCT_1$). Similarly as described above, the triplet term (=state) consists of three substates. Considering additionally electron–electron interaction (exchange interaction) between the electrons in the two orbitals (d_1 and π_1^*), the singlet and triplet states split, for example, by ΔE (S_1–T_1) of 2000–4000 cm^{-1} [49, 56, 57].

A different type of excited states results from an excitation of the same ground state configuration ($\pi_3^2\pi_2^2\pi_1^2d_3^2d_2^2d_1^2$) to the excited state configuration $\pi_3^2\pi_2^2\pi_1^1d_3^2d_2^2d_1^2\pi_1^{*1}$, which is abbreviated as $\pi_1\pi_1^*$ excitation. This leads to the ligand-centered (LC) states $^1\pi_1\pi_1^*$ and $^3\pi_1\pi_1^*$ ($^1LC_1$ and $^3LC_1$ states). In this situation, the singlet–triplet splitting can be as large as almost 10^4 cm^{-1}. The $\Delta E(S_1$–$T_1)$ splitting is determined by the orbital parentages of the states. In particular, the interaction between the unpaired electrons, and hence the exchange interaction, is smaller for an on average larger spatial separation of the involved orbitals than for distinctly overlapping MOs. Therefore, the singlet–triplet splitting of $d\pi^*$ states is usually much smaller than that of $\pi\pi^*$ states.

Furthermore, if SOC is taken into account, the triplet state splits into three substates. The corresponding zero-field splittings (ZFS) lie in the range of less than 1 cm^{-1} up to more than 200 cm^{-1}, depending on the orbital character of the state, on the strength of SOC according to the position of the central metal in the periodic table, and on the extent of spin–orbit coupling of this specific triplet state with higher lying $^{1,3}MLCT$ states of different d-orbital involvements. Consequently, the amount of the ΔE(ZFS) values allows us to assign details of the corresponding triplet state (see Section 13.3.3).

Figure 13.3 also displays d*-orbitals. This means that metal-centered (MC) $^{1,3}dd^*$ states ($^{1,3}MC$) also have to be taken into account. However, for the discussions with respect to red and green light emitters, these states can usually be ignored due to the relatively large energy separations from the emitting $^3\pi\pi^*$ or $^3d\pi^*$ states. On the other hand, for blue light emitters, as discussed in Section 13.4, the $^{1,3}dd^*$

states are highly important, since they may become involved in emission quenching and dissociation reactions.

In summary, an excitation from an occupied orbital to an unoccupied orbital leads to four energy states (one singlet state and one triplet state that consists of three triplet substates). Consequently, excitations involving the MOs shown in Figure 13.3 (18 excitations without including the d*-orbitals) give 72 energy states.[2] A quantitative description taking configuration interaction (CI) and spin–orbit coupling into account will lead to significant energy shifts and modifications of the electronic states. Thus, it becomes clear that a simple HOMO–LUMO consideration can be very misleading. This is in particular the case, since organotransition metal complexes have a high density of states lying close in energy, which entails large mixings by configuration interaction and SOC interaction.

For completeness, it is remarked that, according to a quantum mechanical investigation of $Ir(ppy)_3$ (**23**) by Nozaki [58], even the 72 states of our model would not be sufficient to approach the experimental situation. Only an inclusion of about 200 states, meaning 32 additional excitations between MOs, may result in a somewhat more realistic description. Interestingly, about 70 states lie within an energy range of about 8000 cm^{-1} ($\approx$ 1 eV) above the emitting state [58]. This demonstrates the high density of energy states and the complexity of a reliable calculation (compare Refs [59–61]). Nevertheless, relatively simple guidelines for the evaluation of the dominating SOC routes (Section 13.3.2) [36, 56, 62, 63] and an experimentally based systematics (Section 13.3.3) allow us to develop a deeper understanding of how spin–orbit coupling, zero-field splittings, and emission decay times are related.

13.3.2
The Triplet State and Spin–Orbit Coupling

In this section, we want to discuss aspects of spin–orbit coupling and its impact on the properties of the emitting triplet state. It is not intended to provide detailed theoretical formalisms, but we want to present some general schemes and useful trends that are understandable also for nonspecialists.

An introduction to relevant MOs of organotransition metal compounds and the resulting singlet and triplet states is already given in the preceding section. In general, for the type of compounds discussed, the lowest excited state is a triplet state (T_1) and the ground state is a singlet state (S_0). Due to the different spin multiplicity of these states and the selection rules for electronic transitions, the $T_1 \leftrightarrow S_0$ transition would be strictly forbidden without SOC. However, the metal d-orbitals, especially those of the 5d shell, being partially occupied in the third period of transition metal ions, such as Ir(III) and Pt(II), have high SOC constants of about 4000 cm^{-1} [64] and thus can induce the required singlet character to the lowest triplet state.

2) Here, we count only states resulting from excitations of one single electron, since double excitations, that is, states that result from excitations of two electrons from the occupied to the unoccupied orbitals, lie much higher in energy.

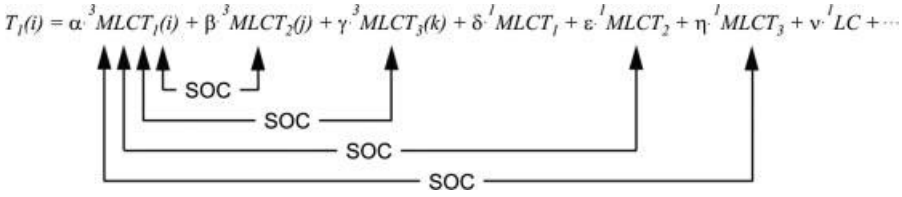

Figure 13.4 Schematic illustration of leading admixtures to substate *i* of the $^3MLCT_1$ state by direct spin–orbit coupling (SOC). *j* and *k* denote specific substates. $MLCT_1$, $MLCT_2$, and $MLCT_3$ denote the unperturbed states that involve the orbitals d_1, d_2, and d_3, respectively.

In this chapter, we are mainly interested in good emitters for OLEDs. Therefore, SOC has to be significant. If this is realizable, high radiative rates and high emission quantum yields are obtainable. It can be shown that this requirement can only be fulfilled if the emitting triplet is largely of MLCT character or at least contains a distinct ^{3}MLCT contribution. In this situation, an efficient *direct*[3] SOC to higher lying ^{1,3}MLCT states is possible according to specific SOC routes [36, 56, 62, 63]. These will be illustrated below.

At first sight, a very large number of higher lying singlet and triplet states seems to be important for SOC. Indeed, many of these states can contribute to the emitting triplet substates via direct or indirect SOC. However, several selection rules for SOC have to be fulfilled [36, 56, 62, 63]. Thus, a number of mixing routes can be ignored. In particular, nonnegligible SOC can only occur between triplet and singlet MLCT states that result from different d-orbitals. In other words, a T_1 state of ^{3}MLCT character does not exhibit SOC with a ^{1}LC state. Moreover, SOC to the ^{1}MLCT state that results from the same d-orbital can also be ignored [36, 56, 62, 63]. In this respect, compare also the valuable investigations carried out in Refs [65–69].

A detailed discussion of the leading admixtures to the emitting triplet state T_1 has to take into account that it consists of three substates ($T_1(i)$, $T_1(j)$, and $T_1(k)$ (or as used later I, II, and III) and that every substate will exhibit its individual SOC to higher lying states. This is schematically depicted in Figure 13.4. The parameters α, β, γ, and so on represent the respective mixing coefficients with a specific $^3MLCT_1(i)$ substate. As described above, the diagram also shows that mixing of $^3MLCT_1(i)$ with the singlet $MLCT_1$ state stemming from the *same* d-orbital can be neglected. Moreover, any mixings with singlet or triplet LC states are also negligible.

In a somewhat more quantitative treatment of SOC, the energies and radiative rates can, at least in principle, be expressed by Eqs. (13.1) and (13.2) as given below. These expressions result from second-order perturbation theory. Here, we apply the nomenclature that is also used for the case studies presented later in this chapter. This means that the lowest triplet term consists of

3) Direct SOC describes a direct mixing of singlet and triplet states via SOC, while indirect SOC refers to a less efficient two-step coupling route that consists of configurational mixing of states of the same spin multiplicity and subsequent direct SOC with ^{1}MLCT states [36, 61, 62].

the substates I, II, and III (corresponding to $T_1(i)$, $T_1(j)$, and $T_1(k)$). If only direct SOC is considered, the energy $E(i)$ of the ^{3}MLCT substate i (with $i = $ I, II, III) is given by [29 (page 201), 56, 63, 70][4)]

$$E(i) = E_{T_1} + \sum_{n,j} \frac{|\langle T_n(j)|H_{SO}|T_1(i)\rangle|^2}{E[T_1] - E[T_n]} + \sum_m \frac{|\langle S_m|H_{SO}|T_1(i)\rangle|^2}{E[T_1] - E[S_m]} \tag{13.1}$$

while the radiative rate $k^r(i)$ can be expressed (in the cgs system) by [29, 56, 63, 70]

$$k^r(i) = \frac{64\pi^4\nu^3}{3hc^3} \cdot \sum_m \left|\frac{\langle S_m|H_{SO}|T_1(i)\rangle}{E[T_1] - E[S_m]}\right|^2 |\langle S_0|\mathrm{er}|S_m\rangle|^2 \tag{13.2}$$

$E[S_m]$ and $E[T_n]$ are the unperturbed energies of higher lying (pure) singlet states S_m and (pure) triplet states T_n. $T_n(j)$ represents a substate j of T_n. H_{SO} is the SOC Hamiltonian, ν is the frequency of (emitted) light, measured in s^{-1}. The corresponding matrix elements are difficult to calculate, but the coupling routes as discussed above provide substantial qualitative information for an assessment of $E(i)$ and $k^r(i)$.

Equation (13.2) contains dipole matrix elements of the type $\langle S_0|\mathrm{er}|S_m\rangle$ with the dipole operator er. Consequently, the radiative rate $k_r(i)$ of a transition from a triplet substate $T_1(i)$ to the singlet ground states depends on the allowedness (oscillator strength or molar extinction coefficient) of the singlet–singlet transition $S_0 \leftrightarrow S_m$, whereby S_m is the singlet that mixes with $T_1(i)$ via direct SOC according to the coupling routes, as symbolized in Figure 13.4.

A discussion of the energy denominators and their magnitudes is particularly helpful. Presumably, SOC with the energetically most proximate ^{3}MLCT state(s) of different d-orbital nature represents a leading contribution to energy stabilizations of the individual T_1 substates and, thus, to the amount of the zero-field splitting ΔE(ZFS). This is simply a consequence of the smaller energy separation ($E[T_1] - E[T_n]$) compared to ($E[T_1] - E[S_n]$). On the other hand, an admixture of triplets can be neglected for the determination of the radiative rates, since the corresponding dipole matrix elements vanish.

Relations between effects of SOC, such as the amount of ΔE(ZFS) and the radiative rates, are discussed in Section 13.3.3 for a series of compounds, some of them representing good OLED emitters.

The energy denominators, that is, the energy differences between the mixing (unperturbed) states, also play an important role when different molecular geometries of emitter complexes are compared. Simple considerations allow us to work out very useful guidelines for the effectiveness of SOCs and their impact on the emission properties. This becomes clear, if one takes into account that these energy separations significantly depend on the geometry of a compound, the number of ligands coordinating to the central metal ion, and ligand field splittings [72]. In a

4) For completeness, it is remarked that the situation is different, if the lowest triplet state represents a ^{3}LC ($^3\pi\pi^*$) state. In this case, SOC can become effective only indirectly via configuration interaction. A corresponding discussion is found in Refs [63–65, 71].

first approximation, if one assumes that for different MLCT states, for example, $d_1\pi^*$, $d_2\pi^*$, and so on, the singlet–triplet splittings (given by exchange interactions) are similar, one can consider just the energy separations between the occupied d-orbitals. This concept often meets the chemical intuition [36, 56, 62, 63].

Figure 13.5 depicts the splittings of the central metal d-orbitals (a) for an octahedral and a distorted octahedral compound and (b) for a square planar and a distorted square planar compound. For this model discussion, one π^*-orbital, representing the lowest unoccupied molecular orbital, is also given. Other unoccupied π^*-orbitals and occupied π-orbitals are neglected here for clarity. Thus, all resulting low-lying electronic states are MLCT states with a central metal d-orbital as HOMO, HOMO-1, and so on.

In the case of a perfect octahedral symmetry, the d-orbitals split into sets of three t_{2g} (d_{xy}, d_{xz}, d_{yz}) and two e_g ($d_{x^2-y^2}$, d_{z^2}) orbitals, separated by the energy of 10 Dq with Dq being the ligand field parameter [72]. For metal ions with a d^6 configuration, such as Ir(III), Os(II), and Ru(II), the t_{2g} shell is fully occupied. For compounds of relevance for OLED applications, the unoccupied e_g orbitals have to lie high above the LUMO to prevent quenching by dd* states (see Section 13.4). For most octahedrally coordinated complexes discussed in this chapter, the symmetry is lower than C_3. As a consequence, the orbitals of the t_{2g} manifold are no longer degenerate and split into three orbitals d_1, d_2, and d_3,

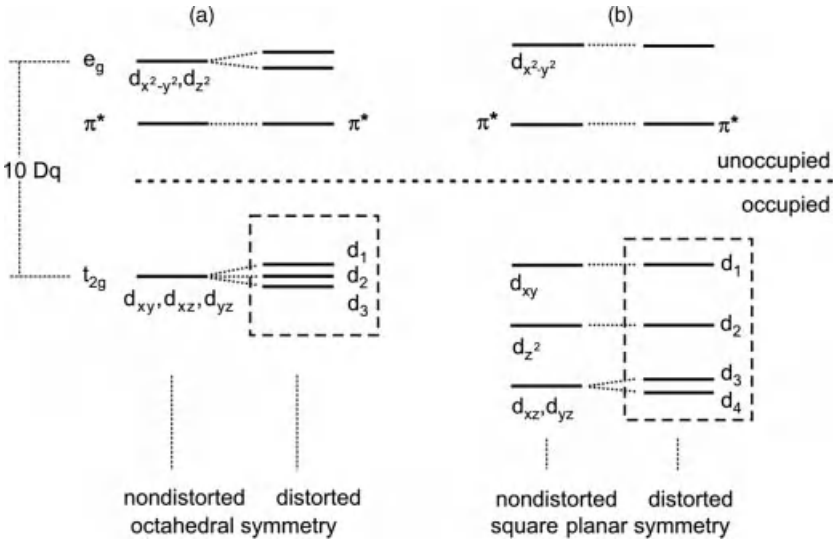

Figure 13.5 Schematic splittings of the d-orbitals in (a) an octahedral and a distorted octahedral compound with a d^6 configuration and (b) in a square planar and a distorted square planar compound with a d^8 configuration. The frames show the different splittings of the occupied d-orbitals. In all cases, a π^*-orbital, representing the LUMO, is also displayed. Population of the unoccupied d^*-orbitals would lead to quenching of the emission and, therefore, these orbitals should have sufficiently high energy. Adapted from Ref. [63].

according to the respective geometrical distortion. However, they will still be rather proximate in energy. For example, t_{2g} splittings of only a few hundred wavenumbers are reported for $[Ru(bpy)_3]^{2+}$ (**16**) [73–75]. According to the relations derived above, the substates of the lowest ^{3}MLCT state $^3(d_1\pi^*)$ can experience efficient SOC with the relatively close-lying singlet states $^1(d_2\pi^*)$ and $^1(d_3\pi^*)$ and the substates of the corresponding triplets $^3(d_2\pi^*)$ and $^3(d_3\pi^*)$, since the energy denominators are relatively small. As a consequence, large zero-field splittings and relatively high radiative rates can occur for the $^3(d_1\pi^*)$ substates of octahedrally coordinated complexes.

For quasi-square planar compounds, a different situation is found. For central metal ions having a d^8 electron configuration, the four lower lying d-orbitals are occupied. The ordering of these orbitals depends strongly on the nature and the bonding abilities of the coordinating ligands [72, 76, 77]. The sequence, as shown in Figure 13.5, is obtained from ligand field theory without considering additional (back)bonding effects. The splittings between the occupied d-orbitals of quasi-square planar compounds are larger than that of quasi-octahedrally coordinated compounds. Similarly, for the square planar situation, the unoccupied antibonding $d_{x^2-y^2}$ orbital lies also at high energy for strong-field ligands. The substates of the lowest ^{3}MLCT $^3(d_1\pi^*)$ state can exhibit SOC with the singlet states $^1(d_2\pi^*)$, $^1(d_3\pi^*)$, and $^1(d_4\pi^*)$ and with the substates of the corresponding triplets $^3(d_2\pi^*)$, $^3(d_3\pi^*)$, and $^3(d_4\pi^*)$. However, in this case, the energy differences between d_1 and the other occupied d-orbitals d_2, d_3, and d_4 are, for most compounds, distinctly larger than for quasi-octahedrally coordinated compounds (Figure 13.5). For $[Pt(CN)_4]^{2-}$, for example, the energy difference between the two highest occupied d-orbitals (HOMO and HOMO-1) is as high as about 4000 cm^{-1} (0.5 eV) [77]. Consequently, the energy denominators, which govern the mixings between the MLCT states, are significantly larger in this case than for a quasi-octahedral coordination. Thus, for quasi-square planar compounds, the efficiency of SOC will not attain the efficiency of quasi-octahedral compounds. This has consequences for the choice of triplet emitters for OLEDs. In Sections 13.3.3 and 13.4, we will come back to this important result and give examples to what extent the amount of zero-field splitting and the radiative rate of an emitting state is related to the coordination geometry of a compound.

13.3.3
Emission Decay Time and Zero-Field Splitting: A General Trend

Triplet emitters applied in OLEDs should exhibit short radiative emission decay times (high radiative rates) to induce high emission quantum yields and to reduce the effects of efficiency roll-off of an OLED. Therefore, a deeper understanding of the factors that control these rates is of crucial importance. As described in Section 13.3.2, spin–orbit coupling opens a radiative path from a triplet substate i (i = I, II, III) to the singlet ground state. Equation (13.2) gives the radiative rate $k^r(i)$. It is determined by SOC matrix elements, energy denominators, and the allowedness(es) (oscillator strengths) of the transition(s) between the mixing singlet state(s) and the ground state. On the other hand, similar and even the same

matrix elements are responsible for energy shifts of the individual triplet substates. The corresponding expression is displayed in Eq. (13.1). Since in most cases each triplet substate experiences a specific but different SOC-induced energy stabilization, energy differences between the substates result. This gives the zero-field splitting parameters $\Delta E_{\mathrm{II-I}}$ and $\Delta E_{\mathrm{III-I}} = \Delta E(\mathrm{ZFS})$, respectively.

It should be possible to relate both photophysical effects. An analytical approach, however, seems to be difficult to achieve and has not yet been carried out. On the other hand, a very large number of experimental data are available. By use of these data, a valuable relation between the emission decay time τ and the total zero-field splitting energy $\Delta E(\mathrm{ZFS})$ can be obtained (Figure 13.6). The data are determined from highly resolved emission and excitation spectra that are measured at

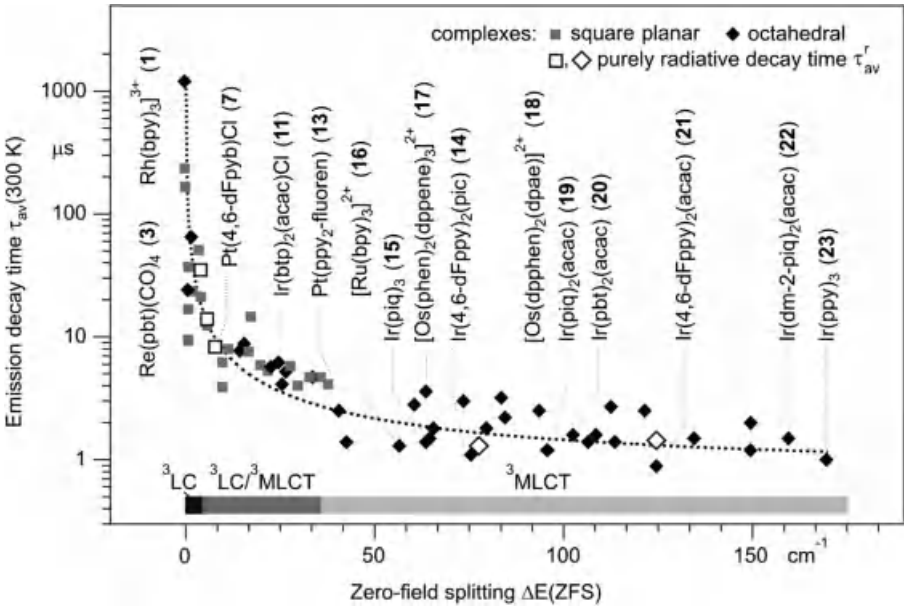

Figure 13.6 Emission decay time τ_{av} at $T = 300$ K versus the total zero-field splitting $\Delta E(\mathrm{ZFS})$ of the emitting triplet. The data points refer to different organotransition metal compounds and/or the same compounds in different environments [36]. τ_{av} (300 K) represents the averaged and Boltzmann-weighted emission decay time of the three triplet substates (full symbols) and the purely radiative decay time (open symbols), respectively. The squares and the rhombs label (approximate) square planar and octahedral geometries of the complexes, respectively. The dashed curve represents an eye-guiding function. Empirically, this curve may be described by $\tau_{av}(300\ \mathrm{K}) = a(\Delta E(\mathrm{ZFS}) + b)^{-1} + 0.75\ \mu s$ with $a = 70\ \mu s\ cm^{-1}$ and $b = 0.02\ cm^{-1}$. τ_{av}(300 K) and $\Delta E(\mathrm{ZFS})$ are measured in microseconds and cm^{-1}, respectively [36]. A qualitative interpretation is given in the text. The bar in the lower part of the diagram gives a classification of the emitting triplet as ^{3}LC ($^3\pi\pi^*$), ^{3}LC/^{3}MLCT (^{3}LC with significant ^{3}MLCT admixtures), and ^{3}MLCT (^{3}dπ^*), respectively. Compounds with ^{3}LC/^{3}MLCT or ^{3}MLCT character are potentially suited for OLED applications. The chemical structures of the compounds are shown in Figure 13.7. Adapted from Ref. [36].

cryogenic temperatures and from an analysis of the temperature dependence of the emission decay time. Only a smaller number of selected data points in Figure 13.6 is marked by the compounds' abbreviations in order not to overload the diagram. A more comprehensive summary of data is found in Ref. [36], where the procedures and strategies for a determination of the experimental data are also illustrated (see also the descriptions presented in Section 13.4).

It is remarked that the emission decay times to be taken in this context should be the purely radiative ones. However, this information is available only for a few compounds that are marked in Figure 13.6. On the other hand, the use of the measured emission decay time is not always reasonable, since at ambient temperature nonradiative deactivation may often distinctly reduce the decay time or even quench the emission completely. Therefore, we calculated an averaged (Boltzmann-weighted) decay time τ_{av} from low-temperature values of the individual substate emission decay times τ_I, τ_{II}, and τ_{III}. These data are obtainable at cryogenic temperatures and represent reasonable approximations for the radiative decay times. This procedure is described in Ref. [36] and in Section 13.4 (Eq. (13.3)).

The relation between the emission decay time and the total zero-field splitting ΔE(ZFS) depicted in Figure 13.6 displays several important trends, which may also help to select good OLED emitters. The trend observed is valid for a large number of organotransition metal compounds even with various central metal ions, such as Ru(II), Rh(III), Pd(II), Re(I), Os(II), Pt(II), or Ir(III), and it is shown that the emission decay time decreases by more than three orders of magnitude with increasing ΔE(ZFS) (note the logarithmic scale). This effect is induced by an increasing effectivity of SOC between the substates of the emitting triplet state and higher lying singlet states (see Eq. (13.2)).

Figure 13.6 displays a very interesting trend that merits special comments. With increasing effectivity of SOC and thus increasing ΔE(ZFS), the emission decay time τ_{av} (300 K) does not seem to decrease to below $\approx$1 μs. The plot appears to exhibit an asymptotic behavior. Qualitatively, this can be easily explained, if one takes into account that, at ambient temperature, all three triplet substates are responsible for the emission decay time. In particular, the highest triplet substate III mostly exhibits by far the shortest (radiative) decay time, at least for Ir(III) complexes with large ΔE(ZFS) values. However, substate III contributes only according to its Boltzmann-governed population. Consequently, although an increasing effectivity of SOC induces a higher radiative rate (shorter radiative decay time) (Eq. (13.2)), the splitting between the substates is also growing. Hence, the Boltzmann-weighted population of the short-lived substate III decreases. This prevents further significant reductions of a compound's decay time and leads to the observed asymptotic behavior. It is remarked that the systematics presented in Figure 13.6 is valid only for the types of organometallic compounds as discussed in the context of this section. Much shorter radiative decay times, being a target for bright and efficient OLED lighting, might be attainable with other electronic structures. In this respect, we proposed to investigate compounds with low-lying and strongly emitting singlet states and introduced the singlet harvesting effect (see Sections 13.2 and 13.5) [24, 36, 45–48].

On the basis of the magnitude of the ΔE(ZFS) value, it is possible to characterize the orbital nature of the emitting triplet state, as has been shown by extensive investigations by Yersin's group [34–36, 49, 56, 62, 63]. From these, it can be concluded that the compounds grouped on the left-hand side of the diagram, shown in Figure 13.6, with ΔE(ZFS) values of less than a few wavenumbers represent states of largely ^{3}LC ($^3\pi\pi^*$) character. For these emitters, SOC is not very effective and therefore ΔE(ZFS) is small. The radiative decay time can be as long as several milliseconds. According to the spin–orbit coupling routes explained in Section 13.3.2, this situation can be described by weak indirect spin–orbit coupling. On the other hand, the triplet states of compounds with large zero-field splittings, for example, being greater than 50 cm^{-1}, are assigned as being mainly of ^{3}MLCT ($^3d\pi^*$) character. These states experience efficient direct SOC with other ^{1,3}MLCT states as described in Section 13.3.2 and visualized in Figure 13.4. Thus, the radiative rates are larger and the corresponding decay times shorter. For example, for Ir(ppy)$_3$ (**23**) in frozen CH_2Cl_2, a ΔE(ZFS) value of 170 cm^{-1} and a radiative decay time of only 1.6 μs were determined [52]. The triplet states of compounds that have ΔE(ZFS) values in the intermediate range of several cm^{-1} up to roughly 30 cm^{-1} may be classified as ^{3}LC ($^3\pi\pi^*$) states with significant ^{3}MLCT admixtures. Accordingly, the radiative decay times are longer than for emitting ^{3}MLCT states and mostly lie in the range of 5–15 μs.

Interestingly, all compounds with ΔE(ZFS) values greater than about 50 cm^{-1} have (distorted) octahedrally coordinated central metal ions. In contrast, the largest ΔE(ZFS) value observed so far for a square planar Pt(II) complex amounts only to 46 cm^{-1} [78]. This behavior is ascribed to be a consequence of relatively large energy separations between admixing MLCT states in square planar compounds, leading to less effective SOCs than in compounds with octahedral coordination (see Figure 13.5). Another example is also very illustrative. The lowest triplet state of the (distorted) octahedral $[Ru(bpy)_3]^{2+}$ complex (**16**) shows a value of ΔE(ZFS) = 61 cm^{-1} [79–82]. This is significantly larger than found for any Pt(II) complex, although the SOC constant of Ru(II) is by more than a factor of 4 smaller than that of Pt(II) [64].

In Table 13.1, we summarize emission data of some representative (octahedrally coordinated) Ir(III) complexes that exhibit short emission decay times and high photoluminescence quantum yields ϕ_{PL}. Moreover, for all these compounds, the lowest triplet states show relatively high zero-field splittings. Thus, the states may be assigned to represent ^{3}MLCT states that experience relatively strong direct SOC to higher lying ^{1,3}MLCT states that involve different d-orbitals than the emitting T_1 state.

As already pointed out, the emission decay time should be as short as possible to reduce roll-off effects. This is especially important for lighting applications. Indeed, all OLED triplet emitters with acceptable performance studied so far exhibit zero-field splittings of the emitting triplet term larger than about 8–10 cm^{-1} [56, 90]. These complexes are well suited to exploit the triplet harvesting effect. Especially, the most efficient triplet emitters are (octahedrally

Table 13.1 Emission data of representative Ir(III) complexes with large ΔE(ZFS) values, high emission quantum yields ϕ_{PL}, and short emission decay times.

Compound	λ_{max} (nm)	ϕ_{PL} (%)	τ (300 K) (μs)	ΔE(ZFS) (cm^{-1})	References
$Ir(piq)_3$[a] (**15**)	629	57	1.3	57	88, 89
$Ir(4,6\text{-}dFppy)_2(pic)$[a] (**14**)	470	83	1.9	76	84, 86, 87
$Ir(4,6\text{-}dFppy)_2(acac)$[a] (**21**)	484	64	1.0	109	63, 84, 85
$Ir(dm\text{-}2\text{-}piq)_2(acac)$[b] (**22**)	624	80	1.7	160	36
$Ir(ppy)_3$[a] (**23**)	519	90	1.4	170	52
$Ir(ppy)_3$[b] (**23**)	508	96	1.6	85–150	52, 83

For these compounds, SOC is highly effective.
a) Measured in deaerated CH_2Cl_2.
b) Measured in PMMA under N_2 atmosphere.

coordinated) Ir(III) compounds with zero-field splittings greater than about $50\,cm^{-1}$. Examples are: $Ir(piq)_3$ (**15**): $57\,cm^{-1}$; $Ir(4,6\text{-}dFppy)_2(pic)$ (**14**): $76\,cm^{-1}$; $Ir(dm\text{-}2\text{-}piq)_2(acac)$ (**22**): $160\,cm^{-1}$; $Ir(ppy)_3$ (**23**): $170\,cm^{-1}$ (Table 13.1). However, this classification is not very strict, since several Pt(II) complexes, lying in the intermediate range, can also represent attractive OLED emitters [5, 7–9, 11, 91–96]. Chemical structures of the compounds discussed in this chapter are given in Figure 13.7.

13.4 Case Studies: Blue Light Emitting Pt(II) and Ir(III) Compounds

In the last years, efficient green- and red-emitting organotransition metal triplet emitters have been reported that exhibit emission quantum yields of almost 100%. However, complexes that show a saturated blue emission of high quantum yield and that are sufficiently stable are still rare. As main reason for these difficulties, the thermal population of higher lying metal-centered states has been identified [97, 98] (compare Section 13.3.1). Such states are strongly distorted with respect to the complex geometry in the ground state and the (emitting) T_1 state due to the population of an antibonding d^* orbital. Therefore, these antibonding states exhibit high nonradiative decay rates (compare to Ref. [99]). Especially, blue emitters are affected by this mechanism, since the activation energy for the population of metal-centered states decreases with increasing emission energy. Moreover, populated metal-centered states can also promote degradation of the molecules by the breaking of metal–ligand (ML) bonds [97, 100], which would drastically reduce the device lifetime of an OLED. In this section, we want to study and compare photophysical properties of several blue-emitting Pt(II) and Ir(III) compounds. Our focus will be on a detailed investigation of the emitting triplet state.

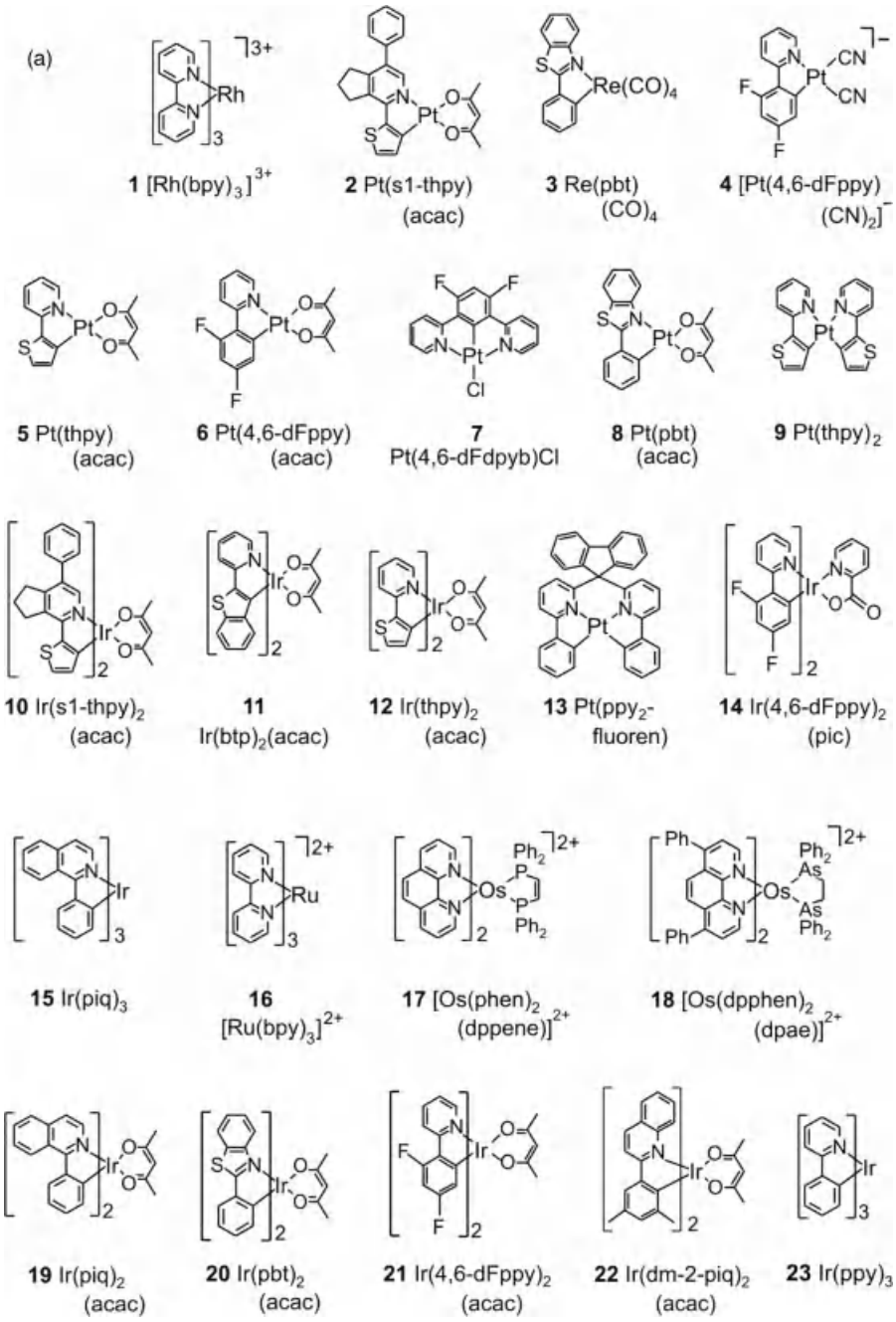

Figure 13.7 Chemical structures of (a) triplet emitters and (b) singlet emitters (at ambient temperature), as discussed in Section 13.5.

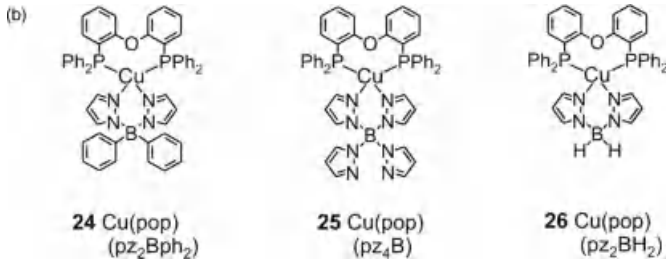

Figure 13.7 (*Continued*).

13.4.1 Pt(II) Compounds

The chemical structures of the studied compounds Pt(4,6-dFppy)(acac) (**6**), [*n*-Bu_4N][Pt(4,6-dFppy)$(CN)_2$] (**4**), and Pt(4,6-dFdpyb)Cl (**7**) can be found in Figure 13.7a. Pt(4,6-dFppy)(acac) (**6**) and [*n*-Bu_4N][Pt(4,6-dFppy)$(CN)_2$] (**4**) were first reported by the groups of Thompson [101] and Yersin [102], respectively, while Pt(4,6-dFdpyb)Cl (**7**) is characterized in Ref. [103]. The materials emit in the blue spectral range. Compounds **6** and **7** have a strong tendency to form excimers or aggregates of strongly interacting monomers in concentrated solutions and doped films. For compound **6**, the excimer formation in solution and the dynamics of aggregate formation in polymer films have been studied experimentally [104, 105] and theoretically [106]. For both Pt(4,6-dFppy)(acac) (**6**) and Pt(4,6-dFdpyb)Cl (**7**), a balanced combination of the monomer and the aggregate emission covers a large spectral range of the visible light. Thus, these materials can be utilized as emitters in single dopant white light emitting OLEDs [8, 107]. On the other hand, blue electroluminescence was obtained when applied in devices with low dopant concentrations [9].

13.4.1.1 Photophysical Properties at Ambient Temperature

Figure 13.8 shows the emission spectra of Pt(4,6-dFppy)(acac) (**6**), [*n*-Bu_4N][Pt(4,6-dFppy)$(CN)_2$] (**4**), and Pt(4,6-dFdpyb)Cl (**7**) dissolved at low concentration in CH_2Cl_2, as well as the emission spectrum of neat [*n*-Bu_4N][Pt(4,6-dFppy)$(CN)_2$] (**4**) measured at ambient temperature [63, 102, 103]. The high-energy maxima corresponding to the electronic transitions between the respective T_1 states and the singlet ground states lie at 468 nm (**6**), 466 nm (**4**), and 473 nm (**7**), respectively. The emission of neat [*n*-Bu_4N][Pt(4,6-dFppy)$(CN)_2$] is distinctly blueshifted with respect to the other spectra, its high-energy maximum lies at 459 nm. Obviously, dipole relaxation of the environment, which can be distinct for electronically excited molecules, is largely suppressed in the rigid crystalline material [108]. Apart from this

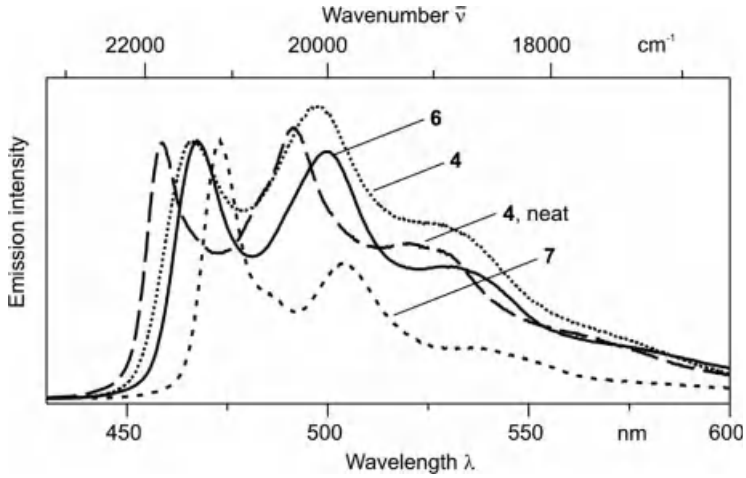

Figure 13.8 Emission spectra of Pt(4,6-dFppy)(acac) (**6**) (solid line), [*n*-Bu_4N][Pt(4,6-dFppy)$(CN)_2$] (**4**) (dotted line), and Pt(4,6-dFdpyb)Cl (**7**) (short dashed line) at ambient temperature dissolved in CH_2Cl_2. The spectrum of neat [*n*-Bu_4N][Pt(4,6-dFppy)$(CN)_2$] (**4**) (dashed line) is also depicted.

blueshift, the spectra of neat [*n*-Bu_4N][Pt(4,6-dFppy)$(CN)_2$] (**4**) and of the dissolved compound are very similar.[5] The spectra of all compounds are structured, indicating emitting triplet states that are largely centered at the chromophoric ligands [101–103].

The peaks at lower energy of the spectra depicted in Figure 13.8 correspond to overlapping vibrational satellites of ground-state modes and combinations/progressions of these modes. The intensities of these bands relative to high-energy bands are distinctly lower for Pt(4,6-dFdpyb)Cl (**7**), being coordinated by a terdentate ligand, than for Pt(4,6-dFppy)(acac) (**6**) and [Pt(4,6-dFppy)$(CN)_2]^-$ (**4**) with bidentate ligands. This intensity distribution has important consequences on the color of the emitted light. The compounds with bidentate ligands exhibit turquoise luminescence due to the intense vibrational satellite bands in the green spectral range, while for Pt(4,6-dFdpyb)Cl (**7**), the contributions of the low-energy vibrational satellite bands are much weaker. Thus, a deeper blue emission results, although the purely electronic transition of **7** lies at lower energy than those of compounds **4** and **6**. As will be discussed below, these differences are consequences of the higher rigidity of the terdentate compared to the bidentate ligands [103].

5) This is uncommon for Pt(II) compounds, since very frequently adjacent complexes (monomers) in the solid state or in highly concentrated doped films interact strongly. This leads to broad and redshifted emission bands that distinctly differ from the monomer emission [109, 110]. In contrast, the crystal structure of [*n*-Bu_4N][Pt(4,6-dFppy)$(CN)_2$] (**4**) reveals large Pt–Pt separations of more than 8 Å, which are a consequence of steric demands of the bulky [*n*-$Bu_4N]^+$ cations [102]. Therefore, no strong interactions between adjacent [Pt(4,6-dFppy)$(CN)_2]^-$ anions occur and the emission of the neat material results from largely isolated monomers.

Table 13.2 Emission properties of different blue light emitting Pt(II) compounds at ambient temperature.

Compound	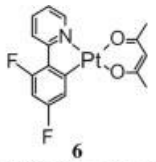 **6** Pt(4,6-dFppy)(acac)	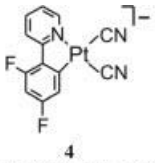 **4** [*n*-Bu$_4$N][Pt(4,6-dFppy)(CN)$_2$]	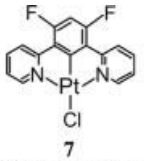 **7** Pt(4,6-dFdpyb)Cl

Environment	**CH_2Cl_2**	**CH_2Cl_2**	**Neat material**	**CH_2Cl_2**
λ_{max} (nm)	467	466	459	472
τ (μs)	0.25	0.26	19	6.4
ϕ_{PL} (%)	2	$\ll 1$	60	80
k_r (s^{-1})[a]	7.7×10^4		3.2×10^4	1.2×10^5
k_{nr} (s^{-1})[a]	3.8×10^6		2.1×10^4	3.6×10^4
{*x*; *y*}[b]	{0.22; 0.40}	{0.19; 0.41}	{0.20; 0.37}	{0.18; 0.38}

a) Radiative and nonradiative rate constants are calculated from the quantum yields and emission decay times according to $\phi_{PL} = k_r \cdot \tau = k_r/(k_r + k_{nr})$.
b) CIE 1931 color space coordinates [111].

Photophysical data of the materials measured at ambient temperature are summarized in Table 13.2. Distinct differences can be observed for the emission quantum yields and decay times. In fluid solution, **7** shows a very high emission quantum yield of $\phi_{PL} = 80\%$, while the yields measured for **6** and **4** are significantly smaller and amount to 2% and $\ll$1%, respectively. (All samples were carefully deaerated.) Together with the short emission decay times of 250 ns (**6**) and 260 ns (**4**), this indicates that thermally populated metal-centered states become involved and lead to high nonradiative rates. On the other hand, for neat [*n*-Bu$_4$N][Pt(4,6-dFppy)(CN)$_2$] (**4**) and for Pt(4,6-dFdpyb)Cl (**7**) in solution, the nonradiative rates are significantly lower. Thus, it is obvious that the quenching states are less populated in these cases of a more rigid environment or a more rigid complex. As a consequence, the quantum yields are distinctly higher and the decay times are longer[6] [63, 102, 103].

The observed behavior can be rationalized when taking into account that the geometries of metal-centered dd* states are strongly distorted with respect to the electronic ground state [96, 99, 112]. It is not straightforward to predict the type of geometry change, but it can be assumed that elongations of Pt–N and Pt–C bonds as well as slight tetrahedral distortions are important factors. Both effects lead to a decrease of the ligand field strength and thus to an energy stabilization of quenching dd* states. Especially, for Pt(4,6-dFppy)(acac) and [Pt(4,6-dFppy)(CN)$_2$]$^-$, the

6) For completeness, it is remarked that for the neat material **4**, effects of energy transfer between the emitter complexes, as well as self-quenching and triplet–triplet annihilation, do not seem to be important.

bidentate ligands can potentially twist in the "soft" fluid environment. Thus, a thermally activated population of metal-centered states becomes more effective at ambient temperature. For Pt(4,6-dFdpyb)Cl, on the other hand, it can be assumed that the quenching states are not significantly shifted to lower energy even in solution, since the described geometry changes are suppressed by the higher molecular rigidity of the complex with the terdentate ligand. Moreover, Pt(4,6-dFdpyb)Cl exhibits a distinctly shorter platinum–carbon bond length (1.91 Å versus ≈2.0 Å for **4**) [102, 113], which leads to a higher ligand field strength of the N^C^N ligand (4,6-dFdpyb) compared to the N^C ligand (4,6-dFppy). Consequently, the dd* states lie at higher energy for **7** and, thus, emission quenching is less probable [103].

The high quantum efficiency of neat [*n*-Bu_4N][Pt(4,6-dFppy)$(CN)_2$] can be explained in an analogous manner. The described distortions are largely suppressed in the rigid crystalline environment, and thus an energy stabilization of the quenching dd* states is largely prevented, in contrast to the situation in fluid solution. Similar models have also been applied to explain the relatively high emission quantum yields of Ru(II) polypyridine compounds in rigid host media, like zeolites [114], glasses [115], or polymeric matrices [116] compared to fluid solutions.

Differences between the materials can also be observed in the radiative decay rates at ambient temperature, amounting to $3.2 \times 10^4\,s^{-1}$ (**4** neat), $7.7 \times 10^4\,s^{-1}$ (**6**), and $1.2 \times 10^5\,s^{-1}$ (**7**) (Table 13.2). This indicates that spin–orbit coupling with higher lying singlet MLCT states, which promotes the radiative decay from the T_1 state to the singlet ground state, is more effective for the terdentate compound than for the bidentate ones. A more detailed analysis of these effects is not possible with ambient temperature measurements, which only lead to broad and unresolved spectra. Therefore, we studied the materials' photophysical properties with methods of high-resolution optical spectroscopy at cryogenic temperatures (next section). In particular, this allows us to determine the photophysical properties of the T_1 substates (zero-field splitting, individual decay times, etc.). Based on these parameters, assignments of the nature of the emitting triplet states become possible [36, 49, 56, 63].

13.4.1.2 High-Resolution Spectroscopy: Triplet Substates and Vibrational Satellite Structures

At ambient temperature, much information on the emitting triplet state and the related photophysical properties is lost due to thermal broadening, electron–phonon coupling, and thermalization effects. On the other hand, at cryogenic temperatures, highly resolved and thus very informative emission and excitation spectra are often obtainable. However, this requires suitable host matrices. For example, for planar molecules, such as Pd(II) or Pt(II) complexes as well as many organic molecules, it has been shown that by use of linear *n*-alkanes as host materials, the so-called Shpol'skii matrices [117], highly resolved electronic and vibronic spectra, can be obtained [36, 49, 56, 62, 63, 78, 88, 103, 118–121]. In such polycrystalline alkane matrices, the guest molecules (dopants) substitute host molecules and thus lie at defined positions in relatively rigid cages. The resulting spectra are often more than a hundred times better resolved than found with glass-forming or amorphous matrices.

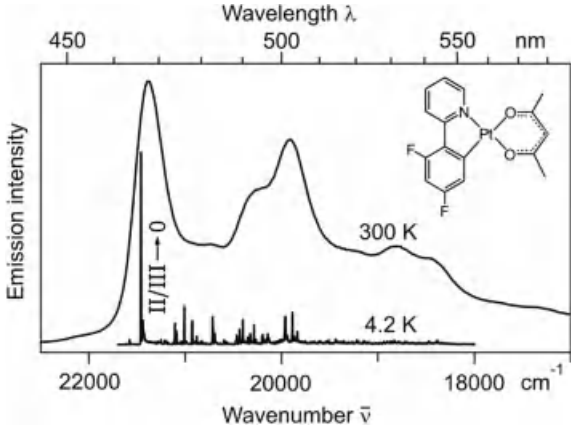

Figure 13.9 Emission spectra of Pt(4,6-dFppy)(acac) (**6**) at 300 K ($\lambda_{exc} = 370$ nm) and at 4.2 K in *n*-octane. The spectrum at 4.2 K represents a site-selective spectrum of the site of lowest energy. The electronic 0–0 transitions between the triplet substates II/III and the electronic ground state 0(S_0) lie at 21 461 cm^{-1}. For further discussions of the vibrational satellite structure, see Figure 13.14 and below in this section. Adapted from Ref. [63].

This technique has successfully been applied for Pt(4,6-dFppy)(acac) (**6**) and Pt(4,6-dFdpyb)Cl (**7**) by using *n*-alkane matrices and measuring at cryogenic temperatures[7] [63, 103, 119–121]. The procedure is shortly exemplified for Pt(4,6-dFppy)(acac) in *n*-octane. After cooling the sample to 4.2 K and exciting it unselectively with UV light, the emission spectrum consists of a manifold of narrow lines with halfwidths of only a few cm^{-1} and a weak background (not shown). These lines correspond to a number of discrete sites of dopant molecules in the *n*-octane matrix. Using a tunable dye laser, a specific site can be excited selectively. For this purpose, the site of lowest energy was chosen, since its emission is well detectable and a perturbing excitation of higher lying sites can be avoided. In Figure 13.9, the drastic effects of this strategy are illustrated by comparing the selectively excited emission spectrum measured in *n*-octane at $T = 4.2$ K with the emission recorded at ambient temperature in the same solvent.

It will be shown below that the most intense line in the selectively excited emission of Pt(4,6-dFppy)(acac) represents the electronic 0–0 transition from two specific substates of the emitting triplet state T_1, denoted as substates II and III, to the singlet ground state S_0. The lines of minor intensity at lower energy correspond to vibrational satellites stemming from ground-state modes.

Electronic 0–0 Transitions and Energy Level Diagrams of the T_1 States In the following, we focus on the purely electronic transitions of the three Pt(II) compounds,

7) For $[Pt(4,6\text{-dFppy})(CN)_2]^-$ (**4**), highly resolved spectra could be registered using the neat crystalline material with the $[n\text{-}Bu_4N]^+$ counterion [102].

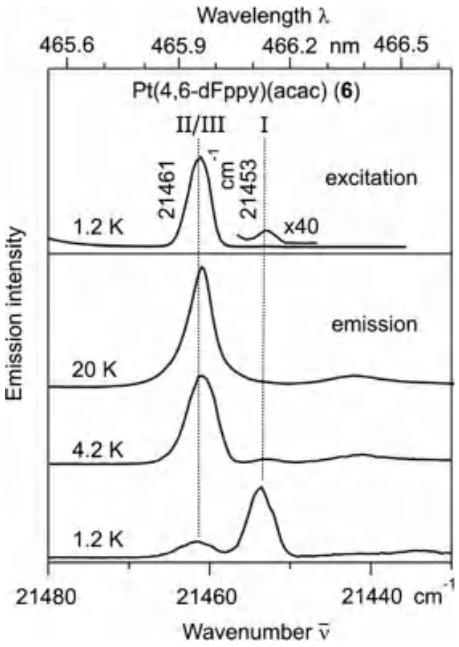

Figure 13.10 Site-selective excitation and emission spectra of Pt(4,6-dFppy)(acac) (**6**) in *n*-octane at different temperatures in the range of the electronic 0–0 transitions ($T_1 \leftrightarrow S_0$ transitions). I, II, and III represent the substates of the emitting triplet state. Adapted from Ref. [63].

that is, on the electronic 0–0 transitions between the substates of the emitting T_1 state and the S_0 ground state.

Figures 13.10 and 13.11 show selectively excited emission and excitation spectra of **6** and **7** for the region of the electronic 0–0 transitions. For both materials, the three substates of the emitting triplet state T_1 can be identified [63, 103, 120, 121].

For Pt(4,6-dFppy)(acac) (**6**) in *n*-octane, only two lines corresponding to electronic 0–0 transitions can be observed in excitation and emission spectra at zero magnetic field, lying at 21 453 and 21 461 cm^{-1}. The high-energy transition carries a distinctly higher oscillator strength (higher allowedness) than the lower lying one. It has been shown by Zeeman experiments that the line at 21 461 cm^{-1} corresponds to the two higher lying T_1 substates II and III, since this line splits into two lines in emission and excitation when high magnetic fields of up to $B = 12$ *T* are applied [121]. As a consequence, the zero-field splitting of Pt(4,6-dFppy)(acac) in *n*-octane amounts to $\Delta E_{II-I} \approx \Delta E_{III-I} = \Delta E(ZFS) = 8.3\ cm^{-1}$. It is stressed that other sites of the material in *n*-octane and even in CH_2Cl_2 exhibit very similar zero-field splittings [63]. Thus, the triplet state properties do not strongly depend on the host environment, in contrast to the situation found for the Ir(III) compounds discussed in Section 13.4.2.

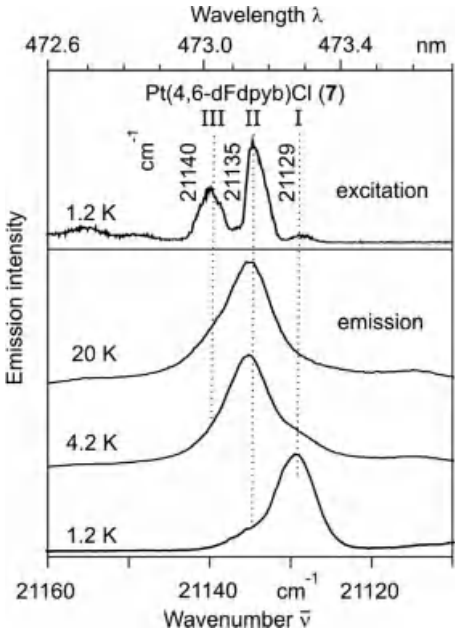

Figure 13.11 Site-selective excitation and emission spectra of Pt(4,6-dFdpyb)Cl (**7**) in *n*-decane at different temperatures in the range of the electronic 0–0 transitions ($T_1 \leftrightarrow S_0$ transitions). Adapted from Ref. [103].

Pt(4,6-dFdpyb)Cl (**7**) was studied in *n*-decane, which allowed to obtain better resolved spectra than in the more common *n*-octane host [103]. All three triplet substates can be observed in excitation, the corresponding 0–0 transitions lie at 21 129 ($0 \rightarrow$ I), 21 135 ($0 \rightarrow$ II), and 21 140 cm^{-1} ($0 \rightarrow$ III). An intensity ratio of $Int(0 \rightarrow II)/Int(0 \rightarrow III)/Int(0 \rightarrow I) = 15/10/1$ is found. This reflects the ratio of the oscillator strengths of these 0–0 transitions. According to its very low allowedness, the weak transition $I \rightarrow 0$ can be observed in emission only at very low temperatures, for example, at 1.2 K. At higher temperatures, the emission from substate II dominates, while the transition $III \rightarrow 0$ occurs only as a shoulder. The spectra depicted in Figure 13.11 allow us to determine the zero-field splitting parameters of Pt(4,6-dFdpyb)Cl (**7**) (in *n*-decane) to $\Delta E_{II-I} = 5.8\,cm^{-1}$ and $\Delta E_{III-I} = \Delta E(ZFS) = 11.3\,cm^{-1}$.

The individual decay times of the T_1 substates of **6** and **7** have been determined by temperature-dependent measurements of the emission decay times. For a system of three thermally equilibrated excited states (i.e., the triplet substates I, II, and III), the temperature-dependent averaged decay time τ_{av} is given by the expression [36, 56, 63, 83, 122]

$$\tau_{av} = \frac{1 + \exp((-\Delta E_{II-I})/(k_B T)) + \exp((-\Delta E_{III-I})/(k_B T))}{k_I + k_{II} \cdot \exp((-\Delta E_{II-I})/(k_B T)) + k_{III} \cdot \exp((-\Delta E_{III-I})/(k_B T))} \qquad (13.3)$$

wherein $k_i = 1/\tau_i$ (i = I, II, III) is the rate constant for the depopulation of substate i to the ground state and ΔE_{II-I} and ΔE_{III-I} are the energy separations between the substates as determined from highly resolved spectra. Applying Eq. (13.3) to the measured decay times, one can determine the individual substate decay times to $\tau_I = 28.0\,\mu s$, $\tau_{II} = 2.0\,\mu s$, and $\tau_{III} = 3.2\,\mu s$ for **7** [103]. For **6**, a modified equation, considering the energetic quasi-degeneracy of the substates II and III, was applied. The following decay times were obtained: $\tau_I = 85\,\mu s$ and $\tau_{II/III} = 2.6\,\mu s$ [52, 63].

The [n-Bu_4N][Pt(4,6-dFppy)$(CN)_2$] salt is insoluble in n-alkanes. However, the material's properties could be investigated by studying the emission of a single crystal at cryogenic temperatures and, in addition, by carrying out temperature-dependent measurements of the emission decay time in a THF (tetrahydrofuran) host [102]. In this chapter, we will focus on the latter investigation.

The emission decay curves of [n-Bu_4N][Pt(4,6-dFppy)$(CN)_2$] (**4**) in THF, measured at 1.2, 20, and 100 K, are depicted in Figure 13.12. A distinctly non-monoexponential decay is observed at 1.2 K. It can be fit with a three-exponential decay function. This indicates that the three T_1 substates are not in a thermal equilibrium at this low temperature and emit independently according to their initial population with their individual decay times. These are determined to $\tau_I = 100\,\mu s$, $\tau_{II} = 31.5\,\mu s$, and $\tau_{III} = 11.5\,\mu s$ [102]. The occurrence of three individual decay times at 1.2 K indicates very small energy separations between the T_1 substates and thus a very small total zero-field splitting. Presumably it is smaller than 1 or $2\,cm^{-1}$ [102].

With temperature increase, the relaxation processes between the T_1 substates (spin–lattice relaxation (SLR)) [49, 123] become faster and a thermal equilibrium establishes. At 10 K, a monoexponential decay with a time constant of $\tau_{av} = 23.8\,\mu s$ is observed. This value decreases only slightly with further temperature increase. At 20 K, for example, the decay constant amounts to 22.7 μs, at 77 K to 21.5 μs, and at 100 K to 21.2 μs. Thus, no higher lying electronic state is thermally populated in this temperature range.

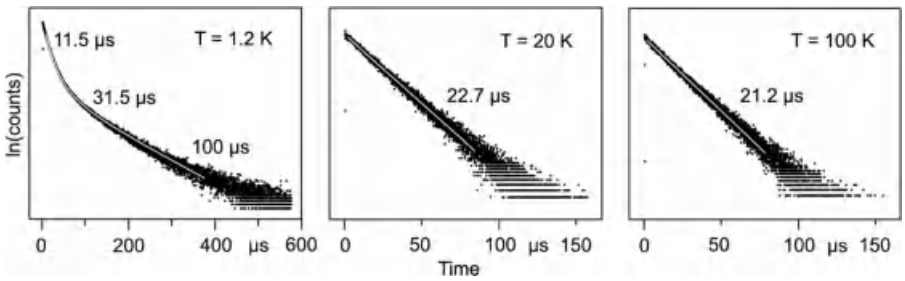

Figure 13.12 Emission decay curves of [n-Bu_4N][Pt(4,6-dFppy)$(CN)_2$] (**4**) in THF at different temperatures. The lines depicted in the diagrams represent fits of the measured data with a triple exponential (1.2 K) and monoexponential decay functions (20 and 100 K), respectively. The emission was detected at $\lambda_{det} = 460$ nm.

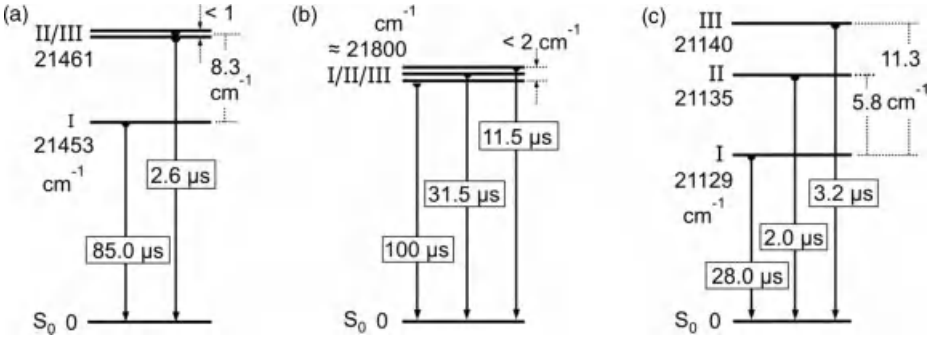

Figure 13.13 Energy level diagrams and individual decay times of the emitting triplet substates of (a) Pt(4,6-dFppy)(acac) (**6**), (b) [*n*-Bu_4N][Pt(4,6-dFppy)$(CN)_2$] (**4**), and (c) Pt(4,6-dFdpyb)Cl (**7**).

For a compound that exhibits three triplet substates with energy separations ΔE_{II-I} and $\Delta E_{III-I} \ll k_B T$ and relaxation times much faster than the individual decay times of the three substates τ_I, τ_{II}, τ_{III} to the electronic ground state, Eq. (13.3) simplifies to [36, 49, 102, 123, 124]

$$\tau_{av} = 3\left(\frac{1}{\tau_I} + \frac{1}{\tau_{II}} + \frac{1}{\tau_{III}}\right)^{-1} \tag{13.4}$$

At higher temperatures, when the substates are in a fast equilibration, an average decay time τ_{av} is expected to occur and it should remain constant with temperature increase. Indeed, this behavior is found for [*n*-Bu_4N][Pt(4,6-dFppy)$(CN)_2$] (**4**). Inserting the individual decay times as determined at 1.2 K into Eq. (13.4), one obtains a value of $\tau_{av} = 23.2\,\mu s$, which matches very well with the experimentally determined decay time of 23.8 µs measured at 10 K.

The information worked out for the emitting triplet states of the compounds Pt(4,6-dFppy)(acac) (**6**), Pt(4,6-dFdpyb)Cl (**7**), and [*n*-Bu_4N][Pt(4,6-dFppy)$(CN)_2$] (**4**) is summarized in energy level diagrams as displayed in Figure 13.13.

According to an empirical ordering scheme, which relates the magnitude of ΔE(ZFS) to the orbital nature of the lowest triplet state [36, 49, 56, 63], the T_1 states of Pt(4,6-dFppy)(acac) and Pt(4,6-dFdpyb)Cl with ΔE(ZFS) values of 8.3 and 11.3 cm^{-1}, respectively, can be classified as largely ligand-centered states with moderate metal-to-ligand charge transfer admixtures. The ΔE(ZFS) value of [*n*-Bu_4N][Pt(4,6-dFppy)$(CN)_2$] is smaller than 1 or 2 cm^{-1}. This indicates a ligand-centered T_1 state with only very small MLCT contributions. Thus, spin–orbit coupling is weaker for the ionic compound than for the other two materials. These aspects will be further discussed in the following section.

Vibrational Satellite Structures Exemplified on Pt(4,6-dFppy)(acac) High-resolution spectroscopy at cryogenic temperatures not only allows us to gain detailed information on the electronic properties of organotransition metal compounds, but

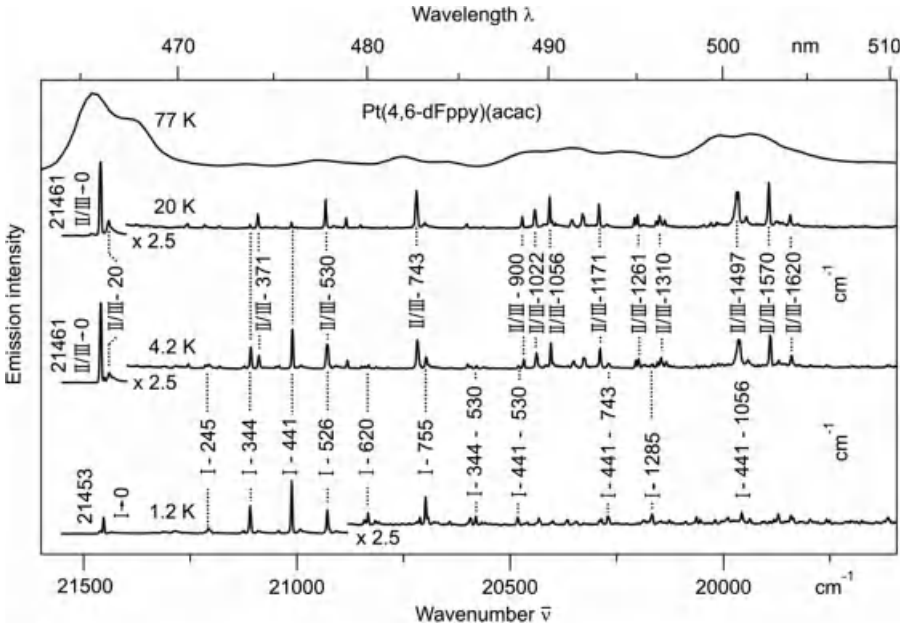

Figure 13.14 Site-selective emission spectra of Pt(4,6-dFppy)(acac) (**6**) in *n*-octane measured at different temperatures. For comparison, a spectrum obtained at 77 K in the same host is also shown. The energies of the vibrational satellites are given relative to the respective electronic 0–0 transitions. Adapted from Ref. [63].

is also a powerful tool to study the vibrational satellite structures and their underlying mechanisms. As an example, we will focus on Pt(4,6-dFppy)(acac) (**6**). Figure 13.14 shows selectively excited emission spectra of **6** dissolved in *n*-octane at $T = 1.2$, 4.2, and 20 K, together with a spectrum obtained at 77 K for comparison.

The low-temperature spectra consist of sharp lines corresponding to the electronic 0–0 transitions, as discussed above, and to a large number of vibrational satellites. An inhomogeneous background, which frequently occurs in addition, is almost absent. Many of the observed vibrational lines represent fundamentals stemming from vibrational ground-state modes. Low-energy modes with energies up to $\approx 100\,cm^{-1}$ relative to the electronic origins are mainly governed by vibrations of the dopant in its matrix cage, representing so-called local phonon modes [125, 126]. Overlapping with this energy range up to $500/600\,cm^{-1}$, vibrations with considerable metal–ligand character can be found (e.g., I – $441\,cm^{-1}$, II/III – $530\,cm^{-1}$) [49, 127]. Modes with energies higher than $\approx 600\,cm^{-1}$ can usually be assigned as internal vibrations of the chromophoric ligand that are not strongly affected by the metal center [49, 128, 129].

The spectrum at $T = 1.2$ K almost completely consists of an emission from the lowest T_1 substate I, since the higher lying substates II and III are barely populated at this temperature. It can clearly be seen that the electronic 0–0 transition $I \rightarrow 0$ is less

intense than several vibrational satellites that lie mainly in the ML range, such as the I – 344 cm^{-1} and I – 441 cm^{-1} satellites. Obviously, the radiative deactivation via the purely electronic transition is less efficient than the radiative deactivation involving vibrational modes. Moreover, for these fundamental vibrations, no progressions occur. Similarly, as extensively demonstrated for $Pt(thpy)_2$ (**9**) [49, 56, 130], it has been shown that the observed vibrational satellite structure in the emission of substate I of Pt(4,6-dFppy)(acac) in *n*-octane is mainly induced by processes of vibronic coupling to higher lying states [121]. This type of coupling, often called Herzberg–Teller (HT) coupling [49, 56, 131, 132], represents the dominating radiative deactivation mechanism, if the electronic 0–0 transition is only weakly allowed.

A completely different situation is observed when the temperature is increased to 4.2 K. Now, the spectrum is dominated by an emission stemming from the substates II/III. They carry a much higher allowedness with respect to the 0–0 transition to the electronic ground state. As a consequence, the vibrational modes involved in the emission of these substates are different from those found for substate I. In particular, for several fundamentals, such as the 1056 and 1497 cm^{-1} vibrational modes, second (weak) members of progressions can be observed (not displayed in Figure 13.14). Thus, it can be concluded that these modes represent totally symmetric Franck–Condon (FC) active modes [49, 63, 118, 121, 132, 133].

Further temperature increase from 4.2 to 20 K does not lead to significant changes of the emission spectrum. Interestingly, the most intense HT-induced satellites of substate I (e.g., the satellites corresponding to the 344 and 441 cm^{-1} vibrational modes) can still be detected at 20 K. Vibronic coupling with respect to substate I seems to be very strong for these specific HT active vibrations. Nevertheless, the vibrational satellite structure at $T = 20$ K is dominated by the emission stemming from the substates II/III. Even at this temperature, the spectrum still consists of sharp emission lines. Only weak temperature-dependent broadening effects occur. This indicates that the coupling between the electronic and vibronic transitions of the compound and the host environment, the electron–phonon coupling [125, 134], is very weak. This can mainly be ascribed to the largely ligand-centered character of the T_1 state of Pt(4,6-dFppy)(acac) (**6**), with only small charge transfer contributions occurring upon the $T_1 \leftrightarrow S_0$ transition, and the non-polar *n*-octane matrix.

As already mentioned, the spectra at 4.2 and 20 K show weak FC progressions. In this situation, one can determine the corresponding Huang–Rhys parameter S according to Eq. (13.5) [49, 133, 135]:

$$S = v \cdot \frac{I_v}{I_{v-1}} \tag{13.5}$$

wherein v is the vibrational quantum number and I_v is the intensity of the respective member of the Franck–Condon progression. The Huang–Rhys parameter is related to the Franck–Condon factor of the corresponding vibrational transition and allows to obtain quantitative information on the shifts ΔQ of the potential energy surfaces of the involved electronic states along the respective vibrational

normal coordinate. For the vibrational modes of 1056 and 1497 cm^{-1}, one finds values of $S = 0.2$ [63]. This indicates very small geometry changes between the singlet ground state and the T_1 substates II/III, at least in the crystalline and rigid *n*-octane matrix at cryogenic temperatures.

Interestingly, the Huang–Rhys parameters obtained for the Franck–Condon active modes of Pt(4,6-dFdpyb)Cl (**7**) with the terdentate ligand are at cryogenic temperatures by a factor of 2 smaller than those observed for Pt(4,6-dFppy)(acac) (**6**) with bidentate ligands, although both materials exhibit similar zero-field splittings [103]. This can be explained by the chelate effect. In particular, geometry changes occurring with an electronic excitation are expected to be smaller for complexes with terdentate than with bidentate ligands. In Pt(4,6-dFppy)(acac), the bidentate (4,6-dFppy) ligand can twist relative to the plane containing the (acac) ligand, in contrast to the situation of Pt(4,6-dFdpyb)Cl. Furthermore, changes of metal–ligand bond lengths are also expected to be less distinct in the latter case. Consequently, smaller displacements ΔQ of the potential energy surfaces of the involved states are expected for **7** than for **6**. Thus, smaller Huang–Rhys parameters result for compound **7** with the more rigid terdentate ligand than for compound **6**. This trend concerning the Huang–Rhys parameters is also reflected in the ambient temperature emission spectra of both compounds. A comparison clearly shows that the intensities of the vibrational satellite bands are significantly smaller for Pt(4,6-dFdpyb)Cl (**7**) than for Pt(4,6-dFppy)(acac) (**6**) (see Figure 13.8).

Comparative Discussion In summary, the compounds Pt(4,6-dFppy)(acac) (**6**), [*n*-Bu_4N][Pt(4,6-dFppy)$(CN)_2$] (**4**), and Pt(4,6-dFdpyb)Cl (**7**) exhibit similar energies of their lowest triplet states and show blue phosphorescence. However, the emission quantum yields and decay times vary significantly, as well as the color purity of the emitted light.

The substitution of acac by two CN^- ancillary ligands results in a higher mean ligand field strength and thus leads to a stabilization of occupied and a destabilization of unoccupied central metal d-orbitals. Therefore, it is expected that the MLCT states are shifted to higher energy, while the π- and π*-orbitals of the chromophoric ligand can be assumed to remain largely unaffected. As a consequence, this leads to decreasing ^{1,3}MLCT contributions in the T_1 state (via indirect SOC) (see Section 13.3.2). Indeed, this is supported by the experimental results. The zero-field splitting of the T_1 state of **4** is distinctly smaller than that of **6** and **7** and the averaged radiative rate at ambient temperature of **4** is lower than that of the two other compounds (Table 13.2). Moreover, since the strong-field CN^- ligands also destabilize the (quenching) metal-centered dd* states, the emission quantum yield at ambient temperature increases compared to compound (**6**). This is at least valid for neat [*n*-Bu_4N][Pt(4,6-dFppy)$(CN)_2$] (**4**). The dissolved material (**4**) is almost non-emissive. Possibly, the ionic compound **4** undergoes an even larger geometrical distortion upon excitation, leading to a larger decrease of the activation energy for the dd* states in a fluid environment than Pt(4,6-dFppy)(acac) (**6**) [102].

The emission quantum yield of the terdentate compound Pt(4,6-dFdpyb)Cl (**7**) in solution is much higher than that of the compounds with bidentate ligands

(Table 13.2). This shows that the strategy of using terdentate instead of bidentate ligands and thus minimizing geometrical distortions in the excited state is successful. Furthermore, this structural aspect significantly improves the color purity of the blue emission, since the intensities of vibrational bands are distinctly smaller as compared to those of the compounds with bidentate chromophoric ligands. This is also reflected in the smaller Huang–Rhys parameters of intraligand modes determined from highly resolved spectra at cryogenic temperatures [103].

13.4.2 Ir(III) Compounds

Cyclometalated octahedral Ir(III) compounds, such as the famous $Ir(ppy)_3$ (**23**), represent the most efficient phosphorescent emitters used in OLEDs. In this chapter, we present investigations of the blue light emitting materials $Ir(4,6\text{-}dFppy)_2(pic)$ (**14**) and $Ir(4,6\text{-}dFppy)_2(acac)$ (**21**) [84, 86]. These complexes contain the same chromophoric ligands as the Pt(II) compounds, discussed in Section 13.4.1. Moreover, $Ir(4,6\text{-}dFppy)_2(acac)$ (**21**) also has the same ancillary ligand as Pt(4,6-dFppy)(acac) (**6**). Thus, a comparison of the photophysical properties of the Pt(II)- and Ir(III)-based materials allows to obtain additional information on the influence of the central metal ion and the coordination sphere on the emitting triplet states. Both Ir(III) compounds were first reported by Thompson and coworkers [87].

Especially, $Ir(4,6\text{-}dFppy)_2(pic)$, often called FIrpic, represents an efficient phosphorescent emitter for blue light emitting OLEDs [136–138]. Furthermore, it was applied in multilayer white light emitting OLEDs in combination with other dopants [139, 140] and as hole-blocking and electron-transporting material [141]. Also, energy transfer and emission quenching processes in various matrices have been studied [142, 143]. Moreover, both Ir(III) compounds (**14** and **21**) were investigated theoretically [144, 145] and by detailed photophysical studies [84, 86].

13.4.2.1 Photophysical Properties at Ambient Temperature

Figure 13.15 shows the emission spectra of $Ir(4,6\text{-}dFppy)_2(pic)$ (**14**) and $Ir(4,6\text{-}dFppy)_2(acac)$ (**21**) in CH_2Cl_2 measured under ambient conditions. The emission spectrum of $Ir(4,6\text{-}dFppy)_2(pic)$ (**14**) has its maximum at 470 nm, the decay time is 1.9 μs, and the phosphorescence quantum yield amounts to 83% (in deaerated solution). The spectrum of $Ir(4,6\text{-}dFppy)_2(acac)$ (**21**) is slightly less structured and lies at lower energy with an emission maximum at 484 nm, a decay time of 1.0 μs, and a photoluminescence quantum yield of 64%. These photophysical data are summarized in Table 13.3 [84, 86].

At ambient temperature, the emission spectra of both compounds are significantly less resolved than the spectra of the Pt(II) compounds studied in Section 13.4.1. This already indicates a considerably larger MLCT character in the emitting states of $Ir(4,6\text{-}dFppy)_2(pic)$ (**14**) and $Ir(4,6\text{-}dFppy)_2(acac)$ (**21**). This is associated with pronounced metal–ligand vibrational satellites with energies below 600 cm^{-1} relative to the electronic origin. These satellites lead to a smearing out of

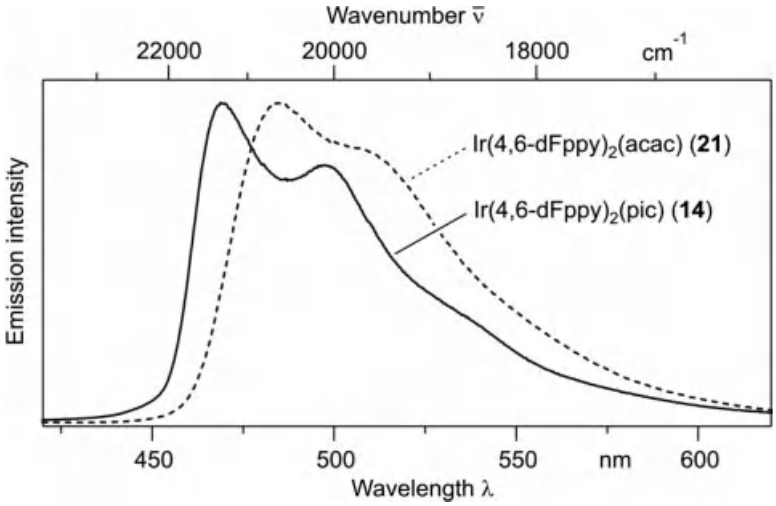

Figure 13.15 Emission spectra of Ir(4,6-dFppy)$_2$(pic) (**14**) (= FIrpic) and Ir(4,6-dFppy)$_2$(acac) (**21**) dissolved in CH_2Cl_2 at ambient temperature. Adapted from Ref. [84].

the emission spectra at ambient temperature [146, 147]. Furthermore, smearing out is also a consequence of stronger electron–phonon coupling that occurs with an MLCT transition. Moreover, the large halfwidths of the emission spectra are determined by overlapping vibrational satellites that correspond to vibrational fundamentals, progressions, and combinations (see also Section 13.4.2.3). Interestingly, the radiative rate of the $T_1 \rightarrow S_0$ transition of compound (**21**) is by 45% larger than that of compound **14**, but **14** has a significantly higher emission quantum

Table 13.3 Emission properties of Ir(4,6-dFppy)$_2$(pic) and Ir(4,6-dFppy)$_2$(acac) in CH_2Cl_2 at ambient temperature.

Compound	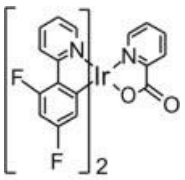 **14** Ir(4,6-dFppy)$_2$(pic)	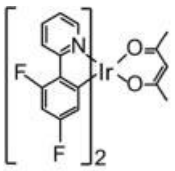 **21** Ir(4,6-dFppy)$_2$(acac)
λ_{max} (nm)	470	484
τ (μs)	1.9	1.0
ϕ_{PL} (%)	83	64
k_r (s^{-1})	4.4×10^5	6.4×10^5
k_{nr} (s^{-1})	0.9×10^5	3.6×10^5
$\{x; y\}^{a)}$	{0.16; 0.35}	{0.18; 0.48}

a) CIE1931 color space coordinates [111].

yield. This is a consequence of the distinctly smaller nonradiative rate of **14** compared to **21**. These effects will be discussed further in Section 13.4.2.4.

For completeness, it is referred to Section 13.4.3, in which photophysical properties of the Ir(III) compounds **14** and **21** are compared with those of the Pt(II) complexes **4**, **6**, and **7**.

13.4.2.2 Electronic 0–0 Transitions and Energy Level Diagrams of the Emitting Triplet States

In Section 13.4.1, it has been shown that *n*-alkanes cooled to cryogenic temperatures can represent well-suited host materials for high-resolution optical spectroscopy of Pt(II) compounds. For Ir(III) compounds, on the other hand, only a few such studies in *n*-alkanes are known [62, 90]. However, recently it has been shown that CH_2Cl_2 can represent a suitable low-temperature host for Ir(III) complexes, allowing to obtain optical spectra of good quality [52, 62, 148, 149].

Figure 13.16 shows site-selective emission and excitation spectra of Ir(4,6-dFppy)$_2$(pic) (**14**) and Ir(4,6-dFppy)$_2$(acac) (**21**) measured in CH_2Cl_2 in the region of the electronic 0–0 transitions at different temperatures [84, 86]. For both compounds, the highest triplet substate III strongly dominates the excitation spectrum. Consequently, the corresponding transition carries by far the

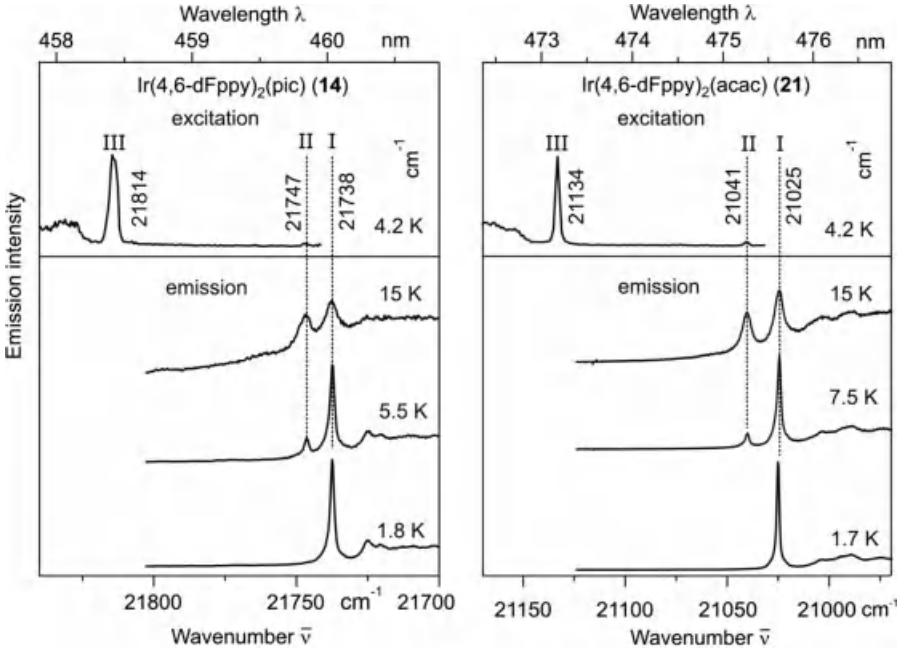

Figure 13.16 Site selective excitation and emission spectra of Ir(4,6-dFppy)$_2$(pic) (**14**) and Ir(4,6-dFppy)$_2$(acac) (**21**) measured in CH_2Cl_2 at different temperatures in the range of the electronic 0–0 transitions ($T_1 \leftrightarrow S_0$ transitions). Adapted from Refs [84, 86].)

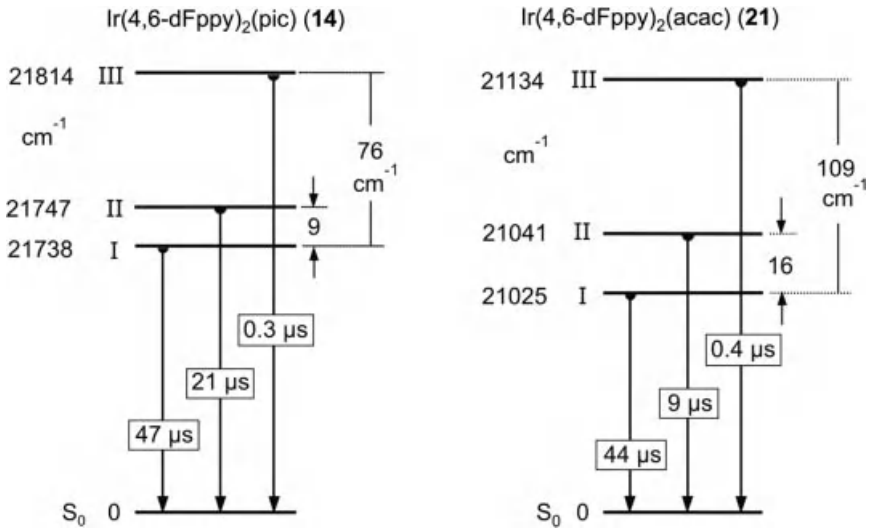

Figure 13.17 Energy level diagrams and individual decay times of the emitting triplet substates of Ir(4,6-dFppy)$_2$(pic) (**14**) and Ir(4,6-dFppy)$_2$(acac) (**21**).

largest allowedness of the three T_1 substates. However, at low temperatures, the emission behavior is governed by the substates I and II. From the spectra shown in Figure 13.16, one can directly deduce the zero-field splitting energies of the compounds' T_1 states. These data are summarized in the energy level diagrams depicted in Figure 13.17. The total zero-field splitting ΔE(ZFS) of Ir(4,6-dFppy)$_2$(acac) (**21**) is with 109 cm^{-1} higher than the value of 76 cm^{-1} found for Ir(4,6-dFppy)$_2$(pic) (**14**). This indicates a slightly higher MLCT character of the emitting state and a higher spin–orbit coupling efficiency with respect to the T_1 state of the compound **21**. This is in line with the trend observed for the radiative rates determined at ambient temperature (Table 13.3).

The diagrams shown in Figure 13.17 also display the decay times of the individual T_1 substates. These data have been determined by fitting equation (13.3) to the measured emission decay times at different temperatures [84, 86]. It is stressed that the relatively short emission decay times of the substates III, amounting to τ_{III}(**14**) = 0.3 µs and τ_{III}(**21**) = 0.4 µs, respectively, correspond to the relatively high allowedness of the $0 \rightarrow$ III transitions. This has already been deduced from the excitation spectra depicted in Figure 13.16. Especially, if high transition probabilities or high radiative rates are connected with high emission quantum yields, a corresponding material is potentially well suited for OLED applications. This situation is met particularly with Ir(4,6-dFppy)$_2$(pic) (**14**).

Interestingly, and in contrast to the Pt(II) compounds studied in Section 13.4.1, the T_1 state properties of Ir(4,6-dFppy)$_2$(pic) (**14**) and Ir(4,6-dFppy)$_2$(acac) (**21**) strongly depend on the host environment. For example, other sites of the compounds in CH_2Cl_2 exhibit significantly different zero-field splitting parameters. Furthermore, in host matrices, in which only broadband spectra can be obtained

even at cryogenic temperatures, it was observed that the zero-field splittings and T_1 sublevel decay times are spread over a relatively broad range [63, 84, 86]. This behavior can be attributed to a high metal-to-ligand charge transfer character of the materials' emitting states and a strong sensitivity of these MLCT states to influences of the host environment [36, 52, 90, 108].

13.4.2.3 Vibrational Satellite Structures Exemplified on Ir(4,6-dFppy)$_2$(acac)

The studied Ir(III) compounds differ from the Pt(II) compounds discussed in Section 13.4.1 not only in the electronic but also in the vibronic properties. As an example, we will shortly discuss the vibrational satellite structure that is observable in the highly resolved emission of Ir(4,6-dFppy)$_2$(acac) (**21**) in CH_2Cl_2 [63]. Figure 13.18 shows site-selective emission spectra measured at 1.7 and 10 K. The 77 K spectrum is also shown for comparison.

The spectrum at 1.7 K shows a series of narrow emission lines. However, a broad spectral background is also present. It is much more intense than that observed for Pt(4,6-dFppy)(acac) (**6**) in *n*-octane. This is probably a consequence of stronger electron–phonon coupling (see below) and of contributions of inhomogeneously distributed emitter molecules in the CH_2Cl_2 environment. At 1.7 K, only the lowest triplet substate I emits, with the electronic 0–0 transition I → 0 being much more intense than the vibrational satellite lines. This demonstrates that the electronic 0–0 transition I → 0 of Ir(4,6-dFppy)$_2$(acac) (**21**) in CH_2Cl_2 carries distinct

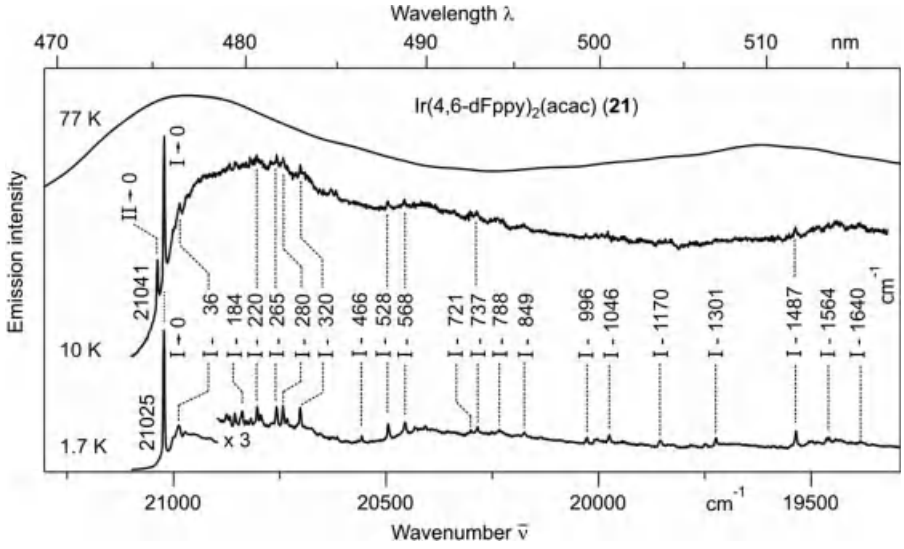

Figure 13.18 Site-selective emission spectra of Ir(4,6-dFppy)$_2$(acac) (**21**) in CH_2Cl_2 at 1.7 and 10 K. For comparison, a spectrum obtained at 77 K in the same host is also shown. The energies of the vibrational satellites are given relative to the electronic 0–0 transition I → 0. Adapted from Ref. [63].

allowedness. Thus, processes of vibronic HT coupling, being important for Pt(4,6-dFppy)(acac) (**6**) at 1.2 K (Section 13.4.1), are of minor importance for this Ir(III) compound. Presumably, most of the vibrational satellites in the emission of substate I can be assigned to result from the Franck–Condon activity. However, second members of FC progressions could not be resolved due to the high background emission, the weak intensities of the fundamental vibrations, and the small Huang–Rhys parameters (being presumably smaller than 0.1).

In the range of vibrational metal–ligand modes at energies below $\approx 600\,cm^{-1}$, distinctly more satellites are observed in the emission of substate I of the Ir(III) compound **21** than found for the Pt(II) compound **6** with the same ligands (compare Figures 13.14 and 13.18). The relatively high intensities of ML satellites are characteristic of a large MLCT character of the emitting triplet state of Ir(4,6-dFppy)$_2$(acac) (**21**) [146, 147]. As already mentioned, these ML vibrational satellites are also responsible for the smearing out the emission spectra at higher temperatures [63].

The highly resolved emission spectrum of Ir(4,6-dFppy)$_2$(acac) (**21**) shows a pronounced temperature dependence, which, however, is strongly different from the situation observed for Pt(4,6-dFppy)(acac) (**6**). When the temperature is increased from 1.7 to 10 K, the electronic 0–0 transition II $\rightarrow$ 0 grows in, but the line I $\rightarrow$ 0 still exhibits the highest intensity at that temperature. Independent of this effect, the spectrum broadens and, thus, narrow vibrational satellite lines can be observed only weakly. This temperature-dependent broadening is assigned to be a consequence of relatively strong electron–phonon coupling, being connected with a large charge transfer character of the lowest ^{3}MLCT state of Ir(4,6-dFppy)$_2$(acac) (**21**) and with the polar nature of the CH_2Cl_2 host [62, 125, 134, 150].

13.4.2.4 Effects of the Nonchromophoric Ligands

For Ir(4,6-dFppy)$_2$(pic) (**14**) and Ir(4,6-dFppy)$_2$(acac) (**21**), the (4,6-dFppy) ligands are mainly involved in the electronic MLCT transitions. Therefore, they are regarded as chromophoric ligands, while (pic) and (acac) represent nonchromophoric or ancillary ligands. This distinction mainly refers to the energy positions of the corresponding states. Obviously, the states lie at significantly higher energies in (pic) and (acac) compared to (4,6-dFppy). Nevertheless, the two compounds **14** and **21** exhibit systematic differences in their photophysical properties.

The emission energy of Ir(4,6-dFppy)$_2$(pic) (**14**) is about $700\,cm^{-1}$ (≈ 0.09 eV) higher than that of Ir(4,6-dFppy)$_2$(acac) (**21**). Although this energy difference is not large, it significantly contributes to the color purity of the blue emission. This difference can mainly be ascribed to influences of the ancillary ligands on the 5d (Ir)-dominated HOMO. Usually, the coordination of nitrogen to a central metal ion leads to a stronger metal–ligand bond than the coordination to oxygen [72]. DFT calculations performed on both compounds display that this trend is also valid for the two studied compounds, since the Ir$-$N bond length of picolinate was determined to be substantially shorter than the Ir$-$O bond lengths of picolinate and acetylacetonate [144]. Different lengths of Ir$-$N and Ir$-$O bonds are also observed in the X-ray structure of **14**, where the respective distances are 1.138 Å (Ir$-$N) and

1.153 Å (Ir−O) for the Ir–picolinate bonds [151]. Therefore, a higher mean ligand field strength is expected for the (pic) ligand compared to the (acac) ligand. As a consequence, the occupied d-orbitals of the t_{2g} manifold experience on average a larger energy stabilization in Ir(4,6-dFppy)$_2$(pic) than in Ir(4,6-dFppy)$_2$(acac).

Interestingly, our simple model is supported by the oxidation potentials E_{ox} measured for the two compounds. For Ir(4,6-dFppy)$_2$(pic) (**14**) and Ir(4,6-dFppy)$_2$ (acac) (**21**), potentials of 0.90 V [152] and 0.74 V (Djurovich, P.I., private communication) (measured versus ferrocene), respectively, were determined. On the other hand, the π- and π*-orbitals of the chromophoric (4,6-dFppy) ligand are expected to remain almost unchanged. Thus, the d–π* energy separations are larger for Ir(4,6-dFppy)$_2$(pic) (**14**) than for Ir(4,6-dFppy)$_2$(acac) (**21**). Indeed, corresponding energy differences are displayed in the emission spectra.

Since the emitting states of both compounds exhibit a high MLCT character, it can be expected that the occupied d-orbitals lie energetically above the ligand π-orbitals. However, close-lying occupied d- and π-orbitals of adequate symmetry will combine to strongly mixed molecular orbitals. Because of the smaller d–π energy separation as resulting from a stabilization of the d-orbitals in compound **14**, it is expected that the d–π mixing and thus the π contribution in the occupied frontier orbitals is larger in **14** than in **21**. Consequently, the MLCT character of the resulting states is slightly smaller for **14**. This also affects the effectiveness of spin–orbit coupling, which is dominantly carried by the metal d-orbital contributions [36, 56, 63]. Therefore, it is expected that those photophysical properties that are related to the effectiveness of SOC, such as the magnitude of ΔE(ZFS) and the radiative decay rates, are strongly influenced by the discussed mixings. Indeed, this trend is observed. ΔE(ZFS) values and radiative rates are larger for Ir(4,6-dFppy)$_2$ (acac) (**21**) (with less π-admixtures to the occupied d-orbitals) than for Ir(4,6-dFppy)$_2$(pic) (**14**) (Table 13.3 and Figure 13.17). For a more detailed discussion of these trends, see Ref. [84].

The two compounds Ir(4,6-dFppy)$_2$(pic) (**14**) and Ir(4,6-dFppy)$_2$(acac) (**21**) exhibit different emission quantum yields (Table 13.3). The lower quantum yield of compound **21** compared to **14** is not expected at a first sight, since the radiative rate k^r for **21** is distinctly larger than for **14**. This behavior can be ascribed to differently effective deactivation processes by molecular vibrations. In particular, the "higher symmetry" of Ir(4,6-dFppy)$_2$(acac) (**21**) might be connected with an involvement of the two chromophoric ligands in the emitting triplet state, whereas in the "less symmetric" Ir(4,6-dFppy)$_2$(pic) (**14**), the triplet state will probably be confined to only one chromophoric ligand. This is also indicated by DFT calculations [144]. In the latter case, the number of vibrational modes that can deactivate nonradiatively is substantially lower. Interestingly, investigations on Os(II) compounds have shown that materials with only one chromophoric ligand tend to exhibit higher photoluminescence quantum yields than corresponding complexes with two chromophoric ligands [127]. However, we cannot rule out that vibrational modes of (acac) and (pic), respectively, might also affect the radiationless deactivation of the Ir(III) compounds **14** and **21**. Furthermore, thermal population of quenching metal-centered (dd*) states might have an additional impact on the emission

quantum yield. Because of the lower ligand field strength of (acac) compared to that of (pic), the dd* states are supposed to lie at a somewhat lower energy in compound **21** than in **14**. Thus, population of these quenching dd* states at room temperature might be more pronounced in Ir(4,6-dFppy)$_2$(acac) (**21**).

13.4.3
Comparison of Photophysical Properties of Pt(II) and Ir(III) Compounds

A comparison of the photophysical properties of the Pt(II) compounds studied in Section 13.4.1 with those of the Ir(III) compounds investigated in Section 13.4.2 reveals that the latter ones exhibit distinctly higher zero-field splittings of the emitting T_1 states, shorter decay times of the T_1 substates, and higher radiative rates of the $T_1 \leftrightarrow S_0$ transitions. All photophysical differences indicate that spin–orbit coupling is more effective in the octahedrally coordinated Ir(III) complexes than in the square planar Pt(II) complexes. This is a consequence of a larger MLCT character and thus a higher SOC efficiency for the emitting T_1 states of the discussed Ir(III) complexes. The experimental results are in agreement with the discussion presented in Section 13.3.2, where it was derived that spin–orbit coupling can – for materials with comparable ligands – principally be more efficient in octahedrally coordinated than in square planar emitters. This is due to smaller splittings between the occupied d-orbitals in the former case.

The photophysical data listed in Table 13.4 show that this general trend is also valid for other "couples" of Ir(III) and Pt(II) compounds with the same chromophoric and nonchromophoric ligands. Also, in these cases, the octahedral Ir(III)-based materials exhibit higher total zero-field splittings ΔE(ZFS) and higher radiative rates at ambient temperature, showing that spin–orbit coupling is more effective than in the related square planar Pt(II) complexes. This indicates that Ir(III) complexes are mostly better suited for OLED applications than Pt(II) complexes.

Table 13.4 Selected photophysical properties of several Ir(N^C)$_2$(acac) and Pt(N^C)(acac) compounds with *ortho*-metalating chromophoric ligands.

Compound[a)]	λ_{em} (300 K) (nm)	ΔE(ZFS) (cm^{-1})	k^r(300 K) (s^{-1})	References
Ir(4,6-dFppy)$_2$(acac) (**21**)	484	109	6.4×10^5	63, 84
Pt(4,6-dFppy)(acac) (**6**)	467	8	7.7×10^4	63, 120, 121
Ir(thpy)$_2$(acac) (**12**)	567	34	1.2×10^5	36, 155
Pt(thpy)(acac) (**5**)	559	4	2.6×10^4	36, 155
Ir(s1-thpy)$_2$(acac) (**10**)	586	16	1×10^5	36, 154, 155
Pt(s1-thpy)(acac) (**2**)	578	<1	1.8×10^4	153–155
Ir(pbt)$_2$(acac) (**20**)	557	103	1.4×10^5	36, 156
Pt(pbt)(acac) (**8**)	539	10	6.0×10^4	36

a) The chemical structures are displayed in Figure 13.7.

13.5
Case Studies: Singlet Harvesting and Blue Light Emitting Cu(I) Complexes

The case studies presented in Section 13.4 show that blue light generation can be successfully realized with suitable Pt(II) and Ir(III) complexes. However, these classes of emitters often show some shortcomings. For example, in many cases, the color of the emitted light is not truly blue and emission quenching or dissociation reactions frequently occur (see Section 13.4.1.1 [97, 100]. The latter problems are connected with the presence and thermal population of metal-centered dd* states, which often lie only a few thousand cm^{-1} above the phosphorescent state. Consequently, Pt(II)- and Ir(III)-based compounds with sufficiently high triplet energy, required for deep blue emission, are often not at all emissive at ambient temperature, since their emission is totally quenched by the described mechanisms (see also Section 13.4.1).

For these reasons, alternative emitter materials have come into the focus of research. In this respect, Cu(I) complexes are attractive since, due to the d^{10} ground state configuration, no unoccupied d* orbitals are present. At first sight, these complexes do not seem to be suited as emitters in OLEDs, since, due to the relatively weak SOC effectivity of the first-row transition metal ion Cu(I), the triplet T_1 state of such materials mostly exhibits decay times of several hundreds to thousand microseconds. As a consequence this would result in a drastic roll-off of the device efficiency and frequently also in small emission quantum yields. However, for specific Cu(I) complexes, the lowest excited singlet S_1 state has a relatively small energy separation from the T_1 state, for example, being only on the order of $10^3\ cm^{-1}$. Thus, a thermally activated fluorescence can occur from the S_1 state. Hence, these complexes can principally achieve high emission quantum yields with short (radiative) emission decay times and, therefore, should be applicable in OLEDs taking advantage of the singlet harvesting effect (see Section 13.2.2 and Figure 13.2).

Recently, we proposed the use of Cu(pop)(pz_2Bph_2) (**24**), Cu(pop)(pz_4B) (**25**), and Cu(pop)(pz_2BH_2) (**26**) as OLED emitters (Figure 13.7b) [24, 36, 48]. With these materials, photoluminescence quantum yields as high as 90% and emission decay times at ambient temperature of only several microseconds can be realized. This is due to the involvement of the S_1 state in the emission process. Cu(I) complexes are also attractive from another point of view. Their costs are significantly lower than those of Pt- or Ir-based emitters, making them better suited for large-scale applications. In this section, we focus on photophysical properties of Cu(pop)(pz_2Bph_2) (**24**) and shortly address the related complexes Cu(pop)(pz_4B) (**25**) and Cu(pop)(pz_2BH_2) (**26**).

13.5.1
Photophysical Properties at Ambient Temperature

Cu(pop)(pz_2Bph_2) (**24**) is strongly emissive as neat material or if doped into a PMMA (poly-methyl methacrylate) matrix. Figure 13.19 shows the emission and

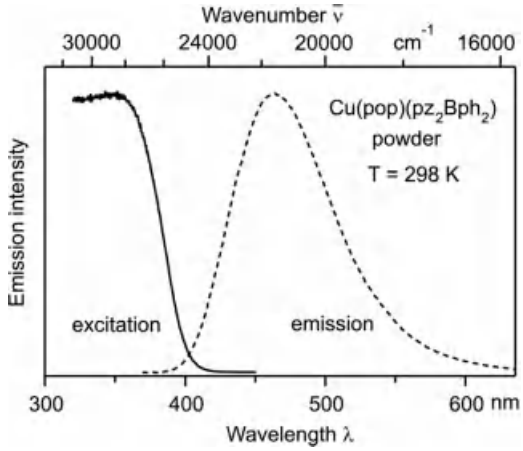

Figure 13.19 Emission and excitation spectra of neat Cu(pop)(pz_2Bph_2) (**24**) at ambient temperature.

excitation spectra of this compound measured as powder at ambient temperature. The emission spectrum is broad and unstructured with the maximum at $\lambda_{max} = 464$ nm. The excitation spectrum reveals absorptions from the ground state to higher lying states, in particular, to the lowest excited state S_1 at wavelengths below ≈400 nm. In the spectral region near 400 nm, the excitation and emission bands overlap indicating that in this spectral range the same electronic transition, that is, the $S_0 \leftrightarrow S_1$ transition, is responsible for both processes. Accordingly, it is indicated that the emission of Cu(pop)(pz_2Bph_2) can be assigned as fluorescence stemming from the lowest excited singlet state S_1. Further evidence will be given in Section 13.5.2.

The character of the S_1 state can be assigned by comparing luminescence data of different complexes [24]. In particular, modifications of the bis(pyrazol-1-yl)borate ligand do not lead to significant spectral shifts of the emission. Even a replacement of (pz_2Bph_2) by acetylacetonate results only in small changes. For example, neat Cu(pop)(acac) emits at $\lambda_{max} = 461$ nm [157] compared to $\lambda_{max} = 464$ nm of neat **24**. On the other hand, a replacement of the (pop) ligand by (dppb) (=1,2-bis(diphenylphosphino)benzene), giving Cu(dppb)(pz_2BH_2), results in an intense yellow emission with $\lambda_{max} = 570$ nm (powder sample at ambient temperature) [158]. Moreover, the π–π* transitions of both (pop) and (pz_2BH_2) lie at much higher energies than the transitions observed in Figure 13.19. Consequently, we assign the emitting S_1 state of Cu(pop)(pz_2Bph_2) (**24**) as ^{1}MLCT ($^1d\pi^*$) state with a significant involvement of the (pop) ligand. This is also valid for Cu(pop)(pz_4B) (**25**) and Cu(pop)(pz_2BH_2) (**26**). For completeness, it is mentioned that the lowest excited states of many other Cu(I) complexes have also been assigned to be of MLCT character [27, 28, 159–165].

Table 13.5 summarizes photophysical data of the compounds **24–26** determined at ambient temperature. All three compounds show strong blue luminescence as

Table 13.5 Emission properties of different Cu(I) complexes at ambient temperature [24].

Compound	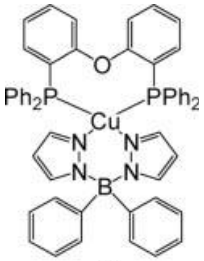 **24** Cu(pop)(pz_2Bph_2)	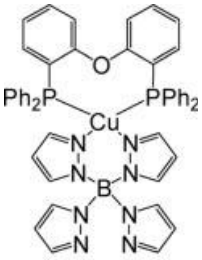 **25** Cu(pop)(pz_4B)	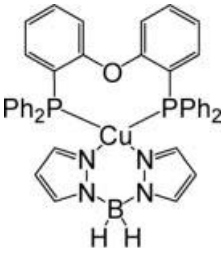 **26** Cu(pop)(pz_2BH_2)			
Environment	**Powder**	**PMMA**	**Powder**	**PMMA**	**Powder**	**PMMA**
λ_{max} (nm)	464	466	447	457	436	462
τ (μs)	13	23	22	24	20	22
ϕ_{PL} (%)	90	41	90	30	45	35
$\{x; y\}^{a)}$	{0.16; 0.22}	{0.17; 0.21}	{0.14; 0.11}	{0.17; 0.18}	{0.15; 0.11}	{0.17; 0.21}

a) CIE 1931 color space coordinates [111].

neat materials. For instance, the samples emit with maxima at 464 (**24**), 447 (**25**), and 436 nm (**26**), respectively. The {*x*; *y*} color space coordinates are also given. Slight spectral differences are observed. These are related to different influences of the substituents on the bis(pyrazol-1-yl)borate spectator ligand. The different functional groups exhibit different electron-withdrawing/electron-donating properties and have different steric requirements, resulting in slightly different molecular geometries. It is indicated that these effects slightly modify the energies of the 3d orbitals of Cu(I).

For all three complexes, the emission maxima found in PMMA are shifted to longer wavelengths compared to the solid samples. The redshift is largest for Cu(pop)(pz_2BH_2) (**26**), amounting to 26 nm. On the other hand, for Cu(pop)(pz_2Bph_2) (**24**), a spectral redshift of only 2 nm is observed. Moreover, the luminescence quantum yields measured in PMMA are considerably smaller than found for the neat samples. For instance, for Cu(pop)(pz_2Bph_2) (**24**), ϕ_{PL} drops from 90% (powder) to 41% (doped into PMMA). These effects are much more pronounced in liquid solution. For example, Cu(pop)(pz_2Bph_2) (**24**) dissolved in CH_2Cl_2 experiences a redshift of 34 nm to $\lambda_{max} = 498$ nm, the quantum yield drops to only $\phi_{PL} = 8\%$, and the emission decay time is reduced to $\tau = 1.8$ μs [24]. These observations can be explained by taking changes of the molecular geometry occurring after MLCT excitation into consideration. In the electronic ground state, a pseudo-tetrahedral orientation of the ligands is energetically favored, while in the excited MLCT state, a flattening distortion of the molecular structure can occur [162–165]. Such a structural rearrangement leads to a smaller energy gap between the excited states and

the electronic ground state. Furthermore, due to the distortion of the molecular geometry, the radiationless deactivation is strongly enhanced [30, 36, 166]. Obviously, such distortions are largely suppressed in rigid environments and blue light emission with high quantum yields is possible. The flattening distortion is also influenced by the steric demands of the ligands. This is exemplified by the data listed in Table 13.5. The largest effects are observed for Cu(pop)(pz_2BH_2) (**26**) with the relatively small and flexible (pz_2BH_2) ligand, while the smallest changes are found for Cu(pop)(pz_2Bph_2) (**24**) with bulky phenyl substituents.

For completeness, it is remarked that the very high ϕ_{PL} values obtained for the studied complexes in the solid state indicate that effects of energy transfer between adjacent emitter molecules as well as of triplet–triplet annihilation do not seem to be important. This can be rationalized by assuming at least a small geometry change in the excited state even for a complex "sitting" in the neat material. This results in an energy stabilization at that site (self-trapping effect). Accordingly, the resonance condition required for the occurrence of energy transfer processes between excited and nonexcited complexes is no longer fulfilled. Consequently, emission self-quenching and quenching by triplet–triplet annihilation become less probable.

13.5.2
Triplet State Emission and Thermally Activated Fluorescence

The emission behavior of Cu(pop)(pz_2Bph_2) (**24**) was investigated in the temperature range of $T = 1.6$–300 K. In order to minimize effects of molecular geometry changes induced by flattening distortions occurring upon the MLCT excitation as described above, powder samples were studied. In the whole temperature range,

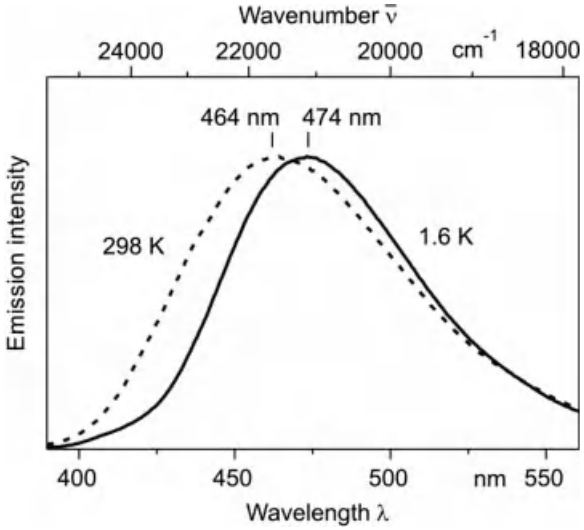

Figure 13.20 Emission spectra of neat Cu(pop)(pz_2Bph_2) (**24**) at 1.6 and 298 K.

the emission spectra of neat Cu(pop)(pz_2Bph_2) are broad and unstructured. At 1.6 K, the complex emits with $\lambda_{max} = 474$ nm (Figure 13.20). With temperature increase to about 100 K, the emission maximum does not markedly change. However, with further temperature increase, the spectra become broader and a blueshift is observed. At temperatures above $T = 200$ K, the emission maximum approaches the ambient temperature value of $\lambda_{max} = 464$ nm.

The emission decay behavior of neat Cu(pop)(pz_2Bph_2) shows a very pronounced temperature dependence. At $T = 1.6$ K, the decay profile is distinctly nonexponential (inset of Figure 13.21). It can be described by a triexponential decay function with individual components of 2 ms (τ_I), 600 µs (τ_{II}), and 170 µs (τ_{III}). A similar behavior has been discussed for [Pt(4,6-dFppy)$(CN)_2$)]$^-$ (**4**) (Figure 13.12). The explanation given here applies also to the Cu(I) compound **24**. Thus, at $T = 1.6$ K, the emission is assigned to originate from the three triplet substates I, II, and III, which are not thermally equilibrated and emit independently. This is often found at very low temperatures and at energy separations between the substates of only a few cm^{-1}. Indeed, it is predicted by theoretical investigations that the zero-field splitting of the emitting ^{3}MLCT state of a comparable compound lies in this energy range [167]. In this situation, processes of spin–lattice relaxation between the substates are much slower than the emission decay times of the transitions to the electronic ground state [49, 123, 168, 169]. Generally, with temperature increase, thermal equilibration between the triplet substates becomes fast and the decay finally becomes monoexponential [123, 124]. In this case, Eq. (13.4) can be applied

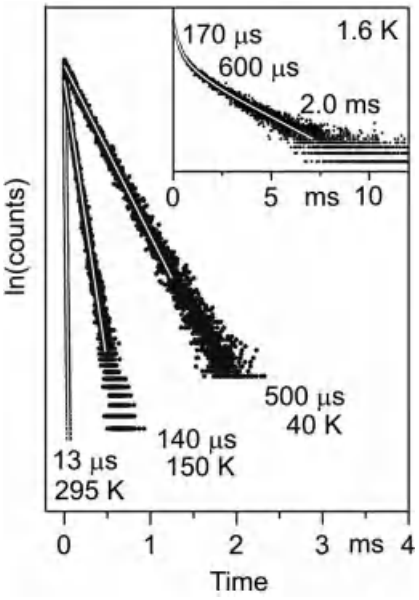

Figure 13.21 Emission decay recorded for neat Cu(pop)(pz_2Bph_2) (**24**) at different temperatures after pulsed excitation at $\lambda_{exc} = 355$ nm and detected at 470 nm. Adapted from Ref. [24].

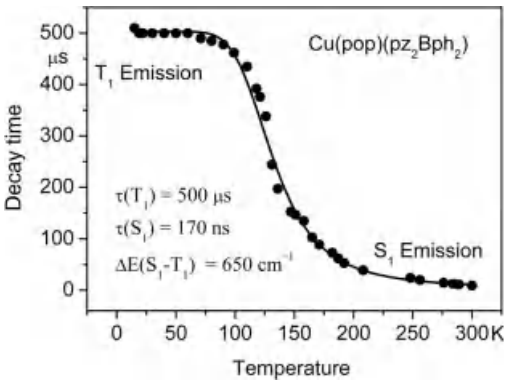

Figure 13.22 Emission decay time of Cu(pop)(pz_2Bph_2) (**24**) versus temperature. The solid line represents a fit of Eq. (13.6) to the experimental data. For this fit, $\tau(T_1) = 500\,\mu s$ is kept constant.

to determine the average decay time $\tau_{av}(T_1)$ for the ^{3}MLCT state. By use of the three decay components given above, an average decay time $\tau_{av}(T_1)$ of slightly less than 400 μs is obtained. As expected in the scope of this model, this value corresponds approximately to the decay time of 500 μs measured at $T = 40$ K (Figure 13.21).

The emission decay time of **24** is displayed in Figure 13.22 for the temperature range of $T = 30$–300 K. Interestingly, the decay time is almost constant between about 30 and 100 K and amounts to about 500 μs. Accordingly, this value can be assigned to represent the decay time $\tau(T_1)$ of the emitting ^{3}MLCT state. Obviously, this decay time is extremely long, compared to the values found for Ir(III) or Pt(II) complexes with significant MLCT character of the emitting triplet states (Figure 13.6). This is related not only to the smaller SOC constant of Cu(I), being about five times smaller than that of iridium(III) or platinum(II) [64], but also to the influence of another effect. Especially, the radiative rate of the $T_1 \rightarrow S_0$ transition is determined by the dipole matrix elements (or the allowednesses) of the transitions between the singlet ground state and the ^{1}MLCT states that mix with the emitting ^{3}MLCT state (Section 13.3.2). For Cu(I) complexes, these states are of $^1(3d\pi^*)$ character and it is expected that the corresponding matrix elements are significantly smaller than those involving the $^1(5d\pi^*)$ states, for example, of Ir(III) complexes.

The situation with respect to the extremely long decay time changes drastically with temperature increase. For $T > 100$ K, the decay time becomes distinctly shorter (Figure 13.22). This observation, together with the blueshift of the emission spectra (Figure 13.20), indicates that a higher lying electronic state with a distinctly greater deactivation rate becomes thermally populated. As discussed above and in analogy to a number of other investigations with Cu(I) complexes [25–28], this higher lying state is assigned as the lowest excited singlet state S_1 of ^{1}MLCT character. Above 200 K, the singlet state emission strongly dominates. It represents a thermally activated delayed fluorescence [24, 36].

Under the assumption of a fast thermalization between the $T_1(^3MLCT)$ and the $S_1(^1MLCT)$ state, an average decay time $\tau_{av}(S_1,T_1)$ will result. For a model including two excited states, one triplet (consisting of three triplet substates) and one singlet state, as well as the ground state, one obtains Eq. (13.6) which is easily derived from Eq. (13.3):

$$\tau_{av}(S_1, T_1) = \frac{3 + \exp(-\Delta E(S_1\text{-}T_1)/k_B T)}{3/\tau(T_1) + \{1/\tau(S_1)\}\exp(-\Delta E(S_1\text{-}T_1)/k_B T)} \tag{13.6}$$

where $\tau(T_1)$ and $\tau(S_1)$ are the intrinsic decay times of the emitting triplet and singlet state, respectively, and $\Delta E(S_1–T_1)$ is the energy separation (activation energy) between these two states. With $\tau(T_1) = 500\,\mu s$, as determined above (plateau between about 30 and 100 K), the values of $\tau(S_1)$ and $\Delta E(S_1–T_1)$ can be obtained by fitting Eq. (13.6) to the measured decay times. The respective fit curve is displayed in Figure 13.22 as solid line. The resulting fit parameters are $\tau(S_1) = 170\,ns$ and $\Delta E(S_1–T_1) = 650\,cm^{-1}$.

Figure 13.23 depicts the data determined for Cu(pop)(pz_2Bph_2) (**24**) in an energy level diagram, while Table 13.6 summarizes the data for the three studied Cu(I) complexes **24–26**.

The lowest excited singlet states S_1 of the studied Cu(I) complexes lie between $\Delta E(S_1–T_1) = 650$ and $1300\,cm^{-1}$ above the triplet states T_1 (Table 13.6). These energy separations are determined as activation energies from the temperature-dependent decay behavior. They are also displayed in the emission spectra, if the spectra measured at 40 and 300 K are compared. In a very coarse model, this energy separation is roughly proportional to the quantum mechanical exchange interaction integral [30, 31, 56, 170]. In particular, this interaction decreases with increasing charge transfer character, which is roughly related to the spatial separation of the orbitals involved in the excitation process. This trend can be illustrated by comparing molecules with different charge transfer contributions in the lowest excited states. (See also

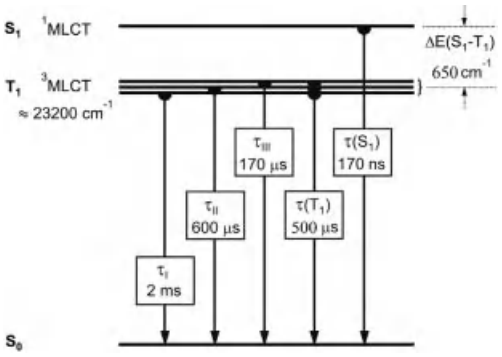

Figure 13.23 Energy level scheme for the lowest excited states and emission decay times of Cu(pop)(pz_2Bph_2) (**24**) powder. The decay time of the prompt fluorescence of $\tau(S_1) = 170$ ns and the singlet–triplet energy separation of $\Delta E(S_1–T_1) = 650\,cm^{-1}$ are determined by fitting of Eq. (13.6) to the experimental data as shown in Figure 13.22.

Table 13.6 Energies and decay times of the investigated Cu(I) complexes.

	Cu(pop)(pz_2Bph_2) (24)	**Cu(pop)(pz_4B)** (25)	**Cu(pop)(pz_2BH_2)** (26)
$E(T_1)$[a)]	$\approx$23 200 cm^{-1}	$\approx$24 000 cm^{-1}	$\approx$23 800 cm^{-1}
$E(S_1)$[b)]	$\approx$24 000 cm^{-1}	$\approx$24 700 cm^{-1}	$\approx$25 100 cm^{-1}
$\Delta E(S_1\text{-}T_1)$[c)]	650 cm^{-1}	1000 cm^{-1}	1300 cm^{-1}
$\tau(T_1)$[d)]	500 µs	450 µs	610 µs
$\tau(S_1)$[e)]	170 ns	80 ns	10 ns
τ_{DF}(300 K)[f)]	13 µs	22 µs	20 µs

Adapted from Ref. [24].

a) $E(T_1)$: Energy determined from the high-energy flank of the emission spectrum (phosphorescence) at 40 K (at 15% of the peak intensity).

b) $E(S_1)$: Energy determined from the high-energy flank of the emission spectrum (fluorescence) at ambient temperature (at 15% of the peak intensity).

c) $\Delta E(S_1–T_1)$: Activation energy as determined from a fit of Eq. (13.6) to the measured decay times.

d) $\tau(T_1)$: Decay time of the T_1 state at $30\,K < T < 100\,K$ (plateau).

e) $\tau(S_1)$: Decay time of the prompt fluorescence determined from a fit of Eq. (13.6) to the measured decay times.

f) τ_{DF} (300 K): Delayed fluorescence decay time measured at 300 K.

Ref. [56], p. 13). For example, the lowest singlet and triplet $\pi\pi^*$ states of purely organic aromatic molecules (with essentially no spatial separation between π and π^* orbitals) are usually separated by many thousand cm^{-1} [30]. For instance, for the free (pop) ligand, the S_1 state lies about 6700 cm^{-1} above the lowest triplet state T_1 [24]. For Pt(thpy)$_2$ (**9**), a $\Delta E(S_1–T_1)$ value of $\approx$3300 cm^{-1} was determined [49]. Its emitting triplet state was assigned to be of ligand-centered character, however, containing significant metal-to-ligand charge transfer contributions [49]. Interestingly, the $\Delta E(S_1–T_1)$ splittings found for the Cu(I) complexes investigated here are even by a factor of 3–4 smaller. This can be rationalized by a distinctly more pronounced charge transfer or charge separation in the HOMO and LUMO, respectively. These considerations represent an additional support for the ^{1,3}MLCT assignment of the lowest excited states of the studied Cu(I) complexes. For completeness, it is also mentioned that an equivalent model explains the small energy separations between the $^1n\pi^*$ and $^3n\pi^*$ states of about 1500 cm^{-1} of organic molecules, such as ketones [30].

The emission decay times determined for the singlet states $\tau(S_1)$, lying between 10 and 170 ns (Table 13.6), are much longer than typically found for allowed $S_1 \rightarrow S_0$ transitions of organic molecules [30]. Obviously, for the studied Cu(I) compounds, the oscillator strengths of the corresponding $^1(3d\pi^*) \rightarrow S_0$ transitions are relatively low.

13.5.3
Singlet Harvesting: Cu(I) Complexes as OLED-Emitters

The analysis of the emission decay behavior of several blue light emitting Cu(I) complexes shows that, at ambient temperature, the luminescence is dominated by a (delayed) fluorescence stemming from the thermally populated S_1 state of ^{1}MLCT character. The direct involvement of this fast-decaying singlet state in the emission

process accounts for relatively high radiative decay rates. This has important practical implications when the use of Cu(I) complexes in OLEDs or light-emitting electrochemical cells (LEECs) is concerned. A device based on a triplet emitter with an emission decay time of many hundred microseconds would show only very poor performance, for example, because of saturation effects already occurring at very low current densities. This problem can be largely overcome, when a thermally activated fluorescence dominates the emission. For Cu(pop)(pz_2Bph_2), for instance, the decay time of the delayed fluorescence is by a factor of more than 35 shorter than the phosphorescence decay time of the T_1 state.

Interestingly, the involvement of both singlet and triplet excited states also allows to harvest all excitons formed in the course of an electroluminescence process. This is illustrated in Figure 13.24. After electron–hole recombination, the S_1 and T_1

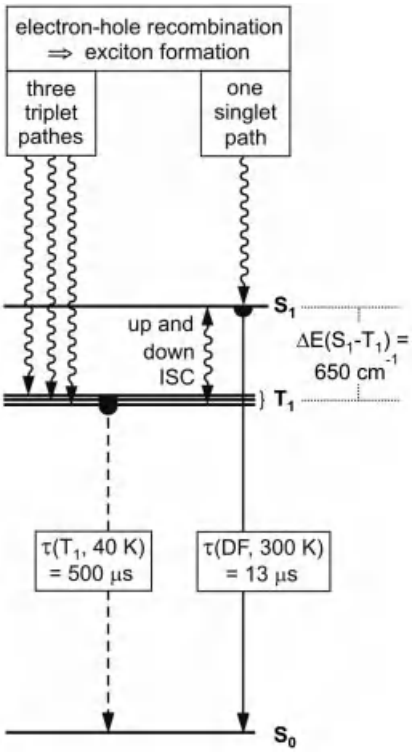

Figure 13.24 Emission behavior of neat Cu(pop)(pz_2Bph_2) (**24**) and proposed mechanism for singlet harvesting to be applied in OLEDs. At $T = 40$ K, the luminescence stemming from the lowest triplet state T_1 decays with $\tau(T_1) = 500\,\mu s$. At ambient temperature, a thermally activated delayed fluorescence from the lowest singlet state S_1 exhibits a decay time of $\tau_{DF} = 13\,\mu s$, while the decay time of prompt fluorescence is 170 ns. In the emitting layer of an electroluminescent device, one singlet and three triplet paths populate the S_1 and T_1 states of the complex. Because of the efficient up-ISC from the T_1 to the S_1 state, all excitations can be harvested in the S_1 state and can potentially be used for light generation at ambient temperature [24, 36, 45].

states of the emitter molecule are populated by fast internal conversion processes by one singlet path and three triplet paths, respectively. Furthermore, SOC induced by the Cu(I) ion is strong enough to enable fast intersystem crossing (ISC), which also leads to a fast thermal equilibration between the S_1 and T_1 states. Provided that $\Delta E(S_1–T_1)$ is small enough, up-ISC processes become important at ambient temperature. Thus, the radiative deactivation is accessible for all triplet and singlet excitations as $S_1 \rightarrow S_0$ fluorescence. In other words, the singlet state S_1 harvests all singlet and triplet excitations and emits according to its high radiative deactivation rate (and to its Boltzmann-governed population). Interestingly, a participation of the singlet state in the emission has already been investigated for several green to orange light emitting Cu(I) complexes [25–28] and OLED tests with Cu(I) complexes have also been carried out [28, 171–179]. These successful realizations strongly support the strategy of applying luminescent compounds with small ΔE $(S_1–T_1)$ separations in light-emitting devices by use of the singlet harvesting effect. Potentially, the relatively cheap Cu(I) complexes may replace emitter materials based on more expensive noble metals in future. (Compare also Ref. [180]) This will become particularly attractive, if even smaller $\Delta E(S_1–T_1)$ values and thus shorter decay times of the delayed fluorescence are found, which would be advantageous to minimize saturation and roll-off effects.

13.6 Conclusion

For efficient OLEDs, it is a crucial requirement to optimize the emitters with respect to high emission quantum yields, short (radiative) emission decay times, and chemical stability and – besides other important factors – to allow harvesting of all excitons that are generated by electron–hole recombination. For the emission behavior of organotransition metal compounds, spin–orbit coupling is essential, since triplet–singlet transitions are forbidden without SOC. In particular, this quantum mechanical effect determines the radiative (and nonradiative) decay rates, the amount of splitting of the triplet into substates (zero-field splitting, ZFS), and the intersystem crossing rates between the higher lying singlet state and the emitting triplet state.

In this investigation, a deeper understanding of these properties is presented by analyzing selected Pt(II) and Ir(III) complexes on the basis of high spectral and time resolution methods. Indeed, these studies combined with an extensive data set with respect to emission properties of a large number of organotransition metal compounds allow us to reveal important trends.

In particular, the effects of SOC depend on the geometry of the complexes, that is, SOC can be more effective in octahedral than in square planar complexes. This explains why octahedral Ir(III) complexes are so attractive as emitters in OLED, for example, with respect to short (radiative) emission decay times and high quantum yields. Moreover, since SOC regulates the amount of energy splitting of the triplet state into substates, effective SOC induces large

ΔE(ZFS) values and usually also high radiative rates in these compounds. Especially, in Ir(III) complexes, the transition from the highest triplet substate to the singlet ground state becomes particularly allowed. However, at a large total zero-field splitting ΔE(ZFS), the average emission decay time of the three triplet substates at ambient temperature is not significantly reduced with further increasing SOC. This is a consequence of the fact that the emission properties are governed not only by the shortest-lived triplet substate but also by all three substates weighted by a Boltzmann distribution. Thus, based on an extensive data set, a trend becomes evident. It is indicated that the shortest (radiative) emission decay time of the type of materials investigated, which are usually applied in OLEDs, cannot be reduced significantly to below about 1 μs. This implicates problems concerning the development of emitter materials with less roll-off of efficiency for high-brightness OLED lighting.

At present, extensive research is carried out to develop highly luminescent and stable triplet emitters, especially, for blue light generation. It is indicated that these compounds should be characterized by emitting ^{3}MLCT (^{3}dπ^*) states or should at least exhibit significant MLCT contributions. Problems concerning blue light emission are discussed on the basis of detailed case studies. For example, in many cases, quenching dd* states are thermally activated at ambient temperature from the necessarily high-lying (emitting) ^{3}MLCT states. Therefore, deep blue ambient temperature emission often occurs only with low quantum yield (if it is not totally quenched at all) and even dissociation processes involving ligand losses with consequences for the device stability are often observed. Therefore, it is aimed to energetically destabilize the lowest dd* states. Principally, this can be achieved by coordinating either chromophoric or ancillary ligands with very high ligand field strengths (high Dq values). On the other hand, these ligands also stabilize the populated d-orbitals in the HOMO range. Thus, the ^{3}MLCT states are also shifted to higher energies and as a consequence, the lowest triplet state, that is the emitting state, may become a ^{3}LC ($^3\pi\pi^*$) state, which would exhibit an undesirably long radiative emission decay time. Such a material would not be well suited for OLED applications. Obviously, only a detailed balance concerning the involvements of d- and π-orbitals in the lowest excited states might solve these problems. On the other hand, blue emission color is not exclusively determined by the electronic energy of the emitting state. Generally, vibrational satellites (sidebands) occur in addition and mostly show high intensities in the green region of the spectrum. As a consequence, the total emission will not be blue but green-blue. We address this problem by also investigating the vibrational satellite structures and show that a high molecular rigidity plays a crucial role in minimizing the intensities of these satellite bands. Thus, it is possible to obtain color coordinates more suited for blue emission. This is in line with the requirement that high rigidity is also a very good basis for obtaining compounds with high emission quantum yields. Obviously, material design demands a deep understanding of the compounds' electronic and vibronic properties.

The discussion shows that triplet emitters, in particular Ir(III) complexes, such as $Ir(4,6\text{-dFppy})_2(pic)$ (sky blue emitter), $Ir(ppy)_3$ (green emitter), and $Ir(dm\text{-}2\text{-}piq)_2(acac)$ (red emitter), with photoluminescence quantum yields between 80% and almost 100% represent materials that are very well suited for OLED applications based on the triplet harvesting effect.

Interestingly, a different exciton harvesting mechanism may also be highly successful in future. Therefore, the new singlet harvesting effect is discussed in detail. This mechanism is based on a thermally activated fluorescence involving the lowest excited singlet state. It works as follows. After electron–hole recombination and generation of excitons, one singlet path and three triplet paths populate the S_1 and T_1 states of the emitter molecule. Usually, SOC induced by the metal ion is strong enough and enables fast intersystem crossing. At small $\Delta E(S_1\text{–}T_1)$ separations, both up- and down-ISC processes occur at ambient temperature. Since the rate for a $T_1 \rightarrow S_0$ transition is much smaller than the up-ISC rate, the excitation gathered in the triplet state is at ambient temperature radiatively deactivated via the S_1 state. The excitation that originally populates the singlet state also takes part in the equilibration process and finally is also deactivated as $S_1 \rightarrow S_0$ emission. Thus, the singlet state harvests all excitons and emits a (delayed) fluorescence according to its high radiative deactivation rate. A corresponding emission behavior is studied using blue light emitting Cu(I) complexes. Interestingly, since Cu(I) has a d^{10} ground state configuration, these materials do not have excited dd^* states und thus cannot show thermally activated emission quenching by such states. Consequently, blue light emitters are more easily developed. The Cu(I) compounds studied are singlet emitters at ambient temperature and exhibit emission quantum yields as high as $\phi_{PL} = 90\%$. However, the emission decay times of the delayed fluorescence of about 10 μs are still relatively long. Therefore, the materials require some further improvements. Nevertheless, the singlet harvesting effect may successfully be applied in future not only to develop new and cheaper emitters but also to possibly reduce the average (radiative) emission decay time of the thermally activated fluorescence to below the limit of about 1 μs, which is indicated to exist for typical triplet emitters. If successful, this strategy will help to reduce the roll-off of the OLED efficiency for lighting, even at high-brightness applications.

Acknowledgments

The BMBF (German Federal Ministry of Education and Research) is acknowledged for the funding of our research. We are grateful to Prof. Dr. Mark E. Thompson (University of Southern California), Dr. J. A. Gareth Williams (University of Durham), and Dr. Uwe Monkowius (Johannes Kepler Universität Linz) for enjoyable and fruitful cooperations, which were partly supported by the DAAD (German Academic Exchange Service) and BaCaTeC (Bavaria California Technology Center). The COST project is also acknowledged for financial support within the action D35 (WG 10).

References

1 Yersin, H. (ed.) (2008) *Highly Efficient OLEDs with Phosphorescent Materials*, Wiley-VCH Verlag GmbH, Weinheim.
2 Chou, P.T. and Chi, Y. (2007) *Chem. Eur. J.*, **13**, 380.
3 Borek, C., Hanson, K., Djurovich, P.I., Thompson, M.E., Aznavour, K., Bau, R., Sun, Y., Forrest, S.R., Brooks, J., Michalski, L., and Brown, J. (2007) *Angew. Chem., Int. Ed.*, **46**, 1109.
4 Evans, R.C., Douglas, P., and Winscom, C.J. (2006) *Coord. Chem. Rev.*, **250**, 2093.
5 Williams, J.A.G., Develay, S., Rochester, D.L., and Murphy, L. (2008) *Coord. Chem. Rev.*, **252**, 2596.
6 Xiao, L., Chen, Z., Qu, B., Luo, J., Kong, S., Gong, Q., and Kido, J. (2011) *Adv. Mater.*, **23**, 926.
7 Che, C.-M., Kwok, C.-C., Lai, S.-W., Rausch, A.F., Finkenzeller, W.J., Zhu, N., and Yersin, H. (2010) *Chem. Eur. J.*, **16**, 233.
8 Kalinowski, J., Fattori, V., Cocchi, M., and Williams, J.A.G. (2011) *Coord. Chem. Rev.*, **255**, 2401.
9 Yang, X., Wang, Z., Makaduni, S., Li, J., and Jabbour, G.E. (2008) *Adv. Mater.*, **20**, 2405.
10 Ma, B., Djurovich, P.I., Garon, S., Alleyne, B., and Thompson, M.E. (2006) *Adv. Funct. Mater.*, **16**, 2438.
11 Murphy, L. and Williams, J.A.G. (2010) *Top. Organomet. Chem.*, **28**, 75.
12 Su, H.-C., Chen, H.-F., Fang, F.-C., Liu, C.-C., Wu, C.-C., Wong, K.-T., Liu, Y.-H., and Peng, S.-M. (2008) *J. Am. Chem. Soc.*, **130**, 3413.
13 Bolink, H.J., Coronado, E., Costa, R.D., Lardiés, N., and Ortő, E. (2008) *Inorg. Chem.*, **47**, 9149.
14 Slinker, J., Bernards, D., Houston, P.L., Abruña, H.D., Bernhard, S., and Malliaras, G.G. (2003) *Chem. Commun.*, 2392.
15 Kapturkiewicz, A. (2010) Electrochemiluminescent systems as devices and sensors, in *Electrochemistry of Functional Supramolecular Systems* (eds P. Ceroni, A. Credi, and M. Venturi), John Wiley & Sons, Inc., Hoboken, p. 477.
16 Lo, K.K.-W., Louie, M.-W., and Zhang, K. Y. (2010) *Coord. Chem. Rev.*, **254**, 2603.
17 O'Neil, E.J. and Smith, B.D. (2006) *Coord. Chem. Rev.*, **250**, 3068.
18 Keefe, M.H., Benkstein, K.D., and Hupp, J.T. (2000) *Coord. Chem. Rev.*, **205**, 201.
19 Zhao, Q., Li, F., and Huang, C. (2010) *Chem. Soc. Rev.*, **39**, 3007.
20 Fernández-Moreira, V., Thorp-Greenwood, F.L., and Coogan, M.P. (2010) *Chem. Commun.*, **46**, 186.
21 Botchway, S.W., Charnley, M., Haycock, J.W., Parker, A.W., Rochester, D.L., Weinstein, J.A., and Williams, J.A.G. (2008) *Proc. Natl. Acad. Sci. USA*, **105**, 16071.
22 Stephenson, K.A., Banerjee, S.R., Besanger, T., Sogbein, O.O., Levadala, M. K., McFarlane, N., Lemon, J.A., Boreham, D.R., Maresca, K.P., Brennan, J.D., Babich, J.W., Zubieta, J., and Valliant, J.F. (2004) *J. Am. Chem. Soc.*, **126**, 8598.
23 Zhao, Q., Li, F., and Huang, C. (2010) *Chem. Soc. Rev.*, **39**, 3007.
24 a) Czerwieniec, R., Yu, J., and Yersin, H. (2011) *Inorg. Chem.*, **50**, 8293.
b) Czerwieniec, R., Yu, J., and Yersin, H. (2012) *Inorg. Chem.*, **51**, 1975.
25 Blasse, G. and McMillin, D.R. (1980) *Chem. Phys. Lett.*, **70**, 1.
26 Breddels, P.A., Berdowski, P.A.M., Blasse, G., and McMillin, D.R. (1982) *J. Chem. Soc., Faraday Trans. 2*, **78**, 595.
27 Felder, D., Nierengarten, J.-F., Barigelletti, F., Ventura, B., and Amaroli, N. (2001) *J. Am. Chem. Soc.*, **123**, 6291.
28 Deaton, J.C., Switalski, S.C., Kondakov, D.Y., Young, R.H., Pawlik, T.D., Giesen, D.J., Harkins, S.B., Miller, A.J.M., Mickenberg, S.F., and Peters, J.C. (2010) *J. Am. Chem. Soc.*, **132**, 9499.
29 McGlynn, S.P., Azumi, T., and Kinoshita, M. (1969) *Molecular Spectroscopy of the Triplet State*, Prentice-Hall, Eaglewood Cliff.
30 Turro, N.J. (1978) *Modern Molecular Photochemistry*, Benjamin Inc., Menlo Park.

31 Klessinger, M. and Michl, J. (1995) *Excited States and Photochemistry of Organic Molecules*, Wiley-VCH Verlag GmbH, New York.

32 Helfrich, W. and Schneider, W.G. (1966) *J. Chem. Phys.*, **44**, 2902.

33 Adachi, C., Baldo, M.A., Forrest, S.R., and Thompson, M.E. (2000) *Appl. Phys. Lett.*, **77**, 904.

34 Yersin, H. (2004) *Top. Curr. Chem.*, **241**, 1.

35 Yersin, H. (2004) *Proc. SPIE*, **5214**, 124.

36 Yersin, H., Rausch, A.F., Czerwieniec, R., Hofbeck, T., and Fischer, T. (2011) *Coord. Chem. Rev.*, **255**, 2622.

37 Reineke, S., Walzer, K., and Leo, K. (2007) *Phys. Rev. B*, **75**, 125328.

38 Giebink, N.C. and Forrest, S.R. (2008) *Phys. Rev. B*, **77**, 235215.

39 Tanaka, D., Sasabe, H., Li, Y.-J., Su, S.-J., Takeda, T., and Kido, J. (2007) *Jpn. J. Appl. Phys.*, **46**, L10.

40 Reineke, S., Schwartz, G., Walzer, K., and Leo, K. (2007) *Appl. Phys. Lett.*, **91**, 123508.

41 Kalinowski, J., Stampor, W., Szmytkowski, J., Virgili, D., Cocchi, M., Fattori, V., and Sabatini, C. (2006) *Phys. Rev. B*, **74**, 085316.

42 Hertel, D. and Meerholz, K. (2007) *J. Phys. Chem. B*, **111**, 12075.

43 Köhler, A. and Bässler, H. (2009) *Mater. Sci. Eng. R*, **66**, 71.

44 Baldo, M.A., Lamansky, S., Burrows, P. E., Thompson, M.E., and Forrest, S.R. (1999) *Appl. Phys. Lett.*, **75**, 4.

45 Yersin, H., Czerwieniec, R., and Hupfer, A. (2012) Proc. SPIE 8435, 843508.

46 Yersin, H. and Monkowius, U. (2008) German Patent No. DE 10 2008 033 563 A1 and Yersin, H. (2006) Internal Invention Disclosure. University of Regensburg, Germany.

47 Yersin, H., Czerwieniec, R., and Monkowius, U. (2011) German Patent No. DE 10 2011 000 406.8.

48 Yersin, H. (2010) Controlling photophysical properties of metal complexes: toward molecular photonics, Book of Abstracts, COST D35 Workshop, Prague, Czech Republic, p. 6.

49 Yersin, H. and Donges, D. (2001) *Top. Curr. Chem.*, **214**, 81.

50 Hedley, G.J., Ruseckas, A., and Samuel, I.D.W. (2008) *Chem. Phys. Lett.*, **450**, 292.

51 Goushi, K., Kawamura, Y., Sasabe, H., and Adachi, C. (2004) *Jpn. J. Appl. Phys.*, **43**, L937.

52 Hofbeck, T. and Yersin, H. (2010) *Inorg. Chem.*, **49**, 9290.

53 Parker, C.A. and Hatchard, C.G. (1961) *Trans. Faraday Soc.*, **57**, 1894.

54 Brown, R.E., Singer, L.A., and Parks, J.H. (1972) *Chem. Phys. Lett.*, **14**, 193.

55 Saltiel, J., Curtis, H.C., Metts, L., Miley, J. W., Winterle, J., and Wrighton, M. (1970) *J. Am. Chem. Soc.*, **92**, 410.

56 Yersin, H. and Finkenzeller, W.J. (2008) *Highly Efficient OLEDs with Phosphorescent Materials* (ed. H. Yersin), Wiley-VCH Verlag GmbH, Weinheim, p. 1.

57 Donges, D., Nagle, J.K., and Yersin, H. (1997) *J. Lumin.*, **72–74**, 658.

58 Nozaki, K. (2006) *J. Chin. Chem. Soc.*, **53**, 101.

59 Jansson, E., Minaev, B., Schrader, S., and Ågren, H. (2007) *Chem. Phys.*, **333**, 157.

60 Hay, P.J. (2002) *J. Phys. Chem. A*, **106**, 1634.

61 Li, X., Minaev, B., Ågren, H., and Tian, H. (2011) *J. Phys. Chem. C*, **115**, 20724.

62 Rausch, A.F., Homeier, H.H.H., Djurovich, P.I., Thompson, M.E., and Yersin, H. (2007) *Proc. SPIE*, **6655**, 66550F.

63 Rausch, A.F., Homeier, H.H.H., and Yersin, H. (2010) *Top. Organomet. Chem.*, **29**, 193.

64 Murov, S.L., Carmichael, J., and Hug, G. L. (1993) *Handbook of Photochemistry*, 2nd edn, Marcel Dekker, New York, p. 340.

65 Azumi, T. and Miki, H. (1997) *Top. Curr. Chem.*, **191**, 1.

66 Miki, H., Shimada, M., Azumi, T., Brozik, J.A., and Crosby, G.A. (1993) *J. Phys. Chem.*, **97**, 11175.

67 Kimachi, S., Satomi, R., Miki, H., Maeda, K., and Azumi, T. (1997) *J. Phys. Chem. A*, **101**, 345.

68 Obara, S., Itabashi, M., Okuda, F., Tamaki, S., Tanabe, Y., Ishii, Y., Nozaki, K., and Haga, M.-A. (2006) *Inorg. Chem.*, **45**, 8907.

69 Siddique, Z.A., Ohno, T., Nozaki, K., and Tsubomura, T. (2004) *Inorg. Chem.*, **43**, 663.

70 Ikeda, S., Yamamoto, S., Nozaki, K., Ikeyama, T., Azumi, T., Burt, J.A., and Crosby, G.A. (1991) *J. Phys. Chem.*, **95**, 8538.

71 Miki, H. and Azumi, T. (1994) *J. Phys. Chem.*, **98**, 6059.

72 Schläfer, H.L. and Gliemann, G. (1969) *Basic Principles of Ligand Field Theory*, Wiley-Interscience, London.

73 Ceulemans, A. and Vanquickenborne, L. G. (1981) *J. Am. Chem. Soc.*, **103**, 2238.

74 Kober, E.M. and Meyer, T.J. (1982) *Inorg. Chem.*, **21**, 3967.

75 Daul, C., Baerends, E.J., and Vernooijs, P. (1994) *Inorg. Chem.*, **33**, 3538.

76 Figgis, B.N. (1987) Ligand field theory, in *Comprehensive Coordination Chemistry*, Pergamon, Oxford.

77 Ziegler, T., Nagle, J.K., Snijders, J.G., and Baerends, E.J. (1989) *J. Am. Chem. Soc.*, **111**, 5631.

78 Bossi, A., Steward, T., Djurovich, P.I., Thompson, M.E., Leitl, M.J., Rausch, A.F., Huber, R., and Yersin, H. (2011) submitted.

79 Yersin, H., Humbs, W., and Strasser, J. (1997) *Coord. Chem. Rev.*, **159**, 325.

80 Elfring, W.H. and Crosby, G.A. (1981) *J. Am. Chem. Soc.*, **103**, 7061.

81 Kato, M., Yamauchi, S., and Hirota, N. (1989) *Chem. Phys. Lett.*, **157**, 543.

82 Yersin, H. and Braun, D. (1991) *Chem. Phys. Lett.*, **179**, 85.

83 Finkenzeller, W.J. and Yersin, H. (2003) *Chem. Phys. Lett.*, **377**, 299.

84 Rausch, A.F., Thompson, M.E., and Yersin, H. (2009) *J. Phys. Chem. A*, **113**, 5927.

85 Li, J., Djurovich, P.I., Alleyne, B.D., Yousufuddin, M., Ho, N.N., Thomas, J.C., Peters, J.C., Bau, R., and Thompson, M.E. (2005) *Inorg. Chem.*, **44**, 1713.

86 Rausch, A.F., Thompson, M.E., and Yersin, H. (2009) *Inorg. Chem.*, **48**, 1928.

87 Adachi, C., Kwong, R.C., Djurovich, P.I., Adamovich, V., Baldo, M.A., Thompson, M.E., and Forrest, S.R. (2001) *Appl. Phys. Lett.*, **79**, 2082.

88 Deaton, J.C., Young, R.H., Lenhard, J.R., Rajeswaran, M., and Huo, S. (2010) *Inorg. Chem.*, **49**, 9151.

89 Tsuboyama, A., Iwawaki, H., Furugori, M., Mukaide, T., Kamatani, J., Igawa, S., Moriyama, T., Miura, S., Takiguchi, T., Okada, S., Hoshino, M., and Ueno, K. (2003) *J. Am. Chem. Soc.*, **125**, 12971.

90 Finkenzeller, W.J., Hofbeck, T., Thompson, M.E., and Yersin, H. (2007) *Inorg. Chem.*, **46**, 5076.

91 Xiang, H.-F., Lai, S.-W., Lai, P.T., and Che, C.-M. (2008) in: *Highly Efficient OLEDs with Phosphorescent Materials* (ed. H. Yersin), Wiley-VCH Verlag GmbH, Weinheim, page 259.

92 Che F C-.M., Chan, S.-C., Xiang, H.-F., Chan, M.C.W., Liu, Y., and Wang, Y. (2004) *Chem. Commun.*, 1484.

93 Kalinowski, J., Cocchi, M., Virgili, D., Fattori, V., and Williams, J.A.G. (2007) *Adv. Mater.*, **19**, 4000.

94 Chang, S.-Y., Kavitha, J., Li, S.-W., Hsu, C.-S., Chi, Y., Yeh, Y.-S., Chou, P.-T., Lee, G.-H., Carty, A.J., Tao, Y.-T., and Chien, C.-H. (2006) *Inorg. Chem.*, **45**, 137.

95 Ma, B., Djurovich, P.I., Garon, S., Alleyne, B., and Thompson, M.E. (2006) *Adv. Funct. Mater.*, **16**, 2438.

96 Vezzu, D.A.K., Deaton, J.C., Jones, S.J., Bartolotti, L., Harris, C.F., Marchetti, A.P., Kondakova, M., Pike, R.D., and Huo, S. (2010) *Inorg. Chem.*, **49**, 5107.

97 Sajoto, T., Djurovich, P.I., Tamayo, A.B., Oxgaard, J., Goddard, W.A., III, and Thompson, M.E. (2009) *J. Am. Chem. Soc.*, **131**, 9813.

98 Yang, L., Okuda, F., Kobayashi, K., Nozaki, K., Tanabe, Y., Ishii, Y., and Haga, M.A. (2008) *Inorg. Chem.*, **47**, 7154.

99 Williams, J.A.G. (2007) *Top. Curr. Chem.*, **281**, 205.

100 Treboux, G., Mizukami, J., Yabe, M., and Nakamura, S. (2007) *Chem. Lett.*, **36**, 1344.

101 Brooks, J., Babayan, Y., Lamansky, S., Djurovich, P.I., Tsyba, I., Bau, R., and Thompson, M.E. (2002) *Inorg. Chem.*, **41**, 3055.

102 Rausch, A.F., Monkowius, U., Zabel, M., and Yersin, H. (2010) *Inorg. Chem.*, **49**, 7818.

103 Rausch, A.F., Murphy, L., Williams, J.A. G., and Yersin, H. (2012) *Inorg. Chem.*, **51**, 312.

104 Ma, B., Djurovich, P.I., and Thompson, M.E. (2005) *Coord. Chem. Rev.*, **249**, 1501.

105 D'Andrade, B. and Forrest, S.R. (2003) *Chem. Phys.*, **286**, 321.

106 Kim, D. and Brédas, J.-L. (2009) *J. Am. Chem. Soc.*, **131**, 11371.

107 Adamovich, V., Brooks, J., Tamayo, A., Alexander, A.M., Djurovich, P.I., D'Andrade, B.W., Adachi, C., Forrest, S.R., and Thompson, M.E. (2002) *New J. Chem.*, **26**, 1171.

108 Chen, P. and Meyer, T.J. (1998) *Chem. Rev.*, **98**, 1439.

109 Gliemann, G. and Yersin, H. (1985) *Struct. Bond.*, **62**, 87.

110 Lai, S.-W., Chan, M.C.-W., Cheung, T.-C., Peng, S.-M., and Che, C.-M. (1999) *Inorg. Chem.*, **38**, 4046.

111 Smith, T. and Guild, J. (1932) *Trans. Opt. Soc.*, **33**, 73.

112 Thompson, D.W., Fleming, C.N., Myron, B.D., and Meyer, T.J. (2007) *J. Phys. Chem. B*, **111**, 6930.

113 Wang, Z., Turner, E., Mahoney, V., Madakuni, S., Groy, T., and Li, J. (2010) *Inorg. Chem.*, **49**, 11276.

114 Forniés, J., Fuertes, S., López, J.A., Martin, A., and Sicilia, V. (2008) *Inorg. Chem.*, **47**, 7166.

115 Maruszewski, K., Strommen, D.P., and Kincaid, J.R. (1993) *J. Am. Chem. Soc.*, **115**, 8345.

116 Danielsson, E., Lumpkin, R.S., and Meyer, T.J. (1987) *J. Phys. Chem.*, **81**, 1305.

117 Shpol'skii, E.V. (1960) *Sov. Phys. Usp.*, **3**, 372.

118 Yersin, H., Humbs, W., and Strasser, J. (1997) *Top. Curr. Chem.*, **191**, 153.

119 Rausch, A.F., Murphy, L., Williams, J.A. G., and Yersin, H. (2009) *Inorg. Chem.*, **48**, 11407.

120 Rausch, A.F., Thompson, M.E., and Yersin, H. (2009) *Chem. Phys. Lett.*, **468**, 46.

121 Rausch, A.F. and Yersin, H. (2010) *Chem. Phys. Lett.*, **484**, 261.

122 Harrigan, R.W. and Crosby, G.A. (1973) *J. Chem. Phys.*, **59**, 3468.

123 Yersin, H. and Strasser, J. (2000) *Coord. Chem. Rev.*, **208**, 331.

124 Tinti, D.S. and El-Sayed, M.A. (1971) *J. Chem. Phys.*, **54**, 2529.

125 Friedrich, J. and Haarer, D. (1984) *Angew. Chem., Int. Ed.*, **23**, 113.

126 Becker, D., Yersin, H., and von Zelewsky, A. (1995) *Chem. Phys. Lett.*, **235**, 490.

127 Kober, E.M., Caspar, J.V., Lumpkin, R.S., and Meyer, T.J. (1986) *J. Phys. Chem.*, **90**, 3722.

128 Colombo, M.G., Hauser, A., and Güdel, H.U. (1993) *Inorg. Chem.*, **32**, 3088.

129 Mallick, P.K., Danzer, G.D., Strommen, D.P., and Kincaid, J.R. (1988) *J. Phys. Chem.*, **92**, 5628.

130 Wiedenhofer, H., Schützenmeier, S., von Zelewsky, A., and Yersin, H. (1995) *J. Phys. Chem.*, **99**, 13385.

131 Albrecht, A.C. (1963) *J. Chem. Phys.*, **38**, 354.

132 Fischer, G. (1984) *Vibronic Coupling*, Academic Press, London.

133 Solomon, E.I. (1984) *Comments Inorg. Chem.*, **3**, 225.

134 Rebane, K.K. (1988) *Zero-Phonon Lines and Spectral Hole Burning in Spectroscopy and Photochemistry* (eds O. Sild and K. Haller), Springer, Berlin.

135 Seiler, R., Kensy, U., and Dick, B. (2001) *Phys. Chem. Chem. Phys.*, **3**, 5373.

136 Su, S.-J., Sasabe, H., Takeda, T., and Kido, J. (2008) *Chem. Mater.*, **20**, 1691.

137 Shih, P.-I., Chien, C.-H., Wu, F.-I., and Shu, C.-F. (2007) *Adv. Funct. Mater.*, **17**, 3514.

138 Vecchi, P.A., Padmaperuma, A.B., Qiao, H., Sapochak, L.S., and Burrows, P.E. (2006) *Org. Lett.*, **8**, 4211.

139 D'Andrade, B.W., Thompson, M.E., and Forrest, S.R. (2002) *Adv. Mater.*, **14**, 147.

140 Yu, X.-M., Kwok, H.-S., Wong, W.-Y., and Zhou, G.-J. (2006) *Chem. Mater.*, **18**, 5097.

141 Adamovich, V., Cordero, S.R., Djurovich, P.I., Tamayo, A., Thompson, M.E., D'Andrade, B.W., and Forrest, S.R. (2003) *Org. Electron.*, **4**, 77.

142 Tanaka, I., Tabata, Y., and Tokito, S. (2004) *Chem. Phys. Lett.*, **400**, 86.

143 Huang, S.-P., Jen, T.-H., Chen, Y.-C., Hsiao, A.-E., Yin, S.-H., Chen, H.-Y., and Chen, S.-A. (2008) *J. Am. Chem. Soc.*, **130**, 4699.

144 Gu, X., Fei, T., Zhang, H., Xu, H., Yang, B., Ma, Y., and Liu, X. (2008) *J. Phys. Chem. A*, **112**, 8387.

145 You, Y., Kim, K.S., Ahn, T.K., Kim, D., and Park, S.Y. (2007) *J. Phys. Chem. C*, **111**, 4052.

146 Yersin, H., Huber, P., and Wiedenhofer, H. (1994) *Coord. Chem. Rev.*, **132**, 35.

147 Colombo, M.G., Brunold, T.C., Riedener, T., Güdel, H., Förtsch, M., and Bürgi, H.-B. (1994) *Inorg. Chem.*, **33**, 545.

148 Marchetti, A.P., Deaton, J.C., and Young, R.H. (2006) *J. Phys. Chem. A*, **110**, 9828.

149 Finkenzeller, W.J., Thompson, M.E., and Yersin, H. (2007) *Chem. Phys. Lett.*, **444**, 273.

150 Bauer, R., Finkenzeller, W.J., Bogner, U., Thompson, M.E., and Yersin, H. (2008) *Org. Electron.*, **9**, 641.

151 Xu, M.-L., Che, G.-B., Li, X.-Y., and Xiao, Q. (2009) *Acta Cryst. E*, **65**, m28.

152 Orselli, E., Kottas, G.S., Konradsson, A. E., Coppo, P., Fröhlich, R., De Cola, L., van Dijken, A., Büchel, A., and Börner, H. (2007) *Inorg. Chem.*, **46**, 11082.

153 Kozhevnikov, D.N., Kozhevnikov, V.N., Ustinova, M.M., Santoro, A., Bruce, D. W., Koenig, B., Czerwieniec, R., Fischer, T., Zabel, M., and Yersin, H. (2009) *Inorg. Chem.*, **48**, 4179.

154 Fischer, T., Czerwieniec, R., Hofbeck, T., Osminina, M.M., and Yersin, H. (2010) *Chem. Phys. Lett.*, **486**, 53.

155 Fischer, T. (2006) PhD thesis. Pt(II) and Ir(III) triplet emitters for OLED applications. Detailed characterizations of luminescence properties. Universität Regensburg.

156 Pentlehner, D. (2006) Diplom thesis. Universität Regensburg.

157 Xie, Y.-M. and Wu, J.-H. (2007) *Chem. Inorg. Commun.*, **10**, 1561.

158 Yersin, H., Czerwieniec, R., Monkowius, U., and Yu, J. (2008) Ger. Patent DE 10 2008 048 336 A1.

159 Ichinaga, A.K., Kirchhoff, J.R., McMillin, D.R., Dietrich-Buchecker, C.O., Marnot, P.A., and Sauvage, J.P. (1987) *Inorg. Chem.*, **26**, 4290.

160 Scaltrito, D.V., Thompson, D.W., O'Callaghan, J.A., and Meyer, G.J. (2000) *Coord. Chem. Rev.*, **208**, 243.

161 Sakaki, S., Mizutani, H., and Kase, Y. (1992) *Inorg. Chem.*, **31**, 4575.

162 Shaw, G.B., Grant, C.D., Shirota, H., Castner, E.W., Jr., Meyer, G.J., and Chen, L.X. (2007) *J. Am. Chem. Soc.*, **129**, 2147.

163 Iwamura, M., Takeushi, S., and Tahara, T. (2007) *J. Am. Chem. Soc.*, **129**, 5248.

164 Miller, M.T., Gantzel, P.K., and Karpishin, T.B. (1998) *Inorg. Chem.*, **37**, 2285.

165 Vorontsov, I.I., Graber, T., Kovalevsky, A. Y., Novozhilova, I.V., Gembicky, M., Chen, Y.-S., and Coppens, P. (2009) *J. Am. Chem. Soc.*, **131**, 6566.

166 Siebrand, W. (1967) *J. Chem. Phys.*, **46**, 440–447.

167 Siddique, Z.A., Yamamoto, Y., Ohno, T., and Nozaki, K. (2003) *Inorg. Chem.*, **42**, 6366.

168 Donges, D., Nagle, J.K., and Yersin, H. (1997) *Inorg. Chem.*, **36**, 3040.

169 Czerwieniec, R., Finkenzeller, W.J., Hofbeck, T., Starukhin, A., Wedel, A., and Yersin, H. (2009) *Chem. Phys. Lett.*, **468**, 205.

170 Cohen-Tannoudji, C., Diu, B., and Laboë, F. (1977) *Quantum Mechanics*, vol. I, John Wiley & Sons, Inc., New York, p. 109.

171 Si, Z., Li, J., Liu, S., and Li, W. (2009) *J. Lumin.*, **129**, 181.

172 Hashimoto, M., Igawa, S., Yashima, M., Kawata, I., Hoshino, M., and Osawa, M. (2011) *J. Am. Chem. Soc.*, **133**, 10348.

173 Zhang, D. (2010) *J. Lumin.*, **130**, 1419.

174 Ge, H., Wie, W., Shuai, P., Lei, G., and Qing, S. (2011) *J. Lumin.*, **131**, 238.

175 Zhang, Q., Zhou, Q., Cheng, Y., Wang, L., Ma, D., Jing, X., and Wang, F. (2006) *Adv. Funct. Mater.*, **16**, 1203.

176 Sun, W., Zhang, Q., Qin, L., Cheng, Y., Xie, Z., Lu, C., and Wang, L. (2010) *Eur. J. Inorg. Chem.*, 4009.

177 Che, G., Su, Z., Li, W., Chu, B., Li, M., Hu, Z., and Zhang, Z. (2006) *Appl. Phys. Lett.*, **89**, 103611.

178 Zhang, Q., Ding, J., Cheng, Y., Wang, L., Xie, Z., Jing, X., and Wang, F. (2007) *Adv. Funct. Mater.*, **17**, 2983.

179 Zhang, Q., Zhou, Q., Cheng, Y., Wang, L., Ma, D., Jing, X., and Wang, F. (2004) *Adv. Mater.*, **16**, 432.

180 Zink, D.M., Bächle, M., Baumann, T., Nieger, M., Kühn, M., Wang, C., Klopper, W., Monkowius, U., Hofbeck, T., Yersin, H., and Bräse, S. (2012) *Inorg. Chem.*, in press.

Part Four
Device Physics

Physics of Organic Semiconductors, Second Edition. Edited by Wolfgang Brütting and Chihaya Adachi

14
Doping of Organic Semiconductors

Björn Lüssem, Moritz Riede, and Karl Leo

14.1
Introduction

In today's production of semiconductor devices, single-crystalline silicon is by far the most frequently used material among other inorganic crystalline materials like GaAs by a wide margin. These materials are stable and offer room temperature mobilities up to 1000 $cm^2/(V\,s)$. However, they are less suitable for low-cost or large area applications. For optoelectronic applications like solar cells and light-emitting diodes, silicon is again less appropriate because it is an indirect semiconductor. Therefore, silicon solar cells need rather thick material layers, resulting in higher cost and long payback time.

A recently much-noticed alternative is organic semiconductor, that is, molecular semiconductor consisting of carbon-based molecular entities. Although early research on organic semiconductors focused on single-crystalline organics whose mobilities, which were investigated in the pioneering work of Karl [1], reach from a few $cm^2/(V\,s)$ at room temperature to a much higher values at reduced temperatures, the thin-film organic semiconductors are preferred today due to practical reasons. The two groups of such materials, the polymers processed from solution and the evaporated small-molecule compounds, are already included in present products, for example, as photoconductors in copiers and laser printers. The field has been recently reviewed by several authors; we however refer here to Refs [2–4] (organic light-emitting diodes (OLEDs)), [5, 6] (organic electronics in general), and [7–9] (organic solar cells (OSCs)).

Organic semiconductors are superior to inorganic semiconductors in the field of low-cost and large area optoelectronics due to their wide variety, making tailor-made materials possible. For example, there are organic dyes with exceptionally high absorption coefficients in the visible range, allowing the realization of ultra-thin photovoltaic cells and photodetectors. The most important problems of inorganic LEDs like reabsorption losses can be avoided by using organic fluorescent dyes with low refraction indices and large redshifts from absorption to emission. In addition, disordered systems of organic semiconductors result in a low

Physics of Organic Semiconductors, Second Edition. Edited by Wolfgang Brütting and Chihaya Adachi

concentration of intrinsic defects due to their saturated electron systems: this compares with the dangling bonds of inorganic amorphous semiconductors that generate a high trap density. Finally, most organics are much easier to process, for example, allowing deposition on flexible substrates at room temperature.

Light emission and photovoltaic effects in organics have been known for a long time. However, the possibility of organic light-emitting diodes and solar cells was hardly noted by researchers until the pioneer work of Tang and Vanslyke [10, 11], who realized thin-film devices by basically inserting an organic double layer between an anode and a cathode, a structure that is fundamental to both LEDs and solar cells.

Figure 14.1 shows schemes for OLED and organic solar cell devices. The key property of both devices is the transport of charge carriers through thin films either from the contacts to the active zone in OLEDs or in the opposite direction in OSCs. It is desirable to minimize any kind of losses in this flow, so highly conductive transport layers are most suitable. Because a transition of charge carriers between the contacts and the active media is necessary for both kinds of devices, a material choice resulting in low energetic barriers or space charge layers thin enough for charge carriers to tunnel through provides the most efficient devices.

These two requirements, high conductivity and efficient injection, are the main topics of this chapter: The possibility of controlled doping was an extremely important factor for the success of inorganic semiconductor technology because it allows having control over conduction properties. Although today's organic semiconductors are usually undoped, the prospective creation of efficient organic-based devices will require controlled and stable doping to adjust the Fermi levels to the transport states. This way ohmic losses can be lowered while the charge carrier injection is supported. Furthermore, it would enable one to raise the built-in potential of Schottky or p–n junctions, which is, for example, helpful in OSC.

This chapter discusses recent work on both fundamental principles and device applications of doping, focusing primarily on doping of evaporated organic layers

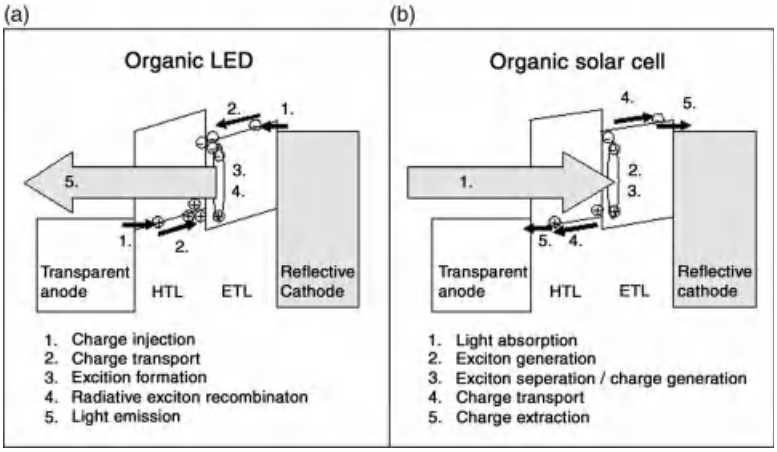

Figure 14.1 Operation principles of an OLED (a) and an organic solar cell (b). Two-layer devices are shown. Reprinted with permission from Walzer et al. Chemical Reviews 107, 1233, 2007. Copyright 2007 American Chemical Society.

with a molecular dopant using coevaporation. Contrary to other conceivable dopants like gases or metals, molecular dopants enable very stable doping. We will begin by describing the basic physics of doping, covering both p-type [12–15] and n-type [16–19] doping. Conductivity increases by several orders of magnitude are possible in both cases, However, the energetic positions of the orbitals in materials used as transport layers in OLEDs and OSCs are facilitating p-type doping compared to n-type doping, making the latter a challenge for recent research. To support the understanding of the basic device principles, this chapter includes some elementary model devices such as organic p–n homojunctions, which have just been realized for the first time [20]. These structures show huge internal voltages and reveal the limits of current semiconductor models as they provide experimental data that are not compatible with the Shockley model usually used for inorganic semiconductors. We will end by discussing devices based on electrically doped organic layers, especially OLEDs, on which the application of these layers has multiple positive effects.

Decreasing the ohmic resistance of the transport layers is crucial to more efficient devices. Figure 14.2 presents a comparison between inorganic and organic LEDs. Figure 14.2a shows a scheme of band structure for a typical inorganic LED. The emitter layer has a smaller bandgap and is placed inbetween two transport layers, one of them being highly n-doped and the other one highly p-doped. The high conductivity of these layers results in very low ohmic losses and almost flat band edges because of the extremely low voltage drop. Therefore, the device operates at a voltage nearly identical to the photon energy of the emitted light.

If the transport layers are not doped as in the early organic light-emitting diodes, the lower carrier density increases ohmic losses and the fields necessary to drive the currents. High fields are needed since the carriers need to be injected and driven through low-conductivity layers, as shown in Figure 14.2b. The high losses can be reduced by very thin films, which is however a disadvantage for process stability. Also, the optical design of the thin-film devices profits from the thickness variations that are possible with doped layers without changing the electrical properties of the devices.

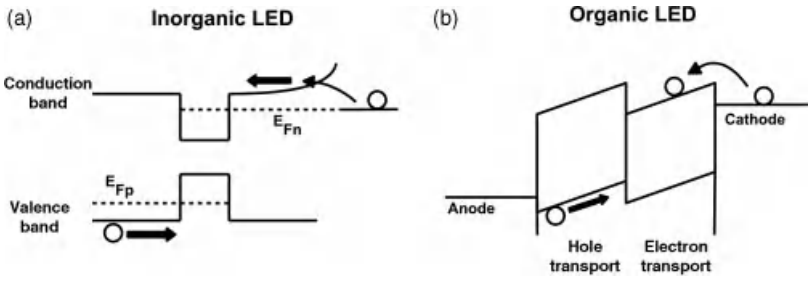

Figure 14.2 (a) Scheme of a typical inorganic LED, which operates close to flat band erated condition. The injection at the contacts is by tunneling through thin-space charge layers. (b) Scheme of an undoped organic LED. Due to the low charge carrier concentration, a high field is needed to drive the lower number of injected carriers. Reprinted with permission from Walzer et al. Chemical Reviews 107, 1233, 2007. Copyright 2007 American Chemical Society.

Furthermore, as shown in Figure 14.2a, doped transport layers generate narrow space charge regions at the contacts, allowing efficient injection by charge carrier tunneling. Despite a potentially large energy barrier between the contacts and the transport layers, ohmic contacts are possible. This is a big advantage since it allows avoiding contact materials with unstable work functions, which would be necessary for adjusting the barriers to optimal levels, and saves additional efforts in preparation compared to OLEDs with undoped layers. The improved flexibility in material choice is of special importance to the field of top-emitting or inverted OLEDs.

Doped transport layers can also be applied in organic solar cells, where they result in similar advantages:

- They allow to virtually freely choose the thickness of doped window layers, enabling efficient optical design, that is, for placing the field maxima.
- Since solar cells operate at very low voltages, avoiding voltage drops by creating ohmic contacts via doping is even more crucial to efficiency than in LEDs.
- In stacked cell structures, doping can significantly improve the efficiency of charge recombination.

The key materials used in this chapter are enlisted in Figure 14.3.

14.2 Doping Fundamentals

Due to the very different structures of organic and inorganic semiconductors, one can expect significant differences in the properties of doped layers. However, as we will discuss in the following section, there are many similarities in the basic properties of the doping process. The key differences in the doping behavior are caused by the transport in organic semiconductors occurring due to hopping in a distribution of more or less localized states. Additional effects are the large Coulomb correlation between charge carriers and strong polaronic coupling between localized hopping states.

The basic principle of doping is like that in inorganic semiconductors. Electron donors or acceptors are added to the material, generating additional mobile charge carriers. To obtain n-type doping in organics, the dopant has to donate electrons to the lowest unoccupied orbital (LUMO) states, while the p-type dopants extract electrons from the highest occupied orbital (HOMO) states thereby creating holes (Figure 14.4.)

Doping in organic semiconductors using strongly oxidizing gases, for example, iodine or bromine, has been addressed quite early: the doping of materials such as phthalocyanines lead to high conductivities [21]. However, these dopants are too small to provide thermally stable doped layers of bipolar devices like p–n- or p–i–n junctions due to their large tendency to diffuse.

Small atoms like lithium, caesium, or strontium [22, 23] and even small molecules like Lewis acids [24] have often been used. A report on the previously described effects has been exemplarily given by Parthasarathy and coworkers who used UPS to measure the Fermi level of the well-known organic electron

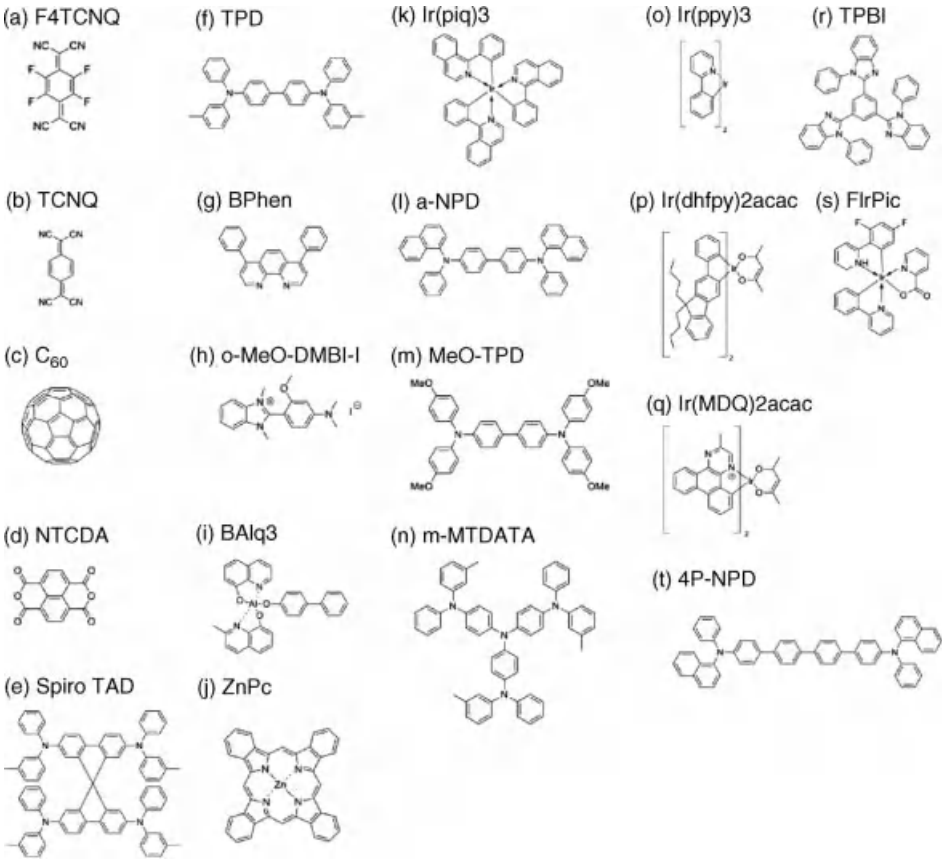

Figure 14.3 Key materials used in this paper (a) F4-TCNQ: 2,3,5,6-tetrafluoro-7,7,8,8-tetracyano-quinodimethane (b)TCNQ: 7,7′,8,8′-tetracyanoquinodimethane (c) C60 (d) NTCDA: 1,4,5,8-naphthalenetetacarboxylic dianhydride (e) Spiro-TAD: 2,2′,7,7′-Tetrakis-(*N*,*N*-diphenylamino)-9,9'-spirobifluoren (f)TPD: *N*,*N*′-bis(3-methylphenyl)-*N*,*N*′-diphenylbenzidine (g) BPhen: 4,7-diphenyl-1,10-phenanthroline (h) o-MeO-DMBI-I: 2-(2-methoxyphenyl)-1,3-dimethyl-1H-benzoimidazol-3-ium iodide (i) BAlq: aluminum (III) bis(2-methyl-8-quninolinato)-4-phenylphenolate (j) ZnPc: zinc phthalocyanine (k) Ir(piq)3: Tris(1-phenylisoquinoline) iridium(III) (l) a-NPD: *N*,*N*′-di(naphthalen-2-yl)-*N*,*N*′-diphenyl-benzidine (m) MeO-TPD: (*N*,*N*,*N*′,*N*′-tetrakis(4-methoxyphenyl)-benzidine (n) m-MTDATA: 4,4′,4″-tris(3-methylphenylphenylamino) triphenylamine (o) Ir(ppy)3: Tris(2-phenylpyridin) iridium(III) (p) Ir(dhfpy)2(acac) Bis(2-(9,9-dihexylfluorenyl)-1-pyridine) (acetylacetonate)iridium(III) (q)Ir(MDQ)2 (acac): Iridium(III)bis(2-methyldibenzo-[f,h] chinoxalin)(acetylacetonat) (r) TPBi: 2,2′,2″-(1,3,5-Phenylen)tris(1-phenyl-1H-benzimidazol) (s) FIrpic: iridium(III)bis[(4,6-difluorophenyl)-pyridinato-N,C2]picolinate (t)4P-NPD: *N*,*N*′-di-1-naphthalenyl-*N*,*N*′-diphenyl-[1,1′:4′,1″:4″,1‴-Quaterphenyl]-4,4‴-diamine.

transporter BCP when doped with lithium. The result is shown schematically in Figure 14.5, where it can be observed that the lithium ions occupy states in the BCP gap. For practical applications, the doping with ions or very small molecules usually suffers from device instability due to diffusion.

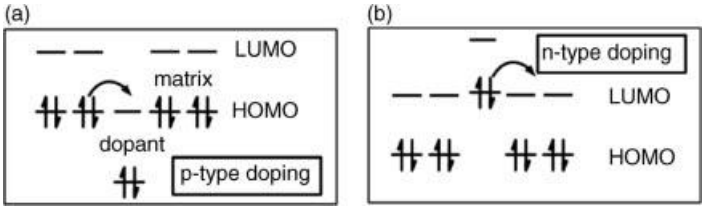

Figure 14.4 Scheme of the doping process for molecular p-type (a) and n-type doping (b). In p-type doping, the dopant is an acceptor; in n-type doping, it is a donor. Adapted with permission from Walzer et al. Chemical Reviews 107, 1233, 2007. Copyright 2007 American Chemical Society.

The preparation of stable devices is easier when using larger, in particular aromatic, molecules acting as good donors or acceptors. In the last decades, many possible combinations of materials and dopants have been reported, such as phthalocyanines doped by organic acceptor molecules like *ortho*-chloranil [25], tetracyano-quinodimethane (TCNQ) or dicyano-dichloroquinone (DDQ) [26, 27]. The latter has also been used to dope covalently bound stacked phthalocyanines [28] and oligothiophenes [29]. However, these dopants usually had a rather small effect. Furthermore, there was a general lack of systematic research on the impact that doping has on key properties of semiconductors as the charge carrier density or the Fermi level and on device performance [26, 29].

Our group has recently systematically investigated the physics underlying molecular doping [12, 15, 16, 20, 30–32], which lead to the development of electrically doped transport layers that were successfully applied in both OLEDs [33–40] and organic solar cells [41–46]. The following sections will address our approach to doping via coevaporation of dopants and organic matrices. Regarding p-type doping, we did extensive research on different matrix materials, including both amorphous

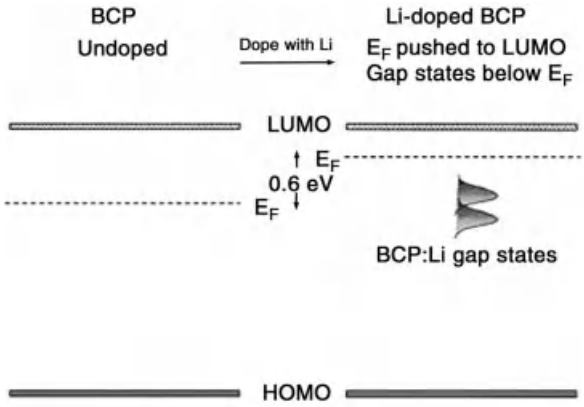

Figure 14.5 Energy levels of undoped (left) and Li-doped (right) bathocuproine (BCP) thin films. Reprinted with permission from Parthasarathy et al, Journal of Applied Physics 89, 4986, 2001. Copyright 2001, American Institute of Physics [22].

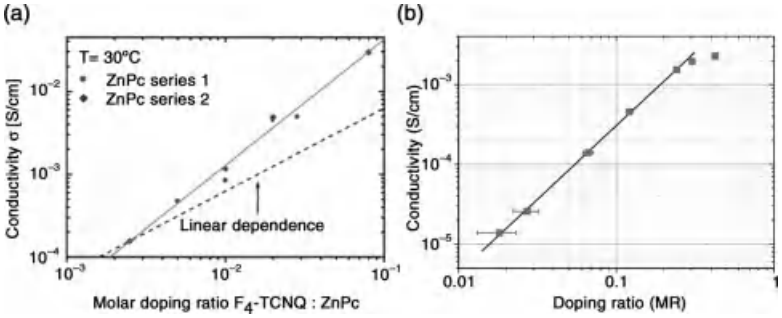

Figure 14.6 Doping of different host materials (ZnPc - left Reprinted with permission from Walzer et al. Chemical Reviews 107, 1233, 2007. Copyright 2007 American Chemical Society. [47] and MeO-TPD - right Reprinted with premission from Olthof et al., Journal of Applied Physics 106, 103711, 2009. Copyright 2009, American Institute of Physics.[32]) by the strong electron acceptor F_4-TCNQ . The conductivity of both layers increases with increasing F_4-TCNQ concentration.

and polycrystalline materials, which will be presented in this chapter. The n-type doping is more complex as there are not many molecules combining stability with sufficiently high energy levels to reach the LUMO states of typical organic semiconductors. Nevertheless, some important results will be discussed in this chapter.

14.2.1 p-Type Doping

The p-type doping has been shown for a wide range of different matrix/dopant combinations [47]. Both, polycrystalline and amorphous materials have been studied [15] and conductivities above 10^{-4} S/cm have been reached, which is sufficient for charge transport layers of organic solar cells and organic light-emitting diodes.

In Figure 14.6, two examples of p-doping are shown. In Figure 14.6a, the conductivity of a layer of a phthalocyanine, ZnPc, doped with the strong electron acceptor F_4-TCNQ, is shown. Phthalocyanines are stable molecules with a low-lying HOMO state and have been used as model system for many early studies of doping. In Figure 14.6b, doping of an amorphous material, MeO-TPD, with F_4-TCNQ is shown. MeO-TPD is a common hole transport material in highly efficient OLEDs.

In the following, two aspects of the doping mechanism will be discussed. It is shown how doping can be used to control the Fermi level position, which is related to the number of free charge carriers created in the organic semiconductors. Furthermore, the efficiency of the doping process, that is, how many free charge carriers are created per dopant molecule, is discussed.

14.2.1.1 Control of the Position of the Fermi Level by Doping

By doping, the concentration of free charge carriers is increased or remains equivalent, the Fermi level moves toward the transport level of the organic semiconductor.

The distance between the transport states and the Fermi level E_F can be measured by the Seebeck effect [12, 15]. The Seebeck coefficient S depends on the distance between the transport states E_μ and the Fermi level E_F:

$$S(T) = \frac{k_B}{e}\left[\left(\frac{E_F(T) - E_\mu}{k_B T}\right) + A\right] \tag{14.1}$$

where A is a numerical factor that can be neglected for organic systems, k_B is the Boltzmann constant, T is the temperature, and e is the elementary charge. Seebeck measurements show that the difference between the Fermi level and the transport state decreases with increasing doping concentrations [48]. However, a discrete transport level E_μ is assumed in Eq. (14.1), which neglects the commonly observed Gaussian distribution of transport states. Although correct qualitative conclusions can be drawn from these measurements, many doping-induced effects cannot be understood if a discrete transport level is assumed.

A technique that is able to resolve the distribution of transport (HOMO) states and to determine the position of the transport states in relation to the Fermi level is *ultraviolet photoelectron spectroscopy* (UPS). Olthof *et al.* [32] used UPS to study metal/p-doped organic semiconductor junctions, which lead to a deeper understanding of the doping mechanisms.

In Figure 14.7a, the energy level alignment of a metal/p-doped organic layer junction is sketched. After a contact between the semiconductor and the metal is established, the Fermi level E_F of the organic layer aligns with the work function of the metal (Wf_n). The hole injection barrier at the interface ϕ_0 is determined by the

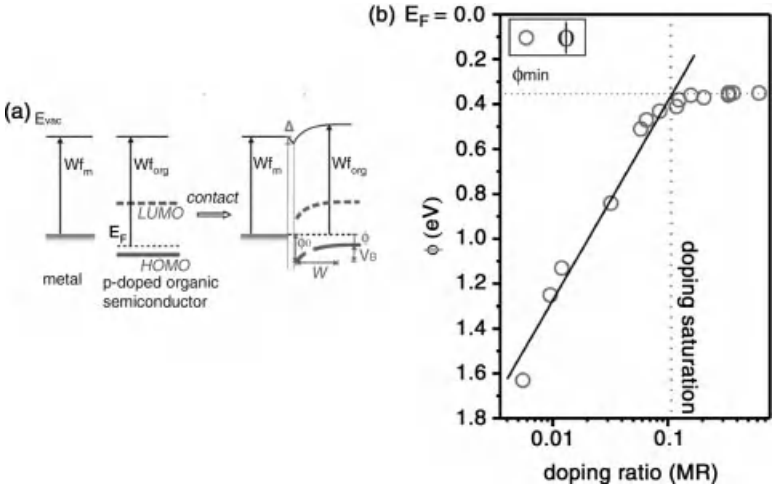

Figure 14.7 (a) Energy level alignment in a metal/organic semiconductor junction. (b) The distance ϕ between the Fermi level and the HOMO states in the bulk of the organic layer consisting of MeO-TPD doped with F_4-TCNQ is plotted as a function of the doping ratio. Although for low doping concentrations, ϕ decreases, it saturates at high doping concentrations [32]. Reprinted with premission from Olthof et al., Journal of Applied Physics 106, 103711, 2009. Copyright 2009, American Institute of Physics.

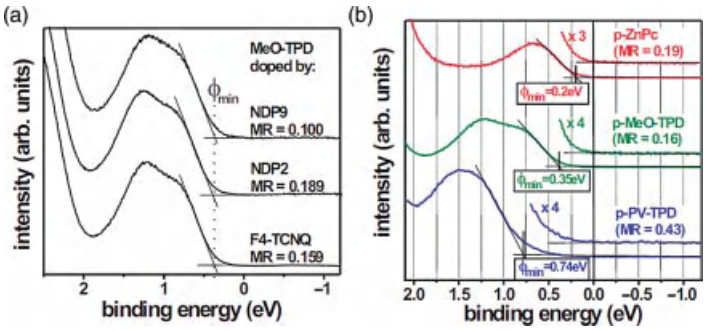

Figure 14.8 (a) The HOMO region of MeO-TPD doped with F_4-TCNQ and the commercially available dopants NDP2 and NDP9. Although all dopants have different doping strengths, the shift of the Fermi level toward the HOMO saturates at $\phi = 0.35$ eV. (b) Doping of different matrix materials (ZnPc, MeO-TPD, and PV-TPD) by F_4-TCNQ is shown. ϕ_{min} strongly depends on the matrix material. In the enlarged plots, it can be seen that a significant density of state tails into the transport gap and pins the Fermi level [32]. Reprinted with premission from Olthof et al., Journal of Applied Physics 106, 103711, 2009. Copyright 2009, American Institute of Physics.

metal work function, the ionization potential of the semiconductor I_P, and an interface dipole $\Delta(\phi_0 = I_P + \Delta - Wf_m)$. Due to a charge depletion zone at the interface, the HOMO states bend upward and the distance between the HOMO and the Fermi level decreases with increasing distance from the interface. At the end of the charge depletion zone, the distance between HOMO and E_F saturates at its bulk value ϕ. All these parameters can be determined by UPS, so a full characterization of the contact and the position of the Fermi level in the bulk is possible.

In Figure 14.7b, the distance between the Fermi level and the HOMO states in the bulk ϕ of the organic semiconductor MeO-TPD is plotted versus the doping ratio of F_4-TCNQ [32]. For intrinsic MeO-TPD, the Fermi level is close to the midgap ($\phi = 1.68$ eV). Increasing the doping ratio leads to a steep decrease in ϕ until it saturates at approximately $\phi_{min} = 0.35$ eV.

The shift of the Fermi level at low concentrations proves that doping is effective. However, the saturation of the Fermi level shift can be understood only by a detailed analysis of the doping process. In Figure 14.8a, the HOMO region of the UPS signal of MeO-TPD doped with F_4-TCNQ and two commercially available dopants (NDP2 and NDP9[1)]) is shown. Although all dopants F_4-TCNQ, NDP2, and NDP9 have different doping strengths and different electron affinities, the distance between the Fermi level and HOMO states at saturation ϕ_{min} does not depend on the dopant.

In contrast, in Figure 14.8b, the matrix material has been varied. In addition to MeO-TPD, ZnPc and PV-TPD have been doped by F_4-TCNQ. It can be seen that the choice of the matrix material has a strong influence on the saturation behavior. Whereas MeO-TPD saturates at 0.35 eV, PV-TPD saturates at $\phi_{min} = 0.74$ eV and ZnPc at 0.2 eV.

1) Novaled AG.

The dependence of the saturation effect on the matrix material can be understood by the insets in Figure 14.8b, which show an enlarged view of the UPS signal between the HOMO energy and the Fermi level. Commonly, the HOMO cutoff energy is defined as the intersection of a tangent and the background. However, as shown in Figure 14.8b, there is a significant density of states that extends into the gap and reaches up to the Fermi level at saturation. Thus, at high doping ratios, the Fermi level is pinned by a significant density of tailing states in the transport gap, which leads to a saturation of the Fermi level shift [32].

In conclusion, by UPS it can be shown that the Fermi level is shifted toward the transport states, which implies that the number of free charge carriers in the matrix materials is increased by doping. However, up to now, it has not been discussed how efficient this process is, that is, how many dopant molecules are ionized and how many free charge carriers are generated for a given doping concentration.

14.2.1.2 **Doping Efficiency**

To determine the efficiency of charge transfer between the dopant and the host molecule, Fourier transform infrared spectroscopy (FTIR) can be used. The absorption of the CN-stretching mode of F_4-TCNQ depends on the charging state Z of the dopant. It shifts from 2228 cm^{-1} ($Z = 0$) to 2194 cm^{-1} ($Z = 1$) [30].

In Table 14.1, the charge transfer ratio of different dopant/matrix combinations is shown [47]. It can be seen that phthalocyanines and TDATA derivatives can be easily doped, that is, a complete charge transfer from the dopant to the matrix is observable ($Z = 1$). This efficient charge transfer can be explained by the electron affinity of these materials ($\sim$ 5.2 eV) [12, 32], which is larger than the ionization energy of the matrix materials. If the electron affinity of the dopant is reduced (e.g., TCNQ that has an electron affinity of only 4.5 eV), the charge transfer is much less efficient ($Z = 0.2$ for the combination ZnPc/TCNQ). Similarly, if a host material with a higher I_P (e.g., TPD) is used, the charge transfer is less efficient (0.64 for the combination TPD/F_4-TCNQ). Charge transfer for TPD derivatives can be enhanced, if the I_P is lowered by electron pushing methoxy groups at the outer benzene rings, as in MeO-TPD. A charge transfer ratio of 0.74 is reached for the combination of MeO-TPD/F_4-TCNQ.

Thus, the degree of charge transfer strongly depends on the electron affinity and the ionization energy of the dopant and host molecule, respectively. However, a

Table 14.1 P-doping of various hole transport materials by TCNQ derivates.

Matrix	**ZnPc**	**ZnPc**	**m-MTDATA**	**TPD**	**MeO-TPD**
Dopant	**F4-TCNQ**	**TCNQ**	**F4-TCNQ**	**F4-TCNQ**	**F4-TCNQ**
I_P (eV)	5.1 [14]	5.1	5.1 [49]	5.4 [50]	
Z	1	0.2	1	0.64	0.74
σ (S/cm)	1×10^{-3}	1×10^{-6}	3×10^{-7}	1×10^{-7}	1×10^{-5}

The table shows the solid-state ionization energy I_P of the matrix materials, the degree of charge transfer Z from the matrix to the dopant, derived from the position of the $b_{1u}\nu_{18}$ mode of the TCNQ derivates, and the conductivity σ at a doping level of 2 mol% for a series of matrix/dopant combinations [47].

charge transfer ratio Z of unity does not necessarily mean that one *free* electron is generated per dopant molecule. The hole that has been transferred to the matrix molecule still feels the attractive force of the negatively charged dopant molecule. In contrast to inorganic semiconductors, organic materials have a lower dielectric constant, which leads to stronger Coulomb interactions. The attractive force between the negatively charged dopant molecule and the generated hole on the matrix is strong, and a charge carrier transferred to a matrix molecule is not necessarily free. The doping efficiency, defined as ratio of the number of free charge carriers to the number of dopants, can be below unity, even if all dopant molecules transfer charge to a matrix molecule.

To measure the density of free charge carriers in an organic semiconductor, the thickness of charge depletion zones w in p–i–n and in m–i–p diodes can be measured. Olthof *et al.* [32] studied the thickness of the depletion zone in m–i–p junctions consisting of a silver anode, an intrinsic layer of MeO-TPD ($d = 5$ nm), and a p-doped layer of MeO-TPD by UPS. Using the common assumption that the intrinsic layer and the charge depletion zones are fully depleted ($p = 0$, p: density of holes), one can solve Poisson's equation:

$$\frac{d^2\phi}{dx^2} = -\frac{\varrho}{\varepsilon\varepsilon_0} = \begin{cases} 0 & 0 < x \leq d \\ \dfrac{eN_A^-}{\varepsilon\varepsilon_0} & d < x \leq d + w \end{cases} \tag{14.2}$$

where d is the thickness of the intrinsic layer, ϕ is the electric potential, ϱ is the space charge density, $\varepsilon_0\varepsilon$ is the permittivity of the organic layer, N_A^- is the number of ionized dopants, that is, density of dopant states that have generated a *free* hole, and w is the thickness of depletion zone in the p-doped layer. Integration of Eq. (14.2) leads to an expression for N_A^-, which equals the number of free holes p in the bulk of the organic layer:

$$N_A^- = -\frac{2\varepsilon\varepsilon_0 V_B}{e(w^2 + 2wd)} \tag{14.3}$$

where V_B is the built-in voltage (cf. Figure 14.7a). By UPS, the built-in potential and the thickness of the depletion zone can be measured experimentally for different doping concentrations. Using Eq. (14.3), the density of free charge carriers and thus the doping efficiency can be calculated. The result is summarized in Table 14.2. In addition to the analytical solution of the Poisson equation (14.3), the number of free

Table 14.2 Efficiency of doping MeO-TPD with F_4-TCNQ at different doping concentrations.

Doping ratio (MR)	w (nm)	ϕ_0 (eV)	ϕ (eV)	eV_B (eV)	p(cm^{-3}) Analytic/numerical	Ionized dopants (%) analytic/numerical
0.032	8 ± 1	1.5	0.84	0.66	$1.5 \times 10^{18}/2.0 \times 10^{18}$	3.3/4.3
0.065	5 ± 0.5	1.36	0.47	0.89	$4.0 \times 10^{18}/6.0 \times 10^{18}$	4.2/6.4
0.205	2.8 ± 0.3	1.63	0.38	1.25	$1.2 \times 10^{19}/1.5 \times 10^{19}$	3.9/5.0
0.370	0.6 ± 0.2	1.75	0.35	1.4	$7.3 \times 10^{19}/1.0 \times 10^{20}$	13.6/18.6

The number of free charge carriers are either determined by Eq. (14.3) or by a numerical simulation [32].

charge carriers has been determined by a refined numerical calculation. At low doping densities, the doping efficiency is as low as 3–4%, which means that only a fraction of dopant molecules generates free holes. At higher concentrations, the efficiency seems to increase, but the thin depletion layer thickness (below one monolayer) can lead to additional effects that are unaccounted for in this model.

14.2.2 n-Type Doping

Finding suitable materials for n-type doping is much more challenging than for p-type doping, but essential to realize efficient devices based on the p–i–n concept [47]. In addition to be large enough to not migrate to thin films and not to act as trap, they have to be able to add electrons to the LUMO of ideally a wide variety of matrix materials. For a direct electron transfer from a dopant, its HOMO has to lie above the LUMO of the matrix material, making n-doping fundamentally more difficult, because a high HOMO reduces the stability of the dopant against oxidation. Figure 14.9 shows a couple of materials and illustrates the challenges.

Of the various ways for n-doping of organic semiconductors, the following three approaches are discussed.

- Using alkali metals.
- Using molecular compounds with very high HOMO levels.
- Using air-stable precursor molecules that can donate an electron to the matrix material in the deposited film.

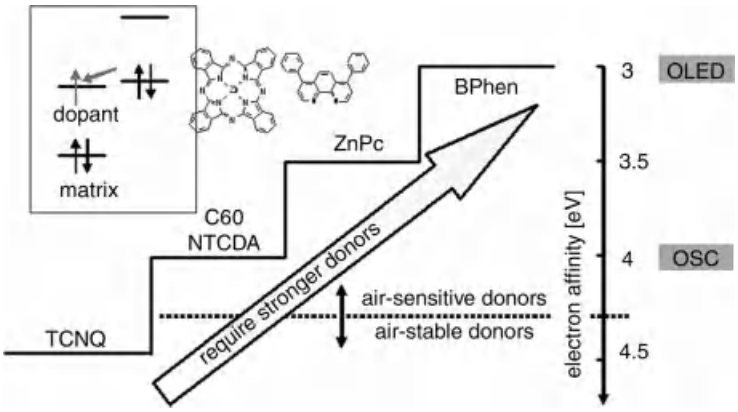

Figure 14.9 A series of typical electron transport materials for organic solar cells and OLEDs. Because the electron transport materials for organic solar cells typically have an electron affinity (EA) of about 4.0 eV, the requirements for n-doping materials for organic solar cells are more relaxed than for OLEDs. For the latter application, electrons have to be added to matrix materials with an EA of about 3 eV, generally requiring materials that increasingly require handling under inert conditions. Reprinted with permission from Walzer et al. Chemical Reviews 107, 1233, 2007. Copyright 2007 American Chemical Society [47].

14.2.2.1 n-Type Doping Using Alkali Metals

The first use of n-type doping using alkali metals like potassium or sodium was reported in the 1970s [51] and subsequently investigated both theoretically and experimentally in more detail [52]. Doping using Li was first reported to dope an OLED cathode in the early 1990s [53, 54]. Li is still commonly used today and typically applied as a thin layer of pristine Li, Li_2, or LiF before deposition of the metal cathode.

The deposition of the metal cathode onto such a Li-containing layer plays an important role in doping and the energy input from the metal deposition supports the diffusion of the Li into the organic layer. The most investigated interface is Alq_3/LiF/Al, because of its frequent use in OLEDs and Figure 14.10 shows the UPS studies on this interface by Mori *et al.* [55]. They showed that the Fermi levels align well in the presence of the LiF interlayer, that is, a reduction of barrier height, leading to a good electron injection and explaining the reduced driving voltage for OLEDs.

To determine the species responsible for the doping, Hung *et al.* [56] investigated this particular interface by XPS, showing that after LiF deposition, the LiF remains undissociated. If Al is subsequently deposited onto the LiF, LiF and Al were said to undergo an exothermic reaction on Alq_3. However, no Li+ ions were detected in their experiments [57]. Other groups obtained different results. Grozea *et al.* [58] lifted off the Al electrode after its deposition and found both Li—F and C—F bonds in the layers underneath, an indication that LiF had dissociated. However, the diffusion of Li is not controllable, resulting in a usually unknown thickness of the doped layer. Parthasarathy *et al.* [22] therefore carried out a study of Li doping from an interface layer and its diffusion into the bulk of BCP, CuPc, and Alq_3, that is, common materials for OLEDs. They found using current–voltage measurements, UPS and secondary

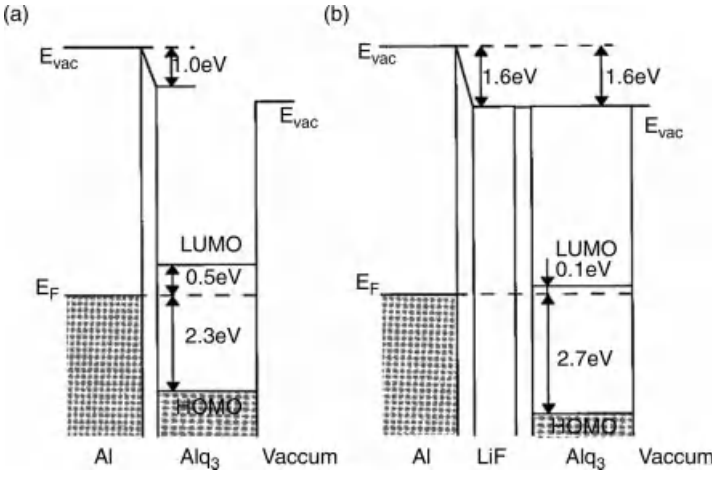

Figure 14.10 The results of a UPS study on the interface between Alq_3 (1.7 nm) and Al (50 nm) without (a) and with (b) a 0.5 nm LiF interlayer. The energy diagrams show the difference between the undoped (a) and doped (b) interface. Reprinted with permission from Hung et al. Applied Physics Letters 70, 152, 1997. Copyright 2007 American Institute of Physics [55].

ion mass spectrometry (SIMS) depth profiling that they could obtain a peak conductivity of $\approx 10^{-5}$ S/cm, that is, high enough for applications, and that Li diffused nearly up to 100 nm into the bulk for BCP and CuPc after evaporation of a metal electrode. How much exactly Li diffuses into the bulk very much depends on the matrix and the preparation conditions, as another study determined that Li diffuses from a 0.8 nm layer to only 10 nm into BPhen without the deposition of a metal electrode [59].

An alternative to n-type doping by diffusion from the interface is coevaporating Li with an organic material typically at high doping ratios, leading to bulk doping. Here, the thickness of the initially doped layer is more controllable, but can also lead to a good Fermi level alignment at the interface. Kido *et al.* showed efficient OLEDs with a Li-doped Alq_3 or BPhen as electron injection layer [23]. Both approaches, interface and bulk doping with alkali metals, are frequently used for OLEDs and the beneficial effect of an LiF interlayer between the organic material and the Al electrode was also shown for organic solar cells [60, p. 215].

Other alkali metals like Cs and their salt or alloy compounds can also be used for efficient n-doping of organic materials. Here, Cs is often codeposited with organic electron transport layers and can lead to highly efficient OLEDs [40]. Given that Cs has larger atomic dimensions, its main advantage is the reduced diffusivity compared to Li. Thus, such devices show a higher stability with respect to device temperatures as Cs remains better localized in the transport layers.

However, independent of interface or bulk doping, alkali metal ions used to generate a doped layer can still diffuse due to their small size, which is a serious disadvantage. Their uncontrolled diffusion in the organic layers is generally detrimental to the device lifetime, as they may get into layers where it is not desired, for example, acting as luminescence quencher in OLEDs [23, 22].

14.2.2.2 n-Type Doping Using Molecular Compounds with Very High HOMO Levels

The first publication of controlled n-type doping using an organic molecule was presented by Nollau *et al.* in 2000 [16]. They showed how naphthalenetetracarboxylic dianhydride (NTCDA) could be doped by the electron-donating molecule bis (ethylenedithio)-tetrathiafulvalene (BEDT-TTF). The proof of n-type doping was a clearly observable shift of the Fermi level toward the electron transport level and an increase in conductivity by one–two orders of magnitude. This study showed that it is possible to n-dope organic semiconductors using molecular compounds and as such has the potential to be much more thermally stable than using alkali metals because of the reduced diffusivity. Thus, much research was carried out and several other material classes have been found.

The molecule tetrathianaphthacene (TTN, HOMO $\approx$ 4.7 eV) was shown in an UPS study to n-dope hexadecafluoro-zinc-phthalocyanine (F16ZnPc) well, but not Alq_3 [61]. Given the energy levels of F16ZnPc (LUMO $\approx$ 4.5 eV) and Alq_3 (LUMO $\approx$ 2.5 eV), it is not surprising that TTN works more efficiently as electron donor for the former matrix molecule, highlighting that the HOMO level of a dopant has to lie above the LUMO of the matrix for direct n-doping.

Another compound for n-doping is the strongly reducing molecule bis(cyclopentadienyl)-cobalt(II) (cobaltocene, CoCp2) as shown by Chan *et al.* [62]. Their

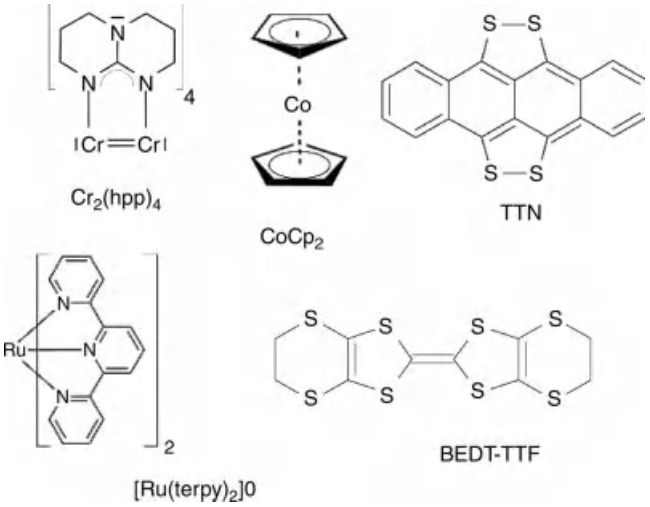

Figure 14.11 The chemical structures of some complexes used for direct n-doping: Cr_2 (hpp)$_4$, cobaltocene ($CoCp_2$), tetrathianaphthacene (TTN), $[Ru(terpy)_2]^0$, and bis-ethylenedithio-tetrathiafulvalene (BEDT-TTF).

thorough investigation included conductivity measurements, X-ray studies for analyzing the structure of the vacuum-deposited films, and UPS. Their matrix material was a tris(thieno)hexaazatriphenylene derivative, an electron transporter. CoCp2 has an ionization potential of only 4 eV and was able to shift the Fermi level of their matrix material by more than 0.5 eV toward the electron transport level, a clear proof of n-type doping. Consequently, the conductivity of the investigated films were found to increase by about three orders of magnitude, making CoCp2 an interesting n-dopant and leading to further work with this material class (see Section 14.2.2.3).

Using metal complexes in general appears to be a good approach for n-doping, as they are also the basis for other n-type dopants. Bloom *et al*. suggested the compounds $[Ru(terpy)_2]^0$, $[Cr(bpy)_3]^0$, and $[Cr(TMB)_3]^0$ as n-dopants [63]. The electron-donating character of these compounds is strong enough to dope materials used in organic solar cells [31], but was found to be not sufficiently n-doping for general application in OLEDs because of the higher lying LUMO values of the electron-transporting materials.

To directly n-dope OLED materials, dopants with higher lying HOMO are required. Novaled AG investigated two compounds first described by Cotton *et al*. [64–66] and recently characterized in more detail by Menke *et al*. [67]. The dimetal complexes of chromium or tungsten with the anion of 1,3,4,6,7,8-hexahydro-2*H*-pyrimido[1,2-*a*]pyrimidine (hpp), forming $Cr_2(hpp)_4$ and $W_2(hpp)_4$ (Figure 14.11) were shown to effectively dope C60 with conductivities reaching well above 1 S/cm. It was found that $Cr_2(hpp)_4$ doped C60 more effectively than $W_2(hpp)_4$, although the ionization potential of $W_2(hpp)_4$ is with 2.68 ± 0.13 eV even lower than Cs (IP = 3.9 eV) [64]. A strong shift in Fermi level toward the electron transport

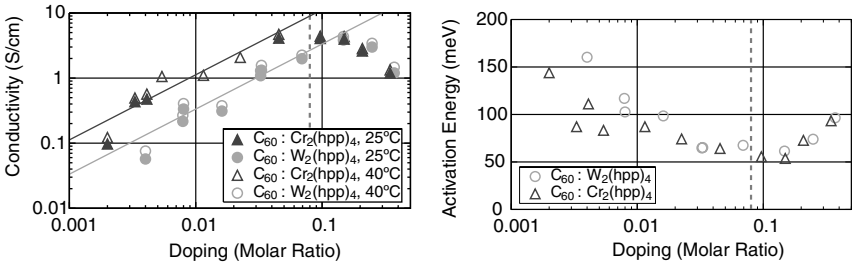

Figure 14.12 Lateral conductivity of C60 (30 nm) at 40 °C (a) and activation energy of the conductivity (b) as function of the doping concentration with either $Cr_2(hpp)_4$ or $W_2(hpp)_4$. Reprinted with permission from Menke et al. Applied Physics Letters 100, 093304, 2012. Copyright 2012 American Institute of Physics. [67].

level was observed and the corresponding increase in conductivity is shown in Figure 14.12. Furthermore, both dopants were found to lead to a stable n-doping in C60 up to 100 °C most likely due to their molecular dimensions.

However, one general drawback of this approach for n-type doping is the increasing instability of the dopants with respect to oxygen for higher HOMO values, requiring a continuous handling of the materials under inert conditions.

14.2.2.3 n-Type Doping Using Precursors

Given the challenges in synthesis and handling of oxygen-sensitive substances, much research in recent years has been devoted to finding n-dopants that do not directly dope the matrix materials, but via an intermediate form with the precursor being less or not at all sensitive to oxygen.

One possible approach is to use precursors that donate an electron to the matrix by being activated by heat or illumination. Werner *et al.* showed that cationic dyes like pyronin B chloride can be used as stable precursors for strong molecular donors [18, 17]. Figure 14.13 illustrates this effect of pyronin B chloride coevaporated with the matrix material NTCDA where it turns into the strong donor pyronin B and the conductivity of NTCDA is increased by about four orders of magnitude up to 10^{-4} S/cm. Cationic dyes were chosen, because these molecules consist of an organic cation and an often inorganic counterion, and as the corresponding neutral radicals have strong electron donor character, the closed-shell cations are of interest for n-type doping.

Also, Chan *et al.* investigated the doping process of pyronin B in NTCDA in great detail, using UPS/IPES and current–voltage measurements [68]. They confirmed the n-doping process by observing a shift in Fermi level toward the electron transport level and an increase in conductivity by more than four orders of magnitude. Combining their experimental data with calculations using density functional theory (DFT), they concluded that two species of pyronin B are present in the deposited thin film: the leuco and the neutral radical of pyronin B, although they attributed the doping effect to the neutral radical.

Other stable precursor molecules are triphenylmethane cationic dyes crystal violet [19] and acridine orange base [3,6-bis(dimethylamino)acridine (AOB)] [69]. The

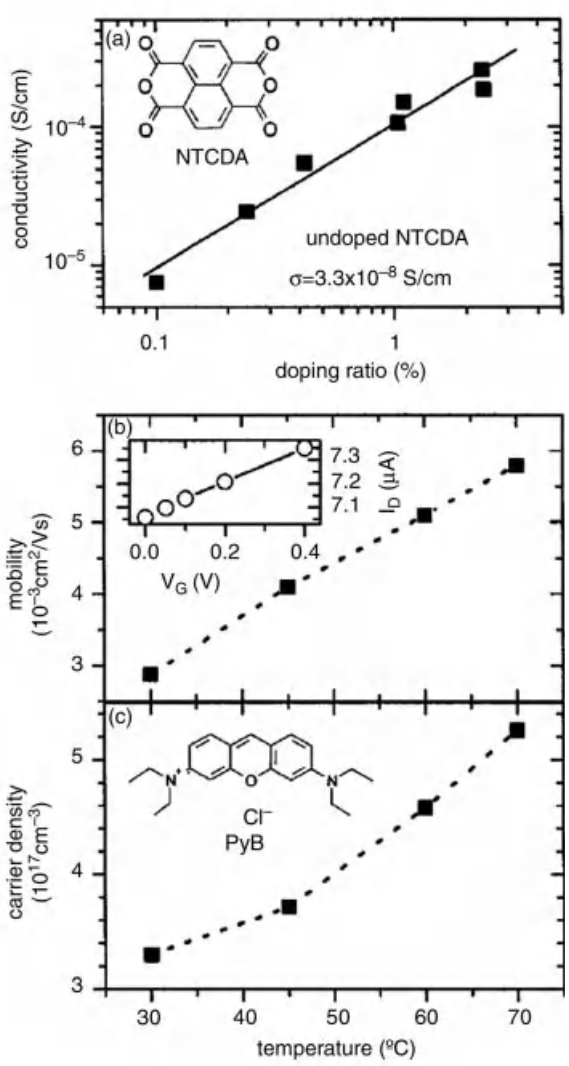

Figure 14.13 The conductivity of NTCDA layers versus doping concentration with pyronin B chloride. Reprinted with permission from Werner et al. Applied Physics Letters 82, 4495, 2003. Copyright 2003 American Institute of Physics [18].

common process is that these molecules can become *in situ* a volatile electron donor for n-doping of a matrix.

Further investigations using FTIR, UV/VIS/NIR, and mass spectroscopy showed that during the sublimation of triphenylmethane cationic dyes (malachite green, crystal violet) and xanthene cationic dyes (pyronin B, Rhodamine B), leuco bases are formed [17, 19]. Once the leuco forms oxidize, the original cationic dye is recreated. Using leuco bases like leuco crystal violet (LCV) and

leuco malachite green, the intermediate role of the leuco bases was inferred as the leuco form is only a weak electron donor, not able to directly donate electrons to most matrix materials.

The proposed mechanism of this doping process is illustrated for LCV and C60 in Figure 14.14. The initial step is the illumination with light that excites LCV, that is, lifting an electron from its HOMO to LUMO. From there, an electron transfer to the LUMO of C60 can take place, leading to an LCV cation and a C60 anion. The probability of a back reaction of the electron from the LUMO of C60 to the HOMO of LCV is reduced by an apparently irreversible hydride reaction of LCV to CV. Through this hydride transfer, the LCV with a half-filled HOMO is converted into a nonradical CV with a filled HOMO. As a consequence, the electron back transfer from C60 is no longer possible and a stable doping has been obtained. The same effect has been observed for stronger acceptors like DDQ or TCNQ where LCV is directly oxidized to CV by the hydride transfer without requiring illumination to reach an excited state as it is the case for weaker acceptors like C60 [70–72].

Recently, another material class for efficient n-type doping via a precursor has been introduced by Wei *et al*. [73, 74]. They introduced (4-(1,3-dimethyl-2,3-dihydro-1*H*-benzoimidazol-2-yl)phenyl)dimethylamine (*N*-DMBI) as a solution-processable n-dopant [73] and its cationic derivative, 2-(2-methoxyphenyl)-1,3-dimethyl-1*H*-benzoimidazol-3-ium iodide (*o*-MeO-DMBI-I) as vacuum-processable n-dopant [74] for fullerenes. Using *o*-MeO-DMBI-I, they were able to obtain conductivities of about more than 1 S/cm for vacuum-deposited C60. Their hypothesis for this stable doping process was that *o*-MeO-DMBI-I was reduced during evaporation to its neutral radical that has a much higher SOMO level. From there, an electron transfer to the LUMO of C60 can take place, and thus the neutral radical is assumed to be responsible for the strong n-type doping effect in C60.

For organic solar cells, doping via such precursors has frequently been used as the LUMO of C60 or other electron transport materials like NTCDA [75, 76] can effectively be doped with electrons. A low doping concentration of less than 5 wt% is generally enough to reach conductivities of 10^{-5} S/cm, that is, high enough for negligible ohmic losses in the transport layers. However, the LUMOs of common OLED materials are too high for cationic dyes to reach a significant doping effect and, consequently, this approach is hardly used for efficient OLEDs.

A novel and different approach based on air-stable dimers that can dissociate into strong n-dopants and may allow the doping of OLED materials has recently been presented by Guo *et al*. [77]. Although CoCp2 is air sensitive, rhodocene can dimerize giving a much more air-stable compound [78]. However, when heated in vacuum, the rhodocene dimer can dissociate, resulting in a monomer with strong doping capabilities, as they illustrate for several matrix materials. Furthermore, they show that this approach is not limited to Rh as metal atom for the dopant and also can be used for solution-processable films.

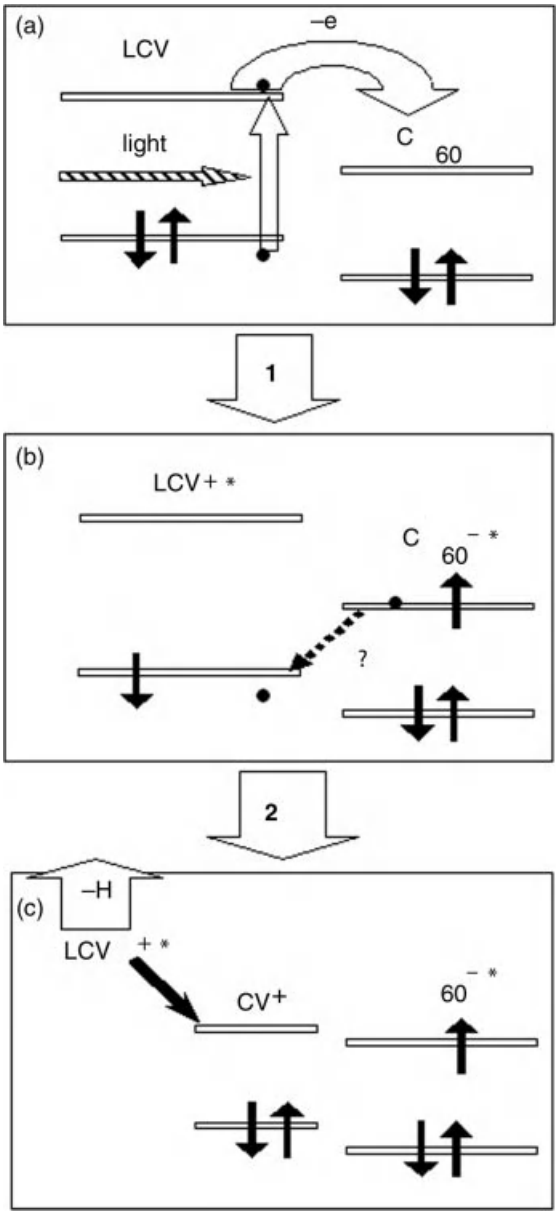

Figure 14.14 Schematic sketch of the proposed mechanism of the n-doping effect of LCV on C60. The n-doping effect becomes permanent by the stabilization of the positive charge on the dopant by hydride transfer to C60. Reprinted with permission from Li et al., Journal of Physical Chemistry B 108, 17076, 2004. Copyright 2004 American Chemical Society [19].

14.2.3
Contacts with Doped Semiconductors

Doping leads to an increase in the number of free charges in organic layers and thus to an increase in conductivity. However, in organic devices, much voltage drops across the interface between metals and organic layer. It has been tried to reduce this voltage drop by the use of metals with a work function that closely matches the transport level of the organic layer, but for electron injection this often requires highly reactive metals.

Doping can also be used to optimize injection and to reduce voltage losses at the interface to metals. The energy alignment of a doped organic layer at the metal interface has already been shown in Figure 14.7. Due to the difference in work function of the metal and the organic, the organic layer is depleted at the interface and the remaining ionized dopant molecules generate a space charge region. According to Eq. (14.2), the space charge region leads to a bending of the transport states in the organic layer toward the Fermi level. The thickness of the depletion region depends on the doping concentration (Table 14.2). If the doping concentration is high, the transport states in the organic layer are close to the Fermi level and the depletion zone is very thin. Thus, charges can easily tunnel through the very thin injection barrier at the interface to the metal and a so-called quasi-ohmic contact is formed.

This mechanism has been studied by UPS. In Figure 14.15, the energy alignment of intrinsic ZnPc and that of ZnPc doped with F_4-TCNQ are compared [14]. As expected, the Fermi level of the doped organic layer is shifted by ~0.6 V compared to the intrinsic case. The level bending is stronger in the doped case and consequently the depletion zone is reduced to less than 5 nm. Although the injection barrier is the same for both cases (1.2 eV), the depletion zone is much thinner in the doped case leading to an effective tunnelling and to a quasi-ohmic contact.

Ohmic contacts can be realized by a wide range of electrode/organic semiconductor combinations [32]. In Figure 14.16, the energy diagrams of doped MeO-TPD deposited onto Ag, ITO, and PEDOT:PSS are shown. In all cases, level bending is strong leading to a thin depletion layer and effective injection.

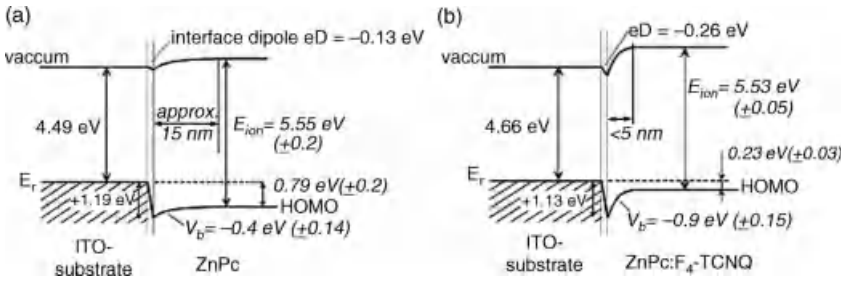

Figure 14.15 Alignment of HOMO level for undoped (a) and F_4-TCNQ-doped ZnPc (b). Doping shifts the Fermi level toward the HOMO position and leads to a stronger level bending and a thinner injection barrier.

Reprinted from Organic Electronics 2, Blochwitz et al., "Interface Electronic Structure of Organic Semiconductors with Controlled Doping Levels", 97, Copyright 2001, with permission from Elsevier [14].

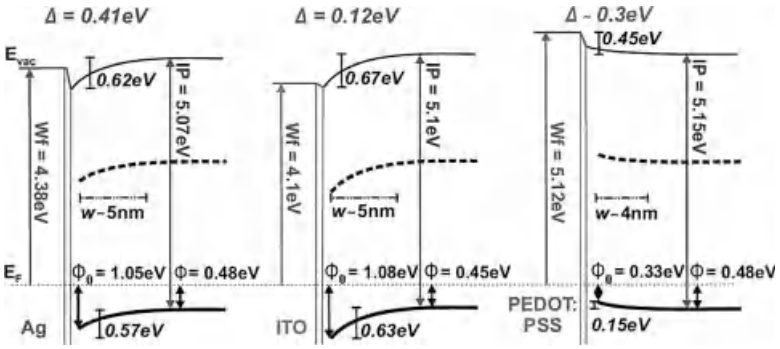

Figure 14.16 Energy diagram of doped MeO-TPD (4 mol% F_4-TCNQ) deposited onto Ag, ITO, and PEDOT:PSS. Despite the difference in work function of the electrode material, the difference between the Fermi level and the HOMO position in the bulk of the organic layer and the thickness of the depletion layer is almost constant. Reprinted with premission from Olthof et al., Journal of Applied Physics 106, 103711, 2009. Copyright 2009, American Institute of Physics [32].

14.3
Organic p–n Junctions

14.3.1
p–n-Homojunctions

The basic element of every classical semiconductor device is a diode using a semiconductor in its both p- and n-doped forms, that is, a homojunction. Thus, one would assume that the same applies to organic semiconductors. However, the challenges of p- and n-doping for organic materials described in the previous section may explain why despite of intense research in organic semiconductors for decades it took until 2005 when Harada *et al.* presented the first stable and reproducible p–n-homojunction or more precisely a p–i–n homojunction with organic materials [20]. A p–i–n structure turned out to be necessary, because given the required high doping concentration used for organic materials, an intrinsic interlayer is required to achieve the blocking behavior.

There were some earlier attempts with less well-defined systems [79, 80], however, they did not yield reproducible and stable p–n homojunction. Thus, no extensive investigations on the properties or mechanisms of these structures were possible. This also implied that there was no answer whether or not the standard Shockley model p–n-junctions [81] was suitable for describing organic p–n homojunctions. This was a particularly interesting question, because other material systems, for example, p–n junctions in amorphous silicon, were shown to deviate from the Shockley model due to recombination processes occurring at defects that are distributed in the intrinsic layer in energy and space [82, 83].

The material choice for organic p–n homojunctions is highly restricted by energy level requirements: p-type dopant molecules need to have a LUMO similar to or even below the HOMO of the matrix (see Section 14.2.1) and even more

challenging is finding suitable dopants for the n-doping (see Section 14.2.2). Given that organic molecules are typically wide-gap materials, doping the same matrix with p- and n-doping required dopants with an extraordinary low LUMO and with a very high HOMO, respectively. Thus, in many cases, heterojunctions had been chosen for devices where the realization of a p–n (hetero)junction relaxed the requirements: the materials for p- and n-regions can be chosen separately and in such a way obtain high HOMO and low LUMO, respectively, that are readily dopable with weaker dopants. However, the open-circuit voltage of such heterojunctions is limited and much lower than the open-circuit voltage of a real homojunction. In addition, having a heterojunction introduces additional effects by having two dissimilar matrix materials that one wants to avoid from a scientific point of view when characterizing junction properties.

Harada *et al.* eventually succeeded in finding a suitable combination of p- and n-dopants for an organic matrix material, and their materials and a corresponding energy scheme is shown in Figure 14.17 [20].

14.3.1.1 **Experiments**

As described in Section 14.2.1, p-doping of various organic hole transport materials including ZnPc has been shown before [12, 15] where is was possible to achieve high carrier concentrations up to $10^{20}/cm^3$. One consequence of such a high

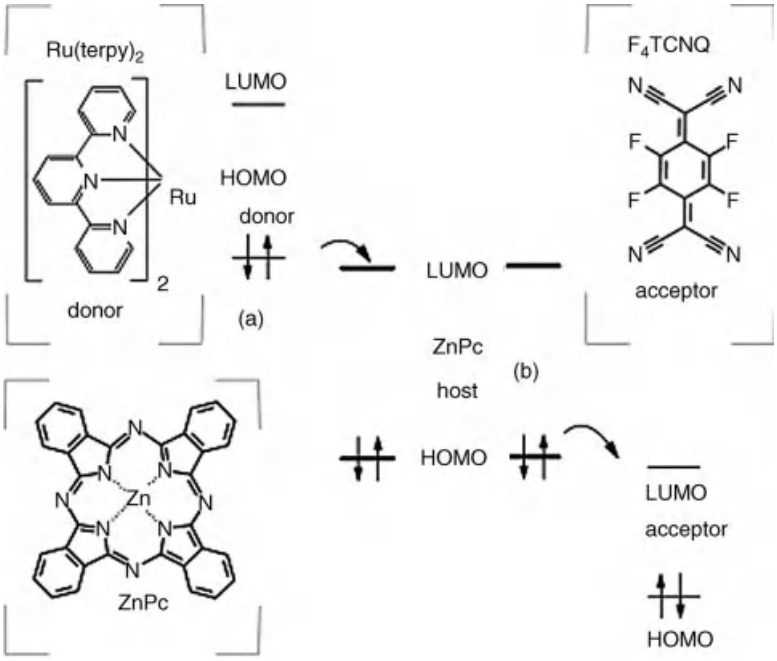

Figure 14.17 Materials and energy-level scheme of n-type (a) and p-type (b) used to create an organic p–n homojunction. (from Ref. [20]. Copyright 2005 by The American Physical Society.

Table 14.3 Details of doping ratios and layer thickness for the investigated junctions.

	Doping ratio (molar)/thickness of layer (nm)		
Junction type	**p-ZnPc**	**ZnPc**	**n-ZnPc**
p–i–n	1 : 38/15	–/30	1 : 46/40
m–i–p	–	–/30	1 : 41/100

Data from Ref. [20]. Other thicknesses of the ZnPc layer were also investigated.

number of charge carriers is that the space charge regions are typically very small and in the range of a few nanometers [14]. Putting p- and n-doped organic materials directly in contact would lead to a barrier at the p–n junction that can easily be tunnelled through and no diodelike behavior, that is, a rectification effect, would be observed.[2)] Thus, so far, instead of a direct contact between p- and n-doped layers, organic diodes require an intermediate intrinsic layer leading to a p–i–n junction. Then, good rectification ratios can be observed and will be described for a homojunction of ZnPc.

The investigated stacks of Harada *et al*. were ITO/p-ZnPc/ZnPc/n-ZnPc (p–i–n) and as comparison ITO/ZnPc/n-ZnPc (m–i–n) [20], where p-doping was achieved using F_4-TCNQ [12, 15] and n-doping using $[Ru(terpy)_2]^0$ [63]. Table 14.3 summarizes the layer structures and doping parameters of the investigated devices that are sketched as insets in Figure 14.17a. The characterization was carried out with impedance spectroscopy and current–voltage (I–V) characteristics, and the results are shown in Figure 14.17.

Figure 14.18a shows the capacitance–voltage (C–V) spectra that were used to determine the built-in potential V_{bi} for both p–i–n and m–i–n diodes. As the capacitance of the diodes is mainly controlled by the depletion layer width, it can be changed by different voltage bias, and at a voltage equal to V_{bi} the space charge region vanishes. In the experiments, the capacitance collapsed in both the cases at bias voltages of about 0.8 V, implying that both p–i–n and m–i–n stacks have a similar V_{bi} of 0.8 V at room temperature. This is considerably larger than the V_{bi} of heterojunction solar cells based on ZnPc and C60, but only about half of the gap expected from the onset of the optical absorption (≈1.6 eV) [42]. The 0.8 V were also shown to be independent of the electrode as exchanging the Al ($W_f = 4.3$ eV) of top contact with Au ($W_f = 5.0\,\text{eV} \approx W_f$ (ITO)) lead to the same results for V_{bi} as well as to similar I–V curves. Thus, V_{bi} can only be due to the difference in Fermi levels of the doped p- and n-layers of ZnPc, independent of the metal work functions. In the case of m–i–n, the similar value of V_{bi} can be explained by the fact that ITO approximately has the same work function as the pristine ZnPc [14].

2) Although this behavior is not desirable for diodes, it is successfully exploited in the recombination contact of organic tandem solar cells (see Section 14.5.2.4).

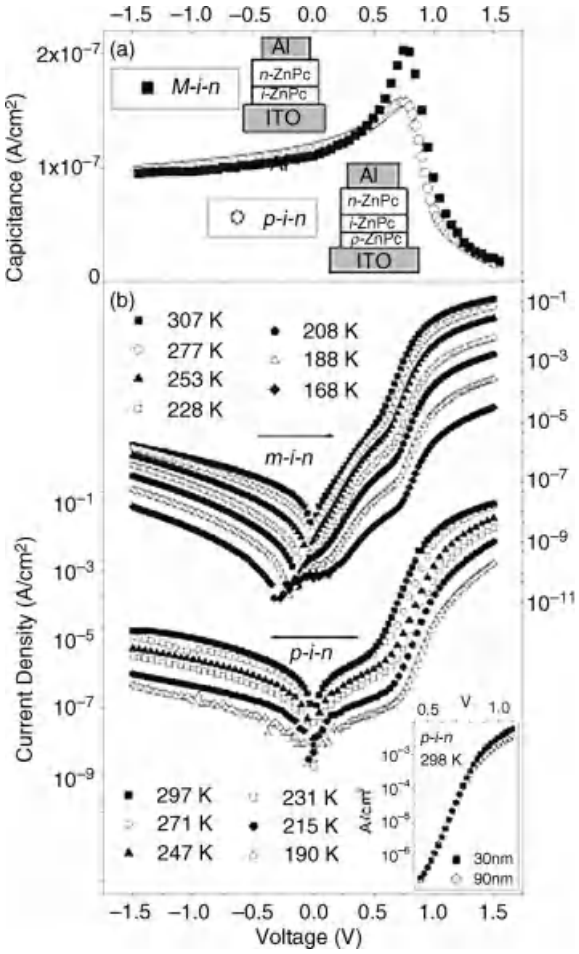

Figure 14.18 (a) Capacitance–voltage spectra of a ZnPc p–i–n homojunction measured at 3 kHz and a corresponding m–i–n junction measured at 2 kHz. The insets show the stack schematics of both devices. (b) *I–V* characteristics of the same devices at various measurement temperatures from 168 to 307 K. The junction properties are reflected in the linear part between 0.5 and 0.8 V. Below 0.5 V, the characteristics are controlled by an inevitable shunt. *Inset*: *I–V* characteristics of p–i–n samples with a ZnPc thicknesses of 30 and 90 nm at room temperature. Copyright 2005 by The American Physical Society. Taken from Ref. [20]).

The *I–V* characteristics taken at different temperatures in Figure 14.18b appear diodelike. Both types of junctions show blocking behavior in reverse bias. In forward bias at voltages below 0.5 V, shunts are dominating the curves. Between 0.5 and 0.8 V, the *I–V* characteristics are determined by the junction and show the corresponding linear increase. Above 0.8 V, the current levels off due to the series

resistance of the device. Using the standard Shockley equation for p–n junctions,

$$J = J_0\left[\exp\left(\frac{eV}{nkT}\right) - 1\right] \tag{14.4}$$

where J_0 is the dark saturation current, e is the unit charge, n is the diode ideality factor, k is the Boltzmann constant, and T is the temperature, the validity of the Shockley model for this organic homojunction was tested [20]. In Shockley theory for p–n junctions, n is the unity in the absence of recombination, as well as for thermionic emission theory and diffusion theory for Schottky diodes. J_0 and n can be fitted from the slope and the intercept of the linear part, being between approximately 0.5–0.8 V in the semilogarithmic plot. However, fitting the data of Figure 14.18 revealed that a temperature-dependent n is required, because the slope between 0.5–0.8 V only weakly depends on the temperature. n was found at room temperature to be between 1.8 and 2, a value that can also be found for inorganic semiconductors. For decreasing temperatures, however, n increases up to 4 as shown in Figure 14.19a, but such behavior has not been observed in crystalline inorganic semiconductors and is not explicably with the Shockley model for p–i–n-diodes.

Also, the Schottky model failed to describe the observed behavior. Fitting J_0 at different temperatures to estimate the Schottky barrier, a barrier of less than half of V_{bi} was calculated and both p–i–n and m–i–n showed a similar temperature dependence. Thus, Harada *et al.* proceeded to suggest their own model, a changed version of the diffusion theory, that quantitatively explain the observed behavior [20].

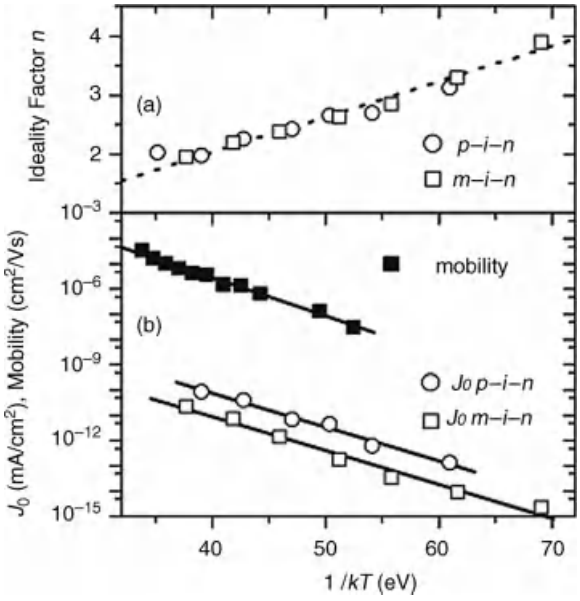

Figure 14.19 The temperature dependence of (a) the ideality factors n and (b) the saturation current J_0 of both p–i–n and m–i–n devices. In addition, the field-effect mobility of a [Ru(terpy)$_2$]^0:ZnPc (molar ratio 1 : 41) layer is given in (b) as comparison. Copyright 2005 by The American Physical Society. Taken from Ref. [20].

Their central component is that the deviations from the Einstein relation in disordered systems were taken into account. As a consequence, both the $1/T$ temperature dependence of n and the thermal activation of J_0 in the experimental data could be explained. The latter was said to be mainly determined by the temperature behavior of the mobility, because OFET measurements of *n*-ZnPc (molar doping ratio 1 : 41) yielded an activation energy of 0.34 eV being comparable to the slopes of $\ln J_0$ versus $1/T$ for both p–i–n and m–i–n stacks (Figure 14.19).

After the initial studies and a demonstration for organic solar cells [31], very recently with the availability of more materials and dopants, the concept of organic homojunctions has been investigated further. The main focus of research appears to be on OLEDs, both for solution-processed [84] and vacuum-processed devices [85, 86] with the goal to simplify the device architecture.

14.3.2
Reverse Currents in p–n-Junctions

In contrast to the forward characteristic of p–n junctions, the reverse currents are due to a zener-like tunneling behavior, which can be controlled by the doping concentration of the p- and n-layers.

The behavior of an organic p–i–n junction consisting of aluminum (100 nm) as anode, $Ir(piq)_3$ [3] doped with NDP2 as p-doped layer, a mixed layer consisting of $BAlq_2$ [4] and NPB as intrinsic layer (7 nm), $Ir(piq)_3$ doped with NDN1[5] (16 wt%, 50 nm) as n-doped layer, and aluminum (100 nm) as cathode is shown in Figure 14.20 [87]. At

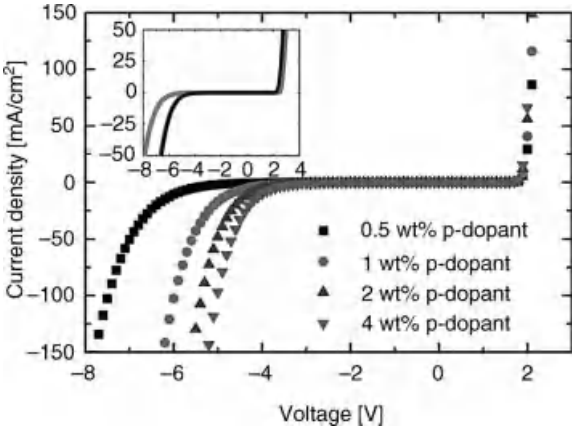

Figure 14.20 Organic zener diode based on electrically doped layers. The breakdown voltage can be precisely tuned by the doping concentration of the doped layers, whereas the forward direction is not affected by the change in doping concentration. Reprinted with permission from Kleemann et al., Nano Letters 10, 4929, 2010. Copyright 2010 American Chemical Societ [87].

3) Tris(1-phenylisoquinoline) iridium(III).
4) Aluminium-(III) bis(2-methyl-8-quninolinato)-phenylphenolate.
5) Novaled AG.

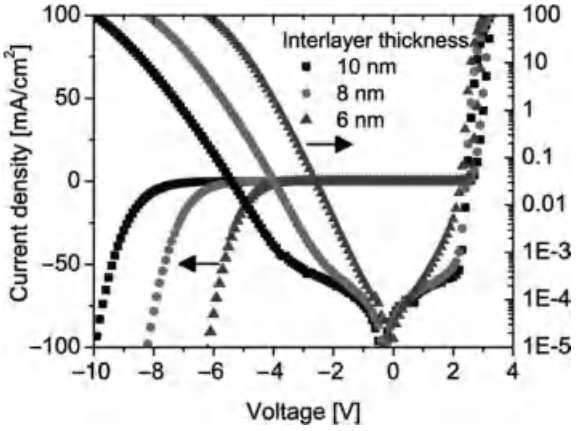

Figure 14.21 Control of the backward current by the intrinsic interlayer thickness of organic p–i–n junctions [87]. The breakthrough voltage shifts by approximately 2 V due to an increase of the interlayer thickness of 2 nm. Reprinted with permission from Kleemann et al., Nano Letters 10, 4929, 2010. Copyright 2010 American Chemical Society.

approximately 2 V, the current rises sharply. At negative voltages, the device shows a reversible breakdown. The breakdown voltage depends on the doping concentration in the p-doped layer.

The backward current can also be controlled by the thickness of the intrinsic interlayer, as shown for a device consisting of Al (100 nm), MeO-TPD doped with F_4-TCNQ (4 wt%, 50 nm), a mixed layer consisting of $BAlq_2$,[6] and NPB as intrinsic layer (6–10 nm), BPhen-doped Cs (50 nm), and Al (100 nm) in Figure 14.21. The breakdown voltage shifts by approximately 2 V for an increase of 2 nm in intrinsic interlayer thickness.

The backward current can be understood by zener tunnelling of electrons from the HOMO to the LUMO of adjacent molecules, which generates a free electron and a free hole in the n- and p-doped layers, respectively [87]. The tunnelling process depends on the electrical field inside the intrinsic layer and the depletion zone of the p–i–n junction. By increasing the intrinsic interlayer or the thickness of the depletion zone by lowering the doping concentration, the electrical field and the tunneling current are reduced.

This mechanism has many applications. First, these devices can be used as zener diodes, which are used, for example, for overvoltage protection or as selection element in passive matrix memory structures. Furthermore, such p–i–n junctions can be used as charge generation layers in stacked OLEDs. As will be shown in Section 14.4, p–i–n diodes can connect two individual OLEDs. The p–i–n diodes are biased in reverse direction and generate holes and electrons that are injected into the individual OLEDs. It can be shown that this process is very effective, that is, no voltage is lost at the charge generation unit and that the *I–V* characteristic of the stacked unit equals the characteristic of a series connection of two individual OLEDs.

6) Aluminium-(III) bis(2-methyl-8-quninolinato)-phenylphenolate.

14.4 OLEDs with Doped Transport Layers

The first observation of electroluminescence from organic single crystals stems back to the 1950s [88]. Although these early devices showed reasonable quantum efficiencies, high voltages needed to drive current through these rather thick crystals resulting in a poor power efficiency [89, 90]. The driving voltage was reduced significantly when thin and amorphous layers of organic materials were used instead of single crystals [91, 92]. A breakthrough was achieved when Tang and VanSlyke used an organic heterojunction consisting of an organic hole transporter and an organic electron transporter [11]. Tang and VanSlyke were the first to reach a luminous efficacy beyond 1 lm/W.

Since then, progress in the field has been vast. Further milestones in organic light-emitting diode development were the use of phosphorescent emitters that utilize all excitons formed electrically in the OLEDs [93] and the use of electrically doped transport layers that lead to driving voltages close to the thermodynamic limit [94]. Nowadays, monochrome OLEDs with external quantum efficiencies beyond 50% [95] and white OLEDs with power efficiencies beyond the efficiency of fluorescent tubes have been reported [40], which has led to significant interest from the industry.

OLEDs are currently used as active matrix displays by many handheld devices. Furthermore, several companies such as Sony and LG have developed large OLED TV sets. Besides display applications, another future market of OLEDs is the lighting industry. OLEDs are highly efficient, can produce high-quality white light, and are a large area light source, which sets OLEDs apart from other lighting technologies. Currently, demonstrator kits of white OLEDs are sold by Philips[7)] and OSRAM.[8)]

14.4.1 Efficiency of OLEDs

In the past, OLED research was mainly driven by the need to further improve the efficiency of OLEDs. To optimize the efficiency, all elementary processes involved in photon generation have to be understood and improved.

The working mechanism of a simple OLED is shown in Figure 14.22. A single organic layer described by its HOMO and LUMO energy is enclosed by two contacts, an anode, which often consists of the transparent conductive oxide ITO deposited onto a glass substrate, and a cathode consisting of a thin layer of metal. The contacts are depicted by their work function Φ_C and Φ_A.

Electrons and holes are injected into the cathode and anode (1), they drift toward the middle of the layer due to the applied electrical field (2), and recombine and

7) https://www.lumiblade-shop.com/.
8) http://www.osram-os.com/osram_os/EN/Press/Press_Releases/Organic_LED/ORBEOS-OLED-light-source.html.

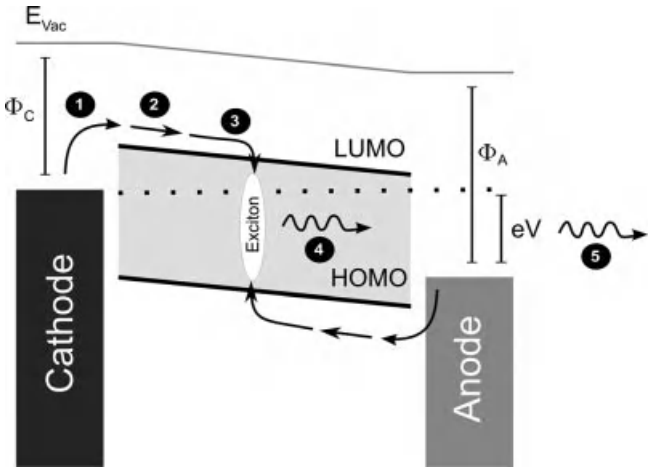

Figure 14.22 Working mechanism of a simple OLED. Charges are injected into the organic layer (1) and transported to the middle of the layer (3), where they recombine and form an exciton (3). The exciton relaxes to the ground state and emits a photon (4), which is finally extracted from the planar device (5).

form an exciton (3). To generate light, the exciton has to decay to the ground state and to emit a photon (4). However, many photons generated inside the OLED are trapped inside the planar device and only a fraction of photons are extracted (5).

14.4.1.1 External Quantum Efficiency η_q

The external quantum efficiency η_q, which is the ratio of the number of emitted photons to the number of injected charge carriers (either holes or electrons), is given by [96]

$$\eta_q = \gamma\chi \int_\lambda \eta_r(\lambda)\xi(\lambda)s_{PL}(\lambda)d\lambda \tag{14.5}$$

where γ denotes the electrical efficiency or charge balance, χ is the exciton spin factor, η_r is the efficiency of radiative decay, ξ is the outcoupling efficiency, and $s_{PL}(\lambda)$ is the normalized photoluminescence spectrum of the emitter. Both the efficiency of radiative decay and the outcoupling efficiency are wavelength dependent.

Processes (1)–(3) of Figure 14.22 are usually described by the so-called electrical efficiency or *charge carrier balance* γ, which is defined as the probability that an injected charge carrier finds a charge of opposite polarity and forms an exciton. The charge carrier balance γ is a measure for the bipolar character of the device. If the same amounts of electrons and holes are injected into the device, the charge carrier balance is unity and all charges find a charge of opposite sign and can form an exciton. If there is an excess of one type of charge carrier and either more holes or more electrons are injected into the device, not all charges contribute to exciton formation and hence light emission.

Process (4), the emission of a photon, is influenced by two factors, the *exciton spin factor* χ and the *probability of radiative decay* η_r. In OLEDs, two types of excitons are formed: singlets and triplets. Due to spin statistics, approximately three triplets per singlet are formed. In fluorescent emitters, the transition of the molecules from the triplet state to the ground state is spin forbidden, limiting the efficiency of these emitters or the exciton spin factor χ to 0.25. Using phosphorescent emitters, all excitations of the molecule are directed to the triplet state, which, due to a strong spin–orbit coupling, can relax into the ground state. Thus, both, triplets and singlets, take part in the emission process and the exciton spin factor is unity.

Even though all excitons can take part in the emission process, the radiative decay into the ground state always competes with nonradiative relaxation processes. The *efficiency of radiative decay* η_r is defined as

$$\eta_r = \frac{\Gamma_r}{\Gamma_r + \Gamma_{nr}} \tag{14.6}$$

where Γ_r and Γ_{nr} denote the rate constants of radiative and nonradiative decay of excitons. The rate of radiative decay Γ_r of the molecular emitter strongly depends on its optical environment. Due to the difference in the refractive index of the organic layers and ITO ($n \approx 1.7 - 1.8$), the glass substrate ($n \approx 1.5$), and air, light is reflected at the interface between organic layers and glass and between the glass substrate and air (see Figure 14.23). Furthermore, as photons are also reflected at the metallic cathode, the OLED essentially forms an optical cavity. Depending on the strength of the cavity, the radiative rate is altered by the factor $F(\lambda)$ (Purcell effect):

$$\Gamma_r = F(\lambda)\Gamma_{r,inf} \tag{14.7}$$

where $\Gamma_{r,inf}$ is the radiative rate in an infinite medium, that is, if all cavity effects can be neglected. The efficiency of radiative decay can therefore be refined to

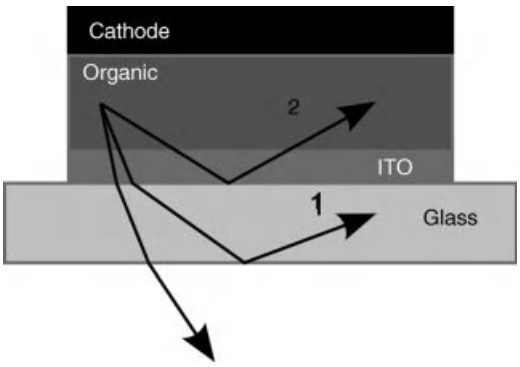

Figure 14.23 Due to the difference in refractive index of the organic layers including ITO, glass, and air, total reflection occurs at the interfaces. Light generated inside the OLED cavity is trapped in organic (2) and glass (1) modes.

incorporate cavity effects:

$$\eta_r = \frac{F(\lambda)\Gamma_{r,inf}}{F(\lambda)\Gamma_{r,inf} + \Gamma_{nr}} = \frac{qF(\lambda)}{q(F(\lambda) - 1) + 1} \tag{14.8}$$

where q denotes the efficiency of radiative decay in an infinite medium.

Finally, the *outcoupling efficiency* $\xi(\lambda)$ quantifies process (5) of Figure 14.22. Even though a photon has finally been generated, it can be trapped inside the OLED cavity and is hence lost for light generation. Photons that are reflected at the interface between organic layers and glass are feeding waveguided modes, the so-called organic modes (arrow 2 in Figure 14.23), and the light reflected at the interface between glass and air is lost in the so-called glass modes (arrow 1 in Figure 14.23). The probability that a photon, which was generated inside the OLED, is extracted from the cavity is given by the outcoupling efficiency $\xi(\lambda)$. Simplifying calculations show that for a normal planar device, the outcoupling efficiency is in the range of 20% [97].

14.4.1.2 Power Efficiency or Luminous Efficacy

The external quantum efficiency alone is not sufficient to characterize the efficiency of an OLED, as it only accounts for the number of injected charge carriers and the number of emitted photons, but does not take into account their energy. An energy balance is given by the power efficiency or luminous efficacy η_p:

$$\eta_p = \eta_q \frac{\overline{h\nu}}{eV} \tag{14.9}$$

Here, $\overline{h\nu}$ denotes the average energy of an emitted photon and eV is the energy of the injected charge carriers. For display and lighting applications, the emitted light output is often weighted by the sensitivity of the human eye. Thus, the power efficiency is given in photometrical quantities (lm/W).

14.4.2 p–i–n OLEDs

The OLED presented in Figure 14.22 is simple, but for highly efficient OLEDs, at least five different layers are needed (Figure 14.24): an electron and a hole transport layer (ETL and HTL), which are electrically doped, an emission layer (EML), where excitons are generated, and finally two charge-blocking layers (electron-blocking layer, EBL, and hole-blocking layer, HBL), which confine all charges inside the emission layer.

In this so-called p–i–n setup, both the quantum and the power efficiency are optimized [47, 96]. The *driving voltage* of the OLED is reduced by the doped transport layers. Doped transport layers improve the charge carrier injection at the contacts. As discussed in Section 14.2.3, a very thin depletion zone is generated at the contact to the electrodes, which can be easily tunnelled through. Thus, an ohmic contact is established, which avoids a large voltage drop at the contacts. Furthermore, due to the high conductivity of the doped transport layer, charges are efficiently

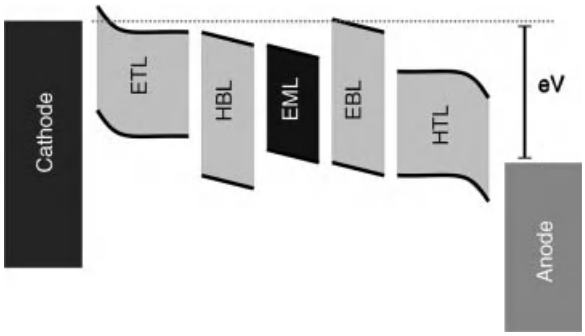

Figure 14.24 Five layer p–i–n OLED. The OLED consists of electron and hole transport layers (ETL and HTL), electron- and hole-blocking layers (EBL and HBL), and an emission layer (EML).

transported toward the emission layer, which results in low driving voltages and high power efficiencies.

The *charge carrier balance* γ is optimized by the electron-blocking layers. Once an electron or a hole has been injected into the emission layer, it is confined in the EML by a large offset in the transport level of the blocking layer. Furthermore, the blocking layers separate the EML from the doped transport layers and therefore avoid quenching of excitons.

The *exciton spin factor* χ and the *efficiency of radiative decay* η_r are optimized by the choice of the emission layer. First, to maximize the exciton spin factor, phosphorescent emitters have to be used. As these emitters usually suffer from the so-called concentration quenching if used as bulk layer [98, 99], they are doped at low concentrations into a suitable matrix. To optimize the efficiency of radiative decay, emitters with high photoluminescence efficiency have to be chosen. However, as discussed above, the efficiency of radiative decay of the emitters will also be influenced by the optical cavity of the OLED.

Doping allows to optimize the optical cavity of the OLED and, therefore, improves the *outcoupling efficiency* ξ. To obtain efficient emission of light from the OLED, the resonance, that is, the thickness of the OLED, has to be tuned to the wavelength of the emitted light and the emitters have to be placed into the antinode of the optical field inside the OLED. Doping provides sufficient free charges in the doped layer to reach a conductivity above 10^{-4}S/cm, which is much higher than the conductivity of the undoped emission layers. Thus, almost all voltage drops across the thin emission layers and not across the charge transport layers, and the thickness of the charge transport layers can be used to optimize the optical cavity without introducing additional voltage losses. An example of an optimization of OLED efficiency by variation of the electron transport layer thickness will be discussed in Section 14.4.2.1. Besides the optimization of the stack design of the OLEDs, there are many other techniques to optimize the outcoupling efficiency [100]. The most successful techniques are scattering layers inside the OLED, microlens foils attached to the glass substrate, or the use of index-matched glass substrates. Some of these techniques are discussed in Sections 14.4.2.1 and 14.4.2.2.

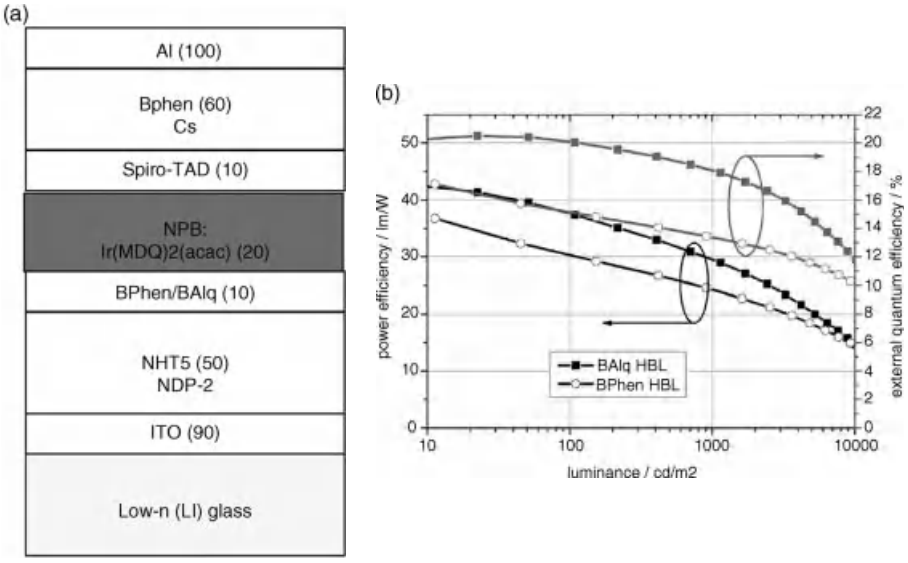

Figure 14.25 Design of a highly efficient orange/red OLED (a). The external quantum efficiency reaches 20% if the material BAlq is used as hole blocker (b) [101]. Reprinted with permission from Meerheim et al, Journal of Applied Physics 104, 14510, 2008. Copyright 2008, American Institute of Physics.

14.4.2.1 Highly Efficient Monochrome Devices

Bottom Emission OLEDs Monochrome OLEDs with an external quantum efficiency above 20% are well established nowadays for all monochrome colors [37, 101, 102]. The design of a highly efficient red-orange OLED is shown in Figure 14.25a. It consists of 90 nm ITO as anode, 50 nm NHT5 doped with NDP2,[9] 10 nm Spiro-TAD as EBL, 20 nm of NPB doped with the red-orange emitter Ir(MDQ)2(acac) (10%), either BPhen or BAlq as HBL (10 nm), BPhen doped with Cs as ETL (60 nm), and Al (100 nm) as cathode [101].

The device shows the expected orange-red emission. The external quantum efficiency and power efficiency of the two samples with varying hole-blocking layers are shown in Figure 14.25b. The OLED using BAlq is clearly superior to BPhen as blocking layer, which can be explained by a more efficient injection of electrons into the emission layer [101].

The device using BAlq as blocking layer reaches an external quantum efficiency of 20% at a luminance of 100 cd/m^2. Considering that these results were obtained without the use of outcoupling enhancement methods and that only one out of five photons is coupled out of these devices, the internal quantum efficiency (IQE), that is, the efficiency of photon generation inside the OLED, is already very high. This

9) Novaled AG.

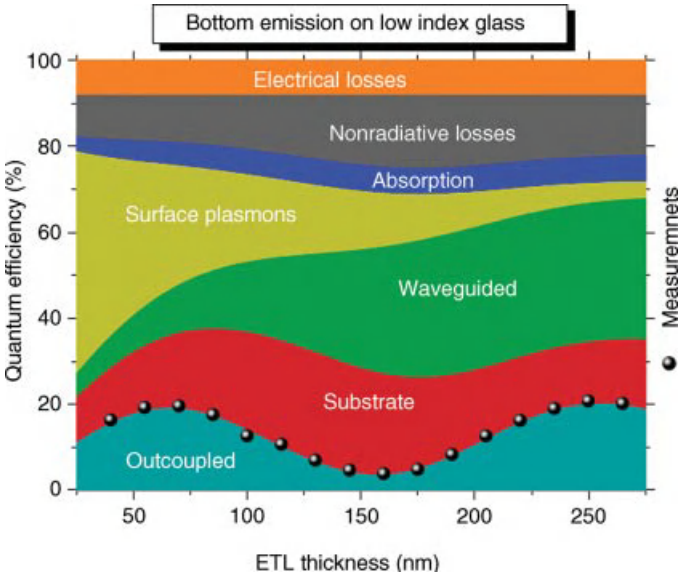

Figure 14.26 Influence of the OLED cavity on the external quantum efficiency of an OLED. The different loss mechanisms in a red OLED are quantified. Experimentally obtained external quantum efficiencies are shown as black dots [95]. Reprinted with permission from Meerheim et al. Applied Physics Letters 97, 253305, 2010. Copyright 2010 American Institute of Physics.

shows that the largest improvements in efficiency of OLEDs can be reached by an improvement of the outcoupling efficiency.

Doping is a key technology to study cavity and outcoupling effects as it allows to vary the thickness of the transport layers and to tune the cavity. The measured and calculated quantum efficiency of a series of similar orange/red OLEDs with varying ETL thickness is shown in Figure 14.26. The red OLED consists of 60 nm NHT-5 doped with 4% NDP-2[10] as HTL, 10 nm of Spiro-TAD as EBL, 20 nm of NPB doped with the red phosphorescent emitter Ir(MDQ)2(acac) as EML, 10 nm of BAlq as HBL, and BPhen doped with Cs as ETL. The thickness of the ETL has been varied from 25 to 275 nm [95]. The measured external quantum efficiency for varying thickness of the electron transport layer is shown by black dots. The plot shows two distinct peaks corresponding to the first and the second resonance condition of the cavity. At these peaks, the emission layer is positioned at the maximum of the optical field in the device, which results in an optimal outcoupling efficiency.

Apart from the measured external quantum efficiency, the different optical loss channels inside the OLED are quantified. The calculation is based on an optical model of the OLED, which treats the emitting molecules as point dipoles to calculate the radiative molecular transitions [103]. The electromagnetic field inside the OLED is calculated by a transfer matrix approach. The electrical behavior of the device is taken into account by the electrical efficiency or charge carrier balance γ.

10) Novaled AG.

In the OLED, energy is lost due to electrical losses (i.e., a low γ), nonradiative losses (i.e., a low η_r), absorption in the organic layers, coupling to surface plasmons located at the metallic cathode, coupling to waveguided (organic) modes, and finally due to light that is trapped in the substrate (cf. Figure 14.26). A large share of the losses in the first-order devices is due to a strong coupling of the emission to surface plasmons. If the distance between emitter and cathode is increased by increasing the ETL thickness, coupling to surface plasmons decreases. However, the decrease in surface plasmons is almost completely compensated by an increase in coupling to waveguided modes, so that the overall increase in external quantum efficiency is small.

The calculations shown in Figure 14.26 show that a large increase in quantum efficiency is possible if all waveguided and substrate modes are extracted from the device. One method to extract these modes is the use of an index-matched glass substrate ($n = 1.78$), which avoids total reflections at the interface ITO/glass. To extract all light out of the substrate, a half lense is attached to the substrate.

The resulting external quantum efficiencies and the distribution of loss channels are shown in Figure 14.27. All waveguided and substrate modes are avoided. In the second-order device, the external quantum efficiency is as high as 54% (104 lm/W), that is, more than every second electron injected into the device generates a photon, which is extracted out of the device.

In summary, monochrome OLEDs with an extremely high internal quantum efficiency of 20% can be designed. To increase the efficiency further, the outcoupling efficiency of the OLED has to be improved. If the distance between the emitter and

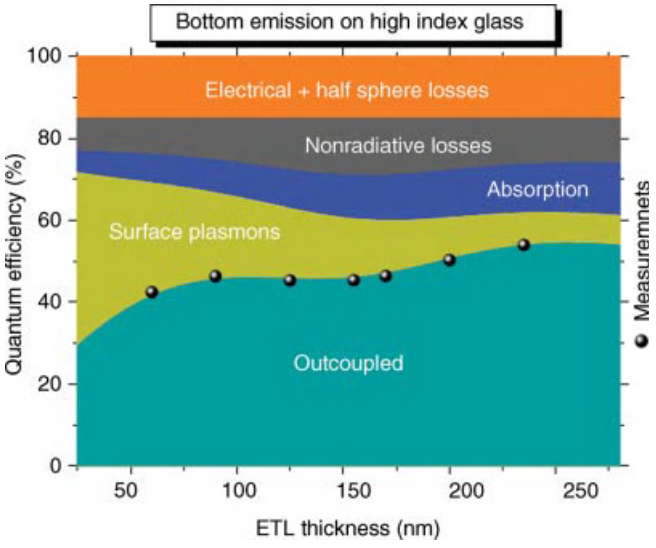

Figure 14.27 Simulated distribution of loss channels in a red OLED on high-index glass. A half lense is used to extract all substrate modes. The measured external quantum efficiency of these devices is shown by black dots [95]. Reprinted with permission from Meerheim et al. Applied Physics Letters 97, 253305, 2010. Copyright 2010 American Institute of Physics.

the cathode is increased by the thicker ETL layers, the coupling to plasmons is reduced. Furthermore, by high-index glass substrates and an index-matched half-lense, the waveguided modes can be avoided, resulting in an external quantum efficiency beyond 50%.

Top Emission OLEDs All OLEDs discussed so far are bottom emission devices, that is, light is emitted through a transparent anode and a glass substrate. However, there is a great need to use low-cost and flexible substrates, which would allow a roll-to-roll production and a significant reduction in OLED cost. One alternative for thick glass substrates are flexible metal foils, which also provide a sufficient barrier to humidity and oxygen, so that high OLED lifetimes can be reached.

However, these metal substrates are opaque and light emission is possible only through a thin, semitransparent metal-top electrode. These so-called top emission OLEDs show an even more enhanced microcavity, which is also observable in the calculated external quantum efficiency for varying ETL thickness, as shown in Figure 14.28. The device consists of 36 nm MeO-TPD doped with 4% NDP-2[11] as HTL, 10 nm of NPB as EBL, 20 nm of NPB doped with the red phosphorescent emitter Ir(MDQ)2(acac) as EML, 10 nm of BPhen as HBL, and BPhen doped with Cs as ETL. As for the bottom devices, the thickness of the ETL has been varied from 25 to 275 nm [95].

Figure 14.28a shows the external quantum efficiency and luminous efficiency for the first-order device (ETL thickness of 64 nm). For these devices, a maximum external quantum efficiency of 29% is reached, which exceeds the efficiency of bottom emission devices without outcoupling enhancement [104].

The measured external quantum efficiency and the calculated loss channels for varying ETL thickness are shown in Figure 14.28b. In comparison to bottom-emitting devices, the two peaks at the first- and second-order resonances are sharper, which can be explained by a stronger microcavity of top-emitting OLEDs. Furthermore, the first-order devices are always more efficient than the second-order devices, which is due to a stronger Purcell effect.

In summary, top-emitting devices can be highly competitive with bottom-emitting devices, at least for monochrome devices. However, for white OLEDs, the strong cavity and the need to precisely adjust the thickness of the cavity to the emission wavelength of the emitter make the design of a broadly emitting white top emission OLED challenging. Thus, the discussion will be focused on bottom-emitting white OLEDs in the following section.

14.4.2.2 p–i–n Devices: White OLEDs

To generate white light, the emission of several emitters has to be mixed. The most common approach to combine the emission of several emitters is to stack distinct emission layers for all colors.

11) Novaled AG.

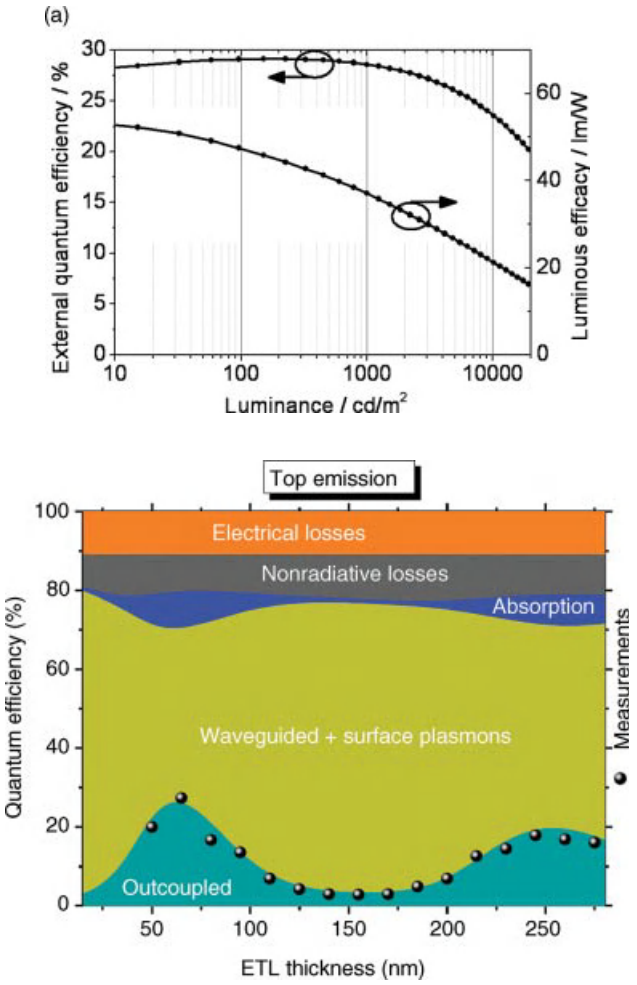

Figure 14.28 (a) External quantum efficiency of a red top-emitting OLED. An external quantum efficiency of 29% is reached. Reprinted with permission from Hofmann et al. Applied Physics Letters 97, 253308, 2010. Copyright 2010 American Institute of Physics. [104] b) Distribution of loss channels in the top-emitting OLED. Measured external quantum efficiencies are marked by black dots. Reprinted with permission from Meerheim et al. Applied Physics Letters 97, 253305, 2010. Copyright 2010 American Institute of Physics [95].

Figure 14.29 shows the design of a highly efficient white OLED. The device is based on the p–i–n concept. It consists of an ITO anode (on high-index glass, $n_{high} = 1.78$ or low-index glass $n_{low} = 1.51$, devices HI and LI), MeO-TPD doped with NDP-2[12] (4 mol%, 60 nm for the OLEDs on low n glass and 45 nm on high n glass) as HTL, NPB (10 nm) as EBL, red, blue, and green emission layers, TPBi (10 nm) as hole-blocking layer, BPhen doped with Cs as ETL, and Ag as cathode.

12) Novaled AG.

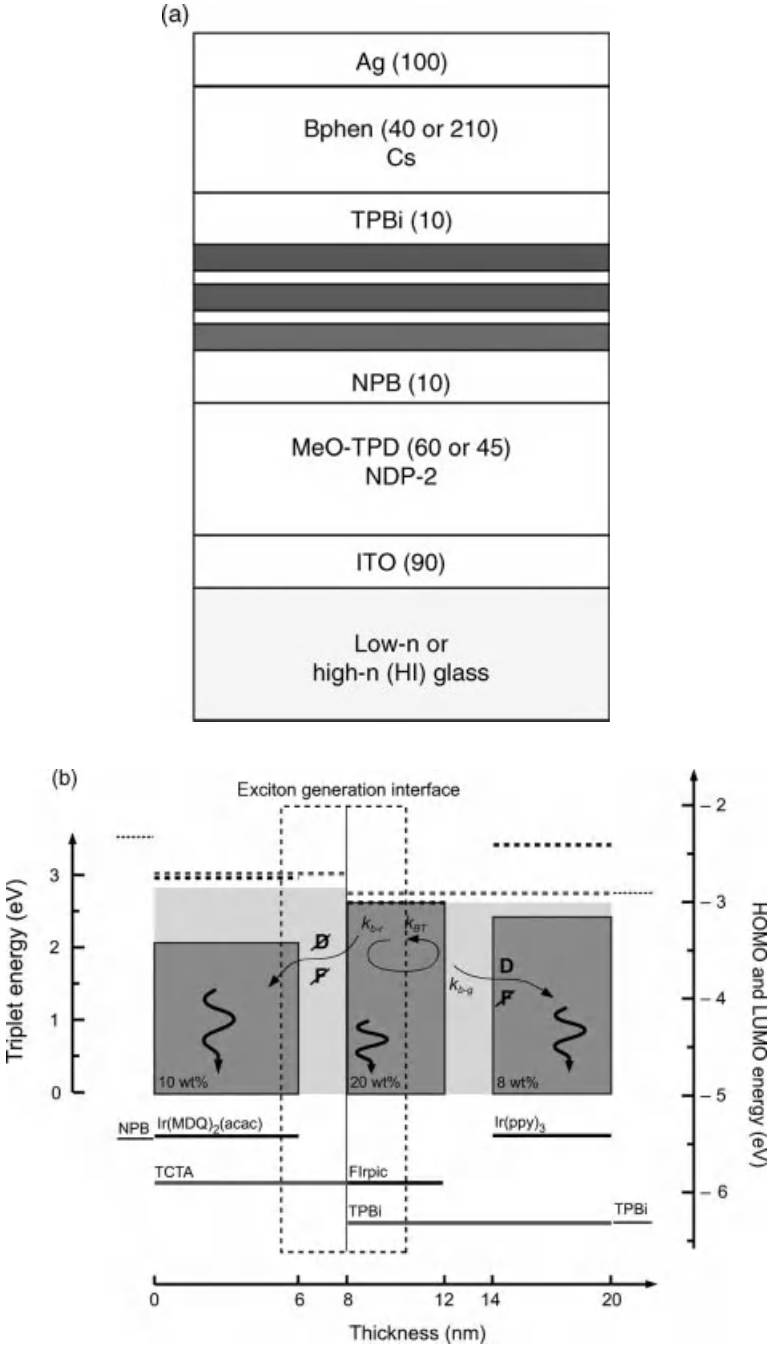

Figure 14.29 Highly efficient white OLED based on the p–i–n concept. (a) Green, blue, and red emission are generated in separate layers. (b) The design of the emission layer is shown [40, 105]. Reprinted with permission from Luessem, Reineke et al., Proceedings of the SPIE 7617, 761712, 2010.

Two thickness values for the ETL layer are used (40 and 210 nm) for the first- and second-order cavities (denoted as HI-1 or LI for the first maximum and HI-2 and HI-3 for the second maximum) [40].

The emission layers are designed to ensure a distribution of excitons on all monochrome emitters (Figure 14.29b) leading to white emission. The emission layer consists of two matrix materials: TCTA, which is preferentially hole transporting, and TPBi, which is preferentially electron transporting. In such a double-emission layer (DEML) [37], the exciton generation zone is located at the TPBi/TCTA interface. It extends across the part of the TCTA matrix, which is doped by a red emitter Ir(MDQ2(acac) (10 wt%) and across the FIrpic-doped region of TPBi (20 wt %). Thus, either red or blue excitons are generated. As the triplet energy of FIrpic is in resonance with the triplet energy of TPBi, excitons are not confined to the FIrpic molecule and can diffuse toward the green emitter Ir(ppy)3 (8 wt%). The overall distribution of excitons can be tuned by thin undoped layers between the doped layers.

The efficiency of these OLEDs is shown in Figure 14.30. The same variations of layer structure as for the monochrome devices in Section 14.4.2.1 have been done,

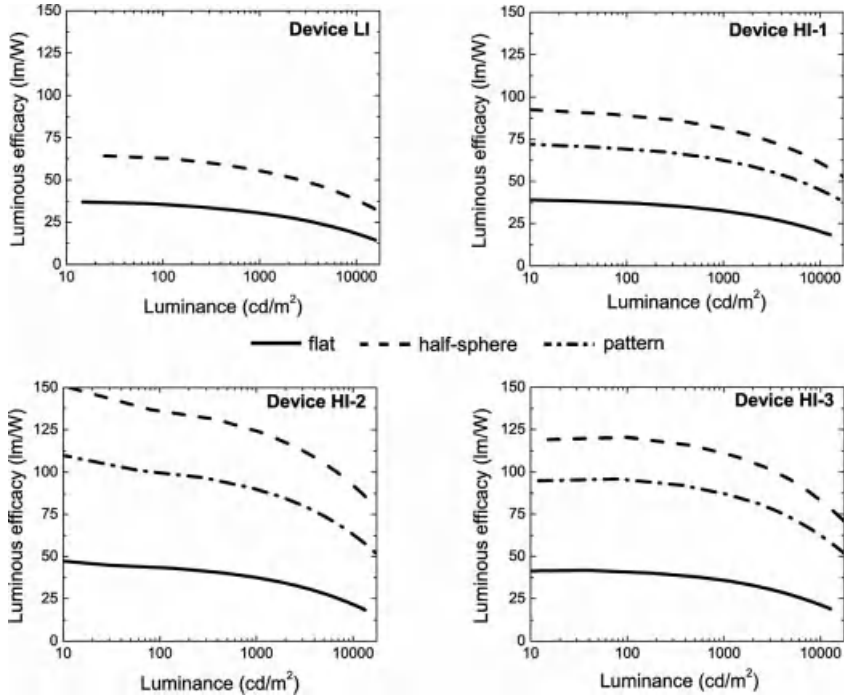

Figure 14.30 Efficiency of the white OLED as shown in Figure 14.29 Devices are prepared on high-index (HI) and low-index (LI) glass. The ETL thickness has been varied to obtain OLEDs in the first (LI and HI-1) and second order (HI-2 and HI-3). The efficiency is measured without any further outcoupling enhancement methods, with a large half-lense and with a pyramidal high-index structure (pattern) [40, 105]. Reprinted with permission from Luessem, Reineke et al., Proceedings of the SPIE 7617, 761712, 2010.

that is, the thickness of the ETL has been varied to obtain the first- (LI and HI-1) and second-order devices (HI-2 and HI-3). Furthermore, devices were prepared on low-index (LI) and on high-index glass (HI). In Figure 14.30, the efficacy measured without any outcoupling enhancement is shown by continuous lines, the dotted line is obtained by applying a structure of small pyramids cut into a sheet of high-index glass applied to the substrate to enhance the outcoupling efficiency, and the dashed line is obtained by applying a half lense to the substrate.

As already shown for monochrome devices, the use of high-index glass leads to a significant improvement in the luminous efficacy (e.g., compare the efficacy of the devices LI and HI-1), if either the pyramidal outcoupling structure or the half-sphere is used.

Furthermore, the second-order devices are generally more efficient. Less emission is lost to plasmonic modes and waveguided modes are suppressed due to the use of high-index glass. A luminous efficacy as high as 90 lm/W at 1000 cd/m^2 is obtained using the pyramidal outcoupling structure, measured in the second maximum of the cavity of the OLED structure (HI-2).

These experiments show that it is possible to very efficiently generate white light. However, one drawback of these devices is the color point (0.41, 0.49), which contains too less blue emission and which is off the Planckian locus. The color could be enhanced by a deep blue phosphorescent emitter. However, even FIrpic is very unstable, which leads to low lifetimes of these white OLEDs. Deep blue emitters such as FIr6 show a comparable efficiency at smaller wavelengths compared to FIrpic, but are even less stable. Hence, there is a dire need to find alternatives to the all-phosphorescent approach, which avoid the use of unstable blue phosphorescent emitters, but still keep the potential of 100% internal quantum efficiency. One alternative is the triplet harvesting approach [106–112].

14.4.2.3 Triplet Harvesting OLEDs

In the so-called hybrid white OLEDs, emission from a fluorescent blue emitter is mixed with emission from phosphorescent red and green emitters. Triplets generated on the fluorescent blue emitter are usually lost, as the transition to the ground state is nonradiative. However, if the triplet level of the fluorescent blue emitter exceeds the triplet level of the red and green phosphorescent emitter, triplets can be transferred to the phosphorescent emitter and decay radiatively. Thus, all excitons are utilized and it is possible to reach high efficiencies, although a fluorescent blue emitter is used.

A possible blue emitter is 4P-NPD [107–109]. 4P-NPD has a triplet level of 2.3 eV [108] and allows to transfer triplets to a red emitter. The design of a red/blue triplet harvesting OLED is shown in Figure 14.31a [113]. As 4P-NPD preferentially conducts holes, excitons are generated at the interface between the hole-blocking layer (BPhen) and the 4P-NPD layer. Starting from this interface, excitons start to diffuse toward the 4P-NPD layer doped with the red emitter Ir(MDQ)2(acac).

Figure 14.31b shows the emission spectra of the device for varying thickness of the undoped 4P-NPD layer at a constant current. It can be seen that the blue emission remains constant for different 4P-NPD layer thickness, whereas the intensity

(a)

material	thickness
ITO	
MeO-TPD:NDP2	20 nm
Spiro-TAD	10 nm
4P-NPD:	10 nm
$Ir(MDQ)_2acac$	8 wt%
4P-NPD	0–30 nm
BPhen	10 nm
BPhen:Cs	30 nm
Al	

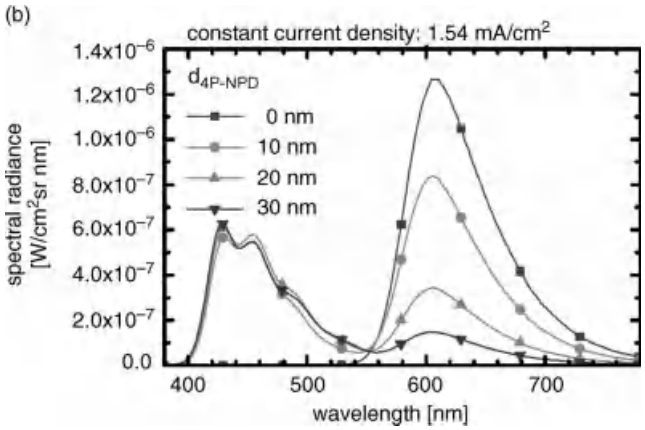

Figure 14.31 Triplet harvesting red/blue OLED. Excitons are generated at the interface between the hole-blocking layer BPhen and the blue emitter 4P-NPD and diffuse toward the 4P-NPD layer doped with the red emitter Ir(MDQ)2(acac) (a). Depending on the thickness of the 4P-NPD layer, more or less triplets reach the red emitter, which is visible in the spectrum in part (b). As the singlet diffusion length is shorter compared to the triplet diffusion length, all singlets decay on the blue 4P-NPD layer and the blue emission does not depend on the thickness of the intrinsic 4P-NPD layer. Reprinted with permission from Rosenow et al., Journal of Applied Physics 108, 113113, 2010. Copyright 2010, American Institute of Physics [113].

of the red emission increases for decreasing 4P-NPD layer thickness. This behavior can be understood by the different diffusion lengths of singlets and triplets. Due to their longer diffusion length, triplets can reach the doped 4P-NPD layer and recombine on the red emitter, whereas the singlets decay on the blue 4P-NPD. Therefore, depending on the thickness of the undoped 4P-NPD layer, more or less triplets are harvested on the red emitter. At a thickness of 5 nm, an optimum is

reached: almost all triplets are harvested on the red emitter, but blue singlets are not quenched by the triplet emitter. A quantum efficiency of 16% is reached at 1000 cd/m^2.

However, the triplet level of 4P-NPD is not sufficient to harvest triplets on green phosphorescent emitters. To fill the spectral gap in Figure 14.31, a second yellow/greenish emitting OLED can be stacked onto the red/blue triplet harvesting OLED [113]. The design of such a stacked OLED is shown in Figure 14.32a. The emission layer of the bottom OLED consists of the matrix TCTA doped with the green emitter Ir(ppy)3 and the yellow emitter Ir(dhfpy)2(acac). The top OLED is the same OLED as shown in Figure 14.31a. The two individual OLEDs are connected by a doped p–n junction consisting of BPhen:Cs, a thin layer of Al, and MeO-TPD:NDP2. In this p–n junction, which is biased in reverse direction, electrons and holes are generated (cf. Section 14.3.2), which are injected into the upper and lower OLEDs.

The spectrum of the OLED is shown in Figure 14.32b. A broad spectrum with color coordinates close to the warm white point A (x, y) = (0.462, 0.429), CRI = 80) is obtained. The power efficiency is presented in Figure 14.32c. As for all other OLEDs discussed so far, the highest efficiency is reached for OLEDs on high-index glass with a half-lense applied to the substrate (90 lm/W). For the array of pyramids cut into a high-index glass, an efficiency of 47.5 lm/W is reached.

14.4.2.4 **Conclusion**

Doping of transport layers helps to design OLEDs with high efficiencies. The driving voltage is reduced and the thickness of the OLED cavity can be adjusted to reach a high outcoupling efficiency. Efficiencies reached by monochrome and white OLEDs are already exceeding 20% without outcoupling enhancement methods, which indicates that the internal quantum efficiency is impressively high. Hence, the largest improvements in efficiency can be expected by an optimization of the outcoupling efficiency ξ, which is currently a topic of intense research.

14.5
Organic Solar Cells with Doped Transport Layers

Directly harnessing the energy from the sun will play an important role in creating a sustainable energy supply system and organic solar cells have the potential to become a low-cost, large area photovoltaic technology. Thus, they have received increasing attention in recent years and have been developed toward market introduction. Some of their main advantages are that OSC can be produced using large area coating technologies at low temperatures on flexible plastic substrates for the typically 100–200 nm thin organic films. Consequently, both energy and material consumption are low during production and require less than 1 g organic semiconductor per square meter.

First experiments on the photovoltaic effect in organic semiconductors began in the 1950s with vacuum-deposited small molecules [114] and the first major

(a)

material	thickness
ITO	90
MeO-TPD:NDP2	40: 2wt%
Spiro-TAD	10
4P-NPD: $Ir(MDQ)_2acac$	5: 5 wt%
4P-NPD	5
BPhen	10
BPhen:Cs	90
Al	0.5
MeO-TPD:NDP2	65: 2 wt%
Spiro-TAD	10
TCTA: $Ir(ppy)_3$: $Ir(dhfpy)_2acac$	10: 8 wt% 1 wt%
TPBi	10
Bphen:Cs	75
Al	100

(b)

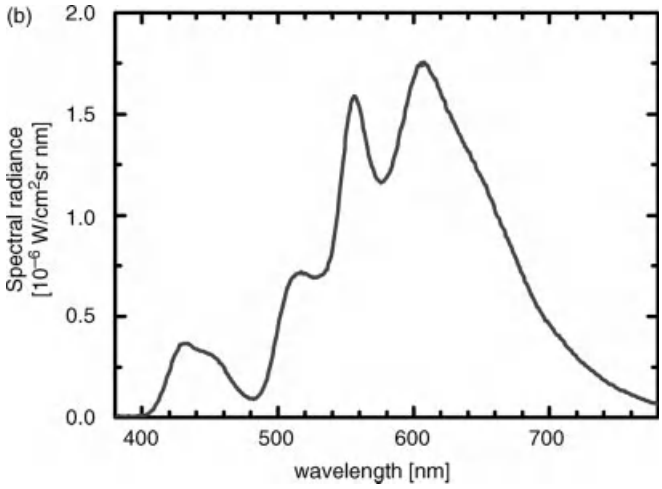

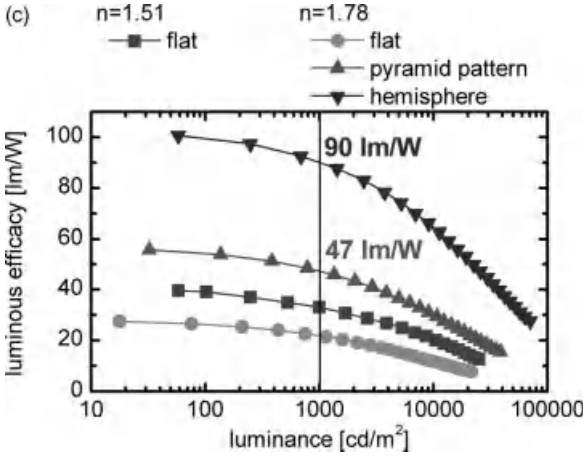

Figure 14.32 (a) Stacked white OLED based on the triplet-harvesting concept. The device consists of a green/yellow and a red/blue triplet-harvesting unit. The two OLEDs are connected by a charge generating p–n junction. (b) The emission spectrum of the device is shown. The spectrum is close to color point A. (c) Using a high-index hemisphere and high-index substrates, an efficiency of 90 lm/W has been reached. Reprinted with permission from Rosenow et al., Journal of Applied Physics 108, 113113, 2010. Copyright 2010, American Institute of Physics [113].

breakthrough was published in 1986 by Tang [10]. He introduced the concept of the planar heterojunction, that is, using two different kinds of small molecules with dissimilar energy levels on top of each other, to facilitate the separation of the photogenerated exciton that is strongly bound. This strongly bound exciton is the main difference between OSC and standard inorganic solar cells made from, for example, silicon where light absorption instantaneously creates free charge carriers under normal operating conditions. In organic molecules, optical excitations are typically bound with energies of several 100 meV, leading to Frenkel excitons. The required electric field to separate them is with more than 10^6 V/cm and thus much higher that what is obtained in a working OSC. Tang's heterojunction concept provided a solution, because the energetic difference of electron donor and electron acceptor molecules at the heterojunction creates an interface for efficient exciton separation. The basic stack structure of Tang's OSC and a conceptual illustration of the heterojunction is shown in Figure 14.33.

In addition to their strong binding energy, the diffusion length of photogenerated excitons is typically on the order of only 10 nm. Thus, only excitons that are generated within their diffusion length of the heterojunction can contribute to the generation of free charge carriers. This significantly limits the photovoltaic active volume and leads to far too little absorption for efficient light harvesting even for organic materials with absorption coefficients exceeding 10^5/cm. In 1991, Hiramoto *et al*. presented a solution to this problem by coevaporating donor and

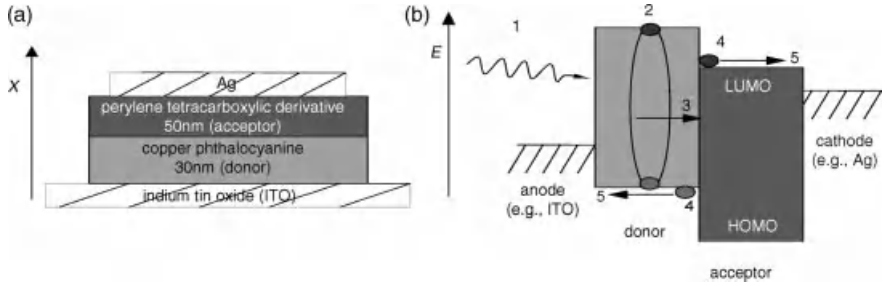

Figure 14.33 Basic layer sequence of Tang's organic solar cell (a) and a conceptual illustration of the exciton separation at the interface between two organic materials with different energy levels (b). (1) light exposure, (2) light absorption and exciton generation, (3) exciton diffusion, ideally to the heterojunction, (4) exciton separation, and (5) charge carrier separation and extraction at opposite electrodes.

acceptor molecules, that is, creating a bulk heterojunction by mixing of donor and acceptor into one layer with phase separation on the order of exciton diffusion length [115]. This second major breakthrough showed that an efficient exciton dissociation through the complete absorbing layer is possible. If suitable energy levels of donor and acceptor are chosen, this approach works very well. However, both the detailed processes and limits for free charge carrier generation at the heterojunction as well as for establishing percolation paths to the respective electrode and maintaining good transport of charge carriers in the mixed layer have remained a challenge and focus of much research both on the synthesis and processing sides in recent years [116–118].

Today, all efficient OSC are based on the bulk heterojunction concept and the power conversion efficiencies starting with around 1% for Tang's device have steadily been improved since then using various strategies like better tailoring of the organic semiconductors or optimizing the stack. Current OSC efficiencies have reached about 9% on application-relevant sizes of more than 1 cm^2 [119]. There are different approaches for making organic solar cells and they are typically categorized by their processing technology: (a) physical vapor deposition of the organic layers in vacuum, that is, the method with which most of the initial research has been carried out [7, 76, 114, 120], and (b) processing the organic layers from solution by, for example, spin-coating or printing, which is the process that most of the current OSCs are being made with [121, 122]. In solution processing, both soluble small molecules and polymers can be used as organic semiconductors. Vacuum processing limits the suitable organic semiconductors to small molecules that can be thermally evaporated without being damaged by the elevated temperatures. Since doping of organic semiconductors is most extensively being used for the latter approach, the focus will be on vacuum processing. However, in recent years, the benefits of doping have led to an increased research effort to find ways for realizing efficient doping in solution-processed devices.

14.5.1 Solar Cell Characteristics

Before discussing the application and benefits of doping in OSC, the standard measurements and parameters will be introduced. The main figures of merit for solar cells in general are depicted in Figure 14.34. Much of the OSC research is driven by attempts to increase the power conversion efficiency η, that is, the ratio of maximum power P_{MPP} delivered by the OSC and the power of the incoming light P_{ill}. The extractable power is given by

$$P_{MPP} = V_{MPP} I_{MPP} = V_{oc} I_{sc} FF \tag{14.10}$$

where V_{MPP} and I_{MPP} are the voltage and current, respectively, at the maximum power point (MPP), V_{oc} is the open-circuit voltage, I_{sc} is the short circuit current, and FF is the fill factor. Thus, the efficiency is defined as

$$\eta = \frac{V_{MPP} I_{MPP}}{P_{ill}} = \frac{V_{oc} I_{sc} FF}{P_{ill}} \tag{14.11}$$

As η of a particular solar cell very much depends on the illumination spectrum, international standards have been defined for characterizing solar cells and measuring the device efficiency [123]. These should also be followed for OSC, but special care is necessary, because up to now no organic reference diodes are available and the spectral responses of the OSC and the reference diode used to determine P_{ill} differ very much [124]. Figure 14.34 illustrates this difference in spectral response $SR(\lambda)$ that is defined as

$$SR(\lambda) = \frac{q\lambda}{hc} EQE(\lambda) \tag{14.12}$$

where q is the elementary charge, λ is the wavelength, h is the Planck's constant, c is the speed of light in vacuum, and $EQE(\lambda)$ is the external quantum efficiency, that is, the ratio between extracted electron–hole pairs and incoming photons at λ [124]. Having determined the absorption of the solar cell and the EQE, the internal quantum efficiency gives the ratio between extracted electron–hole pairs and absorbed photons and can be calculated as

$$EQE(\lambda) = \frac{EQE(\lambda)}{\eta_a(\lambda)} \tag{14.13}$$

where $\eta_a(\lambda)$ is the absorption of the solar cell. Here, either the absorption of the complete stack or the absorption only in the photovoltaic active layers can be used [125, 126].

Knowing the spectrum of the illumination source and the standard reference solar spectrum AM1.5g as well as the spectral response of reference diode and

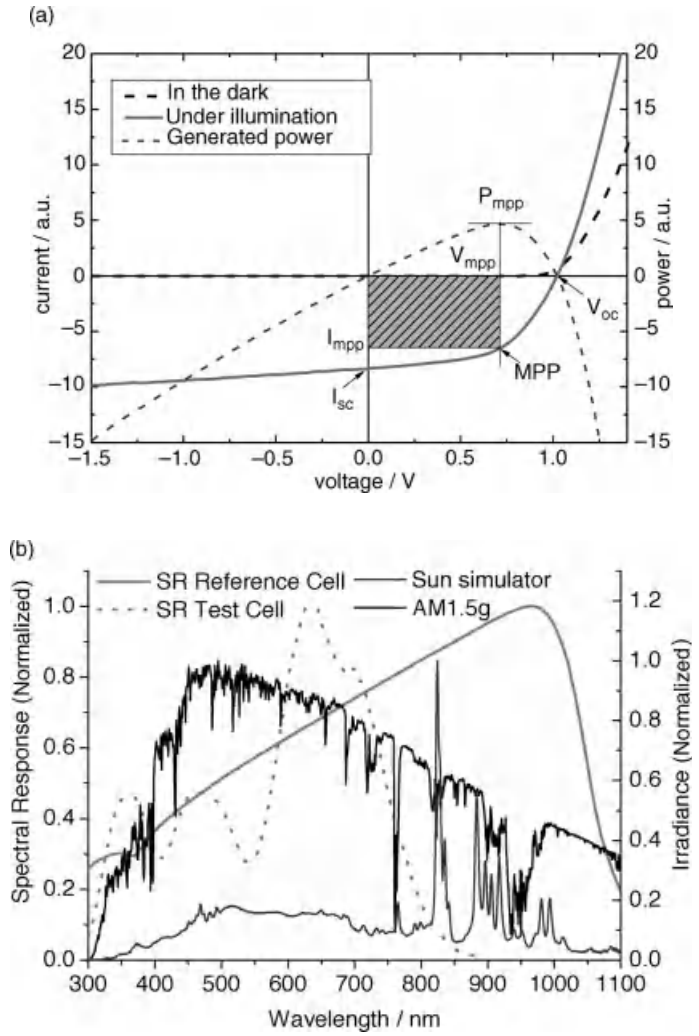

Figure 14.34 (a) A typical current–voltage curve of a solar cell in the dark (black dashed) and under illumination (red) with the main parameters and the generated power (blue dashed). (b) A comparison between the spectral response of a typical Si reference diode (pink solid) and an OSC (red dotted) having four times fluorinated zinc phthalocyanine and C60 as photovoltaic active layer. In addition, the differences in the reference illumination spectrum AM1.5g (black solid) and a typical solar simulator (300 W Xe high-pressure lamp with AM1.5 filter, blue solid) are shown.

OSC, the efficiency can be calculated correctly using a mismatch factor for the light intensity [124, 127]. Generally, additional great care has to be taken when measuring the active area of the OSC, because the typical size for laboratory OSC is only a few square millimeter that makes them prone to measurement errors [128]. For independent verification and additional certification of efficiencies, several institutions and companies around the world offer their service [119].

14.5.2
Organic p–i–n Solar Cells

To further improve the efficiency, all processes from photon absorption to the extraction of charge carriers have to be better understood and optimized. Concerning the device architecture, vacuum processing and controlled doping of transport layers have several advantages. In the early days, vacuum deposition was the simplest way of making thin films of organic semiconductors, because these materials were generally hard to process. Furthermore, vacuum processing allows an excellent control of the thickness of the deposited layers and easy fabrication of multilayer structures. This control is also key during coevaporation of doped layers and D-A heterojunctions of two materials where fine adjustments of the composition ratio and even concentration gradients can easily be realized.

14.5.2.1 **Brief History of Vacuum-Deposited Organic Solar Cells**

Before the discovery of the heterojunction concept, organic solar cells were basically Schottky diodes in which an organic semiconductor was sandwiched between two electrodes [114]. Due to the strongly bound photogenerated excitons, charge separation inside the organic layer was very ineffective, and the metal contacts were efficient exciton quenchers. Consequently, power conversion efficiencies were well below 1%. These issues were solved by Tang and published in 1986 [10]. His bilayer solar cells were made of a metal–phthalocyanine as electron donor and a perylene derivative as electron acceptor (Figure 14.33). Being stacked on top of each other, the planar heterojunction offered an interface for efficient exciton separation, leading to efficiencies of about 1%. However, this approach still has one major drawback: due to an exciton diffusion length that is typically on the order of nanometers to a few tens of nanometers, only excitons generated within the exciton diffusion length from the heterojunction can reach the separating interface. Consequently, the effective photovoltaic active volume is very limited and despite absorption coefficients exceeding 10^5/cm only a small fraction of the incident light can be converted into free charge carriers.

Hiramoto *et al.* were the first to introduce a new concept to OSC: given the limited volume of efficient exciton separation in a planar heterojunction, they adapted the concept of tandem devices, well known from inorganic solar cells, to OSC (Figure 14.35) [129]. Using gold nanoparticles in the recombination zone between

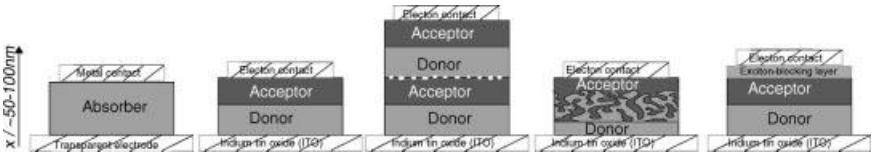

Figure 14.35 Illustration of various OSC stacks. *Left to right*: A pre-Tang single-layer device, Tang's planar heterojunction device concept, a tandem stack using metal clusters as recombination centers, Hiramoto's planar–bulk–planar heterojunction stack, and a stack using an exciton-blocking layer.

both subcells, they showed that this concept is feasible for OSC and can lead to improved device performances. Today, having a better understanding of the underlying device physics and a systematic tailoring of new materials, tandem devices currently have the champion efficiencies of OSC [130].

However, this would not have been achieved without the bulk heterojunction concept that is often called the second breakthrough in organic solar cells, that is, mixing of donor and acceptor into one layer. Again in 1991, Hiramoto *et al.* coevaporated a perylene tetracarboxylic derivative and metal-free phthalocyanine into a mixed layer surrounded by pristine layers, thus publishing the first bulk heterojunction [115].[13] In this general concept, the phase separation between the donor and the acceptor can be made to be on the order of the exciton diffusion length. Thus, excitons can be separated throughout the complete layer. However, the challenge is to establish percolation paths to the respective electrode and maintain good transport of charge carriers through the mixed layer. This challenge still remains today.

Efficiencies remained at about 1%, but starting from about 2000 onward, significant progress in the understanding of OSCs and improvements in device efficiency were made. The number of available organic semiconductors has considerably grown since then, stacks have been optimized, and various strategies followed to investigate the OSC fundamentals and to create a viable product.

In 2000, Rostalski and Meissner [131] used the fullerene C60 as electron acceptor in a bulk heterojunction with a stack similar to the one used by Hiramoto *et al.* in 1990. Fullerenes have very strong electron-accepting character and had been shown to be an excellent acceptor material in solution-processed organic solar cells with polymers as donor [132]. Up to now, they have remained the main choice of materials for the acceptor due to its unique properties.

Progress in the stack design was shown by Peumans *et al.* in 2003 who introduced a dedicated thin exciton-blocking layer of bathocuproine (BCP) between the acceptor layer and the cathode, thus efficiently blocking excitons and preventing damage to the active layer during metal deposition and leading to power conversion efficiencies of about 3.6% [7]. With rising efficiencies, blocking excitons from being quenched at the contacts has become a very relevant step.

An important milestone in the development of efficient OSC was finding an efficient way to tune the morphology of the bulk heterojunction. This technique was first discovered for solution-processed OSC [133, 134] and later adapted for vacuum-processed solar cells [135, 136]. The method for extrinsically tuning the morphology is heating the substrate during the film formation, allowing molecules to better diffuse and rearrange on the surface. Overall, this has become a key component in realizing the most efficient OSC in vacuum.

The concept of deliberate molecular doping of organic materials, the main focus of this section, has also found its way in organic solar cells. Pfeiffer *et al.* [41] used

13) Sometimes the used stack is denoted as "'p–i–n"' stack in literature, because it consists of a pristine donor layer/mixed donor:acceptor layer/pristine acceptor layer. However, it does not deliberately use doped layers and thus is not a p–i–n stack in the general sense.

F4-TCQN (Figure 14.3) as strong electron acceptor for p-doping. Doping on the p-side was later complemented with doping on the n-side, leading to the p–i–n concept for OSC, that uses both p- and n-doped layers surrounding the photovoltaic active layer [75]. The advantages of this concept will be the focus of the remaining part of this section.

14.5.2.2 **Advantages of Molecular Doping in OSC**

The doping fundamentals were already described in Section 14.2 and doped wide-gap transport layers can extensively be used with similar advantages, that is, control of Fermi levels, quasi-ohmic contacts to electrodes, for OSC as for OLEDs.

Tang's solar cell of 1986 had a planar heterojunction for efficient exciton separation. However, given the strongly bound nature of the photogenerated excitons and their short diffusion length, most of the excitons in the absorbing volume could not reach the heterojunction and contribute to the photocurrent. This is illustrated in Figure 14.36a. Reducing the layer thickness to the photovoltaic active volume generally does not work because of the short circuits and recombination at the organic–metal interfaces. Thus, the parasitic absorption in the volume that cannot contribute to the photocurrent is a severe limitation.

Using doped wide-gap transport layers, the donor–acceptor layer thickness can be reduced to the photovoltaic active volume without risking short circuits and recombination at the organic–metal interfaces. The corresponding layer structure for a typical p–i–n stack is illustrated in Figure 14.36b. It consists of a transparent hole contact, a p-doped wide-gap hole transport layer, a photovoltaic active layer, a n-doped wide-gap electron transport layer, and an electron contact. This stack is not only advantageous for planar heterojunctions but is also used for bulk heterojunctions or a combination of both.

By replacing the absorbing but not the photovoltaic active volume of Tang's solar cell with wide-gap materials, the parasitic absorption is significantly reduced. Ideally, light absorption then takes place only in the photovoltaic active layers that are positioned such that photon absorption and internal quantum efficiency are

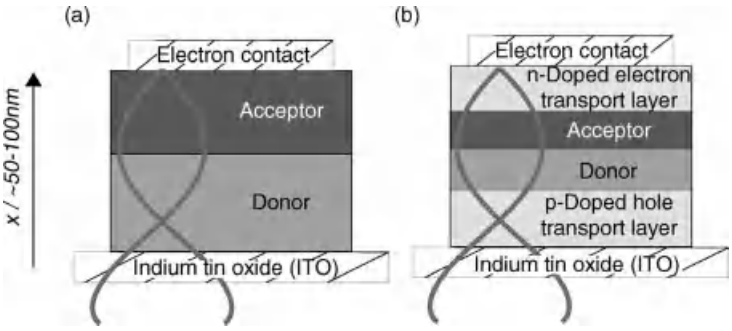

Figure 14.36 Comparison of Tang's solar cell (1986) and a p–i–n solar cell structure with doped wide-gap transport materials (2004), including a schematic illustration of the optical interference pattern.

maximized. If the wide-gap materials are doped, as described in Section 14.2, the layers can reach conductivities of more than 10^{-5} S/cm, that is, values will allow an extension of the layer thickness to 100 nm and more without introducing noticeable ohmic losses. Consequently, such layers not only serve as efficient charge transport layers but can also be used as optical spacers of an optical device optimization. Second, doping commonly ensures ohmic contact between electrodes and organic layers [14] and, for example, ITO can be used as either hole or electron contact [125]. Finally, by choosing suitable wide-gap materials, the contacts can be made semipermeable: excitons are blocked from reaching the typically quenching electrode interface and charge carriers can only reach their contact, ideally without a barrier or a loss in free energy. The energy-level diagram of a p–i–n solar cell structure is shown in Figure 14.37 and is close to the generic and ideal solar cell structure proposed by Würfel [137].

Overall, the p–i–n concepts allow many degrees of freedom in optimizing the absorption of the active layers, choosing the contact materials, as well as the order of the layers. In recent years, the p–i–n concept has been proven to be a versatile concept for investigation of both the fundamental processes in organic solar cells and a solid base for device optimization. In the meantime, other OSC approaches,

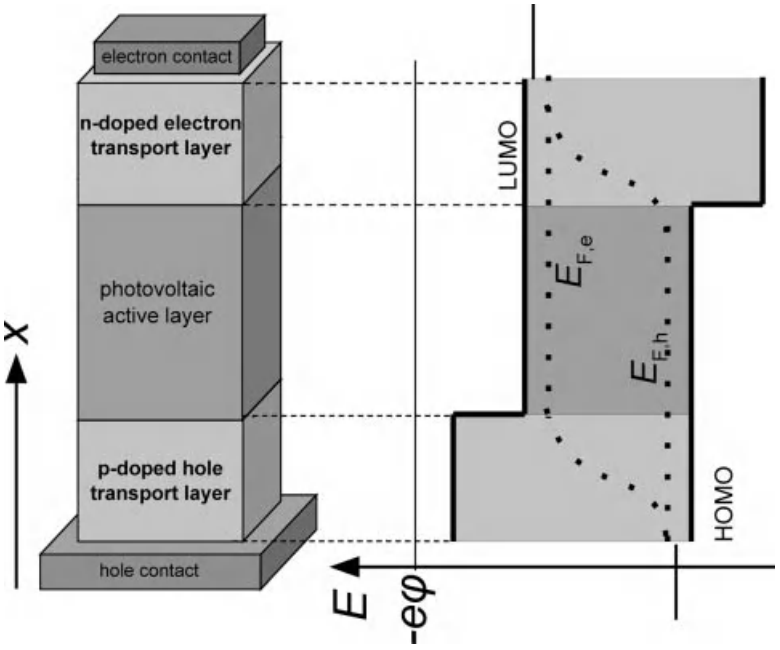

Figure 14.37 The stack of p–i–n OSC schematically shown in spatial coordinates (top) and a simple energy diagram (bottom). The photovoltaic active layer can be a planar heterojunction, a bulk heterojunction, or a combination of both. Both for electron and hole transport layers, wide-gap materials are used leading to an energetic offset to the photovoltaic active layer.

particularly those based on solution processing, also started looking closer into doping of organic materials, thus trying to realize a full p–i–n concept.

14.5.2.3 Optical Optimization

There are various ways of optimizing OSC, and one important way is putting the absorbing layers where they can absorb most. For the nontransparent OSC, the reflecting metal electrode creates an interference pattern with a node at the organic–metal interface. Thus, the light intensity close to the metal contact is low. Since the useful thickness of the absorbing layers is limited either by the exciton diffusion length in the case of a planar heterojunction of charge carrier transport to the electrodes in the case of a bulk heterojunction, placing the photovoltaic active layer close to the metal contact will limit the achievable photocurrent. Often, a thin transparent buffer layer of BCP or bathophenanthroline (BPhen) is used to shift the absorbing layers closer to the maximum of the optical interference pattern [44, 138]. Although these layers have advantages over putting the metal contact directly into contact with the absorbing heterojunction, the thickness of this kind of buffer layer is typically limited to ≤ 15 nm due to low conductivity and charge carrier mobility [7]. Here, doped transport layers again have significant advantages, because doping leads to a high conductivity allowing spacer layer thicknesses of more than 100 nm without causing significant transport losses.

Figure 14.38 shows a p–i–n stack where the thickness d_{ETL} of the n-doped electron transport layer (ETL), using 2,3,8,9,14,15-hexachloro-5,6,11,12,17,18-hexaazatrinaphthylene (HATNA-Cl_6), is varied between 0 and 140 nm [139]. HATNA-Cl_6

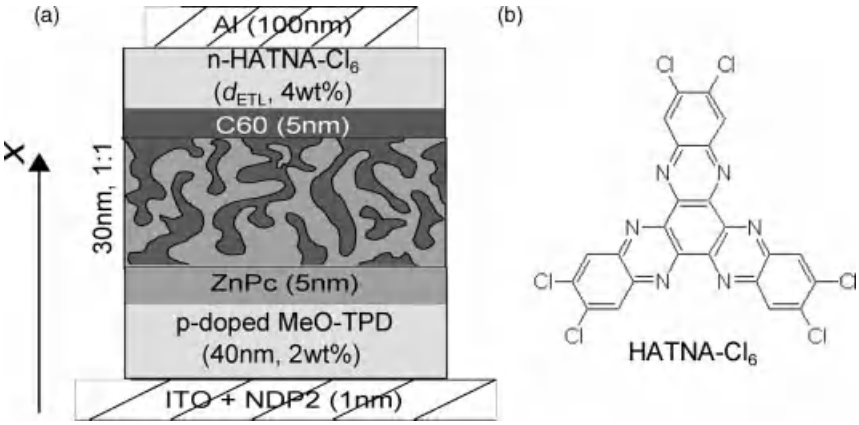

Figure 14.38 (a) Simple test stack to illustrate the advantages of doped transport layers for optical optimization of the stack. The stack uses a combination of a planar and bulk heterojunction (1 : 1 volume ratio ZnPc:C60) as photovoltaic active volume. (b) The structure of the electron transport material 2,3,8,9,14,15-hexachloro-5,6,11,12,17,18-hexaazatrinaphthylene (HATNA-Cl_6). p- and n-Doping are realized using NDP2 and NDN1 (both Novaled AG), respectively. d_{ETL} of the n-doped HATNA-Cl_6 is systematically varied between 0 and 140 nm to move the photovoltaic active volume with respect to the Al mirror and thus into the interference pattern forming in the stack under illumination.

has an optical gap of 2.7 eV, that is, it is mostly transparent in the visible region of the sun spectrum, and an electron affinity (EA) of 4.07 eV [140]. Thus, the value closely matches the EA of C60 (4.0 eV) [141], the standard electron acceptor, and therefore allows a barrier-free extraction of electrons from C60. Doping HATNA-Cl_6 with a few wt% of NDN1, a commercial dopant by Novaled AG, leads to a conductivity on the order of 10^{-3} S/cm, a value high enough for realizing even thick electron-transporting layers.

Optical simulations were carried out using a numerical algorithm based on the transfer matrix formalism and Poynting vector calculation (Furno, M. (2010) Osolemio. Unpublished.) [142]. The optical constants of the organic materials were determined using transmission and reflection measurements [143], but other methods like ellipsometry could also be used. From the calculated absorption in each photovoltaic active layer (here ZnPc/ZnPc:C60/C60), it is possible to calculate the maximum possible current that can be extracted from the solar cell by assuming an IQE of unity. Figure 14.39 shows the comparison of j_{sc} determined in experiments and simulations [139]. As the solar cells were measured with a solar simulator, its illumination spectrum was used as input for the optical simulation for a better comparability to the measurements and as the optical simulations are based on a series of assumptions, for example, IQE = 1 at 0 V, the absolute values of j_{sc} will be different, most likely lower.

Depending on where the photovoltaic active layers are positioned, a variation in j_{sc} of a factor of more than 4 is observed. This is a direct result of shifting the absorbing layers with respect to the optical interference pattern. The optimum j_{sc} is found at d_{ETL} of 50 nm. Increasing d_{ETL} to about 140 nm puts the absorbing layer into the first interference minimum and thus much fewer photons can be absorbed. The small variations in FF between the maximum and the minimum illustrate the good transport through the doped electron transport layer. V_{oc} varies slightly due to changes in the splitting of the quasi-Fermi levels, because the absorption in the photovoltaic active layers changes with varying d_{ETL}. Consequently, η is mainly determined by the variations in j_{sc}.

These results show that doped transparent transport layers, here in the example of n-doped HATNA-Cl_6, are a key to optical optimization of OSC. This principle applies not only to vacuum-processed OSC but also to all kinds of OSC as long as the well-reflecting electrodes are used and the film thickness is below the coherence length of the sunlight. Also, for semitransparent OSC, the optical optimization and the use of window layers are crucial to achieving efficient devices [144]. However, the effects of thin-film optics are generally less dominant in solution-processed OSC, because the thickness of the absorbing layer often exceeds 200 nm.

14.5.2.4 **Tandem Devices**

With certified single-heterojunction OSC, efficiencies of above 8% have been reported in press releases and literature [145, 146]. Still under discussion is how high the efficiencies of single-heterojunction devices can be pushed; however, estimates based on theoretical considerations put the limit to between 10 and 11%, depending on the assumptions [147, 148]. However, these values are just about the

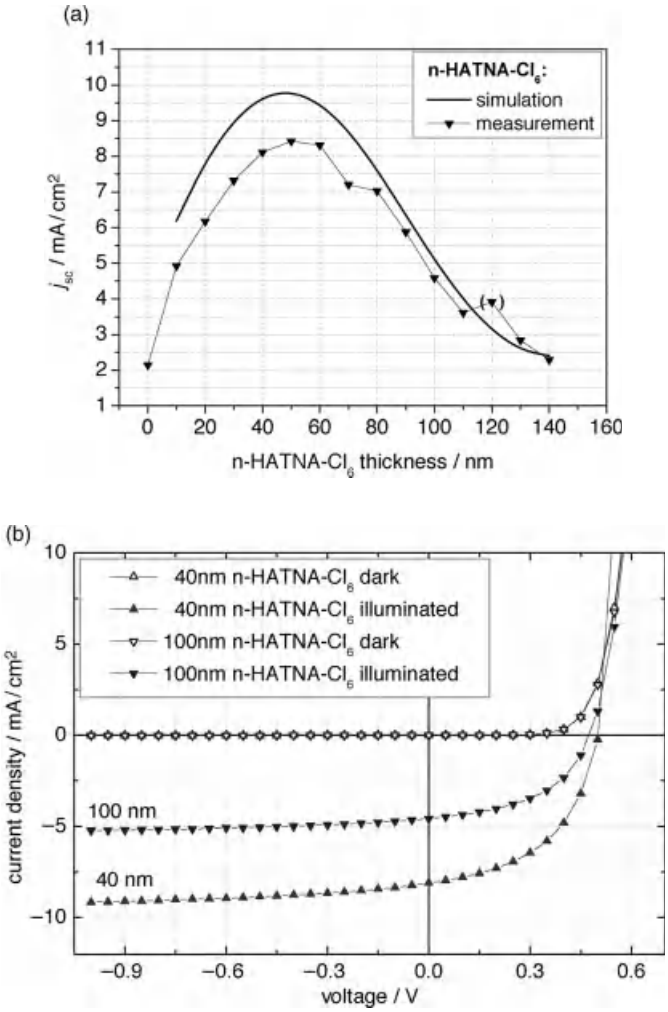

Figure 14.39 Short circuit current density j_{sc} from experiment and optical simulations assuming an IQE of unity using the sun simulator spectrum for varying thicknesses d_{ETL} of the n-doped transport layer HATNA-Cl_6 (a) and selected *I–V* curves to demonstrate the photovoltaic performance (b). The value at 120 nm is the only outlier in the j_{sc} measurements. The corresponding efficiencies for 40 and 100 nm *n*-HATNA-Cl_6 are 2.1 and 1.1%.

supposedly required values for large-scale applications. Consequently, tandem concepts involving the stacking of single-junction solar cells as shown in Figure 14.40 are used to exceed the 10–11% limits. Their efficiencies are estimated to potentially reach about 15% [149, 150], because transmission and thermalization losses, two major loss mechanisms, can in principle be reduced. Thus, much research has been devoted in recent years to realizing tandem OSC [151] that are currently leading the device efficiencies both for solution-processed and vacuum-processed OSC

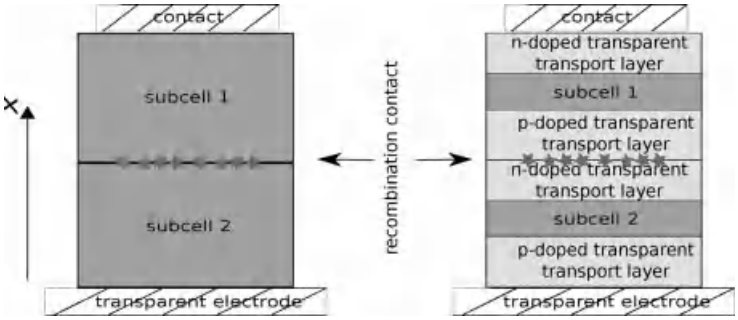

Figure 14.40 Stack of a generic two-terminal tandem stack consisting of two subcells connected by a recombination contact and a p–i–n tandem stack.

[152, 153]. Here, the ease and control of multilayer deposition in vacuum as well as the doping prove to be big advantages of this approach. In addition to complementary absorbers, efficient tandem devices require a well working and versatile recombination contact and current matching between the subcells, both of which can be well realized based on the p–i–n single concept, as shown in Figure 14.40. There are various concepts for tandem devices [151] and in the following the focus will be on the two-terminal design.

Recombination Contact One central component of any two-terminal tandem is a versatile recombination contact that leads to a recombination of electrons from one subcell and holes from the other subcell without loss in free energy at all applied voltages. Hiramoto *et al.* have already showed in the first OSC tandem publication in 1990 that metal clusters can be used as recombination centers between donor and acceptor. This approach is still used in many vacuum-deposited tandem OSC, because it can prevent the splitting of the quasi-Fermi levels at this interface between the subcells. However, it has some drawbacks, as it is not a generic solution and thus does not work for any material combination of donor and acceptor. In addition, optical optimization would be difficult, because donor and acceptor are directly next to each other. Other approaches, like the use of absorbing molecules that have the right energy levels for the recombination contact [154] or the incorporation of metal oxide interlayers [155, 156], have similar drawbacks.

Here, doping of organic layers was found to be very beneficial, as evaporating highly doped electron and hole transport layers on top of each other allows the creation of a well-working recombination contact [157, 158]. This approach has the advantage that it leads to a complete addition of the open-circuit voltages of the subcells in most cases and a high FF in tandem devices. By shifting the recombination contact into transport layers, it can be used independent of the absorber materials, that is, it provides a generic solution for the recombination contact. Furthermore, the use of wide-gap materials ensures high transparency, separates the recombination areas of charge carriers and excitons, and can be created using the same processes as for the rest of the tandem stack. Figure 14.41 shows

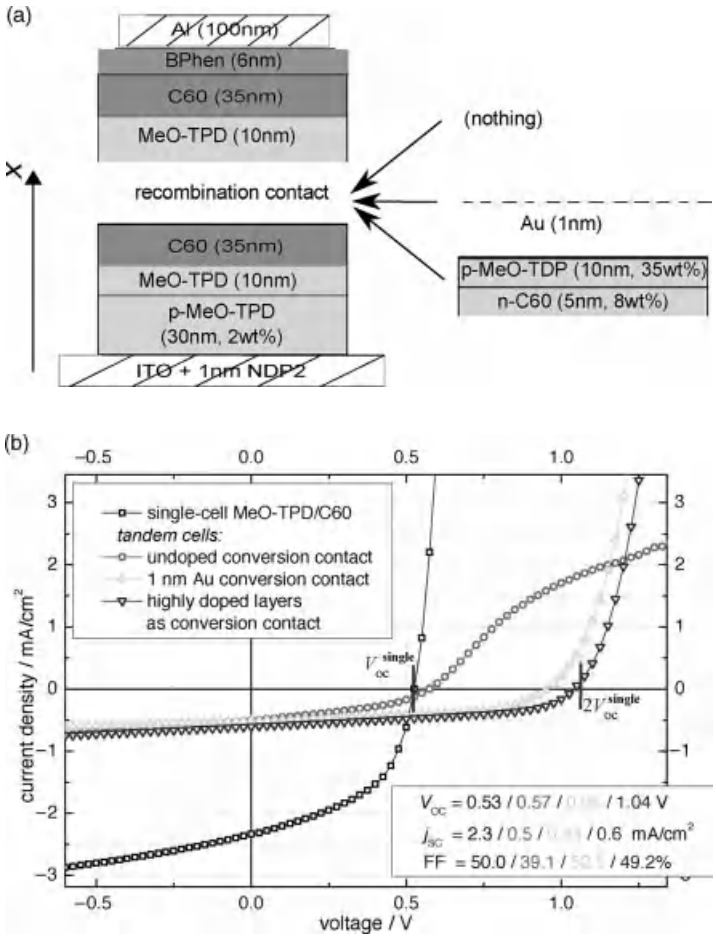

Figure 14.41 A simple test stack for investigating the recombination contact based on doped transport layers (a) and the corresponding results (b). A recombination contact with either no interlayer, 1 nm Au, or highly doped transport layers are inserted. The transport layers are doped at the given percentage (n-doping: AOB, p-doping: F4-TCNQ).

the difference between using undoped layers, using gold clusters, and using doped transport layers as recombination contact in a test stack.

The very simple stack shown in Figure 14.3 uses MeO-TPD for both the p-doped transparent hole transport layer and electron donor. C60 is used as electron acceptor and n-doped electron transport layer. All three tandem devices shown have similar current in reverse direction, indicating that they generate the same amount of free charge carriers. The *I–V* characteristics show that without doped or Au nanoclusters, the forward current is limited because of the backward directed heterojunction between the undoped MeO-TPD and C60. The V_{oc} of the tandem OSC

reaches a value only close to that of the single heterojunction. Inserting 1 nm Au between the subcells introduces metal clusters that act as efficient recombination centers leading to nearly twice the V_{oc} of the single cell. By inserting highly doped transport layers for the recombination contact, an addition of V_{oc} values of the subcells is reached retaining also a good FF. The general applicability of this approach has further been tested with transport materials of various energy levels, where it was found that thin interlayers of Au or Ag do not work well [157]. Due to its versatility, this kind of recombination contact is used in most efficient p–i–n tandem OSC [159, 160].

The reason for the differences between the three recombination contacts was investigated using UPS for the material combination MeO-TPD and C60 as displayed in Figure 14.41. The results show that using metal nanoclusters or doped transport layers are significantly different. In comparison to an interface between the two subcells without modification, both approaches reduce the tunneling distance between the donor HOMO and the acceptor LUMO. However, while metal clusters lead to an accumulation of charge carriers, the high doping of the layers in the recombination zone allows a tunneling of charge carriers through a thin depletion layer [158].

Complementary Absorption Although the first tandem devices used the same absorbing molecules in both subcells [129], the number of available materials has grown considerably. Figure 14.42 shows only a small selection of light-absorbing molecules and their corresponding extinction coefficients. This figure also illustrates why organic materials are particularly interesting for tandem concepts: the used organic semiconductors have typical absorption coefficients above 10^5/cm at their absorption maximum and can be tailored to have well-defined absorption bands. Thus, the thickness limit of the light-absorbing layers due to excitonic effects, low charge carrier

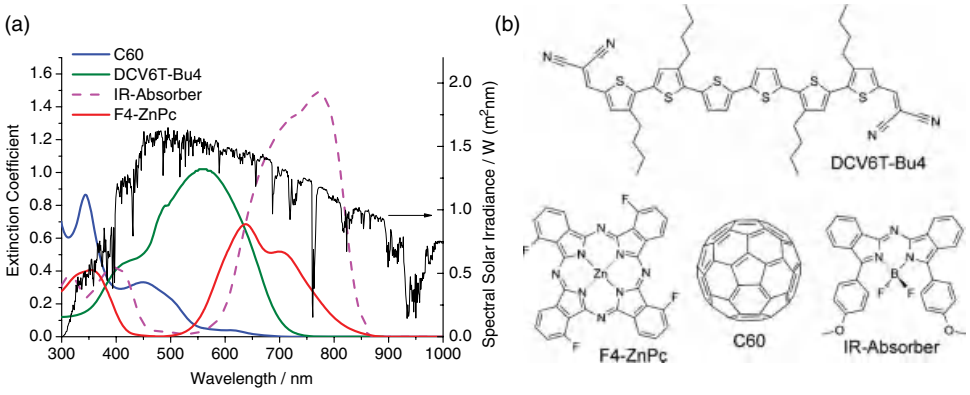

Figure 14.42 Extinction coefficients of some selected small molecules versus the solar spectrum. Shown are the values for C60, a dicyanovinyl-substituted sexithiophene with four butyl side chains (DCV6T-Bu4, Heliatek GmbH) [46], a four times fluorinated zinc phthalocyanine (F4-ZnPc, BASF SE) [161], and a NIR absorber based on AZA-bodipys [162].

mobilities, and lifetime can be circumvented by stacking single-heterojunction solar cells and by choosing subcells with complementary absorption. Hence, a large spectral coverage of the solar spectrum with efficient absorption can be realized. However, efficiently harvesting the NIR is still a challenge.

Current Matching Given that the current through a two-terminal tandem device is limited by the current of the weaker subcell, optimization of absorption and current generation in the subcells is key to efficient tandem solar cells independent of the used semiconductors. Although tandem OSC are thicker than the single-heterojunction OSC, their absorption is still subjected to interference and microcavity effects. Taking these effects into account is crucial.

Yakimov and Forrest who used only Ag nanoclusters in their tandem devices found that the efficiency increased from one to two stacked heterojunction, but it did not increase when adding more than two subcells [163]. Although they were able to fit two heterojunctions into the first interference maximum, because the organic layers were thin enough, some of the following subcells had to be in an optical interference minimum due to the missing optical spacers and thus were limiting the current of the tandem devices.

Stacking p–i–n OSC into tandem devices allows a simple way of using the interference pattern as advantage, because the doped transport layers can be used as optical spacer between the absorbing layers of the subcells. If the subcells are thin and can be positioned in the first interference maximum ($\leq$100 nm), usually no optical spacer between the subcells is required [159]. However, despite the high absorption coefficients of the organic absorbers, the tandem OSC would be optically thin. Once the absorbing layers of the subcells become thick to not to fit best into the first interference maximum anymore, an optical spacer is required. Both subcells can be made thick enough to each cover their complete interference maximum. The former condition is currently the case for the best vacuum-processed OSC and much work is devoted to further increase the thickness of the absorption layers.

Figure 14.43 shows the stack of a recently published two-terminal tandem OSC based on the p–i–n concept [160]. The stack consists of two subcells with nearly complementary absorption (F4-ZnPc:C60 and DCV6T-Bu4:C60) covering most of the spectrum between 300–800 nm (see Figure 14.42). The stack design is inverted, that is, the ITO is used as electron contact through a thin n-doped C60, thus demonstrating the one degree of freedom that doping creates. The recombination contact between the subcells is realized using doped transport layers as, described in Section 14.5.2.4. An additional recombination contact is used below the Al electrode due to processing reasons, but is not essential, as it has successfully been removed in later stack designs.

The importance of the doped transparent spacer is illustrated in Figure 14.43b showing the optical simulations of the stack. The curves illustrate how much the absorption of the F4-ZnPc-based subcell varies as function of the spacer thickness even though all other layers were kept the same, as they were made in the same process. This directly translates into the experimental results presented in Figure 14.44 that shows the characteristic parameters of the *I–V* curves versus the

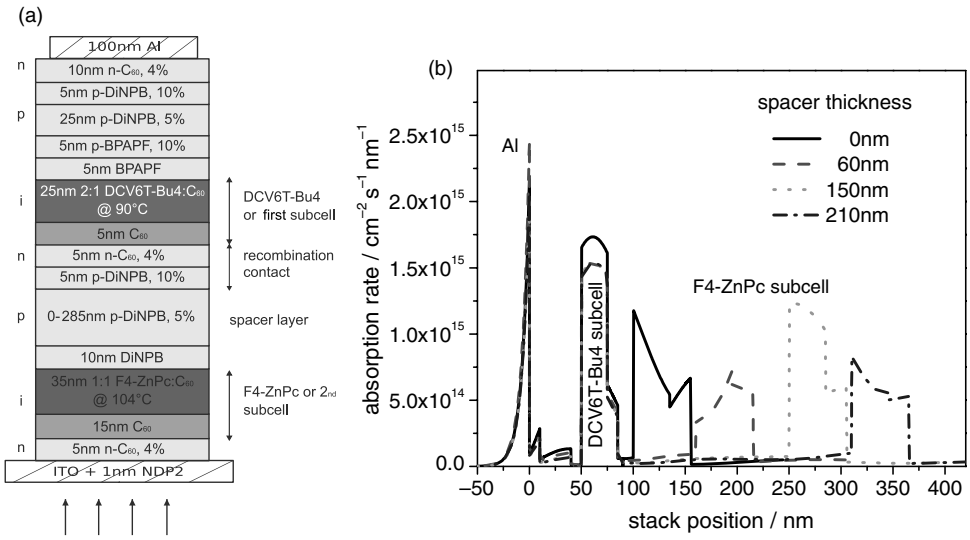

Figure 14.43 The stack structure of the tandem device used for the spacer variations, based on two inverted p–i–n OSC with complementary absorbing subcells of F4-ZnPc: C60 and DCV6T-Bu4:C60 (a) and the results of the optical simulation (b) that shows the absorption rate as function for four different spacer layer thicknesses.

thickness of the transparent spacer. V_{oc} is the sum of the voltages generated by the subcells and FF is above 70% all the time. Furthermore, V_{oc} and FF remain nearly constant through the complete spacer range indicating a very well working recombination contact.

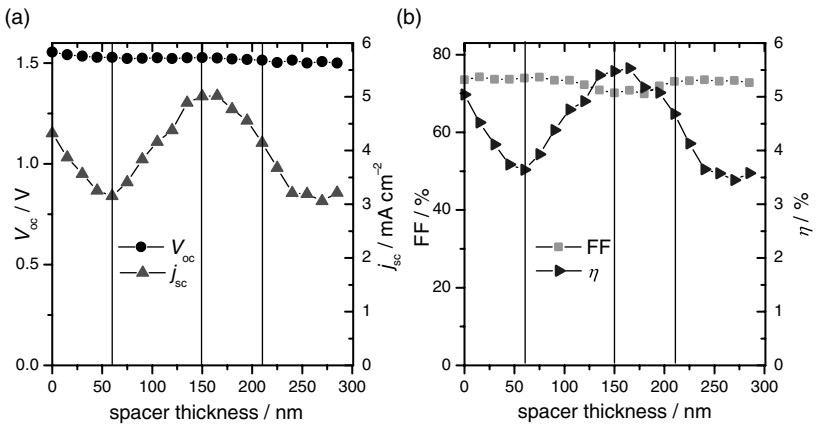

Figure 14.44 The parameters extracted from the *I–V* curves of tandem devices with a variation of the spacer layer thickness between 0 and 285 nm. All measurements were carried out at the same, but not mismatch, corrected intensity of 98 mW/cm^2 (Si reference diode). The vertical lines indicate the values used for the simulations shown in Figure 14.43.

The main difference in varying spacer thicknesses is observed in j_{sc} and subsequently in η of the tandem device. As shown by the optical simulations in Figure 14.43b, the variations in j_{sc} are a clear consequence of the thin-film optics. Starting without spacer, both subcells are just too thick to fit into the first interference maximum. With increasing spacer thickness, the red absorbing subcell (F4-ZnPc:C60) is shifted through an interference minimum of the wavelengths it absorbs (about 60 nm spacer thickness) before arriving at the second interference maximum at about 150–165 nm spacer thickness. Here, j_{sc} of the tandem device reaches its maximum and hence η is also maximized.

The optical simulations also clearly show why it makes sense to put the red (lower optical gap) absorbing subcell in front of the green (higher optical gap) absorbing subcell in this example. The red interference maximum forms further away from the Al mirror than the green interference maximum. Given that the absorption bands of organic semiconductors can be made narrow and really complementary, both subcells are positioned where they absorb most.

Although tandem OSC heavily rely on interference effects, their performance under different angles of illumination seems to be hardly affected. For the example above, simulations showed that the absorption in both subcells is reduced in a nearly equal way for off-angle illumination and, thus, no subcell becomes dominantly current limiting. This was also experimentally confirmed [160].

This optical optimization using doped and transparent spacer layers is one of the key stack components for the world record OSC that are based on vacuum-deposited small molecules [130].

14.6 Conclusion

Doping of organic materials has several distinct advantages for OSC, the main being that using doped transparent transport layers to sandwich the photovoltaic active layers allows to create stacks with energy levels that closely resemble the ideal solar cell structure as proposed by Würfel [164]. Furthermore, doping of transport layers creates many degrees of freedom in the choice of electrode materials, layer sequence, and optical optimization, because it allows controlling the position of the Fermi levels. To sum up, doped organic layers create a very versatile basis for both the investigation of fundamental processes in organic solar cells and the systematic optimization of single and tandem OSC.

14.7 Summary and Outlook

In this section, we have discussed results on the doping of organic semiconductor, addressing both the fundamentals of the process and the device applications. When seen from a perspective of the established inorganic semiconductors, it seems

obvious that doping is a key technology to make useful devices. However, in the community working on organic semiconductors, the opinion was for a long time that doping is less relevant. This was probably because of the following facts:

- Organic devices are typically large area devices and need only low current densities; in the FET with higher densities, doping was replaced by gate-induced carrier generation.
- Organic devices have used extremely thin layers where charge injection is often reasonably effective.
- Doping was actually used, but disguised as injection layer or interface effect.
- Finally, organic materials are often that impure that they are unintentionally highly doped.

The controlled doping work discussed in this section allows to systematically use the doping effect. Although a microscopic understanding is still missing (the simple hydrogen model that works well in inorganics is not applicable), work in recent years has convincingly shown that electrical doping can lead to superior device properties. This proof was first obtained for OLED: The voltage of these devices can be significantly lowered using doped transport layers, and the devices become virtually independent of the choice of contact material. Due to the low ohmic losses in the bulk at interfaces, the devices have improved stability. Not surprisingly, doping techniques have been commercially successful and are now used in millions of active matrix OLED displays. Similarly, it can be expected that doped transport layers will play a significant role in OLED lighting where low voltage is even more important.

Even more useful is doping in organic cells: In a solar cell, *every meV counts*, and thus ohmic losses should be kept as low as possible. Furthermore, a high built-in voltage helps in a solar cell, and is much more convenient to create such a built-in voltage by doped layers than by electrodes where materials with more extreme work function usually create stability problem.

Tandem solar cells are so to say the paradise for doping: First, they need an efficient recombination contact, and by far the easiest way to generate an efficient and stable recombination contact is a highly doped p–n junction. If one stacks to p–i–n cells, this junction is created automatically. Now, in tandem cells, optical design is also crucial because both absorbers need to be placed in the field maxima for their wavelength, and this is again quite well possible using doped window layers.

For switching devices, such as organic field-effect transistors, doping has been used much less. As said above, the charge carrier density control in the channel is done here by gate effects. However, doping can help to improve the contact properties. This would need a structured deposition of doping that requires more effort.

What is the outlook for the doping technology in organic semiconductors? First, the technology could grow with the markets: After long years of delay, the technology of organic semiconductors has finally achieved great success with small active matrix displays, and it appears that like those of larger TV displays they also have a rosy future. OLED lighting is still in infancy, but has a chance for a great success if

efficiency, lifetime, and cost requirements are met. Similar arguments hold for organic solar cells.

Scientifically, it seems obvious that more effort should be put into a microscopic understanding of the doping processes. This is very difficult, since the molecular doping of molecular organic semiconductors leaves very large freedom in the morphology of the system and it will be hard to design a system where the electronic effects can be isolated. Ideally, this should be a single crystal that remains same when doped.

Obviously, there is also a need for further dopant materials. One aspect is to obtain dopants that can dope organic semiconductors with more extreme energies, that is, hole-transporting materials with very low HOMO and electron-transporting materials with very high LUMO. For n-doping, this dopant should be air stable so that only the strong reduction properties materialize when the dopant is incorporated in the matrix.

Furthermore, doping should be broadly extended to organic systems prepared from solution. Although majority of commercial organic devices sold today are largely prepared by vacuum evaporation, it can be expected that more and more liquid processing will be integrated to lower cost. Therefore, it would be of interest to develop host:dopant combinations that can easily be deposited by liquid processing.

Acknowledgments

The authors would like to thank Christiane Falkenberg, Torben Menke, Max Tietze, and Hans Kleemann for proofreading. The authors gratefully acknowledge the results of Martin Pfeiffer, Jan Blochwitz-Nimoth, Christiane Falkenberg, Ronny Timmreck, BASF SE, Heliatek GmbH, Roland Gresser, Melanie Lorenz, Rico Schüppel, Sebastian Reineke, Rico Meerheim, Mauro Furno, Selina Olthof, Thomas Rosenow, and Simone Hofmann on which the results of this chapter are based. We would also like to thank the European Commission, BMBF, DFG, Novaled AG, and Heliatek GmbH for funding.

References

1 Karl, N. (1990) *Defect Control in Semiconductors*, vol. II, Amsterdam, North Holland.
2 Hung, L. and Chen, C. (2002) Recent progress of molecular organic electroluminescent materials and devices. *Mat. Sci. Eng. R Rep.*, **39**, 143–222.
3 Berner, D., Houili, H., Leo, W., and Zuppiroli, L. (2005) Insights into OLED functioning through coordinated experimental measurements and numerical model simulations: review article. *Phys. Status Solidi A*, **202**, 9–36.
4 Gather, M.C., Köhnen, A., and Meerholz, K. (2011) White organic light-emitting diodes. *Adv. Mater.*, **23** (2), 233–248.
5 Jenekhe, S.A., (2004) *Chem. Mater.*, **16** (23), (Special Issue on Organic Electronics).

6 Arias, A.C., MacKenzie, J.D., McCulloch, I., Rivnay, J., and Salleo, A. (2010) Materials and applications for large area electronics: solution-based approaches. *Chem. Rev.*, **110** (1), 3–24.

7 Peumans, P., Yakimov, A., and Forrest, S. R. (2003) Small molecular weight organic thin-film photodetectors and solar cells. *J. Appl. Phys.*, **93** (7), 3693–3723.

8 Shakeen, S.E., Giuley, D.S., Jabbour, G.E., (2005) *MRS Bulletin*, **30** (1).

9 Hains, A.W., Liang, Z., Woodhouse, M. A., and Gregg, B.A. (2010) Molecular semiconductors in organic photovoltaic cells. *Chem. Rev*, **110** (11), 6689–6735.

10 Tang, C.W. (1986) Two-layer organic photovoltaic cell. *Appl. Phys. Lett.*, **48** (2), 183–185.

11 Tang, C. and Vanslyke, S. (1987) Organic electroluminescent diodes. *Appl. Phys. Lett.*, **51**, 913.

12 Pfeiffer, M., Beyer, A., Fritz, T., and Leo, K. (1998) Controlled doping of phthalocyanine layers by cosublimation with acceptor molecules: a systematic Seebeck and conductivity study. *Appl. Phys. Lett.*, **73**, 3202.

13 Zhou, X., Blochwitz, J., Pfeiffer, M., Nollau, A., Fritz, T., and Leo, K. (2001) Enhanced hole injection into amorphous hole-transport layers of organic light-emitting diodes using controlled p-type doping. *Adv. Funct. Mater.*, **11**, 310.

14 Blochwitz, J., Fritz, T., Pfeiffer, M., Leo, K., Alloway, D.M., Lee, P.A., and Armstrong, N.R. (2001) Interface electronic structure of organic semiconductors with controlled doping levels. *Org. Electron.*, **2**, 97.

15 Männig, B., Pfeiffer, M., Nollau, A., Zhou, X., and Leo, K. (2001) Controlled p-type doping of polycrystalline and amorphous organic layers: self-consistent description of conductivity and field-effect mobility by a microscopic percolation model. *Phys. Rev. B*, **64**, 195208.

16 Nollau, A., Pfeiffer, M., Fritz, T., and Leo, K. (2000) Controlled n-type doping of a molecular organic semiconductor: naphthalenetetracarboxylic dianhydride (NTCDA) doped with bis(ethylenedithio)-tetrathiafulvalene (BEDT-TTF). *J. Appl. Phys.*, **87**, 4340.

17 Werner, A., Li, F., Harada, K., Pfeiffer, M., Fritz, L., Leo, K., and Machill, S. (2004) n-Type doping of organic thin films using cationic dyes. *Adv. Funct. Mater.*, **14**, 255–260.

18 Werner, A., Li, F., Harada, K., Pfeiffer, M., Fritz, T., and Leo, K. (2003) Pyronin B as a donor for n-type doping of organic thin films. *Appl. Phys. Lett.*, **82**, 4495–4497.

19 Li, F., Werner, A., Pfeiffer, M., Leo, K., and Liu, X. (2004) Leuco crystal violet as a dopant for n-doping of organic thin films of fullerene C60. *J. Phys. Chem. B*, **108**, 17076.

20 Harada, K., Werner, A.G., Pfeiffer, M., Bloom, C.J., Elliott, C.M., and Leo, K. (2005) Organic homojunction diodes with a high built-in potential: interpretation of the current–voltage characteristics by a generalized Einstein relation. *Phys. Rev. Lett.*, **94**, 036601.

21 Yamamoto, Y., Yoshino, K., and Inuishi, Y. (1979) Electrical properties of phthalocyanine halogen complexes. *J. Phys. Soc. Jpn.*, **47** (6), 1887–1891.

22 Parthasarathy, G., Shen, C., Kahn, A., and Forrest, S. (2001) Lithium doping of semiconducting organic charge transport materials. *J. Appl. Phys.*, **89**, 4986–4992.

23 Kido, J. and Matsumoto, T. (1998) Bright organic electroluminescent devices having a metal-doped electron-injecting layer. *Appl. Phys. Lett.*, **73**, 2866.

24 Endo, J., Matsumoto, T., and Kido, J. (2002) Organic electroluminescent devices with a vacuum-deposited Lewis-acid-doped hole-injecting layer. *Jpn. J. Appl. Phys. 2*, **41**, L358–L360.

25 Kearns, D., Tollin, G., and Calvin, M. (1960) Electrical properties of organic solids: 2. Effects of added electron acceptor on metal-free phthalocyanine. *J. Chem. Phys.*, **32** (4), 1020–1025.

26 Maitrot, M., Guillaud, G., Boudjema, B., Andre, J., and Simon, J. (1986) Molecular material based junctions: formation of a Schottky contact with metallophthalocyanine thin films doped by the cosublimation method. *J. Appl. Phys.*, **60**, 2396.

27 Andre, J., Simon, J., Even, R., Boudjema, B., Guillaud, G., and Maitrot, M. (1987) Molecular semiconductors and junction formation: phthalocyanine derivatives. *Synth. Met.*, **18**, 683–688.

28 Marks, T. (1985) Electrically conductive metallomacrocyclic assemblies. *Science*, **227**, 881.

29 Lous, E., Blom, P., Molenkamp, L., and Deleeuw, D. (1995) Schottky contacts on a highly doped organic semiconductor. *Phys. Rev. B*, **51**, 17251–17254.

30 Pfeiffer, M. (1999) *Controlled doping of organic vacuum deposited dye layers: basics and applications.* PhD thesis. TU Dresden.

31 Harada, K., Riede, M., Leo, K., Hild, O. R., and Elliott, C.M. (2008) Pentacene homojunctions: electron and hole transport properties and related photovoltaic responses. *Phys. Rev. B*, **77**, 195212.

32 Olthof, S., Tress, W., Meerheim, R., Lüssem, B., and Leo, K. (2009) Photoelectron spectroscopy study of systematically varied doping concentrations in an organic semiconductor layer using a molecular p-dopant. *J. Appl. Phys.*, **106** (10), 103711.

33 Blochwitz, J., Pfeiffer, M., Fritz, T., and Leo, K. (1998) Low voltage organic light emitting diodes featuring doped phthalocyanine as hole transport material. *Appl. Phys. Lett.*, **73**, 729.

34 Huang, J., Pfeiffer, M., Werner, A., Blochwitz, J., Leo, K., and Liu, S. (2002) Low-voltage organic electroluminescent devices using pin structures. *Appl. Phys. Lett.*, **80**, 139–141.

35 Zhou, X., Pfeiffer, M., Huang, J., Blochwitz-Nimoth, J., Qin, D., Werner, A., Drechsel, J., Maennig, B., and Leo, K. (2002) Low-voltage inverted transparent vacuum deposited organic light-emitting diodes using electrical doping. *Appl. Phys. Lett.*, **81**, 922.

36 Blochwitz, J., Pfeiffer, M., Hofmann, M., and Leo, K. (2002) Non-polymeric OLEDs with a doped amorphous hole transport layer and operating voltages down to 3.2V to achieve 100 cd/m^2. *Synth. Met.*, **127**, 169–173.

37 He, G., Pfeiffer, M., Leo, K., Hofmann, M., Birnstock, J., Pudzich, R., and Salbeck, J. (2004) High-efficiency and low-voltage p–i–n electrophosphorescent organic light-emitting diodes with double-emission layers. *Appl. Phys. Lett.*, **85**, 3911.

38 Huang, Q., Walzer, K., Pfeiffer, M., Lyssenko, V., He, G., and Leo, K. (2006) Highly efficient top emitting organic light-emitting diodes with organic outcoupling enhancement layers. *Appl. Phys. Lett.*, **88**, 113515.

39 Meerheim, R., Walzer, K., Pfeiffer, M., and Leo, K. (2006) Ultrastable and efficient red organic light emitting diodes with doped transport layers. *Appl. Phys. Lett.*, **89**, 061111.

40 Reineke, S., Lindner, F., Schwartz, G., Seidler, N., Walzer, K., Lüssem, B., and Leo, K. (2009) White organic light-emitting diodes with fluorescent tube efficiency. *Nature*, **459**, 234.

41 Pfeiffer, M., Beyer, A., Plönnigs, B., Nollau, A., Fritz, T., Leo, K., Schlettwein, D., Hiller, S., and Wöhrle, D. (2000) Controlled p-doping of pigment layers by cosublimation: basic mechanisms and implications for their use in organic photovoltaic cells. *Sol. Energy Mater. Sol. Cells*, **63**, 83.

42 Gebeyehu, D., Maennig, B., Drechsel, J., Leo, K., and Pfeiffer, M. (2003) Bulk-heterojunction photovoltaic devices based on donor–acceptor organic small molecule blends. *Sol. Energy Mater. Sol. Cells*, **79**, 81–92.

43 Drechsel, J., Maennig, B., Kozlowski, F., Pfeiffer, M., Leo, K., and Hoppe, H. (2005) Efficient organic solar cells based on a double p–i–n architecture using doped wide-gap transport layers. *Appl. Phys. Lett.*, **86**, 244102.

44 Schulze, K., Uhrich, C., Schueppel, R., Leo, K., Pfeiffer, M., Brier, E., Reinold, E., and Baeuerle, P. (2006) Efficient vacuum-deposited organic solar cells based on a new low-bandgap oligothiophene and fullerene C-60. *Adv. Mater.*, **18**, 2872–2875.

45 Uhrich, C., Wynands, D., Olthof, S., Riede, M.K., Leo, K., Sonntag, S., Maennig, B., and Pfeiffer, M. (2008)

Origin of open circuit voltage in planar and bulk heterojunction organic thin-film photovoltaics depending on doped transport layers. *J. Appl. Phys.*, **104**, 043107.

46 Wynands, D., Levichkova, M., Leo, K., Uhrich, C., Schwartz, G., Hildebrandt, D., Pfeiffer, M., and Riede, M. (2010) Increase of internal quantum efficiency in small molecular oligothiophene:C_{60} mixed heterojunction solar cells by using substrate heating. *Appl. Phys. Lett.*, **97**, 073503.

47 Walzer, K., Maennig, B., Pfeiffer, M., and Leo, K. (2007) Highly efficient organic devices based on electrically doped transport layers. *Chem. Rev.*, **107**, 1233.

48 Pfeiffer, M., Leo, K., Zhou, X., Huang, J., Hofmann, M., Werner, A., and Blochwitz-Nimoth, J. (2003) Doped organic semiconductors: physics and application in light emitting diodes. *Org. Electron.*, **4**, 89.

49 Adachi, C., Kwong, R., and Forrest, S. (2001) Efficient electrophosphorescence using a doped ambipolar conductive molecular organic thin film. *Org. Electron.*, **2**, 37.

50 Yoshida, M., Fujii, A., Ohmori, Y., and Yoshino, K. (1996) Three-layered multicolor organic electroluminescent device. *Appl. Phys. Lett.*, **69**, 734–736.

51 Ivory, D., Miller, G., Sowa, J., Shacklette, L., Chance, R., and Baughman, R. (1979) Highly conducting charge-transfer complexes of poly(*para*-phenylene). *J. Chem. Phys.*, **71** (3), 1506–1507.

52 Ramsey, M.G., Steinmüller, D., and Netzer, F.P. (1990) Explicit evidence for bipolaron formation: Cs-doped biphenyl. *Phys. Rev. B*, **42**, 5902–5905.

53 Itoh, Y., Tomikawa, N., Kobayashi, S., and Minato, T. (1990) Extended abstracts. The 51st Autumn Meeting, The Japan Society of Applied Physics, p. 1040.

54 Kido, J., Nagai, K., and Okamoto, Y (1993) Bright organic electroluminescent devices with double-layer cathode. *IEEE Trans. Electron Dev.*, **40**, 1342–1344.

55 Mori, T., Jujikawa, H., Tokito, S., and Taga, Y. (1998) Electronic structure of 8-hydroxyquinoline aluminum/LiF/Al interface for organic electroluminescent device studied by ultraviolet photoelectron spectroscopy. *Appl. Phys. Lett.*, **73**, 2763.

56 Hung, L.S., Tang, C.W., and Mason, M.G. (1997) Enhanced electron injection in organic electroluminescence devices using an Al/LiF electrode. *Appl. Phys. Lett.*, **70** (2), 152–154.

57 Mason, M.G., Tang, C.W., Hung, L.-S., Raychaudhuri, P., Madathil, J., Giesen, D.J., Yan, L., Le, Q.T., Gao, Y., Lee, S.-T., Liao, L.S., Cheng, L.F., Salaneck, W.R., dos Santos, D.A., and Bredas, J.L. (2001). Interfacial chemistry of Alq_3 and LiF with reactive metals. *J. Appl. Phys.*, **89** (5), 2756–2765.

58 Grozea, D., Turak, A., Feng, X.D., Lu, Z. H., Johnson, D., and Wood, R. (2002) Chemical structure of Al/LiF/Alq interfaces in organic light-emitting diodes. *Appl. Phys. Lett.*, **81** (17), 3173–3175.

59 D'Andrade, B.W., Forrest, S., and Chwang, A. (2003) Operational stability of electrophosphorescent devices containing p and n doped transport layers. *Appl. Phys. Lett.*, **83**, 3858.

60 Brabec, C.J., Dyakonov, V., Parisi, J., and Sariciftci, N.S. (eds.) (2003) *Organic Photovoltaics*, Springer, Berlin.

61 Tanaka, S., Kanai, K., Kawabe, E., Iwahashi, T., Nishi, T., Ouchi, Y., and Seki, K. (2005) Doping effect of tetrathianaphthacene molecule in organic semiconductors on their interfacial electronic structures studied by UV photoemission spectroscopy. *Jpn. J. Appl. Phys.*, **44**, 3760–3763.

62 Chan, C.K., Amy, F., Zhang, Q., Barlow, S., Marder, S., and Kahn, A. (2006) n-Type doping of an electron-transport material by controlled gas-phase incorporation of cobaltocene. *Chem. Phys. Lett.*, **431** (1–3), 67–71.

63 Bloom, C.J., Elliott, C.M., Schroeder, P. G., France, C.B., and Parkinson, B.A. (2003) Low work function reduced metal complexes as cathodes in organic electroluminescent devices. *J. Phys. Chem. B*, **107** (13), 2933–2938.

64 Cotton, F.A., Gruhn, N.E., Gu, J., Huang, P., Lichtenberger, D.L., Murillo, C.A., Van Dorn, L.O., and Wilkinson, C.C.

(2002) Closed-shell molecules that ionize more readily than cesium. *Science*, **298**, 1971–1974.

65 Cotton, F.A., Donahue, J.P., Lichtenberger, D.L., Murillo, C.A., and Villagrán, D. (2005) Expeditious access to the most easily ionized closed-shell molecule, W_2 (hpp)$_4$. *J. Am. Chem. Soc.*, **127** (31), 10808–10809.

66 Wellmann, P. (2009) *Lebensdauer und Stabilität elektrisch dotierter OLEDs*. Dissertation. TU Dresden.

67 Menke, T., Ray, D., Olthof, S., Meiss, J., Leo, K., and Riede, M. (2012) *In-situ* conductivity and Seebeck measurements of highly efficient n-dopants in fullerene C_{60}. *Appl. Phys. Lett.*, **9**, 1.

68 Chan, C., Kim, E.-G., Bredas, J.-L., and Kahn, A. (2006) Molecular n-type doping of 1,4,5,8-naphthalene tetracarboxylic dianhydride by pyronin B studied using direct and inverse photoelectron spectroscopies. *Adv. Funct. Mater.*, **16** (6), 831–837.

69 Li, F., Pfeiffer, M., Werner, A., Harada, K., Leo, K., Hayashi, N., Seki, K., Liu, X., and Dang, X.-D. (2006) Acridine orange base as a dopant for n doping of C_{60} thin films. *J. Appl. Phys.*, **100** (2), 023716.

70 Lewis, E.S., Perry, J.M., and Grinstein, R. H. (1970) Mechanism of hydride transfer. III. Rates and isotope effects in the quinone oxidation of leuco triphenylmethane dyes. *J. Am. Chem. Soc.*, **92** (4), 899–905.

71 Naguib, Y.M.A., Cohen, S.G., and Steel, C. (1986) Reduction of crystal violet by diphenylketyl radicals. *J. Am. Chem. Soc.*, **108** (1), 128–133.

72 Yamamoto, S., Sakurai, T., Yingjin, L., and Sueishi, Y. (1999) Mechanism of hydride transfer reaction from 4-(dimethylamino)phenyl methane derivatives to 2,3-dichloro-5,6-dicyano-*p*-benzoquinone. *Phys. Chem. Chem. Phys.*, **1**, 833–837.

73 Wei, P., Oh, J.H., Dong, G., and Bao, Z. (2010) Use of a 1*H*-benzoimidazole derivative as an n-type dopant and to enable air-stable solution-processed n-channel organic thin-film transistors. *J. Am. Chem. Soc.*, **132** (26), 8852–8853.

74 Wei, P., Menke, T., Naab, B.D., Leo, K., Riede, M., and Bao, Z. (2012) 2-(2-Methoxyphenyl)-1,3-dimethyl-1*H*-benzoimidazol-3-ium iodide as a new air-stable n-type dopant for vacuum processed organic semiconductor thin films. *J. Am. Chem. Soc.*, **134** (9), 3999–4002.

75 Maennig, B., Drechsel, J., Gebeyehu, D., Kozlowski, F., Werner, A., Li, F., Grundmann, S., Sonntag, S., Koch, M., Leo, K., Pfeiffer, M., Hoppe, H., Meissner, D., Sariciftci, N., Riedel, I., Dyakonov, V., and Parisi, J. (2004). Organic p–i–n solar cells. *Appl. Phys. A*, **79** (1), 1–14.

76 Riede, M., Mueller, T., Tress, W., Schueppel, R., and Leo, K. (2008) Small-molecule solar cells: status and perspectives. *Nanotechnology*, **19**, 424001.

77 Guo, S., Kim, S.B., Mohapatra, S.K., Qi, Y., Sajoto, T., Kahn, A., Marder, S.R., and Barlow, S. (2011) n-Doping of organic electronic materials using air-stable organometallics. *Adv. Mater.*, **24** (5), 699–703.

78 Fischer, E.O. and Wawersik, H. (1966) Über Aromatenkomplexe von Metallen: LXXXVIII. Über monomeres und dimeres dicyclopentadienyl-rhodium und dicyclopentadienyliridium und über ein neues Verfahren zur Darstellung ungeladener Metall-aromaten-komplexe. *J. Organomet. Chem.*, **5** (6), 559–567.

79 Yamashita, K., Kunugi, Y., Harima, Y., and Chowdhury, A.-N. (1995) Fabrication of an organic p–n homojunction diode using electrochemically cation- and photochemically anion-doped polymer. *Jpn. J. Appl. Phys.*, **34** (7B), 3794–3797.

80 Hamm, S. and Wachtel, H. (1995) Rectifying organic junctions of molecular assemblies based on perylene ion salts. *J. Chem. Phys.*, **103** (24), 10689–10695.

81 Shockley, W. (1949) The theory of p–n junctions in semiconductors and p–n junction transistors. *BELL Syst. Tech. J.*, **28**, 435–489.

82 van Berkel, C., Powell, M.J., Franklin, A. R., and French, I.D. (1993) Quality factor in α-Si:H nip and pin diodes. *J. Appl. Phys.*, **73** (10), 5264–5268.

83 Kroon, M.A. and van Swaaij, R.A.C.M.M. (2001) Spatial effects on ideality factor of amorphous silicon pin diodes. *J. Appl. Phys.*, **90** (2), 994–1000.

84 Tsuji, H., Mitsui, C., Sato, Y., and Nakamura, E. (2009) Bis(carbazolyl) benzodifuran: a high-mobility ambipolar material for homojunction organic light-emitting diode devices. *Adv. Mater.*, **21**, 3776–3779.

85 Cai, C., Su, S.-J., Chiba, T., Sasabe, H., Pu, Y.-J., Nakayama, K., and Kido, J. (2011) High-efficiency red, green and blue phosphorescent homojunction organic light-emitting diodes based on bipolar host materials. *Org. Electron.*, **12**, 843–850.

86 Hamwi, S., Riedl, T., and Kowalsky, W. (2011) An organic p–i–n homojunction as ultra violet light emitting diode and visible-blind photodiode in one. *Appl. Phys. Lett.*, **99**, 053301.

87 Kleemann, H., Gutierrez, R., Lindner, F., Avdoshenko, S., Manrique, P.D., Lussem, B., Cuniberti, G., and Leo, K. (2010) Organic zener diodes: tunneling across the gap in organic semiconductor materials. *Nano Lett.*, **10**, 4929–4934.

88 Bernanose, A. (1955) Electroluminescence of organic compounds. *Br. J. Appl. Phys*, **6**, (Suppl. 4), S54–S56.

89 Helfrich, W. and Schneider, W.G. (1965). Recombination radiation in anthracene crystals. *Phys. Rev. Lett*, **14** (7), 229–231.

90 Williams, D. and Schadt, M. (1970) A simple organic electroluminescent diode. *Proc. IEEE*, **58** (3), 476.

91 Kampas, F. and Gouterman, M. (1977) Porphyrin films: electroluminescence of octaethylporphyrin. *Chem. Phys. Lett.*, **48** (2), 233–236.

92 Vincett, P., Barlow, W., Hann, R., and Roberts, G. (1982) Electrical-conduction and low-voltage blue electro-luminescence in vacuum-deposited organic films. *Thin Solid Films*, **94** (2), 171–183.

93 Baldo, M., O'Brien, D., You, Y., Shoustikov, S., Sibley, S., Thompson, M., and Forrest, S. (1998) Highly efficient phosphorescent emission from organic electroluminescent devices. *Nature*, **395**, 151.

94 Meerheim, R., Walzer, K., He, G., Pfeiffer, M., and Leo, K. (2006) Highly efficient organic light emitting diodes (OLED) for displays and lighting. *Proc. SPIE*, **6192**, 22.

95 Meerheim, R., Furno, M., Hofmann, S., Luessem, B., and Leo, K. (2010) Quantification of energy loss mechanisms in organic light-emitting diodes. *Appl. Phys. Lett.*, **97**, 253305.

96 Meerheim, R., Luessem, B., and Leo, K. (2009) Efficiency and stability of p–i–n type organic light emitting diodes for display and lighting applications. *Proc. IEEE*, **97**, 1606–1626.

97 Greenham, N.C., Friend, R.H., and Bradley, D.D.C. (1994) Angular dependence of the emission from a conjugated polymer light-emitting diode: implications for efficiency calculations. *Adv. Mater.*, **6**, 491.

98 Baldo, M., Lamansky, S., Burrows, P., Thompson, M., and Forrest, S. (1999) Very high-efficiency green organic light-emitting devices based on electrophosphorescence. *Appl. Phys. Lett.*, **75**, 4–6.

99 Kobayashi, T., Ide, N., Matsusue, N., and Naito, H. (2005) Temperature dependence of photoluminescence lifetime and quantum efficiency in neat fac-Ir(ppy)$_3$ thin films. *Jpn. J. Appl. Phys.*, **44**, 1966–1969.

100 Meerholz, K. and Müller, D. (2001) Outsmarting waveguide losses in thin-film light-emitting diodes. *Adv. Funct. Mater.*, **11**, 251.

101 Meerheim, R., Scholz, S., Olthof, S., Schwartz, G., Reineke, S., Walzer, K., and Leo, K. (2008) Influence of charge balance and exciton distribution on efficiency and lifetime of phosphorescent organic light-emitting devices. *J. Appl. Phys.*, **104**, 014510.

102 Chopra, N., Lee, J., Zheng, Y., Eom, S.-H., Xue, J., and So, F. (2008) High efficiency blue phosphorescent organic light-emitting device. *Appl. Phys. Lett.*, **93**, 143307.

103 Furno, M., Meerheim, R., Thomschke, M., Hofmann, S., Lüssem, B., and Leo, K. (2010) Outcoupling efficiency in

small-molecule OLEDs: from theory to experiment. *Proc. SPIE*, **7617**, 761716.
104 Hofmann, S., Thomschke, M., Freitag, P., Furno, M., Luessem, B., and Leo, K. (2010) Top-emitting organic light-emitting diodes: influence of cavity design. *Appl. Phys. Lett.*, **97**, 253308.
105 Lüssem, B., Reineke, S., Rosenow, T., Schwartz, G., and Leo, K. (2010) Novel concepts for OLED lighting. *Proc. SPIE*, **7617**, 761712.
106 Sun, Y., Giebink, N., Kanno, H., Ma, B., Thompson, M., and Forrest, S. (2006) Management of singlet and triplet excitons for efficient white organic light-emitting devices. *Nature*, **440**, 908.
107 Schwartz, G., Pfeiffer, M., Reineke, S., Walzer, K., and Leo, K. (2007) Harvesting triplet excitons from fluorescent blue emitters in white organic light-emitting diodes. *Adv. Mater.*, **19**, 3672.
108 Schwartz, G., Reineke, S., Rosenow, T.C., Walzer, K., and Leo, K. (2009) Triplet harvesting in hybrid white organic light-emitting diodes. *Adv. Funct. Mater.*, **19**, 1319–1333.
109 Schwartz, G., Reineke, S., Walzer, K., and Leo, K. (2008) Reduced efficiency roll-off in high-efficiency hybrid white organic light-emitting diodes. *Appl. Phys. Lett.*, **92**, 053311.
110 Lee, J.-Y., Connor, S.T., Cui, Y., and Peumans, P. (2008) Solution-processed metal nanowire mesh transparent electrodes. *Nano Lett.*, **8**, 689–692.
111 Lee, J.-I., Chu, H.Y., Lee, J., and Chung, S.M. (2008) Triplet harvesting for efficient white organic light emitting diodes. *J. Nanosci. Nanotechnol.*, **8**, 5602–5605.
112 Kondakova, M.E., Giesen, D.J., Deaton, J. C., Liao, L.-S., Pawlik, T.D., Kondakov, D. Y., Miller, M.E., Royster, T.L., and Comfort, D.L. (2008) Highly efficient fluorescent/phosphorescent OLED devices using triplet harvesting. *SID Symp. Digest Tech.*, **39**, 219.
113 Rosenow, T.C., Furno, M., Reineke, S., Olthof, S., Luessem, B., and Leo, K. (2010) Highly efficient white organic light-emitting diodes based on fluorescent blue emitters. *J. Appl. Phys.*, **108**, 113113.
114 Chamberlain, G. (1983) Organic solar cells: a review. *Solar Cells*, **8** (1), 47–83.
115 Hiramoto, M., Fujiwara, H., and Yokoyama, M. (1991) Three-layered organic solar-cell with a photoactive interlayer of codeposited pigments. *Appl. Phys. Lett.*, **58** (10), 1062–1064.
116 Vandewal, K., Tvingstedt, K., Gadisa, A., Inganas, O., and Manca, J.V. (2009) On the origin of the open-circuit voltage of polymer-fullerene solar cells. *Nat. Mater.*, **8**, 904–909.
117 Hoppe, H. and Sariciftci, N. (2006) Morphology of polymer/fullerene bulk heterojunction solar cells. *J. Mater. Chem.*, **16** (1), 45–61.
118 Salleo, A., Kline, R., Delongchamp, D., and Chabinyc, M. (2010) Microstructural characterization and charge transport in thin films of conjugated polymers. *Adv. Mater.*, **22**, 3812–3838.
119 Green, M.A., Emery, K., Hishikawa, Y., Warta, W., and Dunlop, E.D. (2011) Solar cell efficiency tables (Version 38). *Prog. Photovolt. Res. Appl.*, **19**, 565–572.
120 Rand, B.P., Genoe, J., Heremans, P., and Poortmans, J. (2007) Solar cells utilizing small molecular weight organic semiconductors. *Prog. Photovolt. Res. Appl.*, **15**, 659–676.
121 Brabec, C.J. (2004) Organic photovoltaics: technology and market. *Sol. Energy Mater. Sol. Cells*, **83** (2–3), 273–292.
122 Dennler, G., Scharber, M.C., and Brabec, C.J. (2009) Polymer-fullerene bulk-heterojunction solar cells. *Adv. Mater.*, **21**, 1323–1338.
123 ASTM (2010) *ASTM Standard G173, Standard Tables for Reference Solar Spectral Irradiances: Direct Normal and Hemispherical on 37° Tilted Surface.*
124 Shrotriya, V., Li, G., Yao, Y., Moriarty, T., Emery, K., and Yang, Y. (2006) Accurate measurement and characterization of organic solar cells. *Adv. Funct. Mater.*, **16** (15), 2016–2023.
125 Wynands, D., Levichkova, M., Leo, K., Uhrich, C., Schwartz, G., Hildebrandt, D., Pfeiffer, M., and Riede, M. (2010) Increase in internal quantum efficiency in small molecular oligothiophene: C60 mixed heterojunction solar cells by

substrate heating. *Appl. Phys. Lett.*, **97**, 073503.

126 Burkhard, G.F., Hoke, E.T., and McGehee, M.D. (2010) Accounting for interference, scattering, and electrode absorption to make accurate internal quantum efficiency measurements in organic and other thin solar cells. *Adv. Mater.*, **22**, 3293–3297.

127 Seaman, C.H. (1982) Calibration of solar cells by the reference cell method: the spectral mismatch problem. *Sol. Energy*, **29**, 291–298.

128 Cravino, A., Schilinsky, P., and Brabec, C.J. (2007) Characterization of organic solar cells: the importance of device layout. *Adv. Funct. Mater.*, **17** (18), 3906–3910.

129 Hiramoto, M., Suezaki, M., and Yokoyama, M. (1990) Effect of thin gold interstitial-layer on the photovoltaic properties of tandem organic solar cell. *Chem. Lett.*, **3**, 327–330.

130 Heliatek (2011) Heliatek achieves new world record for organic solar cells with certified 9.8% cell efficiency. http://www.heliatek.com/?p=1346&lang=en.

131 Rostalski, J. and Meissner, D. (2000) Monochromatic versus solar efficiencies of organic solar cells. *Sol. Energy Mater. Sol. Cells*, **61**, 87–95.

132 Sariciftci, N.S., Smilowitz, L., Heeger, A. J., and Wudl, F. (1992) Photoinduced electron-transfer from a conducting polymer to buckminsterfullerene. *Science*, **258** (5087), 1474–1476.

133 Shaheen, S.E., Brabec, C.J., Sariciftci, N. S., Padinger, F., Fromherz, T., and Hummelen, J.C. (2001) 2.5% efficient organic plastic solar cells. *Appl. Phys. Lett.*, **78** (6), 841–843.

134 Padinger, F., Rittberger, R.S., and Sariciftci, N.S. (2003) Effects of postproduction treatment on plastic solar cells. *Adv. Funct. Mater.*, **13** (1), 85–88.

135 Suemori, K., Miyata, T., Hiramoto, M., and Yokoyama, M. (2004) Enhanced photovoltaic performance in fullerene: phthalocyanine codeposited films deposited on heated substrate. *Jpn. J. Appl. Phys.*, **8**, 1014–1016.

136 Pfuetzner, S., Meiss, J., Petrich, A., Riede, M., and Leo, K. (2009) Thick C60: ZnPc bulk heterojunction solar cells with improved performance by film deposition on heated substrates. *Appl. Phys. Lett.*, **94**, 253303.

137 Würfel, P. (2004) *Physics of Solar Cells: From Principles to New Concepts*, Wiley-VCH Verlag GmbH, Weinheim.

138 Peumans, P., Bulovic, V., and Forrest, S. R. (2000) Efficient photon harvesting at high optical intensities in ultrathin organic double-heterostructure photovoltaic diodes. *Appl. Phys. Lett.*, **76** (19), 2650–2652.

139 Falkenberg, C., Leo, K., and Riede, M.K. (2011) *Improved photocurrent by using n-doped 2,3,8,9,14,15-hexachloro-5,6,11,12,17,18-hexaazatrinaphthylene (HATNA-Cl6) as optical spacer layer in p–i–n type organic solar cells. J. Appl. Phys.*, **110**, 124509.

140 Barlow, S., Zhang, Q., Kaafarani, B.R., Risko, C., Amy, F., Chan, C.K., Domercq, B., Starikova, Z.A., Antipin, M.Y., Timofeeva, T.V., Kippelen, B., Bredas, J. L., Kahn, A., and Marder, S.R. (2007). Synthesis, ionisation potentials and electron affinities of hexaazatrinaphthylene derivatives. *Chem. Eur. J.*, **13** (12), 3537–3547.

141 Zhao, W. and Kahn, A. (2009) Charge transfer at n-doped organic–organic heterojunctions. *J. Appl. Phys.*, **105**, 123711.

142 Centurioni, E. (2005) Generalized matrix method for calculation of internal light energy flux in mixed coherent and incoherent multilayers. *Appl. Opt.*, **44**, 7532–7539.

143 Fritz, T., Hahn, J., and Böttcher, H. (1989) Determination of the optical constants of evaporated dye layers. *Thin Solid Films*, **170**, 249.

144 Meiss, J., Allinger, N., Riede, M.K., and Leo, K. (2008) Improved light harvesting in tin-doped indium oxide (ITO)-free inverted bulk-heterojunction organic solar cells using capping layers. *Appl. Phys. Lett.*, **93** (10), 103311.

145 Solarmer (2010) *Solarmer energy, Inc. breaks psychological barrier with 8.13% OPV efficiency*. http://tinyurl.com/28nyg7d.

146 Konarka (2010) *Konarka's power plastic achieves world record 8.3% efficiency certification from national energy renewable laboratory (NREL)*. http://tinyurl.com/25gdcm5.

147 Koster, L.J.A., Mihailetchi, V.D., and Blom, P.W.M. (2006) Ultimate efficiency of polymer/fullerene bulk heterojunction solar cells. *Appl. Phys. Lett.*, **88** (9), 093511.

148 Scharber, M.C., Mühlbacher, D., Koppe, M., Denk, P., Waldauf, C., Heeger, A.J., and Brabec, C.J. (2006) Design rules for donors in bulk-heterojunction solar cells: towards 10% energy-conversion efficiency. *Adv. Mater.*, **18**, 789–794.

149 Rand, B.P., Burk, D.P., and Forrest, S.R. (2007) Offset energies at organic semiconductor heterojunctions and their influence on the open-circuit voltage of thin-film solar cells. *Phys. Rev. B*, **75**, 115327.

150 Dennler, G., Scharber, M.C., Ameri, T., Denk, P., Forberich, K., Waldauf, C., and Brabec, C.J. (2008) Design rules for donors in bulk-heterojunction tandem solar cells: towards 15% energy-conversion efficiency. *Adv. Mater.*, **3**, 579–583.

151 Ameri, T., Dennler, G., Lungenschmied, C., and Brabec, C.J. (2009) Organic tandem solar cells: a review. *Energy Environ. Sci.*, **2**, 347–363.

152 NREL (2011) *Presentation, value certified by NREL*.

153 Heliatek (2010) *Heliatek and IAPP achieve production relevant efficiency record for organic solar cells*. http://tinyurl.com/cd5xnbg.

154 Yu, B., Zhu, F., Wang, H., Li, G., and Yan, D. (2008) All-organic tunnel junctions as connecting units in tandem organic solar cell. *J. Appl. Phys.*, **104**, 114503.

155 Kim, J.Y., Lee, K., Coates, N.E., Moses, D., Nguyen, T.Q., Dante, M., and Heeger, A.J. (2007) Efficient tandem polymer solar cells fabricated by all-solution processing. *Science*, **317** (5835), 222–225.

156 Gilot, J., Wienk, M.M., and Janssen, R.A. J. (2007) Double and triple junction polymer solar cells processed from solution. *Appl. Phys. Lett.*, **90**, 143512.

157 Timmreck, R., Olthof, S., Riede, M.K., and Leo, K. (2010) Highly doped layers as electron–hole recombination contact in organic tandem cells. *J. Appl. Phys.*, **108**, 033108.

158 Olthof, S., Timmreck, R., Luessem, B., Riede, M., and Leo, K. (2012) Photoelectron spectroscopy investigations of recombination contacts for tandem organic solar cells based on metal clusters and pn junctions. *Appl. Phys. Lett.*, **100** (11), 3302–3306.

159 Schueppel, R., Timmreck, R., Allinger, N., Mueller, T., Furno, M., Uhrich, C., Leo, K., and Riede, M. (2010) Controlled current matching in small molecule organic tandem solar cells using doped spacer layers. *J. Appl. Phys.*, **107**, 044503.

160 Riede, M., Uhrich, C., Widmer, J., Timmreck, R., Wynands, D., Schwartz, G., Gnehr, W.-M., Hildebrandt, D., Weiss, A., Hwang, J., Sundarraj, S., Erk, P., Pfeiffer, M., and Leo, K. (2011) Efficient organic tandem solar cells based on small molecules. *Adv. Funct. Mater.*, **21**, 3019–3028.

161 Meiss, J., Merten, A., Hein, M., Schuenemann, C., Schäfer, S., Tietze, M., Uhrich, C., Pfeiffer, M., Leo, K., and Riede, M. (2011) Fluorinated zinc phthalocyanine as donor for efficient vacuum-deposited organic solar cells. *Adv. Funct. Mater.*, **22** (2), 405–414.

162 Gresser, R., Hummert, M., Hartmann, H., Leo, K., and Riede, M. (2011) Synthesis and characterization of near-infrared absorbing benzannulated aza-bodipy dyes. *Chem. Eur. J.*, **17**, 2939–2947.

163 Yakimov, A. and Forrest, S.R. (2002) High photovoltage multiple-heterojunction organic solar cells incorporating interfacial metallic nanoclusters. *Appl. Phys. Lett.*, **80** (9), 1667–1669.

164 Würfel, P. (2007) Photovoltaic principles and organic solar cells. *Chimia*, **61**, 770–774.

15
Device Efficiency of Organic Light-Emitting Diodes

Wolfgang Brütting and Jörg Frischeisen

15.1
Introduction

The availability of artificial light has been a seminal cultural development of mankind. After open fires for thousands of years, the introduction of electricity together with the invention of the light bulb in the second half of the nineteenth century has revolutionized our daily life. Having dominated the lighting market for more than 100 years, however, the light bulb faces its decline due to the need for technologies that convert electricity more efficiently into visible light. Besides fluorescent lamps, which are already well established in the market, the availability and progress in white light-emitting diodes, both inorganic and organic, over the last decade has led to a new lighting technology called solid-state lighting [1]. Its working principle, namely, the radiative recombination of injected electron–hole pairs in a solid, a process termed electroluminescence, is fundamentally different from thus far existing techniques and holds the promise for highly efficient, long-lived, and environment-friendly light sources. In contrast to their inorganic counterparts, organic light-emitting diodes (OLEDs) are flat and thin large-area light sources that could rather lead to complementary luminaires than competitors to existing technologies.

Historically speaking, electroluminescence in organic molecular crystals dates back to the early 1960s [2, 3], however, the important step toward applicable devices was the demonstration of thin-film organic light-emitting diodes by researchers at Eastman Kodak in 1987 [4] using vacuum-deposited molecular materials and by a group at Cambridge University in 1990 [5] making use of a solution-processed conjugated polymer. Inspired by these publications, intense research and development has led to the introduction of first commercial products based on OLED displays in the late 1990s. Since 2000, however, the focus in many laboratories shifted toward OLEDs for lighting applications, that is, to white OLEDs. After steady improvements in efficiency and lifetime over the years, the commercialization of OLEDs for general lighting has just recently started [6].

The scope of this chapter is to present the working principles of OLEDs and to review ongoing efforts to improve their efficiency, in particular through enhanced light outcoupling. Thus, we will restrict ourselves to devices fabricated by vacuum

Physics of Organic Semiconductors, Second Edition. Edited by Wolfgang Brütting and Chihaya Adachi

deposition of low-molecular weight materials (small molecules). Nevertheless, most of the following discussion is equally valid for polymer OLEDs where thin films are prepared by solution processing of large macromolecules. For an overview of various technical aspects of OLED fabrication and the current state of the art of white OLEDs for lighting applications see Refs [7–10].

15.2 OLED Operation

15.2.1 OLED Architecture and Stack Layout

In principle, an OLED can consist of only one organic layer sandwiched between two electrodes, that is, the anode and the cathode [5]. However, a multilayer OLED made of several different functional organic layers is superior in terms of efficiency and lifetime because the properties of the individual layers can be tuned through the proper choice of materials. A typical stack layout of such an OLED is displayed in Figure 15.1. The positively biased anode is required in order to inject holes into the hole transport layer (HTL). Similarly, electrons are injected from the cathode into the electron transport layer (ETL). The emission layer (EML) comprises one or more dyes, emitting light in different regions of the visible spectrum. High-efficiency OLEDs often contain several additional layers like separate blocking and injection layers.

The most common substrate material is glass, but it is also possible to employ other materials, like polymer or metal foils or semiconductor substrates. One of

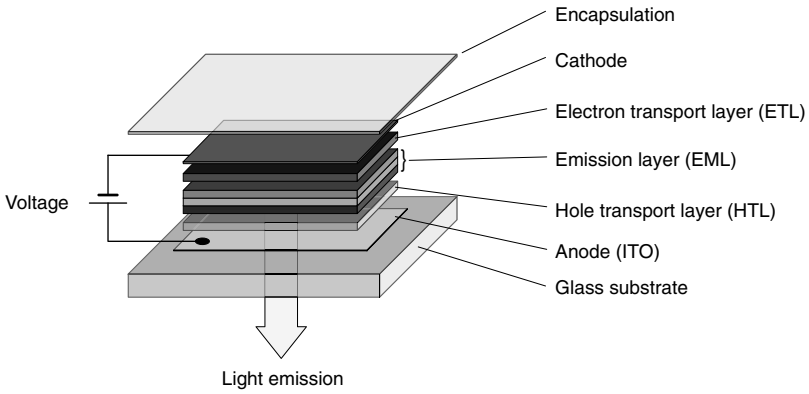

Figure 15.1 Simplified illustration of a three-layer OLED stack. ETL, EML, and HTL denote the electron transport layer, the emission layer(s), and the hole transport layer, respectively. In order to obtain light emission, a positive voltage must be applied to the anode, which often consists of optically transparent indium tin oxide.

the two metallic or metallic-conducting electrodes must be semitransparent so that the produced light can leave the device either to the substrate side (bottom emission) or to the upper electrode (top emission). The anode of an OLED often consists of indium tin oxide (ITO), which is highly transparent and shows a good electrical conductivity. In general, anode materials need a high work function that also makes metals like gold a suitable choice. For the cathode, low work function metals like calcium or magnesium are often used in combination with highly reflective and less reactive metals like aluminum or silver.

Since many organic materials and low work function metals are not stable under ambient conditions [11], that is, they react with oxygen and moisture, it is necessary to protect the materials with an encapsulation. The most common method utilizes a cover glass that is glued to the substrate, thus creating a cavity filled with inert gas or a desiccant acting as a getter to absorb small amounts of oxygen and water that penetrate through the encapsulation in the course of time. The active area of the OLED is defined as the overlap of the two electrodes. Hence, OLEDs can in principle have any shape and size and they are therefore suited for a wide range of applications. Laboratory OLEDs have typical dimensions of a few square millimeter. In industrial prototypes, the active area of the OLEDs has already been scaled up to around 50 cm^2 and beyond. The thickness of the organic layers is typically in the range between 10 and a few hundred nanometers.

15.2.2 Working Principles of OLEDs

The basic processes in an OLED under operation are illustrated in Figure 15.2 for a device with three organic layers. An external voltage source of typically a few volts is applied to the device so that the two types of charge carriers are injected from the opposite electrodes, that is, electrons from the cathode and holes from the anode, and drift toward each other. When the initially free electrons and holes meet, they form strongly bound electron–hole pairs (excitons) in the emission layer, which then may decay radiatively and emit photons. In detail, the whole process can be separated into four fundamental steps as denominated in Figure 15.2:

1) Injection of electrons and holes at the electrodes
2) Transport of charge carriers through the organic layers
3) Formation of bound electron–hole pairs (excitons)
4) Radiative exciton decay and emission of light

One distinct difference between OLEDs based on molecular materials and polymer OLEDs is the extent and location of the recombination zone inside the device. While in the latter case the emission zone is spread over a sizable fraction of the light-emitting polymer layer (depending of course on the detailed material properties) [12], in small-molecule OLEDs the generation of light can be confined by a proper choice of materials with suitable energy levels and layer thicknesses to a relatively narrow zone sandwiched between HTL and ETL. Moreover, if doped hole and electron injection layers are used [13], this region can be placed at almost

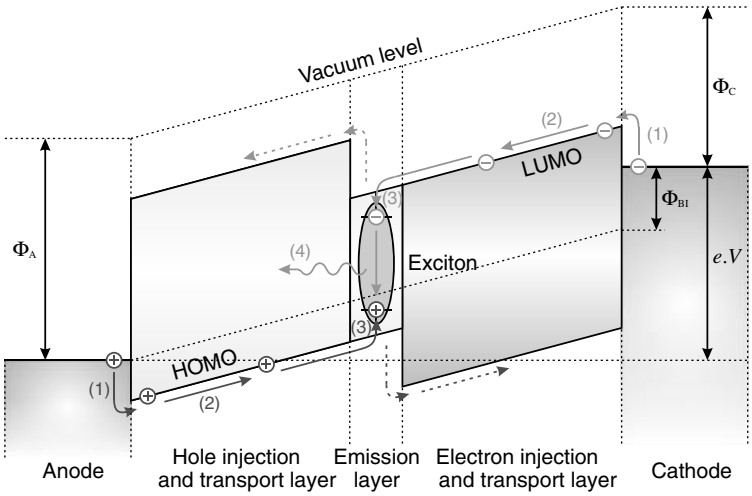

Figure 15.2 Schematic energy diagram of a three-layer OLED illustrating the basic processes of electroluminescence. Electrons are injected from the cathode into the LUMO of the ETL, while holes are injected from the anode into the HOMO of the HTL. Since the anode and cathode have different work functions Φ_A and Φ_C, respectively, a built-in voltage Φ_{BI} exists in the device, which has to be overcome by an external voltage V before current can flow through the device. If materials are properly chosen, recombination of electrons and holes will be confined to the EML and the flow of excess carriers not recombining will be minimized. It should be noted that owing to disorder, the energy levels of all involved states are not discrete but distributed in energy, thus leading to important consequences for charge-carrier transport and recombination (for further details on this aspect, refer to Chapter 6). Furthermore, vacuum level shifts and other effects occurring at interfaces between different materials are not taken into account in this diagram (again, for a discussion of such phenomena, see Chapters 2 and 5).

arbitrary distance away from the electrodes. This is favorable because recombination near the electrodes usually causes quenching and therefore a reduction in efficiency. Furthermore, as will be discussed later in this chapter, this additional degree of freedom is a handle to improve OLEDs with respect to light outcoupling by making use of optical interference effects.

15.2.3 OLED Materials

The development of OLEDs has been enabled by and will continue to rely on the availability of tailor-made functional organic materials that can be applied to well-controlled thin films. Thus, the requirements to the materials are manifold: starting from processability and film formation, via electrical transport, to optical properties. The key factor is obviously the availability of efficient and stable light emitters in the full visible spectral range. In this respect, one has to distinguish between fluorescent and phosphorescent materials. A seminal step was the

introduction and further development of emitters based on heavy metal-centered metal–organic complexes, as shown in Figure 15.3 (see also Chapter 13). In these compounds, strong spin–orbit coupling mixes singlet and triplet states much more than in pure hydrocarbons, so that phosphorescence becomes an allowed transition [14]. In the meantime, impressive efficiency data have been published for OLEDs

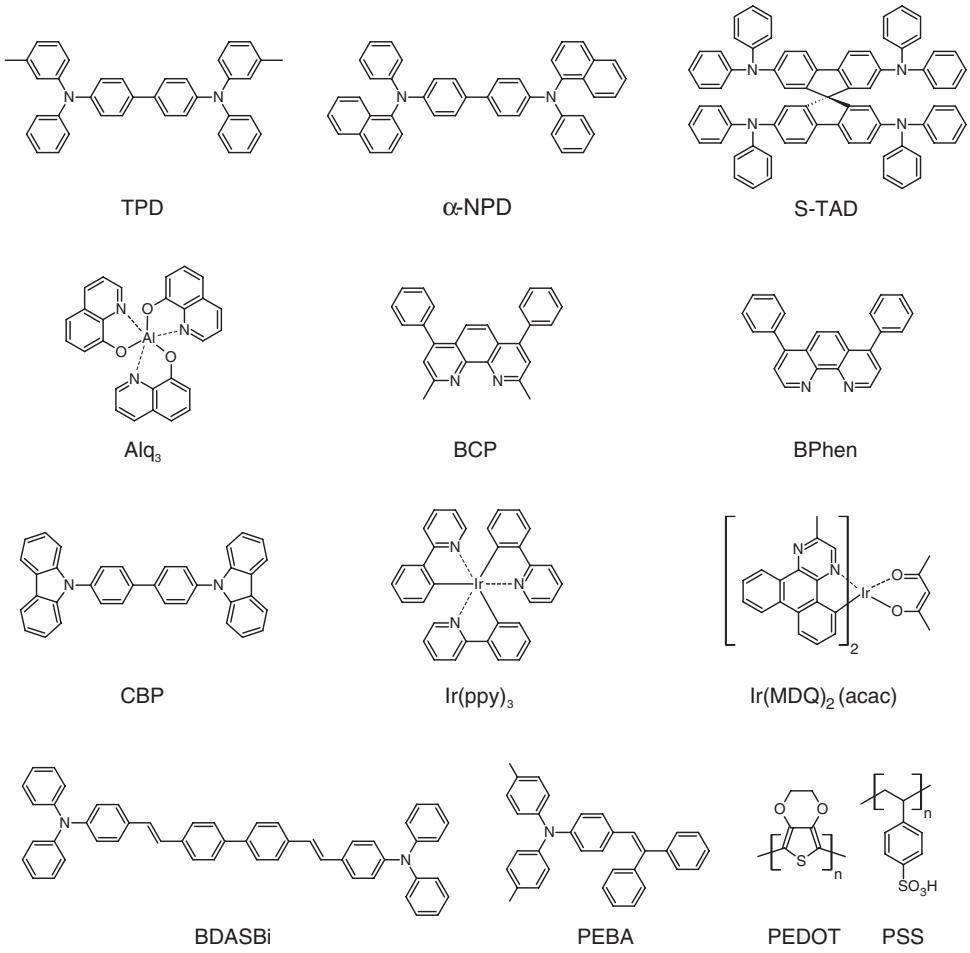

Figure 15.3 Selection of organic materials used for OLEDs that are discussed in this chapter. TPD, α-NPD, and S-TAD are hole transport materials. Alq_3, BCP, and BPhen are electron transport materials, with Alq_3 often being used as green fluorescent emitter material. CBP serves as matrix material for the green phosphorescent emitter $Ir(ppy)_3$ or the two blue fluorescent emitters BDASBi and PEBA. The red phosphorescent emitter $Ir(MDQ)_2(acac)$ is doped into an α-NPD host layer. PEDOT:PSS is a conducting polymer that can be used as hole injection layer, because it effectively increases the work function of ITO and serves as a planarization layer.

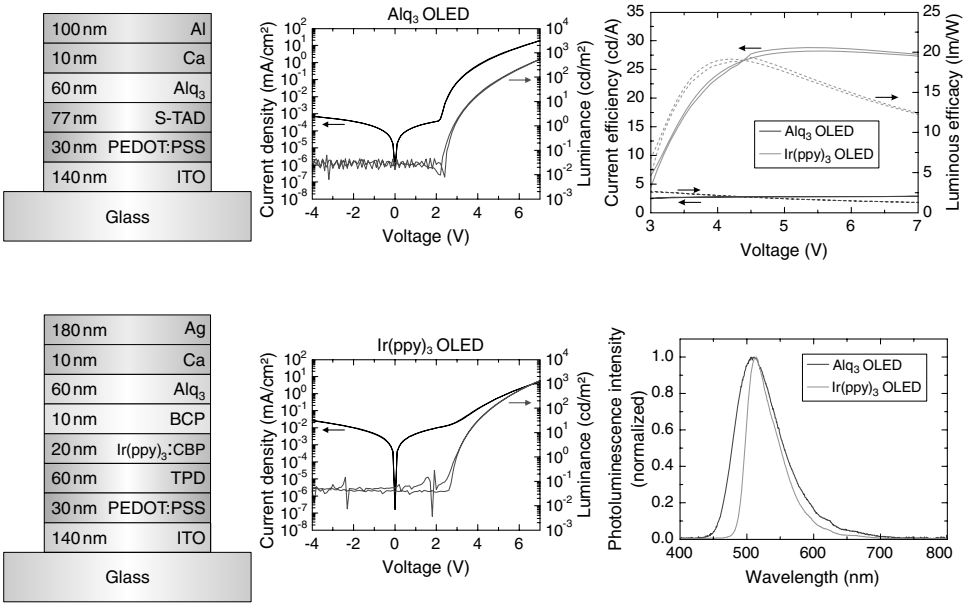

Figure 15.4 Layer structures of two prototypical OLEDs with Alq_3 as fluorescent and $Ir(ppy)_3$ as phosphorescent green emitters, respectively. Also shown are their current–voltage–luminance characteristics as well as their electroluminescence emission spectra and their efficiency.

based on these materials [15], however, the bottleneck is still the limited availability and stability of deep blue phosphorescent emitters.

A selection of common organic materials that were used for fabricating OLEDs in our group are displayed in Figure 15.3. Figure 15.4 shows electroluminescence characteristics of two prototypical OLEDs, one with the fluorescent emitter Alq_3 and the other one with the phosphorescent material $Ir(ppy)_3$. Both will serve as reference devices throughout this chapter.

15.2.4 White OLEDs

One of the peculiarities of organic emitters is their intrinsically broad luminescence spectrum. By the combination of several organic emitters with different emission colors, it is possible to generate light spreading over the whole visible spectral range, thus having an excellent color-rendering index (CRI), that is, the ability to reproduce the color of illuminated objects. There are several methods in order to create such white OLEDs. The first report dates back to 1994, when a Japanese group combined red, green, and blue (RGB) laser dyes in a common matrix and achieved light emission over a broad spectral range [16]. Despite its simplicity in preparation, achieving white light emission with good and stable color

quality in this way is not that straightforward, because charge recombination and energy transfer processes between the different dyes need to be well controlled. Thus, it is nowadays more common to employ distinct emission layers for RGB that can either be directly stacked on top of each other in one OLED (Figure 15.1) or in three separated OLEDs – one for each color – that are in turn vertically stacked by optically transparent electrical interconnecting units. In addition, white light from OLEDs may be produced similar to inorganic LEDs, that is, by combining a blue OLED with either red and green or yellow color conversion layers [17]. Depending on the method and the choice of materials, it is thus possible to cover a large variety of colors and color temperatures within the CIE 1931 color space (*Commission internationale de l'éclairage*). Further details about different concepts of white OLEDs and the current state of the art can be found in Refs [8–10].

15.3
Electroluminescence Quantum Efficiency

15.3.1
Factors Determining the EQE

Apart from its spectral characteristics, the most important parameter characterizing an OLED is the external electroluminescence quantum efficiency (EQE) that describes the ratio between the number of emitted photons and injected charge carriers [18]:

$$\eta_{\mathrm{EQE}} = \gamma \cdot \eta_{\mathrm{S/T}} \cdot q_{\mathrm{eff}} \cdot \eta_{\mathrm{out}} \tag{15.1}$$

Here, γ is the charge-carrier balance factor, describing whether or not equal amounts of electrons and holes are injected and what fraction of them recombines to form an exciton. The second factor $\eta_{\mathrm{S/T}}$ gives the fraction of excitons that is allowed to decay radiatively by spin statistics. The third factor q_{eff} indicates how many of the spin-allowed excitons actually do decay by emitting a photon (instead of dissipating the excitation energy nonradiatively to their environment). Finally, the last factor η_{out} determines what fraction of the generated photons are in the end able to leave the device to the outside world. Hence, the external quantum efficiency can be split into an internal quantum efficiency $\eta_{\mathrm{IQE}} = \gamma \cdot \eta_{\mathrm{S/T}} \cdot q_{\mathrm{eff}}$ times the outcoupling factor η_{out}.

In detail (Figure 15.2), the charge-carrier balance γ depends on the numbers of electrons and holes that are injected and the fraction of them, which is consumed by recombination:

$$\gamma = \frac{j_{\mathrm{R}}}{j_{\mathrm{tot}}} \tag{15.2}$$

where $j_{\mathrm{tot}} = j_{\mathrm{h}} + j'_{\mathrm{e}} = j_{\mathrm{e}} + j'_{\mathrm{h}}$ is the total current density and $j_{\mathrm{R}} = j_{\mathrm{h}} - j'_{\mathrm{h}} = j_{\mathrm{e}} - j'_{\mathrm{e}}$ is the recombination current density. Here, $j_{\mathrm{h,e}}$ are the injected hole and electron currents, respectively, and the primed quantities are the corresponding fractions of

carriers leaving the device at the opposite electrode without recombination. Under ideal conditions, the latter will be zero and consequently $\gamma = 1$. However, if there is an imbalance in the numbers of injected electrons and holes or if recombination is not complete, then there is excess of charge carriers that does not contribute to the production of light, and the efficiency of the OLED is reduced. In small-molecule multilayer OLEDs, the charge-carrier balance can be brought close to unity by using doped transport layers and additional selective carrier- and exciton-blocking layers [13, 19].

The so-called singlet/triplet factor $\eta_{S/T}$ describes the probability for the formation of an exciton that is allowed to decay radiatively according to the spin selection rules. Under electrical operation, singlet and triplet excitons are formed by recombination of electrons and holes, each of them carrying spin 1/2. The probability of forming a triplet exciton with total spin $S = 1$ is statistically three times higher than the probability of forming a singlet exciton with $S = 0$, because the spin orientations of the injected electrons and holes are random and every triplet state is threefold degenerate. Therefore, $\eta_{S/T}$ is believed to have a value of 25% for fluorescent emitters that make use of only singlet excitons, while it can be 100% for phosphorescent emitters, where both singlets and triplets contribute to light emission [20, 21].

We note that even for singlet emitters, $\eta_{S/T}$ might be enhanced beyond 25% by triplet–triplet annihilation (TTA) in certain material systems [22, 23]. In the context of conjugated polymer systems, there has been a debate whether $\eta_{S/T}$ might intrinsically be larger than 25% (even in the absence of TTA) [24–26], however, recent results indicate that this is probably not the case [27]. As will be discussed below, an unambiguous assignment requires a careful efficiency analysis, including effects of nonisotropic orientation of the light-emitting chromophores. All in all, a significant efficiency enhancement can be obtained by using phosphorescent materials; hence, $\eta_{S/T}$ can be raised to 1 [14, 28].

The effective radiative quantum efficiency q_{eff} is derived from the intrinsic radiative quantum efficiency q of the emitter material, which is obtained if the emitting species is surrounded by an unbounded medium in the limit of very low excitation densities. Usually the photoluminescence quantum efficiency measured by using a thin film of the emitter embedded in the same matrix as in the OLED comes close to this value. As per definition, q is given as

$$q = \frac{\Gamma_r}{\Gamma_r + \Gamma_{nr}} \tag{15.3}$$

where Γ_r is the radiative decay rate of the excited state and Γ_{nr} is the sum of all competing nonradiative decay rates. It is apparent that every nonradiative contribution to the exciton decay reduces the radiative quantum efficiency. In addition, in an OLED environment, the presence of stratified media with different refractive indices as well as the vicinity to metallic electrodes lead to a modification of the radiative decay rate of an exciton via the Purcell effect: $\Gamma_r \rightarrow \Gamma_r^* = F \cdot \Gamma_r$ (with F being the Purcell factor) [29–31]. In contrast, the nonradiative decay rates, for example, the dissipation of excitation energy into heat, are not affected by the cavity

environment [32]. Thus, the effective radiative quantum efficiency q_{eff} can be defined as

$$q_{\mathrm{eff}} = \frac{\Gamma_{\mathrm{r}}^{*}}{\Gamma_{\mathrm{r}}^{*} + \Gamma_{\mathrm{nr}}} = \frac{F \cdot \Gamma_{\mathrm{r}}}{F \cdot \Gamma_{\mathrm{r}} + \Gamma_{\mathrm{nr}}} \tag{15.4}$$

Depending on the details of the layer stack, the cavity effect can either increase or reduce q_{eff} with respect to the intrinsic value q. Consequently, the optimization of the OLED cavity is very important not only in terms of the light outcoupling efficiency, as will be discussed below, but also to enhance the radiative decay processes in cases where the emitter does not *a priori* have $q = 1$. And even if q is close to 1, one has to be aware that in an operating device the radiative quantum efficiency can be significantly reduced by bimolecular quenching of excitons or interactions with charge carriers at high current densities [33]. This is especially relevant for long-lived triplet excitons (triplet–triplet quenching, triplet–polaron quenching) as will be shown later on.

With the above said, the internal quantum efficiency of OLEDs can be brought toward the theoretical limit of 100%, if charge-carrier injection and recombination are well balanced, if phosphorescent emitters are used, and if nonradiative exciton quenching processes are suppressed [19]. Nevertheless, only a fraction of light will in the end be able to leave the device to the outside world. The reason is that light is generated in a region of the OLED stack with higher refractive index than the glass substrate and, obviously, ambient air. In a simple model based on ray optics, the light outcoupling efficiency is given by [34]

$$\eta_{\mathrm{out}} = \frac{1}{2n^2} \tag{15.5}$$

where n denotes the (average) refractive index of the organic layer stack. With typical values of $n = 1.6 - 1.8$, one immediately finds that only 15–20% of the optical power is actually extracted from an OLED. However, this should only be taken as a rough estimation; a more sophisticated analysis has to take the coupling of the excited molecules to the modes of the OLED cavity into account, as will be discussed in detail in the next section.

15.3.2
Luminous Efficacy

Finally, to quantify the amount of visible light reaching the observer, one has to consider the sensitivity of the human eye. The luminous flux Φ_{L} (measured in lumen (lm)) is obtained by multiplying the spectral flux of radiation Φ_{R} (measured in watt per nanometer) with the response curve of the eye ($V(\lambda)$) and integrating over the whole visible spectral range [35]:

$$\Phi_{\mathrm{L}} = K_{\mathrm{m}} \int_{400\ \mathrm{nm}}^{800\ \mathrm{nm}} V(\lambda) \cdot \Phi_{\mathrm{R}}(\lambda)\, \mathrm{d}\lambda \tag{15.6}$$

with the photopic constant $K_m = 683$ lm/W determining the maximum luminous efficacy obtainable for a monochromatic green emitter at a wavelength of 555 nm. Given the electrical drive conditions (voltage V and current I) and the luminous flux Φ_L, it is possible to calculate the luminous efficacy η_P of a light source according to [36]

$$\eta_P = \frac{\Phi_L}{V \cdot I} \tag{15.7}$$

For a Lambertian light source, where the luminous intensity $L_v(\theta)$ at an angle θ with respect to the surface normal follows $L_v(\theta) = L_0 \cdot \cos\theta$ with L_0 being the luminous intensity (also called luminance in units of cd/m^2) measured perpendicular to the surface, one obtains $\eta_P = \pi \cdot L_0/(j \cdot V)$ with j being the current density [34]. Another quantity that characterizes an OLED is the current efficiency η_L (expressed in cd/A). It is defined as the ratio between luminance and current density [36]:

$$\eta_L = \frac{L_0}{j} \tag{15.8}$$

For the OLED device characteristics shown in Figure 15.4, one obtains peak values of about 2.5 cd/A at 3 V corresponding to an EQE of a little less than 1% in the case of Alq_3 as emitter material and about 27 cd/A at 5 V corresponding to an EQE of 8% for $Ir(ppy)_3$, which is in good agreement with published results [37, 38].

15.4 Fundamentals of Light Outcoupling in OLEDs

15.4.1 Optical Loss Channels

As already mentioned above, a ray optical model can only give a rough estimate of the light extraction efficiency η_{out} of an OLED. For a more accurate treatment, wave optical methods are required, which will be addressed in this section. An excited molecule can couple to different optical modes in such a thin-film structure (Figure 15.5). Viewed from the emitter position, the light escape cone has an opening angle of some 30° with respect to the surface normal and the energy contained in it typically amounts to less than 20% of the total energy. This is followed by the contribution of substrate modes, where total internal reflection at the glass–air interface is the limiting process. This contribution is also comparable in energy at around 20%. For higher emission angles, the light cannot even reach the glass substrate, but is waveguided in the organic layers (including the transparent indium tin oxide electrode) and in the end lost by residual absorption or edge emission. Finally, the emitter can couple to the evanescent field of surface plasmon polaritons (SPP) traveling at the interface between the metal electrode and the organic layers. Quantitative calculations, treating the emitting molecules as classical electrical dipoles (for details see below), reveal that in planar OLED stacks, typically around

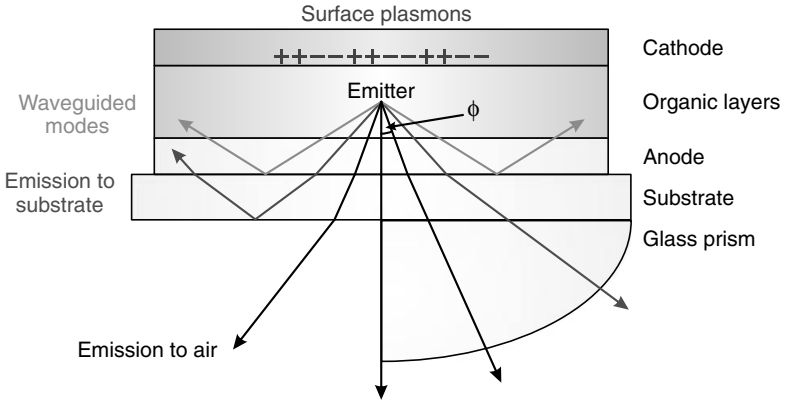

Figure 15.5 Schematic illustration of an OLED showing different optical loss channels. Without outcoupling enhancement, only a small fraction of light is directly emitted to air, as shown in the left part of the figure. By applying a macroextractor, for example, an index-matched glass hemisphere, the substrate emission can also be extracted (cf. the right part of the figure).

50% of the light is trapped in waveguided and plasmon modes [30, 39, 40]. As an example, Figure 15.6 shows the contribution of different optical channels for the prototypical Alq_3 OLED stack discussed before in Figure 15.4. Note that this chart is obtained with a radiative quantum efficiency $q = 1$. It thus describes the maximum light outcoupling of the stack under ideal conditions. The given numbers are valid regardless of whether emitter is fluorescent (e.g., Alq_3) or phosphorescent (e.g., $Ir(ppy)_3$), as long as the layer stack has comparable thicknesses and refractive indices and the emission spectra are not too different. Given the low number of directly emitted light, it is therefore not surprising that developing new concepts for improving light extraction efficiency has been a major issue over recent years (for an overview, see Ref. [41]). Some of these approaches (including our own results) will be presented in Section 15.5.

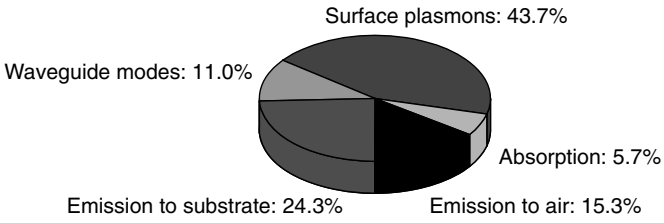

Figure 15.6 Amount of power coupled to different optical channels in the prototypical Alq_3 OLED from Figure 15.5. The numbers are obtained by integrating each region in the power dissipation spectrum shown in Figure 15.8a. In this diagram, a radiative quantum efficiency of $q = 1$ is assumed. The influence of q-values below unity is discussed in the text.

15.4.2
Optical Modeling of OLEDs

Fluorescence and phosphorescence of excited molecules are not intrinsic properties of a material, but are modified by the optical environment of the emitting species. Originally discovered for magnetic resonance, this so-called Purcell effect [42] has been found to be also relevant in experiments with fluorescent molecules near interfaces [43, 44]. After its experimental demonstration, Chance, Prock, and Silbey (CPS) developed a theoretical framework by applying the classical theory of an oscillating electrical dipole near a dielectric interface to the problem of molecules fluorescing near a surface [45, 46]. Thus, they made use of the fact that the probability for the emission of a photon by an excited molecule via a dipole transition is equivalent to the power radiated by a classical dipole antenna. The formalism has later on been extended to structures where the emitter is embedded in a layer stack with multiple interfaces [47] and to microcavity structures [48, 49].

Here, we follow the approach by Wasey and Barnes [50], where the problem of an incoherent ensemble of dipole emitters being embedded in a planar thin-film structure is solved by a plane wave expansion of the electric field with appropriate consideration of the electromagnetic boundary conditions (Figure 15.7). Formally the whole OLED stack is split into an upper and a lower half with respect to the emitter position and the propagation of radiation in both directions is calculated by taking into account the Fresnel reflection and transmission coefficients at the

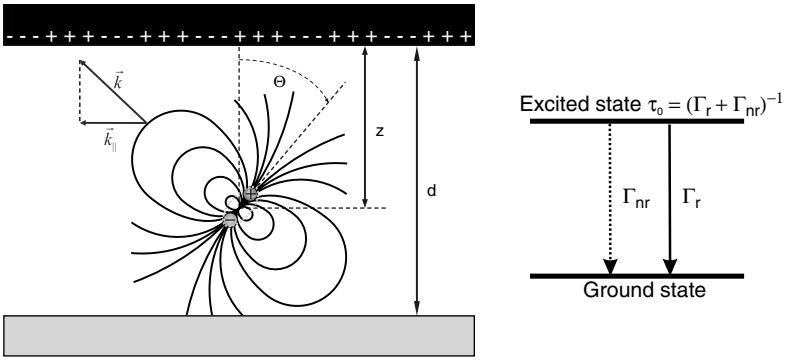

Figure 15.7 Schematic illustration of an oscillating electrical dipole embedded in a dielectric layer, which is sandwiched between two interfaces. The upper material is assumed to be a metal, so that surface plasmon polaritons are supported at this interface. The other parameters are the layer thickness d, the distance z of the dipole to the metal, its relative orientation Θ to the surface normal, the wave vector $\vec{k}$, and its in-plane component $\vec{k}_{\parallel}$. The quantum mechanical analogue is a two-level system consisting of the energy levels of the excited state of the molecule and the ground state with radiative and nonradiative decay rates between them, leading to a finite lifetime of the excited state. Note that if the dipole is embedded in a cavity, the radiative rate will be modified to become $\Gamma_r^* = F \cdot \Gamma_r$ (with F being the Purcell factor, see text) and the excited state lifetime accordingly $\tau = (\Gamma_r^* + \Gamma_{nr})^{-1}$.

involved interfaces. Key parameters entering into the model are the position (z) of the emitter with respect to interfaces (in particular, the highly reflective cathode in bottom-emitting structures), the emitter orientation (Θ), the thicknesses (d) and optical constants (refractive index n, extinction coefficient κ) of all involved layers, and the intrinsic radiative quantum efficiency (q) of the emitter (often embedded in a matrix material). The presence of the OLED cavity now has a twofold effect on the properties of light emission with respect to the case when the emitter resides in an infinite medium with the same index of refraction: It will modify the radiative decay rate of the emitter (thus leading to an effective radiative quantum efficiency q_{eff} in Eq. (15.1)) and it will redistribute the optical power between different channels (thus determining the light outcoupling factor η_{out}).

According to Ref. [50], the relative decay rate (Γ/Γ_0) of an ensemble of isotropically oriented and mutually incoherent dipoles emitting at a single wavelength λ takes the following form:

$$\tilde{P} = \frac{\Gamma}{\Gamma_0} = (1-q) + q \cdot \int_0^{\infty} P(k_{\parallel}, \lambda, z)\mathrm{d}k_{\parallel} \tag{15.9}$$

Here, $\Gamma = \Gamma_{\mathrm{r}}^{*} + \Gamma_{\mathrm{nr}}$ is the decay rate of the emitter modified by the presence of the cavity, $\Gamma_0 = \Gamma_{\mathrm{r}} + \Gamma_{\mathrm{nr}}$ is the original decay rate without a cavity, q is the intrinsic radiative quantum efficiency (again for the emitter in a homogeneous unbounded medium), and P is the layer-specific power dissipation function depending on the in-plane wave vector $k_{\parallel}$, the wavelength λ, and the emitter position within the layer stack denoted by z. For the sake of simplicity, we will always use a discrete emitter position, that is, an infinitely sharp recombination zone inside the OLED. This assumption is not so far from reality for small-molecule OLEDs, where the exciton formation zone is confined by using a thin dye-doped emission layer surrounded by selective carrier-blocking layers. It is, however, quite straightforward to extend the formalism to an extended emission zone by introducing some distribution function in z and averaging over all emitter positions [12, 51]. The same holds for the emitter orientation. The calculation is actually performed for the three fundamentally different dipole orientations:

- $P_{\perp,\mathrm{TM}}$: Dipoles oriented perpendicular to the substrate plane (vertical), which emit p-polarized (transverse magnetic (TM)) light.
- $P_{\parallel,\mathrm{TM}}$: Dipoles oriented parallel to the substrate plane (horizontal), which emit p-polarized (transverse magnetic) light.
- $P_{\parallel,\mathrm{TE}}$: Dipoles oriented parallel to the substrate plane (horizontal), which emit s-polarized (transverse electric (TE)) light.

For symmetry reasons, the contributions of the two horizontal dipole components are equal, so that in the case of a random distribution of dipole orientations P is given as $P_{(\mathrm{iso})} = 1/3P_{\perp} + 2/3P_{\parallel}$. If not otherwise stated, we will in the following assume isotropic emitter orientation. The effect of nonisotropic orientation on the light outcoupling efficiency will be discussed separately at the end of Section 15.5.

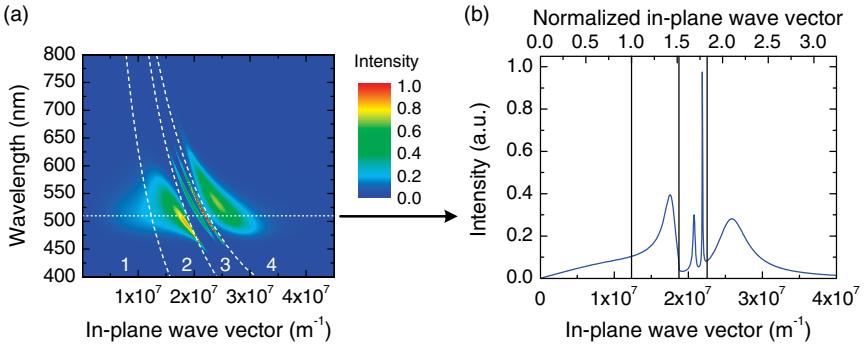

Figure 15.8 (a) Simulation of the total dissipated optical power for the Alq_3 OLED shown in Figure 15.4. The emitter position is assumed at the interface between Alq_3 and S-TAD. The result is shown for an isotropic dipole orientation. Red and yellow areas indicate a high amount of dissipated power. The dashed white lines divide the graph into four regions: (1) emission into air, (2) emission into substrate, (3) waveguide modes, and (4) coupling to surface plasmons. (b) Cross section of (a) at a wavelength of 510 nm, that is, at the emission maximum. The upper axis shows the normalized in-plane wave vector with respect to the vacuum wave vector at a wavelength of 510 nm. See also Ref. [30].

Figure 15.8 shows the power dissipation spectrum corresponding to the prototypical OLED stack shown in Figure 15.4, where the emission is assumed to take place in Alq_3 directly at the interface to the HTL. Furthermore, we have used a hypothetical radiative quantum efficiency $q = 1$ and weighted the simulation results for different wavelengths between 400 and 800 nm with the normalized photoluminescence spectrum $S(\lambda)$ of the emitter. Also shown in the figure is a cross section at a wavelength of 510 nm, where the different optical loss channels can be clearly identified.

According to Eq. (15.9), this power dissipation spectrum can now be used to calculate the total relative decay rate by integrating over all relevant wavelengths (between $\lambda_1 = 400$ nm and $\lambda_2 = 800$ nm) and in-plane wave vectors:

$$\tilde{P}_{\text{tot}} = \frac{\Gamma}{\Gamma_0} = (1-q) + q \cdot \int_{\lambda_1}^{\lambda_2} S(\lambda) \int_0^{\infty} P(k_{\parallel}, \lambda, z) \mathrm{d}k_{\parallel} \mathrm{d}\lambda \equiv (1-q) + q \cdot F \tag{15.10}$$

The latter equivalence follows from the definition of the decay rates in free space $\Gamma_0 = \Gamma_r + \Gamma_{nr}$ and inside the cavity $\Gamma = \Gamma_r^* + \Gamma_{nr} = F \cdot \Gamma_r + \Gamma_{nr}$. Thus, the integral of the spectrally weighted power dissipation directly yields the Purcell factor F. With that, the effective radiative quantum efficiency of the emitter in the OLED cavity is given by

$$\frac{q_{\text{eff}}}{q} = \frac{F \cdot (\Gamma_r + \Gamma_{nr})}{F \cdot \Gamma_r + \Gamma_{nr}} = F \cdot \frac{\Gamma_0}{\Gamma} = \frac{F}{(1-q) + q \cdot F} \tag{15.11}$$

Of course, this concept is equally valid for nonisotropic emitter orientation, if the calculation of the Purcell factor is performed by taking deviations from randomness into account. For details, refer to Ref. [52].

We note that in this terminology, the coupling of the excited molecules to modes of the cavity that do *a priori* not radiate into the far-field, such as waveguide modes or surface plasmons, are radiative processes, since they contribute to F and thus change the radiative emission rate Γ_r. (Also note that in practice the integration over $k_\parallel$ is only carried out up to a finite cutoff value, where the contribution of surface plasmons has decayed to sufficiently small values – in most cases at around $4 \times 10^7\ \mathrm{m}^{-1}$.)

The simulated power dissipation spectrum can furthermore be used to calculate the fraction of power of the dipole that goes into different optical channels as discussed in the previous section:

$$\tilde{P}_{\mathrm{mode}} = q \cdot \int_{\lambda_1}^{\lambda_2} S(\lambda) \int_{k_l}^{k_u} P(k_\parallel, \lambda, z)\mathrm{d}k_\parallel \mathrm{d}\lambda \tag{15.12}$$

with suitable lower (k_l) and upper (k_u) integration limits for each channel. For this purpose, the spectrum shown in Figure 15.8 has to be subdivided into different regions according to the allowed range of the in-plane wave vector of the radiation to be able to couple to distinct optical modes. For example, for direct emission into air ($\tilde{P}_{\mathrm{air}}$), the in-plane wave vector must satisfy the condition $0 \leq k_\parallel \leq (n_{\mathrm{air}} \cdot k_0)$ where $k_0 = 2\pi/\lambda$ is the vacuum wave vector at a given wavelength λ. In addition, in this case transmission losses are also included in the calculation. Finally, by dividing the power contribution of the air mode by the total power dissipation, one arrives at

$$q_{\mathrm{eff}} \cdot \eta_{\mathrm{out}} = \frac{\tilde{P}_{\mathrm{air}}}{\tilde{P}_{\mathrm{tot}}} \tag{15.13}$$

from which the outcoupling factor (for direct emission to air) is easily obtained, if q_{eff} is known from Eq. (15.11).

As an example, Figure 15.6 shows a pie chart of the different fractions of power to which the emitting molecules in a prototypical OLED dissipate their excitation energy. Obviously, the aforementioned $1/(2n^2)$ estimation based on ray optics is not that far from the calculated value of about 15% for the air mode. However, this is due to the fact that the distance of the emitter to the cathode was chosen not too far from the values favorable for light outcoupling (see also Figure 15.12). As will be shown below, this number can vary strongly if the spacing between the emitter and a metallic electrode is varied. It is further evident from this chart that the amount of light that is accessible directly and via substrate light extraction is limited to about 40% in this particular OLED stack. The biggest loss is the coupling to surface plasmons, amounting to more than 40% of the total power.

In order to verify simulation results with experimental data, one can on the one hand use measured EQE values (without and with a macroextractor attached to the glass substrate), which is an angle-integrated quantity. However, as expressed in

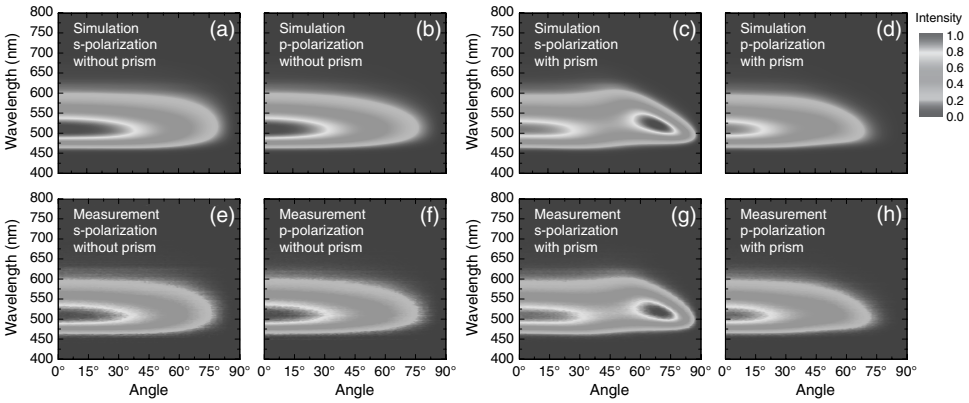

Figure 15.9 Simulation (a–d) and measurement (e–h) of the spectrally resolved angle-dependent emission of the Alq_3 OLED in the case of s- and p-polarized light. Left half is data for the planar OLED, while right half shows the results for an index-matched fused silica half-cylinder prism attached as a macroextractor to the glass substrate. See also Ref. [30].

Eq. (15.1), η_{EQE} is a product of four factors so that additional assumptions are necessary. On the other hand, one can also use angular and polarization-dependent emission spectra containing much more information. Figures 15.9 and 15.10 show a comparison of measured and simulated spectra where all observed features (in particular, the appearance of an s-polarized substrate mode) are well reproduced. Moreover, a detailed analysis of the angular emission spectra allows to recalibrate the layer thicknesses of the OLED stack (as shown in Figure 15.10) and to determine the spatial extent of the emission profile as well as the orientational distribution of the transition dipole moments, which is particularly important in polymer OLEDs [12, 51, 53, 54].

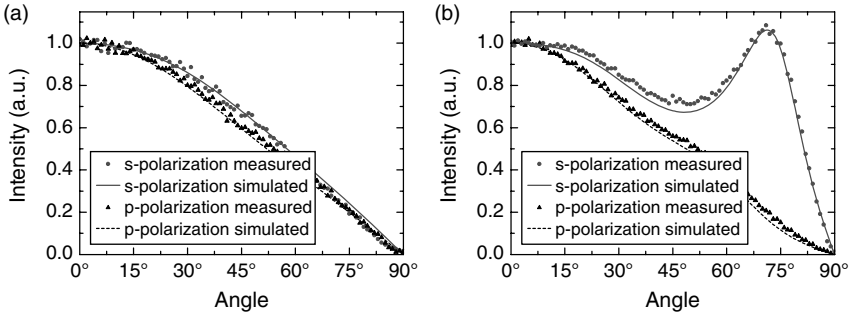

Figure 15.10 Cross section at a wavelength of 510 nm of the s- and p-polarized angle-dependent measurement and simulation of Figure 15.9. (a) Direct emission to air. (b) Emission with attached macroextractor. Best agreement is obtained with layer thicknesses of 60 nm for Alq_3 and 77 nm for S-TAD, as given in Figure 15.4.

15.4.3
Simulation-Based Optimization of OLED Layer Stacks

The real benefit of optical simulations is to study and optimize OLED stacks without the need for elaborate and time-consuming experiments. In this section, the prototypical Alq_3 OLED introduced in Section 15.2 will be investigated in terms of thickness variations of the electron transport layer (ETL) and hole transport layer. This basically corresponds to a variation of the distance between the emitter position and the interfaces to the metallic electrode and the glass substrate. Thus, the cavity will be strongly modified, which results in changes of the outcoupling efficiency into air and into the substrate. We will assume a radiative quantum efficiency of $q = 1$ in this example. Thus, variations of the cavity environment will only affect the light outcoupling factor η_{out}; the effect on q will be discussed separately in the next section.

Figure 15.11 shows how the fraction of power that is dissipated into different optical modes varies as a function of the ETL thickness in the prototypical Alq_3 OLED. Oscillations are clearly observable for direct emission into air and for substrate emission. As the distance increases, the strength of the oscillations decreases because the intensity of the dipole radiation field weakens with increasing distance from the dipole, thus the strength of the reflected field will also be decreased [49]. It is noteworthy that the optimum for extraction to air is not in the first cavity maximum at about 75 nm ETL thickness but in the second antinode at about 220 nm (in agreement with similar results by Lin *et al.* [55]; for further details, see Chapter 16). However, if the contribution of both the direct and the substrate emission are considered, that is, if substrate light extraction enhancement tools are used, then the optimum ETL thickness will be at about 90 nm.

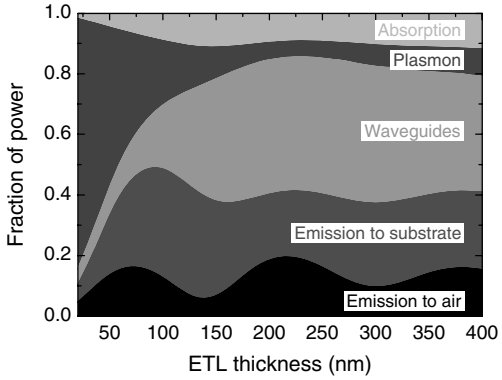

Figure 15.11 Amount of power coupled to different optical channels for the Alq_3 OLED as depicted in Figure 15.4 in dependence of the electron transport layer (Alq_3) thickness assuming a radiative quantum efficiency of $q = 1$. The simulation was performed polychromatically according to the emission spectrum of Alq_3. See also Ref. [30].

Power dissipation to waveguide modes and surface plasmons shows a quite different progression. Coupling to waveguides is very low for small ETL thicknesses, but it is strongly enhanced with increasing thickness. This can be explained by the fact that there is a lower limit for the thickness of an asymmetric waveguide before a waveguide mode can exist. Above this limit, an increasing number of modes are supported for larger thicknesses. In contrast, power dissipation to SPPs is strongest for a small ETL thickness, that is, if the emitter is positioned close to the metallic cathode. This is obvious, because SPPs are evanescent waves that are only excited if the dipole couples to the metal in the near-field. This contribution is reduced with increasing distance of the dipole to the metal. It should be noted that the simulation does not differentiate between coupling to surface plasmons and nonradiative energy transfer to lossy surface waves, that is, luminescence quenching at the metal, which especially dominates for very small distances below about 25 nm and significantly reduces the efficiency [31, 49, 56].

Further optimization of the OLED layer stack is possible if both the ETL and HTL are systematically varied in thickness, as shown in Figure 15.12. For the sake of simplicity, these simulations have been carried out at a single wavelength of 510 nm only (in the emission maximum of Alq_3). It is again found that changing the ETL thickness has the strongest impact on EQE as the distance to the cathode is the main determining factor for interference effects. Moreover, reducing the HTL thickness (or in practice the ITO thickness) will lead to a further improvement of the efficiency [57].

As a result, modifying the cavity environment of the emitting molecules allows optimizing the light outcoupling of an OLED. Nevertheless, coupling to both

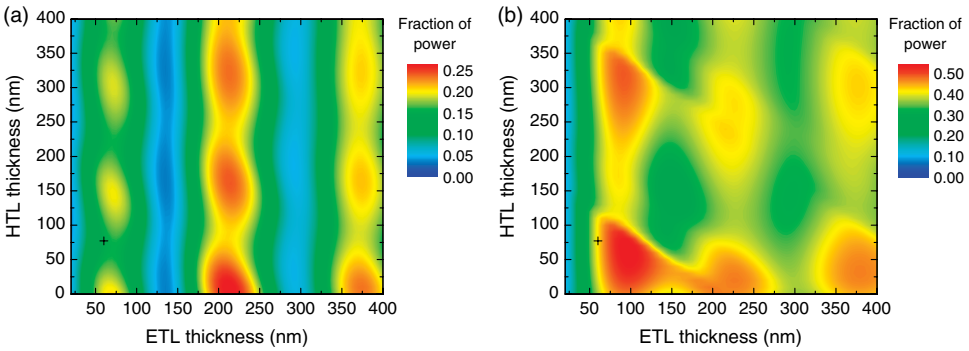

Figure 15.12 Optical power coupled directly into air (a) and into the glass substrate for an applied macroextractor (b) in dependence of the electron and hole transport layer thicknesses. The stack consists of a glass substrate, 140 nm ITO, 30 nm PEDOT:PSS, varying thicknesses of S-TAD (HTL) and Alq_3 (ETL), 10 nm Ca, and 100 nm Al. The position of the prototypical OLED stack used in this work (cf. Figure 15.4) is marked by a cross in the diagram. The simulations were performed at a single wavelength of 510 nm, that is, close to the emission maximum of Alq_3. The ETL and HTL thicknesses were varied in steps of 5 and 10 nm, respectively. A radiative quantum efficiency of $q = 1$ was assumed.

surface plasmons and waveguide modes causes combined losses of around 50% of the total available power – almost independent of the chosen thickness. Therefore, it is inevitable to either reduce coupling to these unfavorable loss channels or at least to partially recover some of the dissipated energy in order to develop highly efficient OLEDs. For this reason, we will later on present several promising approaches.

15.4.4 Influence of the Emitter Quantum Efficiency

In the discussion so far, we have assumed that the intrinsic radiative quantum efficiency q of the emitter material is equal to one. In real OLEDs, however, and in particular in the considered prototypical Alq_3 OLED, this quantity is often significantly less than unity. According to the above said, the cavity environment will then modify not only the light outcoupling factor η_{out} but also the overall decay rate and thus lead to an effective radiative quantum efficiency q_{eff} (Eq. (15.11)). Figure 15.13 shows the effect on q_{eff} of the distance of Alq_3 emitter molecules with $q = 0.2$ to the cathode in the prototypical OLED given in Figure 15.4 [30]. It is found that q_{eff} oscillates around the value of q and reaches the true value only asymptotically for very large distances. For small distances (less than about 120 nm), however, q_{eff} strongly increases due to constructive interference, but most importantly due to coupling to SPPs at the metal–organic interface. We note that for distances less than about 25 nm, the radiative quantum efficiency should strongly decrease again due to nonradiative energy transfer to the metal and subsequent quenching of the excitation [46, 49, 56], which is not distinguished for SPPs in our analysis.

The consequences for the efficiency of OLEDs with emitters having $q \ll 1$ are manifest. Due to the enhancement of q_{eff} for smaller distances to the metal cathode, the first cavity maximum will gain in power relative to the second one, where

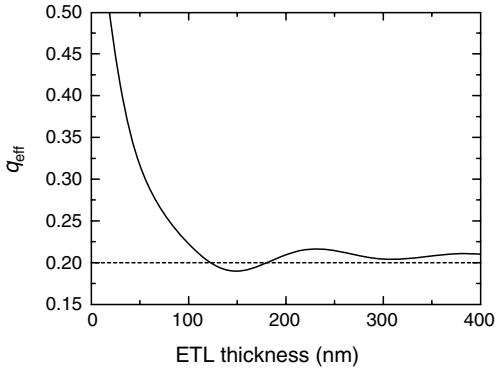

Figure 15.13 Variation of q_{eff} with the distance of the emitting dipoles to the cathode in the prototypical OLED given in Figure 15.4. The emission layer is assumed to be an infinitely thin sheet of Alq_3 molecules with $q = 0.2$ residing immediately at the Alq_3/S-TAD interface. See also Ref. [30].

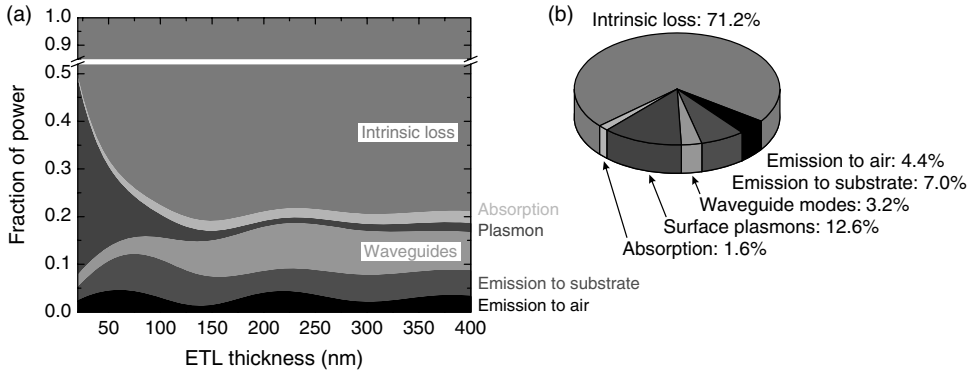

Figure 15.14 Amount of power coupled to different optical channels as in Figure 15.11 in dependence of the electron transport layer (Alq_3) thickness assuming a radiative quantum efficiency of $q = 0.2$. Also shown is a pie chart of the different fractions of power for an Alq_3 thickness of 60 nm. See also Ref. [40].

the cavity effect on the radiative rate is much weaker. This is directly observable in Figure 15.14, where the dissipation of power to different optical channels is shown for the same prototypical Alq_3 OLED stack as before (Figure 15.11), but now with a realistic value of $q = 0.2$ [40]. As expected, the biggest loss is now due to intrinsic nonradiative exciton decay; however, for both direct emission to air and emission to substrate, the optimum thickness is at the first cavity maximum below 100 nm distance to the cathode. It is also worth noting that the fraction of power that can be coupled out of the device is significantly more than what would be expected by taking the simulation for $q = 1$ and simply multiplying with the lower q-value 0.2. Thus, the correct value of q_{eff} is essential for making reliable OLED efficiency predictions according to Eq. (15.1).

15.4.5
Comprehensive Efficiency Analysis of OLEDs

As outlined in the previous section, the knowledge of the intrinsic radiative quantum efficiency is of paramount importance for OLED optimization, in particular for designing the optimum layer stack. In many cases, however, this information is not available or the value of q is taken from photoluminescence measurements performed on films fabricated under quite different conditions than an OLED. Furthermore, in an operating OLED, the excitation profile is usually different than in an optical experiment and excitons can be quenched at interfaces or due to interactions with other excited molecules or charge carriers residing in the emission layer. Thus, a method for the determination of q applicable directly in an OLED environment or even in an operating OLED will give the most direct information on the value of the radiative quantum efficiency [58]. We have recently shown that the above-described variation of the distance between the emitter and a metal electrode,

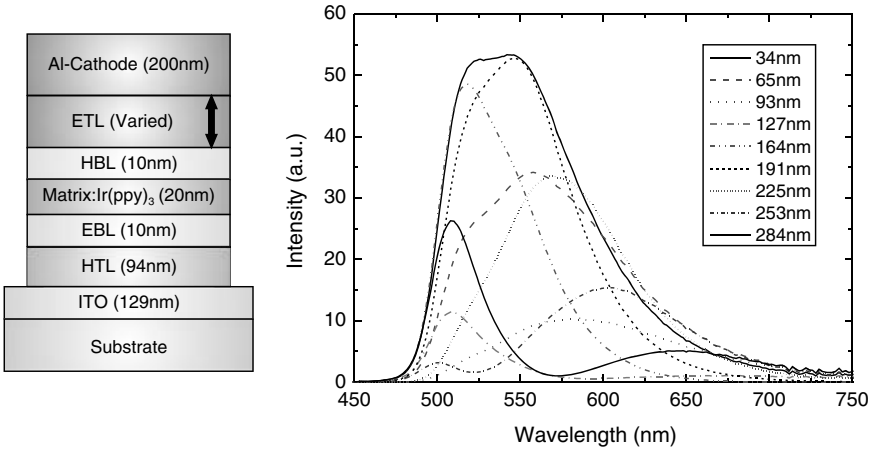

Figure 15.15 Green phosphorescent OLED stack with $Ir(ppy)_3$ as emitter, where the ETL thickness is systematically varied. Simulated emission spectra show both spectral and intensity changes, indicating strong effects of the variation of the optical cavity, while the electrical characteristics (not shown) are not affected. See also Ref. [59].

which changes the optical environment most significantly, can be performed in real OLEDs without changing the electrical properties, provided that a doped electron transport layer is used [29, 59].

In order to prove the feasibility of this approach, a green phosphorescent OLED based on $Ir(ppy)_3$ as emitter was chosen (Figure 15.15) (for details, refer to Ref. [59]). Photoluminescence lifetime measurements were performed on a variety of OLED stacks with different ETL thickness. As shown in Figure 15.16, the

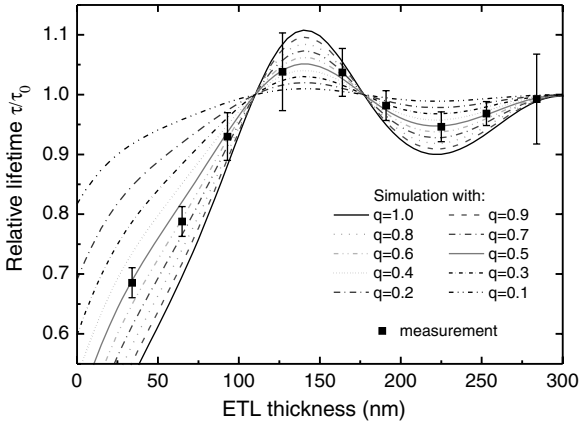

Figure 15.16 Experimentally determined phosphorescence lifetimes of $Ir(ppy)_3$ in OLED stacks with different ETL thickness, as shown in Figure 15.15. The lines are simulations for the given stacks with different values of the intrinsic radiative quantum efficiency *q*. See also Ref. [59].

phosphorescence lifetime of $Ir(ppy)_3$ is not constant, but varies with the ETL thickness. This directly reflects the influence of the optical cavity on the radiative decay rate of the emitter. With the above-presented optical modeling, a quantitative analysis is now possible. Recall that the measured PL lifetime τ in the presence of a cavity is given by $\tau = \Gamma^{-1} = (\Gamma_r^* + \Gamma_{nr})^{-1}$ and in the absence of the cavity by $\tau_0 = \Gamma_0^{-1} = (\Gamma_r + \Gamma_{nr})^{-1}$. Thus, according to Eq. (15.10), the ratio between these two values depends only on the cavity enhancement factor F and the intrinsic radiative quantum efficiency of the emitter q, but is independent of the light outcoupling factor:

$$\frac{\tau}{\tau_0} = \frac{\Gamma_0}{\Gamma} = [(1-q) + q \cdot F]^{-1} \tag{15.14}$$

As F is obtained independently from simulation for each of the used OLED stacks with different ETL thicknesses, the two free parameters q and τ_0 are easily determined by comparing measured lifetime data with simulation results. As shown in Figure 15.16, the best agreement is obtained with $q_{(PL)} = 0.5 \pm 0.1$ and an intrinsic phosphorescence lifetime $\tau_0 \approx 700$ ns. Remarkably, the value of the quantum efficiency is significantly less than unity. Thus, care should be taken when published IQE values for the emitter $Ir(ppy)_3$ [38] are generalized to other OLED stacks containing this emitter. q should rather be considered as an OLED stack-specific quantity, depending, for example, on the type of matrix material for the emitting dye or the materials in the immediate vicinity of the emission layer.

The same series of OLEDs with systematic variation of the ETL thickness can now be used for the determination of the radiative quantum efficiency $q_{(EL)}$ under electrical operation, which need not necessarily be identical to $q_{(PL)}$ as will be seen below. For this purpose, the EQE of the complete series of OLEDs was measured in an integrating sphere, once without any substrate modification and once with an index-matched hemispherical lens attached to the glass substrate to extract all the substrate modes. Both measurements were performed for various current densities to investigate possible effects of exciton quenching with increasing currents. Again, the experimental results can nicely be reproduced by optical simulation as shown in Figure 15.17 with q being the only free parameter. As demonstrated in Ref. [59], the charge balance factor γ can thereby be assumed to be close to unity. The analysis now allows extracting the radiative quantum efficiency $q_{(EL)}$ at each current density, as shown in Figure 15.18. It is evident that only in the limit of very small currents, $q_{(PL)}$ and $q_{(EL)}$ take almost the same value of 0.5; however, with increasing current density, $q_{(EL)}$ rapidly decreases and may only be some 20% in the range where OLEDs are typically operated for lighting applications. Thus, one has to conclude that for simulation-based optimization of OLEDs, that is, the question whether the emitter should be placed in the first or second cavity maximum, not only the radiative quantum efficiency q in the limit of low excitation densities has to be known but also its value under realistic operating conditions.

Finally, a comprehensive efficiency analysis of OLEDs has to include the investigation of the radiation pattern, that is, the angular and polarization-dependent emission spectra as mentioned before, to obtain information about the emitter

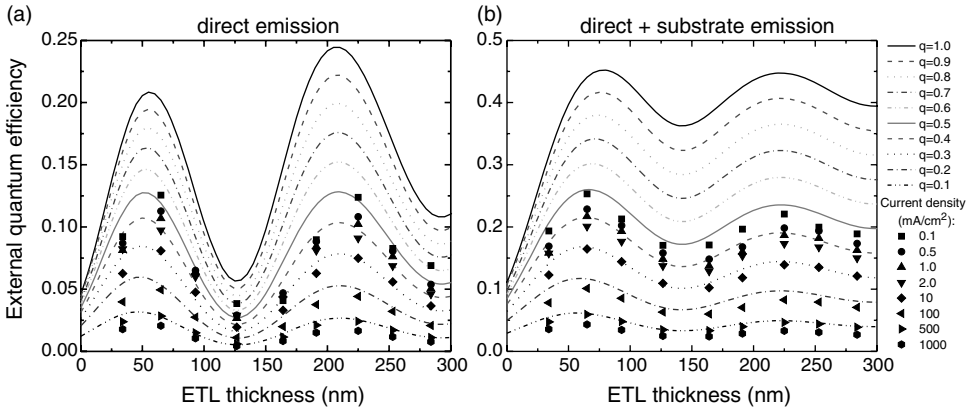

Figure 15.17 Experimentally determined external quantum efficiencies of OLED stacks with different ETL thicknesses, as shown in Figure 15.15 – (a) direct emission to air; (b) values obtained with a macroextractor. The lines are simulations for the given stacks with different values of the intrinsic radiative quantum efficiency *q*. See also Ref. [59].

orientation [53, 54] and the spatial extent of the emission zone [12, 51]. We have performed this analysis for the series of $Ir(ppy)_3$ OLEDs (not shown here) and found no evidence for a nonisotropic emitter orientation of $Ir(ppy)_3$ as well as good agreement with the assumption of a sharply localized emission zone in the middle of the only 10 nm wide EML [59]. We will later on come back to the issue of nonisotropic emitter orientation when rodlike dyes (e.g., BDASBi) [60] or

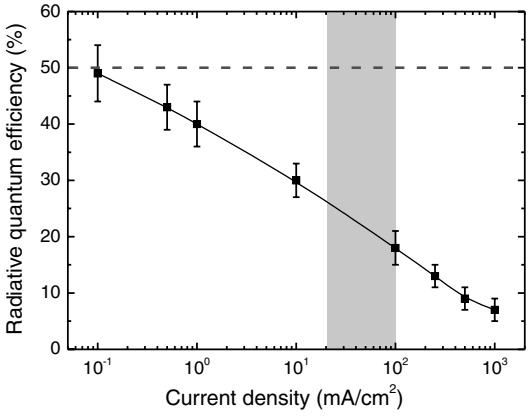

Figure 15.18 Dependence of the extracted radiative quantum efficiency from Figure 15.17 as a function of the driving current of the OLEDs. The horizontal dashed line corresponds to a *q*-value of 0.5 determined from photoluminescence measurements; the vertical shaded area indicates the typical drive conditions for OLEDs in lighting applications. See also Ref. [59].

asymmetrically substituted metal–organic complexes (e.g., $Ir(MDQ)_2(acac)$) [52, 61] are used as emitters.

15.5 Approaches to Improved Light Outcoupling

15.5.1 Overview of Different Techniques

As shown above, in planar bottom-emitting OLEDs, typically around 50% of the generated light is trapped in waveguided and surface plasmon modes and only a fraction of about 20% of it is directly radiated into air. In Section 15.4, we have already made use of the fact that light captured in the glass substrate can be fully extracted if an index-matched macroscopic lens is used and if the active pixel area is not too large. However, if the unique form factor (thin and flat) is to be preserved, this method is not practicable in large area devices. Thus, the development of new concepts for improving light extraction efficiency has been a major issue over recent years (for reviews, see Refs [41, 62]).

The different approaches can roughly be distinguished into techniques staying with planar structures and others utilizing scattering methods [63, 64]. Among the former ones are approaches toward further optimization of the OLED cavity, that is, modifications of the layer stack with respect to thicknesses, refractive indices, or reflectivity. A relatively simple method is to place the emission zone in the second antinode of the interference pattern relative to the cathode [55] and thus reduce the coupling to SPPs. As discussed before, however, this will be beneficial only if the radiative quantum efficiency of the emitter is very high; otherwise, the emitter will experience a stronger enhancement of its radiative rate when placed in the first cavity maximum. Alternatively, the excitation of SPPs can be completely avoided if metal-free OLEDs are used [65], but there is usually no overall gain in light outcoupling since the reduction of SPP losses is mostly at the expense of enhanced waveguiding [40].

Another way of boosting the direct emission to air is the use of microcavity structures, that is, OLEDs with two (partially) reflecting electrodes, where the radiation is directed more toward small angles with respect to the surface normal. This can be achieved, for example, by (aperiodic) dielectric Bragg reflectors placed underneath the ITO electrode [66] or in top-emitting devices with a highly reflective anode on glass and a semitransparent metallic cathode, often followed by a dielectric capping layer as antireflection coating [67–69]. Though very high EQE values close to 30% have recently been published for a red phosphorescent top-emitting OLED [70], these structures usually have non-Lambertian emission characteristics with nonnegligible spectral shifts as a function of the viewing angle. We also want to note that in case of particular red phosphorescent dye $Ir(MDQ)_2(acac)$ used in Ref. [70], nonisotropic emitter orientation might at least partially contribute to the high EQE values as will be discussed below [52, 61].

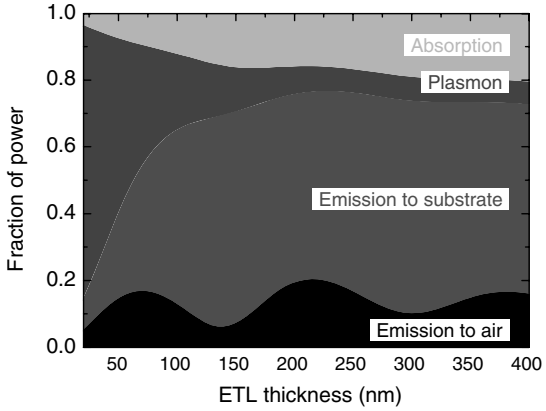

Figure 15.19 Amount of power coupled to different optical channels in dependence of the electron transport layer thickness for the Alq_3 OLED, as depicted in Figure 15.4, but now with a high-index substrate (SF6 glass with $n = 1.82$). The simulation was performed polychromatically according to the emission spectrum of Alq_3, and a radiative quantum efficiency of $q = 1$ was assumed.

A third method where the planar layer structure is preserved lies in matching the refractive indices of the emission layer, where the light is generated, and the outside world, either by bringing the refractive index of the EML down to one or by using a high-index (HI) substrate. Simulations show that if the refractive index of the EML could be reduced to $n = 1$, a theoretical limit of almost 70% direct emission to air would be possible [71]. An experimental realization might be difficult simply because no such materials are available, but lowering n_{EML} below the value of glass would bring an enormous boost in EQE.

The use of glass substrates with higher refractive index than the organic layers (including ITO) is possible [72, 73]. Simulations for the prototypical Alq_3 OLED demonstrate (Figure 15.19) that in this way all the light from waveguided modes goes into the HI glass substrate from where it can be extracted more easily. Combining HI substrates with a macroextractor (an index-matched lens) record EQEs in excess of 40% have been achieved in this way [15, 74]. Nevertheless, one has to be aware that HI glass substrates would increase the overall cost of OLEDs considerably. Thus, for practicable devices, thin-film solutions have to be applied.

A fundamentally different approach to extract trapped light in OLEDs is the use of scattering structures. Here, one has to distinguish between periodic and nonperiodic (random) structures on the one hand and internal or external scattering on the other (Figure 15.20). The latter realization is quite straightforward and can be any modification of the backside of the glass substrate that serves to scatter out light rays that would otherwise suffer from total internal reflection at the glass/air interface. Examples are ordered microlens arrays [75, 76], scattering particles [77], or mechanical roughening of the glass substrate [78]. In the meantime, light scattering foils are commercially available, but in contrast to a macroextractor these

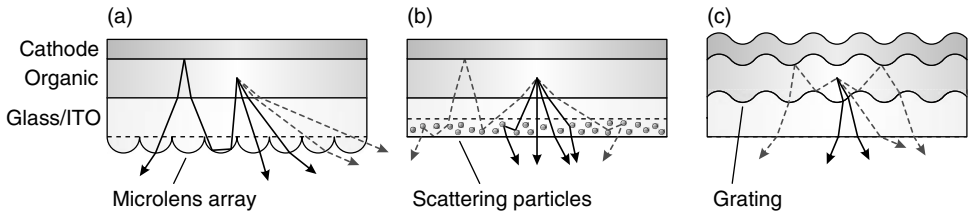

Figure 15.20 (a) Schematic illustration of substrate mode extraction by a microlens array. Light paths indicated in dashed lines correspond to radiation that would normally not be able to leave the device due to total internal reflection at the glass/air interface. Multiple reflections inside the stack reduce the efficiency due to absorption in the organic layers and in ITO as well as due to reflection losses at the cathode. (b) Concept of light outcoupling by scattering particles in a film applied to the backside of the substrate. (c) Realization of an internal scattering structure by a periodic grating placed between the glass substrate and the thin-film stack.

techniques typically extract only part of the light trapped in the substrate and the reflecting appearance of the OLED in the off-state changes to a milky, nonreflecting one.

If one wants to get access to waveguided modes, an internal scattering structure, for example, placed between the glass substrate and the ITO layer, has to be used. Thus, both periodic gratings (photonic crystals) and random scattering structures are possible. The effectiveness of this approach relies on the spatial overlap of the waveguide modes with such features; in other words, they have to be employed close to the emission zone of the OLED [79]. In general, photonic crystal structures with periodicities on a length scale comparable to optical wavelengths have the disadvantages that they require elaborate fabrication techniques and that they induce a wavelength and angle-dependent scattering efficiency. Other interesting approaches are therefore the use of so-called low-index grids with periods on the micron scale [80] or random structures fabricated by morphological instabilities of thin-film structures [81]. The above said is also true for the extraction of surface plasmons by scattering structures that consequently need to be in the vicinity of the metal cathode [82]. This boundary condition is even more challenging since many of the established patterning techniques are not compatible with OLED technology as they would damage or destroy the underlying organic films.

15.5.2 Reduction of Surface Plasmon Losses

15.5.2.1 Basic Properties of SPPs

Before presenting our own results on the reduction of surface plasmon losses, some general properties of SPPs will be discussed (for details, refer to Refs [83–85]). Surface plasmon polaritons are longitudinal, p-polarized waves traveling at the interface between a metal and a dielectric with evanescent fields decaying

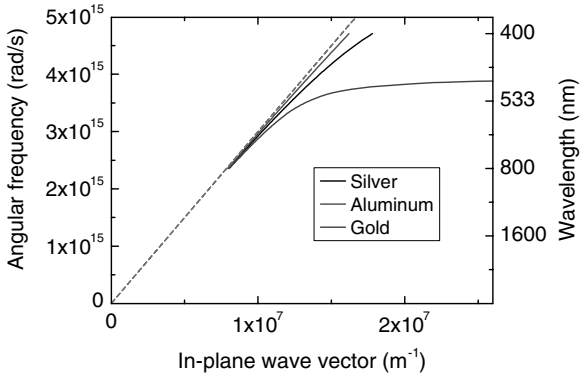

Figure 15.21 Dispersion relation of surface plasmon polaritons at metal/air interfaces for three different metals in the visible spectral range. The dashed line is the light line in air following the relation $\omega = c \cdot k_{\parallel}$.

exponentially into both adjacent media. For semi-infinite layers, their dispersion relation is given by

$$k_{\mathrm{SPP}}(\omega) = k_0 \sqrt{\frac{\varepsilon_1 \cdot \varepsilon_2}{\varepsilon_1 + \varepsilon_2}} = \frac{\omega}{c} \sqrt{\frac{\varepsilon_1(\omega) \cdot \varepsilon_2(\omega)}{\varepsilon_1(\omega) + \varepsilon_2(\omega)}} \tag{15.15}$$

where $\varepsilon_{1,2}(\omega)$ is the complex dielectric functions of the metal and the adjacent dielectric layer and k_0 is the vacuum wave vector. This relation is shown in Figure 15.21 for three different metal surfaces adjacent to air as dielectric for the range of frequencies and in-plane wave vectors relevant in this context. It is obvious that the SPP dispersion curve and the light line in air do not intersect for finite frequencies; thus, energy and momentum conservation cannot be fulfilled simultaneously and as a consequence SPPs cannot couple to far-field radiation. The application to OLEDs, however, requires an important modification due to the fact that the involved layers are not thick enough to be treated as bulk material. Thus, the evanescent field of the SPP can extend through an adjacent thin organic layer and sense an *effective* refractive index and, if the metal is thin enough, SPPs can exist on both sides of the metal layer and couple with each other [86].

15.5.2.2 **Scattering Approaches**

There are well-established methods how SPPs can be excited by far-field radiation, most importantly by grating coupling or prism coupling [83, 84]. Making use of reciprocity in optics, it is quite straightforward to transfer these techniques to light-emitting structures [82, 87]. The first approach uses a periodic grating with period λ_g to scatter SPPs so that they gain an extra momentum $k'_{\mathrm{SPP}} = k_{\mathrm{SPP}} \pm m \cdot (2\pi/\lambda_g)$ (with an integer number m) (Figure 15.22). This scattering approach relies on the fact that there is sufficient overlap between the SPP mode and a periodic modulation of the refractive index, which implies that the grating has to be placed next to the metal layer (or there has to be a height modulation reaching through the

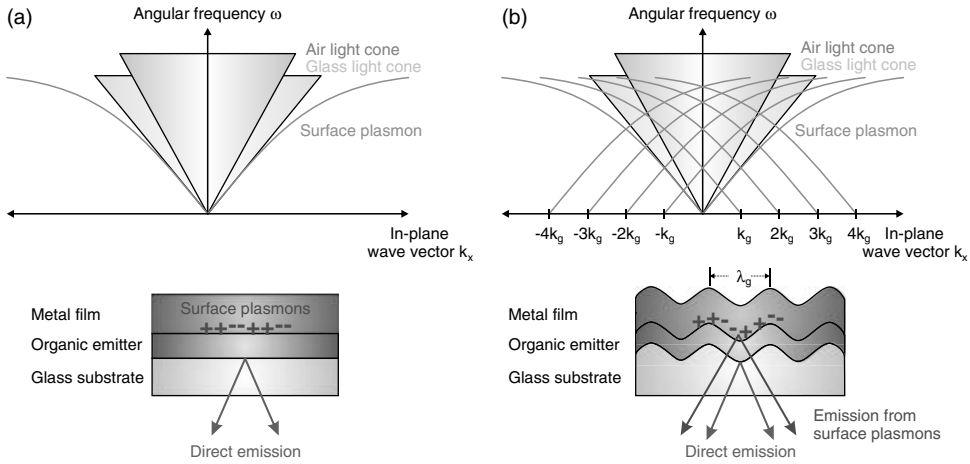

Figure 15.22 Simplified layer structure to demonstrate the principle of SPP grating coupling. The SPP dispersion relation, lying below the glass light cone in planar layered structures (a), is scattered by multiples of the grating wave vector to result in several branches being located within the glass light cone (b), so that light from SPPs can be coupled out. See also Ref. [89].

complete layer stack including the cathode). The fabrication of OLEDs fulfilling this condition is still challenging [88], as not only the optical properties have to be tuned but also the electrical functioning has to be ensured. For this reason, we have investigated this coupling approach only in simplified structures comprising a luminescent film adjacent to a metal layer [89, 90].

Figure 15.23 shows experimentally measured angle-dependent p-polarized emission spectra for photoluminescence excitation of a 30 nm thick Alq_3 film adjacent to a silver layer, both deposited on a line grating that was nanoimprinted into a PMMA layer. One can clearly see that SPPs, which are excited by fluorescent Alq_3 molecules via near-field coupling, are scattered back into the substrate up to the fifth diffraction order. There is excellent agreement between the measured angular dispersion and the simulated curves using the above-described methods. One can also readily show that waveguided modes that will become relevant for thicker organic layers are equally well scattered out in this way. Furthermore, we have demonstrated that even structures containing some randomness, produced, for example, by an ordinary DVD stamp, can be used [90]. Nevertheless, one has to be aware that periodic structures will induce a pronounced angular dependence of the perceived color of the OLED [91]. Thus, for white OLEDs with color coordinates independent of the viewing angle, random scattering structures have to be used [81].

15.5.2.3 **Index Coupling**

Figure 15.24 shows the principle of index (or prism) coupling utilizing the so-called inverse Kretschmann configuration [92]. This technique makes use of the fact that the in-plane wave vector within the prism is stretched by a factor given by the

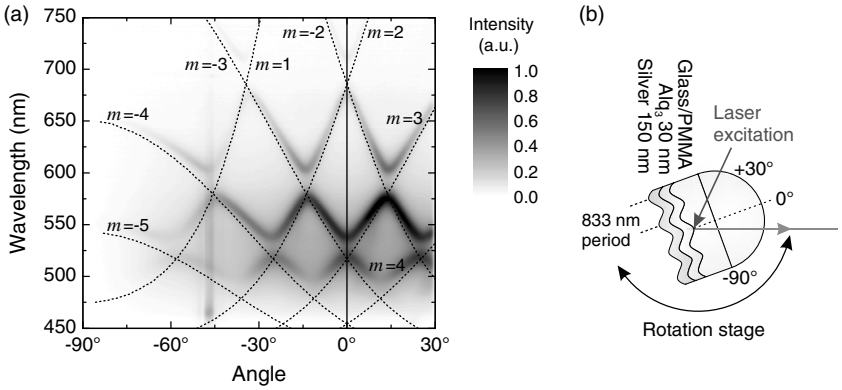

Figure 15.23 (a) Experimentally measured angle-dependent p-polarized emission spectra after photoluminescence excitation of a 30 nm thick Alq_3 film adjacent to a silver layer, both deposited on an 833 nm periodic line grating that was nanoimprinted into a PMMA layer. The dotted lines show simulated SPP dispersions of the corresponding planar structure, where the curves were shifted by integer multiples of the grating wave vector. (b) Schematic sample layout used in the experiment; both excitation and detection are through the glass prism. Excitation is made by a 375 nm laser diode incident at a fixed angle of 45°, detection is performed by a fiber optical spectrometer through a linear polarizer in front of which the sample is rotated on a motorized turntable. See also Ref. [90].

refractive index of the prism, so that energy and momentum conservation are fulfilled. If the refractive indices are properly chosen, it is possible to extract SPPs that are evanescent modes at the metal/organic interface (the bottom side in Figure 15.24a) to become radiative modes at the opposite side of the metal layer (here the topside). To realize this concept, however, some prerequisites have to be fulfilled. First, the metal film obviously has to be semitransparent. Since there are two counteracting processes, namely, an enhanced coupling of the emitting dipoles to SPPs with an increasing metal thickness on the one hand and a concomitant

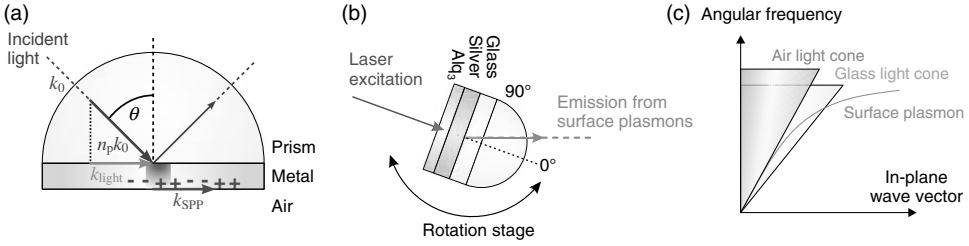

Figure 15.24 Principle of SPP index coupling. (a) The excitation of SPPs by light from the far-field in the so-called Kretschmann configuration. (b) Inverse Kretschmann configuration to extract SPPs that are excited by near-field coupling from a luminescent organic film. (c) The dispersion relation of the SPP traveling at the interface to air overlaps with the light cone for the attached glass prism. See also Ref. [89].

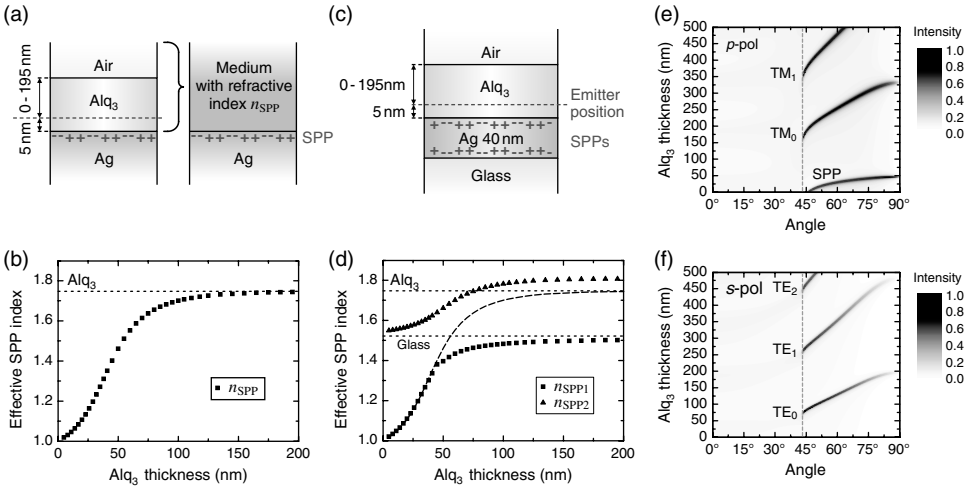

Figure 15.25 Concept of the effective refractive index of the adjacent dielectric medium that is probed by an SPP for a thick metal layer (a and b) and for a thin metal layer (c and d). Also shown is the simulated angular dispersion of the modes that can be extracted through a fused silica prism as a function of the organic layer thickness: p-polarized (e) and s-polarized (f). See also Refs [89, 94].

reduced optical transmission on the other hand, there is typically an optimum thickness at around 50 nm (see below) [89, 93]. More importantly, the refractive index on the extraction side of the metal has to be larger than on the other side in order to match the dispersion relation of the plasmon (traveling at the bottom side) with the far-field light line in the prism at the topside. Due to the evanescent nature of SPPs, this condition not only depends on the bulk values of the organic material and the prism but in particular also on the thickness of the organic layer. Since the decay length of the SPP field amplitude perpendicular to the metal/dielectric interface is typically on the order of half a wavelength, the SPP field probes an extended vertical distance to the metal surface. In order to account for this feature, we have introduced an effective refractive index that has to be entered in Eq. (15.15) to calculate the correct SPP dispersion relation. This concept of the effective index of SPPs and its dependence on the thickness of the organic layer for a one-sided SPP (thick metal) and a two-sided SPP configuration (thin metal) is shown in Figure 15.25. Without going into the details, it is clear from the figure that only for thin Alq_3 layers (up to about 50 nm), ordinary glass can be used to extract SPPs. For larger organic layer thickness and in particular for the thicknesses typically used in OLEDs, the extraction of SPPs (in addition to waveguided modes that can also be extracted by this method) requires a medium on the topside of the metal that has a significantly higher refractive index.

Figure 15.26 shows the basic experimental realization of this concept with a fused silica glass prism and a thin Alq_3 layer. With photoluminescence excitation of Alq_3 molecules and near-field coupling to SPPs in Ag, the radiation can be

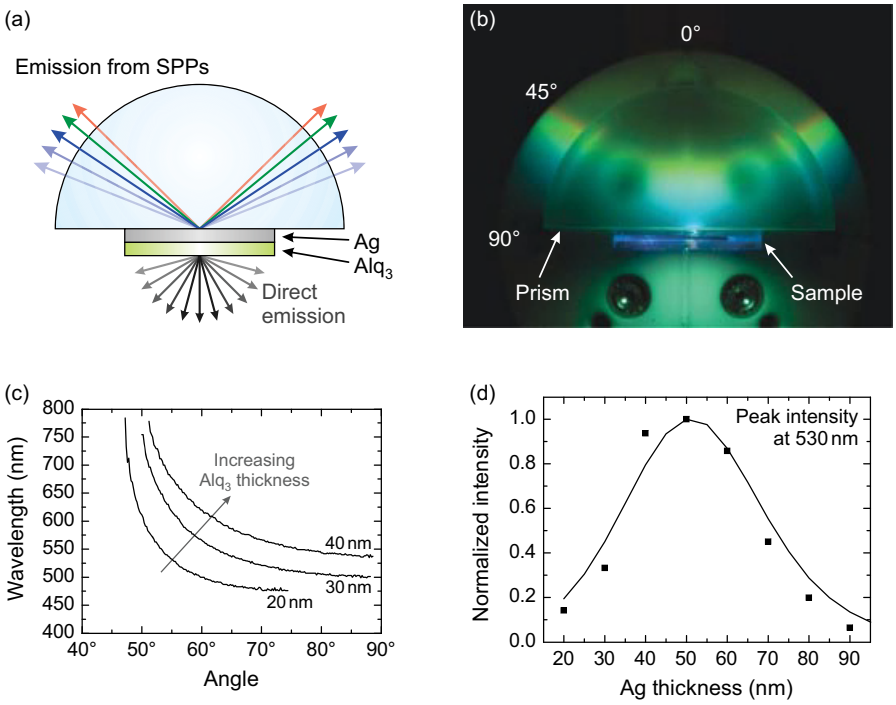

Figure 15.26 (a) Schematic experimental setup for measuring the angular dispersion of SPPs extracted by a fused silica half-cylinder prism. As sketched in Figure 15.24, while excitation of the organic film is made by a 375 nm laser diode incident at a fixed angle of 90° from air, detection is performed through the prism by a fiber optical spectrometer combined with a linear polarizer in front of which the sample is rotated on a motorized turntable. (b) The photograph directly visualizes the angular dispersion of the SPP emission. (c) and (d) show the dependence of the SPP dispersion on organic layer thickness and the extraction efficiency depending on metal layer thickness. See also Ref. [89].

extracted to the far-field. Thus, the angle-dependent emission spectra show the characteristic dependence on wavelength and organic layer thickness. Furthermore, due to the above-mentioned counteracting effects, there is a maximum of the extraction efficiency at a silver thickness of about 50 nm, in agreement with previously published results [93].

In order to make this concept working also for larger organic layer thickness being typically used in OLEDs, one has to increase the refractive index of the adjacent medium. Figure 15.27 shows exemplarily the calculated angular dispersion of p-polarized modes that can be extracted when a high-index glass (SF6, $n = 1.82$) or a $LiNbO_3$ ($n = 2.28$) prism is used. In the former case, SPP modes can now be extracted up to an Alq_3 thickness of about 100 nm; in the latter case, the index is so high that there is no limit anymore and all modes regardless of the thickness of the organic film can be extracted under an angle of not more than 60°.

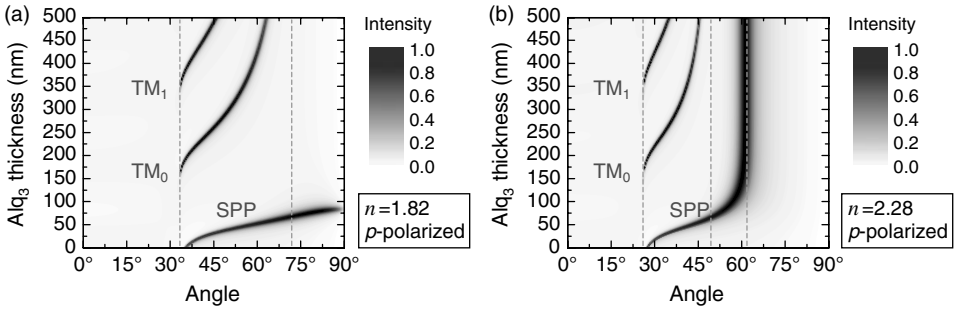

Figure 15.27 Simulated angular dispersion of the p-polarized modes extracted through a high-index SF6 glass prism (a) and a $LiNbO_3$ prism (b) as a function of the organic layer thickness. See also Ref. [94].

The application of this concept to a white bottom-emitting OLED with a thin semitransparent Ag top contact is shown in Figure 15.28. The photograph clearly shows that only the air mode is emitted to the bottom side, whereas all other modes (including substrate, waveguide, and SPP modes) are emitted in characteristic angular ranges to the topside. We note that the index of the used SF6 prism was

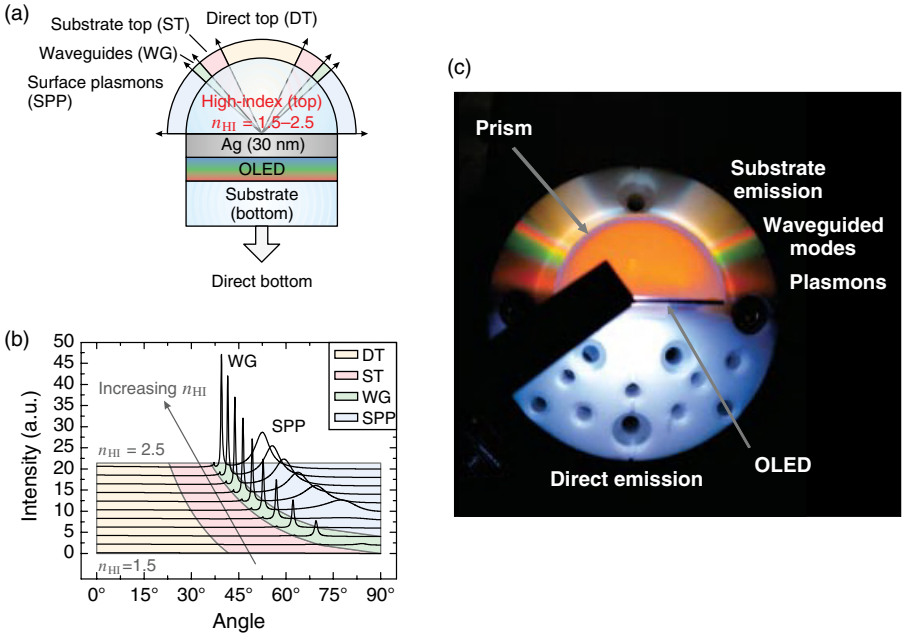

Figure 15.28 Sample layout (a) and angular dispersion of the modes extracted through a high-index glass prism (b) as a function of the refractive index of the prism. Note that for the simulation shown in (b), a semi-infinite glass substrate was assumed to avoid back reflected light from the glass–air interface appearing as top emission. The photograph in (c) shows the realization with a white OLED using an SF6 prism with $n = 1.82$. See also Refs [94, 95].

not high enough to extract the SPP completely, so that only the red part of the SPP branch is seen under large angles close to 90°. Furthermore, the used index-matching fluid was strongly absorbing in the short wavelength range so that the substrate light has a brownish appearance. Nevertheless, this is a clear demonstration that the concept of high-index coupling is applicable not only to extract waveguided modes in bottom-emitting OLEDs, as was demonstrated before by different authors [15, 73], but also to get access to *all trapped modes* – including surface plasmons [94].

It should be noted, however, that these results can only serve as a proof of principle, because using a high-index prism is not practicable in OLED applications. It would therefore be necessary to develop thin-film solutions to get rid of the viewing angle-dependent color shift. In this context, it should be noted that top-emitting OLEDs with high-index capping layers have been known for many years [67, 68]; however, the connection to SPPs was not made. Only recently it has been shown that including a fluorescent dye in such a capping layer can allow to extract energy from SPPs in top-emitting OLEDs [96]. This SPP-mediated energy transfer will be discussed in more detail in Chapter 16.

15.5.2.4 **Emitter Orientation**

Instead of developing tools to extract energy from surface plasmons, one can consider means to reduce their excitation in OLEDs. Apart from the already mentioned distance-dependent coupling between a radiating dipole and the SPPs, there is also a characteristic dependence on the orientation of the dipole [45, 49]. Thus, another way to avoid the excitation of surface plasmons, even if the emitter is rather close to the metal, is to control the orientation of the emitting molecules and thereby their transition dipole moments. Keeping the radiation pattern of a classical electrical dipole in mind (Figure 15.7) and considering that surface plasmons are transverse magnetic modes, one readily concludes that perfectly horizontally oriented dipoles would only very weakly couple to SPPs [39]. This effect has been known for many years in polymeric OLEDs [97]; however, only very recently we have been able to show that orientation effects also play a role in small-molecule OLEDs fabricated by vacuum evaporation, where the fluorescent or phosphorescent dyes are embedded with only a few percent content in a matrix material [52, 60, 61].

To demonstrate the potential of controlling the emitter orientation for efficiency enhancement in OLEDs, Figure 15.29 shows simulated power dissipation spectra separately for each of the three orthogonal dipole orientations in the prototypical Alq_3 OLED (structure shown in Figure 15.4). From this plot one can clearly see that horizontal dipoles (p_x and p_y) couple to various optical channels, whereas vertical (p_z) dipoles dissipate their energy almost exclusively to SPPs. It is furthermore instructive to look at the power dissipation of both dipole orientations into different optical channels as a function of the distance to the cathode, as displayed in Figure 15.30 (cf. Figure 15.11 for the isotropic case). It is obvious from these simulations that the light outcoupling efficiency (be it only direct emission or including substrate emission) can be enhanced by about a factor of 1.5 with respect to the case of random emitter orientation, which is mostly due to the strongly reduced coupling

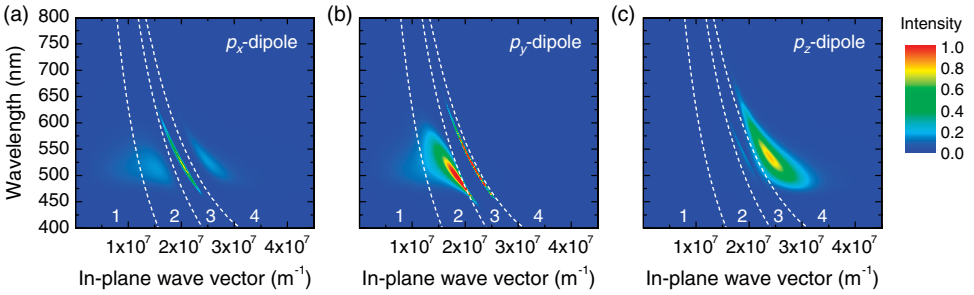

Figure 15.29 Simulation of power dissipation for the prototypical Alq_3 OLED (structure shown in Figure 15.4) for the three orthogonal dipole orientations separately (x, y in the substrate plane, z perpendicular to the substrate plane). In all cases, the radiative quantum efficiency was set to $q = 1$. The dashed lines separate the power dissipation spectra into different regions as denoted in Figure 15.8. See also Ref. [40].

to SPPs, if vertical dipoles are absent. Thus, from the point of view of efficiency, the vertical dipole orientation should be avoided in OLEDs. It is also interesting to note in this context that vertical dipoles exhibit markedly different distance-dependent coupling to the various optical channels compared to horizontal ones, which is due to different interference conditions. First, the coupling to SPPs has a longer range than in the horizontal case (as predicted already in Ref. [98] for energy transfer of dyes to a metal surface). Second, for vertical dipoles, the maximum outcoupling efficiency to air is achieved for an ETL thickness of about 135 nm, exactly where the outcoupling from horizontal ones has an interference node. As will be discussed below, this property can be used for the determination of the amount of vertical dipoles in an OLED with nonisotropic emitter orientation [54].

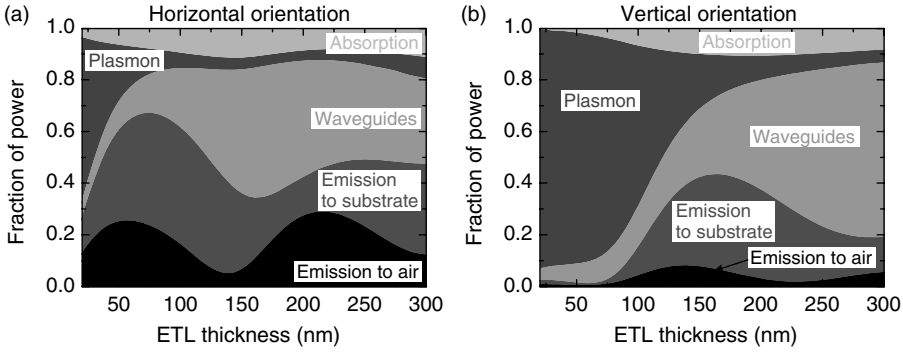

Figure 15.30 Simulation of power dissipation for exclusively horizontal (a) or vertical dipole orientation (b) in the prototypical Alq_3 OLED (structure shown in Figure 15.4) as a function of the ETL thickness. In both cases, the radiative quantum efficiency was set to $q = 1$ (compare with Figure 15.11 for the isotropic case).

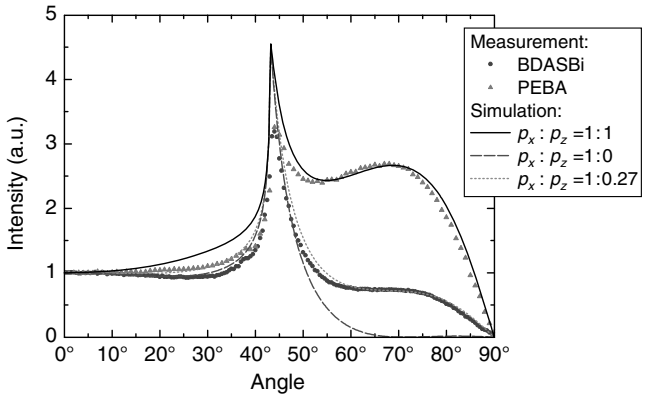

Figure 15.31 Angle-dependent p-polarized photoluminescence intensity of simplified structures with two fluorescent dyes (BDASBi and PEBA) embedded in a CBP matrix on glass substrates together with simulations for exclusively horizontal and fully random emitter orientation. Note that neat films of Alq_3 and films of $Ir(ppy)_3$ doped into CBP (not shown here) show perfectly random emitter orientation, as in the case of PEBA. For details, see Ref. [100].

To realize this concept, one needs emitter molecules that show nonisotropic orientation in a small-molecule OLED environment, where the emission layer is usually a thin dye-doped layer prepared by coevaporation on top of the other – usually amorphous – layers. Good candidates are rodlike chromophores with a large shape anisotropy, such as the blue fluorescent dye BDASBi shown in Figure 15.3. This material has already been known to exhibit nonisotropic orientation in neat evaporated films [99], but interestingly it preserves this feature even when it is doped into a CBP matrix [100]. As already mentioned, the fact that vertically oriented chromophores more or less completely couple to SPPs makes it difficult to detect them in OLEDs, for example, from angle-dependent emission spectra of OLEDs. As a workaround, we have therefore developed a method that is based on photoluminescence excitation of layer stacks that contain the same EML as the corresponding OLED but no metal layer [100]. It is thus possible to quantitatively determine the orientational distribution from angular and polarization-dependent photoluminescence spectra. As an example, Figure 15.31 shows the measured angle-dependent spectra for BDASBi and another blue fluorescent dye (PEBA) in comparison to simulation results. A careful analysis shows that in the former case, one has almost 90% contribution of horizontal dipole orientation compared to 66% for isotropic orientation in the latter case.

As described in detail in Ref. [60], we have compared OLEDs incorporating these two blue emitting dyes exhibiting different emitter orientation with respect to their external quantum efficiency. In the actual OLEDs investigated by us (as shown in Figure 15.32), the emitter orientation is not perfectly horizontal and the emitter quantum efficiency is less than unity. Nevertheless, the experimentally observed increase in EQE with respect to the isotropic reference OLED can consistently be

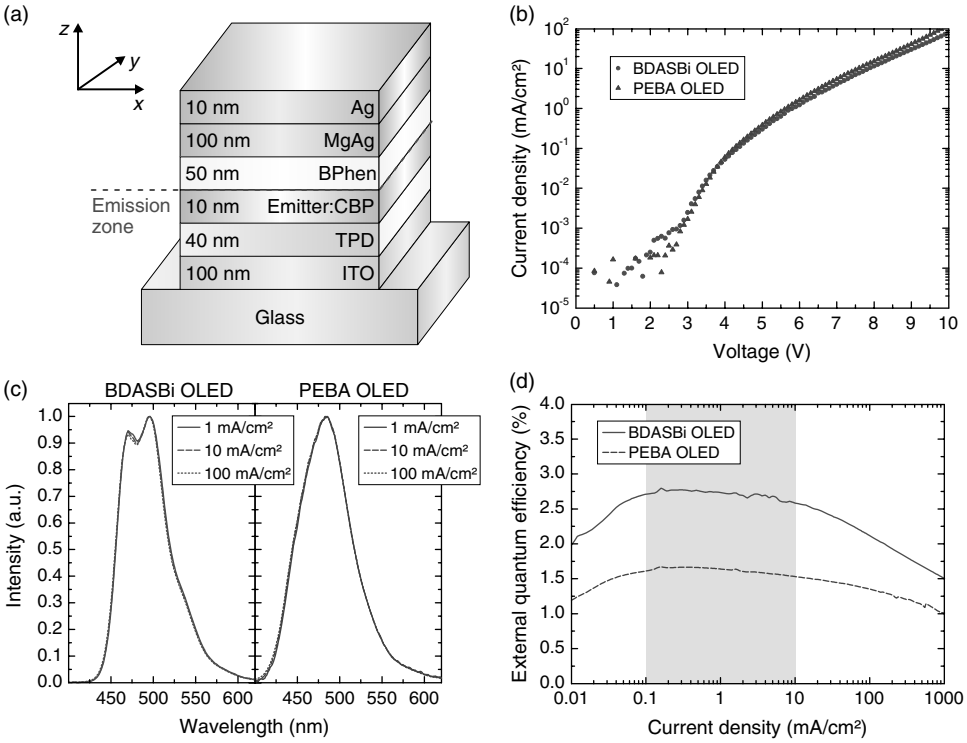

Figure 15.32 (a) Structure of blue fluorescent OLEDs with two different dyes (BDASBi and PEBA) doped in a CBP matrix as EML together with (b) their current–voltage characteristics, (c) their emission spectra, and (d) their EQE versus current. For details, see Ref. [60].

explained by the preferentially horizontal emitter orientation in case of BDASBi as emitting dye. Though in absolute numbers the EQE values of these devices are not that high (which is due to the fact that the used emitters are fluorescent making $\eta_{S/T} = 0.25$, their q-values are only between 0.55 and 0.65 and the charge balance factor γ is significantly less than one), these data demonstrate the huge potential of efficiency enhancement by this technique.

In the meantime we have extended these studies toward highly efficient phosphorescent emitters. As expected, symmetrically substituted metal–organic emitter complexes such as $Ir(ppy)_3$ have random emitter orientation when doped in a CBP matrix; however, in the case of complexes with different ligands, there is evidence for nonisotropic emitter orientation. For example, the well-known red phosphorescent emitter system $Ir(MDQ)_2(acac)$ doped into an α-NPD matrix also exhibits predominantly horizontal orientation of the emitting dipoles [52, 61]. If this circumstance is ignored, efficiency analysis based on the assumption of isotropic emitter orientation will lead to an overestimation of the radiative quantum efficiency [101], as has been worked out in detail in Ref. [52]. This again emphasizes the importance of radiation pattern analysis of OLEDs to detect such deviations

from random dipole orientation. However, as nicely shown in Ref. [54], this analysis should not be done with optimized ETL thickness corresponding to the first cavity maximum, because in this case the fraction of vertical dipoles is not detectable as they almost completely couple to SPPs. It should rather be performed in devices with ETL thickness fulfilling destructive interference conditions for horizontal dipoles so that the radiation from vertical emitters is visible.

15.6 Conclusion

After more than 20 years of research on OLEDs, the microscopic understanding of the underlying processes has progressed substantially. With respect to the expression for the external quantum efficiency (Eq. (15.1)) put forward by Tsutsui in 1997 [18], we now have a sound understanding of all four factors allowing quantitative calculations of OLED efficiencies and predictions toward the potential in improvement of it by newly developed OLED materials, structures, and concepts. Moreover, these methods are the basis for a reliable experimental determination of the relevant factors for the OLED efficiency. Nevertheless, the development is ongoing and important new physical concepts, such as the importance and the implications of disorder, are still being elucidated and integrated into OLED modeling (see Chapter 6).

By now, commercially available white OLEDs are specified with luminous efficacies of about 25 lm/W [6], that is, they are comparable to the best halogen lamps. However, several laboratories have reported values exceeding 60 lm/W for devices with good color compliance being currently under development [10]. Of course, there is room for improvement regarding the impressive numbers obtained with inorganic LEDs reaching more than 100 lm/W. But as already mentioned, the comparison with them is of limited relevance. A strong benefit of OLEDs is their unique form factor, with the light being distributed homogeneously over large area and thus being glare-free. Hence, (almost) no additional fixtures are needed: the OLED already is the luminaire!

Beyond general lighting, the compatibility of organic materials with various kinds of substrates and the ease of processing could also open possibilities for new appliances in other fields. In particular, the topics relevant for light extraction could have fruitful overlap with other fields of optics, for example, cavity physics, photonic crystals, and plasmonics – and we are still waiting to see the electrically pumped organic laser diode.

Acknowledgments

The authors thank the German Ministry of Education and Research (BMBF) for funding within the TOPAS project (FKZ 13N10474) and the Elite Network of Bavaria for financial support through the graduate school Materials Science of

Complex Interfaces (CompInt). We are grateful to colleagues from Osram Opto Semiconductors (Regensburg, Germany) and Fraunhofer Institute for Applied Optics and Precision Engineering (Jena, Germany) as well as the groups of P. Lugli (TU Munich, Germany) and C. Adachi (Kyushu University, Japan) for continuous support and fruitful discussions.

Furthermore, the contributions of Nils A. Reinke, Stefan Nowy, Bert J. Scholz, Tobias D. Schmidt, Thomas Wehlus, and Jörg Kinzel at Augsburg University, Daniel S. Setz and Arndt Jäger at Osram OS as well as Daisuke Yokoyama at Kyushu University/Yamagata University to part of the results shown in this chapter are gratefully acknowledged.

References

1 Humphreys, C.J. (2008) Solid-state lighting. *MRS Bull.*, **33**, 459–470.
2 Pope, M., Kallmann, H.P., and Magnante, P. (1963) Electroluminescence in organic crystals. *J. Chem. Phys.*, **38** (8), 2042–2043.
3 Helfrich, W. and Schneider, W.G. (1965) Recombination radiation in anthracene crystals. *Phys. Rev. Lett.*, **14** (7), 229–231.
4 Tang, C.W. and VanSlyke, S.A. (1987) Organic electroluminescent diodes. *Appl. Phys. Lett.*, **51** (12), 913–915.
5 Burroughes, J., Bradley, D., Brown, A., Marks, R., Mackay, K., Friend, R., Burns, P., and Holmes, A. (1990) Light-emitting diodes based on conjugated polymers. *Nature*, **347**, 539.
6 Osram and Philips (2010) Commercial white OLEDs are offered since 2010. www.osram.com and www.lighting.philips.com.
7 D'Andrade, B. and Forrest, S. (2004) White organic light-emitting devices for solid-state lighting. *Adv. Mater.*, **16** (18), 1585–1595.
8 Schwartz, G., Reineke, S., Rosenow, T.C., Walzer, K., and Leo, K. (2009) Triplet harvesting in hybrid white organic light-emitting diodes. *Adv. Funct. Mater.*, **19** (9), 1319–1333.
9 Gather, M.C., Köhnen, A., and Meerholz, K. (2011) White organic light-emitting diodes. *Adv. Mater.*, **23** (2), 233–248.
10 Tyan, Y.S. (2011) Organic light-emitting-diode lighting overview. *J. Photon. Energy*, **1**, 011009.
11 Hung, L.S., Tang, C.W., and Mason, M.G. (1997) Enhanced electron injection in organic electroluminescence devices using an Al/LiF electrode. *Appl. Phys. Lett.*, **70** (2), 152–154.
12 van Mensfoort, S.L.M., Carvelli, M., Megens, M., Wehenkel, D., Bartyzel, M., Greiner, H., Janssen, R.A.J., and Coehoorn, R. (2010) Measuring the light emission profile in organic light-emitting diodes with nanometre spatial resolution. *Nat. Photon.*, **4**, 329–335.
13 Pfeiffer, M., Forrest, S., Leo, K., and Thompson, M. (2002) Electrophosphorescent pin organic light-emitting devices for very-high-efficiency flat-panel displays. *Adv. Mater.*, **14** (22), 1633–1636.
14 Baldo, M.A., O'Brien, D.F., You, Y., Shoustikov, A., Sibley, S., Thompson, M.E., and Forrest, S.R. (1998) Highly efficient phosphorescent emission from organic electroluminescent devices. *Nature*, **395** (6698), 151–154.
15 Reineke, S., Lindner, F., Schwartz, G., Seidler, N., Walzer, K., Lüssem, B., and Leo, K. (2009) White organic light-emitting diodes with fluorescent tube efficiency. *Nature*, **459** (7244), 234–238.
16 Kido, J., Hayase, H., Hongawa, K., Nagai, K., and Okuyama, K. (1994) Bright red light-emitting organic electroluminescent devices having a europium complex as an emitter. *Appl. Phys. Lett.*, **65**, 2124.
17 So, F., Krummacher, B., Mathai, M.K., Poplavskyy, D., Choulis, S.A., and

Choong, V.E. (2007) Recent progress in solution processable organic light emitting devices. *J. Appl. Phys.*, **102** (9), 091101.

18 Tsutsui, T., Aminaka, E., Lin, C.P., and Kim, D.U. (1997) Extended molecular design concept of molecular materials for electroluminescence: sublimed-dye films, molecularly doped polymers and polymers with chromophores. *Philos. Trans. R. Soc. Lond. A*, **355** (1725), 801–814.

19 Adachi, C., Baldo, M.A., Thompson, M. E., and Forrest, S.R. (2001) Nearly 100% internal phosphorescence efficiency in an organic light-emitting device. *J. Appl. Phys.*, **90** (10), 5048–5051.

20 Baldo, M.A., O'Brien, D.F., Thompson, M.E., and Forrest, S.R. (1999) Excitonic singlet–triplet ratio in a semiconducting organic thin film. *Phys. Rev. B*, **60** (20), 14422–14428.

21 Segal, M., Baldo, M.A., Holmes, R.J., Forrest, S.R., and Soos, Z.G. (2003) Excitonic singlet–triplet ratios in molecular and polymeric organic materials. *Phys. Rev. B*, **68** (7), 075211.

22 Kondakov, D.Y., Pawlik, T.D., Hatwar, T. K., and Spindler, J.P. (2009) Triplet annihilation exceeding spin statistical limit in highly efficient fluorescent organic light-emitting diodes. *J. Appl. Phys.*, **106** (12), 124510.

23 Luo, Y. and Aziz, H. (2010) Correlation between triplet–triplet annihilation and electroluminescence efficiency in doped fluorescent organic light-emitting devices. *Adv. Funct. Mater.*, **20** (8), 1285–1293.

24 Wohlgenannt, M., Tandon, K., Mazumdar, S., Ramasesha, S., and Vardeny, Z.V. (2001) Formation cross-sections of singlet and triplet excitons in π-conjugated polymers. *Nature*, **409** (6819), 494–497.

25 Shuai, Z., Beljonne, D., Silbey, R.J., and Brédas, J.L. (2000) Singlet and triplet exciton formation rates in conjugated polymer light-emitting diodes. *Phys. Rev. Lett.*, **84** (1), 131–134.

26 Rothe, C., King, S.M., and Monkman, A.P. (2006) Direct measurement of the singlet generation yield in polymer light-emitting diodes. *Phys. Rev. Lett.*, **97** (7), 076602.

27 van Mensfoort, S.L.M., Billen, J., Carvelli, M., Vulto, S.I.E., Janssen, R.A.J., and Coehoorn, R. (2011) Predictive modeling of the current density and radiative recombination in blue polymer-based light-emitting diodes. *J. Appl. Phys.*, **109**, 064502.

28 Wilson, J.S., Dhoot, A.S., Seeley, A.J.A. B., Khan, M.S., Kohler, A., and Friend, R.H. (2001) Spin-dependent exciton formation in π-conjugated compounds. *Nature*, **413** (6858), 828–831.

29 Krummacher, B.C., Nowy, S., Frischeisen, J., Klein, M., and Brütting, W. (2009) Efficiency analysis of organic light-emitting diodes based on optical simulation. *Org. Electron.*, **10** (3), 478–485.

30 Nowy, S., Krummacher, B.C., Frischeisen, J., Reinke, N.A., and Brütting, W. (2008) Light extraction and optical loss mechanisms in organic light-emitting diodes: influence of the emitter quantum efficiency. *J. Appl. Phys.*, **104** (12), 123109.

31 Becker, H., Burns, S.E., and Friend, R.H. (1997) Effect of metal films on the photoluminescence and electroluminescence of conjugated polymers. *Phys. Rev. B*, **56** (4), 1893–1905.

32 Wasey, J.A.E., Safonov, A., Samuel, I.D.W., and Barnes, W.L. (2001) Efficiency of radiative emission from thin films of a light-emitting conjugated polymer. *Phys. Rev. B*, **64** (20), 205201.

33 Giebink, N.C. and Forrest, S.R. (2008) Quantum efficiency roll-off at high brightness in fluorescent and phosphorescent organic light emitting diodes. *Phys. Rev. B*, **77**, 235215.

34 Greenham, N.C., Friend, R.H., and Bradley, D.D.C. (1994) Angular dependence of the emission from a conjugated polymer light-emitting diode: implications for efficiency calculations. *Adv. Mater.*, **6** (6), 491–494.

35 Diekmann, K. (2008) OLLA White paper on the necessity of luminous efficacy measurement standardization of OLED light sources. http://www.hitech-projects.

com/euprojects/olla/news/press_release_4_september_2007.
36 Forrest, S., Bradley, D., and Thompson, M. (2003) Measuring the efficiency of organic light-emitting devices. *Adv. Mater.*, **15** (13), 1043–1048.
37 Brütting, W., Berleb, S., and Mückl, A.G. (2001) Device physics of organic light-emitting diodes based on molecular materials. *Org. Electron.*, **2** (1), 1–36.
38 Baldo, M.A., Lamansky, S., Burrows, P.E., Thompson, M.E., and Forrest, S.R. (1999) Very high-efficiency green organic light-emitting devices based on electrophosphorescence. *Appl. Phys. Lett.*, **75** (1), 4–6.
39 Smith, L.H., Wasey, J.A.E., Samuel, I.D. W., and Barnes, W.L. (2005) Light out-coupling efficiencies of organic light-emitting diode structures and the effect of photoluminescence quantum yield. *Adv. Funct. Mater.*, **15** (11), 1839–1844.
40 Nowy, S., Frischeisen, J., and Brütting, W. (2009) Simulation based optimization of light-outcoupling in organic light-emitting diodes. *Proc. SPIE*, **7415** (1), 74151C.
41 Saxena, K., Jain, V., and Mehta, D.S. (2009) A review on the light extraction techniques in organic electroluminescent devices. *Opt. Mater.*, **32** (1), 221–233.
42 Purcell, E. (1946) Spontaneous emission probabilities at radio frequencies. *Phys. Rev.*, **69**, 681.
43 Drexhage, K.H. (1970) Influence of a dielectric interface on fluorescence decay time. *J. Lumin.*, **1-2**, 693–701.
44 Drexhage, K.H. (1974) Interaction of light with monomolecular dye layers. *Prog. Opt.*, **12**, 165.
45 Chance, R.R., Prock, A., and Silbey, R. (1974) Lifetime of an emitting molecule near a partially reflecting surface. *J. Chem. Phys.*, **60** (7), 2744–2748.
46 Chance, R.R., Prock, A., and Silbey, R. (1978) Molecular fluorescence and energy transfer near interfaces. *Adv. Chem. Phys.*, **37**, 1–65.
47 Lukosz, W. (1981) Light emission by multipole sources in thin layers: I. Radiation patterns of electric and magnetic dipoles. *J. Opt. Soc. Am.*, **71**, 744–754.
48 Neyts, K.A. (1998) Simulation of light emission from thin-film microcavities. *J. Opt. Soc. Am. A*, **15**, 962–971.
49 Barnes, W.L. (1998) Fluorescence near interfaces: the role of photonic mode density. *J. Mod. Opt.*, **45** (4), 661–699.
50 Wasey, J.A.E. and Barnes, W. (2000) Efficiency of spontaneous emission from planar microcavities. *J. Mod. Opt.*, **47**, 725–741.
51 Gather, M.C., Flaemmich, M., Danz, N., Michaelis, D., and Meerholz, K. (2009) Measuring the profile of the emission zone in polymeric organic light-emitting diodes. *Appl. Phys. Lett.*, **94** (26), 263301.
52 Schmidt, T.D., Setz, D.S., Flämmich, M., Frischeisen, J., Michaelis, D., Krummacher, B., Danz, N., and Brütting, W. (2011) Evidence for non-isotropic emitter orientation in a red phosphorescent organic light-emitting diode and its implications for determining the emitter's radiative quantum efficiency. *Appl. Phys. Lett.*, **99**, 163302.
53 Flämmich, M., Gather, M.C., Danz, N., Michaelis, D., Braeuer, A.H., Meerholz, K., and Tuennermann, A. (2010) Orientation of emissive dipoles in OLEDs: quantitative *in situ* analysis. *Org. Electron.*, **11** (6), 1039–1046.
54 Flämmich, M., Michaelis, D., and Danz, N. (2011) Accessing OLED emitter properties by radiation pattern analyses. *Org. Electron.*, **12** (1), 83–91.
55 Lin, C.L., Cho, T.Y., Chang, C.H., and Wu, C.C. (2006) Enhancing light outcoupling of organic light-emitting devices by locating emitters around the second antinode of the reflective metal electrode. *Appl. Phys. Lett.*, **88** (8), 081114.
56 Celebi, K., Heidel, T.D., and Baldo, M.A. (2007) Simplified calculation of dipole energy transport in a multilayer stack using dyadic Green's functions. *Opt. Express*, **15** (4), 1762–1772.
57 Kim, S.Y. and Kim, J.J. (2010) Outcoupling efficiency of organic light emitting diodes and the effect of ITO thickness. *Org. Electron.*, **11**, 1010–1015.
58 Flämmich, M., Gather, M.C., Danz, N., Michaelis, D., and Meerholz, K. (2009) *In situ* measurement of the internal

luminescence quantum efficiency in organic light-emitting diodes. *Appl. Phys. Lett.*, **95**, 263306.

59 Setz, D.S., Schmidt, T.D., Flämmich, M., Nowy, S., Frischeisen, J., Krummacher, B.C., Dobbertin, T., Heuser, K., Michaelis, D., Danz, N., Brütting, W., and Winnacker, A. (2011) Comprehensive efficiency analysis of organic light-emitting devices. *J. Photon. Energy*, **1** (1), 011006.

60 Frischeisen, J., Yokoyama, D., Endo, A., Adachi, C., and Brütting, W. (2011) Increased light outcoupling efficiency in dye-doped small molecule organic light-emitting diodes with horizontally oriented emitters. *Org. Electron.*, **12** (5), 809–817.

61 Flämmich, M., Frischeisen, J., Setz, D.S., Michaelis, D., Krummacher, B.C., Schmidt, T.D., Brütting, W., and Danz, N. (2011) Oriented phosphorescent emitters boost OLED efficiency. *Org. Electron.*, **12**, 1663.

62 Meerholz, K. and Müller, D.C. (2001) Outsmarting waveguide losses in thin-film light-emitting diodes. *Adv. Funct. Mater.*, **11** (4), 251–253.

63 Greiner, H. (2007) Light extraction from organic light emitting diode substrates: simulation and experiment. *Jpn. J. Appl. Phys.*, **46**, 4125–4137.

64 Greiner, H. (2010) Light extraction from OLEDs. OLED100 Summer School, (Krutyn, June 2010, unpublished).

65 Meyer, J., Winkler, T., Hamwi, S., Schmale, S., Johannes, H.H., Weimann, T., Hinze, P., Kowalsky, W., and Riedl, T. (2008) Transparent inverted organic light-emitting diodes with a tungsten oxide buffer layer. *Adv. Mater.*, **20** (20), 3839–3843.

66 Agrawal, M., Sun, Y., Forrest, S.R., and Peumans, P. (2007) Enhanced outcoupling from organic light-emitting diodes using aperiodic dielectric mirrors. *Appl. Phys. Lett.*, **90** (24), 241112.

67 Riel, H., Karg, S., Beierlein, T., Ruhstaller, B., and Rieß, W. (2003) Phosphorescent top-emitting organic light-emitting devices with improved light outcoupling. *Appl. Phys. Lett.*, **82** (3), 466–468.

68 Riel, H., Karg, S., Beierlein, T., Riess, W., and Neyts, K. (2003) Tuning the emission characteristics of top-emitting organic light-emitting devices by means of a dielectric capping layer: an experimental and theoretical study. *J. Appl. Phys.*, **94** (8), 5290–5296.

69 Thomschke, M., Nitsche, R., Furno, M., and Leo, K. (2009) Optimized efficiency and angular emission characteristics of white top-emitting organic electroluminescent diodes. *Appl. Phys. Lett.*, **94** (8), 083303.

70 Hofmann, S., Thomschke, M., Freitag, P., Furno, M., Luessem, B., and Leo, K. (2010) Top-emitting organic light-emitting diodes: influence of cavity design. *Appl. Phys. Lett.*, **97** (25), 253308.

71 Smith, L. and Barnes, W. (2006) Using a low-index host layer to increase emission from organic light-emitting diode structures. *Org. Electron.*, **7** (6), 490–494.

72 Nakamura, T., Tsutsumi, N., Juni, N., and Fujii, H. (2005) Thin-film waveguiding mode light extraction in organic electroluminescent device using high refractive index substrate. *J. Appl. Phys.*, **97**, 054505.

73 Gaertner, G. and Greiner, H. (2008) Light extraction from OLEDs with (high) index matched glass substrates. *Proc. SPIE*, **6999** (1), 69992T.

74 Mladenovski, S., Neyts, K., Pavicic, D., Werner, A., and Rothe, C. (2009) Exceptionally efficient organic light emitting devices using high refractive index substrates. *Opt. Express*, **17** (9), 7562–7570.

75 Madigan, C.F., Lu, M.H., and Sturm, J.C. (2000) Improvement of output coupling efficiency of organic light-emitting diodes by backside substrate modification. *Appl. Phys. Lett.*, **76** (13), 1650–1652.

76 Möller, S. and Forrest, S.R. (2002) Improved light out-coupling in organic light emitting diodes employing ordered microlens arrays. *J. Appl. Phys.*, **91** (5), 3324–3327.

77 Yamasaki, T., Sumioka, K., and Tsutsui, T. (2000) Organic light-emitting device with an ordered monolayer of silica

microspheres as a scattering medium. *Appl. Phys. Lett.*, **76** (10), 1243–1245.
78 Riedel, B., Kaiser, I., Hauss, J., Lemmer, U., and Gerken, M. (2010) Improving the outcoupling efficiency of indium-tin-oxide-free organic light-emitting diodes via rough internal interfaces. *Opt. Express*, **18** (23), A631–A639.
79 Lupton, J.M., Matterson, B.J., Samuel, I.D.W., Jory, M.J., and Barnes, W.L. (2000) Bragg scattering from periodically microstructured light emitting diodes. *Appl. Phys. Lett.*, **77** (21), 3340–3342.
80 Sun, Y. and Forrest, S.R. (2008) Enhanced light out-coupling of organic light-emitting devices using embedded low-index grids. *Nat. Photon.*, **2** (8), 483–487.
81 Koo, W.H., Jeong, S.M., Araoka, F., Ishikawa, K., Nishimura, S., Toyooka, T., and Takezoe, H. (2010) Light extraction from organic light-emitting diodes enhanced by spontaneously formed buckles. *Nat. Photon.*, **4** (4), 222–226.
82 Wedge, S., Hooper, I.R., Sage, I., and Barnes, W.L. (2004) Light emission through a corrugated metal film: the role of cross-coupled surface plasmon polaritons. *Phys. Rev. B*, **69** (24), 245418.
83 Raether, H. (1988) *Surface Plasmons on Smooth and Rough Surfaces and on Gratings*, Springer.
84 Maier, S.A. (2007) *Plasmonics: Fundamentals and Applications*, Springer.
85 Atwater, H.A. (2007) The promise of plasmonics. *Sci. Am.*, **296** (4), 56–63.
86 Andrew, P. and Barnes, W.L. (2004) Energy transfer across a metal film mediated by surface plasmon polaritons. *Science*, **306** (5698), 1002–1005.
87 Barnes, W.L. (1999) Electromagnetic crystals for surface plasmon polaritons and the extraction of light from emissive devices. *J. Lightwave Technol.*, **17**, 2170–2182.
88 Wedge, S., Giannattasio, A., and Barnes, W. (2007) Surface plasmon–polariton mediated emission of light from top-emitting organic light-emitting diode type structures. *Org. Electron.*, **8** (2–3), 136–147.
89 Frischeisen, J., Scholz, B.J., Arndt, B.J., Schmidt, T.D., Gehlhaar, R., Adachi, C., and Brütting, W. (2011) Strategies for light extraction from surface plasmons in organic light-emitting diodes. *J. Photon. Energy*, **1** (1), 011004.
90 Frischeisen, J., Niu, Q., Abdellah, A., Kinzel, J.B., Gehlhaar, R., Scarpa, G., Adachi, C., Lugli, P., and Brütting, W. (2011) Light extraction from surface plasmons and waveguide modes in an organic light-emitting layer by nanoimprinted gratings. *Opt. Express*, **19** (S1), A7–A19.
91 Hauss, J., Riedel, B., Gleiss, S., Geyer, U., Lemmer, U., and Gerken, M. (2011) Periodic nanostructuring for guided mode extraction in organic light-emitting diodes. *J. Photon. Energy*, **1** (1), 011012.
92 Kretschmann, E. (1971) Die Bestimmung optischer Konstanten von Metallen durch Anregung von Oberflächenplasmaschwingungen. *Z. Physik*, **241**, 313–324.
93 Winter, G. and Barnes, W.L. (2006) Emission of light through thin silver films via near-field coupling to surface plasmon polaritons. *Appl. Phys. Lett.*, **88** (5), 051109.
94 Scholz, B.J., Frischeisen, J., Jaeger, A., Setz, D.S., Reusch, T., and Brütting, W. (2012) Extraction of surface plasmons in organic light-emitting diodes via high-index coupling. *Opt. Express*, **20** (S2), A205.
95 Brütting, W., Frischeisen, J., Scholz, B.J., and Schmidt, T.D. (2011) More light from organic light-emitting diodes. *Europhys. News*, **42** (4), 20.
96 Tien, K.C., Lin, M.S., Lin, Y.H., Tsai, C.H., Shiu, M.H., Wei, M.C., Cheng, H.C., Lin, C.L., Lin, H.W., and Wu, C.C. (2010) Utilizing surface plasmon polariton mediated energy transfer for tunable double-emitting organic light-emitting devices. *Org. Electron.*, **11** (3), 397 –406.
97 Kim, J.S., Ho, P.K.H., Greenham, N.C., and Friend, R.H. (2000) Electroluminescence emission pattern of organic light-emitting diodes: implications

for device efficiency calculations. *J. Appl. Phys.*, **88** (2), 1073–1081.

98 Weber, W.H. and Eagen, C.F. (1979) Energy transfer from an excited dye molecule to the surface plasmons of an adjacent metal. *Opt. Lett.*, **4**, 236–238.

99 Yokoyama, D., Sakaguchi, A., Suzuki, M., and Adachi, C. (2009) Horizontal orientation of linear-shaped organic molecules having bulky substituents in neat and doped vacuum-deposited amorphous films. *Org. Electron.*, **10** (1), 127 –137.

100 Frischeisen, J., Yokoyama, D., Adachi, C., and Brütting, W. (2010) Determination of molecular dipole orientation in doped fluorescent organic thin films by photoluminescence measurements. *Appl. Phys. Lett.*, **96** (7), 073302.

101 Meerheim, R., Furno, M., Hofmann, S., Luessem, B., and Leo, K. (2010) Quantification of energy loss mechanisms in organic light-emitting diodes. *Appl. Phys. Lett.*, **97** (25), 253305.

16
Light Outcoupling in Organic Light-Emitting Devices

Chih-Hung Tsai and Chung-Chih Wu

16.1
Introduction

Since the first reports of efficient and practical organic light-emitting devices (OLEDs) in 1987 by Tang and VanSlyke [1], OLEDs have been the subjects of intensive studies owing to their advantageous flat panel displays and lighting applications, such as high efficiency, wide viewing angle, fast response, and potentially low cost. In addition, their low processing temperatures and thus versatility in substrates render them suitable for some novel applications, such as flexible displays and lighting. Over the past two decades, the OLED technology has made rapid progresses and various types of OLED displays have been demonstrated and commercialized. With the continuous improvements of OLED efficiencies and white-emitting OLEDs, the application of OLEDs in solid-state lighting is also getting realistic [1–3].

Currently, the optical outcoupling technique for OLEDs has become an important issue for achieving high efficiencies [3–8] compatible with other solid-state lighting techniques, like fluorescent tubes and LEDs. Indeed, by adopting the phosphorescence mechanisms, the internal quantum efficiencies of OLEDs can reach nearly 100% [9, 10]. However, due to the significant refractive index mismatches at air/substrate and substrate/ITO interfaces, OLED internal emission usually suffers total internal reflection and hence most of internal radiation is trapped and guided inside the device [11]. Thus, the outcoupling efficiency of conventional bottom-emitting devices is usually only about 20%, and there is a great potential for a significant enhancement in external quantum efficiency (EQE) by increasing the light outcoupling [12–18], in particular for applications that impose strong requirements on power efficiencies (e.g., lighting and mobile applications).

In this contribution, the general theories and discussions of optical structures and characteristics of OLEDs are first given. Based on these basic understandings, various OLED structures that might be useful to enhance the optical outcoupling of the devices will be discussed in sequence.

Physics of Organic Semiconductors, Second Edition. Edited by Wolfgang Brütting and Chihaya Adachi

16.2
Theories and Properties of OLED Optics

The basic structure of OLEDs consists of multilayers of organic materials sandwiched between two electrodes (Figure 16.1). The total thickness of organic materials is usually on the order of 100 nm and is comparable to the emission wavelength. Therefore, emission properties of devices not only depend on intrinsic properties of emitting materials but also often are modified significantly by the optical structures of OLEDs. One popular and common treatment of OLED optics is to use Fabry–Perot formulation [8], which, however, treats only the optical characteristics along the forward direction of an OLED, in which there is no difference for s- or p-polarizations. However, when considering detailed emission characteristics along the different viewing angles of an OLED, the dependence on both wavelength and polarization must be considered. Furthermore, in the more accurate treatment of optical characteristics of OLEDs, the influence of cavity on the transition rate of molecular excited states must be included. All these can be considered by adopting the rigorous and full vectorial electromagnetic modeling of OLEDs.

Such a rigorous electromagnetic model adopts a classical approach based on the equivalence between the emission of a photon due to an electrical dipole transition and the radiation from a classical electrical dipole antenna, which can take into account losses due to electrodes and absorption [19–22]. The formulations are rather complicated and therefore in the following only brief outlines of the treatment are given. First, consider the radiation field from a single dipole of particular position, orientation, and frequency embedded in a general layered structure, as

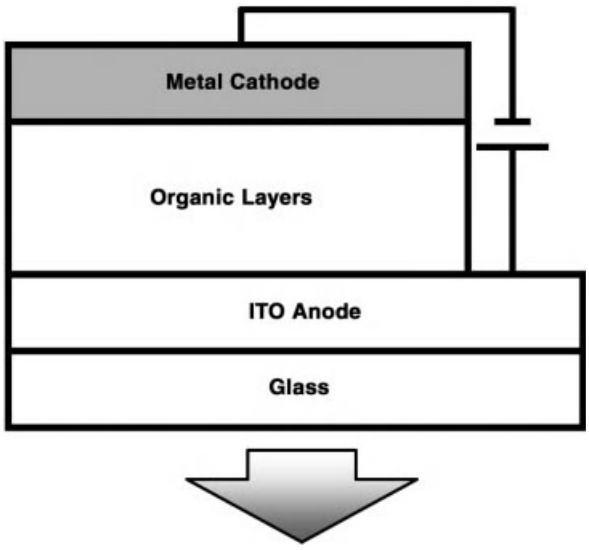

Figure 16.1 The device structure of a conventional bottom-emitting OLED. With permission from Ref. [23].

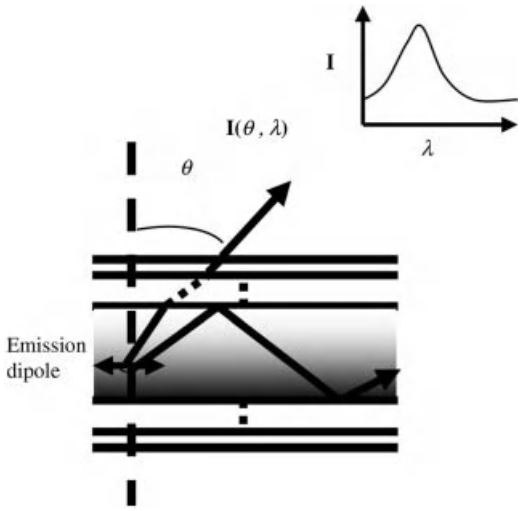

Figure 16.2 Illustration of radiation from an oscillating dipole of a particular position, orientation, and frequency embedded in a general layered structure. With permission from Ref. [23].

illustrated in Figure 16.2 [23]. With plane wave expansion of the dipole field, the full vectorial electromagnetic fields generated by a radiation dipole embedded in a layered structure are calculated, from which the distribution of the radiation power into different plane wave modes and the far-field radiation related to emission characteristics of an OLED are obtained [19–22]. In the plane wave expansion, each plane wave mode can be characterized by an in-plane wave vector k_t, where k_t is the component of the wave vector parallel to the layer surface. To model emission characteristics of a real OLED, one treats the emitting layer as an ensemble of mutually incoherent dipole radiators with distributions in dipole orientations, locations, and frequencies (using the photoluminescence (PL) spectrum of the emitter as the intrinsic spectral distribution of the dipole radiators) [22]. It has been shown that the quantum efficiency of the emitter might influence the simulation results and the power dissipation into different modes [24]. The optical model discussed here indeed has included the influences of the optical structures on the quantum yields (transition rates) of the emitters and the internal quantum efficiencies of OLEDs. The total emission intensity I from the OLED as a function of the wavelength λ and the viewing angle θ (i.e., $I(\theta,\lambda)$, with θ measured relative to the surface normal) (Figure 16.2) is then obtained by averaging contributions over these distributions. Color coordinates of emission at various angles can then be calculated from $I(\theta,\lambda)$.

Take a typical bottom-emitting OLED, which has the organic layer(s) sandwiched between one reflective metal cathode and one transparent indium tin oxide (ITO) anode on glass substrates (Figure 16.1) as an example. The distribution of OLED internal radiation power coupled into different plane wave modes (represented by the in-plane wave vector k_t) can be calculated. Figure 16.3 shows the normalized

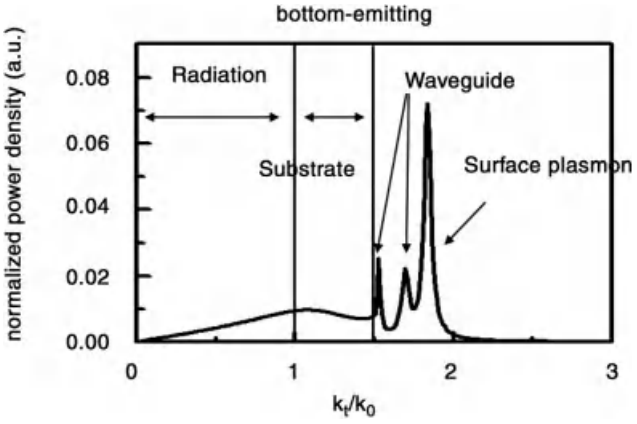

Figure 16.3 Normalized power density at a single emission wavelength of 520 nm as a function of the in-plane wave vector k_t (normalized to the free-space wave vector k_0).

power density at a single emission wavelength of 520 nm as a function of the in-plane wave vector k_t (normalized to the free-space wave vector k_0). In general, internal radiation in OLEDs is coupled into four different modes [25]: radiation modes that are outcoupled as useful emission, substrate modes that are trapped and waveguided in the substrate, waveguided modes that are trapped and waveguided in the high-index organic/ITO layers, and surface plasmon (SP) modes that are guided along the organic/metal interface. In this case of Figure 16.3, roughly speaking, modes with the in-plane wave vector k_t of $0 < k_t < k_0$ are associated with free radiation modes, modes with the in-plane wave vector k_t of $k_0 < k_t < n_{sub}k_0$ (where n_{sub} is the refractive index of the substrate material, that is, glass here) are associated with substrate (waveguided) modes, modes with the in-plane wave vector k_t of $n_{sub}k_0 < k_t < n_{ITO}k_0$ (where n_{ITO} is the refractive index of the transparent indium tin oxide) are associated with organic/ITO waveguided modes, and modes with the in-plane wave vector k_t of $n_{ITO}k_0 < k_t < \infty$ are associated with surface plasmon modes. By integrating the area in the free radiation modes relative to the total radiation, the optical outcoupling efficiency of the device can be calculated. In the case of Figure 16.3, the outcoupling efficiency of conventional bottom-emitting devices is usually only about 20%.

16.3
A Few Techniques and Device Structures to Enhance Light Outcoupling of OLEDs

16.3.1
Second-Antinode OLED

In a typical bottom-emitting OLED structure as shown in Figure 16.1, due to strong reflection of the metal electrode, directly outgoing beams of the emission interfere

with the beams reflected from the metal electrode, influencing outcoupled emission intensity [8, 26]. To obtain constructive interference and to optimize light extraction from the device, it roughly requires the locations of emitters to the metal electrode be consistent with the antinode condition of major emission wavelengths (i.e., the emitter-to-metal round-trip phase change equals multiple integers of 2π) [8, 26]. Due to generally low conductivity and low carrier mobilities of organic materials, OLEDs are typically optimized by locating emitters around the first antinode of the metal electrode to minimize the layer thickness and device voltage. Furthermore, placing emitters at a farther antinode by using a thicker carrier transport layer may significantly disturb and complicate the scenario of carrier recombination (e.g., the location and distribution). Recent advances in conductive doping of organic semiconductors and high-mobility materials [27–30], however, may remove such constraints. By utilizing device structures containing conductive doping, it is interesting to see theoretically and experimentally the influences of the location of emitters relative to the metal electrode on OLED emission [31].

Consider an inverted OLED structure: glass/ITO (120 nm)/Bphen:Cs (5 wt%, 20 nm)/Bphen (20 nm)/Alq_3:C545T (1 wt%, 20 nm)/α-NPD (40 nm)/m-MTDATA:F4-TCNQ (1.5 wt%, x nm)/Ag (100 nm), which adopts the inverted structure with conductive doping in carrier transport layers for current conduction and carrier injection [31]. ITO and Ag serve as the bottom cathode and the top anode, respectively. Other layers in sequence consist of 4,7-diphenyl-1,10-phenanthroline (Bphen) doped with 5 wt% Cs as the n-doped electron injection layer [28], undoped Bphen as the electron transport layer, tris-(8-hydroxyquinoline) aluminum (Alq_3) doped with the fluorescent dye C545T as the emitting layer [1, 8], α-naphthylphenylbiphenyl diamine (α-NPD) as the hole transport layer [32], 4,4′,4″-tris(3-methylphenylphenylamino)triphenylamine (m-MTDATA) doped with 1.5 wt% of tetrafluorotetracyano-quinodimethane (F4-TCNQ) as the p-doped hole injection layer [27]. The thickness of m-MTDATA:F4-TCNQ is varied to adjust the distance between emitters and the metal electrode. The rigorous electromagnetic model described in the previous section is used for performing the analysis, which can take into account loss due to electrodes. To model emission characteristics of an OLED, it is assumed that the emitting layer contains an ensemble of mutually incoherent dipole radiators with distributions in dipole orientations (a random isotropic distribution), locations (a decaying exponential distribution from the α-NPD/Alq_3 interface into Alq_3 with an exciton diffusion length of 15 nm) [33], and frequencies (using the photoluminescence spectrum of Alq_3:C545T as the intrinsic spectral distribution of the dipole radiators). Radiation characteristics of OLEDs are then obtained by averaging contributions over these distributions.

As mentioned in the previous section, radiation in OLEDs is in general coupled into four different modes [25]: radiation modes, substrate modes, organic/ITO waveguided modes, and surface plasmon modes. The partition of OLED radiation into these modes strongly depends on the location of emitters relative to the metal electrode [31]. As an instance, Figure 16.4a shows the fractions of radiation from single-frequency (520 nm, corresponding to the peak wavelength of C545T emission) and single-position (the α-NPD/Alq_3 interface) emitting dipoles coupled into

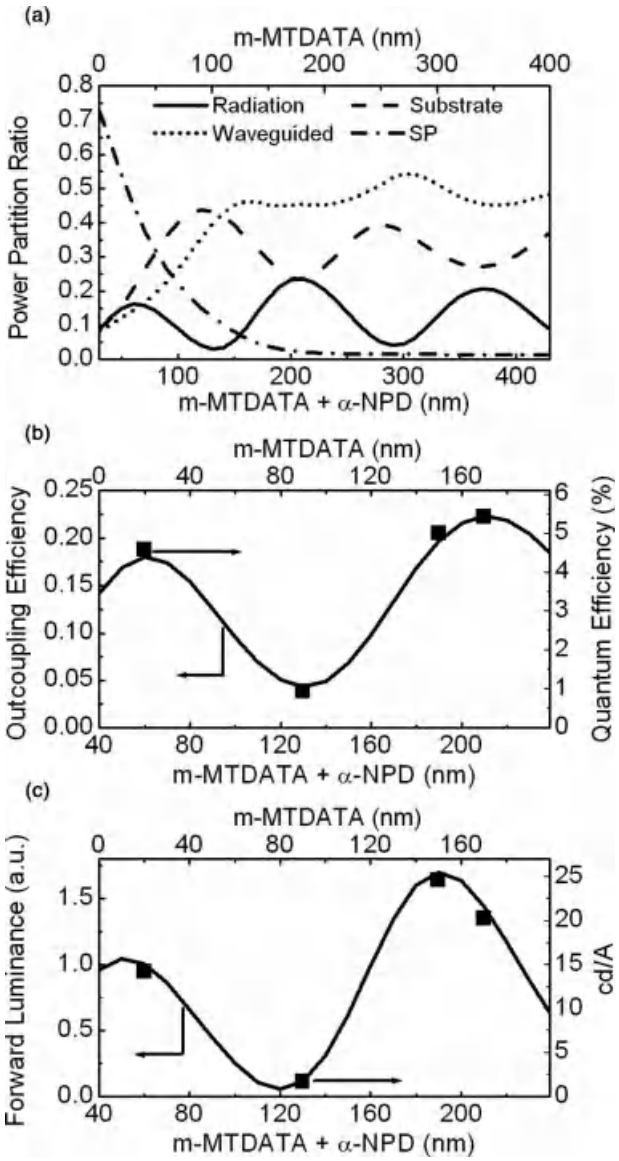

Figure 16.4 Efficiency characteristics of the device of glass/ITO (120 nm)/Bphen:Cs (5 wt%, 20 nm)/Bphen (20 nm)/Alq_3:C545T (1 wt%, 20 nm)/α-NPD (40 nm)/m-MTDATA:F4-TCNQ (1.5 wt%, *x* nm)/Ag (100 nm). (a) Calculated fractions of radiation coupled into different modes. (b) Calculated (line) and measured (symbol) outcoupling efficiency. (c) Calculated (line) and measured (symbol) forward luminance (normalized to $x = 20$ nm case) as a function of the distance between emitters and the reflective Ag electrode (by varying m-MTDATA thickness). Results of (a) are calculated with single-frequency (520 nm) and single-position (α-NPD/Alq_3 interface) emitting dipoles, while those of (b) and (c) are calculated with the complete dipole distributions. With permission from Ref. [31].

different modes as a function of its distance to the Ag electrode (by varying m-MTDATA thickness). With emitting dipoles getting close to the metal (and thus smaller thickness of the overall structure), ratios of substrate modes and waveguided modes are low, yet most of the radiation is coupled into SP modes and OLED emission is significantly quenched. With increasing the distance of emitting dipoles to the reflective metal, coupling into SP modes drops rapidly and those into other modes first rise and then become somewhat periodic with the distance. The maxima and minimum occurring in outcoupling (i.e., fraction of radiation modes) roughly correspond to antinodes and nodes of the metal electrode, respectively. Interestingly, the second antinode gives the highest outcoupling efficiency than other antinodes, particularly the first antinode condition that is typically implemented in optimized OLEDs. One notices that around the second antinode, the highest efficiency is achieved because the coupling into SP modes has dropped to an almost negligible level and both substrate and waveguided modes happen to be around their local minima.

Taking into consideration the complete distributions of dipole frequencies and locations [31], Figure 16.4b and c also shows the calculated outcoupling efficiency and the forward luminance, respectively, as a function of the distance to Ag (by varying m-MTDATA thickness). In Figure 16.4c, the forward luminance is normalized to that of a conventional OLED optimized around the first antinode, that is, the device with the structure of glass/ITO (120 nm)/Bphen:Cs (5 wt%, 20 nm)/Bphen (20 nm)/Alq_3:C545T (1 wt%, 20 nm)/α-NPD (40 nm)/m-MTDATA: F4-TCNQ (1.5 wt%, 20 nm)/Ag (100 nm) (device A). In Figure 16.4b and c, one observes that locating emitters around the first node (m-MTDADA = 90 nm, device B) gives the least outcoupling, while locating emitters around the second antinode enhances both outcoupling and forward luminance. The conditions for obtaining maximal outcoupling and maximal forward luminance are slightly different. The maximal forward luminance (∼1.6 times larger than that of device A) occurs around m-MTDADA = 150 nm (device C), at which the antinode condition is exactly satisfied by 520 nm. The maximal outcoupling (∼1.2 times larger than that of device A) occurs around m-MTDATA = 170 nm (device D), at which the antinode condition is exactly satisfied by a wavelength (560 nm) larger than the peak wavelength of C545T. Experiments indeed were conducted on devices A–D for comparison with analyses [31]. Electrical properties of these devices are almost identical despite very large variation in thickness of the hole injection layer (m-MTDATA:F4-TCNQ), indicating the effectiveness of the conductive doping in enhancing conductivity. In Figure 16.4b and c, measured efficiencies of devices A–D (symbols) are compared with calculated ones (lines). Fairly good agreement is obtained between calculated and experimental values.

The angular dependence of electroluminescence (EL) characteristics is also an important concern in applications. Along with photoluminescence of Alq_3:C545T, Figure 16.5a–c shows measured (symbols) and simulated (lines) EL spectra with relative intensities at viewing angles of 0° and 60° off the surface normal for devices A, C, and D, respectively, in which again fairly good agreement is obtained [31]. Figure 16.5d compares angular distributions of the measured EL intensity

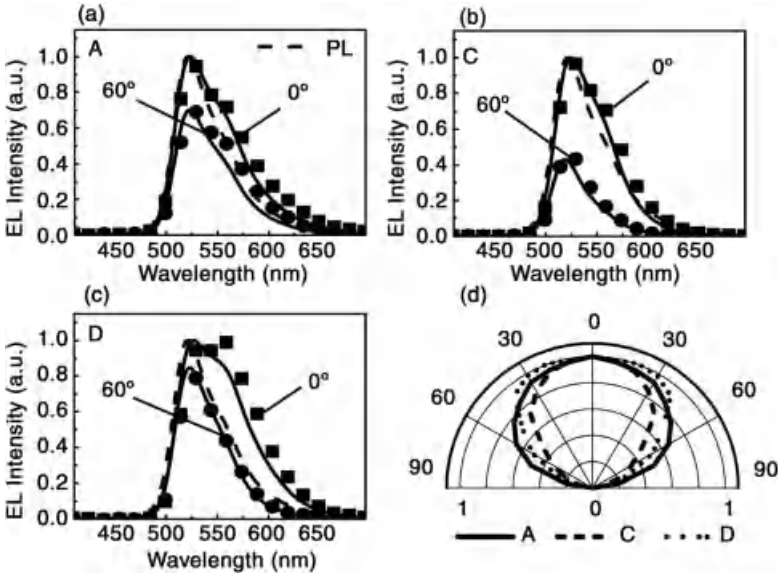

Figure 16.5 Measured (symbols) and calculated (lines) EL spectra with relative intensities at viewing angles of 0° and 60° for (a) device A, (b) device C, and (c) device D. (d) Polar plots of measured EL intensities (normalized to the 0° intensity) for devices A, C, and D. In (a)–(c), PL of Alq_3:C545T is also shown for comparison. With permission from Ref. [31].

(normalized to 0° intensity) for the same three devices. Because the antinode condition is set for a larger wavelength, EL of device D at small angles is broader than PL of C545T. Besides, devices C and D do not exhibit obvious color shift with viewing angles. For device C (with highest forward luminance), due to the enhanced forward luminance, it also exhibits more directed emission (Figure 16.5d) as often observed in the strong microcavity devices, yet without suffering color shift with viewing angles [8, 22]. Such characteristics may be useful for display applications, since without involving more complicated fabrication and tuning of microcavity OLED structures, advantages similar to those of microcavity OLEDs can be obtained by simply increasing layer thickness.

In 2009, Leo and coworkers [3] and Neyts and coworkers [34] independently reported high-EQE OLEDs by combining the second-antinode OLED structure and other optical outcoupling schemes, such as high-index substrates and other external light extraction structures like half-sphere outcoupling lens or patterned/textured substrate surfaces. When Leo and coworkers [3] fabricated a standard (first-antinode) phosphorescent white OLED on a high-index substrate, an EQE of 14.45% and a power efficiency of 33 lm/W (at the brightness of 1000 nits) were achieved. By attaching a large index-matched hemisphere to the device substrate for optical outcoupling, the EQE and power efficiency were increased by a factor of 2.4–34% and 81 lm/W (at the brightness of 1000 nits), respectively. By replacing the OLED structure with the second-antinode structure, the EQE and power efficiency

were further increased to 46% and 124 lm/W. In their another set of experiments, with the application of the patterned high-index substrate surface (i.e., periodical pyramids) for optical outcoupling, similarly, the EQE and power efficiency of the device were increased from 26%, 63 lm/W to 34%, 90 lm/W by replacing the first-antinode structure with the second-antinode structure. When Neyts and coworkers [34] fabricated a standard (first-antinode) phosphorescent green OLED on a high-index substrate, an EQE of 15% and a power efficiency of 70 lm/W were achieved (at the brightness of 1000 nits). By attaching a large index-matched hemisphere to the device substrate for optical outcoupling, the EQE and power efficiency were increased by a factor of 2.8–42% and 183 lm/W (at the brightness of 1000 nits), respectively. All these results clearly demonstrate that, by placing the emitters farther away from the reflective metal electrode, the second-antinode OLED structure can effectively reduce the plasmonic losses to the metal electrode and can be used to enhance the optical extraction efficiency of OLEDs.

These results discussed in this section also have certain implications to tandem OLEDs that have multiple OLED units stacked vertically in series [35–39]. In the simplest viewpoint, one would expect proportional increase in the luminance efficiency (i.e., cd/A) with the number of emitting units. The results here, however, suggest that the enhancement in cd/A efficiency could significantly exceed such proportional increase (extra efficiency gain from the tandem structure), since the emitting unit farther away from the reflective metal electrode could contribute a larger cd/A efficiency or total outcoupling.

16.3.2
Top-Emitting OLEDs Capped with Microlens or Scattering Layers

According to discussions in the previous sections, in conventional OLED structure as shown in Figure 16.1, the OLED emission is outcoupled through the substrate (i.e., the bottom-emitting structure) and there is a significant portion of the internal radiation being trapped in the substrate modes, contributing to a significant outcoupling loss. If one instead makes the bottom electrode of OLED reflective and the top electrode transparent, outcoupling OLED internal radiation through the topside (i.e., the top-emitting OLED structure), one could avoid the loss in substrate modes and increase the outcoupling efficiency [40]. With the top-emitting structure, one could possibly further make some optical micro- or nanostructures on atop the top electrode to access/manipulate/outcouple the internal organic waveguided modes [6, 15], further boosting the OLED outcoupling efficiency. In this section, examples of combining top-emitting OLED structures with microlens and scattering layers for enhancing OLED light extraction are discussed [6, 15].

In the first case, by integrating top-emitting OLEDs with microlenses, the enhancements in external quantum efficiency, cd/A efficiency, and color performances (small color shift with viewing angles) can be simultaneously achieved [15]. Consider the top-emitting OLEDs without microlenses shown in Figure 16.6a [36]: glass/Ag (100 nm)/m-MTDATA:F_4-TCNQ (2 wt%, 30 nm)/α-NPD (20 nm)/Alq_3: C545T (1wt%, 20 nm)/Alq_3 (40 nm)/LiF (0.5 nm)/Al (1 nm)/Ag (20 nm)/

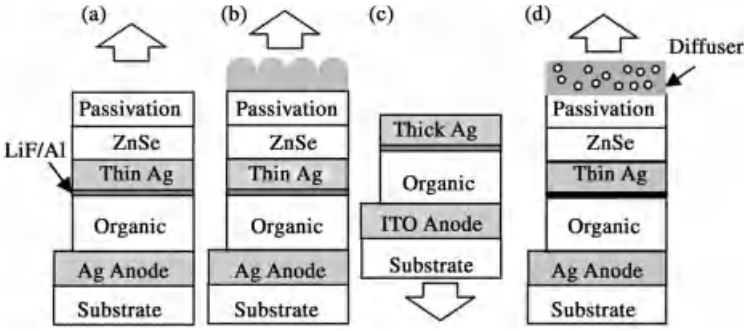

Figure 16.6 Device structures of (a) top-emitting OLED without microlenses, (b) top-emitting OLED with microlenses, (c) conventional bottom-emitting OLED, and (d) top-emitting OLED capped with a scattering layer. With permission from Refs [6, 15].

ZnSe(45 nm)/parylene (1 μm). The top-emitting microcavity OLED is based on the efficient fluorescent green emitter C545T, whose PL shows a peak around 521 nm and a FWHM (full width at half maximum) of ∼60 nm. It adopts the high-reflectivity Ag (100 nm) as the bottom anode and the thin Ag (20 nm) as the semitransparent top cathode. The organic multilayer structure in sequence consists of m-MTDATA doped with F_4-TCNQ as the p-doped hole injection layer, α-NPD as the hole transport layer, Alq_3 doped with C545T as the emitting layer, and undoped Alq_3 as the electron transport layer. Ultrathin layers of LiF (0.5 nm) and Al (1 nm) serve as the electron injection layer [41, 42]. The ZnSe and micrometer-thick parylene layers were coated by the room-temperature vapor-phase deposition on top of the device as the passivation layer [43]. For the top-emitting OLED with microlenses (Figure 16.6b), all the layer structures were the same, except that a thin sheet of polydimethylsiloxane (PDMS, ∼50 μm) with the microlens array was further laminated on top of the parylene. For comparison, a roughly optimized conventional bottom-emitting OLED (Figure 16.6c) was also tested. The microlens array on PDMS was fabricated by the micromolding technique using the Si master mold [44]. The fabricated thin PDMS sheets (∼50 μm thick) with microlens arrays (Figure 16.7a) were examined with the scanning electron microscopy (SEM). The top-view SEM micrograph (Figure 16.7b) shows the hexagonal arrangement of the microlens array, while the oblique-view SEM micrograph in Figure 16.7c indicates the nearly hemisphere shape (with the diameter of ∼10 μm) of the microlenses [15].

Figure 16.8a and b shows the measured electroluminescence spectra with relative intensities for the top-emitting OLED without and with microlenses, respectively, at viewing angles of 0°, 30°, and 60° off the surface normal, compared to the (normalized) 0° EL spectrum of the conventional bottom-emitting device [36]. Figure 16.8c shows the polar plots of the emission intensities (normalized to the 0° intensity of the conventional device) for the three devices [15]. Compared to the conventional bottom-emitting device, the top-emitting devices show both the narrowed EL spectra and the enhanced forward emission intensities. The enhancement of the 0° intensity is up to 2.5× and 3× for top-emitting devices without or

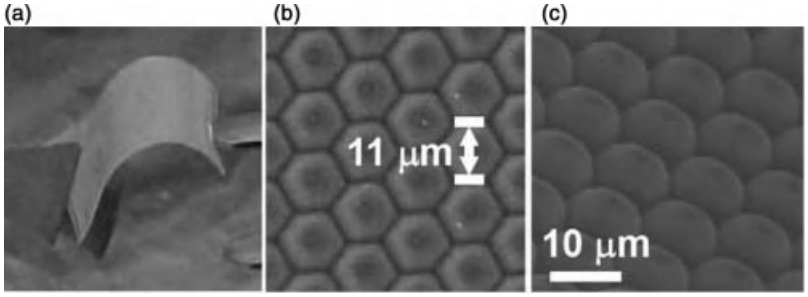

Figure 16.7 (a) Photo of the PDMS sheet with microlens arrays. (b) Top-view SEM image of the microlenses. (c) Oblique-view SEM image of the microlenses. With permission from Ref. [15].

with microlenses, respectively. For the top-emitting OLED without microlenses (Figure 16.8a), the EL shows a sharp emission peak at 538 nm at 0° and a significant shift to shorter wavelengths with the viewing angles due to microcavity effects. Interestingly, with microlens lamination (Figure 16.8b), the 0° emission peak slightly blueshifts to 527 nm and the shift of EL spectra with viewing angles is eliminated. It is also noted that the spectral shapes are modified with microlens lamination. By considering results of Figure 16.8a–c, it may be concluded that lamination of microlenses has led to mixing/averaging EL of different angles and redirecting more light into the forward direction, consequently giving stable/saturated colors over angles.

Figure 16.9a and b shows the cd/A efficiencies and the external quantum efficiencies, respectively, of the three devices [15]. The conventional bottom-emitting device, the top-emitting device without microlenses, and the top-emitting device with microlenses show efficiencies up to 14.5 cd/A, 4%; 36.3 cd/A, 5.7%; and 43.8 cd/A, 6.4%, respectively. The top-emitting device shows not only enhanced cd/A efficiency (2.5×) but also substantially enhanced external quantum efficiency (1.42×), compared to the conventional bottom-emitting device. With microlens lamination, the top-emitting OLED shows even larger enhancement in both quantum efficiency (1.6×) and cd/A efficiency (3.0×).

The case above demonstrates that by integrating top-emitting OLEDs with microlens, simultaneous enhancements in both color and efficiency performances may be obtained. Such a microlens approach, however, leads to even more strongly directed emission (large deviation from the desired Lambertian distribution). Besides, microlenses are more complicated in fabrication and are less convenient for integration. The second case to be discussed here shows that by using the microparticle diffusers (scattering layers) instead of microlenses [6], enhancements in both color and efficiency performances are kept, and yet the enhancement in quantum efficiencies is even more significant (∼2.1×) and the emission pattern can be made closer to the Lambertian distribution [6]. Importantly, the fabrication of the diffuser (scattering) films is much simpler, making it attractive for use in enhancing OLED performances.

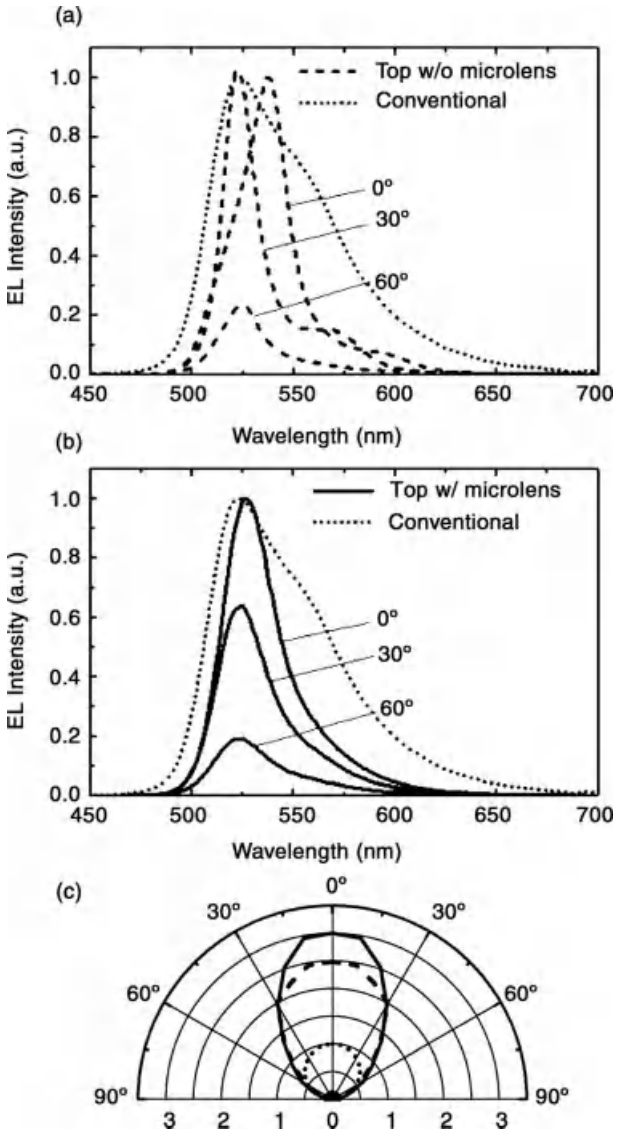

Figure 16.8 EL spectra with relative intensities at viewing angles of 0°, 30°, and 60° for top-emitting device (a) without and (b) with microlenses. In (a) and (b), the EL spectrum of the conventional bottom-emitting OLED is also shown for comparison. (c) Polar plots of emission intensities of the three devices (normalized to the 0° intensity of the conventional bottom-emitting device). With permission from Ref. [15].

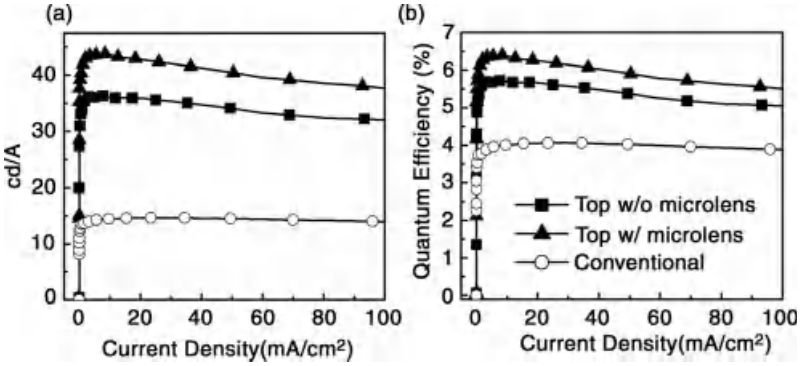

Figure 16.9 (a) cd/A efficiencies and (b) quantum efficiencies of the three devices. With permission from Ref. [15].

For the top-emitting OLED with the diffuser (scattering) films (Figure 16.6d), the entire layer structures are similar to those in Figure 16.6a and b, except that a thin sheet of polydimethylsiloxane (PDMS) (~100 μm) dispersed with the high-index dielectric microparticles (ZrO_2) is laminated on the top of parylene. The fabrication of the microparticle diffuser (scattering) films is illustrated schematically in Figure 16.10 [6]. The zirconium dioxide (ZrO_2) microparticles (with a refractive index of ~2.0, average particle sizes of 10–20 μm) were first dispersed into the poly (dimethylsiloxane) (PDMS) matrix with a concentration of 25 wt%. The microparticle diffuser (scattering) film was then formed by the doctor blading technique, as shown in Figure 16.10a, with the thickness controlled by the gap between the blade and the substrate. After curing, the free-standing diffuser (scattering) sheets were then lifted (from the carrier substrate) for device use. The microscopic view

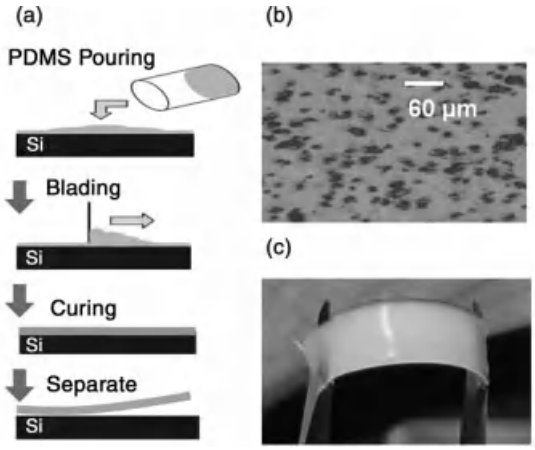

Figure 16.10 (a) Fabrication processes of the diffuser (scattering) film. (b) The microscopic view and (c) photo of the microparticle diffuser film. With permission from Ref. [6].

and the photograph of the fabricated diffuser (scattering) film (~100 μm) are shown in Figure 16.10b and c [6].

Figure 16.11a and b shows the measured electroluminescence spectra with relative intensities for the top-emitting OLED without and with diffuser (scattering) films, respectively, at viewing angles of 0°, 30°, and 60° off the surface normal, compared to the (normalized) 0° EL spectrum of the conventional bottom-emitting device. Figure 16.11c shows the polar plots of the emission intensities (normalized to the 0° intensity of the conventional device) for the three devices. Compared to the conventional bottom-emitting device, top-emitting devices show both narrowed EL spectra and enhanced forward emission intensities. The enhancement of the 0° intensity is up to 2.7× and 2.9× for top-emitting devices without or with diffusers (scattering films), respectively. For the top-emitting OLED without diffusers (Figure 16.11a), the EL shows a significant shift to shorter wavelengths with the viewing angles due to microcavity effects. Interestingly, with diffuser films (Figure 16.11b), the shift of EL spectra with viewing angles is eliminated. Also, the incorporation of diffusers had modified the emission pattern of the top-emitting OLED (Figure 16.11c), making it closer to the desirable Lambertian distribution (compared to more directed emission from top-emitting OLEDs without diffusers). Such characteristics are in contrast to those obtained with the previous microlens approach. Results of Figure 16.11a–c indicate that microparticle diffusers had led to mixing/averaging EL of different angles and redistributing light into different directions, consequently giving stable/saturated colors over angles and the more desired emission pattern [6].

Figure 16.12a and b shows the cd/A efficiencies and the external quantum efficiencies, respectively, of the three devices: the conventional bottom-emitting device, the top-emitting device without diffusers, and the top-emitting device with diffusers show efficiencies up to 14.5 cd/A, 4%; 39 cd/A, 6.1%; and 42 cd/A, 8.4%, respectively. The top-emitting device shows not only enhanced cd/A efficiency (2.6–2.7×) but also substantially enhanced external quantum efficiency (1.6×) compared to the conventional bottom-emitting device. With diffusers, the top-emitting OLED shows even larger enhancement in both quantum efficiency (2.1×) and cd/A efficiency (2.9×). Particularly, the quantum efficiency enhancement obtained using the microparticle diffusers is significantly larger than that obtained with the previous microlens approach [6].

16.3.3
OLED with Internal Scattering

Recent studies reveal that the light extraction of OLEDs can be enhanced by using external extraction structures (EES) [3, 13, 14, 16–18, 45] and/or internal extraction structures (IES) [4, 5, 46–49]. EES are optical micro/nanostructures implemented at the outside surface of the device substrate and can extract the substrate modes of the OLED emission. IES are optical micro/nanostructures inserted between the device substrate and the ITO anode layer of OLEDs. Such structures can extract/impact both the ITO/organic waveguide modes and the substrate modes, since

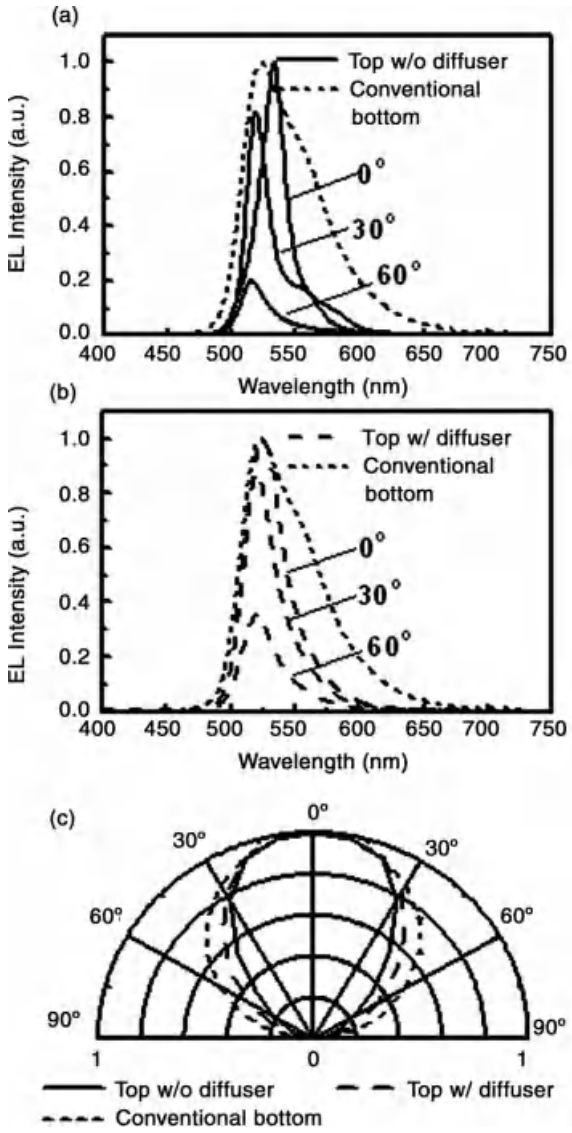

Figure 16.11 EL spectra with relative intensities at viewing angles of 0°, 30°, and 60° for top-emitting device (a) without and (b) with diffusers. In (a) and (b), the EL spectrum of the conventional bottom-emitting OLED is also shown for comparison. (c) Polar plots of emission intensities of the three devices (normalized to the 0° intensity). With permission from Ref. [6].

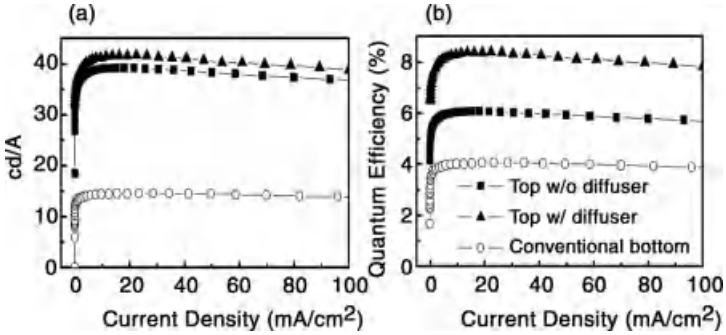

Figure 16.12 (a) cd/A efficiencies and (b) quantum efficiencies of the three devices. With permission from Ref. [6].

the micro/nanostructures between the substrate and the ITO anode can disturb the total internal reflection at the ITO/substrate interface and also redirect the radiation reflected from the substrate/air interface by the total internal reflection for outcoupling. Thus, the IES technique is thought to potentially yield higher extraction efficiency than the EES technique [4, 5, 46–49].

Among various IES techniques reported for OLEDs [4, 5, 46–49], the ones employing the scattering mechanism appear to be relatively more feasible [4, 5, 17, 18], since the more complicated and expensive microfabrication or even nanofabrication may be avoided. In fabricating the internal scattering structures, the most important issue is to achieve optical nonuniformity for light scattering and yet also surface flatness for device integration simultaneously. The internal scattering structures may be fabricated in two different ways. One is to construct the light-scattering structure first and then use the planarization layer to smooth the surface [4, 5]; the other is simply mixing the light-scattering objects (e.g., particles) into a matrix material and directly coating the scattering films with relatively smooth surface. The quality of the first approach depends on the planarization technique [4, 5, 46–48, 50–52], such as "thermal reflow," "etch back," "chemical mechanical polish," and so on. Furthermore, the refractive index of the planarization layer must be high enough to extract light from the ITO/organic waveguide modes effectively. For instance, the structure and processes proposed by Tyan *et al.* belong to the first approach [5]. This first approach in general is still relatively complicated. Here, we place more emphasis on the second approach: fabricating the scattering films with nanoparticle dispersed in the matrix with smooth enough surfaces for the subsequent device integration [49]. By inserting a nanoparticle-based scattering film (by spin-coating) between the OLED and the glass substrate as the internal extraction structure, the external quantum efficiencies of conventional bottom-emitting OLEDs can be significantly improved [49]. The fabrication of nanoparticle-based scattering films is simple and effective, attractive for mass production and cost reduction.

Two types of devices were compared [49]. The first one was the conventional bottom-emitting OLEDs without internal scattering films, which were used as the

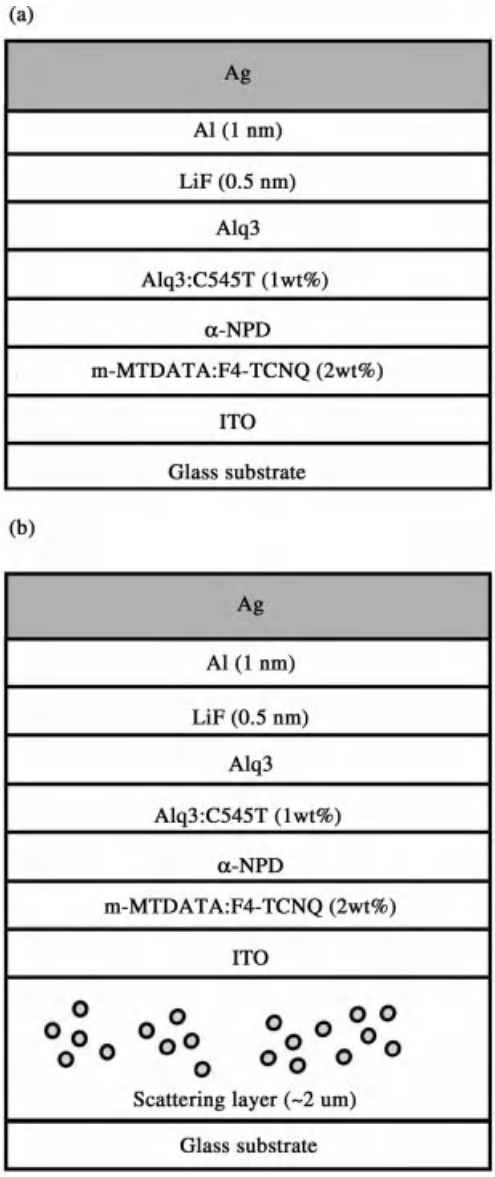

Figure 16.13 Device structures of bottom-emitting OLEDs (a) without the internal nanocomposite scattering layer, and (b) with the internal nanocomposite scattering layer. With permission from Ref. [49].

reference device (Figure 16.13a). The device structure was glass/ITO (120 nm)/m-MTDATA:F4-TCNQ (2wt%, 30 nm)/α-NPD (20 nm)/Alq_3:C545T (1 wt%, 20 nm)/Alq_3 (45 nm)/LiF (0.5 nm)/Al (1 nm)/Ag (200 nm). It adopted the high-reflectivity Ag (200 nm) as the top cathode and the transparent ITO deposited by magnetron

sputtering as the bottom anode. For the bottom-emitting OLED with the internal scattering film, as shown in Figure 16.13b, all the materials and the layer structures were the same as those of the conventional bottom-emitting device, except that a nanoparticle-based scattering film was spin-coated onto the glass substrate and was inserted between the substrate and the ITO anode.

For OLED IES applications, in general it is desired that both the host and nanoparticle materials of the nanocomposite scattering films possess high transparency and low absorption, while the nanocomposite scattering films possess strong enough optical scattering, high integrated transmittance, and appropriate surface flatness for subsequent device integration. In addition, the host material/nanocomposite should have good enough adhesion to the glass substrate and enough toughness to endure the ITO sputtering on top. With these requirements, the materials used for internal scattering films were different from those described in the previous section (external scattering films for top-emitting OLEDs). The host material used was a transparent photoresist (TPR). The light-scattering particles used were TiO_2 nanoparticles with average diameters of about 100 and 400 nm. Nanoparticles of different sizes were well dispersed into the TPR host with different concentrations (by adjusting the mixing ratios of the nanoparticles and the TPR host solutions). Three compositions were tested for the smaller 100 nm nanoparticles: 0.5 g TiO_2 particles in 10 cc TPR (composition A), 2 g TiO_2 particles in 10 cc TPR (composition B), 3 g TiO_2 particles in 10 cc TPR (composition C). The solid content of the TPR solution is about 30%. Similarly, three compositions were tested for the larger 400 nm nanoparticles: 0.8 g TiO_2 particles in 10 cc TPR (composition D), 1.6 g TiO_2 particles in 10 cc TPR (composition E), 2.4 g TiO_2 particles in 10 cc TPR (composition F). The procedure for the preparation of the nanocomposite materials and films was similar to those shown in Figure 16.10a. Nanoparticle-based scattering films were then made by spin-coating the filtered nanocomposite solutions onto the glass substrates, with the thickness of about 2 μm. After spin-coating, the film was cured at 130 °C for 10 min.

The UV-Vis spectrophotometer equipped with an integrating sphere was often used to characterize the transmittance and scattering properties of the samples having a single nanocomposite layer on the glass substrate: the total transmittance (T_{total}), the direct transmittance (T_{direct}), and the diffuse transmittance ($T_{diffuse}$). T_{total} was measured by using a monochromatic light beam normally incident onto the film side and then using an integrating sphere to collect transmitted light over all angles from the substrate side. On the other hand, T_{direct} was measured by using a monochromatic light beam normally incident onto the film side and then collecting transmitted light only in the normal direction (within a 5° collection angle) from the substrate side. $T_{diffuse}$ and the Haze were then obtained by $T_{diffuse} = T_{total} - T_{direct}$ and $\text{Haze} = T_{diffuse}/T_{total}$, both being useful indication of the optical scattering capability of the fabricated scattering films.

T_{total}, T_{direct}, $T_{diffuse}$, and Haze values of the nanocomposite films of compositions A–F at the wavelength of 520 nm are also summarized in Table 16.1 [49]. Compared to the pure TPR host film, the addition of the smaller 100 nm nanoparticles gives slight optical scattering capability ($T_{diffuse} = 2$–3% versus $T_{diffuse} = 1\%$ at 520 nm),

Table 16.1 Physical and optical properties of nanocomposite scattering films having TiO_2 nanoparticles of different sizes and concentrations (compared to the pure TPR host film).

Composition N.P.(g)/P.R. (c.c.)	Pure TPR (0/10)	A (0.5/10)	B (2/10)	C (3/10)	D (0.8/10)	E (1.6/10)	F (2.4/10)
		100 nm nanoparticles			400 nm nanoparticles		
Roughness (nm)	0.5	0.5	0.5	0.4	0.4	4.8	5.6
T_{total} (%)	92	90	91	89	81	71	71
T_{direct} (%)	91	87	89	87	56	25	19
$T_{diffuse}$ (%)	1	3	2	2	25	46	52
Haze (%)	1	3	2	2	31	65	73

Values of T_{total}, T_{direct}, $T_{diffuse}$, and Haze are for the wavelength of 520 nm.
With permission from Ref. [49].

but the scattering capability is still rather limited. As shown in Table 16.1, the use of the larger nanoparticles (400 nm) largely raises $T_{diffuse}$ and Haze values, and thus the optical scattering capability. Roughly, $T_{diffuse}$ and Haze values increase with the nanoparticle size and concentration, and $T_{diffuse}$ up to 52% and Haze up to 73% were obtained in nanocomposites with the highest concentration of 400 nm nanoparticles shown. Even stronger optical scattering capability could be obtained with even higher concentrations, but the large surface roughness limited the use in device integration.

The integrated transmittance T_{total} of the scattering films is also critical for the overall enhancement of the OLED optical outcoupling, in addition to the strong enough scattering capability. A low T_{total} implies that most of the light cannot transmit through the film (either directly or scatteringly) and be outcoupled, but can be scattered backward instead. Therefore, upon raising the scattering capability, simultaneously maintaining a high enough T_{total} is also important. In Table 16.1, it is seen that T_{total} decreases when larger nanoparticles are used and when the nanoparticle concentration increases. Nevertheless, even for the highest concentration shown (for 400 nm nanoparticles), T_{total} remains above the high value of 70% at major emission wavelengths around 520 nm. Even stronger optical scattering capability could be obtained with even higher concentrations, but T_{total} will drop below a useful value for enhancing optical outcoupling of OLEDs.

Figure 16.14a–c shows the representative *I–V*, cd/A efficiency, and external quantum efficiency characteristics, respectively, of a bottom-emitting OLED incorporating the nanocomposite internal scattering layer (of composition F) [49]. For comparison, corresponding characteristics of the bottom-emitting device without the internal scattering layer (the reference device) are also shown in Figure 16.14a–c. The device with the internal scattering layer exhibits significantly higher cd/A and external quantum efficiencies (Figure 16.14b and c). Table 16.2 summarizes the cd/A efficiencies and external quantum efficiencies of both the reference device and the devices using nanocomposite scattering films of compositions A–F. The percentages of the efficiency enhancement of all devices with internal scattering

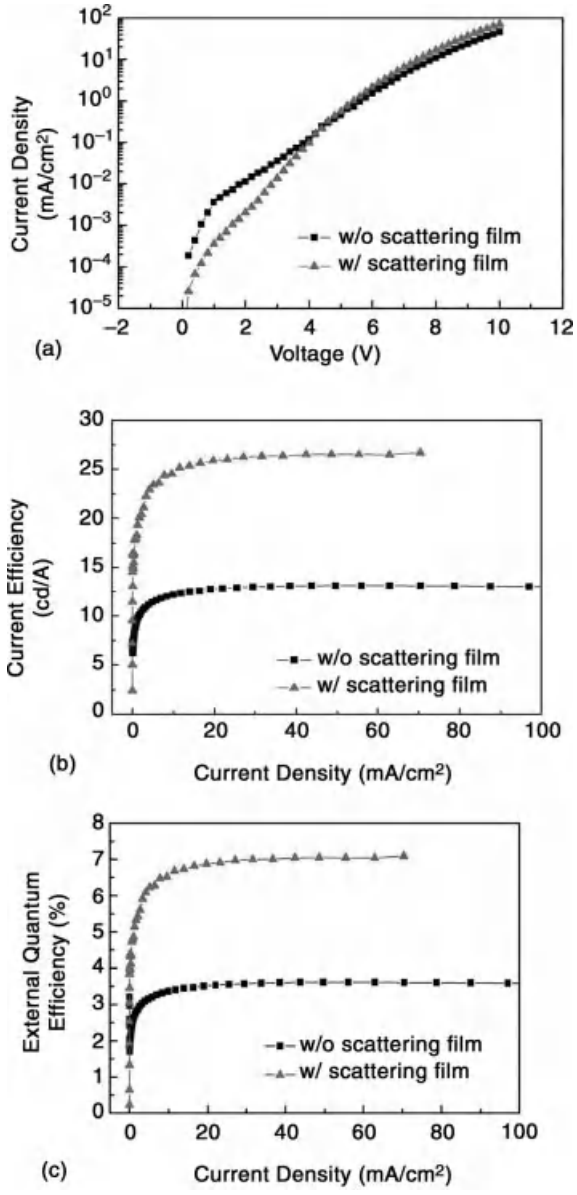

Figure 16.14 (a) *I–V*, (b) cd/A efficiencies, and (c) external quantum efficiencies of a bottom-emitting OLED integrated with the nanocomposite scattering layer (with composition F) and the bottom-emitting device without the internal scattering layer (the reference device). With permission from Ref. [49].

Table 16.2 cd/A efficiencies and external quantum efficiencies of the reference device and the devices using nanocomposite scattering films of compositions A–F.

Composition N.P.(g)/P.R.(c.c.)	Reference device	A (0.5/10)	B (2/10)	C (3/10)	D (0.8/10)	E (1.6/10)	F (2.4/10)
		100 nm nanoparticles			400 nm nanoparticles		
EQE (%)	3.6	3.9	4.6	4.0	4.9	5.8	7.1
cd/A	13.1	13.7	16.1	14.9	18.8	21.9	26.7
QE enhancement (%)	N.A.	7.0	29.4	11.2	38.3	60.9	96.2
cd/A Enhancement (%)	N.A.	4.2	23.3	14.0	37.7	73.2	104.0

With permission from Ref. [49].

layers, in relation to the reference device, are also listed in Table 16.2. Results of Table 16.2 indicate that the nanocomposite scattering films with stronger scattering capability (as indicated by larger T_{diffuse} and Haze values) in general give larger enhancement in optical outcoupling and EL efficiencies, as long as the total transmittance remains high enough. Among all the devices, the device using the nanocomposite scattering film of composition F (with the highest concentration of larger 400 nm nanoparticles) shows the highest efficiency enhancement (Figure 16.14 and Table 16.2). With efficiencies of 26.7 cd/A, 7.1%, they represent a $>2\times$ and a $>1.9\times$ enhancement in the cd/A and external quantum efficiency, respectively, compared to efficiencies (13.1 cd/A, 3.6%) of the reference device.

Figure 16.15a and b shows the electroluminescence spectra over several viewing angles (0°, 30°, and 60°) for the bottom-emitting OLED without and with internal scattering films (with composition F, highest EL efficiency), respectively [49]. Compared to the reference device, the incorporation of the nanocomposite scattering film in general does not alter the EL spectra and color of the OLED, but one sees that the slight color shift with viewing angles occurring in the reference device is completely eliminated in the device with the nanocomposite scattering film. Thus, the color and viewing angle characteristics of the OLED indeed are improved by incorporating the internal scattering layer. Such color stability over viewing angles may be due to the mixing/averaging of EL over angles and redistribution into different directions, as a result of the optical scattering mechanism. Figure 16.15c compares the emission patterns (polar plots of EL intensities) of the reference device, the device with the scattering layer (composition F), and the Lambertian pattern. The device with the scattering layer shows an emission pattern very close to the ideal Lambertian pattern, similar to the reference device.

16.3.4
OLED Utilizing Surface Plasmon Polariton-Mediated Energy Transfer

Surface plasmon polaritons (SPPs) are guided electromagnetic waves propagating at the interface between a dielectric and a conductor, which arise via the coupling of

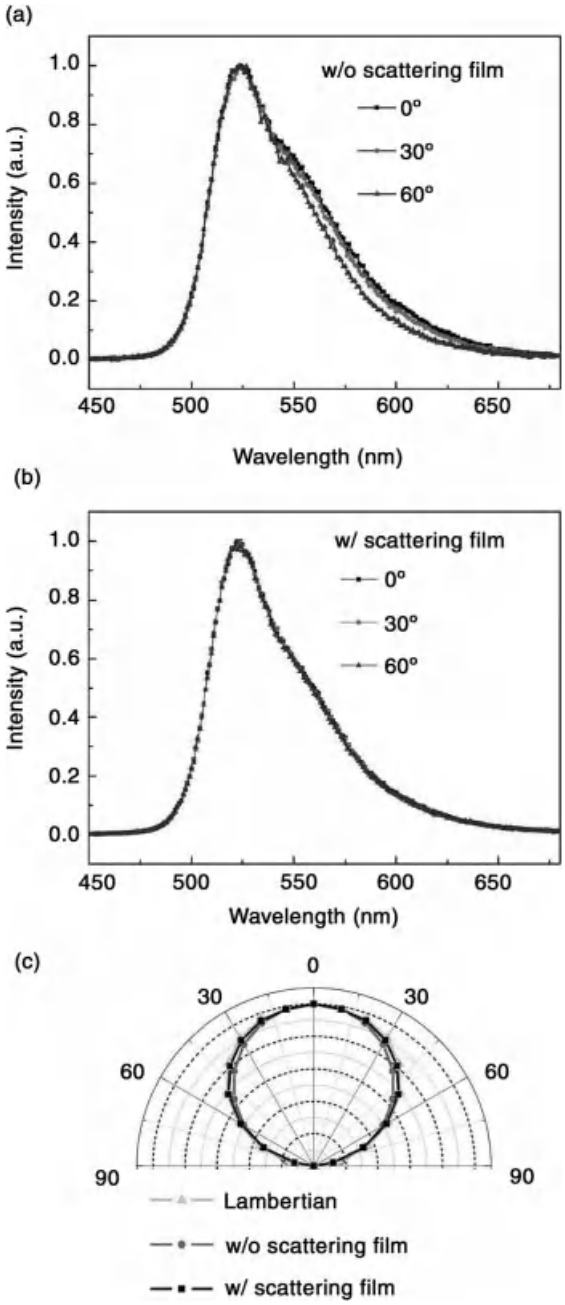

Figure 16.15 EL spectra over several viewing angles (0°, 30°, 60°) for the bottom-emitting OLEDs (a) without the internal scattering film and (b) with internal scattering film (with composition F, highest EL efficiency). (c) Polar plots of EL intensities of the reference device, the device with the scattering layer (composition F), in comparison with the Lambertian pattern. With permission from Ref. [49].

the electromagnetic fields to oscillations of the conductor's electron plasma and are evanescently confined near the interface [53–60]. In typical organic light-emitting devices, emitters are located close enough to the metal electrode, and thus a large portion of internally generated radiation is trapped into SPP modes (20–40%, depending on the device structure) and is not available for external use [31–38]. Thus, an effective approach/structure that is able to access/recycle SPP modes for external use and compatible with typical OLED fabrication is certainly desired.

In a conventional OLED with a thick top metal electrode, the SPP modes are mainly distributed from the bottom surface of the metal layer downward into the organic layer, thereby making it difficult to access/manipulate the SPP modes from outside of the device. Some periodically corrugated structures were proposed previously to outcouple the SPPs [61], although in general they are less compatible with typical OLED fabrication and also result in strong wavelength and angular dependence in emission characteristics. In extensive studies of SPP optics in recent years, it has been shown that by thinning the thickness of a metal layer, the originally independent SPPs on two sides of a metal layer could interact with each other, resulting in coupled SPPs that have modal field distributions spanning on two sides of the metal layer [56–58]. As such, by making OLEDs with thinner metal electrodes, SPPs of the devices could exhibit a significant field distribution outside the devices, giving a possibility to access/manipulate SPPs from outside of the device for external emission. In this section, we discuss the use of such a principle to manipulate SPPs of OLEDs for external use [62].

The OLED device structures (Figure 16.16) under discussion [62] were glass substrate/ITO (120 nm)/m-MTDATA (30 nm)/α-NPD (20 nm)/Alq_3:C545T (1 wt%, 20 nm)/Alq_3 (35 nm)/LiF (0.5 nm)/Al (1 nm)/Ag (X nm)/Alq_3 (80 nm, for type IA devices with nondoped capping) or Alq_3:DCJTB (1 wt%, 80 nm, for type IB devices with doped capping). Nondoped or doped Alq_3 were used as the capping layer.

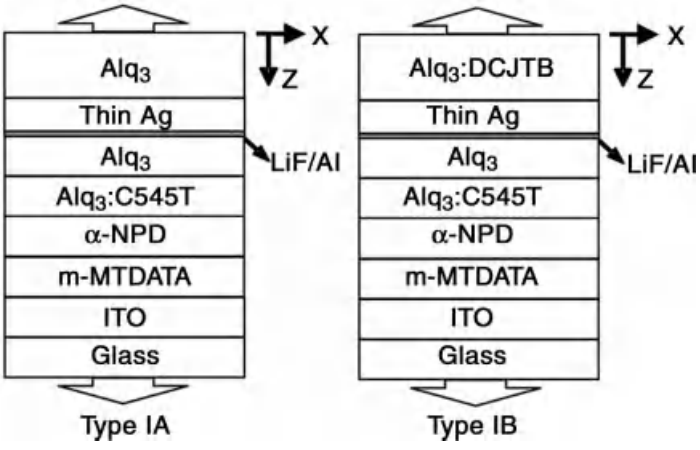

Figure 16.16 Schematic device structures of IA and IB. With permission from Ref. [62].

The thickness of Ag cathode ($X = 20$, 30, 40, 50, and 120 nm) was varied to investigate the SPP properties. The Alq_3 was used as the capping so that the dielectrics on both sides of the metal layer would have same/similar refractive indices to ensure effective generation of coupled SPP modes [56, 57]. The 1 wt% DCJTB [4-(dicyanomethylene)-2-*tert*-butyl-6-(1,1,7,7-tetramethyljulolidin-4-yl-vinyl)-4*H*-pyran] doped in the Alq_3 capping is used to absorb the SPPs propagating in the capping layer for reemission (i.e., recycling SPPs), thus inducing the donor–acceptor (C545T–DCJTB) energy transfer mediated by coupled SPPs across the metal layer [56]. The thickness of the electron transport layer (undoped Alq_3) was adjusted in a way to increase fraction of internally generated radiation coupled into SPP modes and to make the SPP effects more easily observable [60, 41].

Based on the rigorous electromagnetic model of OLED discussed in the previous section, Figure 16.17a shows the calculated mode distributions (fraction of radiation coupled into different modes) of internally generated radiation (at 525 nm) as a function of k_t/k_0 (k_t is the in-plane component of the wave vector and k_0 is the free-space wave vector) from a conventional OLED with thick Ag cathode (i.e., 120 nm Ag) and from an OLED with thin Ag cathode (40 nm) [62]. With the confining nature of the SPPs, modes with $k_t/k_0 > 1.75$ (where $n = 1.75$ is the refractive index of the bounding medium of Alq_3 at 525 nm) are associated with the SPP modes [55, 57]. The conventional OLED with the thick Ag cathode (120 nm) has only one major SPP mode peaking at $k_t = 2.05k_0$, which is the typical SPP having only one-side distribution (i.e., from the Ag/Alq_3 interface downward into the Alq_3). The OLED with thin Ag (40 nm), on the other hand, has two major SPP modes peaking at $k_t = 1.84k_0$, and $k_t = 2.28k_0$. These two modes, one with k_t lower than $2.05k_0$ and one with k_t higher than $2.05k_0$ indeed are the coupled SPP modes resulting from the interaction and splitting of two one-side SPP modes (i.e., one above and one below the metal cathode) [56]. Further analyses on polarization properties (Figure 16.17b) reveal that these coupled SPP modes associated with thin Ag are mainly of TM (transverse magnetic mode) nature, similar to conventional one-side SPP modes associated with the thick metal layer [62]. The distributions of the field intensity for these two modes (transverse magnetic field H_x, since they are of TM nature) along the z-axis (from the Alq_3/air interface downward as shown in Figure 16.16) are shown in Figure 16.18a and b [62]. From Figure 16.18, it is seen that the mode at $k_t = 1.84k_0$ is of symmetric nature and the mode at $k_t = 2.28k_0$ is of antisymmetric nature (i.e., with a node located within the thin metal layer). Both modes span from the inside to the outside of the thin Ag cathode and exhibit significant distributions in the capping layer.

In Table 16.3, the peak k_t/k_0 values for symmetric SPP modes and antisymmetric SPP modes associated with different Ag thicknesses are listed [62]. The peak k_t/k_0 values for these two types of SPP modes are splitted farther away from each other when the Ag thickness is reduced (i.e., the coupling/interaction between SPPs on two sides of the metal layer increases).

Since these symmetric or antisymmetric modes propagate horizontally and have rather long propagation lengths (of micrometer scale), in type IB devices, by doping into the capping layer a small amount of DCJTB dyes (e.g., 1 wt%) whose

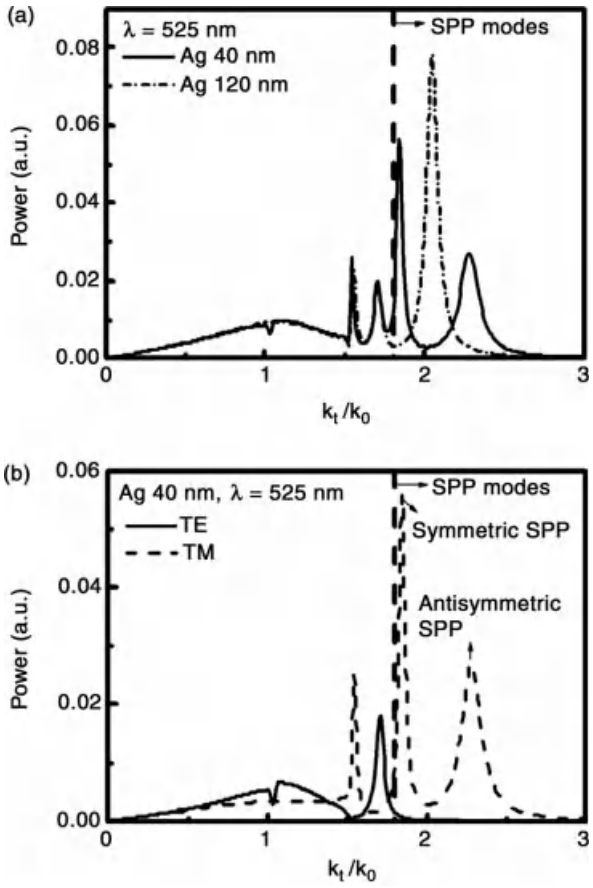

Figure 16.17 (a) Calculated mode distributions (power dissipation) of internally generated radiation ($\lambda = 520$ nm) as a function of the normalized in-plane wave vector k_t/k_0 for a conventional OLED with thick Ag cathode (120 nm) and for a type IA double-emitting OLED with thin Ag cathode (40 nm). (b) Calculated mode distributions (power dissipation) for the same type IA double-emitting OLED with thin Ag cathode (40 nm), with TE and TM modes separated. With permission from Ref. [62].

absorption matches C545T emission, the SPPs in the capping can be effectively absorbed and then be re-emitted, thus recycling a portion of SPPs for external emission [62]. In Figure 16.19a–d, the (0°) EL spectra with relative intensities measured from the topside of the type IA device (with nondoped capping) and the type IB device (with doped capping) are compared for each of the Ag cathode thicknesses (20, 30, 40, and 50 nm), respectively. Without DCJTB dopants in the capping, pure C545T emission is observed, while with DCJTB dopants in the capping, the emission combines both DCJTB and C545T emission. The observed DCJTB emission from the topside of type IB devices cannot be complete due to reabsorption/reemission of the directly outcoupled top (donor) emission, since for

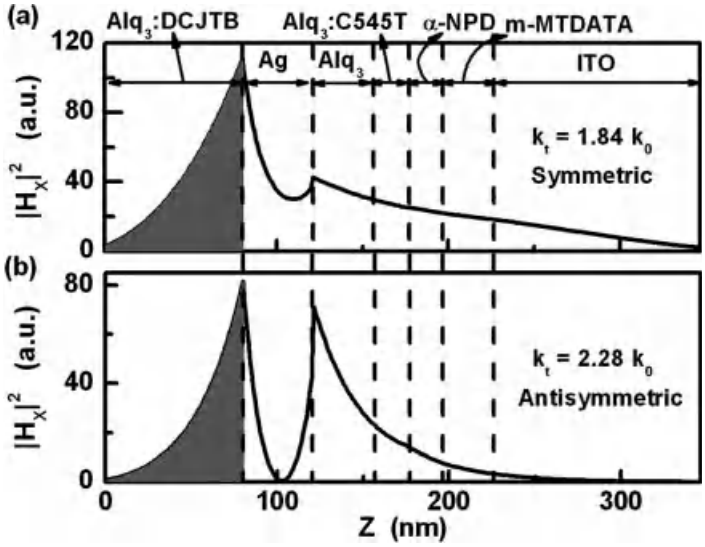

Figure 16.18 The distributions of the field intensity for the (a) symmetric and (b) antisymmetric SPP modes of the type IA double-emitting OLED with thin Ag cathode (40 nm), at the wavelength of 520 nm, and along the *z*-axis. The transverse magnetic field H_x is shown, since SPP modes are of TM nature. With permission from Ref. [62].

each type IB device C545T emission from the topside only drops slightly compared to those of type IA devices. Instead, the significant DCJTB emission from the topside is mainly due to recycled SPPs, which in some sense can be regarded as the SPP-mediated energy transfer from the C545T donor to the DCJTB acceptor and is a rather long-range energy transfer process. Figure 16.19e shows the (0°) EL spectra with relative intensities for bottom emission of type IB devices (with doped capping) with different Ag cathode thicknesses (20, 30, 40, 50, and 120 nm). The EL spectra are basically the same as those of type IA devices and are not dependent on the Ag thickness. Yet, in general, the intensity of bottom emission (for both type IA and type IB) drops gradually with the reducing Ag thickness, mainly due to lowered

Table 16.3 SPP characteristics of type IA devices versus Ag thickness.

Ag (nm)	Symmetric SPP (k_t/k_0)	Antisymmetric SPP (k_t/k_0)	$ET_{d\text{-}a}$ (%)
20	1.75	2.94	5.29
30	1.79	2.49	6.77
40	1.84	2.28	6.43
50	1.89	2.17	4.92

With permission from Ref. [62].

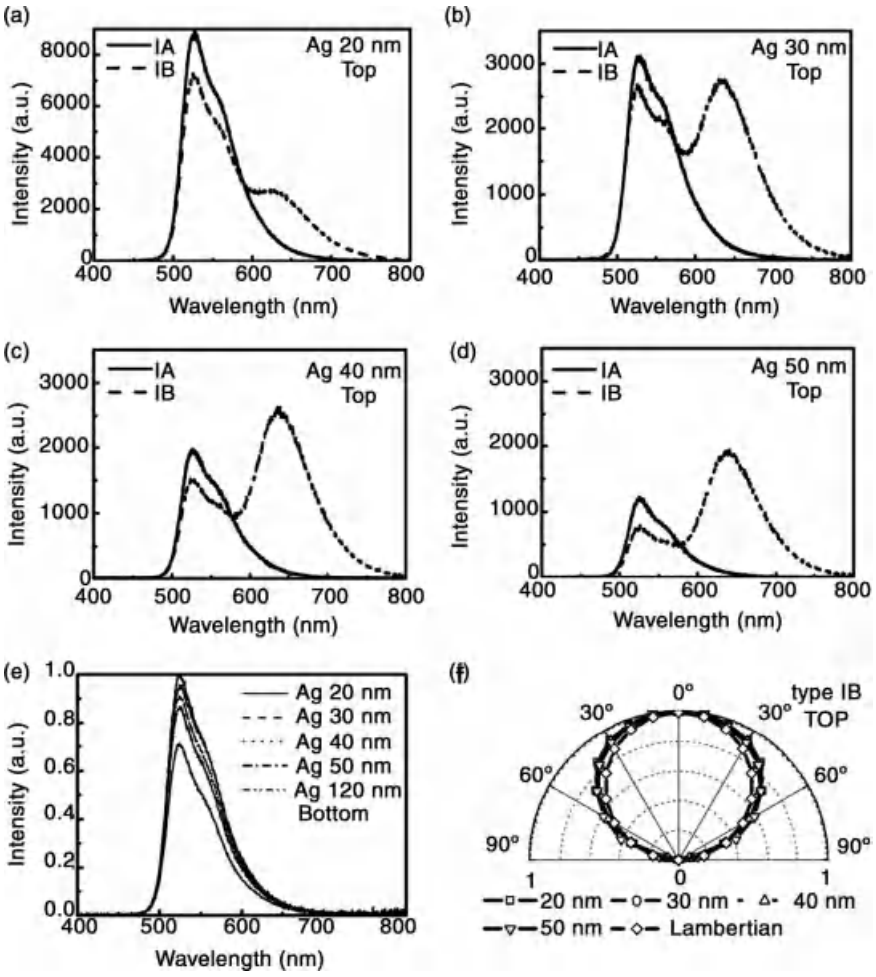

Figure 16.19 The (0°) EL spectra with relative intensities measured from the topside of the type IA device (with nondoped capping) and the type IB device (with doped capping) are compared for each of the Ag cathode thickness: (a) 20, (b) 30, (c) 40, (d) 50 nm. (e) (0°) EL spectra with relative intensities for bottom emission of type IB devices with different Ag cathode thicknesses (20, 30, 40, and 50 nm) compared to that of the conventional bottom-emitting device (Ag = 120 nm). (f) Polar plots of the top-emission intensity for type IB devices with different Ag cathode thicknesses (20, 30, 40, and 50 nm) compared to the Lambertian pattern. For (a)–(f), measurements were performed at a current density of 100 mA/cm^2. With permission from Ref. [62].

reflection of the Ag cathode. Figure 16.19f shows the polar plots of the top-emission intensity for type IB devices (similar for type IA devices, data not shown), which are all nearly Lambertian regardless of the Ag thickness (since there is no strong microcavity structure in these devices).

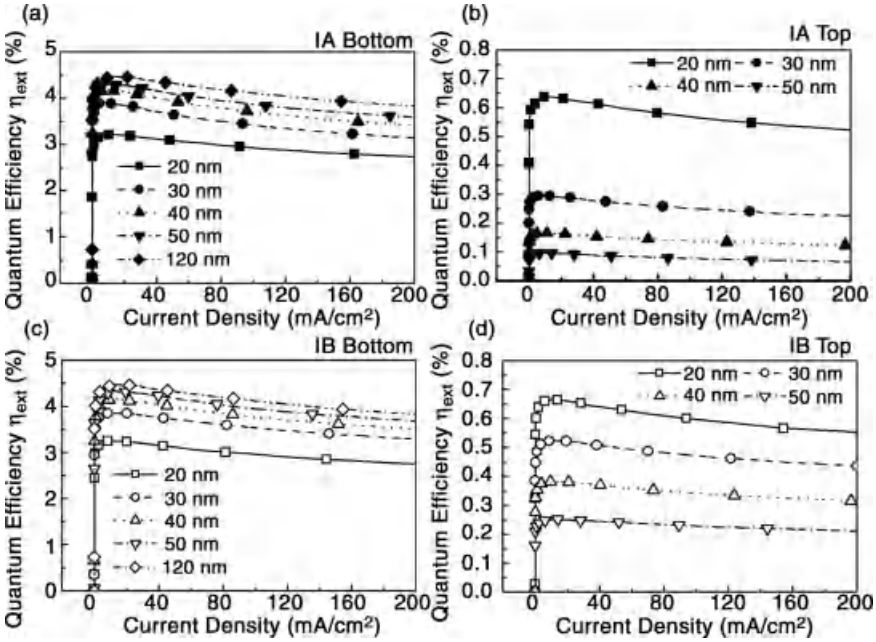

Figure 16.20 (a) and (b) show the external quantum efficiencies for bottom emission and top emission of type IA devices (with nondoped capping), respectively. (c) and (d) show the external quantum efficiencies for bottom emission and top emission of type IB devices (with doped capping), respectively. With permission from Ref. [62].

In type IB devices, as the Ag thickness increases, the directly outcoupled top radiation (C545T emission) decays rapidly due to reduced transmission of the semitransparent cathode. Yet, interestingly, the intensity of the SPP-recycled top emission (DCJTB emission) stays rather constant versus the Ag cathode thickness (which will be explained later in this section). As such, for the top emission, the ratio of the DCJTB emission relative to the directly outcoupled C545T emission rises when the Ag thickness increases, providing a capability of color tuning. Due to the capability to tune emission colors with the metal thickness, the SPP-mediated energy transfer can be used for implementing double-emitting OLEDs with different emission colors on two sides or with color tuning capability.

Figure 16.20a and b shows the external quantum efficiencies for bottom emission and top emission of type IA devices (with nondoped capping), respectively [62]. Figure 16.20c and d shows the external quantum efficiencies for bottom emission and top emission of type IB devices (with doped capping), respectively [62]. Magnitudes and trends of efficiencies (versus Ag thickness) for bottom emission of both type IA and type IB devices are basically the same; they however differ for top emission of type IA and type IB devices. The top-emission quantum efficiency of type IA devices drops rapidly with increasing Ag thickness, but the efficiency drop is more gradual for type IB devices. In Table 16.4, the measured quantum

Table 16.4 The measured external quantum efficiencies of various IA and IB devices.

Ag (nm)	IA				IB			
	Bottom (%)	Top (%)	Total (%)	Enhancement	Bottom (%)	Top (%)	Total (%)	Enhancement
20	3.21	0.64	3.85	0.86	3.25	0.68	3.93	0.88
30	3.90	0.3	4.20	0.94	3.85	0.52	4.37	0.98
40	4.17	0.17	4.34	0.97	4.14	0.38	4.53	1.014
50	4.30	0.10	4.40	0.99	4.3	0.3	4.6	1.03
120	4.46	0.0	4.46	1.00	4.46	0.0	4.46	1.00

"Enhancement" indicates the ratio of the total efficiency of various devices relative to that of the conventional bottom-emitting device (Ag = 120 nm).
With permission from Ref. [62].

efficiencies of the bottom emission, the top emission, and the total emission (including both top and bottom emission) of both type IA and type IB devices are listed and are compared with those of the conventional bottom-emitting device (with Ag = 120 nm). All these efficiencies are also plotted in Figure 16.21 as a function of the Ag thickness for comparison. For type IA devices (with nondoped capping), the total efficiency drops monotonically in reducing the Ag thickness. Yet for type IB devices (doped capping), enhanced total efficiency is observed for Ag = 50 and 40 nm, although the enhancement by up to 3% is modest. It however may be further optimized. For instance, with changing the top mirror structure/property of the devices, the organic layer structures in the device should be modified

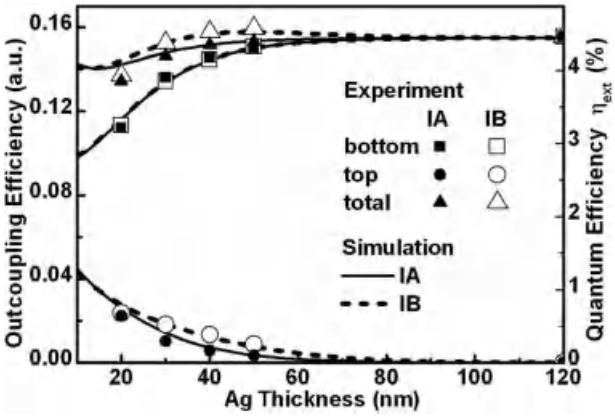

Figure 16.21 The measured quantum efficiencies of the bottom emission, the top emission, and the total emission (including both top and bottom emission) as a function of the Ag cathode thickness for both type IA/type IB devices, compared with the calculated outcoupling efficiencies for top emission, bottom emission, and total emission. With permission from Ref. [62].

accordingly for maximizing optical output. Preliminary analyses show that further enhancement should be achievable.

In Figure 16.21, the measured quantum efficiencies are also compared with the calculated outcoupling efficiencies for top emission ($\eta_{\text{device,top}}$), bottom emission ($\eta_{\text{device,bot}}$), and total emission ($\eta_{\text{device}} = \eta_{\text{device,top}} + \eta_{\text{device,bot}}$). $\eta_{\text{device,top}}$ is calculated by $\eta_{\text{device,top}} = \eta_{\text{d-out,top}} + \text{ET}_{\text{d-a}} \times \text{QY}_{\text{a}} \times \eta_{\text{a-out,top}} + \text{A}_{\text{d-a,direct}} \times \text{QY}_{\text{a}} \times \eta'_{\text{a-out,top}}$. $\eta_{\text{d-out,top}}$ is the direct outcoupling efficiency for donor (C545T) top emission. By taking into consideration the complex optical index (i.e., both n and k) of the DCJTB-doped Alq_3 capping, the $\eta_{\text{d-out,top}}$ for type IB devices would suffer ~10% decrease compared to $\eta_{\text{d-out,top}}$ for type IA devices due to direct absorption by acceptors, which is consistent with the experiment results shown in Figure 16.19a–d). $\text{ET}_{\text{d-a}}$ is the efficiency of the donor (C545T)-to-acceptor (DCJTB) energy transfer mediated by coupled SPPs for type IB devices (e.g., ~6.43% for the OLED with Ag = 40 nm) (Table 16.3). QY_{a} is the emission quantum yield of the acceptor (1 wt% DCJTB doped in the Alq_3 capping, ~70%). $\eta_{\text{a-out,top}}$ is the outcoupling efficiency for acceptor top emission (through SPP-mediated energy transfer). $A_{\text{d-a,direct}}$ is the efficiency of the donor (C545T)-to-acceptor (DCJTB) energy transfer through direct absorption for type IB devices ($\sim 0.1 \times \eta_{\text{d-out,top}}$). $\eta'_{\text{a-out,top}}$ is the outcoupling efficiency for acceptor top emission (through direct acceptor absorption). Since $\eta_{\text{d-out,top}}$ is much larger than $A_{\text{d-a,direct}} \times \text{QY}_{\text{a}} \times \eta'_{\text{a-out,top}}$, indeed it results in $\eta_{\text{device,top}} = \eta_{\text{d-out,top}} + \text{ET}_{\text{d-a}} \times \text{QY}_{\text{a}} \times \eta_{\text{a-out,top}} + A_{\text{d-a,direct}} \times \text{QY}_{\text{a}} \times \eta'_{\text{a-out,top}} \approx \eta_{\text{d-out,top}} + \text{ET}_{\text{d-a}} \times \text{QY}_{\text{a}} \times \eta_{\text{a-out,top}}$. In calculating $\text{ET}_{\text{d-a}}$, the emission properties of the donor emitter, the SPP modal field distribution, the propagation properties of the SPP modes, and the complex dielectric constants of related media are used. The calculated $\text{ET}_{\text{d-a}}$ values (for C545T donor and DCJTB acceptor) for different Ag thicknesses are listed in Table 16.3, which are basically consistent with the variation of the DCJTB top emission intensity versus Ag thickness shown in Figure 16.19a–d. The $\text{ET}_{\text{d-a}}$ values do not vary significantly versus the Ag thickness (20–40 nm) till the Ag thickness increases to 50 nm. Meanwhile, the transmission of thin Ag drops significantly when its thickness increases from 20 to 50 nm. These explain why the intensity of the SPP-recycled top emission (DCJTB emission) stays rather constant versus the Ag cathode thickness, in contrast to that of the directly outcoupled C545T top emission. On the other hand, $\eta_{\text{device,bot}}$ is calculated by $\eta_{\text{device,bot}} = \eta_{\text{d-out,bot}} + \text{ET}_{\text{d-a}} \times \text{QY}_{\text{a}} \times \eta_{\text{a-out,bot}}$, where $\eta_{\text{d-out,bot}}$ is the direct outcoupling efficiency for donor bottom emission and $\eta_{\text{a-out,bot}}$ is the outcoupling efficiency for acceptor bottom emission. Since $\eta_{\text{d-out,bot}}$ is much larger than $\text{ET}_{\text{d-a}} \times \text{QY}_{\text{a}} \times \eta_{\text{a-out,bot}}$ ($\eta_{\text{d-out,bot}} \gg \text{ET}_{\text{d-a}} \times \text{QY}_{\text{a}} \times \eta_{\text{a-out,bot}}$), indeed it results in $\eta_{\text{device,bot}} = \eta_{\text{d-out,bot}} + \text{ET}_{\text{d-a}} \times \text{QY}_{\text{a}} \times \eta_{\text{a-out,bot}} \approx \eta_{\text{d-out,bot}}$. Thus, in bottom emission of all type IB devices (Figure 16.19e), the DCJTB acceptor emission (recycled SPP emission) is hardly visible. As can be seen in Figure 16.21, overall rather good agreement between calculation and experiment results of efficiencies is obtained.

In summary, by thinning the metal electrode, the SPP modes can be coupled to the outside surface of the device. As such, one can recycle a portion of SPPs by capping the thinned metal electrode with an appropriate absorbing/reemission medium, inducing SPP-mediated energy transfer and reemission. Such an

approach may be used for implementing double-emitting OLEDs with different emission colors on two sides and with a broad color tuning capability.

16.4 Summary

In summary, the general theories and discussions of optical structures and characteristics of OLEDs are first given. Based on these basic understandings, various OLED structures that might be useful to enhance the optical outcoupling of the devices are discussed in sequence. These include (i) second-antinode OLED structure, (ii) top-emitting OLEDs capped with microlenses or scattering layers, (iii) OLEDs with internal scattering, and (iv) OLED utilizing surface plasmon polariton-mediated energy transfer.

References

1 Tang, C.W. and VanSlyke, S.A. (1987) Organic electroluminescent diodes. *Appl. Phys. Lett.*, **51**, 913–915.

2 Kido, J., Kimura, M., and Nagai, K. (1995) Multilayer white light-emitting organic electroluminescent device. *Science*, **267**, 1332–1334.

3 Reineke, S., Lindner, F., Schwartz, G., Seidler, N., Walzer, K., Lüssem, B., and Leo, K. (2009) White organic light-emitting diodes with fluorescent tube efficiency. *Nature*, **459**, 234–239.

4 Tyan, Y.S., Rao, Y.Q., Wang, J.S., Kesel, R., Cushman, T.R., and Begley, W.J. (2008) Fluorescent white OLED devices with improved light extraction. *SID Symp. Dig. Tech.*, **39** (1), 935.

5 Tyan, Y.S., Rao, Y.Q., Ren, X.F., Kesel, R., Cushman, T.R., Begley, W.J., and Bhandari, N. (2009) Tandem hybrid white OLED devices with improved light extraction. *SID Symp. Dig. Tech.*, **40** (1) 895.

6 Liu, C.C., Liu, S.H., Tien, K.C., Hsu, M. H., Chang, H.W., Chang, C.K., Yang, C.J., and Wu, C.C. (2009) Microcavity top-emitting organic light-emitting devices integrated with diffusers for simultaneous enhancement of efficiencies and viewing characteristics. *Appl. Phys. Lett.*, **94**, 103302.

7 Takada, N., Tsutsui, T., and Saito, S. (1993) Control of emission characteristics in organic thin-film electroluminescent diodes using an optical-microcavity structure. *Appl. Phys. Lett.*, **63**, 2032.

8 Lin, C.L., Lin, H.W., and Wu, C.C. (2005) Examining microcavity organic light-emitting devices having two metal mirrors. *Appl. Phys. Lett.*, **87**, 021101.

9 Adachi, C., Baldo, M.A., Thompson, M.E., and Forrest, S.R. (2001) Nearly 100% internal phosphorescence efficiency in an organic light emitting device. *J. Appl. Phys.*, **90**, 5048.

10 Baldo, M.A., O'Brien, D., You, Y., Shoustikov, A., Sibley, S., Thompson, M. E., and Forrest, S.R. (1998) Highly efficient phosphorescent emission from organic electroluminescent devices. *Nature*, **395**, 151–154.

11 Chutinan, A., Ishihara, K., Asano, T., Fujita, M., and Noda, S. (2004) Theoretical analysis on light-extraction efficiency of organic light-emitting diodes using FDTD and mode-expansion methods. *Org. Electron.*, **6**, 3–9.

12 Chen, C.W., Lin, C.L., and Wu, C.C. (2004) An effective cathode structure for inverted top-emitting organic light-emitting devices. *Appl. Phys. Lett.*, **85**, 2469–2471.

13 Möller, S. and Forrest, S.R. (2002) Improved light out-coupling in organic light emitting diodes employing ordered microlens arrays. *J. Appl. Phys.*, **91**, 3324–3327.

14 Peng, H., Ho, Y.L., Yu, X.J., Wong, M., and Kwok, H.S. (2005) Coupling efficiency enhancement in organic light-emitting devices using microlens array-theory and experiment. *J. Disp. Technol.*, **1**, 278–282.

15 Yang, C.J., Liu, S.H., Hsieh, H.H., Liu, C. C., Cho, T.Y., and Wu, C.C. (2007) Microcavity top-emitting organic light-emitting devices integrated with microlens arrays: simultaneous enhancement of quantum efficiency, cd/A efficiency, color performances, and image resolution. *Appl. Phys. Lett.*, **91**, 253508.

16 Shiang, J.J. and Duggal, A.R. (2004) Application of radiative transport theory to light extraction from organic light emitting diodes. *J. Appl. Phys.*, **95**, 2880–2888.

17 Shiang, J.J., Faircloth, T.J., and Duggal, A.R. (2004) Experimental demonstration of increased organic light emitting device output via volumetric light scattering. *J. Appl. Phys.*, **95**, 2889–2895.

18 Bathelt, R., Buchhauser, D., Gärditz, C., Partzold, R., and Wellmann, P. (2007) Light extraction from OLEDs for lighting applications through light scattering. *Org. Electron.*, **8**, 293–299.

19 Neyts, K.A. (1998) Simulation of light emission from thin-film microcavities. *J. Opt. Soc. Am. A*, **15**, 962–971.

20 Lukosz, W. and Kunz, R.E. (1977) Light emission by magnetic and electric dipoles close to a plane dielectric interface. II. Radiation patterns of perpendicular oriented dipoles. *J. Opt. Soc. Am.*, **67**, 1615–1619.

21 Wasey, J.A.E. and Barnes, W.L. (2000) Efficiency of spontaneous emission from planar microcavities. *J. Mod. Opt.*, **47**, 725–741.

22 Wu, C.C., Lin, C.L., Hsieh, P.Y., and Chiang, H.H. (2004) Methodology for optimizing viewing characteristics of top-emitting organic light-emitting devices. *Appl. Phys. Lett.*, **84**, 3966–3968.

23 Wu, C.C., Chen, C.W., Lin, C.L., and Yang, C.J. (2005) Advanced organic light-emitting devices for enhancing display performances. *J. Disp. Technol.*, **1**, 248–266.

24 Nowy, S., Krummacher, B.C., Frischeisen, J., Reinke, N.A., and Brutting, W. (2008) Light extraction and optical loss mechanisms in organic light-emitting diodes: influence of the emitter quantum efficiency. *J. Appl. Phys.*, **104**, 123109.

25 Lu, M.H. and Sturm, J.C. (2002) Optimization of external coupling and light emission in organic light-emitting devices: modeling and experiment. *J. Appl. Phys.*, **91**, 595–604.

26 So, S.K., Choi, W.K., Leung, L.M., and Neyts, K. (1999) Interference effects in bilayer organic light-emitting diodes. *Appl. Phys. Lett.*, **74**, 1939–1941.

27 Zhou, X., Pfeiffer, M., Blochwitz, J., Werner, A., Nollau, A., Fritz, T., and Leo, K. (2001) Very-low-operating-voltage organic light-emitting diodes using a p-doped amorphous hole injection layer. *Appl. Phys. Lett.*, **78**, 410–412.

28 He, G., Schneider, O., Qin, D., Zhou, X., Pfeiffer, M., and Leo, K. (2004) Very high-efficiency and low voltage phosphorescent organic light-emitting diodes based on a p-i-n junction. *J. Appl. Phys.*, **95**, 5773–5777.

29 Wu, C.C., Liu, T.L., Hung, W.Y., Lin, Y.T., Wong, K.T., Chen, R.T., Chen, Y.M., and Chien, Y.Y. (2003) Unusual nondispersive ambipolar carrier transport and high electron mobility in amorphous Ter(9,9-diarylfluorene)s. *J. Am. Chem. Soc.*, **125**, 3710–3711.

30 Chen, L.Y., Hung, W.Y., Lin, Y.T., Wu, C. C., Chao, T.C., Hung, T.H., and Wong, K. T. (2005) Enhancement of bipolar carrier transport in oligofluorene films through alignment in the liquid-crystalline phase. *Appl. Phys. Lett.*, **87**, 112103.

31 Lin, C.L., Cho, T.Y., Chang, C.H., and Wu, C.C. (2006) Enhancing light outcoupling of organic light-emitting devices by locating emitters around the second antinode of the reflective metal electrode. *Appl. Phys. Lett.*, **88**, 081114.

32 Hung, L.S., Tang, C.W., Mason, M.G., Raychaudhuri, P., and Madathil, J. (2001) Application of an ultrathin LiF/Al bilayer in organic surface-emitting diodes. *Appl. Phys. Lett.*, **78**, 544–546.

33 Tang, C.W., VanSlyke, S.A., and Chen, C.H. (1989) Electroluminescence of doped organic thin films. *J. Appl. Phys.*, **65**, 3610–3616.

34 Mladenovski, S., Neyts, K., Pavicic, D., Werner, A., and Rothe, C. (2009) Exceptionally efficient organic light emitting devices using high refractive index substrates. *Opt. Express*, **17**, 7562–7570.

35 Matsumoto, T., Nakada, T., Endo, J., Mori, K., Kavamura, N., Yokoi, A., and Kido, J. (2003) Multiphoton organic EL device having charge generation layer. *SID Symp. Dig. Tech.*, **34** (1), 979–983.

36 Liao, L.S., Klubek, K.P., and Tang, C.W. (2004) High-efficiency tandem organic light-emitting diodes. *Appl. Phys. Lett.*, **84**, 167–169.

37 Chang, C.C., Hwang, S.W., Chen, C.H., and Chen, J.F. (2004) High-efficiency organic electroluminescence device with multiple emitting units. *Jpn. J. Appl. Phys.*, **43**, 6418–6642.

38 Cho, T.Y., Lin, C.L., and Wu, C.C. (2006) Microcavity two-unit tandem organic light-emitting device having a high efficiency. *Appl. Phys. Lett.*, **88**, 111106.

39 Cho, T.Y., Lin, C.L., Chang, C.H., and Wu, C.C. (2006) Optical characteristics of tandem and microcavity tandem organic light-emitting devices. *J. SID*, **14**, 1063–1070.

40 Lu, M.H., Weaver, M.S., Zhou, T.X., Rothman, M., Kwong, R.C., Hack, M., and Brown, J.J. (2002) High-efficiency top-emitting organic light-emitting devices. *Appl. Phys. Lett.*, **81**, 3921–3923.

41 Lin, C.L., Chang, H.C., Tien, K.C., and Wu, C.C. (2007) Influences of resonant wavelengths on performances of microcavity organic light-emitting devices. *Appl. Phys. Lett.*, **90**, 071111.

42 Hung, L.S., Tang, C.W., Mason, M.G., Raychaudhuri, P., and Madathil, J. (2001) Application of an ultrathin LiF/Al bilayer in organic surface-emitting diodes. *Appl. Phys. Lett.*, **78**, 544–546.

43 Yamashita, K., Mori, T., and Mizutani, T. (2001) Encapsulation of organic light-emitting diode using thermal chemical-vapour-deposition polymer film. *J. Phys. D Appl. Phys.*, **34**, 740–743.

44 Xia, Y. and Whitesides, G.M. (1998) Soft lithography. *Angew. Chem., Int. Ed.*, **37**, 550–575.

45 Gu, G., Garbuzov, D.Z., Burrows, P.E., Vendakesh, S., Forrest, S.R., and Thompson, M.E. (1997) High-external-quantum-efficiency organic light-emitting devices. *Opt. Lett.*, **22**, 396–398.

46 Do, Y.R., Kim, Y.C., Song, Y.W., Cho, C.O., Jeon, H., Lee, Y.J., Kim, S.H., and Lee, Y.H. (2003) Enhanced light extraction from organic light emitting diodes with 2D SiO_2/SiN_X photonic crystals. *Adv. Mater.*, **15**, 1214–1218.

47 Do, Y.R., Kim, Y.C., Song, Y.W., and Lee, Y.H. (2004) Enhanced light extraction efficiency from organic light emitting diodes by insertion of a two-dimensional photonic crystal structure. *J. Appl. Phys.*, **96**, 7629–7636.

48 Sun, Y. and Forrest, S.R. (2008) Enhanced light out-coupling of organic light-emitting devices using embedded low-index grids. *Nat. Photonics*, **2**, 483–487.

49 Chang, H.W., Tien, K.C., Hsu, M.H., Huang, Y.H., Lin, M.H., Tsai, C.H., Tsai, Y.T., and Wu, C.C. (2011) Organic light-emitting devices integrated with internal scattering layers for enhancing optical out-coupling. *J. SID*, **19**, 196–204.

50 Malshe, A.P., Park, B.S., Brown, W.D., and Naseem, H.A. (1999) A review of techniques for polishing and planarizing chemically vapor-deposited (CVD) diamond films and substrates. *Diam. Relat. Mater.*, **8**, 1198–1213.

51 Hung, L.S., Tang, C.W., Mason, M.G., Raychaudhuri, P., and Madathil, J. (2001) Application of an ultrathin LiF/Al bilayer in organic surface-emitting diodes. *Appl. Phys. Lett.*, **78**, 544–546.

52 Burdeaux, D., Townsend, P., and Carr, J. (1990) Benzocyclobutene (BCB) dielectrics for the high density, thin film multichip modules. *J. Elect. Mater.*, **19**, 1357–1366.

53 Sarid, D. (1981) Long-range surface-plasma waves on very thin metal films. *Phys. Rev. Lett.*, **47**, 1927–1930.

54 Burke, J.J., Stegeman, G.I., and Tamir, T. (1986) Surface-polariton-like waves guided by thin, lossy metal films. *Phys. Rev. B*, **33**, 5186–5201.

55 Raether, H. (1988) *Surface Plasmons*, Springer, Berlin.

56 Andrew, P. and Barnes, W.L. (2004) Energy transfer across a metal film mediated by surface plasmon polaritons. *Science*, **306**, 1002–1005.

57 Maier, S.A. (2007) *Plasmonics: Fundamentals and Applications*, Springer.

58 Smith, L.H., Wasey, J.A.E., and Barnes, W.L. (2004) Light outcoupling efficiency of top-emitting organic light-emitting diodes. *Appl. Phys. Lett.*, **84**, 2986–2988.

59 Ford, G.W. and Weber, W.H. (1984) Electromagnetic interactions of molecules with metal surfaces. *Phys. Rep.*, **113**, 195–287.

60 Weber, W.H. and Eagen, C.F. (1979) Energy transfer from an excited dye molecule to the surface plasmons of an adjacent metal. *Opt. Lett.*, **4**, 236–238.

61 Wedge, S., Wasey, J.A.E., Sage, I., and Barnes, W.L. (2004) Coupled surface plasmon-polariton mediated photoluminescence from a top-emitting organic light-emitting structure. *Appl. Phys. Lett.*, **85**, 182–184.

62 Tien, K.C., Lin, M.S., Lin, Y.H., Tsai, C.H., Shiu, M.H., Wei, M.C., Cheng, H.C., Lin, C.L., Lin, H.W., and Wu, C.C. (2010) Utilizing surface plasmon polariton mediated energy transfer for tunable double-emitting organic light-emitting devices. *Org. Electron.*, **11**, 397–406.

17
Photogeneration and Recombination in Polymer Solar Cells

Carsten Deibel, Andreas Baumann, and Vladimir Dyakonov

17.1
Introduction

Organic solar cells have a strong potential to complement and enhance the application areas of their inorganic counterparts [1]. They can be processed with mass production compatible printing techniques on flexible substrates at room temperature [2], leading to a low-energy footprint. The absorption coefficient of photoactive organic semiconductors is very high, leading to low material consumption. The focused efforts on research and development of these systems have led to notable increases in their performance and lifetimes. Recently, power conversion efficiency of 10% was reported [3], and lifetimes for encapsulated devices exceeding several years [4]. Even if these values remain below the corresponding figures of merit for inorganic solar cells, the lower cost structure can make organic photovoltaics attractive for a range of applications. In order to get on par with established solar cell technologies, the investigation of the fundamental mechanisms of charge photogeneration and intrinsic stability are a prerequisite for a guided device optimization. Here, we give an overview on the elementary processes determining the conversion from light to current in polymer-based organic solar cells.

The first organic solar cells were made of a single layer of organic semiconductor with two metal contacts with asymmetric work functions for the extraction of photogenerated charges. However, due to the low dielectric constant in organic semiconductors of only between 3 and 4, in contrast to inorganic ones, two charge carriers of opposite charge at a given distance are strongly Coulomb bound. Thus, the photogenerated electron–hole pairs are difficult to separate in a single organic layer, leading to power conversion efficiencies far below 1% [5]. Only in 1979, C.W. Tang was able to show an organic bilayer solar cell, with a planar heterojunction of thermally evaporated CuPc as light absorbing material and a perylene carboxylic derivative to assist in the separation of the strong electron–hole pair of the first material [6, 7]. The strongly bound electron–hole pair as primary photoexcitation in organic semiconductors, a singlet exciton, has a lifetime below 1 ns; the corresponding diffusion length being limited to a few nanometers only [8], much less

Physics of Organic Semiconductors, Second Edition. Edited by Wolfgang Brütting and Chihaya Adachi

than the absorption length and therefore not sufficient for a high exciton to charge conversion ratio. An advanced concept to circumvent this limiting factor by reducing the length of exciton diffusion before reaching an acceptor for dissociation was introduced more than a decade later: mixing the two materials, donor and acceptor. The resulting devices were called bulk heterojunction solar cells due to their distributed heterointerface. The concept was implemented by solution processing a donor–acceptor blend for the first time in 1992 by Sariciftci *et al*. [9]: as light absorbing material, polyphenylenevinylene (PPV) was used, whereas the charge generation was assisted by blending it with the fullerene C_{60}. The photoinduced electron transfer to the fullerene acceptor – the actual process of separating the strongly bound electron–hole pair of the light absorbing donor material – was shown to be on the femtosecond timescale [10]. A more soluble fullerene derivative, PCBM ([6,6]-phenyl-C_{61} butyric acid methyl ester), was introduced briefly thereafter as better acceptor [11] – and even today this type of acceptor is still the best performing one for solution-processed organic solar cells. An important optimization parameter is the phase separation and its spatial dimensions: too large phases limit the photocurrent due to the low exciton diffusion length, whereas a too fine-grained intermixing hinders the charge extraction. In 2001, Shaheen *et al*. [12] adjusted the phase separation of PPV:PCBM-based solar cells by selecting solvents with a higher boiling point, allowing for a slower drying time and thus better self-organization. This led to enhancement of the power conversion efficiencies from around 1 to 2.5%. Two years later, Padinger *et al*. [13] showed that the semicrystalline donor material poly(3-hexyl thiophene) (P3HT) in conjunction with PCBM could be improved, again in terms of phase separation, by post treatment, that is, by applying thermal treatment and electric field after the film deposition. The efficiency could be improved from 0.4 to 3.5%. Subsequently, more and more donor materials were tried, going beyond polythiophenes to block copolymers [14], partly with the aid of processing additives [15, 16], and other material classes [17]. Also, solar cells from polymer–polymer blends have been presented, but with below 2% efficiency [18]. In the meantime, solution-based processing of copolymer–fullerene blends has already led to organic solar cells with power conversion efficiencies of beyond 8% [19].

In order to understand how these performances are reached, and what the limiting factors for organic bulk heterojunction solar cells are, the fundamental function of charge carrier generation and recombination in these devices needs to be considered more closely. In Figure 17.1, the different steps necessary from light absorption to photocurrent are depicted and described. This chapter is divided into different parts accordingly, that is, in the sequence of photon-to-current conversion: first, the photogeneration of charge carriers is discussed (Section 17.2), followed by the charge transport of the separated free polarons to the respective electrodes (Section 17.3). On their way, the charge carriers may also undergo nongeminate recombination, as described in Section 17.4. In addition to the resulting photocurrent, the performance of a solar cell is also determined by its open-circuit voltage (Section 17.5). Finally, the chapter is briefly summarized (Section 17.6).

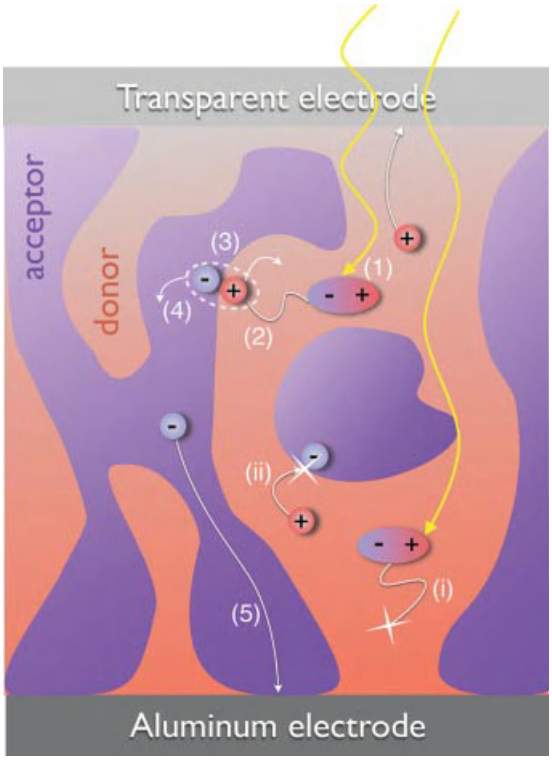

Figure 17.1 From light absorption to photocurrent in a polymer–fullerene solar cell. (1) Incoming light is absorbed in both constituents of the donor–acceptor blend, generating singlet excitons in each material phase. As these excitons are strongly bound, they can be separated only at a heterojunction interface. Thus, the singlet excitons generated within the bulk of a material phase have to (2) diffuse to such a donor–acceptor heterojunction. (i) If they do not reach the junction in their lifetime, they can recombine, partly by emitting photoluminescence. (3) The ultrafast charge transfer occurs, after which the electron resides on the acceptor phase, whereas the hole is on the donor material. This electron–hole pair may still be bound, requiring a (4) polaron pair dissociation step, although direct generation of charge carriers from singlet excitons is also reported in literature. (5) The separated charge carriers are transported to the respective electrodes. They may (ii) recombine nongeminately; otherwise, they are extracted at the electrodes, leading to the photocurrent.

17.2
Photogeneration of Charge Carriers

In principle, both photoactive constituents of the bulk heterojunction solar cell, the donor and the acceptor materials, can absorb light. In particular conjugated polymers, mostly applied as donors, have very high absorption coefficients on the order of 10^7 m^{-1}, although the optical bandgap is rather high with 1.5–2.0 eV. Also, the absorption range is narrower compared to inorganic semiconductors. Other

organic semiconductors such as fullerene derivatives usually have somewhat lower absorption coefficients.

For simplicity, we will discuss the photogeneration upon absorption in the donor polymer: light above its optical bandgap leads to the generation of singlet excitons [20] as primary photoexcitations (see Figure 17.1, step 1). As the dielectric constant of most organic semiconductors is between 3 and 4, the screening of electric fields is rather weak, which implies that the mutual Coulomb binding of electrons to holes is much higher compared to inorganic semiconductors. Similarly, the binding energy of the singlet exciton is much higher than the thermal energy, and amounts to between 0.4 and 0.7 eV for conjugated polymers [21–23]. Thus, the primary photoexcitation needs a driving force to dissociate the singlet excitons into free charge carriers – which are called polarons in organic semiconductors, as each charge leads to deformation of the polymer chain or small molecule it is residing on (see also Section 17.3) – as a prerequisite for a photocurrent generation. The singlet exciton dissociation relies on charge transfer [24]. In case of a singlet exciton on the donor polymer, an electron transfer to the acceptor material – usually a fullerene derivative – is the crucial step for the free charge photogeneration. Thus, if the singlet exciton is in the vicinity of a donor–acceptor heterointerface, a charge transfer can occur if it is energetically viable, that is, if the final energy of electron on PCBM and hole on polymer is below the singlet exciton energy [25]. The charge transfer is possible from polymer to fullerene [9, 26] – for MDMO-PPV to PCBM, it was reported to occur within the first 45 fs [10] – and vice versa [27] on a similar timescale.

As already pointed out in the introduction, the spatial dimensions of the donor–acceptor phase separation determine how efficiently charges are photogenerated in bulk heterojunction devices. Polymer-based solar cells are solution-cast, and are rather disordered and at best semicrystalline on a local scale. The diffusion length of singlet excitons, L_S, is accordingly short. During their lifetime τ_S, the excitons can diffuse with the diffusivity D_S, leading to $L_S = \sqrt{D_S \tau_s}$. With τ_S between 300 [28] and 400 ps [8] for P3HT, singlet exciton diffusion lengths of 2.5–8.5 nm were reported [8, 29–31], with one report claiming (27 ± 12) nm [32]. The fullerene derivative PCBM, the most prominent acceptor material, has been found to inhibit $L_S \approx 5$ nm [27]. The exciton diffusion length being much less than the absorption length in disordered organic semiconductors is the reason why bilayer solar cells with planar heterojunction do perform well, and why the phase separation and its optimization are so important for a high device performance.

The ideal dimensions of the donor–acceptor phase separation are given if the maximum distance to the next heterointerface never exceeds the singlet exciton diffusion lengths. Of course, the real devices are much more complicated, as phase separation occurs on different length scales, with both pure and intermixed material phases being present [33]. Nevertheless, the primary photoexcitations that are not directly located at the heterointerface can diffuse to it, followed by a charge transfer to the other semiconductor (see Figure 17.1, steps 2 and 3). If the primary photoexcitation is not dissociated, it recombines geminately – partly radiatively by emitting photoluminescence – in a first-order process with a concentration-

independent decay time (see Figure 17.1, process (i)). For annealed P3HT:PCBM blends, about 5% of the singlet excitons are lost in this way.

After successful singlet exciton dissociation, two scenarios are possible: either the generated separated charges still Coulomb interact with one another – the interacting charge pair is called polaron pair or charge transfer (CT) exciton [34–36] – or they do not and thus are free (see Figure 17.1, step 4). Recent evidence favors the direct charge generation, although it remains unclear if a polaron pair is formed as an intermediate step, which may dissociate with near-unity efficiency. We point out that a polaron pair describes a pair of a positive and a negative polaron that are mutually Coulomb bound, with a wide distribution of interpair radii and binding energies. Here, we will briefly discuss both processes.

If a polaron pair or CT exciton is generated upon singlet exciton dissociation, this implies that this bound electron–hole pair has a finite Coulomb binding energy that needs to be overcome by an external driving force. As the charge carriers are already on different materials, the electron on the acceptor and the hole on the donor, it is more difficult to find an energetically favorable dissociation site in comparison to the separation of the primary photoexcitation. In 1938, Onsager described the separation of an ion pair by an applied electric field [37], and later Braun based an empirical model for charge pair separation on its foundation [38]. The Braun–Onsager model mathematically describes the field-dependent dissociation yield $P(F)$ by weighing the rates for escape $k_{\mathrm{diss}}(F)$ and recombination to the ground state k_{f} against one another,

$$P(F) = \frac{k_{\mathrm{diss}}(F)}{k_{\mathrm{diss}}(F) + k_{\mathrm{f}}} \tag{17.1}$$

The field-dependent dissociation rate was given as

$$k_{\mathrm{diss}}(F) = \frac{e\mu}{\varepsilon_r \varepsilon_0} \cdot \frac{3}{4\pi a^3} \exp\left(-\frac{E_b}{k_{\mathrm{B}} T}\right) \cdot \left(1 + b + \frac{b^2}{3} + \frac{b^3}{18} + \cdots\right) \tag{17.2}$$

The first factor is derived from the Langevin recombination [39, 40] of free charge carrier recombination (see also Section 17.4); it is proportional to the sum of electron and hole mobility μ and the average dielectric constant ε_r. $E_b = \mathrm{e}^2/4\pi\varepsilon_r\varepsilon_0 a$ is the binding energy of the charge pair, a the initial distance of its constituents, $k_{\mathrm{B}}T$ the thermal energy. The last factor of Eq. (17.2) in brackets is the Taylor expansion of a first-order Bessel function [41], with the reduced electric field $b = \mathrm{e}^3 F/8\pi\varepsilon_r\varepsilon_0(kT)^2$. As the dissociation rate is independent of the species concentration, and thus independent of the illumination density, this geminate recombination inhibits a first-order decay. Other similar theories for charge carrier pair losses have also been presented [42, 43], but are less commonly used.

Thus, geminate recombination to the ground state is the major competing process to the generation of free charges, as expressed in Eq. (17.1). The binding energy of the CT exciton has been determined to be 200 meV for a PPV derivative: PCBM blend [44]. For copolymer–copolymer heterojunctions, 250 meV was reported [45]. Both values go clearly beyond the thermal energy kT at room temperature, implying that the dissociation of these bound states should heavily rely on

external factors such as the electric field in the device. However, this has not been reconciled with field-dependent photocurrent measurements. The impact of geminate recombination seems to be lower than expected, which is also true for a more common organic photovoltaic material combination: The binding energy of the P3HT:PCBM CT exciton has not been experimentally determined, which leads to a large uncertainty for the applicability of the Braun–Onsager model. In addition, it has been found that in regioregular P3HT blended with PCBM, about 95% of charge generation seems to be direct [28], leading to an almost field-independent photocurrent in the working regime of organic solar cells [46–49], as shown in Figure 17.2a. Using the macroscopic charge carrier mobility as the input parameter for Eq. (17.1), recombination rates k_f much longer [50] than the experimentally observed 5 ns [28] or 4–30 ns for copolymers [51, 52] had to be used. The potential reasons for the high polaron pair dissociation yield will be discussed next.

An important reason for the efficient dissociation mechanism has been given by Veldman *et al*. [51]. They performed a Braun–Onsager fit, Eq. (17.1), to their photophysical data of copolymer:PCBM films and achieved good agreement when using a mobility exceeding the macroscopically measured charge carrier mobility by orders of magnitude. They explained their finding by proposing a high local mobility in crystalline PCBM clusters of about 15 nm diameter. Indeed, PCBM nanocrystals were experimentally observed [54, 55]. Similarly, polymer chains allow high local mobilities along their conjugated segments [56, 57], as described in Section 17.3. By Monte Carlo simulations of polaron pair dissociation, it was shown that delocalization along polymer chains [58] with high local mobility can increase the photogeneration yield by more than one order of magnitude, leading to an almost field-independent photocurrent [53]. The results are shown in Figure 17.2b. The delocalization leads to a larger interpair radius of the CT complex or polaron pair, implying a lower effective binding energy.

Thus, one interpretation of the expected generation of a bound state after singlet exciton dissociation, and its seemingly effortless dissociation into free charges, is the high local mobility found for at least one of the blend materials. Another explanation is that singlet excitons are dissociated into free charges directly without precursor state [28, 59], with close to unity yield for P3HT:PCBM [28]. In this scenario, only a small fraction of singlets is transferred into a CT complex instead, all of them recombining to the ground state [28]. In the first instance, CT complexes would contribute a positive effect to photovoltaics [36], in the latter case they would be a loss mechanism only. Scharber *et al*. found that by increasing the acceptor content in PPV derivative:PCBM solar cells, they could tune the amount of direct charge generation up to 100% for a 1:4 ratio. On the other hand, though, the voltage bias dependence of the CT complex quenching in P3HT:PCBM compared to the photocurrent gave the same behavior [60], which is expected only if the emissive CT state serves as precursor for charge generation. Thus, the role of the bound polaron pair in organic solar cells is not yet completely resolved.

Despite these open questions, it is known that additional factors do have an impact of the dissociation yield in polymer–fullerene blends.

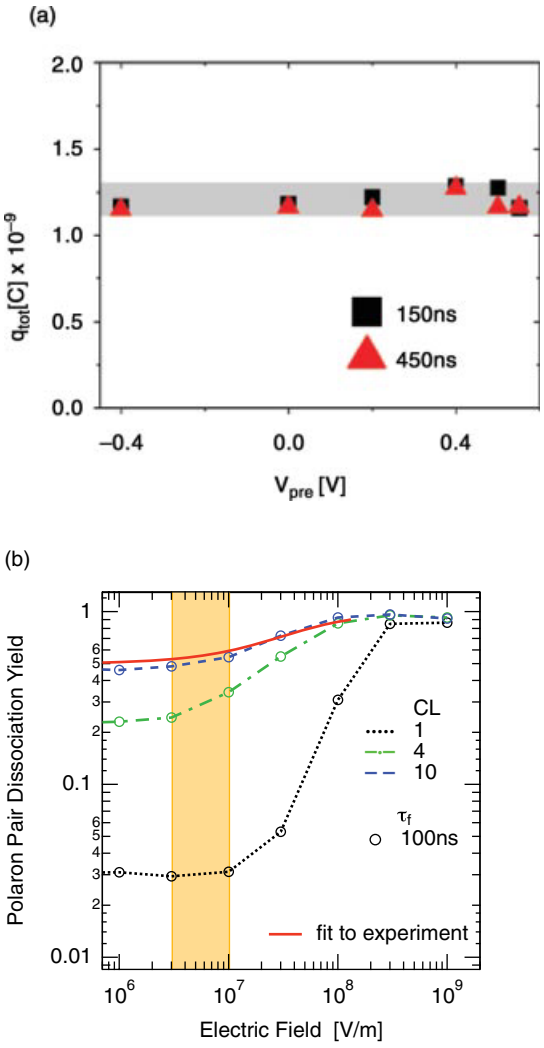

Figure 17.2 Field dependence of photogeneration. (a) For a P3HT:PCBM solar cell, the photogeneration of charges q_{tot} is field independent for the voltage range of −0.4 to 0.55 V at room temperature, as shown by time-delayed collection field measurements. (b) The polaron pair dissociation yield was computed by Monte Carlo simulations for a polymer–fullerene blend with different lengths of the effective polymer chain length CL [53]. For comparison, the Braun–Onsager fit to the experimental photocurrent of a P3HT:PCBM solar cell is shown [46]. In the working regime of organic solar cells, with electric fields smaller than 10^7 V/m, the photogeneration is almost field independent. Reproduced with permission from Ref. [48]. Copyright 2011 American Chemical Society.

One important contribution is made by the excess energy ΔG (see Figure 17.3) of the dissociated singlet excitons, given by the difference of their energy to that of the resulting (bound or free) electron–hole pairs. The Durrant group found that the initial polaron density in polymer–PCBM blends is proportional to $exp(\Delta G)$ [61, 62], with the ΔG and the resulting highest free carrier concentration – and thus the highest polaron pair dissociation yield – for P3HT:PCBM. Furthermore, they later reported that the short-circuit current density is also proportional to this initial polaron concentration [63]. Despite this intriguing dependence, it became clear that this is not a universal law: solar cells made from P3HT:PCBM and with P3HT with an endohedral fullerene [64], in which the latter has an excess energy ΔG that is one third lower, still feature almost the same short-circuit current.

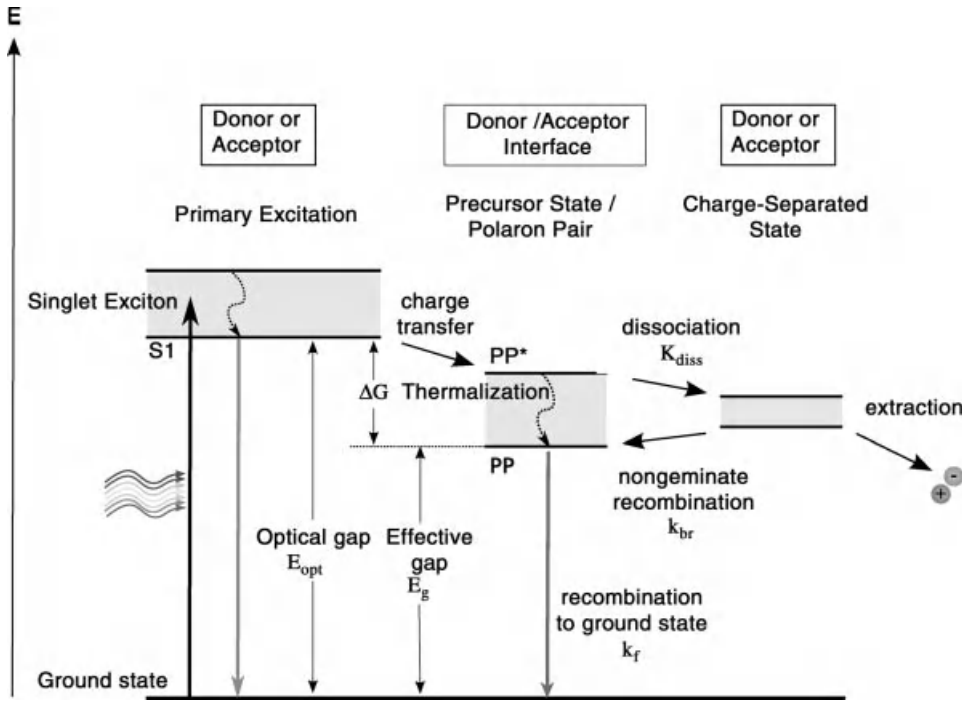

Figure 17.3 The energy states involved in the photogeneration in organic solar cells, complementing the kinetic picture shown in Figure 17.1. The light absorption occurs in either donor or acceptor material, generating singlet excitons S_1 with an energy at least corresponding to the absorption edge or optical gap E_{opt}. The energy of the polaron pair PP at the donor–acceptor interface resulting from the charge transfer is lower by the free energy ΔG, which may play an important role in the charge separation process, as described in the text. The dissociation process occurs with a rate k_{diss}, which needs to exceed the PP recombination to the ground-state k_f in order to photogenerate charge carriers with a significant yield. The reverse process of recombination of free charges into bound PP is also indicated, and takes place with the rate k_{br}. The remaining charges can be extracted at the electrodes.

Similarly, P3HT:bis-PCBM solar cells have no significant short-circuit current reduction, despite ΔG being reduced by 100 meV as compared to P3HT:PCBM [65].

Also, dipole layers can be a driving force for charge photogeneration. Dipole layers were found experimentally at organic–organic interfaces [66], and their influence on polaron pair dissociation was described theoretically [67, 68]. For pentacene/C_{60} planar heterojunctions as model systems, the orientation of the pentacene layers relative to the symmetric buckyballs was found to be decisive by electrostatic calculations [69, 70]: two different orientations lead to varying energetic environments. The one in which the pentacene is flat on the fullerene surface, exposing the former's p-orbital, favors polaron pair dissociation, while the other orientation suppresses it [69]. The authors point out that the impact of the interfacial dipole is due to polarization rather than ground-state charge transfer [70].

For polymer–fullerene bulk heterojunctions, Pensack *et al*. [71] proposed that PCBM domains have a higher order in their bulk and a low order at their interface to the polymer. In this scenario, charge pairs can be spatially separated more easily after charge transfer, an effect that might increase the effective lifetime of polaron pairs due to suppression (or delay) of geminate recombination.

As described above, the charge photogeneration is based on rather efficient processes and therefore has a high yield in polymer–fullerene solar cells. The separated charge pairs are finally transported to their respective electrodes: their charge transport is described in the next section, whereas nongeminate recombination of already free charge carriers is described in Section 17.4.

17.3
Charge Carrier Transport in Disordered Organic Semiconductors

After being photogenerated and successfully separated at the donor–accepter heterointerface, the electrons and holes are transported in the corresponding phase to the respective electrodes (see step 5 in Figure 17.1). Thereby, the holes are typically transported in the donor material – that is, the polymer – and the electrons in the acceptor phase, in this case the fullerene. The charge carrier transport in organic semiconductors, such as polymers and fullerene derivatives, is mainly characterized by the disordered nature of the materials. The charge carriers are localized to molecular sites with respect to the Anderson localization [72] due to energetic and spatial disorder in the bulk. In case of a conjugated polymer, a molecular site, which can be occupied by a charge carrier, is defined by the conjugation length of a polymer segment, that is, the overlap of neighboring sp_2-hybridized orbitals forming a delocalized π-bonding. The delocalized polymer segments are disrupted by breaks in the conjugation causing an energetic barrier for the charge carriers [73]. Along a delocalized state, a charge carrier can move barrier free. The distribution of these electronic sites in an organic disordered semiconductor is often described to be Gaussian density of states distribution (GDOS) [74], which also accounts for the random distribution of the molecular sites.

Due to strong electron–phonon interaction in organic materials, a charge carrier residing on a molecule results in the deformation of the latter: an electron or hole distorts the molecular lattice and is hence known as a negative or positive polaron, respectively. To participate in the charge transport, a localized polaron has to proceed from one state to another by a hopping process, which is in general characterized by a combination of tunneling from one site to the next neighboring site and a thermally activated process [75, 76].

In 1956, Marcus [24] proposed a rate describing the electron transfer from molecule i to j as a process of reduction followed by oxidation of the participating molecules by

$$\nu_{ij} = \frac{|I_{ij}|^2}{\hbar}\sqrt{\frac{\pi}{\lambda k_B T}}\exp\left(-\frac{(\Delta G_{ij}+\lambda)^2}{4\lambda k_B T}\right) \tag{17.3}$$

for which he was awarded the Nobel Prize in chemistry in 1992. I_{ij} in Eq. (17.3) corresponds to the transfer integral, that is, the wave function overlap between site i and site j, which is equivalent to a tunneling contribution. λ represents the reorganization energy related to the relaxation of the molecule upon charge transfer, ΔG_{ij} is the energy difference between the two sites i and j, k_B is the Boltzmann constant, and T is the temperature. In the same year, Mott [77] and Conwell [78] used the concept of hopping transport in order to describe impurity band conduction in semiconductors.

An often-used equation to determine the transition rate for a charge carrier was given by Miller and Abrahams in 1960 [79]. They calculated the rate ν_{ij} for a phonon-assisted hopping process from an occupied state i with an energy E_i to an unoccupied state j with energy E_j by [79]

$$\nu_{ij}(E_i, E_j, R_{ij}) = \nu_0 \exp(-2\gamma R_{ij})\begin{cases}\exp\left(-\dfrac{E_j - E_i}{k_B T}\right) & E_j > E_i \\ 1 & E_j < E_i\end{cases} \tag{17.4}$$

ν_0 is the maximum hopping rate, also known as attempt-to-escape frequency, R_{ij} is the spatial distance between the states i and j, γ is the inverse localization radius being proportional to the transfer integral, and $k_B T$ is the thermal energy. The first exponential term in Eq. (17.4) describes the overlap of the wave function of the states i and j representing again the tunneling contribution – similar to I_{ij} in Marcus theory – whereas the second exponential term accounts for the temperature dependence of the phonon density described by a Boltzmann term in analogy to the Marcus theory in Eq. (17.3). However, the energy difference ΔE_{ij} usually considers only energetic disorder and not the polaron relaxation, which is regarded by the reorganization energy λ in the Marcus model. Furthermore, the Boltzmann term in Eq. (17.4) is assigned to be one for jumps down in energy. Both the rate equations given by Marcus (Eq. (17.3)) and Miller–Abrahams (Eq. (17.4)) describe the hopping transport of charge carriers as a combination of a tunneling process (spatial contribution) and an energy activation process (energetic contribution) with respect to the absorption or emission of phonons. In contrast to the Miller–Abrahams equation, the Marcus theory includes polaronic effects, such as the

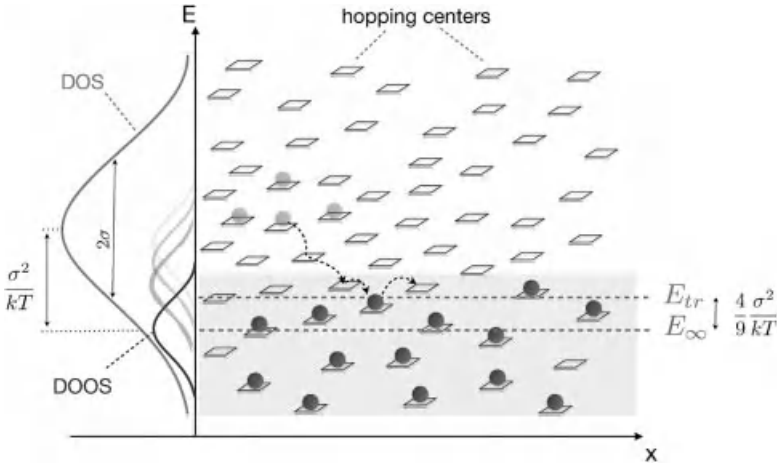

Figure 17.4 Schematic overview of the charge carrier hopping transport in disordered systems. The density of states distribution is assumed to be Gaussian (GDOS) [74]. Charge carriers generated by a light pulse first follow the DOS and finally thermalize to deep states toward equilibrium (E_∞). To participate in the transport, a charge carrier has to be thermally activated to the transport energy level E_{tr}.

change in molecular confirmation upon charge transfer. The hopping rates given by both theories are typically applied in Monte Carlo simulations [74, 80, 81] or hopping master equations [82, 83] to study the macroscopic charge carrier transport properties in organic disordered semiconductors. The Marcus theory is usually applied in multiscale simulations [84], whereas Miller–Abrahams rate equation is used for generic simulations without specifying the considered molecules [85].

In Figure 17.4, the hopping transport of charge carriers in a Gaussian density of states distribution is illustrated. Directly after being photogenerated the density of occupied states (DOOS) follows exactly the GDOS of available states. With increasing time, the charge carriers relax down in energy by thermalization to unoccupied states until an equilibrium level is reached (E_∞). In order to participate in the transport, the charge carriers have to be thermally activated to the so-called transport energy level E_{tr} (see Figure 17.4) [75, 86]. With less energy available for the hopping motion, the charge carriers may get trapped by deep states in the DOS due to the absence of sufficient activation energy. This phenomenon is often described by the multiple trapping and release (MTR) model [87–89], which accounts for this trapping and detrapping of charge carriers. Thereby, charge carriers on hopping sites below the transport energy E_{tr} are assumed to be immobile and first have to be activated to a site above E_{tr} in order to participate in the charge transport.

A macroscopic parameter describing the charge transport properties in general is the charge carrier mobility μ, which is defined as the proportionality constant between the drift velocity v_{d} and the electric field F

$$v_{\text{d}} = \mu F \tag{17.5}$$

In contrast to inorganic semiconductors with delocalized band transport, the charge carrier mobility in organic disordered materials obeys a different dependence on electric field F and temperature T. From experiments, a typical Poole–Frenkel-type behavior can be found ($\mu \propto \exp\sqrt{F}$) as well as an increasing charge carrier mobility with temperatures [74, 90], which indicates that the hopping transport is a thermally activated process. Depending on the shape of the density of states distribution (DOS) in organic semiconductor, the temperature dependence of the charge carrier mobility varies: in case of an exponential DOS $\mu \propto \exp(-E_a/k_B T)$ behavior with E_a as the activation energy, whereas $\mu \propto \exp(-(\sigma/k_B T)^2)$ for a Gaussian DOS (GDOS) with the energetic width of the GDOS given by the standard deviation or disorder parameter σ [76, 91].

Usually, the intrachain mobility, that is, the mobility of a charge carrier along a polymer chain or within a nanocrystal in case of the fullerene phase, and the interchain mobility have to be distinguished. The latter usually describes the charge transport throughout the bulk of the material from the front contact to the back contact in a diode configuration, where the charge carriers have to hop from one molecular site to another. In organic field effect transistors (OFET), the transport typically occurs in a lateral configuration, that is, a thin sheet of layer at the surface. Depending on the direction of the molecules, the charge carrier mobility measured in a lateral configuration and in the diode configuration, that is, in solar cell architecture, is somewhat different and cannot be directly compared. Moreover, the charge carrier concentration in the channel of a field effect transistor is generally much higher (2–4 orders of magnitude) than the concentration of photogenerated charge carriers in an organic solar cell. In such a high charge carrier concentration regime ($n > 10^{24}$ m^{-3}), the charge carrier mobility increases distinctly with n [82, 92, 93].

An experimental technique studying the local charge carrier mobility on a molecular chain (intrachain mobility) is the transient microwave conductivity (TRMC) experiment, where the charge carrier mobility is studied in an electrode-less configuration [29, 94]. In another experiment, the charge carrier relaxation on an ultrafast timescale can be probed by a combination of conventional time-of-flight and time-resolved electric-field-induced second-harmonic generation [95]. It was found that the excess energy given after photogeneration results in a very high initial charge carrier mobility. The subsequent relaxation of charge carriers within the DOS (see Figure 17.4) leads to a rapid decrease in the charge carrier mobility by several orders of magnitude, which suggest a time-dependent charge carrier mobility in organic solar cells. However, in the μs to ms regime, usually no charge carrier relaxation is observed for most organic compounds [96]. A commonly used experimental technique to determine the bulk charge carrier mobility in low mobility materials such as organic disordered semiconductors is the method of transient photoconductivity, also known as time of flight (TOF) (e.g., Refs [90, 97–99]). The charge carrier mobility μ can be calculated from the transit time t_{tr}, the sample thickness d, and the applied electric field F by

$$\mu = \frac{d}{t_{tr} \cdot F} \tag{17.6}$$

Thereby, the active layer of the investigated sample structure has to be much thicker than the penetration depth of the laser. This often limits the active layer of the device to thickness larger than 1 μm. However, in organic bulk heterojunction solar cells, usually the thickness of the blend layer is on the order of 100–200 nm. Thus, TOF measurements are mostly used to study the transport properties in the bulk of an organic solar cell (see Refs [100–103]).

An important prerequisite for the performance of an organic BHJ solar cell is that the electron and hole mobilities are rather balanced to avoid a space charge piling up in the device, which lowers V_{oc} (see Section 17.5). Furthermore, the charge carriers have to find distinct percolation pathways to the respective electrode in order to be extracted efficiently. For many conjugated polymers, such as PPV [12], an excess of PCBM content (67–80 wt.%) was found to optimize the solar cell performance, even though the cell harvests less sunlight. This was related to an improved charge transport and hence increased short-circuit current density due to a better phase separation boosting the charge separation process (see Section 17.2) [50]. Furthermore, it could be shown that depending on the size of the fullerene as well as on the size and density of side chains of the polymer, intercalation of the fullerenes between the side chains can occur [104, 105]. The latter is beneficial for an efficient charge separation at the donor–acceptor heterointerface. However, the excess of fullerene is necessary for a favorable phase separation in the bulk so that charge carrier can be collected efficiently at the electrodes [104, 106]. In Figure 17.5a, the electron and hole mobility in MDMO-PPV:PCBM blend devices, respectively, are shown as a function of the PCBM fraction. Both the electron and the hole mobility rise with fullerene content. At a PCBM loading of around 70%, the electron and hole mobilities are almost balanced with a relatively high mobility on the order of 10^{-4}–10^{-3} cm^2/V s. The blend system of P3HT:PCBM has a special role in this context, as it has its best performance at a ratio of 1: 0.8–1: 1, in contrast to many other systems. Due to rather short side chains of the polymer P3HT, neither intercalation of the fullerene has to occur for an efficient charge separation nor an excess of fullerene is needed for favorable phase separation. Moreover, it could be shown that with increasing PCBM content in the blend, the overall crystallinity of the P3HT decreases [107, 108], which limits the charge transport and hence leads to a decrease in hole mobility. Furthermore, it was reported that both P3HT [100] and PCBM [102] have an ambipolar character, that is, both electron and holes can be transported, similar to many other conjugated polymers [109]. In P3HT:PCBM, indeed, two transit times were found for some blend ratios, as can be seen in Figure 17.5b by t_1 and t_2. The observation of two independent transit times was assigned to a hole and electron transport on different percolation pathways, which are not necessarily restricted to one material phase [103].

A method, which can be applied to organic solar cells with typical device thicknesses on the order of 100–200 nm, is the technique of charge carrier extraction by linearly increasing voltage (photo-CELIV) [110]. It is often used to study the charge carrier recombination in organic solar cells as the charge carrier mobility μ and the concentration of the extracted charge carriers n can be probed simultaneously [101, 111, 112]. Thereby, the time between the charge photogeneration and the

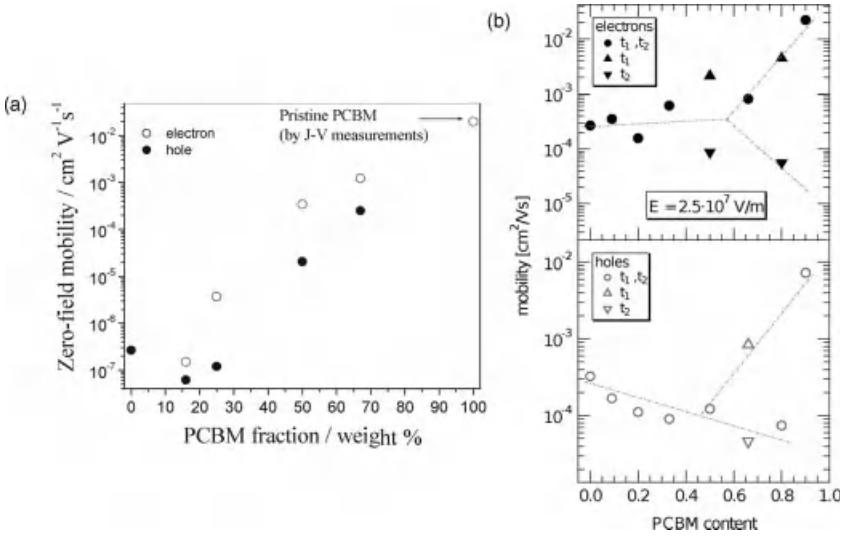

Figure 17.5 (a) Electron and hole mobilities in MDMO-PPV:PCBM blend films as a function of the PCBM content. The values were obtained by extrapolating the field-dependent (Poole–Frenkel-like) mobility to zero field ($F = 0$). (b) Electron and hole mobilities in P3HT:PCBM blend devices as a function of the PCBM content at an electric field of 2.5×10^7 V/m. The two transit times were assigned to different percolation pathways for the charge carriers. Reproduced with permission from Ref. [102]. Copyright 2005, John Wiley & Sons.

charge extraction is varied [101]. A drawback of this versatile technique is that it is insensitive to the polarity of the extracted species.

In the next section, the charge carrier recombination in organic bulk heterojunction solar cells will be discussed.

17.4 Recombination of Photogenerated Charge Carriers

During the charge transport of the photogenerated charge carriers to their respective electrodes, the charge carriers can meet each other and recombine, which describes a loss mechanism for the photocurrent and hence limits the efficiency of the solar cell (Figure 17.1, step (ii)). The current continuity equation can be written as

$$\frac{\mathrm{d}n}{\mathrm{d}t} = G - R - \frac{1}{q}\frac{\partial j}{\partial x} \tag{17.7}$$

with the generation rate G, the recombination rate R, and $\partial j/\partial x$ as the spatial current derivative representing a diffusion current. The recombination of already separated polarons is typically a nongeminate process, in contrast to the geminate recombination, where charge carriers originating from the same precursor state

recombine (see Section 17.2). Furthermore, the nongeminate recombination of an electron and a hole is found to be bimolecular [113–115]. The recombination rate is described by

$$R = k_{\mathrm{br}} \cdot (np - n_{\mathrm{i}}^2) \tag{17.8}$$

with the recombination coefficient k_{br}, the charge carrier concentration of photogenerated electrons (n) and holes (p), and n_{i} the concentration of intrinsic charge carriers. In case of charge neutrality ($n = p$) with $np > n_{\mathrm{i}}^2$ and that both electrons and holes are mobile and not trapped, the recombination order is two ($R \propto n^2$). However, charge carriers may also be trapped during the transport as already mentioned in Section 17.3, which will have an impact also on the charge carrier recombination.

A model, which is often used in literature to describe the bimolecular recombination in materials with low charge carrier mobility ($\mu < 1\ \mathrm{cm}^2/\mathrm{V\,s}$), is the one introduced by Langevin [39, 40]. In his model [39], Langevin proposed a rate describing the recombination of two opposite charged ions in a large ion reservoir. In the absence of an electric field, the two ions can circumvent recombination only if their kinetic energy is larger than the Coulomb attraction. In other words, the two oppositely charged carriers will recombine if the distance is smaller than the Coulomb radius r_{c} [40]

$$r_{\mathrm{c}} = \frac{e^2}{4\pi\varepsilon\varepsilon_0 kT} \tag{17.9}$$

which is also known as the Onsager radius. In case of organic materials with $\varepsilon \approx 3.4$, this distance can be as large as 17 nm, which is far beyond the distance of adjacent molecules.

In analogy to Eq. (17.8), the recombination rate in the Langevin model is described by

$$R_{\mathrm{L}} = \gamma \cdot (np - n_{\mathrm{i}}^2) \tag{17.10}$$

with the intrinsic charge carrier concentration n_{i}^2, which is usually much smaller than the product np. The recombination coefficient γ is proportional to the sum of the charge carrier mobility of electron μ_n and hole μ_p and is given by

$$\gamma = \frac{q}{\varepsilon\varepsilon_0}(\mu_n + \mu_p) \tag{17.11}$$

Thus, the finding of the charge carriers is a crucial parameter limiting the charge carrier recombination. From experiments, however, often a deviation from Langevin recombination can be observed [111, 116–119], as will be shown in the following.

Commonly used experimental techniques to determine the charge carrier recombination rate in organic bulk heterojunction solar cells are, among others, the technique of transient absorption (TA) [28, 61, 120, 121], transient photovoltage and photocurrent (TPV/TPC) [115], and charge carrier extraction by linearly increasing voltage (photo-CELIV) [110, 122]. As already mentioned earlier, the last

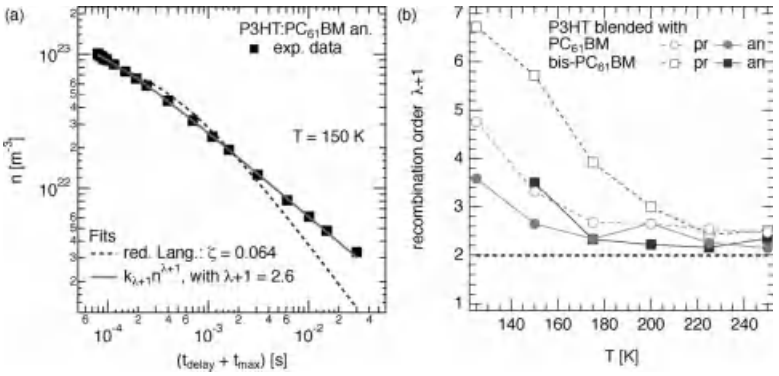

Figure 17.6 (a) Charge carrier concentration revealed by the photo-CELIV experiment on P3HT:PCBM 1: 0.8 BHJ solar cell at $T = 150$ K as a function of the sum of delay time t_{delay} and the position of the maximum extraction peak t_{max}. Fits: (dashed line) reduced Langevin recombination: $R = \zeta\gamma_L n^2$; (solid line) empirical approach: $R = k_{\lambda+1}\, n^{\lambda+1}$; (b) charge carrier recombination order $\lambda + 1$ as a function of the temperature for P3HT:PCBM and P3HT:bis-PCBM pristine and annealed devices.

technique is feasible for measuring the charge carrier mobility and concentration simultaneously. In Figure 17.6a, the time-dependent charge carrier concentration n revealed by photo-CELIV measurements on P3HT:PCBM at $T = 150$ K is shown. The experimental data are fitted with respect to the current continuity equation (see Eq. (17.7)) assuming charge neutrality ($n = p$) as well as the spatial derivative of the current to be zero ($\partial j/\partial x = 0$). The Langevin theory with the experimentally determined charge carrier mobility can partly describe the experiment with an additional constant prefactor ζ [111] in Eq. (17.10). However, especially for long delay times, the corresponding fit still deviates from the experimental data. The latter can be better described by an empirical approach assuming the recombination term to be $R = k_{\lambda+1} n^{\lambda+1}$ [115]. In many organic BHJ systems, a recombination order $\lambda + 1 > 2$ [106, 115, 123, 124] is observed by complementary experimental techniques, whereas the order typically increases with decreasing temperature [106]. In Figure 17.6b, for example, the charge carrier decay order $\lambda + 1$ is shown for two different blend systems – P3HT:PCBM and P3HT:bis-PCBM pristine and annealed – as a function of the temperature. Both blend systems obey an increase in the recombination order with decreasing temperature. Thereby, $\lambda + 1$ in pristine devices increases more strongly and reaches even $\lambda + 1 = 7$ for P3HT:bis-PCBM at $T = 150$ K. The question now arises how such a deviation from recombination order of 2 can be explained.

If the recombination of free polarons in organic bulk heterojunction solar cells is considered, one has to bear in mind that the bulk of the solar cell consists mainly of two materials mixed together on the nm scale [125]. Typically, the donor material serves as a hole conductor and the acceptor as the electron conducting material. Thus, the recombination of mobile electrons and holes can take place only at the heterointerface of the donor and the acceptor [126], which already leads to a reduced

recombination probability [111]. Moreover, the transport of the charge carriers to the heterointerface is affected by the disorder in the blend system. Thus, not only the charge carrier transport is influenced by the disorder, which is widely accepted in literature, but also the charge carrier recombination is influenced by the disorder.

As already mentioned in Section 17.3, the charge carrier transport in organic BHJ solar cells is influenced by multiple trapping and release processes. Especially at low temperatures with less activation energy available, a certain amount of charge carriers is trapped in deep states of the broad DOS. Thereby, the molecular packing in a donor–acceptor blend system is crucial for the energetic ordering in the latter, which has an important impact on the performance of the solar cell [127]. In the P3HT:bis-PCBM blend system shown here, the ordering of the fullerene cages is reduced due to the additional side chain in bis-PCBM, which immediately leads to an increase in energetic disorder. In thermally annealed blend devices, typically the donor and acceptor phase increases, party crystallizes, which leads to a more favorable design for the charge transport (see Section 17.3) with a narrower DOS (small σ) compared to thermally untreated devices. Models have been presented [119, 120] to describe the charge carrier recombination in organic BHJ solar cells by taking into account the recombination of free charge carriers as well as the recombination of free and trapped charge carriers with respect to Shockley–Read–Hall (SRH) recombination [40]. These models are derived from amorphous semiconductors, which usually deal with an exponential band-tail of localized states lying at the bottom of the conduction band [128–130]. In Figure 17.7a, possible capture and recombination mechanism is depicted, whereas electrons and holes – besides recombining as free charge carriers – can be trapped in states below the conduction band (E_C) or the valence band (E_V). Free mobile charge carriers can recombine with these trapped charge carriers, which is described by SRH recombination. Thereby, the charge carrier trapping and detrapping processes implicitly cause the charge carrier mobility to become dependent on the charge carrier concentration [119], which of course also has an impact on the charge carrier recombination. With respect to Eq. (17.11) the recombination coefficient γ becomes concentration dependent and a recombination order $\lambda + 1 > 2$ can be observed [124]. Especially at low temperatures, the charge transport becomes more and more trap limited, which causes the charge decay order to increase (see Figure 17.6a). However, the high recombination order at low temperatures cannot be explained solely by the charge carrier concentration-dependent charge carrier mobility. Moreover, the phase separation in the blend system plays a major role in this context. In Figure 17.7b, different scenarios of possible nongeminate recombination pathways in an organic BHJ solar cells are shown: (i) In the simplest case, both electrons and holes are mobile (n_c, p_c) and can recombine at the heterointerface. However, charge carriers can also be trapped (n_t) either at the heterointerface or away from it. (ii) In case of being trapped at the interface, the charge carrier can recombine with a free mobile counterpart passing the interface. (iii) If the charge carrier is trapped within a material phase apart from the heterointerface, it has to be first released before it can recombine. The latter is an energy

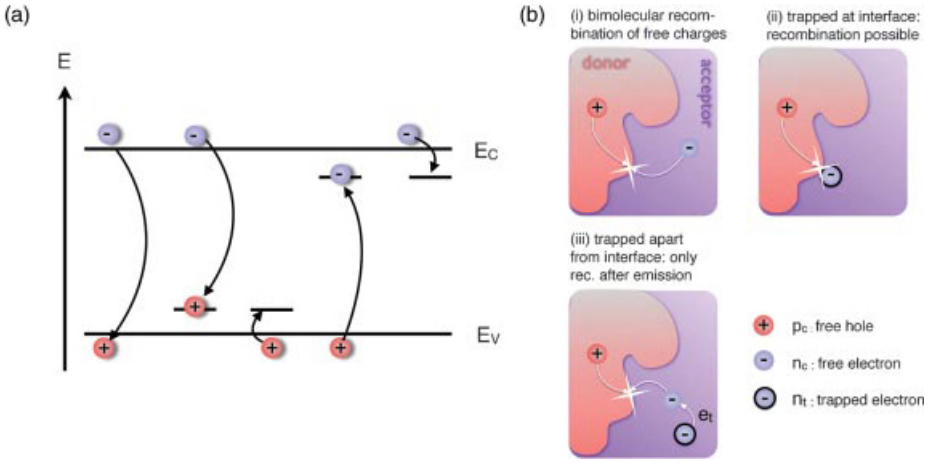

Figure 17.7 (a) Energetic schematics of different possible capture and recombination processes via tail states in the DOS: besides the recombination of free electrons and holes, they can also be trapped in states below the conduction (E_C) or above the valence band (E_V), respectively, before they recombine with a free mobile counterpart. (b) Charge carrier trapping and recombination in a phase-separated donor–acceptor blend system from morphological point of view: (i) recombination of free mobile charge carriers at the heterointerface. (ii) Trapped (energetically) electron directly at the interface can recombine with a free hole from the donor side. (iii) Electron trapped apart from the heterointerface first has to be released before it can recombine at the interface with a free hole. reproduced from Ref. [119]

activated process and leads to a delay in recombination [106, 120]. This delay can be observed in the experiment as a reduced charge carrier decay in time (see Figure 17.6a) and hence in an increased charge carrier recombination order.

Depending on the concentration of trapped charge carriers, the experimentally observed charge carrier recombination order, however, can be even smaller than 2. Considering the continuity equation of free holes p_c, we find

$$dp_c/dt = -kp_c n_c - k' p_c n_t \tag{17.12}$$

with n_c and n_t as the free and trapped electrons, respectively, and k and k' as the relevant recombination prefactors. In the case, when $n_t \gg n_c, p_c$, the recombination dynamics can be written as

$$dp_c/dt \approx -k' p_c n_t = p_c/\tau \tag{17.13}$$

with $\tau = 1/k' n_t \approx$ const, which is a first-order process. Thus, even the charge carrier recombination is bimolecular, the recombination order, which is observed in the experiment, can be even 1 [131].

So, both the impact of charge trapping and the donor–acceptor phase separation, and hence the morphology, are responsible for the experimentally observed recombination order.

17.5
Open-Circuit Voltage

The previous sections of this chapter outlined the steps of conversion from light to photocurrent. However, the performance of organic solar cells is also determined by the open-circuit voltage, V_{oc}. It is given by the balance of charge generation and recombination in the device, $G = R$, with the maximum possible V_{oc} being due to the energetics of the donor–acceptor material system.

Already in 2001, a linear dependence of the open-circuit voltage on the energy difference between the acceptor's lowest unoccupied molecular orbital and the donor's highest occupied molecular orbital (HOMO) was reported [132]. This effective bandgap E_g is indicated in Figure 17.3. The empirical finding was that $V_{oc} \approx E_g - 0.3$ eV for a wide range of polymer–fullerene combinations. Later on, E_g was attributed to the energy of the donor–acceptor CT complex (see Section 17.2) [36, 133].

Analytically, the open-circuit voltage can be described by

$$V_{oc} = \frac{E_g}{e} - \frac{kT}{e} \ln\left(\frac{N_{eff}^2}{\Delta n \cdot \Delta p}\right) \tag{17.14}$$

where N_{eff} is the effective density of states, and Δn and Δp are the excess steady-state carrier concentration of electrons and holes due to photogeneration, respectively [134, 135]. Here, the diode ideality factor was neglected. As pointed out above, the effective bandgap is given by the donor–acceptor combination. In principle, it should always be smaller than the energy of the primary excitation in order to have a driving force for singlet exciton dissociation, but can be almost as high [25]. The excess polaron concentration should be as high as possible under steady-state conditions in order to maximize V_{oc} within the bounds set by E_g. This is achieved by a maximum generation rate of polarons for a given illumination intensity (see Section 17.2 for photogeneration), and a minimum polaron recombination rate (see Section 17.2 for geminate recombination and Section 17.4 for nongeminate losses). We point out that recently, the impact of energetic disorder typically found in these solution-processed systems on the open-circuit voltage was described [136].

Figure 17.8a shows the temperature dependence of the open-circuit voltage for two P3HT:fullerene bulk heterojunction experiments and also macroscopic device simulations [137]. Clearly, V_{oc} is raised with decreasing temperature, and then levels off. V_{oc} is increased as the steady-state carrier concentration is higher at low temperatures due to the diminishing nongeminate recombination, which is thermally activated due to its proportionality to the charge carrier mobility (see Section 17.4). At 0 K, without any nongeminate recombination, the maximum open-circuit voltage with the value of E_g could ideally be reached. However, experimentally, already at intermediate temperatures, the open-circuit voltage does not increase any more, but remains constant. In this case, the carrier concentration may still increase [137], but the electrode work functions limit the quasi-Fermi-level splitting [138]. Thus, under these conditions, V_{oc} becomes contact limited.

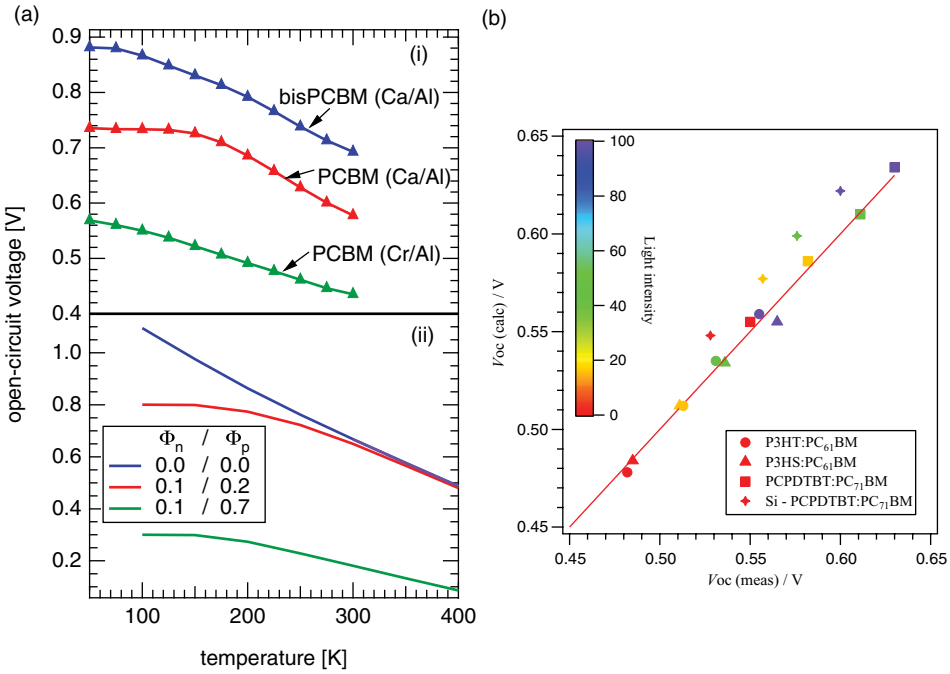

Figure 17.8 (a) The open-circuit voltage of polymer–fullerene solar cells increases toward the effective bandgap with lower temperature, but becomes limited by the electrode work function at some point. (i) Experimental V_{oc} of P3HT:fullerene solar cells with different electrodes, (ii) macroscopic device simulations with different injection barriers Φ showing the contact limitation of V_{oc}. The open-circuit voltage can also be reconstructed experimentally from Eq. (17.15) by (b) the loss current at open-circuit conditions from time-resolved recombination measurements. Reproduced with permission from Ref. [137]. Copyright 2011, American Institute of Physics.

The open-circuit voltage can alternatively be written as

$$V_{oc} = \frac{kT}{e} \ln\left(\frac{j_{sc}}{j_0} + 1\right) \tag{17.15}$$

which is based on the well-known Shockley diode equation. Of course, this equation implies that the photogeneration is field independent. Then, the open-circuit voltage can be reconstructed from the short-circuit current and the dark saturation current, even without explicitly including the effective bandgap. The information on recombination, or – according to a detailed balance approach [133] – the spectral information of CT absorption and emission, is included in the dark saturation current. By measuring them, the open-circuit voltage could be reconstructed for a wide range of polymer–fullerene solar cells. This strongly indicates that the maximum open-circuit voltage is given by the CT complex.

The open-circuit voltage can also be reconstructed by measurements of the recombination dynamics, and thus the nongeminate loss current. The latter is

included in Eq. (17.15) as j_0, and the V_{oc} of several polymer–fullerene solar cells could be predicted with a small error (Figure 17.8b). Clearly, the open-circuit voltage can be optimized only by either increasing the effective bandgap toward the absorption gap [25] or finding ways to decrease the nongeminate recombination (Section 17.4) [134, 136]. Vandewal *et al.* pointed out that of the about 0.6 V difference from E_g to the actually measured V_{oc} at room temperature under 1 sun for typical polymer–fullerene solar cells, about 0.25 eV is due to radiative losses and 0.35 eV is due to nonradiative recombination [140]. In addition to bulk recombination, the open-circuit voltage can also be lowered by surface recombination, that is, when a low charge extraction rate from the solar cell leads to space charge accumulation. This behavior is connected to s-shaped current–voltage characteristics [141–143].

17.6 Summary

In this chapter, we discussed the subsequent steps from light absorption to photocurrent extraction in polymer based on the light-to-current generation in polymer–fullerene bulk heterojunction solar cells. In the fundamental understanding, significant progress has been made, although some controversial issues remain. For instance, quantitative investigations on the origin and impact of radiative and nonradiative recombination on the solar cell performance have been started only recently. However, further progress is expected in the years to come, and conversion efficiencies exceeding 10 % for single junction devices are in close reach already now.

References

1 Deibel, C. and Dyakonov, V. (2010) Polymer–fullerene bulk heterojunction solar cells. *Rep. Prog. Phys.*, **73**, 096401.
2 Hübler, A., Trnovec, B., Zillger, T., Ali, M., Wetzold, N., Mingebach, M., Wagenpfahl, A., Deibel, C., and Dyakonov, V. (2011) Printed paper photovoltaic cells. *Adv. Energy Mater. Adv. Energy Mater.* **1**, 1018.
3 Green, M.A., Emry K., Hishikawa, Y., Warta, W., and Dunlop, E.D. (2012) Solar cell efficiency tables (Version 39), *Prog. Photovolt.: Res. Appl.* **20**, 12.
4 Peters, C.H., Sachs-Quitana, I.T., Kastrop, J.P., Beaupré, S., Leclerc, M., and McGehee, M.D. (2011) High efficiency polymer solar cells with long operating lifetimes. *Adv. Energy Mater., Adv. Energy Mater.* **1**, 491.
5 Chamberlain, G.A. (1983) Organic solar cells: a review. *Solar Cells*, **8**, 47.
6 Tang, C.W. (1979) US Patent **4**, 164, 431.
7 Tang, C.W. (1986) Two-layer organic photovoltaic cell. *Appl. Phys. Lett.*, **48**, 183.
8 Shaw, P.E., Ruseckas, A., and Samuel, I.D.W. (2008) Exciton diffusion measurements in poly(3-hexylthiophene). *Adv. Mater.*, **20**, 3516.
9 Sariciftci, N.S., Smilowitz, L., Heeger, A.J., and Wudl, F. (1992) Photoinduced electron-transfer from a conducting polymer to buckminster fullerenes. *Science*, **258**, 1474.
10 Brabec, C.J., Winder, C., Scharber, M.C., Sariciftci, N.S., Hummelen, J.C., Svensson, M., and Andersson, M.R. (2001) Influence of disorder on the photoinduced excitations in phenyl substituted polythiophenes. *J. Chem. Phys.*, **115**, 7235.

11 Yu, G., Gao, J., Hummelen, J.C., Wudl, F., and Heeger, A.J. (1995) Polymer photovoltaic cells: enhanced efficiencies via a network of internal donor–acceptor heterojunctions. *Science*, **270**, 1789.

12 Shaheen, S.E., Brabec, C.J., and Sariciftci, N.S. (2001) 2.5% efficient organic plastic solar cells. *Appl. Phys. Lett.*, **78**, 841.

13 Padinger, F., Rittberger, R.S., and Sariciftci, N.S. (2003) Effects of postproduction treatment on plastic solar cells. *Adv. Funct. Mater.*, **13**, 85.

14 Kim, J.Y., Lee, K., Coates, N.E., Moses, D., Nguyen, T.Q., Dante, M., and Heeger, A.J. (2007) Efficient tandem polymer solar cells fabricated by all-solution processing. *Science*, **317**, 222.

15 Peet, J., Kim, J.Y., Coates, N.E., Ma, W.L., Moses, D., Heeger, A.J., and Bazan, G.C. (2007) Efficiency enhancement in low-bandgap polymer solar cells by processing with alkane dithiols. *Nat. Mater.*, **6**, 497.

16 Park, S.H., Roy, A., Beaupre, S., Cho, S., Coates, N., Moon, J.S., Moses, D., Leclerc, M., Lee, K., and Heeger, A.J. (2009) Bulk heterojunction solar cells with internal quantum efficiency approaching 100%. *Nat. Photon.*, **3**, 297.

17 Brabec, C.J., Gowrisanker, S., Halls, J.J. M., Laird, D., Jia, S., and Williams, S.P. (2010) Polymer–fullerene bulk-heterojunction solar cells. *Adv. Mater.*, **22**, 3839.

18 McNeill, C.R., Halls, J.J.M., Wilson, R., Whiting, G.L., Berkebile, S., Ramsey, M. G., Friend, R.H., and Greenham, N.C. (2008) Efficient polythiophene/polyfluorene copolymer bulk heterojunction photovoltaic devices: device physics and annealing effects. *Adv. Funct. Mater.*, **18**, 2309.

19 Green, M.A., Emery, K., Hishikawa, Y., and Warta, W. (2010) Solar cell efficiency tables (version 35). *Prog. Photovolt.*, **18**, 144.

20 Brazovskii, S. and Kirova, N. (2010) Physical theory of excitons in conducting polymers. *Chem. Soc. Rev.*, **39**, 2453.

21 Conwell, E.M. and Mizes, H.A. (1995) Photogeneration of polaron pairs in conducting polymers. *Phys. Rev. B*, **51** (11), 6953.

22 Hertel, D. and Bässler, H. (2008) Photoconduction in amorphous organic solids. *Chem. Phys. Chem.*, **9**, 666.

23 Deibel, C., Mack, D., Gorenflot, J., Schöll, A., Krause, S., Reinert, F., Rauh, D., and Dyakonov, V. (2010) Energy levels and exciton binding energy in the conjugated polymer poly(3-hexyl thiophene). *Phys. Rev. B*, **81**, 085202.

24 Marcus, R.A. (1956) On the theory of oxidation–reduction reactions involving electron transfer. I. *J. Chem. Phys.*, **24**, 966.

25 Veldman, D., Meskers, S.C.J., and Janssen, R.A.J. (2009) The energy of charge-transfer states in electron donor–acceptor blends: insight into the energy losses in organic solar cells. *Adv. Funct. Mater.*, **19**, 1939.

26 Brabec, C.J., Zerza, G., Cerullo, G., de Silvestri, S., Luzzati, S., Janssen, R.A.J., and Sariciftci, N.S. (2001) Tracing photoinduced electron transfer process in conjugated polymer/fullerene bulk heterojunctions in real time. *Chem. Phys. Lett.*, **340**, 232.

27 Cook, S., Katoh, R., and Furube, A. (2009) Ultrafast studies of charge generation in PCBM:P3HT blend films following excitation of the fullerene PCBM. *J. Phys. Chem. C*, **113**, 2547.

28 Howard, I.A., Mauer, R., Meister, M., and Laquai, F. (2010) Effect of morphology on ultrafast free carrier generation in polythiophene:fullerene organic solar cells. *J. Am. Chem. Soc.*, **132**, 14866.

29 Kroeze, J.E., Savenije, T.J., Vermeulen, M.J.W., and Warman, J.M. (2003) Contactless determination of the photoconductivity action spectrum, exciton diffusion length, and charge separation efficiency in polythiophene-sensitized TiO_2 bilayers. *J. Phys. Chem. B*, **107**, 7696.

30 Lüer, L., Egelhaaf, H.J., Oelkrug, D., Cerullo, G., Lanzani, G., Huisman, B.H., and de Leeuw, D. (2004) Oxygen-induced quenching of photoexcited states in polythiophene films. *Org. Electron.*, **5**, 83.

31 Goh, C., Scully, S.R., and McGehee, M.D. (2007) Effects of molecular interface modification in hybrid organic–inorganic

photovoltaic cells. *J. Appl. Phys.*, **101**, 114503.
32 Cook, S., Liyuan, H., Furube, A., and Katoh, R. (2010) Singlet annihilation in films of regioregular poly(3-hexylthiophene): estimates for singlet diffusion lengths and the correlation between singlet annihilation rates and spectral relaxation. *J. Phys. Chem. C*, **114**, 10962.
33 Dennler, G., Scharber, M.C., and Brabec, C.J. (2009) Polymer–fullerene bulk-heterojunction solar cells. *Adv. Mater.*, **21**, 1323.
34 Frankevich, E.L., Lymarev, A.A., Sokolik, I., Karasz, F.E., Blumstengel, S., Baughman, R.H., and Hörhold, H.H. (1992) Polaron-pair generation in poly (phenylene vinylene). *Phys. Rev. B*, **46**, 9320.
35 Zhu, X.Y., Yang, Q., and Muntwiler, M. (2009) Charge-transfer excitons at organic semiconductor surfaces and interfaces. *Acc. Chem. Res.*, **42**, 1779.
36 Deibel, C., Strobel, T., and Dyakonov, V. (2010) Role of the charge transfer state in organic donor–acceptor solar cells. *Adv. Mater.*, **22**, 4097.
37 Onsager, L. (1938) Initial recombination of ions. *Phys. Rev.*, **54**, 554.
38 Braun, C.L. (1984) Electric field assisted dissociation of charge transfer states as a mechanism of photocarrier production. *J. Chem. Phys.*, **80**, 4157.
39 Langevin, P. (1903) Recombinaison et mobilites des ions dans les gaz. *Ann. Chim. Phys.*, **28**, 433.
40 Pope, M. and Swenberg, C.E. (1999) *Electronic Processes in Organic Crystals and Polymers*, 2nd edn., Oxford University Press, USA.
41 Onsager, L. (1934) Deviations from Ohm's law in weak electrolytes. *J. Chem. Phys.*, **2**, 599.
42 Burshtein, A.I. (2004) Non-Markovian theories of transfer reactions in luminescence and chemiluminescence and photo- and electrochemistry. *Adv. Chem. Phys.*, **129**, 105.
43 Wojcik, M. and Tachiya, M. (2009) Accuracies of the empirical theories of the escape probability based on eigen model and Braun model compared with the exact extension of Onsager theory. *J. Chem. Phys.*, **130**, 104107.
44 Kern, J., Schwab, S., Deibel, C., and Dyakonov, V. (2011) Binding energy of singlet excitons and charge transfer complexes in MDMO-PPV:PCBM solar cells. *Phys. Stat. Sol.* **5**, 364 (RRL).
45 Gélinas, S., Paré-Labrosse, O., Brosseau, C.N., Albert-Seifried, S., McNeill, C.R., Kirov, K.R., Howard, I.A., Leonelli, R., Friend, R.H., and Silva, C. (2011) The binding energy of charge-transfer excitons localized at polymeric semiconductor heterojunctions. *J. Phys. Chem. C*, **115**, 7114.
46 Limpinsel, M., Wagenpfahl, A., Mingebach, M., Deibel, C., and Dyakonov, V. (2010) Photocurrent in bulk heterojunction solar cells. *Phys. Rev. B*, **81**, 085203.
47 Street, R.A., Cowan, S., and Heeger, A.J. (2010) Experimental test for geminate recombination applied to organic solar cells. *Phys. Rev. B*, **82**, 121301(R).
48 Kniepert, J., Schubert, M., Blakesley, J.C., and Neher, D. (2011) Photogeneration and recombination in P3HT/PCBM solar cells probed by time-delayed collection field experiments. *J. Phys. Chem. Lett.*, **2**, 700.
49 MacKenzie, R.C.I., Kirchartz, T., Dibb, G. F.A., and Nelson, J. (2011) Modeling nongeminate recombination in P3HT: PCBM solar cells. *J. Phys. Chem. C*, **115**, 9806.
50 Mihailetchi, V.D., Koster, L.J.A., Blom, P. W.M., Melzer, C., de Boer, B., van Duren, J.K.J., and Janssen, R.A.J. (2005) Compositional dependence of the performance of poly(*p*)-phenylene vinylene):methanofullerene bulk-heterojunction solar cells. *Adv. Funct. Mater.*, **15**, 795.
51 Veldman, D., Ipek, Ö., Meskers, S.C.J., Sweelssen, J., Koetse, M.M., Veenstra, S. C., Kron, J.M., van Bavel, S.S., Loos, J., and Janssen, R.A.J. (2008) Compositional and electric field dependence of the dissociation of charge transfer excitons in alternating polyfluorene copolymer/fullerene blends. *J. Am. Chem. Soc.*, **130**, 7721.

52 De, S., Pascher, T., Maiti, M., Jespersen, K.G., Kesti, T., Zhang, F., Yartsev, O.I.A., and Sundström, V. (2007) Geminate charge recombination in alternating polyfluorene copolymer/fullerene blends. *J. Am. Chem. Soc.*, **129**, 8466.

53 Deibel, C., Strobel, T., and Dyakonov, V. (2009) Origin of the efficient polaron pair dissociation in polymer–fullerene blends. *Phys. Rev. Lett.*, **103**, 036402.

54 Campoy-Quiles, M., Ferenczi, T.A.M., Agostinelli, T., Etchegoin, P.G., Kim, Y., Anthopoulos, T.D., Stavrinou, P.N., Bradley, D.D.C., and Nelson, J. (2008) Morphology evolution via self-organization and lateral and vertical diffusion in polymer:fullerene solar cell blends. *Nat. Mater.*, **7**, 158.

55 Bull, T.A., Pingree, L.S.C., Jenekhe, S.A., Ginger, D.S., and Luscombe, C.K. (2009) The role of mesoscopic PCBM crystallites in solvent vapor annealed copolymer solar cells. *ACS Nano*, **3**, 627.

56 Hoofman, R.J.O.M., de Haas, M.P., Siebbeles, L., and Warman, J.M. (1998) Highly mobile electrons and holes on isolated chains of the semiconducting polymer poly(phenylenevinylene). *Nature*, **392**, 54.

57 Grzegorczyk, W.J., Savenije, T.J., Dykstra, T.E., Piris, J., Schins, J.M., and Siebbeles, L.D. (2010) Temperature-independent charge carrier photogeneration in P3HT–PCBM blends with different morphology. *J. Phys. Chem. C*, **114**, 5182.

58 Köhler, A., dos Santos, D.A., Beljonne, D., Shuai, Z., Brédas, J.L., Holmes, A.B., Kraus, A., Müllen, K., and Friend, R.H. (1998) Charge separation in localized and delocalized electronic states in polymeric semiconductors. *Nature*, **392**, 903.

59 Guo, J., Ohkita, H., Benten, H., and Ito, S. (2010) Charge generation and recombination dynamics in poly(3-hexylthiophene)/fullerene blend films with different regioregularities and morphologies. *J. Am. Chem. Soc.*, **132**, 6154.

60 Lee, J., Vandewal, K., Yost, S.R., Bahlke, M.E., Goris, L., Baldo, M.A., Manca, J.V., and Voorhis, T.V. (2010) Charge transfer state versus hot exciton dissociation in polymer–fullerene blended solar cells. *J. Am. Chem. Soc.*, **132**, 11878.

61 Ohkita, H., Cook, S., Astuti, Y., Duffy, W., Tierney, S., Zhang, W., Heeney, M., McCulloch, I., Nelson, J., Bradley, D.D. C., and Durrant, J.R. (2008) Charge carrier formation in polythiophene/fullerene blend films studied by transient absorption spectroscopy. *J. Am. Chem. Soc.*, **130**, 3030.

62 Shoaee, S., Clarke, T.M., Huang, C., Barlow, S., Marder, S.R., Heeney, M., McCulloch, I., and Durrant, J.R. (2010) Acceptor energy level control of charge photogeneration in organic donor/acceptor blends. *J. Am. Chem. Soc.*, **132**, 12919.

63 Clarke, T.M., Ballantyne, A., Shoaee, S., Soon, Y.W., Duffy, W., Heeney, M., McCulloch, I., Nelson, J., and Durrant, J.R. (2010) Analysis of charge photogeneration as a key determinant of photocurrent density in polymer: fullerene solar cells. *Adv. Mater.*, **22**, 5287.

64 Liedtke, M., Sperlich, A., Kraus, H., Baumann, A., Deibel, C., Wirix, M., Loos, J., Cardona, C., and Dyakonov, V. (2011) Triplet exciton generation in bulk-heterojunction solar cells based on endohedral fullerenes. *J. Am. Chem. Soc.*, **133**, 9088.

65 Jarzab, D., Cordella, F., Lenes, M., Kooistra, F.B., Blom, P.W.M., Hummelen, J.C., and Loi, M.A. (2009) Charge transfer dynamics in polymer–fullerene blends for efficient solar cells. *J. Phys. Chem. B*, **113**, 16513.

66 Osikowicz, W., de Jong, M.P., and Salaneck, W.R. (2007) Formation of the interfacial dipole at organic–organic interfaces: C_{60}/polymer interfaces. *Adv. Mater.*, **19**, 4213.

67 Arkhipov, V.I., Heremans, P., and Bässler, H. (2003) Why is exciton dissociation so efficient at the interface between a conjugated polymer and an electron acceptor? *Appl. Phys. Lett.*, **82** (25), 4605–4607.

68 Wiemer, M., Nenashev, A.V., Jansson, F., and Baranovskii, S.D. (2011) On the efficiency of exciton dissociation at the

interface between a conjugated polymer and an electron acceptor. *Appl. Phys. Lett.*, **99**, 013302.

69 Verlaak, S., Beljonne, D., Cheyns, D., Rolin, C., Linares, M., Castet, F., Cornil, J., and Heremans, P. (2009) Electronic structure and geminate pair energetics at organic–organic interfaces: the case of pentacene/C_{60} heterojunctions. *Adv. Funct. Mater.*, **19**, 3809.

70 Linares, M., Beljonne, D., Cornil, J., Lancaster, K., Brédas, J.L., Verlaak, S., Mityashin, A., Heremans, P., Fuchs, A., Lennartz, C., Ide, J., Mereau, R.L., Aurel, P., Ducasse, L., and Castet, F. (2010) On the interface dipole at the pentacene–fullerene heterojunction: a theoretical study. *J. Phys. Chem. C*, **114**, 3215.

71 Pensack, R.D. and Asbury, J.B. (2009) Barrierless free carrier formation in an organic photovoltaic material measured with ultrafast vibrational spectroscopy. *J. Am. Chem. Soc.*, **131**, 15986.

72 Anderson, P.W. (1958) Absence of diffusion in certain random lattices. *Phys. Rev.*, **109**, 1492.

73 Heeger, A.J., Kivelson, S., Schrieffer, J.R., and Su, W.P. (1988) Solitons in conducting polymers. *Rev. Mod. Phys.*, **60**, 781–850.

74 Bässler, H. (1993) Charge transport in disordered organic photoconductors: a Monte Carlo simulation study. *Phys. Stat. Sol. B*, **175**, 15.

75 Baranovskii, S.D., Cordes, H., Hensel, F., and Leising, G. (2000) Charge-carrier transport in disordered organic solids. *Phys. Rev. B*, **62**, 7934.

76 Baranovski, S. (ed.) (2006) *Charge Transport in Disordered Solids with Applications in Electronics*, John Wiley & Sons, Inc.

77 Mott, N.F. (1956) On the transition to metallic conduction in semiconductors. *Can. J. Phys.*, **34**, 1356.

78 Conwell, E.M. (1956) Impurity band conduction in germanium and silicon. *Phys. Rev.*, **103** (1), 51.

79 Miller, A. and Abrahams, E. (1960) Impurity conduction at low concentrations. *Phys. Rev.*, **120**, 745.

80 Schönherr, G., Eiermann, R., Bässler, H., and Silver, M. (1980) Dispersive exciton transport in a hopping system with Gaussian energy distribution. *Chem. Phys.*, **52**, 287.

81 Offermans, T., van Hal, P.A., Meskers, S. C.J., Koetse, M.M., and Janssen, R.A.J. (2005) Exciplex dynamics in a blend of μ-conjugated polymers with electron donating and accepting properties: MDMO-PPV and PCNEPV. *Phys. Rev. B*, **72** (4), 045213.

82 Pasveer, W.F., Cottaar, J., Tanase, C., Coehoorn, R., Bobbert, P.A., Blom, P.W. M., de Leeuw, D.M., and Michels, M.A.J. (2005) Unified description of charge-carrier mobilities in disordered semiconducting polymers. *Phys. Rev. Lett.*, **94**, 206601.

83 Houili, H., Tutis, E., Batistic, I., and Zuppiroli, L. (2006) Investigation of the charge transport through disordered organic molecular heterojunctions. *J. Appl. Phys.*, **100**, 033702.

84 Kirkpatrick, J., Marcon, V., Nelson, J., Kremer, K., and Andrienko, D. (2007) Charge mobility of discotic mesophases: a multiscale quantum and classical study. *Phys. Rev. Lett.*, **98**, 227402.

85 Strobel, T., Deibel, C., and Dyakonov, V. (2010) Role of polaron pair diffusion and surface losses in organic semiconductor devices. *Phys. Rev. Lett.*, **105**, 266602.

86 Arkhipov, V.I., Emelianova, E.V., and Adriaenssens, G.J. (2001) Effective transport energy versus the energy of most probable jumps in disordered hopping systems. *Phys. Rev. B*, **64**, 125125.

87 Monroe, D. (1985) Hopping in exponential band tails. *Phys. Rev. Lett.*, **54**, 146.

88 Marshall, J.M. (1983) Carrier diffusion in amorphous semiconductors. *Rep. Prog. Phys.*, **46**, 1235.

89 Chesterfield, R.J., McKeen, J.C., Newman, C.R., Ewbank, P.C., da Silva Filho, D.A., Bredas, J.L., Miller, L.L., Mann, K.R., and Frisbie, C.D. (2004) Organic thin film transistors based on *N*-alkyl perylene diimides: charge transport kinetics as a function of gate voltage and temperature. *J. Phys. Chem. B*, **108**, 19281.

90 Gill, W.D. (1972) Drift mobilities in amorphous charge-transfer complexes of trinitrofluorenone and poly-*n*-vinylcarbozole. *J. Appl. Phys.*, **43**, 5033.

91 Tessler, N., Preezant, Y., Rappaport, N., and Roichman, Y. (2009) Charge transport in disordered organic materials and its relevance to thin-film devices: a tutorial review. *Adv. Mater.*, **21**, 2741.

92 Tanase, C., Meijer, E.J., Blom, P.W.M., and de Leeuw, D.M. (2003) Unification of the hole transport in polymeric field-effect transistors and light-emitting diodes. *Phys. Rev. Lett.*, **91**, 216601.

93 Baranovskii, S.D., Rubel, O., and Thomas, P. (2006) On the concentration and field dependences of the hopping mobility in disordered organic solids. *J. Non-Cryst. Sol.*, **352**, 1644.

94 Huijser, A., Savenije, T.J., Kroeze, J.E., and Siebbeles, L.D.A. (2005) Exciton diffusion and interfacial charge separation in meso-tetraphenylporphyrin/TiO_2 bilayers: effect of ethyl substituents. *J. Phys. Chem. B*, **109**, 20166.

95 Devižis, A., Serbenta, A., Meerholz, K., Hertel, D., and Gulbinas, V. (2009) Ultrafast dynamics of carrier mobility in a conjugated polymer probed at molecular and microscopic length scales. *Phys. Rev. Lett.*, **103**, 027404.

96 Savenije, T.J., Murthy, D.H.K., Gunz, M., Gorenflot, J., Siebbeles, L.D.A., Dyakonov, V., and Deibel, C. (2011) Absence of post-nanosecond charge carrier relaxation in poly(3-hexyl-thiophene): fullerene blends. *J. Phys. Chem. Lett.*, **2**, 1368.

97 Scher, H. and Montroll, E.W. (1975) Anomalous transit-time dispersion in amorphous solids. *Phys. Rev. B*, **12**, 2455.

98 Borsenberger, P.M., Pautmeier, L.T., and Bässler, H. (1992) Nondispersive-to-dispersive charge-transport transition in disordered molecular solids. *Phys. Rev. B*, **46**, 12145.

99 Mozer, A.J. and Sariciftci, N.S. (2004) Negative electric field dependence of charge carrier drift mobility in conjugated, semiconducting polymers. *Chem. Phys. Lett.*, **389**, 438.

100 Choulis, S.A., Kim, Y., Nelson, J., Bradley, D.D.C., Giles, M., Shkunov, M., and McCulloch, I. (2004) High ambipolar and balanced carrier mobility in regioregular poly(3-hexylthiophene). *Appl. Phys. Lett.*, **85**, 3890.

101 Mozer, A.J., Sariciftci, N.S., Pivrikas, A., Österbacka, R., Juška, G.G., Brassat, L., and Bässler, H. (2005) Charge carrier mobility in regioregular poly(3-hexylthiophene) probed by transient conductivity techniques: a comparative study. *Phys. Rev. B*, **71**, 035214.

102 Tuladhar, S.M., Poplavskyy, D., Choulis, S.A., Durrant, J.R., Bradley, D.D.C., and Nelson, J. (2005) Ambipolar charge transport in films of methanofullerene and poly(polyphenylenevinylene)/methanofullerene blends. *Adv. Funct. Mater.*, **15**, 1171.

103 Baumann, A., Lorrmann, J., Deibel, C., and Dyakonov, V. (2008) Bipolar charge transport in poly(3-hexyl thiophene)/methanofullerene blends: a ratio dependent study. *Appl. Phys. Lett.*, **93**, 252104.

104 Mayer, A.C., Toney, M.F., Scully, S.R., Rivnay, J., Brabec, C.J., Scharber, M., Koppe, M., Heeney, M., McCulloch, I., and McGehee, M.D. (2009) Bimolecular crystals of fullerenes in conjugated polymers and the implications of molecular mixing for solar cells. *Adv. Funct. Mater.*, **19**, 1173.

105 Cates, N.C., Gysel, R., Beiley, Z., Miller, C.E., Toney, M.F., Heeney, M., McCulloch, I., and McGehee, M.D. (2009) Tuning the properties of polymer bulk heterojunction solar cells by adjusting fullerene size to control intercalation. *Nano Lett.*, **9**, 4153.

106 Baumann, A., Savenije, T.J., Murthy, D. H.K., Heeney, M., Dyakonov, V., and Deibel, C. (2011) Influence of phase segregation on the recombination dynamics in organic bulk heterojunction solar cells. *Adv. Funct. Mater.*, **21**, 1687.

107 van Bavel, S.S., Sourty, E., de With, G., and Loos, J. (2009) Three-dimensional nanoscale organization of bulk heterojunction polymer solar cells. *Nano Lett.*, **9**, 507.

108 van Bavel, S.S., Bärenklau, M., de With, G., Hoppe, H., and Loos, J. (2010) P3HT/PCBM bulk heterojunction solar cells: impact of blend composition and 3D morphology on device performance. *Adv. Mater.*, **20**, 1458.

109 Chua, L.L., Zaumseil, J., Chang, J.F., Ou, E.C.W., Ho, P.K.H., Sirringhaus, H., and Friend, R.H. (2005) General observation of n-type field-effect behaviour in organic semiconductors. *Nature*, **434**, 194.

110 Juška, G., Arlauskas, K., Viliūnas, M., and Kočka, J. (2000) Extraction current transients: new method of study of charge transport in microcrystalline silicon. *Phys. Rev. Lett.*, **84**, 4946.

111 Deibel, C., Baumann, A., and Dyakonov, V. (2008) Polaron recombination in pristine and annealed bulk heterojunction solar cells. *Appl. Phys. Lett.*, **93**, 163303.

112 Pivrikas, A., Sariciftci, N.S., Juška, G., and Österbacka, R. (2007) A review of charge transport and recombination in polymer/fullerene organic solar cells. *Prog. Photovolt. Res. Appl.*, **15**, 677.

113 Pivrikas, A., Juška, G., Mozer, A.J., Scharber, M., Arlauskas, K., Sariciftci, N. S., Stubb, H., and Österbacka, R. (2005) Bimolecular recombination coefficient as a sensitive testing parameter for low-mobility solar-cell materials. *Phys. Rev. Lett.*, **94**, 176806.

114 Soci, C., Moses, D., and Heeger, A.J. (2005) Effects of bimolecular recombination and charge-trapping on the transient photoconductivity of poly (*p*-phenylene vinylene). *Synth. Met.*, **153**, 145.

115 Shuttle, C.G., O'Regan, B., Ballantyne, A. M., Nelson, J., Bradley, D.D.C., and Durrant, J.R. (2008) Bimolecular recombination losses in polythiophene: fullerene solar cells. *Phys. Rev. B*, **78**, 113201.

116 Juška, G., Arlauskas, K., Stuchlik, J., and Osterbacka, R. (2006) Non-Langevin bimolecular recombination in low-mobility materials. *J. Non-Cryst. Sol.*, **352**, 1167.

117 Pivrikas, A., Österbacka, R., Juška, G., Arlauskas, K., and Stubb, H. (2005) Time-dependent Langevin-type bimolecular charge carrier recombination in regiorandom poly(3-hexylthiophene). *Synth. Met.*, **155**, 242.

118 Adriaenssens, G.J. and Arkhipov, V.I. (1997) Non-Langevin recombination in disordered materials with random potential distributions. *Sol. State Commun.*, **103**, 541.

119 Kirchartz, T., Pieters, B.E., Kirkpatrick, J., Rau, U., and Nelson, J. (2011) Recombination via tail states in polythiophene:fullerene solar cells. *Phys. Rev. B*, **83**, 115209.

120 Nelson, J. (2003) Diffusion-limited recombination in polymer–fullerene blends and its influence on photocurrent collection. *Phys. Rev. B*, **67**, 155209.

121 Clarke, T.M., Jamieson, F.C., and Durrant, J.R. (2009) Transient absorption studies of bimolecular recombination dynamics in polythiophene/fullerene blend films. *J. Phys. Chem. C*, **113**, 20934.

122 Mozer, A.J., Sariciftci, N.S., Lutsen, L., Vanderzande, D., Österbacka, R., and Westerling, M., and Juška, G. (2005) Charge transport and recombination in bulk heterojunction solar cells studied by the photoinduced charge extraction in linearly increasing voltage technique. *Appl. Phys. Lett.*, **86**, 112104.

123 Foertig, A., Baumann, A., Rauh, D., Dyakonov, V., and Deibel, C. (2009) Charge carrier concentration and temperature dependent recombination in polymer–fullerene solar cells. *Appl. Phys. Lett.*, **95**, 052104.

124 Shuttle, C.G., Hamilton, R., Nelson, J., O'Regan, B.C., and Durrant, J.R. (2010) Measurement of charge-density dependence of carrier mobility in an organic semiconductor blend. *Adv. Funct. Mater.*, **20**, 698.

125 Blom, P.W.M., Mihailetchi, V.D., Koster, L.J.A., and Markov, D.E. (2007) Device physics of polymer:fullerene bulk heterojunction solar cells. *Adv. Mater.*, **19**, 1551.

126 Koster, L.J.A., Mihaletchi, V.D., and Blom, P.W.M. (2006) Bimolecular recombination in polymer/fullerene bulk heterojunction solar cells. *Appl. Phys. Lett.*, **88**, 052104.

127 Chu, C.W., Yang, H., Hou, W.J., Huang, J., Li, G., and Yang, Y. (2008) Control of the nanoscale crystallinity and phase separation in polymer solar cells. *Appl. Phys. Lett.*, **92**, 103306.

128 Joannopoulos, J.D. and Lucovsky, G. (eds) (1983) *The Physics of Hydrogenated Amorphous Silicon II*, Springer.

129 Dylla, T., Finger, F., and Schiff, E.A. (2004) Hole drift-mobility measurements and mulitple-trapping in microcrystalline silicon. *Mat. Res. Soc. Symp. Proc.*, **808**, A8.101.

130 Emelianova, E.V., Brinza, M., Arkhipov, V.I., and Adriaenssens, G.J. (2005) Study of a-Si:H tail state distributions through analytical multiple trapping modelling. *J. Optoelectron. Adv. Mater.*, **7**, 951–954.

131 Cowan, S.R., Leong, W.L., Banerji, N., Dennler, G., and Heeger, A.J. (2011) Identifying a Threshold Impurity Level for Organic Solar Cells: Enhanced First-Order Recombination Via Well-Defined PC84BM Traps in Organic Bulk Heterojunction Solar Cells, *Adv. Func. Mat.* **21**, 3083.

132 Brabec, C.J., Cravino, A., Meissner, D., Sariciftci, N.S., Fromherz, T., Rispens, M.T., Sanchez, L., and Hummelen, J.C. (2001) Origin of the open circuit voltage of plastic solar cells. *Adv. Funct. Mater.*, **11**, 374.

133 Vandewal, K., Tvingstedt, K., Gadisa, A., Inganäs, O., and Manca, J.V. (2009) On the origin of the open-circuit voltage of polymer–fullerene solar cells. *Nat. Mater.*, **8**, 904.

134 Koster, L.J.A., Mihailetchi, V.D., Ramaker, R., and Blom, P.W.M. (2005) Light intensity dependence of open-circuit voltage of polymer:fullerene solar cells. *Appl. Phys. Lett.*, **86, 123**, 509.

135 Cheyns, D., Poortmans, J., Heremans, P., Deibel, C., Verlaak, S., Rand, B.P., and Genoe, J. (2008) Analytical model for the open-circuit voltage and its associated resistance in organic planar heterojunction solar cells. *Phys. Rev. B*, **77**, 165332.

136 Blakesley, J. C. and Neher D. (2011) Relationship between energetic disorder and open-circuit voltage in bulk heterojunction solar cells, *Phys. Rev. B*, **84**, 075210.

137 Rauh, D., Wagenpfahl, A., Deibel, C., and Dyakonov, V. (2011) Relation of open circuit voltage to charge carrier density in organic bulk heterojunction solar cells. *Appl. Phys. Lett.*, **98**, 133301.

138 Mihailetchi, V.D., Blom, P.W.M., Hummelen, J.C., and Rispens, M.T. (2003) Cathode dependence of the open-circuit voltage of polymer:fullerene bulk heterojunction solar cells. *J. Appl. Phys.*, **94**, 6849.

139 Maurano, A., Hamilton, R., Shuttle, C. G., Ballantyne, A.M., Nelson, J., O'Regan, B., Zhang, W., McCulloch, I., Azimi, H., Morana, M., Brabec, C.J., and Durrant, J.R. (2010) Recombination dynamics as a key determinant of open circuit voltage in organic bulk heterojunction solar cells: a comparison of four different donor polymers. *Adv. Mater.*, **22**, 4987.

140 Vandewal, K., Tvingstedt, K., Gadisa, A., Inganäs, O., and Manca, J.V. (2010) Relating the open-circuit voltage to interface molecular properties of donor: acceptor bulk heterojunction solar cells. *Phys. Rev. B*, **81, 125**, 204.

141 Scott, J.C. and Malliaras, G.G. (1999) Charge injection and recombination at the metal-organic interface. *Chem. Phys. Lett.*, **299**, 115.

142 Wagenpfahl, A., Rauh, D., Binder, M., Deibel, C., and Dyakonov, V. (2010) S-shaped current–voltage characteristics of organic solar devices. *Phys. Rev. B*, **82, 115**, 306.

143 Wagenpfahl, A., Deibel, C., and Dyakonov, V. (2010) Organic solar cell efficiencies under the aspect of reduced surface recombination velocities. *IEEE J. Sel. Top. Quantum Electron.*, **16**, 1759.

18
Light-Emitting Organic Crystal Field-Effect Transistors for Future Organic Injection Lasers

Hajime Nakanotani and Chihaya Adachi

18.1
Introduction

Organic semiconductor-based light-emitting devices such as organic light-emitting diodes (OLEDs) and light-emitting organic field-effect transistors (LE-OFETs) have demonstrated the tremendous potential of organic semiconducting materials. In OLEDs, a maximum external quantum efficiency (η_{ext}) of 20%, corresponding to an internal quantum efficiency (η_{int}) of nearly 100%, has been achieved through the use of phosphorescent emissive materials such as Ir complexes [1, 2]. However, unipolar, ambipolar, or static induction transistor-type LE-OFETs have been produced by careful selection of organic semiconductors and optimization of device fabrication procedures [3]. Although light-emitting organic semiconductors possess excellent light amplification characteristics [4–7] and existing OLEDs and LE-OFETs exhibit exceptional light-emitting performance, challenges still remain in the field of organic light-emitting devices such as the development of organic injection lasers.

To realize an organic injection laser, the principal requirements are (i) injection and transport of very high current density in organic semiconductors, (ii) suppression of exciton annihilation, and (iii) minimization of waveguide loss by the electrodes. Previous results and problems preventing the realization of organic injection lasers include the following:

i) Injection and transport of a high current density of greater than a few hundred A/cm^2 has been achieved in not only small molecule-based OLEDs [8] but also polymer-based [9] OLEDs using short-pulse excitation combined with high thermal conductivity from a silicon substrate or configuration with a small active area. However, the principal limitation for injection and transport of current in many OLEDs arises from the use of amorphous organic semiconductors, which possess low carrier mobilities (10^{-5}–10^{-3} cm^2/(V s)). Organic semiconductors with high carrier mobilities, such as polycrystalline materials, could be used to overcome this problem. However, these materials produce

Physics of Organic Semiconductors, Second Edition. Edited by Wolfgang Brütting and Chihaya Adachi

films with rough, nonuniform morphology, making them inappropriate for OLED fabrication.

ii) Efficient carrier recombination and confinement of the recombination zone have been realized at the organic/organic interface in OLEDs by layering of p-type and n-type organic semiconductors. In fact, complete carrier recombination, that is, carrier balance (γ) of almost unity, can be achieved by optimization of device structure as evidenced by the realization of the theoretical limit of η_{ext} of 20%. However, a significant decrease of η_{ext} is typically observed at high current density ($J > 1\,A/cm^2$) in OLEDs because of the formation of high exciton and carrier densities at the organic/organic interface. The decreased η_{ext} of the OLED can be explained by the exciton–exciton annihilation model [10–12]. Furthermore, we also observed a significant decrease in the η_{ext} of laser dye-based OLEDs and concluded that the major exciton annihilation process in such OLEDs was exciton–polaron annihilation [11, 13]. Because the trapped or accumulated charge carriers in OLEDs significantly affect the exciton annihilation process, carrier trapping states created by dopant or impurity molecules and organic/organic interfaces should be removed. Furthermore, γ depends on the driving voltage because carrier mobilities of organic semiconductors in OLEDs depend on the electric field.

iii) To avoid waveguide loss by the electrodes and introduce optical resonators, a transparent OLED containing an optical resonator needs to be developed. Oscillation of the amplified spontaneous emission (ASE) under optical excitation from an OLED containing transparent electrodes such as indium tin oxide (ITO) or aluminum-doped zinc oxide (AZO) has been demonstrated [14–18]. In particular, Görrn *et al.* [17] demonstrated that the oscillation of ASE arose from the planar waveguide structure of the OLED of bottom AZO electrode/BN-PFO: MEH-PPV (5 wt%)/top AZO electrode without increasing the ASE threshold. However, because the distances between the electrodes and recombination zone are very small (typically less than 100 nm) in such a configuration, a thick carrier transport layer is required to avoid waveguide loss. This helps to prevent propagation loss of light from the electrodes even when a transparent electrode such as ITO is used. However, a thick carrier transport layer increases the driving voltage because of the low carrier mobilities of amorphous organic semiconductors, which results in a decrease in the current density.

From these results, it is considered that the configurations of OLEDs used to date have not been suitable to produce an organic injection laser. The development of a novel architecture is a requisite for the study of carrier transport and injection mechanisms in organic semiconductors, exciton decay under high electrical excitation to avoid exciton annihilation, and material design for low lasing threshold. One possible solution is the realization of highly efficient ambipolar LE-OFETs with high carrier mobilities. The structure of an ambipolar LE-OFET is compared with that of an OLED for the production of an organic injection laser in Figure 18.1. Ambipolar LE-OFETs possess numerous attractive characteristics, including

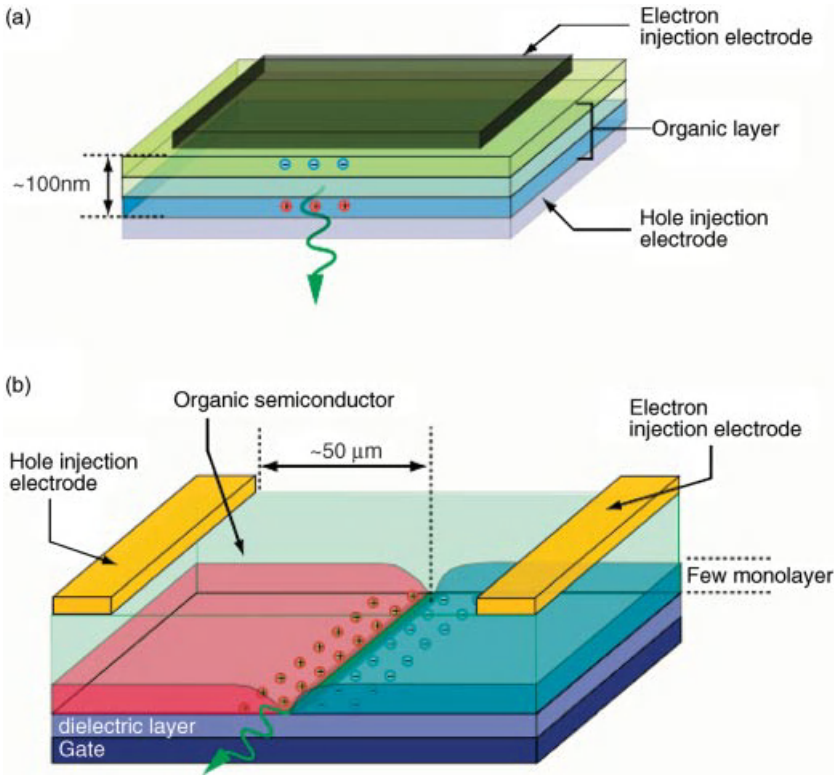

Figure 18.1 Comparison of the structures of an (a) OLED and (b) ambipolar light-emitting transistor.

injection of a very high current density into the organic layer because of a very thin carrier accumulation layer [19], efficient carrier recombination in a single-component organic layer lacking an organic/organic interface, and equal carrier injection with balanced hole and electron transport through careful molecular design. Furthermore, the unique lateral arrangement of electrodes in a LE-OFET configuration provides various options for optical confinement such as distributed-feedback (DFB) and distributed Bragg reflector optical resonators placed on the recombination zone a few micrometers from the electrodes. This allows the propagation loss of light from the metal electrodes to be minimized. In particular, Gwinner *et al.* [20] have demonstrated lasing oscillation from a polymer-based LE-OFET with Ta_2O_5-based rib waveguide DFB feedback resonator under optical excitation. Emission spectra from this LE-OFET containing a rib waveguide DFB feedback resonator are shown in Figure 18.2. Lasing emission was clearly observed at the long-wavelength edge of the Bragg dip without an increase in the ASE threshold compared to that of the sample without a metal electrode, again indicating the strong availability of the LE-OFET structure. Consequently, ambipolar LE-OFETs are a promising structure for organic injection laser.

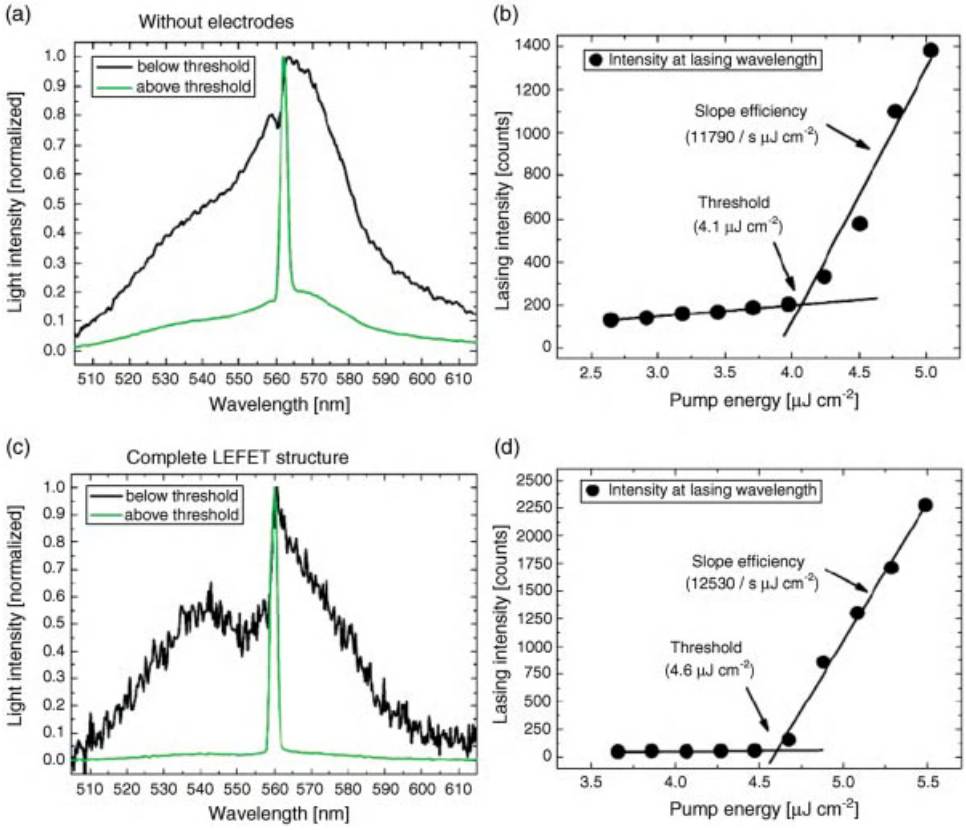

Figure 18.2 The lasing characteristics of a polymer-based LE-OFET containing a rib waveguide DFB feedback resonator. Emission spectra from samples (a) without and (c) with a metal electrode below and above the lasing threshold. Dependence of the emission intensity of samples (b) without and (d) with a metal electrode on excitation power. From Ref. [20].

Light-emitting polymers such as polyphenylene vinylene (PPV) or polyfluorene derivatives are potential candidates for an active gain medium for solid-state organic lasers [21–24]. Light-emitting polymer-based ambipolar LE-OFETs show excellent ambipolar carrier transport characteristics and high η_{ext} because of the high photoluminescence quantum efficiency (Φ_{PL}) of light-emitting polymers [25–30]. Naber *et al.* [30] demonstrated an efficient ambipolar LE-OFET based on poly(9,9-di-*n*-octylfluorene-*alt*-benzothiadiazole) with a high η_{ext} of 0.75% using poly(vinylidene fluoride-trifluoroethylene) as high-k dielectric materials. This structure enabled both high electron and hole mobilities of up to $10^{-2}\,cm^2/(V\,s)$. However, the field-effect mobilities are slightly lower than those of organic single-crystal semiconductors.

Because molecular orientation is completely organized in the bulk of a single crystal without grain boundaries, organic single crystal-based ambipolar LE-OFETs

make an interesting research object for fundamental studies of not only charge-carrier transport processes but also carrier recombination processes in organic semiconductor devices. In 2007, electroluminescence (EL) from a tetracene single crystal-based ambipolar LE-OFET with high electron ($0.037\,cm^2/(V\,s)$) and hole ($0.16\,cm^2/(V\,s)$) mobilities was reported [31]. Furthermore, the injection and transport of an extremely high current density was demonstrated in a transistor channel using organic single crystals of tetracene or rubrene, according to their high field-effect mobilities of $>10^{-1}\,cm^2/(V\,s)$ [32]. In addition, surprisingly, the rubrene and tetracene single crystal-based ambipolar LE-OFETs exhibited stable η_{ext} at high current, as shown in Figure 18.3. These results suggest that γ is perfectly balanced and exciton quenching processes such as exciton–polaron interaction are absent in ambipolar LE-OFETs. However, from the point of view of light-emitting devices, it is difficult to obtain both high carrier mobilities and high Φ_{PL} in organic semiconductors. In fact, although the maximum saturation mobilities of the OFETs were increased to around $10\,cm^2/(V\,s)$ [33], which is significantly higher than that of a *a*-Si:H-based FET, a considerable reduction in Φ_{PL} was generally observed using organic single crystals such as rubrene because of the significant concentration quenching caused by strong intermolecular interactions. Few ambipolar LE-OFETs based on organic single crystals with both high ambipolar mobilities and high Φ_{PL} have been produced to date [34–38].

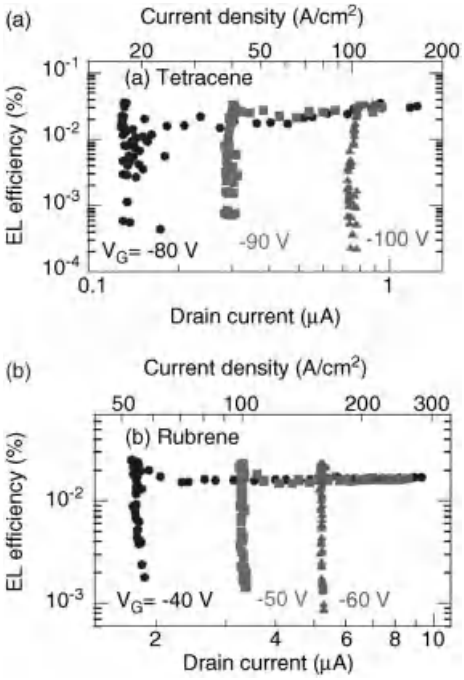

Figure 18.3 Dependence of EL efficiency on drain current in tetracene (a) and rubrene (b) single crystal-based ambipolar LE-OFETs. From Ref. [32].

In Sections 18.2 and 18.3, we will describe our recent results regarding the photoluminescence characteristics of ambipolar LE-OFETs based on oligo(*p*-phenylenevinylene) (OPV) derivatives with the aim of achieving high EL efficiency and constructing organic injection lasers. We especially focused on controlling the energy barriers between metal/organic and oxide/organic interfaces to understand the mechanism of ambipolar FET operation. The importance of energy level alignment for ambipolar operation will be demonstrated. Bright ambipolar LE-OFETs based on organic single crystals with high ambipolar mobilities ($>10^{-1}\,cm^2/(V\,s)$) and intense EL were realized. We believe that our results allow the fundamental carrier transport properties and EL characteristics of organic semiconductors to be understood, making progress toward the realization of high-performance organic light-emitting devices.

18.2
Highly Photoluminescent Oligo(*p*-phenylenevinylene) Derivatives

To achieve highly efficient ambipolar LE-OFETs, it is essential to obtain compatible ambipolar characteristics with both high Φ_{PL} and high carrier mobilities. The Φ_{PL} values of vapor-deposited or polymer films are generally rather high compared to those of single crystals because of the weak intermolecular interactions, although the carrier mobilities are vice versa.

OPV derivatives, which are model compounds of PPV-based polymers, have recently been extensively investigated for use not only in OLEDs [39, 40] but also in OFETs [41, 42]. The chemical structures of some OPV derivatives are shown in Figure 18.4a. Table 18.1 and Figure 18.4b summarize the fundamental PL characteristics of single crystals of P3V2, *para*-methyl-substituted P3V2 (CH_3-P3V2), P4V3, and P5V4. In addition, the PL characteristics of previously reported highly luminescent organic single crystals such as thiophene/phenylene co-oligomers are also summarized in Table 18.1 [43, 44]. We observed pure blue PL with an emission peak at $\lambda = 472$ nm, $\Phi_{PL} = 85 \pm 2\%$, and a fluorescent lifetime (τ_{Flu}) of 2.9 ± 0.1 ns from a single crystal of P3V2. For single crystals of CH_3-P3V2, P4V3, and P5V4, a slight redshift of the PL spectrum and minor decrease of Φ_{PL} were observed compared to those of P3V2, because of the increase in the number of phenylenevinylene units. Interestingly, these crystals maintained a high Φ_{PL} of >40%, resulting in these organic single crystals exhibiting slightly higher Φ_{PL} values than those of light-emitting polymers and small molecules. Conversely, relatively low Φ_{PL} values of 54 ± 2, 39 ± 2, 11 ± 3, and $7 \pm 3\%$ were observed for deposited thin films of P3V2, CH_3-P3V2, P4V3, and P5V4, respectively, indicating that exciton quenching processes that occur in the polycrystalline films are significantly suppressed in single crystals of the OPV derivatives.

Although ASE was not observed in deposited thin films of the OPV derivatives, that is, polycrystalline films, we observed that single crystals of all the OPV compounds show lasing activity under optical excitation. A significant increase in the emission intensity and rapid decrease in the full width half maximum (FWHM)

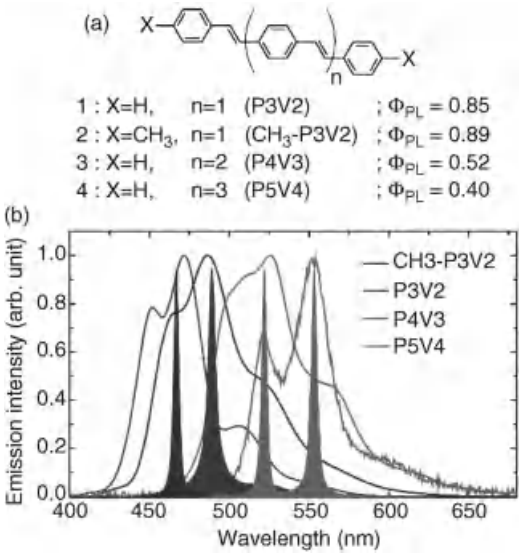

Figure 18.4 (a) Chemical structures of OPV derivatives and corresponding Φ_{PL}. (b) PL and ASE spectra of single crystals of OPV derivatives.

were observed as the excitation intensity was increased, indicating the occurrence of ASE (Figure 18.4b). Kabe *et al*. found that nonradiative deactivation processes were greatly suppressed in the crystalline state compared to that in the polycrystalline state. However, polycrystalline films and single crystals of the OPV derivatives showed nearly identical radiative decay rates (k_r), which relate strongly to the ASE threshold, indicating that the ASE threshold is controlled by not only k_r but also by the surface morphology of the films, which form an optical waveguide

Table 18.1 Photoluminescence characteristics of organic single crystals.

Material	Φ_{PL} (%)	Φ_{PL} (%)[a)]	τ (ns)	ASE threshold (μJ/cm^2)
P3V2[b)]	85 ± 2	54 ± 2	2.9 ± 0.1	18 ± 6
CH_3-P3V2 [43]	89 ± 2	50 ± 2	4.6 ± 0.2	25 ± 5
P4V3[b)]	52 ± 2	11 ± 2	3.0 ± 0.1	11 ± 4
P5V4[b)]	40 ± 2	7 ± 2	2.4 ± 0.1	20 ± 4
AC5[c)] [42]	23 ± 1	N.A.	2.28	21.3
BP3T[c)] [43]	80	NA	NA	8
Tetracene	<1	<1	NA	NA
Rubrene	<1	<1	NA	NA

a) Φ_{PL} of a thin film.
b) The thicknesses of single crystals of P3V2, P4V3, and P5V4 were 690, 480, and 390 nm, respectively.
c) AC5: 1,4-bis(5-phenylthiophen-2-yl)benzene; BP3T: α,ϖ-bis(biphenylyl)terthiophene.

structure [45]. These results indicate that highly luminescent organic single crystals are suitable for use as active gain media in organic injection lasers.

18.3
Ambipolar Light-Emitting Field-Effect Transistors Based on Organic Single Crystals

18.3.1
Ambipolar Carrier Transport Characteristics of Single Crystals of OPV Derivatives

The characteristics of LE-OFETs based on OPV derivatives and previously reported organic single crystals are summarized in Table 18.2. Because it is essential that unwanted electron traps on the gate insulator, such as a SiO_2 surface, are eliminated completely, a 20 nm thick layer of the organic dielectric material poly(methylmethacrylate) (PMMA), which allows the organic semiconductor to show n-type carrier transport [46], was formed on the SiO_2/n^{++}-Si substrate. In addition, these LE-OFETs have an asymmetric gold (work function: WF = −4.5 to −5.1 eV)–calcium (WF = −2.9 to −3.0 eV) contact as source and drain electrodes to reduce both hole and electron injection barriers between the metal electrodes and OPV single crystals.

In all the OPV derivative-based LE-OFETs, both p- and n-type FET operation was clearly observed with EL under applied negative and positive gate voltages (V_G), indicating that the OPV derivatives possess intrinsically bipolar carrier transport characteristics. Conversely, in the P4V3- and P5V4-based LE-OFETs, the electron mobility (μ_e) was one order of magnitude higher (>0.1 $cm^2/(V\,s)$) than those of P3V2 and *p*-CH_3-P3V2-based LE-OFETs and a high hole mobility (μ_h) of >0.1 $cm^2/(V\,s)$ was retained. In the P5V4 single crystal-based LE-OFET, the highest values of μ_h and μ_e were 0.38 and 0.28 $cm^2/(V\,s)$, respectively. μ_e was slightly higher than that of a tetracene-based ambipolar LE-OFET and was comparable to those of rubrene- and pentacene-based ambipolar LE-OFETs [47]. The significant improvement of μ_e was caused by the large reduction in the electron injection barrier

Table 18.2 Ambipolar LE-OFET characteristics of organic single crystals.

Material	Hole mobility (μ_h) ($cm^2/(V\,s)$)	Hole mobility μ_h ($cm^2/(V\,s)$)
P3V2 [37]	0.12	1.3×10^{-2}
CH_3-P3V2 [43]	0.17	0.9×10^{-2}
P4V3 [37]	0.12	0.11
P5V4 [38]	0.38	0.28
BP3T [36]	1.64	0.17
Tetracene [32]	2.3	0.12
Pentacene [47]	0.29	0.35
Rubrene [32]	0.82	0.27

between Ca (WF = 2.9–3.0 eV) and the level of the lowest unoccupied molecular orbital (LUMO) of the single crystal as the energy gap of the OPV derivative was reduced by expanding its conjugation length. Therefore, efficient injection of electrons from a Ca electrode to the LUMO levels of P4V3 and P5V4 resulted in a maximum μ_e of $\sim 0.3\,cm^2/(V\,s)$.

18.3.2
EL Characteristics of LE-OFETs Based on Organic Single Crystals

In ambipolar LE-OFETs, the position of the carrier recombination zone within the transistor channel can be controlled by changing the applied gate and drain voltages [26]. Figure 18.5 shows a top-view photograph of the light emitted from a P5V4-based LE-OFET at a drain–source voltage (V_{DS}) of −100 V and various V_G. No emission was observed at low V_G because electrons are dominant in the channel layer. Conversely, a significant increase in the emission intensity was observed as V_G was increased, indicating simultaneous injection and accumulation of holes in the channel, and a clear linear recombination zone was observed near the source electrode. The recombination zone immediately moved from the source electrode toward the drain electrode as V_G was increased. At $V_G = -27$ V, the recombination zone was almost centered between the source and drain electrodes (Figure 18.5 bottom). At this V_G, a maximum $\eta_{ext} = 0.1\%$ was observed because the hole and electron currents are almost equal. However, despite the fact that the OPV single

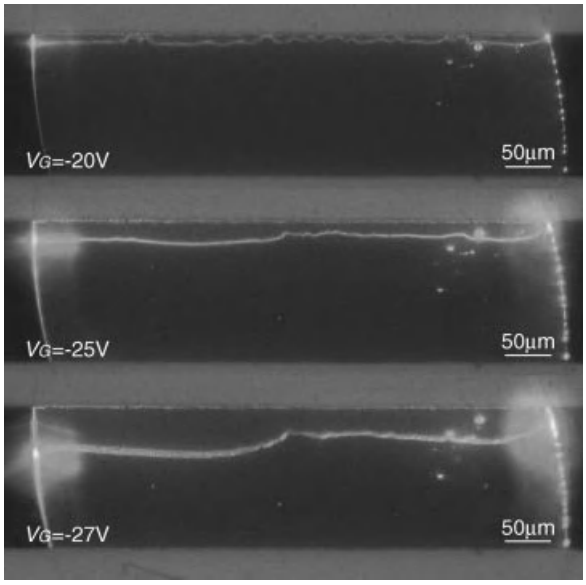

Figure 18.5 Top-view photographs of the light emitted from the channel of a P5V4 single crystal-based LE-OFET obtained under microscope observation at $V_{DS} = -100$ V and $V_G = -20$, −25, and −27 V. From Ref. [38].

crystals show high Φ_{PL} of >40%, the maximum η_{ext} was rather low compared to those of polymer-based ambipolar LE-OFETs.

Here, we discuss the origin of the low η_{ext} observed for the OPV single crystal-based LE-OFETs. η_{ext} is given by $\eta_{ext} = \gamma\eta_r\eta_p\Phi_{PL}$ [48], where γ is the charge balance factor, η_r is the exciton generation efficiency, and η_p is the light outcoupling efficiency. Under ambipolar operating conditions, because the injected holes and electrons should recombine in the channel, γ is almost unity and η_{ext} is controlled by η_r, Φ_{PL}, and η_p. For single crystals of OPV derivatives, η_r is ~25% because of their fluorescent character and Φ_{PL} is 40–90%, depending on the specific compound. Thus, the rather low η_{ext} observed for the OPV single crystal-based LE-OFETs may be because of the significantly low η_p (as discussed below).

In the top-view photographs of light emission (Figure 18.5), the edges of the OPV single crystal showed stronger emission than the surface, indicating that it behaves as an optical slab waveguide. As a result, light is well confined to the bulk of the crystal because of the vertical orientation of the long *c*-axes of OPV molecules, which is evidenced by the fact that OPV single crystals show ASE under optical excitation. Overall, such behavior results in a low η_p. This feature was also observed by Bisri *et al.* [36] for the emission from α,ϖ-bis(biphenylyl)terthiophene (BP3T) single crystal-based LE-OFETs. Interestingly, the emission from the BP3T single crystal-based LE-OFET exhibited spectral dependence on the drain current and was narrower at the edge of the single crystal under ambipolar operation (Figure 18.6),

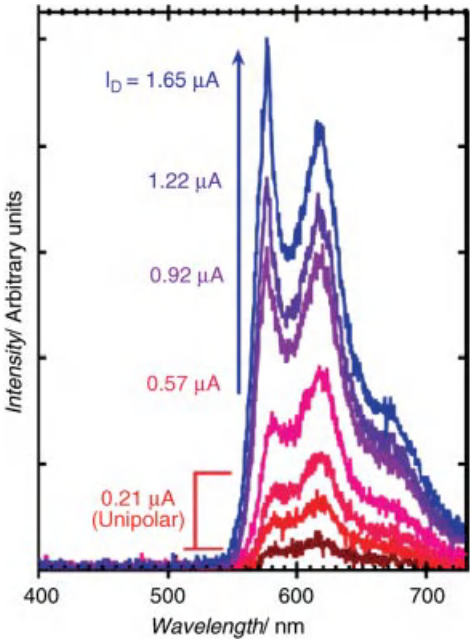

Figure 18.6 EL spectra from the edge of a BP3T single crystal-based ambipolar LE-OFET at various drain currents during a drain voltage sweep. From Ref. [36].

which raised expectations for the realization of an organic injection laser. However, as described by Samuel *et al.* [49], the threshold current ($\sim$229 A/cm^2) was an order of magnitude lower than that of optical excitation, so the mechanism of the dependence of the emission spectrum on the drain current remains unclear.

18.3.3
Tuning of Carrier Density by Interfacial Carrier Doping in Single Crystals of OPV Derivatives

In the previous section, the bright ambipolar characteristics of LE-OFETs based on highly luminescent unsubstituted OPV single crystals were introduced. However, the maximum current density in the ambipolar region still remains very low at $\sim$6 A/cm^2 assuming a carrier accumulation layer with a thickness of 10 nm, which is unacceptable for a current-driven organic laser.

Interfacial carrier doping of organic semiconductors is a possible solution to increase the current density and has been successfully demonstrated using not only organic electron-accepting materials such as tetracyanoquinodimethane [50] and tetrafluorotetracyanoquinodimethane [51] but also metal oxides such as molybdenum oxide (MoO_x) [52–54]. In particular, metal oxides such as vanadium oxide, tungsten oxide, and MoO_x are well known to act as efficient hole injection layers in OLEDs [55–57] and OFETs [58, 59]. Interfacial doping has been achieved electrochemically in a LE-OFET based on a tetracene film [60]. The polymer electrolyte, which induces a dipole layer between the organic and dielectric layers, resulted in a LE-OFET with a very low operating voltage. In this section, we start by discussing the effect of interfacial carrier doping on the characteristics of organic single crystal-based ambipolar LE-OFETs.

18.3.3.1 Interfacial Carrier Doping Based on Electron Transfer from an Organic Single Crystal into a MoO_x Layer

Figure 18.7 shows the typical current–voltage (I–V) characteristics of a P5V4 single crystal (donor)/MoO_x (2 nm, acceptor) bilayer and a P5V4 single crystal. A schematic illustration of the device structure used in this study is shown in the left-hand side inset of Figure 18.7. The P5V4 single crystal showed a very low current of less than 1×10^{-11} A at low voltage. In contrast, the current was 10^5 orders of magnitude higher for a P5V4 single-crystal/MoO_x bilayer even at low voltage.

The significant increase in the current is caused by the formation of P5V4 radical cations at the interface between the P5V4 single crystal and MoO_x layer, as evidenced by the observation of a new broad absorption peak at around 1350 nm in the 50 mol% MoO_x-doped P5V4 film (right-hand inset of Figure 18.7), which is very similar to the absorption spectrum of P5V4 radical cations reported by Spangler and Hall [61]. Therefore, holes are induced at the interface between the organic single crystal and MoO_x layer, which increases the hole current.

Here, we note that a significant increase in the current was also observed after deposition of a MoO_x layer with a thickness of 2 nm on the surface of not only other OPV derivatives but also on single crystals of rubrene and tetracene, as shown in

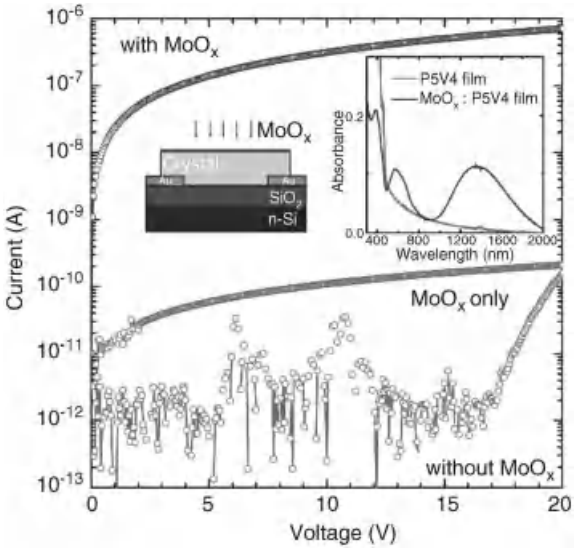

Figure 18.7 Typical *I–V* characteristics of a P5V4 single-crystal MoO_x layer and bilayer of P5V4/MoO_x. *Inset*: Schematic illustration of the (left) fabricated single-crystal device and (right) UV-Vis-NIR absorption spectra of a P5V4 film and MoO_x-doped P5V4 film. From Ref. [38].

Figure 18.8. However, the conductivities at the interface between the organic single crystals and MoO_x layer strongly depended on the highest occupied molecular orbital (HOMO) level of the donor molecules. In fact, because the energy level of MoO_x lies around -5.6 eV [52], the device based on a CH_3-P3V2 single crystal (HOMO level of -5.6 eV) showed a conductivity that was one order of magnitude higher ($\sim$0.01 S/cm) than that of a P3V2-based device (-5.82 eV, $\sim$0.002 S/cm) Nakanotani, H. and Adachi, C. (unpublished work), indicating the importance of the alignment of the energy levels between donor and acceptor materials.

18.3.3.2 Application of Interfacial Carrier Doping for Ambipolar LE-OFETs

The transfer characteristics of LE-OFETs based on P5V4 are shown in Figure 18.9. In contrast to the LE-OFET lacking a doping layer of MoO_x, the threshold voltage (V_{th}) for hole accumulation shifted considerably to more positive voltage from -80 ± 3 V to 2 ± 3V by inserting a 2 nm thick MoO_x layer at the interface between the P5V4 single crystal and Au layer, indicating that the hole injection barrier between Au and the organic interface was significantly reduced.

To estimate the effect of interfacial carrier doping on the current density at the recombination zone in the channel, we assumed that the thickness of the carrier accumulation layer was 10 nm, which corresponds to approximately three monolayers of P5V4 molecules along the long *c*-axis. Here, we explain why the current density was estimated at minimum drain current. Because the recombination zone should be centrally located between the source and drain electrodes at low voltage if the device has similar carrier mobilities, it allows us to neglect the propagation loss

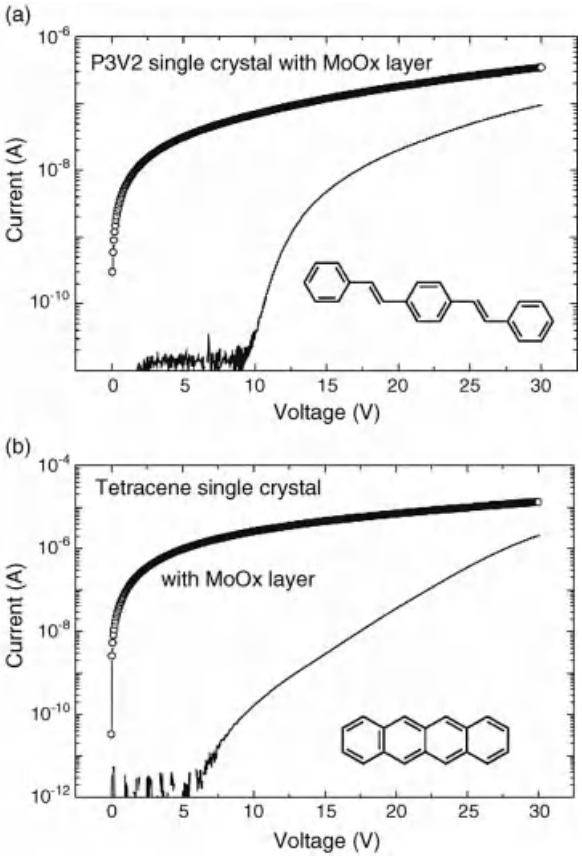

Figure 18.8 Typical *I–V* characteristics of (a) a P3V2 single crystal and bilayer of P3V2/MoO_x and (b) a tetracene single crystal and bilayer of tetracene/MoO_x.

of light from the metal electrodes. In particular, although the current density increases as the drain voltage increases (i.e., I_D–V_D sweep), the recombination zone should move from the center of the FET channel toward the metal electrode, allowing quenching by the metal electrodes. Thus, to achieve lasing oscillation from an ambipolar LE-OFET structure by charge-carrier injection, we have to discuss the current density–luminance characteristics in an ambipolar LE-OFET at low voltage.

The minimum current density in the LE-OFETs lacking a doping layer in the ambipolar region was only $\sim$2 A/cm^2, which is very low compared to those previously reported for ambipolar OFETs [32, 36]. This can be ascribed to the high V_{th} for hole accumulation, leading to a limitation of the hole current in the ambipolar region, that is, a small total current. However, a minimum current density of $\sim$100 A/cm^2, which is two orders of magnitude higher than that of the device lacking a carrier doping layer, was observed for the LE-OFET containing a MoO_x layer,

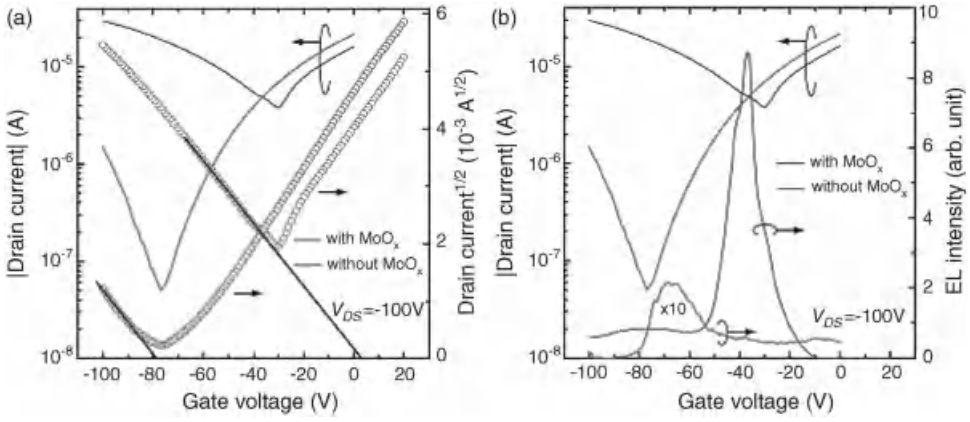

Figure 18.9 (a) Transfer characteristics and (b) dependence of EL intensity on gate voltage in FETs based on P5V4 single crystals with and without a MoO_x layer. From Ref. [38].

indicating that V_{th} for hole accumulation limited the total current under ambipolar operation. As a result, interfacial carrier doping can significantly reduce the driving voltage of ambipolar LE-OFETs based on single crystals of OPV derivatives and other materials such as rubrene.

18.3.3.3 Estimation of Singlet Exciton Density in the Recombination Zone

To realize an inverted population in an organic semiconductor, injection and transport of a very high current density, that is, the formation of an extremely high singlet exciton density, in organic semiconductors is required. The singlet exciton density was calculated using Eq. (18.1) [30]:

$$\sigma_{RZ} = \frac{I_{DS}}{qWW_{RZ}} \cdot \gamma_{ST} \cdot \Phi_{PL} \cdot \tau \tag{18.1}$$

where σ_{RZ} is the exciton density per unit area in the recombination zone, I_{DS} is the drain current, q is the elementary charge, W is the width of the transistor channel, W_{RZ} is the width of the recombination zone, γ_{ST} is the ratio of singlet excitons to the total amount of excitons, and τ is the exciton lifetime. The minimum singlet exciton density in the recombination zone of the LE-OFETs with and without a carrier doping layer in the ambipolar region was calculated to be $6 \times 10^8\,cm^{-2}$ and $1 \times 10^7\,cm^{-2}$, respectively, using $\Phi_{PL} = 40 \pm 2\%$ and $\tau = 2.4$ ns for the P5V4 single crystal, indicating that tuning of V_T increased the singlet exciton density in the recombination zone by more than one order of magnitude. Here, we also note that the maximum η_{ext} of the LE-OFETs both with and without a carrier doping layer was estimated to be ~0.1%, indicating the possibility of only a small contribution from exciton annihilation processes on η_{ext} in ambipolar LE-OFETs.

Here, we discuss the threshold singlet exciton density for ASE under electrical excitation. The singlet exciton density required for ASE under optical excitation was calculated using Eq. (18.2):

$$E_{\mathrm{th}} = n_{\mathrm{ex}} \cdot \frac{hc}{\lambda} \tag{18.2}$$

where h is the Planck constant, n_{ex} is the singlet exciton density, c is the speed of light, and λ is the excitation wavelength. The singlet exciton density was estimated to be $3.4 \times 10^{13}\,\mathrm{cm}^{-2}$, which corresponds to an ASE threshold of $E_{\mathrm{th}} = 20 \pm 4$ $\mu\mathrm{J/cm}^2$. This calculated exciton density is five orders of magnitude lower than the current threshold for lasing, and is caused by the very broad width of the recombination zone (about a few micrometers) in our ambipolar LE-OFETs. Kemerink *et al.* theoretically predicted the recombination width (W) in an ambipolar LE-OFET using Eq. (18.3) [62]:

$$W = \sqrt{4.34 d\delta/\beta} \tag{18.3}$$

where d and δ are the thickness of the gate dielectric and accumulation layer, respectively. β is defined as $\gamma = \beta\gamma_{\mathrm{L}}$, where γ_{L} is the Langevin recombination strength. In our OPV single crystal-based LE-OFET, W was calculated to be $\sim 0.11\,\mu\mathrm{m}$ using $d = 300\,\mathrm{nm}$, $\delta = 10\,\mathrm{nm}$, and $\beta = 1$. There is disagreement between the predicted value and the microscopic observation of W, which indicates that β is orders of magnitude lower than unity. Thus, further mechanisms to increase β in addition to the light confinement by cavity structures are required.

18.4 Summary and the Outlook for Future Organic Injection Lasers

As described in Sections 18.2 and 18.3, high-performance organic single crystal-based ambipolar LE-OFETs provide significant guidance for realizing high-performance organic light-emitting devices such as organic injection lasers. However, we are still far from achieving lasing with electrical pumping because we need to develop a novel device structure and further clarify the mechanisms of exciton formation and decay under electrical excitation. Proposed strategies to realize organic injection lasers are presented below.

i) **Dye-doped organic crystal-based LE-OFETs:** Although the carrier mobilities of organic single crystals are three orders of magnitude higher than those of amorphous organic semiconductors, the ASE thresholds of organic single crystals are only one order of magnitude lower than those of amorphous materials. One possible solution to lower the ASE threshold is doping organic crystals with dyes. Dye doping techniques have been widely applied in the field of organic light-emitting devices, allowing color tunability based on energy transfer from donor to acceptor molecules and improved Φ_{PL} and reduced ASE

threshold by minimizing intermolecular interactions, that is, concentration quenching of dye molecules.

Wang *et al.* recently reported the surprising PL characteristics of tetracene- and pentacene-doped OPV crystals and demonstrated ASE from the doped crystals [63]. Because single crystals of tetracene do not show ASE under optical excitation because of the presence of exciton–exciton annihilation [11], these results indicate that exciton–exciton annihilation can be significantly reduced by dye doping. We recently demonstrated that dye doping can be used for both emission color tuning and improving η_{ext} of organic crystal-based ambipolar LE-OFETs [64]. The doping of tetracene molecules into a host P3V2 crystal had almost no effect on the electron mobility, and the dominant carrier recombination process in the tetracene-doped P3V2 crystal involves direct carrier recombination on the tetracene molecules. We also believe that devices with a low ASE threshold and high ambipolar mobilities can be achieved by alignment of the energy levels of donor and acceptor molecules.

ii) **Formation of extremely high carrier and exciton densities:** As discussed in Section 3.3.3, we need to further reduce the width of the carrier recombination zone in the channel to form an extremely high exciton density in this region. The width of the carrier recombination zone is directly related to the Langevin recombination constant (K):

$$K = \frac{e(\mu_h + \mu_e)}{\varepsilon\varepsilon_0} \tag{18.4}$$

where e is the electronic charge, ε_0 is the permittivity of free space, and ε is the relative dielectric constant, when Langevin-type carrier recombination is assumed. Therefore, the injection of a high current density and confinement of excitons to a recombination zone can be achieved by improving the carrier mobilities of organic semiconductors. Carrier doping of organic semiconductors may be used to increase charge-carrier density, providing one possible solution. This was demonstrated in Section 18.3.3.1, where we demonstrated interfacial "hole" carrier doping based on electron transfer from an organic single crystal into a metal oxide layer. This technique significantly increases the concentration of free carriers in the organic semiconductor, resulting in the formation of a high exciton density. However, interfacial "electron" carrier doping of organic single crystals has not been demonstrated. Selection of appropriate acceptor and donor materials should allow the production of homojunction light-emitting devices based on organic single crystals. Another possibility is the realization of "bandlike" carrier transport in organic semiconductors while maintaining high Φ_{PL}. Once phonon scattering is effectively suppressed at low temperatures, high carrier mobilities can be easily achieved, as demonstrated in single crystals of naphthalene and perylene. Furthermore, by combining this technique with dye doping, the formation of an extremely high exciton density in the recombination zone should be achieved.

iii) **Effect of triplet excitons in the recombination zone:** Because strong triplet–triplet absorption by organic dye molecules readily inhibits light amplification

because of their long excited state lifetime, formation of triplet excitons under electrical excitation is a very serious problem. A possible solution is the use of an exciton decay process based on phosphorescence-sensitizing fluorescence [65]. Under electrical excitation, singlet and triplet excitons are formed in the ratio of 1 : 3 based on classical spin statistics. Efficient energy transfer from a donor triplet state to an acceptor singlet state should not only increase the number of singlet excitons under electrical excitation but must also suppress triplet–triplet absorption. However, light amplification through phosphorescence-sensitizing fluorescence has not been demonstrated to date. Another possibility is the use of a "triplet exciton scavenger." For example, 1,3,5,7-cyclooctatetraene (COT), which has large singlet–triplet splitting and a low-lying relaxed triplet state (0.8 eV) with a short triplet lifetime ($\sim$00 μs), is well known to be a very efficient scavenger of triplet excitons in liquid-state organic dye lasers. Recently, Schols *et al*. reported the efficient quenching of both phosphorescence and delayed fluorescence in a COT-doped poly(2,7-(9,9-bis(2-ethylhexyl))fluorene) thin film [66], indicating that triplet exciton scavengers are applicable even in solid-state thin films. We also need to optimize the driving method of the device, such as using short-pulse operation. By combining these techniques, the unwanted effects of triplet excitons in the recombination zone should be removed.

We believe that the recent development of bright organic single-crystal LE-OFETs lead not only to understanding the fundamental carrier transport properties and carrier recombination processes of organic semiconductors but also to make progress toward future organic injection lasers.

References

1 Adachi, C., Baldo, M.A., Thompson, M.E., and Forrest, S.R. (2001) *J. Appl. Phys.*, **90**, 5048.
2 Ikai, M., Tokito, S., Sakamoto, Y., Suzuki, T., and Taga, Y. (2001) *Appl. Phys. Lett.*, **79**, 156.
3 Cicoira, F. and Santato, C. (2007) *Adv. Funct. Mater.*, **17**, 3421.
4 Tessler, N., Denton, G.J., and Friend, R.H. (1996) *Nature*, **382**, 695.
5 Hide, F., Diaz-Garcőa, M.A., Schwartz, B.J., Andersonn, M.R., Pei, Q., and Heeger, A.J. (1996) *Science*, **273**, 1833.
6 Kozlov, V.G., Bulovic, V., Burrows, P.E., and Forrest, S.R. (1997) *Nature*, **398**, 362.
7 Pauchard, M., Swensen, J., Moses, D., Heeger, A.J., Perzon, E., and Andersson, M.R. (2003) *J. Appl. Phys.*, **94**, 3543.
8 Nakanotani, H., Oyamada, T., Kawamura, Y., Sasabe, H., and Adachi, C. (2005) *Jpn. J. Appl. Phys.*, **44**, 3659.
9 Tessler, N. (1999) *Adv. Mater.*, **11**, 363.
10 Baldo, M.A., Adachi, C., and Forrest, S.R. (2000) *Phys. Rev. B*, **62**, 10967.
11 Baldo, M.A., Holmes, R.J., and Forrest, S.R. (2002) *Phys. Rev. B*, **66**, 035321.
12 Nakanotani, H., Sasabe, H., and Adachi, C. (2005) *Appl. Phys. Lett.*, **86**, 213506.
13 Nakanotani, H., Sasabe, H., and Adachi, C. (2005) *Proc. SPIE*, **5937**, 59370W.
14 Kozlov, G., Bulovic, V., Burrows, P.E., Baldo, M., Khalfin, V.B., Parthasarathy, G., Forrest, S.R., You, Y., and Thompson, M.E. (1998) *J. Appl. Phys.*, **84**, 4096.
15 Yamamoto, H., Oyamada, T., Sasabe, H., and Adachi, C. (2004) *Appl. Phys. Lett.*, **84**, 1401.
16 Reufer, M., Feldmann, J., Rudati, P., Ruhl, A., Müller, D., Meerholz, K., Karnutsch, C., Gerken, M., and Lemmer, U. (2005) *Appl. Phys. Lett.*, **86**, 221102.

17 Görrn, P., Rabe, T., Riedl, T., Kowalsky, W., Galbrecht, F., and Scherf, U. (2006) *Appl. Phys. Lett.*, **89**, 161113.

18 Song, M.H., Kabra, D., Wenger, B., Friend, R.H., and Snaith, H.J. (2009) *Adv. Funct. Mater.*, **19**, 2130.

19 Kiguchi, M., Nakayama, M., Fujiwara, K., Ueno, K., Shimada, T., and Saiki, K. (2003) *Jpn. J. Appl. Phys.*, **42**, L1405.

20 Gwinner, M.C., Khodabakhsh, S., Song, M.H., Schweizer, H., Giessen, H., and Sirringhaus, H. (2009) *Adv. Funct. Mater.*, **19**, 1360.

21 McGehee, M.D. and Heeger, A.J. (2000) *Adv. Mater.*, **12**, 1655.

22 Rabe, T., Hoping, M., Schneider, D., Becker, E., Johannes, H.-H., Kowalsky, W., Weimann, T., Wang, J., Hinze, P., Nehls, B.S., Scherf, U., Farrell, T., and Riedl, T. (2005) *Adv. Funct. Mater.*, **15**, 1188.

23 Turnbull, G.A., Andrew, P., Barnes, W.L., and Samuel, I.D.W. (2006) *Appl. Phys. Lett.*, **89**, 161113.

24 Ribierre, J.C., Tsiminis, G., Richardson, S., Turnbull, G.A., Samuel, I.D.W., Barcena, H.S., and Burn, P.L. (2007) *Appl. Phys. Lett.*, **91**, 081108.

25 Swensen, J.S., Soci, C., and Heeger, A.J. (2005) *Appl. Phys. Lett.*, **87**, 253511.

26 Zaumseil, J., Friend, R.H., and Sirringhaus, H. (2006) *Nat. Mater.*, **5**, 69.

27 Zaumseil, J., Donley, C.L., Kim, J.-S., Friend, R.H., and Sirringhaus, H. (2006) *Adv. Mater.*, **18**, 2708.

28 Zaumseil, J., McNeill, C.R., Bird, M., Smith, D.L., Ruden, P.P., Roberts, M., McKiernan, M.J., Friend, R.H., and Sirringhaus, H. (2008) *J. Appl. Phys.*, **103**, 064517.

29 Bürgi, L., Turbiez, M., Pfeiffer, R., Bienewald, F., Kirner, H.J., and Winnewisser, C. (2008) *Adv. Mater.*, **20**, 2217.

30 Naber, R.C.G., Bird, M., and Sirringhaus, H. (2008) *Appl. Phys. Lett.*, **93**, 023301.

31 Takahashi, T., Takenobu, T., Takeya, J., and Iwasa, Y. (2007) *Adv. Funct. Mater.*, **17**, 1623.

32 Takenobu, T., Bisri, S.Z., Takahashi, T., Yahiro, M., Adachi, C., and Iwasa, Y. (2008) *Phys. Rev. Lett.*, **100**, 066601.

33 De Boer, R.W.I., Gershenson, M.E., Morpurgo, A.F., and Podzorov, V. (2004) *Phys. Status Solidi A*, **201**, 1302.

34 Bisri, S.Z., Takahashi, T., Takenobu, T., Yahiro, M., Adachi, C., and Iwasa, Y. (2007) *Jpn. J. Appl. Phys.*, **46**, L596.

35 Nakanotani, H., Kabe, R., Yahiro, M., Takenobu, T., Iwasa, Y., and Adachi, C. (2008) *Appl. Phys. Express*, **1**, 091801.

36 Bisri, S.Z., Takenobu, T., Yomogida, Y., Shimotani, H., Yamao, T., Hotta, S., and Iwasa, Y. (2009) *Adv. Funct. Mater.*, **19**, 1728.

37 Nakanotani, H., Saito, M., Nakamura, H., and Adachi, C. (2009) *Appl. Phys. Lett.*, **95**, 033308.

38 Nakanotani, H., Saito, M., Nakamura, H., and Adachi, C. (2009) *Appl. Phys. Lett.*, **95**, 103307.

39 Stalmach, U., Detert, H., Meier, H., Gebhardt, V., Haarer, D., Bacher, A., and Schmidt, H.-W. (1998) *Opt. Mater.*, **77**, 98.

40 He, F., Xu, H., Yang, B., Duan, Y., Tian, L.L., Huang, K.K., Ma, Y.G., Liu, S.Y., Feng, S.H., and Shen, J.C. (2005) *Adv. Mater.*, **17**, 2710.

41 Yasuda, T., Saito, M., Nakamura, H., and Tsutsui, T. (2006) *Jpn. J. Appl. Phys.*, **45**, L313.

42 Yasuda, T., Saito, M., Nakamura, H., and Tsutsui, T. (2008) *Chem. Phys. Lett.*, **452**, 110.

43 Nagawa, M., Hibino, R., Hotta, S., Yanagi, H., Ichikawa, M., Koyama, T., and Taniguchi, Y. (2002) *Appl. Phys. Lett.*, **80**, 544.

44 Ichikawa, M., Nakamura, K., Inoue, M., Mishima, H., Haritani, T., Hibino, R., Koyama, T., and Taniguchi, Y. (2005) *Appl. Phys. Lett.*, **87**, 221113.

45 Kabe, R., Nakanotani, H., Sakanoue, T., Yahiro, M., and Adachi, C. (2009) *Adv. Mater.*, **21**, 4034.

46 Chua, L.-L., Zaumseil, J., Chang, J.-F., Ou, E.C.-W., Ho, P.K.-H., Sirringhaus, H., and Friend, R.H. (2005) *Nature*, **434**, 194.

47 Takenobu, T., Watanabe, K., Yomogida, Y., Shimotani, H., and Iwasa, Y. (2008) *Appl. Phys. Lett.*, **93**, 073301.

48 Oyamada, T., Sasabe, H., Adachi, C., Okuyama, S., Shimoji, N., and Matsushige, K. (2005) *Appl. Phys. Lett.*, **86**, 093505.

49 Samuel, I.D.W., Namdas, E.B., and Turnbull, G.A. (2009) *Nat. Photonics*, **3**, 546.

50 Alves, H., Molinari, A.S., Xie, H., and Morpurgo, A.F. (2008) *Nat. Mater.*, **7**, 574.

51 Abe, Y., Hasegawa, T., Takahashi, Y., Yamada, T., and Tokura, Y. (2005) *Appl. Phys. Lett.*, **87**, 153506.

52 Matsushima, T. and Adachi, C. (2008) *J. Appl. Phys.*, **103**, 034501.

53 Shin, W.-J., Lee, J.-Y., Kim, J.C., Yoon, T.-H., Kim, T.-S., and Song, O.-K. (2008) *Org. Electron.*, **9**, 333.

54 Matsushima, T., Jin, G.-H., and Murata, H. (2008) *J. Appl. Phys.*, **104**, 054501.

55 Tokito, S., Noda, K., and Taga, Y. (1996) *J. Phys. D*, **29**, 2750.

56 Reynolds, K.J., Barker, J.A., Greenham, N. C., Friend, R.H., and Frey, G.L. (2002) *J. Appl. Phys.*, **92**, 7556.

57 Matsushima, T., Kinoshita, Y., and Murata, H. (2007) *Appl. Phys. Lett.*, **91**, 253504.

58 Chu, C.W., Li, S.H., Chen, C.W., Shrotriya, V., and Yang, Y. (2005) *Appl. Phys. Lett.*, **87**, 193508.

59 Kumaki, D., Umeda, T., and Tokito, S. (2008) *Appl. Phys. Lett.*, **92**, 013301.

60 Hepp, A., Heil, H., Schmechel, R., and von Seggern, H. (2005) *Adv. Eng. Mater.*, **7**, 957.

61 Spangler, C.W. and Hall, T.J. (1991) *Synth. Met.*, **44**, 85.

62 Kemerink, M., Charrier, D.S.H., Smits, E. C.P., Mathijssen, S.G.J., de Leeuw, D.M., and Janssen, R.A.J. (2008) *Appl. Phys. Lett.*, **93**, 033312.

63 Wang, H., Li, F., Gao, B., Xie, Z., Liu, S., Wang, C., Hu, D., Shen, F., Xu, Y., Shang, H., Chen, Q., Ma, Y., and Sun, H. (2009) *Cryst. Growth Des.*, **9**4945.

64 Nakanotani, H., Saito, M., and Nakamura, H., and Adachi, C. (2010) *Adv. Funct. Mater.*, **20** (10)., 1610–1615.

65 Baldo, M.A., Thompson, M.E., and Forrest, S.R. (2000) *Nature*, **403**, 750.

66 Schols, S., Kadashchuk, A., Heremans, P., Helfet, A., and Scherf, U. (2009) *ChemPhysChem*, **10**, 1071.

Index

Physics of Organic Semiconductors, Second Edition. Edited by Wolfgang Brütting and Chihaya Adachi